ETH zürich

17th Biennial SGA Meeting

ETH Zurich, Switzerland

August 28 – September 1

Proceedings Volume 3

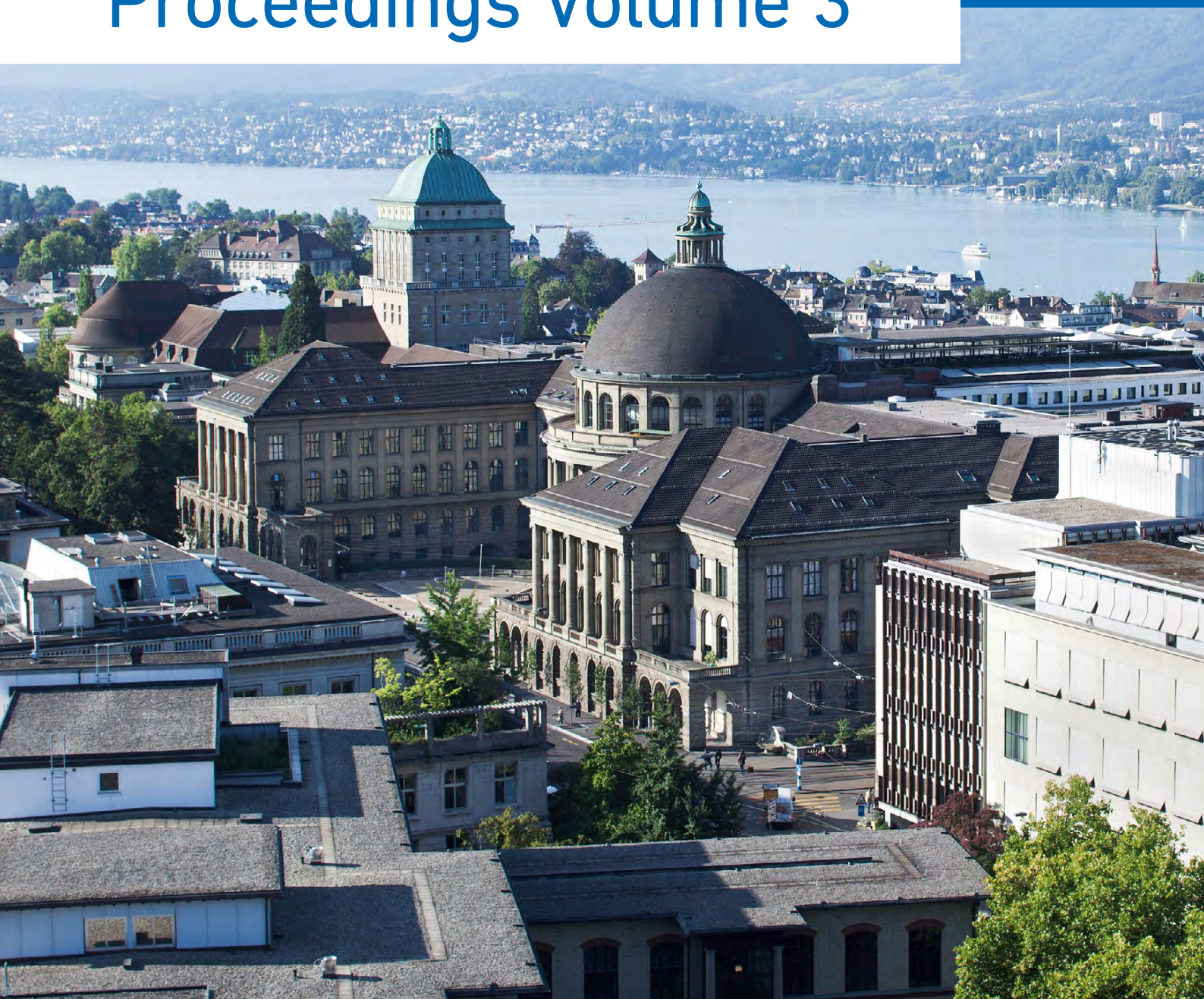

ISBN 978-2-8399-4046-7

The theme for this 17th edition is "Mineral Resources in a Changing World"

Suggested citation for the entire proceedings:

Proceedings of the 17th SGA Biennial Meeting, 28 August – 1 September 2023, Zurich, Switzerland, 1182 pages.

Suggested citation for an individual paper:

Carcamo-Valencia IC, Torró L, Proenza JA, Ramírez-Briones JS, Ayala L, Viveen W, Aiglsperger T, Baby P (2023) Cobalt-rich manganese nodules in Pliocene marine deposits of the onshore forearc Pisco Basin, Peru. In: Proceedings of the 17th SGA Biennial Meeting, 28 August – 1 September 2023, 2:280–283.

Volume 1

Porphyry-type and skarn deposits

Geothermal systems and epithermal ore deposits

Hydrothermal mineralization associated with highly fractionated magmas (e.g., Li, Be, Sn, W, Nb, Ta)

IOCG and magnetite-apatite deposits

Volume 2

VMS and seafloor mineralization

Gold: a journey from sources to precipitation sites and processes

Metallogenesis in sedimentary basins

Supergene ore forming processes

Volume 3

Critical minerals and geo-inspired technologies for a carbon-neutral future

Mineral deposits related to mafic-ultramafic intrusions

Ore genesis associated with alkaline-carbonatite systems

Advances in analytical techniques applied for ore deposits research and mineral exploration

New sensing instruments and processing methods in mineral exploration

Machine learning, data mining and new target generation in mineral exploration

This publication cannot be reproduced in whole or in part without the permission of The Society for Geology Applied to Mineral Deposits (SGA).

A digital version of this Proceedings is available from the SGA website www.e-sga.org

Welcome to SGA2023,
Welcome to Zürich,

Mineral Resources in a Changing World. In the context of an undeniable and threatening climate change, a suite of financial crisis, global sanitary challenges, and geopolitical tensions have stamped in a snowball effect the start of the XXIst century. Yet, we contend that an optimistic and united approach to lead the "Green New Deal" is possible. Thus, we have prepared a conference program comprising (1) the presentation of the latest findings in ore deposit and critical material research, (2) invited talks by plenary speakers to bring concrete insights and inspiring solutions for the challenges our economies need to face and solve in our acute awareness of climate change mitigation, and a reasoned exploitation of resources with optimal management of the environment, and (3) lively and enthusiastic scientific and social exchange between all participants from early-career researchers and students to high-ranking industry delegates and government agency representatives.

We wish you an instructive and rewarding 17th Biennial Meeting of the SGA.

Your Local Organizing Committee

Conference Chairs	Cyril Chelle-Michou (ETH Zurich, Switzerland)
	Nicolas J. Saintilan (ETH Zurich, Switzerland)
Scientific Program Chairs	Massimo Chiaradia (University of Geneva, Switzerland)
	Zoltán Zajacz (University of Geneva, Switzerland)
Field trip Chairs	David Dolejš (University of Freiburg, Germany)
	Jochen Kolb (Karlsruhe Institute of Technology, Germany)
Short Course Chair	Kalin Kouzmanov (University of Geneva, Switzerland)

ETH zürich

UNIVERSITÉ DE GENÈVE

KIT Karlsruher Institut für Technologie

UNI FREIBURG

Preface

With its load of unexplored mineral deposits, Switzerland has no metal mining activity. Yet, it is a country at the heart of the mineral resource industry. Indeed, Switzerland focuses a third of the world metal trading and two thirds of the world gold refinement. It is also in Switzerland that the SGA was legally incorporated back in 1971. Fifty-two years later, the SGA was back in Switzerland with the first SGA Biennial meeting of the post-COVID era, hosted at ETH Zurich between August 28 and September 1 2023. The world SGA community, with over 430 international delegates from 58 countries, gathered in Zurich to share knowledge and understanding of how mineral resources formed in Earth history, and how they may be discovered and exploited in a virtuous manner towards the environment and local communities. Our delegates include students (40%), academics (37%), industry (18%), and government (5%) representative from all regions of the planet.

The conference featured a four-day program with five plenary sessions, up to four concurrent technical sessions and one poster session on display over three full days. The scientific program comprised 21 keynote presentations, 169 regular oral presentations (including 72 students) and 135 posters (including 55 students). The important student contribution was and will remain a highlight of the 17th SGA Biennial meeting. It shows how dynamic our community is with a clear vision into the future of the world supply of metal and study of mineral deposits in a context of unprecedented challenges, yet riddled with what should also be seen as optimistic opportunities to be grasped.

SGA Zurich 2023 would not have been possible without the dedication of the local organizing committee, the ETH event team, Symporg and the strong support from our local and international sponsors. We are deeply indebted to the presenters and their co-authors for their contributions, and the session convenors for organizing and running their session, and for reviewing their session papers.

We are delighted to present you the Proceedings of the 17th SGA Biennial Meeting. With this edition, the SGA council decided to come back exclusively to the 4-page-long peer-reviewed short papers, which has been the distinct signature of the SGA meetings. The Proceedings is made up of three volumes totaling almost 1200 pages and includes 309 short papers.

Cyril Chelle-Michou
Nicolas Saintilan
Conference Chairs

Sponsors

Patron Sponsor

BHP

Student Patron Sponsor

GLENCORE

Gold Sponsor

Swiss National Science Foundation

Zürich, Switzerland.

Silver Sponsor

NEW BOLIDEN

PAN AMERICAN SILVER

Teck

Bronze Sponsor

RoyalRoad

FIRST QUANTUM MINERALS LTD.

We thank all convenors of SGA 2023

Session 1a. Porphyry-type and skarn deposits
Andreas Audétat, Bayerisches Geoinstitut, Germany
Bertrand Rottier, Université Laval, Canada

Session 1b. Geothermal systems and epithermal ore deposits
Isabelle Chambefort, GNS Science, New Zealand
Thomas Driesner, ETH Zurich, Switzerland

Session 1c. Hydrothermal mineralization associated with highly fractionated magmas (e.g., Li, Be, Sn, W, Nb, Ta)
Matthieu Harlaux, BRGM, France
Hélène Legros, University of Alberta, Canada
Mathias Burisch, Colorado School of Mines, USA
Celestine Mercer, USGS, USA

Session 1d. IOCG and magnetite-apatite deposits
Adam Simon, University of Michigan, USA
Tobias Schlegel, CSIRO Mineral Resources, Australia
Irene del Real, Universidad Austral de Chile, Chile

Session 2. VMS and seafloor mineralization
Clifford Patten, Karlsruhe Institute of Technology, Germany
Ana Patrícia Jesus, Universidade de Lisboa, Portugal
Rémi Coltat, Instituto Andaluz De Ciencias De La Tierra, Spain
Melissa Anderson, University of Toronto, Canada

Session 3. Gold: a journey from sources to precipitation sites and processes
Georges Beaudoin, Université Laval, Canada
Steffen Hagemann, CET - University of Western Australia, Australia
Crystal LaFlamme, Université Laval, Canada

Session 4a. Metallogenesis in sedimentary basins
Philippe Muchez, KU Leuven, Belgium
Garth Graham, USGS, USA
Sam Spinks, Teck Resources, Australia

Session 4b. Supergene ore forming processes
Nicola Mondillo, Università degli Studi di Napoli Federico II, Italy
Cristina Villanova-de-Benavent, Universitat De Barcelona, Spain

Session 5. Critical minerals and geo-inspired technologies for a carbon-neutral future
Alexander Gysi, New Mexico Institute of Mining and Technology, USA
Katharina Pfaff, Colorado School of Mines, USA
Daniel Harlov, Deutsches GeoForschungsZentrum GFZ, Germany

Session 6a. Mineral deposits related to mafic-ultramafic intrusions
Eduardo Mansur, Geological Survey of Norway, Norway
Giada Iacono-Marziano, CNRS-ISTO, France
William Smith, Carleton University, Canada

Session 6b. Ore genesis associated with alkaline-carbonatite systems
Sophie Decrée, Royal Belgian Institute of Natural Sciences, Belgium
Francesco Stoppa, Università Gabriele d'Annunzio, Italy
Benjamin Walter, Karlsruhe Institute of Technology, Germany

Session 7a. Advances in analytical techniques applied for ore deposits research and mineral exploration
Marco Fiorentini, CET - University of Western Australia, Australia
Amanda Stoltze, Ivanhoe Mines Exploration, DRC

Session 7b. New sensing instruments and processing methods in mineral exploration
Doug Schouten, Ideon Technologies, Inc., Canada
Glenn Chubak, Dias Geophysical, Canada
Thibaut Astic, KoBold Metals, Canada

Session 7c. Machine learning, data mining and new target generation in mineral exploration
Daniel Gregory, University of Toronto, Canada
Chetan Nathwani, ETH Zurich, Switzerland
Francisca Maepa, BHP, Canada

Critical minerals and geo-inspired technologies for a carbon-neutral future

Critical cobalt and where to find it: distribution of cobalt in the Dolostone Ore Formation deposit, Namibia 1
V. Bertrandsson Erlandsson, R. Ellmies, P. Gopon, H. Waldl, D. Misch, F. Melcher

Geostatistical and geometallurgical investigation of Co in the Rocklands tailings deposit, Queensland, Australia 5
R. Blannin, L. Jackson, A. Parbhakar-Fox

Copper in Onshore New Zealand: Mineral Deposit Types, Occurrences and Potential for this Critical Metal 9
T. Christie

New paradigms on phosphate mining in the Colombian industry: Crystallochemistry and geochemistry of phosphorites from the Lidita Superior Formation, Colombia 13
J. Felipe Correa Briceño, J. Felipe Galán Palacios, T. Cramer

Fluid inclusions host germanium in acicular sphalerite from the carbonate-hosted Zhulingou Pb-Zn deposit, South China 17
A. Cugerone, K. Luo, D. Fougerouse, J-X Zhou, V. Motto-Ros

Critical raw material potential of the North Pennine Orefield, England 21
D. Currie, E. Deady, A. Lacinska, K. Goodenough

Towards a better understanding of a Co-rich hydrothermal system: Punta Corna (Western Alps, Italy) 25
G. Domenighini, L. Santoro, M. Moroni

A lithological context for stratabound REE mineralisation at the birthplace of REEs – Bastnäs, Riddarhyttan, Sweden 29
R. Dunst, I. Pitcairn, H. Raat, N. F Jansson, A. Karlsson

Genesis, Sedimentology, and Geochemical Features of Phosphorite Deposit in Colombia and his content on Rare Earth Elements 33
J. F. Galan Palacios, J. F. Correa Briceño

The Circular Economy Challenge: Re-use of processing granite wastes for REEs-recovery: preliminary results. 37
S. Gioiello, L. Santoro, A. Cazzaniga

The world-class Schlema-Alberoda U-(Ag-Co-Ni) deposit (Germany): mineralogy and fluid characteristics 41
M. Guilcher, J. Gutzmer, A. Hiller, J. Krause, N. Blamey, B. Härtel, M. Burisch

The MINES thermodynamic database for simulating the hydrothermal mobilization of REE in critical mineral deposits 45
A. P. Gysi

A green future from a contentious past: Gold and critical metals in a historic arsenic mining district Strassegg (Styria) 49
J. Mareen Hiller, V. Bertrandsson Erlandsson, C. Mottram, P. Gopon

Critical Minerals Potential of Armenia: An Overview for Future Exploration 52
S. Hovakimyan, R. Moritz, M. Harutunyan, K. Hambaryan, K. Charatanyan

Environmentally sustainable production of critical metals: a Tasmanian approach 56
J. Hunt, M. Roach, L. Zhang, S. Fraser, Y. Cajal, M. Fathi, W. Hong, O. Missen, D. Cooke

Potential for sulfide-hosted by-products from the iron oxide-apatite deposits at Kiruna? A mineralogical perspective 60
P. Krolop, U. Andersson, K. McFall, J. Kalmbach, S. Gilbricht, T. Seifert

Geochemical trends of lithium-bearing minerals in LCT-pegmatites in Central Namibia 64
N. Kropp, G. Borg

Can the mining industry meet global demand for critical minerals? 67
J. L. Mauk, J. A. Funk, N. A. Karl

Exploration of indium in sulfidic mine waste and acid mine drainage environments 71
O. Mejías, L. Jackson, A. Parbhakar-Fox

Tracking cobalt deportment from primary ore to copper tailings and determining reprocessing potential
L. Nicholls, E. Wightman, C. Evans, L. Casey, A. Parbhakar-Fox

Invisible metals for a green future: Au associated critical elements in historic mining districts Murtal (Styria) 79
S. Niederl, V. Bertrandsson Erlandsson, P. Felfer, P. Gopon

Comparison of the Wilson and Ivan monazite-bearing high-grade mineralization at Alces Lake, SK (Canada): Mineralogy, composition, and U-Pb chemical ages 81
K. Poliakovska, I. R. Annesley, O. Ivanik, K. Branning

Forensic geometallurgy of Ni-Co laterites: Sustainable processing of Europe's low-grade ores and tailings into battery-grade metals 85
F. Prado Araujo, P. Muchez, J. Andersen, N. Magalhães, R. Crane, H. Hughes

A mineralogical characterization of an antimony tailings dam: Implications for antimony recovery. 88
R. Ravele, K. Viljoen, D. Rose

Distribution of critical elements in rocks and fluids, Taupo Volcanic Zone, New Zealand 92
A. Reyes

Ni-Co-As-Bi minerals in the Silius vein system, (SE Sardinia, Italy): The polymetallic evolution of a word-class fluorspar deposit 96
I. Scano, A. Attardi, F. Cocco, D. Fancello, A. Murroni, F. Zara, S. Naitza

Critical Metal Resources Required for the Green Energy Transition 100
A. Simon, L. Cathles

Hyperspectral cathodoluminescence of REE-bearing agpaitic minerals from Pajarita Mountain, USA 103
P. Slezak, S. Simonsen, F. Wilke, D. Chew, R. Wendlandt, M. Berger, M. Hitzman

The typology of Czech graphite raw materials 107
M. Poňavič, F. Pticen, B. Kříbek, A. Vymazalova

The Northern Copper Belt—a chance for a new giant copper district in Poland 110
K. Zieliński, S. Speczik

Mineral deposits related to mafic-ultramafic intrusions

Geochemical thresholds for vanadium throughout Korea and at potential development sites 114
J. Sung Ahn, S-J Youm, Y-C Cho

Reassessing the source controls of Ni sulfide mineral systems 118
D. Blanks, D. Holwell, M. Fiorentini, I. Ezad, J. Bennett, S. Foley, W. Gorczyk, N. Januszczak, L. Hart-Madigan, S. Rennick

Mafic magmatism in the Central Iberian Zone: Towards a better understanding of Sb mineralization? 121
H. R. Campos Rodríguez, E. Gloaguen, A. Pochon, J. Tuduri, S. Sizaret, P. Higueras, G. Iacono-Marziano, S. Lorenzo, J. María Esbrí Víctor, M. Poujol, V. Mollé

On the origin of volatile-rich minerals associated with magmatic sulfides 125
M. Cherdantseva, M. Fiorentini, C. Fisher, L. Martin, M. Aleshin

Role of carbon in the formation of Ni-Cu-PGE mineralization in the Valmaggia ultramafic pipe: Insights from laser-ablation-time-of-flight ICP-MS 129
S. Clark, M. Locmelis, D. Savard, M. Moroni, M. Fiorentini

Ni-Cu-Co-Bi mineralization in Valea Muntelui ultramafic complex (Cindrel Mountains, Romania) 133
G. Dincă, G. Săbău, A. Filiuță

Magmatic sulphide mineralization and prospectivity in the Tantalite Valley Complex, Namibia 137
D. Ferreira, B. Von Der Heyden, M. Klausen, L. Martin

A new look to the high-PGE chromitites from the Cabo Ortegal Complex (NW Spain) 141
M. García-Tudela, J. Proenza, J. Farré-de-Pablo, T. Aiglsperger, N. Pujol-Solà, J. M. González-Jiménez

Characterization of the UG2 Reef split-facies types, Eastern Bushveld Complex, South Africa: A mineralogical perspective 145
C. Hlongwani, K. S. Viljoen, D. H. Rose, L. C. Blignaut

Towards a genetic model for the unusual Cu-Au-Te(-PGE) sulfide and Ni sulfide deposits of the Curaçá Valley, Brazil 149
D. Holwell, D. Blanks, J. Thompson, F. Tomazoni, F. Porto, A. Lima, R. D'Altro, P. Graia, T. Sant'Ana, E. Oliviera

The importance of volatiles in the formation of magmatic sulphide ore deposits: experimental constraints 152
G. Iacono Marziano, M. Le Vaillant, S. J. Barnes

Cobalt–nickel–copper arsenide, sulfarsenide and sulfide of Bou Azzer (Anti-Atlas – Morocco): Lithological and structural control 155
M. Jabbour, Z. ELOuad, M. Ezzghoudi, M. Souhassou, Y. Moundi, N. Saintilan, S. Ilmen, A. Bajjaddi, L. Maacha, F. Haissen, M. Zouhair, M. Ikenne

Prospects on platinoids of the mafic-ultramafic belt of the Sultanuvais mountains (UZBEKISTAN) 159
N. Jurabekov, A. Khaydarova, R. Khalmatov, A. Kholikov

Insights into genesis of Pt-Fe minerals, laurite and kashinite from clinopyroxenite-dunite massifs: evidence from compositional and Cu-S isotope data 163
H. Kreshimir Malich, I. Badanina, N. Soloshenko, S. Votyakov, T. Velivetskaya, A. Ignatiev

The Ni-Cu-Co mineralisation of the Espedalen Complex, southern Norway: constraints for the distribution of magmatic sulphides within an anorthosite intrusion 167
E. Mansur, T. Slagstad, J. Sverre Sandstad, S. Dare

Ni-Cu Sulphidic deposits in Sweden - general characteristics, genetic aspects, and economic potential 171
O. Martinsson

Post-volcanic modification of komatiite associated nickel sulfide mineralization: A case study of the Cassini deposit, Yilgarn Craton 175
H. McFarlane, M. Le Vaillant, S. Barnes, S. Hu

Mineralogical study of Co-Ni-As of the F53 vein deposit of the Aït Ahmane area (Bou Azzer-El Graara inlier, Morocco) 179
M. Ez-zghoudy, M. Ikenne, M. Souhassou, S. Ilmen, I. R. Prokopyev, Z. Hajjar, M. Ousbih, F. Askour, L. Maacha, M. Zouhair

Mineralogical distribution of platinum-group elements (PGE) in the UG2 and Merensky Reefs at the Kalkfontein farm, Bushveld Igneous Complex 183
A. Nailana, N. Q. Hammond

Mineralogical constraints and evidence for crustal interaction in the Ni-rich systems of the Curaçá Valley mineral district, Bahia, Brazil. 187
T. Nunes, G. Olivo, J. Thompson, F. Porto, A. Lima, P. Graia

Chemistry of major sulfides from Ni-Cu (PGE) mineralization at the Ransko ore district (Bohemian Massif): A result from LA-ICPMS study 191
J. Pasava, I. Andronikova, V. Wertich, L. Ackerman, P. Rambousek, O. Pour, K. Malý

Ilmenite-hosted fluid inclusions: Snapshot of magmatic fluid chemistry in mafic rocks 196
A. Pochon, D. J. Kontak, E. Gloaguen, J. Tuduri, G. Iacono-Marziano, H. Campos Rodriguez, V. Mollé, T. Chatelin

Magnetite composition as petrogenetic and fertility indicator for Fe-Ti-V-(P) mineralization in Archean mafic-ultramafic intrusions within the Superior Province, Canada 200
A-A Sappin, M. G. Houlé

Crustal S sources for komatiite hosted Ni deposits and implications for sulfide transport and deposition 204
A. Brandt Virnes, M. Fiorentini, S. Caruso, K. Baublys, Q. Masurel, N. Thebaud

Magmatic Black Shale Assimilation and the Formation of Sulphide Deposits – Perspectives from Experiments and Thermodynamic Simulations 208
V. J Virtanen

Solubility of selected elements in the synthetic analogue of kotulskite (PdTe) 212
A. Vymazalova, F. Laufek, M. Tuhý, J. Kamenský

Ore genesis associated with alkaline-carbonatite systems

Mineralogical and geochemical insights of Fe-Ti-P-REE mineralization in alkaline igneous complexes: example from the Kodal deposit, Oslo Rift, Norway 215
P. Buelens, V. Debaille, S. Decrée, N. Coint

Magmatic and hydrothermal processes in a carbonatite-related REE mineralization system: insights from the Maoniuping deposit, southwestern China 219
Z. Chi, P. Ni, J. Pan, Z. Hou, D. Szymanowsk, C. Chelle-Michou

Dating multi-stage REE mineralization in Canada: the example of Thor Lake and Saint Honoré deposits 223
H. Legros, G. Pearson, S. Dare, P. Bédard

Stable isotope constraints on the source of ore fluids for the Hicks Dome REE+Y-HFSE-fluorspar deposit 225
J. McIntosh, C. Johnson, A. Andersen, A. Hofstra

Iron-Ti oxide and apatite mineralisation associated with alkaline monzonitic rocks: An example from the Kodal deposit, Permian Oslo Rift, Norway 229
A. C. Miranda, N. Coint, S. Dare, E. Mansur

Fengchengite from Sierra La Vasca Complex, Mexico 233
M. Grazia Perna, A. Rodriguez Vega, E. Humpreys-Williams, F. Nestola, C. Biagioni, F. Stoppa, G. Rosatelli

The Mount Weld rare earth element deposit, Western Australia: a carbonatite-derived laterite 236
P. Verplanck, H. Lowers, A. Boehlke, J. Thompson, G. Bhat, C. Mercer

Advances in analytical techniques applied for ore deposits research and mineral exploration

Delineating the sulfur isotope signature of a VMS district by LA-ICP-QQQ-MS 240
G. Barré, C. Laflamme

Application of Next Generation Technology in Undercover Exploration 244
N. Brand, D. Crook

Cassiterite: the zircon of mineral systems 247
P. Carr, D. Szymanowski, L. Tavazzani, B. Pulitz, T. Vennemann, C. Chelle-Michou, Q. Charbonnier, Z. Galazka, J. Mercadier

Zircon and whole-rock geochemical fertility tools applied to porphyry copper deposits: Case study, Chachimbiro Volcanic Complex and Cerro Tolondro, Ecuador 251
F. Del Rio, M. Chiaradia, H. Carrasco, A. Ulyanov, A. Aguilar, S. Cubelli, C. Rodríguez, C. Urrutia

Identification and characterization of indicator minerals using µ-XRF 255
L. Géring, A. Nadeau, G. Beaudoin, C. Guilmette

Compositional variations of olivine in kimberlites: A new tool for diamond exploration 259
A. Giuliani, D. Phillips, G. Pearson, S. Sarkar, Y. Weiss, R. Preston, M. Seller, Z. Spetius

In-situ Rb-Sr dating of mica: method refinement and application to mineral resources 262
A. Giuliani, M. Guillong, S. Oesch, R. Maas, G. H. Howarth, M. L. Fiorentini

Standardized and Automated 3D Mineralogy of Ores 265
J. Godinho

How trace elements are incorporated into pyrite, a view from mm- to nano-scale 268
D. Gregory, A. Chappaz, S. Taylor, D. Perea, L. Kovarik, J. Cliff

Mineralization age of the Kar'ernoe ore occurrence, Polar Urals revealed by the U-Th/He dating of pyrite 271
E. Ivanova, O. Yakubovich, M. Anosova, E. Tuykova, I. Sobolev

Hyperspectral mineral mapping on exploration core from the Au-rich from LaRonde Penna VMS deposit, Quebec, Canada in the shortwave infrared.....275
F. Körting, J. Hernandez, P. Koirala, M. Lehman, T. Monecke, D. Lindblom, O. Jonsson, C. Hildebrand

Characterisation of apatite-bearing magnetite ore in drillcores using µ-XRF 279
C. Månbro, J. Kolodziejczyk, P. Krolop, E. Öberg, M. Parian

Continuous X-Ray Fluorescence Core Scanning: Application Examples and Methodology Developments.....284
M. Lehman, T. Monecke, E. Tharalson, A. Tod, A. Lundström, A. Seyfarth, S. Stolze, K. Pfaff

XRD clustering and quantitative analysis as a fingerprinting technique to study ore deposits 288
S. Makvandi, J. Cauzid, A. Tarantola, V. Melfos, P. Voudouris

Integrated analysis of the Consorcio prospect in Cunas emerald mine (Colombia), tool to determine mineralization stages and related by-products 292
A. S. Martín-Ravelo

LA-ICP-MS trace element composition of stibnite from the Kizhnica-Hajvalia-Badovc ore field, Kosovo.....296
S. Mederski, J. Pršek, K. Kluza, D. Dimitrova

Rapid and on-site elemental quantitative analyses using handheld LIBS: the Beauvoir granite case study 300
N. Mezoued, C. Fabre, J. Cauzid, M. Cathelineau, C. Ballouard

Pyrite analysis enhanced by dimensionality reduction: investigating texture, trace elements, and sulphur isotope signatures in the Kibali gold district, DRC 304
Y. Mpaka Waku, B. P. von der Heyden, G. Hurst, D. Lawrence, E. Mwandale, S. Glynn

Phytoremediation, a less costly prospect for tailings rehabilitation.....308
P. Gift Munyai, H. R. Mundalamo, J. O. Ogola, L. Chimuka

Continuous element mapping of drill cores from the Bushveld Complex, SA using LIBS and µEDXRF 311
W. Nikonow, D. Rammlmair, J. A. Meima

Exploring mineral chemistry variations in tourmaline and chlorite at the Triangle orogenic gold deposit (Val-d'Or, Québec): Implications for mineralisation vectors.....315
G. Pedemonte, B. Rottier, G. Beaudoin, J. Simoneau, P. Mactar-Dieng

Exploring semi-supervised generation of mineral list for automated mineralogy systems 319
L. Pereira, R. Tolosana-Delgado, S. Thiele, R. Japarov, M. Frenyel, K. Bachmann, G. van den Boogaart, J. Gutzmer

Critical Minerals: Germanium and Cobalt in the Bornite Deposit, Southwestern Brooks Range, Alaska 321
K. Pfaff, G. Graham, A. Jones, K. Kelley

Exploring the preservation potential of mineral deposits in the northern Canadian Cordillera through low temperature thermochronology: preliminary insights 325
N. Pinet, D. Kellett, I. Coutand, P. Sack

A hyperspectral detailed view on a magnetitite horizon in the Bushveld Complex, SA 329
D. Rammlmair, W. Nikonow

Petrography and geochemistry of rare earth element occurrences in the Koumbizick Massive (South Region, Cameroon).....333
B. Ndobe Tarkang, W. Tasing Ngirnyu

U-Pb dating and trace-element characterisation of potential cassiterite reference materials applicable to Sn-W mineralisation systems 336
T. B. Thomsen, B. Heredia, J. Ryznar, W. Zygo, H. O'Brien, M. Goodey, S. Tapster, A. M. Borst, N. Keulen, S. Malkki, D. Rosa

Nation-wide low-density geochemical mapping using composite sample, Korea.....339
S-J Youm, J. Sung Ahn, Y-C Cho, G-J Yim, S-W Ji, J-H Lee, J-H Lee

New sensing instruments and processing methods in mineral exploration

Resistivity imaging over porphyry copper systems in the Red Mountain district, southwest Colorado, USA.....343
E. Anderson, M. Deszcz-Pan, D. Yager, K. Eastman, B. Hoogenboom

Multi-scale and multi-source hyperspectral imaging for mapping lithium-bearing minerals.....347
R. Booysen, M. Kirsch, S. Thiele, S. Lorenz, Y. Madriz, P. Nex, J. Kinnaird, R. Gloaguen

Remote sensing and radiometric data for the detection of hydrothermal alteration zones with mineral potential at Yarra Wurta cliff, Australia 351
J. Mosquera

The use of total-field data for mineral exploration.....355
C. Parker

New lithostructural map of the Doropo region, northeast Côte d'Ivoire: Insight from structural and aeromagnetic data 359
Z. Hervé Siagné, T. Aïfa, A. Nicaise Kouamelan, H. N'guessan Nestor, W. Digbeu, B. Koffi Fidèle Kakou, P. Couderc

Machine learning, data mining and new target generation in mineral exploration

National- to continental-scale governmental geophysical efforts for critical mineral mapping, USA....363
A. E. McCafferty, C. M. Amaral, G. E. Graham

A GIS-based mineral prospectivity analysis of the Neoproterozoic Arabian Shield....367
C. Bonnetti, A. Fontaine, C. Berthier, J. Feneyrol, J. Corbet, V. Masson, R. Bosc, A. Hashim

Large-scale structural controls on hot spring mineral deposits of geothermal systems (Mt. Amiata, Italy) highlighted by machine learning algorithms?....371
P. S. Garofalo, L. Capitanio, E. Mariarosaria Farella, S. Rigon, F. Remondino, I. Callegari, D. Rappuoli

Imputation methods for REE and Y in zircon....375
C. Carrasco-Godoy, I. Campbell

Zircon geochemistry: insights into porphyry copper deposits fertility from machine learning applications....379
C. Carrasco-Godoy, I. Campbell, Y. Cajal

Building up a new mineral exploration indicator (MEI) system based on big data and AI technology....383
J. Zhang, H. Chen

Plate convergence, orogenic uplift, and tectonic preconditioning for giant porphyry copper formation in the central Andes....385
A. Farrar, M. Cracknell, D. Cooke, T. Schaap

The importance of hierarchical data structures for the interpretation of mineral trace-element data....389
M. Frenzel

The role of data science in modern mineral exploration and mining: adding machine learning tools to the geoscientist's toolbox....393
D. Klimentyeva, B. Bluemel, McL. Trott

Predicting mineral abundances from geochemistry in a heavy mineral sand deposit....396
K. Lilly, M. Gazley, M. Kartal, T. Ritchie

Machine learning in mineral prospectivity mapping and target generation for critical raw materials....398
V. Nykänen

Navigating the complexities of decision-making for Critical Mineral Exploration Campaigns: Insights form AI-based Geological Prospectivity and Risk Models....402
M. Parsa

Assessing tourmaline as an indicator mineral using multivariate statistics....404
E. Valentin Dos Santos, G. Beaudoin, B. Rottier

Critical cobalt and where to find it: distribution of cobalt in the Dolostone Ore Formation deposit, Namibia

Viktor Bertrandsson Erlandsson[1], Rainer Ellmies[2], Phillip Gopon[1], Helene Waldl[3], David Misch[1], Frank Melcher[1]
[1]Department of Applied Geosciences and Geophysics, University of Leoben, Austria
[2]Gecko Namibia, Swakopmund, Namibia
[3]Christian Doppler Laboratory for Advanced Coated Cutting Tools, University of Leoben, Austria

Abstract. In the pursuit of new sources of the critical metal Co, we investigate the sediment-hosted Cu-Co-Zn Dolostone Ore Formation (DOF) deposit in Namibia. Besides the stoichiometric Co-phase linnaeite, all sulfides associated with the main Co-forming ore stage (pyrite, sphalerite, and chalcopyrite) are enriched in Co, with significant concentrations found in sphalerite and pyrite. Sphalerite was measured to contain up to 1.5 wt% Co, which is the highest Co concentration reported in sphalerite. Atom probe tomography measurements of the Co-rich sphalerite demonstrates that these high Co concentrations occur homogeneously distributed. Petrographic evidence suggests that the Co was originally hosted in the pyrite, which was later remobilized during metamorphism to get incorporated into sulfides that formed during later ore stages. The Co finally got incorporated into the Co-rich sphalerite and to a lesser extend chalcopyrite. This study showcases the potential of secondary Co-bearing minerals as a source for the future of exploration and production of the critical metal Co.

1 Introduction

Cobalt is one of the many metals now classified as “critical” (European Commission 2020; USGS 2022) largely due to its use large demand in high-tech and green technologies, in particular high capacity batteries for electric cars (e.g. Alves Dias et al. 2018). Around 68 % of the global Co production comes from the Central African Copperbelt, in particular from the sediment-hosted Cu-Co deposits in the Democratic Republic of Congo (European Commission 2020; USGS 2020).

This study focuses on a recently discovered Co mineralization outside the Central African Copper Belt, the Dolostone Ore Formation (DOF) Cu-Co-Zn deposit in northwestern Namibia. To better define the distribution and mode of occurrence of Co in the sulfides of the DOF deposit, we use a correlative approach. Alongside with petrographic work with reflective light microscopy and scanning electron microscopy (SEM), we used laser ablation inductively coupled plasma mass spectrometry (LA-ICP-MS) to quantify the trace element composition of the various sulfides of the DOF deposit.

Electron probe micro analyzer (EPMA), electron backscattered diffraction (EBSD), and atom probe tomography (APT) were used to comprehend and visualize the Co distribution in Co-rich sphalerite. By applying all of these methods, we hope to better understand the occurrence and processes required to form Co-bearing phases in sediment-hosted deposits.

2 Geological setting

2.1 Regional geology

The DOF deposit is hosted in the Neoproterozoic Ombombo Subgroup of the Damara Supergroup (Allen 2016). The Damara Supergroup contains a sediment succession derived from the break-up of Rodinia with initial rifting with sandstones and conglomerates into carbonate platform environment with interlayered shales, siltstones and carbonates (Hoffman & Halverson 2008; Miller 2008; Porada 1989; Guj 1970). The Abenab Subgroup overlays the Ombombo Subgroup in the DOF area, containing the Chuos Formation diamictite and Rasthof Formation cap-carbonates (Allen 2016; Hoffman 2011; Hoffman & Prave 1996). The DOF deposit is located within the Eastern Foreland of the Kaoko Belt, the northern branch of the Damara orogen (Goscombe et al. 2005). The Eastern Foreland Zone experienced low-grade greenschist facies metamorphism (300 – 400 °C) during two stages of the Damara orogeny: the Kaoko Phase (590 – 535 Ma) and Damara Phase (555 – 505 Ma; Goscombe et al. 2017, 2003; Foster et al. 2009; Guj 1970).

2.2 Geology of the DOF deposit

The DOF Cu-Co-Zn mineralized horizon has been traced for at least 43 km E-W extension, dipping to the north, and is hosted in siltstones, shales, and carbonates within the Ombazu Trough in the Kunene region of northwestern Namibia (Figure 1). The mineralization has been subdivided into the main Cu-Co-Zn stage, expressed as sulfides disseminated in the host rock along with mineralized nodules and polysulfide aggregates. The second Cu-Zn stage occurs primarily within veins and pressure shadow mineralization. The main sulfides are pyrite, pyrrhotite, chalcopyrite, sphalerite, and linnaeite with lesser amounts of cobaltpentlandite, galena, and cobaltite. Linnaeite is restricted to the main stage mineralization (Bertrandsson Erlandsson 2022). The Ge-Ga-In-Mn-Fe (GGIMF) in sphalerite geothermometer (Frenzel 2016) indicates formation temperatures of all sphalerite to be above 310 ± 50 °C (Bertrandsson Erlandsson 2022).

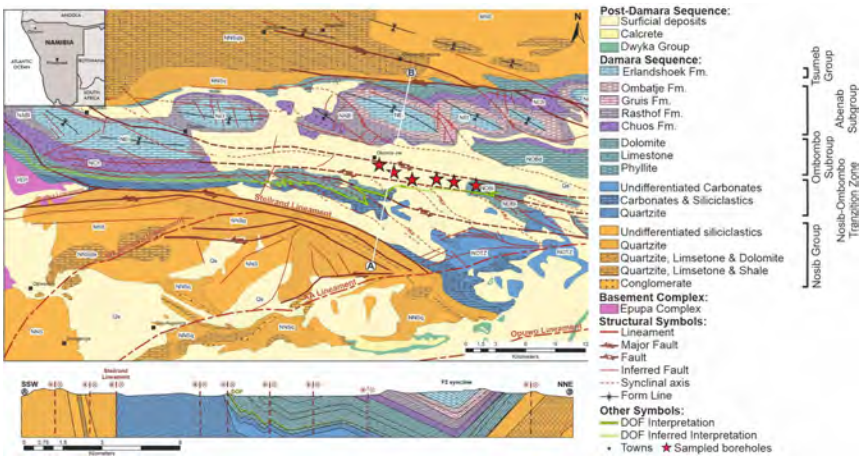

Figure 1. Geological map of the DOF deposit (green line) with sampled boreholes marked by stars. With schematic profile through the Ombazu Trough (white line). Modified after Bertrandsson Erlandsson (2022).

3 Methods

3.1 Sampling and petrographic methods

Polished mounts were made from sampling of six different exploration boreholes drilled by Celsius Resources (Figure 1), along the E-W extent of the DOF horizon. Boreholes are located approximately 2 km apart from each other. Mineral identification and textural observations were primarily done using reflective light microscopy and a Zeiss EVO MA 10 (SEM) coupled with a Bruker Quantax EDX detector.

3.2 LA-ICP-MS trace element analyses

An ESI Nd:YAG NWR213 laser ablation system coupled to an Agilent 8800 QQQ ICP-MS was used for in-situ trace element analyses of sphalerite, chalcopyrite, pyrite, and pyrrhotite. Masses analyzed were: ^{34}S, ^{51}V, ^{52}Cr, ^{55}Mn, ^{57}Fe, ^{59}Co, ^{60}Ni, ^{63}Cu, ^{67}Zn, ^{71}Ga, ^{74}Ge, ^{75}As, ^{82}Se, ^{95}Mo, ^{107}Ag, ^{111}Cd, ^{115}In, ^{118}Sn, ^{121}Sb, ^{125}Te, ^{197}Au, ^{201}Hg, ^{205}Tl, ^{208}Pb, and ^{209}Bi. Element concentrations were calculated using Iolite 4 (Paton et al. 2011), using two reference materials: the sphalerite standard MUL-ZnS1 (Onuk et al. 2017) and the polysulfide standard MASS-1 (Wilson et al. 2002).

3.3 EPMA mapping

Element maps of linnaeite, Co-rich sphalerite and pyrite were done using a JEOL Superprobe JXA 8200 EPMA equipped with five wavelength-dispersive spectrometers and one energy dispersive spectrometer. Maps were made with a 15 keV and 100 nA beam in stage scan mode.

3.4 EBSD mapping

A FEI Versa 3D Dual Focused Ion Beam FE-SEM was utilized to carry out EBSD mapping. Measurements were carried out with 20 keV electron-beam, with phase cubic scan parameters and a 500 nm step size in beam scanning mode.

3.5 APT measurements

Sphalerite APT analyses were carried out in laser mode with a 355 nm UV laser using a CAMECA LEAP 5000 XR. The measurements were done at a stage temperature of 50 K with 125 Hz pulse rate and laser pulse energy between 40 – 80 pJ. These parameters were adapted after the successful APT analyses of pyrite by Gopon et al. (2022). Sample preparation was done after Thompson et al. (2007) using a FEI Versa 3D Dual Focused Ion Beam FE-SEM equipped with a focused ion beam (FIB). Data reconstructions and peak ranging were done in IVAS 3.8.

4 Results

4.1 Mineralization styles of the DOF

Disseminated sulfides in the DOF deposit occur in several mineralization styles: disseminated, clusters, nodules, veins and in pressure shadows. There are also the locally termed “Events” that are vein-like but show both brittle and ductile deformation. Petrography of the sulfides from the main Cu-Co-Zn mineralization shows sphalerite overgrowing, and chalcopyrite forming rims around linnaeite and iron sulfides, indicating a more complex genesis of the main stage. The linnaeite is almost exclusively enveloped in pyrite and often appears partially altered. Main stage mineralization is associated with host rock alteration containing stilpnomelane and euhedral siderite, both which crosscut the pyrite. Disseminated sulfides occur oriented along the schistosity and mineralization styles such as the polysulfide cluster seems to be ripped apart in the orientation of the schistosity. See Bertrandsson Erlandsson (2022) for more details.

4.2 Sulfide trace element composition

Trace element LA-ICP-MS analyses revealed two main groups between the different mineralization styles. Group 1 is primarily recognized by the

elevated concentrations of Co in sphalerite (Figure 2), chalcopyrite, and pyrite. Other trace elements also differ significantly between the two groups, e.g. Ni and Se in sphalerite and chalcopyrite. Sphalerite contains up to 1.5 wt% Co.

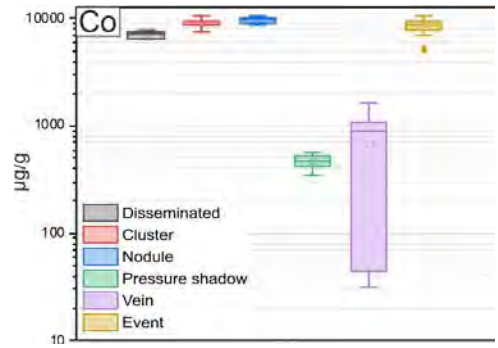

Figure 2. Cobalt concentrations in sphalerite showing distinct grouping between Co-rich and Co-poor sphalerite. Mineralization styles in legend are briefly explained in section 4.1.

4.3 EPMA and EBSD mapping of Co-sphalerite

EPMA mapping shows homogeneous distribution of Co within the Co-rich sphalerite, but also revealed a Co-poor and Zn-rich network (Figure 3). EBSD mapping shows subgrains within sphalerite that seem to correlate with the network feature identified by the EPMA. EPMA mapping shows oscillatory Co-zoning in the pyrites from the main Cu-Co-Zn stage mineralization, where the innermost zones show higher Co concentrations (Figure 4).

4.1 APT data reconstruction

3D reconstructions of the APT needle shaped sample reveal that Co occur homogenously within the Co-rich sphalerite, with no evidence for nano-inclusions (Figure 5).

5 Discussion

Based off the LA-ICP-MS analyses, all sulfides that occur are associated with the stoichiometric Co-mineral linnaeite have elevated Co contents. Both the Co-rich sphalerite and chalcopyrite crosscut the linnaeite and pyrite of the main Cu-Co-Zn mineralization, suggesting a relatively later formation of these phases. As linnaeite contains Co^{3+} and pyrite, which envelops the linnaeite, should only include 2+ cations, it is assumed that different physiochemical changes were involved in the remobilization of Co in the DOF deposit (Bertrandsson Erlandsson et al. 2023). The sphalerite and chalcopyrite formation would also imply an additional source of Zn and Cu, as these elements are not significantly elevated in the earlier pyrite (Bertrandsson Erlandsson et al. 2022).

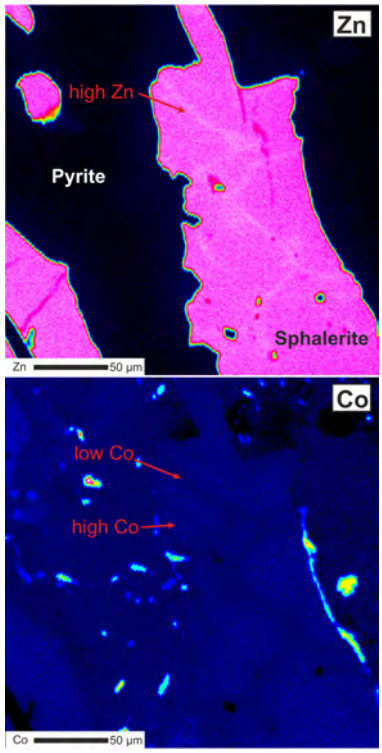

Figure 3. EPMA element maps of Zn and Co from Co-rich sphalerite. Cobaltpentlandite inclusions in pyrite are visible as spots of high Co. Note that the high Co on the right-side of the sphalerite-pyrite contact is an edge artifact from holes in the sample, and not trustworthy data.

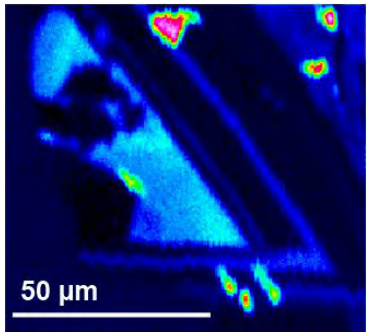

Figure 4. EPMA map of cobalt zonation within pyrite from another part of the cluster mineralization style, with crosscutting cobaltpentlandite inclusions (high Co in map).

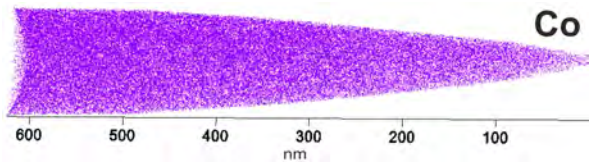

Figure 5. Tip reconstructions of homogenously distributed Co ions from the APT data. X-axis showing scale of the APT tip.

The observation of Cu-Co-Zn stage sulfides being aligned with the host rock schistosity and the GGIMF in sphalerite geothermometer yielding formation temperatures 310 ± 50 °C (in agreement with regional metamorphic temperatures) strongly suggests that the DOF mineralization formed during the Damara orogeny. The vein-hosted Cu-Zn

mineralization is believed to have formed later and is thus related to a late orogenic stage. It is worth noting that the network feature, identified by EPMA in the Co-rich sphalerite (Figure 3), has lower Co concentrations than the rest of the sphalerite, as the later Cu-Zn mineralization sulfides were also shown to also contain significantly lower Co concentrations by LA-ICP-MS (Figure 2). This later Cu-Zn mineralization occurs predominantly within veins and is believed to have formed later than the Co-mineralization (Bertrandsson Erlandsson et al. 2022). Attempts of dating have so far been unsuccessful and therefore these mineralization stages cannot be attributed to the different Damara orogenic phases.

6 Conclusions

This study highlights the widespread Co-enrichment in all sulfides associated with the main Cu-Co-Zn mineralization stage (pyrite, sphalerite, and chalcopyrite) of the DOF deposit. Whilst the later vein-hosted Cu-Zn mineralization lacks stochiometric Co-phases and has low Co trace element concentrations. APT analyses of sphalerite containing up to 1 wt% Co, shows homogenous distribution of Co. The petrographic evidence suggests that the Co in the sphalerite is the result of Co remobilization through several stages related to metamorphism and physiochemical changes. The presence of additional Co-rich minerals (e.g. sphalerite and pyrite) may be important as additional sources of Co in future exploration as the demand of critical metals increases.

Acknowledgments

The authors would like to acknowledge funding and support from the Gecko Namibia exploration team, M. Zimmermann for his assistance with the EPMA, and G. Hawranek for assistance with EBSD analyses.

References

Allen NK (2016) Structurally controlled Cu-Zn-(Co-Pb) mineralization in the Neoproterozoic Ombombo Subgroup, Kaokoland, Namibia. Colorado School Mines.

Alves Dias P., Blagoeva D, Pavel C, Arvanitidis N (2018) Cobalt: demand-supply balances in the transition to electric mobility. Publications Office of the European Union 10:97710.

Bertrandsson Erlandsson V, Gopon P, Waldl H, Misch D, Ellmies R, Melcher F (2023) Sphalerite as a non-traditional critical metal source: correlative microscopy (EPMA, EBSD, APT) of cobalt-enriched sulfides from the sediment-hosted copper-cobalt Dolostone Ore Formation deposit, Namibia. Front Earth Sci 11:543. doi: 10.3389/feart.2023.1171859

Bertrandsson Erlandsson V, Wallner D, Ellmies R, Raith JG, Melcher F (2022) Trace element composition of base metal sulfides from the sediment-hosted Dolostone Ore. Formation (DOF) Cu-Co deposit in northwestern Namibia: Implications for ore genesis. J Geochem Explo: 107105.

European Commission (2020) Communication from the Commission to the European Parliament, the Council, the Economic and Social Committee and the Committee of the Regions. Critical Raw Materials Resilience: Charting a Path towards greater Security and Sustainability. Online: https://eur-lex.europa.eu/legal-content/EN/TXT/?uri=CELEX%3A52020DC0474.

Foster DA, Goscombe BD, Gray DR (2009) Rapid exhumation of deep crust in an obliquely convergent orogen: The Kaoko Belt of the Damara Orogen. Tectonics 28:1–24.

Frenzel M, Hirsch T, & Gutzmer J (2016) Gallium, germanium, indium, and other trace and minor elements in sphalerite as a function of deposit type—A meta-analysis. OGR:52–78.

Gopon P, Douglas JO, Meisenkothen F, Singh J, London AJ, Moody MP (2022) Atom probe tomography for isotopic analysis: development of the 34S/32S system in sulfides. Microsc Microanal 28:1127–1140.

Goscombe BD, Foster DA, Gray DR, Wade B (2017) Metamorphic response and crustal architecture in a classic collisional orogen: The Damara Belt, Namibia. Gondwana Res 52:80–124.

Goscombe BD, Gray DR, Hand M (2005) Extrusional Tectonics in the Core of a Transpressional Orogen; the Kaoko Belt, Namibia. J Petro 46: 1203–1241.

Goscombe BD, Hand M, Gray DR (2003) Structure of the Kaoko Belt, Namibia: progressive evolution of a classic transpressional orogen. J Struc Geo 25:1049–1081.

Guj P (1970): The Damara Mobile Belt in the south-western Kaokoveld South West Africa (PhD Thesis). Uni Cape Town / Precambrian Research Unit, Cape Town, South Africa.

Haley D (2018) 3Depict: Valued Point Cloud Visualization and Analysis Software. Retrieved from http://threedepict.sourceforge.net/

Hoffman PF, Halverson GP (2008) Otavi Group of the western Northern Platform, the Eastern Kaoko Zone and the western Northern Margin Zone. In R. M. Miller (Ed.), The Geology of Namibia: Neoproterozoic to Lower Palaeozoic (2nd ed., 13-69–13-136). Windhoek, Namibia: Geo Survey.

Hoffmann KH, Prave AR (1996) A preliminary note on a revised subdivision and regional correlation of the Otavi Group based on glaciogenic diamictites and associated cap dolostones. Com Geo Survey Namibia 77–82.

Onuk, P, Melcher F, Mertz-Kraus R, Gäbler HE, Goldmann S (2017) Development of a matrix-matched sphalerite reference material (MUL-ZnS-1) for calibration of in situ trace element measurements by laser ablation-inductively coupled plasma-mass spectrometry. Geost Geoanal Res 41:263-272.

Paton C, Hellstrom J, Paul B, Woodhead J, Hergt J (2011) Iolite: Freeware for the visualisation and processing of mass spectrometric data. J Ana Atomic Spectrometry 26:2508-2518.

Porada H (1989) Pan-African rifting and orogenesis in southern to equatorial Africa and eastern Brazil. Precambrian Research:103–136.

Thompson K, Lawrence D, Larson DJ, Olson JD, Kelly TF, Gorman B (2007) In situ site-specific specimen preparation for atom probe tomography. Ultramicroscopy 107:131–139.

Wilson SA, Ridley W I, Koenig AE (2002) Development of sulfide calibration standards for the laser ablation inductively-coupled plasma mass spectrometry technique. J Analy Atomic Spectrometry 17:406–409.

USGS (2020) Mineral commodity summaries 2020. Advance online publication. https://doi.org/10.3133/mcs2020

USGS (2022) 2022 Final List of Critical Minerals. Notices. https://www.usgs.gov/news/national-news-release/us-geological-survey-releases-2022-list-critical-minerals.

Geostatistical and geometallurgical investigation of Co in the Rocklands tailings deposit, Queensland, Australia

Rosie Blannin[1], Laura Jackson[1], Anita Parbhakar-Fox[1]
[1]WH Bryan Mining Geology Research Centre, Sustainable Minerals Institute, University of Queensland, QLD, 4072, Australia

Abstract. Historical mining and processing operations did not always target critical minerals, and typically had lower efficiencies than present day. As a result, mine wastes have the potential to become unconventional resources of critical minerals. To assess this potential, the contents and mode of occurrence of critical minerals in the mine wastes must be investigated through sampling, characterisation and modelling. This study applied several analytical methods to identify critical minerals in the Rocklands tailings deposit in Queensland, Australia, and characterise their deportment. The Co and Cu grades of the tailings deposit were modelled with co-kriging, a geostatistical method. The results were assessed in combination with mineralogical, textural and mineral chemistry data to investigate the resource potential of the Rocklands tailings. Cobalt and Cu are found to be hosted by a range of both primary and secondary sulphide and oxide minerals. Due to the complex nature of the materials, recovery of the critical minerals from the Rocklands tailings may require a range of processing technologies.

1 Introduction

Critical minerals are those of high importance for the economy and green energy transition, often with supply chain risks, e.g., Co, In, REEs, Sn, Ge, Ga and W. Many deposits in Queensland, Australia, are known to be endowed in critical minerals alongside the main commodities (Fig. 1). There is great potential to explore mine wastes in Australia and elsewhere as unconventional resources for critical minerals. In order to assess resource potential of mine wastes, the contents and mode of occurrence of critical minerals must be investigated through sampling, characterisation and modelling.

The Rocklands mine is one example of a deposit hosting critical minerals in Queensland (Fig. 1). The main commodity at Rocklands is Cu, but the deposit also hosts Au and Co, the latter of which is critical. The mineralisation at Rocklands comprises an enriched supergene oxide zone overlying a hypogene copper sulphide zone. The supergene zone reaches depths of up to 100 m, with variable development of chalcocite and secondary native copper and chalcocite. Surface outcrops comprise siliceous breccias with minor malachite and azurite. Primary copper sulphide mineralisation comprises coarse intergrowths of chalcopyrite as breccia infill, with pyrite, calcite, actinolite, magnetite and quartz. Cobalt grades range from 500 to 1,800 g/t and up to 3,390 g/t in the hypogene zones (Beams, 2009).

Rocklands was mined as an open pit operation between 2012 and 2018, targeting Cu, Co, Au and Fe. Native copper was recovered with gravity separation (jigs, gravity spirals, tables), while separate copper sulphide and pyrite concentrates were recovered with flotation. Magnetic separation of the flotation tailings was performed to recover magnetite. CuDeco (2018) reported that 2.3 Mt of ore was processed between 2015 and 2017, with a Cu recovery of 78 % (CuDeco 2017). As a result, significant volumes of tailings, possibly enriched in Co and Cu, were produced and stored in the Rocklands tailings facility.

This study aimed to sample, analyse and spatially model tailings deposit at Rocklands in order to assess the resource potential of Co, as well as Cu. Geostatistical modelling was implemented in 3D to model the Co and Cu grades in the tailings. Previous studies have successfully applied geostatistical modelling to tailings deposits (e.g., Parviainen et al. 2020; Wilson et al. 2021; Blannin et al. 2022, 2023). Furthermore, mineralogical and textural properties related to the recoverability of Co were investigated to evaluate the potential for re-processing of the Rocklands tailings.

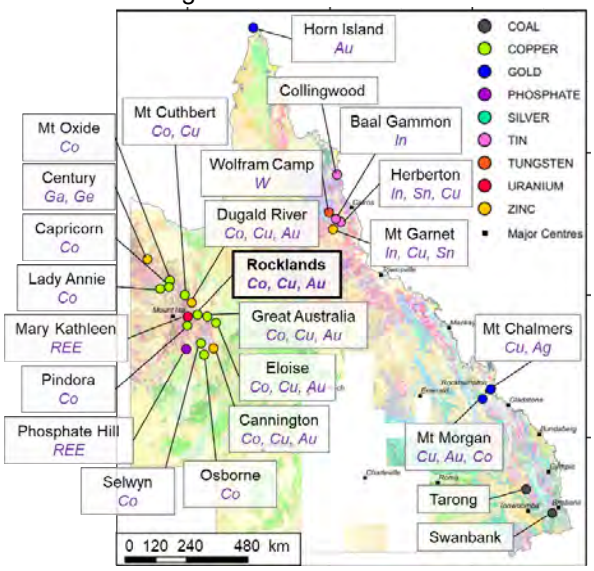

Figure 1. Map of critical minerals, alongside the main commodities, at operating mines and major deposits in Queensland, Australia. The Rocklands mine, the tailings of which are the focus of this study, is highlighted.

2 Methodology

2.1 Sampling and analysis

The tailings facility at the Rocklands mine was sampled with an auger at 24 locations (Fig. 2). A total of 139 samples were taken up to a maximum depth of 7 m. The base of the tailings was not intersected as to not damage the basal lining.

Figure 2. Map of the sample locations at the Rocklands tailings facility in Queensland, Australia.

The samples were sent to Australian Laboratory Services in Brisbane for sample preparation and geochemical analysis with inductively coupled plasma atomic emission spectroscopy or mass spectroscopy (ICP-AES/MS). The thirty samples with the highest Co assays were selected for mineralogical studies to determine the dominant modes of occurrence of Co, as well as Cu. Bulk mineralogy was measured by X-ray Diffractometry (XRD) at Queensland University of Technology, using a PANalytical X'Pert Pro powder diffractometer and cobalt Kα. The mineral liberation analyser (MLA), an automated mineralogy tool, was used to collect mineralogical and textural data on the potentially Co-bearing sulphide minerals, namely pyrite. The MLA measurements were performed at the Sustainable Minerals Institute, University of Queensland with the XBSE measurement mode. Laser ablation analyses were carried out to investigate the trace element distributions in the sulphide minerals. The analyses were performed at CODES Analytical Laboratories, University of Tasmania, using a RESOlution laser platform, equipped with a Coherent COMPex Pro 193 nm excimer laser and Lauren Technic S155 large format sample cell, coupled to an Agilent 7700 quadrupole ICP-MS.

2.2 Geostatistical modelling of chemistry

In order to investigate the spatial variability of critical minerals in the Rocklands tailings facility and estimate their average grades, geostatistical modelling was performed. Specifically, Co and Cu grades were interpolated using co-kriging, (Wackernagel 1995; Goovaerts 1997). The modelling was performed in R studio (R Core Team 2021), making use of the "gstat" package (Pebesma 2004; Gräler et al. 2016).

First, the Co and Cu grades were log-transformed. Variograms and cross-variograms were computed for the log-transformed variables with the following parameters: horizontal lag distance of 25 m; maximum horizontal distance of 375 m; vertical lag distance of 0.25 m; maximum vertical distance of 3.75 m; vertical angle tolerance of 2°. The variogram and cross-variogram models were automatically fitted by the "gstat" program, using exponential models and a range of 100 m. The sedimentary-style deposition of tailings forms a horizontally layered structure, resulting in a greater continuity in the horizontal direction than the vertical direction. An anisotropy factor of 0.00625 was calculated for fitting the variogram models, based on the horizontal and vertical ranges of the variograms.

Leave-one-out cross validation was performed to validate the geostatistical model (e.g., Goovaerts, 1997). This involves sequentially removing each sample from the dataset and using the geostatistical model to predict the value at that location. By comparing the original (observed) and predicted values, the quality of the modelling results can be evaluated. Following this, the Co and Cu grades were interpolated into a 3D grid across the tailings using co-kriging with the geostatistical model. The 3D grid had a horizontal spacing of 15 m and a vertical spacing of 1.5 m. The grid extended to a depth of 7.5 m, based on the available samples.

3 Results and discussion

3.1 Geochemistry

Geochemical analysis revealed that the Co grade varies from 200 to 1,275 g/t (average: 570 g/t) whilst Cu ranges from 304 g/t to 6,960 g/t (average: 2,021 g/t). Cobalt is strongly correlated with both S and Fe. However, there is a bimodal association pattern of Co and S, suggesting that Co is hosted in both sulphide and Fe oxides phases, and potentially a secondary sulphate or jarosite. The Cu remaining in the Rocklands tailings is potentially economically significant, with an average grade of 0.2 %. Positive Cu associations are seen with Zn, Ni and Au while a negative correlation is observed with S, suggesting that little Cu is sequestered in sulphides.

3.2 3D grade models

The cross-validation of the geostatistical model showed that there is an excellent correspondence between the observed (assay) values and those predicted by the geostatistical model, as seen by the observed-predicted (Obs-Pred) R^2 values of 89 % for Co and 75 % for Cu (Table 1, Fig. 4). The mean errors (ME) and correlations between the predicted and residual values (Pred-Res R^2) are low, showing that the geostatistical model is unbiased (Table 1). Therefore, co-kriging is shown to be an appropriate method for geostatistical modelling of the Rocklands tailings and should be applicable to other studies.

Table 1. Cross validation results for co-kriging.

	ME	Obs-Pred R^2	Pred-Res R^2
Co	7.0×10^{-5}	0.89	0.01
Cu	0.004	0.75	0.07

The summary statistics of the predicted Co and Cu grades are shown in Table 2. The mean grades of Co and Cu are around 535 and 1,631 g/t, respectively. This demonstrates that there are potentially economic grades of critical minerals in the Rocklands tailings. The Cu grade is more variable than the Co grade, with a relative standard deviation (standard deviation divided by mean) of ~ 40 % compared to ~ 15 % for Co.

Table 2. Summary statistics of the predicted Co and Cu grades (g/t). SD = standard deviation.

	2.5th perc.	Median	97.5th perc.	Mean	SD
Co	334	538	680	535	82
Cu	820	1,493	3,371	1,631	686

The spatial distribution of the critical minerals throughout the tailings is also of importance when investigating resource potential, as it may influence appropriate mining methods and re-processing routes. As such, horizontal maps of Co and Cu grades at 1.5 m depth intervals are plotted in Fig. 4.

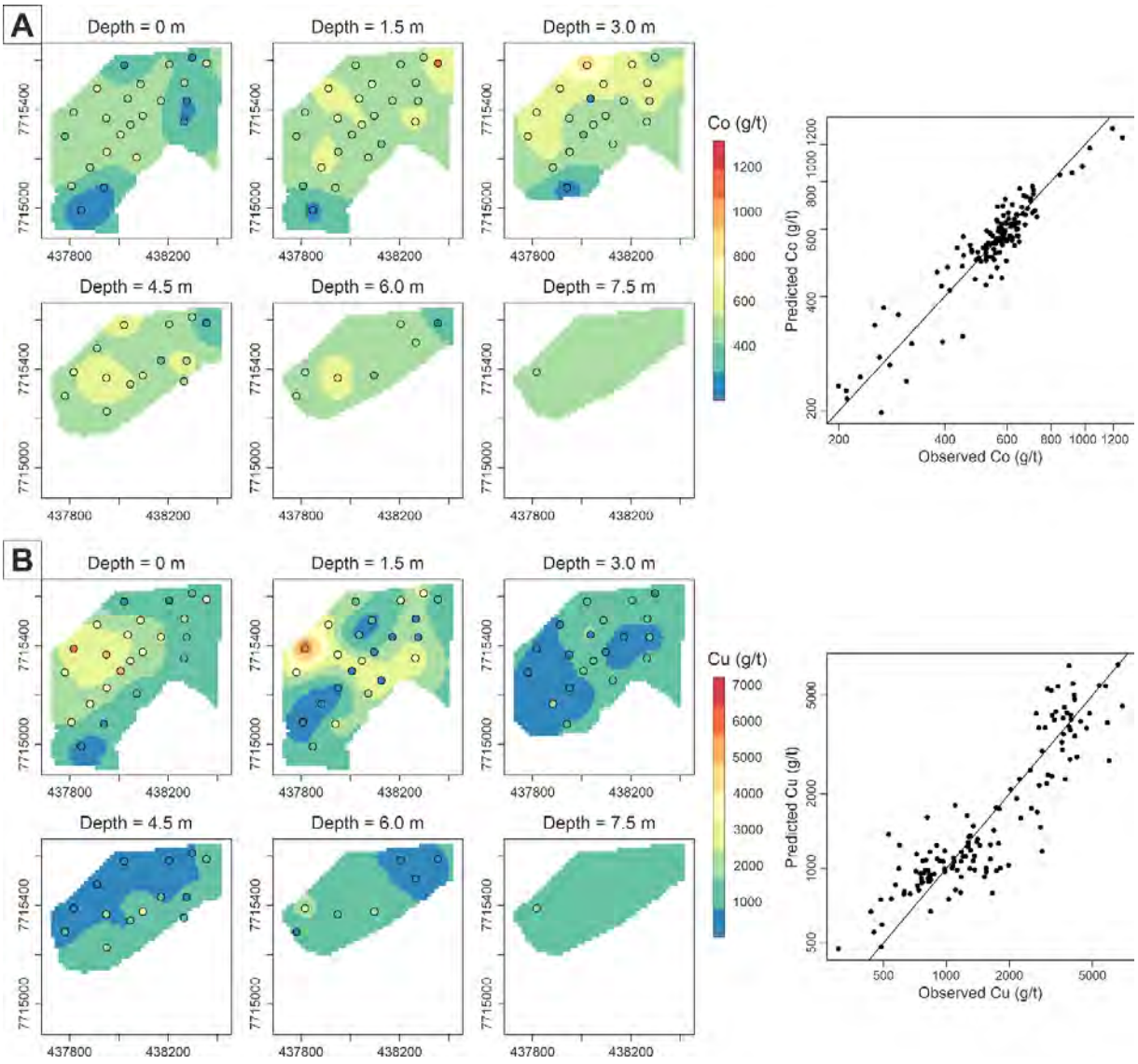

Figure 4. Heatmaps of the interpolated Co (A) and Cu (B) grades at 1.5 m depth intervals are shown on the left. The color-coded points show the sample locations and assay values. Cross-validation plot for the co-kriging of the Co and Cu grades are shown on the right, with the 1:1 line to show the good correspondence between the observed and predicted values.

Cobalt and Cu follow rather different spatial distribution trends (Fig. 4), suggesting that they are not (always) hosted by the same mineral(s) and may be concentrated in different tailings facies. Higher Co grades are concentrated in the central-north zone of the tailings, particularly at a depth of 3 m. In contrast, copper grades are higher at the surface, in the north-west and central zones. This may be in relation to the oxidised zone in the near surface of the tailings.

3.3 Mineralogy and textural properties

A total of 38 minerals were identified by MLA. The modal mineralogy of the tailings is dominated by quartz (~ 13.5 wt. %), plagioclase (~ 16 wt. %), Ca-amphibole (~ 15.3 wt. %), chlorite (~ 8.9 wt. %) and Fe oxide / magnetite (~ 12.8 wt. %). Pyrite was present in all samples (~ 3.1 wt. %) with two notably high samples (9.1 and 8.6 wt. %). Minor amounts of carrollite (up to 0.04 wt. %), a Cu-Co-bearing sulphide, were identified but cobaltite was not. A wide range of Cu sulphides (chalcopyrite, bornite, chalcocite, covellite) and Cu oxide or silicate minerals (cuprite, malachite/ azurite, chrysocolla) are present at varying concentrations. Jarosite was identified in all samples at < 1 wt. %. Notably, calcite contents of around 14.7 wt. % indicate that intrinsic neutralising potential is available within the tailings, reducing the potential for acid mine drainage.

Overall, there are likely to be at least three hosts of Co in the tailings: pyrite, pyrite weathering products and Fe oxide. The p80 of the pyrite grains ranges from ~ 75 to 180 µm. The abundance of fully liberated pyrite varies between ~ 44 and 75 %. Lower pyrite grades generally coincide with higher oxidisation and therefore poorer liberation of pyrite due to the formation of surface coatings. Pyrite also exhibits minor associations with pyrrhotite, jarosite and amphibole. Similarly, Fe oxide particles have mineral associations with plagioclase, chlorite and amphibole and similar liberation degrees to pyrite (between 32 and 78 % fully liberated).

Cobalt occurs in pyrite in the form of micro-inclusions and larger inclusions, leading to an average Co concentration of 10,412 ppm, and up to 51,815 ppm. For Cu, an average and maximum of 2,331 and 277,167 ppm occur, respectively, suggesting that pyrite contains intercalations of chalcopyrite. Corresponding to these Co and Cu concentrations in pyrite, and assuming an average pyrite grade of 3.1 wt. % in the tailings, around 60 % of the Co content in the Rocklands tailings is hosted by pyrite compared to only 5 % of the Cu content. The remainder of the Co may be (partially) hosted by Fe oxides. Copper appears to be dominantly hosted by Cu oxide minerals. Overall, Co and Cu are present in different mineral phases and their recovery from the range of sulphide and oxide phases present, both primary and secondary, will require different processing methods.

Whitworth et al. (2022) reviewed re-processing methods for mine wastes and found that different challenges are faced for the recovery of critical minerals when compared to primary deposits. For instance, the pyrite particle sizes observed would be amenable to flotation. However, the relatively poor liberation of pyrite, combined with weathering and surface coatings, would require additional processing steps to produce fresh surfaces prior to flotation. Additionally, the abundance of secondary phases may impact flotation responses. As a result, leaching or bioleaching may be preferable to recover Co and Cu from the Rocklands tailings.

4 Conclusions

This work aimed to demonstrate the importance of mine wastes as sources of critical minerals. By characterising the Rocklands tailings with a range of analytical methods, the critical minerals and the opportunities and challenges for their recovery were identified. Additionally, 3D models of Co and Cu in the Rocklands tailings deposit were produced as a first step to assessing the resource potential. Metallurgical test work should be performed to optimise the recovery of the critical minerals present in the Rocklands tailings.

Acknowledgements

The authors would like to thank the Department of Resources, Queensland, for providing funding (NEMI-UQ-06) to enable completion of this work.

References

Beams SD (2009) Geology and mineralisation at the Rocklands Copper-Cobalt deposits, Cloncurry District, Northwest Queensland, Australia. Proc 10th Bienn SGA Meet, Townsville, 17-20th August 2009.

Blannin R, Frenzel M, Tolosana-Delgado R, et al (2023) 3D geostatistical modelling of a tailings storage facility: resource potential and environmental implications. Ore Geol Rev 154. https://doi.org/10.1016/j.oregeorev.2023.105337

Blannin R, Frenzel M, Tolosana-Delgado R, Gutzmer J (2022) Towards a sampling protocol for the resource assessment of critical raw materials in tailings storage facilities. J Geochem Explor 236. https://doi.org/10.1016/j.gexplo.2022.106974

CuDeco (2017) Annual Report, CuDeco Ltd, pp 45.

CuDeco (2018) Rocklands Ore Reserve Update. Market release dated 22 March 2018, pp 45.

Goovaerts P (1997) Geostatistics for Natural Resources Evaluation. Oxford University Press, New York

Gräler B, Pebesma E, Heuvelink G (2016) Spatio-Temporal Interpolation using gstat. R J 8:204–218. https://doi.org/10.32614/RJ-2016-014

Parviainen A, Soto F, Caraballo MA (2020) Revalorization of Haveri Au-Cu mine tailings (SW Finland) for potential reprocessing. J Geochem Explor 218. https://doi.org/10.1016/j.gexplo.2020.106614

Pebesma EJ (2004) Multivariable geostatistics in S: the gstat package. Comput Geosci 30:683–691

R Core Team (2021) R: A language and environment for statistical computing. R Foundation for Statistical Computing, Vienna, Austria

Wackernagel H (1995) Ordinary Kriging. In: Multivariate Geostatistics. Springer Berlin Heidelberg, pp 74–81

Whitworth AJ, Forbes E, Verster I, et al (2022) Review on advances in mineral processing technologies suitable for critical metal recovery from mining and processing wastes. Clean Eng Technol 7. https://doi.org/10.1016/j.clet.2022.100451

Wilson R, Toro N, Naranjo O, et al (2021) Integration of geostatistical modeling into discrete event simulation for development of tailings dam retreatment applications. Miner Eng 164. https://doi.org/10.1016/j.mineng.2021.106814re

Copper in Onshore New Zealand: Mineral Deposit Types, Occurrences and Potential for this Critical Metal

Anthony (Tony) B. Christie
[1]GNS Science, Lower Hutt, New Zealand

Abstract. New Zealand has intermittently produced small quantities of Cu ore between 1846 and 1972. Most of the known Cu deposits are classified into four main types:

1.) Porphyry Cu deposits that consist of stockwork quartz veins deposited from hydrothermal fluids generated by Miocene stocks and dikes of diorite to granodiorite composition (e.g. Coppermine Island, Miners Head, Paritu, Ohio Creek);

2.) VMS hydrothermal deposits related to submarine volcanic activity, including Mesozoic deposits associated with chert and pillow lava in greywacke sequences (e.g. Kawau Island, Te Kumi, Maharahara, Moke Creek, Waitahuna), and Cretaceous deposits associated with marine basalts (e.g. Pupuke, Pakotai, Parakao, Lottin Point) and the Pounamu Ultramafics;

3.) Serpentine-hosted Fe-Cu deposits that are shear-controlled massive sulfide lenses in serpentinised ultramafic rocks of the Permian Dun Mountain Ophiolite Belt (e.g. D'Urville Island, Dun Mountain, Red Mountain); and

4.) Gabbroid-associated Ni-Cu/Cu-Ni deposits formed by magmatic crystallization in mafic magma chambers or conduits (e.g. Riwaka, Blue Mountain, Otama and Longwood igneous complexes).

Porphyry Cu deposits represent the best exploration target in terms of size potential, but higher Cu grades of the other deposit types may enable production from smaller deposits or as a by-product.

1 Introduction

Copper is a critical element required for electricity generation and transmission in the carbon neutral future and therefore it is timely to review New Zealand's Cu deposits and their exploration potential. A little more than 7500 t of Cu ore has been mined in New Zealand since the country's first underground mine was opened on Kawau Island in 1846. This production was mainly from porphyry Cu (Miners Head, Great Barrier Island), volcanogenic massive sulfide (Kawau Island, Pakotai, Pupuke, Parakao, Te Kumi, Maharahara, Moke Creek, Waitahuna), serpentine-hosted (D'Urville Island, Dun Mountain), and epithermal vein (Tui) deposits (Fig. 1 and Table 1). Occurrences of other types of Cu-bearing deposits include: porphyry Mo-Cu, gabbroid associated Ni-Cu and Cu-Ni, and skarn Cu deposits (Table 1). This study reviews available information on New Zealand Cu deposits to highlight their exploration potential.

Some small quartz vein and disseminated stratabound/stratiform Cu-bearing deposits, particularly in Fiordland National Park, are not described here because of their apparent small size and insufficient information available to determine their deposit type and genesis. See Williams (1974), Brathwaite and Pirajno (1993), and Christie and Brathwaite (1994) for additional information.

Figure 1. Location of Cu occurrences in New Zealand.

2 Porphyry Cu deposits

Porphyry Cu style mineralization occurs associated with the intrusion of Miocene quartz diorite, diorite and granodiorite stocks and dikes into Permian-Jurassic greywacke metasedimentary rocks and Miocene andesite in Northland (Knuckle Point, Coppermine Island) and the Hauraki Goldfield - Coromandel Volcanic Zone (Miners Head of Great Barrier Island, Paritu, Manaia, and Ohio Creek).

Exploration from the 1960s to 1980s included geochemical and geophysical surveys, and drilling of diamond drill holes (DDH) at Coppermine Island (4 DDH; Wodzicki and Thompson 1970), Paritu (3 DDH totalling 357 m; Bates 1980) and Ohio Creek (6 DDH totalling 2530 m; Brathwaite et al. 2001).

At Paritu, Cu mineralization is associated with a pluton (Paritu Plutonics) predominantly of quartz diorite to granodiorite composition. Exploration in the 1970s identified anomalous Cu geochemistry in Ongohi and Stony Bay streams (Bates 1980). Three DDH totalling 357 m were drilled in the Ongohi zone and intersected disseminated chalcopyrite, magnetite and pyrite in biotite quartz diorite, averaging 0.16% Cu. At Ohio Creek, a dacite stock and surrounding intrusion breccia host a quartz vein stockwork containing pyrite-chalcopyrite and returning an average grade of 0.18% Cu (Brathwaite et al. 2001). Some of the mineralization contains significant concentrations of gold, e.g. a 2.1 m interval of 17.3 g/t Au was intersected in drillhole OC6.

Table 1. New Zealand Cu deposit types and occurrences (source: Williams 1974; Brathwaite and Pirajno 1993; Christie and Brathwaite 1994).

	Form	Setting	Age	Minerals	Examples	Production (ore or conc)
Porphyry Cu	stockwork vn, dissem, breccia	stocks and dikes of diorite, quartz diorite, granodiorite, and dacite intruded into Jurassic metasediments	Miocene (~17-10 Ma)	py, cp (po, mo)	Knuckle Point, Coppermine Is, Miners Head, Paritu, Ohio Ck	Miners Head, Otea mine (2325 t, 1857-1867)
VMS, Ophiolite-hosted (Cyprus) type	stratiform lens, dissem	basalt, dolerite, chert	Cretaceous-Tertiary	py, cp, (mc, sp, gn, mt, hm)	Pupuke, Pakotai, Parakao, Purua, Lottin Point	Pupuke (30 t, 1892-1912 & 1964-1968), Pakotai(1400 t, 1947-1951), Parakao (1040 t, 1961-1966)
VMS associated with chert and pillow lava in greywacke	stratiform lens, dissem	chert and basalt in greywacke sequences	Permian-Jurassic	py, mc, cp, (po, sp, mt)	Kawau Is, Te Kumi, Maharahara, Moke Ck, Waitahuna	Kawau Is (2500 t, 1846-1860), Maharahara (50 t. 2% Cu, 1881-1891 & 1930), Moke Ck (1880s, 1917 &1968), Waitahuna (minor, late 1800s)
VMS in the Pounamu Ultramafics	stratiform lens, dissem	greenschist (metabasalt) and metaserpentinite	Permian-Triassic	py, cp	Newton, Diedrich, Meta, Bowen & Wilberg ranges, Whitcombe R	None
Serpentine-hosted Fe-Cu	lenses in shear zones	serpentinized ultramafic rocks of the Dun Mt Ophiolite Belt	Permian	py, cp, po, (mt)	D'Urville Is, Dun Mt	D'Urville Is (minor, 1879-1880), Dun Mt (930 t, 1886 & 1908-1909)
Gabbroid-associated Ni-Cu and Cu	dissem, lenses	gabbro, peridotite, trondhjemite, diorite, anorthosite, troctolite	Devonian-Permian (ca. 364 Ma for Riwaka)	po, cp, pent, py, mt (il, PGE)	Riwaka, Cobb Valley, Blue Mt, Mt Tapuaenuku, Otama IC, Longwood IC	None
Epithermal quartz vein	vn	andesite and dacite	Miocene	py, sp, gn, cp, Ag, Au	Monowai, Tui, Waiorongomai	Tui (404 t, 1967-1974)
Porphyry Mo	vn, stockwork vn, dissem	stocks of granite, granite geniss, quartz monzonite, granodiorite intruded into metasediments	Cretaceous (most between 100 and 120 Ma; ca. 122.5 Ma for Copperstain Ck)	py, mo, cp, (mt, gn, sp, Bi-min)	Eliot Ck, Copperstain Ck, Burgoo Stm, Karamea Bend, Mt Radiant, Taipo Spur, Bald Hill, McConnochie Ck	None
Skarn	dissem	skarn, schist, marble, granodiorite porphyry	Cretaceous (ca. 122.5 Ma)	py, cp, mo	Copperstain Ck	None

Ck = Creek, conc = concentrate, dissem = disseminated, IC = Igneous Complex, Is = Island, Mt = Mountain, R = River, Stm = stream, vn = vein. Minerals: Bi-min = Bi-minerals, cp = chalcopyrite, gn = galena, hm = hematite, il = ilmenite, mc = marcasite, mo = molybdenite, mt = magnetite, PGE = platinum group elements, po = pyrrhotite, py = pyrite, sp = sphalerite, () = minor metallic minerals

3 Volcanogenic massive sulfide deposits

Volcanogenic massive sulfide (VMS) hydrothermal deposits are formed in association with submarine volcanic activity. The first metalliferous mining in New Zealand was production of Cu ore from a VMS deposit on Kawau Island from 1846 to 1860. The known VMS deposits in New Zealand consist of small sulfide lenses composed mainly of pyrite and chalcopyrite that are associated with: (a) marine basalts of Cretaceous-Tertiary age in Northland and East Cape

(mafic-ultramafic or Cyprus type VMS; Shanks and Thurston 2010), (b) chert and pillow lava in greywacke sequences of Permian-Jurassic age, and their metamorphic equivalents (siliclastic-mafic or Besshi type VMS: Shanks and Thurston 2010), and (c) greenschists (metabasalts) and metaserpentinite of the Cretaceous Pounamu Ultramafics in Westland (Brathwaite and Pirajno 1993).

3.1 Mafic-ultramafic (Cyprus type) VMS deposits in Northland and East Cape

Previously mined Cu deposits at Pupuke, Pakotai and Parakao, and several other Cu deposits in Northland and at Lottin Point in East Cape are associated with allocthonous ophiolite sequences of Cretaceous-Tertiary age: the Tangihua Complex in Northland (Brathwaite et al. 2012) and Matakoa Volcanics in East Cape (Brathwaite et al. 2008). Geochemical trace and rare earth element studies (e.g. Whattam et al. 2004, 2005) have indicated that they contain island arc tholeiites, in addition to mid-ocean ridge basalts, and were formed in a suprasubduction zone setting close to their Late Oligocene obduction site. Exploration in East Cape from the 1980s, including reconnaissance and detailed geochemical, and airborne and ground based geophysical surveys, and 5 DDH at the Lottin Point prospect have so far failed to locate significant Cu resources.

3.2 Siliclastic-mafic or Besshi type VMS deposits associated with chert and pillow lava in greywacke

In both the North and South islands, several small siliclastic-mafic or Besshi type Cu deposits occur in Torlesse Supergroup and Waipapa Group greywacke, and Haast Schist associated with cherts and/or spilitic pillow lavas (Brathwaite and Pirajno 1993; Christie and Brathwaite 1994). The mineralization forms single or multiple stratiform bands, layers and lenses up to 6.7 m thick (Te Kumi) and 46 m long (Maharahara). Modern exploration has been limited to reconnaissance geochemical sampling.

3.3 Massive sulfide lenses in the Pounamu Ultramafics

Small massive sulfide lenses are present in Cretaceous greenschist metavolcanics and metaserpentinite of the Pounamu Ultramafics on the western side of the Southern Alps in Westland. The Pounamau Ultramafics are interpreted as ophiolite (ocean crust) basement to the Torlesse terrane (Cooper and Reay 1983). The sulfide lenses in the Wilberg Range appear to be the largest, with a 3 m to 9 m wide and 1500 m long mineralized zone containing numerous pyrite-chalcopyrite lenses (30 cm to 90 cm wide) (McPherson et al. 1970). Later exploration in the same area (Coleman 1980) identified a more extensive zone of mineralization comprising many small pods of massive sulfide within greenschist, with grades between 0.5 and 2.0% Cu. Higher grades, up to 5.1% Cu and 3.9 ppm Ag, were reported from sulfide lenses in the Diedrich Range.

4 Serpentine-hosted Fe-Cu

Small shear-controlled lenses of Cu mineralization are present in serpentinised ultramafic rocks of the Permian Dun Mountain Ophiolite Belt in the Nelson region (D'Urville Island and Dun Mountain) and in Southland (Red Mountain) (Williams 1994; Brathwaite and Pirajno 1993). Dun Mountain is the largest lens group, although even here the lenses are discontinuous and of small extent, with maximum dimensions of less than 150 m in length by 4 m in width. Primary ore was typically in the range of 1-1.5% Cu.

5 Gabbroid-associated Ni-Cu, Cu-Ni and Cu

In the South Island, several Paleozoic and Mesozoic mafic and ultramafic intrusive complexes, stocks and dikes have associated Ni-Cu, Cu-Ni or Cu mineralization formed from magmatic crystallization. The most significant occurrence is the Riwaka Complex in Northwest Nelson. The complex is a Late Devonian (ca. 364 Ma), SSW-NNE striking, elongate intermediate-mafic-ultramafic intrusive body 50 km long and ≤6 km wide representing a vertically sheeted conduit emplaced in an extensional back-arc post-orogenic setting (Turnbull et al. 2017). It intrudes metasedimentary rocks of Ordovician to Devonian age. The Ni-Cu mineralization occurs mainly in a 12 km long section of gabbro and pyroxenite between the Graham Valley and Prices Creek, where sulfide content ranges from 1-50%, characteristically with Ni>Cu. Drilling of 33 DDH between 1968 and 1976 gave best intersections of 0.60% Cu and 2.2% Ni over 1.4 m, 0.22% Cu and 1.52% Ni over 2.5 m, and 0.42% Cu and 1.42% Ni over 3.6 m (Christie and Turnbull 2016)

Nickel-Cu, Cu-Ni and Cu sulfide mineralization is also associated with mafic-ultramafic rocks in other areas (Table 1), some of which have received exploration attention for PGE, e.g. The Longwood Complex in Southland (Ashley et al. 2012).

6 Epithermal quartz veins

Chalcopyrite is present in several epithermal Au-Ag-base metal quartz vein deposits hosted in Miocene andesite and dacite of the Coromandel Group (Christie et al. 2007). The most Cu-rich veins are in the former gold mines between Tapu and Thames (e.g. Zeehan, Paroquet, Monowai, Comstock and Sylvia), and in the former base metal and gold mines at Tui and Waiorongomai respectively. Mining on the Champion and Ruakaka veins at Tui between 1967 and 1974, produced a concentrate containing 404 t of Cu, along with Zn, Pb, Ag, Au (Christie et al. 2007).

7 Porphyry Mo

Exploration in the late 1960s to early 1980s discovered a number of porphyry Mo deposits in the northwestern part of the South Island (Table 1). They are related to the emplacement of Late Cretaceous (120-106 Ma) I-type Separation Point suite granitoids into the Paleozoic S-type granites of the Karamea suite (e.g. Karamea Batholith) or quartzose metasedimentary rocks, mostly of the Aorere Group and Greenland Group (Eggers and Adams 1979; Brathwaite and Pirajno 1993). Most of the deposits are hosted by the metasedimentary rocks or by the intrusive Cretaceous granitic stocks, with a few hosted in Paleozoic Karamea suite granite (e.g. Taipo Spur). The geochemistry of the Mo-bearing granitoids is characterised by low K_2O, Rb, and F, and high Sr and Ti, confirming the classification of the deposits as Mo end members of the porphyry Cu-Mo family (Tulloch and Rabone 1993).

A slightly older (133.5 Ma) porphyry Mo deposit at Copperstain Creek occurs where granodiorite stocks and sills intrude lower Paleozoic Mount Arthur Marble and Onekaka Schist (Brathwaite et al. 2004). Skarn Cu mineralization is also present (see below). Exploration, including 14 DDH, outlined a Cu-bearing zone about 60 m wide and 760 m long, dipping steeply to the west and grading 0.06-0.6% Cu.

8 Skarn deposits

Copper occurrences with a skarn association include: Copperstain Creek, Mount Arthur, Arthur Range and Leslie River (Christie and Brathwaite 1994). At Copperstain Creek, skarns are developed in the calcareous rocks and exhibit a zonal pattern from an outer tremolite-actinolite-epidote±talc zone, through an intermediate diopside zone, to an inner garnet-magnetite±hedenbergite zone. Lateral zonation ranges from Mo in the granodiorite, out through Cu, to Pb-Zn in peripheral locations.

9 Conclusions

New Zealand has intermittently produced small quantities of Cu ore between 1846 and 1972, from several deposit types including porphyry Cu, VMS, serpentine-hosted Fe-Cu, and epithermal vein deposits. Although the known Cu deposits are all small, the varied geology and number of Cu occurrences offers exploration potential for future Cu production, possibly as a by-product of mining other metals (e.g. Au, Ni, PGE). Based on international examples, the porphyry Cu deposits are likely to yield the largest resources of Cu although other types may provide higher grades of Cu.

References

Ashley P, Craw D, MacKenzie D, Rombouts M, Reay A (2012) Mafic and ultramafic rocks, and platinum mineralization potential, in the Longwood Range, Southland, New Zealand. NZ J Geol Geophys 55:3–19

Bates TE (1980) Final report on EL 33-066 Paritu area, Coromandel Peninsula: Otter Mineral Exploration Ltd. NZ Petroleum & Minerals, MBIE unpublished report MR0378

Brathwaite RL, Christie AB, Lukovic B (2012) Desktop study documenting the occurrence and geological characteristics of known VMS deposits associated with Northland's Tangihua Complex. GNS Science Report 2012/08. 43 p

Brathwaite RL, Kamo SL, Faure K (2004) U-Pb geochronology and geochemistry of molybdenum-bearing granodiorite porphyry at Copperstain Creek, west Nelson, New Zealand. NZ J Geol & Geophys 47:219-225

Brathwaite RL, Pirajno F (1993) Metallogenic map of New Zealand. Institute of Geological and Nuclear Sciences Monograph 3.

Brathwaite RL, Sewell RJ, Christie AB (2008) Nature and tectonic setting of massive sulfide mineralization and associated sediments and volcanics in the Matakaoa Volcanics, Raukumara Peninsula, New Zealand. NZ J Geol Geophys 51:349-366

Brathwaite RL, Simpson MP, Faure K, Skinner DNB (2001) Telescoped porphyry Cu-Mo-Au, advanced argillic alteration and polymetallic quartz-sulfide-gold-anhydrite veins in the Thames District, New Zealand. Mineral Deposita 36:623-640

Christie AB, Brathwaite RL (1994) Mineral commodity report 4 - copper. New Zealand Mining 14:32-42

Christie AB, Simpson MP, Brathwaite RL, Mauk JL, Simmons SF (2007) Epithermal Au-Ag and related deposits of the Hauraki Goldfield, Coromandel Volcanic Zone, New Zealand. Econ Geol 102:785-816

Christie AB, Turnbull RE (2016) Exploration of nickel–copper mineralization in mafic and ultramafic rocks of the Riwaka Complex, West Nelson, South Island. AusIMM Monograph 31:453-462

Coleman AC (1980) Final report on the Wilberg area (PL 31527) Westland, New Zealand. Amoco Minerals NZ Ltd. NZ Petroleum & Minerals, MBIE unpublished report MR1664

Cooper AF, Reay A (1983) Lithology, field relationships, and structure of the Pounamu Ultramafics from the Whitcombe and Hokitika Rivers, Westland, New Zealand. NZ J Geol Geophys 26:359-380

Eggers AJ, Adams CJ (1979) Potassium-argon ages of molybdenum mineralization and associated granites of Bald Hill and correlation with other molybdenum occurrences in the South Island, New Zealand. Econ Geol 74:628-637

McPherson RI, Babcock RC, Howitt, G (1970) Final report on MPWs 8502, 8504 Wilberg Range, Westland. Kennecott Exploration Aust Pty Ltd. NZ Petroleum & Minerals, MBIE unpublished report MR1622

Shanks WCP, Thurston R eds (2012) Volcanogenic massive sulfide occurrence model.. U.S. Geological Survey Scientific Investigations Report 2010–5070–C, 345 p.

Tulloch AJ, Rabone SDC (1993) Mo-bearing granodiorite porphyry plutons of the Early Cretaceous Separation Point Suite, west Nelson, New Zealand. NZ J Geol Geophys 36:401–408, DOI: 10.1080/00288306.1993.9514586

Turnbull RE, Size WB, Tulloch AJ, Christie AB (2017) Theultramafic–intermediate Riwaka Complex, New Zealand: summary of the petrology, geochemistryand related Ni–Cu–PGE mineralization. NZ J Geol Geophys 60:270–295, DOI: 10.1080/00288306.2017.1316747

Whattam SA, Malpas JG, Ali JR, Smith IEM, Lo Ching-hua (2004). Origin of the Northland Ophiolite, northern New Zealand: discussion of new data and reassessment of the model. NZ Jour Geol & Geophys 47:383-389

Whattam SA, Malpas JG, Ali JR, Lo Ching-hua, Smith IEM. 2005. Formation and emplacement of the Northland Ophiolite, northern New Zealand: SW Pacific tectonic implications. Journal of the Geological Society, London 162:225-241.

Williams GJ (1974) Economic geology of New Zealand. AusIMM Monograph 4

Wodzicki A, Thompson BN (1970) The geology and mineralization of Coppermine Island. NZ J Geol Geophys 13:631-646, DOI: 10.1080/00288306.1970.10431334

New paradigms on phosphate mining in the Colombian industry: Crystallochemistry and geochemistry of phosphorites from the Lidita Superior Formation of Quebrada Talora, Colombia

Juan F. Correa-Briceño[1], Juan F. Galán-Palacios[1], Thomas Cramer[1]
[1]Departamento de Geociencias, Universidad Nacional de Colombia, Sede Bogotá

Abstract. X-ray-fluorescence (XRF) analysis and X-ray diffraction (XRD) techniques reveal rare earth elements (REEs) enrichment in granular sedimentary phosphorite rocks near the town of Piedras, Tolima, Colombia. These phosphorites are part of the Lidita Superior Formation, which is a Campanian-aged lithostratigraphic unit located in the Upper Magdalena Valley**.** High radiation levels of up to 0.6 µSv/h in these phosphorus strata stem from uranium found in concentrations of 65 ppm. Additionally, these intervals are rich in benthic foraminifera and bone remains and have shown an enrichment of up to 800 ppm of the sum of Rare Earth Elements and yttrium (ΣRE-Y). Based on a combined petrographic study that incorporates both X-ray diffraction (XRD) and X-ray fluorescence (XRF) analyses, we present a discussion on the potential of using radioactivity as an indicator of REEs enrichment. Furthermore, we propose that this approach can be utilized as an exploratory tool to optimize beneficiation processes and maximize the exploitation of these elements. Ultimately, our proposal aims to promote a transition towards a circular mining model.

1 Introduction

In Colombia, studies about the distribution of phosphatic deposits mainly in sedimentary rocks, phosphate prospecting techniques, and mining as well as fertiliser development were carried out since the 1960s by the Colombian Geological Survey (SGC, former Ingeominas) and other authors (Burgl et al. 1967; McKelvey 1967; Cathcart et al. 1967; Irving E 1967). About 90% of phosphatic rocks are used as raw material for producing fertilizers. Colombia is currently the fifth largest producer of phosphates on the continent, after the United States, Brazil, Peru and Mexico. In the last 5 years, approximately 65 thousand tonnes of phosphate have been produced on average per year in Colombia, and total World market demand is estimated to grow from 250 Mt in 2024 to 263 Mt in 2035, driven by the need to feed a growing world population and by the constraints of arable land expansion, which will require higher fertiliser application rates (UPME 2018).

Marine phosphorites may be interesting because of their potential to enrich rare earth elements and yttrium (RE-Y) (e.g. Hein et al. 2016) as well as U, Th and other incompatible elements, mainly incorporating them in different crystallographic sites of apatite-series minerals [$Ca_5(PO_4)_3(Cl,F,OH)$]. Global REE demand is increasing by 8-12% per year and is expected to double from 300,000 tonnes in 2022 to 600,000 tonnes in 2030 (World Energy Trade Platform 2022). So, obtaining REEs as a by-product of phosphorite mining becomes increasingly attractive and necessary. About this, the systematic exploration and extraction of REEs in Colombia is still in its beginnings and focus more on associated magmatic-hydrothermally formed minerals like monazite, coltan, cassiterite or uranium phases in the NW-Amazonian Craton region, with informal mining, if any.

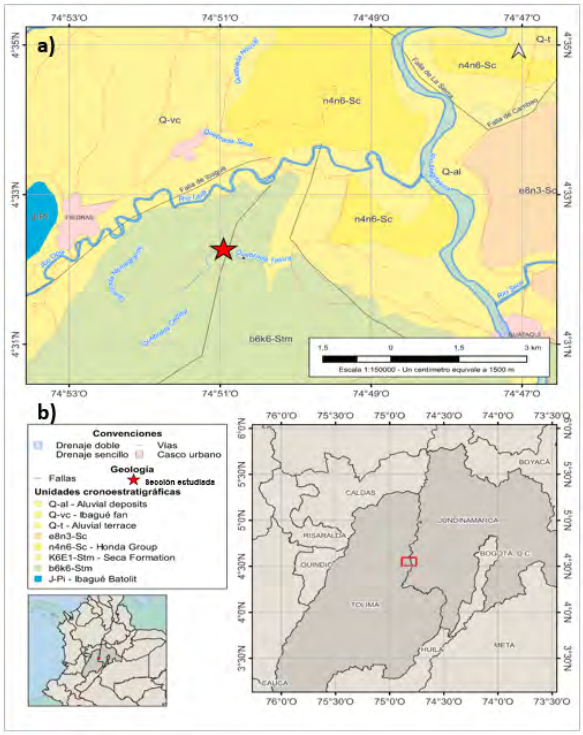

Figure 1. a Simplified geological map of the study area at scale 1:100,000, modified from the cartographic base of Girardot plate 245 of Acosta et al. (1999). See the lithostratigraphic unit studied, the Lidita Superior Formation, and the location of the Quebrada Talora. **b.** Location of the section studied. Physiographically, it is the northernmost part of the Upper Magdalena Valley, 40 km east of Ibague and 75 km west of Bogotá.

Much less is known in Colombia about REEs distributions in marine phosphorite deposits formed in different Cretaceous sedimentary rocks. Therefore, this study tries to fill partly this gap by determining whether phosphorite layers in the Cretaceous Upper Lidita Formation deposited in the

Upper Magdalena River Valley (Fig 1a) host economically interesting REEs concentrations.

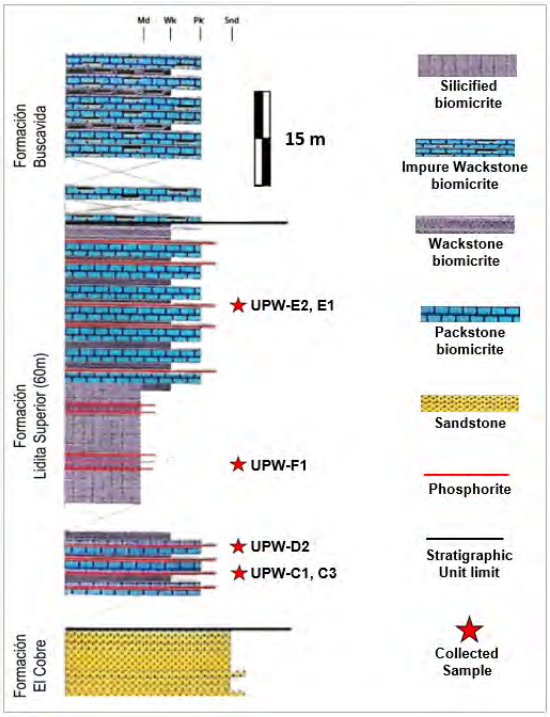

Figure 2. Stratigraphic column with the studied Upper Lidita Formation, showing, as red lines, the phosphorus-rich levels, and as red stars, the sampling sites. Modified from Guerrero et al. (2000).

2 Methodology

2.1 Sample collection and petrography

Two field trips to Quebrada (=Creek) Talora, east of Piedras town, in the Tolima Department, allowed field descriptions and collecting of 30 samples of the phosphorus-rich levels (Fig 2) previously reported by Guerrero et al. (2000) in the Lidita Superior Formation. From the 10 most significant samples, considering their texture, facial changes and distribution in the stratigraphic column, ten polished thin sections were prepared in the MinerLab laboratory.

2.2 X-ray fluorescence geochemistry

Phosphorite samples UPW-E2 and UPW-C3 were analysed at the X-ray spectroscopy laboratory of the Universidad Nacional de Colombia using a MagixPro PW 2440 Philips (WDXRF) X-ray fluorescence spectrometer, equipped with a rhodium tube, a maximum power of 4 kW and a sensitivity of 100 ppm for heavy metallic elements. Samples were powdered and dried at 105°C for 12 hours, then mixed with Merck spectrometric wax in a 10:1 ratio, homogenized by stirring, and compacted in a hydraulic press at 120 kN for one minute, to produce two pellets of 37 mm diameter. The measurement applying 11 scans was performed using the Semio5 software, in order to detect all the elements present in the sample, excluding H, Li, Be, B, N, C, O, noble gases and transuranic elements.

2.3 X-ray diffraction and γ-ray spectroscopy

Seven samples (UPW-C1, UPW-C3B, UPW-D1, UPW-E1, UPW-C3TF, UPW-E2 and UPW-C3TL) were analysed by means of a Bruker D2-Phaser diffractometer using Cu-K-alpha radiation without monochromator, 100 W, steps of 0.019° in a range of 4° to 60° 2theta. Following Thorez (1976), first the non-oriented sample powder <50 micrometers were analysed, then the finer fraction was suspended in deionized water and placed on a slide for subsequent desiccation and orientation of the clay minerals. For the analysis of expansive clays, ethylene glycol was included in their crystalline structure to increase the interlaminar distance (Thorez, 1976). Finally, the samples were heated at 515°C to extract the water molecules from the hydrated mineral structure. The diffraction patterns were analysed using the Rietveld method integrated in the Profex v5.1 software.

In addition, for radiation measurement on the UPW-E2 sample, a Probe VB6 VGO 2 gamma-ray spectrometer was used (Fig 5).

3 Comparison of results from XRD- and XRF analyses

The average P_2O_5 concentration in active phosphorite mines in Colombia was assumed to be 30% (Cantera et al. 2008). Our XRD phosphorite analyses reveal an average fluorapatite concentration of 49% in rocks ranging in thickness from 2 to 30 cm (Figs 2 and 3). Figure 4 compares XRF values in phosphorite samples UPW-E1 and UPW-C3TF, showing enrichment of Si, Al, Fe, S, Ce, Pb, and U at similar values of ~25% P_2O_5 and 300 ppm Cl in the Si-richer and Ca-poorer level UPW-C3TF. The 300 ppm Cl indicates a certain Cl-apatite content in the F-apatite determined by XRD. Total cerium of 600 ppm, lanthanum of 300 ppm and yttrium of 195 ppm are comparable to those obtained in seamount phosphorites described by Hein et al. (2016). Figure 6 shows a 124-fold enrichment process for Y, 1265-fold for La and 978-fold for Ce in the studied phosphorites compared to chondrites.

Figure 3 exhibits an inverse relationship between the amount of quartz and the amount of fluorapatite + calcite. This reflects a sedimentological process where the richest phosphate levels also show enriched Ce-La-Y concentrations and low silicification, which determines the ease of extraction of the material because silicification increases the costs of the beneficiation processes.

Data on REEs concentrations presented by Grosz et al. (1995) report on average 460 ppm REEs in phosphorite commonly contained in the francolite (a CO_2- and F-rich apatite) crystal structure. The phosphorites studied in this work (from the Lidita Superior Formation) contain up to 800 ppm Ce-La-Y contained in the fluorapatite structure, a 73% enrichment with respect to those compiled by Grosz et al. (1995). Assuming a typical phosphorite used in fertilizer manufacturing has the same REEs content, the amount of phosphate rocks mined worldwide annually contains more than 70,000 t of REEs.

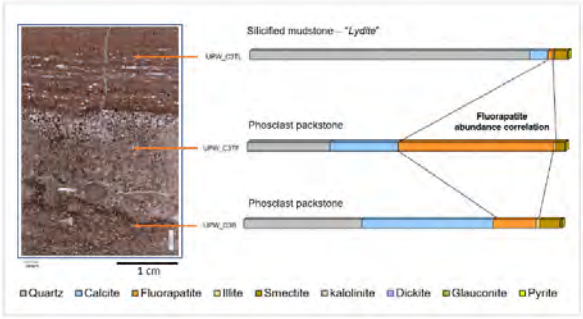

Figure 3. XRD results at three levels with distinguishable sedimentological features in the digitalized thin section C3A which shows the predominant lithologies (silicified mudstone "lydite" and phosphorites) in the lower and upper segment of the studied lithostratigraphic unit (Fig 2). Nomenclature after Trappe (2001).

4 Approach to new paradigms for phosphate rock exploration and exploitation in Colombia

From sixty-three phosphatic rocks mining titles in Colombia, 70% were being exploited and 30% were under construction and assembly (UPME 2018). The production of phosphate rock in Colombia in 2016 was 66,324 tonnes per year. Assuming a 50% benefaction rate when extracting RE-Y as a co-product of phosphoric acid, considering the average production of phosphate rock in Colombia and the total values of ∑Ce-La-Y exposed in this work, Colombia has the potential to extract up to 1300 tonnes of RE-Y and become one of the main REE-producers in Latin America.

Wu et al. (2018) and Emsbo et al. (2015) demonstrated the feasibility of solvent extraction of REEs as a co-product of phosphate mining, thus phosphorites are now considered an important potential source for industrial REEs supply. This work may awake the interest of private exploration companies and public entities such as the SGC or the ANM in a new exploration target which includes REEs beneficiation processes during the phosphate extraction emulating the circular mining models of developed countries such as China, USA and Russia, thus providing an opportunity for Colombia to diversify its mineral basket, provide competitive conditions that promote the exploration and exploitation of REEs, generate new sources of employment and tax revenues for the regions, making the country more attractive to investors and, at the same time, allowing the areas to be exploited in an orderly and efficient manner, contributing to social development, in harmony with the environment and with other economic activities.

Different methods exist to extract REEs from phosphorites, including acid leaching, solvent extraction and precipitation; these methods are expensive and require specialized technologies, but the growing demand for REEs has prompted research and development of more efficient and economic processes that will have to be implemented to optimize the beneficiation process. Recovery of these marine-sediment-hosted REEs would require the addition of costly infrastructure and changes in extractive processing to the existing mining operations. Production of RE-Y as a co-product of phosphorite mining would be advantageous if considered in the early stages of planning a new mining operation.

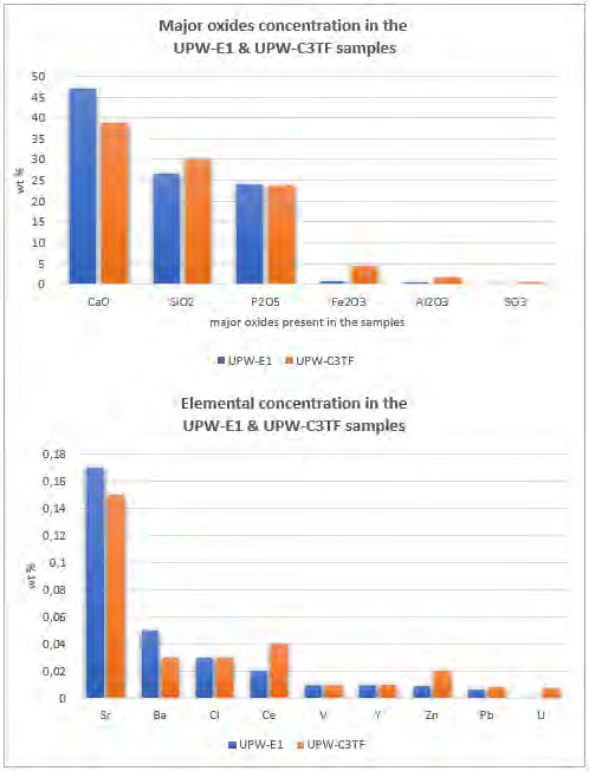

Figure 4. Bar charts of XRF-element concentrations in phosphorite samples UPW-E1 and UPW-C3TF.

Isotope	Concentration	Contribution of total radioactivity
Uranium	8.0 ppm	59.7%
Thorium	5.4 ppm	40.3%

Figure 5. Gamma-ray spectroscopy results for sample UPW-E2.

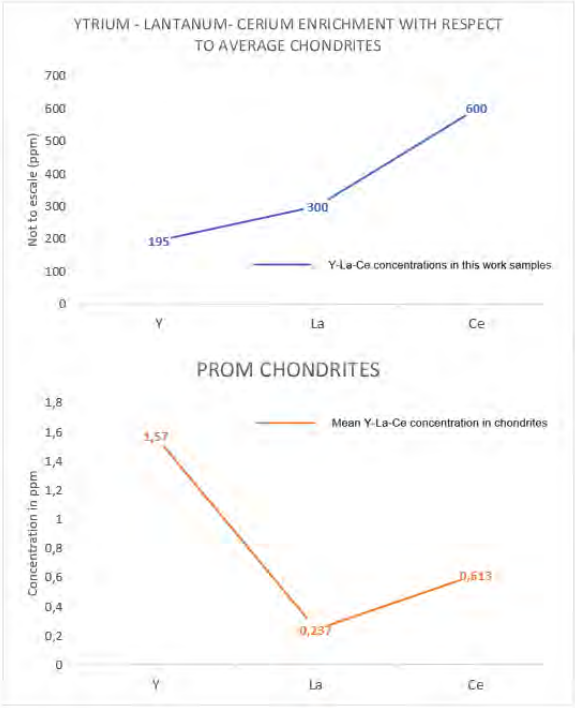

Figure 6. Ce-La-Y abundance of the UPW-E1 & UPW-C3TF samples and the average abundance of Ce-La-Y in chondrites after McDonough and Sun (1995).

5 Conclusions

Deposits with high RE-Y contents, such as the marine phosphorites analysed in this research, could help supply the RE-Y needed for high-tech and green technology applications without creating an oversupply. The Ce-La-Y concentrations (up to 800 ppm in total) are high enough to be considered as a co-product of phosphorite extraction. Combined XRF and XRD analysis indicates that fluorapatite is the main host of P and REE; elements such as Ce, La, Y, Sr and U replace Ca- cations in the crystal structure of fluorapatite (Trappe 1998). This inquiry provides evidence that Colombia's phosphate exploration and extraction endeavours must be invigorated by novel exploratory paradigms that allow for the assessment of beneficial phosphate recovery processes. Phosphorite, a potentially economic REEs resource, represents a prospect that warrants extensive and systematic investigation to ensure that its extraction not only persists but is optimized to capitalize on elements that will be instrumental in the nation's development and energy transition.

Acknowledgments

We are grateful to the SGA for the financial support to present this work at the 17th SGA Biennial Meeting, also to Professor Carlos Alberto Sánchez for his advice and support, as well as to Denis Oi Ulu for giving us his time and experience to carry out this research, to the Lattice laboratory with Professor Gustavo Sarmiento for supporting us in carrying out the XRD-analysis and to the MicrofluidSpectral Laboratory for the digitization of the thin sections.

References

Acosta J, Guatame R, Torres O, Solano F (1999) Geología de la Plancha 245 Girardot [Map]. INGEOMINAS.

Bürgl H, Botero D (1967) Las capas fosfáticas de la Cordillera oriental. Boletín Geol 15:7-44.

Cantera V (2008) Selección de la mejor alternativa para la industrialización de la roca fosfórica del Dpto. del Huila. Gobernación Huila 1:1-33

Catchcart J, Zambrano F, Mojica P (1967) Roca fosfática en Colombia. Boletín Geol 15:65-162.

Emsbo P, McLaughlin P, Breit G, du Bray E, Koenig A (2015) Rare earth elements in sedimentary phosphate deposits: Solution to the global REE crisis? Gondwana Research Int Geol J 27(2):776–785. https://doi.org/10.1016/j.gr.2014.10.008

Grosz A, Meier A, Clardy B (1995) Rare earth elements in the Cason Shale of Northern Arkansas: a geochemical reconnaissance. Arkansas Geological Commission Circular IC-33:22-55

Guerrero J, Sarmiento G, Navarrete R (2000) The Stratigraphy the W Side the Cretaceous Colombian Basin in the Upper Magdalena Valley. Reevaluation of Selected Areas and Type Localities Including Aipe, Guaduas, Ortega, and Piedras. Geol Colombina 25:45-110.

Hein J, Koschinsky A, Mikesell M, Mizell K, Glenn C, Wood R (2016) Marine Phosphorites as Potential Resources for Heavy Rare Earth Elements and Yttrium. Min: 6:88-92. doi:10.3390/min6030088

Irving E (1967) Conceptos preliminares sobre el Desarrollo y uso de fertilizantes en Colombia. Boletín Geol 15:163-174.

McDonough W, Sun S (1995) The composition of the Earth. Chemical Geol 120(3-4):223–253. doi:10.1016/0009-2541(94)00140-4.

McKlevey V (1967) Nuevas técnicas en la prospección para yacimientos de fosfatos. Boletín Geológico 15:45-64.

Thorez J (1976). Practical identification of clay minerals. Min 13(2): 238–239. doi.org/10.1180/claymin.1978.013.2.11.

Trappe J (1998) Phanerozoic Phosphorite Depositional Systems. A Dynamic Model for a Sedimentary Resource System. Springer, Germany

Trappe J (2001) A nomenclature system for granular phosphate rocks according to depositional texture. Sedimentary Geol 145(1–2): 135–150. doi.org/10.1016/s0037-0738(01)00103-8

Unidad de Planeación Minero-Energética (2018) Informe de gestión. https://www1.upme.gov.co/InformesGestion. Accessed 05 January 2023.

World Energy Trade (2021) Canada's first rare earth producer begins shipping concentrate. https://www.mining.com/canadas-first-rare-earth-producer-begins-shipping-concentrate/. Accessed 26 December 2022.

Wu S, Wang L, Zhao L, Zhang P, El-Shall H, Moudgil B, Huang X, Zhang L (2018) Recovery of rare earth elements from phosphate rock by hydrometallurgical processes – A critical review. Chem Eng J 335:774–800 doi.org/10.1016/j.cej.2017.10.143

Fluid inclusions host germanium in acicular sphalerite from the carbonate-hosted Zhulingou Pb-Zn deposit, South China

Alexandre Cugerone[1], Kai Luo[2], Denis Fougerouse[3,4], Jia-Xi Zhou[2], Vincent Motto-Ros[5]
[1] *Department of Earth Sciences, University of Geneva, Switzerland*
[2] *Key Laboratory of Critical Minerals Metallogeny in Universities of Yunnan Province, Yunnan University, China*
[3] *School of Earth and Planetary Sciences, Curtin University, Australia*
[4] John de Laeter Centre, Curtin University, Australia
[5] *Institut Lumière Matière UMR 5306, Université Lyon 1 - CNRS, France*

Abstract. Sphalerite is frequently considered to host critical metal concentrations such as Ge, Ga and In. These elements are thought to be mainly incorporated via substitution mechanisms into the sphalerite lattice. However, the nanoscale distribution of Ge, Ga and In is still poorly understood, especially if these elements are incorporated in the sphalerite crystal lattice or in other discrete mineral and/or fluid phases. Using a combination of microstructural, geochemical and nanoscale observations, a new type of Ge occurrence is recognized in stratabound sphalerite from the Zhulingou carbonate-hosted Zn(-Ge) deposit. Early stage sphalerite is represented by acicular crystals with high Ge concentrations (up to ~2000 ppm), which are positively correlated with Pb, Fe, and Mn concentrations. High Ge concentrations usually occur in dark brown oscillatory coloured bands, which are interpreted to have formed through rapid precipitation of sphalerite. Preliminary nanoscale data, performed with atom probe tomography (APT), indicate that Ge and related elements are mainly found in nanoscale fluid inclusions, and subordinately in nanoscale Ge-Pb rich phases. This study promotes the use of nanoscale studies to better understand the sequestration of critical metals in sulfides.

1 Introduction

Sphalerite frequently contains significant quantities of critical metals such as Ge, Ga and In. Solely based on chemical data conducted at the micron scale, these concentrations are frequently considered to be hosted in the sphalerite lattice (Cook et al. 2009; Belissont et al. 2016; Hu et al. 2021). The distribution of Ge, Ga and In in sphalerite may be complex and trace elements might be hosted in various microscale chemical zones such as sector zones, micrometric rhythmic bands or millimetric oscillatory color bands.

Acicular sphalerite frequently exhibits millimeter scale oscillatory color bands and can host significant amount of Ge (Cook et al. 2015; Luo et al. 2022). In this case, Ge is frequently correlated with Pb, Mn, Fe. However, in euhedral sphalerite, Ge is commonly correlated with Cu (Belissont et al. 2016).

Very few studies exist at the nanoscale, and presently, they don't consider all the sphalerite types, especially acicular sphalerite. A recent study describes the nanoscale distribution of Ge in Cu-rich sphalerite, showing Ge mostly occurring in sphalerite lattice in euhedral sphalerite, or Ge hosted in Ge-Cu rich minerals (briartite) in deformed sphalerite (Cugerone et al. 2021; Fougerouse et al. 2023).

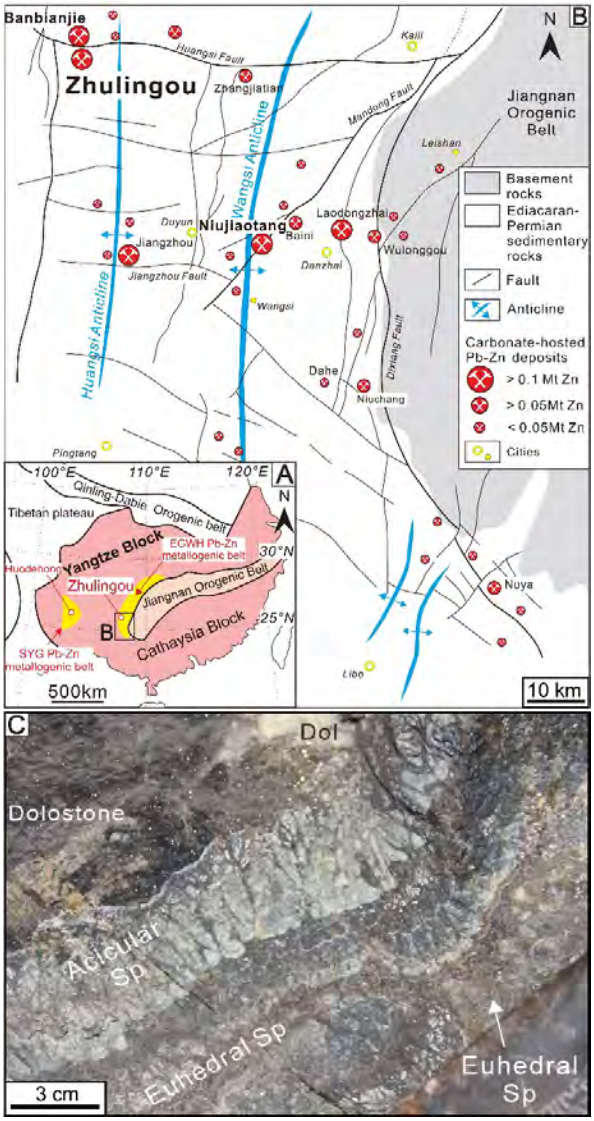

Figure 1. A. Location of the Zhulingou deposit in the eastern Guizhou-western Hunan (EGWH) metallogenic belt, South China. B. Simplified structural map showing the location of Zhulingou and the E-W Huangsi fault. C. Outcrop photo of a typical stratabound Pb-Zn ore body from Zhulingou. Note the presence of euhedral sphalerite generally more developed at the center of the stratabound bodies.

At Zhulingou, a mix of acicular and euhedral sphalerite represent a perfect material to study the incorporation of Ge depending on the sphalerite texture and their related formation conditions. In this study, we performed textural and chemical measurements with multiple techniques, from the microscale with electron back-scattered diffraction (EBSD), laser ablation coupled plasma mass spectrometry (LA-ICPMS), and laser-induced breakdown spectroscopy (LIBS), to the nanoscale with high-angle annular dark-field scanning transmission electron microscopy (HAADF-STEM) and atom probe tomography (APT) measurements.

2 The Zhulingou deposit

South China is known to host about one thousand Pb-Zn(-Ge) carbonate-hosted deposits. The Zhulingou Zn-Ge deposit (0.28 Mt Zn and >400 t Ge @ 97.9 g/t) is part of the eastern Guizhou-western Hunan (EGWH) metallogenic belt, South China (Figure 1A). This deposit is hosted in Devonian carbonate rocks and is lithologically and structurally controlled. The deposit is composed of stratabound orebodies hosted in carbonate-mudstone facies transition zones and late Paleozoic faults (Huangsi fault; Figure 1B).

At Zhulingou, two hydrothermal (< 200 °C) stages are recognized (Figure 1C; Luo et al. 2022): i) an early stage is composed of acicular sphalerite with oscillatory color bands and ii) a late stage is constituted of euhedral sphalerite with sector zones. From acicular to euhedral sphalerite, Ge concentrations decrease progressively with mean contents from 1009 to 490 ppm Ge, respectively (Luo et al. 2022).

3 Methods

In this study, we have analysed two representative samples where acicular and acicular-euhedral sphalerite are well preserved. These two samples were selected among sixty samples collected at Zhulingou.

EBSD analyses were carried out by the NordlysNano + AZtecHKL electron backscattered diffraction (EBSD) system from Oxford Instruments, on a FEI Quanta 450 FEG environmental scanning electron microscope at China University of Geosciences, Wuhan, China. Working conditions were as follows: 20 kV accelerating voltage, 25 mm working distance, 70°sample tilt angle. The sample was uncoated and well-polished for better pattern quality in a low-vacuum mode of 30 Pa. A step size of 1 µm was chosen. The Channel 5+ software was used for processing the data and generating the maps.

Laser-Induced Breakdown Spectroscopy (LIBS) multi-elemental imaging was performed at the Institute Lumière Matière, University of Lyon 1 (France). The two samples were analysed using a nanosecond Nd:YAG laser with a pulse energy of 600 IJ operating at 100 Hz at the fundamental wavelength (1064 nm). A 15x magnification lens (LMM-15X-P01, Thorlabs, Germany) was used to focus the laser pulses on the sample surface. In this configuration, the size of the ablation craters for a single laser shot was in the range of 8 µm. In the shown images, the lateral resolution (step size) was 19 µm. All experiments were conducted at room temperature under ambient pressure conditions. In addition, the laser pulse energy and its focus onto the sample were strictly controlled. Two spectrometers were configured to detect intense lines of Ge, Pb and Fe. The general protocol used for the construction of the elemental images is described in Motto-Ros et al. (2019).

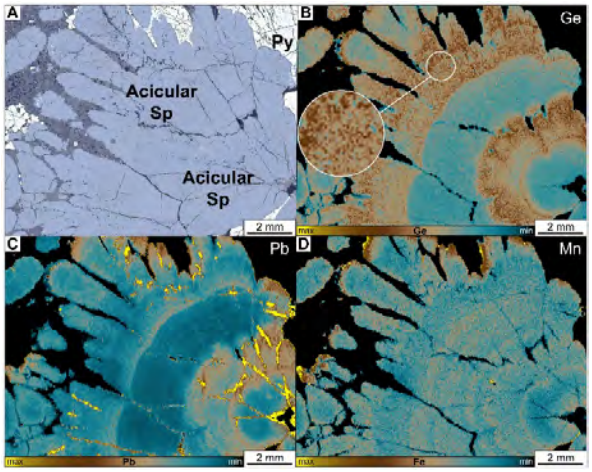

Figure 2. A. Reflected light microphotograph of acicular sphalerite from Zhulingou. B-D. LIBS Ge, Pb and Mn maps of the area in (A). Note the positive correlation in Ge and Pb in acicular sphalerite. In oscillatory bands, Ge does not show a homogeneous distribution in the Ge-rich oscillatory bands. Very high Pb concentrations are observed in fractures associated with organic matter.

LA-ICP-MS mapping was performed on a sphalerite sample with a mix of acicular and euhedral textures to determine minor and trace element concentrations, using a NWR ablation system (λ = 193 nm) coupled to an iCAP RQ ICP-MS instrument at Guangzhou Tuoyan Analytical Technology Co., Ltd., Guangzhou, China. LA-ICP-MS elemental mapping was performed using the same laser ablation system with similar carrier gas settings as for spot analysis. The selected area (~1 mm * 5 mm) was mapped using laser energy of 3.5 J/cm^2, a repetition rate of 20 Hz, 10 µm spot size, and stage translation speed of 40 µm/s. The following isotopes were selected: ^{23}Na, ^{29}Mg, ^{32}S, ^{55}Mn, ^{57}Fe, ^{65}Cu, ^{70}Zn, ^{71}Ga, ^{74}Ge, ^{75}As, ^{107}Ag, ^{111}Cd, and ^{208}Pb. Data were processed using an Excel-based software Iolite 3.6 to perform off-line selection and integration of background and analysed signals, time-drift correction, and quantitative calibration.

Transmission electron microscopy (TEM) on the acicular sphalerite was prepared by Ga-ion milling using a Focused Ion Beam device (FEI-FIB200) at the Institute of Geochemistry, Chinese Academy of Sciences, Guiyang, with an acceleration voltage of

30 kV. High-angle annular dark-field scanning transmission electron microscopy (HAADF-STEM) and high-resolution TEM (HRTEM) analyses were performed at the Electron Microscopy Center of the Guangzhou Institute of Geochemistry, Chinese Academy of Sciences, Guangzhou.

Five APT specimens adjacent to TEM targets were prepared from the investigated sphalerite to investigate the detailed chemical composition. A TESCAN Lyra3 Ga^+ focused ion beam scanning electron microscopy (FIB-SEM) was used to prepare atom probe needle-shaped specimens. The specimens were then analysed by the CAMECA LEAP 4000X HR Geoscience Atom Probe in the John de Laeter Centre at Curtin University (Perth, Australia). During the ~ 5 h acquisitions, 15 million ions were collected from each of two specimens (specimen 1 and 2) at an evaporation rate of 0.01 ions/pulse, a UV laser (l = 355 nm) energy of 45-50 pJ per pulse, and a pulse rate of 125 kHz. The data was reconstructed in 3D using parameters suggested by Fougerouse et al. (2022).

4 Trace element distribution in acicular sphalerite

Acicular sphalerite is composed of pluri-centimeter-size crystals (Figure 2A) with radial shapes which can be observed with light grey to brown colors in hand specimens (Figures 1C and 2A). Oscillatory zoning coloured from dark to light brown under plane polarized light are perpendicular to the maximum length of acicular crystals (Figures 2 and 3). Importantly, Ge and Pb concentrations (up to few thousands of ppm) are noticed, with a generally positive correlation, except in fractures where Pb-rich organic matter is noticed (Figures 2B-C). Manganese concentrations are also broadly correlated but occur in lower concentrations than Pb and Ge in sphalerite (up to ~ 100ppm Mn; Figure 2D).

In Figures 3A-B, EBSD maps show higher amounts of low-angle misorientation (1-5°) as well as twin boundaries (Figures 3C-E) in acicular sphalerite compared to euhedral sphalerite. LA-ICP-MS maps (Figures 3F-L) show important zoning patterns. Dark brown bands are rich in Mn, Ge, Fe, and Pb. Zones with high Ge concentrations generally correspond to zones with high Na concentrations. Gallium and Cd are negatively correlated to Ge.

5 Nanoscale study in acicular sphalerite

At nanoscale, APT measurements were performed on acicular sphalerite to detect the distribution of Ge and related elements. Numerous up to ~ 60 nm-sized clusters are identified and contain Na, Fe, Ca, Ga, Ge, Cd, H_3O^+, and Pb (Figure 4). They are generally distributed homogeneously but locally depleted close to twin boundaries (low cluster density area in Figure 4A). Germanium and Ga reach up to 2516 ppm and 416 ppm in the clusters, and 285 ppm and 173 ppm in the lattice, respectively. Hydrogen concentrations in Na-Pb clusters are up to 4230 ppm, considerably higher than in the lattice (10 ppm) and suggest the presence of aqueous fluids in the clusters based on the geometrical outlines and relatively light contrast TEM/HAADF bright-field image. HAADF and TEM images show the occurrence of germanium particles associated with galena and porosity in acicular sphalerite (Figure 4).

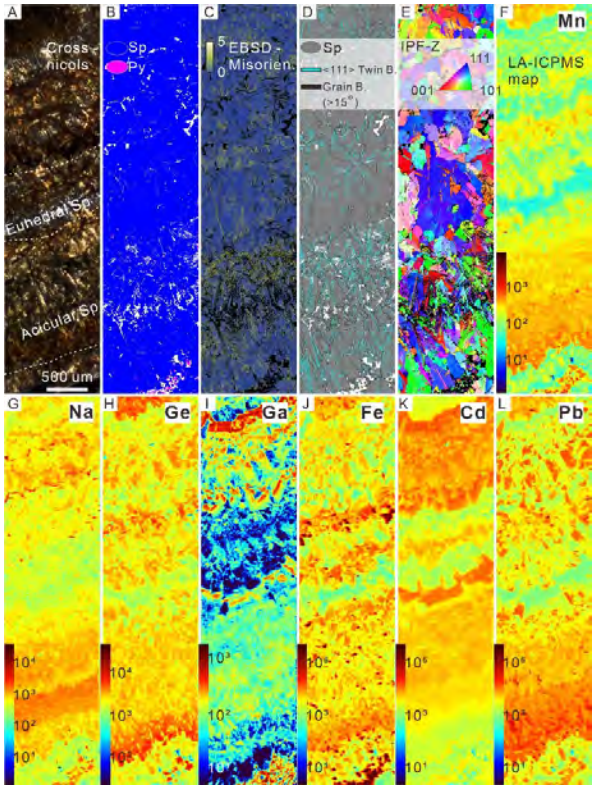

Figure 3. Micro-textures and LA-ICP-MS maps of acicular-euhedral sphalerite. A. Plane polarized transmitted light scan. B. Phase map acquired with EBSD. C. EBSD map showing low angle misorientation (1-5°). C. EBSD map showing high angle misorientation boundaries such as twins (60°) and grain boundaries (15°). D. EBSD inverse pole figure according to the Z-axis map. F-L. LA-ICP-MS maps of Mn, Na, Ge, Ga, Fe, Cd and Pb.

6 Discussion and implications

One of the most common sulphides with observed oscillatory banded textures is sphalerite (Ramdohr 1969; Barrie et al. 2009). These textures can be associated with acicular crystals (Ramdohr 1969; Beaudoin 2000) typically formed by supercooling (< 150 °C) and/or supersaturation conditions, inducing rapid crystal growth. Based on our observation at Zhulingou, we suggest that these conditions of quick precipitation of zinc sulphide are optimal for the preservation of significant concentrations of critical metals (Ge, Ga). Paradoxically, these conditions may not be ideal for the incorporation of trace metals in the sphalerite lattice. Most of the Ge and other elements like Na, K, Pb, Mn are observed in nanoscale clusters. These

clusters are interpreted as nanoscale fluid inclusions because of their concentrations in light elements (Na, Ca, K, H) and their characteristic rounded to elongated shapes. These nanoscale fluid inclusions are primary and not associated to late structures such as fractures or low angle misorientation (1-5°). Local nanoscale mineral phases are also inferred but directly associated with nanoscale fluid inclusions.

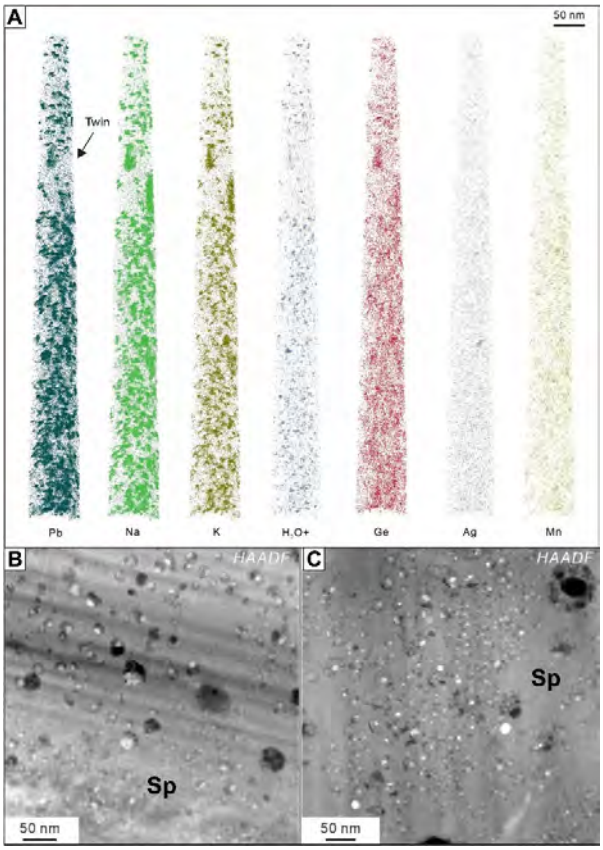

Figure 4. Nanoscale distribution of Ge and related elements in clusters/fluid inclusions hosted in acicular sphalerite. A. Atom probe map showing the distribution of Pb, Na, K, H3O+, Ge, Ag and Mn. B-C. HAADF images showing random distribution of the clusters at nanoscale. In these clusters, two phases (presumably liquid+vapor) are frequently observed, indicating occurrence of fluid inclusions. Brighter spots represent Pb(-Ge) solids.

Nanoscale studies are key to understanding the precise incorporation mechanism of critical metals in sphalerite. Although previous studies interpreted (based on geochemical analyses) that Ge was mostly incorporated in the sphalerite crystal lattice (Cook et al. 2009; Belissont et al. 2016), our results could indicate that Ge and associated elements such as Pb, Ca, K are generally associated with nanoscale fluid inclusions in acicular sphalerite. This study shows that Ge enrichment is higher in acicular sphalerite, and we interpret this relationship to be caused by the quick precipitation of acicular sphalerite. These conditions are not favorable to the incorporation of Ge in the sphalerite lattice but then preserves considerable amounts of Ge (up to 2000 ppm Ge) in nanoscale particles associated with the primary fluid phase.

Acknowledgements

This research was financially supported by the National Natural Science Foundation of China (42172082 and 92162218), Major collaborative innovation projects for prospecting breakthrough strategic action of Guizhou Province, China ([2022] ZD004), Guangdong Basic and Applied Basic Research Foundation (2022B1515020007), and Youth Innovation Promotion Association CAS (2021353).

References

Barrie CD, Boyce AJ, Boyle APP, Williams PJJ, Blake K, Wilkinson JJJ, Lowther M, McDermott P, Prior DJ, MacDermott P, Prior DJ (2009) On the growth of colloform textures: a case study of sphalerite from the Galmoy ore body, Ireland. J Geol Soc London 166:563–582. doi: 10.1144/0016-76492008-080

Beaudoin G (2000) Acicular sphalerite enriched in Ag, Sb, and Cu embedded within color-banded sphalerite from the Kokanee Range, British Columbia, Canada. Can Mineral 38:1387–1398. doi: 10.2113/gscanmin.38.6.1387

Belissont R, Munoz M, Boiron M-C, Luais B, Mathon O (2016) Distribution and oxidation state of Ge, Cu and Fe in sphalerite by µ-XRF and K-edge µ-XANES: Insights into Ge incorporation, partitioning and isotopic fractionation. Geochim Cosmochim Acta 177:298–314. doi: 10.1016/j.gca.2016.01.001

Cook N, Etschmann B, Ciobanu C, Geraki K, Howard D, Williams T, Rae N, Pring A, Chen G, Johannessen B, Brugger J (2015) Distribution and Substitution Mechanism of Ge in a Ge-(Fe)-Bearing Sphalerite. Minerals 5:117–132. doi: 10.3390/min5020117

Cook NJ, Ciobanu CL, Pring A, Skinner W, Shimizu M, Danyushevsky L, Saini-Eidukat B, Melcher F (2009) Trace and minor elements in sphalerite: A LA-ICPMS study. Geochim Cosmochim Acta 73:4761–4791. doi: 10.1016/j.gca.2009.05.045

Cugerone A, Cenki-tok B, Muñoz M, Kouzmanov K, Oliot E, Motto-ros V, Goff E Le, Motto-ros V (2021) Behavior of critical metals in metamorphosed Pb-Zn ore deposits : example from the Pyrenean Axial Zone. Miner Depos 56:685–705. doi: doi: 10.1007/s00126-020-01000-9

Fougerouse D, Cugerone A, Reddy SM, Luo K, Motto-ros V (2023) Nanoscale distribution of Ge in Cu-rich sphalerite. Geochim Cosmochim Acta 346:223–230. doi: 10.1016/j.gca.2023.02.011

Fougerouse D, Saxey DW, Rickard WDA, Reddy SM, Verberne R (2022) Standardizing Spatial Reconstruction Parameters for the Atom Probe Analysis of Common Minerals. Microsc Microanal 28:1221–1230. doi: 10.1017/S1431927621013714

Hu X, Chen Y, Liu G, Yang H, Luo J, Ren K, Yang Y (2021) Numerical modeling of formation of the Maoping Pb-Zn deposit within the Sichuan-Yunnan-Guizhou Metallogenic Province, Southwestern China: Implications for the spatial distribution of concealed Pb mineralization and its controlling factors. Ore Geol Rev 140:104573. doi: 10.1016/j.oregeorev.2021.104573

Luo K, Cugerone A, Zhou M-F, Zhou J-X, Sun G-T, Xu J, He K-J, Lu M-D (2022) Germanium enrichment in sphalerite with acicular and euhedral textures: an example from the Zhulingou carbonate-hosted Zn(-Ge) deposit, South China. Miner Depos. doi: 10.1007/s00126-022-01112-4

Motto-Ros V, Moncayo S, Trichard F, Pelascini F (2019) Investigation of signal extraction in the frame of LIBS imaging. Spectrochim Acta - Part B At Spectrosc 155:127–133. doi: 10.1016/j.sab.2019.04.004

Ramdohr P (1969) The ore minerals and their intergrowths. Pergamon Press Ltd, Head Hill Hall, Oxford 4 5 Fitzroy Square, London W 1 1179

Critical raw material potential of the North Pennine Orefield, England

David Currie[1] Eimear Deady[2], Alicja Lacinska[1], Kathryn M Goodenough[2]
[1] *British Geological Survey, Keyworth, Nottingham NG12 5GG, UK*
[2] *British Geological Survey, The Lyell Centre, Research Avenue South, Edinburgh, EH14 4AP, UK*

Abstract. In 2019, the UK became the first major economy to legislate a net zero emissions target by 2050. The process of achieving this goal is multifaceted and, to do so, a robust understanding of the critical raw material (CRM) potential of the UK is essential. CRMs are commonly associated with base metal sulfides and other common metals as minor and trace elements and can play a key role in increasing the economic feasibility and circularity of an ore deposit throughout its lifecycle. The North Pennine Orefield (NPO) was selected as an area of interest by using GIS-based mineral systems analysis for exploration targeting. Historically, the NPO has produced approximately 4 Mt Pb, 0.3 Mt Zn, 2.1 Mt fluorite, 1.5 Mt barite, 1 Mt witherite ($BaCO_3$) plus a substantial amount of Fe and Cu ore from vein-hosted, stratabound, and skarn mineralisation in Carboniferous limestones. In this study, petrographic and geochemical data on CRM deportment in ore minerals across the NPO will be incorporated into a larger scale future project, aimed at creating a series of data-driven studies on areas of CRM potential across the UK.

1 Introduction

Over the coming decades, the mining of minerals and metals, with an emphasis on CRMs, is likely to increase as economies progress toward net zero emission targets (Lusty et al. 2021). Technologies needed to combat the effects of climate change, and decarbonise energy generation, transport, and digital systems, will consume increasing amounts of minerals and metals for decades (Bloodworth et al. 2019). This increase in demand coupled with potential issues with future supply chains has led governments to conduct criticality assessments to understand which materials are at risk of supply disruption, to assess the severity of impacts resulting from disruption and to recognise appropriate mitigation of these risks (Lusty et al. 2021; Australian Government 2022). Therefore, it is necessary for governments to understand domestic CRM supply chains and resources.

Tracing back ~6000 years, the United Kingdom has an extensive history of resource extraction (Edinborough et al. 2020). Metals like Fe, Pb, Cu, Zn, Au, Ag, and Sn dominated production during this time. Cornwall, for example, supplied up to 45% of world copper between 1800 and 1860 (Culver and Reinhart 1989). Renewed interest in Li, Sn and W has attracted investors to the area and sparked further exploration across the UK including the North Pennine Orefield (NPO) (Cornish Lithium 2023).

The NPO has produced approximately 4 Mt Pb, 0.3 Mt Zn, 2.1 Mt fluorite, 1.5 Mt barite, 1 Mt witherite plus a substantial amount of Fe and Cu ore from vein-hosted, stratabound, and skarn mineralisation in Carboniferous limestones (Dunham 1990). However, no systematic assessment of CRM potential has been conducted despite known occurrences of uneconomic Co, Ni, Bi, and Sb mineralisation across the orefield (Ixer et al. 1996; Fairbairn et al. 2020). Here, we provide a framework for the analysis of Pb, Zn, Cu, and Fe sulfides to assess the association of CRMs, chiefly In, Ga, and Ge, with these minerals. Ultimately, this petrographic and geochemical workflow can then be replicated for any geographical area for any CRM to create a user-friendly resource for future exploration and resource security analysis.

2 The North Pennine Orefield

2.1 Setting, geology, and ore mineralisation

Covering approximately 1500 km^2 across northern England, the NPO was the most significant UK producer of Pb and Zn through the 18th and 19th centuries (Stone et al. 2010). Commercial mining ceased in 1999, but collector specimens of fluorspar are still mined at the Diana Maria mine.

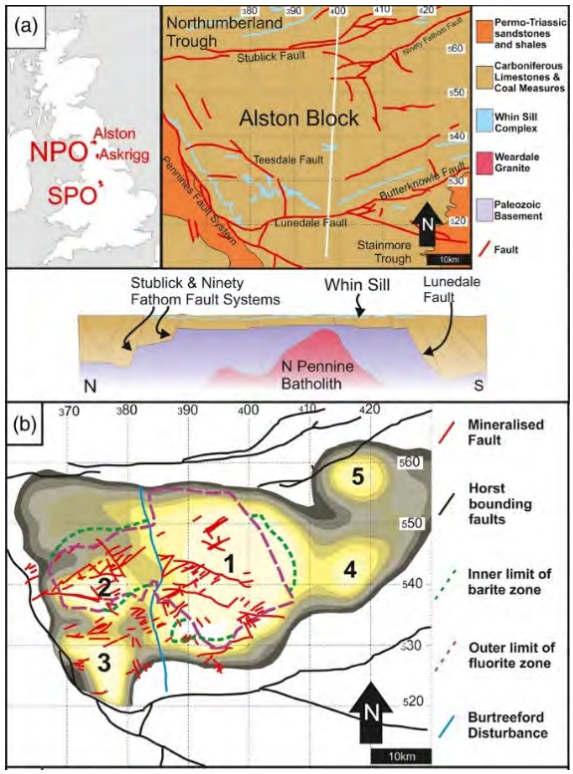

Fig. 1 (a) Simplified geological map and cross-section of the Alston Block. (b) Main mineralised faults in red with bounding structures in black. Green and purple

dashed lines represent the inner limit of the barite zone and outer limit of the fluorite zone, respectively. Image from Dempsey et al. (2021).

The Alston Block of the NPO comprises Lower Palaeozoic sedimentary and volcanic rocks intruded by Caledonian-aged granite (Selby et al. 2008; Kimbell et al. 2010) and overlain by up to 600 m of cyclothemic limestones, sandstones, mudstones, and minor coals (Dunham 1990). It is a horst structure bound by crustal-scale faults and suggested to have come in to existence due to north-south Carboniferous extension above the Iapetus Convergence Zone (Chadwick et al. 1995). The thin cyclothem sequences are attributed to the Alston Block being underlain by a concealed relatively buoyant batholith (Dunham et al. 1965). An Early Permian phase of transtensional deformation and magmatism resulted in the emplacement of a doleritic complex across the NPO known as the Whin Sill. It is recorded across northern Britain (Dempsey et al. 2021).

Veins and stratabound 'flats' are hosted in Carboniferous limestone sequences. Minor skarn mineralisation was also mined (Young et al. 1985). The main ore phases are galena, sphalerite, siderite, ankerite, limonite, fluorspar, witherite, barite, and chalcopyrite (Dunham 1990). NPO deposits are structurally controlled along faults and steeply dipping conjugate fracture systems (Dunham 1990). Stratabound deposits are often overlain by impervious mudstone, whereas vein ore-shoots are overlain by sandstones thus suggesting a hydrological and lithological control on ore mineralisation styles (Dunham 1990). Stratabound mineralisation is typically 5 to 20 m wide and up to 3 m thick and can extend for hundreds of metres laterally (Dunham 1990), whereas veins can extend for 10s of km and be hundreds of metres thick; the Great Sulphur vein for example.

2.2 Existing geochemistry and geochronology

Ore fluid temperatures range from >200°C in the central fluorite zone to around 100 °C at the margins (Cann and Banks 2001; Sawkins 1966). Homogenisation temperature of sphalerite in stratabound mineralisation ranged between 80-150°C (Bouch et al. 2008). Barite zone temperatures ranged from 120°C to 50°C (Cann and Banks 2001).

Salinities of fluid inclusions in ore, gangue, and host rock range from around 2 to about 25 wt.% NaCl equivalent (Cann and Banks 2001; Bouch et al. 2008). Fluids are reported to be enriched in K and Li relative to oil field brines (Rankin and Graham 1988; Cann and Banks 2001) and interpreted as a mixed $CaCl_2$–NaCl-bearing brine containing significant dissolved Fe, Cu, Zn and Pb.

The timing of ore mineralisation across the NPO is thought to be restricted to the time of Whin Sill emplacement and cooling (~295 Ma; Fitch and Miller 1967; Young et al. 1985; Dunham 1990; Dempsey et al. 2021). However, other data suggest that the main phase of mineralisation was restricted to between the latest Permian (~250–260 Ma) (Dunham et al. 1968; Davison et al. 1992; Lenehan 1997) and end Triassic (~210-200 Ma; Cann and Banks 2001; Shepherd et al. 1982; Halliday et al. 1990).

2.3 Ore-forming processes

It has been suggested the NPO is a fluoritic sub-type of Mississippi-Valley type deposits (Dunham 1983; Halliday et al. 1990). Cann and Banks (2001) proposed deep fluid circulation and interaction with underlying granite and country rock allowed fluid temperature and salinity to rise and scavenge metals during Late Permian extension. They suggest chimney-like systems drove convection above hotter granitic centres leading to zoning of ore mineralisation in host rock (Cann and Banks 2001). An 'emanative centres' hypothesis was also proposed by Johnson and Dunham (1963) and supported by Ixer et al. (1996). Bouch et al. (2006) suggest that the zonation may be due to two distinct phases of ore mineralisation.

Bott and Smith (2018) used geophysical modelling to suggest that the underlying batholith was not hot enough to facilitate a chimney effect of heat channelling, rather the batholith was underplated by alkali magma associated with the intrusion of the Whin Sill. Dempsey et al. (2021) rule out any link between granite-related hydrothermal fluid circulation and/or MVT models previously proposed and link ore mineralisation with Whin Sill emplacement.

3 CRMs in MVT and skarn sulfides

3.1 Sphalerite

Mississippi-Valley type (MVT) and related carbonate-hosted vein, breccias and skarn deposits are distributed globally and, in a few cases, have been assessed for CRM potential. Textural characterisation of sphalerite from MVT deposits in Peru revealed some of the most Ge- and Ga-rich samples ever reported (Torró et al. 2023). Ga in reddish-brown sphalerite from the Chilpes prospect reached 4000 ppm, whilst Ge in Fe-poor orange sphalerite from San Vicente deposit reached >1800 ppm (Torró et al. 2023). Fe-poor sphalerite is preferred for Ge enrichment (Frenzel et al. 2014; Cook et al. 2009), though sphalerite from the Tres Marias Zn deposit in Mexico showed Ge is preferentially incorporated within Fe-rich bands (Cook et al. 2009).

MVT deposits across South China have elevated amounts of Ge in sphalerite, whilst skarn deposits across the same area have shown incorporation of Co and Mn (Ye et al. 2011). Fe-poor sphalerite with up to 2300 ppm Co is noted at Ocna de Fier skarn, Romania (Cook et al. 2009).

Frenzel et al. (2016) show that Ga and Ge concentration will tend to increase with decreasing formation temperature whilst In will do the opposite.

Higher temperature sphalerite-bearing ore deposits, like skarns, are the primary source of global In supply (Xu et al. 2021). Fractionation of a given element into sphalerite is also influenced by metal source and the amount of sphalerite in the deposit relative to other metallic minerals (Cook et al. 2009).

3.2 Galena

Galena is the preferred host for Ag, Bi, Sb, Se, Te, and Tl in co-existing sphalerite-galena-chalcopyrite bearing ore systems (George et al. 2015). Bi and Sb are more likely to favour higher temperature zones of ore deposits like in skarns where concentrations in galena can reach >6400 ppm and 4600 ppm respectively like at Herja epithermal deposit, Romania (George et al. 2015). Tellurium in galena has been recorded at >1000 ppm at the Baita Bihor skarn, Romania (George et al. 2015)

3.3 Fe and Cu sulfides

Pyrite is the most common sulfide mineral on Earth and is known to incorporate several CRMs during the crystallization process or during reprecipitation (Dmitrijeva et al. 2020). Across the Beishan Pb-Zn MVT ore zone, south China, pyrite is enriched in Co, Ni, and Sb (Zhou et al. 2022). The Illinois-Kentucky fluorite district, Co and Ni are recorded at up to 10,000 ppm in early pyrite (Hall and Heyl 1968). Partitioning of CRMs in marcasite is not known across MVT-type deposits, though it can act like pyrite in massive sulfide deposits (Grant et al. 2018). Chalcopyrite is a known host of several CRMs (George et al. 2018), although it will not be studied here as it forms a minor component of the NPO.

4 Future work

Collection of sample material from spoil heaps related to historic underground mine sites began in late 2022. We propose the following petrographic and geochemical analysis framework to quantify CRM potential of the NPO: reflected light petrography to initially identify sulfides (Fig. 2); cathodoluminescence imaging to identify areas of zonation, particularly in sphalerite; quantitative microanalysis using scanning electron microscopy energy-dispersive X-ray microanalysis (SEM-EDXA); and trace element analysis of ore sulfides by laser ablation - inductively coupled plasma - mass spectrometry (LA-ICP-MS). Data collected form part of a larger UK scale reassessment of UK CRM potential.

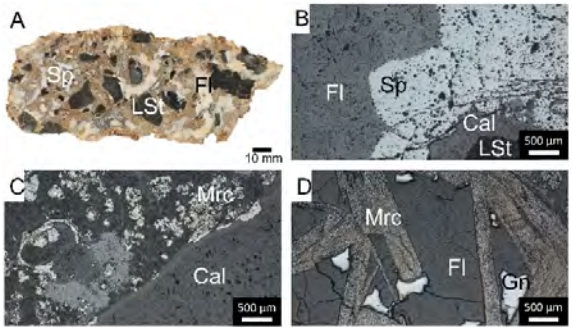

Fig. 2 Representative images from Lady's Rake Mine. A) Hand sample showing breccia with sphalerite, fluorspar, and calcite-rimmed limestone country rock. B) Reflected light image of image A. C) Reflected light image of marcasite mineralisation adjacent to calcite veining in nodule. D) Marcasite, galena, and fluorspar.

Acknowledgements

This work was carried out as part of the British Geological Survey Critical Minerals Intelligence Centre programme. Thanks to Nenthead Mining Museum, Brian Young, and Dr Charlotte Vye-Brown for field assistance and their invaluable knowledge of the North Pennine Orefield. Thanks to Richard Shaw for providing internal peer review.

References

Australian Government (AG) (2022) Critical Minerals Strategy, Department of Industry, Science, Energy and Resources, Australian Government.

Bott MH and Smith FW (2018) The role of the Devonian Weardale Granite in the emplacement of the North Pennine mineralization. Proceedings of the Yorkshire Geological Society 62(1):1-15.

Bloodworth A, Petavratzi E, Gunn G (2019) METALS AND DECARBONISATION: A GEOLOGICAL PERSPECTIVE.

Bouch JE, Naden J, Shepherd TJ, McKervey JA, Young B, Benham AJ, Sloane HJ (2006) Direct evidence of fluid mixing in the formation of stratabound Pb–Zn–Ba–F mineralisation in the Alston Block, North Pennine Orefield (England). Mineralium Deposita 41:821-835.

Bouch J, Naden J, Shepherd T, Young B, Benham A, McKervey J, Sloane H (2008) Stratabound Pb-Zn-Ba-F mineralisation in the Alston Block of the North Pennine Orefield (England): origins and emplacement.

Cann JR, Banks DA (2001) Constraints on the genesis of the mineralization of the Alston Block, Northern Pennine Orefield, northern England. Proceedings of the Yorkshire Geological Society 53(3):187-196.

Chadwick RA (1995) The structure and evolution of the Northumberland-Solway Basin and adjacent areas: Subsurface Memoir. HM Stationery Office.

Cook NJ, Ciobanu CL, Pring A, Skinner W, Shimizu M, Danyushevsky L, Saini-Eidukat B, Melcher F (2009) Trace and minor elements in sphalerite: A LA-ICPMS study. Geochimica et Cosmochimica Acta 73(16):4761-4791.

Cook NJ, Ciobanu CL, George LL, Crowe B, Wade BP (2014) December. Trace element distributions in sulphides: Progress, problems and perspectives. In Acta Geologica Sinica-English Edition; 88:1444-1446.

Cornish Lithium (2023) Cornish lithium and northern lithium announce collaboration to deliver domestic supply of lithium for the UK, Cornish Lithium Plc. Available at: https://cornishlithium.com/company-announcements/cornish-lithium-and-northern-lithium-

announce-collaboration-to-deliver-domestic-supply-of-lithium-for-the-uk/ (Accessed: March 6, 2023).
Culver W, Reinhart CJ (1989) Capitalist Dreams: Chile's Response to Nineteenth-Century World Copper Competition. Comparative Studies in Society and History 31(4):722-744.
Davison JM, Ineson PR, Mitchell JG (1992) Potassium-argon isotopic age determinations from the metasomatic alteration of the Great Limestone, Northern Pennine Orefield. Proceedings of the Yorkshire Geological Society 49:71-74.
Dempsey ED, Holdsworth RE, Selby D, Bird A, Young B, Le Cornu C (2021) A revised age, structural model and origin for the North Pennine Orefield in the Alston Block, northern England: intrusion (Whin Sill)-related base metal (Cu–Pb–Zn–F) mineralization. Journal of the Geological Society 178(4).
Dmitrijeva M, Cook NJ, Ehrig K, Ciobanu CL, Metcalfe AV, Kamenetsky M, Kamenetsky VS, Gilbert S, (2020) Multivariate statistical analysis of trace elements in pyrite: Prediction, bias and artefacts in defining mineral signatures. Minerals 10(1):61.
Dunham KC (1990) Geology of the Northern Pennine Orefield Volume I—Tyne to Stainmore Economic memoir covering the areas of 1: 50 000 and one-inch geological sheets 19 and 25, and parts of 13, 24, 26, 31, 32 (England and Wales).
Dunham KC, Dunham AC, Hodge BL, Johnson GAL (1965) Granite beneath Viséan sediments with mineralization at Rookhope, northern Pennines. Quarterly Journal of the Geological Society 121(1-4):383-414.
Dunham KC, Fitch FJ, Ineson PR, Miller JA, Mitchell JG (1968) The geochronological significance of argon-40/argon-39 age determinations on White Whin from the northern Pennine orefield. Proceedings of the Royal Society of London. Series A. Mathematical and Physical Sciences 307(1490):251-266.
Edinborough K, Shennan S, Teather A, Baczkowski J, Bevan A, Bradley R, Cook G, Kerig T, Pearson MP, Pope A Schauer P (2020) New radiocarbon dates show Early Neolithic date of flint-mining and stone quarrying in Britain. Radiocarbon 62(1):75-105.
Fairbairn RA, Ixer RA,Young B, (2020) Ore mineralogy of the Clargillhead Vein, Tynehead, Cumbria: the first report of native silver from the Northern Pennine Orefield. Journal of the Russell Society 23:48-52.
Fitch FJ, Miller JA (1967) The age of the Whin Sill. Geological Journal 5(2):233-250.
Frenzel M, Ketris MP Gutzmer J (2014) On the geological availability of germanium. Mineralium Deposita 49:471-486.
Frenzel M, Hirsch T, Gutzmer J (2016) Gallium, germanium, indium, and other trace and minor elements in sphalerite as a function of deposit type—A meta-analysis. Ore Geology Reviews 76:52-78.
George L, Cook NJ, Ciobanu CL, Wade BP (2015) Trace and minor elements in galena: A reconnaissance LA-ICP-MS study. American Mineralogist 100(2-3):548-569.
George L, Cook NJ, Ciobanu CL (2015) August. Trace element partitioning between co-existing sphalerite, galena and chalcopyrite. In Mineral Resources in a Sustainable World, 13th Biennial SGA Meeting, Nancy, France, Proceedings:737-740
George LL, Cook NJ, Crowe BB, Ciobanu CL (2018) Trace elements in hydrothermal chalcopyrite. Mineralogical Magazine 82(1):59-88.
Grant HL, Hannington MD, Petersen S, Frische M Fuchs SH (2018) Constraints on the behavior of trace elements in the actively-forming TAG deposit, Mid-Atlantic Ridge, based on LA-ICP-MS analyses of pyrite. Chemical Geology 498:45-71.
Hall WE, Heyl AV (1968) Distribution of minor elements in ore and host rock, Illinois-Kentucky fluorite district and Upper Mississippi Valley zinc-lead district. Economic Geology 63(6):655-670.
Halliday AN, Shepherd TJ, Dickin AP, Chesley JT (1990) Sm–Nd evidence for the age and origin of a Mississippi Valley Type ore deposit. Nature 344(6261):54-56.
Ixer RA, Young B, Stanley CJ (1996) Bismuth-bearing assemblages from the Northern Pennine Orefield. Mineralogical Magazine 60(399):317-324.
Johnson GAL, Dunham KC (1963) The geology of Moor house. HM Stationery Office.
Kimbell GS, Young B, Millward D, Crowley QG (2010) November. The North Pennine batholith (Weardale Granite) of northern England: new data on its age and form. Geological Society of London.
Lenehan T (1997) An investigation into thermo-tectonic and maturation histories in north-west Britain. Ph.D. Thesis, University of Leeds
Lusty PAJ, Shaw RA, Gunn AG, Idoine NE (2021) UK criticality assessment of technology critical minerals and metals. British Geological Survey Commissioned Report, CR/21/120:76pp
Rankin AH, Graham MJ (1988) Na, K and Li contents of mineralizing fluids in the Northern Pennine Orefield, England, and their genetic significance. Transactions of the Institution of Mining and Metallurgy. Section B. Applied earth science 97:99-107.
Sawkins FJ (1966) Ore genesis in the North Pennine orefield, in the light of fluid inclusion studies. Economic Geology 61(2):385-401.
Selby D, Conliffe J, Crowley QG Feely M (2008) Geochronology (Re–Os and U–Pb) and fluid inclusion studies of molybdenite mineralisation associated with the Shap, Skiddaw and Weardale granites, UK. Applied Earth Science 117(1):11-28.
Shepherd TJ, DPF D, GR M, DA G (1982) Rare earth element and isotopic geochemistry of the North Pennine ore deposits.
Stone P, Millward D, Young B, Merritt J, Clarke S, McCormac M,Lawrence D (2010) Northern England. British Geological Survey.
Torró L, Millán-Nuñez AJ, Benites D, González-Jiménez JM, Laurent O, Tavazzani L, Vallance J, Chelle-Michou C, Proenza JA, Flores C. Melgarejo JC (2023) Germanium- and gallium-rich sphalerite in Mississippi Valley–type deposits: the San Vicente district and the Shalipayco deposit, Peru. Mineralium Deposita, 1-28.
Xu J, Cook NJ, Ciobanu CL, Li X, Kontonikas-Charos, A, Gilbert S,Lv Y (2021) Indium distribution in sphalerite from sulfide–oxide–silicate skarn assemblages: a case study of the Dulong Zn–Sn–In deposit, Southwest China. Mineralium Deposita 56:307-324.
Ye L, Cook NJ, Ciobanu CL, Yuping L, Qian Z, Tiegeng L, Wei G, Yulong Y, Danyushevskiy L (2011) Trace and minor elements in sphalerite from base metal deposits in South China: A LA-ICPMS study. Ore Geology Reviews 39(4):188-217.
Young B, Styles MT, Berridge NG (1985) Niccolite-magnetite mineralization from Upper Teesdale, North Pennines. Mineralogical Magazine 49(353):555-559.
Zhou C, Yang Z, Sun H, Koua KAD, Lyu C, (2022) LA-ICP-MS trace element analysis of sphalerite and pyrite from the Beishan Pb-Zn ore district, south China: Implications for ore genesis. Ore Geology Reviews, p.105128.

Towards a better understanding of a Co-rich hydrothermal system: Punta Corna (Western Alps, Italy)

Giulia Domenighini[1], Licia Santoro[1], Marilena Moroni[2]
[1]Department of Earth Sciences University of Torino, Italy.
[2]Department of Earth Sciences "Ardito Desio" University of Milan, Italy.

Abstract. This study presents new geochemical, mineralogical, and petrographic data on the Co-Fe-Ni vein system of Punta Corna (PC) in the Western Alps, Italy. The mineralogical phases identified include arsenides belonging to the skutterudite and safflorite (Fe-Co-Ni tri- and di-arsenides) solid solutions, tetrahedrite, and sulfides (chalcopyrite, minor pyrite and rare sphalerite and galena). Gangue minerals comprise carbonates (mainly siderite, ankerite and calcite) and quartz. Field and mineralogical observations show a distinct geochemical zonation within the deposit system. No Co or Ni occur to the west, with only Fe-bearing minerals observed. Co-Ni arsenides are present in the central region, with a higher proportion of Ni di-arsenides than Co-bearing phases. To the east, Co arsenides prevail. Additional sampling, micro-textural characterization and geochemical investigations are ongoing, yet these preliminary observations agree with the genetic model recently proposed for similar types of deposits and suggest that the hydrothermal system may have formed through a complex geological history, with multiple mineralizing events and variations in fluid composition and possibly temperature.

1 Introduction

The Co-Ni-bearing Punta Corna (PC) hydrothermal vein system is located in the western sector of the Alpine belt near the Lanzo Massif, Northern Italy. Despite being a historically known mining complex, exploited until the 20th century, formerly for Fe and later for Co (used as a pigment), this vein system has received little scientific attention until recently. In 2020, the Australian Junior Mining Company (Altamin l.t.d.) acquired the exploration license of ca. 22 Km^2 area around ancient mining galleries. The PC mining complex holds great potential from an economic standpoint, both for the main ores consisting of Co-rich arsenides, and for the poor exposure of the vein system, likely preserved at depth.

The literature lacks detailed information on the geochemistry of the deposit and high-resolution geological maps. Preliminary paragenetic studies based on museum samples (Moroni et al., 2019 andref. therein) suggest a multi-stage mineralizing process with early siderite, ankerite, quartz and baryte followed by deposition of Fe-Co-Ni di- triarsenides with native elements (As, Bi), and thenbase metal sulphides and tetrahedrite with siderite, ankerite, quartz and late baryte gangue.

There are analogies between the PC mineralization and the five-element vein-type deposits according to Kissin' (1992), to more recent studies (e.g., Markl etal 2016) as well as the mineralized veins in theworld-class Bou Azzer ore district (Tourneur et al 2021). Nevertheless, definitive constraints on the genetic conditions of the PC hydrothermal vein system are still missing.

In this work, we summarize geological, mineralogical, and geochemical data of a new set of surface samples of the poorly known Fe-Co-Ni- bearing Punta Corna ore deposit. Drilling is plannedin order to verify the features of the vein system at depth. Moreover, we illustrate some investigations inprogress about the possible sources of Co in the mineralization, the age of the mineralizing process and the properties of the fluid and its origin.

2 Geological setting

The ore bodies of the PC hydrothermal vein systemare located in the Arnàs, Servin, Veil, and Autour valleys, some small offshoots of the Viù valley, close to the village of Usseglio (TO, Fig1 A, B).

The Fe-Co-Ni-bearing veins extend for 2 Km along an east-west axis, from the "Lago dietro la Torre" lake to the "Torre d'Ovarda" peak, with elevations ranging from 2200 to 2900m. The average thickness of the outcropping veins is in the cm/dm range. Mineralized bodies are hosted in metabasites and, subordinately, in heavily foliated calcschists of the Internal Piedmont Zone tectonic unit (IPZ), a portionof oceanic lithosphere and its sedimentary cover related to the Middle-Jurassic Piedmont-Ligurian Ocean (Dal Piaz 1999, Fig1). The IPZ is structurallylocated above the Gran Paradiso (to the North) and the Dora Maira (to the South) Units, which representthe external continental margin of the EuropeanPlate. With the subduction of the oceanic crust below the Adria plate leading to the Alpine orogenesis (90-35 Ma), the oceanic rocks of the IPZregistered an eclogitic peak metamorphism followed by green-schist facies re-equilibration during exhumation (35-23 Ma, Sandrone 1986). The rocks record several ductile deformations phases, while the mineralized veins are related to a post-metamorphic brittle event and are associated with faults and fractures. Two late steep E-W trending fault systems occur throughout the whole deposit. The first system is represented by a subvertical normal fault system, interacting with a diverging high-angle transtensional fault system.

Field evidence of a geochemical zonation affecting the vein system occurs across the mining district. The presently accessible portions of the veins in thewestern sector are characterized by siderite- ankerite, once exploited for Fe. In contrast, the eastern sector displays high Co/Ni ore minerals

(di-and tri-arsenides). It is worth mentioning the presence of Ag, mined since historical times, in the southernmost part of the district.

The ophiolite terranes in the surroundings of the studied area host several metamorphosed volcanogenic massive sulfides deposits (VMS) exploited in historical mines like Fragnè-Chialamberto, Uja di Calcante and Beth-Ghinivert, where recent studies signalled anomalous Co contents in the pre-metamorphic pyrite (Giacometti et al 2014). For this reason, we have started sampling variably deformed portions of some of these volcanogenic sulfides layers for evaluating them as possible sources for Co in the PC vein system.

3 Methods

Several samples collected in the field, both on surface and in the ancient mining tunnels, were cut to obtain thin and polished sections for optical microscopy (OM). The powder x-ray diffraction (PXRD) analyses of carbonates, alteration and supergene phases were carried out using a Rigaku SmartLab XE diffractometer in Bragg-Brentano geometry (Cu-Kα radiation, Ni filter, generator operating at 40 kV and 30 mA, soller slit 2.5 deg) equipped with a 2D HyPix-3000 detector. The detector was employed in 1D XRF-reduction mode to increase peak resolution and limit the background signal due to the fluorescence from Fe. In addition, each measurement was collected by mounting a frontal knife edge and a direct beam stop to reduce the background. The patterns were collected from 5to 75º 2θ angles, with a step size of 0.02º and a scan speed of 1 º/min. The qualitative analysis was carried out with EVAluation software (Bruker) and employing the PDF-2 database.

Scanning electron microscope (SEM) equipped with an energy dispersive spectrometer (EDS) was employed for preliminary petrography and chemical semi-quantitative analyses. Carbon-coated polished thin sections were analysed with a JEOL JSM-IT300LV SEM equipped with an EDS Energy 200 and an SDD X-Act3 detector (Oxford Inca Energy). The operating conditions were 20 kV accelerating voltage, 5 nA probe current, 30 s counting time. Thedata were acquired and processed using the Suite AzTec ID, version 6.0 (Oxford Instruments). Samplepreparation, PXRD, and SEM-EDS were carried out at the Department of Earth Sciences, University of Turin, Italy.

Quantitative electron probe microanalysis (EPMA) was performed at the University of Milan "Ardito Desio" on carbon-coated polished thin sections using a JEOL JXA — 8200 EPMA equipped with five wavelength-dispersive spectrometers (WDS). The analytical conditions for the electron beam were an accelerating voltage of 15 kV, a beam current of 5 nA, and a beam diameter of 1-2 µm. Counting timesfor each element (Sb, Co, Bi) were 30 s on peaks and 10 s on the background. Elemental concentrations were determined after applying the

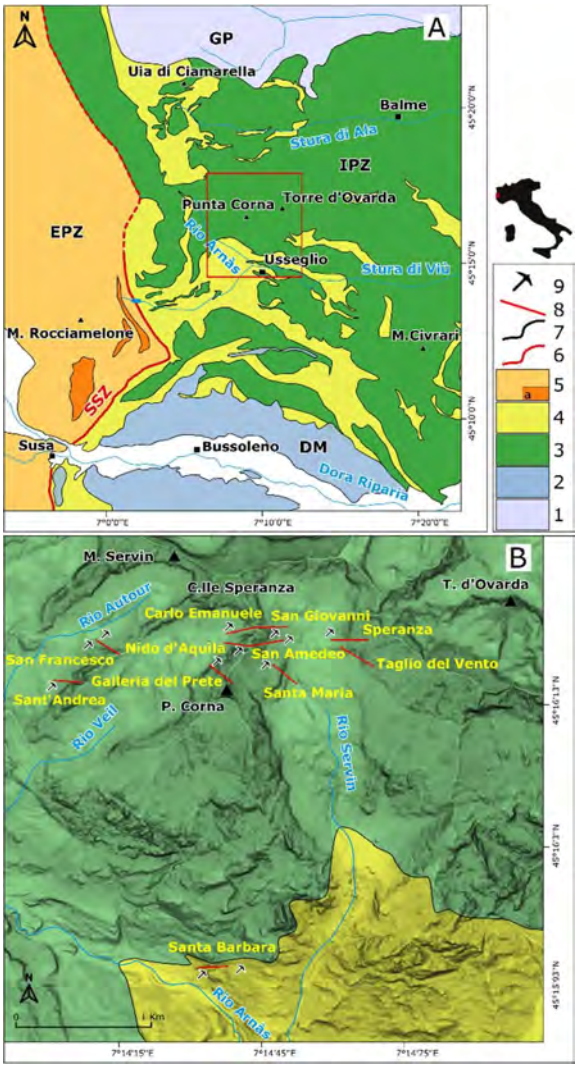

Fig 1. A) simplified tectonic sketch-map of the central sector of the Western Alps, modified after De Togni et al. 2021. In red is marked the location of the studied area. B) geological map of the studied area. 1 Gran Paradiso (GP); 2 Dora Maira (DP); 3 meta-ophiolites of the Internal Piedmont Zone (IPZ); 4 metasedimentary coverof IPZ; 5 oceanic metasediments with a) meta-ophiolite bodies of the External Piedmont Zone (EPZ); 6 Susa Shear Zone (SSZ); 7 tectonic contacts; 8 main mineralized veins; 9 ancient mining adits.

φ(ρz) algorithm and corrections for X-ray fluorescence, absorption, atomic number (Z), and matrices and by evaluating spectral interferences.

4. Petrography, Mineralogy and Geochemistry

The new surface samples display abundant gangue minerals encompassing calcite, dolomite, siderite, ankerite, quartz, and baryte. Hydrothermal alterations of wall rock commonly result in the presence of very fine-grained chlorite and white mica. Supergene oxidation of primary arsenides sulphides and siderite results in erythrite, annabergite, and abundant goethite. The veins exhibit a brecciated texture with clasts from the host

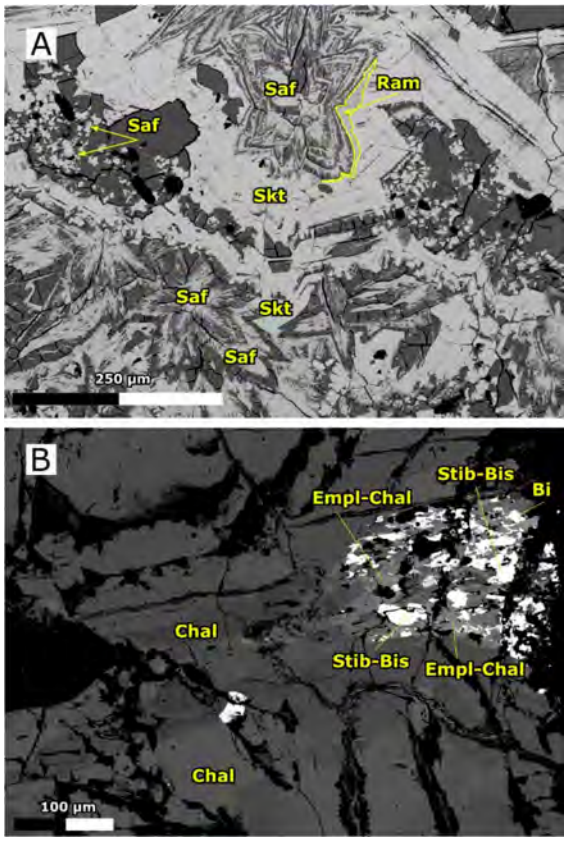

Fig 2. BSE images of Nido d'aquila vein, A and Santa Barbara vein, B. A) coarse-grained safflorite (Saf) crystals exhibiting star-shaped twinning alternating with thin grained disseminated aggregates of safflorite. Rammelsbergite (Ram) rim and well-formed euhedral crystals of skutterudite (Skt) can be observed. B) Sulfosalt belonging to emplectite-chalcostibite (Empl-Chal) solid solution and stibnite-bismiuthinite (Stib-Bis) solid solution. Chal = chalcopyrite, Bi = native bismuth.

rock, sometimes reaching centimetric sizes, cemented by a fine-grained gangue minerals matrix. Bladed siderite and euhedral quartz growing radially around brecciated clasts is also a typical texture of the mineralized veins. Veins can also present a banded structure with different compositional and textural layers. The ore minerals observed so far are represented by dominant Co-Ni di-triarsenides and base metal sulfides as those previously mentioned, although SEM and EPMA analyses helped in detecting additional sulfosalt minerals. Ore minerals show variable textures from well-preserved coarse-grained to brecciated or fine-grained disseminated crystals. The precipitation sequence starts with carbonates and quartz, followed by arsenides. They are characterized by di-arsenides either overgrowing coarse-grained tri-arsenides Fig2A,B) or disseminated along preferential directions or bands throughout the veins. Tri-arsenides (skutterudite series: $(Fe,Co,Ni)As_3$) are often zoned, with banding marked by alteration products (erythrite,annabergite). Di-arsenides belong to the safflorite series: loellingite ($FeAs_2$), clinosafflorite ($CoAs_2$), and rammelsbergite ($NiAs_2$)**.** The latter commonly occur as a rim on di- and tri-arsenides. The last precipitation stage is represented by base metal sulfides (chalcopyrite, minor pyrite and rare sphalerite and galena), tetrahedrite and several Bi- rich sulfosalts intergrown with native Bi (Fig **2**B). Rare droplets of secondary Ag sulfides were observed along rims of altered tetrahedrite crystals. Skutterudite composition is characterized by an average Co content of 9,25 wt%, Ni content of 7,65 wt% and Fe content of 4,93 wt%, but the compositions are quite homogeneous (Fig **2**A). Di- arsenides, on the other side, present wide variation in composition, with a range in Co content varying from 3,16 wt% to 16,52, Ni content from 0 to 30,23 wt% and Fe content from 0,12 to 19,94 wt% (**Error! Reference source not found.**A,B**)**. Tetrahedrite belong to the tetrahedrite end memberof the tennantite-tetrahedrite series: $Cu_6(Cu_4\mathbf{C}_2{}^{2+})As_4S_{12}S$ - $Cu_6(Cu_4\mathbf{C}_2{}^{2+})Sb_4S_{12}S$, where **C** can be Zn, Fe, Hg, Cd, etc.

The analysed samples show low values of both Zn (ranging from 0,88 wt% to 6,46 wt%) and Ag (ranging from 0 to 0,87 wt%).

Beside Bi-Sb alloys, Bi-rich sulfosalts display highly variable compositions including horobetsuite (related to stibnite - bismuthinite solid solution) and Cu-rich varieties like wittichenite and emplectite-chalcostibite solid solution. It is worth noting that

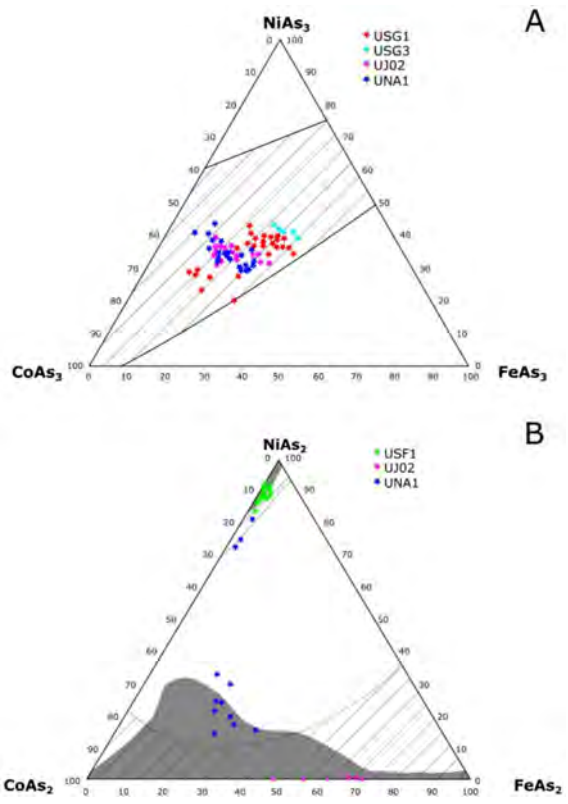

Fig 3. A) plot of skutterudite mineral series for the investigated veins. The solid-solution field for the system FeAs3–CoAs3–NiAs3 is defined by shaded area, according to Roseboom (1962). B) plot of safflorite mineral series (system FeAs2–CoAs2–NiAs2), compositional limits of natural Fe, Co, Ni diarsenides, according to Roseboom (1963) in dashed areas and Radcliffe & Berry (1968), full areas.

these Bi sulfosalts are especially characteristic of the post-metamorphic Au-bearing veins of the nearby Gran Paradiso nappe.

5. Work in progress

We are preparing a set of double polished sections from the new samples for fluid inclusion analyses in gangue minerals. From the same samples we are selecting portions with ore-related and post ore carbonates for performing U-Pb geochronology, together with carbonates from other post-metamorphic mineralized veins in the Gran Paradiso and Monte Rosa nappes. Carbon isotope analyses will be performed for obtaining indications about the origin of C-bearing gases in the fluids. Also, the origin of the great amount of Co in the PC vein system is a topic of interest. Therefore, a series of pyrite-rich samples from the VMS deposits in the Western Alpine ophiolites are in preparation for testing their possible role as sources for hydrothermal Co enrichment. Preliminary EMPA analyses on cm-sized metamorphosed py-cpy layerslocated at the contact between metabasites and calcschists, in the Arnàs valley, have been promising so far by revealing anomalous Co contents (up to 2%) in irregularly zoned pyrites.

6. Conclusion

The data from the characterization of the new surface samples from the Co-rich post-metamorphicveins in the Western Alpine ophiolites at Punta Corna — Usseglio are revealing that the mineralized system is more complex than previously indicated from historical samples. Beside indications about the distribution of Co and Ni, the new data suggest a role to previously unknown Bi enrichment which also contributes to establishing a possible link with the nearby domain of the Pennidic Gran Paradiso nappe. Therefore, the upcoming drilling campaign isbringing great expectations.

Because of the poor exposure of the PC veins, plenty of work is still needed to fully understand the features and the genetic process that led to the deposition of the hydrothermal system associated with the Fe-Co-Ni arsenides. To gain further insight into these issues, fluid inclusion, geochronological and isotopical analyses will likely provide significant data for better defining the hydrothermal fluids and their components, the origin of the vein system and potentially explain the zonation. The fluid inclusion analyses will be focused in particular on potential reduction mechanisms/agents (e.g. hydrocarbons) proposed in various models in literature for hydrothermal Co-Ni mineralization. Last but not least, the study of the metamorphosed exhalative pyrite ores in the western alpine ophiolites will be interesting for tracing possible Co sources for the PC mineral system and beyond. Further research and investigations could have significant implications for the evaluation of mineral resources and mining exploration in the region.

Acknowledgements

The project is part of the “Progetto Nazionale Operativo” (PON) “Ricerca e Innovazione” 2014-2020, of the Ministry of Education, University and Research dedicated to PhD Research Projects on green topics reducing the impacts of climate change and promoting sustainable development.
(DM 1061/2021). The authors would like to acknowledge AltaMin L.d.t. for co-founding the project. Furthermore, the authors would like to extend their thanks to the lab technicians at UniTo and UniMi as well as the staff at AltaMin for their assistance in preparing the samples and accompanying the research team in the field. Their expertise and support have been invaluable to the success of this project.

References

Dal Piaz GV (1999) The Austroalpine-Piedmont nappe stack and the puzzle of Alpine Tethys. Mem. Sci. Geol. 51:155-176.

De Togni M, Gattiglio M, Ghignone S, Festa A (2021) Pre-Alpine Tectono-Stratigraphic Reconstruction of the Jurassic Tethys in the High-Pressure Internal Piedmont Zone (Stura di Viù Valley, Western Alps). Minerals 11:361.

Giacometti F, Evans KA, Rebay G, Cliff J, Tomkins AG, Rossetti P, Adams DT (2014) Sulfur isotope evolution in sulfide ores from Western Alps: Assessing the influence of subduction-related metamorphism. Geochemistry, Geophys. Geosystems 15:3808-3829.

Kreissl S, Gerdes A, Walter BF, Neumann U, Wenzel T, MarkIG (2018) Reconstruction of a> 200 Ma multi-stage “five element” Bi-Co-Ni-Fe-As-S system in the Penninic Alps, Switzerland. Ore Geol. Rev. 95:746-788.

Moroni M, Rossetti P, Naitza S, Magnani L, Ruggieri G, AquinoA, Secchi F (2019) Factors controlling hydrothermal nickeland cobalt mineralization—Some suggestions from historical ore deposits in Italy. Minerals 9:429.

Markl G, Burisch M, Neumann U (2016) Natural fracking and the genesis of five-element veins. Miner Deposita 51:703-712.

Peucker-Ehrenbrink B, Hofmann AW, Hart SR (1994) Hydrothermal lead transfer from mantle to continentalcrust: the role of metalliferous sediments. Earth Planet. Sci. Lett. 125:129-142.

Radcliffe D, Berry LG (1968) The safflorite-loellingite solid solution series. Am Min 53:1856-1881.

Roseboom EH (1962) Skutterudites (Co, Ni, Fe) As3− x: composition and cell dimensions. Am Min 47:310-327.

Roseboom EH (1963) Co-Ni-Fe diarsenides: compositions and cell dimensions. Am Min 48:271-299.

Sandrone R, Leardi L, Rossetti P, Compagnoni R (1986) P-T conditions for the eclogitic re-equilibration of the metaophiolites from Val d’Ala di Lanzo (Internal Piedmontese Zone, Western Alps). J. Metamorph. Geol. 4:161-178.

A lithological context for stratabound REE mineralisation at the birthplace of REE – Bastnäs, Riddarhyttan, Sweden

Robert Dunst[1], Iain Pitcairn[1], Hein Raat[2], Nils F Jansson[3], Andreas Karlsson[4]
[1]Department of Geological Sciences, Stockholm University, Stockholm, Sweden
[2]EMX Royality Corp., Vancouver, Canada
[3]Division of Geosciences and Environmental Engineering, Luleå University of Technology, Luleå, Sweden
[4]Department of Geosciences, Swedish Museum of Natural History, Stockholm, Sweden

Abstract. The Bastnäs ore field, in central Sweden, is the cradle of the rare earth elements (REE). It is the place of the discovery of several REE and important REE-minerals (e.g., Bastnäsite one of the primary REE-ore minerals). In recent years there has been an increased interest due to rising demand of REE for technological applications. Several recent studies have focused on the mineralogy and geochemistry but a lack of fresh in situ samples has meant that textural and stratigraphic relationships are not as well described. Recent exploration in the area has produced drill core traverses across the host stratigraphy of the Bastnäs deposit, allowing the collection of relatively fresh in situ samples which can be placed in lithological context. Here we present new mineralogical and textural information linked to the lithology indicating that the REE-mineralisation in Bastnäs is commonly associated with magnetite skarn and that it occurs over a wide range of stratigraphic levels.

1 Introduction

The Bastnäs deposit in central Sweden played an important role in the discovery of the rare earth elements (REE) in the mid 19th century. Chemists tried to identify the constituents of samples from Bastnäs called “Bastnäs-Tungsten” (heavy rock from Bastnäs) and found several new elements with very similar properties. Cerium, Lanthanum and Didymium (a mixture of Praseodymium and Neodymium) were isolated from the material (Öhman et al. 2004). The mining field which originally produced Fe-oxide and Cu-sulphide became the first hard-rock REE-mine. The REE ore sat in two small bodies of mainly cerite-(Ce) and ferriallanite-(Ce) (the larger one: 6–7 m long and 0.6 m wide) up to a depth of 30 m (Geijer 1921). Circa 160 t of REE ore was produced in the Ceritgruvan and Sankt Göransgruvan (both primarily Cu-mines) in the late 19th to early 20th century before the mine was closed (Andersson et al. 2004).

The Riddarhyttan ore field (of which Bastnäs is part) has been recently explored for polymetallicsulphide deposits. Drill core from this exploration campaign have also intersected REE-enrichedzones, allowing this mineralisation type to be investigated in lithological context. For this study twodrill cores were studied, RID-19-008 which was drilled under Gamla Bastnäsfältet (the old Bastnäs mines) and RID-19-013 drilled in the Morbergfältet roughly a km northwest of Gamla Bastnäs.

Previous studies of the Bastnäs mineralisation have mainly been mineralogical and geochemical in nature. They include detailed isotopic analyses on a small number of samples. The mineralised samples were collected from mine waste pile and old samples in archives from the time of active mining (Geijer 1921; Ulf B. Andersson et al. 2004; Holtstam and Andersson 2007; Jonsson and Högdahl 2013; Holtstam et al. 2014; Sahlström et al. 2019).

2 Geological setting

The Bastnäs deposit lies within a inlier of Paleoproterozoic metavolcanic andmetasedimentary rocks with ages of ~1.91–1.88 Ga (Holtstam et al. 2014). These dominantly felsic metavolcanics show commonly volcanoclastic textures if they are not overprinted by intense synvolcanic hydrothermal alteration. This alterationoccurs in zones of different intensity and is very widespread in the Riddarhyttan area. It led to rocksstrongly enriched in either K, Na and Mg and depleted in most other elements. Mg-enriched varieties are especially common in the Riddarhyttan area, where least-altered metavolcanic rocks are almost completely lacking (Trägårdh 1988). Metasediments and marble occur as interlayers in the metavolcanic rocks. The iron oxide deposits are historically the most economically important ores in the region. They occur as banded magnetite or hematite ores as well as associated with the marbles in magnetite skarns. Sulphide mineralisation is subordinate even though some of the mines in the area were producing Cu sulphide ore.

The metavolcanic succession was intruded by plutonic rocks of two generations. The first generation has dominantly a granitic composition butranges from granodiorite to tonalite and subordinate mafic compositions. It intruded between 1.90–1.85 Ga (Holtstam et al. 2014) and is spatially dominant.A later generation intruded between 1.81–1.75 Ga (Holtstam et al. 2014) and has more strictly granitic compositions.

Several stages of Svecokarelian metamorphism and deformation complicate the geology in the region. Svecofennian metamorphism peaked at

1.85–1.80 Ga reaching greenschist to amphibolite facies (Stephens and Jansson 2020).

2.1 REE-mineralisation in western Bergslagen

After the discovery of the Bastnäs REE-deposits several additional iron oxide deposits strongly enriched in REE were recognized. These deposits are all of similar geology and mineralogy and are classified as Bastnäs type deposits. They occur along a narrow strip of over 100 km length in western Bergslagen called the REE-line (**Figure 1**).Holtstam and Andersson 2007 introduced a classification of the Bastnäs type deposits in twogroups. Type 1 with the type deposits Bastnäs, and Rödbergsgruvan at the southern end of the REE line which shows enrichment in LREE and Fecharacterised by cerite-(Ce) and ferriallanite-(Ce) as primary ore minerals. Type 2 is relatively enriched in,HREE, Y and Mg, Ca, F and occurs mainly in theNorberg district at the northern end of the REE line.

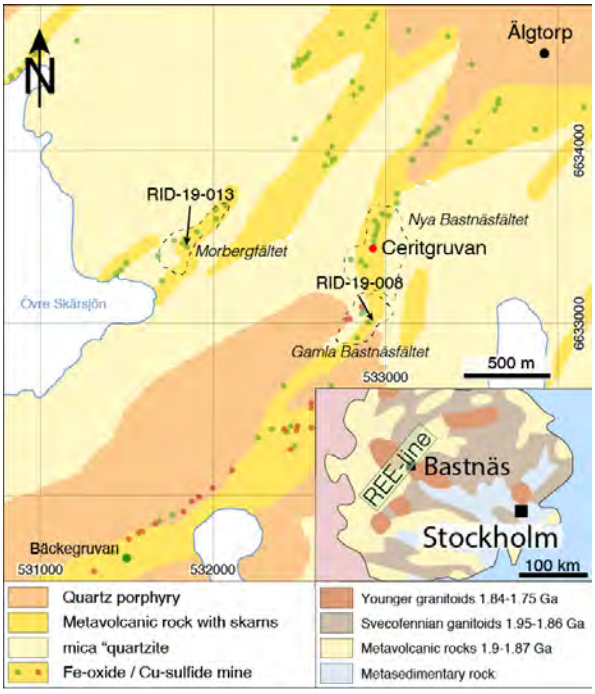

Figure 1. Geological map of the Bastnäs ore field (after Holtstam et al. 2014). The two studied drill cores are shown by arrows, both plunge with -50° while the generalbedding is sub-vertical, striking NO-SW. The location of the Nya Bastnäs iron oxide deposit and the Ceritgruvan isshown by the alchemical iron symbol. The coordinate frame is in SWEREF99. The location of Bastnäs in Bergslagen is given in the inset geological map.

3 Existing data, sampling, and methods

As part of this study, two drill cores from a drilling campaign in 2019 were re-logged and selectively sampled. The sampled sections were scanned by X-ray tomography to identify the 3-dimensional textures of the REE-bearing minerals. Samples representing the different structural and textural REE-ore types were then selected for thin sections. Twelve thin sections were examined at the SEM (Scanning Electron Microscope) at the Swedish Museum of Natural History. Mineral compositions were semi-quantitively analysed by EDS (energy-dispersive X-ray spectroscopy).

4 Lithological controls

The bulk rock assay data shows that all magnetite skarn units in the two studied drill cores contain very high REE concentrations, whereas the magnetite and hematite banded iron formations (BIF) are not significantly enriched in REE (Figure 2). Within the magnetite skarns there is no correlation between magnetic susceptibility (as a proxy for magnetite) and REE concentration. The magnetite and REE mineralisation in drill core RID-19-008 occur mainlyat the margins of the marble unit. In drill core RID- 19-013, the whole upper marble/skarn unit is strongly mineralised with magnetite whereas the REE mineralisation is more pronounced in the lowerpart of the skarn.

5 Mineralogy and Textures

The REE-rich sections in the drill cores are typically characterised by mm- to cm-sized grains or massive veins and bands of dark brown to black epidote supergroup REE-minerals (ESM) (~80-90%; e.g. ferriallanite-(Ce), dollaseite-(Ce) and dissakissite-(Ce)), which strongly dominate the REE paragenesis. REE-carbonates and halides are rare,an exception is bastnäsite-(Ce), which is a more common accessory phase. There are two main groups of REE-mineralisation textures and paragenesis described below.

The first and most common REE mineral paragenesis is a granoblastic intergrowth of magnetite and ESM (dominantly ferriallanite-(Ce), dissakisite-(Ce) and dollaseite-(Ce)) in a matrix of tremolite and in some samples (mostly magnetite free samples) actinolite; diopside and serpentineoccur in the lower part of drillhole RID-19-013. The matrix generally shows a granoblastic to fibrousunoriented texture which appears recrystallised. However, the skarn shows decimeter scale variations in magnetite content and type of tremolitetextures (massive fine grained to asbestiform). ESMcontain inclusions of britholite-(Ce) and gadolinite- (Y, Ce, Nd). Bastnäsite-(Ce) occurs at the contact tocalcite and calcsilicates (Figure 3a) as well as fibrous loose clusters in the vicinity of other REE phases (Figure 3c). This style of mineralisation is the dominant REE mineralisation type in drillhole RID- 19-013.

The second group is associated with structures such as veins, faults, and shear bands. The REEs are almost exclusively hosted by ESM whilexenotime-(Y) occurs as accessory phase. The REE paragenesis is commonly associated withserpentine, calcite (as vein, fracture-filling) and talc. Ferriallanite-(Ce) is the dominant REE. It commonly

occurs as overgrowth and rims on, and as veins in allanite-(Ce) (Figure 3d). As in the first group bastnäsite-(Ce) occurs as secondary mineral in contact to calcite and calc-silicates but also as fracture filling in allanite-(Ce). In some samples ESM bearing veins crosscut older REE mineralisation in skarn.

A notable exception to the above-described groupings is a sample at 230 m in core RID-19-008 which shows cerite-(Ce) as an intergrowth with magnetite and chalcopyrite (Figure 3b).

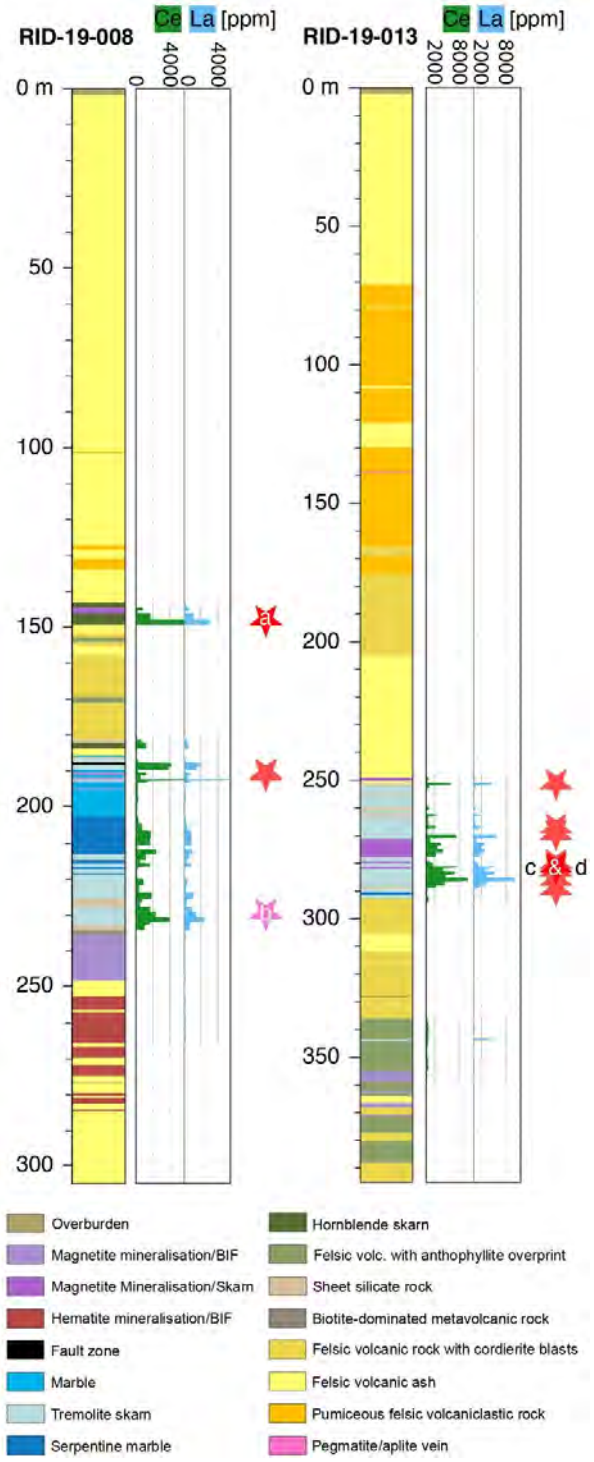

Figure 2. Simplified core logs (EMX) of the twoinvestigated drillcores showing the stratigraphy with the position of the iron ores and in separate columns the sections of high REE concentration according to assay data from EMX. The two drill cores are from different stratigraphic intervals (position shown in Figure 1). The stars indicate the position of the analysed samples, (the letters refer to the images in Figure 3). The sample containing cerite is shown by the pink star.

6 Discussion and conclusions

The results show that the REE mineralisation at Bastnäs is associated with skarn horizons as previously reported (e.g. Jonsson and Högdahl 2013, Holtstam et al 2014). However, the drill cores investigated in this study allow this relationship to be seen in more detail. We report two main textural groups of REE mineralisation. The first and most common group comprises a recrystallised intergrowth of REE-minerals and magnetite hosted in tremolite skarn and in some sections also by actinolite or diopside skarn. Group 2 mineralisation shows evidence of extensive remobilisation and recrystallisation, such as strongly foliated chlorite and talc layers (5-20 cm thick) containing coeval intergrown ferriallanite-(Ce). The intensity of REE mineralisation appears to peak at lithological boundaries such as with BIF in RID-19-008 which is not mineralised with REE (Fig. 2).

The mineralogy we observe is generally similar to the type 1 mineralisation (Riddarhyttan area / Rödbergsgruvan) reported by Holtstam et al. (2014) as the mineralisation is dominated by REE-silicates, but there are some key differences and variations. Cerite-(Ce) which is described as a major constituent by Holtstam and Andersson (2007) only occurs as a minor constituent in one layer at the bottom of the thick marble/skarn unit in RID-19-008.Old mine maps (Mannerstråle 1886) indicate the cerite ore at Nya Bastnäs at a similar stratigraphic position. The differences in REE mineralogy between Nya Bastnäs and Gamla Bastnäs which appear to lie in the same stratigraphic position possibly indicate lateral variability in REE mineralisation style. We observe bastnäsite-(Ce) but contrary to the observations of Holtstam and Andersson (2007), only as minor, secondary mineralat the contact of REE-silicates and Ca-bearing phases (Figure 3c). Furthermore, in our textural group 1, gadolinite-(Ce, Y, Nd) occurs as a common mineral, and britholite-(Y, Ce) and fluorbritholite-(Ce)as rarer mineral forming inclusions in ESM (Figure 3a) whereas Holtstam et al. (2014) describes fluorbritholite-(Ce) only in type 2 mineralisation (Norberg district) and gadolinite-(Y) only as accessory phase in type 1. Britholite-(Y) and britholite-(Ce) have previously not been reportedfrom Bastnäs type deposits.

Our observations combined with those previously reported indicate a large variety of REE mineralisation with different styles possibly occurring at different stratigraphic levels, laterally within the same horizon and due to recrystallisation driven by

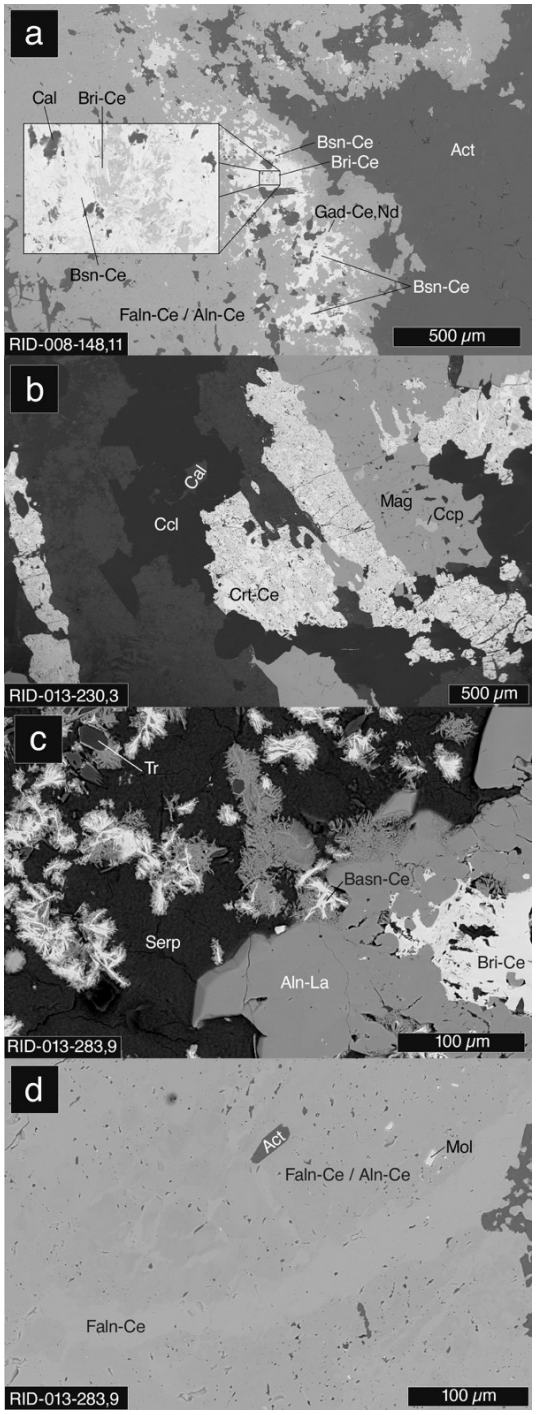

Figure 3. Backscattered electron images showing the textural relationships between different REE phases. The position of the samples is referenced with the letters in the top left corner corresponding to Figure 2. The sample ID is given in the lower left corner. **a**) shows the typical paragenesis in magnetite skarns (group 1), **b**) shows the cerite ore, **c**) shows secondary Basn-Ce and **d**) shows Faln-Ce veins in Aln-Ce (group 2).
Abbreviations: Act=actinolite; Aln=allanite; Bsn=bastnäsite;Bri=britholite; Cal=calcite; Ccl=clinochlore; Ccp=chalcopyrite; Crt=cerite; Faln=ferriallanite; Gad=gadolinite; Mag=magnetite; Mol=molybdenite; Serp=serpentine; Tr=tremolite.

deformation. The stratigraphic sections from Gamla Bastnäs (RID-19-008) and Morbergfältet (RID-19-013) contain different styles of REE mineralisation and most likely represent different stratigraphic levels. The higher abundance of minerals rich in HREE and Y in RID-19-013 indicates some similarities with the REE mineralisation described atNorberg (Holtstam et al. 2014). The abundance of heavily remobilised group 2 mineralisation and the occurrence of wide, talk and chlorite filled fractures in RID-19-008 may indicate proximity to a fault zone (also indicated by Öhman et al. 2004). The combined observations indicate a complex mineralisation history with several temporal stages and later remobilisation. The REE-ore is best described as stratabound. Most REE mineral textures are paragenetically late, but it remains unclear whether primary REE mineralisation occurred during initial skarn formation or at a later stage.

Acknowledgements

EMX Royalties Corp. are thanked for the access to the drill cores logs and assay data.

References

Andersson UB, Holtstam D, Lundström I, Langhof J, Nysten P (2004) The Bastnäs-type REE-mineralisations in north-western Bergslagen, Sweden: a summary with geological background and excursion guide. Geological Survey of Sweden, Uppsala

Geijer P (1921) The cerium minerals of Bastnäs at Riddarhyttan. Geological Survey of Sweden, Uppsala, C304:1–24

Holtstam D, Andersson UB (2007) The REE minerals of the Bastnäs-type deposits, south-central Sweden. CanMineral 45: 1073-1114. https://doi.org/10.2113/gscanmin.45.5.1073

Holtstam D, Andersson UB, Broman C, Mansfeld J (2014) Origin of REE mineralization in the Bastnäs-type Fe-REE-(Cu-Mo-Bi-Au) deposits, Bergslagen, Sweden. Miner Deposita 49:933-966. https://doi.org/10.1007/s00126-014-0553-0

Jonsson E, Högdahl K (2013) New evidence for the timing of formation of Bastnäs-type REE mineralization in Bergslagen, Sweden. Mineral deposit research for a high-tech world: Proceedings of the 12th SGA Biennial Meeting 2013 pp 1724–1727.

Mannerståle CM (1910) Karta över Bastnäs Gruvfält i Skinnskattebergs Bergslag av Westerås län, Gruvkarta 491.

Öhman L, Nysten P, Langhof J (2004) The Bastnäs Mines, Riddarhyttan ore field, Bergslagen district, Västmanland, Sweden. The minerlogical Record 35:187-200

Sahlström F, Jonsson E, Högdahl K, Troll VR, Harris C, Jolis EM, Weis F (2019) Interaction between high-temperature magmatic fluids and limestone explains 'Bastnäs-type'REE deposits in central Sweden. Sci Rep 9:15203. https://doi.org/10.1038/s41598-019-49321-8

Stephens MB, Jansson NF (2020) Chapter 6 Paleoproterozoic (1.9-1.8 Ga) syn-orogenic magmatism, sedimentation and mineralization in the Bergslagen lithotectonic unit, Svecokarelian orogen. Geological Society, London, Memoirs 50:155–206. https://doi.org/10.1144/M50-2017-40

Trägårdh J (1988) Cordierite-mica-quartz schists in a Proterozoic volcanic iron ore-bearing terrain, Riddarhyttan area, Bergslagen, Sweden. Geol Mijnb 67:397–409

Genesis, Sedimentology, and Geochemical Features of Stratiform Phosphorites of the Upper Lydite Formationand Rare Earth Element Content

Juan F. Galán[1], Juan F. Correa[1]
[1]Departamento de Geociencias, Universidad Nacional de Colombia, Sede Bogotá

Abstract. This study presents a petrological and geochemical analysis of phosphorites deposited during the Upper Cretaceous near the municipality of Piedras, inthe department of Tolima, Colombia and found within the Upper Lydite Formation of the Oliní Group characterized by a sedimentary sequence composed of fine-grained terrigenous and calcareous marine. rocks. The objective is to provide a better understanding of the mineralogy, genesis, and formation environments of these phosphorus-rich rocks, as well as their economic viability for exploitation. Petrographic analysis reveal that the rocksare mainly composed of fluorapatite, calcite, and quartz, with accessory minerals such as glauconite, pyrite, smectite, and other clay minerals, which were confirmed by crystallographic results obtained using XRD. Sedimentological analysis from petrography indicate that the rocks belong to a calcareous sequence of benthic foraminiferal biomicrites, which are highly silicified, suggesting that the entire sequence was formed in an offshore marine environment with an influence of upwelling currents and processes of increasing and decreasing system energy. Geochemical analysis using X-ray fluorescence showed the presence of REE such as cerium, lanthanum, and yttrium in appreciable concentrations in the phosphorite using a semi- quantitative method, which opens the possibility of future exploitation of this type of deposit focused on obtaining these elements in Colombia. This would be of great scientific and economic interest as these elements are key in various technological applications, have high demand inthe global market, and especially in the energy transition that is beginning in the country. The importance and detailed information of this type of reservoir in global REE demand is discussed in depth in McLaughlin et al. (2016). The relatively high concentrations of REE in the rocks were associated with the replacement of calcium in the structure of fluorapatite by these elements during their formation.

1 Introduction

Phosphorites are sedimentary rocks that contain high concentrations of phosphate (P_2O_5), an essential element for life and agriculture. Colombia has important phosphorite deposits, mainly in the Eastern Cordillera, where phosphorites of marine origin of Cretaceous age are found (Cathcart et al. (1967)). These rocks have been exploited for decades to produce fertilizers. Colombia is the 5th largest producer of phosphates in the continent, after the United States, Brazil, Peru, and Mexico. Currently, Colombia has been extracting the mineral, with an average annual production of 60,377 tons in the last 5 years (ANM 2021). However, domestic demand exceeds the national supply, so it is necessary to import this mineral from other countries, which makes it necessary to increase the production of this resource in a sustainable manner and with world standards of environmental care.

In addition to their importance for agriculture and life in general, in recent years it has become evident that these rocks present concentrations of rare earth elements, which are a group of elements considered critical due to their unique properties and strategic applications in various industrial sectors. The high REE concentrations in phosphorites have been explained that their relatively high concentrations are due to the substitution of Ca2+ cations, which is the most common cation in phosphates. These are similar in size to rare earths (REE), which facilitates substitution. In addition, rare earths have a charge of 3+, which is the same as that of the anionic group of (PO4)3-phosphates, which promotes electrical neutrality and stability of the crystal structure.

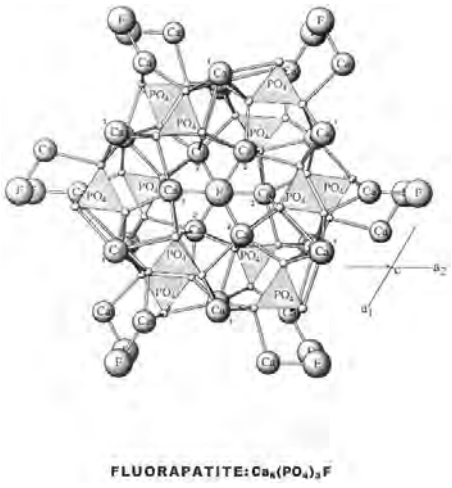

Figure 1. Molecular structure of fluorapatite ($Ca_5(PO_4)_3F$) taken from Skinner (2004).

Constituent ion	Substituting ion
Ca^{2+}	Na^+, K^+, Ag^+ Mg^{2+}, Sr^{2+}, Ba^{2+}, Cd^{2+}, Mn^{2+}, Zn^{2+} Bi^{3+}, Sc^{3+}, Y^{3+}, REE^{3+} U^{4+}
PO_4^{3-}	CO_3^{2-}, SO_4^{2-}, CrO_4^{3-} CO_3, BF^{3-}, CO_3, OH^{3-}, AsO_4^{3-}, VO_4^{3-} SiO_4^{4-}
F^-	OH^-, Cl^-, Br^- O^{2-}

Figure 2. Possible substitutions in the fluorapatitestructure. taken from Jarvis et al. (1994).

Phosphorites are formed through a complex series of geological processes that involve the concentration of phosphorus and other elements in sedimentary deposits. Understanding these processes and the factors that control the formation and distribution of phosphorites is essential for identifying potential deposits and developing sustainable strategies for their extraction.

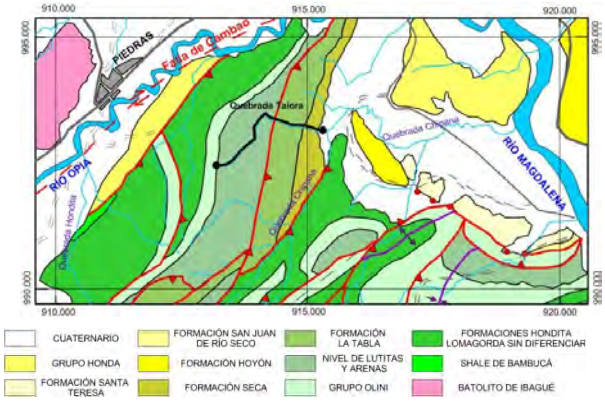

Figure 3. Regional geology and location of the study area taken from Hernández Duran (2021).

2 Methodology

Two field trips were made to Piedras town to collect representative samples of the bedrock (silicified calcareous rocks) and especially of the phosphorites. We also tried to know the general formation environment of the outcropping units in the area, through sedimentological and stratigraphic observations, and with the support of a bibliographic review of previous studies of the area, such as Guerrero et al. (2000) and De Porta (1965). A mostly marine environment was interpreted, with evidence of transgressive and regressive events, but with a trend towards marine regression towards the end of the Cretaceous. The samples were then observed and analysed macroscopically and microscopically, from hand samples and thin sections prepared for petrographic analysis.

XRD and XRF methods were used to compare and quantify the mineralogical and chemical composition of the samples. XRD was carried out with a D2 Phaser equipment, following the methodology of Thorez (1976), which consists of crushing the sample to a size <50 um and then making the 4 analyses which are disoriented powder, natural orientation, ethylene glycol and calcined at 515 °C. This allows a correct and unbiased interpretation of the semi-quantitative composition of the samples, which was performed in the profex program. XRF was performed on phosphorite samples UPW-E2 and UPW-C3 (Fig. 4), which were reduced to powder, dried at 105 °C for 12 hours, mixed with Merck spectrometric wax in a 10:1 ratio, homogenized by shaking and pressed at 120 kN for one minute, forming two granules of 37 mm diameter and measured in the SEMIQ-2020 application. Semiquantitative analysis was performed with Semio 5 software, with 11 scans, to detect all elements present in the sample, except H, C, Li, Be, B, N, O, and transuranic elements. An X-ray fluorescence spectrometer, MagixPro PW 2440 Philips (WDXRF) with a rhodium tube and a maximum power of 4 KW was used. This equipment has a sensitivity of 100ppm (0.01%) for heavy metallic elements.

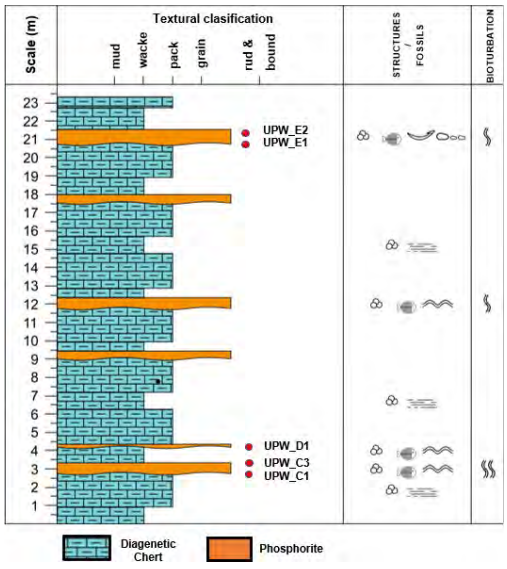

Figure 4. Generalized stratigraphic column of the last 24 meters of the top of the Upper Lidita Formation modified from Guerrero et al. (2001).

3 Petrography analysis

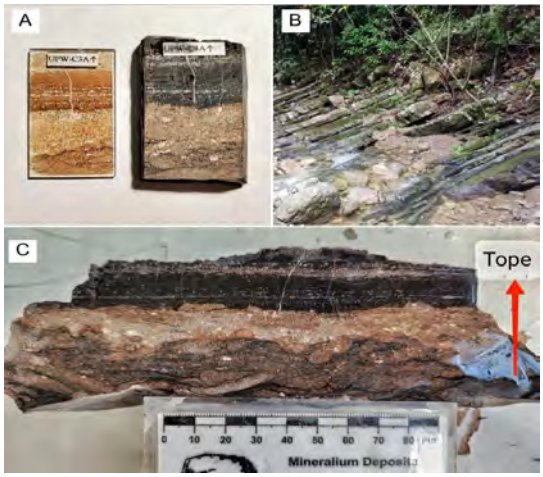

Figure 5. Thin section and rock slice of phosphorite sample. B: outcrop view of Upper Lydite Formation. C: Cut and polished hand phosphorite sample.

The petrographic analysis was performed on 10 thin sections of the Upper Lidita formation, this analysis showed two types of sedimentary rocks: cherts and phosphorites. The cherts are siliceous rocks that originated from the silicification of carbonate rocks of marine origin, which formed in a low-energy

environment, possibly in the lower off-shore. These rocks were classified as wackstone biomicrites and benthic foraminiferal packstones, according to Dunham's (1962) classification. The cherts contain mainly benthic foraminifers as allochems and micrite as matrix. The samples show plane-parallel lamination, indicating settling sedimentation, and an absence of bioturbation, indicating little biological activity. Silicification was aided by ions in solution brought by upwelling currents, which precipitated in the pores of the carbonate rocks, replacing micrite and foraminifera. The presence of framboidal pyrites within some foraminifera suggests that conditions were reducing and that sulfate-reducing bacteria were involved in diagenesis.

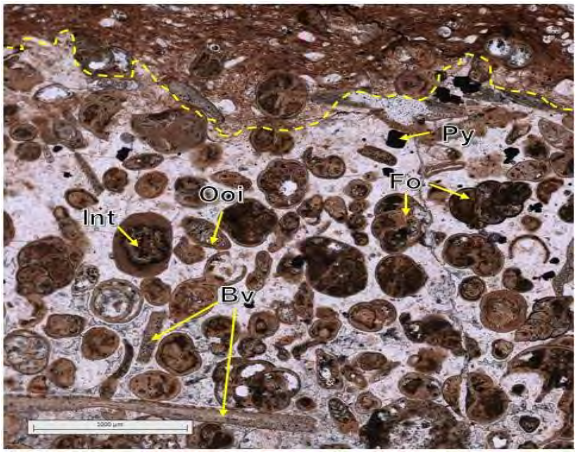

Figure 6. Phosclast-grainstone of Benthic foraminifera (C3TF sample): Benthic foraminifera (Fo), phosphate intraclasts (Int), bivalve fragments (Bv), immature phosphate ooids (Ooi) with benthic foraminifera cores, pyrite (Py).

Phosphorites originated from the accumulation of remains of phosphorus-rich marine organisms such as fish bones and from the replacement of calcium carbonate by dissolved phosphate in the water largely contributed by upwelling currents (e.g.: Föllmi 1995). These rocks were classified as phosclast packstone and grainstone of benthic foraminifera, fish remains, intraclasts and bivalve fragments, as classified by Trappe (1998). The phosphorites also contain quartz, clay minerals indicating a greater terrigenous input than in the cherts. The phosphorites show an absence of sedimentary structures such as lamination but some bioturbation structures, indicating higher energy and greater biological activity. The net increase in grain size and the presence of erosional surfaces towards the base of the phosphorite indicate sudden changes in the energy of the environment that reworked and concentrated the phosphate particles. A noticeable increase in pyrite and glauconite concentrations was also observed with respect to the chert layers.

4 X-ray diffraction quantification

X-ray diffraction (XRD) analysis was carried out to corroborate the information obtained by petrography and to complete the mineralogical part of the investigation. This analysis revealed the presence of fluorapatite, quartz and calcite as rock-forming minerals (Fig. 7). Smectite and kaolinite were identified as main clay minerals, and pyrite and glauconite as accessory minerals. In addition to knowing the specific composition of each sample some additional interpretations were reached, such as that the clay minerals and quartz content increase towards the top of the studied section. Also, from sample C3 which was divided into 3 parts, the whole history of the rocks was better understood.

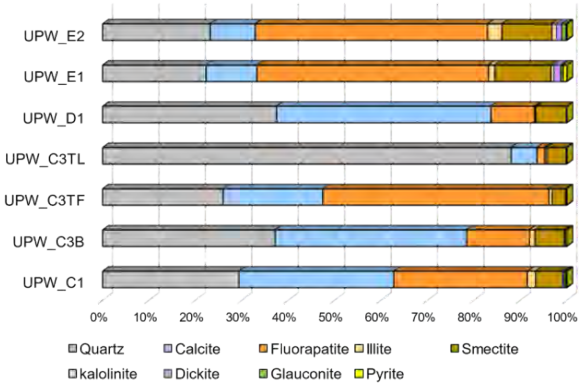

Figure 7. Semi-quantitative mineral composition of phosphorite and lydite samples analysed by X-ray diffraction.

Higher concentrations of fluorapatite are observed in lydite samples (Samples C3B and D1) stratigraphically located just before a phosphorite genesis event compared to lydite samples located just after the event (C3TL). Phosphorite samples (E1, E2, C3TF, and C1) yielded a maximum of 50% by weight of the total rock, and it was discovered that the thickness of the phosphorite layer is directly related to the percentage of phosphate. Furthermore, the phosphate content is inversely proportional to the silica content of the phosphorite samples.

5 XRF Analysis

According to the results obtained by X-ray fluorescence, these rocks were identified as containing a high percentage of P2O5 (~25 wt%), which is the main indicator of the quality of phosphate rocks. In addition, the rocks present considerable concentrations of REE, such as cerium (~400 ppm), lanthanum (~300 ppm) and yttrium (~100 ppm), the relationship of P2O5 with other major oxides such as CaO and SiO2 is not clear, and more information is needed to correctly interpret these associations. Other components found in the samples are shown in detail in Figure 8.

Further geochemical analysis is needed on the phosphorites and especially on associated rocks such as lydites to identify if there are compositional variations and what they might be associated with.

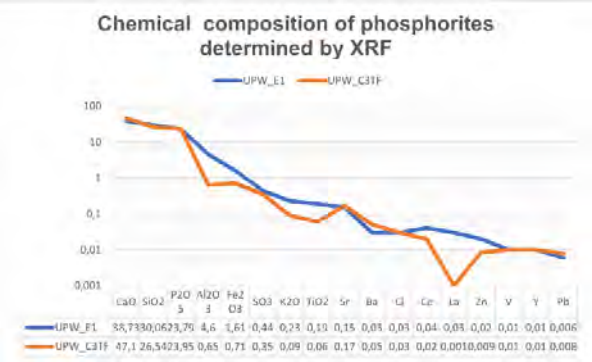

Figure 8. Chemical composition in weight percent of total rock from two samples of phosphorites C3TF and E1 determined by XRF.

6 Conclusions

The Upper Lidita Formation consists of two types of sedimentary rocks: cherts and phosphorites. Petrographic analysis reveals their different origins and environments. The cherts have planoparallel lamination, with calcareous allochemicals and orthochemicals replaced by silica. They lack erosional structures, suggesting that they formed from the silicification of carbonate rocks in a low energy setting. The phosphorites have microerosive structures at the base, randomly arranged allochemicals, no matrix, calcite cementation and phosphatization of the fossils. These features indicate that they resulted from the accumulation of phosphorus-rich marine organisms, with substitution of calcium carbonate by dissolved phosphate, in a higher-energy setting. Possible upwelling currents may have contributed phosphate to the system. The petrographic results agree with previous studies that interpret the Upper Lidita Formation as a transgressive-regressive sequence, reflecting changes in sea level and tectonics during the Upper Cretaceous (Guerrero et al. 2001).

The phosphorites contain fluorapatite, quartz, calcite, smectite, kaolinite, pyrite and glauconite, as confirmed by X-ray diffraction analyses. They also show evidence of a phosphorite genesis event, which started with a rapid enrichment of fluorapatite in the rock. After a high-energy event, fluorapatite reached up to 50% by weight of the rock. When the system returned to normal (low energy environment producing biomicrites), fluorapatite decreased to only 3%.

The phosphorites have a high percentage of P2O5 and significant concentrations of REE such as cerium, lanthanum, and yttrium. These make them potentially valuable as a source of these elements, which are highly demanded and scarce. Most of the production of REE is concentrated in a few countries, such as China. Phosphate rocks are an abundant and accessible resource that can also provide phosphorus, which is a critical element for food security and economic development.

Acknowledgements

I would like to express my sincere thanks to Professor Carlos Sánchez for his guidance and support throughout the project. I also thank the Lattice and MicroFluidSpectral laboratories for facilitating the use of their analytical equipment. I would also like to acknowledge the help and advice of Denis Oi ulu and Carlos Esquivel in the final part of the project. Finally, thanks to SGA UNAL Bogota and Professor Thomas Heinrich Cramer for doing everything.

References

ANM (2021). “Los fosfatos son un mineral de interés estratégico para Colombia”: presidente ANM. Agencia Nacional de Minería ANM. https://www.anm.gov.co/?q=los-fosfatos-son-un-mineral- de-interes-estrategico-para-colombia

Cathcart JB, Zambrano F, Mojica PE (1967). Roca fosfática en Colombia, con una sección sobre fosfatos de Turmequé, Boyacá. Boletín Geológico, 15(1-3): 65-162.

De Porta J (1965). La estratigrafía del Cretácico Superior y Terciario en el Extremo S del valle Medio del Magdalena. Boletín De Geología 19: 5-50

Dunham RJ (1962). Classification of carbonate rocks according to depositional texture. American Association of Petroleum Geologists Memoir 1(108): 108–121.

Föllmi KB (1995). The phosphorus cycle, phosphogenesis and marine phosphate-rich deposits. Earth-Science Reviews, 40(1-2): 55-124.

Guerrero J (2000). The Stratigraphy of the W Side of the Cretaceous Colombian Basin in the Upper Magdalena Valley. Reevaluation of Selected Areas and Type Localities Including Aipe, Guaduas, Ortega, and Piedras. Geología Colombiana 25:45-110

Hernández Duran S (2021). Litogeoquímica de las unidades del Cretácico Superior, su relación con las áreas de aporte y evolución de los medios sedimentarios, Cuenca del Valle Superior del Magdalena, Colombia; M.Sc. thesis, Universidad Nacional de Colombia, 225 p. https://repositorio.unal.edu.co/handle/unal/80337

Jarvis I, Murphy AM, Gale AS, Thirlwall MF, Busfield ME (1994). Phosphorus cycling in the sedimentary record. Philosophical Transactions of the Royal Society B: Biological Sciences 346(1318): 27–35.

McLaughlin PI, Emsbo P, Breit GN, du Bray EA, Koenig AE (2016). Rare earth elements in sedimentary phosphate deposits: Solution to the global REE crisis? Gondwana Research 36(1): 145-157.

Skinner C (2004). Molecular structure of fluorapatite. https://serc.carleton.edu/download/images/1809/CatherineS_ice.jpg

Thorez J (1976). Practical Identification of Clay Minerals: A Handbook for Teachers and Students in Clay Mineralogy. 90 p.

Trappe J (1998). Phanerozoic phosphorite depositional systems: A dynamic model for a sedimentary resource system. Lecture Notes in Earth Sciences, v. 76, 323 p. https://doi.org/10.1007/BFb0009670

The Circular Economy Challenge: Re-use of processing granite wastes for REEs-recovery: preliminary results

Silvia Gioiello[1], Licia Santoro[1], Alberto Cazzaniga[2]
[1] Department of Earth Sciences, University of Torino, Italy
[2] Minerali Industriali S.r.l., Italy

Abstract. Chemical and minero-petrographic analyses by ICP-MS, XRPD, and SEM-EDS have been performed on scraps from the industrial processing of granite. The work aims to study the optimization of industrial processes by re-using the feldspar-treated waste material to recover Critical Raw Materials in the view of economic circularity and sustainable mining. The material used for this work derives from Montorfano quarry wastes (Piemonte, Italy). The ICP-MS analyses on the 1.2 to 0.1 mm fraction discarded after magnetic separation of granitic material for pure feldspar production show enrichment in Rare Earth Elements (REEs), mainly Ce, La, Nd, and Y. The XRPD and SEM-EDS analyses indicate that monazite, allanite, and xenotime are the main REE-bearing minerals, commonly locked within phyllosilicates. The results suggest that a further grinding on the unprocessed material is probably required to enhance particle liberation. Comminution to a particle size smaller than 0.1 mm, will lead to a more effective concentration of REEs minerals during magnetic separation.

1 Introduction

The growing economic importance and high supply risk make the availability of Critical Raw Materials (CRMs) a crucial issue for the European Union, which translates into the need to promote their exploration and recovery optimization to meet the foreseeable increase in demand. Most of these materials are essential for transitioning from the traditional energy system to a more sustainable one. However, domestic production is severely limited, resulting in a strong dependence on imports and uncertain access to resources. The present study focuses particularly on Rare Earth Elements (REEs), mainly used to manufacture components for high-tech and green technologies applications (European Comission 2017, 2021; Bobba et al. 2020). Currently, China holds the monopoly on REEs production. Moreover, mineral processing to recover such materials still represents a considerable challenge. Re-processing and re-use from quarry and mining wastes represent a good option to face the supply risk, leading to diversification of the supply chain and likely enhancement of domestic supply. In light of the above, this work aims to assess the viability of REEs recovery from mineral-processing industrial wastes, hence favoring a possible valorization and sustainable management of the processing scraps through their re-use in the frame of the Circular Economy.

The object of this research is a quarry disposal site located in the Lake District of the Verbano-Cusio-Ossola area (Piedmont, Italy), on the southern slope of the Montorfano massif (Figure 1a), where granite bodies were quarried as dimension stones for ornamental purposes, producing a huge volume of waste material. Such material is presently exploited to recover feldspar for ceramic and glass industries. The Montorfano pluton is intruded into gneissic rocks of the *Scisti dei Laghi* subunit, belonging to the *Serie dei Laghi* unit (Figure 1b). It is part of a NE-SW elongated batholith composed of many plutons occurring from the Biella area to the western shore of Lago Maggiore (Boriani et al. 1988).

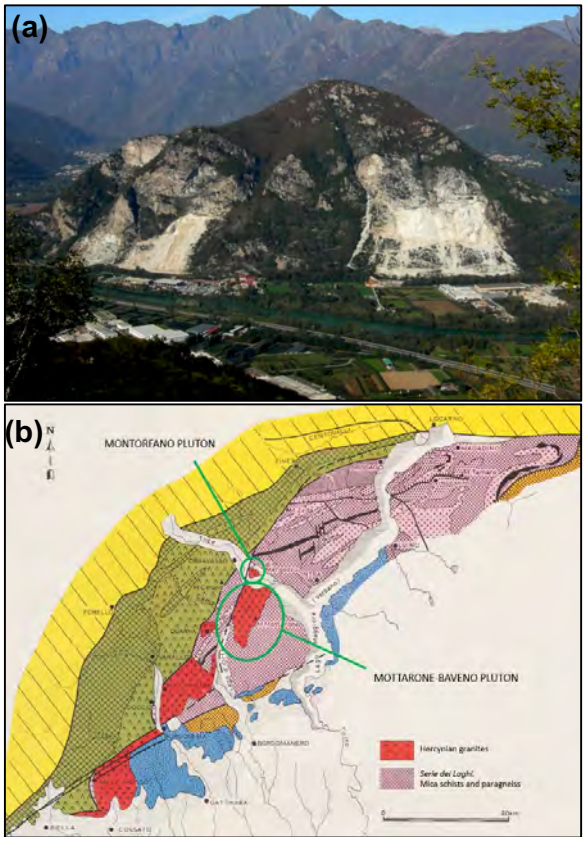

Figure 1. a Granite quarries on the southern side of Montorfano massif (Dino et al. 2012). **b** Tectonic sketch map of a portion of the central-southern Alps (Piedmont, Italy) and location of Montorfano and Mottarone-Baveno granitic plutons into *Serie dei Laghi* unit. Adapted from 1:50.000 geological map of the Verbania area (Boriani A et al. 1977).

The pluton is a medium-grain white granite, whose mineralogical assemblage consists primarily of plagioclase, quartz, K-feldspar, and biotite, including typical accessory minerals such as apatite, zircon, and allanite (Boriani et al. 1988). The occurrence of allanite-(Ce), together with other REEs-bearing minerals (e.g., Y-Sc-REEs-silicates, Y-REEs phosphates and Nb-Ta-Y-REEs oxides) has already been described in previous studies on the niobium-yttrium-fluorine (NYF) granitic pegmatite at Baveno (Guastoni et al. 2017).

A key purpose of the study was to evaluate the concentration process of ore minerals during the granite waste treatment aimed at feldspar production, performing detailed mineralogical and geochemical analyses on milled samples coming from different processing stages, as described in the following paragraph.

2 Methodology

Granite waste rock samples were collected in the Montorfano quarry and subsequently prepared and analyzed to define the behavior of REEs minerals in different types of concentrates resulting from industrial processing. All samples were crushed and ground in appropriate mills to achieve a grain size between 0.1 and 1.2 mm and then subjected to two different steps of magnetic separation, thus replicating the method used to obtain a pure feldspar concentrate. This process produces a "waste" magnetic fraction. The first separation step was applied on unprocessed material with grain size between 0.1 and 1.2 mm using a current of 2.5 Amp. Subsequently, the magnetic concentrate was sieved, and a second step was carried out on grain size of 0.1-0.6 mm using 2.5 Amp.

Wet chemical analyses by Inductively Coupled Plasma Mass Spectrometry (ICP-MS) were performed by ALS Laboratories on both the unprocessed material and the magnetic fraction for a large number of elements, including REEs (Sc, Ce, La, Nd, Sm, Pr, Eu, Dy, Er, Y, Gd, Ho, Lu, Tb, Tm and Yb) and other critical metals (e.g., Nb, Ta). Furthermore, the magnetic concentrates were investigated in terms of mineralogical and chemical composition through qualitative and quantitative analyses. Particularly, X-Ray Powder Diffraction (XRPD) analyses were carried out at the Minerali Industriali Engineering's central laboratory to characterise the material. The acquisitions were carried out by using a Siemens D5000 Diffraktometer, operating at 40 kV, 40 mA, divergence slit 1, antiscatter slit 1, rotation 30, start 4 and stop 70. SEM-EDS analyses were carried out with a JEOL IT300LV Scanning Electron Microscope at the Department of Earth Sciences, University of Torino. The instrument was equipped with an energy dispersive spectrometry (EDS) Energy 200 system and an SDD X-Act3 detector (Oxford Inca Energy). Operating conditions were: 20 kV accelerating voltage, 5 nA probe current, 30 s counting time. SEM data were acquired and processed using the AzTec software (Oxford Instrument), version 6.0. In detail, microanalyses were acquired by using AzTec point ID suite. The use of SEM-EDS was combined with Automated Mineralogy (AM) analytical systems using a specific software package for data processing and automation (i.e., AztecFeature), which provides detailed particle analyses to be classified on the morphology and on the chemistry and combination of the two.

3 Results

Preliminary results described below refer to a representative sample indicated as *SNG*, which consists of a magnetic concentrate resulting from the first separation step, sieved to a grain size greater than 0.6 mm.

3.1 Wet chemical analyses (ICP-MS)

As shown in Table 1, chemical analysis on samples from different processing stages highlights a REEs enrichment in the magnetic concentrate compared to unprocessed material, particularly on the course fraction obtained from the first separation step. Light REEs (from Sc to Eu) are generally more abundant than heavy REEs (from Dy to Yb), and the highest values, are found for Ce, La and Nd. In addition, there is an increase in P from the unprocessed material to the magnetic fraction coinciding with the trend in REEs concentrations.

Table 1. ICP-MS results for REEs and P. (TQ = unprocessed material; SNG = magnetic fraction >0.6 mm, 1st separation step) SNS = magnetic fraction <0.6 mm, 2nd separation step).

		TQ	SNG	SNS			TQ	SNG	SNS
Sc	ppm	8.6	55.3	32.9	**Dy**	ppm	4.86	22.2	12.45
Ce	ppm	89.9	434	256	**Er**	ppm	2.25	9.78	5.53
La	ppm	42	197	118	**Y**	ppm	22.8	99	64.3
Nd	ppm	40.5	198.5	125	**Gd**	ppm	6.76	32	17.9
Sm	ppm	8.34	39.2	23.3	**Ho**	ppm	0.86	3.82	2.19
Pr	ppm	10.8	51.9	32.5	**Lu**	ppm	0.28	1.13	0.69
Eu	ppm	0.77	1	0.82	**Tb**	ppm	0.92	4.24	2.28
					Tm	ppm	0.3	1.28	0.79
P	ppm	280	1460	700	**Yb**	ppm	1.91	8	4.95

3.2 Mineralogy and petrography (XRPD/SEM-EDS)

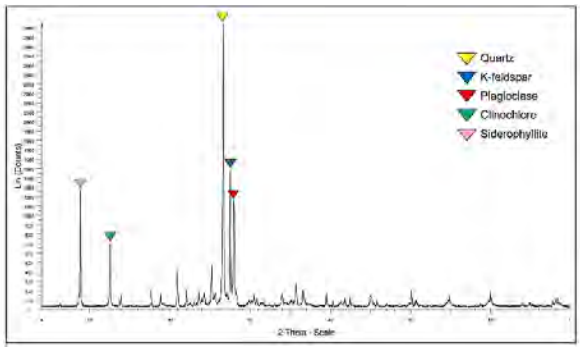

Figure 2. XRPD pattern showing prevailing gangue minerals in the coarse magnetic fraction (SNG sample).

Mineralogical characterization by XRPD helped identify the dominant gangue minerals in the SNG sample, represented by quartz, K-feldspar, plagioclase, clinochlore, and mica group minerals (e.g., siderophyllite), as shown in Figure 2. Peaks representative of REEs-minerals in the diffractogram are absent due to their concentrations falling below the instrument's detection limit.

Backscatter Electron (BSE) images and EDS on target minerals are presented respectively in Figure 3 and Table 2. The most common REEs mineral is monazite-(Ce), in agreement with the high P concentration of ICP-MS analyses (Table 1). Monazite locally shows tiny inclusions of thorite. Additionally, xenotime-(Y) and allanite (light grey) grains were

spotted. REEs-bearing minerals seem generally associated with phyllosilicates (e.g., biotite, annite, siderophyllite, clinochlore) also observed on the XRPD pattern but are characterized by far smaller grain size. However, allanite has a larger grain size than monazite and xenotime. Zircon and ilmenite, often Nb-bearing, were also detected.

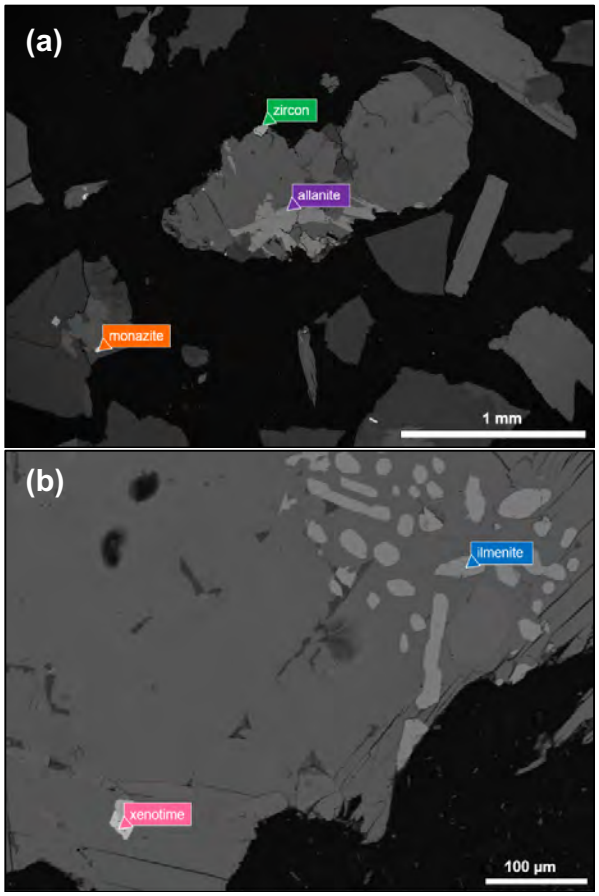

Figure 3. BSE images of selected areas on SNG sample, showing target minerals: **a** zircon (green, Spectrum 24), allanite (purple, Spectrum 25), monazite (orange, Spectrum 32) and **b** xenotime (pink, Spectrum 23), ilmenite (blue, Spectrum 22).

Table 2. EDS analyses of target minerals.

Monazite

	Spectrum 26 (normalised)				Spectrum 32 (normalised)				
	Oxide	Oxide %	Oxide % Sigma	Number of Ions		Oxide	Oxide %	Oxide % Sigma	Number of Ions
O				4	O				4
Si	SiO2	3.3	0.05	0.13	Al	Al2O3	2.45	0.22	0.11
P	P2O5	24.47	0.15	0.83	Si	SiO2	5.45	0.21	0.22
Ca	CaO	6.28	0.05	0.27	P	P2O5	22.21	0.52	0.74
La	La2O3	9.85	0.1	0.14	Ca	CaO	1.26	0.08	0.05
Ce	Ce2O3	27.41	0.18	0.4	Fe	Fe2O3	1.75	0.19	0.05
Pr	Pr2O3	2.74	0.11	0.04	Y	Y2O3	0.08	0.37	0
Nd	Nd2O3	10.2	0.12	0.15	La	La2O3	9.87	0.35	0.14
Sm	Sm2O3	9.62	0.49	0.13	Ce	Ce2O3	25.57	0.64	0.37
Gd	Gd2O3	1.43	0.09	0.02	Pr	Pr2O3	2.53	0.38	0.04
Th	ThO2	4.69	0.09	0.04	Nd	Nd2O3	8.82	0.4	0.12
Total		100		2.15*	Sm	Sm2O3	11.18	1.77	0.15
					Gd	Gd2O3	1.13	0.34	0.01
					Tb	Tb2O3	0.07	0.35	0
					Dy	Dy2O3	0.41	0.33	0.01
					Ho	Ho2O3	0.07	0.3	0
					Th	ThO2	7.16	0.35	0.06
					Total		100		2.10*

* Cation Sum

Allanite

	Spectrum 1				Spectrum 25				
	Oxide	Oxide %	Oxide % Sigma	Number of Ions		Oxide	Oxide %	Oxide % Sigma	Number of Ions
O				12	O				12
Mg	MgO	0.13	0.33	0.02	Al	Al2O3	20.2	0.07	2.04
Al	Al2O3	13.65	0.09	1.47	Si	SiO2	32.43	0.09	2.77
Si	SiO2	30.09	0.09	2.76	Ca	CaO	11.72	0.04	1.07
Ca	CaO	10.65	0.04	1.05	Mn	MnO	1.02	0.05	0.07
Ti	TiO2	2.17	0.05	0.15	Fe	Fe2O3	11.18	0.07	0.72
Mn	MnO	0.29	0.05	0.02	Y	Y2O3	1.14	0.07	0.05
Fe	Fe2O3	14.81	0.08	1.02	La	La2O3	3.59	0.07	0.11
Y	Y2O3	0.49	0.07	0.02	Ce	Ce2O3	8.7	0.11	0.27
La	La2O3	3.58	0.1	0.12	Pr	Pr2O3	1.03	0.08	0.03
Ce	Ce2O3	10.11	0.12	0.34	Nd	Nd2O3	3.58	0.09	0.11
Pr	Pr2O3	1.11	0.09	0.04	Sm	Sm2O3	5.96	0.46	0.18
Nd	Nd2O3	4.21	0.1	0.14	Gd	Gd2O3	0.77	0.1	0.02
Sm	Sm2O3	6.03	0.52	0.19	Dy	Dy2O3	0.26	0.1	0.01
Eu	Eu2O3	0.08	0.1	0	Total		101.58		7.46*
Gd	Gd2O3	0.93	0.12	0.03					
Tb	Tb2O3	0.15	0.13	0					
Dy	Dy2O3	0.41	0.12	0.01					
Er	Er2O3	0.09	0.1	0					
Lu	Lu2O3	0.07	0.09	0					
Total		99.05		7.39*					

* Cation Sum

Xenotime

	Spectrum 23			
	Oxide	Oxide %	Oxide % Sigma	Number of Ions
O				4
Si	SiO2	1.42	0.07	0.05
P	P2O5	34.14	0.13	0.98
Fe	FeO	0.92	0.05	0.03
Y	Y2O3	38.66	0.16	0.7
Ce	Ce2O3	0.03	0.06	0
Nd	Nd2O3	0.44	0.06	0.01
Pm	Pm2O3	-0.13	0.07	0
Sm	Sm2O3	4.17	0.42	0.05
Gd	Gd2O3	2.43	0.08	0.03
Dy	Dy2O3	5.13	0.11	0.06
Ho	Ho2O3	1.34	0.11	0.01
Er	Er2O3	4.38	0.11	0.05
Tm	Tm2O3	0.44	0.11	0
Yb	Yb2O3	3.11	0.12	0.03
Lu	Lu2O3	0.44	0.11	0
Th	ThO2	0.97	0.09	0.01
U	UO2	1.31	0.08	0.01
Total		99.2		2.00*

Ilmenite

	Spectrum 22			
	Oxide	Oxide %	Oxide % Sigma	Number of Ions
O				3
Si	SiO2	0.16	0.03	0
K	K2O	0.07	0.01	0
Ti	TiO2	50.79	0.09	0.99
Mn	MnO	7.03	0.05	0.15
Fe	FeO	39.11	0.1	0.85
Nb	Nb2O5	0.47	0.05	0.01
Total		97.63		2.00*

* Cation Sum

Zircon

	Spectrum 24				Spectrum 18 (normalised)				
	Oxide	Oxide %	Oxide % Sigma	Number of Ions		Oxide	Oxide %	Oxide % Sigma	Number of Ions
O				4	O				4
Si	SiO2	30.85	0.09	0.98	Si	SiO2	32.06	0.13	0.99
K	K2O	0.12	0.02	0	Ca	CaO	0.42	0.02	0.01
Ca	CaO	0.24	0.02	0.01	Fe	FeO	0.63	0.04	0.02
Fe	FeO	0.38	0.04	0.01	Zr	ZrO2	65.9	0.21	0.99
Zr	ZrO2	64.35	0.18	1	Pr	Pr2O3	0.06	0.06	0
Sm	Sm2O3	0.47	0.38	0.01	Nd	Nd2O3	0.08	0.06	0
Eu	Eu2O3	0.08	0.07	0	Eu	Eu2O3	0.04	0.07	0
Gd	Gd2O3	0.11	0.09	0	Gd	Gd2O3	0.02	0.09	0
Tb	Tb2O3	0.12	0.09	0	Tb	Tb2O3	0.1	0.09	0
Dy	Dy2O3	0.09	0.09	0	Ho	Ho2O3	0.16	0.09	0
Ho	Ho2O3	0.1	0.09	0	Er	Er2O3	0.15	0.09	0
Er	Er2O3	0.11	0.09	0	Yb	Yb2O3	0.11	0.09	0
Tm	Tm2O3	0.08	0.09	0	Hf	HfO2	0.27	0.2	0
Yb	Yb2O3	0.14	0.09	0	Total		100		2.02*
Hf	HfO2	0.51	0.21	0					
U	UO2	0.19	0.07	0					
Total		97.93		2.02*					

* Cation Sum

4 Discussion and conclusions

Chemical and minero-petrographic analyses pointed out an enrichment in REEs (mostly Ce, La, Nd in monazite and allanite and Y in xenotime) in the magnetic fraction resulting from the industrial processing of the Montorfano granite. The results show that magnetic separation enhances the concentration of REEs minerals in the source rock. However, SEM-EDS-based automated analysis (AZtecFeature Suite) used for automatic identification of REEs-bearing minerals (Figure 4a) and particles/grain size revealed likely liberation issues preventing the effectiveness of the magnetic separation process; the average grain size of target minerals is extremely small compared to the associated gangue phases, although slight

differences in size are noticeable between allanite, monazite, zircon, and ilmenite (Figure 4b).
Preliminary results of the work indicate that the major problem encountered lies in the limited particle liberation of REEs-bearing minerals, which are always locked within micas. It denotes that the particle size obtained by crushing and grinding the material before the magnetic separation process is too big to allow the liberation of monazite and other REEs minerals and their subsequent concentration in the following processing stages.

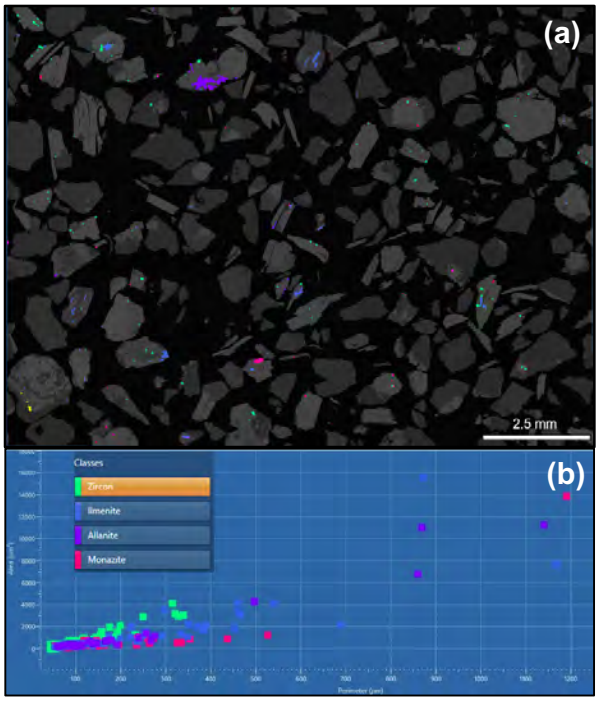

Figure 4. a Particle classification of ore minerals referring to the selected area of the SNG sample **b** Binary diagram showing the correlation between grain size area (μm^2) and perimeter (μm) of target minerals.

Hence, an additional grinding step on the unprocessed material is probably required to achieve a roughly homogeneous grain size below 0.1 mm. This could make the particle liberation more effective, leading to a better concentration of ore minerals during magnetic separation and the possible consequent extraction of REEs metals through specific techniques.

In conclusion, the work assesses that the concentration of the REEs-bearing minerals in magnetic scraps from feldspar production, aiming at reusing such processing waste with economic benefits and reducing landfill volumes, is potentially feasible upon further concentration. Additional lab tests (i.e., hydrometallurgy tests on improved concentrated material) will confirm the viability of the recovery.

Acknowledgements

The work is part of the Ph.D. project “Exploration and recovery optimization of Critical Raw Materials for the green transition, toward zero-waste Circular Economy model” in the framework of “National Recovery and Resilience Plan (PNRR)”- PHD-Innovation 352. The project is partially co-funded by Minerali Industriali S.r.l., which provides part of the facilities and equipment. The authors thank Minerali Industriali Engineering’s laboratory staff for their support during the sample preparation and analysis procedures.

References

Bobba S, Carrara S, Huisman J, Mathieux F, Pavel C (2020) Critical Raw Materials for Strategic Technologies and Sectors in the EU - a Foresight Study. Publications Office of the EU, 98pp

Boriani A, Bigioggero B, Giobbi Origoni E (1977) Geological map of the Verbania area. Mem Sci Geol 32

Boriani A, Buruni L, Caironi V, Giobbi Origoni E, Sessa ANGEUCA, Sesana ELENA (1988) Geological and petrological studies on the hercynian plutonism of Serie dei Laghi-geological map of its occurrence between Valsesia and Lago Maggiore (N-Italy). Rend Soc It Mineral Petrol 43:367-384

Dino GA, Fornaro M, Trentin A (2012) Quarry Waste: Chances of a Possible Economic and Environmental Valorisation of the Montorfano and Baveno Granite Disposal Sites. J Geol Res 2012:1–11. https://doi.org/10.1155/2012/452950

European Comission (2017) Study on the review of the list of critical raw materials. Publications Office of the EU, 153pp

European Comission (2021) Critical Raw Materials Resilience: Charting a Path towards greater Security and Sustainability

Guastoni A, Nestola F, Schiazza M (2017) Post-magmatic solid solutions of CaCeAl2(Fe3+2/3□1/3)[Si2O7][SiO4]O(OH),allanite-(Ce) and REE-bearing epidote in miarolitic pegmatites of Permian Baveno granite (Verbania, central-southern alps, Italy). Mineral Petrol 111:315-323. https://doi.org/10.1007/s00710-016-0475-x

The world-class Schlema-Alberoda U-(Ag-Co-Ni) deposit (Germany): mineralogy and fluid characteristics

Marie Guilcher[1,2], Jens Gutzmer[1,2], Axel Hiller[3], Joachim Krause[1], Nigel Blamey[4], Birk Härtel[5], Mathias Burisch[1,2,6]
[1]Helmholtz-Zentrum Dresden-Rossendorf, Helmholtz Institute Freiberg for Resource Technology, Chemnitzer Straße 40, 09599 Freiberg, Germany
[2]Institute of Mineralogy, Technische Universität Bergakademie Freiberg, Brennhausgasse 14, 09599 Freiberg, Germany
[3]Wismut GmbH, Talstraße 7, 08118 Hartenstein, Germany
[4]Department of Earth Sciences, Western University, London (Ontario), N6A 5B7, Canada
[5]Department of Geoscience, University of Calgary, Calgary (Alberta), T2N 1N4, Canada
[6]Mineral Systems Analysis Group, Department of Geology and Geological Engineering, Colorado School of Mines, 1516 Illinois Street, Golden, CO, 80401, USA

Abstract. The Schlema-Alberoda deposit is one of the largest uranium deposits in Europe with uranium ores closely associated with native metal-arsenide ore shoots. All ore styles occur in veins and stockwork zones that crosscut carbon-rich Devonian to Silurian metasediments and metabasites. This study investigates the native metal-arsenide veins in the district and provides an update on mineral paragenesis and novel fluid inclusion data. Native metal-arsenide ore occurs as vein-hosted ore shoots with native metals (Ag, Bi, As) and Co-Ni-Fe arsenides. Within the native metal-arsenide stage, five mineral associations are identified: (i) bismuth-skutterudite-safflorite, (ii) silver-rammelsbergite-skutterudite, (iii) arsenic-silver-loellingite, (iv) loellingite and (v) arsenic-sulfosalt-sulphide. Fluid inclusions measured in dolomite-ankerite that occur as gangue minerals have homogenization temperatures of ~115-150°C with fluid salinities of ~24.4-27.3 wt. % ($NaCl+CaCl_2$) eq. The spatial relationship between native metal-arsenide across the deposit and carbon-rich lithologies suggest reduction of the ore fluid as a decisive precipitation process. Microthermometric data indicate mixing of a sedimentary and a basement brine, which is also documented for other occurrences of native metal-arsenide ore across Europe that are all related to Mesozoic continental rifting.

1 Introduction

The world-class uranium deposit of Schlema-Alberoda is part of the Erzgebirge metallogenic province located in the European Variscan belt. Whilst ages for uranium mineralisation range between Permian and Mesozoic (Hiller and Schuppan 2008 and references therein), closely associated native metal-arsenide veins have recently been found to have a Cretaceous age (Guilcher et al. 2021a).

The native metal-arsenide veins consist of native metal (Ag, Bi, As) followed by arsenides within a quartz/carbonate gangue (Markl et al. 2016). The exploitation focused on uranium resources in Schlema-Alberoda between 1945 and 1991 (~80,000 t of U produced; Hiller and Schuppan 2008). The other metals (e.g., Ag, Co, Ni) were of minor relevance. Only 199 t of Co metal were extracted from ore with grades from 0.51% to 3.78 % between 1958 and 1978. Except for mineralogical studies published by Lipp and Flach (2003), no modern investigation has been carried out to understand the genesis of the native metal-arsenide veins in the Schlema-Alberoda district.

Here, we provide new petrographic observations and microthermometric measurements, complemented by mineral chemistry and fluid inclusion bulk-gas analysis aiming to better understand the origin of the native metal-arsenide veins in the Schlema-Alberoda district.

2 Geological setting of the Schlema-Alberoda district

The Erzgebirge is located within the Saxo-Thuringian zone of the Variscan Orogen. Following peak regional metamorphism at ca. 340 Ma the metamorphic units of the Variscan basement were rapidly exhumed and intruded by post-collisional granitoids followed by voluminous rhyolitic volcanic rocks between ~335 and 290 Ma (Förster and Romer 2010; Tichomirowa and Leonhardt 2010; Tichomirowa et al. 2022). Extensional tectonics dominated from the Permian to the Jurassic and were associated with rapid erosion. Extensive subsidence formed a ~2-3 km thick sedimentary cover on top of the crystalline basement (Ziegler and Dèzes 2006; Wolff et al. 2015).

In the western part of the Erzgebirge, the Schlema-Alberoda district mainly comprises phyllites and carbonaceous schist of Ordovician to Devonian age, marble and metabasic rocks; this succession experienced greenschist facies regional metamorphism. Exhumation is associated with the intrusion of the Aue granite at 328.6±2 Ma and the development of a ~1,000 m wide contact metamorphic halo (Fig. 1; Tichomirowa and Leonhardt 2010; Hiller and Schuppan 2008). The lithological units are crosscut by a NW-SE fault system hosting three main ore stages: (1) quartz-calcite-uraninite association (~280-267 Ma; Förster and Haak 1995; Golubev et al. 2000); (2) dolomite-uraninite-fluorite association (~190-140 Ma; Förster and Haak 1995; Golubev et al. 2000) and (3) native metal-arsenide ± uranium association (~129-86 Ma, Guilcher et al. 2021a). Textural observations suggest extensive remobilization and reprecipitation of uranium from the quartz-calcite-uraninite association during the dolomite-uraninite-fluorite stage (Hiller and Schuppan 2008). The native metal-arsenide ore shoots represent a second and minor remobilization of uranium. All three associations occur within a

distance of 200-800 m from the contact of the metamorphic rocks to the Aue granite. Importantly, veins pinch out or become barren beyond the limit of the contact metamorphic aureole (800-1,100 m; Lipp and Flach 2003; Hiller and Schuppan 2008). Only a few uranium and native metal-arsenide mineralised veins were observed at the contact or within the granite (less than 10 m inside the granite; Lipp and Flach 2003; Hiller and Schuppan 2008).

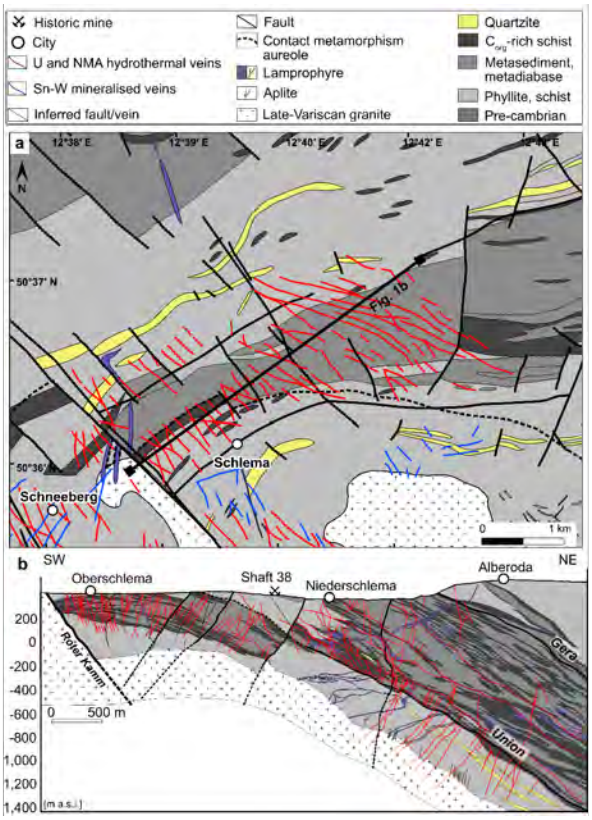

Figure 1. a Simplified geological map of the Schlema-Alberoda deposit (modified after Hoth et al. 1980; Hiller and Schuppan 2008). Red lines represent major hydrothermal veins hosting U and NMA ores. **b** SW-NE cross-section of the Schlema-Alberoda deposit.

3 Methods

Forty-nine mineralised hand specimens were selected from a large suite of well-documented samples in the geoscientific collections (including the Flach collection of U. Lipp) of the TU Bergakademie Freiberg (TU BAF) and the archives of the Wismut GmbH. Samples were selected to represent a wide range of sample depth from different veins. Petrographic descriptions are based on optical microscopy and mineral identification were supported by scanning electron microscopy (SEM) and high-resolution backscattered electron (BSE) images carried out on a FEI Quanta 650F SEM equipped with two Bruker Quantax X-Flash 5030 energy-dispersive X-ray spectrometers (EDS) at the Helmholtz Institute Freiberg for Resource Technology (HIF). The instrument was operated with a 25 kV acceleration voltage and a beam current of 13 nA to produce the BSE images. A total of 20 samples were selected for investigation of fluid inclusions in carbonates related to the native metal-arsenide mineral associations identified. Fluid inclusions suitable for microthermometric analysis were measured in 6 samples using a Linkam THMSG600 heating-cooling stage at TU BAF. Total salinities (wt. % [$NaCl+CaCl_2$] eq.) and the Na/(Na+Ca) ratio were calculated according to Steele-MacInnis et al. (2011) in the ternary $NaCl+CaCl_2-H_2O$ system. Fluid inclusions showing post-entrapment modifications (e.g., necking) were excluded. The bulk composition of gases in fluid inclusions was analysed using the crush-fast scan (CFS) method at University of Western Ontario, London, Canada (Blamey 2012). Mineral separates of carbonates were cleaned with H_2O_2 and were incrementally crushed (typically 10 crushes per sample) at room temperature under vacuum of about 10^{-7} to 10^{-8} Torr.

4 The native metal-arsenide veins

4.1 Mineral associations

Based on petrographic observations and in good agreement with mineral descriptions from Lipp and Flach (2003), we identified five distinct native metal-arsenide subtypes, namely (i) bismuth-skutterudite-safflorite, (ii) silver-rammelsbergite-skutterudite, (iii) arsenic-silver-loellingite, (iv) loellingite and (v) arsenic-sulfosalt-sulphide.

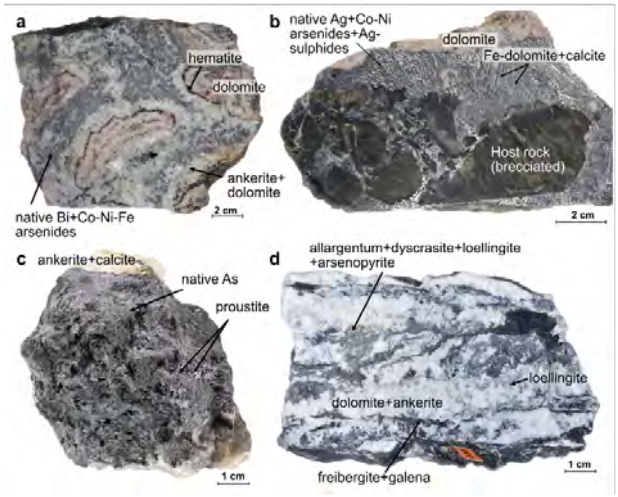

Figure 2. Main native metal-arsenide subtypes observed in the Schlema-Alberoda district. **a** Bismuth-skutterudite-safflorite with pink dolomite from the dolomite-uraninite-fluorite association. **b** Silver-rammelsbergite-skutterudite. **c** Arsenic-silver-loellingite. **d** Loellingite with Ag-sulfosalts, arsenopyrite and galena.

The bismuth-skutterudite-safflorite subtype comprises skeletal crystals or irregularly shaped grains of native bismuth overgrown by euhedral, often zoned, (nickel-)skutterudite followed by safflorite and rare loellingite (Fig. 2a). Rammelsbergite and nickeline are scarce. Occasionally, multiple layers of gersdorffite and cobaltite occur in between layers of rammelsbergite and safflorite. Dolomite, ankerite, and siderite occur

as gangue minerals either coeval with safflorite and loellingite or they overgrow arsenides. Calcite and quartz usually form the youngest minerals in this mineral paragenesis.

The silver-rammelsbergite-skutterudite subtype consists of fern-like dendritic native silver overgrown by rammelsbergite, nickeline, safflorite, and euhedral (nickel-)skutterudite (Fig. 2b). Loellingite, if at all present, invariably occupies the youngest paragenetic position within the arsenide sequence. Iron-dolomite, dolomite-ankerite, calcite, and paragenetically younger quartz compose the gangue minerals that accompany the arsenides.

The arsenic-silver-loellingite subtype shows native silver and rammelsbergite encapsulated by aggregates of fine-grained native arsenic (Fig. 2c). The latter minerals are either rimmed by a thin layer of loellingite or overgrown by euhedral loellingite crystals. Loellingite is accompanied by ankerite and dolomite, followed by younger calcite.

Native elements are rarely present in the loellingite subtype (Fig. 2d). Loellingite is the main arsenide and often replaces or encapsulates relics of uraninite, freibergite, sphalerite, galena, nickeline or (nickel-)skutterudite. Scarce native As occasionally overgrows loellingite. The main gangue minerals are dolomite, ankerite and calcite. This subtype is often associated with the paragenetically younger arsenic-sulfosalt-sulphide subtype.

This arsenic-sulfosalt-sulphide subtype overgrows or replaces paragenetically older native metal-arsenide subtypes described above. Arsenides are usually not replaced but overgrown, whereas native metals tend to be replaced by minerals related to the arsenic-sulfosalt-sulphide subtype. This mineral association encompasses secondary native silver, acanthite, proustite, cobaltite, gersdorffite, bismuthinite, arsenopyrite, argentopyrite, chalcopyrite, pyrite, galena, realgar, Bi-tennantite, allargentum, dyscrasite, Fe-oxides, REE minerals, dolomite-ankerite, calcite and quartz.

4.2 Vertical mineral zoning

All investigated native metal-arsenide subtypes, except for the silver-rammelsbergite-skutterudite and loellingite subtypes, occur across the entire vertical profile from ~200 to –1,155 m a.s.l. (meter above sea level) exposed by uranium exploitation. The silver-rammelsbergite-skutterudite subtype, however, appears absent from deeper portions of the Schlema-Alberoda deposit (-350 to -1,155 m a.s.l.), whereas the loellingite subtype mainly occurs in the deepest parts (between -650 and -1,155 m a.s.l.). Rammelsbergite, safflorite and nickeline are rarely recognized below ~ -500 m a.s.l. and loellingite abundance increases towards depth.

4.3 Mineralizing fluid

Primary and pseudosecondary fluid inclusion assemblages (*n*=23, *n*FIs=122) hosted in dolomite and ankerite coeval with safflorite and loellingite in bismuth-skutterudite-safflorite, silver-rammelsbergite-skutterudite, and loellingite subtypes have homogenization temperature (Th) between 115° and 150°C. There is no systematic variation in Th of various native metal-arsenide subtypes. Hydrohalite nucleation was observed in 6 fluid inclusion assemblages with average salinities of ~26.4 wt. % ($NaCl+CaCl_2$) eq. and Na/(Na+Ca) ratios between 0.61 and 0.78. Fluid inclusion gas compositions span a large range with respect to their CO_2/CH_4 and N_2/Ar ratios (Fig. 3).

5 Discussion and conclusions

At Schlema-Alberoda, the native metal arsenide tenor locally varies, including Ag-, Bi-, or As-dominated veins. Nickel-richer arsenides tend to be associated with native Ag, whereas Co-richer arsenides tend to be associated with native Bi. Similar observations were reported from other native metal-arsenide localities in Central Europe (e.g., Mackenheim and Urberg; Burisch et al. 2017; Scharrer et al. 2022).

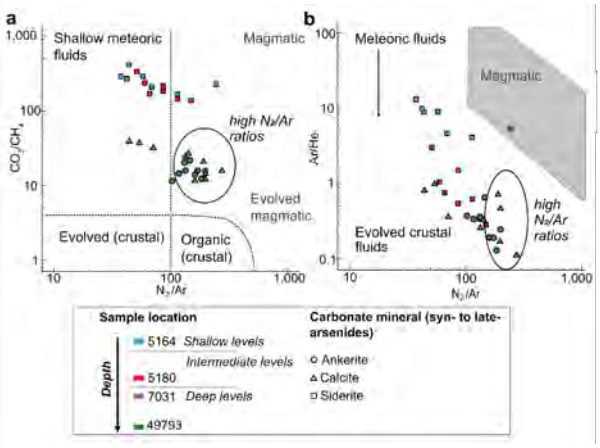

Figure 3. Crush-fast scan data for fluid inclusions. All data are in mol. %. **a** CO_2/CH_4 versus N_2/Ar. **b** Ar/He versus N_2/Ar. Field boundaries are from Blamey and Norman (2002) and Blamey (2012). Samples are classified according to the levels of the deposit they originate.

The spatial relationship between the native metal-arsenide veins and carbon-rich metasediments is striking. It supports the notion of recent studies (Markl et al. 2016; Burisch et al. 2017) that ore formation is likely related to reduction caused by interaction of the metal-bearing fluids with carbonaceous host rocks.

Microthermometric data of native metal-arsenide veins show that the ore fluids are of low temperature and high salinity. A wide range of Na/(Na+Ca) ratios (0.61-0.78) supports fluid mixing of two saline fluids, again consistent with evidence from other native metal-arsenide occurrences (Burisch et al. 2017; Scharrer et al. 2022). Although, not as obvious as for other localities, fluid mixing is furthermore supported by the large scatter in CO_2/CH_4 and N_2/Ar ratios of the fluid inclusions. The presented data is thus in agreement with previous studies, which proposed that the formation of native metal-arsenide veins in

Europe, is related to mixing between a metal-rich basement brine and a sedimentary-derived fluid under anomalously low fO_2 conditions (Markl et al. 2016; Burisch et al. 2017; Guilcher et al. 2021b).

Laser-ICP-MS U-Pb carbonates ages (113.1±1.8 Ma; Guilcher et al. 2021a) of the native metal-arsenide stage at Schlema-Alberoda constrain the timing of arsenide mineralisation to Mesozoic continental rifting in conjunction with the disintegration of the supercontinent Pangea (Guilcher et al 2021a; Burisch et al. 2022). Progressive mantle exhumation and crustal thinning in continental rift zones (Staude et al. 2009; Burisch et al. 2022) are assumed to be the driving mechanism for episodic injection of deep-seated basement brines into shallower aquifers across Europe (Bons et al. 2014; Burisch et al. 2016, 2022). Hence, we also assume this process is to have caused local formation of native metal-arsenide ore shoots, where metal-bearing basement fluids encountered carbon-rich lithologies at the Schlema-Alberoda deposit.

Acknowledgements

We thank our colleagues from the Helmholtz Institute Freiberg for Resource Technology (HIF) and the Technische Universität Bergakademie Freiberg (TU BAF) for their support with sampling, sample preparation and SEM work. This project was partly funded by the European Social Fund and the Federal State of Saxony (Project no. 100339454 received by M. Burisch).

References

Blamey N, Norman D (eds) (2002) New interpretations of geothermal fluid inclusion volatiles: Ar/He and N2/Ar ratios-a better indicator of magmatic volatiles, and equilibrium gas geothermometry, 27th edn.

Blamey NJF (2012) Composition and evolution of crustal, geothermal and hydrothermal fluids interpreted using quantitative fluid inclusion gas analysis. Journal of Geochemical Exploration 116-117:17–27. https://doi.org/10.1016/j.gexplo.2012.03.001

Bons PD, Fusswinkel T, Gomez-Rivas E, Markl G, Wagner T, Walter B (2014) Fluid mixing from below in unconformity-related hydrothermal ore deposits. Geology 42:1035–1038. https://doi.org/10.1130/G35708.1

Burisch M, Walter BF, Wälle M, Markl G (2016) Tracing fluid migration pathways in the root zone below unconformity-related hydrothermal veins: insights from trace element systematics of individual fluid inclusions. Chemical Geology 429:44–50. https://doi.org/10.1016/j.chemgeo.2016.03.004

Burisch M, Gerdes A, Walter BF, Neumann U, Fettel M, Markl G (2017) Methane and the origin of five-element veins: mineralogy, age, fluid inclusion chemistry and ore forming processes in the Odenwald, SW Germany. Ore Geology Reviews 81:42–61. https://doi.org/10.1016/j.oregeorev.2016.10.033

Burisch M, Markl G, Gutzmer J (2022) Breakup with benefits - hydrothermal mineral systems related to the disintegration of a supercontinent. Earth and Planetary Science Letters 580:117373. https://doi.org/10.1016/j.epsl.2022.117373

Förster B, Haack U (1995) U/Pb-Datierungen von Pechblenden und die hydrothermale Entwicklung der U-Lagerstätte Aue-Niederschlema (Erzgebirge). Zeitschrift für Geologische Wissenschaften 23:581–588

Förster H-J, Romer RL (2010) Carboniferous magmatism. In: Linnemann U, Romer RL (eds) Pre-Mesozoic geology of Saxo-Thuringia: from the Cadomian active margin to the Variscan Orogen. Schweizerbart, Stuttgart, pp 287–308

Golubev VN, Cuney M, Poty B (2000) Phase composition and U-Pb pitchblende systems of quartz-calcite-pitchblende veins at the Schlema-Alberoda deposit (Erzgebirge). Geology of Ore Deposits 42:513–525

Guilcher M, Albert R, Gerdes A, Gutzmer J, Burisch M (2021a) Timing of native metal-arsenide (Ag-Bi-Co-Ni-As±U) veins in continental rift zones – in situ U-Pb geochronology of carbonates from the Erzgebirge/Krušné Hory province. Chemical Geology 584:120476. https://doi.org/10.1016/j.chemgeo.2021.120476

Guilcher M, Schmaucks A, Krause J, Markl G, Gutzmer J, Burisch M (2021b) Vertical zoning in hydrothermal U-Ag-Bi-Co-Ni-As systems: a case study from the Annaberg-Buchholz district, Erzgebirge (Germany). Economic Geology 116:1893–1915. https://doi.org/10.5382/econgeo.4867

Hiller A, Schuppan W (2008) Geologie und Uranbergbau im Revier Schlema-Alberoda. Bergbau in Sachsen Bergbaumonographie, vol 14. Sächsisches Landesamt für Umwelt und Geologie (LfUG), Germany

Hoth K, Tischendorf G, Berger HJ, et al. (1980) Geologische Karte Erzgebirge/Vogtland. Sächsisches Landesamt für Umwelt, Landwirtschaft und Geologie, Dresden

Lipp U, Flach S (2003) Wismut-, Kobalt-, Nickel- und Silbererze im Nordteil des Schneeberger Lagerstättenbezirkes. Bergbau in Sachsen Bergbaumonographie, vol 10. Sächsisches Landesamt für Umwelt und Geologie, Dresden

Markl G, Burisch M, Neumann U (2016) Natural fracking and the genesis of five-element veins. Mineralium Deposita 51:703–712. https://doi.org/10.1007/s00126-016-0662-z

Scharrer M, Epp T, Walter B, Pfaff K, Vennemann T, Markl G (2022) The formation of (Ni-Co-Sb)-Ag-As ore shoots in hydrothermal galena-sphalerite-fluorite veins. Mineralium Deposita 57:853–885. https://doi.org/10.1007/s00126-021-01059-y

Staude S, Bons PD, Markl G (2009) Hydrothermal vein formation by extension-driven dewatering of the middle crust: an example from SW Germany. Earth and Planetary Science Letters 286:387–395. https://doi.org/10.1016/j.epsl.2009.07.012

Steele-MacInnis M, Bodnar RJ, Naden J (2011) Numerical model to determine the composition of H2O–NaCl–CaCl2 fluid inclusions based on microthermometric and microanalytical data. Geochimica et Cosmochimica Acta 75:21–40. https://doi.org/10.1016/j.gca.2010.10.002

Tichomirowa M, Leonhardt D (2010) New age determinations (Pb/Pb zircon evaporation, Rb/Sr) on the granites from Aue-Schwarzenberg and Eibenstock, Western Erzgebirge, Germany. Zeitschrift für Geologische Wissenschaften 38:99–123

Tichomirowa M, Käßner A, Repstock A, Weber S, Gerdes A, Whitehouse M (2022) New CA-ID-TIMS U–Pb zircon ages for the Altenberg–Teplice Volcanic Complex (ATVC) document discrete and coeval pulses of Variscan magmatic activity in the Eastern Erzgebirge (Eastern Variscan Belt). International Journal of Earth Sciences (Geologische Rundschau) 111:1885–1908. https://doi.org/10.1007/s00531-022-02204-2

Wolff R, Dunkl I, Lange J-M, Tonk C, Voigt T, Eynatten H von (2015) Superposition of burial and hydrothermal events: post-Variscan thermal evolution of the Erzgebirge, Germany. Terra Nova 27:292–299. https://doi.org/10.1111/ter.12159

Ziegler PA, Dèzes P (2006) Crustal evolution of western and central Europe. In: Gee DG, Stephenson RA (eds) European Lithosphere Dynamics, vol 32. Geological society, London, pp 43–56

The MINES thermodynamic database for simulating the hydrothermal mobilization of REE in critical mineral deposits

Alexander P. Gysi[1,2]
[1]*New Mexico Bureau of Geology & Mineral Resources, New Mexico Institute of Mining and Technology, Socorro, NM 87801, USA*
[2]*Department of Earth and Environment Science, New Mexico Institute of Mining and Technology, Socorro, NM 87801, USA*

Abstract. The rare earth elements (REE) are essential for the high-tech and green technology industries, and used, for example, in computers, smartphones, and wind turbines. The REE are considered critical minerals and can be highly enriched in certain magmatic-hydrothermal systems including alkaline complexes and carbonatites. Almost all of the critical mineral deposits show a complex overprint by hydrothermal processes during their genesis. However, our understanding of the mobility in these ore-forming systems and our knowledge about the stability of REE minerals is still very limited. The MINES thermodynamic database is an open-access database and continuously updated with the most up to date thermodynamic data for REE aqueous species and minerals. This database also includes rock-forming minerals and permits simulating the mineralogy and alteration geochemistry that relates to the formation of these critical mineral deposits. This study gives a short overview of the MINES thermodynamic database and the GEMS code package for simulating the formation of hydrothermal calcite, fluorite and bastnäsite-(Ce) veins relevant to interpreting critical mineral deposits.

1 Introduction

Critical mineral deposits evolve through a complex sequence of magmatic-hydrothermal processes, and most of them, are overprinted by late auto-metasomatic processes (e.g. Gysi et al. 2016; Elliott et al. 2018). The mobilization, fractionation and/or enrichment of critical elements, such as the rare earth elements (REE), can be predicted using thermodynamic modeling (Migdisov et al. 2016; Perry and Gysi 2018). These geochemical models yield insights about the controls and distribution of REE in these deposits and can potentially be used together with field geochemical data to predict alteration vectors for mineral exploration. However, our current ability to predict the behavior of REE in high temperature aqueous fluids and interpret these natural systems depends on the availability of thermodynamic data for the REE minerals and aqueous species.

The hydrothermal solubility of the REE phosphates, monazite and xenotime, has only recently been determined experimentally (Gysi et al. 2015, 2018; Van Hoozen et al. 2020; Gysi and Harlov 2021). The same applies to the thermodynamic properties of bastnäsite-(Ce) (e.g. Gysi and Williams-Jones 2015; Shivaramaiah et al. 2016; Goncharov et al. 2022). Furthermore, new models are developed based on experimental work, which aid in simulating the mechanisms of REE incorporation into gangue vein minerals such as apatite, calcite, and fluorite (Perry and Gysi 2020; Payne et al. 2023).

Thermodynamic data are available to predict the mobility of REE in acidic aqueous fluids to ~350-400ºC, whereas more experimental work is needed to simulate the mobility of REE in alkaline and supercritical fluids >350-400ºC. The properties of many aqueous REE species have been determined experimentally, including fluoride, sulfate, and chlorite complexes that control REE transport in acidic fluids (Migdisov et al. 2016). Previous modeling studies further indicate the potential importance of REE hydroxyl and carbonate complexes in alkaline fluids (Perry and Gysi 2018). The thermodynamic properties of these aqueous species are, however, still poorly known at elevated temperature, and the properties of a few of the REE carbonate complexes were determined only recently in hydrothermal solutions (Louvel et al. 2022; Nisbet et al. 2022).

Here, I present the MINES thermodynamic database and a modeling study using the GEMS code package (Kulik et al. 2013) to show an application of geochemical modeling in economic geology. This study gives an example of the replacement of a calcite vein by hydrothermal fluorite and bastnäsite-(Ce), and related compositional changes in fluorite to highlight advances and capabilities for modeling critical mineral deposits.

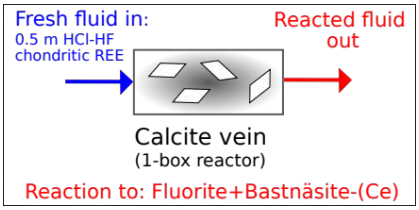

Figure 1. Conceptual model of a multipass leaching model (or 1-box flow-through reactor model), showing the input/output of fresh/reacted aliquots of acidic REE-F-bearing fluids passing through a calcite vein.

2 Methods

The MINES thermodynamic database (https://geoinfo.nmt.edu/mines-tdb) is an open-access database updated on a rolling release model (i.e., as new data become available, andhave been implemented and tested). The current database comprises >700 aqueous species and minerals relevant to modeling hydrothermal ore-

forming processes and fluid-rock interaction. The database includes aqueous REE species (Migdisov et al. 2009, 2016), REE phosphate minerals, and REE fluorocarbonates (Gysi and Williams-Jones 2015; Gysi et al. 2015, 2018; Van Hoozen et al. 2020; Gysi and Harlov 2021). The database also includes rock-forming minerals (Robie and Hemingway 1995; Holland and Powell 1998), zeolites, and clay minerals (Gysi and Stefánsson 2011).

The program GEM-Selektor (https://gems.web.psi.ch) was used with the MINES thermodynamic database to simulate the replacement reaction of calcite vein by secondary fluorite and REE fluorocarbonates (Fig. 1); a typical reaction texture observed in many critical mineral deposits. The simulations were carried out in the Ca-REE-F-Cl-C-H-O system at 400ºC and 500 bar with an acidic REE-F-Cl-bearing starting fluid (0.5 m HCl/HF) interacted with a calcite vein. The REE concentrations used are the chondrite values listed in McDonough and Sun (1995).

The first model is a multipass leaching model (Figs. 1-3) where at each step a fresh aliquot of acidic REE-F-Cl-bearing fluid interacts with the calcite vein while the alteration mineralogy, fluid chemistry, and the compositions of both calcite and fluorite can be monitored. The second model is a 1-D reactive transport model (Fig. 4), which permits simulating fluid-flow using the GEM2MT module implemented in the GEMS code package. In this model, 50 sequential rock nodes containing calcite were interacted simultaneously with the acidic fluid, which is flushed as sequential "waves" through each of the rock nodes. The resulting mineral distribution is then recorded after 200 and 2000 steps or waves.

3 Modeling examples

3.1 Multipass leaching model

Figure 2 shows the progressive replacement of the calcite vein by fluorite and bastnäsite-(Ce) upon increased fluid-rock interaction (i.e., aliquots of fluid added). The pH is initially buffered by calcite to a value slightly below ~6.5. Interaction of the acidic REE-F-bearing fluid with calcite leads to the formation of bastnäsite-(Ce) and fluorite according to:

$CaCO_3$ (calcite) + $3F^-$ + REE^{3+} = CaF_2 (fluorite) + $REEFCO_3$ (bastnäsite) **(Eq. 1)**

Once all calcite is consumed (~140 aliquots of fluidin Fig. 2), bastnäsite-(Ce) becomes unstable and all the remaining REE (i.e., not flushed out through the reactor box) are retained in fluorite. Figure 3 shows the compositional evolution of the simulatedREE-bearing fluorite. These preliminary simulations indicate that fluid-rock reaction can lead to significant REE variations in fluorite including the light (L) and heavy (H) REE. Furthermore, the simulations show a REE enrichment in fluorite of up to ~100 times chondrite.

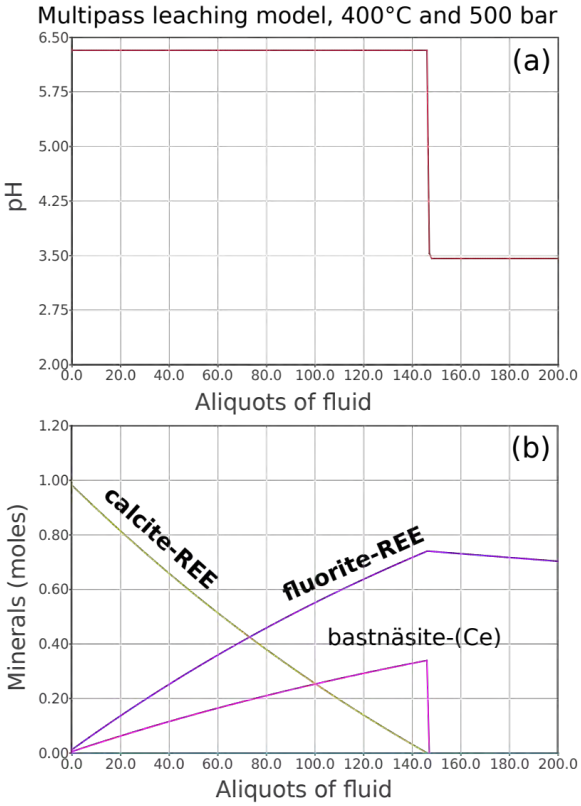

Figure 2. Multipass leaching model (or 1-box reactorflow-through) showing (a) the simulated pH and (b) the simulated mineralogy as a function of aliquots of fluids flushed through the calcite vein. Calcite-REE and fluorite-REE both indicate that the REE concentrations were simulated for these minerals.

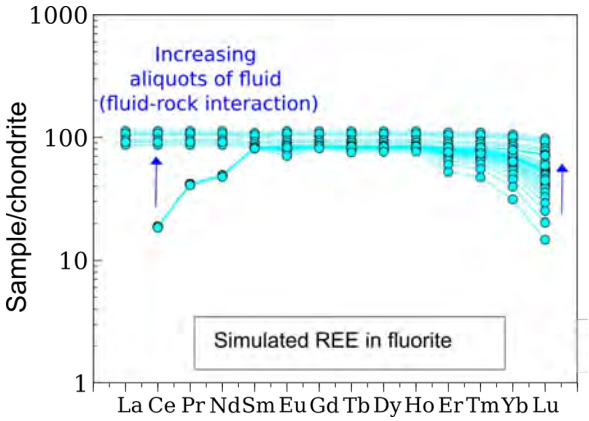

Figure 3. Simulated REE variations in fluorite normalized to chondrite. The stability of fluorite is shown in Figure 2 and variations correspond to various degrees of fluid- rock interaction or aliquots of fluid flushed through the rock.

3.21-D reactive transport model

Figure 4a shows the evolution of a calcite vein after 200 steps, with the development of a large zone of REE mineralization (i.e., fluorocarbonate veins) and a smaller zone of fluorite plus bastnäsite-(Ce). Upon increased fluid-rock interaction (Fig. 4B; after 2000 simulations steps), a large zone of fluorite develops at the input side of the acidic REE-F-

bearing fluid, and a large zone of calcite plus bastnäsite-(Ce) forms on the output side of the reactive fluid flow path. A smaller zone comprising fluorite plus bastnäsite-(Ce) forms at the interface between the calcite and fluorite rich zones.

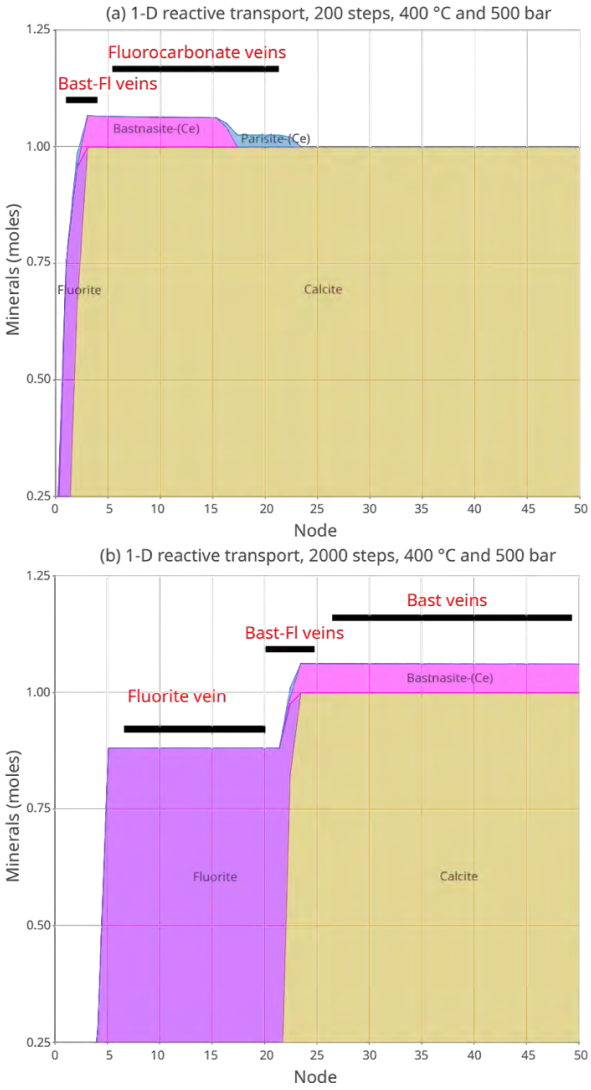

Figure 4. 1-D reactive transport simulations showing the mineralogy in 50 nodes or boxes of rock after (a) 200 steps and (b) 2000 steps, representing the number of fluid "waves" flushed through all the calcite boxes.

4 Conclusions

Numerical modeling provides a powerful tool to interpret the mineralogy, geochemistry, and alteration zones developed in natural critical mineral deposits. The MINES thermodynamic database was used here to show an example application to fluid-rock interaction processes that control REE mobilization. This can be extended to different mineral systems (Gysi and Williams-Jones 2013; Perry and Gysi 2018; Payne et al. 2023). Many of the REE mineral deposits associated with carbonatites and alkaline deposits contain hydrothermal barite, calcite, fluorite, and/or bastnäsite-(Ce) bearing veins. Hence the simulations presented in Figures 2-4 provide a first step in quantifying the processes that affect the stability of these minerals and concurrent change in fluorite REE chemistry. Prominent examples where this type of reactions could be of importance include the hydrothermal fluorite-REE-bearing breccia/vein deposit in Gallinas Mountains in New Mexico (McLemore et al. 2021), Bear Lodge in Wyoming (Andersen et al. 2019), the giant Bayan Obo carbonatite deposit in China (Gao et al. 2021), and the Mianning-Dechang REE belt in China (Guo and Liu 2019).

Acknowledgments

I like to thank my colleagues who contributed to the project including Nicole Hurtig and Ruiguang Pan (New Mexico Tech), Dan G. Miron and Dmitrii Kulik (Paul Scherrer Institute). The work on the MINES thermodynamic database and REE experimental data acquired were supported through the following National Science Foundation (NSF) and U.S. Department of Energy (DOE) grants: NSFCAREER EAR-2039674 and EAR-2032761; DOE DE-SC0021106 and DE-SC0022269.

References

Andersen AK, Larson PB, Cosca MA (2019) C–O stable isotope geochemistry and $^{40}Ar/^{39}Ar$ geochronology of the Bear Lodge carbonatite stockwork, Wyoming, USA. Lithos 324:640-660.

Chappell JC, Gysi AP, Monecke T, Chang Z (in press) Experimental apatite-fluid interaction and partitioning of rare earth elements at 150 and 250°C. Am Mineral. https://doi.org/10.2138/am-2022-8589

Elliott HAL, Wall F, Chakhmouradian AR, Siegfried PR, Dahlgren S, Weatherley S, Finch AA, Marks MAW, Dowman E, Deady E (2018) Fenites associated with carbonatite complexes: A review. Ore Geol Rev 93:38-59.

Gao Z, Liu Y, Jing Y, Hou Z, Liu H, Zheng X, Shen N (2021) Mineralogical characteristics and Sr–Nd–Pb isotopic compositions of banded REE ores in the Bayan Obo deposit, Inner Mongolia, China: Implications for their formation and origin. Ore Geol Rev 139:104492.

Goncharov VG, Nisbet H, Strzelecki A, Benmore CJ, Migdisov AA, Xu H, Guo X (2022) Energetics of hydroxyl bastnäsite solid solutions, $La_{1-x}Nd_xCO_3OH$. Geochim Cosmochim Acta 330:47-66.

Guo D, Liu Y (2019) Occurrence and geochemistry of bastnäsite in carbonatite-related REE deposits, Mianning–Dechang REE belt, Sichuan Province, SW China. Ore Geol Rev 107:266-282.

Gysi AP, Harlov D (2021) Hydrothermal solubility of $TbPO_4$, $HoPO_4$, $TmPO_4$, and $LuPO_4$ xenotime endmembers at pH of 2 and temperatures between 100 and 250°C. Chem Geol 567:120072.

Gysi AP, Stefánsson A (2011) CO_2–water–basalt interaction. Numerical simulation of low temperature CO_2 sequestration into basalts. Geochim Cosmochim Acta, 75:4728-4751.

Gysi AP, Williams-Jones AE (2013) Hydrothermal mobilization of pegmatite-hosted REE and Zr at Strange Lake, Canada: A reaction path model. Geochim Cosmochim Acta 122:324-352.

Gysi AP, Williams-Jones AE (2015) The thermodynamic properties of bastnäsite-(Ce) and parisite-(Ce). Chem Geol 392:87-101.
Gysi AP, Williams-Jones AE, Collins P (2016) Lithogeochemical vectors for hydrothermal processes in the Strange Lake peralkaline granitic REE-Zr-Nb deposit. Econ Geol 111:1241-1276.
Gysi AP, Harlov D, Miron GD (2018) The solubility of monazite ($CePO_4$), $SmPO_4$, and $GdPO_4$ in aqueous solutions from 100 to 250°C. Geochim Cosmochim Acta 242:143-164.
Holland TJB, Powell R (1998) An internally consistent thermodynamic data set for phases of petrological interest. J Metamorph Geol 16:309-343.
Kulik DA, Wagner T, Dmytrieva SV, Kosakowski G, Hingerl F F, Chudnenko KV, Berner UR (2013) GEM-Selektor geochemical modeling package: revised algorithm and GEMS3K numerical kernel for coupled simulation codes. Comput Geosci 17:1-24.
Louvel M, Etschmann B, Guan Q, Testemale D, Brugger J (2022) Carbonate complexation enhances hydrothermal transport of rare earth elements in alkaline fluids. Nature Commun 13:1456.
McDonough WF, Sun SS (1995) The composition of the Earth. Chem Geol 120:223-253.
McLemore VT, Kelley S, Zimmerer MJ, Owen E, Haft EB, Cantrell T, Gysi AP, Dietz H, Cherotich S, Trivitt A (2021) Geology and mineral deposits of the Gallinas Mountains, Lincoln and Torrance counties, New Mexico. New Mexico Bureau of Geology and Mineral Resources, Open-File Report 617.
Migdisov AA, Williams-Jones AE, Wagner T (2009) An experimental study of the solubility and speciation of the Rare Earth Elements (III) in fluoride-and chloride-bearing aqueous solutions at temperatures up to 300°C. Geochim Cosmochim Acta 73:7087-7109.
Migdisov A., Williams-Jones AE, Brugger J, Caporuscio FA (2016) Hydrothermal transport, deposition, and fractionation of the REE: Experimental data and thermodynamic calculations. Chem Geol 439:13-42.
Nisbet H, Migdisov AA, Goncharov V, van Hinsberg V, Williams-Jones AE, Xu H, Guo X (2022) The solubility and speciation of Nd in carbonate-bearing hydrothermal fluids up to 250°C. Chem Geol 611:121122.
Payne MR, Gysi AP, Hurtig NC (2023) Hydrothermal fluorite solubility experiments and mobility of REE in acidic to alkaline solutions from 100 to 250°C. Chem Geol 617:121256.
Perry EP, Gysi AP (2018) Rare earth elements in mineral deposits: speciation in hydrothermal fluids and partitioning in calcite. Geofluids 2018:1-19.
Perry EP, Gysi, AP (2020) Hydrothermal calcite-fluid REE partitioning experiments at 200°C and saturated water vapor pressure. Geochim Cosmochim Acta 286:177-197.
Robie RA, Hemingway BS (1995) Thermodynamic properties of minerals and related substances at 298.15 K and 1 bar (10^5 Pascals) pressure and at higher temperatures. U.S. Geological Survey Bulletin Vol. 2131.
Shivaramaiah R, Anderko A, Riman RE, Navrotsky A (2016) Thermodynamics of bastnaesite: A major rare earth ore mineral. Am Mineral 101:1129-1134.
Van Hoozen CJ, Gysi AP, Harlov DE (2020) The solubility of monazite ($LaPO_4$, $PrPO_4$, $NdPO_4$, and $EuPO_4$) endmembers in aqueous solutions from 100 to 250°C. Geochim Cosmochim Acta 280: 302-316.

A green future from a contentious past: Gold and critical metals in a historic arsenic mining district Strassegg (Styria)

Hiller, J.M.[1], Bertrandsson Erlandsson, V.[1], Mottram, C.[2], Gopon, P.[1]
[1] *Chair of Geology and Economic Geology, Montanuniversität Leoben, Peter-Tunner Straße, 8770, Leoben, Austria*
[2] *School of the Environment, Geography and Geosciences, University of Portsmouth, Burnaby Building, Portsmouth, PO 1 3QL, United Kingdom*

Abstract. Metals such as Bi, Co, Sb, Te, and W are needed in large amounts for renewable technologies central to reaching net-zero carbon and have therefore been termed as critical metals by the European Union. A stable supply chain for these raw materials into the EU is urgently needed, especially considering the current geo-political instabilities. In light of this, domestic production of raw materials is a priority, and we therefore investigate the historic Au-Ag-As mining district Strassegg in the north of Graz (Styria) for precious and critical metals. Our study combines whole rock geochemistry from tailings piles as well as scanning electron microscope (SEM) and laser ablation inductively coupled plasma mass spectrometry (LA-ICP-MS) analyses of sulfide minerals to show the amount precious and critical metals still present, as well as characterizing in what form these metals are found (i.e., inclusions or lattice bound). Additionally, in-situ calcite U-Pb dating was done for Strassegg and other Au-Cu deposits in the eastern Alps to constrain the age of ore mineralization in the region.

1 Introduction

The European Union and the USGS regularly update their lists of critical metals, i.e., those of importance to national security and industry whose sourcing has been deemed at risk. Most of the producers of these important commodities lie outside of the EU / North America, putting this nations at a supply risk. Therefore, the EU has decided to promote raw material production in their own territory.

The mining in EU already has a long history, with many documented historic deposits, which potentially still contain abundant resources. One such mining area is the historic mining district of Strassegg (Styria, Austria), which was mined for Au, Ag, and As (Figure 1) (Bojar 1989). The rudimentary mining and ore processing methods used at the time, however, means that there is a potential for a significant portion of the ore underground as well as significant quantities of raw materials in the tailings.

The fact that many of the elements that remain in the tailings piles are important for modern technologies, and pose a potential environmental risk, is a strong argument to re-process these materials. For example, As is an important dopant in Si based semi-conductors but is also poisonous when ingested. These As containing minerals are therefore hugely important, even more so because they are known for being hosts for several trace elements that are needed for the green energy transition (i.e., Sb, Te, Bi, W, etc.).

1.1 Ore mineralization and mining history

The mineralization at Strassegg, occurs in the Graz Paleozoic nappe system both in the form of vein-type as well as stratabound bodies hosted in greenschists (Figure 1). The mineralization generally strikes NNW and lies subparallel, cross-cutting the

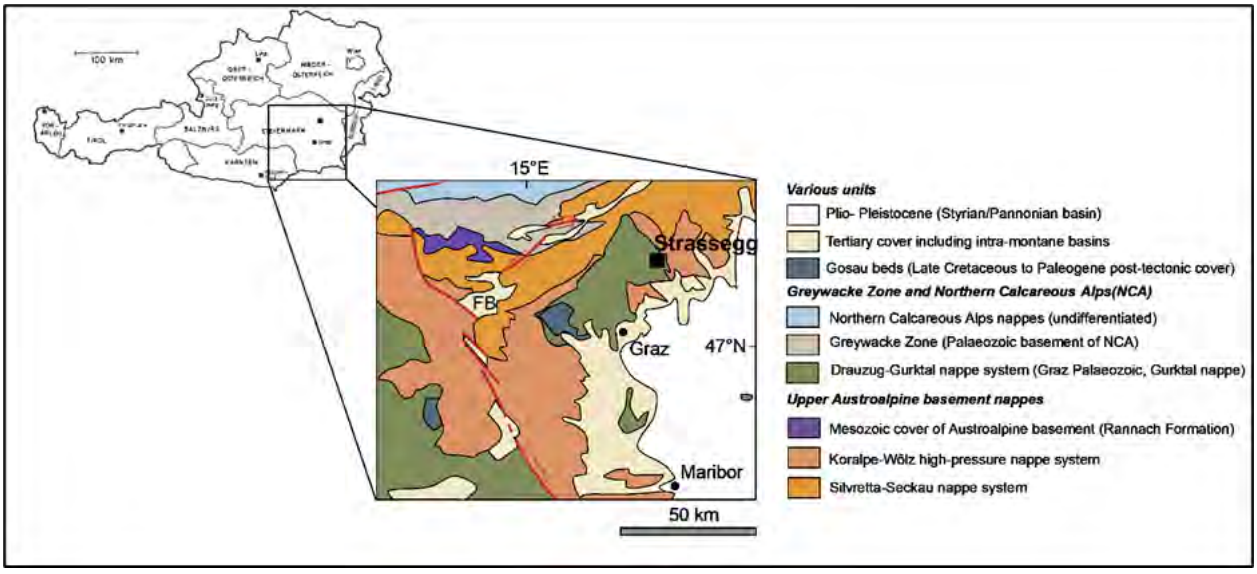

Figure 1. Geologic map of the Eastern-Alps with Strassegg noted (modified after MINEREX report 1987; Raith et al.2015)

low angle NW-SE foliation of the host rock (MINEREX report 1987; Bojar et al. 2002).

The mineralization formed through two main stages. The first mineralization stage is dominated by arsenopyrite-pyrite-gold, and the second by e.g. galena, Pb-sulfosalts, and minor Cd-, Ni-, and Te-phases.

The main mining activity stopped in the 18th century due to the high number of miner/ore processers deaths, combined with a poor economic situation. Most of the deaths were associated with long term arsenic exposure from the ore roasting. However, artisanal workings continued into the 20th century (Bojar 1989), and much of the old ore processing facilities and tailing piles still contain appreciable amounts of arsenic. In fact, the central ore processing waste dump (from which sample 21TB01 is taken from; Figure 2) is so contaminated that the local farmers have been barred from grazing their livestock in a 500m radius from the site.

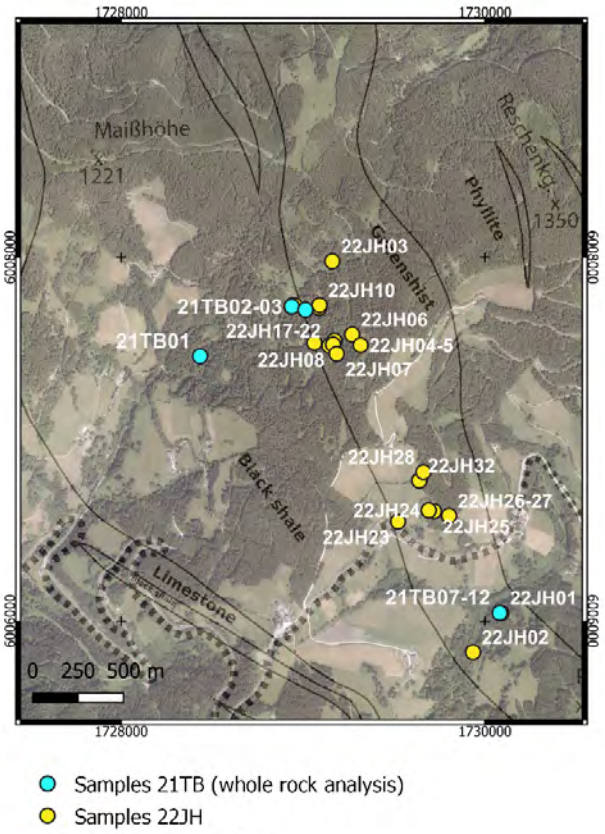

Figure 2. Sample map of Strassegg. On the sample map are the geologic unit boundaries, taken from Antes (1998). Whole rock analysis has been done on sample 21TB, whilst the petrogical work presented herein is from sample 22JH.

Much of the mining was conducted at or near the surface, and it is suspected that the main ore vein was mostly untouched at depth.

Additionally, at the time little was known of the ability of sulfide minerals to host significant quantities of Au. Most of these sulfides were disposed of in tailings which are still present in the area. The aim of our work is to examine the potential of these tailing piles for the primary elements (As, Au, and Ag) as well as critical metals that might be won as a byproduct (esp. Bi, Co, Sb, Te, and W).

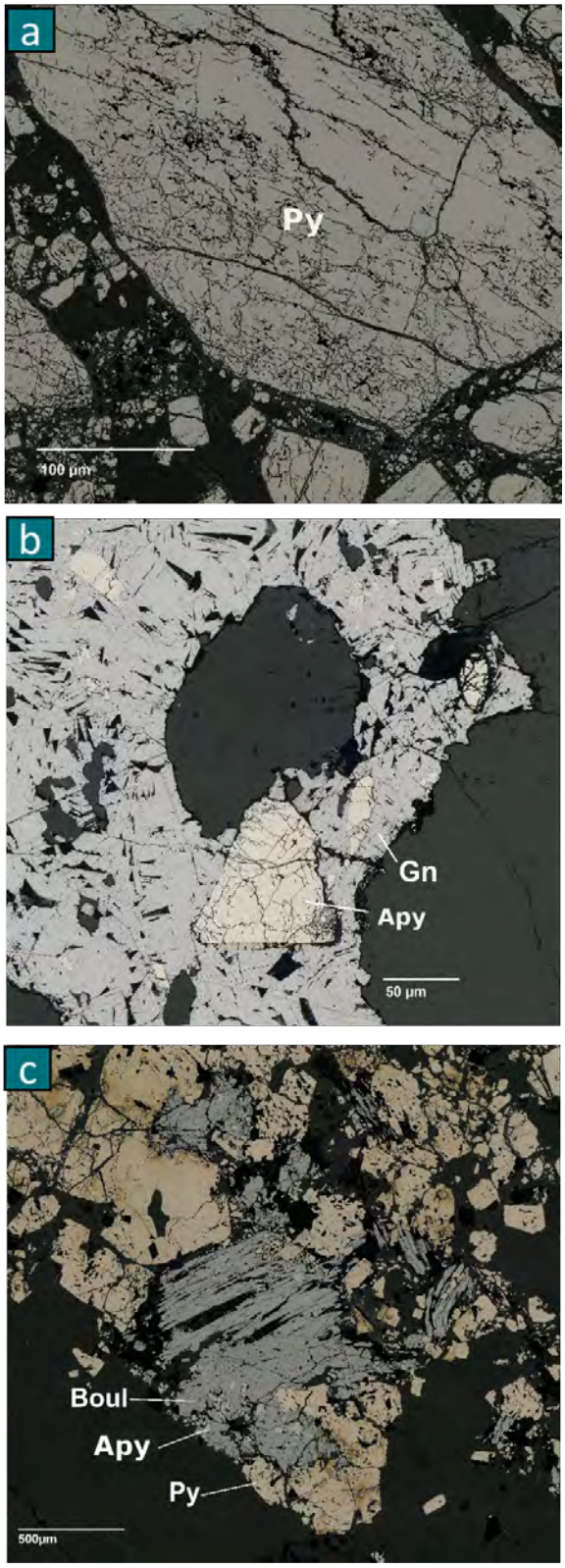

Figure 3. a) Cracked pyrite (Py) in a quartz; **b)** two stages of ore mineralisation – stage 2 galena (Gn) surrounding cracked stage 1 arsenopyrite (Apy); c) Boulangerite (Boul), arsenoypyrite (Apy) and pyrite (Py). Boulangerite filling cracked zones in the other ore minerals.

2 Analytical Methods

We collected 34 ore samples from tailing piles in the historic mining district of Strassegg, Styria, Austria (Figure 2). These 34 samples were supplemented with polished sections from the ore geology collection of the Montanuniversität Leoben (Austria). Samples were investigated using a combination of whole rock geochemistry, optical microscopy, SEM, and laser ablation inductively coupled mass spectrometry. A first impression of optical microscopy is given in Figure 3. Different ore phases are indicated.

Additional LA-ICP-MS U-Pb analyses (methods after Roberts et al. 2020) where conducted on calcite veins from Strassegg and three additional closely associated deposits (Pusterwald, Flatschach, and Kothgraben) to constrain the age of mineralization.

3 Futher work

Further work is planned to investigate exactly how these sulfide minerals are able to host concentrations of Au, Ag, and to see if critical metals are associated with Au/Ag at the atomic scale. Therefore, we plan to use atom probe tomography (APT) to investigate is the gold is hosted as nanoparticles (Fougerouse et al. 2016), lattice bound (Gopon et al. 2019), or in deformation-related dislocation sites (Fougerouse et al. 2021).

Acknowledgements

The work is financed by in part by the State of Styria (Green Transformations grant, ABT08-247901/2021), as well AUREX Biomining AG.

References

Antes G (1998) Geochemische und geophysikalische Anomalien im Bereich des Arsenkies-Goldvorkommens Strassegg, Steiermark (die „Straßegger Anomalie“). – Unveröff. Dissertation Geol. Inst. Univ. Wien, III + 92

Bojar H-P (1989) Zur Geschichte der Bergbaue am Straßegg. -In: CHRISTIAN, G. (Hrsg.): Die Breitenau. Marktgemeinde am Fusse des Hochlantsch.- Eigenverlag d. Marktgemeinde Breitenau am Hochlantsch:19-22.

Bojar H-P, Mogessie A, Bojar AV (2002) The genesis of the gold-arsenopyrite mineralisation Strassegg, Styria: evidence for local fluid flow during late Cretaceous extension. PANGEO Austria, 2002:23

Fougerouse D, Reddy SM, Saxey DW, Rickard WDA, Riessen A Van, Micklethwaite S (2016) Nanoscale gold clusters in arsenopyrite controlled by growth rate not concentration: Evidence from atom probe microscopy k: American Mineralogist, v. 101:1916–1919.

Fougerouse D, Reddy SM, Aylmore, M, Yang L, Guagliardo P, Saxey DW, Rickard WDA, Timms N, (2021) A new kind of invisible gold in pyrite hosted in deformation-related dislocations: v.XX:1–5

Gopon P, Douglas JO, Auger MA, Hansen L, Wade J, Cline JS, Robb LJ, Moody MP (2019) A Nanoscale Investigation of Carlin-Type Gold Deposits: An Atom-Scale Elemental and Isotopic Perspective: Economic Geology, v. 114: 1123–1133, doi:10.5382/econgeo.4676.

MINEREX (1987) Statusbericht Projekt: Gold - Strassegg. Berichtszeitraum VII - XII / 1986.- Unveröff. Ber. (Lagerst. Arch. Geol. B.-A.), 13 S.

Raith JG, Leitner T, Paar WH (2015) Orogenic-type copper-gold-arsenic-(bismuth) mineralization at Flatschach (Eastern Alps), Austria. Mineralogy and Petrology 109:531–553

Roberts NM, Drost K, Horstwood MS, Condon DJ, Chew D, Drake H, Milodowski AE, McLean NM, Smye AJ, Walker RJ, Haslam R (2020) Laser ablation inductively coupled plasma mass spectrometry (LA-ICP-MS) U–Pb carbonate geochronology: strategies, progress, and limitations. Geochronology, *2*(1):33-61

Critical Minerals Potential of Armenia: An Overview for Future Exploration

Samvel Hovakimyan[1], Robert Moritz[2], Marianna Harutunyan[3], Karen Hambaryan[3], Kima Charatanyan[3]
[1]*Institute of Geological Sciences of the National Academy of Sciences of the Republic of Armenia*
[2]*Department of Earth Sciences, University of Geneva, Switzerland*
[3]*Institute of Geological Sciences of the National Academy of Sciences of the Republic of Armenia*

Abstract. Armenia is well endowed with significant mineral resources, including copper, molybdenum and gold, that can be found in different metallogenic belts recording diverse geological and geodynamic environments, ranging from island-arc to collisional and post-collisional settings. Critical metals potential in Armenia is related to alkaline complexes, granitic pegmatite and tourmaline-bearing intrusions, but also various ore deposit types, such as porphyry Cu-Mo, Au and base metal epithermal, Cu-rich and polymetallic deposits, magnetite-apatite deposits, mine tailings andwaste rocks, as well as metamorphic basement rocks. They contain variable amounts of critical minerals, including REE, chromium, cobalt, nickel, PGE, rhenium, selenium, tellurium, titanium, tungsten, vanadium, and zirconium, which are considered as by-products, and are typically not recovered during mining. The potential of these metals remains largely unknown and requires future investigations.

1 Introduction

The Armenian mountain belts belong to the Caucasian segment of the Tethyan metallogenic belt, located between the Black Sea and the Caspian Sea (Fig.1, inset). The Lesser Caucasus contains two metallogenic belts, including the Late Jurassic - Early Cretaceous Somkheto-Karabagh island arc and the Kapan block, and the Cenozoic Gondwana-derived South Armenian block (Fig. 1).

Critical minerals occur in diverse geological environments and mineralized systems in Armenia, including alkaline complexes, epithermal Au and base metal, Cu-rich and polymetallic type deposits, porphyry Cu-Mo deposits, as well as granitic pegmatite and carbonatite (Fig. 1).

The existing mines (e.g. Kadjaran, Agarak, Teghout etc.) generate huge volumes of waste rock and tailings. They can be source of significant amounts of critical minerals, including REE, Cr, Ni, Co, Li, PGE, Re, Se, Te, Bi, Ti, W, V, Zr etc., whichare considered as by-products, and are typically not recovered (Avagyan 2004). Consequently,characterization and reprocessing of existing surface waste materials at active and inactive mines have the potential to transform waste into a resource by providing new sources of critical minerals. Recovery of these metals from mine wastes and tailings can be an environmentally friendly alternative to opening new mines.

This contribution provides an overview on critical minerals potential of Armenia based on literature review, with the aim to highlight the critical minerals distribution in different ore deposit types, and in various magmatic settings. Future investigations are required to evaluate the potential of critical metals for exploration to meet their growing demands for technological development in fields such as renewable energy and clean technologies.

2 REE in nepheline syenite complexes

Two major alkaline complexes are known in Armenia, which are the Cenozoic Tejsar and Meghri alkaline syenite complexes (Meliksetian 1971). They are situated at the northern and southern edges of the South Armenian Block, respectively (Fig. 1). They formed during the Cenozoic Arabia-Eurasia collision and post- collision evolution of the Lesser Caucasus (Grosjean et al. 2022).

2.1 The Tejsar alkaline syenite complex

The Tejsar alkaline complex consists of mid- Eocene to Pliocene magmatic rocks (Bagdasaryan et al. 1969), and includes a mid-Eocene nepheline syenite (Meliksetian 1971; Sokoł et al. 2018; Grosjean et al. 2022), which has been identified as a major source of lanthanides, Sc, and Y in Armenia. Nepheline syenite of this complex contains 457Mt grading at 21.49 % Al_2O_3 (Uzumova 1983). The magmatic rocks of the Tejsar complex are also characterized by high concentrations of Zr, Hf, Ga, Th, Ce and Nb. Other elements that have been reported (Maghakyan et al. 1972; Grosjean et al. 2022) include: 0.3 wt% Li; 0.0008 wt % Be; 0.008 wt % Rb; 0.03 wt % La; 0.01 wt % Sr; 0.03 wt % Ce; 0.001 wt % Sc; 0.003 wt % Cs; 0.003 wt % Ga, 0.003 wt % Tl, and 0.001 wt % Y.

The Tejsar alkaline syenite complex may also be interesting for Sc resources. Scandium is dominantly sourced by magmatic deposits (about 90% of the total), where it is primarily hosted in clinopyroxene ± amphibole in mafic–ultramafic intrusions (Wang et al. 2021). The recent discoveryof a Sc deposit in the Crater Lake syenite complex,

Canada (Beland and Williams-Jones 2023) documents that carbonatite-related metasomatic deposits provide an alternative resource for Sc in magmatic rocks. At the Tejsar alkaline complex, Sc concentrations range from 3.8 to 39.8 ppm (Grosjean et al. 2022).

2.2 The Meghri-Ordubad pluton

The highly mineralized Cenozoic Meghri-Ordubad pluton was formed by repeated intrusive activity from mid-Eocene subduction to Miocene post- collisional evolution of the southernmost Lesser Caucasus (Moritz et al. 2016b; Rezeau et al. 2016, 2019). It hosts major porphyry Cu-Mo and epithermal Au and base metal deposits, many of which are currently under production (Moritz et al. 2016a). Dextral strike-slip tectonics controlled mid- Eocene ore deposit and magma emplacement during the convergence between the Arabian and Eurasian plates. This tectonic system has been repeatedly reactivated during Neogene collision and post-collision ore formation and magmatism (Hovakimyan et al. 2019). The Meghri alkaline syenite complex within the Meghri-Ordubad pluton is characterized by high Zr,Hf, Be, Nb, and Th concentrations (Maghakyan et al. 1972; Rezeau et al. 2019). Concentrations of 0.025 wt% Zr, 0.0003 wt% Hf, and 0.01 wt% Nb have been reported (Maghakyan et al. 1972). The Li potential of granitic pegmatite and tourmaline-bearing intrusions of the Meghri-Ordubad pluton is still unknown and requires future investigations. An additional potential source of Li might be clay minerals, such as hectorite, which might be related to hydrothermally altered rhyolite.

3 Critical minerals in epithermal gold and base metal deposits

Gold deposits of Armenia are located in both the Mesozoic Somkheto-Karabagh belt and the Kapan block, and the Cenozoic South Armenian Block. They are highly prospective for Cu, Se, Te, Bi, Cd, Ga, In, Ge, Zr, Ti, REE, Co, Sb, W, Sc and other associated critical minerals, which are considered as by-product commodities with further unexplored potential (Maghakyan et al. 1972; Amiryan 1984; Avagyan 2004). Tellurium is present in most of the epithermal Au deposits (e.g., Meghradzor, Tey- Lichkvaz, Sotk, Terterasar etc.), generally together within common sulfides (pyrite, arsenopyrite) and as discrete Te minerals (Amiryan 1984).

The Armanis high-sulfidation and the Sotk low-sulfidation epithermal Au deposits are hosted by the Jurassic-Cretaceous Amasia-Sevan-Akera ophiolite suture zone (Fig. 1), and contain significant concentrations of Se, Te, Bi, and Cd (Maghakyan et al. 1972; Amiryan 1984).

The Azatek deposit (Fig. 1) is characterized by a Au-Pb-Sb type mineralization, with significant concentrations of Te, Bi, Ga, In, Ge, and Cd in polymetallic ores (Amiryan 1984).

The Shahumyan gold – polymetallic deposit in the Kapan block is hosted by Middle Jurassic subvolcanic rocks (Fig. 1). Gold-polymetallic veins are characterized by significant Te concentrations with Au–Ag-tellurides (Mederer et al. 2014). Indium (0.008%), gallium (0.01%), cadmium (1%), and germanium (0.003%) have also been reported in sphalerite (Maghakyan et al. 1972).

4 Critical minerals in porphyry Cu-Mo deposits

Porphyry Cu-Mo deposits in Armenia are characterized by high concentrations of Re, Se, Te, Ge, Bi, Ag and other critical metals as by-products. They include the Late Jurassic Teghout deposit (Fig. 1), where molybdenite-rich ore contains up to 0.073 wt% Re (Avagyan 2004).

Cenozoic porphyry Cu-Mo deposits in southernmost Armenia are the major sources of Cu and Mo, and critical minerals like Re, Se, and Te. They include the mid-Eocene subduction-related Agarak (0.038 wt% Re, 0.0275 wt% Se, 0.003 wt% Te), Aygedzor (0.13 wt% Re; 0.05 wt% Se; 0.0055 wt% Te, 0.0016 wt% Bi), and Dastakert (0.0212 wt% Re, 0.0055 wt% Se, 0.0035 wt% Te) deposits,and the Oligocene to early Miocene collisional to post-collisional giant Kadjaran deposit (0.04 wt% Re, 0.018 wt% Se, 0.0066 wt% Te) in the Meghri- Ordubad pluton (Fig. 1; Faramazyan et al. 1970; Avagyan 2004).

Another Cenozoic porphyry Cu-Mo deposit at Hanqavan is located in the northern part of the Gondwana-derived South Armenian Block (Fig. 1), where the molybdenite ores contain significant amounts of Re (0.015-0.034 wt%), Se (0.112 wt%), Te (0.072 wt%), and Bi (0.03-0.3 wt%) (Maghakyanet al. 1972).

5 Critical minerals in Cu-rich and polymetallic deposits

The major Cu pyrite and polymetallic deposits are located along the Jurassic- Cretaceous Somkheto –Karabagh belt of the Eurasian margin and its southern extension the Jurassic Kapan block. They include the Alaverdi Cu–Au, the Shamlugh Cu-rich pyrite, and the Akhtala Ba-rich polymetallic deposits in the Alaverdi mining district (Fig. 1; Moritz et al. 2016a; Calder et al. 2019), and the Kapan Cu mines in the Kapan block (Mederer et al. 2014). These deposits and their tailings are characterized by significant concentrations of Se, Te, as well as Bi and Ga. Selenium and Tellurium concentrations at the Alaverdi deposit are, respectively 52.1 ppm and 83.9 ppm, and 10.5 ppm Se and 25.4 ppm Te at the Shamlugh deposit. At the Kapan Cu deposit, 19.25 ppm Se, and 12.38 ppm Te have been reported (Maghakyan et al.1972).

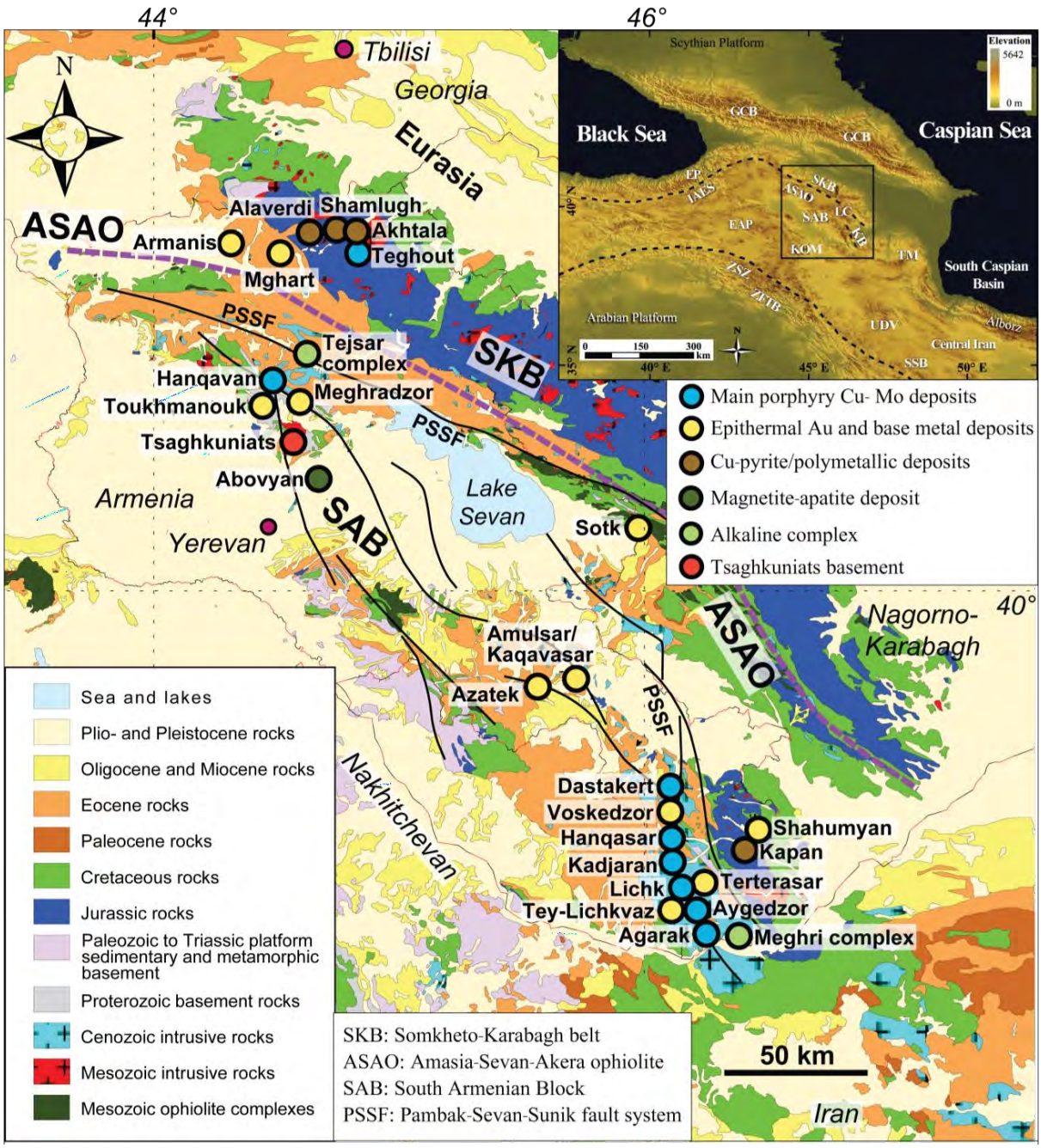

Figure 1. Geology of the Lesser Caucasus (modified after Mederer et al. 2014), with locations of the intrusive complexes and mineral deposits described in this abstract.

6 REEs in the Abovyan Kiruna-type magnetite-apatite deposit

The Abovyan magnetite-apatite deposit is a Kiruna-type iron oxide - apatite deposit (Fig. 1; Frietsch and Perdahl 1995). It is hosted by post-Middle Miocene andesite porphyritic rock, tuff and tuffite (Sarukhanyan and Mkrtchyan 1968). Apatite and magnetite in various ore types at Abovyan make upto 85-90% of the total volume. The ore consists of massive and breccia type ores with a subvolcanic character connected to fault zones (Sarukhanyan and Mkrtchyan 1968; Frietsch and Perdahl 1995).

The interest for this deposit has increased recently,because apatite can have significant REEs concentrations (Chakhmouradian and Wall 2012). Apatite from the Abovyan deposit belongs to an alkaline trend, and has a high concentration of REEs (Frietsch and Perdahl 1995). The apatite ores contain 0.64-1.10 wt% La, 1.36-2.30 wt% Ce, 0.22-0.44 wt% Nd, and 0.10-0.14 wt% Y (Sarukhanyan and Mkrtchyan 1968), which can be considered as a potential source of REEs. Further investigations are required to understand the originof this deposit.

7 Critical minerals potential of the Neoproterozoic basement

The Tsaghkuniats massif consists of Neoproterozoic metamorphic basement rocks (Fig. 1). These rocks are potential targets for criticalminerals, because of the presence of granitic rockswith high silica content (Critical Minerals Mapping Initiative). Fertility of these rocks for critical minerals have been recognized in several districts of the Tsaghkuniats massif, such as the Arzakan titanium prospect, where the mineralization is related to schist, and silicified zones of the Arzakanmetamorphic complex. This prospect contains 2.35wt% of TiO_2, with an estimated 14,075 tons of probable reserves of Ti (Harutchyan 1995).

8 Conclusions

The Armenian segment of the Tethyan metallogenic belt represents a potential target for some critical metals, including Re, Te, Se, REE, PGE, and potentially Li, associated with various geological environments and mineralized systems. Significant potential resources of critical metals in existing mines, in mine wastes and tailings remain underexplored. Reprocessing and recoveries of existing deposits and their tailings are required, aimed at an environmentally sustainable production of critical metals. For instance,significant quantities of Re and Te can be recovered from most of the porphyry Cu-Mo and epithermal Au deposits, respectively. Further investigations are required for the assessment of critical metals enrichment of alkaline complexes, granitic pegmatite, and Neoproterozoic metamorphic basement rocks.

Acknowledgements

This study was financially supported by the Science Committee of Republic of Armenia (Research project № 22IRF-08), and by the Swiss National Science Foundation grant200021_188714.

References

Amiryan ShH (1984) Gold ore formation of Armenian SSR. Pub House Acad Sci Arm SSR p 304 (in Russian)

Avagyan H (2004) Armenian mineral resources: “Gitutyun” publishing house of the National Academy of Sciences of the Republic of Armenia, Yerevan, p 432 (in Armenian)

Bagdasaryan GP, Ghukasian RKh, Karamyan KA (1969) Absolute dating of Armenian ore formations. Int Geol Rev 11:1166-1172

Beard ChD, Goodenough KM, Borst AM, Wall F, Siegfried PR et al (2023) Alkaline-Silicate REE-HFSE Systems. Econ Geol 118:177–208

Beland CMJ, Williams-Jones AE (2023) The genesis of a potential scandium ore deposit at Crater Lake, Canada. Chemical Geology 615:121223

Calder MF, Moritz R, Ulyanov A, Chiaradia M, Spangenberg J E, Melkonyan RL (2019) Jurassic ore-forming systems during the Tethyan orogeny: Constraints from the Shamlugh deposit, Alaverdi district, Armenia, Lesser Caucasus. Miner Deposita 54:1011–1032

Chakhmouradian AR, Wall F (2012) Rare earth elements: minerals, mines, magnets (and more). Elements 8 (5): 333–340

Critical Minerals Mapping Initiative (CMMI) https://portal.ga.gov.au/persona/cmmi

Faramazyan AS, Kalinin SK, Terekhovich SL (1970) Geochemistry of PGE in ores of Cu-Mo deposits of Armenia: Proceedings of the Academy of Sciences of the Armenian SSR. Earth Sciences 23(4):25–32 (in Russian) Frietsch R, Perdahl JA (1995) Rare earth elements in apatiteand magnetite in Kiruna-type iron ores and some other iron ore types. Ore Geol Rev 9:489-510

Grosjean M, Moritz R, Rezeau H, Hovakimyan S, Ulianov A, Chiaradia M, Melkonyan R (2022) Arabia-Eurasia convergence and collision control on Cenozoic juvenile K-rich magmatism in the South Armenian block, Lesser Caucasus. Earth-Science Reviews, Vol. 226:103949

Harutchyan AG (1995) The Arzakan titanium prospect. Ministry of Energy and Natural Resources of the Republic of Armenia, Unpublished report 105:6 (in Russian)

Hovakimyan S, Moritz R, Tayan R et al (2019) Cenozoic strike-slip tectonics and structural controls of porphyry Cu-Mo and epithermal deposits during geodynamic evolution of the southernmost Lesser Caucasus, TethyanMetallogenic Belt. Econ Geol 114:1301–1337

Maghakyan HG, Pidjyan GO et al (1972) Rare and precious elements in ore formations of the Armenian SSR. Publishing House of the Academy of Sciences of the Armenian SSR, Yerevan, p 393 (in Russian)

Mederer J, Moritz R, Zohrabyan S, Vardanyan A (2014) Base and precious metal mineralization in Middle Jurassic rocks of the Lesser Caucasus: a review of geology and metallogeny and new data from the Kapan, Alaverdi and Mehmana districts. Ore Geol Rev 58:185–207

Meliksetian BM (1971) Mineralogy, geochemistry and petrology of Tezhsar Alkaline Complex. In: Intrusive Complexes of Principal Ore Provinces of Armenia. Academy of Sciences, Armenian SSR, Yerevan: pp 117–298 (in Russian)

Moritz R, Melkonyan R, Selby D et al (2016a) Metallogeny of the Lesser Caucasus: From Arc Construction to Postcollision Evolution. Special Publication of the Societyof Economic Geology 19:157–192

Moritz R, Rezeau H, Ovtcharova M, Tayan R et al (2016b) Long-lived, stationary magmatism and pulsed porphyry systems during Tethyan subduction to postcollision evolution in the southernmost Lesser Caucasus, Armenia and Nakhitchevan. Gondwana Res 37:465-503

Rezeau H, Moritz R, Wotzlaw JF, Tayan R, Melkonyan R et al (2016) Temporal and genetic link between incremental pluton assembly and pulsed porphyry Cu-Mo formationin accretionary orogens. Geology 44:627–630

Rezeau H, Moritz R, Wotzlaw J-F, Hovakimyan S, Tayan RN (2019) Zircon petrochronology of the Meghri-Ordubad pluton, Lesser Caucasus: fingerprinting igneous processes and implications for the exploration of porphyry Cu-Mo deposits. Econ Geol 114:1365–1388

Sarukhanyan LB, Mkrtchyan GM (1968) Distribution of accessory rare earth elements in apatite. Proceedings of the Academy of Sciences of Armenian SSR, Earth Sciences 21(4):16–27 (in Russian)

Sokół K, Halama R, Meliksetian K, Savov IP, Navasardyan G, Sudo M (2018) Alkaline magmas in zones of continental convergence: The Tezhsar volcano- intrusive ring complex, Armenia. Lithos 320–321:172–191

Uzumova AI (1983) The Tejsar aluminum deposit. Ministry of Energy and Natural Resources of the Republic of Armenia, Unpublished report 13 (in Russian)

Wang Zh, Li MYH, Liu ZRR, Zhou MF (2019) Scandium: Ore deposits, the pivotal role of magmatic enrichment and future exploration. Ore Geol Rev 128:103906

Environmentally sustainable production of critical metals: a Tasmanian approach

Julie Hunt[1], Michael Roach[2], Lejun Zhang[1], Sharon Fraser[3], Yamila Cajal[1], Mohammad Fathi[1], Wei Hong[1], Owen Missen[1], David R Cooke[1]
[1]Centre for Ore Deposit and Earth Sciences (CODES), University of Tasmania, TAS, Australia
[2]Earth Sciences, College of Science and Engineering, University of Tasmania, TAS, Australia
[3]School of Education, College of Arts, Law and Education, University of Tasmania, TAS, Australia

Abstract. Tasmania, Australia is host to significant critical metal resources and currently produces tungsten (W) and tin (Sn). Exploration is underway for rare earth elements (REE) and magnesium (Mg). Additional critical metals, e.g. cobalt (Co), occur as minor components in operating base and ferrous metals mines and in legacy waste materials. A partnership between industry, academic and government organisations focused on the characterisation of critical metal deportment, pathways to production, plus education and engagement, has been commenced to aid growth of the critical metals industry in Tasmania. This includes outreach and training to engage with regional communities. Innovative tools are being developed including immersive 3D visualisations of mining operations. Example visualisations have been completed for the Dolphin tungsten deposit and the Savage River mining operations. Development of visualisations for the Kara iron-tungsten mine and processing plant are underway.

1 Introduction

Critical metals (including cobalt, magnesium, nickel REE, tin, and tungsten) are essential to industry in developed economies but are vulnerable to market uncertainties and supply chain disruptions. Domestic production of critical metals is therefore of strategic importance to individual countries or regions from a resource security perspective. Within Australia, Tasmania has a significant critical metals resource and currently produces tungsten (used in steel manufacturing and superalloys) and more than 95% of Australia's tin (important for renewables such as electric vehicles, photovoltaics, batteries etc; Geoscience Australia 2023). Tasmania's existing base and ferrous metal mines also have potential to produce critical metals such as cobalt either as a by-product of existing processing operations and/or from historical waste repositories. Recent discoveries of unconventional REE occurrences and significant discoveries of magnesium are currently being evaluated for potential development (ABx 2023; Australian Resources 2023).

The growth of a sustainable critical metals industry in Tasmania is being supported by an innovative collaboration between industry, academic, and government partners centred on three themes: novel tools for characterisation of critical metals deportment; optimisation and development of methods and workflows for critical metals processing and waste management strategies; and innovative community education and outreach strategies. Besides the University of Tasmania, there are nine industry partners, plus the University of Liege, the University of Queensland, Mineral Resources Tasmania (MRT), and the Tasmanian Minerals, Manufacturing and Energy Council (TMEC) involved in the collaboration.

The collaborative project includes fundamental research into deposit characterisation and genesis as well as detailed studies of mineral and element deportment that will inform mineral processing options. Sources of critical metals being examined include primary ore deposits plus mine waste materials. Processing options are also being addressed. In addition, there is a significant focus on outreach and training targeted at regional communities to help with workforce capacity building.

2 Critical metals in Tasmania

Most of the known critical metal resources are in north-western Tasmania as shown by the distribution of properties owned by collaborating organisations (Fig. 1). This area is largely underlain by Proterozoic sedimentary and volcanic rocks; Middle Cambrian sedimentary and felsic rocks, including the Mt Read Volcanics; Cambrian medium to high grade metamorphic complexes, including the Arthur Lineament; and Devonian granites (e.g., Rawlinson et al. 2010). Recent discoveries of REE-bearing clays have been made further east (9 on Fig. 1).

At the Dolphin mine (1 on Fig. 1) scheelite is hosted within carbonate-rich rocks proximal to granite. The site is currently undergoing re-development due to increased tungsten prices and contained high grade reserves (4.43 Mt of 0.92% WO_3) and resources (Group6 Metals, 2023). Prospect Ridge (2 on Fig. 1) hosts magnesium in a number of magnesite deposits (e.g., Perry 2011). At the Kara mine (3 on Fig. 1) iron and tungsten are hosted by limestone and calcareous sandstones proximal to Devonian granite (e.g., Singoyi 2001). Savage River (4 on Fig. 1) is an operating mine producing Fe from magnetite but has potential for production of Co and Ni from legacy waste materials (Grange Resources, 2023). Rosebery (5 on Fig.1) is a world class polymetallic volcanic-hosted massive sulphide deposit producing Cu, Pb, Ag, Zn and Au (Denwer et al. 2017). It also has potential to produce W, Sn and In as by-products (Geoscience Australia

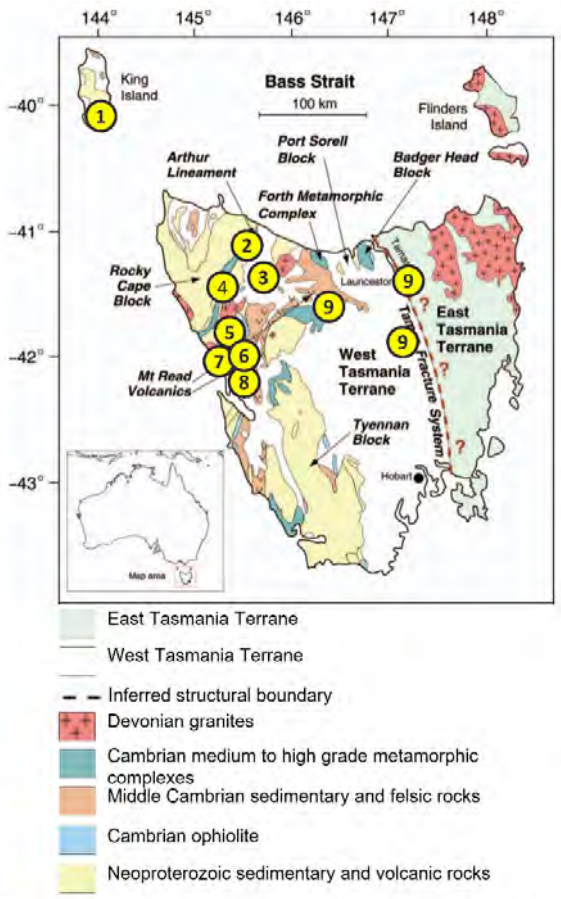

Figure 1. Simplified geology map of Tasmania (after Rawlinson et al. 2010) showing the location of industry partner properties. 1: Dolphin (W). 2: Prospect Ridge (Mg). 3: Kara (Fe, W). 4: Savage River (Fe, Mg, Co). 5: Rosebery (Zn-Pb-Ag-Au-Cu, Cu, In). 6: Renison (Sn). 7: Avebury (Ni, Co). 8: Mount Lyell (Cu, Co). 9: Deep Leads (REE).

2023). Renison (6 on Fig. 1) is a carbonate replacement tin deposit and is Australia's largest tin producer (Patterson et al. 1981; Metals X 2023). The potential for recovery of critical metals (e.g., In, Co, Ni) from ores, gangue and waste is being explored. Avebury (7 on Fig. 1) is a Ni sulphide deposit associated with an ophiolite sequence that has been intruded by granite (Kamenetsky et al. 2016). Portions of the ultramafic rocks are variably enriched in critical metals (W, Sn, Co). Mount Lyell (8 in Fig. 1) is a copper deposit hosted in volcanic rocks and has significant Co potential contained in legacy mine wastes (van Balen 2019). Deep Leads (9 on Fig. 1) are unconventional REE prospects associated with bauxite (Abx Group 2023).

3 Outreach and community engagement

A significant part of the project is targeted at outreach and training to engage with and educate regional communities. Innovative tools are being developed including immersive 3D visualisations of mining operations. Example visualisations have been completed for the Dolphin tungsten deposit and the Savage River mining operations. Development of visualisations for the Kara mine and processing plant are underway. The visualisations are created from various types of photography, including aerial images from drones, images from multi-lens 360° cameras, still and video photography, and detailed 3D renderings of rock samples. Also included are videos and sound for individual pieces of equipment along with oral descriptions and interviews with equipment operators. Snapshots are shown in Figures 2 and 3. In the visualisations information is available at a variety of scales from regional to local to outcrop to hand specimen to microscopic, as shown by the examples in Figures 4 and 5.

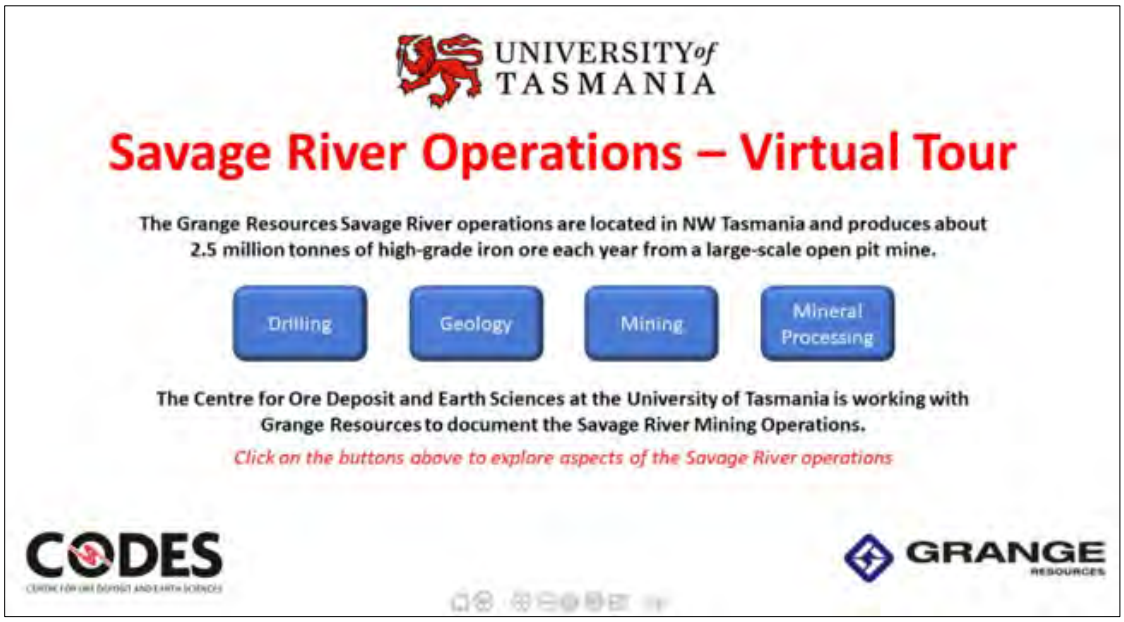

Figure 2. Snapshot of 3D visualisation for the Savage River mining operations. Buttons provide links to additional information, videos etc. All visualisations by M. Roach.

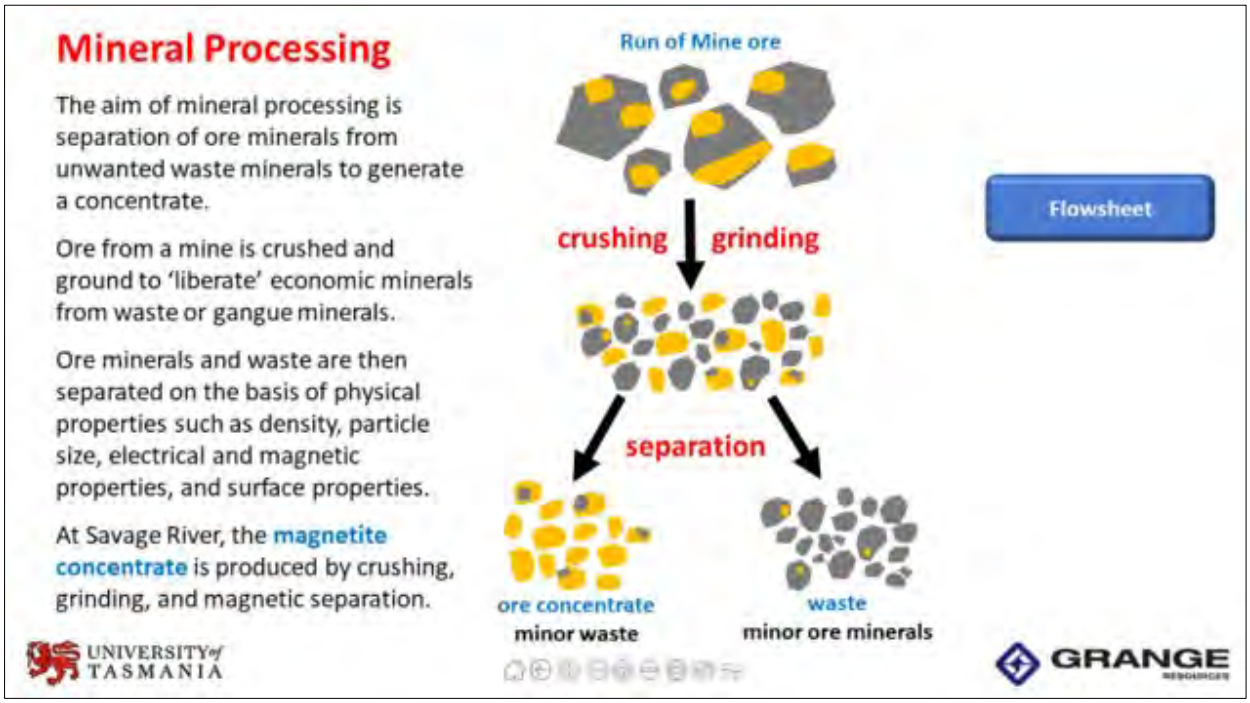

Figure 3. Information for the Savage River mining operations that can be seen by clicking on the mineral processing button shown in Figure 2. Clicking on the flowsheet button takes the user to details and videos of the processing plant.

Figure 4. Snapshot of 3D visualisation for the Dolphin mine showing the variety of scales of information available to the viewer. This includes regional geology, a virtual tour of the mine area, details of hand samples, as well as zoomable 3D renderings of samples.

Figure 5. Illustration of Information types available for sample K12LZ003 from the Dolphin tungsten deposit, including: visible light, ultra violet (UV) light, high resolution imagery, back-scattered electron (BSE), SEM-based automated mineral classification (AMICS), cathode luminescence (CL), and hyperspectral (TIR = thermal infra-red). Buttons at the bottom show links to geochemical data available for specific minerals.

Acknowledgements

The authors would like to thank all industry, academic and government collaborators for their participation and enthusiasm for the project. They have all been very generous with access to field sites, data and their time.

References

ABx Group (2023) Rare earth elements (REE) discovery. ABx Group website. https://www.abxgroup.com.au/site/about/about-us. Accessed 21 February 2023.

Australian Resources (2023) GWR to acquire Prospect Ridge magnesite project in Tasmania. Australian Resources website. https://www.australianresources.com.au/gwr-to-acquire-prospect-ridge-magnesite-project-in-tasmania/. Accessed 21 February 2023.

Denwer K, Garrick L and Robertson M (2017) Rosebery Cu-Pb-Zn-Ag-Au volcanogenic massive sulphide deposit. In Phillips GN (Ed) 2017 Australian Ore Deposits. Australasian Institute of Mining and Metallurgy, Monograph 32, p. 817-822.

Geoscience Australia (2023) Australia's potential for critical commodities. Geoscience Australia website. https://www.ga.gov.au/data-pubs/data-and-publications-search/publications/critical-commodities-for-a-high-tech-world/australias-potential. Accessed 21 February 2023.

Grange Resources (2023) Annual Report 2022. Grange Resources website. https://grange.blob.core.windows.net/public/2327e5a5-7a9e-453a-9fcd-89a142dc7e76.pdf. Accessed 8 May, 2023.

Group6 Metals (2023) Dolphin project. Group6 Metals website. https://g6m.com.au/dolphin-project/overview/. Accessed 15 February 2023.

Kamenetsky VS, Lygin AV, Foster JG, Meffre S, et al. (2016) A story of olivine from the McIvor Hill complex (Tasmania, Australia): Clues to the origin of the Avebury metasomatic Ni sulfide deposit. American Mineralogist 101:1321-1331

Metals X (2023) Renison tin operation. Metals X website. https://www.metalsx.com.au/renison-tin-operation/. Accessed 21 February 2023.

Patterson DJ, Ohmoto HH, Solomon M (1981) Geological setting and genesis of cassiterite-sulfide mineralisation at Renison Bell, western Tasmania. Economic Geology 76:393-438.

Perry OC (2011) A geophysical and geological study of the Arthur River magnesite deposit, northwest Tasmania. Dissertation, University of Tasmania.

Rawlinson N, Tkalcic H, Reading AM (2010) Structure of the Tasmanian lithosphere from 3D seismic tomography. Australian Journal of Earth Sciences 57:381-394.

Singoyi B, Zaw K (2001) A petrological and fluid inclusion study of magnetite-scheelite skarn mineralization at Kara north-western Tasmania: implications for ore genesis. Chemical Geology 173:239-253.

van Balen JFM (2019) Determining the mineralogical and geochemical properties of tailings at Copper Mines of Tasmania. Honours thesis, University of Tasmania, 126 p.

Potential for sulfide-hosted by-products from the iron oxide-apatite deposits at Kiruna? A mineralogical perspective

Patrick Krolop', Ulf B. Andersson[1], Katie McFall[2], Jana Kalmbach[3], Sabine Gilbricht[4], Thomas Seifert[4]
[1]*Luossavaara Kiirunavaara AB (publ), Kiruna, Sweden*
[2]*University College London, Department of Earth Sciences, London, UK*
[3]*Avannaa Exploration Services AB, Kiruna, Sweden*
[4]*TU Bergakademie Freiberg, Institute of Mineralogy, Freiberg, Germany*

Abstract. Sulfide mineralisation types in the Kiirunavaara and Per Geijer iron oxide-apatite deposits in the Kiruna district have been studied by mineralogical means to infer a preliminary potential for future by-products of Co, Cu, and sulfuric acid. Based on the dominance of pyrite over other sulfides, e.g., chalcopyrite and bornite-digenite solid solution series minerals, the main potential can be attributed to pyrite as the source of sulfuric acid. Significant concentrations of cobalt in pyrite types from both deposits may indicate an economic potential if proven processable in the future. Copper minerals have low concentrations of deleterious elements but occur less frequently compared to pyrite, so their potential is not yet tangible. Further studies are planned to evaluate the full potential of sulfides.

1 Introduction

Circular business models are key aspects in all mining operations as they increase materials efficiency, create diversity in assets and thus greater potential financial stability. The need for critical raw materials to the European economy to achieve the green energy transition enhances the investigation for potential by-products from existing mines. Reduction of the environmental impact of mining by recovery of by-products from waste streams is an additional important factor.

Nowadays, upgrading waste material in search for potential by-products is also being evaluated for iron ore mining operations in the Kiruna district. However, the focus is on phosphorus and rare earth elements, based on the high modal abundance of phosphates in tailings and large quantities in current exploration targets, e.g., the Per Geijer (PG) deposits. So far, the potential of Cu, Co, and sulfuric acid from sulfide minerals present in association with the iron ore has not been investigated in detail.

As a first approach, preliminary characterisation studies of the different sulfide species and varying types in the Kiirunavaara (KV) and PG iron oxide-apatite deposits near Kiruna were conducted (Kalmbach 2022, Andersson et al. 2022). Most of the information obtained in these investigations were mainly utilized to decipher the origin of mineralisation. In this contribution, the mineralogical information from previous studies is used to deliver preliminary implications for the potential of Co, Cu, and sulfuric acid as by-products from iron ore mining.

2 General characteristics of Kiruna IOA deposits

Iron oxide-apatite (IOA) deposits are the most important ore deposits in the Kiruna region of northern Sweden. The expression “Kiruna-type” has been introduced to signify the special character of the ores with over 40 orebodies in the Kiruna district (Geijer 1931, Martinsson et al. 2016). Early studies of IOA deposits in Kiruna district (e.g., Geijer 1910, 1931, Parák 1975) revealed high iron grades above 60 % Fe and the large tonnages for the Kiirunavaara deposit. The PG exploration targets potentially display significant mineral resources for future production for Luossavaara-Kiirunavaara Aktiebolag (publ.), known as LKAB, who exploits the iron ores in the district. Most of the IOA deposits in the Kiruna area display almost pure magnetite ores with minor impurities in the form of gangue minerals such as apatite, calcite, actinolite, mica, chlorite, titanite, sulfates, allanite, and quartz (Nordstrand & Andersson 2013, Martinsson et al. 2016). However, large differences in texture, mineralogy and relation to wall rocks occur in the PG deposits (Frietsch 1979, Martinsson 2015, Krolop 2022) compared to KV. Common features are the presence of sulfides hosted both disseminated in the iron ore and wall rocks as well as vein-hosted occurrences.

3 Methodology

Sampling was conducted according to styles of sulfide mineralisation in the deposits with regards to textural variability and mineral associations. Kiirunavaara samples were selected from recently blasted mining areas underground and partly from drill cores while exploration drill cores were sampled from the PG deposits. Samples were prepared by the Helmholtz Institute Freiberg for Resource Technology (PG samples) and the University of Gothenburg (KV samples). All 64 samples were studied with transmitted and reflected light and further investigated by scanning electron microscopy at TU Bergakademie Freiberg. Mineral chemical analysis was obtained on 18 samples by electron probe microanalysis (EPMA) and electron probe mapping with a JEOL JXA-8320 equipped with five wavelength dispersive spectrometers (WDS) at TU Bergakademie Freiberg. Additional trace element analysis was carried out on 14 samples using the

Analyte Excite 193 nm ArF* excimer-based laser ablation (LA) system, coupled to the quadrupole-ICPMS iCAP at the German Research Centre for Geosciences (GFZ).

4 Sulfides in the deposits

Preliminary investigation on sulfides based on textural and mineral chemical observation revealed 5 respective types of sulfides in both the KV and PG IOA deposits (Table 1). Sulphide minerals encountered in the deposits include pyrite, chalcopyrite, bornite, molybdenite, copper-rich minerals (in the bornite-digenite solid solution series), and pyrrhotite in some of the samples.

Table 1. Sulfide types in the Kiirunavaara and Per Geijer deposits and their characteristics.

Type	Sulfides	Setting	Assemblage
K1	Py	diss. in iron ore	Mgt
K2	Py > Cpy	vein-hosted	Mgt-Qtz-Cc
K3	Py > Cpy	vein-hosted	Qtz-Cc-Anh-Spec
K4	Py > Cpy	vein-hosted	Mgt-Clay
K5	Py > Cpy	diss. in wall rocks	Ttn-Act-Qtz-Cc-Alb
PG1	Cpy > Bo	diss. in iron ore	Mgt-Hem
PG2	Py > Cpy > Bo-Dig	vein-hosted	Cc-Qtz-Spec
PG3	Py > Cpy	vein-hosted	Chl-Alb-Cc-Alla
PG4	Py > Cpy	alteration nests	Mus-Chl-Alb-Cc-Qtz
PG5	Py > Cpy > Bo-Dig	vein-hosted	Mgt-Hem-Ap-Cc

Mineral chemical differences are most pronounced in pyrite compared to the other sulfide minerals. Significant variations from the ideal composition of pyrite occur particularly in sulfide types PG2 and PG4 expressed in the stoichiometric variability of $Fe_{0.87\text{-}1.02}Co_{0.00\text{-}0.14}As_{0.00\text{-}0.01}S_{1.93\text{-}2.00}$ and $Fe_{0.61\text{-}1.01}$ $Co_{0.05\text{-}0.38}As_{0.00\text{-}0.27}S_{1.42\text{-}2.01}$, respectively. The fluctuations relate mainly to the incorporation of Co and As. The other pyrite types are rather homogenous showing minor trace element concentrations of < 0.6 wt.% Ni and < 300 ppm As (PG3). Pyrite from the KV deposit reveals less elemental variation compared to PG but can be enriched in cobalt in sulfide type K1 up to 2.3 wt.% Co. Here, cobalt occurs unrelated to As with low concentrations of all trace elements (< 260 ppm). Chalcopyrite composition is relatively homogenous with low amounts of impurities (< 0.2 wt.%) independent of the sulfide type and deposit. However, mineral chemical complexity is introduced by the presence of minerals of the bornite-digenite solid solution series varying in Cu content between 57.7 wt.% and 77.4 wt.% and elevated Bi content up to 880 ppm for $bornite_{ss}$. Generally, the Cu-rich phases are poor in trace elements (< 0.2 wt.%).

5 Implications for potential by-products

5.1 Cobalt (Co)

Cobalt is an important element for the energy transition commonly used in batteries for electric vehicles and regarded a critical element by the European Union (e.g., Blengini et al. 2020).

Cobalt in the studied IOA deposits occurs either in iron oxides or in sulfide minerals, mainly pyrite. The content in Fe oxides, however, is negligible in PG and KV, with mineral chemistry of different Fe oxide types showing < 200 ppm Co (Krolop 2022).

Cobalt is enriched in pyrite from PG (types PG2 and PG4) with concentrations up to 10.2 wt.%. This is higher than Co concentrations in pyrite from KV (up to 2.3 wt.% Co) and other IOA deposits containing up to 3.9 wt.% Co (Reich et al. 2016, Liu et al. 2020). Cobalt in PG and KV does, however, show positive correlation with As in some types (Figure 1). Arsenic is regarded a deleterious element in pyrite (e.g., Anawar et al. 2006, Mileusnić et al. 2014).

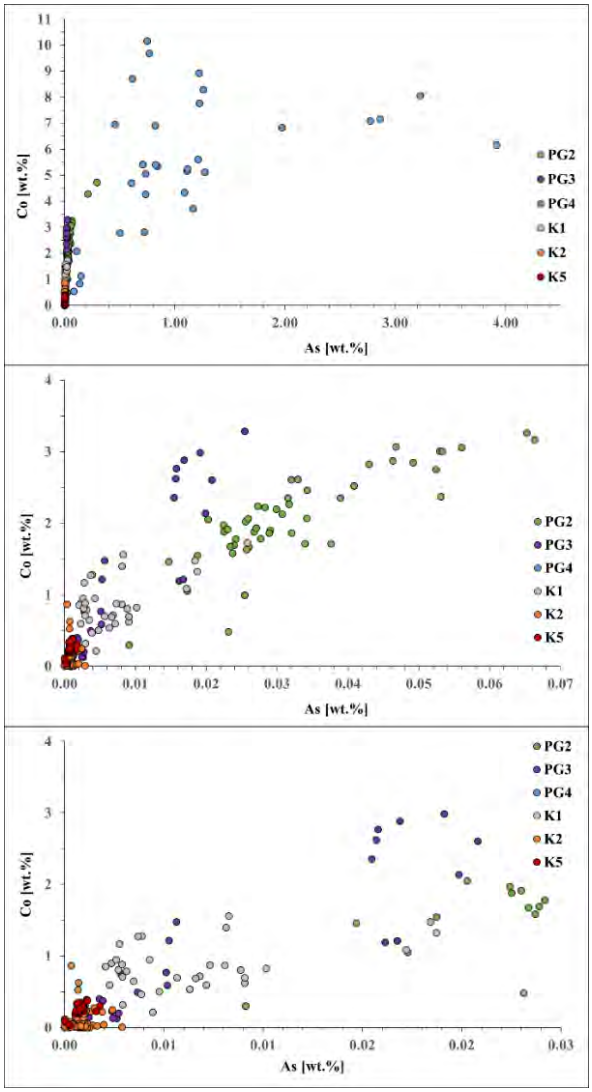

Figure 1. Cobalt vs As plot of sulfide types in the Kiirunavaara and Per Geijer deposits. Note that the x-axis has been adjusted in the lower two plots to illustrate variation at lower As concentration. Data derived by LA-ICP-MS.

Production of Co from sulfide ores is dependent on the parent sulfide mineral. Commonly, cobalt is extracted as a by-product in magmatic Ni-Cu-PGE deposits, therein mainly hosted in pentlandite. According to Moa and Davenport (2014), the process includes: 1) concentration by flotation, 2) concentrate is then smelted in a flash smelter or roasted and then smelted in an electric furnace, 3) the resulting matte treated either hydrometallurgically or pyrometallurgically to produce high-purity nickel and cobalt.

So far, pyrite-hosted Co is only being extracted from the Broken Hill deposit in Australia by Cobalt Blue. The method includes: 1) concentration of pyrite by gravity and flotation operations, 2) thermal treatment producing artificial pyrrhotite (calcine) and elemental sulfur, 3) leaching and further processing for sulfur recovery by remelting, 4) minor metals (Fe, Cu, Zn, Mn) removed by precipitation, ion exchange, and solvent extraction, resulting in final cobalt-hydroxide, which is further refined for production of high purity cobalt sulfate heptahydrate (Washbourne 2018).

However, to date this method has not been utilised by a mine in Europe. The deposit types at LKAB are different to those being processed using this method in Australia. Therefore, detailed characterisation of the Co-bearing sulfides in LKAB's deposits is needed, including the influence of As, before this process can be applied and commercialized if evaluated as positive by further investigation.

5.2 Copper (Cu)

The copper content in drill core assay data from KV seems to be lower than those reported for PG. The higher concentration of Cu in the in-situ ore is also reflected in magnetite concentrates achieved by process mineralogical test work, being elevated in PG compared to KV (Krolop et al. 2022). The relevant source for copper is in Cu-bearing sulfides, e.g., chalcopyrite and minerals of the bornite-digenite solid solution series (Figure 2).

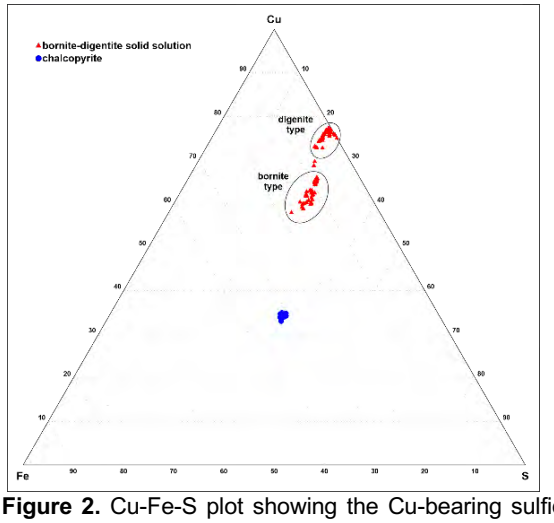

Figure 2. Cu-Fe-S plot showing the Cu-bearing sulfides based on EPMA-derived composition.

Other minerals that incorporate Cu as a trace element, e.g., magnetite, hematite, pyrite etc. can be neglected based on insignificant concentrations (< 100 ppm; Krolop 2022)

Chalcopyrite can function as a scavenger for other elements that may be regarded as economically relevant, such as Ag (Ayres et al. 2013). Furthermore, Cu-mineral concentrates can become enriched during processing in elements including As, Sb, Hg, Bi and Se. The concentration of those elements is regarded crucial in terms of financial penalties applicable when sold as a by-product on the world market (Fountain 2013). However, on the positive side the deleterious elements in the investigated chalcopyrite grains are entirely below the reported concentrate limits, being As < 0.2 wt.%, Sb = 0.05 wt.%, Bi = 0.02 wt.%, Cd = 0.03 wt.%, Hg = 0.0005 wt.%, Ni+Co = 0.5 wt.%, and Zn = 3 wt.% following Salomon-de-Friedberg and Robinson (2014).

5.3 Sulfuric acids

Sulfuric acid is predominantly used in the production of phosphate fertilizers, chemical (e.g., detergents, resins, coatings, water treatment) or other industrial applications, such as manufacture of explosives or automobile batteries. Since sulfuric acid is planned for use in recovering phosphorus (and REE) as side products from apatite during iron ore mining, this is also of importance for LKAB. Sulfuric acid is commonly produced from pyrite. Pyrite is the most common sulfide in both studied deposits, KV and PG, based on its relative abundance (Andersson et al. 2022). Nevertheless, pyrite can also host a range of elements that are deleterious from a processing and/or environmental perspective. The latter is predominantly influenced by Hg, Tl, and As (Deditius and Reich 2016, George et al. 2019) having ramifications for environmental management at mine sites, especially waste piles and tailings treatment.

Pyrite has been characterised in different textural and mineral chemical composition in the IOA deposits (see chapter 4). Notably, the contents of Hg and Tl are generally below detection limit and can be regarded as negligible for processing and environmental aspects. Arsenic, however, occurs in significant concentration in the weight percentage range in pyrite of some sulfide types, as shown in Figure 1. However, As has been shown to be treatable from copper concentrates by recovering the metal value (Salomon-de-Friedberg et al. 2014).

Recently, the two Swedish mining companies LKAB and Boliden agreed to investigate the possibility of extracting pyrite concentrate from mining waste at Boliden's Aitik mine. Subsequently, LKAB will process the concentrate into fossil-free sulfuric acid, to be further used in processes for extracting rare earth elements and phosphorus from LKAB's mining waste. However, it can be expected that the volumes of pyrite concentrate from Aitik are unlikely to cover the full amount of what LKAB requires in the future. To produce the predicted

volume of sulfuric acid needed to process the high modal abundance of phosphates in the Per Geijer deposits (8 times as much as the currently operated mines), additional pyrite concentrate is needed that could originate from LKAB's mine waste. However, the full potential is under investigation.

In addition, if pyrite could be added from LKAB's own deposits to the supplied waste stream from the Aitik mine, this will reduce the cost and environmental impact of this processing method as it would remove the need to import sulfuric acid to cover the shortfall for this process left by the current arrangement. This will continue the move towards a circular business model and will allow the production of these critical and strategic metals in Europe from mine waste, while also reducing the amount of waste from the mines.

6 Conclusions

The economic potential of pyrite is investigated, as the most abundant sulfide mineral in both the KV and PG deposits, both for producing sulfuric acid and cobalt based on preliminary mineralogical investigation. However, further information, e.g., distribution and quantity in the deposits, contents in current waste and tailing material, possibilities for processing and other economic criteria need to be addressed to evaluate the full potential of sulfides in IOA deposits.

Acknowledgements

The authors acknowledge colleagues at LKAB for support during sample acquisition. Personnel at the sample preparation laboratories are thanked for high quality thin sections and embeddings. We further acknowledge Marcus Oelze for LA-ICP-MS data acquisition and LKAB for approval of publication.

References

Anawar HM, Garcia-Sanchez A, Murciego A, Buyolo T (2006) Exposure and bioavailability of arsenic in contaminated soils from the La Parrilla mine, Spain. Environ Geol 50:170-179. https://doi.org/10.1007/s00254-006-0196-2

Andersson UB, Kalmbach J, Gilbricht S, Seifert T, Karlsson A, Krolop P (2022) Preliminary data on sulphides at Kiruna, Sweden. In 16th SGA Biennial Meeting, Proceedings, Rotorua, New Zealand, Proceedings volume 1, 1 (Vol. 4).

Ayres RU, Ayres LW, Råde I (2013) The life cycle of copper, its co-products and by-products. Eco-efficiency in industry and science, Vol. 13. Kluwer Academic Publishers, Amsterdam

Blengini GA, El Latunussa C, Eynard U, De Matos CT, Wittmer DMAG, Georgitzikis K, Pavel CC, Carrara S, Mancini L, Unguru M, Blagoeva D (2020) Study on the EU's list of critical raw materials. Publications Office of the European Union, Luxembourg

Deditius AP, Reich M (2016) Constraints on the solid solubility of Hg, Tl, and Cd in arsenian pyrite. Am Min, 101(6):1451-1459. https://doi.org/10.2138/am-2016-5603

Fountain C (2013) The whys and wherefores of penalty elements in copper concentrates. MetPlant 2013: Metallurgical Plant Design and Operating Strategies, Australasian Institute of Mining and Metallurgy, Melbourne, Australia

Frietsch R (1979) Petrology of the Kurravaara Area Northeast of Kiruna northern Sweden; Serie C; Sveriges Geol Undersoekg, Uppsala

Geijer P (1910) Igneous rocks and iron ores of Kiirunavaara, Luossavaara and Tuollavaara. Econ Geol 5 (8):699–718

Geijer (1931) The iron ores of the Kiruna type. Sveriges Geol Undersoekg, Uppsala

George LL, Biagioni C, Lepore GO, Lacalamita M, Agrosì, G, Capitani GC, Bonaccorsi E and d'Acapito F (2019) The speciation of thallium in (Tl, Sb, As)-rich pyrite. Ore Geol Rev 107:364-380. https://doi.org/10.1016/j.oregeorev.2019.02.031

Kalmbach J (2022) Sulfides in iron oxide-apatite and greenstone-hosted copper deposits in the Kiruna area, northern Sweden – characterization by mineralogy, mineral chemistry and sulfur isotopy. M. Sc. Thesis, TU Bergakademie Freiberg

Krolop P (2022) The Per Geijer iron ore deposits: Characterization based on mineralogical, geochemical and process mineralogical methods. Dissertation, TU Bergakademie Freiberg

Krolop P, Larsson A, Körtge M (2022) Per Geijer Deep geometallurgical tests. LKAB internal report

Liu Y, Fan Y, Zhou T, Wang J, Fu B, Ireland TR, White NC, Zhang L (2020) Geochemical characteristics of pyrite in the Dabaozhuang deposit in the Middle-Lower Yangtze River Metallogenic Belt, Eastern China, Ore Geol Rev 124:103-662. https://doi.org/10.1016/j.oregeorev.2020.103662

Martinsson O (2015) Genesis of the Per Geijer apatite iron ores, Kiruna area, northern Sweden. Proceedings of the SGA Biennal Meeting, 23–27.

Martinsson O, Billström K, Broman C, Weihed P, Wanhainen C (2016) Metallogeny of the northern Norrbotten ore province, northern Fennoscandian Shield with emphasis on IOCG and apatite-iron ore deposits. Ore Geol Rev 78:447-492. https://doi.org/10.1016/j.oregeorev.2016.02.011

Mileusnić M, Mapani BS, Kamona AF, Ružičić S, Mapaure I, Chimwamurombe PM (2014) Assessment of agricultural soil contamination by potentially toxic metals dispersed from improperly disposed tailings, Kombat mine, Namibia. J Geochem Explor 144: 409-420. https://doi.org/10.1016/j.gexplo.2014.01.009

Moats MS, Davenport WG 2014. Nickel and cobalt production. In Seetharaman S (ed) Treatise on process metallurgy, 3rd edn. Elsevier, Amsterdam, pp 625-669

Nordstrand J, Andersson UB (2013) Mineral chemistry of gangue minerals of the Kiirunavaara iron ore, evidence for a transition from magmatic to hydrothermal conditions. 12th SGA Biennial Meeting, Proceedings, Geological Survey of Sweden, 1663, 1666.

Reich M, Simon AC, Deditus A, Barra F, Chryssoulis S, Lagas G, Tardani D, Knipping J, Bilenker L, Sanchez-Alfaro P, Roberts MP, Munizaga R (2016) Trace element signature of pyrite from the Los Colorados iron oxide-apatite (IOA) deposit, Chile: a missing link between Andean IOA and iron oxide copper-gold systems? Econ Geol 111 (3):743-761. https://doi.org/10.2113/econgeo.111.3.743

Salomon-De-Friedberg H, Robinson T, Lossin A, Omaynikova V (2014) Developing copper arsenic resources with CESL technology. In Proceedings of the COM 2014, 53rd Annual Conference of Metallurgists, Vancouver

Parak T (1975) Kiruna iron ores are not" intrusive-magmatic ores of the Kiruna type". Econ Geol 70(7):1242-1258. https://doi.org/10.2113/gsecongeo.70.7.1242

Washbourne M (2018) Cracking the cobalt code. Australia's Paydirt, 1(258):86

Geochemical trends of lithium-bearing minerals in LCT-pegmatites in Central Namibia

Nico Kropp[1, 2], Gregor Borg[1,2]
[1]Martin Luther University Halle-Wittenberg, Institute for Geoscience and Geography, Economic Geology and Petrology Research Unit, Von-Seckendorff-Platz 3, 06120 Halle (Saale)
[2]ITEL- Institute for Technologies and Economics of Lithium - Deutsches Lithiuminstitut GmbH, Leipziger Str. 70, 06108 Halle (Saale)

Abstract. In the central area of Namibia, between the Erongo, Swakopmund, and the Brandberg, five separate pegmatite belts run in a southwest-northeast direction, which have been previously explored primarily for tin ("tin belts") and uranium ("Rössing belt") and have also been commercially mined from various deposits. Since the demand for lithium has increased drastically worldwide, lithium minerals, which are especially associated with tin-bearing pegmatites, have also become the new focus of exploration and mining. Besides spodumene-bearing pegmatites, petalite and lepidolite-bearing pegmatites are also attracting the interest of industry and researchers.
For a feasibility study on lithium fingerprinting, as proof of origin of mineral sources of lithium, three pegmatite provinces in Namibia were sampled and are now being investigated for their distinguishability using geochemical analyses. The investigations cover the mineralogy, the isotopic signature, and the trace element composition of different lithium minerals (spodumene, petalite and lepidolite) from several deposits.

1 Introduction

In the past, intensive exploration and mining for tin in cassiterite-bearing pegmatites was the most common exploration target in Central Namibia because of several pegmatite swarms in this region. Nowadays, these pegmatites are of interest since they contain lithium-bearing minerals such as spodumene, petalite, and lepidolite.

Lithium-Caesium-Tantalum pegmatites (LCT) are the most important hard rock source of lithium, which is a key element for the green energy transition and is needed as an accumulator material in the electronic vehicles industry and for energy storage in general.

Transparency and regulations for the traceability of products and raw materials need a database, which verifies the origin of raw materials by the natural properties or with artificially added tracers. To decide, which methods will be used in the future, case studies are necessary, which generate data of the different lithium deposits and compare data sets to use them as a database for a possible lithium fingerprint as proof of origin. The idea of fingerprinting mineral raw materials is not new and has already been applied for columbite-tantalite minerals (Melcher et al. 2008), gold (Schlosser et al. 2009), and ancient building material such as marble (Antonelli and Lazzarini 2015). In the field of lithium minerals, there have only been a few studies dealing with primary raw materials so far (Desaulty et al. 2022).

In this study, preliminary data from samples of different deposits in Central Namibia is presented.

2 Geological Setting

The Neoproterozoic Damara Belt in Namibia was formed during the different phases of rifting, spreading, subduction, and continental collision, which resulted in the amalgamation of Gondwana between the Kalahari, Congo, and Rio de la Plata Cratons between 900 and 460 Ma with the formation of two coastal and one inland branching orogenic belts (Borg and Gauert 2018, Ashworth 2020).

The Pre-Damaran Abbabis Complex, as basement of the Damara Belt, is overlain by metasedimentary complexes. Granitic intrusions of Pan-African age divide the belt into tectono-stratigraphic units of different metamorphic overprint and igneous activity (Ashworth 2020).

Different pegmatite swarms occur in the central portion, i.e., close to the triple point of the three orogenic branches (Ashworth 2020). According to the mining history of Central Namibia, these swarms are called Northern Tin Belt, Central Tin Belt (CTB), Southern Tin Belt, Karibib Pegmatite Belt (KPB), and Rössing Pegmatite Belt (Fig. 1).

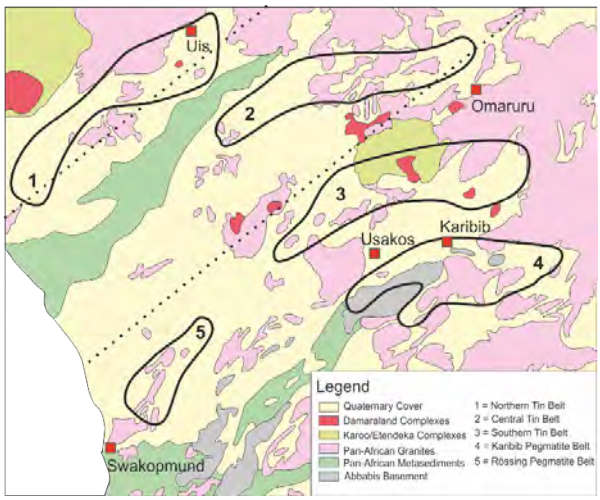

Figure 1. The regional geology of Central Namibia with five pegmatite belts, showing a similar orientation (modified after Ashworth 2014).

The Northern Tin Belt is a northeast-trending zone between the Brandberg and Cape Cross with different pegmatite swarms (Uis, Karlowa, and Strathmore swarms) intruded in Damara meta-

sediments (Diehl 1986). The pegmatites are commonly unzoned and intrude as sigmoidal structures into biotite-schists.

Pegmatites of the Central Tin Belt intruded into mica schists of the Kuiseb Formation and show minor textural internal zonation.

The Karibib Pegmatite Belt, as the southernmost pegmatite belt in this area, is host to the Rubicon and Helikon pegmatites. The Rubicon pegmatites show an internal zonation with separate zones of petalite and lepidolite-rich units and are enclosed in granodioritic host rocks. In contrast, the Helikon pegmatites are similar in orientation but intruded into marbles (Ashworth 2020).

3 Material and Methods

3.1 Samples and Sample Preparation

Sample material from three different pegmatite belts was analysed: Four Lepidolite samples and one petalite sample from two deposits in the Karibib Pegmatite Belt, two spodumene samples and four petalite samples from the Northern Tin Belt, as well as one lepidolite sample from the Central Tin Belt.

Thin sections were used to determine the mineral paragenesis by polarisation microscopy.

3.2 SEM-EDX and Electron Microprobe

For the mineralogical investigation of the sample material, thin sections were characterised using scanning electron microscopy-assisted energy dispersive spectroscopy (EDX) at the Martin Luther University Halle-Wittenberg. A SEM JSM 6300 149 (JEOL, Akishima - Tokyo, Japan) was used for this purpose. The excitation voltage was 20 kV and an XFlash 5010 EDX detector with a resolution of 123 eV and a working distance of 25 mm was used.

For further mineral chemistry, trace elements were measured using wavelength dispersive spectroscopy (WDX) on a JEOL JXA-8230 equipped with WDX-spectrometers at Friedrich Schiller University Jena. For the measurements at 15 kV and 15 nA with a measurement time of 20s for point measurements, standards were used for the following elements (as oxides): bismuth (Mα, Bi-100, DL 0.09 mass%), caesium (Lα, Cs glass, DL 0.09 mass%), iron (Kα, Fe_2O_3, DL 0.05 mass%), manganese (Kα, Rhodonite, DL 0.05 mass%), sodium (Kα, Albite, DL 0.04 mass%), niobium (Lα, Nb-100, DL 0.13 mass%), rubidium (Lα, Rb glass, DL 0.12 mass%), zinc (Kα, ZnS, DL 0.09 mass%).

4 Results

The petalite samples from the Northern Tin Belt are fresh and show only minor occurrences of clay minerals along some fissures. Different colour variations are visible, from slightly orange to salmon-coloured and greenish to white. Only small inclusions of cassiterite and minerals from the columbite-tantalite series occur. The petalites contain only minor concentrations of trace elements like rubidium (0.14 mass%), niobium (0.08 mass%), bismuth (0.11 mass%), and zinc (0.089 mass%), which seems to occur randomly. The spodumene from the Karlowa pegmatite swarm can reach large crystal sizes of about 1 metre. The analysed hard rocks contain only spodumene with minor inclusions of cassiterite, sphalerite, and apatite. The WDX data indicate minor concentrations of sodium (0.12 mass%), niobium (0.08 mass%), and bismuth (0.11 mass%). Spodumene from the DeRust pegmatite swarm shows similar niobium concentrations (0.09 mass%), but higher rubidium concentrations (0.16 mass%). In general, the concentrations of trace elements detectable with the electron microprobe are low for both, spodumene and petalite.

Lepidolite from the Central Tin Belt is only found in minor amounts closely associated with feldspar and quartz in small artisanal pits. The lepidolites are intergrown with feldspar, quartz, topaz, apatite, and minor cassiterite. The mineral chemistry of the pinkish mica shows low contents of rubidium (0.45 mass%), manganese (0.19 mass%), and caesium (0.31 mass%, Fig. 2) and concentrations for iron are below the detection limit.

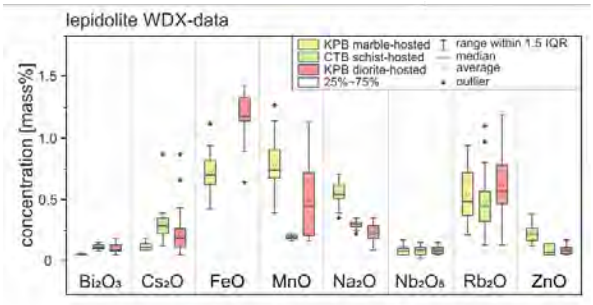

Figure 2. Comparison of selected trace elements in lepidolite from Karibib Pegmatite Belt (KPB) and Central Tin Belt (CTB), showing minor variations for bismuth, niobium, and zinc, whereas the variation is bigger for iron, manganese, and sodium.

The pegmatites in the Karibib area contain mainly petalite and lepidolite as Li-minerals. The lepidolites from diorite-hosted pegmatites show different colour variations, typically pinkish and greyish mica. The trace element composition shows a difference in rubidium between those two types of samples (pinkish lepidolite with 0.64 mass%, greyish lepidolite with 0.72 mass%), caesium (pinkish lepidolite with 0.15 mass%, greyish lepidolite with 0.32 mass%) and manganese (pinkish lepidolite with 0.46 mass%, greyish lepidolite with 0.82 mass%) concentrations (Fig. 3).

This indicates a wider range for trace element variance in this deposit, compared to lepidolite-bearing pegmatites without colour variations. Additionally, lepidolite from the marble-hosted pegmatites shows also colour variations from pinkish to light greyish. The microprobe data revealed minor zinc concentrations (0.22 mass%), which are higher, than in the other analysed lepidolite samples.

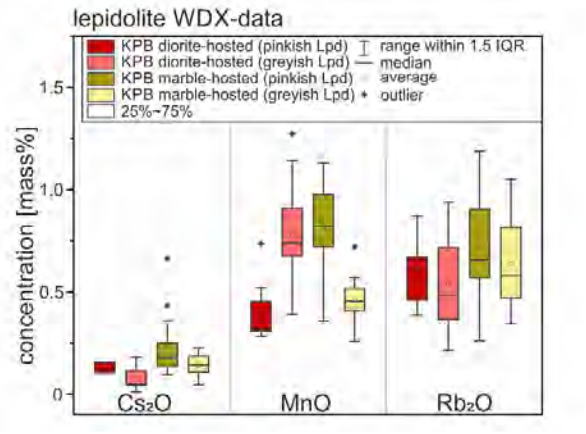

Figure 3. WDX-data of different coloured lepidolite from diorite-hosted pegmatite (n=40) and marble-hosted (n=29) from the Karibib Pegmatite Belt (KPB) shows different concentrations of caesium, manganese, and rubidium where only caesium behaves the same in both deposits.

5 Discussion and Conclusions

Although the petalite samples are of different colours, they are not distinguishable by microprobe analyses alone. If the colour changes are due to the incorporation of trace elements, their concentrations seem to be below the detection limit of microprobe analyses, which can only be investigated by other methods.

The different concentrations of sodium and manganese in the lepidolite from the Central Tin Belt and the Karibib Pegmatite Belt suggest three clusters (Fig. 4). Both elements are common in lepidolite but are present in different positions inside the crystal lattice. In complement with other methods, the trace element composition can be used as a parameter for the differentiation of pegmatite provinces. As already shown by Roda et al. 2007, mica minerals in the Karibib Pegmatite Belt can be chemically differentiated by their location within the pegmatite zonation but are similar on a regional scale.

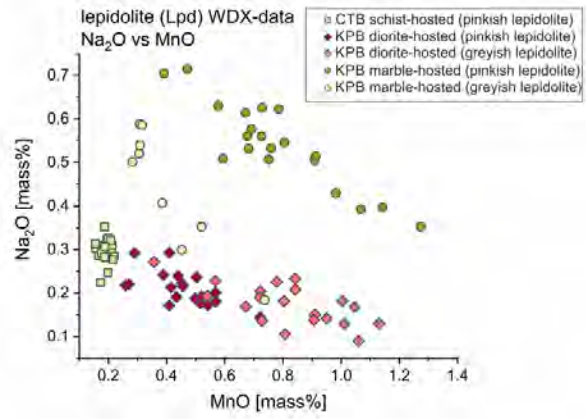

Figure 4. WDX-data of lepidolite from the Central Tin Belt (n=20) and Karibib Pegmatite Belt (n=69) shows different concentrations of manganese and sodium, resulting in three distinguishable clusters probably reflecting the three different host rocks.

Due to the different trace element contents of lithium-rich minerals (spodumene, petalite and lepidolite) in the various pegmatite belts in central Namibia, it is possible to distinguish these based on their geochemical signature.

The different geochemical signatures are probably due to the different genesis of the pegmatites and their zonation, their different metamorphic and deformational history, and the different host rocks.

In order to be able to make reliable statements about the distinguishability also across different sections of pegmatitic lithium deposits, narrower sampling patterns are necessary. However, based on our preliminary data, it is indicated that the pegmatite provinces can be distinguished from each other with the help of the mineral chemistry of the lithium minerals. For the differentiation between individual pegmatite bodies, further analyses are also necessary, including additional methods and parameters, such as the investigation of trace elements by LA-ICP-MS and the behaviour of the lithium isotopes, which are currently carried out.

Acknowledgements

The authors are grateful to Stefan Kiefer for the supply of microprobe analyses at the Friedrich Schiller University Jena. Andreas Kamradt (MLU Halle) and Michael Schmidt (DERA) are gratefully acknowledged for their support during fieldwork and many fruitful discussions.

References

Antonelli F, Lazzarini L (2015) An updated petrographic and isotopic reference database for white marbles used in antiquity. Rend Fis Acc Lincei 26:399–413

Ashworth L (2014) Mineralised Pegmatites of the Damara Belt, Namibia: Fluid inclusion a geochemical characteristic with implications for post collisional mineralisation. Dissertation, University of Witwatersrand. Faculty of Science

Ashworth L, Kinnaird JA, Nex PAM, Harris C, Müller AB (2020) Origin of rare-element-mineralized Damara Belt pegmatites: A geochemical and light stable isotope study. Lithos 372-373(2020):105655

Borg G, Gauert C (2018) The African Metallotects of Southwest Gondwana. In: Siegesmund S, Basei MAS, Oyhantçabal P, Oriolo S (eds) Geology of Southwest Gondwana. Springer International Publishing (Regional Geology Reviews) 615–676

Desaulty AM, Climent MC, Lefebvre G, Cristiano-Tassi A, Peralta D, Perret S (2022) Tracing the origin of lithium in Li-ion batteries using lithium isotopes. Nature communications 13:4172

Diehl M (1986) Preliminary report on the Cape Cross-Uis pegmatite field. Communs geol Surv S W Africa/Namibia 2:37–42

Melcher F, Graupner T, Henjes-Kuns, F, Oberthür T, Sitnikova, M, Gäbler E (2008) Analyitical Fingerprint of Columbite-Tantalite (Coltan) Mineralisation in Pegmatites - Focus on Africa. Ninth International Congress for Applied Mineralogy 2008:615–624

Roda E, Keller P, Pesquera A, Fontan F (2007) Micas of the muscovite–lepidolite series from Karibib pegmatites, Namibia. Mineralogical Magazine 71(1):41-62

Schlosser S, Kovacs R, Pernicka E, Günther D, Tellenbach M (2009) Fingerprints in Gold. In: Reindel M, Wagner GA (eds) New Technologies for Archaeology. Berlin, Heidelberg: Springer Berlin Heidelberg (Natural Science in Archaeology) 409–436

Can the mining industry meet global demand for critical minerals?

Jeffrey L. Mauk[1], Jonathan A. Funk[1], Nicholas A. Karl[1]
[1]U.S. Geological Survey, Denver, Colorado, USA

Abstract. We define U.S. Fortiers as the 5-year average of annual U.S. consumption of a commodity, and global Fortiers as the 5-year average of annual global production of a commodity. Comparison of global Fortiers to previously published mineral deposit size classifications reveals that humankind is consuming approximately one supergiant deposit of Ag, Au, Cu, Pb, and Zn every year. Because increasing environmental, social, and governmental factors make it more difficult to open new mines and expand existing mines, and because new discoveries are increasingly coming from deeper deposits, the mining industry may struggle to meet future needs. We infer that some critical minerals—Bi, Mo, PGE, Sb, Re, REE, Sn, and Te—might have current production rates that are equivalent to the endowment of one of the largest 1-10% of all deposits for each commodity. We conclude that detailed, fit-for-purpose data are required to rigorously evaluate evolving supply risk.

1 Introduction

There is no single unified definition of "critical mineral", but most definitions share common attributes that can be summarized as: a critical mineral is an element or commodity that is essential for modern technologies, economies, or national security, and has a supply chain that is vulnerable to disruption. Many of these critical minerals are essential for 21st century applications such as green energy and technology, so their supply has become an increasing cause for concern for governments and industry.

Mineral deposits can be ranked by size, and classified as large, giant, or supergiant (e.g., Singer 1995; Laznicka 2014). However, despite the increasing visibility of critical minerals, there does not appear to be a definition of whether a critical mineral deposit can play a leading role in addressing humankind's needs for critical minerals. We refer to these as *significant deposits*.

We provide a brief overview of some attempts to quantify giant deposits for base and precious metals to help inform establishing thresholds for significant deposits of critical minerals. We then propose a method that can be applied to determine significant deposits of critical minerals, we provide threshold values for the majority of commodities that are considered critical minerals in the United States, and then we discuss how applying this method sheds some light on the question of whether the global mining industry can meet growing demand for critical minerals.

2 Deposit size and societal significance

2.1 Deposit size

Ranking of mineral deposits by size has mostly used two approaches. One approach is to use the average crustal concentration of each element (Clarke values) to calculate the tonnage of each element in large, giant, and supergiant deposits (Laznicka 2014). For example, Ni has a Clarke value of 5.5×10^1 ppm, and the threshold values for contained metric tons of Ni in different deposit sizes are (I) large: 5.5×10^5; (II) giant: 5.5×10^6; and (III) supergiant 5.5×10^7 (Table 1). The principal benefits of this system are its near-universal applicability and simplicity. Complexities such as political, economic, technical, and geological factors that determine "ore" are not embedded in this classification scheme. Because Clarke values are relatively well-known, mineral deposit size classifications can be calculated for any element, though calculations for actual minerals that are considered critical—such as barite, fluorspar, graphite, and potash—cannot be directly determined.

Another common approach to evaluating deposit size is statistical treatment based on cumulative frequency graphs, with the largest 10% of deposits classified as giant, and the largest 1% of deposits classified as supergiant (Table 1; Singer 1995). By plotting data from actual deposits, this technique assimilates considerations of what determines ore, such as those factors mentioned above. However, the technique requires enough deposits for each commodity to be statistically rigorous, so commodities that are produced from only a few deposits might not yield meaningful results. Conversely, the technique is based on compiling historical records, so some datasets may contain deposits that would not meet current criteria to be classified as orebodies. Furthermore, to our knowledge, byproduct commodities have not been classified by this methodology, perhaps because the economic viability of the deposit depends on factors for the primary commodity, and perhaps because in many cases byproduct production is not reported.

2.2 Societal significance

The transition of the global energy system to clean energy is bringing about unprecedented increases in demand for battery and energy commodities such as Cu, Li, Ni, Co, and REEs (International Energy Agency 2021). There are two main ways to evaluate demand, and both provide valuable insights. On the one hand, forecasting based on assumptions of

future targets and needs can identify possible future demands. For example, the International Energy Agency (2021) projects that to meet the Paris Agreement's climate stabilisation at "well below 2°C global temperature rise", would mean quadrupling mineral requirements for clean energy technologies by 2040.

On the other hand, the winds of change can be fickle, and it is possible to extrapolate demand from current consumption and production. Both approaches are complimentary, but we use the latter to define significant deposits of critical minerals. Herein, we refer to the 5-year average of annual U.S. consumption of a commodity as one U.S. Fortier (Table 1). Loosely translated from the French, a fortier is a fortress, and deposits with endowments of one Fortier or more may help to fortify humankind by helping to meet the need for critical minerals and other commodities.

Metal	Clarke ppm	U.S. Fortier	Global Fortier	Large Deposits			Giant deposits			Supergiant deposits		
		consumption	*production*	Low	Mid	High	Low	Mid	High	Low	Mid	High
Al	8.0×10^{4}	4.7×10^{5}	6.4×10^{7}	8.0×10^{8}	3.2×10^{9}	5.6×10^{9}	8.0×10^{9}	3.2×10^{10}	5.6×10^{10}	8.0×10^{10}	3.2×10^{11}	5.6×10^{11}
Mg	2.2×10^{4}	5.6×10^{4}	1.0×10^{6}	2.2×10^{8}	8.8×10^{8}	1.5×10^{9}	2.2×10^{9}	8.8×10^{9}	1.5×10^{10}	2.2×10^{10}	8.8×10^{10}	1.5×10^{11}
Ti	4.0×10^{3}	1.2×10^{5}	8.1×10^{6}	4.0×10^{7}	1.6×10^{8}	2.8×10^{8}	4.0×10^{8}	1.6×10^{9}	2.8×10^{9}	4.0×10^{9}	1.6×10^{10}	2.8×10^{10}
Mn	7.2×10^{2}	7.1×10^{5}	1.9×10^{7}	7.2×10^{6}	2.9×10^{7}	5.0×10^{7}	7.2×10^{7}	2.9×10^{8}	5.0×10^{8}	7.2×10^{8}	2.9×10^{9}	5.0×10^{9}
Sr	3.3×10^{2}	7.5×10^{3}	2.8×10^{5}	3.3×10^{6}	1.3×10^{7}	2.3×10^{7}	3.3×10^{7}	1.3×10^{8}	2.3×10^{8}	3.3×10^{8}	1.3×10^{9}	3.3×10^{9}
Zr	2.0×10^{2}	4.0×10^{4}	1.4×10^{6}	2.0×10^{6}	8.0×10^{6}	1.4×10^{7}	2.0×10^{7}	8.0×10^{7}	1.4×10^{8}	2.0×10^{8}	8.0×10^{8}	1.4×10^{9}
REE	1.5×10^{2}	8.3×10^{3}	2.1×10^{5}	1.5×10^{6}	6.0×10^{6}	1.1×10^{7}	1.5×10^{7}	6.0×10^{7}	1.1×10^{8}	1.5×10^{8}	6.0×10^{8}	1.1×10^{9}
V	1.0×10^{2}	9.7×10^{4}	8.8×10^{4}	1.0×10^{6}	4.0×10^{6}	7.0×10^{6}	1.0×10^{7}	4.0×10^{7}	7.0×10^{7}	1.0×10^{8}	4.0×10^{8}	7.0×10^{8}
Zn	6.5×10^{1}	8.8×10^{5}	1.2×10^{7}	6.5×10^{5}	2.6×10^{6}	4.6×10^{6}	6.5×10^{6}	2.6×10^{7}	4.6×10^{7}	6.5×10^{7}	2.6×10^{8}	4.6×10^{8}
Ni	5.5×10^{1}	2.3×10^{5}	2.5×10^{6}	5.5×10^{5}	2.2×10^{6}	3.9×10^{6}	5.5×10^{6}	2.2×10^{7}	3.9×10^{7}	5.5×10^{7}	2.2×10^{8}	3.9×10^{8}
Cu	2.5×10^{1}	1.8×10^{6}	2.0×10^{7}	2.5×10^{5}	1.0×10^{6}	1.8×10^{6}	2.5×10^{6}	1.0×10^{7}	1.8×10^{7}	2.5×10^{7}	1.0×10^{8}	1.8×10^{8}
Co	2.4×10^{1}	8.8×10^{4}	1.4×10^{6}	2.4×10^{5}	9.6×10^{5}	1.7×10^{6}	2.4×10^{6}	9.6×10^{6}	1.7×10^{7}	2.4×10^{7}	9.6×10^{7}	1.7×10^{8}
Nb	1.9×10^{1}	8.2×10^{3}	7.8×10^{4}	1.9×10^{5}	7.6×10^{5}	1.3×10^{6}	1.9×10^{6}	7.6×10^{6}	1.3×10^{7}	1.9×10^{7}	7.6×10^{7}	1.3×10^{8}
Li	1.8×10^{1}	2.0×10^{3}	8.8×10^{4}	1.8×10^{5}	7.2×10^{5}	1.3×10^{6}	1.8×10^{6}	7.2×10^{6}	1.3×10^{7}	1.8×10^{7}	7.2×10^{7}	1.3×10^{8}
Ga	1.5×10^{1}	1.6×10^{4}	3.7×10^{5}	1.5×10^{5}	6.0×10^{5}	1.1×10^{6}	1.5×10^{6}	6.0×10^{6}	1.1×10^{7}	1.5×10^{7}	6.0×10^{7}	1.1×10^{8}
Pb	1.5×10^{1}	1.6×10^{5}	4.6×10^{6}	1.5×10^{5}	6.0×10^{5}	1.1×10^{6}	1.5×10^{6}	6.0×10^{6}	1.1×10^{7}	1.5×10^{7}	6.0×10^{7}	1.1×10^{8}
Be	2.4×10^{0}	1.9×10^{3}	2.4×10^{5}	2.4×10^{4}	9.6×10^{4}	1.7×10^{5}	2.4×10^{5}	9.6×10^{5}	1.7×10^{6}	2.4×10^{6}	9.6×10^{6}	1.7×10^{7}
Sn	2.3×10^{0}	4.3×10^{4}	3.0×10^{5}	4.3×10^{4}	9.2×10^{4}	1.6×10^{5}	2.3×10^{5}	9.2×10^{5}	1.6×10^{6}	2.3×10^{6}	9.2×10^{6}	1.6×10^{7}
As	1.7×10^{0}	6.9×10^{3}	4.0×10^{4}	1.7×10^{4}	6.8×10^{4}	1.2×10^{5}	1.7×10^{5}	6.8×10^{5}	1.2×10^{6}	1.7×10^{6}	6.8×10^{6}	1.2×10^{7}
Ge	1.4×10^{0}	3.0×10^{1}	1.3×10^{2}	1.4×10^{4}	5.6×10^{4}	9.8×10^{4}	1.4×10^{5}	5.6×10^{5}	9.8×10^{5}	1.4×10^{6}	5.6×10^{6}	9.8×10^{6}
Ta	1.1×10^{0}	8.8×10^{2}	1.9×10^{3}	1.1×10^{4}	4.4×10^{4}	7.7×10^{4}	1.1×10^{5}	4.4×10^{5}	7.7×10^{5}	1.1×10^{6}	4.4×10^{6}	7.7×10^{6}
Mo	1.1×10^{0}	2.0×10^{4}	2.9×10^{5}	1.1×10^{4}	4.4×10^{4}	7.7×10^{4}	1.1×10^{5}	4.4×10^{5}	7.7×10^{5}	1.1×10^{6}	4.4×10^{6}	7.7×10^{6}
W	1.0×10^{0}	N/A	8.2×10^{4}	1.0×10^{4}	4.0×10^{4}	7.0×10^{4}	1.0×10^{5}	4.0×10^{5}	7.0×10^{5}	1.0×10^{6}	4.0×10^{6}	7.0×10^{6}
Sb	3.0×10^{-1}	2.6×10^{4}	1.3×10^{5}	3.0×10^{3}	1.2×10^{4}	2.1×10^{4}	3.0×10^{4}	1.2×10^{5}	2.1×10^{5}	3.0×10^{5}	1.2×10^{6}	2.1×10^{6}
Bi	8.5×10^{-2}	1.7×10^{3}	2.0×10^{4}	8.5×10^{2}	3.4×10^{3}	6.0×10^{3}	8.5×10^{3}	3.4×10^{4}	6.0×10^{4}	8.5×10^{4}	3.4×10^{5}	6.0×10^{5}
Ag	7.0×10^{-2}	6.9×10^{2}	2.6×10^{4}	7.0×10^{2}	2.8×10^{3}	4.9×10^{3}	7.0×10^{3}	2.8×10^{4}	4.9×10^{4}	7.0×10^{4}	2.8×10^{5}	4.9×10^{5}
In	5.0×10^{-2}	1.2×10^{2}	8.6×10^{2}	5.0×10^{2}	2.0×10^{3}	3.5×10^{3}	5.0×10^{3}	2.0×10^{4}	3.5×10^{4}	5.0×10^{4}	2.0×10^{5}	3.5×10^{5}
PGE	1.3×10^{-3}	1.4×10^{2}	4.1×10^{2}	1.3×10^{1}	5.2×10^{1}	9.1×10^{1}	1.3×10^{2}	5.2×10^{2}	9.1×10^{2}	1.3×10^{3}	5.2×10^{3}	9.1×10^{3}
Te	5.0×10^{-3}	N/A	5.2×10^{2}	5.0×10^{1}	2.0×10^{2}	3.5×10^{2}	5.0×10^{2}	2.0×10^{3}	3.5×10^{3}	5.0×10^{3}	2.0×10^{4}	3.5×10^{4}
Au	2.5×10^{-3}	1.8×10^{2}	3.2×10^{3}	2.5×10^{1}	1.0×10^{2}	1.8×10^{2}	2.5×10^{2}	1.0×10^{3}	1.8×10^{3}	2.5×10^{3}	1.0×10^{4}	1.8×10^{4}
Re	4.0×10^{-4}	4.2×10^{1}	5.4×10^{1}	4.0×10^{0}	1.6×10^{1}	2.8×10^{1}	4.0×10^{1}	1.6×10^{2}	2.8×10^{2}	4.0×10^{2}	1.6×10^{3}	2.8×10^{3}

Table 1. Crustal abundances (Clarkes in ppm), thresholds and ranges of "large", "giant" and "supergiant" accumulations of elements (in metric tons). Modified from Laznicka (2014), with values for Mg, Sr, Rb, and Hf calculated from crustal abundance values in Wedepohl (1995). We have removed Cr, Cs, Hf, Rb, Sc, U, and Y because available data do not allow calculation of global Fortier values. Heavy black outlines show giant deposits, and heavy red outlines show supergiant deposits of Singer (1995). Blue cells show one U.S. Fortier, yellow cells show one global Fortier, and for Re, U.S. and global Fortier values are similar, so the cell is green.

We do not know of any global commodity consumption data that are updated annually, but U.S. Geological Survey (USGS) Mineral Commodity Summary reports provide global production values (e.g., U.S. Geological Survey 2022), so we define a global Fortier as the 5-year average of annual global production of a commodity (Table 1). In this case, we assume that global production is approximately equal to global consumption. We recognize that there are flaws in this assumption, and weaknesses in the underlying data, but this currently appears to be the best metric to capture global need through time.

3 Discussion

3.1 Comparison of size-based classifications

As described above, the crustal concentration method of determining large, giant, and supergiant deposits, and the statistical method of determining giant and supergiant deposits both have merits (Singer 1995; Laznicka 2014). Table 1 presents the Laznicka (2014) endowments of large, giant, and supergiant deposits for commodities that are on the 2022 final list of critical minerals for the United States. (Applegate 2022), or recently were on that list (Petty 2018), plus Ag, Au, Cu, and Pb. Each size category is subdivided into three bins of equal size that are designated "Low", "Mid", and "High".

Superimposed on Table 1, we show the threshold values for giant deposits (the largest 10% of known deposits) of Ag, Au, Cu, Pb, and Zn as defined by Singer (1995), and we also show threshold values for his supergiant deposits (the largest 1% of known deposits). This comparison shows that all "giant"

deposits from Singer (1995) fall within the "large" deposits of Laznicka (2014). Furthermore, most of the "supergiant" deposits of Singer (1995) have threshold values that fall within the range of "giant" deposits of Laznicka (2014); only for Cu is there consensus about what constitutes a supergiant deposit.

On the one hand, this comparison demonstrates that confusion about what constitutes large, giant, and supergiant deposits is fully justified. On the other hand, this graphically demonstrates that the two approaches produce different results. For Ag, Au, and Zn, the giant and supergiant deposits of Singer (1995) vary in size by one order of magnitude, but for Pb the variation is less than one order of magnitude, and for Cu it is more than one order of magnitude. Geological, technical, economical, environmental, social, and governmental factors are significant controls on which mineral deposits will be mined, which then controls the statistical classification of deposits.

3.2 Comparison of U.S. and global Fortier values

Global Fortier values range from 1.3 (Re) to 44 (Li) times greater than U.S. Fortier values, with a median value of 11 times for commodities where both values can be determined. The relative change in values reflects the fact that U.S. Fortier values predominantly reflect the needs of the United States for manufacturing and other sectors, and global Fortier values come closer to approximating the total needs of humankind.

3.3 The needs of humankind versus endowment

The highlighted values in Table 1 provide insights into consumption and production of commodities versus deposit size. Overall, 39% and 16% of the commodities with available data have U.S. Fortier values that exceed the threshold values of Laznicka's (2014) large and giant deposits, respectively, and 56%, 38%, and 3% of the commodities have global Fortier values that exceed the threshold values of Laznicka's (2014) large, giant, and supergiant deposits, respectively. Put another way, for more than half of the commodities in Table 1, humankind is consuming the equivalent endowment of at least one large deposit every year. This consumption must be replaced by increased reserves at existing mines, and by adding new mines to the global supply chain.

Much of the conversation about humankind's ability to mine resources in sufficient quantity can be summarized in two ways: (1) increasing demand compared to known resources or reserves indicates future inability to meet demand, or (2) history shows that production rises to meet demand, and there are much larger resources in Earth than are quantified in formal resource and reserve calculations (e.g., Arndt et al. 2017; Schipper et al. 2018; Jowitt et al. 2020, and references therein). We recognize the strength of these approaches and their importance in assessing whether production of Earth resources will continue to meet the needs of humankind.

In addition to these approaches, evaluation of Table 1 suggests another possible approach. Some commodities—Al, Be, Co, Ga, Ge, Li, Mg, Nb, REE, Sr, Ta, Ti, and V—have U.S. and global Fortier values that are less than Laznicka's (2014) threshold values for large deposits. For these commodities, demand from humankind may still be small enough that Earth resources can meet these demands without significant risk. However, the inclusion of REE in this group underscores a limitation of this approach, because REE are not geochemically rare, but economically viable deposits of REE are rare (Van Gosen et al. 2018). Furthermore, some commodities are byproducts, so their availability is controlled by technological and economic factors that differ markedly from the factors that control production of product commodities.

Some commodities have global Fortier values that fall in Laznicka's (2014) range of large deposits. For these commodities—As, In, Mn, Ni, W, and Zr—consideration of the rate of opening of new mines, and the rate of expansion of reserves at existing mines may provide insight into the likelihood of supply shortages. For example, Mudd and Jowitt (2022) concluded that current Ni resources and reserves can meet the current need for several decades, providing that those materials can be mined. In some cases, such as As, the limitations may not be mining, but rather processing or recovery from waste streams, because As is recovered from smelting operations, and many of those operations in the United States and Europe have closed due to environmental concerns. Arsenic-alkali residue is a hazardous waste produced by antimony smelting operations that is increasing in China at the rate of approximately 5,000 metric tons per year (Long et al. 2020), so recovery of As from waste streams in China and elsewhere might supply any future growth in need.

The base and precious metals considered by Singer (1995)—Ag, Au, Cu, Pb, and Zn—have global Fortier values that exceed the endowments of his giant deposits. For Cu and Zn, global Fortier values are slightly less than the metal content of his supergiant deposits; for Pb and Ag, global Fortier values are approximately equal to the metal content of his supergiant deposits; and for Au, the global Fortier value is greater than the metal content of his supergiant deposits (Table 1). In other words, to a first approximation, humankind is currently consuming approximately one supergiant deposit of these commodities every year. By analogy, we infer that other commodities whose global Fortier values lie within Laznicka's (2014) giant deposit range—Bi, Mo, PGE, Sb, Re, REE, Sn, and Te—are also being produced at a rate that is equivalent to the endowment of one of the largest 1-10% of all deposits for each commodity.

Production can come from primary production from existing and new mines, and secondary

production from recycling. In a world where increasing environmental, social, and governmental factors make it more difficult to open new mines and expand existing mines (e.g., Jowitt et al. 2020), and where new discoveries are increasingly coming from deeper deposits (e.g., Arndt et al. 2017), is it reasonable to expect that the mining industry can keep pace with increasing needs for critical minerals? This question is essentially a practical one, but we know of no publicly available 21st century databases that would allow us to quantitatively address this question. Specifically, there is a need for (1) statistical classifications of critical minerals from global producing orebodies into giant and supergiant deposits, (2) commodity-specific grade-tonnage plots from producing deposits worldwide, (3) quantitative data on the time that it takes to go from discovery to production in the 21st century, and (4) the change in failure rate through time (perhaps averaged over 10 or 20 year increments) to achieve production due to environmental, social, and governmental factors.

4 Conclusions

Records of national and global consumption of commodities can be averaged over five years to derive U.S. and global Fortier values. Comparison of Fortier values to size classifications based on the endowment of mineral deposits (Laznicka 2014) might suggest that some critical minerals—Al, Be, Co, Ga, Ge, Li, Mg, Nb, REE, Sr, Ta, Ti, and V—are sufficiently abundant that their deposits can provide reliable supplies for the future. However, this does not take into consideration the distinction between economic mineral deposits and crustal abundance, nor does it consider the complications of byproduct critical minerals. For other commodities whose global Fortier values fall within the range of Laznicka's (2014) large deposits—As, In, Mn, Ni, W, and Zr—consideration of the rate of opening of new mines, and the rate of expansion of reserves at existing mines may provide insight into the likelihood of supply shortages. Global Fortier values for Ag, Au, Cu, Pb, and Zn indicate that humankind is consuming these commodities in quantities that are approximately equivalent to the endowment in supergiant deposits: the largest 1% of deposits for these commodities on Earth (Singer 1995). It is not known whether the global mining industry can keep pace with this demand. By analogy, other critical minerals—Bi, Mo, PGE, Sb, Re, REE, Sn, and Te—might also be difficult for the mining industry to produce at rates that are commensurate with increasing demand. We conclude that this is a cautionary tale, but more fit-for-purpose granular data are needed to critically compare supply and demand.

Acknowledgements

We thank the current and former members of the U.S. Geological Survey's mineral deposit database project (USMIN) for many helpful discussions that have helped develop the ideas presented herein. We thank Eric Anderson and Katharina Pfaff for thoughtful reviews that helped improve this manuscript. Any use of trade, firm, or product names is for descriptive purposes only and does not imply endorsement by the U.S. Government.

References

Applegate JD (2022) 2022 Final list of critical minerals. Federal Register 87:10381-10382.

Arndt NT, Fontboté L, Hedenquist JW, Kesler SE, Thompson JFH, Wood DG (2017) Future global mineral resources. Geochemical Perspectives 6:1-171. doi: 10.7185/geochempersp.6.1.

International Energy Agency (2021) The role of critical minerals in clean energy transitions. https://www.iea.org/reports/the-role-of-critical-minerals-in-clean-energy-transitions. Accessed 22 January 2022

Jowitt SM, Mudd GM, Thompson JFH (2020) Future availability of non-renewable metal resources and the influence of environmental, social, and governance conflicts on metal production. Communications Earth & Environment 1:13. doi: 10.1038/s43247-020-0011-0.

Laznicka P (2014) Giant metallic deposits—A century of progress. Ore Geology Reviews 62:259-314. doi: http://dx.doi.org/10.1016/j.oregeorev.2014.03.002.

Long H, Zheng Y-j, Peng Y-l, He H-b (2020) Recovery of alkali, selenium and arsenic from antimony smelting arsenic-alkali residue. Journal of Cleaner Production 251:119673. doi: https://doi.org/10.1016/j.jclepro.2019.119673.

Mudd GM, Jowitt SM (2022) The new century for nickel resources, reserves, and mining: Reassessing the sustainability of the devil's metal. Economic Geology 117:1961-1983. doi: 10.5382/econgeo.4950.

Petty TR (2018) Final list of critical minerals 2018. Federal Register 83:23295-23296.

Schipper BW, Lin H-C, Meloni MA, Wansleeben K, Heijungs R, van der Voet E (2018) Estimating global copper demand until 2100 with regression and stock dynamics. Resources, Conservation and Recycling 132:28-36. doi: https://doi.org/10.1016/j.resconrec.2018.01.004.

Singer DA (1995) World class base and precious metal deposits; a quantitative analysis. Economic Geology 90:88-104. doi: 10.2113/gsecongeo.90.1.88.

U.S. Geological Survey (2022) Mineral commodity summaries 2022. Reston, VA, pp 202.

Van Gosen BS, Verplanck PL, Seal RR, II, Long KR, Gambogi J (2018) Chapter O. Rare-earth elements In: Schulz KJ, DeYoung JH, Jr., Seal RR, II, Bradley DC (eds) Critical mineral resources of the United States—Economic and environmental geology and prospects for future supply. U.S. Geological Survey Professional Paper 1802, Reston, Virginia, pp O1-O31.

Wedepohl HK (1995) The composition of the continental crust. Geochimica et Cosmochimica Acta 59:1217-1232. doi: https://doi.org/10.1016/0016-7037(95)00038-2.

Exploration of indium in sulfidic mine waste and acid mine drainage environments

Olivia Mejías[1], Laura Jackson[1], Anita Parbhakar-Fox[1]
[1]W.H. Bryan Mining & Geology Research Centre, Sustainable Minerals Institute, The University of Queensland, Australia

Abstract. Indium (In) is a critical metal essential for the transition to a low-carbon economy including its use in solar panels. However, there is a significant knowledge gap regarding cycling of indium in mine waste environments. This study aims to understand the mobility of indium in two different geological mine waste environments as an essential first step toward designing a remining process. Core, waste rock, acid mine drainage (AMD)-impacted waters and sediment samples were collected from Mt Morgan (Au-Cu VHMS) and Baal Gammon (Sn granite-related) historic/abandoned mines and subjected to geochemical and mineralogical investigations. Preliminary results suggest that core and waste rock from Baal Gammon contain above 500 ppm In, with sphalerite the main endowed In-bearing mineral (up to 3,776 ppm In). High concentrations, up to 73 µm/L In, were measured in AMD waters along with fluoride (38 to 120 mg/L). In contrast, waste rock and AMD water samples from Mt Morgan reported a maximum of 3.53 ppm and up to 5 µm/L In (with elevated chloride) respectively. This study found that indium is significantly enriched in the sampled Sn-granite mine waste and that pH and fluoride can potentially control indium mobility in AMD waters.

1 Introduction

It is estimated that over 3 billion tonnes of critical metals will be needed to provide green energy to reduce the temperature increase resulting from global warming (Hund et al. 2020). A combination of growing global demand for critical metals paired with decreasing ore grades, is anticipated to results in higher volumes of mine waste over next decades (Jowitt et al. 2018; Watari et al. 2020). For example, a current study has estimated that the global community will generate 10 billion m^3 of new tailings per annum that will require storage in existing or planned facilities (Franks et al. 2021). Increasing volumes of mine waste increases the associated risks such as the formation of AMD and geotechnical failure events. To date, consequences from disasters associated with poor mine waste management have included 3,000 known deaths, over 4,000 km of waterways damaged, and >275 billion litres of waste spilt into natural environments. Mine waste valorisation offers a new solution to safely managing mine waste, enabling the mineral industry to reduce risk and supplement critical metal production to sustain future societies (Nwaila et al. 2021).

Indium is an essential component of solar panels. However, its current supply is dependent on zinc production (i.e., it is a by-product). Thus, indium has been declared a critical metal in Australia, and in at least six other mining countries. At least 230,000 tonnes of indium will be needed worldwide to ensure 14,000 GW of solar PV by 2050. Thus, demand for indium is projected to increase by 231 % by 2050. Despite the anticipated high demand for indium, there remains a knowledge gap regarding the geochemistry, mineralogy and cycling of indium in mine waste environments.

Economic concentrations of indium mineralisation are found in various types of deposits, including volcanogenic massive sulfide (VHMS), sediment-hosted base-metal, epithermal, skarn, porphyry, and granite-related deposits (Schwarz-Schampera 2014).

In Queensland, indium has been reported in ore and mine waste in granite-related deposits in the Herberton mineral province, NE Queensland (Lottermoser and Ashley 2006; Fox et al. 2016; Parbhakar-Fox 2020). Furthermore, slag from the VHMS Mt Morgan mine site, located in Central Queensland, reported a maximum of 26 ppm In (Parbhakar-Fox and Jackson 2022). In addition, there is estimated to be at least 3,000 Mt of waste rock, at least 1,250 million m^3 of stored tailings, and there are about 120 complexes abandoned mine sites in Queensland (The Global Tailings Portal 2019; Mudd, pers. comm. 2021; Geological Survey of Queensland 2021). Consequently, the Queensland state provides an excellent study area in which to explore the potential of indium in the context of tracking its cycling in unconventional environments. This article briefly focuses on the ore results as background and presents in-depth detail on the preliminary results of the content of indium in waste rock and AMD-impacted waters of Mt Morgan (an Au-Cu VHMS historic deposit) and Baal Gammon (a Sn granite-relate abandoned deposit).

2 Geology setting

2.1 Baal Gammon and Mt Morgan mine sites

The Mount Morgan Au-mine is located 38 km southwest of Rockhampton in the Central of Queensland (Figure 1). Over the 108-year mine life, approximately 237 t of Au, 37 t of Ag and 387,000 t of Cu were mined from both underground and open-cut operations (Edraki et al. 2005). Messenger et al. (1997) reported the deposit as an end-member class of volcanogenic massive sulfide deposits. The Devonian rhyolitic Mine Corridor Volcanics are the host rocks for Au–Cu mineralisation and are surrounded and intruded by the Devonian Mount Morgan Tonalite (Edraki et al. 2005). The main ore body (Main Pipe mineralisation) corresponded an irregular form of massive and disseminated sulfide mineralisation that transgressed stratigraphic units

but was cross-cut by a relatively unaltered tonalite stock (Messenger et al. 1997). The minerals in the ore zone included: pyrite, quartz, pyrrhotite, chalcopyrite, magnetite and sphalerite, gold, Au-tellurides, and Ag minerals. Whilst the common gangue minerals were quartz, chlorite, with minor amounts of carbonate and apatite (Edraki et al. 2005).

The Baal Gammon Sn-mine is located 70 km southwest of Cairns, in the NE of Queensland (Figure 1). It is one of the largest Sn deposit in the Herberton region, and it is also reported to be a viable source of indium and tungsten. The Baal Gammon orebody is hosted in the UNA Porphyry, a derivative of the Elizabeth Creek Granite (Fraser 1972). The UNA Porphyry sits within the metasedimentary rocks of the Silurian-Devonian Hodgkinson Formation, occurring as stockwork veins in greisenised regions of the host rock (Schwarz-Schampera and Herzing 2002). Baal Gammon has a JORC-compliant Indicated Resource of 2.77 Mt @ 1% Cu, 40 g/t Ag, 0.2% Sn and 39 g/t In (Gow et al. 2021).

Both mine sites are non-active and pose environmental risks due to large volumes of acid-forming waste rock and AMD contamination into the Dee River and Jamie Creek respectively.

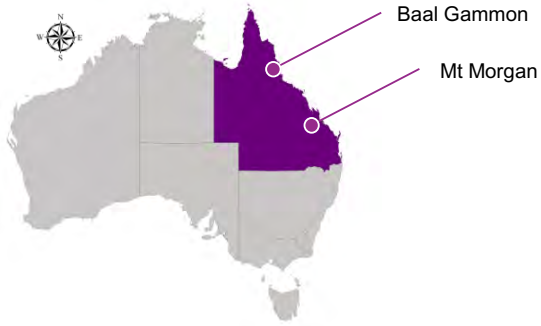

Figure 1. Location map of the mining sites.

3 Methodology

3.1 Sample collection and sample preparation

Fieldwork and sampling (Figure 2) were conducted in November 2022 and February 2023 at Mt Morgan and the Baal Gammon mine sites respectively. Hand-specimen sized waste rock samples (n=66) were selected to provide a range of lithologies from three different locations across the waste rock piles at Mt Morgan, and from one waste rock pile at Baal Gammon; additionally, a few boulders were sampled from along to the Jamie Creek (n=26).

Stream sediment and precipitates samples (n=14 Mt Morgan; n=15 Baal Gammon) were also collected upstream and downstream of the Dee River and Jamie Creek and around districts and represented background and 'mine-impacted' materials. Waste rock samples were cut, as well as a small portion of sediment and precipitates were kept for mineralogical studies. The remaining materials were used for geochemical bulk characterisation.

Figure 2. Plan view of AMD-impacted waters, precipitates, sediments and waste rock at Baal Gammon (A) and Mt Morgan (B).

Surface water samples (n=14 Mt Morgan; n=17 Baal Gammon) were collected around the mine sites (open pit and sumps, Figure 3) to allow for comparison of water quality upstream and downstream of the Dee River and Jamie Creek respectively (Figure 3).

Figure 3. Open pit (A and B), sumps (C and D) and AMD-impacted Dee River and Jamie Creek (E and F) sampling locations from Mt Morgan (left) and Baal Gammon (right).

Water samples were collected for analysis of major cations and anions (unfiltered), and trace metals and metalloids (0.45 µm filtered). Duplicate water samples and blanks were considered every five samples. Oxidation-reduction potential (ORP), temperature, conductivity (SPC), and pH were

measured in the field. These values were measured using a YSI ProDSS multiparameter water quality handheld meter, which was calibrated to pH 4 prior fieldwork. For water analyses, sampling equipment were rinsing prior to each sampling by deionised water.

3.2 Chemical and mineralogical analyses

The bulk elemental composition of all waste rock, sediment, and precipitate samples were assessed by four acid ICP-MS with 48 elements measured. Additionally, comparable geochemical data from a previous at Baal Gammon (Parbhakar-Fox 2020) are included here. The water samples included analysis of alkalinity, acidity, sulfate, chloride, fluoride, ionic balance, dissolved major cations (Ca, Mg, Na, K), and dissolved metals by ICP-MS.

In parallel, polished mounts representative of Baal Gammon ore (n=25) and waste rock (n=6) were prepared for mineralogical characterization to learn more about indium's hosting. The samples were characterised by handheld LIBS at the University of Chile, SEM/EDS at the University of Queensland, electron EPMA at the Queensland University of Technology, LA-ICP-MS at the University of Adelaide. These analyses enabled quantification of indium and others trace elements in sulfides and cassiterite. Whilst investigations on ore samples have concluded, ongoing work is being performed on the waste rock using Maps Mineralogy Software, Thermo Fisher Scientific. Similar analyses on polished mounts from Mt Morgan (and additional Baal Gammon) are pending.

4 Results

4.1 Waste rock chemistry and mineralogy

Waste rock from Mt Morgan reported a maximum of 3.53 ppm In (70 times higher than crustal abundance). Additionally, high concentrations of Cu (up to 6.74 %), Au (up to 6.09 ppm), Ag (up to 6.99 ppm), Re (up to 0.14 ppm), Mo (up to 388 ppm), and Te (up to 81 ppm). These samples comprise mainly massive sulfide minerals, gossan, host rocks (tonalite and porphyry), and country rocks (volcanic breccias and tuffaceous volcanics). The main sulfide is pyrite and a lesser amount pyrrhotite, chalcopyrite, and molybdenite.

Waste rock from Baal Gammon reported above 500 ppm In (10,000 times higher than crustal abundance). Additionally, high concentrations of Cu (up to 18.7 %), and Ag (up to 344 ppm). These samples comprise massive sulfide minerals dominated by arsenopyrite, pyrrhotite and chalcopyrite and a lesser amount sphalerite and stannite group (Figure 4). LA-ICP-MS results from ore samples show a maximum of 1,778 ppm In in the cleanest sphalerite, whilst a maximum of 3,776 ppm In in bulk intervals.

Waste rock from both mines show development of Fe oxides in the exterior rind of samples (Figure 5).

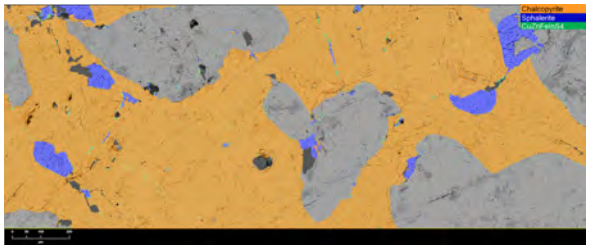

Figure 4. Backscattered electron images of waste rock sample from Baal Gammon using Maps Mineralogy Software.

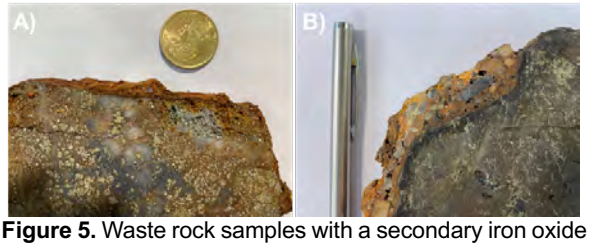

Figure 5. Waste rock samples with a secondary iron oxide rind developed on primary sulfides. A) Mt Morgan; B) Baal Gammon.

4.1 Water chemistry

Background concentrations of metals for surface waters in the Mount Morgan area are represented by a pH of 7.12, 0.02 ppm Al, 0.07 mg/L Fe, 0.53 mg/L Mn and below detection limits for In (<0.001 mg/L), Zn, Co, As, Cd. While fluoride value is 0.2 mg/L and chloride is 42 mg/L. The open pit and seepage sumps at the site contain a range of low pH values (2.79 to 3.06) and high conductivities (6,287 to 12,181 µS/cm). Metal concentrations in the open pit and sumps generally fall in a range from: 1,110 to 2,060 mg/L Al; 94.5 to 578 mg/L Fe; 67.5 to 241 mg/L Mn; 65.5 to 89.3 mg/L Cu; 28.5 to 74.3 mg/L Zn; 2.7 to 6.26 mg/L Co; 0.298 to 0.433 mg/L Cd; and <0.01 mg/L In. Furthermore, 20 to 38 mg/L fluoride; and 2 to 228 mg/L chloride.

Background concentrations of metals for surface waters in the Baal Gammon area are represented by a pH of 6.22, 0.21 ppm Al, 0.07 mg/L Fe, 0.06 mg/L Mn and below detection limits for In (<0.001 mg/L), Zn, Cd. While fluoride value is 0.5 mg/L and chloride is 4 mg/L. The open pit and seepage sumps at the site contain a range of low pH values (2.78 to 4.24) and medium conductivities (135 to 2,437 µS/cm). Metal concentrations in the open pit and sumps generally fall in a range from: 0.79 to 337 mg/L Al; 0.05 to 88.5 mg/L Fe; 0.43 to 36.6 mg/L Mn; 0.67 to 122 mg/L Cu; 0.32 to 62.7 mg/L Zn; 0.005 to 1.19 mg/L Co; 0.007 to 0.4 mg/L Cd; and 0.016 to 0.073 mg/L In. Furthermore, 38 to 120 mg/L fluoride; (Figure 6) and 7 to 9 mg/L chloride.

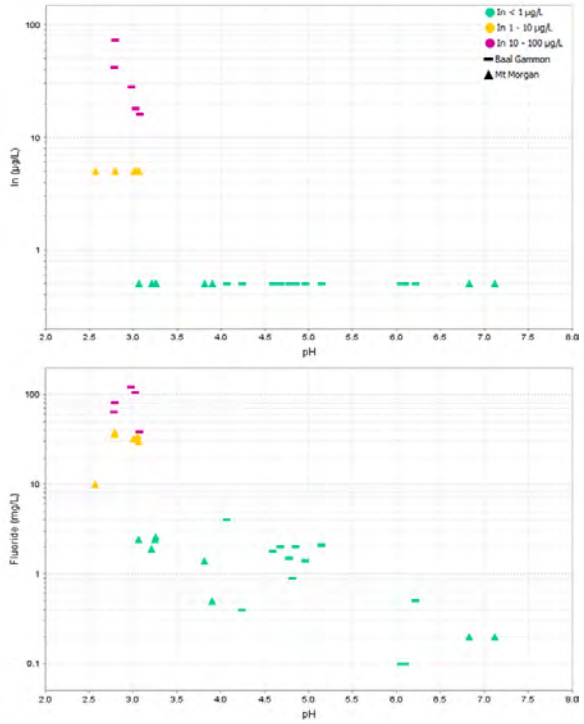

Figure 6. Variations of indium (µg/L) versus contents of pH, and fluoride (mg/L).

5 Conclusions

The highest indium content is reported in waste rock (>500 ppm In) and mine waters (up to 73 µg/L) at the Baal Gammon mine (a granite-related deposit), while low concentrations (3.53 ppm and up to 5 µg/L) were measured at the Mt Morgan mine (Au-Cu VHMS deposit).

Based on this, Mt Morgan is considered an indium-poor system. Therefore, not all VHMS are indium endowed, rather there is a decrease in indium towards Au-rich VHMS. The highest value of indium in mine waters correlate with high content of fluoride and low content of chloride. This observation has been reported in hydrothermal ore-forming systems (i.e., F-rich fluids are commonly related to skarn and greisen-type deposits and Cl-rich fluids with VHMS) showing that the ore geology has an important factor in the indium endowment in the related solid and aqueous mine waste materials. Factors including pH (< 2.8) have a main control of increasing content of dissolved indium, however, the same trend is not observed with the ORP results. Understanding the behaviour of indium (based on an understanding of its mineralogy and geochemistry) in mine waste systems may help identify optimum conditions for its extraction using hydrometallurgical methods, as part of a method to rehabilitate these AMD-forming mine sites.

Acknowledgements

The authors acknowledge the Queensland Department of Resources for supporting this research and allowing access to the Mt Morgan and Baal Gammon sites for sample collection. Thanks are extended to Helen Degeling, Christopher Hansen, Courteney Dhnaram, Sam Pegg, and Mark Eaton. Additional thanks to Kam Bhowany and Thomas Jones for supporting fieldwork and sample preparation respectively. Furthermore, the Thermo Fisher Scientific team for supporting mineral characterization using Maps Mineralogy Software.

References

Edraki M, Golding SD, Baublys KA, Lawrence MG (2005) Hydrochemistry, mineralogy and sulfur isotope geochemistry of acid mine drainage at the Mt. Morgan mine environment, Queensland, Australia. Applied Geochemistry 20:789-805. https://doi.org/10.1016/j.apgeochem.2004.11.004

Fox N, Parbhakar-fox A, Lottermoser B (2016) Critical and Deleterioys Metal Deportment in Sulfidic Waste Rocks, Baal Gammon, North, Queensland. The Third AusIMM International Geometallurgy Conference. Perth, Australia, pp 173-182.

Franks DM, Stringer M, Torres-Cruz LA, Baker E, Valenta R, Thygesen K, Matthews A, Howchin J, Barrie S (2021) Tailings facility disclosures reveal stability risks. Sci Rep 11:5353. https://doi.org/10.1038/s41598-021-84897-0

Gow P, Fox N, Aivazpourporgou S, McGovern J, Valenta R (2021) NE Queensland Mineral Deposit Atlas - Chapter 4 Baal Gammon & Gift. Report, Brisbane, Sustainable Minerals Institute. Sustainable Minerals Institute, pp 25.

Hund K, Porta DL, Fabregas TP, Laing T, Drexhage J (2020) Minerals for Climate Action: The Mineral Intensity of the Clean Energy Transition. The World Bank

Jowitt SM, Mudd GM, Werner TT, Weng Z, Barkoff DW, McCaffrey D (2018) The Critical Metals: An Overview and Opportunities and Concerns for the Future. Metals, Minerals, and Society:25-38. https://doi.org/10.5382/sp.21.02

Lottermoser BG, Ashley PM (2006) Mobility and retention of trace elements in hardpan-cemented cassiterite tailings, north Queensland, Australia. Environmental Geology 50:835-846. https://doi.org/10.1007/s00254-006-0255-8

Messenger PR, Golding SD, Taube A (1997) Volcanic setting of the Mt Morgan Au-Cu deposit, central Queensland: implications for ore genesis. Tectonics and Metallogenesis of the New England Orogen Geological Society of Australia Special Publication 19:109-127.

Nwaila GT, Ghorbani Y, Zhang SE, Frimmel HE, Leon C, Tolmay K, Rose DH, Nwaila PC, Bourdeau JE (2021) Valorisation of mine waste - Part I : Characteristics of , and sampling methodology for , consolidated mineralised tailings by using Witwatersrand gold mines (South Africa) as an example. Journal of Environmental Management 295:113013-113013. https://doi.org/10.1016/j.jenvman.2021.113013

Parbhakar-Fox A (2020) Cobalt and other critical metals in tailings of major mineral deposits in north Queensland: Baal Gammon mine. Report to Government. Sustainable Minerals Institute, University of Queensland, pp 41

Parbhakar-Fox A, Jackson L (2022) Cobalt and other critical metals in tailings of major mineral deposits in north Queensland: Mt Morgan slag study. Report to Government. Sustainable Minerals Institute, University of Queensland, pp 39.

Schwarz-Schampera U (2014) Indium In: Gunn G (ed) Critical Metals Handbook

Watari T, Nansai K, Nakajima K (2020) Review of critical metal dynamics to 2050 for 48 elements. Resources, Conservation and Recycling 155. https://doi.org/10.1016/j.resconrec.2019.104669

Tracking cobalt deportment from primary ore to copper tailings and determining reprocessing potential

Loren Nicholls[1], Elaine Wightman[1], Catherine Evans[1], Lachlan Casey[2], Anita Parbhakar-Fox[1]
[1]Sustainable Minerals Institute, University of Queensland, Australia
[2]Centre of Microscopy and Microanalysis, University of Queensland, Australia

Abstract. The high demand for cobalt in the global energy transition is driving the mining industry to explore alternative and more ethical cobalt sources. Reprocessing of copper flotation tailings is a potential circular economy approach to managing mine waste and supplementing global critical minerals supply. Tracking cobalt deportment from primary ore, through the concentrator and into tailings is a critical first step in assessing the valorisation potential. The mineralogy, particle liberation properties and mineral associations strongly influence the recoverability of cobalt from tailings. This research integrated Micro-X-Ray Fluorescence (μXRF), chemical assay, Mineral Liberation Analysis (MLA) and Advanced Mineral Identification and Characterization System (AMICS) to geometallurgically track cobalt deportment throughout an operating copper flotation circuit and into the fresh tailings. Cobalt was found to be hosted in several mineral phases, including cobaltiferous sulphides and pyrite. Detailed geometallurgical characterisation and deportment studies will assist in identifying mineral processing pathways to recovering value from copper tailings.

1 Introduction

As the global market transitions to more sustainable and green-energy technologies, the demand for critical metals for development is rapidly increasing (Valenta et al. 2023). Cobalt demand is predicted to outpace supply by 2030 with between 235 and 430 kilotonnes required for predominantly the EV lithium-ion battery market, as well as use in superalloys, catalysts, hard metals, permanent magnets and pigments (Hitzman et al. 2017; Fu et al. 2020). Reprocessing of sulfidic tailings for cobalt could supplement the global supply, while also providing an alternative mine waste management approach that incorporates circular economy principles.

The first step in assessing valorisation potential of an ore is to understand cobalt deportment across the mineral processing flow sheet. Given the complexity of cobalt-bearing ores, geometallurgical characterisation is key to recognising cobalt hosts, chemical associations, liberation characteristics and predicting implications for recovery (Dehaine et al. 2021).

In copper sulfide deposits, cobalt tends to occur as a companion metal within cobalt-sulfides and copper-cobalt minerals, or as inclusions in copper-iron sulfides such as chalcopyrite (Mudd et al. 2013). Cobalt can also occur in pyrite as micro-inclusions, as solid-solution in the matrix or as a zonation feature.

Copper flotation circuits are typically optimised to depress pyrite, rejecting it to the tailings stream. An accumulation of cobalt-rich pyrite in the tailings makes for a potential secondary resource for cobalt.

Pyrite is readily recovered by froth flotation under the appropriate conditions and this behaviour may be utilised to generate a pyrite concentrate that can be sold as a cobalt-bearing product for pyrometallurgical or hydrometallurgical extraction and refining.

The case study site for this research is an epigenetic sedimentary copper sulfide deposit that has associated cobalt mineralisation. Trace cobalt minerals have been identified, including carrollite ($CuCo_2S$), linnaeite ($Co^{+2}Co^{+3}{}_2S_4$), cobaltite (CoAsS), siegenite ($(Ni, Co)_3S_4$) and pyrite (FeS_2). Copper and silver are recoverable commodities, but cobalt is yet to be exploited. Understanding cobalt deportment throughout the concentrator is critical to developing a flow sheet to optimise recovery.

A series of plant surveys were conducted over five days to investigate cobalt deportment in the feed, final concentrate and final tail (Fig. 1). Samples of the final tail were then floated in the laboratory to produce a sulfide mineral (mainly pyrite) concentrate and the mineralogy of the concentrate and tail was assessed for mineral liberation and cobalt recovery.

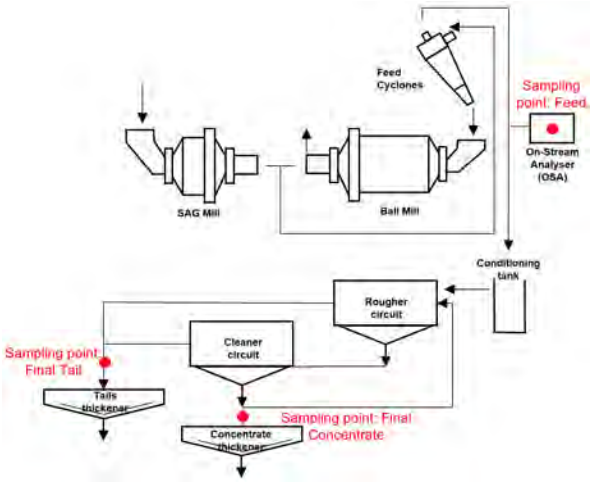

Fig. 1 Simplified schematic of the copper concentrator with plant survey sampling points highlighted.

2 Methodology

2.1 Micro-X-Ray Fluorescence of primary ore

Six (6) slabs of quarter core from the primary ore deposit were scanned using an iXRF ATLAS X XFM (X-ray fluorescence Microscope) at the Centre for Microscopy and Microanalysis, University of Queensland, with a 50W Mo source and 25um polycapillary optic (XOS FlexBeam) and 2x Ketek H150 detectors. Scanning occurred under atmospheric conditions at 40 kV and 200 µA, at 25 ms dwell, 0.5 ms risetime and pixel sizes from 40 to 60 µm. Scans were processed in the GeoPIXE package (CSIRO) via dynamic analysis, assuming a pyrite matrix (Ryan 2001). GeoPIXE generates RGB and spectral intensity images that map elemental distribution and provide qualitative and semi-quantitative data on chemical associations and mineralogy. The overlapping Fe Kβ/Co Kα peaks were excluded from analysis, with abundance calculated only from the Fe Kα and Co Kβ peaks.

2.2 Plant Survey

Representative samples from the flotation feed, final concentrate and final tailings streams of 5 different blend feeds (15 samples in total, ~1.5 kg each) were collected across the plant over 5 days. Samples were weighed (wet), filtered and dried (60 ^{0}C, ~6 hours), weighed (dry), representatively split and bagged. In each plant survey a second tailings sample was split, weighed (wet), stirred to suspend all solids and used for batch flotation tests.

Initially, unsized samples were analysed using the ME MS-61 method (4 acid digest, ICP MS analysis) at ALS Global Brisbane and Mineral Liberation Analysis (MLA) was conducted at the University of Queensland.

Sized fractions included sieved fractions +75, +53, +38 and Cyclosizer C1, C2, C3, C4, C5 and -C5. These fractions were composited into +38 µm (+75, +53, +38), C3 (C1, C2, C3), C5 (C4, C5) and -C5. These composites were also analysed by the same methods at ALS and MLA.

2.3 Batch float tests

Batch flotation laboratory trials were undertaken on four of the tailings samples to produce a pyrite concentrate (Fig. 2) and a desulfurised residual waste product.

The following flotation conditions and reagents were used: Float time: 8 min, Impeller Speed (RPM): 400, pH: 8, adjusted from 11, Frother: Methyl Isobutyl Carbinol (MIBC), Activator: 50g/t CuSO4, Collector: 25g/t Sodium Isobutyl Xanthate (SIBX).

Sized and unsized concentrate and tailings samples were sent for assay using ME MS-61 and to the University of Queensland for MLA.

Fig. 2 Images of the batch float pyrite concentrates floating in float cells from the copper concentrator tailings.

2.4 Advanced Mineral Identification and Characterization System (AMICS)

A Hitachi SU3900 scanning electron microscope (SEM) with a XFlash 6160 Bruker energy dispersive spectroscopy (EDS) detector was used to scan the MLA mounts and generate back scattered electron (BSE) images and X-ray spectra. These data were analysed using the Advanced Mineral Identification and Characterization System (AMICS) software to produce elemental and mineral distribution maps (Bruker 2022).

3 Cobalt distribution in the primary ore

Cobalt occurred in several different phases within the primary deposit. Cobaltiferous pyrite was evident as fine-grained infill around early euhedral pyrites (Fig. 3a). This phase appeared to be deposited post-early pyrite, syn-copper mineralisation and remobilised during supergene enrichment. Cobalt also occurred as carrollite locked in pyrite. A cobaltite-pyrite solid solution was also identified where cobalt was unrelated to copper mineralisation (Fig. 3b).

Variable mineral associations and grain sizes of primary cobalt sulphide hosts inform geometallurgical domaining and cobalt distribution across the flow sheet. Fine-grained cobaltiferous pyrite that is intimately spatially associated with copper minerals will likely deport to the concentrate, whereas more massive cobaltite-pyrite is expected to be rejected to the tailings if the pyrite was sufficiently suppressed during flotation.

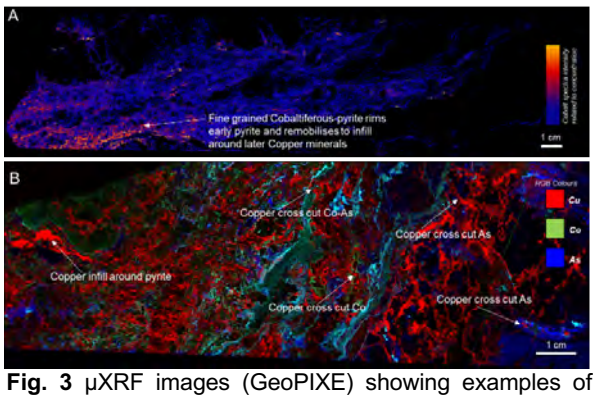

Fig. 3 µXRF images (GeoPIXE) showing examples of cobalt distribution in ¼ core samples of primary ore: A) Spectral intensity image of cobalt rims around early stage pyrite grains and remobilised in copper mineralisation event to infill copper-sulfides, B) Co-As-pyrite solid solution differentiated from Cu-mineralisation event.

4 Cobalt deportment in the concentrator

Four cobalt-bearing sulphide minerals were identified in the plant survey samples: cobaltite, carrollite, alloclasite ((Co,Fe)AsS) and pyrite. MLA modal mineralogy of the final concentrate reported between 33 % and 55 % copper minerals and 33 % to 56 % pyrite (Fig. 4). Copper mineral recoveries were excellent (>80 %), while pyrite recoveries were up to 38 %. Cobalt recovery in the final concentrate was low at approximately 20 % and cobalt sulfides had varying recoveries, indicating poor floatability under the current flotation conditions. The majority of the cobalt was lost to the tailings and may potentially be recovered through reprocessing.

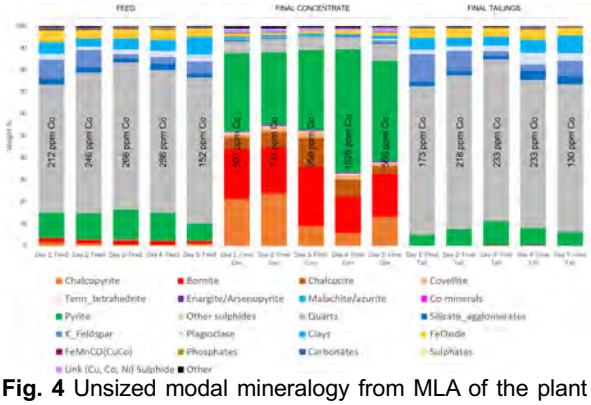

Fig. 4 Unsized modal mineralogy from MLA of the plant survey samples with cobalt assay (mass balanced) data.

In the batch flotation tests, the concentrate was dominated by pyrite up to 65 wt. %. Less than 2 wt. % consisted of other sulfides, including copper and cobalt sulfide minerals (Fig. 5). The non-sulfide gangue (NSG) component ranged between 30 and 50 wt. % of the concentrate and included quartz, K-feldspar, Fe-oxides (<2 wt. %) and clays (<2.5 wt. %). Pyrite recovery to the batch flotation concentrate was excellent, ranging between 87 to 97 % recovery. Recoveries of cobalt minerals carrollite and alloclasite were variable, with some tests recovering as little as 12 %, while others recovered up to 100 %.

The batch flotation tail was almost completely desulfurised, with <1 wt. % sulfide minerals. The tails were predominantly composed of quartz (70 to 85 wt. %), K-feldspar and Fe-oxides (~5 wt. %).

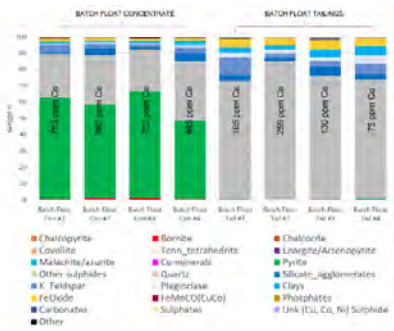

Fig. 5 Unsized modal mineralogy from MLA of the batch float samples with raw cobalt assay data.

Cobalt recovery in the tailings batch float concentrate ranged between 36.5 % and 48.3 %. Several key factors may be controlling cobalt recovery, including fine particle sizes (<10 µm), low primary liberation of cobaltiferous grains (~ 50 to 60 %) (Fig. 6), collector selection for cobalt sulphides or pyrite with trace metal inclusions in the batch float experiment, or unknown cobalt hosts not yet targeted.

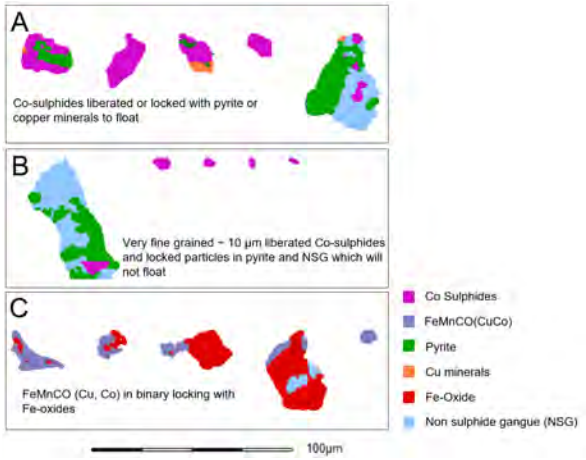

Fig. 6 Individual particles from MLA DataView software from the batch float tests, including: A) Co-sulfide particles in the batch float concentrate, B) Co-sulfide particles in the batch float tailings, C) Co-oxide particles in the batch float tailings.

Elemental distribution mapping using the Bruker EDS detector and processing in AMICS software identified cobaltiferous sulfides (carrollite) locked within NSG minerals in the batch flotation tailings (Fig. 7).

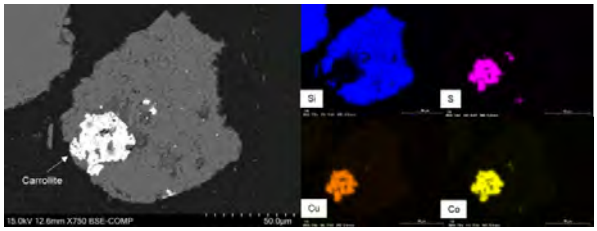

Fig. 7 Cobalt distribution elemental EDS map.

To investigate this further, mass flows were used to identify possible cobalt deportment in the system. The MLA modal mineralogy weight % and MLA estimated assays were generated by grouping key minerals: Cu minerals (chalcopyrite, bornite, chalcocite, covellite, tetrahedrite, enargite, cuprite, malachite, carrollite, FeMnCO, pyrite_group), Co minerals (cobaltite, alloclasite, pyrite_Co-group, FeMnCO and carrollite), pyrite and NSG minerals. The Co mineral mass flows were then calculated using the measured weights of the batch float tests.

Recoveries were calculated from mass flows of cobalt, pyrite, cobalt in pyrite and cobalt not in pyrite. The recoveries of cobalt in pyrite were the same as pyrite recoveries in the system, however the recoveries of cobalt not in pyrite were more

comparable to the measured assay cobalt recoveries (~40 %). This leads to the conclusion that the high-grade cobalt is potentially still sitting in cobaltiferous minerals which are not being optimally recovered in the pyrite concentrate. Carrollite and alloclasite have variable recoveries in the batch float. The elemental distribution of cobalt from the MLA mineralogy shows that a high percentage of cobalt in the batch float tails occurs in carrollite and in the oxide FeMnCO(CuCo), considered to be asbolane.

5 Conclusions

Reprocessing of copper sulfide tailings for secondary cobalt resources is a potential circular economy solution to tailings management and supplement of global critical metal supplies. However, the variability of cobalt mineralogy, locking associations and liberation potential requires detailed geometallurgical characterisation to understand cobalt deportment and opportunities for recovery.

In the case study of a sedimentary copper-sulfide deposit, the dominant cobalt host was expected to be pyrite and therefore floating the pyrite into a pyrite concentrate was expected to also recover the cobalt. Further investigation indicated that fine grained cobalt bearing minerals and pyrite could still be present in the tailings stream, since the pyrite flotation conditions were not optimised to recover these minerals in the batch float experiment.

The integration of chemical, mineralogical and metallurgical data allowed for these key features to be identified and can be used to inform the design of an appropriate mineral reprocessing flow sheet for recovery of cobalt from copper tailings.

Acknowledgements

Many thanks to the case study site and on-site metallurgists (unnamed due to confidentiality reasons) who funded and assisted in this project. The staff at the Julius Kruttschnitt Mineral Research Centre MLA laboratory are thanked for their support and data processing. The Centre for Microscopy and Microanalysis (University of Queensland) is thanked for analytical equipment and technical support.

References

Bruker (2022) ESPRIT 2 – The Powerful 4-in-1 Software for Microanalysis. Bruker https://mbna.bruker.com/acton/fs/blocks/showLandingPage/a/15240/p/p-0036/t/page/fm/2. Accessed 3 March 2023

Dehaine Q, Tijsseling LT, Glass HJ, Törmänen T, Butcher AR (2021) Geometallurgy of cobalt ores: A review. Miner Eng 160:106656. doi: 10.1016/j.mineng.2020.106656

Fu X, Beatty DN, Gaustad GG, Ceder G, Roth R, Kirchain RE, Bustamante M, Babbitt C, Olivetti EA (2020) Perspectives on Cobalt Supply through 2030 in the Face of Changing Demand. Environ Sci Technol 54:2985-2993. doi: 10.1021/acs.est.9b04975

Hitzman M, Bookstrom A, Slack J, Zientek M (2017) Cobalt - Styles of Deposits and the Search for Primary Deposits. USGS https://pubs.usgs.gov/of/2017/1155/ofr20171155.pdf. Accessed 1 March 2023

Mudd GM, Weng Z, Jowitt SM, Turnbull ID, Graedel TE (2013) Quantifying the recoverable resources of by-product metals: The case of cobalt. Ore Geol Rev 55:87-98. doi: 10.1016/j.oregeorev.2013.04.010

Ryan CG (2001) Developments in Dynamic Analysis for quantitative PIXE true elemental imaging. Nucl Instrum Methods in Phys Res Sect B: Beam Interactions with Materials and Atoms 181:170-179. doi: 10.1016/S0168-583X(01)00374-3

Valenta RK, Lèbre É, Antonio C, Franks DM, Jokovic V, Micklethwaite S, Parbhakar-Fox A, Runge K, Savinova E, Segura-Salazar J, Stringer M, Verster I, Yahyaei M (2023) Decarbonisation to drive dramatic increase in mining waste - Options for reduction. Resour, Conserv Recycl 190:106859. doi: 10.1016/j.resconrec.2022.106859

Invisible metals for a green future: Au associated critical elements in historic mining districts Murtal (Styria)

Sandra Niederl[1], Viktor Bertrandsson Erlandsson[1], Peter Felfer[2], Phillip Gopon[1]

[1]*Dept. of Applied Geosciences and Geophysics, University of Leoben, Austria*

[2]*Lehrstuhl für Werkstoffwissenschaften, Friedrich-Alexander-Universität, Erlangen, Germany*

Abstract. Gold is often associated with other critical metals bound in the crystal structure of sulfide minerals. Our study is investigating the possibility of re-mining tailings piles from three former gold mining districts in Styria, with a special focus on precious and critical metal containing sulfides. We combine optical microscopy, electronprobe micro analysis, scanning electron microscopy and whole rock geochemistry to characterize these deposits and where the metals are found. Geochemistry confirms the positive correlation between arsenic and gold as well as other elements. To better understand the atomic relations between the metals and to take a look at the way they occur, nanoscale investigations with atom probe tomography are done on selected grains. Gold is occurring in elevated concentrations in arsenic rich pyrite zonation as well as in nano-inclusions in pyrite and arsenopyrite.

1 Introduction

Tailings piles from mining activities from at least 1000 years of active mining are visible in Austria´s landscape. Due to the increasing need of special metals like bismuth, cobalt, lithium, platinum group elements (PGEs) and tungsten for green technologies, those tailings piles are starting to become a major interest. Most of the mentioned elements are considered critical, but are currently not mined in Europe and there is an ongoing search for local resources. Renewable energies will increase the needed amount of those “green” elements even further. Tailings from old mines are a possible source of those metals all over the EU.

Recent work has shown that gold and a subgroup of critical metals (hereafter referred to as precious metal associated critical metals or PMaCMs) can occur trapped within sulfide minerals often bound with the crystal lattice of e.g. pyrite (Reich et al. 2005; Gopon et al. 2019).

This study is part of a larger project, looking at different tailings piles in Styria, to evaluate their potential according to those PMaCMs. We will

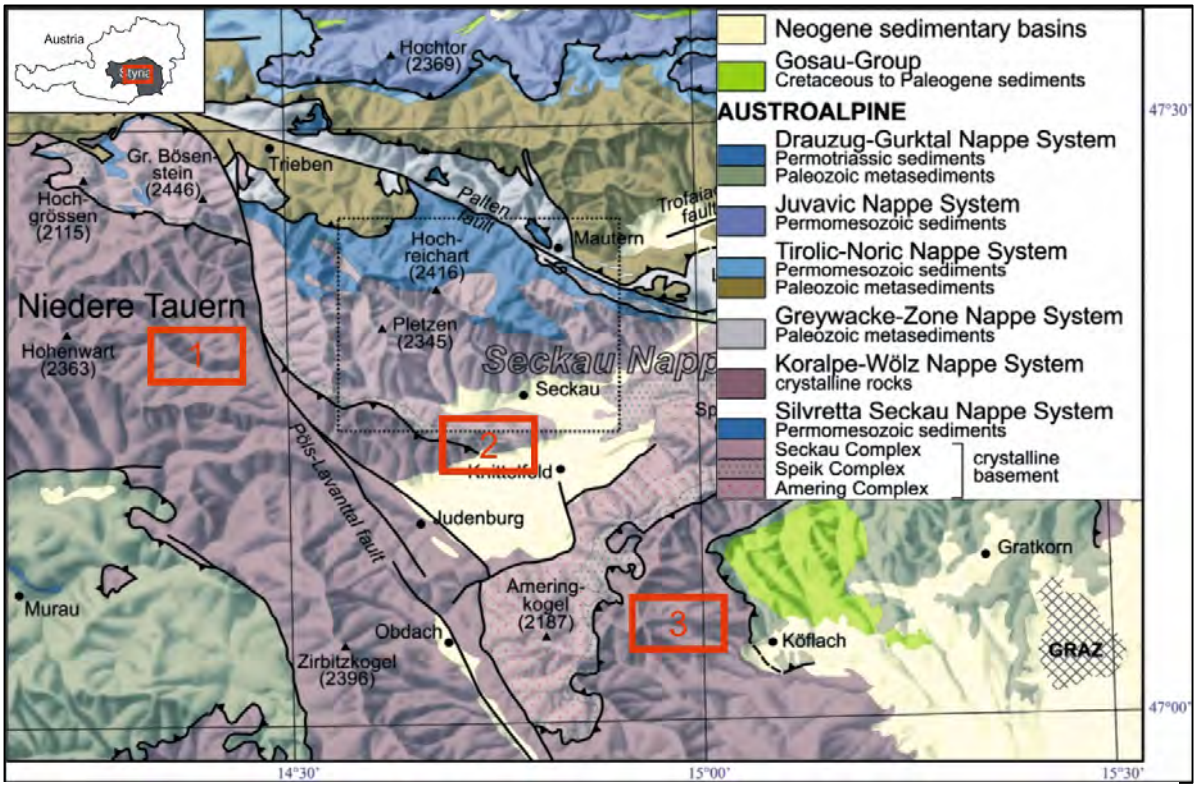

Figure 1. Geological map of Upper Styria with the former mining areas in red: 1= Pusterwald; 2= Flatschach; 3= Kothgraben. (modified after Gasser et al. 2009; Pfingstl et al. 2015)

present results from different tailings piles in three former gold mining districts, operated from the 15th up to the 20th century. These districts are located in Upper Styria and are Flatschach, Kothgraben and Pusterwald (Figure 1). The primary focus of our work is to determine in which quantities PMaCMs are found within these deposits (using whole rock geochemistry) and to characterize how they occur. Not all metals in these deposits are visible with the optical microscope or electron microscopes (i.e. electron probe micro-analyser (EPMA), scanning electron microscope (SEM)), and we report the occurrence of invisible gold within arsenic rich pyrite from at least one of the three deposits (Flatschach). Ongoing work is focusing on other sulfdes in these deposits potentially hosting gold and PMaCMs (using laser ablation inductively coupled plasma mass spectrometry (LA-ICP-MS) and EPMA).

2 Geological overview

The three districts are located in the Silvretta-Seckau and Koralpe- Wölz nappe of the upper lithology consists of medium to high grade metamorphic rocks (Neubauer 2002). The mined ore deposits are mesothermal vein type deposits.

3 Methods

45 samples were taken from different tailings piles in the three districts and 20 of them where send out for geochemical whole rock analysis. Polished sections, from our historic collection, as well as newly prepared ones where scanned with a Keyence VHX 6000 digital microscope. EPMA and SEM work was done with 10 selected samples. The main focus of the petrography was on the district Flatschach, as it seemed most suitable in terms of arsenic contents and existing minerals. The used EPMA was a JEOL JXA 8200 with an acceleration voltage of 15kV and a current of 15µA and the SEM work was done with a Zeiss Evo MA10 with a Bruker Quantax EDX detector. Pyrite as well as arsenopyrite grains where analysed, but major parts of the results are from pyrite analyses.

3.1 Atom probe tomography (APT)

APT is applied to characterize the atomic-scale link between gold, PMaCMs and arsenic (and other minor elements). Analysed were conducted on a CAMECA LEAP 4000 HR, located in the Department of Materials, Friedrich-Alexander-University, Erlangen. Because of the known link between arsenic and gold concentrations in pyrite (Reich et al. 2005), grains with a promising Au/As ratio where chosen. Two liftouts where done on the arsenic rich zones of the pyrites (one is shown in Figure 2).

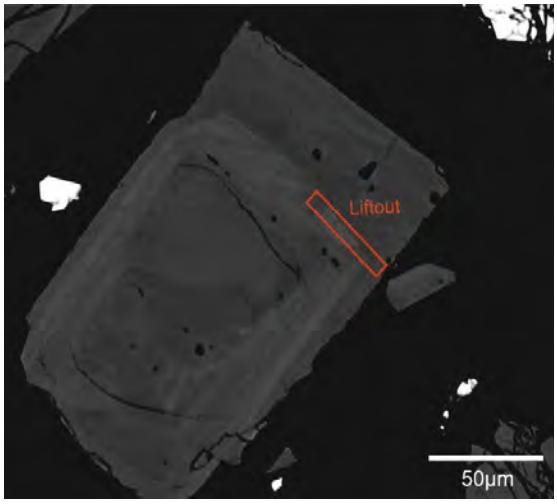

Figure 2. Back scatter image (BSE) image of one of the grains analysed with APT; red= liftout area.

4 Future work

The next step in this project will be the processing of the APT and LA-ICP-MS measurements to get an overall image of the trace element compositions of the grains and not only the selected APT areas. Additionally, we plan to constrain the timing of ore formation and to investigate the trace elemental signature of the ore minerals to determine if there is a geochemical and/or temporal link between these deposits that occur in comparable geological settings.

Acknowledgements

The work is financed by in part by the State of Styria (Green Transformations; ABT08-247901/2021), as well AUREX Biomining AG.

References

Gasser D, Gusterhuber J, Krische O, Puhr B, Scheuchter L, Wagner T, Stüwe K (2009) Geology of Styria: An overview. Mitteilungen des naturwissenschaftlichen Vereines für Steiermark 139:5-36

Gopon P, Douglas J O, Auger M A, Hansen L, Wade J, Cline J S, Robb L J, Moody MP (2019) A Nanoscale Investigation of Carlin-Type Gold Deposits: An Atom-Scale Elemental and Isotopic Perspective. Economic Geology 114:1123–1133

Neubauer F (2002) Evolution of late Neoproterozoic to early Paleozoic tectonic elements in Central and Southeast European Alpine mountain belts. Review and synthesis. Tectonophysics 352:87–103

Pfingstl S, Kurz W, Schuster R, Hauzenberger Ch (2015) Geochronological constraints on the exhumation of the Austroalpine Seckau Nappe (Eastern Alps). Austrian Journal of Earth Science 108/1:172–185

Reich M, Kesler S E, Utsunomiya Satoshi, Palenik C S, Chryssoulis S L, Ewig R C (2005) Solubility of gold in arsenian pyrite. Geochimica et Cosmochimica Acta, 69/11:2781-2796

Schmid S M, Fügenschuh B, Kissling E, Schuster R (2004) Tectonic map and overall architecture of the Alpine orogene. Eclogae geologicae Helvetiae 97:93–117

Comparison of the Wilson and Ivan monazite-bearing high-grade mineralization at Alces Lake, SK (Canada): Mineralogy, composition, and U-Pb chemical ages

Kateryna Poliakovska[1,2], Irvine R. Annesley[1,3,4], Olena Ivanik[2], Kahlen Branning[3]
[1]*GeoRessources, Université de Lorraine, Nancy, France*
[2]*Institute of Geology, Taras Shevchenko National University of Kyiv, Kyiv, Ukraine*
[3]*Appia Rare Earths & Uranium Corp., Toronto, Canada*
[4]*University of Saskatchewan, Saskatoon, Canada*

Abstract. This contribution presents part of an original study that combines field observations, petrography and geochronological constraints of the extremely high-grade REE-Th-U mineralization associated with the pegmatitic bodies of the Alces Lake deposit/prospect (SK, Canada). These pegmatites intrude the metasedimentary and meta-igneous rocks of the Murmac Bay Group with the mineralization hosted in monazite-(Ce) (within the studied Ivan and Wilson zones). The investigated samples display mostly peraluminous signatures and are dominated by the assemblage of quartz + K-feldspar + plagioclase + biotite +/- rutile at the Wilson zone +/- muscovite at the Ivan zone + monazite + zircon. Chemical U-Pb dating of monazite grains of 1.8-2.0 Ga for both studied zones confirm the relation to the Trans-Hudson Orogen metamorphism.

1 Introduction

Rare earth elements (REE) among the rare metals and other critical metals are of great economic interest and have become an irreplaceable part of our lives. However, their genesis often remains poorly defined. Sufficient understanding of the mineral systems of the rare metals is an essential part of discovering new prospects and thus reducing supply deficits, caused by increasing demand worldwide.

This paper focuses on studying and comparing zones of exceptional high-grade monazite (REE-Th-U) mineralization at Alces Lake (Northern Saskatchewan). The current study is a part of a larger research project (Poliakovska et al. 2022) focused on the genesis of the Alces Lake area mineralization (SK, Canada).

One of the key goals of the current research was to analyze the samples from 2 mineralized zones (Ivan and Wilson) of the deposit and ultimately suggest/determine the petrogenesis of the Alces Lake mineralization. This was carried out using field observations data, petrographic observations, and mineral chemistry.

2 Geological Setting

The Alces Lake REE mineralized area is located within the Rae Subprovince in the Churchill Province. Locally it is hosted by the Beaverlodge domain (northern Saskatchewan) at the junction of the Beaverlodge, Train, Zemlak and Ena Domains, approximately 28 km north of the Athabasca Basin
The rocks of the rocks of Alces Lake area (deposit/prospect) have a complex genesis, that is related to 4 major Paleoproterozoic tectonic events that highly deformed and metamorphosed (at mid- to high-pressure amphibolite- and granulite-facies conditions) the predominantly meta-sedimentary and meta-igneous rocks of Paleoproterozoic age (Ashton et al. 2013; Bethune et al. 2013; Regis et al. 2021).

Overall, the crystalline basement complex that comprises the geological suite of the area consists of: Archean to Paleoproterozoic granodioritic and mafic gneisses, amphibolites, granitic gneisses and paragneisses (Ashton et al. 2013) (Fig. 1).

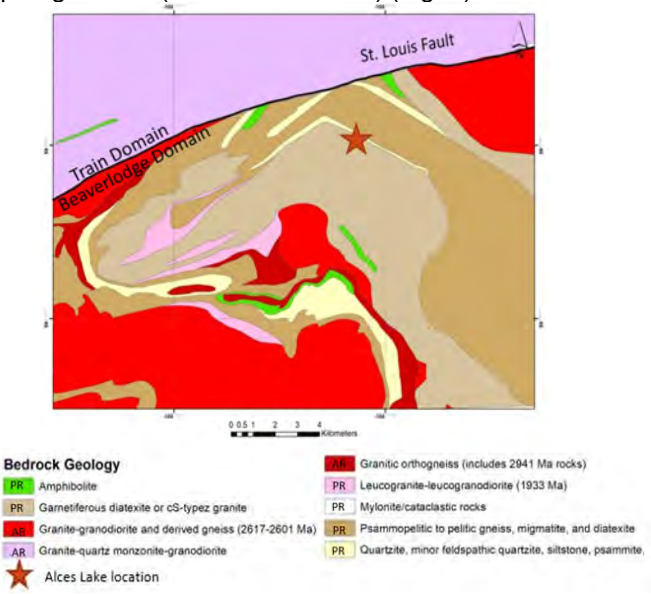

Fig. 1 Geological setting of Alces Lake in the Beaverlodge Domain (modified after the Saskatchewan Geological Atlas)

Alces Lake is ranked as the highest-grade REE occurrence in Canada (Sykes et al. 2018).

The REEs and associated Th, U, Ga, and Zr are hosted in monazite-rich (+/- zircon) granitic to residual melt/cumulate pegmatites, associated with biotite-rich (+/- sulfides) paragneisses. The mineralized pegmatitic bodies are found within/near the Archean/Paleoproterozoic transition zone and are interpreted to have formed under middle crustal P-T conditions (Annesley et al. 2019). At least 3 or 4 generations of pegmatites (biotite-rich mineralized and quartz-feldspar-rich non mineralized) have been identified at the Alces Lake area. The mineralization forms a complex system of pegmatite veins (lenses),

occurring in the form of individual grains, thin lenses from 1 to 3 cm thick, and massive augenitic clusters (i.e. boudins, up to a meter thick) of monazite grains 1 to 3 mm in size (on average).

3 Methodology

After an extensive petrographic study, two thin-sections were selected from a larger suite of thin sections from representative samples. Thus, one thin section was chosen for each study zone – for Wilson (thin-section "172") and for Ivan (thin-section "182"), located around 100 m from each other within the Alces Lake mineralization. The thin-sections were analysed using the micro-XRF – Bruker M4 Tornado µXRF. High-resolution imaging of individual monazite grains from monazite-bearing pegmatoids was performed by using a high-resolution scanning electron microscope (TESCAN VEGA3) in order to find and characterise any internal zoning or other heterogeneities in individual grains of monazite. As a result the backscattered electron (BSE) images have been recorded. Quantitative spot analyses of monazite, as well as X-ray element maps, were performed using the CAMECA SX100 electron microprobe at the SCMEM (Common Service of Electron Microscopy and X-ray Microanalysis) facilities at the GeoRessources laboratory. Monazite was analysed for a number of elements: Si, P, Ca, Y, La, Ce, Pr, Nd, Sm, Gd, Pb, Th, U, and O.

Thirty spot analyses were recorded for the monazite grains of the "182" thin-section and sixty three for the "172" thin-section (due to the larger heterogeneity of the grains within the Wilson zone). Consequently X-ray maps were created for representative monazite grains within the Ivan (5 grains) and Wilson (14 grains) zones.

4 Mineralogy

Petrographic observations have showed that the mineralized samples are composed mainly of feldspar, monazite, quartz, biotite, muscovite, rutile and zircon (Fig. 2, 3). Alteration has led to the chloritization of biotite and the sericitization/ kaolinization of feldspars.

Sample "172" – Wilson zone

In the studied sample, monazite grains are most commonly associated with biotite and feldspar. The monazite forms subhedral to fully rounded, corroded crystals that are variable in size (the grainsize of monazite commonly ranges from 0.1 to over 1 mm diameter) and characterized by extremely high REE, high Th and U contents. Some of the resorbed monazite grains show partial corrosion overgrowths of biotite or quartz. The most common inclusions in monazite are quartz and feldspar. Within the Wilson zone the monazite grains are either homogenous, or weakly to strongly zoned. When present, the chemical zoning can be characterized as: 1) concentric (oscillatory growth zoning), 2) patchy zoning.

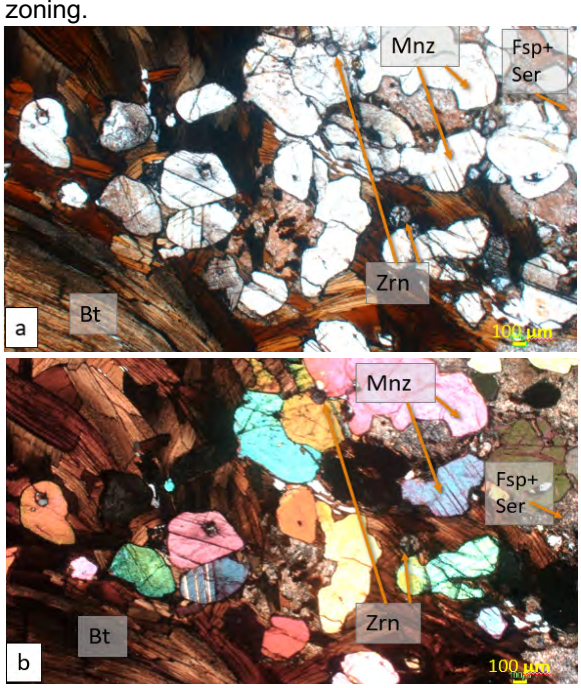

Fig. 2 Photomicrograph of high-grade monazite mineralization. **a** Plane light. **b** XPL image – from "172" – Wilson zone

Sample "182" – Ivan zone

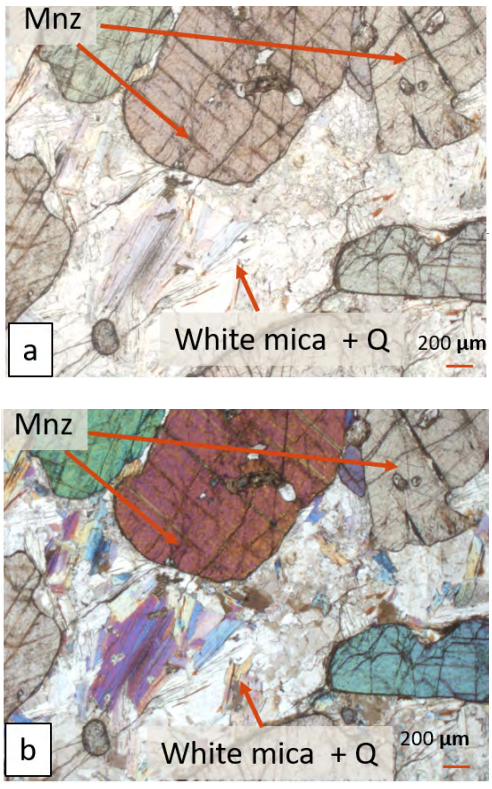

Fig. 3 Photomicrograph of high-grade monazite mineralization in muscovite-quartz matrix. **a** Plane light. **b** XPL image – "182" – Ivan zone

In this sample, monazite grains are associated mainly with biotite, muscovite and quartz. The monazite forms subhedral to fully rounded, corroded

crystals variable in size (the grainsize of monazite commonly ranges from 0.1 to over 1-3 mm diameter) characterized by extremely high REE, high Th and U contents. The most common inclusions in monazite are quartz, feldspar, and also fine-grained white mica. Within the Ivan zone, monazites are overall homogenous. EPMA X-ray mapping revealed slight sector zonation on some of the grains (SEM BSE images did not show any zonation).

EPMA quantifications

Data from 93 monazite spot analysis was compiled and analyzed to better characterize the REE mineralized zones. All the data plotted within the Ce-monazite zone (Fig. 4).

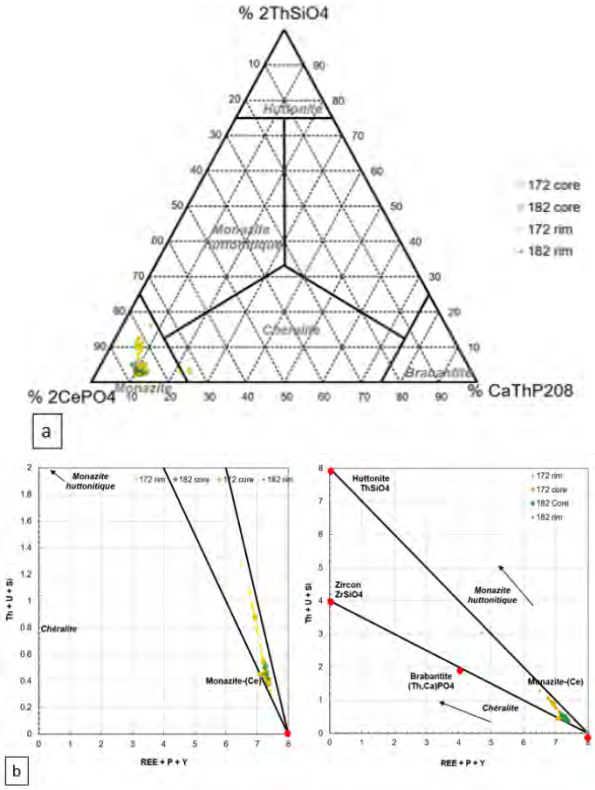

Fig. 4 a Ternary plot of the monazite compositions (in green – Ivan zone, in yellow – Wilson zone). **b** Th + U + Si vs REE + Y + P diagram. For the two identified zones, the monazite grains are dominated by monazite-(Ce) compositions

For sample “182” (Ivan zone), direct correlation between the following elements was observed: Ce and La, and Th and Pb; while inverse correlation was noted between Si and P; and Ce and Pb, Th. For sample “172” (Wilson zone) direct correlation between the following elements was observed P and Ca, Ce, Pr, Nd, Sm, Gd; and Th and Pb; and inverse correlation was noted between Si and P, Ce, Pr, Nd, Sm, Gd; and Ca and Th.

X-ray maps were created for a total of 19 monazite grains from both zones. It was observed that, for all the grains, the lighter colored grey zones (SEM BSE image – Fig. 5a) tend to be more U- and Th-rich and REE-poor (Fig. 5b, 5c) when compared to the darker grey matrix.

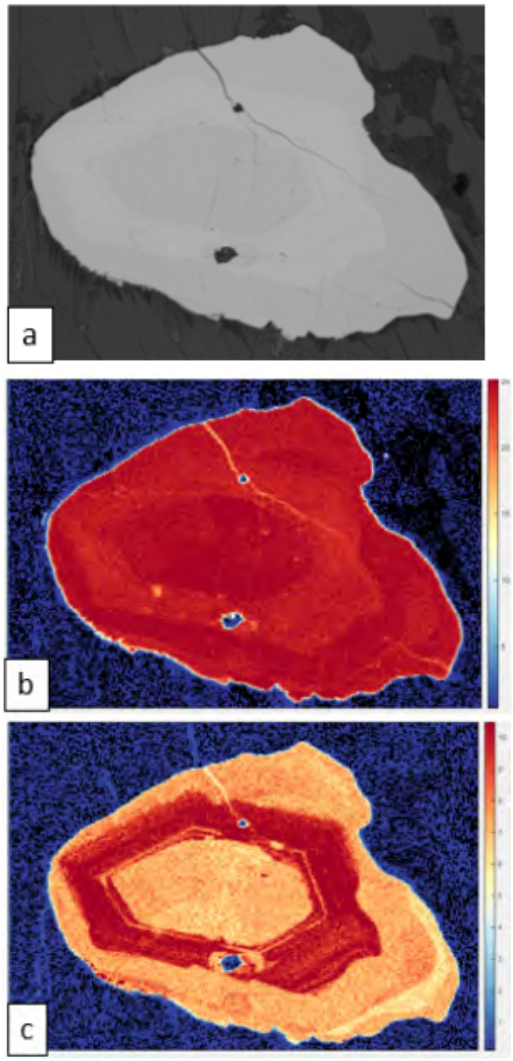

Fig. 5 a BSE SEM. **b** Ce. **c** Th (in weight %) of monazite grain from the Wilson zone of the Alces Lake deposit

U-Pb chemical ages

We attempted to calculate the chemical ages using the EPMA data and the procedures of Montel et. al. 1996. The graphs from the Fig. 6 show the obtained ages for both Wilson and Ivan zones. Most of chemical ages (U-Th-Pb) calculated from monazite EMPA analyses yield ages of 2.0 – 1.7 Ga. We can also observe slightly different age trends for these 2 selected zones where the age range for the Wilson zone is 1.4 – 2.1Ga (average=1.88 Ga, median=1.9 Ga) and for the Ivan one – 1.7 – 2 Ga (average=1.9 Ga, median =1.89 Ga).

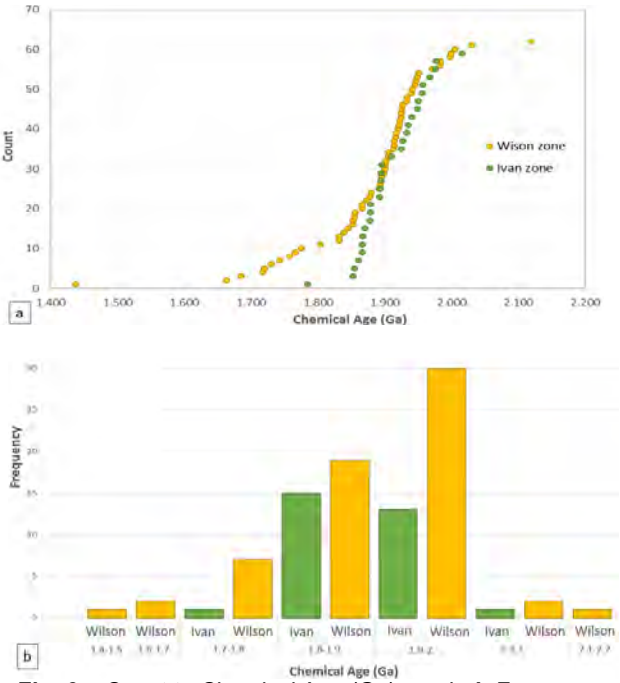

Fig. 6 a Count to Chemical Age (Ga) graph. **b** Frequency to Chemical Age graph

5 Discussions and Conclusions

In this study, we characterized the geological setting, ages, and mineral assemblages, as well as the composition of monazites of the pegmatitic mineralized zones at the Alces Lake deposit/prospect area. The results of this work show that the monazites, the main REE-Th-U bearing mineral identified in the studied samples from the Ivan and Wilson zones, have a complex history and most likely represent a combination of different origins. The studied pegmatites are LREE enriched and are composed of quartz + K-feldspar + plagioclase +/- rutile + biotite +/-muscovite + monazite and zircon.

Taking into account the mostly peraluminous nature of pegmatites along with other evidence they could have formed as a result of partial melting of the ortho and paragneisses (possibly the Murmac Bay Group rocks - a belt of Paleoproterozoic metasedimentary and meta-igneous rocks interleaved with Archean orthogneisses) during high-grade amphibolite to granulite-facies metamorphism related to the Trans-Hudson Orogen in a middle to lower crustal melt-transfer zone, with melt transport preferentially along shear zones and the Archean-Proterozoic transition zone.

Thus, from the field and mineralogical data presented here we interpret that the Alces Lake pegmatitic bodies are of anatectic origin (and not directly related to a parental granitic pluton and are representative of the abyssal REE-Th-U subclass of the Cerny and Ercit (2005) classification.

So, to date, the results of our investigation of the samples from the 2 chosen mineralized zones show that the REEs and associated Th, U, Ga, and Zr are hosted in monazite-rich (+/- zircon) granitic to residual melt/cumulate pegmatites, emplaced within/near the Archean/Paleoproterozoic transition zone under middle to lower crustal P-T conditions.

Both the Ivan and Wilson zones of the Alces Lake deposit/prospect have similar ranges of age (obtained from the chemical dating, thus need to be confirmed using more precise methods, e.g., LA-ICP-MS/ion microprobe dating to properly determine the age of the various stages of growth and recrystallization). The most prominent clusters for both zones are from 1.8 to 2 Ga, which can be interpreted initially as the age of the peak metamorphism, magmatic crystallization, and/or possible age of the source rock area.

We opine that this high-grade Th-rich monazite mineralization represents restitic material formed by disequilibrium melting, which then migrated as a restite-rich melt phase to / emplaced at the presently observed crustal level at Alces Lake (i.e. old middle crust at upper amphibolite/lower granulite facies).

Acknowledgements

This work was carried out thanks to the equipment of the SCMEM (Common Service of Electron Microscopy and X-ray Microanalysis) of the University of Lorraine.

References

Annesley IR, Poliakovska K, Sykes J, Pandur K (2019) The geology and mineralogy of high-grade rare earth element (REE-Th-U) mineralization at Alces Lake, Saskatchewan (Canada). Life With Ore Deposits on Earth, Proceedings of the 15th SGA Biennial Meeting, 2019, Glasgow, Scotland 1-4:1732–1735

Ashton KE, Hartlaub RP, Bethune KM, Heaman LM, Rayner N, Niebergall, GR (2013) New depositional age constraints for the Murmac Bay Group of the southern Rae craton, Canada. Precambrian Res 232:70–88

Bethune KM, Berman RG, Rayner N, Ashton KE (2013) Structural, petrological and U–Pb SHRIMP geochronological study of the western Beaverlodge domain: Implications for crustal architecture, multi-stage orogenesis and the extent of the Taltson orogen in the SW Rae craton, Canadian Shield. Precambrian Res 232:89–118

Černý P, Ercit TS (2005) The classification of granitic pegmatites revisited. Can Mineral 43:2005–2026

Montel J-M, Foret S, Veschambre M, Nicoll C, Provost A (1996) Electron microprobe dating of monazite. Chem. Geol. 131:37-53

Poliakovska K, Annesley IR, Ivanik O, Sykes J, Guest N, Otsuki A (2022) Geological setting, geochemistry and petrology of the granitic pegmatites hosting REE Th U mineralization at the Alces Lake area, Northern Saskatchewan, Canada. Proceedings of the 16th SGA Biennial Meeting, 28-31 March 2022, 1:325-328

Regis D, Pehrsson S, Martel E, Thiessen E, Peterson T, Kellett D (2021) Post-1.9 Ga evolution of the south Rae craton (Northwest Territories, Canada): A Paleoproterozoic orogenic collapse system. Precambrian Res 355(3):106105

Sykes J, Annesley IR, Pandur K (2018) The geological evolution of high-grade rare earth element mineralization on the Alces Lake Property, Northern Saskatchewan. Saskatchewan Geological Survey, Open House 2018 Abstract Volume, Misc Rep 2018-3: p 37

Forensic geometallurgy of Ni-Co laterites: Sustainable processing of Europe's low-grade ores and tailings into battery-grade metals

Fernando Prado Araujo[1], Philippe Muchez[1], Jens C.Ø. Andersen[2], Nívea Magalhães[2], Richard Crane[2], Hannah Hughes[2]
[1]KU Leuven, Department of Earth and Environmental Sciences, Belgium
[2]University of Exeter, Camborne School of Mines, United Kingdom

Abstract. The global nickel (Ni) and cobalt (Co) demand is expected to increase manyfold in the next decades. Both metals are essential components in rechargeable batteries, which are highly required for the energy transition away from fossil fuels. The current European production/refining landscape is not enough to cover such demand (even if recycling rates improve in the future). Additionally, the state-of-the-art processing routes can be energy intensive and not so environmental-friendly. The Horizon Europe-funded ENICON project offers an alternative HCl-based technology, with a lower eco-footprint, to process Europe's Ni-Co ore deposits and tailings into battery-grade metals. The full metal deportment in all products/by-products and valorised residues is done by combining several characterisation techniques into a mineral-focused geometallurgical protocol. This approach minimizes losses and allows the recovery of multiple valuable metals in the flowsheet, effectively improving the sustainability and viability of the European Ni/Co supply chain.

Introduction

Nickel (Ni) and cobalt (Co) are essential components of rechargeable batteries (Nickel Institute 2023). Hence, many studies forecast a sharp increase in their future demand (Campagnol et al. 2017; IEA 2021; Gregoir and van Acker 2022). However, European sources represent only a minor share of the extraction and refinement of battery-grade Ni and Co in the global market (Mudd and Jowitt 2022), leaving Europe mostly dependent on imports of these metals. Additionally, most of the current production practices are energy intensive and can pose environmental hazards (Bartzas et al. 2021). This poses a serious risk to Europe's plans of transitioning away from fossil fuels. Consequently, ensuring the sustainable supply of these critical raw materials is a key priority for Europe (European Commission 2008).

The Horizon Europe ENICON project (https://enicon-horizon.eu/) responds to this issue by enhancing the potential of Ni/Co resources within Europe – i.e. sulphidic ores and limonitic/saprolitic laterite ores – as well as by developing a more sustainable HCl-based processing route for these materials (Figure 4). The project consists of a multidisciplinary approach to (1) track the metals in the supply chain using forensic geometallurgy, (2) develop a new HCl leaching process to extract Ni and Co from ores and tailings, (3) ultra-refine the metals towards battery grade Ni/Co, and (4) provide solutions for the valorisation of residues. All those steps are further integrated into a Life Cycle-Techno Economic Assessment (LCA-TEA) to optimise the performance and decrease the environmental impact of the mining/refining operations (Figure 3). This contribution introduces the geometallurgical protocol for laterite ores (WP1) within the ENICON context.

Ni(/Co) laterites

Ni/Co-lateritic deposits are regoliths formed through weathering of ultramafic rocks and have low metal grades, commonly lower than 5% for Ni and less than 0.1% for Co (Elias 2002). The mineralisation is mainly hosted in two ore zones, saprolitic laterites and limonitic laterites (also known as oxide zone), with saprolite having a slightly higher grade than limonite (Elias 2002). These laterites are mineralogically and texturally complex materials with Ni and Co residing in several silicate and oxide minerals (Andersen et al. 2009). These features compound into a challenging process to release the metals from the mineral matrix.

Europe's two main laterite-processing companies, ENICON partners Larco and Euronickel, transform mixtures of saprolite and limonite laterite ores into an FeNi (Class-II Ni) product by a pyro-metallurgical route. Besides having a large carbon footprint (Bartzas and Komnitsas 2015) this process is unable to produce battery-grade Ni (Class-I Ni) and fails to recover sufficient Co, which largely ends up in the residues sent to landfills. In order to maximise the extraction efficiency of Ni, Co, and other valuable metals from these complex and heterogeneous deposits, it is crucial to understand the geological and mineralogical characteristics of the ore samples and apply a geometallurgical assessment of the processing flowsheet.

Forensic Geometallurgy

Geometallurgy is a multidisciplinary field that combines geology, mineralogy, and metallurgy to optimize mineral processing and increase the recovery of metals from ore deposits.

ENICON's forensic geometallurgy protocol (Figure 5) is a proactive approach that collects mineralogical, textural, and geochemical data of European Ni-Co deposits. It provides information

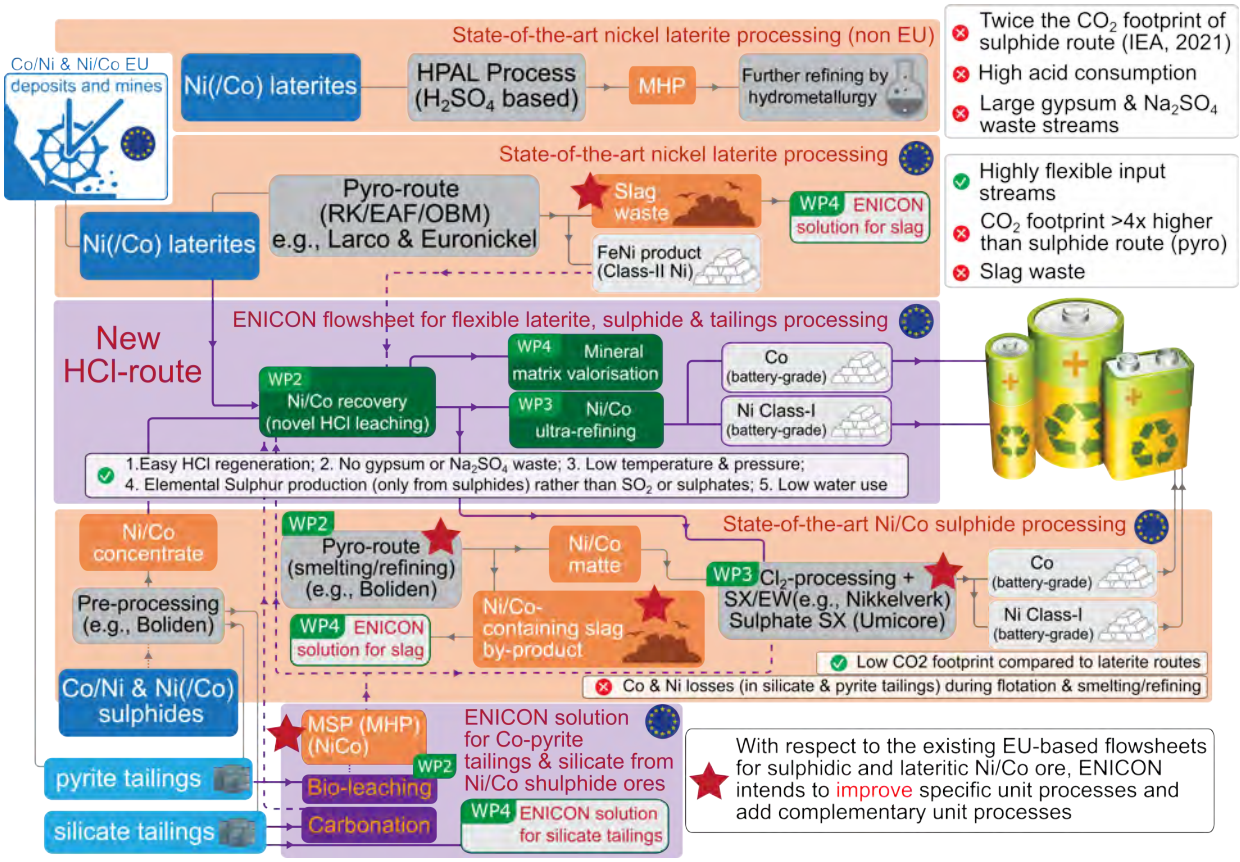

Figure 4. ENICON goes beyond the state-of-the-art for Ni/Co mining, recovery, and refining (orange boxes and grey arrows - source: IEA 2021). The new HCl route (upper purple box and purple arrows) is able to convert both laterite-based and sulphide-based materials into battery-grade Ni and Co, overcoming some of the issues associated with the state-of-the-art routes (green checks and red marks in white boxes near each specific flowsheet). A high-resolution version can be viewed at https://enicon-horizon.eu/.

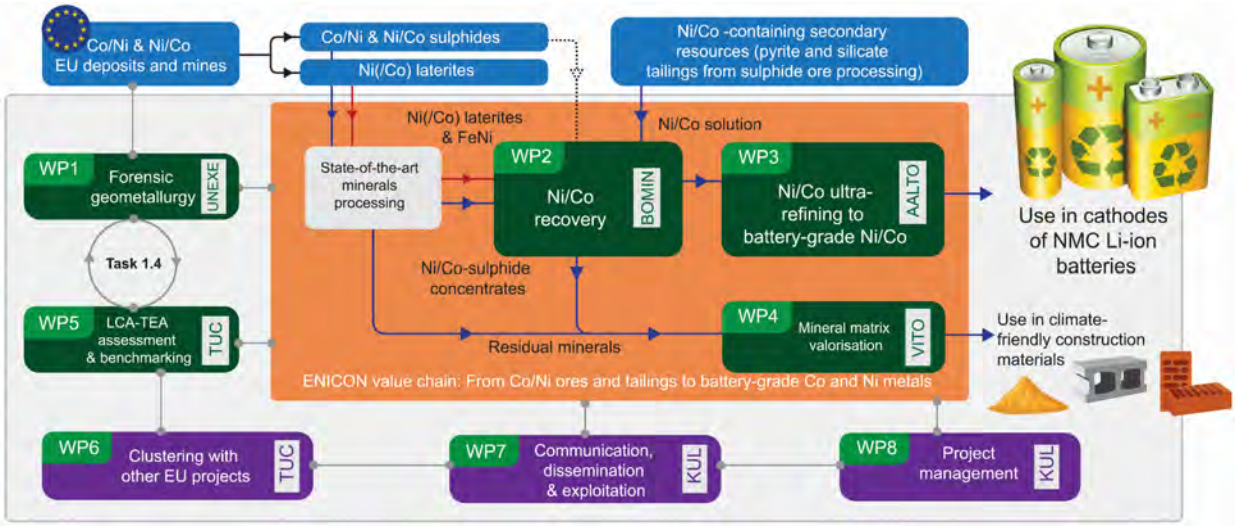

Figure 3. Division of the work package (WP green boxes) structure within the ENICON project. The link between raw material (EU Ni/Co deposits and tailings) to final product (battery-grade metals and climate-friendly construction materials) is monitored by the forensic geometallurgy protocol

about the metal pathways in all processing stages, aiming to track what happens to Ni, Co, potential by-products (e.g., platinum-group elements, Sc), penalty elements (e.g., As, Bi, Te, and Sb), active and passive gangue, and environmentally-deleterious products throughout the flowsheet from ore to battery-grade metal. This approach identifies the mineralogical and textural reasons for processing underperformance and mitigates losses in the Ni/Co mining, processing, and refining flowsheets and for the valorisation of waste materials. Additionally, the data will tell us how metals and minerals behave in the new HCl route compared to traditional stages of processing.

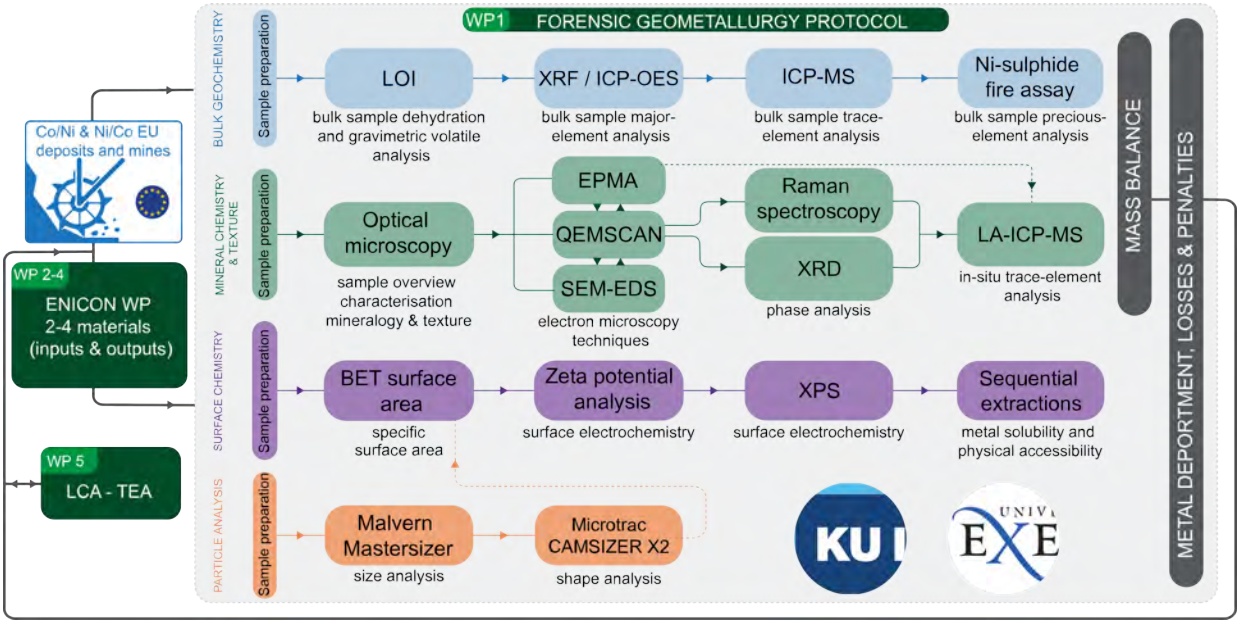

Figure 5. ENICON's forensic geometallurgy protocol & methodology (WP1) describing the main techniques that will be used in the project.

This advanced characterisation of materials involves a holistic investigation of their physical, chemical, and mineralogical parameters and characteristics. An array of techniques such as bulk geochemistry (loss on ignition, X-ray fluorescence, inductively coupled plasma (ICP)-optical emission spectroscopy, ICP-mass spectroscopy, and NiS fire assay), bulk and in situ mineralogy (optical microscopy, X-ray diffraction, scanning electron microscopy, electron microprobe, Raman spectroscopy, and laser ablation ICP-MS), and other analytical tools for particle size and shape distribution analyses are combined. This allows the definition of the metal deportment and losses from ore to battery-grade metal, and in all products/by-products, valorised waste, and residues.

Conclusions

The geometallurgy of nickel laterite deposits is a critical aspect to ensure effective mining and processing of these materials. By optimizing mineral processing and maximizing metal recovery, geometallurgical studies can play a vital role in improving the efficiency and sustainability of Ni and Co production from these ore deposits in Europe. The ENICON project targets to develop a competitive technology to treat the existing, newly exploited, and future low-grade Ni/Co European deposits to produce Class-I (battery-grade) Ni and Co with a lower eco-footprint. This will increase the effectiveness and sustainability of the Co/Ni supply chain in Europe, anticipating the increase in production required to meet Europe's electrification plan. The multi-metal mining approach and the residue valorisation strategies are needed to make the Co/Ni supply chain a near-zero-waste system in the future.

Acknowledgements

The ENICON project (https://enicon-horizon.eu/) has received funding from the European Union's Framework Programme for Research and Innovation Horizon Europe under Grant Agreement No. 101058124.

References

Andersen JCØ, Rollinson G, Snook B, et al (2009) Use of QEMSCAN® for the characterization of Ni-rich and Ni-poor goethite in laterite ores. Miner Eng 22:1119–1129. https://doi.org/10.1016/j.mineng.2009.03.012

Bartzas G, Komnitsas K (2015) Life cycle assessment of ferronickel production in Greece. Resour Conserv Recycl 105:113–122. https://doi.org/10.1016/j.resconrec.2015.10.016

Bartzas G, Tsakiridis PE, Komnitsas K (2021) Nickel industry: Heavy metal(loid)s contamination - sources, environmental impacts and recent advances on waste valorization. Curr Opin Environ Sci Health 21:100253. https://doi.org/10.1016/j.coesh.2021.100253

Campagnol N, Hoffman K, Lala A, Ramsbottom O (2017) The future of nickel: A class act. McKinsey&Company

Elias M (2002) Nickel laterite deposits – geological overview, resources and exploitation. CODES

European Commission (2008) The raw materials initiative — meeting our critical needs for growth and jobs in Europe

Gregoir L, van Acker K (2022) Metals for Clean Energy: Pathways to solving Europe's raw materials challenge. Eurometaux

IEA (2021) The Role of Critical Minerals in Clean Energy Transitions. OECD Publishing, Paris

Mudd GM, Jowitt SM (2022) The New Century for Nickel Resources, Reserves, and Mining: Reassessing the Sustainability of the Devil's Metal. Econ Geol 117:1961–1983. https://doi.org/10.5382/econgeo.4950

Nickel Institute (2023) Nickel in batteries. https://nickelinstitute.org/en/about-nickel-and-its-applications/nickel-in-batteries/. Accessed 9 Feb 2023

A mineralogical characterization of an antimony tailings dam: Implications for antimony recovery

Rembuluwani S. Ravele[1], Karel S. Viljoen[1], Derek H. Rose[1,2]
[1] Department of Geology, University of Johannesburg, P. O. Box 524, Auckland Park, 2006, South Africa
[2] Mintek, 200 Malibongwe Drive, Praegville, Randburg, 2194, South Africa

Abstract. Reprocessing of historical tailings storage facilities (TSFs) has gained momentum worldwide to address the demand for critical metals and minerals. Limited information about these repositories is available, hence the need to fill this knowledge gap. A tailings dam of the Murchison Greenstone Belt (MGB) was characterized to quantify the presence of economic antimony in terms of modal mineralogy, relative mineralogy and their associations (i.e. co-existing phases), and the deportment of antimony in various antimony-bearing minerals. Holes were drilled from the top to the bottom of the tailings dam to acquire samples for chemical and mineralogical characterization. A FEI 600F Mineral Liberation Analyzer (MLA) was used to characterize this tailings dam, accompanied by ICP-MS, XRF and LECO analyses. The MLA results, complemented by ICP-MS analyses revealed the occurrence of considerable amounts of Sb in this TSF. The TSF is mainly comprised of quartz, magnesite, chlorite and dolomite. Chapmanite and stibnite are the most abundant antimony-bearing minerals, along with other antimony minerals such as schafarzikite, senarmontite and berthierite. Significant antimony is mainly deported in stibnite, schafarzikite and senarmontite, with minor deportment into berthierite, cervantite, and other antimony phases.

1 Introduction

The Murchison Greenstone Belt (MGB) was the only antimony producer in South Africa, and produced about 18 % of the total world production by 1986, making it one of the biggest Sb producers in the world (Davis et al. 1986; Poujol and Robb 1999). A total historical estimation of 605 000 tonnes of antimony was mined from the MGB by 2015 (Pearton and Viljoen 2017). However, antimony production is now estimated to occur in a few countries, with China producing roughly 53 % of the world's production with no production from South Africa (Anderson 2019). The U.S. Department of the Interior has listed antimony as a critical mineral following the depletion of global resources and reserves while demand for antimony keeps growing (Anderson 2019).

The depletion of primary ore, coupled with the increase in commodity price and breakthroughs in extraction technology, has led to mine waste being considered as a secondary ore for critical metals and minerals (Lotternoser 2010).

Antimony has been mined along the antimony line (AL) of the east-north-trending MGB as a by-product of gold mining (Poujol and Robb 1999). The Weigel formation of the MGB hosts the prominent AL, where significant antimony mineralization occurs (Jaguin et al. 2012). The Weigel formation occupies the central part of the MGB, consisting of quartzite, quartz-chlorite-schist, quartz-muscovite-schist, minor banded iron formation and conglomerates (Davis et al. 1986; Jaguin et al. 2012). Mineralization along the AL is hosted by quartz-carbonate rocks, mainly quartz, dolomite and magnesite, with minor chlorite, talc and fuchsite. Antimony was mined in the form of stibnite and berthierite associated with pyrite and arsenopyrite from 18 mines (Poujol and Robb 1999).

The current study will only focus on the mineralogical characterization of the MGB antimony tailings dam to reprocess such tailings for antimony recovery. Major emphasis will be on antimony-bearing minerals.

2 Methodology

A total of five holes were drilled from the top to the bottom of the MGB Sb tailings dam with an automated auger drilling machine. Sampling holes were unevenly selected (R1 to R5 in Figure 1) based on accessibility and were selected to ensure representative sampling of the entire tailings repository. Samples were collected at 1.5 m intervals with depth and subsequently composited to produce three samples per hole (top, middle and bottom composite samples).

Each composite sample was split into two representative aliquots for chemical and mineralogical analyses. The first aliquot was sent to Intertek, Perth, Australia for geochemical analyses. Samples were analyzed by X-ray fluorescence spectrometry (XRF) for Al_2O_3, CaO, Cr_2O_3, Fe_2O_3, K_2O, MgO, MnO, Na_2O, SO_3 and SiO_2 (Intertek method FB1/XRF) with detection limits of 0.01 %. A combustion-infrared detection technique (Intertek method /CSA) was used to analyze C and S with detection limits of 0.01 %. Samples were also analyzed for Sb by ICP-MS (Intertek method 4A/MS) with a detection limit of 0.05 ppm. The second aliquot was used to prepare two transverse (90°) resin mounts from each composite sample for bulk modal mineralogical and relative modal mineralogical studies using a FEI 600F Mineral Liberation Analyser (MLA) (Gu, 2003; Fandrich et al. 2007). Bulk modal mineralogical composition was achieved through the XMOD mapping routine, whereas the SPL-GXMAP mapping routine was used for detailed assessment of antimony-bearing minerals. Analytical accuracy and precision of chemical data were monitored through duplicate analysis of selected samples and comparing the assay data to the MLA calculated assay data for quality assurance.

Figure 1. ArcGIS map showing the sampling points where samples were collected (marked R1 to R5).

3 Results

3.1 Tailings chemistry

Assay results of the antimony tailings dam samples from the MGB were combined and an average of the top, middle and bottom composites, are presented in Table 1. The table illustrates major and minor oxides encountered within this tailings dam, Sb, Au, total carbon and sulfur contents, and loss of ignition (LOI). The tailings dam under study contains SiO_2, MgO, Fe_2O_3, Al_2O_3, and CaO making up 78 % of the bulk composition of the samples while LOI makes up 20 %. Antimony was detected with an average value of 6955 ppm. Total C and S contents average 4.76 and 0.34 %, respectively. Minor oxides such as SO_3 (0.8 wt%), Na_2O (0.4 wt%), K_2O (0.2 wt%), Cr_2O_3 (0.2 wt%) and MnO (0.1 wt%) were also detected. Lesser gold was detected with an average of 0.6 ppm.

3.2 Tailings mineralogy

Mineralogical data is presented as a bulk composition of the top, middle and bottom following the observation that the modal mineralogy of the top, middle and bottom of each hole was identical. This study revealed that this tailings dam is primarily made up of quartz, followed by magnesite, chlorite and dolomite occurring at abundances ranging between 27 to 33 wt%, 16 to 22 wt%, 11 to 12 wt% and 8 to 9 wt%, respectively (Figure 2). Antimony-bearing minerals make up 1 to 3 wt% (abundance of each mineral to be discussed under relative modal mineralogy). Other minerals such as amphibole, pyroxene and feldspar were identified at abundances averaging 7 wt%, 5 wt% and 2 wt%, respectively.

Table 1. Analysis (assay data) of the top, middle and bottom composite samples from the MGB's tailings dam.

Elements	Top	Middle	Bottom	Average
Au (ppm)	0.4	0.4	0.9	0.6
Sb (ppm)	5754	6908	8202	6955
S (wt%)	0.2	0.3	0.5	0.3
C (wt%)	5.2	4.7	4.4	4.8
SiO_2 (%)	43.4	45.8	47.6	45.6
MgO (%)	18.1	17.2	15.1	16.8
Fe_2O_3 (%)	6.5	6.6	7.5	6.9
Al_2O_3 (%)	4.7	4.8	4.7	4.7
CaO (%)	4.0	3.9	4.2	4.0
SO_3 (%)	0.5	0.7	1.3	0.8
Na_2O (%)	0.4	0.4	0.4	0.4
K_2O (%)	0.3	0.2	0.2	0.2
Cr_2O3 (%)	0.2	0.2	0.2	0.2
MnO (%)	0.1	0.1	0.1	0.1
LOI (%)	20.1	18.4	17.1	18.5

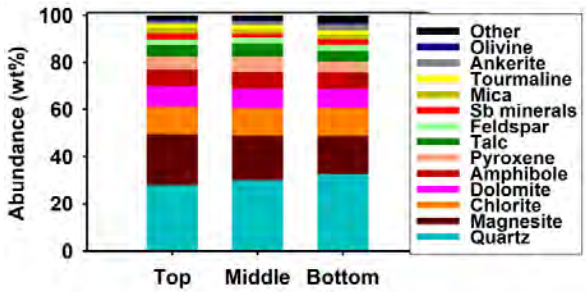

Figure 2. Stacked bar graphs depicting the MGB tailings dam's bulk modal mineralogy. Minerals were plotted in order of abundance with the most abundant mineral at the bottom of the stack and the least abundant mineral at the top.

3.3 Antimony-bearing minerals and their abundances

The MLA identified a total of 11 Sb-bearing minerals and the abundances of these are presented in Figure 3. This includes six Sb-bearing sulfide minerals (berthierite, gudmundite, Ottensite, stibnite, tetrahedrite and ullmannite), four secondary (oxide) Sb minerals (cervantite, schafarzikite, senarmontite and valentinite) and a silicate mineral (chapmanite). The data obtained from the MLA in wt% was normalized to the total Sb-bearing mineral population and presented as a relative percentage. Stibnite (Sb_2S_3) is the most abundant Sb-bearing mineral with values ranging between 28 to 46 % as observed at the top, middle and bottom of the tailings dam. Chapmanite ($Sb^{3+}Fe^{3+}{}_2(SiO_4)_2(OH)$), the only silicate Sb-bearing mineral identified in this study, is the second most abundant Sb-bearing mineral with an average value of 21 %. Gudmundite (FeSbS) and berthierite ($FeSb_2S_4$) form part of the most abundant Sb-bearing sulfide mineralisation with abundances of 7 to 12 %, and 3 to 9 %, respectively. Secondary

Sb-bearing minerals such as schafarzikite ($Fe^2Sb_2O_4$), senarmontite (Sb_2O_3) and valentinite (Sb_2O_3) were also identified with values ranging from 9 to 16 %, 5 to 9 % and <1 %, respectively. Figure 4 shows false colour images of some Sb-bearing minerals that the MLA encountered.

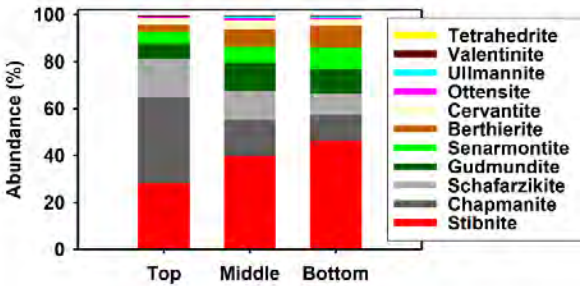

Figure 3. Stacked bar graphs depicting the abundance of antimony-bearing minerals with depth. Minerals were plotted in order of abundance with the most abundant mineral at the bottom of the stack and the least abundant mineral at the top.

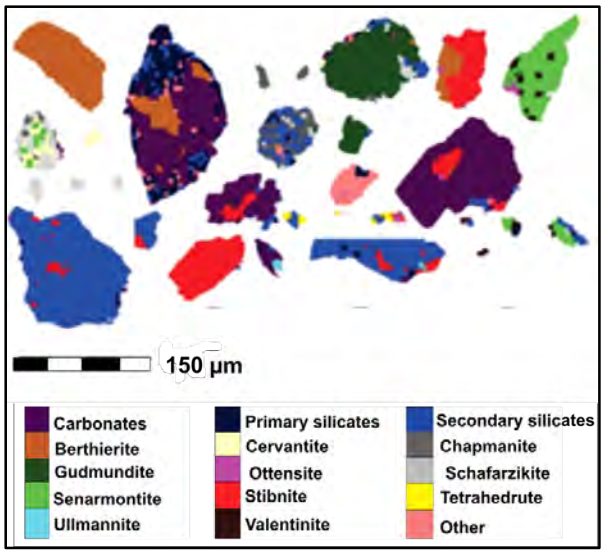

Figure 4. False color MLA images of some selected polished blocks showing antimony-bearing minerals and their association.

3.4 Antimony deportment

The bulk of the antimony from the MGB's tailings dam deports into stibnite (35 to 50 %), followed by schafarzikite (9 to 18 %) and senarmontite (7 to 12 %). Negligible amounts of antimony, 0.04 to 0.1 %, 0.3 to 0.9 and 0.6 to 0.9 %, deports in tetrahedrite, ullmannite and valentinite, respectively (see Figure 5).

3.5 Mineral association

Minerals that are not fully liberated are either associated with one mineral phase (binary) or two or more mineral phases (ternary). Figure 6 clearly illustrates Sb-bearing minerals being highly associated with secondary silicates, followed by primary silicates, carbonates and oxides. For simplicity when presenting the mineral association data, gangue minerals from the same mineral group were combined into four groups (i.e. carbonates, primary silicates, secondary silicates and other). As previously described the tailings consist mainly of quartz, magnesioferrite, chlorite and dolomite. These abundances are evidence of mineral associations as most of the Sb-bearing minerals are associated with these minerals.

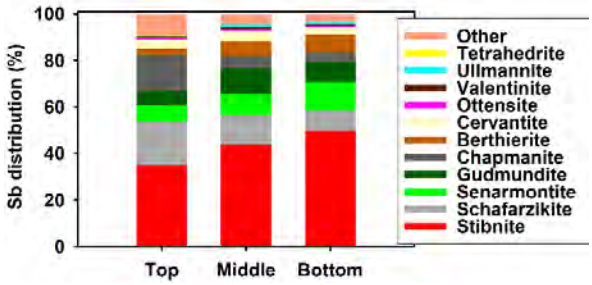

Figure 5. Stacked bar graphs showing the deportment of Sb in antimony-bearing minerals.

4 Discussion and conclusion

Based on the automated mineralogy results, the dominant gangue minerals are quartz, magnesite, chlorite and dolomite and minor amphiboles, pyroxene and feldspars. Antimony-bearing minerals mainly occur as sulfides, making up 56 % of the bulk Sb mineralisation (with stibnite as the main Sb-bearing sulfide), Sb oxides (23 %) and Sb silicates (21 %). Furthermore, about 45 % of Sb is deported into stibnite and approximately 25 % is deported into Sb oxides. The main Sb sulfides are primarily associated with secondary silicates (mostly quartz) and carbonate minerals (mostly magnesite) and have a minor association with primary silicate and other gangue minerals.

Antimony concentrations within the tailings dam under study generally increase with depth with the lowest (5754 ppm) and highest (8202 ppm) values occurring at the top and bottom parts of this tailings dam, respectively.

It was also noted that Sb-mineralisation in sulfide minerals (stibnite, gudmundite and berthierite) increases with depth. Stibnite and other Sb-sulfides oxidize rapidly (within days or weeks), under atmospheric conditions (Klimko et al. 2011; Álvarez-Ayuso et al. 2022) resulting in lower Sb-bearing sulfides at the top of the tailings pile compared to the bottom where oxidation rarely occurs. Secondary antimony-bearing minerals such as senamontite, valentinite and cervantite (the most common secondary antimony minerals) were most likely formed from the oxidation of stibnite and other antimony-bearing sulfides (Álvarez-Ayuso et al. 2022). This is evidence following the abundance of secondary minerals (Sb oxides) being abundant at the top of the tailings dam and less abundant at the bottom. It can be concluded from the deportment

results that bulk of Sb deports into Sb-sulfide mineralisation and less abundance occurs in secondary Sb-minerals. Antimony deportment in Sb-bearing sulfide minerals was less abundant at the top of the pile and more abundant at the bottom.

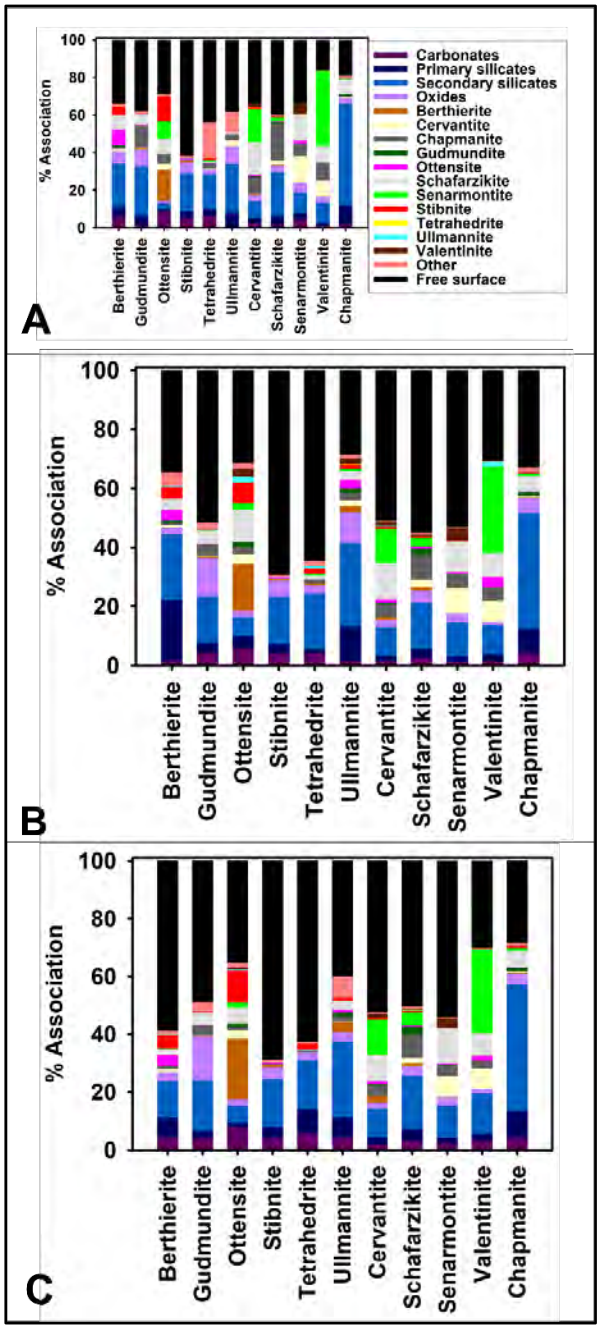

Figure 6. Stacked bar graphs depicting the mineral association of all antimony ore minerals with other minerals. (A) = Mineral association of antimony ore minerals for the top of the TSF. (B) = Mineral association of antimony ore minerals for the middle of the TSF. (C) = Mineral association of antimony ore minerals for the bottom for the TSF.

Since Sb in this TSF mostly deports into stibnite and other Sb-bearing sulfide minerals such as berthierite and gudmundite, alongside gangue minerals such as quartz, magnesite and other carbonate minerals, heavy medium separation and bulk sulfide flotation is recommended for antimony recovery (Anderson 2012). However, laboratory-scale metallurgical test work is recommended to deduce the possible antimony recovery before concluding the economic importance of this TSF.

Acknowledgments

Exceptional gratitude to the mine for granting permission to conduct this study and mine staff who assisted with acquiring samples and data. Prof. K.S. Viljoen acknowledges funding from the South African Department of Science and Innovation under their Research Chairs initiative, as administered by the National Research Foundation. Gabrielle van Heerden is thanked for her guidance on the Mineral Liberation Analyser.

References

Álvarez-Ayuso E, Murciego A, Rodríguez MA, Fernández-Pozo L, Cabezas J, Naranjo-Gómez JM, Mosser-Ruck R (2022) Antimony distribution and mobility in different types of waste derived from the exploitation of stibnite ore deposits. Science of The Total Environment 816: 151566.

Anderson CG (2012) The metallurgy of antimony. Geochemistry 72:3-8.

Anderson CG (2019) Antimony production and commodities. In: Kawatra K, Young CA (ed) SME mineral processing and extractive metallurgy handbook. Society for mining, metallurgy and exploration, Englewood, pp 1557-1568.

Davis DR, Paterson DB, Griffiths DHC (1986) Antimony in South Africa. Journal of the Southern African Institute of Mining and Metallurgy 86:173-193.

Fandrich R, Gu Y, Burrows D, Moeller K (2007) Modern SEM-based mineral liberation analysis. International Journal of Mineral Processing 84:310-320.

Gu Y (2003) Automated scanning electron microscope based mineral liberation analysis. Journal of Minerals and Materials Characterization and Engineering 2:33-41.

Jaguin J, Gapais D, Poujol M, Boulvais P, Moyen JF (2012) The Murchison greenstone belt (South Africa): a general tectonic framework. South African Journal of Geology 115:65-76.

Klimko T, Lalinsk B, Majzlan J, Chovan M, Kucerova G, Paul C (2011) Chemical composition of weathering products in neutral and acidic mine tailings from stibnite exploitation in Slovakia. Journal of Geosciences 56:327-340.

Lottermoser BG (2010) Tailings. In: Mine wastes: characterization, treatment and environmental impacts. Springer, Berlin, Germany, pp 205-241.

Pearton TN, Viljoen MJ (2017) Gold on the Kaapvaal Craton, outside the Witwatersrand Basin, South Africa. South African Journal of Geology 120:101-132.

Poujol M, Robb LJ (1999) New U-Pb zircon ages on gneisses and pegmatite from south of the Murchison greenstone belt, South Africa. South African Journal of Geology 102:93-97.

Distribution of critical elements in rocks and fluids, Taupo Volcanic Zone, New Zealand

Agnes G. Reyes[1]
[1]GNS-Science Lower Hutt, New Zealand

Abstract. Elements with the highest concentrations (>100kg/a) in the Taupo Volcanic Zone (TVZ) geothermal fluids, from lowest to highest, include Mo, Sb, Sr, W, Al, Cs, Rb, As, Li, Ca, B, Si and Na. Although discharge fluids produce only ~1-75 kg/a of Au, Ga, Tl, Ag, Ge, Rb and Cs, their high market prices warrant further study. Amongst gases of economic interest in the TVZ are CO_2 mainly for food processing, C_2H_6 and He. It is estimated that one producing geothermal system has ~NZ$850M/a worth of elements or ~NZ$19.5B/a for 23 systems. However, despite the presence of a wide range of critical elements in the TVZ fluids, only a few can be economically and technologically extracted at present.

1 Introduction

The terms “critical” or “endangered” elements refer to supply risks (https://www.acs.org) of ~90 economically significant natural elements (https://www.euchems.eu). Based on 2021 consumption levels, 12 elements from He to Ta are deemed to be in serious threat in the next 100 years. Another 12 are under rising threat and 19 are of limited availability and at future risk to supply from increasing use in rechargeable batteries and green energy devices, solar panels, aircraft engines, thermal imaging devices, GPS equipment, defense equipment and others (e.g., Geology.com). Supply is plentiful for more than 35 elements. Carbon in the form of gases such as CO_2 and CH_4 is generally plentiful although there is a shortage of CO_2 for food processing in New Zealand. Carbon in the form of oil and natural gas is under serious threat as known subterranean supplies diminish and because some of the most productive oil fields are in regions of political unrest.

There are remediation procedures to decrease the supply risk of elements e.g., recycling, substitution with more abundant materials, devising new ways of manufacturing equipment with an intent to recycle, finding new methods or revamping old methods to extract elements from unconventional sources more economically such as seawater (e.g., https://pubs.usgs.gov), geothermal fluids and precipitates, metal scrap, biological sources and others. Several studies aver, however, that mineral resources in the earth’s crust are by no means depleted, with the search for new resources improved by modern geophysical exploration methods (e.g. Best 2015) and the supply extended by exploitation of resources with lower concentrations.

The focus of this study is the Taupo Volcanic Zone (TVZ) where numerous studies demonstrate the propensity for precious, base, alkaline and alkaline earth metals and non-metals to be precipitated on the surface, in hot springs and geothermal installations (e.g., Weissberg et al. 1979; Hedenquist and Henley 1985; Reyes et al. 2002; Rowland and Simmons 2012; Pope and Brown 2014), subsurface rock formations (e.g. Simmons and Browne 2000) and entrained as solutes in discharge fluids (e.g. Hirner et al 1998; Wood 2003). Most chemical elements precipitate in the well and rock formations resulting to very low concentrations in surface fluid discharges and thus, downhole well samples have been analyzed by various workers (e.g. Simmons et al 2016).

The objectives of this paper are to examine the sources of critical elements (1) from volcanic contributions found in melt inclusions, leached from erupted volcanic ash or held in fresh volcanic rock, (2) contributed by greywacke and (3) enhanced by hydrothermal processes and water-rock interaction. This study also includes an evaluation of the mass (kg) of elements that can potentially be extracted from fluids discharged in TVZ geothermal systems.

2 Geological setting

The TVZ is a back arc rift developed from the oblique convergence of the Australian and Pacific plates along the Hikurangi margin east of the North Island (e.g. Acocella et al. 2003). The region is the locus of unusually voluminous rhyolite volcanism in the last 1.6 Ma and andesitic magmatism since 2.0 Ma with the volume of erupted rhyolites an order of magnitude higher than andesites (Wilson et al. 1995). Andesites occur only in the northernmost and southernmost regions of the TVZ (Rowland and Sibson 2004). There are at least 23 active hydrothermal systems with an estimated heat output of 4.2 GWt expelling at least 10^8 m^3/a (10^{11}kg/a) of aqueous fluids (Bibby et al. 1995). Six to eight of these systems are utilized for power production with an installed net capacity of more than 940 MWe (www.nzgeothermal.org.nz).

Except for magmatic-hydrothermal systems at Tongariro and White Island all other geothermal/hydrothermal systems in the TVZ are liquid-dominated. Two geochemically distinct source fluids were identified by Giggenbach (1995): subduction-related usually associated with andesitic volcanism, and rift-type associated with rhyolites and high-alumina basalts. Subduction-related or arc-type hydrothermal fluids, confined in the eastern side of the TVZ, are characterized by higher CO_2 contents, CO_2/Cl mole ratio, $CO_2/^3$He, N_2/Ar, B/Cl, Li/Cs and magmatic component than rift-type fluids. However, median Cl contents from well discharges are higher in rift-type (~1000 mg/kg) than in arc-type (~600

mg/kg) fluids. The annual mass flow of aqueous fluids and heat output of rift-type systems are 7x and 8x higher, respectively, than arc-type systems.

3 Results

An idealized cross-section of a typical TVZ hydrothermal system (Figure 1A) shows two major lithologies: the Mesozoic greywacke basement at depth overlain by igneous rocks. Sedimentary beds at shallower depths with tuffaceous intercalations are grouped under volcaniclastics due to similarities in chemical compositions.

3.1 Critical elements in greywacke, melt inclusions, fresh volcanic rocks and erupted ash

Concentrations of elements in the Mesozoic greywacke are either similar or less than in the earth's crust except for Au, B, As, Bi and S which are enhanced by 2x to 4x (this study). However, hot water-rock interaction experiments showed that volatile species such as As, Sb, Se and S can be extracted from greywacke in significant amounts (Ewers 1977).

Critical elements in volcanic fluids and rock are gleaned from melt inclusions and glass, and erupted lavas and tephras (2-4 in Figure 1A; e.g. Ewart et al. 1968; Reyes et al. 2012, Johnson et al. 2013; this study). Boron and Cl are more enriched in rhyolitic than andesitic melt inclusions. Melt inclusions show that pre-eruptive rhyolitic and andesitic magmatic fluids contain Fe, Ti, Co, Cu, V, Cr, Zn and Ni in various proportions but Mo, Hg, Pb and As appear to have a stronger affinity for rhyolite melts and Ge for andesite.

Erupted TVZ rhyolitic and andesitic lavas/tephra both show enrichment in Hg, As, B, and Ge relative to normal crustal abundances. However, Sb, Tl, Mo, Au, Cs, Li and Ba abundances are enhanced in rhyolite and I, Br, Se, Bi, Sc, Co and Cu in andesites, relative to the earth's crust (this study).

The volume of critical elements introduced to the surface by ash falls is illustrated by the 1995-1996 eruption of the andesitic Ruapehu volcano albeit mixed with materials from Crater Lake (this study). For a small eruptive episode of 0.04 km^3 of ash (Cronin et al. 1998), $\geq$1 kg each of Tl, Ag, Cd, Se, Cr, As, Li, Co, Ni, Pb, Cu, Zn, Mn, B and Fe together with F, Cl, and SO_4 was expelled from Ruapehu in less than a year.

Knowing that certain elements have a stronger affinity for rhyolite, andesite or greywacke in the TVZ may aide mining companies prospecting for critical elements in fluids. However, elemental affinities for specific rock compositions break down during hydrothermal or magmatic-hydrothermal water-rock interaction, evinced by leachate compositions from erupted ash at Ruapehu, that included materials from Crater Lake.

3.2 Water-rock interaction and critical elements in altered rock and fluid precipitates

Figure 1A shows some of the processes that enhance element deposition in the TVZ including (a) fluid mixing and neutralization of acid fluids, (b) phase separation and changes in redox conditions, (c) changes in temperature and pressure with depth or caused by hydrothermal brecciation and (d) water-rock interaction and rock dissolution.

Intensely altered rhyolite in surface hot springs, contain 2x to 200x, relative to fresh rhyolite, of most elements e.g., Cu, Zn, Sr, Ga, and Au and to 2x to >1000x of volatile elements (Tl, Hg, Sb and As). In contrast, moderately chloritized and silicified rhyolite altered at 270ºC at depth is only enriched by 2x-50x, relative to fresh rock, in Cu, V, Cr, P, Mn, Ti, Mg, Ca and Fe (this study).

At least 24 mineral precipitates have been identified in hot springs, well casings and well surface installations in the TVZ (Figure 1B) containing Fe, As, S, Cu, Sb, Zn, Ag, Te, Pb, Ag and Au (e.g. Weissberg, 1969; Brown, 1986; Krupp and Seward, 1987; Reyes et al. 2002; Pope et al. 2005; Simmons et al. 2016; this study). The main mineral deposited in wells, well surface installations and hot springs is silica, a "sponge" for a several elements including Li, B, Cr, Ni, Cu, Zn, As, Ag, Hg, Sb, Au, Rb and Cs (Brown, 1986; Reyes et al. 2002). Other substrates to which elements preferentially adhere to include biogenic material for Hg, Ge, As, Sb and Te (Hirner et al. 1998) and possibly pyrite and fahlore (e.g. Makovicky and Karup-Moller, 2017). Rare earths have been reported in hot spring silica sinters and rock formations at depth, enhanced where acid waters circulate (e.g. Wood, 2003).

In summary, the chemical compositions of melt inclusions, rock, mineral precipitates and ash leachates in the TVZ show (1) enhanced abundance of a wide number of critical elements including Te, Zn, Ga, As, Ge, Ag, Y, Sr, U, Cu, Cd, Co, Cr, Dy, Li, B, Mg, P, Sc, V, Ni, Zr, Nb, Mo, Sn, Sb, W, Au, Hg, Tl, Pb, Bi and Nd, (2) affinity of various elements for rhyolite or andesite, and (3) variations in element abundances in the rock with alteration intensity/degree of water-rock interaction, type and process, and fluid pH.

3.3 Fluid discharges

Not all elements in the rock have been analyzed or detected in the fluids. Except for halides, concentrations of most "critical" elements in TVZ aqueous fluids are lower than in the rock or precipitates from hydrothermal fluids. But there has been increased interest in extracting "critical" elements from fluids in the TVZ in the past 5 years.

To assess the potential of mining fluids, the annual mass of various "critical" elements produced by a typical geothermal system in the TVZ was calculated assuming a median flowrate of $3x10^6$ m^3/a (340 m^3/h) and a gas:aqueous fluid ratio of 3:7. The highest yield of elements, at >100kg/a include

from lowest to highest: Mo, Sb, Sr, W, Al, Cs, Rb, As, Li, Ca, B, Si and Na. There are two sets of elements that warrant further study: (1) Au, Ga, Tl, Ag and Ge, despite low yields at only ~1-75 kg/a, because of high market prices and (2) Rb and Cs because of high yield from fluids and high market prices. Amongst gases of economic interest in the TVZ are CO_2 mainly for food processing, C_2H_6 and He.

4 Conclusions

Without considering costs of extraction from fluids and mineral substrates, production and research, cut-off concentrations for mining elements, and current technological capabilities to extract elements from aqueous solutions or silica precipitates, a typical TVZ geothermal system contains ~NZ$850M/a worth of elements or ~NZ$19.5B/a for 23 active systems. The estimated value of Mo, As, Ag and CO_2 in fluids from one TVZ system is $10k-100k/a per element; 100k-1M/a for Au, C_2H_6, He, Ge, Tl and B and >1M/a for Li, Na, Cs, Rb and Si. Despite the presence of a wide variety of "critical" elements in TVZ hydrothermal fluids, only a few can be economically and technologically extracted at present e.g., Li, Si, possibly CO_2, and as world-wide supplies rapidly diminish, perhaps He.

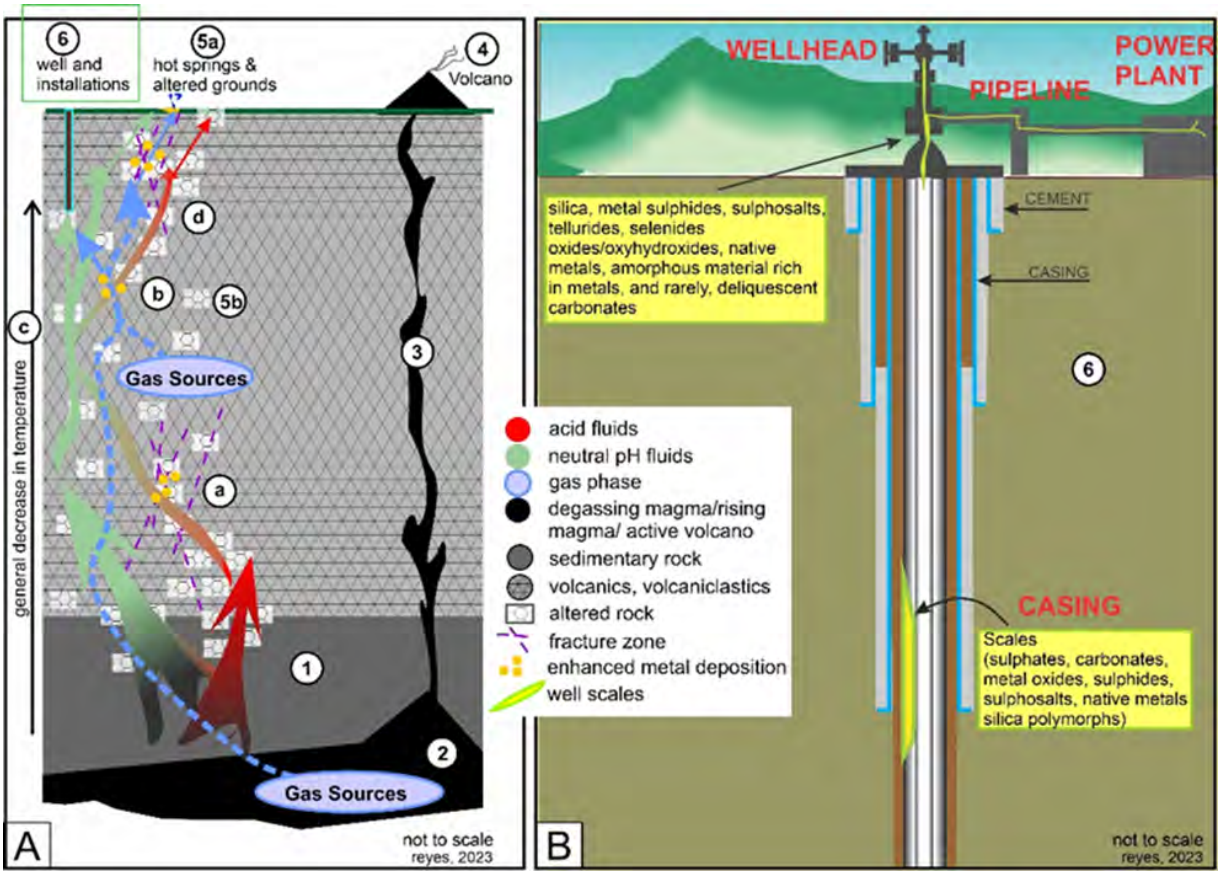

Figure 1. [A] Diagram showing major sources of critical elements in the TVZ marked by numbers and some sites of enhanced metal deposition in the rock formation (a, b, c and d), discussed in the text. Number 6 is shown in detail in [B] main sites and compositions of mineral deposition in a typical TVZ geothermal well and its surface installations (this study).

Acknowledgement

Part of this work was funded by the New Zealand Geothermal Future research programme.

References

Acocella V, Spinks, K, Cole, J, Nicol, A (2003) Oblique back arc rifting of Taupo Volcanic Zone, New Zealand Tectonics 22(4): 19-1 - 19-18

Best ME (2015) Mineral resources, Treatise on Geophysics. 11: 525-556

Bibby HM, Caldwell TG, Davey FJ, Webb TH (1995) Geophysical evidence on the structure of the Taupo Volcanic Zone and its hydrothermal circulation. JVGR, 68(1-3): 29-58.

Brown KL (1986) Gold deposition from geothermal discharges in New Zealand. Econ Geol 81: 979-983.

Cronin SJ, Hedley MJ, Neall VE, Smith RG (1998) Agronomic impact of tephra fallout from the 1995 and 1996 Ruapehu Volcano eruptions, New Zealand. Environ Geol 34(1): 21-30.

Ewart A, Taylor SR, Capp AC (1968) Trace and minor element geochemistry of the rhyolitic volcanic rocks, Central North Island, New Zealand, Contrib Min Petrol 18: 76-104.

Ewers, GR (1977) Experimental hot water-rock interaction and their significance to natural hydrothermal systems in New Zealand. Geochim Cosmochim Acta 41: 143-150.

Giggenbach WF (1995) Variations in the chemical and isotopic composition of fluids discharged over the Taupo Volcanic Zone. JVGR 68(1-3): 89-116.

Hedenquist JW, Henley RW (1985) The importance of CO2 on freezing point measurements of fluid inclusions:

evidence from active geothermal systems and implications for epithermal ore deposition. Econ Geol 80: 1379-1406.

Hirner AV, Feldman J, Krupp E, Grumping R, Goguel R, Cullen WR (1998) Metal(oid)organic compounds in geothermal gases and waters. Org Geochem 29(5-7): 1765-1778.

Johnson ER, Kamenetsky V, McPhie J (2013) The behaviour of metals (Pb, Zn, As, Mo, Cu) during crystallization and degassing of rhyolites from the Okataina Volcanic Centre, Taupo Volcanic Zone, New Zealand J Petrol 54(8): 1641-1659.

Krupp RE, Seward TM (1987) The Rotokawa geothermal system, New Zealand: an active epithermal gold-depositing environment, Econ Geol 82: 1109-1129.

Makovicky E, Karup-Moller, S (2017) Exploratory studies of substitutions in the tetrahedrite/tennantite-goldfieldite solid solution. Canadian Mineral 55: 233-244.

Pope JG, Brown KL (2014) Geochemistry of discharge at Waiotapu geothermal area, New Zealand- trace elements and temporal changes. Geothermics 51: 253-269.

Reyes AG, Trompetter WJ, Graham IJ (2012) Propensity for mineralization in volcanoes- evidence from melt inclusions. Intl J PIXE 22: 157−164.

Reyes AG, Trompetter WJ, Britten K, Searle J (2002) Mineral deposits in the Rotokawa geothermal pipelines, New Zealand. JVGR 119: 215-239.

Rowland JV, Sibson RH (2004) Structural controls on hydrothermal flow in a segmented rift system, Taupo Volcanic Zone, New Zealand. Geofluids4: 259-283.

Rowland JV, Simmons SF (2012) Hydrologic, magmatic, and tectonic controls on hydrothermal flow, Taupo Volcanic Zone, New Zealand: implications for the formation of epithermal vein deposits. Econ Geol 107: 427–457.

Simmons SF, Browne PRL (2000) Hydrothermal minerals and precious metals in the Broadlands-Ohaaki geothermal system: implications for understanding low-sulfidation epithermal environments Econ Geol 95: 971-999.

Simmons SF, Brown KL, Tutolo BM (2016) Hydrothermal transport of Ag, Au, Cu, Pb, Te, Zn, and other metals and metalloids in New Zealand geothermal systems: spatial patterns, fluid-mineral equilibria, and implications for epithermal mineralization, Econ Geol 111: 589-618.

Weissberg BG, Browne PRL, Seward TM (1979) Ore metals in active geothermal systems. In: Barnes HL (editor) Geochemistry of hydrothermal ore deposits, 738-780, John Wiley, New York.

Wilson CJN, Houghton BF, Pillans BJ, Weaver SD (1995) Taupo Volcanic Zone calc-alkaline tephras on the peralkaline Mayor Island volcano, New Zealand: identification and uses as marker horizons. JVGR 69(3-4): 303-311.

Wood SA (2003) The geochemistry of rare earth elements and yttrium in geothermal waters. In: Simmons SF, Graham I (editors) Volcanic, geothermal, and ore-forming fluids: rulers and witnesses of processes within the earth. SEG Special Publication 10: 133–158.

Ni-Co-As-Bi minerals in the Silius vein system, (SE Sardinia, Italy): The polymetallic evolution of a word-class fluorspar deposit

Ignazio Scano[1], Antonio Attardi[1], Fabrizio Cocco[1], Dario Fancello[1], Alessandro Murroni[2], Francesca Zara[1], Stefano Naitza[1]
[1]Università degli Studi di Cagliari, Dipartimento di Scienze Chimiche e Geologiche, Monserrato, Italy
[2]Mineraria Gerrei Srl, Silius, Italy

Abstract. The world-class Silius deposit (NE Sardinia, Italy), exploited for decades, represents a huge ENE-WSW to NE-SW directed vein system, characterized by abundant fluorite, minor barite, and Pb-(Zn-Cu-Fe) sulphides in quartz-carbonate gangue. This deposit shows many similarities to other European unconformity-related F-Ba districts linked to the regional-scale event of the breakup of Pangea, such as ore textures, low-temperature high-salinity fluids, and observed mineral assemblages. Besides fluorite, the mineralogy includes other critical raw materials (CRM) such as disseminated tiny LREE minerals and intergrowths of Ni-Co-Fe arsenides-sulpharsenides such as nickeline (NiAs), rammelsbergite ($NiAs_2$), gersdorffite (NiAsS), cobaltite (CoAsS) and arsenopyrite (FeAsS). Ni-Co assemblages, which were recently discovered in this deposit, were investigated by optical microscopy and SEM-EDS.

1 Introduction

In the last few years, the growing demand for critical raw materials, which are strategic and irreplaceable in many technological and industrial applications, led to a renewed interest in many deposits throughout Europe, even those that until recently were no longer considered worthy of exploitation. An example is the world-class Silius fluorspar deposit (Gerrei district, SE Sardinia, Italy), a hydrothermal vein system that was exploited for fluorite, galena, and barite for over 50 years and is currently on standby. The original size of the deposit was probably over 10 Mt of fluorspar ore; currently certified (proved) reserves consist of over 2.1 Mt at 32% CaF_2 and 3% Pb (Benz et al., 2001). Moreover, following the discovery of LREE minerals in the carbonate gangue, over 1200 tons of LREE are estimated to occur in the deposit (Mondillo et al. 2016, 2017). The reprise of mining led to the resumption of exploration activities, including new structural surveys and new studies on ore mineral associations, to improve the geological model of the deposit and the basic knowledge of its economic potential, particularly in the field of critical metals. This study initially focused on the less investigated sulphide portion of the ore, which led to the unexpected discovery of Ni-Co-Fe arsenide-sulpharsenide mineral associations in the lowest levels of the mine, at 400-500 m under the surface.

2 The Silius deposit

2.1 Geological and structural setting

The Silius mine is set in the External Nappe Zone of the Variscan basement of SE Sardinia. Country rocks are low-grade metamorphic rocks belonging to the Gerrei and Sàrrabus tectonic units, unconformably covered by Cenozoic sediments (Funedda et al. in press, Figure 1). Basement rocks consist of a strongly folded pre-Variscan succession, including a thick Cambrian-Lower Ordovician siliciclastic sequence, arc-related Middle Ordovician calc-alkaline felsic metavolcanics (the “Porfiroidi Auct.” Formation), Upper Ordovician siliciclastics., Silurian and Devonian black shales and meta-limestones.

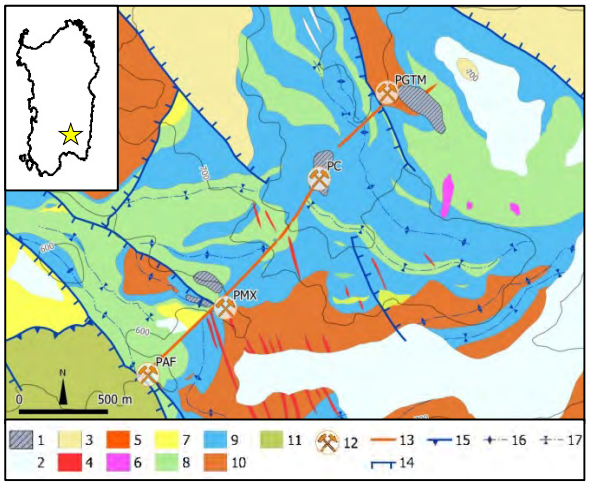

Figure 1. Geological sketch map of the Silius mine area. Legend: 1) Anthropic deposits. Hol.; 2) Recent sediments. Hol.; 3) Marine deposits. Low. Eoc.; 4) Granite porphyry dikes. Perm.; 5) Hydrothermal quartz veins Perm.; 6) Gabbro-diorites. Up. Carb.-Perm.; 7) Black shales and limestones. Sil.-Dev.; 8) Slates and metasandstones Up. Ord.; 9) Metarkose. Up. Ord.; 10) Porphyritic metarhyodacites. Mid. Ord.; 11) Metaquartzarenites. Cambr.-Ord.; 12) Mineshaft; 13) Silius mineralized vein; 14) Normal Fault; 15) Thrust; 16) Anticline fold; 17) Sincline fold

Late Variscan granitoids are poorly exposed in the area, being essentially represented by a large NW-SE swarm of Early Permian felsic dikes that crosses the basement detaching from the Sàrrabus pluton, which emerges more than 15 km further South. The Cenozoic sediments form a series of morphological plateaux resulting from an Eocene transgression over the Paleozoic basement.

The Variscan succession of the Gerrei Unit is located at the hanging wall of the regional "Villasalto Thrust", and it's organized in kilometres-scale recumbent folds verging towards the SW, with their parasitic folds occurring at any scale, producing an increase in the apparent thickness of the involved formations (particularly the Ordovician metavolcanics and metasandstones) and their repetition at depth. The Variscan post-collisional extension (late Carboniferous-Early Permian) resulted in the area as a widespread reactivation of thrust structures, with incremental development of low-angle to high-angle faults. A further reactivation of Paleozoic structures is documented by NW-SE, N-S and E-W directed faults associated with the Sardinian block rotation during Oligo-Miocene; these late structures determined the subdivision into blocks of the basement and the Eocene covers that currently mark the morphology of the area.

2.2 Geology of the deposit

The Silius vein system forms a pinch-and-swell structure, mainly hosted in the "*Porfiroidi Auct*." formation's felsic metavolcanics andOrdovician metasediments. The veins distinctly crosscut all the Variscan structures, including the Early Permian felsic dikes, defining a relative minimum age for the mineralizing event(s) (Natale 1969). The mineralised system consists of two principal parallel veins, namely the San Giorgio and San Giuseppe veins. They strike NE-SW to ENE-WSW, steeply dipping towards NW and coalescing at a depth of about 350 m (about 350m a.s.l.), where they reach 16 m in thickness against the medium thickness of 1 to 3.5 m of a single vein. The overall geometry of the veins, the structural context, and other kinematic features indicate a dextral sense of shearing, prevalent over the vertical component, which kinematic remains unclear, but presumably later reactivated as a high angle normal slip fault. The continuity of the vein system is interrupted to the NE and SW by two major NW-SE normal faults, which give the deposit a trapezoidal shape, with an extension of about 2km on the surface and almost 4km at the deepest exploitation level 100 (the name of the level refers to its location above sea level). Several minor normal faults with a strike-slip component crosscut the deposit at various angles, displacing it from null to about 2m.

The San Giorgio vein formed first and is characterised by alternating bands of chalcedony, pink fluorite, barite, and calcite. The San Giuseppe vein is also banded and shows several generations of fluorite, calcite, and galena (Boni et al. 2009, Mondillo et al. 2016). Both veins show early banded textures, followed by breccias and cockade textures. At the deposit scale, the mineralisation displays an evident vertical compositional evolution. In the shallower part of the deposit, the ore consists of an association of barite (prevalent) + fluorite + quartz ± calcite; the middle zone shows an increase in fluorite content (25% and more), along with calcite and sulphides, with the almost total disappearance of barite; at-depth, calcite is often dolomitised, fluorite is always > 30% and the ore shows a marked increase in sulphide content, mainly galena, observed as veins, aggregates and disseminations (Marino, 1996). Fluid inclusion studies on fluorite and calcite (Boni et al. 2009) indicate ore formation at temperatures in the range of 120–180 °C from fluids with salinities reaching up to ~18wt.% NaCl eq. In addition, Sr-Nd isotopic ratios and (REE + Y) contents in fluorite suggest a crustal origin of mineralising fluids likely from mixing in different proportions of evaporated seawater brines with fluids from the Paleozoic basement and Late Variscan magmatic rocks (Castorina et al. 2020). Moreover, Sm/Nd dating of carbonate gangue of the San Giuseppe vein by Castorina et al. (2020) provided an age of 294±40 Ma, but the Authors suggest as most likely an age around 270 Ma.

3 Methodology

New underground surveys and samplings were performed in three different sites at the 100 and 200 levels of the Silius mine (namely, from E to W, Pozzo Centrale, Muscadroxiu and S'Acqua Frida mineworks) mostly involving the Pb-Zn-Cu sulphide assemblages. The collected samples were studied both by optical microscopy (transmitted and reflected polarized light) and scanning electron microscopy (SEM-EDS), using a FEI Quanta 200 equipped with a ThermoFisher Ultradry EDS detector at CeSAR laboratories of Università di Cagliari (Italy) under high vacuum conditions, acceleration voltage 25–30 Kv, spot size 5 µm.

4. New observations on the Silius sulphide ore: the Ni-Co and Bi assemblages

The sulphide ore of Silius shows a simple mineralogy, mainly represented by galena, sphalerite, and chalcopyrite, followed by pyrite/marcasite (Table 1). Remarkably, no traces of fahlore, a mineral that is commonly associated with galena ores in E Sardinia fluorite-bearing deposits, has been found so far. Galena is the most abundant sulphide; sphalerite is subordinate, found in transparent (colourless to yellow/brown in transmitted light), sometimes idiomorphic individuals and zoned aggregates. Chalcopyrite is much less common and found either alone or intergrown with sphalerite. Marcasite is the last to crystallise and occurs in veinlets that crosscut all the precedent sulphide minerals. It is particularly abundant in the samples from the Pozzo Centrale mineworks sampling zone and contains some relics of pyrite.

In this study, striking evidence derived from optical microscopy work was the discovery of a Ni-Co arsenide/sulpharsenide assemblage, reported here for the first time. This peculiar assemblage was found in samples from every sampling site as

disseminated tiny and complex intergrowths of various Ni-Co-Fe-As-S phases (Figs. 2). They are mainly associated with sulphides (chalcopyrite and less frequently galena) or dispersed in quartz gangue (Figure 2). On SEM-EDS semiquantitative analyses Ni-Co-Fe phases display a large compositional variation (Figure 2): mono- and di-arsenides such as nickeline (NiAs) or rammelsbergite ($NiAs_2$) are overgrown by various mixtures and solid solutions of Ni-Co-Fe sulpharsenides such as gersdorffite (NiAsS), cobaltite (CoAsS) and arsenopyrite (FeAsS). Ni-Co-Fe sulpharsenides also occur in mono- and di-arsenide-free intergrowths, or partly replaced by sulphides.

Rare Bi minerals were found as inclusions in the Ni-Co-Fe arsenide/sulpharsenide assemblages or as complex intergrowths dispersed in fluorite gangue (Figure 3). They mainly consist of probable bismuthinite and of an unknown phase containing bismuth, lead, copper, sulphur and oxygen (possibly a sulphosalt). In the paragenetic succession of the Silius metallic ore, the Bi and Ni-Co arsenide/sulpharsenide assemblage comes first before the sulphides. In Table 1, a first attempt to summarize these observations is shown.

Ore minerals	
Bi minerals	
Ni-Co arsenides/sulfarsenides	
Sphalerite	
Chalcopyrite	
Galena	
Pyrite/marcasite	

Table 1. The schematic paragenetic sequence of the ore mineral assemblages of the Silius deposit.

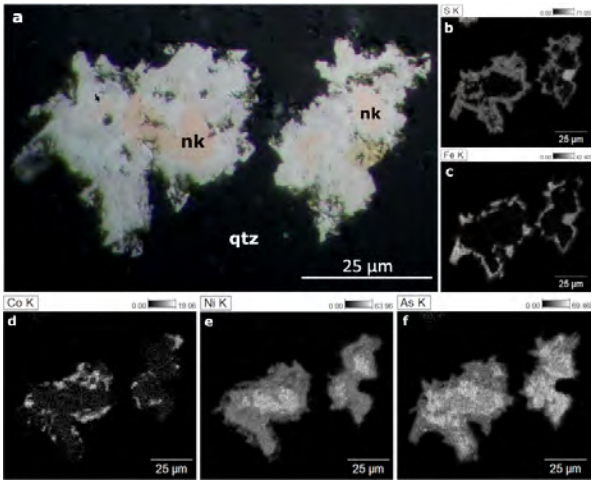

Figure 2. Reflected light photomicrograph (a) and SEM-EDS maps (b-f) showing a complex intergrowth of Ni-Co-Fe arsenides-sulpharsenides in quartz gangue. Nickeline (**nk:** pink) constitutes the core of the aggregate, rimmmed by rammelsbergite (pure white) overgrown by a complex mixture of Ni-Co-Fe sulpharsenides (gersdorffite, cobaltite, arsenopyryte).

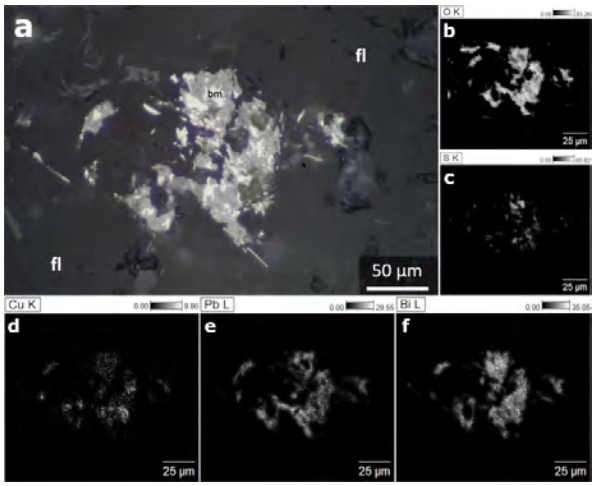

Figure 3. reflected light photomicrograph (a) and SEM-EDS maps (b-f) of an aggregate of Bi minerals (probable bismuthinite (bm) + a Bi-Pb-Cu sulphosalt) in fluorite gangue.

5 Discussion and Conclusions

5.1 Insights for future explorations: polymetallic evolution of the Silius deposit

The geological and mineralogical studies of this research confirm the high prospectivity of the Silius deposit. In detail, the study indicates that a) the ore composition presents an evident vertical variation, becoming progressively more complex with the deepening of the mineworks, and the deposit seems to acquire a true polymetallic character at depth; b) the CRM potential of the deposit, after the LREE phases (synchisite and xenotime-Y; Mondillo et al. 2016) is further expanded with the discovery of Ni-Co arsenides and Bi phases. Moreover, a comparison with the previous literature on fluorite-bearing polymetallic deposits in the Gerrei-Sàrrabus district (i.e., the so-called “Sàrrabus silver lode”; Cortecci et al. 1987 and references therein) in which Ni-Co sulpharsenides were found associated with abundant Ag sulphides and sulphosalts, suggest that this newly found Ni-Co mineral association could be considered as a predictive tool for future exploration in the deeper parts of the Silius deposit, as they may be indicative of the proximity of possible Ag-rich zones of the ore.

5.2 Metallogenic relevance of Ni-Co-Bi discovery: framing the Silius deposit at regional and European scale

Low-temperature (LT) hydrothermal veins are widely spread in the Paleozoic basement of Sardinia and are interpreted to have formed from circulating fluids during the Permian-Triassic time (Boni et al. 1992; 2002; 2009; Castorina et al. 2020). Recent studies on the Arburèse district of SW Sardinia

(Moroni et al. 2019a) allowed expanding this LT mineralisation dataset to the large Montevecchio vein system, whose southern branch has been fully included in the five-element (Ni-Co-As-Bi-Ag) class of hydrothermal deposits, hosting a rich Ni-Co arsenide-sulpharsenide mineral association (Moroni et al., 2019b). Although different in many compositional aspects (Montevecchio polymetallic sulphide ore has a quartz-carbonate gangue, with very rare fluorite), the new findings in the Silius deposit tend to bring these two types of mineralisation closer together, as also suggested by Boni et al. (2009) based on fluid inclusion studies. Thus, a wider metallogenic framework for the Permian-Triassic period in Sardinia, during which it is possible that multiple pulses of shallow crustal fluids mixed with seawater-derived brines (Cortecci et al., 1987; Castorina et al., 2020) is proposed. The reasons that explain the compositional differences between the different LT systems (i.e., Silius-type vs Montevecchio or five-element-type compositions) are speculative, but differences in basement rock geochemistry may have been a critical factor. The LT mineralising fluids that have led to the formation of the fluorite-rich Silius-type ores may have been derived from various F-bearing granite suites of the Sàrrabus pluton that intruded the Variscan basement in Early Permian (Secchi et al. 2021). The main features of the Silius deposit, including ore textures, mineral assemblages, and derivation from low-temperature and highly saline fluids resulting from the mixing of fluids of different origins, allow its comparison with the Mesozoic “unconformity-type” Ba-F and polymetallic deposits of Central Europe (Burisch et al. 2022). These latter were recently referred to late Permian to Cretaceous continental-scale metallogenic events related to the breakup of the Pangea supercontinent and the progressive opening of the Tethys and the North Atlantic Ocean (Burisch et al. 2022). In this large picture, and inside this complex family of deposits, the Silius vein system would therefore assume primary importance.

Acknowledgements

This work was supported by the RAS/FdS grant “Sustainable land management: the tools of geology for the environment” (F72F16003080002). The Authors acknowledge the Mineraria Gerrei Srl and G. Mura, Director of the Silius mine for IGEA SpA, for having allowed us to sample in the underground levels. Thanks are also due to Prof. G.B. De Giudici for SEM-EDS analyses, and equipment kindly provided by the CeSAR laboratory at the University of Cagliari.

References

Benz JP, Féraud J, Save M, Tréhin JL (2001) Expertise technico-économique de la mine de fluorine de Silius (Sardaigne) Rapport final: évaluation des réserves au 27.6.2001 et études de rentabilité. Rapport BRGM/RC-51042-FR

Boni M, Balassone G, Fedele L, Mondillo N (2009) Post-Variscan hydrothermal activity and ore deposits in southern Sardinia (Italy): selected examples from Gerrei (Silius Vein System) and the Iglesiente district. Per Mineral 78: 19–35

Boni M, Iannace A, Köppel V, Hansmann W, Früh-Green G (1992) Late- to post-Hercynian hydrothermal activity and mineralization in SW Sardinia. Econ Geol 87: 2113-2137

Boni M, Muchez P, Schneider J (2002) Permo-Mesozoic multiple fluid flow and ore deposits in Sardinia: a comparison with post-Variscan mineralization of Western Europe. Geol Soc Spec Pub 204: 199 – 211

Burisch M, Frenzel M, Seibel H, Gruber A, Oelze M, Pfänder JA, Sanchez-Garrido C, Gutzmer J (2021) Li-Co–Ni-Mn-(REE) veins of the Western Erzgebirge, Germany—a potential source of battery raw materials. Miner Deposita 56: 1223–1238

Burisch M, Markl G, Gutzmer J (2022) Breakup with benefits - hydrothermal mineral systems related to the disintegration of a supercontinent. Earth Planet Sci Lett 580: 117373

Castorina F, Masi, U, Gorello, I (2020) Rare earth element and Sr-Nd isotopic evidence for the origin of fluorite from the Silius vein deposit (southeastern Sardinia, Italy). J Geoch Explor 215: 106535

Cortecci G, Reyes E, Leone G, Turi, B (1987) Sulfur, Oxygen, Carbon, and Strontium Isotope Geochemistry of the Sarrabus-Gerrei Mining District, Southeastern Sardinia, Italy. Econ Geol 82: 1592–1610

Funedda A, Carmignani L, Pertusati PC, Forci A, Calzia P, Marongiu F, Pisanu G, Serra M (in print) Note illustrative Foglio 548 Senorbì. Note illustrative della Carta Geologica d’Italia 1:50000, ISPRA – RAS

Marino, A (1997) Il giacimento a fluorite e galena di Silius (Cagliari). C. Marini (Ed.): Le materie prime minerali sardi, problemi e prospettive, CUEC, Cagliari 258-268

Mondillo N, Boni M, Balassone G, Spoleto S, Stellato F, Marino A, Santoro L, Spratt J (2016) Rare earth elements (REE)—Minerals in the Silius fluorite vein system (Sardinia, Italy). Ore Geol Rev 74, 211–224

Mondillo N, Balassone G, Boni M, Marino A, Arfè G (2017) Evaluation of the amount of rare earth elements -REE in the Silius fluorite vein system (SE Sardinia, Italy). Per Mineral 86: 121-132

Moroni M, Naitza S, Ruggieri G, Aquino A, Costagliola P, De Giudici G, Caruso S, Ferrari E, Fiorentini M, Lattanzi P (2019a) The Pb-Zn-Ag vein system at Montevecchio-Ingurtosu, southwestern Sardinia, Italy: A summary of previous knowledge and new mineralogical, fluid inclusion, and isotopic data. Ore Geol Rev 115

Moroni M, Rossetti P, Naitza S, Magnani L, Ruggieri G, Aquino A, Tartarotti P, Franklin A, Ferrari E, Castelli D (2019b) Factors Controlling Hydrothermal Nickel and Cobalt Mineralization—Some Suggestions from Historical Ore Deposits in Italy. Minerals 9: 429

Natale P (1969) Il giacimento di Silius nel Gerrei. Boll Ass Miner Subalpina 6: 1–35

Secchi F, Naitza S, Oggiano G, Cuccuru S, Puccini A, Conte AM, Giovanardi T, Mazzucchelli M (2021) Geology of late-Variscan Sàrrabus pluton (south-eastern Sardinia, Italy). J Maps 17: 591-606

Critical Metal Resources Required for the Green Energy Transition

Adam C. Simon[1], Lawrence Cathles[2]
[1]Department of Earth & Environmental Sciences, University of Michigan, Michigan, U.S.A.
[2]Department of Earth & Atmospheric Sciences, Cornell University, New York, U.S.A.

Abstract. What does carbon neutrality mean? What does it require? Is it possible? In this presentation, I will discuss carbon neutrality through the lens of metal resources required to transition from a global energy infrastructure dependent on coal, natural gas, and oil, to one entirely reliant on a combination of photovoltaic solar, wind turbines, battery electric vehicles and grid-scale battery storage. Manufacturing and deploying those renewable energy resources requires dozens of metals, including cobalt, copper, graphite, lithium, manganese, nickel, rare earths, and many others. What types of mineral deposits do those metals come from? What are the geologic constraints on their availability? What are the economic constraints on their availability? What are the environmental permitting constraints on the timeframe for production and delivery to market? What are the political constraints on their availability? Analysis of the current mining supply of all metals required for the green energy transition, and the anticipated production from permitted mines at various stages of development, indicates that the demand for all critical metals required for the green energy transition will exceed supply by 2030. The green energy transition requires production of metals from new mineral deposits on an unprecedented scale.

1 Introduction

Our global society is electric, and copper is the backbone that delivers the electricity. Globally, society uses about 300% more copper every year than it did in 1960 (Figure 1) and demand for copper will increase significantly as renewable energy infrastructure is built (Figure 2).

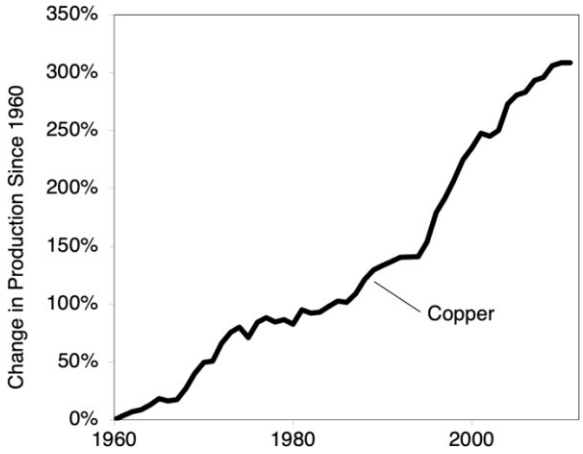

Figure 1. Change in global production (consumption) of copper relative to the year 1960 (Kesler and Simon, 2015).

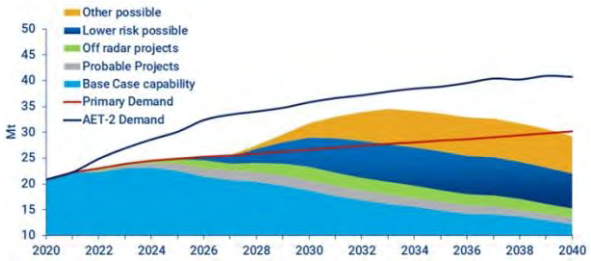

Figure 2. Global copper demand, copper production from operating mines and proposed new mines (Wood Mackenzie, 2023)

For example, using data for the United States, whichis 4% of the global population and consumes 15% ofglobal energy, achieving carbon neutrality by 2050 requires increasing the number of wind turbines andphotovoltaic solar by 5%/y over current levels. This requires 115,000 tonnes per year of copper for windturbines and 685,000 tonnes per year more copper for photovoltaic solar panels. Sixteen million light duty vehicles are sold annually. Replacing these vehicles with battery electric vehicles requires 960,000 tonnes per year more copper. To put this in perspective, the Bingham Canyon porphyry copper mine in Utah produced 144,000 tonnes of copper in2022. Thus, to support just these modest stepstoward a green economy would require the U.S. put 12 new Bingham Canyon copper mines intoproduction each year for the next two decades. Thisseems a practical impossibility. Humans currently extract about 22 million tonnes of copper annually from 250 copper mines operating in 40 countries (Figure 3).

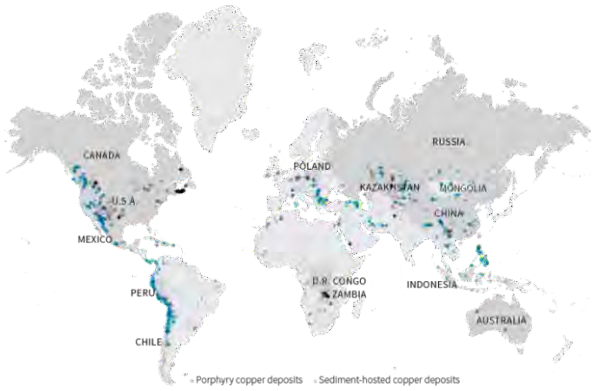

Figure 3. Global porphyry copper mines and sediment copper mines (Thomson Reuters 2023).

Replacing coal, oil, and natural gas, which together account for 85% of global primary energy supply, with a combination of photovoltaic solar, wind turbines, battery electric vehicles, grid-scale batterystorage and significantly expanded electrical grids, will require that annual production of copper increase by at least 50%. The magnitude of this challenge is illustrated in Figure 4 for all countries.

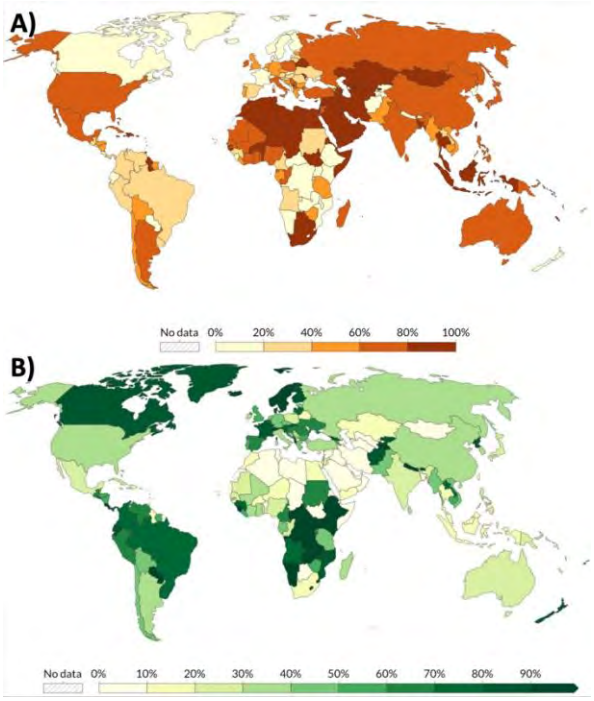

Figure 5. Current percent of total energy met by the sum of coal, oil and natural gas (A) and percent of electricity met by the sum of hydropower, solar, wind, biomass & waste, geothermal, wave, and tidal sources (Our World in Data 2023).

This is not possible from currently operating or planned mines and, considering that permitting and development of a new copper mine takes an average of 16 years, it is projected that there will be an annual global copper shortage of about 10 million tonnes by 2030. In fact, by 2030 there will be a global shortage of cobalt, copper, graphite, lithium, manganese, nickel, dysprosium, neodymium, praseodymium, terbium, and every other metal required for the green energy transition (Figure 5).

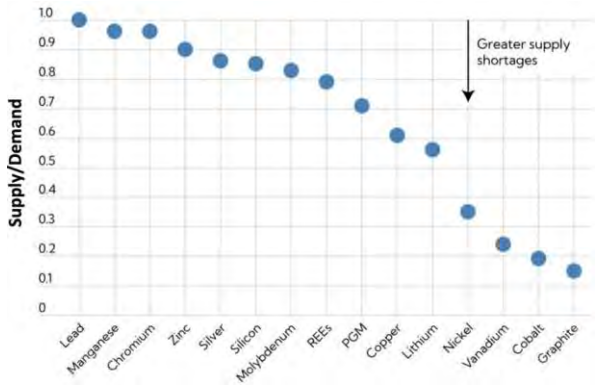

Figure 5. Ratio of supply to demand for energy critical metals required for the green energy transition (IMF, 2021).

These projections just consider the energy transition. They do not include the resources needed to bring the underdeveloped world up to developed world levels of energy use. This is illustrated in Figure 6.

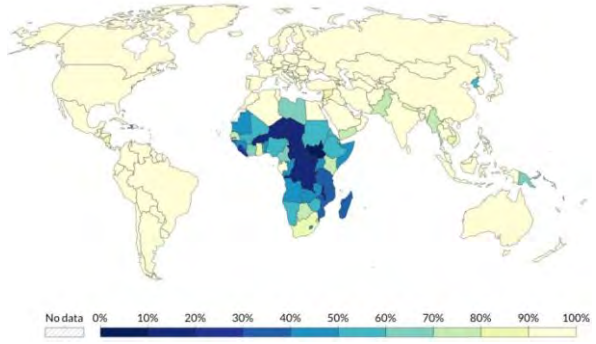

Figure 6. Access to electricity (Our World in Data 2023).

2 Conclusions

It will not be possible to achieve carbon neutrality by building photovoltaic solar and wind energy infrastructure on the timescale established by the International Panel on Climate Change (IPCC, 2023) enough to achieve the stated policy goals of for carbon neutrality. Further, for equity and feasibility, we must consider zero carbon strategies that take the pressure off resource supply.

References

IMF (2021) https://www.imf.org/en/Blogs/Articles/2021/12/08/metals demand-from-energy-transition-may-top-current-global supply. Accessed online 14 March 2023

IPCC (2023) AR6 Synthesis Report: Climate Change 2023. https://www.ipcc.ch/report/sixth-assessment-report cycle/. Accessed online 14 March 2023

Kesler, S.E., Simon, A.C. (2015) Mineral Resources, Economics, and the Environment. Cambridge Press.

Our World in Data based on BP Statistical Review of World Energy (2023); Our World in Data based on Ember's Yearly Electricity Data (2023); Our World in Data based on Ember's European Electricity Review (2022)

Thomson Reuters (2023) http://graphics.thomsonreuters.com/15/chile copper/index.html. Accessed online 14 March 2023

Wood Mackenzie (2021) https://www.woodmac.com/news/opinion/will-a-lack-of- supply-growth-come-back-to-bite-the-copper-industry/. Accessed online 14 March 2023

Hyperspectral cathodoluminescence of REE-bearing zirconosilicate minerals from Pajarito Mountain, USA

Paul Slezak[1], Siri L. Simonsen[2], Franziska D.H. Wilke[3], Dave Chew[4], Richard Wendlandt[5], Michael Berger[5], Murray W. Hitzman[1]

[1]Irish Centre for Research in Applied Geosciences, School of Earth Science, University College Dublin, Dublin 4, Ireland
[2]Department of Geosciences, University of Oslo, P.O. Box 1047, Blindern, N-0316 Oslo, Norway
[3]GFZ German Research Centre for Geosciences, Telegrafenberg, 14473 Potsdam, Germany
[4]Department of Geology, School of Natural Sciences, Trinity College Dublin, Dublin 2, Ireland
[5]Department of Geology and Geological Engineering, Colorado School of Mines, Golden, CO 80401 USA

Abstract. Agpaites are rare igneous rock types containing minerals abundant in high field strength elements (HFSE), rare earth elements (REE), and a variety of other critical metals, making them potentially important resources for critical raw materials. New Mexico (USA) hosts the layered Pajarito Mountain agpaitic complex (PMAC), which is prospective for Y and Zr hosted in abundant eudialyte as a primary cumulus phase. Hyperspectral cathodoluminescence (HyCL) shows that low luminescent minerals such as eudialyte have spectra in the infrared (e.g. 1.37 eV and 1.40 eV), suggesting the presence of Nd^{3+}. Eudialyte has been altered to Ca-zirconosilicate minerals, like gittinsite, which are highly luminescent and contains distinct light and dark CL zones. The lighter zones have much higher counts and peaks from ~2.0 eV to ~4.0 eV and may be related Eu^{3+}, Sm^{3+}, and/or Tb^{3+} to whereas the darker zones show an anomalous, prominent doublet at 1.25 eV and 1.26 eV. Hyperspectral CL imaging, spectral deconvolution, and activator identification provide valuable insights into zirconosilicate chemistry, elemental zonation, and potential element mobility related to alteration, especially regarding highly luminescent and critical metals such as the REE.

1 Introduction

Agpaites are rare, peralkaline igneous rocks — those defined as having a molar ratio of (Na + K)/Al > 1— that typically contain significant amounts of HFSE occurring in complex Na-Ca-HFSE minerals such as the eudialyte group minerals (EGM; Le Maitre et al. 2002; Marks and Markl 2017). Agpaitic rocks may also contain significant amounts of large ionic lithophile elements (LILE), halogens, and REE. Though they typically have lower REE grades than other alkaline igneous rocks such as carbonatites, they may contain higher REE tonnages overall and are also important sources of HFSE in addition to other important commodities including Li, Be, Sn, Ga, and Zn (Wall 2014; Marks and Markl 2017), making them potentially important sources of critical metals for technology items and green energy production (Weng et al 2015). Given the potential for a wide range in valuable elements in these rocks, many of which are critical raw materials (CRM), it is unsurprising that several agpaites have been delineated into mineral deposits such as Ilímaussaq (Greenland), Toongi (Australia), Nechalacho (Canada) and even mined, as is the case with Khibina and Lovozero (Russia; Marks and Markl 2015; Spandler et al. 2016; Möller and Williams-Jones 2016; Kalashnikov et al. 2016).

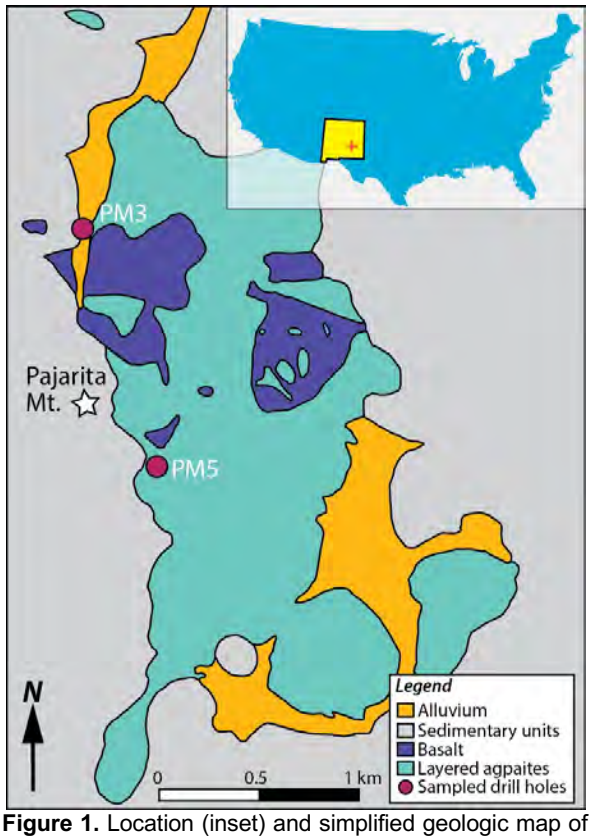

Figure 1. Location (inset) and simplified geologic map of the Pajarito Mountain agpaitic complex showing locations of drillholes PM3 and PM5 (from which the samples in this study were obtained) that intersected the layered intrusions (Modified from Jacobson, 1986; Berger, 2018).

The United States also hosts several agpaitic complexes, most of which are < 200 Ma in age (Marks and Markl 2017 and references therein). The PMAC is one of two Mesoproterozoic agpaitic complexes in the United States (Kelley 1968; Bauer and Pollock 1993). It is located in south-central New Mexico (Fig. 1) and was initially explored in the 1980s and 1990s by Molycorp for Y and Zr with more recent drilling and exploration conducted by the US Division of Energy and Mineral Development (DEMD) on behalf of the Mescalero Apache Tribe (Berger 2018). The drilling conducted by the DEMD and recent work by Berger (2018) indicated it is a layered complex and identified abundant eudialyte $[Na_{15}Ca_6Fe_3Zr_3Si(Si_{25}O_{73})(O,OH,H_2O)_3(Cl,OH)_2]$ as a rock-forming mineral in several layers. This study utilises a combination of petrographic techniques

and HyCL data to elucidate the evolution of the system and the origins of the eudialyte mineralisation, and its critical metal deportment within the eudialyte crystals. Since some critical metals, especially REE, are more desirable than others, identifying the location of specific elements at the mineral scale is important for processing and geometallurgy.

2 Geologic background

The PMAC consists of multiple layers of cumulate, peralkaline intrusions hosted in the southern region of a Grenvillian-aged A-type magmatic belt (see Bickford et al. 2000) and have an age range of 1155 ±25 to 1200 ±25 Ma obtained using K–Ar and Rb–Sr, respectively, on alkali amphiboles and feldspars (Kelley 1968; Bauer and Pollock 1993). The PMAC units are overlain and juxtaposed against younger Phanerozoic sedimentary units, all of which were uplifted during the Permian Pedernal uplift (Kottlowski 1985).

3 Methods

Samples were first analysed at University College Dublin (Ireland) using a Nikon Eclipse LV100NPol optical microscope. Backscattered electron images (BSE) and electron dispersive spectroscopy (EDS) were acquired using a JEOL Superprobe JXA-8230 at GFZ Potsdam (Germany).

Areas of interest were analysed using a Hitachi SU5000 FEG-SEM coupled to a Delmic Sparc HyCL unit at the University of Oslo (Norway). Operating conditions for eudialyte were set to 15 kV, a spot intensity of 50, and an exposure time of 200 ms. Other minerals were analysed at 10 kV, a spot intensity of 50, and an exposure time of 20 ms. Background spectra were obtained from both analytical settings (i.e. 15 kV at 200 ms and 10 kV at 20 ms) for spectral correction and processing. Images were processed and spectral data exported using Delmic's Odemis Viewer. The spectral data were deconvoluted using CSIRO's OpticalFit 21.x (Torpy and Wilson 2008).

4 Petrography

The different cumulate layered units comprising the PMAC have previously been divided into 4 groups by Berger (2018), which all consist of variable proportions of alkali feldspar, eudialyte, arfvedsonite, quartz with minor amounts of apatite and fluorite.

Here we examine PM5-257.25, which is an orthocumulate rock (Type II from Berger 2018) comprised of cumulus alkali feldspar and eudialyte with late cumulus to intercumulus arfvedsonite and intercumulus quartz. The other principal sample from this study is PM3-330.75, which is a mesocumulate rock (Type I from Berger 2018) made of cumulus eudialyte with lesser amounts of alkali feldspars and intercumulus quartz and arfvedsonite.

In all samples, the alkali feldspars are always an early cumulus phase comprised of euhedral albite crystal laths typically ranging in size from 350 µm up to 1000 µm (Fig. 2a) with occasional megacrysts up to 2500 µm. Eudialyte occurs in variable amounts (i.e. it is much more predominant in PM3-330.75) also as a cumulate phase and occasionally as oikocrysts (enveloping apatite). It is often found in higher abundances where quartz is also present. Eudialyte commonly occurs as euhedral, prismatic crystals ranging from 400 µm up to 1100 µm (Fig. 2a). Arfvedsonite is present as a late cumulus and as an early intercumulus phase (Fig. 2a,b). It is typically subhedral to anhedral an occasionally oikocrystic with respect to apatite. Arfvedsonite crystals range in size from 200 µm to 3000 µm. Quartz of variable sizes always occurs as an intercumulus phase (Fig. 2b,c). Apatite occurs as small (75 µm to 200 µm) ovoid crystals, commonly as chadacrysts in eudialyte and arfvedsonite. Fluorite is also present in trace amounts as prismatic, euhedral crystals up to 200 µm in diameter and is typically associated with the quartz-rich domains.

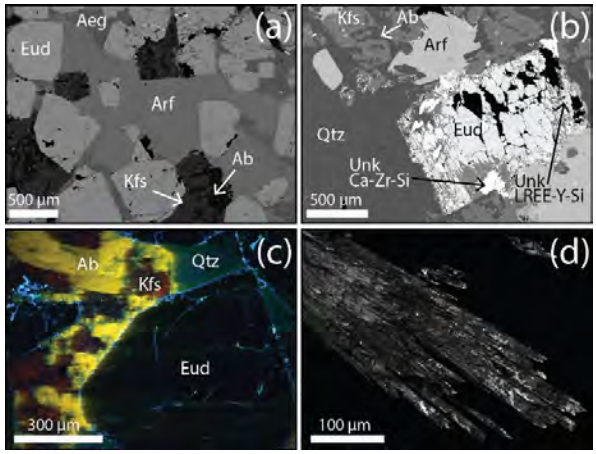

Figure 2. a BSE image from the mesocumulate sample PM3-330.75 (Type I) with cumulus eudialyte and alkali feldspar with intercumulus arfvedsonite displaying minor aegirine alteration. **b** BSE image of the orthocumulate sample PM5-257.25 (Type II) of eudialyte altered to unknown Ca-zirconosilicate and an unknown LREE-Y-silicate minerals. **c** HyCL image of PM3-330.75 with RGB overlay showing prominence of alkali feldspar luminescence compared to quartz and eudialyte. Blue areas are artifacts from cracks and crystal margins. **d** HyCL image of sample PM5-257.25 of an example Ca-zirconosilicate (likely gittinsite) mineral illustrating light and dark luminescent zones. Ab = albite, Aeg = aegirine, Arf = arfvedsonite, Eud = eudialyte, Kfs = potassium feldspar, Qtz = quartz.

Samples display consistent alteration with albite ubiquitously being replaced by patchy, tartan-twinned potassium feldspar (Fig. 2a-c). Arfvedsonite commonly displays minor alteration to aegirine along its crystal margins (Fig. 2a). Moderate to complete alteration to aegirine is present in some other samples but is less common. Eudialyte is occasionally altered (e.g. sample PM5-257.25; Fig.

2b) to a few unknown Ca-zirconosilicate minerals with 2nd order birefringence and crystal lath splays, some of which are likely gittinsite [$CaZrSi_2O_7$], as well as other hydrous and/or carbonated phases (Fig. 2b,d). Eudialyte also alters to an unknown LREE-Y-silicate mineral (Fig. 2b) and rarely, monazite.

5 Spectra results

Hyperspectral CL is a useful tool not only for identifying luminescent features (e.g. REE activators) in minerals outside the visible spectrum (i.e ultraviolet and infrared), but also for acquiring the mineral spectra on different luminescent zones (e.g. MacRae et al. 2012; 2013). Here we present the HyCL spectra on minerals that are not thought to traditionally luminesce, such as eudialyte. In addition we present spectral data on luminescent alteration minerals, like gittinsite, which display small, complex zonation under CL.

5.1 Eudialyte spectra

Compared to other minerals such as albite and potassium feldspar, eudialyte appears to not readily luminesce (Fig. 2c). However, HyCL scans show that eudialyte does have a spectrum (Fig. 3), albeit with count rates several orders of magnitude lower than the associated feldspars (e.g. 20,000 – 40,000 counts for feldspars compared to 80 counts for eudialyte under the same analytical conditions). By focusing on the eudialyte, we were able to obtain spectra (see Fig. 3) illustrating that eudialyte has several prominent peaks outside the visible range in the infrared at 1.27 eV, 1.37 eV, and 1.40 eV.

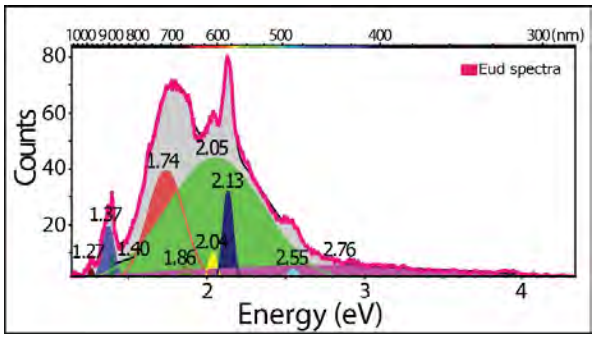

Figure 3. Example eudialyte spectra from PM3-330.75

5.2 Ca-zirconosilicate spectra

Though eudialyte is not the most luminescent mineral in the PMAC, some of its alteration assemblages display significant luminescence (see Fig. 2d), including an unknown Ca-zirconosilicate minerals (potentially gittinsite as determined by EDS). Figure 4a illustrates the difference in counts from the light and dark luminescent zones from Ca-zirconosilicates in Figure 2d. The light zones have significantly higher counts compared to the dark zones except near the 1.26 eV location, which is more prominent in the dark zones (Fig. 4a). This peak only appears as a small bump in the light zones (Fig. 4b), but in the dark zones consists of a distinct doublet at 1.25 eV and 1.25 eV (Fig. 4c). Both spectra show prominent peaks near 2.0 eV. When the spectra are deconvoluted, activators appear in the light and dark zones at or near 1.26 eV, 2.06 eV, 2.78 eV, 3.74 eV, and 4.12 eV (Fig. 4b,c), suggesting similar activators in both zones. However, the light zones have much more pronounced peaks near 3.74 and 4.12 eV (Fig. 4b).

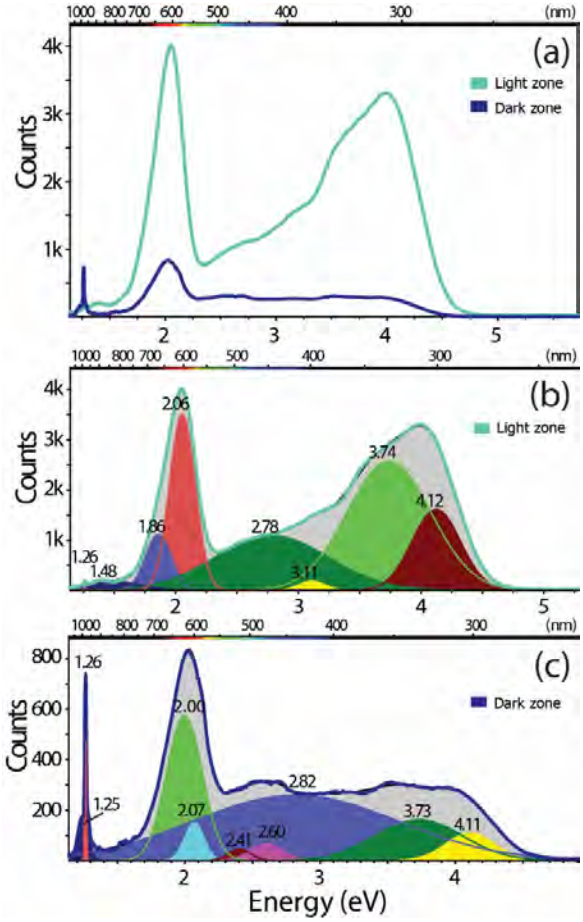

Figure 4. a Comparison of light and dark luminescent zones from the Ca-zirconosilicates in sample PM5-257.25. **b** deconvoluted light CL zone (see Fig. 2d for reference). **c** Deconvoluted dark CL zone (see Fig. 2d for reference)

6 Conclusions

Though eudialyte is typically not analysed for luminescence, many of the spectral peaks in this study are likely associated with REE activators since REE^{3+} activators tend to occur at similar wavelengths/energies in different host materials and minerals (Lenz et al. 2013). The doublet peak at 1.37 eV and 1.40 eV in eudialyte from PM3-330.75 may be attributed to Nd^{3+}. It also exhibits a potential low-level activator in the infrared (i.e. the broad peak centred at 2.76 eV), which may be associated with Y^{3+}(MacRae and Wilson 2008; Lenz et al. 2018).

Ca-zirconosilicate luminescence was first documented by Roelofsen and Veblen (1999) in samples from Strange Lake (Canada). They

described gittinsite as “orange to brownish-orange” under optical CL, but no spectra were captured in their study. Several studies on synthetic gittinsite crystals have been analysed for phosphorescent studies, suggesting that Eu^{3+} may be a potential activator (Bandi et al. 2010). In addition, other possible activators such as Sm^{3+} and Tb^{3+} have been found in similar energy ranges in doped REE^{3+} glasses (MacRae and Wilson 2008). The peak at 1.26 eV is anomalous as this occurs well within the infrared spectrum and outside the region of common CL activators, prompting further investigation.

Acknowledgements

This project has received funding from the European Union’s Horizon 2020 research and innovation programme under grant agreement No. 101005611 for Transnational Access (award code EXCITE_TNA_C2_2022_010) conducted at the SEM lab of the Department of Geosciences, University Oslo. It has also received support from Science Foundation Ireland (SFI) under Grant Number 16/RP/3849 and 13/RC/2092_P2. Lastly, We thank O. Appelt from GFZ Potsdam for their EPMA expertise as well as A. Gysi for their review, which greatly improved this manuscript.

References

Bandi VR, Jayasimhadri M, Jeong J, Jang K, Lee HS, Yi S-S, Jeong J-H (2010) Host sensitized novel red phosphor $CaZrS_2O_7$: Eu^{3+} for near UV and blue LED-based white LEDs. J Phys D Appl Phys 43:395103. doi: 10.1088/0022-3727/43/39/395103

Bandi VR, Grandhe BK, Jang K, Kim S-S, Shin D-S, Lee Y-I, Lim J-M, Song T (2011) Luminescent properties of a new green emitting Eu2+ doped CaZrSi2O7 phosphor for WLED applications. Journal of Luminescence 131:2414–2418. doi: 10.1016/j.jlumin.2011.06.004.

Bauer PW, Pollock TR (1993) Compilation of Precambrian Isotopic Ages in New Mexico. pp 128

Berger M (2018) Geology and mineralization of the Pajarita Mountain layered peralkaline syenitic pluton-hosted REE-Zr prospect, Mescalero Apache Reservation, New Mexico. Colorado School of Mines, USA, pp 84

Bickford ME, Soegaard K, Nielsen KC, McLelland JM (2000) Geology and geochronology of Grenville-age rocks in the Van Horn and Franklin Mountains area, west Texas: Implications for the tectonic evolution of Laurentia during the Grenville. Geol Soc Am Bull 112:1134–1148. doi: 10.1130/0016-7606(2000)112<1134:GAGOGR>2.0.CO2

Jacobson HS (1986) Pajarito Mountain Prospect, Mescalero Apache Indian Reservation, Otero County, New Mexico. Unocal Molycorp internal report, v. I & II

Kalashnikov AO, Konopleva NG, Pakhomovsky YA, Ivanyuk GY (2016) Rare Earth Deposits of the Murmansk Region, Russia—A Review. Econ Geol 111:1529–1559. doi: 10.2113/econgeo.111.7.1529

Kelley VC (1968) Geology of the Alkaline Precambrian Rocks at Pajarito Mountain, Otero County, New Mexico. Geol Soc Am Bull 79:1565–1572. doi: 10.1130/0016-7606(1968)79[1565:GOTAPR]2.0.CO2

Kottlowski FE (1985) Shoreline facies of the Yeso Formation in the northern Pedernal Hills, New Mexico In: Lucas SG, Zidek J (eds) New Mexico Geological Society 36th Annual Fall Field Conference Guidebook: Santa Rosa-Tucumcari Region. New Mexico Geological Society, Socorro, pp 167–169. doi: 10.56577/FFC-36.167

Le Maitre RW, Streckeisen A, Zanettin B, Le Bas MJ, Bonin B, Bateman P, Belleini G, Dukek A, Efremova S, Keller J, Lameyre J, Sabine PA, Schmid R, Sørensen H, Woolley AR (2002) Igneous Rocks A Classification and Glossary of Terms. Cambridge University Press, United Kingdom

Lenz C, Talla D, Ruschel K, Škoda R, Götze J, Nasdala L (2013) Factors affecting the Nd^{3+} (REE^{3+}) luminescence of minerals. Miner Petrol 107:415–428. doi: 10.1007/s00710-013-0286-2

MacRae CM, Wilson NC (2008) Luminescence database I - minerals and materials. Microsc Microanal. Cambridge University Press, Cambridge, U.K., pp 184–204.

MacRae C, Wilson NC, Torpy A, Davidson CJ (2012) Hyperspectral cathodoluminescence imaging and analysis extending from ultraviolet to near infrared. Microsc Microanal 18:1239–1245. doi: /10.1017/S1431927612013505

MacRae C, Wilson NC, Torpy A (2013) Hyperspectral cathodoluminescence. Miner Petrol 107:429-440. doi: /10.1007/s00710-013-0272-8

Marks MAW, Markl G (2015) The Ilímaussaq Alkaline Complex, South Greenland In: Charlier B, Namur O, Latypov R, Tegner C (eds) Layered Intrusions. Springer Netherlands, Dordrecht, pp 649–691. doi: 10.1007/978-94-017-9652-1_14

Marks MAW, Markl G (2017) A global review on agpaitic rocks. Earth-Sci Rev 173:229–258. doi: 10.1016/j.earscirev.2017.06.002

Möller V, Williams-Jones AE (2016) Petrogenesis of the Nechalacho Layered Suite, Canada: Magmatic Evolution of a REE–Nb-rich Nepheline Syenite Intrusion. J Petrol 57:229–276. doi: 10.1093/petrology/egw003

Roelofsen JN, Veblen DR (1999) Relationships among zirconosilicates: examination by cathodoluminescence and transmission electron microscopy. Mineralogy and Petrology 67:71–84. doi: 10.1007/BF01165117.

Spandler C, Morris C (2016) Geology and genesis of the Toongi rare metal (Zr, Hf, Nb, Ta, Y and REE) deposit, NSW, Australia, and implications for rare metal mineralization in peralkaline igneous rocks. CONTRIB MINERAL PETR Contrib Mineral Petr 171:104. doi: 10.1007/s00410-016-1316-y

Torpy A, Wilson NC (2008) OpticalFit Software by CSIRO Australia. http://www.csiro.au/luminescence/opticalfit/

Wall F (2014) Rare earth elements In: Gunn AG (ed) Critical Metals Handbook. John Wiley & Sons, pp 312–339

Weng Z, Jowitt SM, Mudd GM, Haque N (2015) A Detailed Assessment of Global Rare Earth Element Resources: Opportunities and Challenges. Econ Geol 110:1925–1952. doi: 10.2113/econgeo.110.8.1925

The typology of Czech graphite raw materials

Michal Poňavič[1], František Pticen[1], Bohdan Kříbek[1], Anna Vymazalová[1]
[1]Czech Geological Survey, Klárov 131/3, 118 21 Prague 1, Czech Republic

Abstract. Critical Raw Materials (CRM) in the Czech Republic have been studied under the framework of the project "Rock Environment and Natural Resource RENS" (SS02030023) with graphite being one of the CRMs. The purpose of this study is to investigate the processing of graphite raw material from Czech deposits and sources. The goal of this study is to determine the yield and quality of graphite concentrates after the 1st flotation. The different types of graphite raw materials were divided into three quality classes based on their technological treatability. Each class represents a different type of raw material and therefore different conditions for graphite formation.

1 Introduction

This study has been performed under the project "Rock Environment and Natural Resource RENS" (SS02030023), funded by the Technology Agency of the Czech Republic (TA ČR). The main goals of the project are research, monitoring, and evaluation of the state of the rock environment, natural resources, geological hazards, and geological information in the Czech Republic; and to make those findings available to government agencies, organizations within the field, and to the general public. The research is focusing on deposits of strategic mineral resources within the territory of the Czech Republic. The aim is the identification and evaluation of deposits, the study of refining and processing technologies, and evaluation of potential exploitation of these resources in the Czech Republic. One of the most important topics of the project is the detailed study of Czech graphite deposits.

Graphite deposits in the Czech Republic are located in several varied groups of crystalline rocks: In the Český Krumlov and Sušice-Votice Varied Groups (southern Bohemia) and in the Svratka Crystalline Unit (western Moravia) and in the Velké Vrbno Crystalline Unit (northern Moravia) (Fig. 1).

In the Bohemian Massif, graphite deposits were formed by thermal and pressure decomposition of the organic matter, mainly algae, cyanobacteria and bacteria. The products of their decomposition were deposited in shallow pools in the marine environment, probably at the boundary between the Upper Proterozoic and Lower Palaeozoic. In the course of subsequent geological processes (after the overlying of organic matter by sediments and subsequent metamorphism at temperatures of around 550–650 ^{0}C, and pressures of up to 25 kB), the organic matter was gradually decomposed into a mixture of gases, mainly carbon dioxide and methane (Kříbek 1997). Graphite then crystallized from this gas mixture as the rock complex cooled. In later low temperature processes, this crystalline graphite was affected in a number of places by mechanical processes (it was in fact ground up) to form microcrystalline graphite.

A fundamental problem of some South Bohemian graphite deposits is the processability of the raw material, which is adversely affected by its variable grain size composition and the coalescence and intergrowth of graphite flakes with rock-forming minerals, especially micas. Therefore, to release the graphite flake from the raw material by multi-stage flotation, very fine grinding of the raw material is required. However, such an approach degrades the grain size composition of the final product.

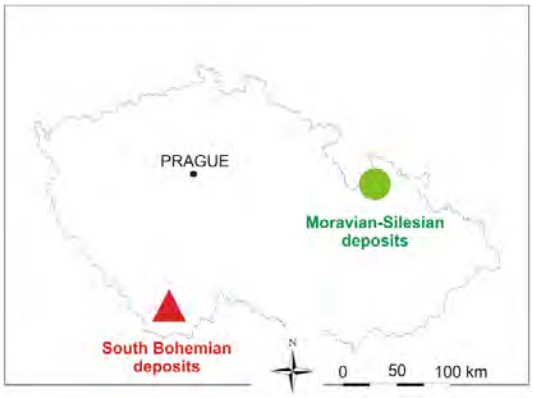

Figure 1. Schematic map of the Czech Republic with locations of the graphite deposits districts.

2 Samples and methods

Within the RENS project, not only archival samples of graphite raw material were studied, but new samples have been collected at available locations. After drying, the samples were crushed and milled to the required grain size (0.015 mm). The samples were further processed at the Central Laboratories of the Czech Geological Survey (CGS). Flotation experiments and detailed analyses of both concentrates and base (silicate analyses, C(tot), C(graph) and detailed trace element analyses) were performed. Graphite mineralogy and morphology were also studied in the CGS laboratories, using a scanning electron microscope. At the same time, rock-slides were made for detailed microscopic investigations.

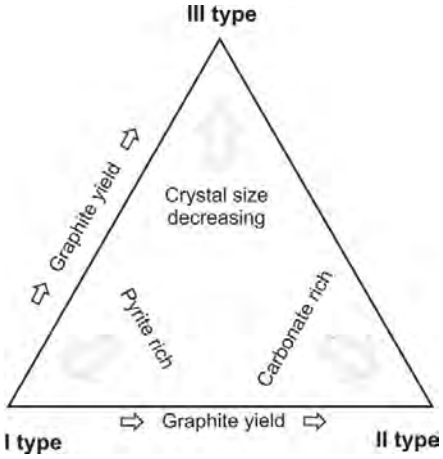

Figure 2. The typology of the Czech graphite raw material based on genetic type and yield of graphite concentrate.

3 Results and discussion

Based on a comparison of the obtained results, from (I) graphite concentration in the feedstock, (II) yield of concentrate after the first flotation, (III) graphite content in this concentrate, and (IV) graphite grain size and ballast mineral content, it is possible to divide the graphite raw materials into three basic groups (Fig. 2). Table 1 shows the average graphitic carbon contents in the raw material (milled to a grain size of 0.10–0.15 mm) and in individual concentrates after the first flotation.

Class I represents graphitic raw materials bound on gneisses. Sulphides (mainly pyrite) are common, and due to their decomposition, the pH of the raw material leachate ranges from 3.5 to 5.0. Graphite is present as small flakes of 0.05–0.15 mm in size. Often there is epitaxial overgrowth of graphite on micas, thus forming a graphite-mica composite (Fig. 3). Microcrystalline graphite (formed by tectonic damage to the gneisses) is also present in small quantities in the raw material. This type of raw material is by far the most common type and is present in the majority of deposits and resources in South Bohemia, with Český Krumlov-Městský vrch being the best known deposit.

Due to the low pH of the raw material, coagulation of particles occurs during flotation and it is therefore necessary to buffer the mixture, for example by adding $Ca(OH)_2$. However, the most important factor is the frequent coalescence of graphite with mica, which leads to low yields and poor quality graphite concentrate (Florena et al. 2016). To achieve acceptable yields it is therefore necessary to incorporate pre-treatment of the raw material, e.g. grinding by ultrasonic treatment (Kang and Li 2019). However, this results in higher energy requirements for the actual treatment.

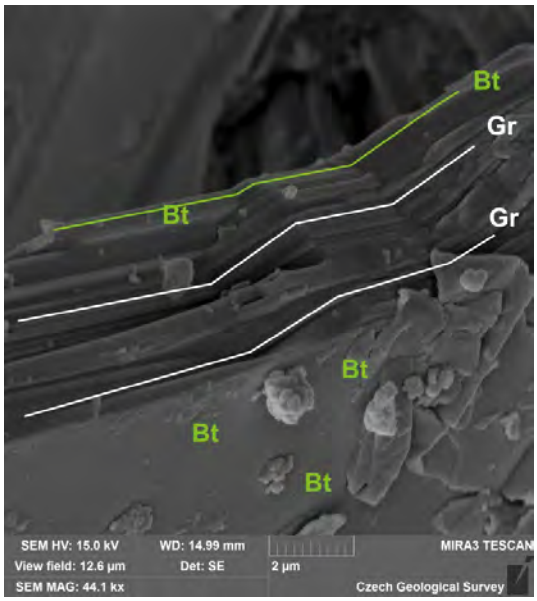

Figure 3. Secondary electron image of alternation between graphite (Gr) and biotite (Bt) in xxx, from the Český Krumlov-Městský vrch deposit.

Input concentrations of graphite are relatively low, ranging between 8–12% C(graph). Yields are also low, the amount of concentrate after the first flotation does not exceed 30 % with a graphitic carbon content of up to 20 % (Table 1).

Class II includes raw materials that may also be associated with gneisses but are predominantly associated with marbles. In this case, the pH of the leachate is between 6.0 and 7.0. Graphite is present as flakes of 0.1–0.25 mm and very often forms separate flakes, without other mineral phases (Fig. 4). This type of raw material is present only in a few deposits in southern Bohemia. The main representative is the Lazec-Křenov graphite deposit.

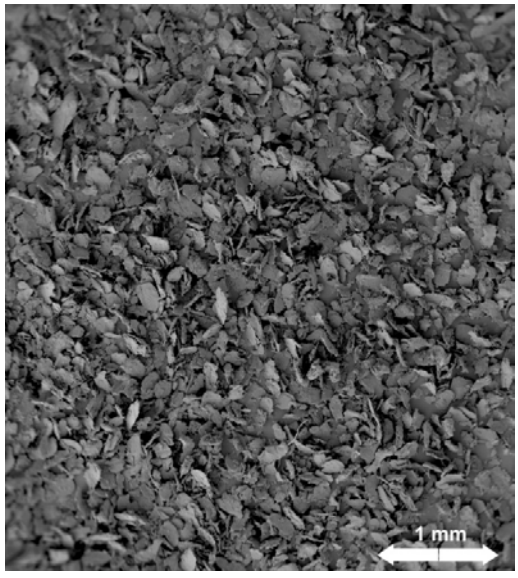

Figure 4. Secondary electron image of graphite flakes from a concentrate after 1st flotation, Lazec-Křenov deposit.

This type of raw material is relatively easy to process, obtaining high yields of high-quality graphite flakes concentrate. The three flotation cycles are sufficient to achieve maximum yields.

The graphite contents in this type of raw material ranges from 12 to 18 %. The yield of concentrate after the first flotation is around 30 % with a C(graph) content between 45 and 50 %.

Class III represents graphitic raw materials bound to gneisses, often tectonically affected. Pyrite may be present, the pH of the leachate ranges from 5.0 to 6.0. Graphite is present in microcrystalline (amorphous) form (Fig. 5). This type of raw material is present in most deposits and sources in the northern Moravia.

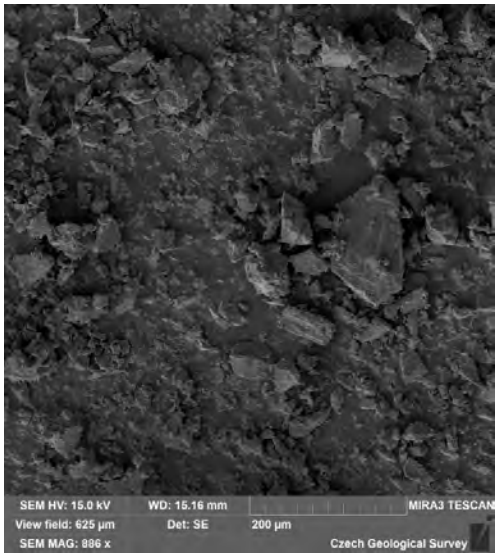

Figure 5. Secondary electron image of amorphous graphite from a concentrate after 1st flotation, Velké Vrbno Konstantin deposit.

This type of raw material is also easy to process, with significant yields of high-quality amorphous graphite concentrate. The graphite content in this type of raw material is very high, ranging from 25 to 30 %. The yield of concentrate after the first flotation is around 50 % with a C(graph) content between 50 and 60 %.

Table 1. Comparison of average graphitic carbon contents in raw materials (milled to a grain size of 0.10–0.15 mm) and in individual concentrates after the first flotation.

Raw material		Concentrate after 1st flotation	
	C(graph)(%)	Concentrate (%)	C(graph) (%)
I type	8–12	40	20–25
II type	18	30	45–50
III type	20–30	50	50–60

5 Conclusions

Samples of Czech graphite raw materials were studied in terms of their workability (yield and quality of graphite concentrate after the first flotation) and also in terms of their mineral association. Table 2 shows the studied graphite deposits. Based on the results so far, it was possible to divide the graphite raw material into three quality classes. They differ in terms of floatability and therefore graphite yield. Each type of graphite raw material thus requires different treatment.

Microcrystalline graphite (Clas III) and graphite associated with carbonates (Clas II) are well treatable and provide concentrates of relatively pure graphite (Jara et al. 2019). In contrast, graphite raw materials bound in gneisses with frequent sulphides requires good physical pre-treatment of the raw material.

This issue will be addressed in the next stages of the SS02030023 RENS project.

Table 2. Studied Czech graphite deposits, and their typology.

Deposit	Num. of samples	Raw material C(graph) average (%)	Category
Český Krumlov-Městský vrch	12	8	I type
Mokrá	8	11	
Chvalšiny	6	12	
Lazec-Křenov	15	18	II type
Velké Vrbno-Konstantin	10	30	III type
Malé Tresné	5	20	

Acknowledgements

Financial support through the project „Rock Environment and Natural Resource (RENS)", No SS02030023 from the state support of the Technological Agency of the Czech Republic (Environment for Life Programme) is gratefully acknowledged.

References

Florena FF, Syarifuddin F, Hanam ES, Trisko N, Kustiyanto E, Enilisiana Rianto A, Arinton G (2016) Floatability study of graphite ore from southeast Sulawesi (Indonesia). In AIP Conference Proceedings. AIP Publishing LLC. 1712, 1.

Jara AD, Betemariam A, Woldetinsae G, Kim JY (2019) Purification, application and current market trend of natural graphite: A review. Int J Min Sci Technol 29: 671–689.

Kang W, Li H (2019) Enhancement of flake graphite cleaning by ultrasonic treatment. R. Soc. open sci. 6191160191160http://doi.org/10.1098/rsos.191160

Kříbek B (1997) Carbonaceous formations of the Bohemian Massif and their mineralization. Czech Geological Survey, Prague, 120 p. (in Czech).

The Northern Copper Belt—a chance for a new giant copper district in Poland

Krzysztof Zieliński[1], Stanisław Speczik[1,2]
[1]Miedzi Copper Corp., Al. Jerozolimskie 96, 00-807 Warsaw, Poland
[2]University of Warsaw, Faculty of Geology, Żwirki i Wigury 93, 02-089 Warsaw, Poland

Abstract. The Northern Copper Belt has been identified recently in south-western Poland as a result of the exploration programme of Miedzi Copper Corp. This zone has great potential to become a new mining district for underground extraction of copper and silver ore. It is located entirely in a geological unit known as the Fore-Sudetic Monocline. The belt includes three newly discovered Cu-Ag ore deposits along with numerous prospective areas scattered around them. The deposits are situated relatively deeply, with an average depth of about 1900 m. The high probability of future extension of these deposits comes from the drillholes of Miedzi Copper Corp., and from the examinations of historical oil and gas exploration boreholes located nearby. Pre-feasibility studies prepared by mining experts confirm the profitability of future extraction of these deposits.
Keywords: Northern Copper Belt, stratiform copper mineralisation; Kupferschiefer-type deposits, deep copper and silver deposits

1 The Northern Copper Belt—an overview

The Northern Copper Belt (NCB) is located in south-western Poland, in the Fore-Sudetic Monocline which is a geological unit already known for its occurrences of stratiform copper and silver deposits. Ore mineralisation is present in the so-called Zechstein copper-bearing series, represented from bottom to top by marine sandstones, shales (the 'Kupferschiefer'), and limestones. The series overlies the barren Rotliegend unit, consisting of continental red bed sediments. The mineralisation occurs directly above the oxidised Rote Fäule zone, the vertical range of which shifts between reaching the sandstone, the Kupferschiefer, or even the limestone. The belt is situated north and east of the existing mines of the Lubin-Sieroszowice District (the so-called New Copper District), which extract ore from shallower parts of the same geological unit.

The NCB has been discovered as a result of an extensive exploration programme of the Miedzi Copper Corp. (MCC) initiated in 2011, which consisted of two stages (Speczik et al. 2021). The first stage involved reprocessing of historical geophysical data, as well as numerous detailed chemical analyses of historical drill core samples of the petroleum industry, irregularly scattered over the investigated area. For this part of the exploration, MCC cooperated with the University of Warsaw and the Polish Geological Institute, the latter of which had earlier performed limited examinations of selected oil and gas exploration boreholes which penetrated the mineralised horizon (Oszczepalski and Speczik 2011). The second stage involved drilling operations performed in areas considered the most promising based on the initial research. A total of 34 exploration boreholes were drilled, with the programme still continuing, and at least two more boreholes scheduled for 2023.

The work performed so far resulted in the discovery of three new Cu-Ag ore deposits (Nowa Sól, Sulmierzyce North, and Mozów) with resources already approved by the Polish government, as well as numerous prospective areas of ore mineralisation, both adjacent to the three deposits and independent therefrom. All these areas collectively form the Northern Copper Belt, which is a name suggested by MCC and already used in other publications on the subject (Speczik et al. 2022).

2 NCB Resources

The three deposits of the NCB have been documented based on MCC's exploration, including its drilling programme. General information about them is presented in Table 2.1.

Table 2.1. Basic characteristics of the Cu-Ag ore deposits of the Northern Copper Belt

Name	Surface area [km^2]	Depth [m b.g.l]	Type of resources (Polish category in brackets)	Cu resources [Mt]	Ag resources [kt]
Nowa Sól	119.2	1780–2160	inferred/ indicated (C_2)	10.96	35.32
Mozów	31.5	2370–2537	inferred/ (C_2)	4.59	6.49
Sulmierzyce North	61.0	1636–2060	inferred/ (C_2+D)	5.65	6.87
			TOTAL:	**21.20**	**48.68**

The resources of the Nowa Sól deposit are described as inferred/indicated, because their relative error of estimation is lower than 30%, which fulfils the requirements of Polish C_1 category, an equivalent of indicated resources according to CRIRSCO (Nieć 2010). The currently continuing exploration of this deposit will upgrade the resources to indicated. These three deposits have been entered into the registry of Polish mineral resources, updated annually by the Polish Geological Institute on commission from the Ministry of Climate and Environment.

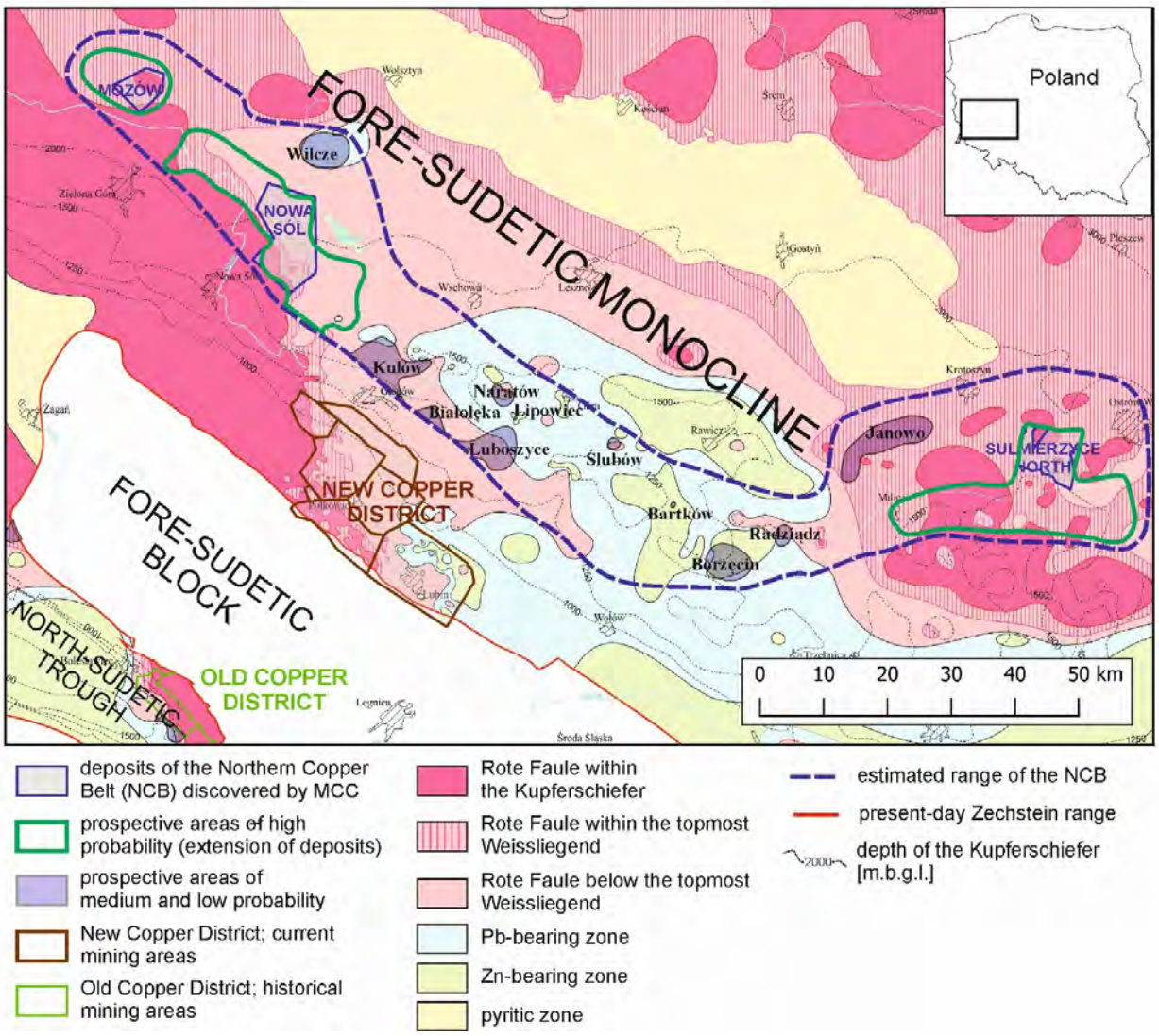

Figure 2.1. Location of the Northern Copper Belt, its ore deposits, and prospective areas.

The NCB also includes areas established as a result of MCC's analyses of old petroleum drill cores. The extent of the belt along with its deposits and prospects are presented in Figure 2.1.

Prospective areas in this part of the Fore-Sudetic Monocline were categorised differently over the years, based on their location with respect to the known deposits, and the degree of their exploration, e.g. as areas of hypothetical resources as well as speculative resources of low and high potential, each one with its own estimated resources (Oszczepalski et al. 2019). In a more recent paper, those among them which are adjacent to the Nowa Sól, Sulmierzyce North, and Mozów deposits were categorised separately as prospective areas allowing for the extension of these deposits (Speczik et al. 2022).

However, the present study uses a new approach, mainly due to the inclusion of additional areas demarcated by historical boreholes, which had been analysed but were not taken into account in previous research. This was because they were represented by incomplete or damaged cores, which could not be used for any official calculations of resources due to their subpar quality. The fragments of intervals with high-grade mineralisation observed in some of those cores make those areas appealing targets for future exploration.

The classification of prospective areas used in the present study is shown in Table 2.2.

Table 2.2. The criteria used to categorise the prospective areas of Cu-Ag ore mineralisation in the Northern Copper Belt.

Type of resources	Description
Prospective of high probability (extension of known deposits)	Adjacent to NCB deposits, identified by historical boreholes with complete core intervals; supplementary boreholes with incomplete cores are allowed
Prospective of medium probability	Distant from NCB deposits, identified by several historical boreholes with complete core intervals; supplementary boreholes with incomplete cores are allowed
Prospective of low probability	Distant from NCB deposits, identified by a single historical borehole with a complete core interval, or only by boreholes with incomplete cores

The prospective areas of the NCB established based on the abovementioned criteria are listed in Table 2.3.

Table 2.3. Basic characteristics of the prospective areas of Cu-Ag ore mineralisation in the Northern Copper Belt.

Type of resources	Name	Surface area [km^2]	Depth [m b.g.l]	Estimated Cu resources [Mt]	Estimated Ag resources [kt]
Prospective of high probability	Nowa Sól (extended)	320*	1600–2200	34.75*	148.26*
	Mozów (extended)	105*	2300–2600	15.27*	23.58*
	Sulmierzyce North (extended)	375*	1400–2100	21.17*	25.71*
Total prospective of high probability:				71.19*	197.55*
Prospective of medium probability	Kulów	50	1500–1800	6.20	16.98
	Białołęka	7	1500–1600	0.33	1.56
	Luboszyce	38	1400–1600	1.21	7.23
	Janowo	56	1700–1800	2.55	5.59
Total prospective of medium probability:				10.29	31.36
Prospective of low probability	Wilcze	36	2400–2500	1.66	18.88
	Naratów	8	1400–1500	0.22	0.91
	Lipowiec	0.2	1400–1500	0.01	0.02
	Ślubów	3	1300–1400	0.11	0.21
	Bartków	0.5	1300–1400	0.02	0.03
	Borzęcin	32	1400–1600	2.01	no data
	Radziądz	6	1600–1800	0.25	0.19
Total prospective of low probability:				4.28	20.24
Total estimated NCB resources:				85.76*	249.15*

*including the deposit(s) from Table 2.1

As seen in Table 2.3, the extensions of the three known deposits (prospective areas of high probability) suggest a considerable increase in their resources, therefore making their future exploration justified and highly appealing.

3 Major ore characteristics

Genetic studies indicate that the richest mineralisation in Fore-Sudetic Monocline is associated with palaeo-elevations like the Wolsztyn High and the Fore-Sudetic Block, and faults, which attracted the flow of mineralising fluids towards those structures and through them. The ore grade is related to the time of the activity of open conduits for mineralising fluids, and on the composition of basement rocks, which also affects the concentrations of accompanying elements, e.g. lead (Borg et al. 2012, Speczik et al. 2021).

The three deposits of the NCB are highly dissimilar from those of the active Lubin-Sieroszowice District. The sole exception is Nowa Sól, which is somewhat comparable to the Polkowice, Sieroszowice, and Rudna deposits of the New Copper District in terms of ore mineralogy (Speczik 2022). This deposit is characterised by eastward dipping of the top of the Rote Fäule horizon. Therefore, the main orebodies of Nowa Sól are located in limestones in its western part; further east they also include shales, and near the eastern edge the ore reaches a few metres deep into the sandstone.

The Mozów deposit is characterised by the prevalence of carbonate ore, related to its close proximity to the vast Zielona Góra oxidised field and the continuously high position of Rote Fäule. Shale ore is present but accounts for only 25% of copper resources, and the underlying sandstones are barren (Speczik 2022).

The Sulmierzyce deposit is peculiar due to its large thickness of the copper-bearing shale, up to 1.5 m, which makes it stand out among both the NCB deposits and the New Copper District Deposits. In fact, the shale resembles the so-called copper-bearing marls (Kupfermergel) of the Old Copper District, currently abandoned and also shown in Figure 2.1. The close proximity of this area to two large oxidised fields resulted in its patchy structure as well as in the mixing of mineralising fluids, which caused the lack of metal zonality. This zonality is typical of the other deposits of the Fore-Sudetic Monocline, and involves the succession of Cu, Pb, and Zn zones in the vertical profile (Borg 2012). Its absence from Sulmierzyce North is another distinguishing feature of this deposit (Speczik 2022).

4 Chances for a new mining district

Even at the current stage of exploration, the Nowa Sol deposit is the largest copper deposit in Poland (Speczik et al. 2022). It also ranks 19th in the world in terms of resources (see Table 4.1), while also occupying the 3rd or 4th place globally with respect to ore grade. The resources of Sulmierzyce North and Mozów are similar to those of the deposits currently mined in the New Copper District.

In 2017, technical reports constituting pre-feasibility studies were prepared for MCC by the Runge Pincock Minarco company—currently RPMGlobal (Bohnet et al. 2017, Goodell et al. 2017). Those documents only considered the resources known at the time, which were lower and less explored. According to them, economically profitable extraction of these deposits is possible, but it would necessitate the application of modern mining technologies, which have not yet been employed in Poland. They include underground flotation performed selectively in order to recover a larger number of valuable elements, the paste backfill technology, cooling of mining headings with ice, and automation of mining machinery (Oszczepalski et al. 2019). These new methods can make the extraction of ore from the NCB deposits more profitable than the mining operations currently continuing in the New Copper District.

Table 4.1. The Nowa Sól deposit among the world's largest copper deposits

No.	Name	Country	Cu resources/ reserves [Mt]	Status
1	Kamoa Kakula	Congo	43.6	in development
2	Escondida	Chile	43.2	active
3	Pebble	USA	37.0	in development
4	Collahuasi	Chile	28.1	active
5	Resolution	USA	27.3	in development
6	Morenci	USA	27.0	active
7	Buenavista	Mexico	26.7	active
8	La Granja	Peru	22.0	in development
9	Andina	Chile	18.8	active
10	Cerro Verde	Peru	18.1	active
11	Toquepala	Peru	17.7	active
12	Tampakan	Phillipines	15.2	in development
13	El Pachon	Argentina	15.0	in development
14	Grasberg	Indonesia	14.6	active
15	Taca Taca	Argentina	12.9	in development
16	Radomiro Tomic	Chile	12.1	active
17	El Teniente	Chile	11.1	active
18	Los Bronces	Chile	11.1	active
19	Nowa Sól	Poland	11.0	in development
20	Cascabel	Ecuador	10.9	in development
21	Baimskaya	Russia	9.5	in development
22	Chuquicamata	Chile	9.4	active
23	Vizcachitas	Chile	7.7	in development
24	Michiquillay	Peru	7.3	in development

The pre-feasibility studies of 2017 estimated the operating costs of future mines at about US $2400–2800 per 1 t of copper, depending on the depth (Bohnet et al. 2017, Goodell et al. 2017). Accounting for inflation, the authors of the present paper believe that these costs should be updated to about $3500. This is still low, considering the current copper prices are about US $9000 per tonne, and according to the predictions of Bank of America and Goldman Sachs, they should reach about $10000–11000 in 2023, and $12000 in 2024 (Christensen 2022).

Another major advantage of the NCB deposits is their continuity. They form relatively uniform orebodies, which may be only locally disrupted by Rote Fäule zones. All three deposits have been identified by regular drilling grids, and new boreholes are currently drilled in the Nowa Sól area. The history of documenting copper and silver ore deposits in the Fore-Sudetic Monocline shows that adding new holes inside the drilling grids of exiting deposits always ends in a slight increase in resources, due to their homogeneity on a macroscale (Speczik et al. 2020).

Further drilling operations are necessary to upgrade the categories of documentation of these deposits to C_1 according to the Polish system, which is an equivalent of indicated resources (Nieć 2010). Pursuant to Polish regulations, this category allows an investor to submit an application for a mining licence. The Nowa Sól deposit is currently at the most advanced stage of exploration, with the largest number of boreholes already drilled, and with a relative error of estimation of resources below 30%, fulfilling the criteria of the C_1 category.

5 Summary

The Northern Copper Belt is a region in south-western Poland, demarcated as a result of the exploration programme of Miedzi Copper Corp. The resources of its three copper and silver ore deposits are already approved by the Polish government, and constitute a major contribution to the country's rich Cu and Ag resources. All three deposits have great potential for growth, and their profitable extraction is already possible, under the condition of utilising modern mining technologies due to their considerable depths.

The NCB also includes numerous prospective areas, with resources estimated at various levels of probability. Further investigation of these areas could lead to the identification of new deposits, some of them shallower than those already documented in the belt. However, already at the current stage of exploration, the NCB presents a proven chance for the development of a new giant mining district for the world's copper industry.

Acknowledgements

The authors would like to thank Prof. Sławomir Oszczepalski of the Polish Geological Institute.

References

Bohnet E, Goodell T, Jorgensen M (2017) Technical Report on Miedzi Copper's Sulmierzyce Project, Poland (Unpublished). RungePincockMinarco, Lakewood

Borg G, Piestrzyński A, Bachmann GH, Püttmann W, Walther S, Fiedler M (2012) An overview of the European Kupferschiefer deposits. Society of Economic Geologists Special Publication 16:455–486

Christensen N (2022) Copper prices to find their groove in the second half of 2023. https://www.kitco.com/news/2022-12-21/Copper-prices-to-find-their-groove-in-the-second-half-of-2023.html (Accessed 28 February 2023)

Goodell T, Jorgensen M, Bohnet E (2017) Technical Report of the Miedzi Copper Project, Poland (Unpublished). RungePincockMinarco, Lakewood

Nieć M (2010) Międzynarodowe klasyfikacje zasobów złóż kopalin. Górnictwo i Geoinżynieria 34(3):33–49 (in Polish)

Oszczepalski S, Speczik S (2011) Rudy miedzi i srebra. In: Wołkowicz S, Smakowski T, Speczik S (eds) Bilans perspektywicznych zasobów kopalin Polski wg stanu na 31 XII 2009 r. Polish Geological Institute, Warsaw, p 76–93 (in Polish)

Oszczepalski S, Speczik S, Zieliński K, Chmielewski A (2019) The Kupferschiefer Deposits and Prospects in SW Poland: Past, Present and Future. Minerals 9. https://doi.org/10.3390/min9100592

Speczik S, Bieńko T, Pietrzela A, Zieliński K (2020) Documenting deep copper and silver deposits—investor's criteria. Górnictwo Odkrywkowe 1:43–54 (in Polish with English abstract)

Speczik S, Zieliński K, Bieńko T, Pietrzela A (2021) The prospecting strategy for a deep Cu-Ag ore deposit in Poland – An anatomy of success. Ore Geol Rev 131. https://doi.org/10.1016/j.oregeorev.2021.104053

Speczik S, Szamałek S, Wierchowiec J, Zieliński K, Pietrzela A, Bieńko T (2022) The new Northern Copper Belt of south-western Poland: a summary. Acta Geol Pol 72(4):469–477

Geochemical thresholds for vanadium throughout Korea and at potential development sites

Joo Sung Ahn[1], Seung-Jun Youm[1], Yong-Chan Cho[1]
[1]Mineral Resources Division, Korea Institute of Geoscience and Mineral Resources, Korea

Abstract. As the industrial demand and use of vanadium increases, it is necessary to explore its new sources in Korea. In this study, using geospatial chemical data, we derived geochemical threshold values for the entire country and identified areas prospective for vanadium deposits. The regional (country-wide) threshold value was derived using logarithmic transformation of raw data (n = 23,548) of the first- and second-order stream sediments collected across the country in the late 1990s and the early 2000s. The median +2 median absolute deviation (MAD) and Tukey inner fence (TIF = Q75 +1.5 interquartile range) values were 116 mg/kg and 200 mg/kg, respectively. Of these, the TIF standard, which showed 0.6 % of data exceeding the threshold, was judged to be appropriate for distinguishing clear enrichment or contamination of vanadium. In the case of the Geumsan and Pocheon, areas with potential for vanadium development, the TIF and median +2 MAD values of 259 mg/kg and 218 mg/kg, respectively, can be used as the criteria for evaluating the impact of environmental pollution before and after deposit development.

1 Introduction

Vanadium is widely used not only in alloys but also for specialized industrial applications, and the demand for vanadium is expected to increase further (Imtiaz et al. 2015). However, most of the world's reserves are stored in three countries, China, Russia, and South Africa, and more than 90% of the world's production is concentrated in these countries. In Korea, the possibility of the existence of vanadium deposits is suggested in the Geumsan area located in the central part and the Pocheon area located in the northern part of the country (Kim et al. 1994; Lee et al. 1997), and high-efficiency beneficiation and smelting technologies are being developed to secure stable vanadium raw materials.

Vanadium, like most heavy metal elements, has no human health effect or may be beneficial at low concentrations; however, it can be toxic at high concentrations. Prolonged exposure to vanadium has been shown to have toxic effects on the respiratory and digestive systems, kidneys, liver, skin, immune system, and cardiovascular system (Jayawardana et al. 2015). However, compared to those on toxic heavy metal elements such as lead and cadmium, environmental studies on vanadium are insufficient, as are worldwide environmental regulations for soils and drinking water.

One of the various purposes of creating a geochemical map is to derive the geochemical background and threshold values. The geochemical background concentration of a specific element can be said to indicate the average concentration exhibited by geological conditions and geochemical reactions in a natural environment where no contamination has occurred. In the case of vanadium, domestically and internationally, environmental standards are insufficient; therefore, the use of regional or local geochemical threshold data is necessary. In particular, this information can be used as a pollution criterion or remediation target value in post-mine development impact assessment and can be applied as basic data for risk assessment. The purpose of this study was to use the national geochemical dataset of Korea (KIGAM 2007) to establish the national-scale regional threshold and the local threshold values of vanadium in the potential mine development areas.

2 Regional geochemical map of Korea

The national geochemical mapping project was performed with the final goal of producing a geochemical map for each element and establishing domestic evaluation criteria for the evaluation of geochemical disasters in Korea (KIGAM 2007). The geochemical map was produced in compliance with the IUGS Global Geochemical Baselines mapping program (Darnley et al. 1995). Sample collection was performed using surficial sediments in first- and second-order streams as representative samples of national catchment basins. Each sample represented composite material over a stream length of 50 m, and approximately 100 g of samples was obtained by wet sieving through a 100-mesh sieve (<150 μm). The entire target area was approximately 97,753 km^2, and 23,696 samples were collected at a density of approximately one site per 4.13 km^2 (Figure 1).

For stream sediment samples, quantitative analyses were performed to determine the concentrations of major and minor oxides, including Al_2O_3, CaO, Fe_2O_3, K_2O, MgO, MnO, Na_2O, P_2O_5, SiO_2, and TiO_2, and 26 trace elements, including As, Ba, Be, Bi, Cd, Ce, Co, Cr, Cs, Cu, Eu, Hf, Li, Mo, Nb, Ni, Pb, Rb, Sb, Sc, Sr, Th, V, Yb, Zn, and Zr using X-ray fluorescence (XRF), inductively coupled plasma-atomic emission spectroscopy (ICP-AES), and neutron activation analysis (NAA). Rigorous quality control was performed using certified reference materials, field duplicate samples and analytical blanks. The precision and accuracy of the analytical data were satisfactory.

Finally, provincial geochemical maps for 22 elements were produced using an interpolation technique of inverse distance weighting (KIGAM 2007).

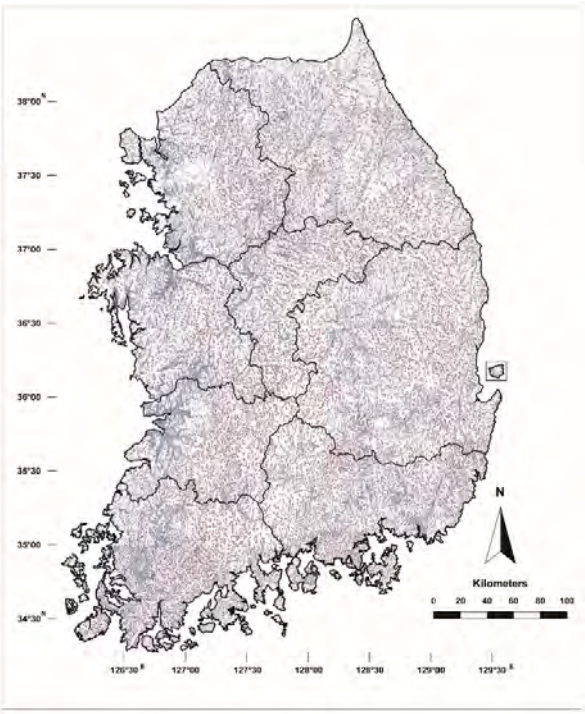

Figure 1. Stream distributions and sampling locations of the Geochemical Atlas of Korea (KIGAM 2007)

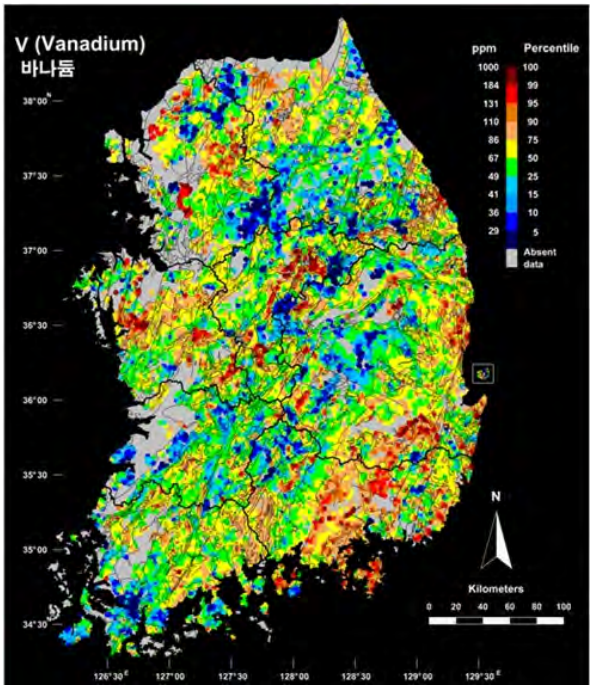

Figure 2. Geochemical map of vanadium in Korea (KIGAM 2007)

3 Geochemical threshold values for vanadium

3.1 Regional distribution

A vanadium geochemical map of Korea is shown in Figure 2. Points in blue indicate a low content of less than 50 mg/kg, and those in red indicate a high content of 100 mg/kg or more. The vanadium content in stream sediments is generally governed by the mineralogical composition of the parent material. Vanadium appears at relatively high concentrations (> 80 mg/kg) in the Okcheon Supergroup, Josen Supergroup, Gyeonggi Gneiss Complex, and Precambrian banded biotite gneiss. In contrast, the concentration is relatively low (< 50 mg/kg) in plutonic rocks, including granites of the Cretaceous, Jurassic, and Permo-Triassic periods. The distribution of vanadium content in the geochemical map agrees well with the distribution of such rock formations (KIGAM 2007). In the geochemical map, specific enriched zones in the range of 100–300 mg/kg are identified. These zones can be considered promising sites for vanadium deposit development.

3.2 Regional geochemical threshold

The vanadium content of the stream sediment samples in Korea was in the range of 2.1–1,000 mg/kg, with a median value of 66.8 mg/kg and an average value of 71.5 mg/kg (Figure 3). As can be seen in the histograms and box plots, the original data (Figure 3) of vanadium content are largely skewed to the right (skewness 4.34) with 821 outliers exceeding the upper inner fence value of 142 mg/kg, which is a typical asymmetric pattern of geochemical data. Therefore, a common logarithm transformation was applied for calculation of the geochemical threshold resulting in a generally symmetrical form as shown in Figure 3.

The calculated median +2 MAD was 116 mg/kg, with 1,908 data points exceeding the threshold value, accounting for 8.1% of the total data (Table 1). This value was higher than the 90th percentile (110 mg/kg) and lower than the 95th percentile (131 mg/kg). In the case of TIF, the threshold value was 200 mg/kg, with 151 data points (corresponding to 0.6%) exceeding this value. The threshold value was much higher than even the 97.5th percentile (151 mg/kg). As expected, the TIF method provided higher threshold values than the more conservative median +2 MAD method. A comparison of the two methods for calculating the geochemical threshold of vanadium in Korea showed that the median +2 MAD method derived a threshold value between the 90th and 95th percentiles, while the TIF approach resulted in a higher threshold value, above the 97.5th percentile. This is similar to the calculations of geochemical thresholds of 59 elements in Australian surface soil in the NGSA project (Reimann & Caritat 2017), 53 elements in European agricultural soil in the GEMAS project (Reimann et. 2018), and eight potentially toxic elements in Bulgarian soil quality monitoring networks (Yotova et al. 2018).

The average upper crust content that can be considered as the geochemical background concentration of vanadium has been suggested to be 53 mg/kg (Wedepohl 1995), 97 mg/kg (McDonough and Sun 1995), 110 mg/kg (Adriano 1986), or 135 mg/kg (Kabata-Pendias 2011). Compared with these values, the median +2 MAD

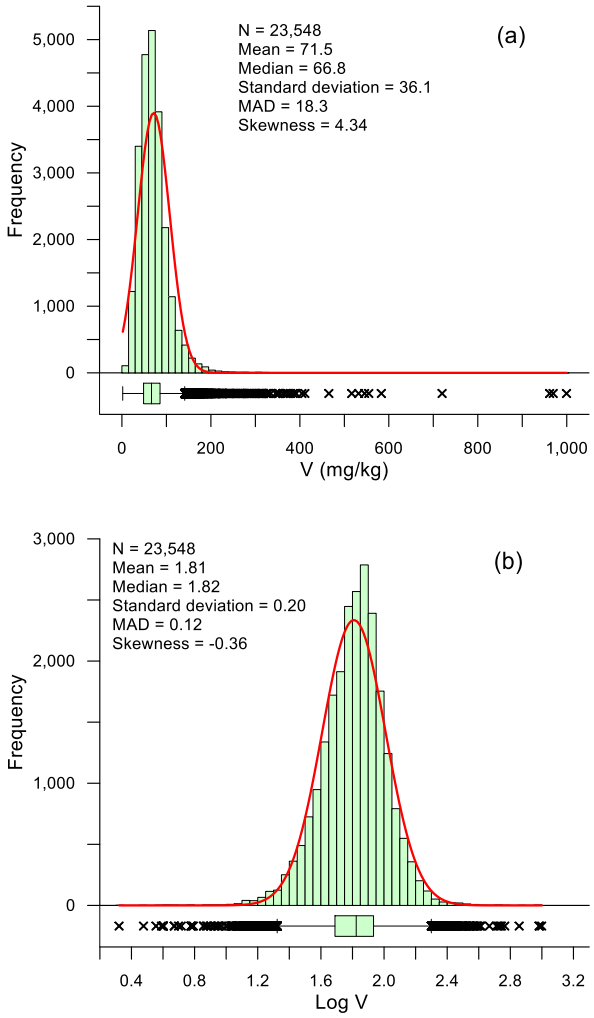

Figure 3. Histograms and boxplots of the raw (a) and log-transformed (b) vanadium data of stream sediments in Korea

value of 116 mg/kg as a geochemical threshold has no discrimination and is a conservatively low standard leading to too many points to be evaluated as a results of vanadium enrichment or contamination. In the case of TIF, the obtained value is two to four times that of these threshold values, and only 0.6% of the total data exceeded the threshold limit. This is much lower than the 2.5% outlier ratio of classical statistics, and can be judged as a completely enriched or contaminated point based on a rather high trend.

3.3 Local distribution and geochemical threshold of vanadium

The distribution of the Okcheon Supergroup in the Geumsan area and the iron mine in the Pocheon area are promising areas for the development of vanadium deposits in Korea. The presence of high vanadium content was known in accordance with the high uranium content in the Geumsan area from previous exploration surveys. The iron mine in the Pocheon area, in which titanium-bearing magnetite

Table 1. Statistics and geochemical threshold values for vanadium of stream sediments in Korea

Statistics	V (mg/kg)	N (> threshold)
N	23,548	
Min	2.1	
Q25	49	
Median	67	
Q75	86	
Q90	110	2,340 (9.9%)
Q95	131	1,168 (5.0%)
Q97.5	151	591 (2.5%)
Max	1,000	
IQR (Q75-Q25)	37	
Median +2 MAD*	116	1,908 (8.1%)
TIF*	200	151 (0.6%)

*Calculated from the log-transformed data
IQR : interquartile range

is concentrated in an alkaline porphyry rock body, also has vanadiferous titanomagnetite ores.

Table 2 shows the results of the geochemical threshold calculation using median +2 MAD and TIF based on log-transformed data for 33 locations in Geumsan and 20 locations in Pocheon around each potential development site. The vanadium content in the Geumsan area ranged from 56 to 270 mg/kg, with an average of 122 mg/kg and median of 116 mg/kg. Regarding geochemical thresholds, the median +2 MAD was 177 mg/kg and the TIF was 259 mg/kg. This is a much higher result than the value derived for the entire country, indicating that vanadium is relatively enriched in this area.

The vanadium content in the Pocheon area ranged from 37 to 236 mg/kg, with an average of 100 mg/kg and median of 93 mg/kg. The median +2 MAD and TIF geochemical thresholds were 218 mg/kg and 377 mg/kg, respectively (Table 2). The derived threshold values were higher than those of the Geumsan area. This is because the difference between the 75th and 25th percentiles is greater, that is, the content dispersion is larger.

When compared to the value of 200 mg/kg determined to be the domestic regional geochemical threshold, we believe that the values of 259 mg/kg and 218 mg/kg obtained using the TIF method for the Geumsan area and the median +2 MAD for the Pocheon area, respectively, are appropriate and valid as the local geochemical thresholds for each research area. The fact that the calculated geochemical thresholds in the Geumsan and Pocheon areas are substantially higher than those of the entire country implies the enrichment of vanadium in these areas, suggesting that in response, environmental management standards should be set high. The derived geochemical threshold can be used as basic data for assessing environmental pollution resulting from surface disturbances or waste generation because of the development of vanadium deposits in these areas.

Table 2. Statistics and geochemical threshold values for vanadium content in stream sediments from the Geumsan and Pocheon areas

Statistics	Geumsan (mg/kg)	Pocheon (mg/kg)
N	33	20
Min	56	37
Q25	94	58
Mean	122	100
Median	116	93
Q75	141	123
Q90	178	177
Q95	211	199
Q97.5	249	217
Max	270	236
IQR (Q75-Q25)	47	65
Standard deviation	49.1	55.1
Skewness	1.20	0.99
Median +2 MAD*	177	218
(N > threshold)	(4)	(1)
TIF*	259	377
(N > threshold)	(1)	(0)

*Calculated from the log-transformed data
IQR : interquartile range

4 Conclusion

Regional and local geochemical thresholds for vanadium, which has insufficient environmental standards, were derived using the first- and second-order sediment geochemical data from the Korean national geochemical map prepared in the early 2000s. A threshold for anomalous vanadium concentrations was determined by using median +2 MAD and TIF statistics. The median +2 MAD and TIF values were derived as 116 mg/kg and 200 mg/kg, respectively, as regional thresholds of vanadium for the country. When applying the TIF, the outlier rate was 0.6%, which is a rather high standard compared to suggested upper crust contents; however, it is expected to be used as a standard to clearly classify enrichment caused either by the presence of vanadium mineralization or by anthropogenic contamination.

Regarding local geochemical thresholds for the Geumsan and Pocheon areas, which were suggested to have potential for vanadium mine development, the derived values were 259 mg/kg (TIF) and 218 mg/kg (median +2 MAD), respectively. We believe that each value will serve as a basis for evaluating the developmental impact in each area.

Acknowledgements

This research was supported by the Basic Research Project (Code: 23-3412-2) of the Korea Institute of Geoscience and Mineral Resources funded by the Ministry of Science and ICT, Korea.

References

Adriano DC (1986) Trace elements in the terrestrial environment. New York: Spring-Verlag.

Darnley AG, Bj€orklund A, Bølviken B, Gustavsson N, Koval PV, Plant JA, Steenfelt A, Tauchid M, Xuejing X, Garrett RG, Hall GEM (1995) A Global Geochemical Database for Environmental and Resource Management. Final Report of IGCP Project 259. Earth Sciences 19. Paris: UNESCO Publishing.

Imtiaz M, Rizwan MS, Xiong S, Li H, Ashraf M, Shahzad SM, Shahzad M, Rizwan M, Tu S (2015) Vanadium, recent advancements and research prospects: A review. Environ Intl 80: 79–88.

Jayawardana DT, Pitawala HMTGA, Ishiga H (2015) Geochemical evidence for the accumulation of vanadium in soils of chronic kidney disease areas in Sri Lanka. Environ Earth Sci 73:5415–5424.

KIGAM (2007) Geochemical Atlas of Korea (1:1,800,000), Series 9. Korea Institute of Geoscience & Mineral Resources

Kim KH, Lee HJ, Chon HT (1994) Ore genesis of the Yonchon titaniferous iron ore deposits, South Korea. Econ Environ Geol 27:117–130.

Lee CH, Lee HK, Shin MA (1997) Barium-vanadium muscovite of coaly metapelite in the Hoenam area of the Ogcheon Supergroup, Korea. J Geol Soc Korea 33:55–64.

McDonough WF, Sun S (1995) The composition of the Earth. Chem Geol 120:223–253.

Reimann C, Caritat Pde (2017) Establishing geochemical background variation and threshold values for 59 elements in Australian surface soil. Sci Tot Environ 578:633–648.

Reimann C, Fabian K, Birke M, Filzmoser P, Demetriades A, Negrel P, Oorts K, Matschullat J, Caritat Pde, The GEMAS Project Team (2018) GEMAS: Establishing geochemical background and threshold for 53 chemical elements in European agricultural soil. Appl Geochem 88:302–318.

Wedepohl KH (1995) The composition of the continental crust. Geochem Cosmochim Acta 59:1217–1232.

Yotova G, Padareva M, Hristova M, Astel A, Georgieva M, Dinev N, Tsakovski S (2018) Establishment of geochemical background and threshold values for 8 potential toxic elements in the Bulgarian soil quality monitoring network. Sci Tot Environ 643:1297–1303.

Reassessing the source controls of Ni sulfide mineral systems

Daryl E. Blanks[1], David A. Holwell[1], Marco L. Fiorentini[2], Isra S. Ezad[3], Jason M. Bennett[2], Stephen F. Foley[3], Weronika Gorczyk[2], Nicole Januszczak[4], Lisa Hart-Madigan[5], Steven Rennick[6]
[1]Centre for Sustainable Resource Extraction, University of Leicester, UK
[2]Centre for Exploration Targeting, School of Earth Sciences, University of Western Australia, Perth, Australia
[3]School of Natural Sciences, Macquarie University, New South Wales, Australia
[4]Resource Centre of Excellence, BHP, Toronto, Canada
[5]Metals Exploration, BHP, London, UK
[6]Metals Exploration, BHP, Perth, Australia

Abstract. The composition of magmatic sulfide deposits is controlled by the metal budget of the magma, which itself is controlled by the composition of the mantle source and degree of partial melting. Traditional models assume that high degrees of partial melting (>15%) are required to sufficiently liberate Cu and PGE from sulfide and Ni from olivine, assuming peridotitic mantle rocks. However, we show that hydrous pyroxenite in the mantle hosts Ni and other critical metals in minerals such as phlogopite and amphibole, which have significantly lower melting temperatures than olivine. We propose a classification of magmatic sulfide deposits that reflects (1) the source composition; and (2) the melting regime. We show that Ni-fertile magmas may be formed in a broader range of geotectonic settings than previously thought if sourced from metasomatised mantle, opening up exploration search spaces for critical battery metals.

1 Mantle source of Ni-Cu-Co-PGE sulfide deposits

Nickel alongside Cu, Co and the platinum-group elements (PGE) are important metals required for sustainable growth and the green energy transition. These metals are concentrated in magmatic sulfide deposits, the crystallise from mantle-derived melts that ascend through the lithosphere. The major depository phases of these metals in the mantle include sulfides, metal alloys, oxides and olivine. All models for the formation of Ni-Cu-Co-(PGE) deposits require the liberation and mobilisation of these metals during partial melting.

The simplistic model of priming mantle-derived melts in Ni, Cu, PGE, etc from the melting of sulfides, oxides and silicates requires high degrees of partial melting (>~15 %) triggered by a significant heat driver (e.g. a mantle plume) that melts the sulfide-bearing and olivine-rich peridotite source. The metals can be later sequestered in the crust by sulfide liquid droplets if the magma undergoes sulfide saturation (Naldrett, 2011).

However, relevant thermal anomalies are isolated in space and time, so that the conditions required to form Ni-Cu-(PGE) deposits have been limited through time. Existing models for mantle melting applied to the formation of mafic-ultramafic magmas that host Ni-sulfide deposits have thus far focussed on ‘dry’ peridotite melting in closed systems (Naldrett, 2011). Although this model is useful to demonstrate the release of Ni from olivine and Cu and PGE from sulfides at varying degrees of mantle melting, it is overly simplistic in terms of the assumed mantle composition. Nonetheless, it has been the basis for most genetic models of magmatic sulfide deposits.

2 Reassessing the source

The mantle is well known to be extremely heterogenous, and therefore, the assumption that the source of all magmatic sulfide deposits is a peridotite is likely a large simplification and, in many cases, inappropriate.

Metasomatised domains in the mantle contain a much more varied mineralogical assemblage, as shown in mantle xenolith datasets from around the globe (e.g. Aulbach et al., 2021). Preliminary results from our work on a series of variably metasomatised mantle xenoliths and from experimental partitioning studies show that a number of other minerals, including phlogopite, amphibole and apatite, can also host significant quantities of Ni and other base metals. We highlight the contrasting mineralogy of two mantle rock types that may be important sources for Ni-Cu-PGE fertile magmas.

2.1 Peridotite mantle

Peridotite is principally comprised of olivine and pyroxene with accessory sulfide, oxide and other trace phases, whereby the bulk of the Ni is hosted in olivine, with some in sulfide. The silicate minerals which host Ni have high melting temperatures, such that a high degree of melting (>20 %) is required to sufficiently liberate the metals from these phases. As such, deposits from this melting scenario are likely to be Ni rich but also host to appreciable Cu and PGE due to the dissolution of sulfide alongside olivine.

2.2 Hydrous pyroxenite mantle

Metasomatically enriched mantle domains are host to more exotic mineralogical assemblages. The composition of these mantle domains can be diverse; they are dominated by clinopyroxene and may comprise hydrous minerals such as amphiboles and micas, in addition to Fe-Ti oxides, phosphates and carbonates.

Critically, the presence of hydrous and volatile-bearing minerals causes these mantle source rocks

to melt at much lower temperatures than dry peridotites. Some of these minerals such as phlogopite, a common mineral in hydrous pyroxenites, have high partition coefficients for Ni (~9), similar to that for olivine (Foley et al., 2022; Ezad and Foley, 2022, Ezad et al., 2023), and may also concentrate other first-row transition elements (Ezad and Foley, 2022). As such, it is possible to form a Ni-rich melt by melting minerals such as phlogopite at lower temperatures without the need to melt significant amounts of olivine and sulfide.

3 Deposit classification as a function of source composition and melting regime

We highlight four scenarios for Ni-Cu-PGE deposit formation from a peridotite and pyroxenite mantle highlighting the controls of the source composition and degree of melting required, as an explanation for the geochemical differences within the Ni-Cu-Co-PGE mineral system.

3.1 High degree melting of a peridotite source (Ni-rich)

This type of deposit forms as a result of high degrees of partial melting (>15%) of a peridotite source where olivine is the dominant source of Ni (Naldrett, 2011). Nickel is liberated at high degrees of partial melting when olivine begins to melt, at the expense of Cu and PGEs which will become diluted at these large volumes. This type of deposit requires a significant heat driver, such as mantle plume or the high mantle potential temperatures such as those known to have existed during the Archean.

3.2 Moderate degree melting of a peridotite source (PGE-rich)

This type of deposit would form at moderate degrees of partial melting from a peridotite source at ~15% partial melting, whereby sulfide (the principal host to Cu and PGE) is completely exhausted, but not diluted by further melting, resulting in significant enrichments in PGEs relative to Ni. This type also requires a significant heat driver required to liberate these metals by S exhaustion in the source and form large, tholeiitic layered igneous complexes that are typical hosts to PGE deposits. Examples of this type include the many PGE deposits of the Bushveld Complex, South Africa; the Stillwater Complex, Montana; and the Duluth Complex, Minnesota.

3.3 High degree melting of a hydrous pyroxenite source (Ni-rich)

The metals in this deposit type are principally hosted within the hydrous minerals, e.g., phlogopite (Ezad et al., 2023), capable of forming Ni-fertile melts. Amphiboles and phlogopite within hydrous pyroxenites melt at lower temperatures than anhydrous peridotite, their exhaustion at approximately 30% partial melting (Foley et al., 2022) results in melts rich in Ni. Due to the low melting temperature of these hydrous and volatile-rich minerals, a plume is not necessary, and thus deposits of this type may form in a wider range of settings, where a heat driver exists. Potential examples of this deposit type include the many deposits of the Central Asian Orogenic Belt, China.

3.4 Low degree melting of hydrous pyroxenite source (Cu-Au-Te-PGE rich)

In cases where hydrous pyroxenite sources contain abundant sulfide and carbonates, their incipient melts (<5% partial melting) are carbonated and can dissolve Cu and PGEs at oxidised conditions (Ezad et al., 2023). These carbonated melts may percolate to shallower depths metasomatising the overlying lithosphere priming it with Cu and PGE rich domains, which may be subsequently remelted and transported in alkaline melts or through physical processes (e.g., Blanks et al., 2020) to form distinct deposit types.

Examples of this process and deposit type being the Cu-Au-Te magmatic sulfide deposits associated with alkaline rocks and include Sron Garbh, Scotland, and Mordor, Australia.

4 Implications

We highlight that partial mantle melts can be enriched in Ni alongside other base metals by melting a range of metasomatised mantle source rocks at lower temperatures than peridotite. We propose that hydrous pyroxenitic mantle offers an alternative source of Ni and other metals and can fertilise partial melts in addition to the conventionally considered olivine and sulfide. Crucially, the implication here is that the lower temperature partial melting of a metasomatised source can produce melts that are fertile in Ni +/- other metals and that Ni sulfide deposits may be found in a more diverse range of geotectonic settings than previously recognised.

Acknowledgements

This work is part of the Craton Margin Exploration Targeting 4D (CMET-4D) project, funded by BHP and involving the University of Leicester, the Centre for Exploration Targeting at the University of Western Australia and Macquarie University. I.S.E and S.F.F acknowledge funding from an ARC Laureate Fellowship (FL180100134) awarded to S.F.F.

References

Aulbach S, Giuliani A, Fiorentini M, et al (2021) Siderophile and chalcophile elements in spinels, sulphides and native Ni in strongly metasomatised xenoliths from the Bultfontein kimberlite (South Africa). Lithos 380–381: 105880

Blanks DE, Holwell DA, Fiorentini M (2020) Fluxing of mantle carbon as a physical agent for metallogenic fertilization of the crust. Nat Comms 11:4342
Ezad I, Saunders M, Scheka S, et al. (2023) Incipient carbonate melting drives precious metal and sulfur mobilisation in the mantle. Nat Comms Preprint
Ezad I and Foley S (2022) Goldschmidt 2022 Abstract 11537
Foley S, Ezad I, van der Laan SR, Shu C (2022) Goldschmidt 2022 Abstract 11550
Naldrett AJ (2011) Fundamentals of magmatic sulfide deposits. Rev Econ Geol 17:1-50

Mafic magmatism in the Central Iberian Zone: Towards a better understanding of Sb mineralization?

Héctor R. Campos-Rodríguez[1], Eric Gloaguen[1,2], Anthony Pochon[2], Johann Tuduri[2], Stanislas Sizaret[1], Pablo Higueras[3], Giada Iacono-Marziano[1], Saturnino Lorenzo[3], José-María Esbri[3], Marc Poujol[4], Valentin Mollé[1]
[1]Université d'Orléans/CNRS/BRGM/ISTO, UMR 7327, F-45071 Orléans, France
[2]BRGM, F-45060 Orléans, France
[3]Instituto de Geología Aplicada & Departamento de Ingeniería Geológica y Minera. E.I.M.I. Almadén, Universidad de Castilla-La Mancha, Plaza Manuel Meca1, E-13400 Almadén (Ciudad Real), Spain
[4]Univ Rennes, CNRS, Géosciences Rennes – UMR6118, F-35000 Rennes, France

Abstract. This work presents the geochemical and geochronological characterization of mafic sills of the Central-Iberian Zone, in order to unveil their possible relationships with Sb mineralization. These sills are located within three different synclines where several Sb mineralization are observed: La Codosera Syncline (CS) hosts the largest Sb mineralisation in Europe; Almadén Syncline (AS) hosts a world-class Hg deposit and some small Sb deposits; Guadalmez Syncline (GS) hosts several Sb±Hg deposits. Whole rock geochemistry of the mafic rocks and U-Pb dating on apatite reveal several differences among the three areas. The rocks from the CS present a sub alkaline affinity, whereas the rocks from AS and GS have an alkaline affinity. Primitive mantle normalized diagrams of the CS mafic samples show E-type MORB patterns with Cs and Pb positive anomalies and K, Ba, and Rb negative anomalies that are more marked in samples spatially related to Sb mineralization. The geochronological data allow to propose the existence of a mafic magmatic event that took place around 357±13Ma in the CIZ. Our data is temporarily concordant with a mafic event reported in the Armorican Massif, which is genetically associated with Sb mineralization in the same domain.

1 Introduction

Most of the Sb deposits are formed in an epigenetic hydrothermal setting (Obolensky et al. 2007) and can be divided into several types considering both the source of metals and fluids: a) epithermal type (veins); b) metamorphic hydrothermal; c) reduced-intrusion related (Schwarz-Schampera 2014). Antimony deposits that formed in tectonic convergence settings underwent strong compressive deformation and the mineralizing fluids are produced by metamorphic reactions (Groves et al. 1998). This classification does not seem very relevant for the formation of Sb±Au deposits in the Massif Central at the end of the Variscan Orogeny (310-300Ma). These deposits formed in an extensive context during a magmatic-hydrothermal event (Bouchot et al. 2005). Within the Armorican Massif, also part of the Variscan Belt (VB) recent studies have demonstrated a strong spatial and genetic relationship between Sb mineralization and a large mafic event dated at 360Ma (Pochon et al. 2016, 2017, 2018, 2019). In other parts of the VB such as the Central Iberian Zone (CIZ), located in the Iberian Massif, several Sb±Hg±W±Au mineralization have also been reported. In the case of the world class Almadén deposit, a link between mafic magmatism and Hg mineralization has been determined (Higueras 1995; Higueras et al. 1995, 2013; Hall et al. 1997). Moreover, a genetic link between the antimony mineralization and the hydrothermal activity associated to Devonian volcanism and with magmatic processes has been suggested (Arribas and Gumiel 1984; Gumiel and Arribas 1987); nevertheless, no studies investigated the possible relationship among mafic rocks and Sb mineralization in the CIZ.

Here we present the geochemical and geochronological characterization of three different structures (synclines) of the CIZ (Figure 1 and Figure **2**). All of them host several mafic sills intruding a metasedimentary sequence (Schist Greywacke Complex, SGC) from Neoproterozoic to Carboniferous age (Bea et al. 2003); as well as Sb±Hg±W±Au mineralization. The Codosera Syncline hosts the Sb±W mineralization of San Antonio; the Almadén Syncline hosts the world class Hg deposit of Almadén and the Guadalmez Syncline hosts several Sb±Hg deposits.

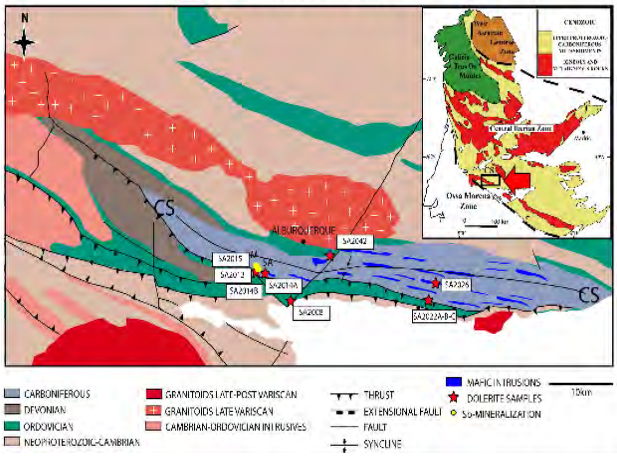

Figure 1. La Codosera Syncline (CS) at the Central Iberian Zone, in the Iberian Massif. Location of the structure and mafic samples studied in this work.

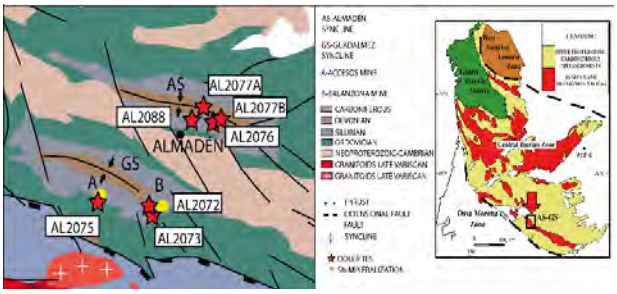

Figure 2. Almadén (AS) and Guadalmez Synclines (GS)at the Central Iberian Zone, in the Iberian Massif. Location of the structures and mafic samples studied in this work.

2 Methodology

2.1 Whole rock geochemistry analyses

Whole rock geochemical analyses of 17 samples were performed at ALS laboratories in Dublin (Ireland). Major elements were analyzed using inductively coupled plasma atomic emissions spectrometry (ICP-AES) after a lithium borate fusion. In order to measure trace elements, the samples were fused using lithium borate ($LiBO_2$), the product (fused beads) underwent acid dissolution for being analyzed by inductively coupled plasma-mass spectrometry (ICP-MS)

2.2 Geochronology- U-Pb dating on apatite

Geochronological analyses were carried out in both thick-polished sections of 150µm and separated crystals of 6 dolerite samples.

The U-Pb geochronology was performed by LA-ICP-MS (Laser ablation-inductively coupled plasma-mass spectrometry) in the facilities of Géosciences Rennes. The Laser ablation system is composed by an Excimer ESI NWR193UC coupled with a Q-ICP-MS Agilent 7700x

Each punctual analysis consisted on 20 seconds of background collection, followed by 60 seconds of ablation and 15 seconds of wash-out delay. Two analytical session were performed. In the first one a rectangular ablation was performed (dimensions 30µm x 40µm) in four samples (SA2022C, SA2026 and AL2073) whereas in the second one a simple spot of 40µm was used for the rest of the samples (SA2014A, AL2075 and AL2076). In both of the analytical sessions the repetition rates were 5Hz.

The analyzed sequence consisted in two analyses of the Madagascar apatite standard (ID-TIMS age of 473±0.7Ma, Thomson et al., 2012), 1 analysis of the Durango apatite standard (31.44±0.18Ma, McDowell et al., 2005), one analysis of the McClure apatite standard (523.51±2.09Ma, Schoene & Bowring, 2006) followed by 6 analyses of apatite samples. The sequence was repeated maximum 6 times and the end of the session consisted of three analyses, 1 of the Durango and 2 of the Madagascar standards.

3 Results and Discussion

3.1 Alteration features

In order to quantify the alteration degree of the dolerites and to investigate the mobility of major elements, all samples have been plotted into the Al-CCPI alteration box plot (Large 2001)

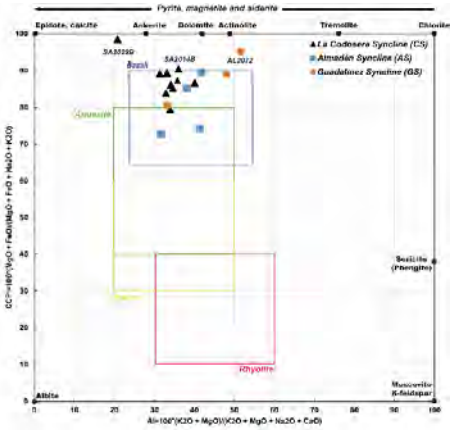

Figure 3. Alteration diagram from Large (2001). Most of the samples fall into the basalt field, showing that the alteration did not compromise their primary geochemical signature.

According to Figure 3 most of the studied samples from the Codosera (CS), Almadén (AS) and Guadalmez Synclines (GS), fall into the basalt field. This means that, even if they experienced some alteration, their primary geochemical signatures are preserved. The three samples that do not fall into the basalt field are not going to be considered in the following discussion.

3.1 Whole rock geochemistry analyses

Whole rock analyses of 14 samples show some differences between CS, AS and GS. According to the Zr/TiO_2 vs Nb/Y diagram (Winchester and Floyd 1977). The CS samples fall into the classical basalt field whereas the AS and GS samples fall into the alkali basalt field. The data is consistent with previous studies regarding the geochemistry of these mafic sills.

Primitive mantle normalized diagrams shown in Figure 4 display high positive anomalies in Cs and Pb suggesting sediment addition and/or the assimilation of country rocks. On the other hand, high negative anomalies in K and Rb, and to a lesser extent in Ba could be associated with both the presence of phlogopite in the source as well as hydrothermal and metamorphic processe (Sun and McDonough 1989). These anomalies are stronger for all the samples spatially related to Sb-mineralization in the CS and the GS. All samples are depleted in HREE and enriched in LREE.

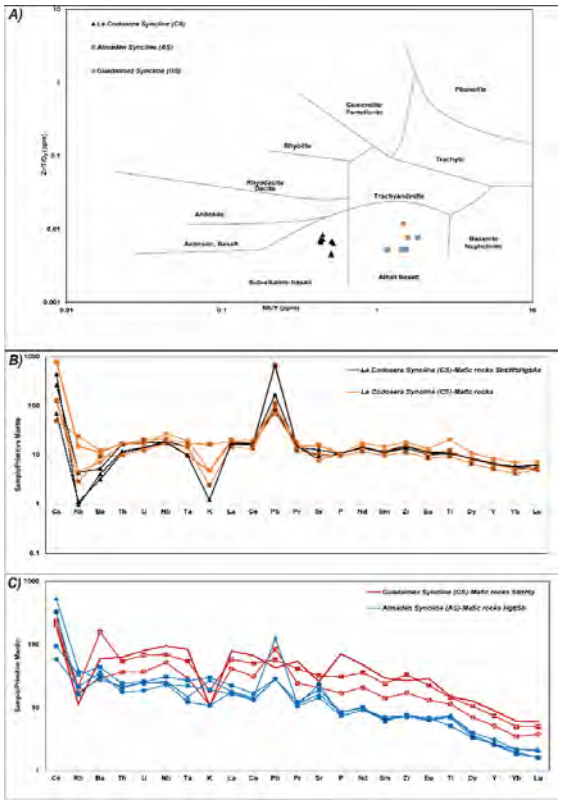

Figure 4. A) Samples from CS, AS and GS plotted into the Zr/TiO2 vs Nb/Y diagram from (Winchester and Floyd 1977). The samples from SA fall into the classical basalt field whereas those coming from GZ fall into the alkali basalt field; B and C) Primitive mantle normalized spider diagram for samples coming from CS (B), AS and GS (C). PM normalizing values taken from (Sun and McDonough 1989).

3.2 U-Pb geochronology apatite

The U-Pb geochronology results are plotted in both, the Tera-Wasserburg diagram using IsoplotR (Vermeesch 2018); as well as in the weighted average ^{207}Pb corrected date (WACD) diagram, which is calculated using the Pb evolution model of Stacey and Kramers (1975).

Regarding the results obtained from samples coming from the CS, AS and GS (**Erreur ! Source du renvoi introuvable.**), two main groups of dates can be observed (considering the errors within each sample). The first group includes samples:

A) SA2014A (CS): Discordia date (Dd)=355.7±17.1Ma/ ^{207}Pb WACD date=357±13Ma.

B) SA2022C (CS) : Dd =352.80±18.9Ma/ ^{207}Pb WACD= 354.5.4±5.4Ma.

C) SA2026 (CS) : Dd=337±23.7Ma/ ^{207}Pb WACD=344.7±4.8Ma.

The second group includes samples.

D) AL2073 (GS) : Dd = 360±25.6Ma / ^{207}Pb WACD=381±7.3Ma.

E) AL2076 (AS): Dd=358.2±11.9Ma / ^{207}Pb WACD=379.3±8.2Ma.

A low-grade metamorphism (up to greenschist facies) has been reported in the studied areas (Higueras et al. 1995, 2013; López-Moro et al. 2007) We assume that sills experienced a fast cooling and solidification (giving their thickness) with no further modification. These dates are thus interpreted as the intrusion age of the mafic sills.

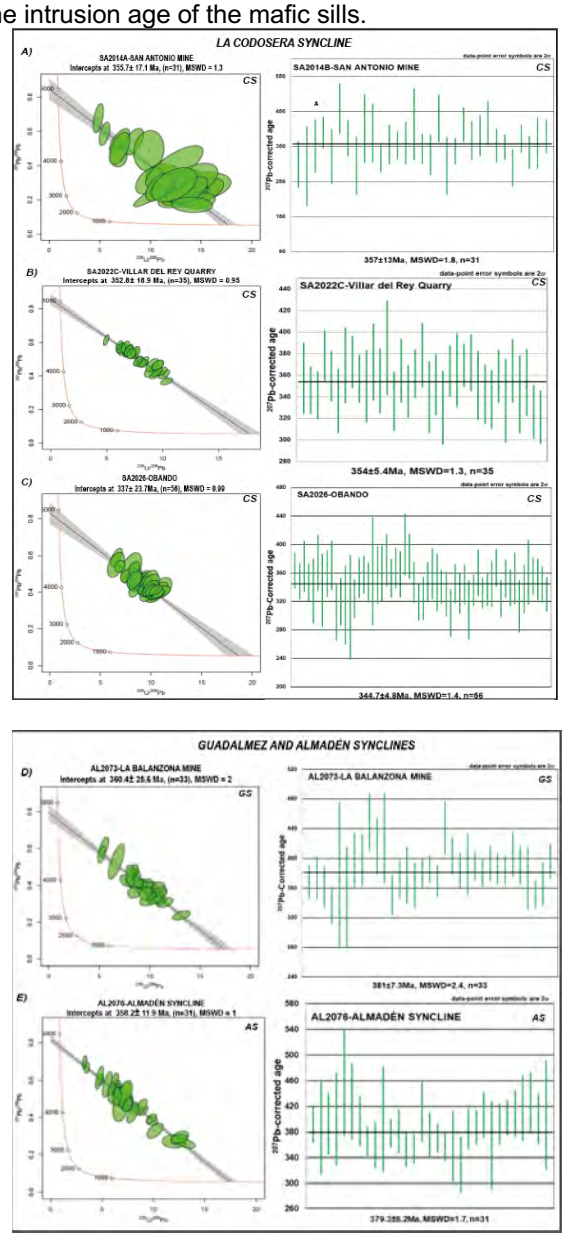

Figure 5. Tera-Wassebourg diagram and their related ^{207}Pb corrected ages for the mafic rocks coming from the Almadén and Guadalmez Synclines.

Our previous intrusion ages show three different stages one at 380Ma, another at 360Ma and the last at 345Ma. The second stage is concordant with the ages reported in the AM by Pochon et al. (2016), which are temporarily related to a peak in Sb mineralization in the AM dated at 360Ma (Pochon et al. 2019).

Conclusions

A spatial link between Sb-mineralization and mafic magmatism is proposed in the CIZ

-Primitive mantle normalized diagrams show negative anomalies in K and Rb that could be

associated with hydrothermal and metamorphic processes. These anomalies are stronger for the samples spatially related to Sb-mineralization. According to these diagrams, all samples are depleted in HREE and enriched in LREE. The samples coming from the GS are more enriched in REE than those coming from AS, suggesting that these magmas could be more differentiated or that the source of both is different.

-Our results allow to propose the existence of three mafic magmatic stages that took place from Late Devonian to Carboniferous times in the CIZ at around 380Ma (AS and GS), 360Ma (CS) and 345Ma (CS). The second stage that we revealed in this study, is concordant with the mafic event dated at 363.4±5.4 in the AM by Pochon et al. (2016), which is related to Sb mineralization peak in the same domain dated at 360Ma (Pochon et al. 2019). In our case, the magmatism that matches temporarily with this peak is located in the CS (related to Sb±W). The rocks in this area present a subalkaline affinity. On the other hand, the magmatism spatially related to Sb±Hg in the GS and Hg±Sb in the AS present an alkaline affinity and is older than the one we reported in the CS.

-The genetical link between Sb-mineralization and mafic magmatism in the CIZ is still a matter of study

Acknowledgements

This work was funded by the ANR (ANR-19-MIN2-0002-01), the AEI (MICIU/AEI/REF.: PCI2019-103779) and author's institutions in the framework of the ERA-MIN2 AUREOLE project, as well as by Project SBPLY/17/180501/000273, Consejería de Educación, Regional Government of Castilla-La Mancha, Spain.

References

Arribas, Gumiel P (1984) First Ocurrece of a Strata-Bound Sb-W-Hg Deposit in the Spanish Hercynian Massif. In: Wauschkuhn A, Kluth C, Zimmerman RH (eds) Syngenesis and epigenesis in the formation of mineral deposits. Spriger-Verlag, Berlin-Heidelberg, pp 469–481

Bea F, Montero P, Zinger T (2003) The nature, origin, and thermal influence of the granite source layer of Central Iberia. J Geol 111:579–595. https://doi.org/10.1086/376767

Bouchot V, Ledru P, Lerouge C, et al (2005) 5: Late Variscan mineralizing systems related to orogenic processes: The French Massif Central. Ore Geol Rev 27:169–197. https://doi.org/10.1016/j.oregeorev.2005.07.017

Groves DI, Goldfarb RJ, Gebre-Mariam M, et al (1998) Orogenic gold deposits: a proposed classification in the context of their crustal distribution and relationship to other gold deposit types. Ore Geol Rev 13:7–27. https://doi.org/10.1016/S0169-1368(97)00012-7

Gumiel P, Arribas A (1987) Antimony deposits in the Iberian Peninsula. Econ Geol 82:1453–1463. https://doi.org/10.2113/gsecongeo.82.6.1453

Hall CM, Higueras PL, Kesler SE, et al (1997) Dating of alteration episodes related to mercury mineralization in the Almadén district, Spain. Earth Planet Sci Lett 148:287–298. https://doi.org/10.1016/s0012-821x(97)00041-1

Higueras P (1995) Procesos petrogenéticos y de alteración de las rocas magmáticas asociadas a las mineralizaciones de mercurio del distrito de Almadén. Universidad de Castilla-La Mancha

Higueras P, Morata D, Munha J (1995) Metamorfismo de bajo grado en facies prehnita-pumpellyita en las metabasitas del Sinclinal de Almadén. Boletín la Soc Española Mineral 18:111–125

Higueras P, Oyarzun R, Lillo J, Morata D (2013) Intraplate mafic magmatism, degasification, and deposition of mercury: The giant Almadén mercury deposit (Spain) revisited. Ore Geol Rev 51:93–102. https://doi.org/10.1016/j.oregeorev.2012.12.004

Large RR (2001) The Alteration Box Plot: A Simple Approach to Understanding the Relationship between Alteration Mineralogy and Lithogeochemistry Associated with Volcanic-Hosted Massive Sulfide Deposits. Econ Geol 96:957–971. https://doi.org/10.2113/96.5.957

López-Moro FJ, Murciego A, López-Plaza M (2007) Silurian/Ordovician asymmetrical sill-like bodies from La Codosera syncline, W Spain: A case of tholeiitic partial melts emplaced in a single magma pulse and derived from a metasomatized mantle source. Lithos 96:567–590. https://doi.org/10.1016/j.lithos.2006.12.006

McDowell FW, McIntosh WC, Farley KA (2005) A precise 40Ar-39Ar reference age for the Durango apatite (U-Th)/He and fission-track dating standard. Chem Geol 214:249–263. https://doi.org/10.1016/j.chemgeo.2004.10.002

Obolensky AA, Gushchina L V., Borisenko AS, et al (2007) Antimony in hydrothermal processes: solubility, conditions of transfer, and metal-bearing capacity of solutions. Russ Geol Geophys 48:992–1001. https://doi.org/10.1016/j.rgg.2007.11.006

Pochon A, Beaudoin G, Branquet Y, et al (2017) Metal mobility during hydrothermal breakdown of Fe-Ti oxides: Insights from Sb-Au mineralizing event (Variscan Armorican Massif, France). Ore Geol Rev 91:66–99. https://doi.org/10.1016/j.oregeorev.2017.10.021

Pochon A, Branquet Y, Gloaguen E, et al (2019) A Sb ± Au mineralizing peak at 360 Ma in the Variscan belt. BSGF - Earth Sci Bull 190:. https://doi.org/10.1051/bsgf/2019004

Pochon A, Gloaguen E, Branquet Y, et al (2018) Variscan Sb-Au mineralization in Central Brittany (France): A new metallogenic model derived from the Le Semnon district. Ore Geol Rev 97:109–142. https://doi.org/10.1016/j.oregeorev.2018.04.016

Pochon A, Poujol M, Gloaguen E, et al (2016) U-Pb LA-ICP-MS dating of apatite in mafic rocks: Evidence for a major magmatic event at the Devonian-Carboniferous boundary in the Armorican Massif (France). Am Mineral 101:2430–2442. https://doi.org/10.2138/am-2016-5736

Schoene B, Bowring SA (2006) U-Pb systematics of the McClure Mountain syenite: Thermochronological constraints on the age of the 40Ar/39Ar standard MMhb. Contrib to Mineral Petrol 151:615–630. https://doi.org/10.1007/s00410-006-0077-4

Schwarz-Schampera U (2014) Antimony. In: Gunn G (ed) Critical Metals Handbook, First Edit. John Wiley & Sons, Ltd., pp 70–98

Stacey JS, Kramers JD (1975) Approximation of terrestrial lead isotope evolution by a two-stage model. Earth Planet Sci Lett 26:207–221. https://doi.org/10.1016/0012-821X(75)90088-6

Sun S-S, McDonough WF (1989) Chemical and isotopic systematics of oceanic basalts: Implications for mantle composition and processes. Geol Soc Spec Publ 42:313–345. https://doi.org/10.1144/GSL.SP.1989.042.01.19

Thomson SN, Gehrels GE, Ruiz J, Buchwaldt R (2012) Routine low-damage apatite U-Pb dating using laser ablation-multicollector- ICPMS. Geochemistry, Geophys Geosystems 13:1–23. https://doi.org/10.1029/2011GC003928

Vermeesch P (2018) IsoplotR: A free and open toolbox for geochronology. Geosci Front 9:1479–1493. https://doi.org/10.1016/j.gsf.2018.04.001

Winchester JA, Floyd PA (1977) Geochemical discrimination of different magma series and their differentiation products using immobile elements. Chem Geol 20:325–343. https://doi.org/10.1016/0009-2541(77)90057-2

On the origin of volatile-rich minerals associated with magmatic sulfides

Maria Cherdantseva[1], Marco Fiorentini[1], Chris Fisher[1], Laure Martin[2], Matvei Aleshin[2]
[1] Centre of Exploration Targeting, School of Earth Sciences, The University of Western Australia, Perth, Western Australia
[2] Centre for Microscopy, Characterisation and Analysis, The University of Western Australia, Perth, Western Australia

Abstract. Magmatic sulfides such as chalcopyrite, pyrrhotite and pentlandite hosted in mafic-ultramafic intrusions are commonly found in intimate spatial association with volatile-rich minerals such as calcite, apatite, amphibole and phlogopite. These volatile-rich minerals have been previously ascribed to form due to late magmatic or secondary processes, involving highly fractionated liquids and/or metamorphic fluids. However, our new results from detailed study of the nature of this association in three different intrusions supported by experiments has led us to the conclusion that these minerals could be, at least in some instances, primary. In this case we explain the presence of halos enriched in volatile-rich silicates, carbonates and phosphates to be a crystallization product of initially immiscible carbonate melt exsolved from silicate magma together with sulfide liquid. Wherein, in our experiments, carbonate melt always envelopes sulfide globules indicating their affinity and presence of wetting agent in carbonate melt. In this study we present isotopic signatures and trace element distributions of three minerals commonly found in spatial association with sulfides (calcite, apatite, and baddeleyite/zircon) to investigate a potential source of carbonate melt in mafic magma.

1 Introduction

The origin of volatile-rich and/or incompatible element-enriched minerals such as calcite, apatite, and baddeleyite/zircon associated with magmatic sulfides in mafic-ultramafic systems has been a topic of debate for decades. Some researchers have suggested that they could form due to precipitation of late magmatic fluids (Aird and Boudreau 2013; Barnes et al. 2017) or as a late hydrothermal overprint (Wernette et al. 2020). However, the morphological and mineralogical features of this association raise questions about these interpretations. In fact, these minerals coat the sulfide globules, forming halos with sharp margins to the host mafic-ultramafic rocks (Schoneveld et al. 2020). Furthermore, distinct mineralogy includes the presence of calcite, which is not typical of fractionated residual liquid, nor are ilmenite or zircon a typical product of late magmatic fluid precipitation (Keevil et al. 2020). On the basis of experimental results, we put forward the hypothesis that this association could reflect the presence of high-temperature immiscible carbonate melt, which exsolved from the silicate magma coevally with sulfide melt. Wherein, we observe that carbonate melt will preferentially adhere to sulfide globules enveloping them, effectively acting as a buoyancy aid facilitating their entrainment in the magma. However, the source of such a carbonate melt has not yet been constrained. To investigate the source and origin of the halos surrounding the compound sulfide globules, we studied the isotopic and trace element compositions of calcite, apatite and zircon/baddeleyite, which are typically found within mineralogical assemblage of these halos, in selected samples from mineralized intrusions from three different systems: Norilsk, Russia; Rudniy, Mongolia and Valmaggia, Italy.

2 Geological background

This research utilized olivine gabbro from the Norilsk1 and Kharaelakh intrusions, which contain sulfide globules from the Norilsk-Talnakh camp in northern Siberia, Russia. These elongated mafic-ultramafic intrusions, also known as chonoliths, can reach up to 360 m in thickness and 25 km in length and were formed in an intracontinental rift. All the intrusions were emplaced at shallow depths and occur as layered sequences of olivine and picritic gabbro-dolerite, gabbronorite-dolerite, gabbro-anorthosite, plagio-lherzolite, troctolite, and gabbro-diorite (Ryabov et al. 2014).

The Rudniy olivine gabbro intrusion in NW Mongolia is a small composite magmatic body with disseminated sulfide globules, representing one of the numerous mafic-ultramafic intrusions in the Torgalyk Complex surrounding the Tuva depression. These intrusions were formed in the Early Devonian as part of the Altai-Sayan large igneous province (Vorontsov et al. 2010).

In contrast, the Valmaggia ultramafic pipe is a small intrusion composed of peridotite with disseminated sulfide globules located in the Ivrea Zone in northwest Italy. This zone represents a part of the lower continental crust and lithospheric mantle exposure formed during the Alpine Orogeny. (e.g., Fiorentini and Beresford 2008).

Selected samples from these localities are characterized by the presence of magmatic sulfide mineralization in the form of disseminated sulfide globules that are commonly composed of pyrrhotite, pentlandite and chalcopyrite. These globules are commonly coated by rounded envelopes of volatile-rich and/or incompatible element-enriched minerals that are distinctly different from the host intrusion. They commonly comprise plagioclase, amphibole (kaersutite, hornblende and hastingsite), phlogopite, clinopyroxene, ilmenite, zircon (and/or baddeleyite),

apatite and calcite. Three of those minerals – calcite, apatite and zircon were chosen to study the trace element and isotope compositions as indicators of the origin of the mineralization and associated haloes.

3 Materials and Methods

Cameca IMS-1280 large-geometry secondary ion mass spectrometry (SIMS) at the Centre for Microscopy, Characterization, and Analysis (CMCA), the University of Western Australia (UWA), has been used to conduct in-situ measurements of oxygen isotopes ($\delta^{18}O$) in zircon and calcite and carbon isotopes ($\delta^{13}C$) in calcite associated with magmatic sulfide globules. To carry out the measurements, fragments of the sulfide globules and haloes around them were mounted in epoxy pucks together with the standard materials: 91500 (9.90 ± 0.3 ‰) and SLZ1 (12.1 ± 0.4 ‰) as primary and secondary standards for oxygen isotopes in zircon, respectively; NSB18 (7.19 ± 0.3 ‰) and 21ca5 (22.2 ± 0.4 ‰) as primary and secondary standards for O isotopes in calcite; NSB18 (-5.014 ± 0.035 ‰) for carbon isotopes in calcite. Before the SIMS analyses, the mounts were coated with a 30 nm-thick Au layer. The drift was monitored by examining standards every five sample analyses.

Laser ablation inductively coupled plasma mass spectrometry (LA-ICP-MS) at the CMCA, UWA, was used to measure trace element concentrations in apatite, calcite and zircon. NIST610 and NIST612 were used as primary standards. They were analyzed before and after every 10 unknown sample spots. Madagascar apatite and 91500 zircon were used as secondary standards for apatite and zircon analyses. Trace element concentrations were within 10% of their certified values. Calcite from the Oka complex was used to monitor calcite analyses. Concentrations of Zr (for zircon) and Ca (for calcite and apatite) were used as internal standard to calculate the trace element concentrations. Major and minor element composition was studied using a JEOL 8530F scanning electron microscope at the CMCA, UWA.

4 Results

Data on $\delta^{18}O$ and rare earth element (REE) distribution in zircon from the Rudniy intrusion are not provided, because the grains were too small to be analyzed.

The chondrite-normalized distribution of REE in zircon and apatite shows enrichments. Specifically, zircon from haloes around sulfide globules from Norilsk and Valmaggia is up to two orders of magnitude more enriched in all REE than zircon derived from highly fractionated magmas (Fig. 1a, e.g., Shi et al. 2022). Apatite from all three localities are characterized by enrichments in light REE with moderate (Rudniy) to steep (Valmaggia) negative slopes in their patterns (Fig. 1b). Apatite from Norilsk and Rudniy intrusions are also characterized by strong to moderate negative Eu anomalies.

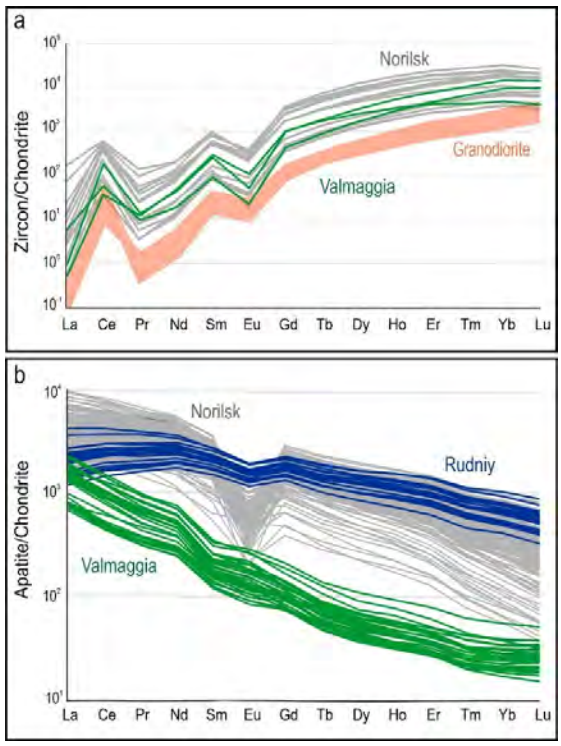

Figure 1. Chondrite-normalized REE distribution in (a) apatite and (b) zircon from Norilsk (Russia), Valmaggia (Italy), Rudniy (Mongolia). Data normalized after (McDonough and Sun 1995)

Oxygen isotope composition of zircon and carbon isotope compositions of calcite from three different deposits are variable for different samples (Figs. 2 and 3). When examining oxygen isotopes in zircon, the Valmaggia intrusion shows values between 4-6 ‰ (Fig. 2), while the zircon from the Norilsk deposit displays a variety of compositions, with values ranging from 1 to 10 ‰ in different samples.

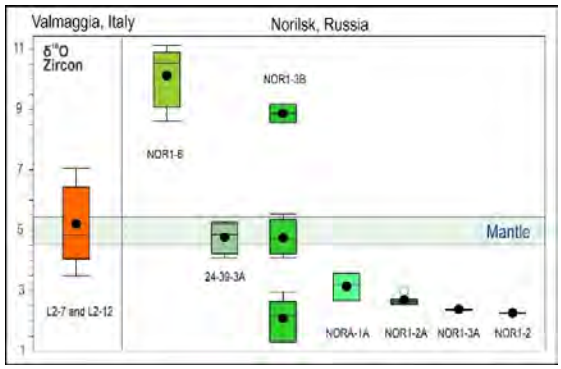

Figure 2. Oxygen (δ18O) isotope compositions of zircon found in haloes enveloping magmatic sulfide globules from Norilsk (Russia) and Valmaggia (Italy) intrusions.

The carbon isotopes in calcite can be divided into two main groups. Samples from the Valmaggia pipe, as well as some samples from the Norilsk deposit,

exhibit values between -16 to -10 ‰ (Fig. 3). In contrast, calcite from the Rudniy and Norilsk intrusions falls in a range between -6 to 0 ‰. The oxygen isotopes for all samples have values ranging from 5 to 15 ‰.

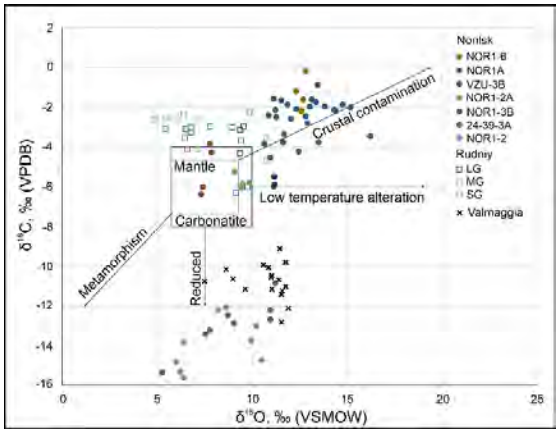

Figure 3. Oxygen (δ18O) and carbon (δ13C) isotope compositions of calcite associated with magmatic sulfide globules from Norilsk (Russia), Rudniy (Mongolia) and Valmaggia (Italy).

3 Discussion and conclusions

The paragenetic association of magmatic sulfides with volatile- and incompatible element-rich phases has been interpreted to reflect the former presence of (supercritical) fluids and/or vapour bubbles, which would physically adhere to the droplets of sulfide liquid upon emplacement and crystallization of the magma. These compound bubbles would significantly increase the buoyancy of sulfide liquid, acting as a natural analogue of an industrial flotation process (Mungall et al. 2015). According to this theory, upon solidification of the magma, these bubbles would form the hollow spaces that would be later filled with late stage highly fractionated magmatic liquid (Le Vaillant et al. 2017). However, our study shows that the specific association, composition, zonation, and trace element geochemistry of accessory minerals contained within the haloes surrounding the sulfides cannot be explained by late filling of former bubbles, nor it can form from primary supercritical fluids (Blanks et al. 2020). In fact, if apatite and zircon had formed from late magmatic fluids, their REE concentrations would have been significantly lower (Fig. 1a, (Shi et al. 2022)). Furthermore, special conditions are required to mobilize Ti and Zr in late hydrothermal fluids (Rubin et al. 1993; Ayers et al. 2012); even crystallization of pure calcite would require the presence of Ca cations in excess of what is anticipated for residual silicate magma, which is very unusual in magmatic environments.

However, this association could have been formed due to exsolution of an immiscible carbonate melt from a mafic magma. The intimate spatial relationship documented in several natural examples suggest that carbonate droplets tend to wet sulfide liquid (Cherdantseva et al., in review). Accordingly, the sharp margins of the haloes could be explained by three liquid immiscibility, rather than by the preservation of gas bubbles, which could be problematic under pressure in a crystal mush, as it could cause the bubbles to explode or escape in low-pressure areas. Also, the unusual enrichment of REE relative to what is expected from fractionated silicate magma in zircon and apatite, especially light REE in apatite, can advocate for the carbonatitic origin of those minerals. In fact, the REE distribution patterns from samples in this study coincide with REE patterns reported for carbonatites and alkali-rich systems, such as Kovdor or Songwe Hill (Broom-Fendley et al. 2017; Milani et al. 2017).

The mineral assemblage crystallized from carbonate melt contains mostly volatile-rich phases, specifically, water-rich amphiboles and phlogopites, as well as hydrous calcium silicates and Cl- and F-rich apatite. Carbonate melts generally have relatively low density (2.7 g/cm^3) and viscosity (0.0067±0.0006 Pa s). Considering volume ratios, the average density of a compound globule made up of carbonate-sulfide liquids would be similar to that of mafic silicate melts; however, the addition of volatiles in carbonate melt could play a role in further increasing the buoyancy of the sulfide compound globules.

We may be able to utilize the geochemical and isotopic data gathered from this study to shed light on the origin of the carbonate melts that appear to surround the sulfide droplets found in the intrusions. These intrusions were observed at varying levels within the Earth's crust, prompting the question of whether the gathered information can be used to provide insight into the unknown source of these liquids. Whereas carbonate liquid is known to form in the mantle (Panina and Motorina 2008), the exsolution of carbonate melts in mafic silicate magmas is not a common occurrence. The data presented here indeed portray a complex scenario. Our study shows that different sources of carbonate liquid could be involved in their origin. For example, the relationship of oxygen and carbon isotopes in calcite indicates that a wide range of sources may be involved (Fig. 1), emphasizing the role of crustal contamination in the genesis of carbonate-rich liquids. This also indicates the variety of crustal material that could be assimilated. Thus, the points that fall in the field of reduced conditions could be formed due to assimilation of carbonaceous graphitic shale. This process could potentially trigger the oversaturation of magma with carbon dioxide (Virtanen et al. 2021) to the extent of exsolution of immiscible carbonate liquid. This process is also generally ascribed to be crucial in adding the additional source of sulfur required to trigger sulfide saturation in magmas emplaced at various depths (Mavrogenes and O'Neill 1999). Specifically, the carbon isotope values characteristic for Valmaggia (deep crust) and several samples from the Norilsk intrusions (shallow crust) could reflect assimilation of some reduced carbon (e.g., coal measures), and/or

reflect mass dependent fractionation due to CO_2 degassing (Gales et al. 2020).

Nevertheless, some of the isotopic signatures still point to a strong mantle contribution as a preferred source for the origin of the immiscible carbonate coats surrounding the sulfide globules (Fig. 3). This piece of evidence indicates that even despite the long and complicated history of crystallization of the magmatic intrusions, a carbonate liquid sourced from the mantle could accompany sulfide droplets all the way across the lithosphere. Along this journey, the carbonate coat may isolate sulfide liquid, preventing it from being re-dissolved in the host silicate melt upon ascent. If this process operated widely, it would be possible to envisage the occurrence of large mineralized camps where mass concentrative processes could have accumulated mantle-derived metal-rich magmatic sulfides without any necessary role for crustal contamination, effectively opening up new search space for nickel-sulfide provinces.

Acknowledgements

We acknowledge the support of the UWA through the SIRF scholarship granted to MC. The funding was provided by the Australian Research Council through grant DP190102422 awarded to MF.

References

Aird HM, Boudreau AE (2013) High-temperature carbonate minerals in the Stillwater Complex, Montana, USA. Contrib to Mineral Petrol 166:1143–1160. https://doi.org/10.1007/s00410-013-0913-2

Ayers JC, Zhang L, Luo Y, Peters TJ (2012) Zircon solubility in alkaline aqueous fluids at upper crustal conditions. Geochim Cosmochim Acta 96:18–28. https://doi.org/10.1016/j.gca.2012.08.027

Barnes SJ, Mungall JE, Le Vaillant M, et al (2017) Sulfide-silicate textures in magmatic Ni-Cu-PGE sulfide ore deposits: Disseminated and net-textured ores. Am Mineral 102:473–506

Blanks DE, Holwell DA, Fiorentini ML, et al (2020) Fluxing of mantle carbon as a physical agent for metallogenic fertilization of the crust. Nat Commun. https://doi.org/10.1038/s41467-020-18157-6

Broom-Fendley S, Brady AE, Wall F, et al (2017) REE minerals at the Songwe Hill carbonatite, Malawi: HREE-enrichment in late-stage apatite. Ore Geol Rev 81:23–41

Fiorentini ML, Beresford SW (2008) Role of volatiles and metasomatized subcontinental lithospheric mantle in the genesis of magmatic Ni-Cu-PGE mineralization: Insights from in situ H, Li, B analyses of hydromagmatic phases from the Valmaggia ultramafic pipe, Ivrea-Verbano Zone (NW Italy). Terra Nov 20:333–340. https://doi.org/10.1111/j.1365-3121.2008.00825.x

Gales E, Black B, Elkins-Tanton LT (2020) Carbonatites as a record of the carbon isotope composition of large igneous province outgassing. Earth Planet Sci Lett 535:116076. https://doi.org/10.1016/j.epsl.2020.116076

Keevil HA, Namur O, Holness MB (2020) Microstructures and late-stage magmatic processes in layered mafic intrusions: Symplectites from the sept iles intrusion, Quebec, Canada. J Petrol 61:1–25. https://doi.org/10.1093/petrology/egaa071

Le Vaillant M, Barnes SJ, Mungall JE, Mungall EL (2017) Role of degassing of the Noril'sk nickel deposits in the Permian-Triassic mass extinction event. Proc Natl Acad Sci U S A 114:2485–2490. https://doi.org/10.1073/pnas.1611086114

Mavrogenes JA, O'Neill HSC (1999) The relative effects of pressure, temperature and oxygen fugacity on the solubility of sulfide in mafic magmas. Geochim Cosmochim Acta 63:1173–1180

McDonough WF, Sun S-S (1995) The composition of the Earth. Chem Geol 120:223–253

Milani L, Bolhar R, Frei D, et al (2017) Light rare earth element systematics as a tool for investigating the petrogenesis of phoscorite-carbonatite associations, as exemplified by the Phalaborwa Complex, South Africa. Miner Depos 52:1105–1125

Mungall JE, Brenan JM, Godel B, et al (2015) Transport of metals and sulphur in magmas by flotation of sulphide melt on vapour bubbles. Nat Geosci 8:216–219. https://doi.org/10.1038/ngeo2373

Panina LI, Motorina I V. (2008) Liquid immiscibility in deep-seated magmas and the generation of carbonatite melts. Geochemistry Int 46:448–464. https://doi.org/10.1134/S0016702908050029

Rubin JN, Henry CD, Price JG (1993) The mobility of zirconium and other "immobile" elements during hydrothermal alteration. Chem Geol 110:29–47. https://doi.org/10.1016/0009-2541(93)90246-F

Ryabov VV, Shevko AY, Gora MP (2014) Trap Magmatism and Ore Formation in the Siberian Noril'sk Region

Schoneveld L, Barnes SJ, Godel B, et al (2020) Oxide-sulfide-melt-bubble interactions in spinel-rich taxitic rocks of the Norilsk-Talnakh intrusions, Polar Siberia. Econ Geol 115:1305–1320. https://doi.org/10.5382/ECONGEO.4748

Shi Q, Guo H, Liu C, Lai Y (2022) Genesis and Metallogenic Characteristics of the Zhunsujihua Granitic Intrusions in Sonid Left Banner, Inner Mongolia, China. Minerals 12:. https://doi.org/10.3390/min12050606

Virtanen VJ, Heinonen JS, Molnár F, et al (2021) Fluids as primary carriers of sulphur and copper in magmatic assimilation. Nat Commun 12:. https://doi.org/10.1038/s41467-021-26969-3

Vorontsov AA, Yarmolyuk V V., Fedoseev GS, et al (2010) Isotopic and geochemical zoning of Devonian magmatism in the Altai-Sayan rift system: Composition and geodynamic nature of mantle sources. Petrology 18:596–609. https://doi.org/10.1134/S0869591110060032

Wernette B, Li P, Boudreau A (2020) Sulfides, native metals, and associated trace minerals of the Skaergaard intrusion, Greenland: evidence for late hydrothermal fluids. Miner Depos 55:1197–1214. https://doi.org/10.1007/s00126-019-00924-1

Role of carbon in the formation of Ni-Cu-PGE mineralization in the Valmaggia ultramafic pipe: Insights from laser-ablation-time-of-flight ICP-MS

Shelby Clark[1], Marek Locmelis[1], Dany Savard[2], Marilena Moroni[3], Marco Fiorentini[4]
[1]Department of Geosciences and Geological and Petroleum Engineering, Missouri University of Science & Technology, Rolla, Missouri, USA
[2]LabMaTer, Département des Sciences Appliquées, Université du Québec à Chicoutimi, Chicoutimi, Québec, Canada
[3]Department of Earth Sciences, University of Milan, Italy
[4]School of Earth Sciences, The University of Western Australia, Perth, Australia

Abstract. Understanding the processes that control sulfide transport and deposition in the deep lithosphere is a critical step in the search for ore deposits in lower crustal rocks. The magmatic sulfide ore-bearing Valmaggia pipe in the Ivrea-Verbano Zone (Italy), an exposed cross section of the subcontinental lithospheric mantle and overlying crust, allows for unique insight into ore-forming processes in the lower crust. Sulfides in the pipe are spatially associated with carbonates and hydrous silicates. Previous studies suggested that the sulfides were physically introduced into the pipe via a bubble-pair transport model, i.e., upward flotation of sulfide droplets attached to vapor bubbles. To further evaluate sulfide ore-forming processes, we integrate new petrographic observations with laser-ablation time-of-flight-ICP-MS trace element mapping of sulfide-carbonate-hydrous silicate relationships. We show that carbonates and hydrous silicates exist in varying sizes, compositions, textures and orientations in relation to sulfide phases, and are not restricted to a singular textural or chemical relationship. Similarly, sulfide textures vary and may or may not exhibit rimming by volatile phases. Our data show that bubble-pair transport cannot fully explain the textural relationships between sulfides and volatile-rich minerals, but rather suggest that at least some of the sulfides and carbonates co-precipitated from the same fluid/melt.

1 Introduction

The number of new and significant ore deposit discoveries is declining (Schodde, 2020). One possible way to increase the discovery of magmatic Ni-Cu-platinum-group element (PGE) sulfide deposits is to open new exploration space in (exhumed) lower crustal rocks that are often neglected in exploration models. However, the chemical and physical processes that form magmatic sulfide deposits in the lower crust remain elusive.

One key area to study the formation of lower crustal magmatic sulfide deposits is the Ivrea-Verbano Zone (IVZ) in northwest Italy (Fig. 1A). The IVZ is a rare example of an exposed cross section of the subcontinental lithospheric mantle and overlying crust (Mehnert, 1975; Garuti et al. 1980). The IVZ hosts five variably metasomatized ultramafic pipes (Fig. 1B) containing Ni-Cu-PGE mineralization with grades of up to 11.9% Cu, 10.7% Ni, and 5 ppm PGE (Zaccarini et al. 2014). The sulfide mineralization appears to be spatially associated with carbonate minerals and hydrous silicates such as phlogopite and amphibole. However, the relationship between volatile-rich minerals and sulfides, and to what extent (carbonated) hydrous fluids played a role in ore genesis, remains to be fully understood.

Previous studies suggested that the sulfides were physically introduced into the pipes via a bubble-pair transport model wherein SCLM sulfides attached to supercritical CO_2 bubbles migrated upwards into the pipes (Blanks et al. 2020; Locmelis et al. 2021). To further test this hypothesis, we integrate new petrographic observations with laser-ablation time-of-flight inductively coupled mass spectrometry (LA-ICP-TOF-MS) trace element mapping of sulfide-carbonate-hydrous silicate relationships for the best preserved IVZ pipe at Valmaggia. The data are used to evaluate whether 1) sulfides were introduced into the Valmaggia pipe attached to CO_2 bubbles, or whether 2) sulfides and carbonates co-precipitated from a high temperature fluid or melt rich in S and CO_2/$CaCO_3$.

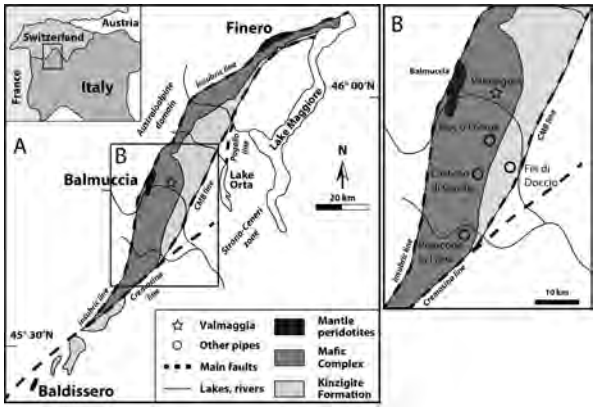

Figure 1. A: Simplified geologic map of the Ivrea Verbano Zone. B: Location of the ultramafic pipes, including Valmaggia (star). Modified after Fiorentini and Beresford (2008) and Locmelis et al. (2016).

2 Geologic Setting

The IVZ (Fig. 1) in the Western Alps, Italy, hosts five discordant ultramafic pipe-like intrusions hosted by the Mafic Complex and Kinzigite Formation (Fig. 1B). Locmelis et al. (2016) showed that the 249 Ma Valmaggia pipe was initially emplaced as an almost pure dunite. Later metasomatic pulses at 209.4 ± 5.1 Ma and 207.8 ± 2.0 Ma (Sessa et al. 2017;

Figure 2. *Reflected light image of sample VMG1B from the core domain of the Valmaggia pipe. Insets show zoomed-in reflected light images of pyrrhotite (Po) and pentlandite (Pn) blebs/globules. The red arrows indicate the perpendicular direction of sulfide-carbonate contacts.*

Locmelis et al. 2021) produced a secondary hydrous assemblage dominated by phlogopite and amphibole with locally abundant carbonates. The Valmaggia pipe hosts blebby and semi-massive sulfide mineralization in its rim portion, compared to a smaller (< 1 mm) disseminated assemblage in the core. Locally, the sulfides are rimmed by and/or intergrown with carbonates, phlogopite and amphibole, particularly in the rim portion.

3 Samples and Methods

Four polished thin sections from the Valmaggia pipe were investigated, i.e., two from the core (VMG1B and VMG7) and two from the rim (I-6A and I6B). The sections were studied using transmitted and reflected light microscopy using a Leica DVM 6 digital microscope in the Department of Geosciences and Geological and Petroleum Engineering (GGPE) at Missouri University of Science and Technology.

Major and minor element compositions of sulfides, carbonates and silicates were determined using a JEOL JXA-8200 electron microprobe equipped with wavelength and energy dispersive spectrometers (EDS and WDS) in the Department of Earth and Planetary Sciences, Washington University, St. Louis, Missouri, USA. Precision and accuracy were better than 3-5% (2σ).

A total of 27 quantitative sets of maps (^{23}Na to ^{238}U) were generated by time-of-flight LA-ICP-TOF-MS (Savard et al. 2023) using a 7, 9, and 19 µm beam size. The analysis focused on sulfide grains that were in contact and/or or spatially close to volatile phases (carbonates and/or hydrous silicates).

4 Sulfide – Carbonate Relationships

Sulfide mineralization in the core of the Valmaggia pipe is commonly disseminated, consisting of < 1 mm patches and composite blebs of pyrrhotite + pentlandite ± chalcopyrite (Fig. 2). Sulfide mineralization in the rim is semi-massive, consisting of polyphase blebs composed of pyrrhotite + pentlandite ± chalcopyrite several microns up to 1 cm in the longest direction (Fig. 3A). In both domains, sulfides are commonly embayed with, or rimmed by, carbonate phases (Fig. 3) and/or hydrous silicates (phlogopite, amphibole). The TOF-LA-ICP-MS data show that sulfides spatially related to carbonates are variably enriched in lithophile elements in the rim (< 20-370 ppm Na, 100-7400 ppm Mg, < 40-390 ppm Al, and < 330-676 ppm Ca) and the core (< 20-530 ppm Na, < 50-1100 ppm Mg, < 40-280 ppm Al, < 330-580 ppm Ca).

Carbonates in the studied samples are generally dolomitic, with less common calcite and Ca-Mg-Fe carbonate phases. The Ca-rich carbonate phases commonly occur adjacent to, or in direct contact with sulfides (Figs. 3A and 4A). Conversely, Ca-poor and Fe-rich phases are mostly surrounded by and intermixed with silicate phases and restricted to sulfide-poor or -absent areas.

Three distinct carbonate groups were identified in this study:

1) Carbonates in direct contact with sulfide grains/blebs in sulfide-rich areas. These grains contain 15-20 wt.% Mg, 20-30 wt.% Ca, 2-3 wt.% Fe, with 1500-2000 ppm Mn, 40-60 ppm Pb, < 90-2780 ppm Ni, and < 30-170 Cu;

2) Carbonates not in direct contact with sulfides, but near small, disseminated sulfide grains (<150 µm) in sulfide-poor areas. These grains contain 34-50 wt.% Mg, < 0.5 wt.% Ca, 10-15 wt.% Fe, 0.5-0.7 wt.% Mn, < 90-120 ppm Ni, and < 30-34 ppm Cu;
3) Carbonates within sulfide grains as vein fill (only in sample VMG7). These grains contain 8-9 wt.% Mg, 20-22 wt.% Ca, 2-3 wt.% Fe, 3-6 wt.% Mn, < 90-265 ppm Ni, and < 30-90 ppm of Cu.

5 Bubble transport vs. chemical precipitation of sulfides in the Valmaggia pipe

Two possible models for the origin of sulfide mineralization in the Valmaggia pipe are discussed: physical bubble-pair transport and chemical sulfide-carbonate co-precipitation.

A physical bubble transport mechanism for sulfides from the upper crustal Norilsk-Talnakh deposit in Russia was recently proposed by Barnes et al. (2019). These authors identified several key characteristics that may be indicative of a bubble transport, including:

1) Crystalline silicate caps uniformly oriented in the direction of lower lithostatic pressure "above" sulfide blebs or globules ("segregation vesicles"), indicating the buoyant migration of the vapor bubble upwards;
2) Flattening of sulfide globules perpendicular to the direction of ascent (gravitational settling);
3) Internal differentiation in the sulfide globule;
4) Differentiation in the silicate "cap".

Similarly, studies by Mungall et al (2015) and Yao and Mungall (2020) conducted experimental and natural studies confirming that under certain conditions, vapors can exsolve from a melt and act as a 'raft' for immiscible sulfide droplets to migrate upwards through a melt.

Here we further investigate the possibility of bubble transport in the Valmaggia pipe via trace element TOF-LA-ICP-MS mapping. Our observations show several lines of evidence that are not consistent with a simple bubble transport model. For example, the mineral textures observed in the samples studied here do not follow the criteria identified by Barnes et al. (2019). There is no obvious uniform orientation of the volatile-rich components associated with sulfides that would indicate pressure-controlled ascent of sulfide-bubble pairs (Fig. 2). Further, uniform flattening of sulfides is not observed although the effect of flattening should theoretically be stronger considering the emplacement depth and impact of high pressure on crystal settling.

Cuspate "embayments" within sulfides are rarely rimmed with carbonates or other volatile-bearing phases. Comb-textured carbonate aggregates

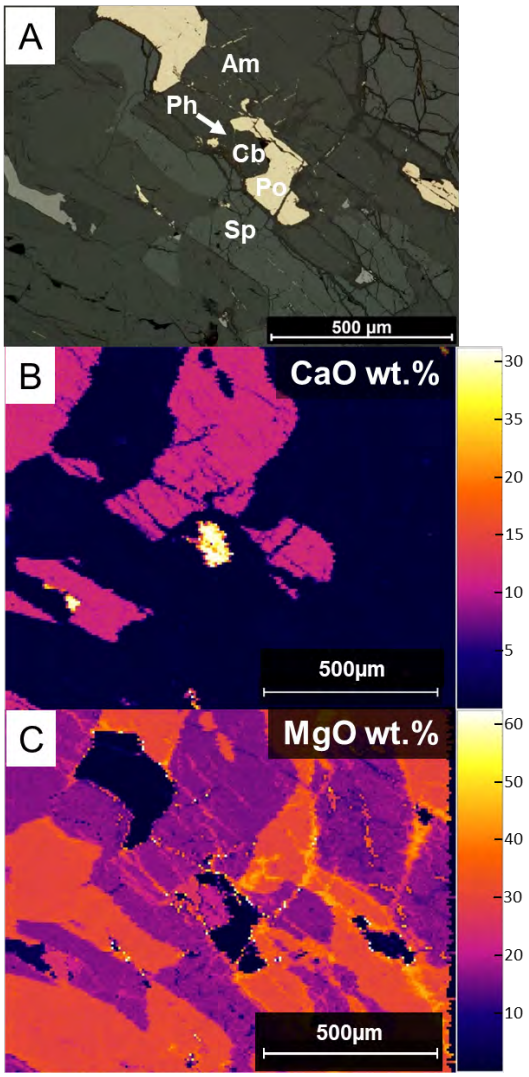

Figure 3. A: Reflected light image of a monophase pyrrhotite grain with a Mg-Ca carbonate grain embayment from sample I6B. B-C: Time-of-flight LA-ICP-MS elemental weight % maps analyzed with a 7 µm beam size. Yellow indicates the highest concentration measured for CaO (B) and MgO (C). Am = amphibole, Cb = carbonate, Po = pyrrhotite, Sp = spinel, Ph = phlogopite.

adjacent to sulfides (which may indicate late-stage carbonate precipitation) were documented by Sessa et al. (2017) and Blanks et al. (2020), but not observed in this study, possibly indicating more than one carbonate mineralization event. The absence of uniform relationships between sulfides and volatile-bearing phases suggests that their formation (or preservation) likely was not uniform throughout the pipe. Furthermore, it is noted that internal differentiation of sulfides and silicate caps (*cf.* Barnes 2019) remain to be fully investigated; however, our currently available data do not show any textural or compositional evidence for mineral-scale differentiation processes.

In contrast to a simple bubble transport model, several textural and geochemical observations appear to favour co-precipitation of sulfides, carbonates, and (metasomatic) silicates. For example, the enrichment of lithophile elements (Ca,

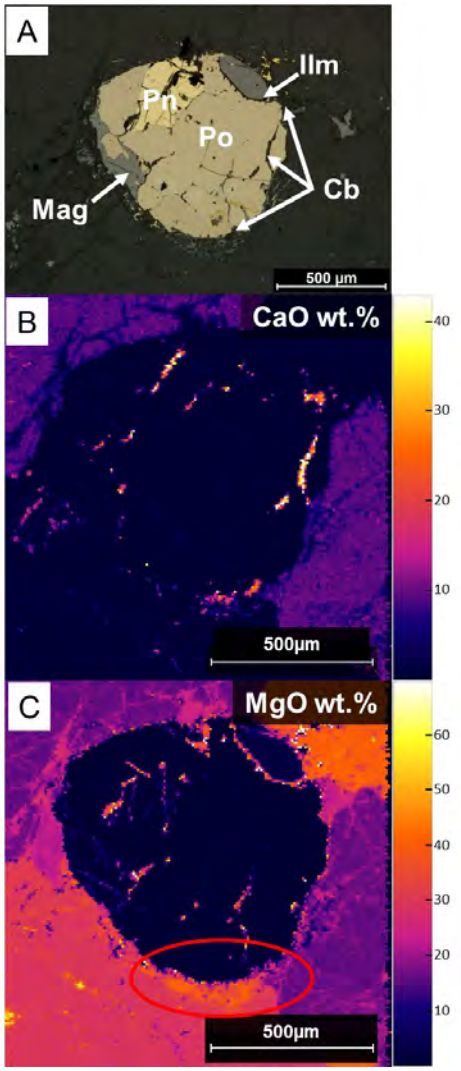

Figure 4. A: Reflected light image of a composite pyrrhotite-pentlandite bleb with accessory ilmenite, magnetite, and carbonate phases surrounding the bleb (center) from sample VMG1B. B-C: Time-of-flight LA-ICP-MS elemental weight % maps analyzed with a 7 µm beam size. Yellow indicates the highest concentration measured for CaO (B) and MgO (C). Am = amphibole, Cb = carbonate, Po = pyrrhotite, Mag = magnetite, Ilm = ilmenite.

Mg, Na, Al) in pyrrhotite and chalcophile elements (Cu, Ni, Fe, Pb) in carbonate phases indicates that the composition of sulfides and carbonates are controlled by the same geochemical process. This is further indicated by the occurrence of varying carbonate compositions (Ca-rich vs Mg- and Fe-rich). Carbonate inclusions in sulfides (Figs. 4B, 4C) have a composition similar to that of the rimming carbonates: this relationship cannot be explained with a simple bubble transport model as it is not physio-chemically compatible. Rather, it indicates that a carbon-rich fluid was present during sulfide ore formation.

The observations presented here possibly indicate co-exsolution of a carbonate phase and sulfide minerals from a S and CO_2 saturated fluid/melt. The findings from this study highlight the need for more comprehensive research on the roles of volatile phases in the transport and deposition of S and metals in the deep lithosphere.

Acknowledgements

M. L. acknowledges support through the National Science Foundation (NSF) CAREER award #1944552 “Investigating the source, transport and deposition of economically important metals in the lower continental crust”.

References

Barnes, S. J., Le Vaillant, M., Godel, B., & Lesher, C. M. (2019). Droplets and bubbles: solidification of sulphide-rich vapour-saturated orthocumulates in the Norilsk-Talnakh Ni–Cu–PGE ore-bearing intrusions. Journal of Petrology, 60(2):269-300.

Blanks, D. E., Holwell, D. A., Fiorentini, M. L., Moroni, M., Giuliani, A., Tassara, S., González-Jiménez, J.M., Boyce, A., & Ferrari, E. (2020). Fluxing of mantle carbon as a physical agent for metallogenic fertilization of the crust. Nat Communications, 11(1):4342.

Garuti, G., Rivalenti, G., Rossi, A., Siena, F., Sinigoi, S., 1980. The Ivrea–Verbano mafic ultramafic complex of the Italian western Alps: discussion of some petrologic problems and a summary. Rendiconti della Societa Italiana di Mineralogia e Petrografia 36:717-749.

Locmelis, M., Fiorentini, M.L., Rushmer, T., Arevalo Jr, R., Adam, J. and Denyszyn, S.W. (2016). Sulfur and metal fertilization of the lower continental crust. Lithos, 244:74-93.

Locmelis, M., Moroni, M., Denyszyn, S.W., Webb, L.E., Fiorentini, M.L., Sessa, G., Caruso, S., Mathur, R. and Nanzad, B. (2021). On the formation of magmatic sulphide systems in the lower crust by long-lived mass transfer through the lithosphere: Insights from the Valmaggia pipe, Ivrea Verbano Zone, Italy. Terra Nova, 33(2):137-149.

Mehnert, K. R. (1975). The Ivrea Zone, a model of the deep crust. Neues Jahrbach fuer Mineralogie: Abhandlungen 125:156-199.

Mungall, J. E., Brenan, J. M., Godel, B., Barnes, S. J. & Gaillard, F. (2015). Transport of S, Cu and Au in magmas by flotation of sulphide melt on vapour bubbles. Nat Geoscience 8:216–219.

Savard, D., Dare, S., Bédard, L.P. and Barnes, S.-J. (2023). A New Mapping Protocol for Laser Ablation (with Fast-Funnel) Coupled to a Time-of-Flight Mass Spectrometer (LA-FF-ICP-ToF-MS) for the Rapid, Simultaneous Quantification of Multiple Minerals. Geostandards and Geoanalytical Research. Accepted Author Manuscript.

Sessa, G., Moroni, M., Tumiati, S., Caruso, S., & Fiorentini, M. L. (2017). Ni-Fe-Cu-PGE ore deposition driven by metasomatic fluids and melt-rock reactions in the deep crust: the ultramafic pipe of Valmaggia, Ivrea-Verbano, Italy. Ore Geol Rev, 90:485-509.

Schodde, R. (2017). Recent trends and outlook for global exploration. In Prospectors & Developers Association of Canada (PDAC) Convention, Conference Proceedings.

Yao, Z., & Mungall, J. E. (2020). Flotation mechanism of sulphide melt on vapour bubbles in partially molten magmatic systems. Earth and Planet Science Lett, 542:116298.

Zaccarini, F., Garuti, G., Fiorentini, M. L., Locmelis, M., Kollegger, P., & Thalhammer, O. A. (2014). Mineralogical hosts of platinum group elements (PGE) and rhenium in the magmatic Ni-Fe-Cu sulfide deposits of the Ivrea Verbano Zone (Italy): an electron microprobe study. Neues Jahrbuch für Mineralogie, 191:169-187.

Ni-Cu-Co-Bi mineralization in Valea Muntelui ultramafic complex (Cindrel Mountains, Romania)

[1]George Dincă, [1]Gavril Săbău, [1]Andra Filiuță
[1]Geological Institute of Romania, 1 Caransebeș St., Bucharest, Romania

Abstract. This paper presents the discovery of Ni-Cu-Co-Bi mineralization in Valea Muntelui ultramafic bodies from the Southern Carpathians. Core samples from two exploration drill holes in the ultramafic body were studied using optical microscopy and SEM/EDS measurements. All of the described ore minerals were discovered in highly serpentinized ultramafic rocks, with the mineral association consisting of ferromagnesian and calcic amphiboles, chlorite, talc, and dolomite, as well as chromiferous spinel grains partially transformed into magnetite. Pentlandite, pyrrhotite, cubanite, cobaltite, chalcopyrite, nickeline, maucherite, parkerite, native Bi, native Pb and natural Cu-Zn alloys were identified. The mineralization process appears to be linked to metasomatic fluids and the redox process leading to the development of a reducing character of the fluids. This research is the first description of Ni-Cu-Co-Bi mineralization in the region, and the first mention of parkerite in Romania and the Balkan Region.

1 Introduction

The studied area is located in the northern part of the Central Southern Carpathians (northeast of the Cindrel Mountains), west of the Olt River Valley, and approximately 2.0 km southwest of the town of Rășinari, Romania.

An unusual Ni-Cu-Co-Bi mineralization appears in Valea Muntelui ultramafic bodies included in the medium-grade Lotru Metamorphic Suite of the South Carpathian basement units.

The mineralization is located along the Valea Muntelui Brook, being hosted in a metamorphosed dunite-peridotite-gabbroic complex preserving abundant textural relics (Codarcea, 1965). The ultramafic rocks, as also amphibolite and eclogite pods equally pointing to mantle- and ocean crust-derived protoliths, appear scattered on a regional scale in the dominantly plagioclase-gneiss matrix of a Variscan tectono-metamorphic complex, marking a suture zone and overlying reworked Early Paleozoic gneissic-granitic basement units (Săbău and Negulescu, 2014).

2 Samples and Methods

Core samples from two exploration drill holes in the ultramafic body were studied. To perform this study, over 20 polished sections of ore samples, were analyzed by optical microscopy under reflected light. The optical microscope used was a Zeiss Imager A2m with an attached Zeiss Axiocam ICc 5 MP camera. Mineral symbols recommended by the Commission on New Minerals, Nomenclature and Classification of the International Mineralogical Association were used for mineral abbreviation in figures and tables (Warr, 2021). For the determination of the chemical composition, SEM/EDS measurements were conducted at the Geological Institute of Romania using a Hitachi TM3030 SEM on uncoated samples with an acceleration voltage of 15 kV, emission current of 25400 nA, focused beam in scanning mode, at a working distance of 7.5-9 mm, and variable counting times averaging 120 s, aimed to optimize noise to signal ratio, visually appreciated from the smoothness of the background spectrum. Elemental analysis was done through Bruker's QUANTAX 70 EDS system.

3 Results

The host rocks are represented by transformed peridotites with a complex history, with medium grade metamorphic and retrograde overprints, as well as attenuation of the chemical gradients towards the host rocks. All of the below-mentioned ore minerals were identified in highly serpentinized and carbonated varieties. Frequent domain textures suggest the preexistence of coarsely developed grains, but their former boundaries appear diffuse, and the composition is exclusively made up of secondary minerals. The mineral association consists of ferromagnesian and calcic amphiboles often with zonal or overgrowth structure, chlorite, talc, and dolomite. The presence of dolomite and talc indicates metasomatic alteration with the contribution of carbonate fluids and silica, of the same nature as listvenitization, but without the installation of a quartz – carbonate – K-white mica association characteristic for the completion of this process (Halls and Zhao, 1995). Several chromiferous spinel grains partly transformed into magnetite were identified, which imply a preliminary stage of iron release during the serpentinization of ultramafic association. Iron oxide crystals with dimensions up to 0.1 mm, sometimes with idiomorphic outlines, are disseminated in the rock. In one of the samples the mineralization is concentrated along former cracks and former grain boundaries.

3.1 Pentlandite, Pyrrhotite, Chalcopyrite and Cubanite

The carbonate+talc altered samples display a noteworthy mineralogical assemblage of: pentlandite, pyrrhotite, cubanite, cobaltite, and chalcopyrite (Fig. 1) disseminated throughout the sample, indicating a higher

concentration of sulfides compared to other serpentinite varieties from the region. The empirical composition of pentlandite from Valea Muntelui is $Ni_{3.51}Co_{0.16}Fe_{5.11}S_{8.22}$, Co varying from 1 to 3 wt%.

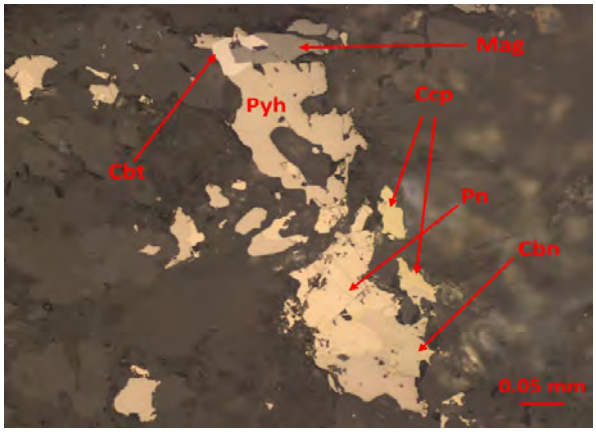

Figure 1. Reflected light photomicrograph of the common ore mineral association, formed by: pentlandite (Pn),, chalcopyrite (Ccp), pyrrhotite (Pyh), cubanite (Cbn) magnetite (Mag) and cobaltite (Cbt).

Chemical analyses of chalcopyrite and cubanite from Valea Muntelui gave the following formulas: $Cu_{1.04}Fe_{0.99}S_{1.97}$ and $Cu_{0.90}Fe_{2.04}S_{3.06}$.

3.2 Nickeline and Maucherite

Nickeline was identified in samples from Valea Muntelui in association with pyrrhotite and magnetite (Fig. 2). The calculated formula is $Ni_{0.93}Fe_{0.05}As_{1.02}$, being slightly enriched in Fe (up to 2.5 wt%).

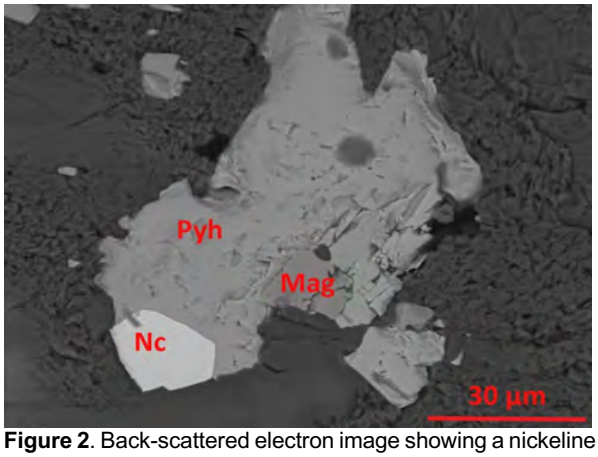

Figure 2. Back-scattered electron image showing a nickeline crystal (Nc) with pyrrhotite (Pyh) and magnetite. (Mag)

Maucherite is a rare Ni arsenide previously described in the South Carpathians by Popescu (1968) in the Bădeni Ni mineralization (Leaota Mountains), in a Ni-Co-Ag mineralization from Nimaia Valley, East Făgăraș Mountains (Lupulescu, 1982), and at Iacobeni, East Carpathians, associated with cobaltite and tučekite (Săbău, 2015). Presence of maucherite in Cindrel Mountains has not been reported so far. In the studied samples maucherite has been found in association with pentlandite and chalcopyrite (Fig. 3). Crystals can reach up to 150 µm in lenght.

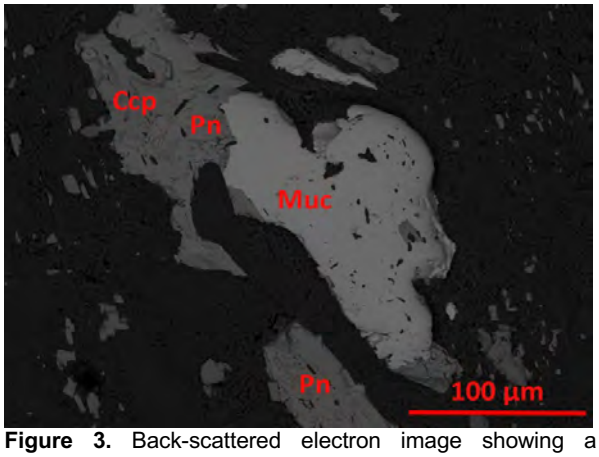

Figure 3. Back-scattered electron image showing a maucherite crystal (Muc) with pentlandite (Pn) and chalcopyrite. (Ccp)

The calculated empirical formula of maucherite is $Ni_{10.91}Fe_{0.34}Co_{0.18}As_{7.50}Sb_{0.07}$.

3.3. Co and Bi minerals

Cobaltite has been identified quite frequently as euhedral singular crystals in serpentine (Fig. 4) and in association with pentlandite, chalcopyrite, pyrrhotite and cubanite (Fig. 1). Chemical analyses of cobaltite from Valea Muntelui gave the following formula: $Co_{0.78}Ni_{0.10}Fe_{0.11}As_{1.05}S_{0.97}$.

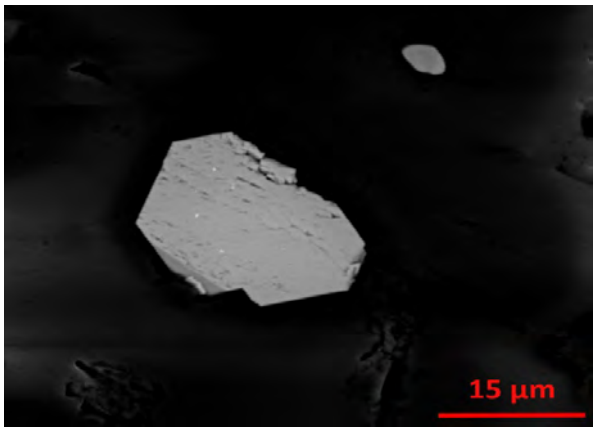

Figure 4. Back-scattered electron image showing a cobaltite crystal**.**

Cobaltite from the studied samples always presents Ni and Fe in the composition, with contents up to 4 wt%.

Parkerite was identified in only one sample from Valea Muntelui. It occurs as a 10 µm inclusion in pyrrhotite, presenting a rim of native Bi (Fig. 5). To our knowledge this is the first mention of parkerite in Romania an in the Balkan Region. The calculated empirical formula of parkerite is $Ni_{2.77}Co_{0.12}Fe_{0.70}Bi_{1.35}As_{0.18}S_{1.89}$. Parkerite from Valea Muntelui is lead free similar to parkerite from the Uralian Emerald Mines, Ural Mountains (Russia) described by Koroteev et al. (2017). The studied parkerite crystal is enriched in Fe and Co as shown in the chemical composition (Table 1).

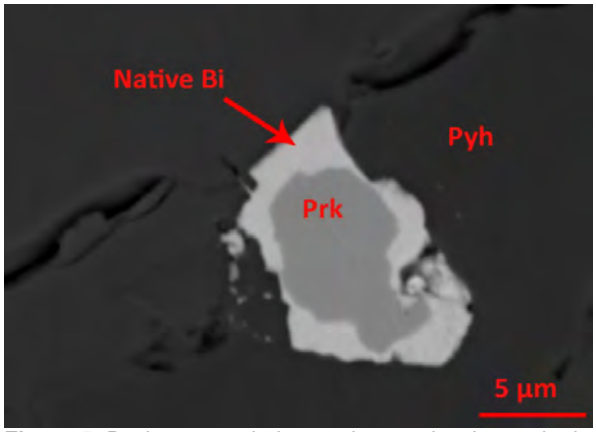

Figure 5. Back-scattered electron image showing parkerite (Prk) with native Bi rim included in pyrrhotite. (Pyh)

Table 1. Representative chemical composition of investigated Ni-Cu-Co-Bi minerals based on SEM-EDS analyses. Pn-pentlandite; Nc-nickeline; Muc-maucherite; Cbt-cobaltite; Prk-parkerite; Cbn-cubanite; Ccp-chalcopyrite

Element (wt%)	Pn	Nc	Muc	Cbt	Prk	Cbn	Ccp
Ni	26.94	40.60	51.60	3.61	28.80	-	-
Co	1.22	-	0.87	27.45	1.22	-	-
Fe	37.33	2.12	1.51	3.57	6.95	41.91	32.49
Cu	-	-	-	-	-	23.73	36.55
As	-	57.27	45.30	46.83	2.41	-	-
Sb	-	-	0.72	-	-	-	-
Bi	-	-	-	-	49.86	-	-
S	34.50	-	-	18.53	10.75	34.36	30.96
Total	100.00	100.00	100.00	100.00	100.00	100.00	100.00

3.4 Cu-Zn natural alloys

Natural Cu-Zn alloy was identified as small disseminated grains in association with native Pb. The natural Cu-Zn alloy shows the dominant composition of $Cu_3(Zn, Fe)_2$, with irregular zones richer in Fe and Ni, corresponding to the approximate composition $Cu_5Zn_3(Ni, Fe)_2$.

Table 2. SEM-EDS analyses of Cu-Zn phases.

Element (wt%)	Phase 1	Phase 2
Cu	56.83	49.31
Zn	38.40	32.67
Ni	-	15.67
Fe	4.77	2.35
Total	100.00	100.00

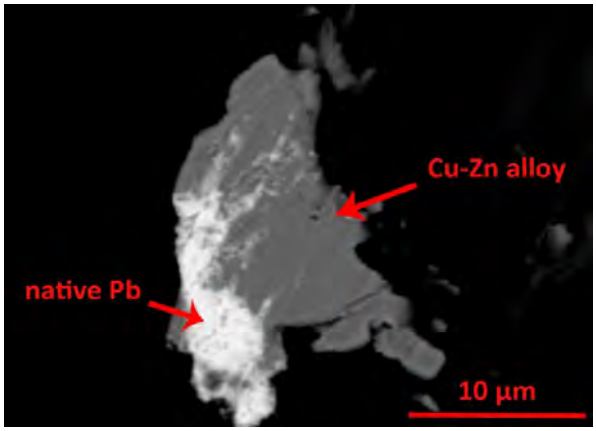

Figure 6. Back-scattered electron image showing association of native Pb with Cu-Zn alloy.

4 Discussion and conclusions

Ni-Cu-Co-Bi mineralization is described for the first time in this area, alongside native elements and alloys indicating a highly reducing chemical environment. The pertaining mineral phases appear in highly serpentinized and metasomatized metaultramafic rocks characterized by a talc-dolomite-chlorite assemblage more or less completely installed. The talc and dolomite-enriched metasomatized samples present a special mineral association, with Ni and Co sulfides and arsenides, native metals (Pb, Cu alloys, Bi) and parkerite, which, to our knowledge, is still unknown from other ultrabasic outcrops. The assemblage is typically represented by small grains disseminated in the altered rock or clustered along micro-lineaments which represent former circulated cracks or grain boundaries, indicating its formation during serpentinization and carbonate metasomatism following it or acting coevally.

The possible source of the elements involved is probably multiple, caused by fluid transport and mixing during metasomatic exchange processes. Decomposing olivine, in which Ni and Co are compatible, as well as pre-existing orthomagmatic Fe-Ni sulfides are the most probable source for siderophile elements. Base metals, As and Bi are most probably externally-derived, transported from the host rocks. Such mineralizations are known in structurally lower positions of the metamorphic basement, where they are considered shear zone-related (Popescu et. al, 2013, and refs. therein).

The onset of a reducing environment is triggered by the serpentinization of Mg-Fe – bearing silicates. Mg is preferentially incorporated in serpentine minerals, from which Fe is expelled and constrained to form magnetite, implying the oxidation of part of Fe^{2+} and the correlative reduction of the coexisting carbonaceous-aqueous fluid phase, which could transiently produce hydrogen and/or highly reduced C-bearing species (Berndt et al., 1996). This mechanism was invoked also for the formation of Fe-Ni alloys in serpentinized peridotites (Frost, 1985).

The complexity and unusual composition of this mineralization is a reflection of the combination of sources and processes operating during incorporation of ultramafic rocks in a tectonic mélange, medium-grade metamorphism, retrograde alteration, and chemical mass-transfer with the surrounding rocks.

Acknowledgements

We thank MINERAL PROIECT INVEST SA for the access to samples from Valea Muntelui. and the GeoEcoLab Laboratory, Geological Institute of Romania, for the acces to the SEM-EDS facilities. The authors acknowledge the financial support by the national research project PN23-39-02-03.

References

Berndt, M.E., Allen, D.E., Seyfried W.E Jr,. Reduction of CO_2 during serpentinization of olivine at 300 °C and 500 bar, *Geology, 24/4, 351-354*

Codarcea-Dessila, M. (1965), Studiul Geologic și Petrografic al Regiunii Răşinari-Cisnădioara-Sadu, *Mem. Com. Geol., Inst. Geol. Rom., Bucureşti vol. 6, 96 pp.*

Frost B.R. (1985) On the Stability of Sulfides, Oxides, and Native Metals in Serpentinite, *J. of Petrology 26/1, 31-63*.

Koroteev, V.A., Popov, M.P., Erokhin Yu. V., Khiller V.V. (2017) Parkerite and bismutohauchecornite in chromitites of the Urals: Example of the Uralian Emerald Mines, *Dokl. Earth Sc. 473, 438–440.*

Lupulescu, M. (1982): Prezenţa unei mineralizaţii de nichel, cobalt și argint în partea estică a Munţilor Făgăraş (V. Bârselor). [On the presence of a Ni-, Co- and Ag-bearing mineralization in the Eastern part of the Făgăraş Mts. (Bârse Valley)], *An. Univ. Bucureşti. Ser. Geol, 30, 27-31.*

Popescu. Gh.C. (1968): Asupra prezenţei maucheritului în mineralizaţia de nichel de la Bădeni (Munţii Leaota). [On the presence of maucherite in the Ni-bearing mineralization at Bădeni. Leaota Mts.], *Stud, cercet. Geol. Geofiz. Geogr., Ser. Geol, 13. 431-435.*

Popescu Gh.C., Neacșu A., Buia G., Damian G., Damian F. (2013) Perspectives of rare metals and dispersed elements ore deposits in Romania. A review. *Romanian J. of Mineral Deposits 86/1, 1-41*

Săbău, G. (2015) Co,Ni – bearing assemblages in the metamorphosed Mn ore from Iacobeni, Sub-Bucovinian Nappe System, East Carpathians, *Presentation, "Mircea Savul" Scientific Symposium, University of Iași, 24 october 2015*

Săbău, G., Negulescu, E. (2014) A monazite U-Th-Pb_T metamorphic ages survey in the South Carpathian basement units: delving into tectonic stacking and differential exhumation. *Buletini i Shkencave Gjeologjike, Special Issue Vol. 1/2014, Proc. XX Congress of Carpathian Balkan Geological Association (CBGA 2014), 24-26 September 2014, Tirana, Albania, 219-222*

Warr, L. N. (2021) IMA–CNMNC approved mineral symbols., *Mineral. Mag. 85, 291–320*.

Magmatic sulphide mineralization and prospectivity in the Tantalite Valley Complex, Namibia

Daniel Ferreira[1], Bjorn Von der Heyden[1], Martin Klausen[1], Laure Martin[2]
[1] *Department of Earth Sciences, Stellenbosch University, South Africa*
[2] *Centre for Microscopy, Characterization, and Analysis, University of Western Australia, Perth, Australia*

Abstract. The formation of immiscible sulphide melt within mafic-ultramafic magmas and its concentration of base-, semi-, and precious metals constitutes an important process in the formation of magmatic sulphide deposits. This study investigates the Tantalite Valley Complex in southern Namibia and the formation of sulphides within the complex and their potential to host valuable metals by examining the processes that led to sulphide melt segregation and accumulation. The research concludes that the TVC comprises a sequence of trough shaped layers of ultramafic dunite, harzburgite, websterite, pyroxenite, as well as troctolite and other gabbroic rock types whose stratigraphy has been complicated by faults and mineralization manifesting as disseminated sulphides within stratiform layers most notably within a pyroxenite layer. Furthermore, the sulphur in the system is derived from the mantle. Sulphide melt saturation is believed to have occurred due to high degrees of fractionation. Precious metals exist in both solid solution and discrete precious metal bearing minerals found within and associated with the sulphide phases. The R-factor for the complex stands at approximately 3 000 suggesting that a small fraction of sulphide melt formed, mixing to moderate degrees with the silicate magma before concentrating in a pyroxenite layer.

1 Introduction

The Tantalite Valley Complex (TVC) is a mafic-ultramafic igneous intrusion found within the core of the Pofadder Shear Zone which crosscuts the Richtersveld Subprovince (Figure 1). To date, previous exploration has been centred on uncovering massive Ni-Cu sulphide deposits. No previous research has been undertaken to investigate the potential for platinum group element (PGE) mineralisation. Mafic-ultramafic intrusions of this nature often yield economic deposits having concentrated base-, semi- and precious-metals, in the form of either sulphur-rich massive Ni-Cu (Co) sulphide deposits or sulphur-poor disseminated PGE deposits. Should a mineralised horizon or reef exist within the complex, its concentration of base-, semi- and precious-metals could warrant further investigation and prompt an in depth look into the economic potential of the complex with regards to PGEs.

Our research aims to analyse the metallogenesis of the complex and to assess its prospectivity for PGE mineralisation. From this we aim to gain better insight into the primary and secondary processes responsible for these concentrations of metals as well as their mineral makeup and associations.

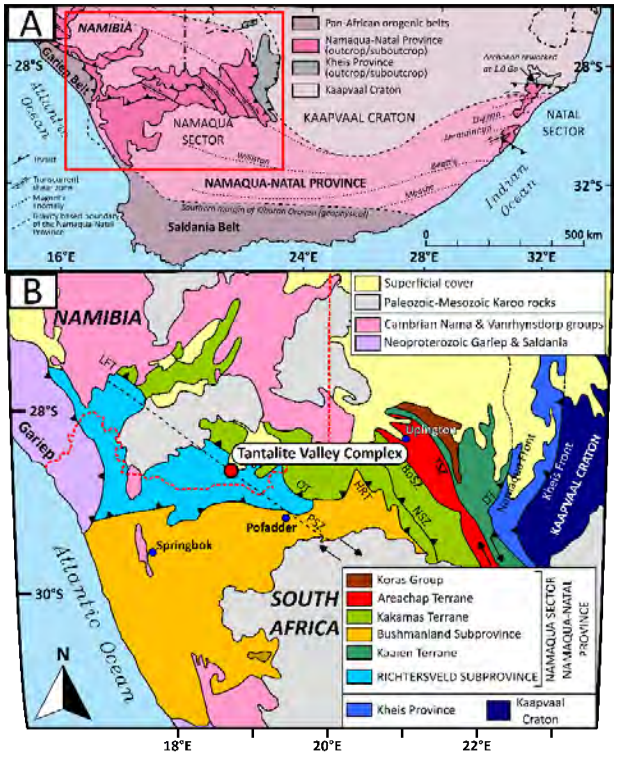

Figure 1. A) Location of the Namaqua Natal Metamorphic belt. B) The Namaqua Sector of the Namaqua Natal Metamorphic Belt. Modified from Macey et al. (2017).

2 Regional and local geology

The Namaqua Natal Metamorphic Province (NNMP) displayed in Figure 1 is a 400 km wide tectono-metamorphic belt bounding the southern and western margins of the Kaapvaal craton (Thomas et al. 1994; Cornell et al. 2006). The province is composed of two sectors, the Namaqua and the Natal sectors in the west and east respectively with the Namaqua sector having five distinct subdivisions, namely; the Richtersveld subprovince, the Bushmanland subprovince, and the Kakamas, Areachap and Kaaien terranes (Thomas et al. 1994; Cornell et al. 2006).

The Tantalite Valley Complex (TVC) is a mafic – ultramafic complex that intruded at 1212 ± 11 Ma into host rocks of the Richtersveld subprovince in the Namaqua-Natal Metamorphic Province (Moore et al. 1979; Macey et al. 2017; Figure 1). The host rocks have experienced numerous metamorphic and deformation events associated with the Orange River and Namaquan orogenies. The Orange River Group host rocks underwent deformation during the Namaquan Orogeny and now form part of the Namaqualand Gneiss Complex (von Backstrom

1976; Schreiber 2016). The approximately 9 x 3 km complex is found within the Pofadder Shear Zone, a dextral shear zone that stretches from the northeast of Luderitz in Namibia to the northeast of Pofadder in South Africa for a distance of 500 km (Kartun 1979). The complex consists of variably altered lithologies of norite, gabbronorite, olivine metagabbro, metagabbro, metagabbronorite, metatroctolite and ultramafic rocks such as dunite, harzburgite, lherzolite, (olivine) websterite and orthopyroxenite along with a thin contact hornfels zone (± 50 m) best seen along the complex's south-eastern and eastern border (von Backstrom 1976; Moore et al. 1979; Schreiber 2016).

3 Methodology

3.1 SEM analysis

Eleven well mineralized polished mounts were selected based on promising assay results and optical microscopy and were then analysed using SEM to ascertain the compositions of the "high contrast minerals" which includes those belonging to the Platinum Group Minerals (PGM).

SEM Energy Dispersive Spectrometer (SEM-EDS) analysis and elemental mapping was accomplished using a Zeiss EVO® MA15 Scanning Electron Microscope. The system is designed to perform high-resolution imaging concurrently with quantitative analysis, with errors ranging from ± 0.6 to 0.01 wt% on the major elements using EDS.

Platinum group minerals were identified with backscattered electron images, and phase compositions were quantified by EDS analysis using an Oxford Instruments® X-Max 20mm^2 detector and Oxford INCA software. Beam conditions during the quantitative analyses were 20 kV and approximately 1.0 A, with a working distance of 8.5 mm and a specimen beam current of - 20.00 nA. For mineral analyses counting time was 10 seconds live-time. Internal Astimex Scientific mineral standards were used for standardization and verification of the analyses. All major elements are below 5% uncertainty of their certified compositions. Pure Co was used periodically to correct for detector drift.

3.2 LA-ICP-MS

Bulk rock chemistry and LA-ICP-MS was undertaken on a subset of polished mounts and crushed country rock samples. The LA-ICP-MS set up follows guidelines set out by Eggins (2003). The methods employed here includes a resolution 193 nm Excimer laser coupled to an Agilent 7700 Q ICP-MS housed at the Central Analytical Facility (CAF), Stellenbosch University. The ICP-MS was optimized for low oxide ratios (less than 0.3%) and sensitivity by ablating a line on NIST612 whilst tuning both the laser parameters and the ICP. Ablation was performed in an atmosphere of Helium gas with a flow rate of 0.45L/min and then mixed with Argon with a flow rate of 1L/min and Nitrogen (0.003L/min) just before introduction into the ICP Plasma. A background acquisition time of 20 seconds was used with an ablation time of 45 seconds followed by a washout time of 25 seconds. Uncertainty for major elements is typically below 6% of their certified compositions. A total of 80 spots were selected for in-situ LA-ICP-MS from four polished mounts spread out across pyrite, pentlandite and pyrrhotite.

3.3 Secondary Ion Mass Spectrometry (SIMS) analysis

Three samples were sent for SIMS analysis at the Centre for Microscopy, Characterisation, and Analysis (CMCA) at the University of Western Australia for triple sulphur isotope analysis (^{33}S, ^{34}S, ^{36}S). The phases tested were pentlandite, pyrrhotite and pyrite for a total of 89 spots. The analysis protocol uses a CAMECA IMS1280 large-geometry ion microprobe with matrix-matched standards (LaFlamme et al. 2016) used to correct for instrumental mass fractionation. The matrix-matched standards are as follows: Sierra pyrite (δ^{34}S = 2.17 ± 0.28‰; Δ^{33}S = -0.02 ± 0.01‰; Alexo pyrrhotite (δ^{34}S = 5.23 ± 0.40‰; Δ^{33}S = -0.96 ± 0.04‰); VMSO pentlandite (δ^{34}S = 3.22 ± 0.51‰; Δ^{33}S = 0.0 ± 0.02‰) (LaFlamme et al. 2016). Uncertainty for isotope concentrations is typically below 6% of their certified compositions.

4 Sulphide and PGM paragenesis

Analysis of all polished mounts made from orthopyroxenite obtained from drill core reveals a primary pristine assemblage of sulphide disseminations with a largely interstitial/intergranular texture or in some rare instances as blebs of magmatic sulphides. The primary magmatic assemblage consists of pentlandite-pyrrhotite-chalcopyrite (Figure 2) with pentlandite having the greatest modal proportion in most cases followed by pyrrhotite and finally chalcopyrite. However, their proportions do vary considerably across drill core samples. Often seen under the microscope is a border of pentlandite separating the chalcopyrite and pyrrhotite indicating it to be peritectic in nature, pentlandite can infrequently be found as exsolved pentlandite flames within pyrrhotite grains. Alteration of the above pristine assemblage within orthopyroxenite manifests as an overprint in which primary pyrrhotite (pyrrhotite$_1$) (and in some instances pentlandite) is replaced by pyrite$_1$ due to late-stage hydrothermal fluids. Pyrite occurs as large euhedral grains with a hexagonal habit but also occurs as anhedral linear arrays within pyrrhotite$_1$ marking the plane of fluid ingress. Alteration further manifests in the gangue silicate assemblage in which amphibole and micas have recrystallized as pyroxene pseudomorphs (not to completion) and overgrowths. Following this, pyrite$_1$ associated with pentlandite and chalcopyrite and the first replacement assemblage is occasionally altered to pyrrhotite$_2$. The two pyrrhotite populations appear the same, however, under cross polarised light, the

primary pyrrhotite$_1$ displays uniform "extinction" within grain boundaries whilst the overprinting pyrrhotite$_2$ can be seen to have smaller euhedral polygonal granoblastic mosaic textured pyrrhotite crystals with a large number of triple junctions.

Analysis under the SEM revealed a number of high contrast minerals of varying compositions. These high contrast minerals are found largely as inclusions/clusters in pentlandite and to a lesser degree in chalcopyrite, even less so in pyrrhotite and pyrite. In some instances, PGMs are found away from sulphides completely, and spatially associated with silicates as opposed to sulphides. Some mineral phases that were found include Hessite (Ag_2Te), Electrum (gold-silver alloy), Merenskyite $(Pt,Pd)(Te,Bi)_2$, Moncheite $Pt(Te,Bi)_2$ and Paolovite (Pd_2Sn).

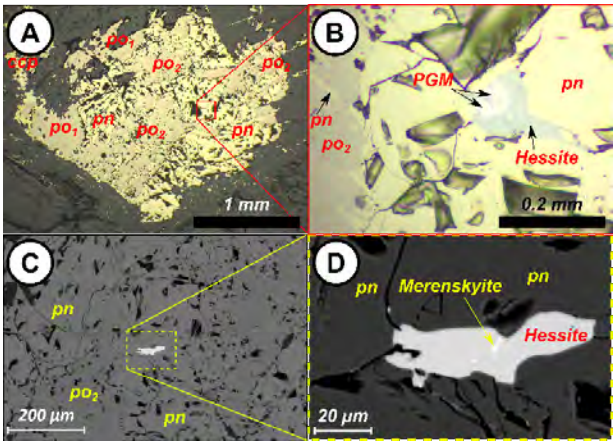

Figure 2. Reflected light microscopy as well as backscattered electron photomicrographs taken from sample D-07 which is particularly well-endowed. A) Pristine sulphide assemblage with overprinting pyrrhotite$_2$. B) Enlarged reflected light image of the PGMs and Hessite encircled in (A). C) Backscattered electron photomicrograph with the area of interest enclosed in yellow. D) Enlarged backscattered electron photomicrograph of the site of interest in (C) showing hessite with inclusions of merenskyite. Abbreviations; pn = pentlandite, po = pyrrhotite, ccp = chalcopyrite.

5 Source of sulphur and degree of silicate melt interaction

Sulphur selenium ratios coupled with multiple sulphur isotope ratios obtained from SIMS analysis (Figure 3), suggest that the sulphur in the system was derived from the mantle. Samples plotting slightly away from the mantle arrays have been the recipients of syn- to post magmatic hydrothermal alteration as well as weathering.

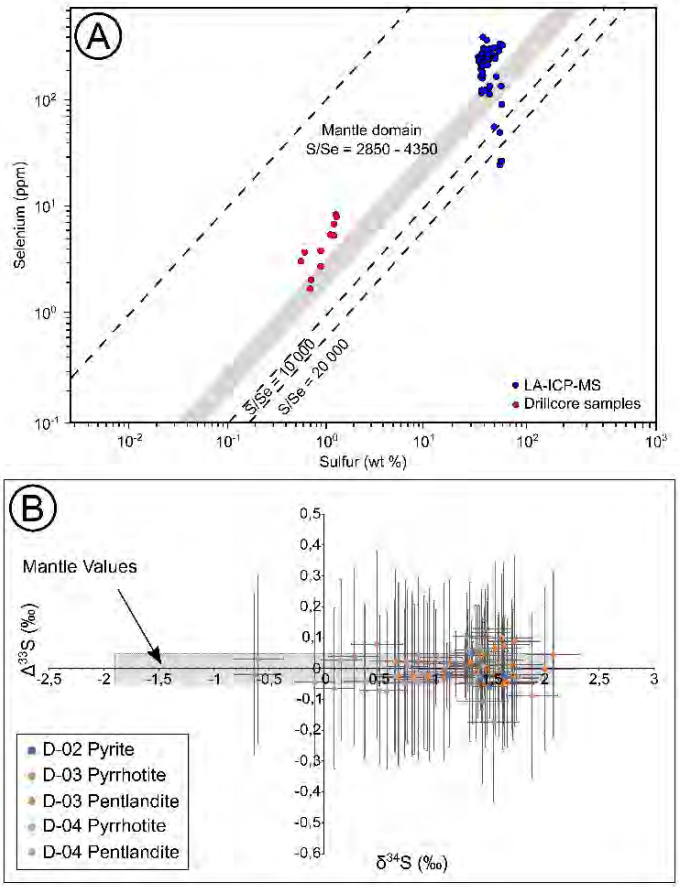

Figure 3. (A) Whole rock and in-situ LA-ICP-MS sulphur versus selenium plot. Modified from Queffurus and Barnes (2015). Mantle values determined by Eckstrand and Hulbert (1987). (B) Multiple sulphur isotope plot of pyrite, pyrrhotite and pentlandite in three different samples, the grey block in the centre represents sulphur isotope concentrations from the mantle as determined by Lesher (2017) for $\delta^{34}S$.

The R-Factor was computed using bulk rock samples from the igneous margin of the TVC as proxies for the parental melt composition. Their assay values for Co, Ni, Cu and Pd were then compared with computed values of 100% sulphides taken from the well-endowed pyroxenites to determine the R-Factor. Unfortunately, the results proved inconclusive due to alteration and metamorphism. As such, several semi-quantitative approaches were applied wherein the complex was compared to various other similar deposits in an effort to gauge its relative R-factor. The results indicate the systems R-Factor value lies between 1000 and 3000.

6 Conclusion

Sulphide saturation has occurred within the TVC resulting in the development of a relatively small fraction of sulphide melt that has preferentially concentrated base-, semi-, and precious metals within ultramafic layers and forming minor amounts

(< 2%) of pentlandite, pyrrhotite, chalcopyrite and pyrite. Based on in-situ multiple sulphur isotope analyses and S/Se values, sulphur saturation did not occur as a result of crustal assimilation of sulphur rich crustal rocks. Instead, sulphur saturation occurred following substantial degrees of fractional crystallization and occurred when orthopyroxene began crystallizing which marks a large decrease in the solubility of sulphur (see Robb 2005). The overprinting sulphides have not sourced sulphur from another reservoir but rather the magma itself, suggesting that they are likely related to syn- to early post-magmatic hydrothermal fluids.

Typically, magmatic sulphide deposits have very small footprints making them easy to miss in the field and through drilling especially if the igneous stratigraphy is poorly constrained and further complicated by structural features. However, the lack of crustal contamination will mean difficulty in obtaining substantial degrees of sulphur saturation or indeed supersaturation needed to generate a massive sulphide deposit. R-factor determinations place this value at approximately 3 000 indicating the TVC to potentially host a sulphide poor PGE deposit should the immiscible sulphide fraction have concentrated within a discrete reef horizon. These findings underpin the prospectivity of the TVC and the need for further exploration.

Acknowledgements

The author would like to thank Orange River Pegmatite (Pty) Ltd for their continued financial support and generosity throughout the course of the study. Our gratitude must also be extended to the staff at the Stellenbosch University Central Analytical Facility (CAF) for their expertise.

References

Cornell, D. H., Thomas, R. J., Moen, H. F. G., Reid, D. L., Moore, J. M., & Gibson, R. L. (2006). The Namaqua-Natal Province. In *Geology of South Africa* (pp. 325–379).

Eckstrand, O. R., & Hulbert, L. J. (1987). Selenium and the source of sulphur in magmatic nickel and platinum deposits (abs.). In *Geological Association of Canada-Minerological Association Canada Program with Abstracts* (p. 40).

Eggins, S. (2003). Laser Ablation ICP-MS Analysis of geological Materials Prepared as Lithium Borate Glasses. *Geostandards and Geoanalytical Research*, *27*, 147–162.

Kartun, K. G. (1979). *The Geology of the Tantalite Valley Mafic-Ultramafic Complex and the Kumkum Metamorphic-Igneous Massif near Warmbad, South West Africa (Namibia)*. University of Cape Town.

Laflamme, C., Martin, L., Jeon, H., Reddy, S. M., Selvaraja, V., Caruso, S., Hao, T., Roberts, M. P., Voute, F., Hagemann, S., Wacey, D., Littman, S., Wing, B., Fiorentini, M., & Kilburn, M. R. (2016). In situ multiple sulfur isotope analysis by SIMS of pyrite, chalcopyrite, pyrrhotite =, and pentlandite to refine magmatic ore genetic models. *Chemical Geology*, *444*, 1–15. https://doi.org/10.1016/j.chemgeo.2016.09.032

Lesher, C. M. (2017). Roles of xenomelts, xenoliths, xenocrysts, xenovolatiles, residues, and skarns in the genesis, transport, and localization of magmatic Fe-Ni-Cu-PGE sulphides and chromite. *Ore Geology Reviews*, *90*, 465–484.

Macey, P. H., Thomas, R. J., Minnaar, H. M., Gresse, P. G., Lambert, C. W., Groenewald, C. A., Miller, J. A., Indongo, J., Angombe, M., Shifotoka, G., Frei, D., Diener, J. F. A., Kisters, A. F. M., Dhansay, T., Smith, H., Doggart, S., Le Roux, P., Hartnady, M. I., & Tinguely, C. (2017). Origin and evolution of the ~1.9 Ga Richtersveld Magmatic Arc, SW Africa. *Precambrian Research*, *292*, 417–451.

Moore, A. C., Kartun, K. G., & Waters, D. J. (1979). Metamorphic history of the Aureole associated with the Tantalite Valley Complex, South West Africa/Namibia. *Transactions of the Geological Society of South Africa*, *82*, 67–80.

Queffurus, M., & Barnes, S. J. (2015). A review of sulphur to selenium ratios in magmatic nickel-copper and platinum-group element deposits. *Ore Geology Reviews*, *69*, 301–324.

Robb, L. (2005). Introduction to ore-forming processes. In *Blackwell Publishing*.

Schreiber, U. M. (2016). *Ministry of Mines and Energy The Geology of Area 2818*.

Thomas, R. J., Cornell, D. H., Moore, J. M., & Jacobs, J. (1994). Crustal evolution of the Namaqua-Natal Metamorphic Province, southern Africa. *South African Journal of Geology*, *97*(1), 8–14.

von Backstrom, J. W. (1976). The Geology and Mineral Deposits of Tantalite Valley, Warmbad District, South West Africa. *Atomic Energy Board, Pelindaba, Pretoria*, *April*, 27.

A new look to the high-PGE chromitites from the Cabo Ortegal Complex (NW Spain)

Matías A. García-Tudela[1], Joaquín A. Proenza[2], Júlia Farré-de-Pablo[2], Thomas H. Aiglsperger[1], Núria Pujol-Solà[2,3] José María González-Jiménez[4]

[1]Department of Civil Engineering and Natural Resources, Luleå University of Technology, SE 97187, Luleå, Sweden
[2]Departament de Mineralogia, Petrologia i Geologia Aplicada, Facultat de Ciències de la Terra, Universitat de Barcelona, Carrer Martí i Franquès, s/n, 08028 Barcelona, Spain
[3]Departamento de Mineralogía y Petrología, Facultad de Ciencias, Universidad de Granada, Av. Fuentenueva s/n, 18071 Granada, Spain
[4]Instituto Andaluz de Ciencias de la Tierra (CSIC-UGR), Avda. de las Palmeras 4, E-18100 Armilla, Granada, Spain

Abstract. The ultramafic rocks of the Herbeira massif in the Cabo Ortegal Complex host chromitite bodies. On the basis of their morphology, host rocks and unaltered chromite cores compositions, they can be grouped into two types: Type-I chromitites, which are massive pods in dunites with Cr# values [Cr/(Cr+Al) atomic ratio] between 0.60-0.63; and Type-II chromitites, which are massive bands in dunites and pyroxenites with Cr# values between 0.80-0.82. Parental melt composition suggests that Type-I chromitites crystallized from melts akin to fore-arc basalt, which probably originated in a mantle wedge during a subduction initiation event, and Type-II chromitites originated from a boninitic parental melt once the subduction zone already developed. Both chromitite types exhibit platinum-group element (PGE) contents exceeding 2,000 ppb and are enriched in PPGE (Rh, Pt, Pd) relative to IPGE (Os, Ir, Ru). Abundant platinum-group minerals (PGM) are found at the edges of chromite grains or embedded by the interstitial serpentinized groundmass. These PGM are associated with base-metal sulfides (mainly pentlandite). The PGE distribution patterns and PGM association with base-metal sulfides suggest that PGEs were concentrated by immiscible sulfide melt. Additionally post-magmatic processes altered the primary PGM, promoting local remobilization of Pt and Pd.

1 Introduction

The high-Cr ophiolitic chromitites of the Herbeira massif in the Cabo Ortegal Complex (NW Spain) reportedly have platinum-group element (PGE) contents up to 13,000 ppb (Moreno et al. 2001), which are higher than those typical of high-Cr ophiolitic chromitites (< 1,000 ppb whole-rock PGE concentrations; Farré-de-Pablo et al. 2020 and references therein).

Moreno et al. (2001) interpreted the ultramafic rocks of the Herbeira massif as a mafic-ultramafic cumulate sequence (above the Moho) characteristic of a magmatic arc-root. According to these authors, the origin of the high-Cr and PGE-rich chromitites from the Herbeira massif was linked to successive injections of Cr- and PGE-rich magmas. However, more recent research interpreted the ultramafic sequence as a part of the mantle, where the interaction between melts and a refractory harzburgite in a sub-arc mantle environment formed chromitites, dunites and pyroxenites (Tilhac et al. 2016, 2020). Therefore, the origin of these chromitites, together with their PGE enrichment, remains unclear.

In this contribution, we present and discuss new petrographic, mineralogical and geochemical data for the chromitites of the Herbeira massif. These new insights, combined with previous knowledge, will help to unravel the origin of these chromitites and understand their enrichment in PGE.

2 Geological setting

The Cabo Ortegal Complex (Fig. 1a) is part of the European Variscan Belt and consists of mafic and ultramafic mantellic rocks and metamorphic rocks (Arenas et al. 2019). The ultramafic rocks of the Cabo Ortegal Complex are found in three massifs: Limo, Herbeira and Uzal (Fig. 1b). All these massifs consist of harzburgites, dunites, and pyroxenites, with subordinate wehrlites and lherzolites (Arenas et al. 2019).

According to Arenas et al. (2019), radiometric age data of ultramafic rocks suggest: 1) the partial melting stages that led to later injections of acidic and basic magma into the ultramafic rocks occurred at 395 Ma, 2) the formation of a garnet-clinopyroxene association (800°C, 16.5 kbar) at 390-395 Ma, and 3) an amphibolitization stage at 380 Ma. The origin of the ultramafic rocks has been established less precisely, at around 500 Ma. The pyroxenites have been interpreted as products of melt–peridotite interaction in a suprasubduction mantle around 459–515 Ma ago (Santos et al. 2002; Tilhac et al. 2017). The P-T conditions of peak

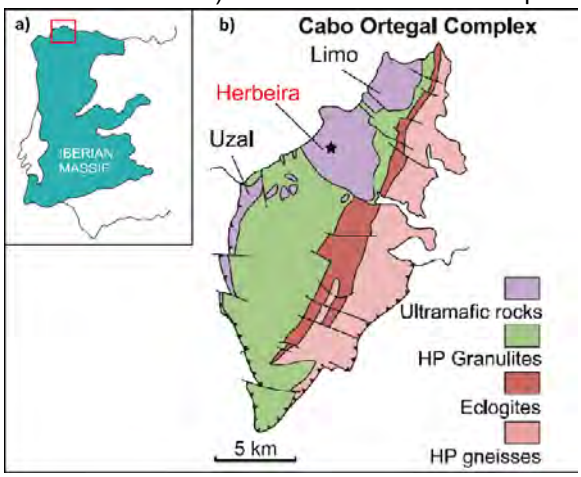

Figure 6. *Geological map of the Herbeira massif of the Cabo Ortegal Complex. The black star indicates the location of the samples. Modified from Tilhac et al. (2020).*

metamorphism of 1.6–1.8 GPa, 780– 800 ºC have been determined in the ultramafic rocks, recorded by undeformed garnet coronas around spinel (Girardeau and Ibarguchi 1991; Tilhac et al. 2016).

The main study area is located at the Herbeira massif (Fig. 1b). The massif is divided into an eastern and a western domain separated by the Herbeira Trans-Fault (Moreno et al. 2001). According to Tilhac et al. (2020), the eastern domain comprises harzburgites and minor pyroxenites, dunites, and chromitites. Meanwhile, the western domain is composed of dunites and chromitites, pyroxenites interlayered with dunites, harzburgites, and local chromitites. The chromitites of this study occur in the western domain of the Herbeira massif. They are massive podiform bodies hosted in dunites and massive bands hosted in dunites with minor pyroxenites layers.

3 Samples and analytical methods

The studied samples include massive chromitites from pods and bands. In this study, the massive chromitites from pods will be referred as Type-I chromitites and the massive chromitites in bands will be referred to as Type-II chromitites.

The mineral chemistry of chromite from both types of chromitites in terms of major and minor elements was analyzed using a JEOL JXA-8230 electron microprobe (EMP) at the Centres Científics i Tecnològics de la Universitat de Barcelona (CCiTUB). The analytical conditions were 15 kV accelerating voltage, 10-20 nA beam current with spot diameter 1-5 µm, and 20s count time. The calibration standards used were: Cr_2O_3 (Cr, PET, Kα), corundum (Al, TAP, Kα), rutile (Ti, PET, Kα), periclase (Mg, TAP, Kα), hematite (Fe, LIF, Kα), rhodonite (Mn, LIF, Kα), NiO (Ni, LIF, Kα), and metallic V (PET, Kα).

Whole-rock PGE analyses were performed on 2 chromitite samples (1 Type-I and 1 Type-II chromitites) at Genalysis Ltd (Perth, Western Australia) after nickel sulfide fire assay collection, following the method described by Chan and Finch (2001).

Hydroseparation was performed at the Laboratories for Quantitative Target Mineralogy (QanTmin) of the Luleå University of Technology; the resulting concentrates were mounted as polished monolayers on resin blocks and analyzed by field emission scanning electron microscope (FE-SEM), using a Zeiss Sigma 300 VP SEM at the same institution.

4 Chromite mineral chemistry

The primary composition (unaltered chromite core) of chromite varies according to the type of chromitite (Fig. 2a-b). Chromite from Type-I chromitites has Cr# values [Cr/(Cr+Al) atomic ratio] ranging from 0.60 to 0.63, TiO_2 contents between 0.08 and 0.29 wt.%, and Mg# values [Mg/(Mg+Fe^{2+}) atomic ratio] between 0.54 and 0.57. The chromite from Type-II chromitites has Cr# values ranging from 0.80 to 0.82, TiO_2 contents between 0.05 and 0.15 wt.%, and Mg# values between 0.42 and 0.44. Both types of chromitites display slightly high Fe_2O_3 contents: Type-I chromitites range between 5.76 and 6.89 wt.% and Type-II chromitites between 7.32 and 8.06 wt.%.

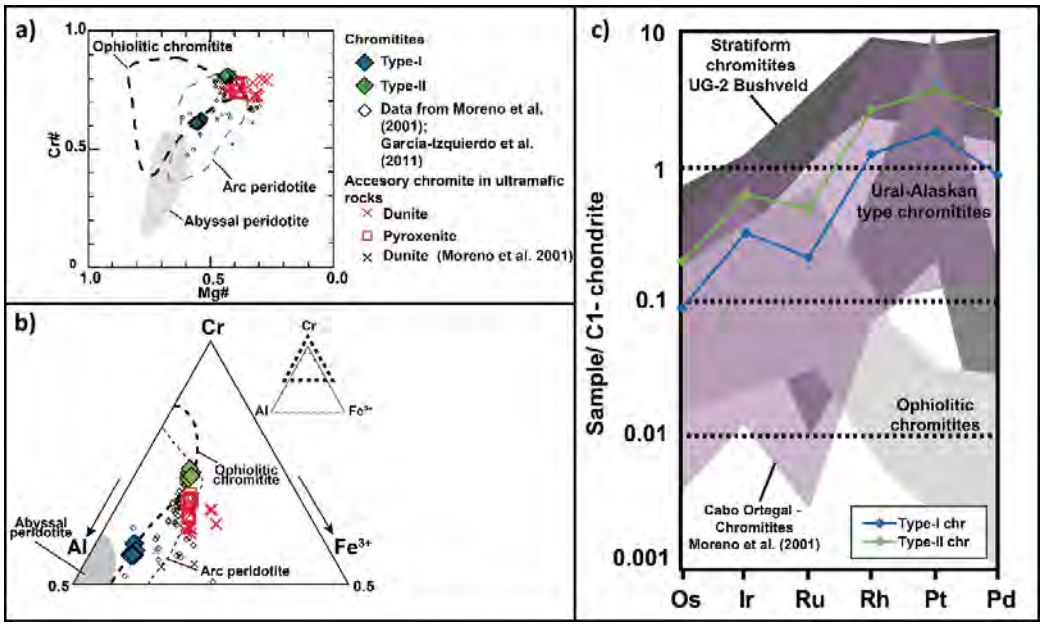

Figure 2. *a-b) Chemistry of chromite from chromitites of the Herbeira massif compared with different tectonic settings. a) Mg# versus Cr# values. b) Al-Cr-Fe^{3+} ternary diagram. Data sources of chromite from different tectonic settings are from Miura et al. (2018). c) C1 chondrite normalized (Naldrett and Duke 1980) PGE contents of the studied chromitites. Data for ophiolitic chromitites, Ural-Alaskan-type complexes and layered UG-2 Bushveld chromitites taken from González-Jiménez et al. (2015). Data for Cabo Ortegal chromitites are from Moreno et al. (2001).*

5 PGE geochemistry and PGM mineralogy

The bulk-rock PGE content of the Type-I chromitites is 2,460 ppb, and the bulk-rock PGE content of Type-II chromitites is 3,600 ppb. These values are higher than the average values for high-Cr ophiolitic chromitites (< 1,000 ppb total PGE; Farré-de-Pablo et al. 2020 and references therein). Chondrite-normalized (Naldrett and Duke 1980) PGE patterns (Fig. 2c) for both types of chromitites show enrichment in Pd-group PGE (PPGE: Rh, Pt and Pd) relative to Ir-group PGE (IPGE: Os, Ir and Ru), defining a positive slope from Ru to Pt and a negative slope between Pt and Pd.

The PGM assemblage observed in situ and in hydroseparated concentrates consists of Rh-Ir-Pt-bearing arsenides and sulfarsenides, Pt-Ir-Pd-base-metal- bearing alloys, and unidentified phases of Pt-Pd-S and Pt-Pd-Fe. In situ observations on thin sections from both types of chromitites reveal that PGM occur as inclusions on the edges of chromite, in fractures along chromite and in the interstitial silicate matrix (Fig. 3a-b). The PGMs located on the edges of chromite are composite grains of Rh-Ir-Pt-bearing sulfarsenides with Ir-Pt-Fe, Pt-Pd sulfides with Pt-Pd-Fe (Fig. 3a), and Ni-Fe sulfide (pentlandite), and Pt-Pd-As with Ni-Fe and Cu-Fe sulfides. The PGMs located in fractures of chromite grains and in the interstitial silicate matrix usually form single grains of Pt-Pd sulfides (Fig. 3b), Pt arsenides and Pt-Fe-Ni sulfides. The PGMs observed in hydroseparated concentrates show that Pt-Fe-Cu(-Ni) alloys occur as single irregular grains with sizes up to 20 µm. Each show porous textures (Fig. 3c). Irregular shaped Pt-Pd-Cu alloys occur with Ni-Fe sulfides. Hollingworthite (RhAsS), irarsite (IrAsS) and platarsite (PtAsS) appear as single allotriomorphic to subidiomorphic grains (Fig. 3d). Sperrylite ($PtAs_2$) occurs as allotriomorphic to idiomorphic grains with sizes up to 50 µm. Zaccariniite (RhNiAs) appears as composite grains associated with Ir-Fe-Ni and Pt-Fe-Cu alloys.

6 Discussion and conclusions

The chromite from the studied chromitite samples systematically have high Cr# values >0.6 (Type-I: 0.60-0.63 and Type-II: 0.80- 0.82) (Fig. 2a). All of them show compositions typical of chromitites hosted in the mantle section of ophiolites, although they have relatively higher Fe_2O_3 contents (5.76-8.06 wt.%; Fig. 2b). We estimated the composition of the melts in equilibrium with the chromite from the studied chromitites, and hence their parental melts, using the Al_2O_3 and the TiO_2 contents of chromite from both types of chromitites according to the approach of Kamenetsky et al. (2001) modified by González-Jiménez et al. (2020). The calculated composition of the parental melt for Type-I chromitites had Al_2O_3 contents between 14.29 and 14.58 wt.%, TiO_2 from 0.15-0.76 wt.%. and FeO/MgO ratio between 1.19 and 1.31. The Al_2O_3 content and FeO/MgO ratio are similar to MORB (e.g., Gale et al. 2013), but the calculated TiO_2 content for the melt is too low (typical MORB 1.68 wt% TiO_2; Gale et al. 2013). Low Ti content in MORB-like melts and low Ti/V ratio (~10-20) are characteristic of fore-arc basalts (Reagan et al. 2010), which are the first products when intra-oceanic subduction begins. On the other hand, the parental melt composition for Type-II chromitites had Al_2O_3 contents between 9.91 and 10.39 wt.%, TiO_2 from 0.15 to 0.25 wt.% and FeO/MgO ratio between 1.57 and 1.74. This composition resembles those from boninitic magmas (e.g., Hickey and Frey 1982).

The two types of chromitites exhibit PGE contents exceeding 2,000 ppb and are enriched in PPGE (Rh, Pt, Pd) relative to IPGE (Os, Ir, Ru) (Fig. 2c). This suggests that the parental melts of both types of chromitites were enriched in PGE. The PPGE enrichment resembles that of the Type II chromitites (especially Type IIA) described in González-Jiménez et al. (2014a, b). According to these authors and references therein, the PPGE enrichment of Type II chromitites may be related to

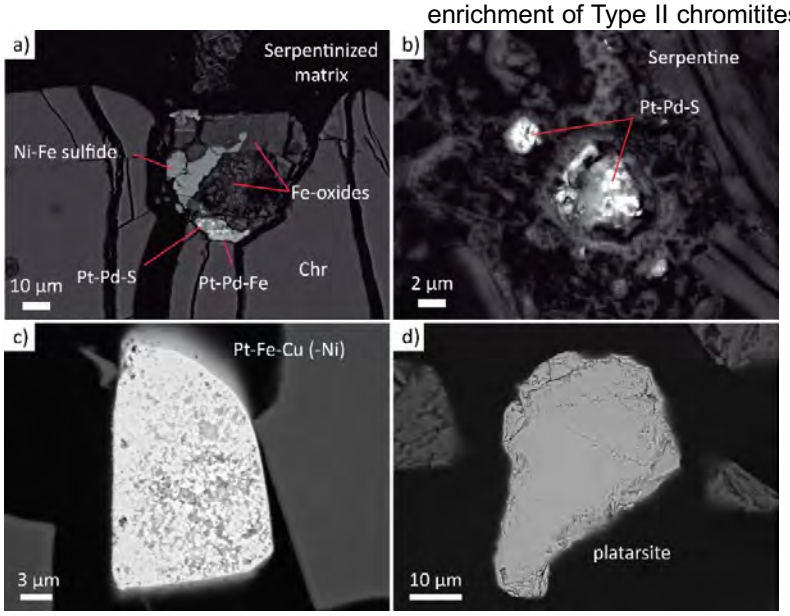

Figure 3. *a) Pt-Pd-S and Pt-Pd-Fe with Ni-Fe sulfide and Fe-oxides on the edge of a chromite grain from a Type-II chromitite. b) Pt-Pd-S grains enclosed by fibrous serpentine in a Type-I chromitite. c) Pt-Fe-Cu (-Ni) alloy grain with porous texture. d) Allotriomorphic platarsite grain.*

the PGE concentration in sulfide melts eventually segregated by immiscibility from evolving volatile-rich small volume melts. This is consistent with observation that PGMs and PGM-bearing sulfides are systematically located at the silicate matrix, thus evidencing that segregation of sulfide melt probably took place after the chromite crystals precipitated. Additionally, sulfide segregation could be favored by decreasing S and volatile solubility in the magma as a result of increasing polymerization degree by differentiation processes that resulted in Si-richer melts of boninitic affinity parental to the pyroxenites of the Herbeira massif too (Tilhac et al. 2016).

Moreover, the observation of Pt-Fe-Cu(-Ni) alloys with porous textures (Fig. 3c) suggest that they were formed by post-magmatic processes as a result of alteration of PGE-rich base metal sulfides or pre-existing PGM. Their location at the edge of chromite or interstitial matrix favored interaction with late metamorphic fluids, whereas porous textures suggest the accumulation of small nanoparticles of Pt, Fe, Cu and Ni precipitated from hydrothermal fluids (Farré-de-Pablo et al. 2022). The presence of zaccariniite with Ir-Fe-Ni alloys (probably garutiite) has also been interpreted to form as secondary minerals due to alteration processes (e.g., serpentinization) (McDonald et al. 2010; Vymazalova et al. 2012). Post-magmatic processes can locally remobilize PGE, especially Pt and Pd as observed in the studied chromitites (Fig. 2c). This can be due to the fact that Pt and specially Pd are relatively mobile during hydrothermal alteration (Barnes and Liu 2012). The PGE remobilization could be related to the percolation of hydrated fluids during amphibolite facies metamorphism (~8 kbar, 500°C; Tilhac et al. 2016) that affected chromitites and ultramafic rocks of the Cabo Ortegal Complex.

Acknowledgements

This research was financially supported by the Spanish Projects CGL2015–65824, RTI2018-099157-A-I00, PID2019-105625RB-C2.

References

Arenas R, Gil Ibarguchi JI, Fernández-Suárez J, et al (2019) El Complejo de Cabo Ortegal: los terrenos alóctonos del NW de Iberia y los episodios iniciales del ensamblado de Pangea. Concello de Cariño

Barnes SJ, Liu W (2012) Pt and Pd mobility in hydrothermal fluids: Evidence from komatiites and from thermodynamic modelling. Ore Geology Reviews 44:49–58.

Chan TK, Finch IJ (2001) Determination of platinum-group elements and gold by inductively coupled plasma mass spectrometry. In: Australian Platinum Conference. Perth, Western Australia, pp 1–9

Farré-de-Pablo J, Proenza JA, González-Jiménez JM, et al (2020) Ophiolite hosted chromitite formed by supra-subduction zone peridotite –plume interaction. Geoscience Frontiers 11:2083–2102.

Farré-de-Pablo J, Proenza JA, González-Jiménez JM, et al (2022) Low-temperature hydrothermal Pt mineralization in uvarovite-bearing ophiolitic chromitites from the Dominican Republic. Miner Deposita 57:955–976.

Gale A, Dalton CA, Langmuir CH, et al (2013) The mean composition of ocean ridge basalts. Geochemistry, Geophysics, Geosystems 14:489–518.

García Izquierdo B, Capote del Villar R, Lunar R, et al (2011) Evolución geodinámica y procesos mantélicos en el Macizo de Herbeira, Complejo de Cabo Ortegal (NO de la Península Ibérica). Instituto Universitario de Geología “Isidro Parga Pondal”, Área de Xeoloxía e Minería do Seminario de Estudos Galegos

Girardeau J, Ibarguchi JIG (1991) Pyroxenite-Rich Peridotites of the Cabo Ortegal Complex (Northwestern Spain): Evidence for Large-Scale Upper-Mantle Heterogeneity. Journal of Petrology Special_Volume:135–154.

González-Jiménez J, Mondal S, Ghosh B, et al (2020) Re-Os Isotope Systematics of Sulfides in Chromitites and Host Lherzolites of the Andaman Ophiolite, India. Minerals 10:686.

González-Jiménez JM, Griffin WL, Gervilla F, et al (2014a) Chromitites in ophiolites: How, where, when, why? Part I. A review and new ideas on the origin and significance of platinum-group minerals. Lithos 189:127–139.

González-Jiménez JM, Griffin WL, Proenza JA, et al (2014b) Chromitites in ophiolites: How, where, when, why? Part II. The crystallization of chromitites. Lithos 189:140–158.

González-Jiménez JM, Locmelis M, Belousova E, et al (2015) Genesis and tectonic implications of podiform chromitites in the metamorphosed ultramafic massif of Dobromirtsi (Bulgaria). Gondwana Research 27:555–574.

Hickey RL, Frey FA (1982) Geochemical characteristics of boninite series volcanics: implications for their source. Geochimica et Cosmochimica Acta 46:2099–2115.

Kamenetsky VS, Crawford AJ, Meffre S (2001) Factors Controlling Chemistry of Magmatic Spinel: an Empirical Study of Associated Olivine, Cr-spinel and Melt Inclusions from Primitive Rocks. J Petrology 42:655–671.

McDonald AM, Proenza JA, Zaccarini F, et al (2010) Garutiite, (Ni,Fe,Ir), a new hexagonal polymorph of native Ni from Loma Peguera, Dominican Republic. ejm 22:293–304.

Miura M, Arai S, Mizukami T, et al (2018) Petrology of Chromitites in the Higashi-Akaishi Ultrahigh-Pressure (UHP) Peridotite Complex, Japan: Toward Understanding of General Features of the UHP Chromitites. Minerals 8:525.

Moreno T, Gibbons W, Prichard HM, Lunar R (2001) Platiniferous chromitite and the tectonic setting of ultramafic rocks in Cabo Ortegal, NW Spain. Journal of the Geological Society 158:601–614.

Naldrett AJ, Duke JM (1980) Platinum metals magmatic sulfide ores. Science 208:1417–1424

Reagan MK, Ishizuka O, Stern RJ, et al (2010) Fore-arc basalts and subduction initiation in the Izu-Bonin-Mariana system. Geochemistry, Geophysics, Geosystems 11:.

Santos JF, Schärer U, Gil Ibarguchi JI, Girardeau J (2002) Genesis of Pyroxenite-rich Peridotite at Cabo Ortegal (NW Spain): Geochemical and Pb–Sr–Nd Isotope Data. Journal of Petrology 43:17–43.

Tilhac R, Ceuleneer G, Griffin WL, et al (2016) Primitive Arc Magmatism and Delamination: Petrology and Geochemistry of Pyroxenites from the Cabo Ortegal Complex, Spain. J Petrology 57:1921–1954.

Tilhac R, Grégoire M, O’Reilly SY, et al (2017) Sources and timing of pyroxenite formation in the sub-arc mantle: Case study of the Cabo Ortegal Complex, Spain. Earth and Planetary Science Letters 474:490–502.

Tilhac R, Oliveira B, Griffin WL, et al (2020) Reworking of old continental lithosphere: Unradiogenic Os and decoupled Hf Nd isotopes in sub-arc mantle pyroxenites. Lithos 354–355:105346.

Vymazalova A, Laufek F, Drabek M, et al (2012) Zaccariniite, RhNiAs, a new platinum-group mineral from Loma Peguera, Dominican Republic. The Canadian Mineralogist 50:1321–1329.

Characterization of the UG2 Reef split-facies types, Eastern Bushveld Complex, South Africa: A mineralogical perspective.

Caroline Hlongwani[1], Karel S. Viljoen[1], Derek H. Rose[1,2], Lauren C. Blignaut[3]
[1]*University of Johannesburg, South Africa*
[2]*Mintek, Randburg, South Africa*
[3]*Kings Christian Collegiate, Oakville, Canada*

Abstract. The Rustenburg Layered Suite of the Bushveld Complex has been extensively exploited for platinum group elements (PGEs), mainly from the Merensky and UG2 Reefs. An exploration drilling programme on the Booysendal Platinum producing Mine on the Eastern Limb of the Bushveld Complex revealed the occurrence of the UG2 Reef split-facies. In comparison to the normal UG2 reef (where the chromitite seam is not separated by pyroxenite), the split reef facies is defined by the splitting of the chromitite layers into multiple layers that are separated by pyroxenite middlings. This is anticipated to pose new challenges during metallurgical processing of the ore. To fully comprehend the mineralogical and metallurgical variations of the UG2 Reef split-facies types, geometallurgical test work was carried out on drill core samples collected from the mine. This was done to determine the bulk modal mineralogy, milling performance, mineral liberation and the flotation response of the various UG2 Reef split-facies types identified. Preliminary results of the study are presented and discussed in this paper.

1 Introduction

Northam Platinum's Booysendal Mine is located on the Eastern Limb of the Bushveld Complex within the Limpopo and Mpumalanga Provinces, in South Africa. It contains both the Merensky and Upper Group 2 (UG2) Reefs and covers a strike length of 14.5 km. The mining operation is divided into the North UG2 mine, North Merensky mine and the newly developed South mine project. Ongoing drilling has revealed that the UG2 reef occurs in several facies types, this includes the normal UG2 (uniform chromitite layer divided into the Upper Group 2 Leader, UL and Upper Group 2 Main member, UM) and the split UG2 Reef (where the chromitite seams are interlayered with pyroxenite units). The UG2 Reef split-facies occurs from the north to the southern portions of the mine premises, with the boreholes investigated in the current study drilled from the north to the central part of the mining right area (Figure 1).

Because the processing behaviour of any ore-type is underpinned by its mineralogical and textural characteristics, an understanding of the various UG2 split reef facies-types is essential to optimize recovery during ore processing. Hence an investigation of the mineralogy and the petrography of the UG2 Reef split-facies types was carried out. A challenge faced by the mine geologists is that the demarcation between the UL and UM units has not always been evident on a mesoscopic scale, and chemical assays data (platinum (Pt)/palladium (Pd) ratio) is used to distinguish the two units. McCall (2016) indicated that the geological contact between the UL and UM units could in fact be marked by the sudden appearance of clinopyroxene oikocrysts from the UL, gradationally moving into the lower UM unit.

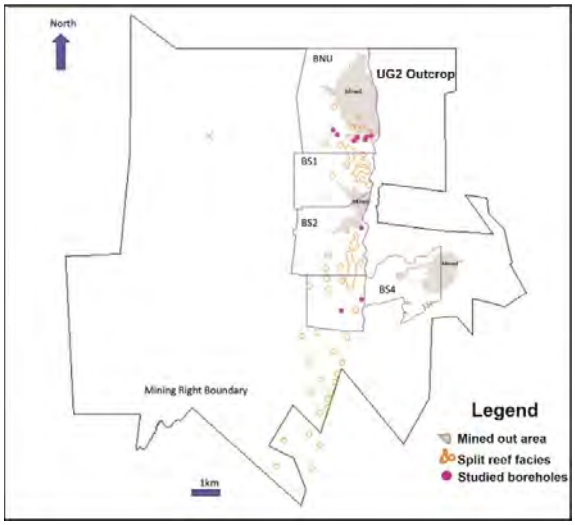

Figure 1. Aerial view of Booysendal Mine, showing the mined-out areas, the split reef and collar position of the studied boreholes (pink circles).

A comparison to previous studies (Dzvinamurungu et al 2013; McCall 2016) is made in the current study and the results are discussed later. Though this is not the first geometallurgical characterization project conducted on a mining operation in the Eastern Bushveld Complex, most of the previous studies however, only considered the Merensky Reef, or the normal UG2 Reef or both (Dzvinamurungu et al 2013; McCall 2016). It was the study by Rose et al. (2018) that investigated the UG2 Reef split-facies at Two Rivers Mine but no such study has been conducted at Booysendal Mine. The results of this study are brought into the discussion of this paper.

For the current study, much emphasis has been placed on the characterization of feed samples (hereby referred to as composite samples) by mineralogical, chemical, and petrographical methods. From the boreholes studied (Figure 1), and based on the UL and UM lithological

proportions, 3 UG2 Reef split-facies types were identified. These were further classified based on qualitative and semi quantitative mineralogical and textural data before any benchtop processing test work was conducted. Characterization of materials (especially feed samples) complemented by benchtop test work results allows for mining operations to build predictive process models by establishing a link between variability in material primary properties and variability resulting from processing (Lotter et al. 2011).

2 Methodology

Seventeen boreholes were logged, thin sections cut, prepared, and studied under optical and scanning electron microscopy fitted with energy dispersive spectrometers (SEM-EDS). Some aliquots were sent to Intertek in Australia for chemical assays (NiS fire assay with inductively coupled plasma-mass spectrometry (ICP-MS) finish; as well as sodium peroxide fusion/inductively coupled plasma-optical emission spectrometry (ICP-OES). The results of the Pt/Pd ratio and 4E PGE grade were used to draw a clear demarcation of the UL versus UM chromitite layers within the split reef-facies. Based on the chemistry, 3 UG2 Reef split-facies types were identified, and composite samples created from the seventeen boreholes and each borehole classified under a specific facies-type. In total, 8 composite samples were defined, and each simulates a possible mining cut that the mine can exploit during production. These composite samples were analysed for bulk mineralogy using X-ray diffraction (XRD) while employing the Rietveldt Refinement method.

3 Lithology, Petrography and Mineralogy

The mining cut varies across the split reef borehole intersections studied. According to mine terminology, the mining cut is stratigraphically divided into the hanging wall, main ore zone and footwall. The hanging wall comprises the following: pyroxenitic units (UP4 and UP1), chromitite stringer (UT3, ca. 1cm), pegmatoidal pyroxenite (UPEG, up to 27cm), and a 20 cm thick chromitite band (UT2). The main ore zone comprises chromitite layers commonly referred to as the leader seam (UL) and main seam (UM). These are parted or separated by a single or multi-pyroxenite unit(s) referred to as (UP which can range between 16 to 600 cm in thickness). The footwall comprises anorthosite, norite or pegmatoidal pyroxenite (UF). Generally, the mining cut starts from the UT3 stringer down to 40 cm into the footwall lithology.

Based on the lithological proportions of the UL and UM seams, mineralogical associations, textural features, and geochemical characteristics, three facies- types are identified and described as facies-type 1, where the UM and UL is separated by a pyroxenite unit (Figure 2), facies-type 2, where the UL remains uniform and directly overlies the UM, which in turn is split by a pyroxenite unit into two layers (Figure 3). The UL and UM in this facies type are distinguished by the change in chemistry, Pd/Pt ratio. Facies-type 3, where the UL and UM seams are collectively split into four or even five layers (Figure 4). Furthermore, 8 composite samples representing 8 mining cuts were collected from the three identified facies-types. The UG2 Reef split-facies types are described in detail subsequently.

Microscopic studies revealed no significant textural variations within the different UG2 Reef split-facies types studied, however, some common mineralogical similarities are noted in the same stratigraphic units across the 3 facies-types. Plagioclase and orthopyroxene occur interstitial to chromite (within the chromitite layers) (Figure 5a). While platinum group minerals (PGMs) seem to occur either as enveloped constituents within the chromite grains (Figure 5b) or at their margins, Base Metal Sulphides (BMS) are restricted to the margins of the chromite grains (Figures 5c, d).

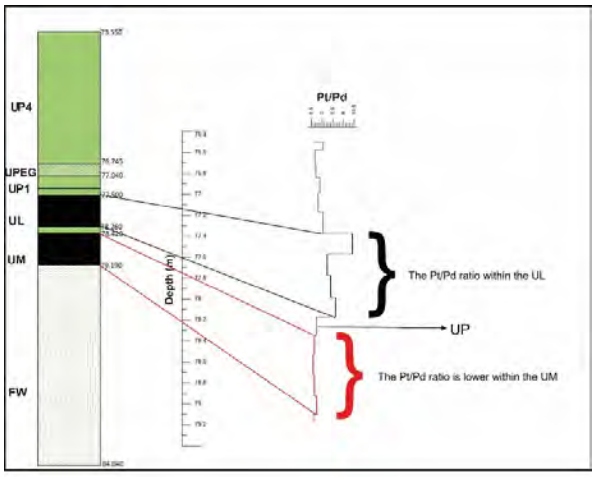

Figure 2. Lithology log of borehole BUT008D1, example of facies-type 1 split reef (right). Chemostratigraphic diagram showing the Pt/Pd variation across different chromitite seams (left). Logs not drawn to the same scale.

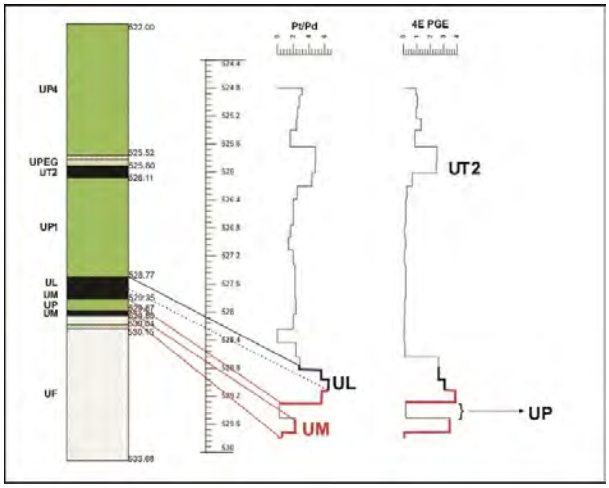

Figure 3. Lithology log of borehole BYS156D1, example of facies-type 2 split reef (right). Chemostratigraphic diagram showing the Pt/Pd and 4E grade variation across different chromitite seams (left). Logs not drawn to the same scale.

The UL typically shows a prominent association of apatite with chromite grains, an occurrence which is only seen in the UL and not the UM (Figure 6a). Platinum group elements-sulphides (PGE-sulphides) such as PtPdS (most likely braggite) and PtS (most likely cooperite) are commonly found in the UL and UM seams (although not described quantitatively here) and generally associated with chalcopyrite and/or pentlandite (Figure 5d). The pyroxenite parting may or may not show specks of BMS on disseminated chromite grains. The pyroxenite is composed of plagioclase, orthopyroxene with exsolution lamellae of clinopyroxene (Figure 6b), with quartz occasionally observed. The footwall lithologies such as norite, anorthosite and/or pegmatoidal pyroxenite may show association with disseminated chromite grains but seem completely devoid of any BMS.

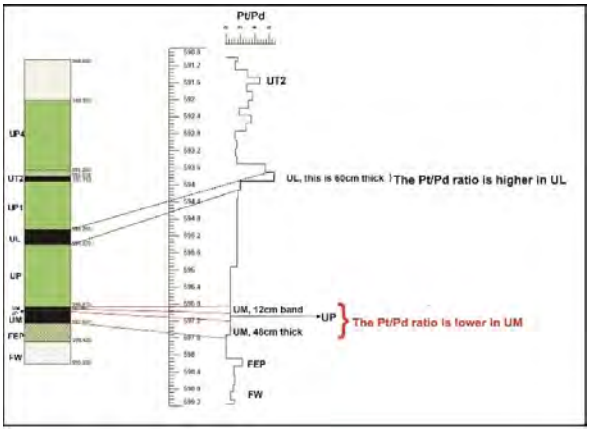

Figure 4. Lithology log of borehole BYS153D1, example of facies-type 3 split reef (right). Chemostratigraphic diagram showing the Pt/Pd variation across different chromitite seams (left). Logs not drawn to the same scale.

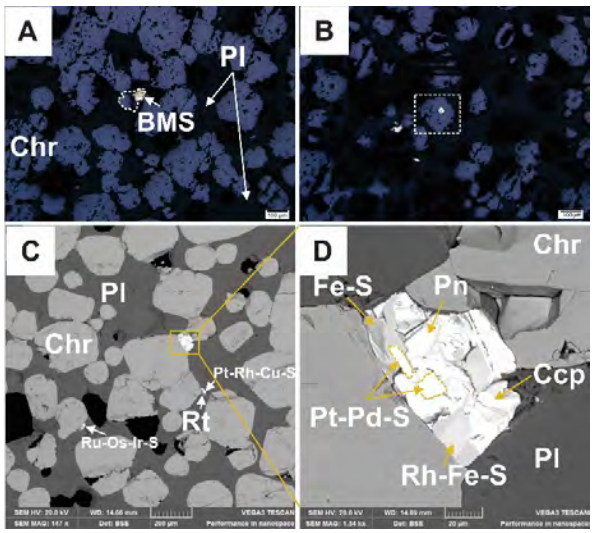

Figure 5. Photomicrographs of various sulphides-gangue mineral textures and association within the chromitite seam (UM). (A) Base metal sulphides (BMS) exsolution in chromite (Chr) grains or (B) interlocked within chromite (Chr) grains or (C) at the interface of chromite (Chr) and plagioclase (Pl). Other mineral associations noted include rutile (Rt) and PGMs alongside the Chr grain margins. (D) Shows a composite grain bounded by chromite (Chr) and plagioclase (Pl) grains.

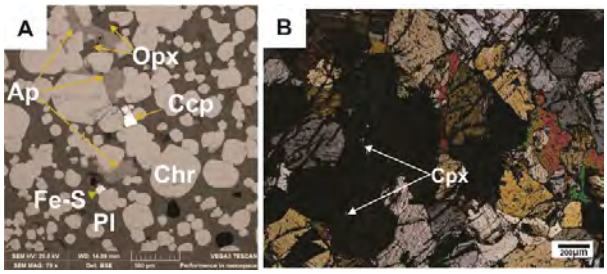

Figure 6. Photomicrographs of (A) mineral associations between apatite (Ap), orthopyroxene (Opx), plagioclase (Pl), and chalcopyrite (Cp) within the UL chromitite seam. (B) shows clinopyroxene (Cpx) exsolution in orthopyroxene (Opx), generally observed within the UP unit.

4 Milling Performance

Milling tests were conducted on 8 composite samples from the three facies types. The milling tests results are presented in the milling curve below (Figure 7) from which the times were then determined. From the three facies types, facies-type 3 composites i.e., UMC and ULT210CUT requires the longest milling times (43 mins) in comparison to LMC, to reach the target grind (70 wt% passing 75µm). Facies-type 2 composite, however, compares relatively well with Facies-type 1 composite LMC, both requiring approximately 40 minutes of milling to reach the target grind. Composite UMC_UT2 of facies-type 1 shows the most milling efficiency with just 37 minutes required to reach the target grind. Lastly, composite UMC of facies-type 1 requires a similar amount of milling time as facies-type 3 LMC composite, at roughly 42 minutes.

5 Discussion and Conclusion

Distinct classification of the various UG2 Reef split-facies types was achieved with respect to the lithological proportions of the UL and UM chromitite seams and to some extent mineralogical characteristics. While the demarcation between the UL and UM seams is remarkably difficult to spot on a mesoscopic scale, the chemistry of the platinum and palladium shows a trend between the two seams, with decreasing Pt/Pd ratio from the UL into the UM seams. This geochemical signature is consistent throughout the boreholes investigated. While McCall (2016) reported that the geological contact between the UL and UM seams is marked by

the sudden appearance of clinopyroxene oikocrysts, these have been noted to occur randomly and not consistently on the geological contact of the UL and UM seams within the drill core investigated. From bench-top milling tests, it is evident that some composites or mining cuts i.e. facies-type 1 UMC_UT2, LMC and facies-type 2 ULT210CUT are the most desirable as they require less milling time ca. 40 minutes) to achieve a target grind of 70wt% passing 75 µm. A study from Rose et al (2018) shows that the UG2 split reef at Two Rivers Mine, north of the current study area (referring to sample S7D) has low PGE grade and poor recoveries. This, however, was only the UG2 Reef split-facies types, there is also the multiple reef split facies which would be equivalent to the Facies-type 3 in the current study, which would most likely have an even lower performance relative to the other two UG2 Reef split-facies types, also judging by the milling times determined in the current study.

The results reported here for the milling times of the UG2 Reef split-facies types contrast with those of the normal UG2 reef, which is reportedly between 27 to 31 minutes to achieve a coarser grind of 60 wt% passing 75µm (Rose et al 2018). The milling times as determined in this study, however, are comparable to those reported by Dzvinamurungu et al (2013) for the Merensky reef in the western limb of the Bushveld Complex, which ranges between 33 to 41 minutes. The differences between the milling times of the normal UG2 and the UG2 split reef facies-types can be attributed to ore mineralogy. The amount of primary silicates such as plagioclase and orthopyroxene in the ore has a direct influence in the amount of energy and time required to reach a specific target grind (Dzvinamurungu et al 2013).

Though the UG2 Reef split-facies types have not been quantitatively described as yet, it would be interesting to see if there is a link between the varied milling performance to the ore mineralogy (or even ore texture) across the facies-types identified, through data to be acquired with the Mineral Liberation Analyzer (MLA).

Acknowledgements

This study would not have been made possible without the initiative of senior management personnel (Dennis Hoffmann, Meshack Mqadi and Arnold Hartzenberg) whose assistance, cooperation and support allowed this study to occur. The staff at the mine (Given, Sipho, Karabo and Tebogo) are thanked for assisting with access to the drill core, core cutting and sample packaging. Funding for this study came from the research grant from the National Research Fund (NRF), and a Department of Science and Innovation (DSI) Geometallurgy Chair grant to Prof. K.S. Viljoen. Additional funding was provided by DHET University Capacity Development Grant (UCDG) administered under the Strategic Initiatives and Administration (SIA) at the University of Johannesburg.

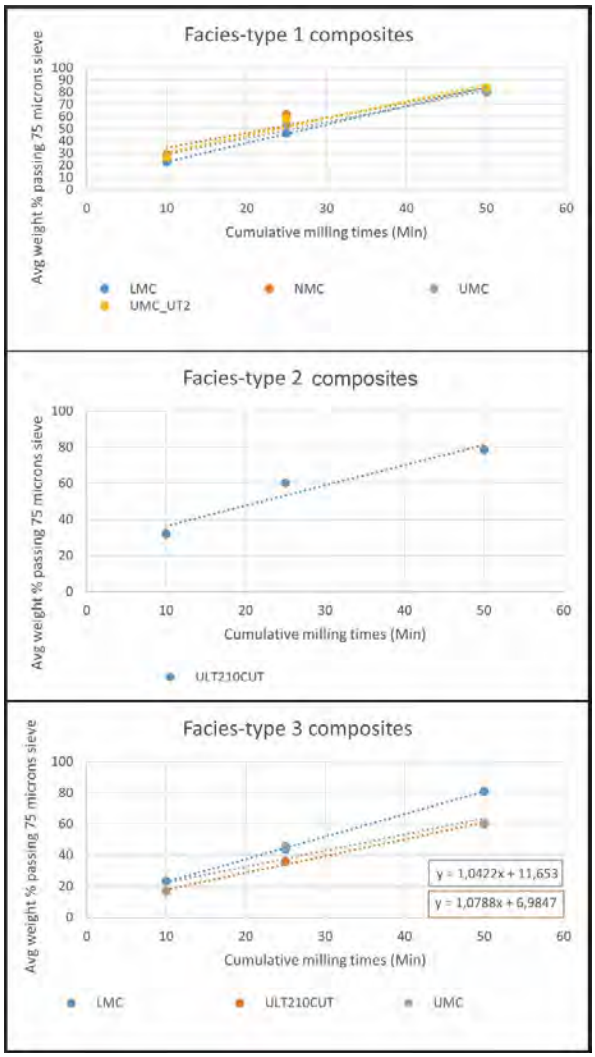

Figure 7. Milling curves of the three facies-types identified. Curves are plotted from average values of two composite samples milled per facies-type.

References

Dzvinamurungu T, Viljoen KS, Knoper MW, Mulaba-Bafubiandi A (2013) Geometallurgical characterisation of Merensky Reef and UG2 at the Marikana Mine, Bushveld Complex, South Africa. Miner.Eng 52: 74-81.

Lotter NO, Kormos LJ, Oliveira J, Fragomeni D, Whiteman E (2011) Modern process mineralogy: two case studies. Miner Eng 24: 638–650.

McCall MJ (2016) Mineralogical and geochemical variations in the UG2 reef at Booysendal and Zondereinde mines, with implications for beneficiation of PGM. Unpublished MSc Dissertation. Stellenbosch University.

Rose DH, Viljoen KS, Mulaba-Bafubiandi A (2018) A mineralogical perspective on the recovery of platinum group elements from the Merensky Reef and UG2 at Two Rivers Platinum mine on the Eastern limb of the Bushveld Complex in South Africa. Mineral. Petrol 112: 881-902.

Towards a genetic model for the unusual Cu-Au-Te(-PGE) sulfide and Ni sulfide deposits of the Curaçá Valley, Brazil

David Holwell[1], Daryl Blanks[1], John Thompson[2], Filipe Porto[3], Eduardo Oliviera[3], Francisco Tomazoni[4], Anderson Lima[4], Rafael D'Altro[4], Pablo Graia[4] and Taila Sant'Ana[4]
[1]Centre for Sustainable Resource Extraction, University of Leicester, UK
[2]PetraScience Consultants, Vancouver, Canada
[3]Ero Copper, Vancouver, Canada
[4]Ero Caraiba, Brazil

Abstract. The Curaçá Valley, Brazil, contains a number of dominantly Cu-rich sulfide deposits hosted by orthopyroxene rich mafic and ultramafic rocks emplaced into the lower crust. The deposits are dominated by chalcopyrite-bornite with elevated Au and Te, and a strong association with abundant phlogopite. Textural evidence indicates emplacement of these sulfides as a migrating Cu-rich sulfide liquid enriched with volatiles. In addition, the Curaçá Valley contains some Ni-rich deposits in identical host rocks, but with interstitial and net textured pyrrhotite-pentlandite-pyrite, with very little Cu, Au and Te. We propose that the Curaçá Valley deposits, and those of the potentially analogous O'okiep district in South Africa, formed from low degree partial melting of a metasomatically enriched mantle source in a collisional setting. Sulfides within the resultant hydrous, alkaline ultramafic rocks were able to fractionate, with Ni sulfides trapped in some bodies, and the Cu-Au-Te sulfide liquid able to migrate through the plumbing system on a district scale at lower crustal temperatures over considerable time. As such, these deposits represent a distinct class of orogenic, lower crustal magmatic sulfide deposits that display sulfide liquid fractionation on a district scale.

1 Magmatic Ni-Cu-PGE sulfide systems

The majority of large magmatic Ni-Cu-PGE sulfide deposits are hosted within mafic-ultramafic complexes thought to have been derived from high degree mantle melts (>15 % partial melting) in rift and/or plume settings. They are typically grouped into three categories: Ni-dominant deposits hosted by komatiites; Ni-Cu-dominant deposits hosted by ultramafic-mafic intrusions such as chonoliths, pipes and conduits; and PGE-dominant reef deposits in layered ultramafic-mafic complexes (e.g. Barnes et al. 2016).

Spatially, the Ni-Cu-dominant deposits are associated with craton margins, (e.g. Noril'sk, Voisey's Bay, Thompson Nickel Belt, Raglan, (e.g. Begg et al. 2010; Maier and Groves 2011); whereas the more PGE-rich layered intrusions are generally found in intracratonic settings (e.g. Bushveld Complex).

Additionally, magmatic sulfide deposits located within collisional settings are being increasingly recognised such as the Finnish Nickel Belt, the Central Asian Orogenic Belt in central China, Aguablanca in Spain, and Älgliden in Sweden.

Furthermore, generally smaller accumulations and occurrences of magmatic sulfides have been recorded in alkaline and hydrous ultramafic intrusions from the lower to mid crust, such as Valmaggia, Italy, Mordor, Australia and Sron Gharb, Scotland (Holwell et al. 2019). These occurrences and deposits are thought to have formed from low degree (<10%) partial melts and have a characteristically elevated Cu-Au-Te signature compared to deposits formed from higher degree melting. In addition, these deposits are almost always associated with magmatic carbonate (Blanks et al. 2020; Holwell and Blanks 2021) and most likely formed in post subduction/collisional regimes.

1.1 Curaçá/O'okiep style deposits

The dominantly Cu-sulfide ores of the Curaçá Valley, Brazil, and those of the O'okiep district, South Africa, form an unusual subgroup of intrusion-related sulfide deposits. They are located in small, hydrous mafic-ultramafic intrusions emplaced into the lower-mid crust around peak metamorphic conditions (Oliviera and Tarney 1995; Robb et al 1999). The metallogeny of both districts is dominated Cu-sulfide deposits with abundant bornite, chalcopyrite with magnetite and hydrous silicates. They both have high Cu/Ni and Au/PGE ratios and have abundant telluride minerals. Both districts have some Ni-dominant deposits in isolated intrusions such that over the districts, there are some intrusions that host Ni sulfide deposits and some that host Cu sulfide deposits.

The recognition of the alkaline metallogenic signature (Holwell et al. 2019; Blanks et al. 2020) raises the question as to whether these deposits are Cu-Au-Te rich due to them having a collisional/post-collisional alkaline affinity, and thus represent some of the most economic concentrations of sulfide in such settings.

However, the depth at which they were emplaced (~20+ km) also raises the possibility that they existed for some time in a temperature window, or 'Goldilock's zone' where Ni sulfide is solid and Cu sulfide is liquid and able to move (Holwell et al. 2022). As such, we also explore the possibility that the Ni and Cu deposits may have had a common sulfide source, that was able to fractionate over considerable distances.

2 The Curaca Valley deposits

2.1 Copper deposits

Copper deposits of the Curaçá Valley, São Francisco Craton, Brazil, such as those at the Pilar mine are located within lozenge shaped, dominantly ultramafic units, emplaced around 2.05Ga. These often follow tight fold structures within the host rock gneisses, which display much higher degrees of deformation showing the intrusion to be late to post tectonic. They are dominated by orthopyroxene rich lithologies devoid of olivine.

The ores are largely chalcopyrite and bornite, with some pyrrhotite, and some rare pentlandite. Associated with the Cu sulfides is abundant phlogopite, some magnetite, Cr-spinel, and rarer apatite and carbonate. Accessory ore minerals include a range of tellurides, mostly melonite ($NiTe_2$), and tellurides of Au, Ag, Pt, Pd and Pb.

The sulfides occur as massive accumulations, typically as veins or breccia fills, with these textural evidence suggesting injection of Cu sulfide into the host rocks, along with some interstitial and net-textured accumulations.

2.2 Nickel deposits

Newly discovered Ni sulfide deposits of the Umburana system in the Curaçá Valley are hosted within orthopyroxene dominant ultramafic intrusions very similar to those that host the Cu ores. The ores are made up of disseminated interstitial, net textured and patchy to massive sulfides made up of pyrrhotite, pentlandite loops and flames, and some euhedral pyrite. Chalcopyrite is rare, but where present forms veins and disseminated patches at the edges or away from the margins of the Ni sulfide accumulations. PGE and Te contents are very low. Some carbonate is present with the sulfide, especially where they are present in more vein like textures.

3 Possible genetic models

3.1 An alkaline system

The characteristics of low degree partial melts are that they are alkaline, typically somewhat hydrous and form in low volumes compared to basaltic magmas derived from higher degrees of partial melt. Whilst the alkaline nature of magmatic rocks can be mimicked by the effects of crustal contamination, metallogenically, mineralisation in such settings is characteristically Cu-Au-Te rich. In particular, the enrichment of Te seems to be an entirely mantle character, with Te enrichments in metasomatized mantle rocks (Blanks et al 2020), and a consistent enrichment in alkaline deposits throughout the lithosphere (Holwell et al. 2019).

The Cu-Au-Te signature of the Curaçá Cu deposits, with abundant hydrous phases, particularly phlogopite, would be supportive of an alkaline interpretation. The question is how do the Ni deposits fit this model? As currently known and explored,, there are many more Cu occurrences identified in the Valley than Ni ones, and if the district is taken as a whole, then the overall metallogenic signature is still Cu-Au-Te dominant with some Ni and PGE. However, the complete lack of IPGE in both styles of deposit would be consistent with a low degree of partial melting that did not melt all sulfide in the mantle, thus allowing the IPGE to remain in mantle restite.

As such, an alkaline affinity does work when assessing the Curaçá Valley as a whole, but it also implies that the sulfides in each individual intrusion may not represent the parental sulfide composition. This can be explained by large scale sulfide liquid fractionation.

3.2 District scale sulfide liquid fractionation

Sulfide liquid fractionation initially produces a crystalline monosulfide solid solution (mss) phase at high temperatures (>1000°C), into which Ni, Co and IPGE and Rh will partition, with Cu, Au, Pt, Pd and semi metals like Te remaining as a liquid (Holwell and McDonald 2010). This allows for the possibility, especially at lower crustal depths where the temperatures of any intrusions will remain hotter for longer, that Cu-Au-Te-(Pt-Pd) sulfide migrated away from the Ni sulfides (Holwell et al. 2022) before crystallising to Cu sulfides like intermediate solid solution (iss).

The general Cu-Au-Te(+Pd) signature of the Cu ores from the Curaçá Valley are entirely consistent with an iss signature, but it would imply sulfide liquid fractionation within the magmatic plumbing system on a district scale of km to tens of km. Whilst this may seem extreme, the process is clearly scalable from the mm to cm scale seen in many sulfide blebs and patches (e.g. Blanks et al. 2022) up to deposit scale such as the Cu-rich veins at Sudbury.

Textural differences are striking, with the Ni ores having sulfides as disseminations, interstitial patches and net textured and massive sulfides representative of sulfide coexisting with silicate minerals. The Cu ores in stark contrast commonly show textures indicative of migrating Cu sulfide liquid, intruding as veins and breccia fills along with net-textures and insterstitial sulfides.

The importance of phlogopite and other volatile-rich mineral phases with the Cu sulfide would also be consistent with a fractionated, volatile-rich sulfide liquid migrating significant distance,

4 Global analogue: O'okiep district

The O'okiep district in South Africa represents a remarkably analogous ore district to the Curaçá Valley albeit of a different age (~1000 Ma). Similarities between the regions include: (1) emplacement in a collisional setting; (2) lower crustal, hot conditions on emplacement ~800-900°C;

(3) tens to hundreds of individual, small (typically <100 m thick and 1000 m long) mafic-ultramafic bodies within the district; (4) mostly Cu-dominant (chalcopyrite-bornite) ores, with some Ni-rich deposits; (5) massive sulfide accumulations and veins with associated magnetite; (6) very low S/Se ratios; (7) abundant volatile phases in the associated ultramafic rocks such as phlogopite.

As such, we consider both these districts to have formed in similar ways and may represent 'typical' conditions of magmatic sulfide genesis in the lower crust from low degree partial melts of metasomatically enriched mantle lithosphere.

Acknowledgements

The staff and management at Ero Copper are thanked for financial and logistical support. Wolf Maier is thanked for access to samples from the O'okiep district.

References

Barnes SJ, Cruden AR, Arndt N, Saumur BM (2016) The mineral system approach applied to magmatic Ni–Cu–PGE sulphide deposits. Ore Geol Rev 76:296–316

Begg GC, Hronsky JA, Arndt NT, et al (2010) Lithospheric, cratonic, and geodynamic setting of Ni-Cu-PGE sulfide deposits. Econ Geol 105:1057–1070

Blanks DE, Holwell DA, Fiorentini ML, et al (2020) Fluxing of mantle carbon as a physical agent for metallogenic fertilization of the crust. Nat Commun 11:1–11

Holwell DA, Blanks DE (2021) Emplacement of magmatic Cu-Au-Te (-Ni-PGE) sulfide blebs in alkaline mafic rocks of the Mordor Complex, Northern Territory, Australia. Miner Deposita 56:789–803

Holwell DA, Fiorentini M, McDonald I, et al (2019) A metasomatized lithospheric mantle control on the metallogenic signature of post-subduction magmatism. Nat Commun 10:1–10

Holwell DA, Fiorentini ML, Knott TR, et al (2022) Mobilisation of deep crustal sulfide melts as a first order control on upper lithospheric metallogeny. Nat Commun 13:1–12

Maier WD, Groves DI (2011) Temporal and spatial controls on the formation of magmatic PGE and Ni–Cu deposits. Miner Deposita 46:841–857

Oliveira EP, Tarney J (1995) Genesis of the Precambrian copper-rich Caraiba hypersthenite-norite complex, Brazil. Miner Deposita 30:351–373

Robb LJ, Armstrong RA, Waters DJ (1999) The history of granulite-facies metamorphism and crustal growth from single zircon U–Pb geochronology: Namaqualand, South Africa. J Petrol 40:1747–1770

The importance of volatiles in the formation of magmatic sulphide ore deposits: experimental constraints

Giada IACONO-MARZIANO[1], Margaux LE VAILLANT[2], Stephen J. BARNES[2]
[1] Institut des Sciences de la Terre d'Orléans, UMR 7327 CNRS-Université d'Orléans-BRGM, 45071 Orléans, France
[2]CSIRO, Mineral Resources, Kensington, WA 6151, Australia

Abstract. Research studies provide growing evidence for the presence of fluids within magmatic mineral systems of mafic-ultramafic composition, despite these ore-forming magmas generally being considered as volatile-poor. Here we summarise the results of two experimental studies that clarify the role of volatiles in the formation of magmatic sulphide ore deposits in mafic-ultramafic magmas: (i) interaction experiments simulating magmatic assimilation of sulfate and/or organic compounds (Iacono-Marziano et al. 2017); (ii) a more recent experimental study shedding light on previously unnoticed physical processes ensuing from the association between sulphide melt and fluid phase (Iacono-Marziano et al. 2022). The silicate melt composition used for both studies is similar to the parental melt of the Noril'sk-Talnakh ore-bearing intrusions in Polar Siberia, and the starting materials of the experiments were samples from the Noril'sk region. Moreover, the experiments were conducted at magmatic conditions relevant to the emplacement pressures and temperatures of the Noril'sk-Talnakh intrusions. Experimental findings are therefore directly applicable to these world-class ores, suggesting that volatiles may have played a crucial role in their formation. Several other magmatic sulphide ores present evidence of the occurrence of a fluid phase during ore formation; hence the mechanisms illustrated by the experiments are likely to be more common than currently considered.

1 Triggering sulphide saturation

The addition of external sulphur to fertile magmas is one of the most common ore-forming processes invoked for magmatic sulphide deposits (e.g., Naldrett 2004). Sulphur can be introduced into the magma by several process: those that have been experimentally documented are anhydrite dissolution (Iacono-Marziano et al. 2017), black shale devolatilization (Virtanen et al. 2021), and black shale assimilation (Deegan et al. 2022). Our experiments at magmatic conditions (1200°C, 80 MPa) show that anhydrite assimilation in the presence of a reducing agent, i.e., organic matter-rich rocks such as coal, is extremely efficient in producing sulphide supersaturation in the magma (Iacono-Marziano et al. 2017).

2 Accumulation of the sulphide melt

The association between the sulphide melt and the fluid phase has been shown to allow the upward transfer of the sulphide melt (Mungall et al. 2015). Our recent experimental results illustrate another physical process that occurs when the proportion of fluid phase in the magma is low: the sulphide-fluid association favours the accumulation of the sulphide liquid, by facilitating the coalescence of the sulphide droplets that are attached to the same fluid bubble (Iacono-Marziano et al. 2022). This consents the accumulation of the sulphide melt in the upper part of the experimental samples (Fig. 1).

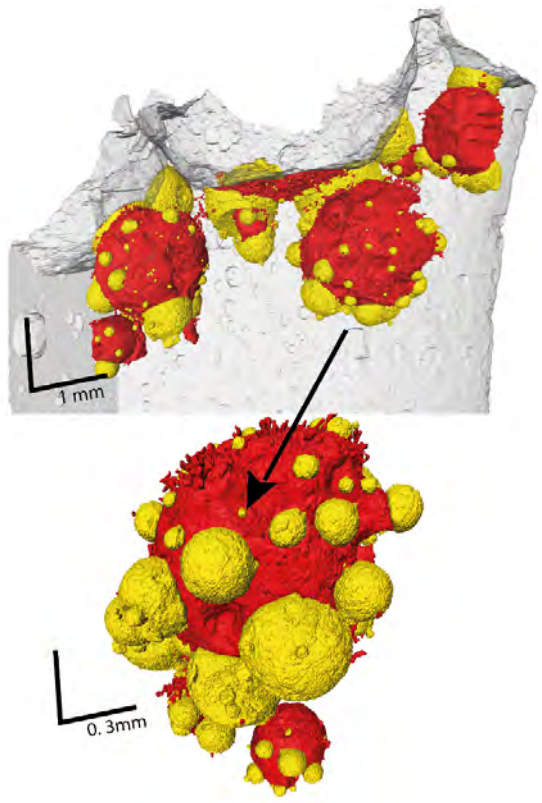

Figure 1. High-resolution X-ray computed tomography rendering of a representative experimental sample showing 3D distribution of sulphide droplets in yellow and fluid bubbles in red (the silicate glass is in grey). The upper image shows a general view of the upper part of the experimental sample, whereas the lower image shows a detail of sulphide-fluid associations, with several sulphide droplets attached to the same fluid bubble. Modified from Iacono-Marziano et al. (2022).

Coalescence of sulphide droplets may be facilitated by the lowering of their interfacial tension induced by the bubble. However, the main driver for coalescence to occur is likely to be the fact that connection to the bubbles keeps the droplets in contact for a long enough time to allow drainage of the melt film between them, as opposed to the situation in a flowing magma where adjacent

droplets are sheared apart before the melt film has time to drain (Robertson et al. 2015). This process may enable sulphide droplets coalescence and deposition in flowing magma, which otherwise have been shown to be unlikely processes (Robertson et al. 2015).

3 Metal enrichment of the sulphide melt

Experimental results indicate that sulphur degassing to the fluid phase increases with increasing proportion of fluid phase, concurrently reducing sulphide melt stability. Consequently, the sulphide melt is consumed and its metal content augments, due to the preferential partitioning of metals into the sulphide melt (Iacono-Marziano et al. 2022). Experimental samples with increasing fluid contents present increasingly Ni- and Cu-rich sulphide melts, illustrating how the metal enrichment of the sulphide melt can be attained by sulphur degassing (Fig. 2). Sulphide upgrading can therefore be achieved by magma degassing.

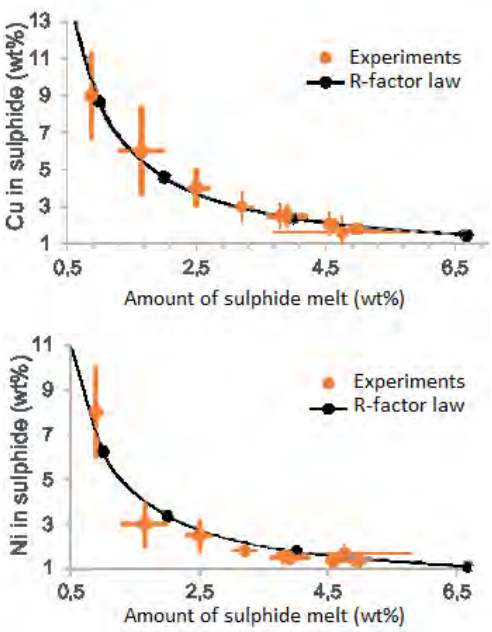

Figure 2. Cu and Ni content of the sulphide melt versus its amount in experimental samples (orange dots) and in theoretical calculations (black line) using the R-factor law of Campbell & Naldrett (1979). Modified from Iacono-Marziano et al. (2022).

4 PGM formation by desulphurisation

Extensive sulphur degassing may completely consume the sulphide melt and form platinum-group minerals (PGMs) at relatively high temperatures (1150°C in the experiments of Iacono-Marziano et al. 2022). Platinum-group mineral formation in the experimental samples (Fig. 3) occurs by desulphurisation of the sulphide melt, while Ni and Cu are partitioned between the silicate melt and the fluid phase. This suggests an unconventional mechanism of PGM formation at temperatures higher than those typical of sulphide melt crystallization.

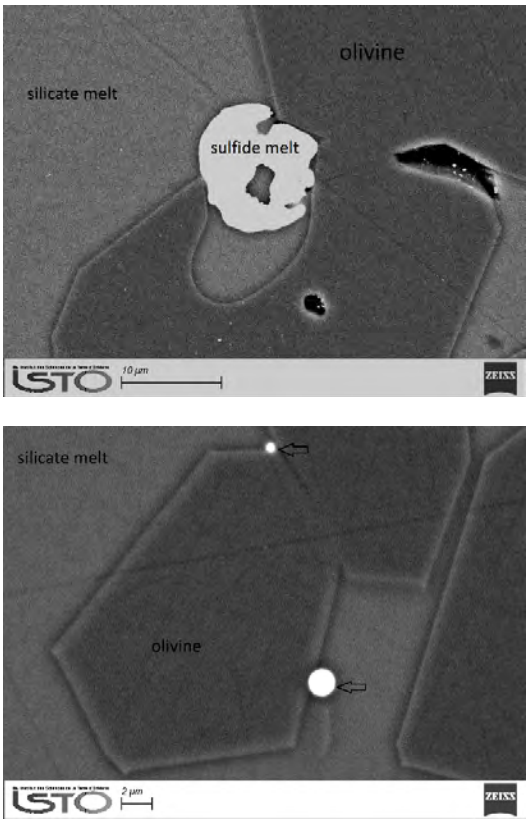

Figure 3. BSE images of an experimental sample with a high proportion of fluid phase (2.2 wt.%), which experienced extensive sulphur degassing. The upper image shows a partially corroded sulphide bleb observed in the upper part of the sample. The lower image shows the Pt-rich, Fe-S-Ni-Cu bearing phase (indicated by the arrows) that commonly occurs at the interface between the olivine and the silicate melt.

5 Application to Noril'sk-Talnakh ores

The experimental results presented above illustrate how the occurrence of a fluid phase in a mafic-ultramafic magma may represent a significant boost for magmatic sulphide ore-forming processes: sulphide melt accumulation, tenor increase, and crystallization of PGMs are indeed key processes in the formation of magmatic Ni-Cu-Co-PGE ore deposits. We use the world-class Noril'sk-Talnakh ore deposits, in Polar Siberia as a case study.

Noril'sk-Talnakh ores are hosted in mafic-ultramafic subvolcanic ribbon-shaped intrusions. Extensive interaction of the ore-forming magmas with evaporitic and carbonaceous rocks has been proposed to be at the origin of the mineralisation and the coexisting abundant fluid phase (e.g. Iacono-Marziano et al. 2017).

The three main ore types are described in ore-bearing intrusions: (i) massive sulphides in the lower

part of the intrusion and largely in the country rocks; (ii) disseminated sulphides (also called globular ores) inside picritic and taxitic rocks, also in the lower part of the intrusion; (iii) low-sulphide PGE ores in the upper part of the intrusion (e.g. Naldrett 2004; Le Vaillant et al. 2017; Schoneveld et al. 2020).

In the second and third ore-types subspherical structures within the crystalline framework have been interpreted as fluid bubbles filled with late magmatic phases or hydrothermal minerals (e.g. Le Vaillant et al. 2017; Schoneveld et al. 2020). In the lower part of the intrusion, these structures are systematically associated with sulphide minerals suggesting they represent sulphide-fluid associations preserved in the olivine-rich magmatic rocks (Le Vaillant et al. 2017). In the upper part of the intrusion, these subspherical structures are even more common and generally contain lower amounts of sulphide minerals but abundant PGMs (Schoneveld et al. 2020), suggesting higher extents of sulphur degassing and sulphide dissolution. On the contrary, massive sulphides are proposed to have experienced low extents of sulphur degassing, attested by the lower metal contents with respect to disseminated sulphides (Iacono-Marziano et al. 2022).

Ore type distribution in Noril'sk-Talnakh intrusions therefore strongly suggests an increasing extent of degassing from the bottom toward the top of the intrusions, implying increasing sulphide melt consumption and metal enrichment. Although a role for volatiles is less clear in other magmatic sulphide deposits, an increasing number of examples of sulphide-fluid associations is reported, as summarised in Iacono-Marziano et al. (2022). This suggests that the role of volatiles in the formation of magmatic sulphide deposits should be re-evaluated.

Acknowledgements

This research received funding from the French agency for research (ANR project #12-JS06-0009-01), the "Equipement d'Excellence" Planex of the University of Orléans (France), and the programme TelluS of the Institut National des Sciences de l'Univers, CNRS.

References

Campbell, I.H., and Naldrett, A.J. (1979): The influence of silicate:sulphide ratios on the geochemistry of magmatic sulphides, Economic Geology, v. 74, p. 1503–1506.

Deegan, F.M., Bédard, J.H., Grasby, S.E., Dewing, K., Geiger H., Misiti, V., Capriolo, M., Callegaro, S., Svensen, H.H., Yakymchuk, C., Aradi, L.E., Freda, C., and Troll, V.R. (2022): Magma-shale interaction in Large Igneous Provinces: Implications for climate warming and sulfide genesis, Journal of Petrology, v. 63, p.1-10.

Iacono-Marziano, G., Ferraina, C., Gaillard, F., Di Carlo, I., and Arndt, N.T. (2017): Assimilation of sulfate and carbonaceous rocks: experimental study, thermodynamic modeling and application to the Noril'sk-Talnakh region (Russia), Ore Geology Reviews, v. 90, p. 399–413.

Iacono-Marziano, G., Le Vaillant, M., Godel B.M., Barnes, S.J., and Arbaret, L. (2022): The critical role of magma degassing in sulphide melt mobility and metal enrichment, Nature Communications, v. 13, 2359.

Le Vaillant, M., Barnes, S.J., Mungall, J.E., and Mungall, E.L. (2017): Role of degassing of the Noril'sk nickel deposits in the Permian-Triassic mass extinction event. Proceedings of the National Academy of Sciences, v. 114, p. 2485–2490.

Mungall, J.E., Brenan, J.M., Godel, B., Barnes, S.J., and Gaillard, F. (2015): Transport of metals and sulphur in magmas by flotation of sulphide melt on vapor bubbles, Nature Geoscience, v. 8, p. 216–219.

Naldrett, A.J. (2004): Magmatic Sulphide Deposits: Geology, Geochemistry and Exploration, Springer Berlin, 728 p.

Robertson, J.C., Barnes, S.J., and Le Vaillant, M. (2015): Dynamics of magmatic sulphide droplets during transport in silicate melts and implications for magmatic sulphide ore formation, Journal of Petrology, v. 56, p. 2445-2472.

Schoneveld, L., Barnes, S.J., Godel, B., Le Vaillant, M., Yudovskaya, M.A., Kamenetsky, V., and Sluzhenikin, S.F. (2020): Oxide-sulphide-melt-bubble interactions in spinel-rich taxitic rocks of the Norilsk-Talnakh intrusions, polar Siberia, Economic Geology, v. 115, p.1305–1320.

Virtanen, V.J., Heinonen, J.S., Molnar, F., Schmidt, M.W., Marxer, F., Skyttä, P., Kueter, N., and Moslova, K. (2021): Fluids as primary carriers of sulphur and copper in magmatic assimilation, Nature Communications, v. 12, 6609.

Cobalt–nickel–copper arsenides, sulfarsenides and sulfides of Bou Azzer (Anti-Atlas – Morocco): Lithological and structural controls

Marieme Jabbour[1], Zoubair ELOuad[2], Mohamed Ez-Zghoudy[1], Mustapha Souhassou[2], Younes Moundi[3], Nicolas Saintilan[4], Said Ilmen[5], Amine Bajddi[3], Lhou Maacha[3], Faouziya Haissen[6], Mohamed Zouhair[3], Moha Ikenne[1]
[1] Laboratory of Applied Geology and Geo-Environment, Ibnou Zohr University, Agadir, Morocco.
[2] Laboratory of Geo-Bio-Environmental Engineering and Innovation, Research, Ibnou Zohr University, Taroudant, Morocco.
[3] MANAGEM Group, Twin Center, Tour A, BP 5199, Casablanca. Morocco
[4] Institute of Geochemistry and Petrology, Department of Earth Sciences, ETH Zurich. Zürich, Switzerland
[5] CAG2M, Polydisciplinary Faculty of Ouarzazate, Ibnou Zohr University, BP 638, 45000 Ouarzazate, Morocco
[6]Department of Geology Faculty of Sciences Ben M'sik, Hassan II University of Casablanca Morocco.

Abstract. The Bou Azzer–El Graara inlier is famous by its Co-Ni deposit associated to a Neoproterozoic ophiolitic complex. This paper aims to present results from three sectors, the Bou-Froukh, the Aghbar, and the Ait Ahmane deposits. Geological investigations (Leblanc, 1975; Saquaque, 1989) and recent radiometric data (Admou 2013) allow recognizing three major formations in the Bou Azzer Inlier: The Bou Azzer group; the Tiddiline Fm., and the Ouarzazate group. These Neoproterozoic formations have undergone the Pan-African events which take place in two episodes. The B1 phase is materialized by the development of a general NW-SE flow cleavage recorded in the Bou Azzer group, whereas the B2 phase is characterized by a fracture cleavage expressed in the Tiddiline Fm. , along with a network of reverse faults and sinistral strike-slip faults crossing the entire region, they are considered to be inherited from the B1 phase and then replayed in the form of sinistral strike-slip faults during the B2 phase, and staked by quartz- carbonate lenses, making them vents for mineralizing fluids. These faults played a significant role in the Bou Azzer district's mineralization by enabling the emplacement of arsenides vein mineralization. The mineralization primarily consists of triarsenides, sulfoarsenides, and sulfides, hosted by quartz and quartz-carbonate veins.

1 Introduction

The Bou Azzer - El Graara inlier (BEI) is famous by its Neoproterozoic ophiolitic complex and its Co-Ni arsenides deposits. It plays a key role in the understanding of geological and geodynamics history of the Anti-Atlas Panafrican belt. This work aims to present new results of three different Co-Ni ore deposits: The Bou-Froukh, Aghbar, and Ait Ahmane deposits. The lithological assemblages in the area are categorized into three primary groups: The Bou Azzer group (serpentinized peridotites, metabasitesand the associated quartz-diorites), the Tiddiline Fm., (detrital and volcani-sedimentary facies), and the Ouarzazate group (volcanic and pyroclastic rocks). These Neoproterozoic terrains have undergone the Panafrican events marked by two deformation phases. The one, B1, is distinguished by a general NW-SE flow cleavage, observed in the Bou Azzer group, whereas the second phase, B2, is defined by a fracture cleavage recorded in the Tiddiline Fm.

Additionally, a network of reverse faults and sinistral strike-slip faults that cut across the entire area is believed to be inherited from the B1 phase and replayed as sinistral strike-slip faults during the B2 phase. These structures were the vents of the mineralizing fluids, particularly Co, Ni, As, Au, and Ag, which have been deposited as triarsenides, sulfoarsenides, and sulfides, primarily hosted by quartz and quartz-carbonate veins. Our investigations aim to provide detailed lithological and structural features from the three deposits help understanding the factors that control the Co- bearing arsenides mineralization within the entire Bou Azzer –El Graara inlier.

2 Geological setting

The BEI is composed of a Neoproterozoic basement consisting of gneiss, amphibolites, serpentinites and mafic rocks, quartz diorites, overlain by volcanic-sedimentary cover represented by Ouarzazate group, divided into two groups: the terrigenous serie of the Tiddiline attributed to the Lower Ediacaran, and the Upper Ediacaran serie of the Ouarzazate Group. These latter are stratigraphically overlain by the early Cambrian series commonly known as the Adoudounian series (Figure 1).

The Aghbar area, located in the central part of the BEI, it is composed of serpentinites representing the Cryogenian ophiolite mantle covered by late Ediacaran volcanic and volcaniclastic rocks, overlain continuously by the lower Cambrian series formed mainly by dolomites and andesites.

The Bou-Froukh sector represents the western end of the BEI. It is composed of Cryogenian formations consisting of serpentinites, mafic rocks, intrusive quartz-diorites, the Tiddiline Fm., to the north, Ediacarian volcanic rocks, and the Adoudounian volcani-sedimentary cover.

The Ait Ahmane area is located in the eastern side of the inlier; it is characterized by the predominance of the ophiolitic rocks and the associated quartz-diorite intrusions (Ikenne et al. 2023). This area is characterized by a NNW-SSE oriented band arrangement of the different terrains

that comprise it, with the serpentinite massifs, gabbro band, and quartz-diorite band arranged from north to south. The quartz diorite band is intersected by veins of quartz, and quartz-carbonate, which serve as the host for cobalt mineralization.

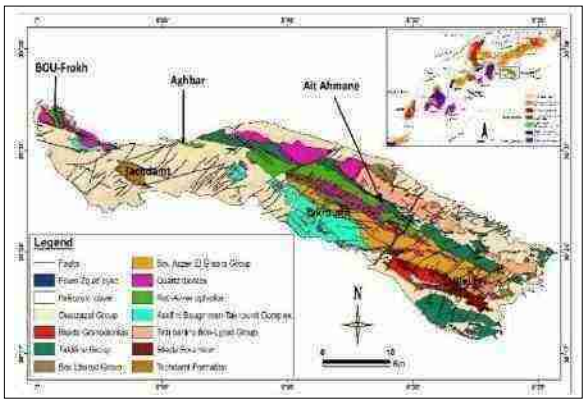

Figure 1. Geological map of the Bou Azzer - El Graara inlier (modified after Leblanc, 1980)

3 Structural data

Leblanc (1975) and Saquaque et al. (1989) highlighted the main events of the Pan-African orogeny in the BEI. They recognized two tectonic phases.

The first one, called phase B1 is a tangential phase that developed a NW-SE metamorphic schistosity in a low grade environment. This phase would have taken place during the obduction of the Bou Azzer ophiolitic complex on the northern border of the West African craton following a shortening in the NE-SW direction (Saquaque et al. 1989). The second, phase B2, is responsible for a fracture cleavage. this second event have also accompaniedby major sinistral strike-slip faults and reverse faults that take up the inherited faults from phase B1, withan average compression direction of N20° to N35° (Figure 2) (Leblanc et Lancelot, 1980; Azizi et al. 1990; Azizi, 1990; Ez-Zghoudy et al., 2023).

In these three studied deposits (Aghbar, Ait Ahmane and Bou Froukh); we identified three main families of structures:

- The E-W to WNW-ESE faults family, associated with major geological events considered as inherited from the B1 phase.
- The ENE-WSW family, recognized mainly in the central and western studied sectors. It consists of reverse faults related to the B2 phase.
- The NNE-SSW to NE-SW family, important because it regularly contains mineralization, is supposed to be related to the Hercynian orogeny (Maacha, 2013) or reactivated during the Hercynian period.

Figure 2. (A) Intra-dioritic quartz-carbonate emplacement, (B) sigmoidal tectonic structure, (C) reverse fault with quartz filling, (D) Fault mirror showing striations and pullout surfaces, (E) S1 flow cleavage across serpentinites, (F) Streaks indicating strike-slip movement (pitch between 5° and 30°).

4 Petrographic study

The three studied deposits are characterized by a large lithological diversity, and several petrographic facies have been mapped and described in these areas. The serpentinites are the predominant rocks in the tree areas; they are the result of the hydration and alteration of the ultramafic rocks that represent the mantle part of the ophiolite (Leblanc, 1980). These serpentinites host several kinds of dykes. The quartz diorites represent the latest element associated with the ophiolitic complex in the BEI terrains, they are anterior or synchronous to the B1 tectonic phase, during which they were tectonized (Leblanc 1981, Ikenne et al.2023).

The formations that post-date the major Pan-African B1 phase are assigned to the Ediacaran age.

During this period, two sedimentary formations were unconformably deposited on the ophiolitic complex and the associated rocks (Leblanc 1980):

- The Tiddiline Fm., which corresponds to detrital (mollasse and arkose) and volcani-detrital (greywackes) facies.
- The Ambed Fm., which is a silici-carbonates shell linked to a meteoric alteration. It constituted the receptacle of mineralizations (Maacha et al. 2011).

After the Pan-African stress, the Bou Azzer domain is exposed to a transtensive regime synchronous with the deposition of the Ouarzazate Fm. (Azizi et al. 1990). This regime favored the development of a system of horsts and grabens associated with the rise of serpentinite domes, alternating with depressions with Ediacaran deposits (Maacha et al. 2011). In the study area and based on the microscopic study, these deposits are represented by andesites, volcanic breccia, and pyroclastic rocks (Figure3).

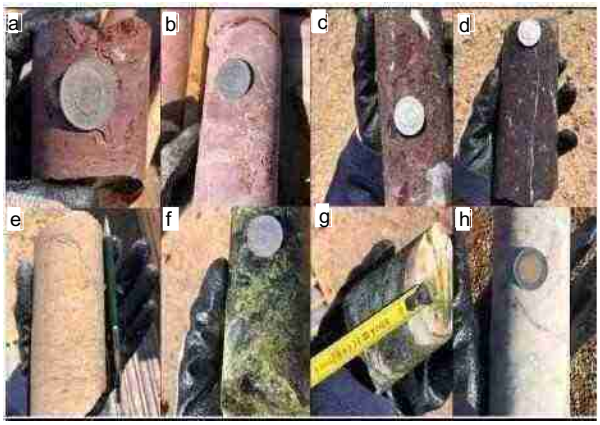

Figure 3. a- Sandstone/ b- Dolomite/ c-Conglomerate/ d-Andesite/ e- Dacite/ f,g- Serpentinite/ h- quartzo-carbonate veins.

5 Co-Ni-Cu mineralization

In all deposits of the Bou Azzer district, mineralized bodies are generally located along major Pan- African faults, and they are spatially and genetically associated with serpentinites (Leblanc. 1975, Maacha et al. 2011, Ikenne et al. 2021, Ez- Zghoudy et al. 2023). The mineralizations consist mainly of cobalt and nickel arsenides which are formed in a polyphase metallogenic system, whose ultimate stage corresponds to a mixing between exogenous fluids enriched in Co, Ni and As chlorides leached from serpentinites, and a volcanogenic fluid carrying selenium, molybdenum, bismuth, and gold (Maacha et al. 1998).

The studied areas contain several mineralized bodies in form of veins and/or lenses of different sizes. These bodies are located along sinistral faults attributed to the B2 Pan-African phase (Maacha et al. 2011). The lenses and veins are composed of quartz-carbonate facies with a late paragenesis of chalcopyrite and malachite (Figure 4).

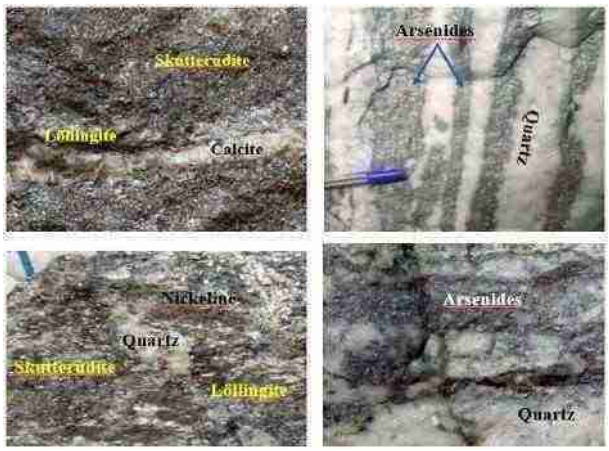

Figure 4. Macroscopic aspects of the mineralization in the Bou Azzer ore deposits.

Morphologically, the main deposits are developed either within the serpentinite or mainly along the contact between the serpentinite and quartz-diorite rocks.

Microscopic examination of these mineralizations shows a predominance of a mineralization consisting of triarsenides (skutterudite), biarsenides (safflorite, löllingite) monoarsenides (nickeline), sulfoarsenides (arsenopyrite), with little sulfides (chalcopyrite, galena) (Figure 5), accompanied by various generations of intercalated calcite, dolomite and quartz. Gold and silver assemblages include mainly native gold and electrum, polybasite, proustite, xanthoconite, argyrodite, stromeyerite and freibergite.

Optical investigations and textural relationships indicate three hydrothermal stages characterized by mineral assemblages of pre-arsenide gold stage I, stage II (Co, Ni, Fe)-arsenide and sulfarsenide, and stage III epithermal sulfide-sulfosalt ± Au ± Ag; a post-ore supergene stage IV is characterized by secondary Co minerals (erythrite, roselite, talmessite) (Bouabdellah et al. 2016).

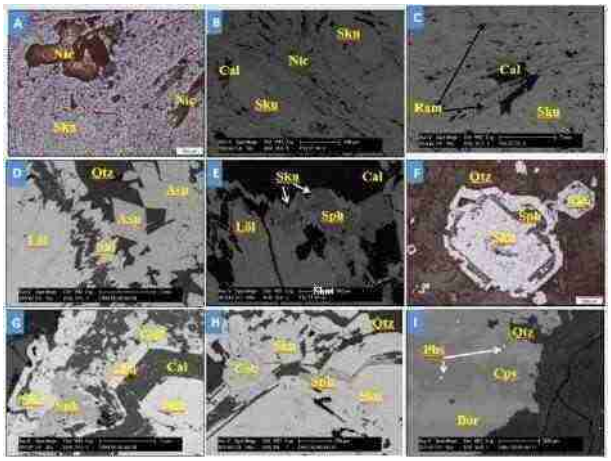

Figure 5. Black scattered images of contact mineralization hosted in calcitic lenses located between serpentinites and quartz diorite. Abbreviations (Nic. Nickeline; Sku. Skutterudite; Ram. Rammelsbergite; Qrz. Quartz; Saf. Safflorite; Löl. Löllingite; Asp. Arsenopyrite; Sph. Sphalerite; Pbs. Galena; Bor.

Bornite; Cpy. Chalcopyrite; Cob. Cobaltite; Gdf. Gersdorffite; Cal. Calcite).

The second type, vein mineralization, consists of mineralized veins that have a banded texture and intersect either quartz diorites or Ediacaran lavas (Figure 6).

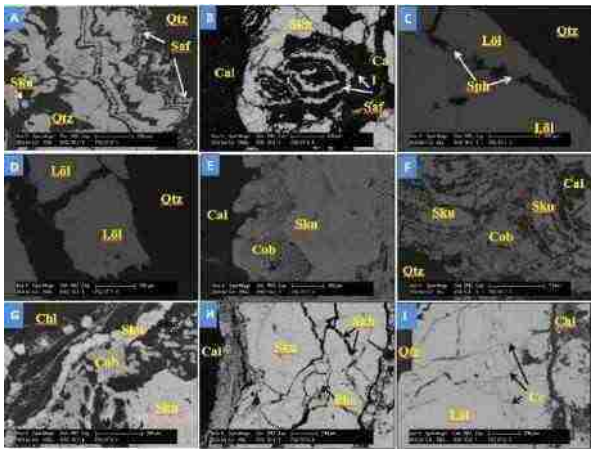

Figure 6. SEM phtomicrographs showing mineral association and mineral textures of the studied veins. Abbreviations (Nic. Nickeline; Sku. Skutterudite; Ram. Rammelsbergite; Qrz. Quartz; Saf. Safflorite; Löl. Löllingite; Asp. Arsenopyrite; Sph. Sphalerite; Pbs. Galena; Bor. Bornite; Cpy. Chalcopyrite; Cob. Cobaltite; Gdf. Gersdorffite; Cal. Calcite).

6 Conclusion

In conclusion, our field investigations in the BEI have revealed that the mineralization in the Aghbar, Ait Ahmane, and Bou-Froukh deposits is controlled by three families of tectonic structures. These structures include an E-W to WNW-ESE trending family inherited from the Pan-African B1 phase, an ENE-WSW trending family of faults related to the Pan-African B2 phase, and an NNESSW to NE-SW trending family related to the Hercynian orogeny. We have redefined two main types of mineralization in these deposits: i) so- called "contact ore bodies with massive lenses structurally controlled by the Pan-African faults and which occur either within serpentinite or mainly along its contact with Cryogenian quartz- diorite (Bou-Froukh and Ait Ahmane) or with Ediacaran volcanic rocks (Aghbar); and ii) the vein systems, which cut the different lithologies and are controlled by an NNE-SSW to NE-SW family, correspond to a reactivation of tension gashes as reverse faults during a shortening phase, probably of Hercynian age. These veins are only mineralized along segments of about 40 m from the contact of the serpentinite massif. The mineralization consists mainly of Co-Ni-Fe-bearing arsenides, sulfarsenides, sulfides, and native elements (Bi, Au), with gangue minerals chiefly represented by quartz, calcite, dolomite, and chlorite.

References

Admou H, Fekkak A., Razin P, Egal E, Youbi N, Soulaimani A, Blein O, Baudin T, Chèvremont P, (2013) Notes et Mémoires du Service Géologique Maroc. N°533. Carte Géologique Maroc (1/50 000). Feuille Aït AAhmane.

Azizi-Samir MR (1990) Géologie du Précambrien terminal (III) et traitement statistique des données géochimiques de prospection, dans la boutonnière de Bou Azzer - El Graara (Anti-Atlas, Maroc). Thèse. Université Joseph Fourier, Grenoble I. 280 p.

Azizi-Samir MR, Ferrandini, J, Tane J.L (1990). Tectonique et volcanisme tardi-Panafricains (580-560 Ma) dans l'Anti-Atlas Central (Maroc) : interprétation géodynamique l'échelle du NW de l'Afrique. J Afri Earth Sci 10:549-563.

Bouabdellah M, Maacha L, Levresse G, Saddiqi O (2016) The Bou Azzer Co–Ni–Fe–As(±Au ± Ag) District of Central Anti-Atlas (Morocco): A Long-Lived Late Hercynian to Triassic Magmatic-Hydrothermal to Low- Sulphidation Epithermal System. In: Bouabdellah, M., Slack, J. (eds) Mineral Deposits of North Africa. Mineral Resource Reviews. Springer, Cham. https://doi.org/10.1007/978-3-319-31733-5_8.

Ez-Zghoudy M, Ikenne M, Souhassou M, Belfoul MA, Gouiza M, Ilmen S, Ousbih M, Karfal, A, Maacha L, Zouhair M (2023) Structural controls on the Co and Ni-bearing arsenides from the Bou Azzer mine (Case of Aït Ahmane F53 vein deposit): Implications for mineral exploration. J Afri Earth Sci 104929. https://doi.org/10.1016/j.jafrearsci.2023.104929.

Ikenne ., Souhassou M, Saintilan N.J, Karfal A, Hassani AE, Moundi Y, Ousbih M, Ezzghoudi M, Zouhir M, Maacha L (2021) Cobalt–nickel–copper arsenide, sulfarsenide and sulfide mineralization in the Bou Azzer window, Anti- Atlas, Morocco: one century of multi-disciplinary and geological investigations, mineral exploration and mining. Geol Soc, London, Special Pub 502: 45-66.

Ikenne M, Souhassou M, Cousens B, Montero PF, Bea F, Askour F, Haissen F, Beraaouz EH, Ernst RE, Bajddi A, Ilmen S, Belkacim S, Toummite A (2023) Zircon U-Pb geochronology and Sm-Nd and Rb-Sr isotope systematics of Neoproterozoic Granitoïds from Bou Azzer (Anti-Atlas - Morocco): the obduction trigger of the Central Anti-Atlas Terrane. J Afr Earth Sci 104900. https://doi.org/10.1016/j.jafrearsci.2023.104900.

Leblanc M (1975) Ophiolites précambriennes et gris arséniés de cobalt (Bou Azzer, Maroc).Ph.D. Thesis Université de Paris VI, 329 p

Leblanc M, Lancelot JR (1980) Interprétationgéodynamique du domaine pan-africain (Précambrienterminal) de l'Anti-Atlas (Maroc) à partir de données géologiques et géochronologiques. Can J Earth Sci 17 : 142–155.

Maacha L (2013) Études métallogéniques et géophysiques des minéralisations cobaltifères et cuprifères de Bou-Azzer El Graara, Anti- Atlas Maroc. Les minéralisations de cuivre de la plateforme de Bleida. Ph.D. Thesis, Université Cadi Ayyad, Marrakech, 748p.

Maacha L, Alansari A, Saquaque A, Soulaimani A (2011) The Bou Azzer Cobalt-Nickel-Arsenic district. In: Les principales mines du Maroc, Michard, A., Saddiqi, O., Chalouan, A., Rjimati, C., Mouttaqi, A. (Eds.). Nouveaux Guides Géologiques et Miniers du Maroc, pp. 91-97.

Maacha L, Azizi-Samir R, Bouchta R (1998) Gisements cobaltifères du district de Bou Azzer (Anti-Atlas) : structure, minéralogie et conditions de genèse. Chron Rech Min 531–532 :65–75.

Saquaque A, Admou H, , Karson J, Hefferan K, Reuber I, (1989) Precambrian accretionary tectonics in the Bou Azzer-El Graara region, Anti-Atlas, Morocco. Geology 17:1107-1110.

PROSPECTS ON PLATINOIDS OF THE MAFIC-ULTRAMAFIC BELT OF THE SULTANUVAIS MOUNTAINS (UZBEKISTAN)

Jurabekov N.J.[1], Khaydarova A.B.[1], Khalmatov R.A.[1] Kholikov A.B.[2]
[1] University of Geological Sciences, Tashkent, Uzbekistan
[2] Institute of Mineral Resources,Tashkent, Uzbekist

Abstract. Mafic-ultramafic belts, tracing zones of deep faults, and suture zones have been discovered in Uzbekistan. Within their limits, in the mountains of Sultanuvais, Bukantau, Tamdytau, Nurata, and Chakylkalyan, studies have been conducted to detect platinum group metals (PGM). The article discusses the prospects for the platinoids of the Tebinbulak intrusion, which is located in the core of a synclinal fold of siliceous rocks. It is an ethmoid-like body (ellipsoid in plan) measuring 4.5x1.8 km, slightly asymmetrical, extending from south to north. The composition of the intrusion is dominated by ultrabasic rocks: peridotites (verlites, schliregeimites), pyroxenites, hornblendites; there are also in some degree mafic rocks. Two promising areas for platinum metals have been identified. Further research is required for an objective assessment of high-category resources.

1 Introduction

The economic significance of platinum group metals (PGM) – ruthenium, rhodium, palladium, osmium, iridium, and platinum – is determined primarily by valuable physical and chemical properties: heat resistance, corrosion and acid resistance, refractory, etc.

The main consumer of platinoids is the modern chemical industry, which uses them as catalysts in the production of nitric and other acids, in hydrogenation reactions of various compounds. The oil refining, automotive, electrical engineering, and jewelry industries are also important areas of application; a small part is used in medicine (surgical instruments, dentures, etc.).

There has been a trend of rapid growth in the consumption of platinoids in the automotive industry in the manufacture of filter-neutralizers of exhaust gases of cars.

The Republic of Uzbekistan does not have its own deposits of platinum metals, and its needs were covered by imports from abroad. However, in the Navoi Mining and Metallurgical Combine (NGMC) in 1980, a technology for extracting palladium from Muruntau ores was developed and implemented.

The Tebinbulak intrusive massif is located at the northwestern end of the Sultanuvais Mountains and includes the Aktau and Jamansai intrusions which are usually considered as large allochthonous blocks juxtaposed with the surrounding schists in a tectonic mélange.The host rocks are represented by metamorphosed Devonian formations (siliceous shales, siltstones, sandstones), forming a synclinal fold, in the core of which the Tebinbulak intrusive massif is located. It is a somewhat asymmetrical, elongated from south to north ethmolith-like body (ellipsoid in plan) measuring 4.5x1.8 km. The composition of the intrusive is dominated by ultrabasic rocks: peridotites (verlites, schliregeimites), pyroxenites, tebinites, hornblendites; there are also mafic rocks - hornblendite gabbro with sections of pyroxene gabbro and gabbro-syenites, gabbro-diorites. This intrusion is promising for the detection of industrial objects of platinum group metals.

2 Methodology

This study summarizes published and archival materials on platinoids of the Tebinbulak intrusion. Field studies sampled the rocks of the intrusive complex in order to determine the industrial significance of the platinoids. The analytical and mineralogical determinations done by the following techniques: primary analytical determination of a wide range of chemical elements by semi-quantitative spectral methods, quantitative determination of concentrations of the main useful components (gold, silver, platinoids, tungsten, etc.) by atomic absorption, quantitative microprobe (Jeol JSM5910LV - Japan) determination by EPMA and elemental determination by ICP (inductively coupled plasma) - mass spectrometric (Elan-G100DRS - USA). All the methods were carried out in the laboratory "Physical-Chemical Research Methods" of SI "IMR", the Institute of Geology and Geophysics of the Academy of Sciences of the Republic of Uzbekistan and the Central Laboratory of the State Committee of Geology of the Republic of Uzbekistan.

3 Discussions of the results

The majority of analysed samples from the Tebinbulak complex, presented by peridotites, pyroxenites and hornblendites with subordinate gabbro and gabbro-diorites.

The average chemical compositions of the main rocks of the Tebinbulak massif are given in Table 1.

Table 1. Chemical composition of rocks of the Tebinbulak massif, weight %

Component	Peridotites (3 an.)	Pyroxenites (8 an.)	Hornblendite (10 an.)	Gabbro (all) (14 an.)
SiO2	42,68	48,64	39,2	42,42
Al2O3	2,55	4,24	11,2	17,92
Fe2O3	6,39	4,22	7,47	6,28
FeO	4,91	4,60	9,93	6,37
MgO	26,97	14,86	11,35	5,89
CaO	8,96	19,60	13,3	13,23
Cr2O3	0,061	0,026	0,015	0,037
NiO	0,007	0,003	0,0014	0,012
CoO	0,001	0,002	0,0016	0,002
CuO	-	-	0,003	0,005
V2O5	0,017	0,0125	0,09	0,02
The amount	92,546	96,2035	92,561	92,186

Ultramafic bodies are exposed mainly in the northern parts of the western and eastern half of the Sultanuizdag ridge. Ten large and a significant number of small lenticular bodies of serpentinites are distinguished. A much smaller volume of ultramafic rocks is exposed in the middle reaches of the Kohrali, Sultan-bobo, Uzunbulak, and Kazgansayas. Several small audited bodies were found in the zone of the Urusai fault. The main mass of serpentinites is located in the form of two bands. The first is traced in the northern part of the ridge and lies among the effusive rocks of the Jamansai formation. Sometimes they come into contact with gabbro amphibolites. The second band is located south of the first, these bodies form interformational lenses by contact with terrigenous-sedimentary and sedimentary-effusive rocks of the Jamansai formation. The total area of Ultramafic bodies is 22 km^2.

The contacts of serpentinites with host rocks are predominantly tectonic and sub-consistent. Ultramafites are characterized by a rather monotonous composition and are represented by serpentinites. Dunites, peridotites, and pyroxenites are poorly expressed; they occur in the form of shlierens in serpentinites.

The objects of the Tebinbulak ore field of Sultanuvais Mountain belong to the titanomagnetite platinum-gold ore formation. They correspond to the riftogenic regime (D-C) with the manifestation of picrite-gabbro-diabase-alkali-olivine-basalt association of formations. Magmatism manifested itself within the long-lived regional Bukantau-South Ferghana zone of deep faults.

The Tebinbulak gabbro-pyroxenite massif is ore-containing and is located in the zone of the submeridional Urusai deep fault, in the core of the synclinal fold among the Lower Devonian rocks (siliceous, shale, sandstones, siltstones) and is a plate-like body. In the near-contact parts of it, the host rocks have been transformed into the plagioclase-micaceous cornea, marbled, scarred limestones (Figure 2).

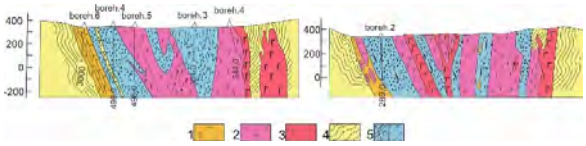

Figure 1. Geological sections of the Tebinbulak intrusive (based on the materials of the Tebinbulak exploration party): Symbols: 1 - peridotites; 2 - pyroxenites; 3 - hornblendites; 4 - ore-bearing Lower Devonian greenstone shales; 5 - zones (areas) of veined-interspersed titanomagnetite mineralization: a - traced; b - isolated from geophysical data.

The composition of the intrusive is dominated by ultrabasic rocks, the most common being hornblendites, pyroxenites, and peridotites. The maximum amount of titanomagnetite is noted in hornblendites and pyroxenites (up to 8.4-10%), where ilmenite and pyrite are present. Gabbroic rocks are represented by hornblendite essexite gabbro, gabbro-monzonites, and gabbro-diorite veins. In gabbro, concentrations of titanomagnetite and ilmenite reach 5.5%. Sphene (up to 1%), apatite, zircon, and rutile are also noted. The third group is the youngest dykes of syenites, leucosienites. The rocks are characterized by increased alkalinity, ferruginousness, and titanicity (maximum in pyroxenites, hornblendites) and are differentiated from basaltic magma. The age of the intrusion according to geological data and the absolute age of potassium-argon 313±8 million years corresponds to C_{1-2}.

Titanomagnetite mineralization with platinum and gold in ultrabasic rock differences extends in a sub-meridional direction near the western contact of the intrusion in the form of a 2.5 km long strip with a width of 100-400m and is traced to a depth of 500m. Mineralization is represented by two associations - titanomagnetite and platinum-gold sulfide. Titanomagnetite mineralization develops in the form of inclusions, and veins of densely interspersed and massive addition, schlieren secretions. 90-95% of the ores consist of magnetite. Its exsolution structures with ilmenite are characteristic, and spinel, hematite, and sphene are also present. The impurities are V, Cr, Mn, Ni, Co (Figure 3).

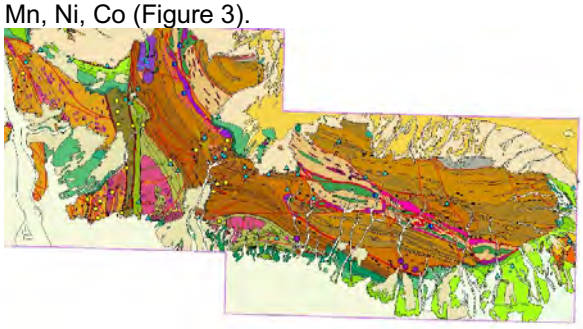

Figure 2. Geological map of the Sultanuvais Mountains in GIS format.

Gold and platinoids are found both in host rocks and in titanomagnetite ores. Their distribution is

extremely uneven and the content increases significantly in the sulfide association. Sulfide paragenesis is represented by chalcopyrite, pyrite, bornite, arsenopyrite, and arsenopyrite. The gold content in pyroxenites, hornblendites, and peridotites averages 0.021 ppm (0.01-0.023), which is five times higher for ultrabasics. There is a positive correlation between gold and platinoid contents. Gold is mainly finely dispersed and pulverized (0.01-0.1mm) high-grade. Gold telluride (Montreuil) has also been found. Gold concentrators are pyrite (up to 1.8 c/u) chalcopyrite (up to 0.5 ppm), its carriers are titanomagnetite (up to 0.7 c/u), hornblendites (up to 0.24 ppm) (Figure 4).

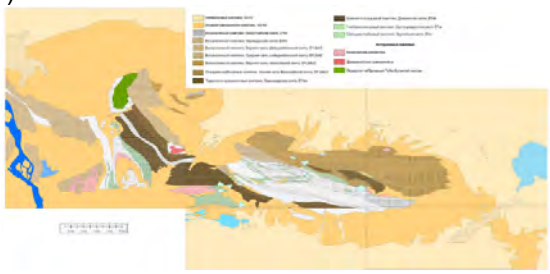

Figure 3. Map of the structural and material complexes of the Sultanuvais mountains.

Platinum and palladium predominate among platinoids, rhodium, traces of ruthenium, and iridium are noted. Peridotites, hornblendites contain PGM close to clarke, and in pyroxenites and gabbro it is 1.5 times higher than clarke.

The maximum amount of palladium (up to 0.06 ppm) is found in pyroxenites, tebinites. The content increases sharply in the presence of sulfide mineralization (the amount of platinoids is up to 1.45 ppm).

According to A.B. Khalikov, more than 25 anomalies with the content of platinum group metals up to 7.73 ppm were detected in the Tebinbulak massif in areas of ferruginization. Sulfides concentrate up to 99.2% of platinum metals with a platinum content from 0.4 to 25 ppm and palladium from 0.24 to 22 ppm. The ratio of palladium to platinum ranges from 0.2-6.7. The main concentrators of platinoids are pyrite (0.64-47 c/u) and chalcopyrite (1.88-4.5 ppm). Platinoids are also present in titanomagnetite (0.01-0.16 ppm), hornblendites (up to 0.24 ppm), pyroxene. Micro inclusions of platinum minerals - cuprite, polyxene, sperrilite - have been found in rocks and sulfides (V.V. Baranov, 1978).

In general, titanomagnetite mineralization with platinum and gold, located in the differentiated gabbro-pyroxenite massif, belongs to the magmatic and late magmatic types. The processes of late magmatic amphibolitization and postmagmatic serpentinization played an important role in the redistribution of ore components. According to the material composition and the nature of the distribution of the main components of the Tebinbulak ore, they are compared with the largest Ural Kachkanar deposit with good reason.

Figure 5 shows histograms of statistical calculations of spectral analysis of rocks of Tebinbulak ore field. Concentrations of most chemical elements: Sb-52.4; Au-39.4; Ta-24.5; Ba-1.4; As-14.7; W-4.6; Cu-9.4; Co-3.6; Cd-3.5; Bi-3.3– V-2.9; Cr-2.9; Mn-2.7; Ni-1.6; Ga-1.5; Ag–1.2; Pb-0.9

Correlations of elements by spectral analysis are shown for the most significant correlations - 84 samples with a critical value of the correlation coefficient for 5% of the significance level of Pk-0.212. noted with Cr, W, Ag, Cd, Sn, Ti, V, Ni, Mn, Co, Pb, Ba, Ga, Cu, Mo, Sb, Ni, As.

According to mass spectrometric analysis, the reduced average content of many elements, including the traditional satellites of gold - As, Ag (24.1 and 0.55 ppm, respectively). And also, the low maximum value–As-249 ppm (0.025%), raises the question of the possibility of its use as an indicator of gold mineralization. Accordingly, for the Tebinbulak expedition, the concentration of most chemical elements was obtained, (concentrations Re-495.1; Se-157.8; Pt-129.2; Te-67.9; Au-25; Pd-19; Si-18.5; As-14.2; Sb-8.7; Ag-7.9; Mo-4.4; Ir-3.2; Ni-3.1; Ca-2.8; Va-2.7; P-2.7; V-2.4; B-2.3; Sr-1.7; Mn-1.6; Fe-1,5; Co-1,4; Ti-1,2; U-1,1; Sc-1,1; Mg-1; W-0,9; Pb-0,9; Cr-0,9; Bi-0,8; Ru-0,6; Rh-0,2; Os-0,02). Normalized according to A.P. Vinogradov. The analysis was performed in Excel and Statistica.

To compare the concentrationsaccording to the regional background with the concentrations according to A.P. Vinogradov (granite-metamorphic shell), c/u. Accordingly, the concentration of most chemical elements by regional background was obtained, (concentrations Pd-72.3; Pt-25.8; Ti-7.8; P-7.6; As-6.3; Re-6.2; V-5.2; Sr-4.8; Ir-4.1; Mg-3.5; Cr-3.4; Co-3.2; Va-3.2; Pb-2.9; Sb-2.3; W-2.3; Sc-2.1; Au-2; Ni-1.8; Mn-1.8; Mo-1.8; Bi-1.7; Rh-1.4; Ag-1.4; Fe-1.3; Ru-1.2; Te-1.1; U-1; B-1; Os-0.9; Ca-0.9; Se-0.9; Si-0.9).

Correlations of elements by mass spectrometric analysis are shown. The most significant correlations - 34 samples with a critical value of the correlation coefficient for 5% of the significance level Rk-0.330) are noted with Fe, V, Pb, Va, Ti, P, V, Mg, Sc, Mn, Co, Ca, Te, Mo, Bi, As, B, Cr, U, Se, Ag, Pt, Rh, Pd, Os, Ru, Au, Ir, Re, Sb, Sr, Si, W, Ni.

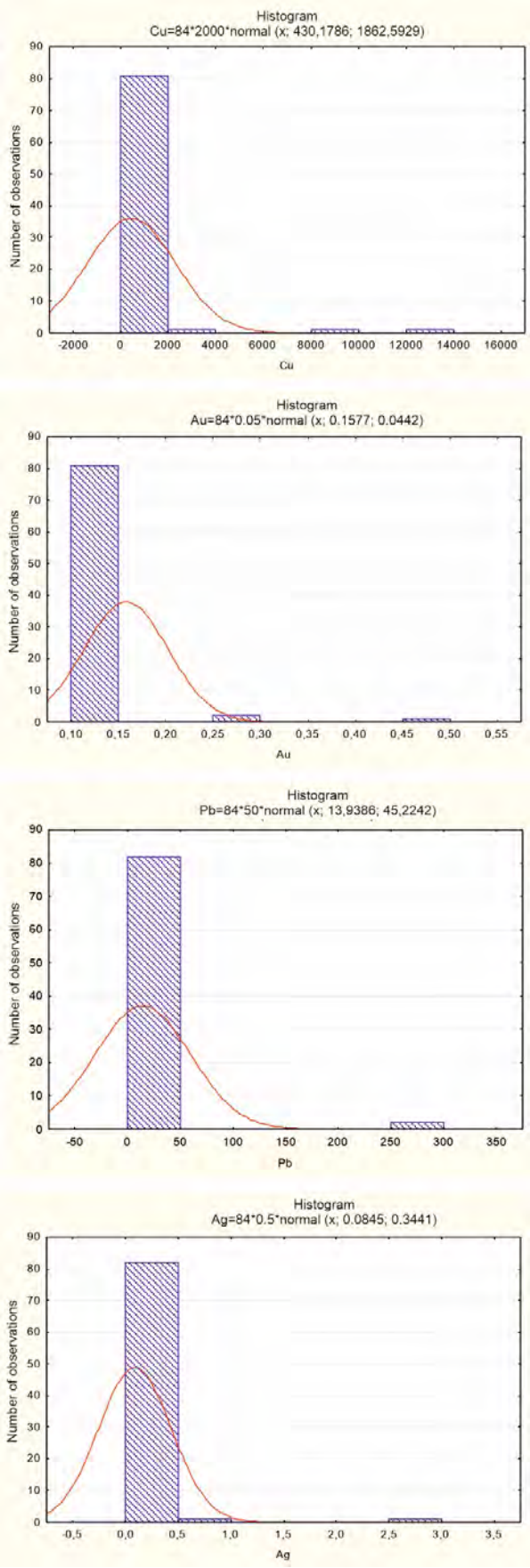

Figure 5. Histograms of the distribution of the contents ofchemical elements in the Tebinbulak ore field.

4 Conclusion

The research results show that in the Sultanuvais mountains, it is possible to expand the mineral resource base of Uzbekistan at the expense of platinum group metals (MPG). The most optimal way to implement these tasks is a detailed study of the areas promising for the MPG.

For a study with the involvement of foreign and domestic investments, 2e areas in the Tebinbulak intrusive massif of the Sultanuvais Mountains are proposed: mineralized zone №Tb-1, mineralized zone №Tb-2 with general forecast resources of platinoids.

References

Akhunjanov R., Zenkova S.O., Karimova F.B. Distinctive features of ultrabasite-basite intrusives of various ore bearing (Western Tien Shan). // Geology and Mineral resources. -2015. - No. 3. – pp.11-26.

Babadzhanov A.A. "Platinum bearing of skarnovo-rare-metal deposits of Western Uzbekistan" (final), - Tashkent, IGiG, 2014

Dalimov T.N., Ganiev I.N. Evolution and types of magmatism of the Western Tien Shan. Tashkent, University, 2010. - 227 p.

Kustarnikova A.A., Usmanov A.I., Babadzhanov A.A., Mansurov M.M., Maripova S.T., Mikhailova Yu.V., Musaev A.M., Smirnova S.K., Turesebekov A.H. – Metallogeny of gold and copper of Uzbekistan. - Institute of Geology and Geophysics named after H.M.Abdullayev. – T., 2012. – 410 p.

Kholikov A.B. Platinum bearing of Sultanuvais mountains // Materials of the International Scientific and Technical Committee / Integration of science and practice as a mechanism for effective development of the geological industry of the Republic of Uzbekistan. - Tashkent, 2014. - pp. 328-331.

Kholikov A.B. Mafit-ultramafic formations of the Western Tien Shan and their platinum bearing // Materials of the International Scientific and Technical Committee / Integration of science and practice as a mechanism for effective development of the geological industry of the Republic of Uzbekistan. - Tashkent, 2022. - pp. 332-337.

Nikitina O.N., Tukhtabayev T.M., etc. "Drawing up a geological map of the Sultanuvais mountains m-a 1:50000 within the sheets to 41-61-B, D; 62-A, B, D; 74-A, B" for 2004-2007. Pos. Eshonguzar, 2007

Artikov T.K., Dementeenko L.I., Nikitina O.N., etc. Geological structure and minerals of the eastern part of the Sultanuvais Mountains. Report on the implementation of GS, GDP1:50000 scale and medium-scale GC of the pre-Mesozoic foundation within the sheets to 41-62- C, D; 74-A, B gor Sultanuvais for 1998-2003. Pos. Eshonguzar, 2003

Insights into genesis of Pt-Fe minerals, laurite and kashinite from clinopyroxenite-dunite massifs: evidence from compositional and Cu-S isotope data

Kreshimir N. Malitch[1], Inna Yu. Badanina[1], Natalia G. Soloshenko[1], Sergey L. Votyakov[1], Tatiana A. Velivetskaya[2], Alexander V. Ignatiev[2]
[1]Institute of Geology and Geochemistry, Ural Branch RAS, Ekaterinburg, Russia
[2]Far East Geological Institute, Far East Branch RAS, Vladivostok, Russia

Abstract. To provide new insights into the origin of platinum-group minerals (PGM), this study presents the mineral chemistry and Cu-isotopic data for primary and secondary Pt-Fe minerals, and in-situ S-isotope data for Ru-Os sulfides and kashinite from chromitites and placer deposits of the Nizhny Tagil and Svetly Bor clinopyroxenite-dunite massifs (Middle Urals) and the Guli clinopyroxenite-dunite massif (Polar Siberia). Collectively the studied samples of primary high-temperature ferroan platinum (Pt_2Fe) and isoferroplatinum (Pt_3Fe) have an overall $\delta^{65}Cu$ range from –0.37 to 0.31‰. Secondary low-temperature PGM represented by the tetraferroplatinum (PtFe) – tulameenite ($PtFe_{0.5}Cu_{0.5}$) solid solutions series have the $\delta^{65}Cu$ values ranging from –1.15 to –0.72‰. The lighter Cu-isotopic composition of secondary Pt-Fe minerals compared to that of primary Pt-Fe minerals ($\delta^{65}Cu$ = –1.01 ± 0.17‰, n = 8 and $\delta^{65}Cu$ = 0.07 ± 0.43‰, n = 14, respectively) is consistent with a secondary nature of isotopic variations, due to evolved composition of the ore-forming fluid during the low-temperature formation of the tetraferroplatinum – tulameenite series. The sulfur isotope results reveal a restricted range of chondritic $\delta^{34}S$ values for laurite (RuS_2) and Rh-bearing kashinite $(Ir,Rh)_2S_3$ ($\delta^{34}S$ = –0.15 ± 0.24‰, n = 4 and $\delta^{34}S$ = –0.23 ± 0.45‰, n = 7, respectively) implying that sulfur derived from a common near-chondritic source.

1 Introduction

A significant number of zoned clinopyroxenite-dunite massifs are located in Russia (the Urals, Eastern Siberia, and the Far East). They are characterized by the presence of dunites, clinopyroxenites and platinum placer deposits. Despite numerous studies of zoned-type ultramafic massifs, the origin of these massifs and of the associated platinum mineralization remains unresolved. Understanding the main events of platinum-metal ore formation is impossible without analyzing the sources and behavior of the main ore-forming components, namely platinum, osmium, sulfur and copper. In contrast to the Re-Os isotope data (Tessalina et al. 2015; Malitch et al. 2020), which previously allowed characterization of distinct sources of platinum-group elements (PGE) and the multi-stage nature of PGE mineralization, the isotopic systematics of platinum, sulfur and copper for platinum-group mienrals (PGM) from this type of geological setting still remains poorly defined. Sulfur isotope data have been restricted to Ru-Os sulfides from the Guli massif (Malitch et al. 2022).

To gain further insights into the genesis of PGM, we have carried out a combined study of primary and secondary Pt-Fe minerals, laurite and kashinite from chromitites and placer deposits of the Nizhny Tagil and Svetly Bor clinopyroxenite-dunite massifs in Middle Urals and the Guli clinopyroxenite-dunite massif in Polar Siberia. We integrate (1) electron microprobe analyses of PGM, (2) in-situ sulfur isotope analyses of laurite and kashinite using a femtosecond laser ablation GC-IRMS at high spatial resolution, and (3) copper isotope analyses using an MC ICP-MS and sample-standard bracketing technique.

2 Geological background and samples

The Nizhny Tagil and Svetly Bor zoned clinopyroxenite-dunite massifs form part of the Platinum Belt of the Urals, which is located along the 60th meridian for more than 900 km. These massifs are famous for platinum deposits; over 330 tonnes of platinum have been mined from associated placer and lode deposits in the past. The most common PGM that occur in bedrocks and placer platinum deposits are Pt-Fe minerals, among which high-temperature ferroan platinum (Pt_2Fe) and isoferroplatinum (Pt_3Fe) dominate over subordinate Os-Ir alloys, Ru-Os sulfides of the laurite–erlichmanite series (RuS_2-OsS_2), Ir-Rh sulfides of the kashinite–bowieite series (Ir_2S_3-Rh_2S_3) and Ir-Rh thioshpinels of the cuproiridsite–cuprorhodsite–ferrorhodsite series ($CuIr_2S4$-$CuRh_2S_4$-$FeRh_2S_4$) (Malitch et al. 2017). Secondary low-temperature PGM assemblages, associated with serpentinization, are represented by the tetraferroplatinum (PtFe) – tulameenite ($PtFe_{0.5}Cu_{0.5}$) – ferronickelplatinum ($PtFe_{0.5}Ni_{0.5}$) solid solutions series and Pt-Cu minerals.

The Guli ultramafic massif, located in the Maimecha-Kotui province Province in northern part of Siberian Craton, is remarkable for its considerable size (about 600 km^2, Malitch and Lopatin 1997). The ultramafic rock assemblage of the Guli massif and its significant potential for placer PGM accumulations make it typical of zoned massifs of the Uralian-Alaskan-Aldan type, whereas the huge size of the ultramafic complex, its shape, the lack of concentrically zoned structure, and the common occurrence of refractory Ir-, Os-, and Ru-rich PGM in chromitite and placer deposits are features more consistent to those of ophiolite massifs (Malitch and Lopatin 1997).

Platinum-group minerals selected for this study were obtained from vein-disseminated chromitite segregations confined to the marginal areas of coarse-grained dunite in the central parts of the Nizhny Tagil (i.e., Krutoy Log and Alexandrovsk Log deposits (Figure 1a, b) and Svetly Bor massifs, and Quaternary deposits of the upper part of the Ingaringda River located within the Guli massif. In total, 19 samples of Pt-Fe minerals from primary (11 samples) and secondary (8 samples) PGM were analyzed (Figure 1c-g). Laurite and kashinite studied are invariably associated with isoferroplatinum of the Svetly Bor massif (Figure 2).

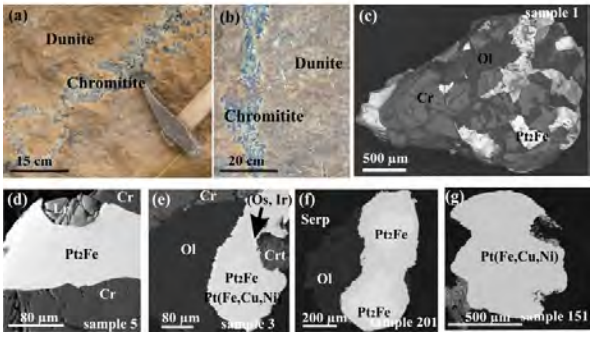

Figure 1. Morphological features of: (**a**, **b**) vein-disseminated chromitites and (**c**) Pt-Fe minerals associated with chromite (Cr) and olivine (Ol) from the Krutoy Log deposit of the Nizhny Tagil massif. Back-scattered images of PGM assemblages from chromitites of the Krutoy Log (**d**, **e**, **g**) and Alexandrovsk Log (**f**) PGE deposits. Pt_2Fe – ferroan platinum, Lr – laurite, (Os, Ir) – iridian osmium, Pt(Fe,Cu,Ni) – minerals of the tetraferroplatinum–tulameenite series, Cr – chromite, Ol – olivine and Serp – serpentine.

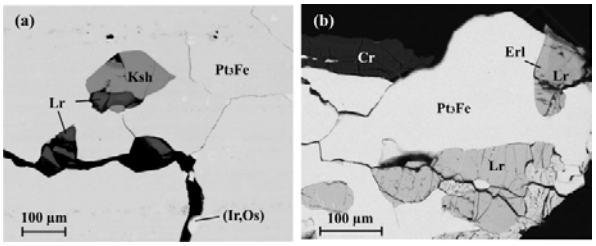

Figure 2. Back-scattered images of PGM assemblages from the Svetly Bor massif. Pt_3Fe – isoferroplatinum, Lr – laurite, Erl – erlichmanite, Ksh – kashinite, (Ir,Os) – osmian iridium, Cr – chromite.

3 Analytical methods

Electron microprobe analyses of PGM were carried out at Common Use Center "Geoanalyst" of the Institute of Geology and Geochemistry, UB RAS, Ekaterinburg, using a CAMECA SX-100 equipped with five WDS spectrometers. Quantitative WDS analyses were performed at 25 kV accelerating voltage and 20 nA sample current, with a beam diameter of ~1 μm. The following X-ray lines and standards have been used: RuLα, RhLα, PdLβ, OsMα, IrLα, PtLα, NiKα (all native element standards); FeKα, CuKα, SKα (all chalcopyrite); AsLα (sperrylite). Corrections were performed for the interferences involving Ru-Rh, Ru-Pd and Ir-Cu.

Eleven S-isotope analyses were subsequently performed at Laboratory of Stable Isotope within Common Use Center of the Far East Geological Institute, Far Eastern Branch of the Russian Academy of Sciences (Vladivostok, Russia). Sample preparation for mass spectrometric isotope analysis of sulfur was carried using a femtosecond laser ablation system NWR Femto in combination with a reactor for sulfide aerosol conversion into SF_6 gas, a cryogenic and chromatographic purification system, and an isotope ratio mass spectrometer (FsLA-GC-IRMS) (Ignatiev et al. 2018; Velivetskaya et al. 2019). Isotope ratio of sulfur were measured using a MAT-253 mass spectrometer (Thermo Fisher Scientific, Germany) equipped with a Faraday cup for simultaneous measurements of the ion currents at m/z 127 ($^{32}SF_5^+$) and 129 ($^{34}SF_5^+$). The measurements were carried out relative to the laboratory working standard, calibrated to the international standards IAEA-S-1, IAEA-S-2 and IAEA-S-3. The sulfur isotope composition in the sample was calculated as $\delta^{34}S=[(^{34}S/^{32}S)_{sample}–(^{34}S/^{32}S)_{std}]/(^{34}S/^{32}S)_{std}*10^3$ and expressed in ‰ with respect to reference standard VCDT (Vienna Canyon Diablo Troilite). Average accuracy of $\delta^{34}S$ analyses was better than 0.2‰ (2σ). Further details of analytical methods are presented elsewhere (Ignatiev et al. 2018).

The method for determining $\delta^{65}Cu$ included the selective chromatographic separation of Cu from a solution of the studied Pt-Fe mineral sample, followed by determination of the $^{65}Cu/^{63}Cu$ isotope ratio using a Neptune Plus multiple-collector inductively coupled plasma mass-spectrometer (Thermo Fisher). A detailed description of the technique is presented by Okuneva et al (2022); digestion and chromatographic separation were carried out in a clean room unit (class 1000, ISO 6) and laminar flow cabinets (class 100, ISO 5). The decomposition stage of Pt-Fe minerals (0.00n mg) included their dissolution in concentrated nitric acid. For chromatographic isolation of pure Cu fraction, AG MP-1 ion-exchange resin (Bio-Rad inc., USA) was used (Maréchal and Albarède 2002); the analyte isolation scheme was detailed in Okuneva et al (2022). The $^{65}Cu/^{63}Cu$ isotope ratios in the analytical copper fraction were measured by sample-standard bracketing technique using a Neptune Plus mass-spectrometer. Measurement sequence was as follows: blank experiment (3% HNO_3 solution) → NIST SRM 976 Cu standard → the studied PGM sample (3% nitric acid solution of the mineral) → NIST SRM 976 Cu standard. Each single measurement of the Cu-isotopic composition consisted of 60 cycles collected at 8-second integrations followed by a baseline measurement for 30 seconds. The copper isotope composition of the sample was calculated as $\delta^{65}Cu=[(^{65}Cu/^{63}Cu)_{sample}/(^{65}Cu/^{63}Cu)_{std} – 1)]\times1000$; the measurement accuracy was ±0.14‰ (2σ).

4 Compositional features of PGM

The majority of the PGM from chromitites and placer deposits of the Nizhny Tagil and Svetly Bor massifs are represented by high temperature ferroan platinum and isoferroplatinum that have compositions close to Pt_2Fe and Pt_3Fe, respectively (where Pt equals to the sum of PGE, at %, Fe is Σ Fe, Cu, Ni, at %). These Pt-Fe minerals are commonly replaced by intermediate members of the tetraferroplatinum (PtFe)–tulameenite ($PtFe_{0.5}Cu_{0.5}$) series and tulameenite ($PtFe_{0.5}Cu_{0.5}$) (Figure 3). Chemically, ferroan platinum and isoferroplatinum carry notable trace concentrations of Ir (up to 4.6 wt. %), besides smaller quantities of Cu (0.4–1.4 wt.%), Ni (0.3–0.4 wt.%), Rh (0.8–1.1 wt.%) and Os (0.3–0.4 wt.%). Copper content in minerals of the tetraferroplatinum (PtFe)–tulameenite ($PtFe_{0.5}Cu_{0.5}$) solid solution series varies within 6.8–11.3 wt.%, reaching 12.3 wt.% in tulameenite. The Pt-Fe minerals from the Nizhny Tagil and Svetly Bor massifs host various inclusions: Ru-Os sulfides of the laurite–erlichmanite series (Figures 1d, 2, 4a, 4b), Ir-Rh sulfides of the kashinite (Ir_2S_3)–bowieite (Rh_2S_3) series (Figures 2a, 4c), Ir-Rh-Pt thiospinels of the cuproiridsite ($CuIr_2S_4$) –cuprorhodsite ($CuRh_2S_4$) – malanite ($CuPt_2S_4$) series (Figure 4d), and Os-Ir(-Ru) alloys (Figures 1e, 2a). Compositional features of Pt-Fe minerals from the Guli massif, including a similar set of PGM inclusions, were characterized in detail by Malitch and Thalhammer (2002).

A common occurrence of inclusions of laurite, kashinite, iridian osmium and osmian iridium in Pt-Fe minerals and the equilibrium phase relations of Os-Ir alloys, deduced from the binary system Os–Ir (Massalski 1993), are indicative of their high-temperature origin. The presence of reaction rims composed of minerals of the tetraferroplatinum (PtFe) – tulameenite ($PtFe_{0.5}Cu_{0.5}$) series, which replace high-temperature ferroan platinum and isoferroplatinum, is indicative of their secondary origin. Most researchers associate the formation of this low-temperature PGM assemblage with serpentinization of ultramafic rocks (Betekhtin 1991).

5 Copper and sulfur isotope data

5.1 Copper isotopic compositions

All the samples of primary Pt-Fe minerals have $\delta^{65}Cu$ values ranging from –0.37 to 0.31‰ (Figure 5). They have a mean $\delta^{65}Cu$ value of 0.07‰, and a standard deviation of 0.43‰ (n=14). We note the pronounced similarity in $\delta^{65}Cu$ values for samples of isoferroplatinum from the Svetly Bor massif, ferroan platinum from the Nizhny Tagil massif, which are close to those for samples of ferroan platinum from the Guli massif (Figure 5). Minerals of the tetraferroplatinum (PtFe) – tulameenite ($PtFe_{0.5}Cu_{0.5}$) solid solution series are characterized by lighter Cu-isotopic compositions ($\delta^{65}Cu$ values range from –1.15 to –0.72‰; Figure 5), with a mean value of –1.01‰ and a standard deviation of 0.17‰ (n=8).

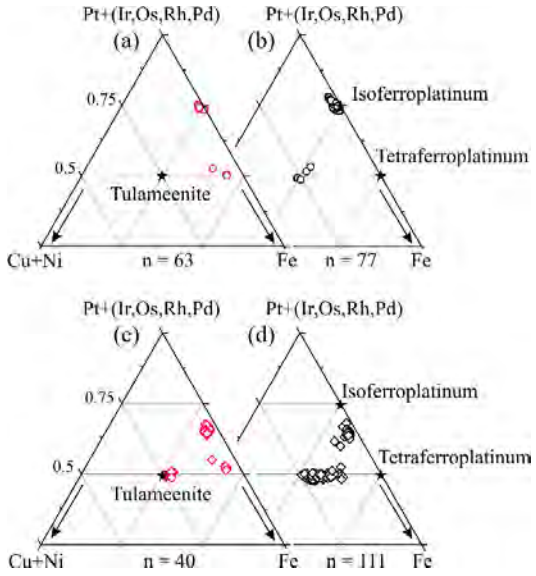

Figure 3. Chemical composition of Pt-Fe minerals from placers (**a**) and chromitites (**b**) of the Svetly Bor massif, placers (**c**) and chromitites (**d**) of the Nizhny Tagil massif in the ternary diagram Pt + (Ir, Os, Rh, Pd) – Cu+Ni – Fe, at.%. Asterisks indicate minerals of the Pt-Fe system.

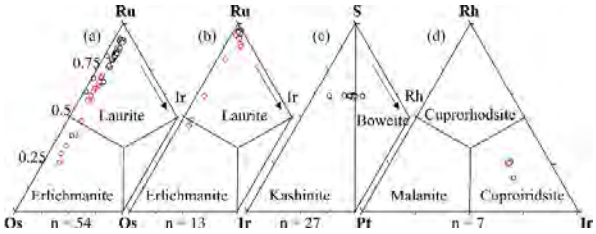

Figure 4. Chemical compositions (at. %) of Ru-Os sulfides in coordinates Ru–Os–Ir (**a**, **b**), Ir-Rh sulfides in coordinates S–Ir–Rh (**c**), and Ir-Rh-Pt thiospinels in coordinates Rh–Pt–Ir (**d**) from placer deposits (open circles in red) and chromitites (open circles in black) from the Svetly Bor, placer deposits (open diamonds in red) and chromitites (open diamonds in black) from the Nizhny Tagil massifs.

It has been shown (Graham et al. 2004) that redox reactions play an important role in the fractionation of Cu isotopes at low temperatures. For example, variations in the Cu-isotopic composition in primary and secondary Cu-bearing minerals may be due to fractionation between different complex species in solution (Maréchal and Albarède 2002) or associated with the influence of isotopically different fluids during hydrothermal processes (Graham et al. 2004). In this context, the lighter Cu-isotopic composition in secondary Cu-bearing PGM compared to that in ferroan platinum ($\delta^{65}Cu$ = –1.01 ± 0.17‰, n = 8 and $\delta^{65}Cu$ = 0.07 ± 0.43‰, n = 14, respectively) is consistent with the secondary nature of isotopic variations, likely due to evolved composition of the ore-forming fluid during the low-temperature formation of the tetraferroplatinum (PtFe) – tulameenite ($PtFe_{0.5}Cu_{0.5}$) solid solution series.

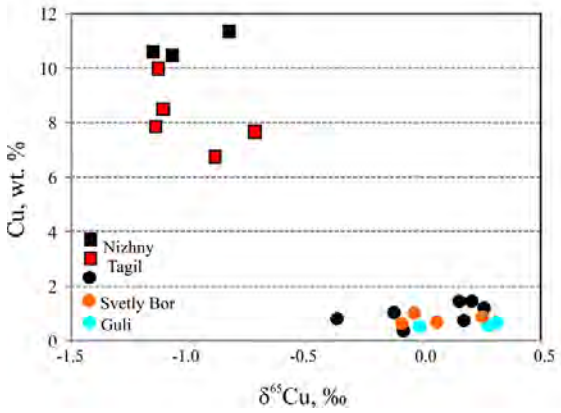

Figure 5. Copper isotope data for Pt-Fe minerals from the Krutoy Log and Alexandrovsky Log deposits of the Nizhny Tagil massif (symbols in black and red color, respectively), Svetly Bor and Guli massifs. Ferroan platinum (black and blue circles), isoferroplatinum (orange circles), minerals of the tetraferroplatinum–tulameenite solid solution series (squares).

5.2 Sulfur isotopic compositions

The $\delta^{34}S$ values in laurite and Rh-bearing kashinite forming part of polymineralic assemblage with isoferroplatinum show a relatively narrow range from –0.8 to 0.4‰. Laurite (Ru#=85-91) have $\delta^{34}S$ values of –0.4–0.00‰ (Figure 6), with a mean of –0.15‰ and a standard deviation of 0.24‰ (n=4), which are similar to Rh-bearing kashinite with $\delta^{34}S$ values ranging from –0.8 to 0.4‰ (a mean value of 0.23‰ and a standard deviation of 0.45‰, n=7). The sulfur isotope signatures of the studied PGM are similar to those of Ru-Os sulfides from the Guli massif (Figure 6). They are indicative of a subchondritic source of sulfur. The deep source of sulfur is consistent with the osmium isotope data obtained for Ru-Os sulfides and Os-Ir alloys from the Nizhny Tagil and Guli massifs (Malitch et al. 2011; Tessalina et al. 2015), implying that HSE and S derived from a near-chondritic source.

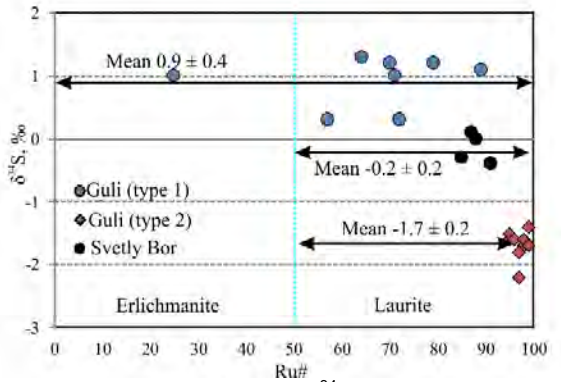

Figure 6. Sulfur isotope data ($\delta^{34}S$, ‰) for Ru-Os sulfides from the Svetly Bor (this study) and Guli (Malitch et al. 2022) massifs.

Acknowledgements

The authors are grateful to T.G. Okuneva, S.V. Karpova and A.R. Sidoruk for valuable analytical assistance, and to Dr. W.D. Smith for useful suggestions and editorial input. This study was financed by the Russian Science Foundation (https://rscf.ru/en/project/22-27-00140/).

References

Betekhtin AG (1935) Platinum and other platinum-group minerals. USSR Academy of Sciences, Moscow, 148 p. [in Russian].

Graham S, Pearson N, Jackson S, Griffin W, O'Reilly SY (2004) Tracing Cu and Fe from source to porphyry: in situ determination of Cu and Fe isotope ratios in sulfides from the Grasberg Cu-Au deposit. Chemical Geology 207: 147–169.

Ignatiev AV, Velivetskaya TA, Budnitskiy SY, Yakovenko VV, Vysotskiy SV, Levitskii VI (2018) Precision analysis of multisulfur isotopes in sulfides by femtosecond laser ablation GC-IRMS at high spatial resolution. Chemical Geology 493: 316–326.

Malitch KN, Lopatin GG (1997) New data on the metallogeny of the unique Guli clinopyroxenite-dunite massif, northern Siberia, Russia. Geology of Ore Deposits 39: 209–218.

Malitch KN, Thalhammer OAR (2002) Pt-Fe nuggets derived from clinopyroxenite-dunite massifs, Russia: a structural, compositional and osmium-isotope study. Can. Mineral. 40: 395–418.

Malitch KN, Efimov AA, Badanina IYu (2011) Contrasting platinum-group mineral from chromitites of the Nizhny Tagil and Guli massifs (Russia): implications for composition, sources and age. Doklady Earth Sciences 441: 1514–1518.

Malitch KN, Stepanov SYu, Badanina IYu, Khiller VV (2017) Bedrock platinum-group element mineralization of zonal clinopyroxenite-dunite massifs of the Middle Urals. Doklady Earth Sciences 476: 1147–1151.

Malitch KN, Puchtel IS, Belousova EA, Badanina IYu (2020) Contrasting platinum-group mineral assemblages of the Kondyor massif (Russia): Implications for the sources of HSE in zoned-type ultramafic massifs. Lithos 376–377: 105800. https://doi.org/10.1016/j.lithos.2020.105800

Malitch KN, Kogarko LN, Badanina IYu, Velivetskaya TA, Ignatiev A.V. (2022) Sulfur isotope composition of Ru-Os sulfides from the Guli massif, Maimecha-Kotui province, Russia: first results. Doklady Earth Sciences 507: 1012–1018. https://doi.org/10.1134/S1028334X22600955

Maréchal C, Albarède F. (2002) Ion-exchange fractionation of copper and zinc isotopes. Geochimica et Cosmochimica Acta 66: 1499–1509.

Massalski TB (1993) (ed) Binary alloy phase diagrams. Amer Soc Metals, Metals Park, Ohio, 2224 pp.

Okuneva TG, Karpova SV, Streletskaya MV, Soloshenko NG, Kiseleva DV (2022) The method for Cu and Zn isotope ratio determination by MC ICP-MS using the AG MP-1 resin. Geodynamics & Tectonophysics 13: 2s. https://doi.org/10.5800/GT-2022-13-2s-0615

Tessalina SG, Malitch KN, Augé T, Puchkov VN, Belousova E, McInnes BIA (2015) Origin of the Nizhny Tagil clinopyroxenite-dunite massif (Uralian Platinum Belt, Russia): insights from PGE and Os isotope systematics. J. Petrol. 56: 2297–2318.

The Ni-Cu-Co mineralisation of the Espedalen Complex, southern Norway: constraints for the distribution of magmatic sulphides within an anorthosite intrusion

Eduardo Mansur[1], Trond Slagstad[1], Jan Sverre Sandstad[1], Sarah Dare[2]
[1]Geological Survey of Norway, PO Box 6315 Torgarden, Trondheim, 7491, Norway
[2]Département de Sciences Appliquées, Université du Québec à Chicoutimi, QC G7H 2B1, Canada

Abstract. The Espedalen Complex, south-central Norway, comprises three main suites (jotunite, charnockite and augengneiss; main anorthosite–ultramafic–norite; and gabbronorite suites) formed between 1520 and 1510 Ma. Several Ni-Cu-Co sulphide occurrences are hosted within the anorthosite-ultramafic-norite suite. Most of the Ni-Cu-Co sulphide occurrences are hosted within anorthosites and norites but spatial association with ultramafic rocks is common. In some cases, the mineralization occurs as predominantly undeformed disseminated sulphides, interstitial to cumulus silicates (olivine, orthopyroxene and plagioclase), whereas in other cases, net-textured and massive sulphide lenses (few-meters thick) are constrained to shear zones. The sulphide assemblage consists mainly of pyrrhotite, followed by pentlandite and chalcopyrite. Primary sulphide assemblages yield Ni and Cu tenors from 4 to 9% and 2 to 4%, respectively. The platinum-group element (PGE) contents are low in the Espedalen Complex, with tenors mostly below 0.5 ppm. Sulphide ore composition can be modelled by variable R-factor (mass ratio of silicate to sulphide liquids) regimes of around 500-1000, and slightly different parental magmas. The Espedalen Complex represents a fertile area with potential for the discovery of new Ni-Cu-Co mineralisation with relatively high Ni and Cu tenors, but low PGE.

1 Introduction and Geological Setting

The Espedalen Complex occurs in the eastern portion of the Jotun–Valdres Nappe Complex, southern Norway (Fig. 1A). It comprises three main suites (jotunite, charnockite and augengneiss; main anorthosite–ultramafic–norite; and gabbronorite suites) that formed between 1520 and 1510 Ma. The complex hosts significant Ni-Cu-Co mineralisation associated with the anorthosite-ultramafic-norite suite, but these have not been systematically investigated. More than 15 mineralised sites were discovered during old mining activities and recent exploration. The largest sites comprise the Dalen and Stormyra deposits, which host 5.3 Mt @ 0.29% Ni, 0.12% Cu and 0.02% Co, and 1.01 Mt @ 1.09% Ni, 0.48% Cu and 0.04%, respectively. This study provides the first systematic characterization of the different Ni-Cu-Co mineralisation from the Espedalen Complex. We combine field work with whole rock and sulphide geochemistry from different mineralisation sites. Our dataset also includes samples and assay results from 165 drill cores.

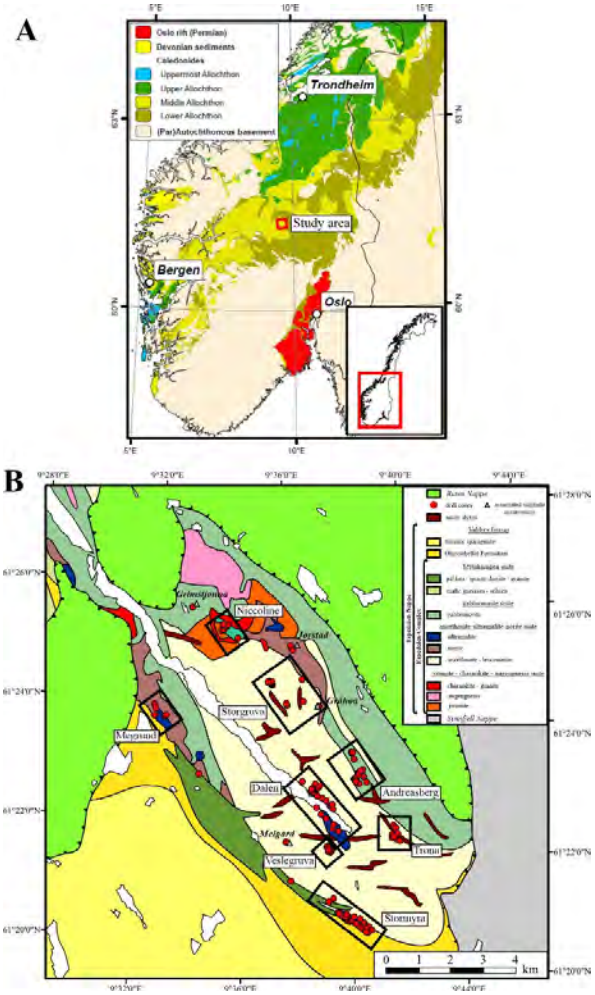

Figure 1. A – Simplified tectonic map of central-south Norway showing the main lithotectonic units. B - Geological map of the surrounding region of the Espedalen Complex and drill hole locations, with highlighted areas (black boxes) for the main magmatic Ni-Cu-Co sulphide occurrences and minor associated occurrences. The map is partially modified from Corfu and Heim (2014).

2 Ni-Cu-Co sulphide mineralisation

Most of the Ni-Cu-Co sulphide mineralisation in the Espedalen Complex is hosted by rocks of the anorthosite-ultramafic-norite suite (Fig. 1B). These areas are commonly marked by old mining excavations, which can vary from pits, only a few metres deep, to excavations that extend to hundreds of metres. However, important resources

that do not crop out were recently discovered by drilling (e.g., Stormyra), and thus, no previous mining activity is observed in these regions. In the areas where previous activity allows for better-exposed ore, the sulphide mineralisation normally defines 50 cm to 2 m-wide zones with variable sulphide contents depending on the location (Fig. 2A). These are commonly deformed and hosted within shear zones, suggesting the displacement and eventual fragmentation of original sulphide bodies (Fig. 2B). In these cases, the host rocks, which vary from anorthosite to melanorite, also display variable degrees of deformation (Fig. 2C). Although Ni-Cu-Co mineralisation is typically hosted by anorthositic to noritic rocks, several occurrences also display a close spatial relation to, or are hosted within, ultramafic cumulates. These medium-grained olivine-orthopyroxenites have preserved their cumulus texture which is commonly poikilitic defined by subrounded olivine crystals enclosed within orthopyroxene oikocrysts (Fig. 2D).

Some of the sulphide occurrences from the Espedalen Complex are associated with shear zones that seem to dislocate the ore bodies from their initial portion within the intrusion. The mineralisation varies from disseminated (Fig. 2D), net-textured (Fig. 2E) and massive sulphides (Fig. 2F). In addition, several zones with locally remobilised sulphides are observed at most occurrences, which are not limited to those hosted within shear zones but also found in less deformed ore bodies. These zones vary from a few metres to several centimetres in scale and consist of deformed rocks with thin sulphide veinlets (Fig. 2G). The secondary mineralogy of the host rocks allows some assessment of the protolith, with ultramafic protoliths normally yielding a chlorite and talc-dominated schist, whereas noritic protoliths yield chlorite, epidote and plagioclase assemblages. We use the terms ‘primary sulphides’ and ‘remobilised sulphides’ to distinguish sulphide occurrences with predominantly magmatic textures, from these thin sulphide veinlets indicating local remobilization, respectively. However, the term ‘remobilised sulphides’ does not refer to the major scale dislocation and/or disruption of some of the sulphide ore bodies within shear zones.

3 Sulphide petrography

The petrographic characteristics of primary and remobilised sulphide ores from the various localities are comparable to each other and thus, these are not individually described to avoid repetition. In disseminated ores, the sulphide assemblage consists mainly of pyrrhotite, followed by pentlandite and minor chalcopyrite, and is interstitial to silicates (Fig. 3A). The presence of magnetite is common and normally occurs as anhedral grains included within pyrrhotite and pentlandite, but small sulphide inclusions in magnetite are also observed. The semi-massive to massive sulphide ores from different localities are also dominated by pyrrhotite and pentlandite with only minor chalcopyrite.

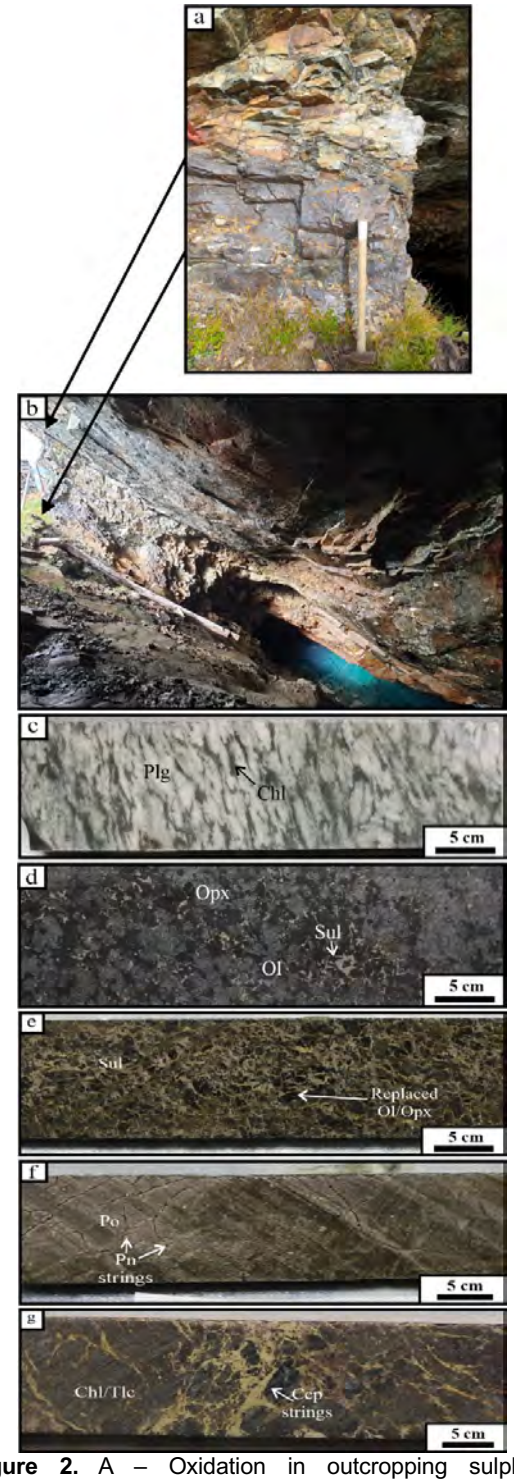

Figure 2. A – Oxidation in outcropping sulphide occurrences partially extracted by previous mining activities. B - Semi-massive sulphide body shown in (A) hosted within a shear zone. C - Deformed anorthosite to leuconorite with strong foliation. D- Medium-grained olivine-orthopyroxenite with poikilitic texture and interstitial sulphides. E - Net-texture sulphide with angular fragments of altered olivine and orthopyroxene. F - Massive sulphide with abundant pyrrhotite and the occurrence of pentlandite strings. G - Chalcopyrite stringers within chlorite-talc schist which represent a transformed ultramafic protolith. Abbreviations: Ccp – chalcopyrite; Chl – chlorite; Ol –

olivine; Opx – orthopyroxene; Plg – plagioclase; Pn – pentlandite; Po – pyrrhotite; Sul – sulphides; Tlc – talc.

Pentlandite normally displays granular texture of individual grains included within pyrrhotite, but in some cases also defines an intergrown mass with pyrrhotite (Fig. 3B).

Secondary alteration and recrystallisation are not ubiquitous features in most primary sulphide occurrences from the Espedalen Complex but are important factors at the Stormyra deposit. Different from other localities, the sulphide assemblage from the Stormyra deposit is marked by variable, but commonly abundant (more than 20%) pyrite. The pyrite grains are predominantly observed in semi-massive and massive ores where they are mostly included within pyrrhotite-dominated masses, but occurrence within chalcopyrite-dominated and even pentlandite-rich portions is also observed. The pyrite grains are mostly subrounded and seem to have grown from the pyrrhotite-pentlandite-chalcopyrite assemblage during post-magmatic alteration (Fig. 3C). Finally, the remobilised sulphide assemblages are dominated by chalcopyrite, mostly associated with secondary silicates (e.g., chlorite and talc), and display ductile structures. The occurrence of anhedral pyrite grains, and less commonly magnetite, within the chalcopyrite in remobilised sulphides domains is recurrent.

4 Sulphide geochemistry

The samples from the different Ni-Cu-Co sulphide mineralisation display very variable sulphide proportions, which result in a wide range of S values ranging from 0.1 to 35 wt.%. The range comprises variations from disseminated, net-textured and massive sulphide ores, respectively, but the values display a continuous trend, suggesting a gradual change in sulphide contents. There is a positive correlation between S and Ni (Fig. 4A), Cu (Fig. 4B) and Co (Fig. 4C) in both primary and remobilised sulphides. However, for all these elements, the concentrations are higher in the former relative to the latter at a given S concentration. For instance, Ni, Cu and Co concentrations in primary sulphides broadly range from 0.05 to 8 wt. %, <0.01 to 4 wt. % and <100 to 3000 ppm, respectively, but from <0.01 to 2 wt. %, <0.01 to 1 wt. % and <100 to 2000 ppm in remobilised sulphides, respectively.

There is also a broad correlation between S and PGE in primary sulphides, which supports their control dominantly by the presence of sulphide minerals (illustrated by Pd in Fig. 4D). However, the concentrations of all PGE are very low and close to detection limits (e.g. horizontal alignments in the plots from 4D), which introduces much scattering in the exploration geochemistry dataset. We have calculated the metal tenors (i.e., concentration of metals in 100% sulphides) for primary and remobilised sulphides from different localities (following Barnes et al., 2011). A distinct feature of the mineralisation in the area is that Ni (Fig. 4E) and Cu (Fig. 4F) tenors from primary sulphides are greater than those from remobilised sulphides.

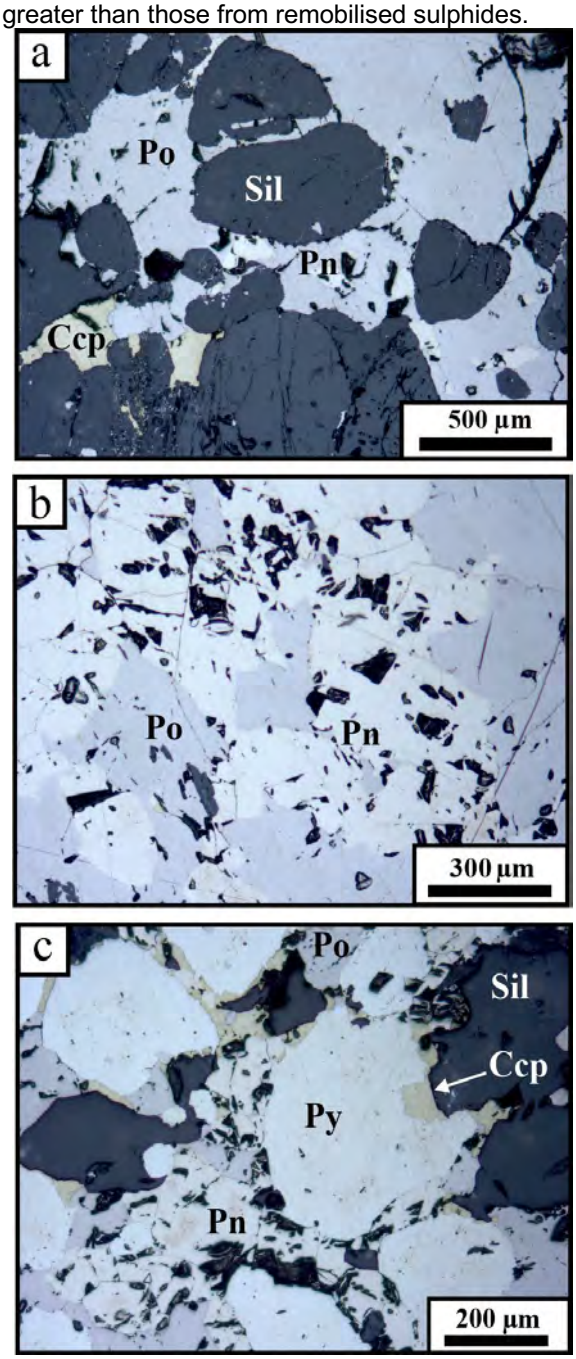

Figure 3. A – Disseminated sulphides comprising pyrrhotite, pentlandite and minor chalcopyrite, interstitial to olivine and orthopyroxene. B - Abundant granular pentlandite enclosed within pyrrhotite. C - Anhedral pyrite crystals enclosed within pyrrhotite and minor pentlandite and chalcopyrite masses. Abbreviations: Ccp – chalcopyrite; Pn – pentlandite; Po – pyrrhotite; Py – pyrite; Sil – silicates.

Moreover, primary sulphides from Stormyra and other minor occurrences display greater tenors relative to the primary sulphides from other locations. For instance, median Ni and Cu tenors vary from 7 to 8.5% and 3 to 3.5% in primary sulphides from Stormyra, Andreasberg and Megrund, followed by 4 to 5.5% and 1.6 to 3% in primary sulphides from other localities, and from 0.3

to 2% and 0.25 to 1.5% in remobilised sulphides, respectively (Fig. 4E and 4F).

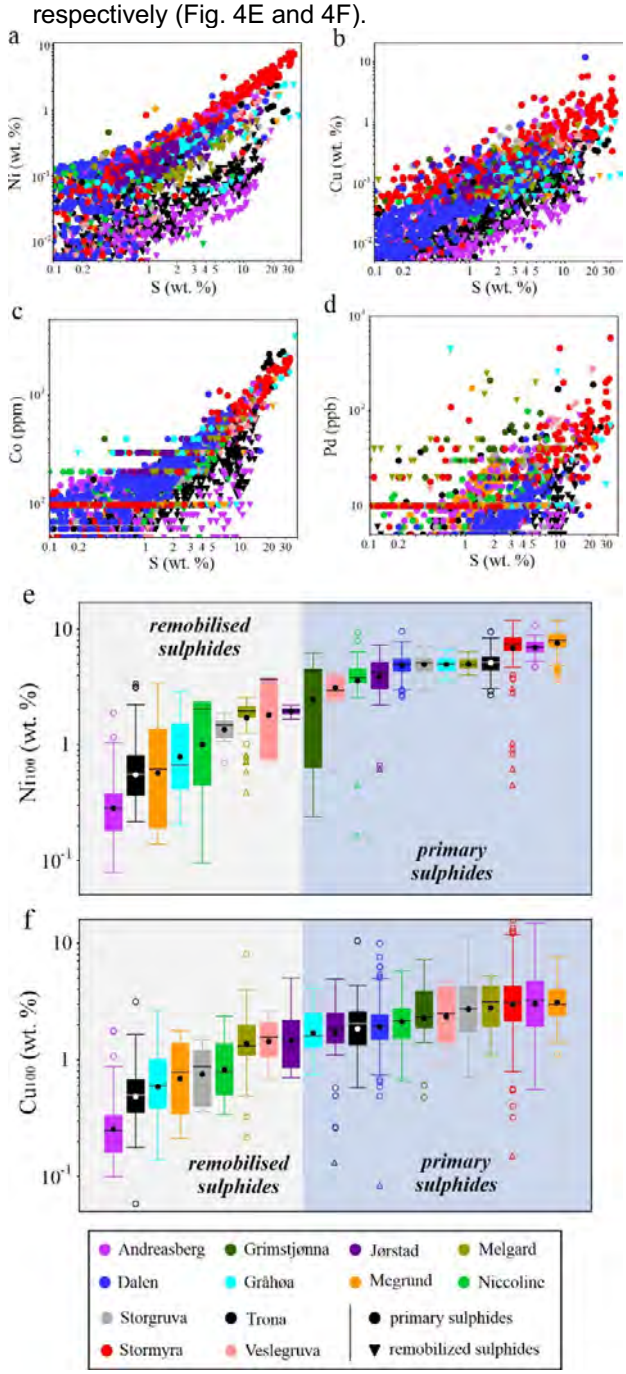

Figure 4. Binary plots of (a) Ni, (b) Cu, (c) Co and (d) Pd, versus S and box and whisker diagrams of (e) Ni and (f) Cu tenors in primary and remobilised sulphides.

5 Interpretations and conclusions

The variations in metal tenors are interpreted to reflect a combination of slightly different, but invariably PGE-depleted, parental magmas and variable R-factor regimes (R-factor varying from 300 to 700; Campbell and Naldrett, 1979) during ore formation (e.g. Lightfoot et al., 2012). The PGE-depleted parental magmas that formed the different sulphide mineralisation of the Espedalen Complex can be modelled as the product of 15% mantle melting (Barnes and Lightfoot, 2005) followed by approximately 2% crystallisation with sulphide removal under cotectic proportions. Moreover, redistribution of magmatic sulphides during post-magmatic deformation and alteration of the Espedalen Complex seems to have taken place at major and local scales. Large-scale displacement has no major geochemical impact, whereas local remobilisation, associated with centimetre-scale local shear zones, formed sulphide veinlets with lower metal tenors (Holwell et al., 2017; Mansur et al., 2021). Overall, the Espedalen Complex, and eventual extensions, offers large potential for further discoveries of magmatic sulphide deposits. We suggest that properly assessing if other geological domains, previously assigned to the Jotun Nappe, are correlated or not with the Espedalen Complex is essential for further expanding this prospective area. If correlated to the Espedalen Complex, these terrains could represent potential targets for Ni-Cu-Co deposits, but not for PGE deposits.

Acknowledgements

Part of the analyses for this study were performed in the Norwegian Laboratory for Mineral and Materials Characterisation (MiMaC) NGU node, supported by the Research Council of Norway project number 269842/F50.

References

Barnes S-J, Lightfoot PC (2005) Formation of magmatic nickel sulfide ore deposits and processes affecting their copper and platinum group element contents. Econ Geol 100th Anniversary: 179–213

Barnes SJ, Osborne GA, Cook D, Barnes L, Maier WD, Godel B (2011) The Santa Rita nickel sulfide deposit in the Fazenda Mirabela intrusion, Bahia, Brazil: geology, sulfide geochemistry, and genesis. Econ Geol 106(7):1083–1110

Campbell IH, Naldrett AJ (1979) The influence of silicate: sulfide ratios on the geochemistry of magmatic sulfides. Econ Geol 74(6):1503– 1506

Corfu F, Heim M (2014) Geology and U–Pb geochronology of the Espedalen Complex, southern Norway, and its position in the Caledonian nappe systems. Geol Soc Lond, Spec Publ 390(1): 223-239

Holwell DA, Adeyemi Z, Ward LA, Smith DJ, Graham SD, McDonald I, Smith, JW (2017) Low temperature alteration of magmatic Ni-Cu-PGE sulfides as a source for hydrothermal Ni and PGE ores: A quantitative approach using automated mineralogy. Ore Geol Rev 91: 718-740

Lightfoot PC, Keays RR, Evans-Lamswood D, Wheeler R (2012) S saturation history of Nain Plutonic Suite mafic intrusions: origin of the Voisey's Bay Ni–Cu–Co sulfide deposit, Labrador, Canada. Mineral Deposita 47: 23-50

Mansur E, Barnes SJ, Ferreira Filho CF (2021) The effects of post-cumulus alteration on the distribution of chalcophile elements in magmatic sulfide deposits and implications for the formation of low-S-high-PGE zones: The Luanga deposit, Carajas mineral province, Brazil. Can Mineral 59(6): 1453-1484

Ni-Cu sulphide deposits in Sweden – general characteristics, genetic aspects and economic potential

Olof Martinsson
Luleå University of Technology, Sweden

Abstract. Several different types of Ni-Cu sulphide deposits have been discovered in Sweden during the last 150 years of exploration and several of them have also been mined in small scale. These deposits share most characteristics with typical magmatic Ni-Cu deposits worldwide but could be divided into at least five different types based on character of host rock and origin of mineralization. Those are deposits related to peridotite sills, mafic dykes, mafic plutons, layered mafic intrusions and serpentinites. In general, the metal composition is related to magma composition with those hosted by ultramafic rocks being more Ni-dominated. Most of the deposits are formed in an arc setting but those related to ultramafic rocks might have formed during events of extension. The economic potential of the known nickel deposits is restricted as most deposits are small in size and/or low grade. However, as several of these deposits are suggested to be part of larger magmatic systems further research and exploration could maybe result in more significant discoveries.

1 Introduction

Sweden is an important mining district in EU with production of mainly Fe, Zn, Cu, Pb, Au, and Ag. Although nickel was discovered from the Co-mine at Los in Sweden 1751 only very limited mining of nickel has occurred. Small scale mining occurred mainly in the 19th century in south Sweden with Kleva as the most important example. In mid 1900s the Lainejaure mine produced 0.1 Mt of ore with 2% Ni and 1% Cu (Grip 1961). Extensive exploration for nickel was done during the later part of the 1900s by Boliden, Swedish Geological Survey, and Swedish Geological AB. This resulted in the discovery of several deposits in the “Nickelbelt” in the eastern part of the Västerbotten County but also in some other areas.

The Ni-deposits are related to ultramafic and mafic intrusive rocks but with slightly different character depending on type of host rock and local geological environment. This paper will give the general characteristics of Ni-deposits occurring in different geological settings and with implications for genetic aspect of mineralization and exploration.

2 Geological setting

The Precambrian part of Sweden belongs to the Baltic shield formed during several orogenic events spanning from 3.0 to 0.9 Ga and including rifting, subduction and collision episodes. To an Archean nucleus several geological sub-provinces has been added and include the 2.5-1.95 Ga Karelian, 1.95-1.86 Svecofennian, 1.86-1.65 Ga Trans-scandinavian Igneous Belt (TIB) and 1.66-0.93 Ga Sveconorwegian provinces. To the west these provinces are bordered by the 0.6-0.4 Ga Caledonides and in the southeast by Fanerozoic sediments.

2.1 Norrbotten province (2.8-1.87 Ga)

The northernmost part of Sweden includes Archean, Karelian and Svecofennian bedrock. The Archean bedrock is dominated by orthogneisses and highly metamorphosed supracrustal units while the Karelian units are dominated by rift-related greenstones. The Svecofennian units are represented by mafic to felsic volcanic rocks formed in shallow marine to terrestrial environment and with interbedded epiclastic sediments. Mafic intrusions are common and may have a layered character with ultramafic cumulates in the lower part. Ultramafic intrusions are rare and mostly small in size. Intrusions hosting Ni mineralization are mainly found in areas dominated by marine sedimentary rocks that often contain Fe-sulphides.

2.1 Västerbotten province (1.90-1.87 Ga)

Northern Västerbotten includes the Skellefte district with important Volcanogenic massive sulphide deposits hosted by submarine volcanic rocks. Those are overlaid and to the south bordered by submarine epiclastic sediments varying from graywacke to shale containing graphite and Fe-sulphides. Small ultramafic (peridotite) intrusions are common in eastern part of Västerbotten whereas mafic intrusions are mostly rare. Several intrusions of both mafic and ultramafic composition contain Ni-mineralization.

2.2 Bothnian Basin province (1.95-1.88 Ga)

The region between Skellefte district and Bergslagen is dominated by epiclastic rocks consisting mainly of graywacke and shale but with locally minor intercalation of volcanic rocks. Mafic intrusions occur locally and may have a layered character. A few of them has low grade Ni-mineralization.

2.3 Bergslagen province (1.90-1.88 Ga)

Bergslagen is the oldest mining district in Sweden with several different types of deposits. The region is dominated by felsic volcanic rocks with epiclastic sedimentary rocks mainly found at the base and the top. Carbonate rocks are common in the upper part of the volcanic sequence. Mafic intrusions occur in several places and have locally a layered character.

Intrusions of ultramafic composition are rare. Ni-mineralization has been discovered in several of the mafic intrusions with small scale mining in some of them.

2.4 TIB province (1.85-1.65 Ga)

TIB is an extensive north-south extending belt of mainly granitoids but locally containing also gabbroic rocks. In a few areas there are preserved associated volcanic rocks of low metamorphic grade and mainly felsic composition. Metasedimentary rocks are mostly rare and of epiclastic origin.

2.5 Sveconorwegian province (1.66-0.93 Ga)

The Sveconorwegian sub-province was formed during several tectonic events including subduction, rifting and collision and is divided in the Gothnian orogeny and the Grenvillian orogeny. Supracrustal rocks are variously metamorphosed and deformed and includes epiclastic sediment and mafic to felsic volcanic rocks. Plutonic rocks are mainly felsic in composition and mafic intrusions are rare.

2.6 Caledonian province (0.6-0.4 Ga)

The Caledonides are the product of a complete Wilson cycle and comprises tectonic units represented different evolutionary steps that are stacked in nappes of different metamorphic grade during the collisional stage. Mafic-ultramafic intrusions were formed mainly in the initial rifting stage and related to late back arc basins. Some of them have minor Ni-sulphide mineralization.

3 Ni-Cu sulphide deposits

Extensive exploration in mid-late 1900s resulted in the discovery of several Ni-Cu sulphide occurrences in northern Sweden and included deposits mainly related to ultramafic intrusions but in some cases also mafic intrusions. A distinctly different type was represented by serpentine altered dunites and peridotites in the Caledonides. Selected representative examples of these different types of Ni-deposits are described more in detail.

3.1 Kukasjärvi

The Kukasjärvi deposit was investigated by the Boliden company drilling in the late 1970s and early 1980s by 15 drill holes. It is hosted by a peridotite sill occurring in metasediments in southeastern Norrbotten. Ore minerals occur disseminated and are dominated by pyrrhotite with small amounts of pentlandite and chalcopyrite. The deposit is calculated to contain 2.6 Mt with 0.4% Ni and 0.4% Cu (Bergman & Kathol 2018).

3.2 Notträsk

Massive Ni-bearing pyrrhotite was first discovered in a road cut at Notträsk and later investigated by drilling. It occurs close to the margin of a 6x4 km large, and concentrically zoned funnel shaped 1.8 Ga intrusion in southern Norrbotten. Modal layering is steep at the margin but becomes gradually almost horizontal in the central part. It has a noritic marginal zone with xenoliths of graphitic metasediments followed by ferrogabbro, olivinegabbro, anorthosite, and troctolite towards the inner part (Arvanitidis 1982; Filén 2001). Massive pyrrhotite and disseminated sulphides comprising pyrrhotite and minor pentlandite and chalcopyrite are found in the marginal norite. Violarite, mackinawite, gersdorffite, cubanite, and cobaltite are rare constituents. The sulphur isotope composition of sulphides is on average 2.2‰ (Arvanitidis 2018).

3.3 Lainijaur

The Lainijaur deposit was discovered in 1940 and mined during 1941-1945 producing in total 0.1 Mt @ 2.2% Ni, 0.9% Cu, and 0.1% Co. It occurs in northern Västerbotten and is hosted by a differentiated intrusion varying in composition from olivine gabbro to granodiorite. The intrusion is hosted by metasediments and has the shape of a narrow laccolite with roots in a mafic dyke striking NE-SW. The ore varies from disseminated to massive consisting of pyrrhotite, chalcopyrite and pentlandite but include also minor vein style mineralization dominated by Ni-As sulphides. The massive ore occurs at the lower contact in close relation to the feeder dyke in the footwall. The disseminated ore occurs in the lower part of the gabbro and in the feeder dyke as sulphide droplets. Veins of nickeline, cobaltite, skutterudite, loellingite, rammelsbergite and asenopyrite occur in the massive ore and in the footwall metasediments (Grip 1961). The deposit is suggested to have an age of c. 1.87-1.89 Ga and to have formed from mantle-derived magmas produced during crustal extension (Martinsson 1996).

3.4 Älgliden

The Älgliden intrusion is a 3-km-long dike, up to 100 m wide in the central part. It strikes SW-NE parallel to steeply dipping extensional faults. It occurs in northern Västerbotten and has an age of 1.88 Ga. It consists mainly of olivine-rich norite with a fosterite content in olivine ranging from 72 to 76, and minor leucogabbro (Beijgarn et al. 2011; Cordier et al. 2019). The mineralization contains 0.2% Ni, 0.69% Cu, and 0.03% Co and consists of sulphide blebs, small stringers, and “net-textured” ore through the dike. The main sulphide minerals are pyrrhotite, pentlandite, and chalcopyrite with pyrrhotite partly replaced by pyrite within 10 m of the dike margins (Bejgarn et al. 2011). Sulphur isotope composition of sulphides have $\delta^{34}S$ values varying from 3.8 to 4.6 ‰ (Cordier et al. 2019).

3.5 Lappvattnet

The Lappvattnet deposit was discovered by drilling in 1973 and later investigated by trial mining. It is the first discovered occurrence related to small peritdotite bodies which intruded graphite bearing biotite gneiss in the Nickelbelt in eastern Västerbotten. Sulphide mineralization occurs in the ultramafic rocks but is most extensively developed in the gneiss occurring disseminated, as veinlets and breccia infill. The most high-grade ore occurs as sulphide rich mylonite and breccia forming lenses and tabular bodies with tectonic and sharp contacts to the gneiss. The mineralized interval is 1-10 m wide and continuous for 620 m and is estimated to contain 1 Mt @ 1.0% Ni and 0.2% Cu (Nilsson 1985). Hexagonal pyrrhotite and minor pentlandite occur disseminated in the peridotite and partly as rounded droplets. Massive and breccia ore is manly hosted by gneiss and consists of rather coarse-grained monoclinic pyrrhotite and minor pyrite, pentlandite, and chalcopyrite. Accessory minerals include mackinawite, sphalerite, gersdorffite, nickeline, and sperrylite (Nilsson 1985).

3.6 Rörmyrberget

Rörmyrberget is also part of the Nickelbelt. Disseminated Ni-mineralization consisting mainly of pyrrhotite and pentlandite is found in a 1700 m long and up to 320 m thick ultramafic intrusion. It comprises multiple sills with modal layering and is hosted by metasediments. Serpentine altered olivine cumulates are found in the lower part of the intrusions followed by peridotite and gabbro. The MgO content is up to 40 % in olivine cumulates and olivine has a forsterite content ranging from 82 to 91. Pentlandite is locally common and is in one orebody the dominating sulphide phase (Nilsson 1985). Later investigations have identified smaller high-grade ore lenses with a combined tonnage of 0.293 Mt @ 1.49% Cu, 0.14% Cu, and 8.54% S (Persson 1991).

3.7 Slättberg

Nickel was discovered in 1817 at Slättberg in northern Bergslagen and mining took place periodically between 1851 and 1943 with a total production of 20 000 tons of ore (Nilsson, 1985). Massive ore occurs in the central part of a 1600 m long and 3-6 m wide mafic dyke, but sulphides are also disseminated in the host rock. Pentlandite, millerite, and chalcopyrite occurs together with pyrrhotite and pyrite with massive ore surrounded by pyrite in a 1.2 to 2.7m wide zone. The pyrrhotite ore contained 1.2-2 % Ni and pyrite contained up to 0.5% Co (Lövstrand 1903).

3.8 Kuså

The Kuså deposit in Bergslagen is hosted by an intrusive complex ranging in composition from quartz monzodiorite through diorite–gabbro to pyroxenite and hornblendite with an age of 1.80 Ga (Ripa et al. 2017). Massive to disseminated ore occurs in a c. 10 m wide and moderately dipping zone having a tectonic lower contact. The ore contained 1.1 to 1.8 % Ni and Cu that was enriched towards the hanging wall (Löfstrand, 1903). Ore minerals are dominated by pyrrhotite, chalcopyrite and pentlandite with bravoite, cobaltite, linneaeite, and sperrylite as minor constituents (Ripa et al. 2017).

3.9 Kleva

Mining for Cu started in 1691 at Kleva but after discovery of high Ni grades in 1842 it was mined for Ni during 1845-1889, and for a few years during World War I. An estimated total production of 55000 tons of ore with 2-2.5% Ni and 0.5% Cu generated approximately 1000 tons of Ni. Sulphide mineralization is related to a 1.79 Ga mafic complex comprising gabbro, diorite, and minor norite and anorthosite within the TIB-province (Bjärnborg et al. 2015). Massive pyrrhotite-dominated mineralization occurs as irregular tabular and vein-shaped bodies in areas of disseminated mineralization. Pentlandite, chalcopyrite, pyrite, sphalerite, violarite, marcasite, mackinawite, magnetite, and ilmenite occur together with pyrrhotite. Chalcopyrite most commonly occurs in the outer parts of the lower grade mineralization, or as fracture fillings. Partly assimilated sedimentary rocks occur in mineralized areas within the gabbro (Grip 1961; Zakrzewski 1988).

3.10 Rönnbäcken

The Rönnbäcken deposit, located in the Caledonides, was discovered in the 1940s. Nickel sulfides occur in a serpentinized ultramafic intrusions originally consisting of olivine and pyroxene. Sulphides are very fine grained and include pentlandite, heazlewoodite and minor millerite and cobaltite. They occur disseminated and were formed during serpentinization by release of Ni from olivine. Metallurgical tests have generated concentrates with high Ni contents in the range of 26–36% Ni. Mineralization occurs in three separate ultramafic bodies and has a total tonnage of 600 Mt @ 0.10% Ni and 0.003% Co (indicated and inferred resource) (SRK Consulting 2022).

4 Discussion

Ni-Cu sulphide deposits occur in geological provinces of different ages in Sweden but most of them are of Paleoproterozoic age. Those related to mafic intrusions occur mainly in bedrock formed in arc settings, whereas those occurring in peridotite intrusions are more likely to have formed during events of extension. The genetic model for Ni-Cu sulphide deposits in general is well constrained and includes source of magma, metals, and sulphur, character of mineralization and ore forming processes (Barnes et al. 2016). The Ni-Cu sulphide

deposits in Sweden share most characteristics with typical magmatic Ni-Cu deposits worldwide, and the generally small size of the mafic hosted deposit is a characteristic feature of Ni-Cu sulphide deposits formed in arc environments.

The known deposits in Sweden could be divided into five different types based on character of host rock and origin of mineralization. Those are deposits related to peridotite sills, mafic dykes, mafic plutons, layered mafic intrusions and serpentinites. In general, the Ni/Cu ratio is related to magma composition with those related to peridotites having a Ni/Ni+Cu ratio less than 0.2, whereas those hosted by mafic rocks mostly vary from 0.3 to 0.5.

The first four types are generally located in areas including sulphide-bearing metasedimentary rocks suggesting external sulphur sources and silica contamination to be important to generate sulphur saturation. This is partly supported by sulphur isotope data and evidence of assimilated metasediments. However, only few of the deposits hosted by mafic intrusions are of typical marginal (or contact) type. Instead, massive and disseminated sulphides occur as irregular accumulations within the intrusions. Only the Lainijaur deposit which is related to a magmatic layered intrusion has massive ore accumulated at the lower contact and especially close to a feeder dyke containing disseminated sulphides. Deposits related to mafic dykes may be disseminated in character (Älgliden) or contain massive ore in the central part of the dyke (Slättberg). They are suggested to represent the roots of possible eroded marginal type deposit emplaced higher up in the crust.

Deposits related to peridotite sills are suggested to also be part of larger magmatic systems as the amount of Ni-Cu sulphide mineralization in these deposits is large in relation to the size of the intrusions. This is the case for most of the deposits occurring in the Nickel Belt in Västerbotten. These deposits are suggested to be related to larger magmatic systems where the main segregation of sulphides occurred deeper in the crust.

The Rönnbäcken deposit is different to traditional Ni-Cu sulphide deposits as it has a very low sulphide content and almost lacks pyrrhotite. During serpentinization low amounts of available sulphur occurring in accessory sulphides was combined with nickel released form olivine resulting in a low-grade dissemination of the Ni-rich sulphide heazlewoodite. Compared to traditional Ni-Cu sulphide deposits that are dominated by pyrrhotite and with pentlandite as main Ni-sulphide it is possible to generate a Ni-concentrate with much higher Ni-contents.

5 Conclusions

Several different types of Ni-Cu sulphide deposits have been discovered in Sweden during the last 150 years of exploration and several of them have also been mined in small scale. But the economic potential of the known Ni deposits is restricted as most deposits are small in size and/or low grade. However, as several of these deposits are suggested to be part of larger magmatic systems, further research and exploration could maybe result in more significant discoveries. The Nickelbelt in Västerbotten may be the most promising area but also mafic layered intrusions with more extensively developed contact-type mineralization could have potential. Deposits related to the serpentinization of peridotites/dunites have large tonnages but low grade. The low sulphide content makes these deposits interesting as tailings will cause less environmental problems and as they will generate Ni-concentrates with a very high Ni-content.

References

Arvanatides (1982) The geochemistry and petrogenesis of the Notträsk mafic intrusion, northern Sweden. PhD Thesis Stockholms Universitet Geological Institution.

Barnes SJ, Cruden AR, Arndt N, Saumur BM (2016) The mineral system approach applied to magmatic Ni-Cu-PGE sulphide deposits. Ore Gel Rev 76: 296–316. http://dx.doi.org/10.1016/j.oregeorev.2015.06.012

Bergman S, Kathol B (2018) Synthesis of the bedrock geology in southern Norrbotten County, northern Sweden. Swedish Geological Survey Rap Medd 144. ISSN 0349-2176 ISBN 978-91-7403-410-3.

Bejgarn T, Årebäck H, Weihed P, Nylander J (2011) Geology, petrology and alteration geochemistry of the Palaeoproterozoic intrusive hosted Älgträsk Au deposit, northern Sweden. Geol Soc Lond Spec Publ 350: 105–132.

Bjärnborg K, Schersten A, Söderlund U, Maier WD (2015) Geochronology and geochemical evidence for a magmatic arc setting for the Ni-Cu mineralized 1.79 Ga Kleva gabbro-diorite intrusive complex, southeast Sweden. GFF 137: 83–101. https://doi.org/10.1080/11035897.2015.1015265.

Cordier C, Coin K, Arndt NT, Cartigny P (2020) The Älgliden Ni-Cu deposit: magmatic sulfides in a subduction setting. Min Dep 55:1173–1196. https://doi.org/10.1007/s00126-019-00921-4

Filén B (2001) Swedish layered intrusions anomalous in PGE-Au. Swedish Geological Survey Res Papers C833 33-45.

Grip E (1961) Geology of the nickel deposit at Lainijaur in northern Sweden. Sveriges Geologiska Undersökning Ser C577.

Löfstrand G (1903) Slättberg och Kuså nickelgrufor. GFF 25:103–122 (in Swedish).

Martinsson E (1996) Geochemistry and petrogenesis of the Palaeoproterozoic nickel-copper bearing Lainijaur intrusion, northern Sweden. GFF 118:97–109. https://doi.org/10.1080/11035899609546234.

Nilsson G (1985) Nickel-copper deposits in Sweden. In: Papunen H, Gorbunov GI (eds) Nickel-copper deposits of the Baltic Shield and Scandinavian Caledonides. Geol Surv Finland Bull 333:313–362.

Persson G (1991) Rörmyrbergets nickelförekomst. Slutrapport etapp VIII. NSG unpublished report 91046 (in Swedish).

Ripa M, Kampmann TC, Hellström FA (2017) SIMS U-Pb zircon geochronology at the Kuså Ni-Cu deposit, sout-central Sweden. GFF 139: 233–240.. https://doi.org/10.1080/11035897.2017.1332096

SRK Consultying (2022) Preliminary economic assessment update for the Rönnbäcken nickel project, Sweden. Unpublished report SRK Consulting UK..

Zakrzewski MA (1988) Mineral parageneses of the sulfide ore-deposits of Bergslagen metallogenic province. 1. Ni-Cu of southern Sweden. Geol en Mijnbouw 67:357–362.

Post-volcanic modification of komatiite-associated nickel sulfide mineralization: A case study of the Cassini deposit, Yilgarn Craton

Helen B. McFarlane[1], Margaux Le Vaillant[1], Stephen J. Barnes[1], Si-Yu Hu[1]
[1]CSIRO Mineral Resources, Australia

Abstract. Representing the first study of the recent greenfields discovery, the Cassini nickel sulfide (NiS) deposit of the Archean Yilgarn Craton, this investigation used an innovative integration of geochemistry and structural geology to elucidate the post-volcanic modification of komatiite associated NiS mineralization. This approach commenced with a new lithological classification, derived from the company whole rock geochemical database, of the host komatiite sequences, basalt and alteration. This was coupled with structural logging to constrain the subsurface geometries of the primary magmatic features and to unravel subsequent overprinting regional Neoarchean deformation. Nickel tenor analysis revealed two possible magmatic flow channels. The earliest deformation generated overthrusts over the massive and net textured sulfides. Both the Cassini ore bodies and the basal contact were passively refolded during ENE-WSW deformation, with the best preservation of the classic mineralization profile associated with parasitic F_2 synclines on the western limb of the Widgiemooltha anticline. The F_2 axial trend is subparallel to the highest tenor channel, providing critical guidance for understanding modification of the primary channel morphology. Analysis revealed significant deformation but limited mechanical remobilization. Furthermore, the study has significant implications for improving prediction of magmatic NiS deposits in poly-deformed terranes.

1 Introduction

Komatiitic ultramafic lavas are a common feature of Archean greenstone belts around the world and are of notable economic significance due to their association with nickel sulfide (NiS) deposits (Lesher et al. 2002). They are characterized by magmas with MgO contents greater than 18 percent, and flow profiles defined by textural features including lower B-zone cumulates underlying spinifex textures of the A-zone and fine-grained flow tops (e.g., Barnes 2006). In an undeformed setting, these classic morphological features develop through the interaction of high flux, ultra-high temperature komatiitic magmas with sediment and hydrated seafloor basalt. Accumulation of a sulfide melt pool or channel at base of the lava tube is associated with the thermal erosion of the footwall basalt and the progressive development of characteristic open basal contacts and pinch out contacts (e.g., Staude et al. 2017).

To enhance exploration for these deposits, it is critical to understand the spatial distribution and morphology of volcanological features to delineate ore bodies within. Identification and prediction of these features is complicated by subsequent post-volcanic modification, however, may be achieved based on our proposed approach. Here we examine the structural history of the recently discovered, and thus far unstudied, Cassini NiS deposit (Mincor Resources) of the Yilgarn Craton in order to unravel the deformation overprint and better understand primary channel geometries and the distribution of economic NiS mineralization.

2 Geological Setting

The Cassini NiS deposit is located in the Kalgoorlie Terrane of the Eastern Goldfields Superterrane (EGST) of the Archean Yilgarn Craton, Western Australia (Cassidy et al. 2006).

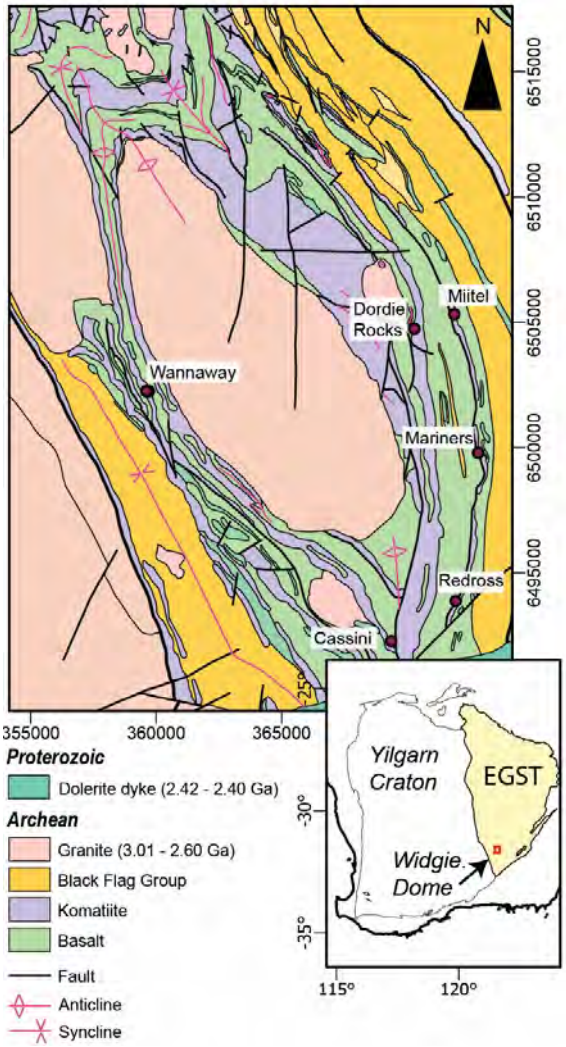

Figure 1. Simplified geological map of the Widgiemooltha Dome showing NiS deposits, including Cassini (modified from GSWA 2022). Inset shows Yilgarn Craton in Western Australia.

The craton comprises expansive granite-greenstone terranes with a dominant NNW-striking crustal architecture. Greenstone belts of the EGST comprise 2.72–2.69 Ga mafic-ultramafic igneous suites and overlying volcaniclastic and siliciclastic units of the Black Flag Group. Ultramafic units contain komatiite associated NiS deposits, including those within the archetypal Kambalda Dome (Barnes and Perring 2007). Approximately 45 km SSW of the Kambalda Dome, the Cassini deposit is located at the southern apex of the Widgiemooltha Dome and is hosted in the Mount Morgan Komatiite (Figure 1). Separated by the tholeiitic Mount Edwards Basalt, the overlying Widgiemooltha Komatiite is host to the Type-1 Wannaway, Mariners, Miitel and Redross deposits (McQueen 1981a; Lesher et al. 2002). Multiple phases of granitic plutonism accompanied polyphase deformation and metamorphism of the mafic-ultramafic rocks in both the Widgiemooltha and Kambalda domes (Witt et al. 2020; Seat et al. 2004; Stone et al. 2005). Peak metamorphic conditions for Widgiemooltha are estimated at ~600 ºC and 4 kbar (McQueen 1981b). Alteration at Cassini is dominated by talc-carbonate assemblages with relict serpentinization preserved in the southern areas. Metamorphic garnet is present in the footwall basalt in the core of the Widgiemooltha anticline.

3 Methodology

Whole rock geochemistry from the company assay database were reprocessed to determine rock types and zonation of the komatiitic flows. From this, a series of geochemical classification plots was generated using ioGas software. Volatile-free and sulfide-free normalisation of whole-rock analyses was performed for lithological classification and excludes rocks with >5% S (>approx. 15% sulfide), according to Barnes (2022). These were visualised in 3D to better constrain the geometries of the host komatiite prior to deformation.

Structural analysis included examination and measurement of magmatic and structural features preserved in oriented diamond drill core and evaluation of the current resource model. Structural investigation of host rock lithologies focussed on the intensity of metamorphism and deformation. Structural observations were integrated with new lithological classifications using the Leapfrog Geo software.

Mineralogical and microstructural analysis of key samples used both transmitted and reflected light microscopy and scanning electron microscope (SEM) analysis. Samples were scanned with an SEM equipped with TESCAN Integrated Mineral Analyser (TIMA) software to automatically generate mineralogy maps for each sample. The scanning electron beam current was approximately 8 nA and accelerating voltage was 25 KV with a dwell time of 125 ms yielding a resolution of 10–12 µm per pixel, with a working distance of 15.0 mm.

4 Geochemistry

Ultramafic rocks at the Cassini deposit are serpentinized, metamorphosed and variably talc-carbonate altered. As such, there is poor preservation of primary magmatic textures classically employed to determine the facies, zonation, and geometries of the primary komatiitic flows and the associated channel. Lithological classification and zonation within the komatiitic sequence (Figure 2) identified from geochemical data was based primarily on a combination of Mg# (molar MgO/(MgO+FeO)), Al_2O_3 and $Al2O_3/TiO_2$, with further information from other alteration-immobile element components including Cr, Zr, and Ti.

Two main komatiite categories were defined, based on MgO weight % (volatile-free), with a third lithology distinguished due to elevated Cr contents but lower MgO numbers than expected, which are interpreted as the result of alteration. Definitions include: komatiitic olivine cumulates (Kom cmlt) with MgO > 32.5%; komatiites flow margins and spinifex textured flows (Kom FT), comprising relatively olivine-poor components of komatiite flows, with

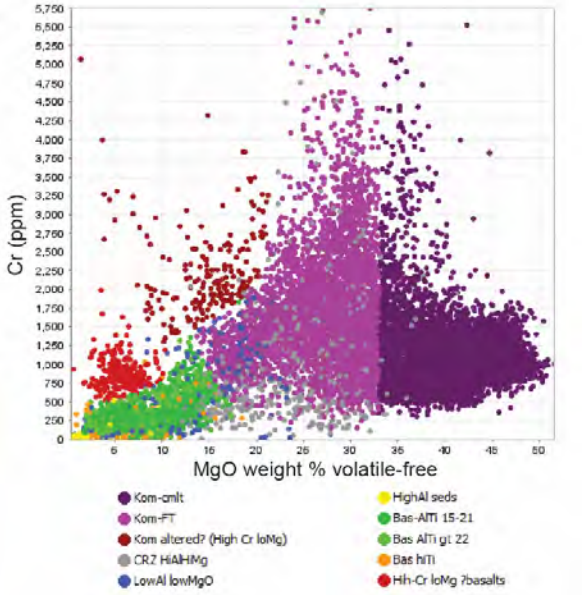

Figure 2. Lithological classification of company whole rock geochemical database showing lithology types grouped by MgO and (wt. %) and Cr concentrations (ppm).

MgO < 32.5%, but above ~ 15% MgO; and, altered komatiite (Kom alt) featuring high Cr but low MgO, likely due to MgO loss with alteration. Altered komatiite was frequently noted along structural trends. Various basalt lithologies were defined, which all have lower MgO contents than the komatiites (<15% MgO) and were divided in function of Al and Ti contents. Classification defined komatiitic basalt, high Al/Ti basalt and high Ti basalt. Nickel tenor (calculated composition in 100% sulfide) showed a wide range independent of the sulfide content in the rock, ranging from around 2.5%

to 20% in disseminated, matrix or net-textured and massive ores. The spatial disposition of these tenor variations in 3D space displayed two shoots with contrasting grade distribution.

5 Cassini mineralization

The current mineral resource of Cassini is 1.4 Mt at 4.0 % Ni for total Ni 58,200t (Mincor Resources 2022). Mineralization at Cassini is characterised as both Type-1, comprising massive sulfides resting on an open contact overlain by net texture and disseminated sulfides, and Type-5 (Lesher et al. 2002). Poor preservation of the classic mineralization profile is consistent with significant post-volcanic deformation. The deposit comprises numerous massive sulfide bodies at the contact between the Mount Morgan Komatiite and the footwall basalt, plunging moderately to the SE to SSE. The orebodies sit on the western limb pf the regional scale Widgiemooltha anticline. The ore assemblages predominantly comprise massive pyrrhotite (Po) and pentlandite (Pn). Few true pinch out structures related to thermal erosion by massive sulfides of the footwall basalt are noted. Localised mechanical remobilization is described below.

6 Structural framework

The structural framework revealed an early deformation event (D_1) associated with low angle shearing and the overthrusting of footwall basalt over disseminated, matrix or net-textured and massive sulfides along the basal contact of the Mount Morgan Komatiite. This creates features that mimic pinch outs. Both textural observations and analysis of new lithological classification from the geochemistry reveal localised overturning of portions of the komatiitic sequences. Evidence of larger scale thrusting and repletion of basalt units was inconclusive given the scale of the study and the available datasets. Massive nickel sulfide occurrences display strong deformation, and patchy development of a ductile Po-Pn S_1 foliation subparallel to magmatic contacts (Figure 3). The deformation event resulted in narrow high strain zones along lithological contacts, extensively overprinting primary textures and geometries, but limited evidence of remobilisation in the central ore zone.

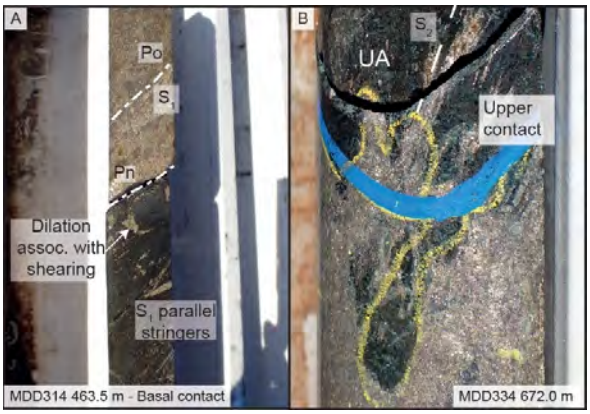

Figure 3. Representative ore textures from Cassini showing (a) Massive sulfides displaying foliation (S_1) parallel to the underlying weakly deformed basal contact containing minor stringer sulfides; and (b) localised mechanical remobilization of sulfides along the S_2 foliation plane, axial planar to the regional folding. UA = amphibole bearing metamorphosed ultramafic.

Rare F_1 folds plunge towards the ENE or SW, suggesting an approximate NNW-SSE shortening regime. The dominant architecture of the deposit is attributed to refolding of the ore body and D_1 low-angle structures by NNW-SSE trending, tight, F_2 folds, with a steeply ENE-dipping axial surface, associated with ENE-WSW D_2 shortening. The bulk of the massive sulfide ore as Cassini is seated in a parasitic F_2 synform on the western limb of the major anticlinal axial surface of the Widgiemooltha Dome. Both the Cassini ore bodies and F_2 folds are co-axial, plunging shallowly to moderately to the SSE, showing parallelism with the highest Ni tenors in the southern portion of the deposit. More intense deformation at Cassini North coincides with more intense deformation and mechanical remobilisation, reflected in associated with widespread Ni tenor distribution, extensive attenuation and dislocation of ore, analogous to the Wannaway N02 ore body (Seat et al., 2004).

These F_2 synforms represent the sites of the best preservation of massive sulfide ore. Mechanical sulfide remobilisation is noted along the S_2 plane (Figure 3b) but is spatially restricted to approximately 50cm above the contact or limited by overlying D_1 overthrusts. More extensive mechanical remobilization associated with shearing and attenuation along the fold limb is noted on the eastern limb of the anticline.

The eastern flank of the antiform is truncated by a high strain to mylonitic, steeply (> 70°) east dipping reverse fault that developed during ongoing E-W to ESE-WNW shortening, juxtaposing the host komatiites with highly altered, low MgO basalt, and altered B zone komatiitic rocks to the east. Both the antiform and reverse faults are gently refolded or displaced during the later minor deformation.

7 Conclusions

The results of this study highlight the control of post-volcanic, polyphase deformation on the subsurface

geometries of the Cassini orebody and the distribution of economic Ni mineralization, linked with the primary channel orientation, relative to the major structures. New geochemical classification of the volcanic facies of the host komatiitic sequence highlight lithological relationships and distribution following deformation. Furthermore, analysis of the distribution and disposition of Ni tenor reveals a high-grade channel in the south, a possible second low-grade channel. The most extensive deformation and sulfide remobilisation is documented in Cassini North. Coupled geochemical and structural analysis has the potential to address some of the significant challenges of defining the geometries of narrow, often geophysically blind, komatiite associated NiS deposits in poly-deformed terranes.

Acknowledgements

The project was co-funded by Mincor and the Australian Government Innovations Connections Program. Mincor Resources NL are thanked for their support, knowledge and enthusiasm during the course of this project.

References

Geological Survey of Western Australia (GSWA) (2022) 1:100 000 State interpreted bedrock geology of Western Australia, April 2022 update. Geological Survey of Western Australia, digital data layer, www.dmp.wa.gov.au/geoview.

Barnes SJ (2022) Lithogeochemistry in exploration for intrusion-hosted magmatic Ni-Cu-Co deposits. Geological Society of London. Collection. https://doi.org/10.6084/m9.figshare.c.6267664.v3

Barnes SJ (2006) Komatiites: Petrology, Volcanology, Metamorphism, and Geochemistry in Nickel Deposits of the Yilgarn Craton: Geology, Geochemistry, and Geophysics Applied to Exploration. Society of Economic Geologists Special Publication 13, pp. 13–49.

Barnes SJ (2006) Komatiite-hosted nickel sulfide deposits: Geology, geochemistry, and genesis. Society Of Economic Geologists, Special Publication 13, pp. 51-97.

Cassidy K, Champion D, Krapez B, Barley M, Brown S, Blewett R, Groenewald P, Tyler I (2006) A revised geological framework for the Yilgarn Craton, Western Australia. Geological Survey of Western Australia, Record 8:1-15.

Lesher C, Keays RR, Cabri L (2002) Komatiite-associated Ni-Cu-PGE deposits: Geology, mineralogy, geochemistry and genesis. Canadian Institute of Mining, Metallurgy and Petroleum 54:579-618.

McQueen K (1981a) Volcanic-associated nickel deposits from around the Widgiemooltha Dome, Western Australia. Economic Geology 76:1417-1443.

McQueen K (1981b) The nature and metamorphic history of the Wannaway nickel deposit, Western Australia. Economic Geology 76:1444-1468.

Mincor Resources NL (2022) Annual Shareholder Report 2022, ASX Announcement https://www.mincor.com.au/site/investor-centre/asx-announcements. Accessed 01 March 2023.

Seat Z, Stone W, Mapleson D, Daddow B (2004) Tenor variation within komatiite-associated nickel sulphide deposits: insights from the Wannaway Deposit, Widgiemooltha Dome, Western Australia. Mineralogy and Petrology 82:317-339.

Staude S, Barnes SJ, Le Vaillant M (2017) Thermomechanical erosion of ore-hosting embayments beneath komatiite lava channels: textural evidence from Kambalda, Western Australia. Ore Geology Reviews 90:446-464.

Stone WE, Beresford SW, Archibald NJ (2005) Structural setting and shape analysis of nickel sulfide shoots at the Kambalda dome, Western Australia: Implications for deformation and remobilization. Economic Geology 100:1441-1455.

Witt WK, Cassidy KF, Lu Y-J, Hagemann SG (2020) The tectonic setting and evolution of the 2.7 Ga Kalgoorlie–Kurnalpi Rift, a world-class Archean gold province. Mineralium Deposita 55:601-631.

Mineralogical study and structural controls of Co-Ni-Fe and Cu of F53 deposit in the Aït Ahmane area (Bou Azzer inlier, Anti-Atlas, Morocco).

Mohamed Ez-Zghoudy [1], Moha Ikenne [1], Mustapha Souhassou [2], Said Ilmen [3], Ilya R PROKOPYEV [4], Zaineb Hajjar [5], Mehdi Ousbih [1], Fatiha Askour [1], Lhou Maacha [6], Mohamed Zouhair [6]

1 LAGAG, Faculty of Sciences, Ibn Zohr University, BP. 8106, Cite Dakhla, Agadir, Morocco

2 EGERNE, Polydisciplinary Faculty of Taroudant, Ibn Zohr University, Agadir, Morocco

3 CAG2M, Polydisciplinary Faculty of Ouarzazate, Ibn Zohr University, BP. 638, 45000, Ouarzazate, Morocco

4 Sobolev Institute of Geology and Mineralogy, Siberian Branch of the Russian Academy of Sciences, 3 Academician Koptyug Ave, Novosibirsk 630090, Russia.

5 Laboratory of Geosciences, Water and Environment (L-G2E), Faculty of Sciences in Rabat, Mohammed V University in Rabat. 4 Avenue Ibn Battouta, B.P. 1014 RP, Rabat, Morocco.

6 MANAGEM Group, Twin Center, Casablanca, Morocco

Abstract. The Bou Azzer mining in the central part of the Anti-Atlas Belt in Morocco is one of the world's main producers of cobalt. The cobaltiferous mineralizations in Bou Azzer are spatially and genetically linked to serpentinized peridotites. Among these deposits is the F53 deposit in the Aït Ahmane area, which is located in the eastern part of the Bou Azzer inlier.

The F53 deposit shows two morphological types of mineralization. The EMPA analysis shows that massive contact mineralizations hosted in quartz-calcite lenses located in the N120° tectonic contact between serpentinized peridotites and quartz diorites is characterized by the presence of Ni and Co monoarsenides (nickeline, langisite, modderite), diarsenides of Co-Ni-Fe (safflorite, löllingite, and rammelsbergite), triarsenides of Co (skutterudite) and Co-Ni-Fe sulfoarsenides marked by a dominance of gersdorffite. The sulfides of Cu, Zn, and Pb are later than the Co-Ni-Fe arsenides.

The vein-type mineralizations hosted in quartz-carbonate veins oriented N00° to N40° intersect the quartz diorite. This mineralization is characterized by the absence of nickel minerals and the presence of Co-Fe diarsenides (safflorite and löllingite), Co triarsenides (skutterudite), and Co-Fe sulfoarsenides with the dominance of cobaltite. Late Cu, Pb, and Zn sulfides are less abundant in this case.

1 Introduction

The deposits of Bou Azzer are located in the Anti-Atlas about 90 km to the south-southeast of the Ouarzazate city in Morocco (Fig. 1A). The mineralization Co-Ni-As is spatially associated with extensive serpentinite bodies which resulted from the alteration of Neoproterozoic ophiolite sequences including peridotite protoliths (Leblanc, 1981). Many deposits and mineralized occurrences were identified along the axis of the inlier over a length of 45 km, from the Mechoui deposit at the western part to the Aït Ahmane eastward (Fig. 1B). These ore deposits are located on the edges or in the immediate vicinity of a wide band of serpentinized peridotites of Neo-proterozoic age.

The Aït Ahmane sector (Fig. 1B) is located, about 35 km from the Bou Azzer Mine, in the eastern part of the Bou Azzer inlier. This sector is characterized by an ophiolitic complex considered one of the oldest known worldwide. In the Aït Ahmane area, several Co–Ni-As-bearing veins are intimately related to the serpentinized peridotite massif (Fig. 1B). Among these mineralized veins, we identify the deposit of F53 which is located about 1.5 km in the south of Aït Ahmane village, and is located at the contact between the serpentinized peridotites massif and quartz diorites (Fig. 2).

The F53 deposit is well-known for its Co–Ni–As mineralizations that are identified in quartz-carbonate veins cutting the quartz diorite and serpentinites, and/or in the faulted contact between quartz diorite and serpentinites (Fig. 2).

Locally, the F53 deposit is formed by the following geological facies (Fig. 2):

- Serpentinized peridotites outcrop in the form of several N120° trending bands or lenses, (2 km wide and 8 km long) from Ightem to Ait Abdellah villages. They are easily recognizable in the field with their visible minerals composed of asbestos-chrysotile, ghosts of pyroxenes, crystals or stringers of magnetite, chromite (Admou et al., 2013).
- Ultramafic cumulates are characterized by a gray color and are essentially magnesian with very large crystals often well-preserved. These cumulates are more or less serpentinized. These are composed mainly of dunites, pyroxenites, wehrlites and sometimes gabbros.
- Isotropic gabbros and microgabbros are outcrop either as isolated intrusions or form the host of the vein complex. Sometimes, they gradually pass to microgabbros and diabases and are more abundant than sheeted gabbros (Admou et al., 2013).

- Quartz diorite: This plutonic intrusion is rich in quartz with a gray to gray-green tint with amphibole, biotite and plagioclase (Admou et al., 2013). This massif outcrops to the south of Aït Ahmane and cutted by dense swarm of quartz-carbonate veins and lenticular quartz veins, which are isolated or in bundles (Fig. 2). Its contact with the serpentinite massif is generally faulted and frequently interspersed with lenses of listvenites and/or quartz and calcite.

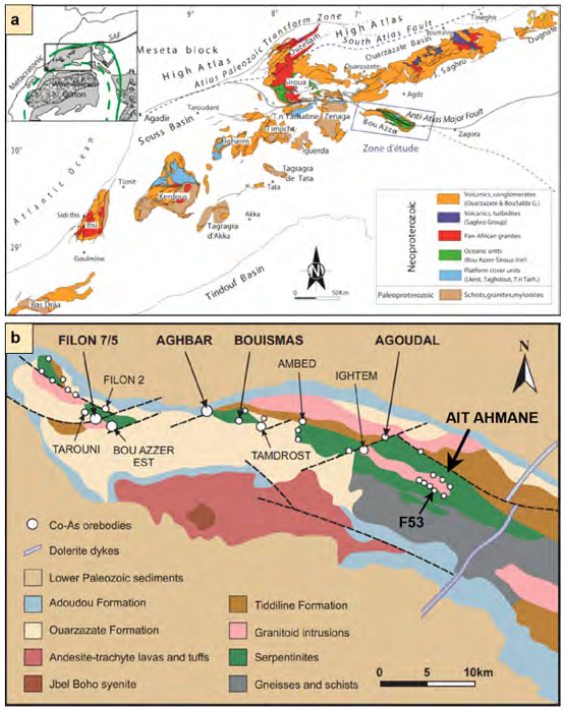

Fig. 1. A: Geological map of the Anti-Atlas mountain showing the position of the Bou Azzer inlier. B: Generalized geological map of the Bou Azzer inlier showing the distribution of the main cobalt-arsenide orebodies in relation to the serpentinized peridotites massifs; the size of the circles is roughly proportional to the size of the orebodies and showing the location of F53 deposit in Aït Ahmane area.

2 Methodology

Field work and sampling of the F53 deposit were undertaken in 2019 and these samples cover the whole mineralogical diversity of the veins. Selected samples were studied by optical microscopy in reflected and transmitted light using an Olympus BX60 polarizing microscope equipped with a Nikon digital camera DXM1200 system. The chemical composition of ore minerals was determined by EMPA using a JEOL JXA8200 electron microprobe equipped with five wavelength dispersive spectrometers (WDS) at the Eugen Stumpfl electron microprobe laboratory of the Siberian Branch of the Russian Academy of Sciences (Novosibirsk, Russia). The mapping and digital collection of geological data and structural measurements in the field was done mainly using the ArcPad 10.2 mobile application and the data processing was done by Win-Tensor software. We use the Win-Tensor software (5.9.2 version) for the structural analysis and paleo stress reconstruction.

3 Results

3. 1 Structural control of mineralization in the F53 deposit

Based on the study of Ez-zghoudy et al., 2023 in the F53 deposit of Aït Ahmane, the mineralization is controlled by two main types of faults. The first family of faults WNW-ESE which is represented by major overlapping faults generally oriented N110° to N120° (WNW-ESE) formed during the Pan-African compressive phase characterized by a maximum compressive stress σ1 horizontal oriented N30°to N40° (Fig. 2).

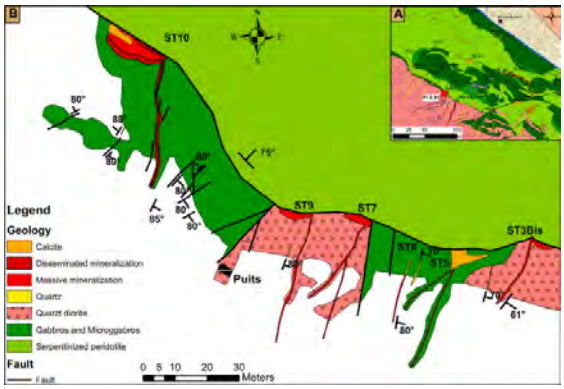

Fig. 2. Geological survey in the underground level − 280 showing the different mineralized veins of the F53 deposit of Aït Ahmane (Ez-Zghoudy et al., 2023).

This family of overlapping faults with a sinistral strike-slip oriented N110° to N120° generally controls the mineralized bodies (contact mineralization) rich in Co–Ni–Fe arsenides in the form of lenses located along the tectonic faults between serpentinized peridotites and quartz diorite or gabbros (Fig. 2). The second family of faults corresponds to tension gashes and normal fault oriented N00° to N40° previously formed and reactivated in sinistral reverse faults oriented N00° to N40° during the NW-SE Hercynian compressional phase (Fig. 2). These faults with quartz-carbonate fillings oriented N00° to N40° with an average dip of 75° to the east intersect the quartz diorite.

3. 2 Mineralogical study of Co-Ni-Fe arsenides and sulfoarsenide

The mineralogical studies of Co-Ni-Fe arsenides and sulfoarsenide by EPMA show that the mineralization of the F53 deposit is mainly composed by:

- Monorsenides: are represented by nickeline which is obviously identified in the contact type of ores as a dendrite in inclusions in the skutterudite, the second mineral is langisite observed in the contact type ore associated with rammelsbergite and gersdorffite. The last is modderite found in inclusions in safflorite.
- Diarsenides (Fig. 3) are composed of the safflorite observed only in the contact type of ore as isolated rosettes surrended by gersdorffite rims, the löllingite occurs in the contact type ore as zoned fibroradial clusters or associated to arsenopyrite grains, the rammelsbergite is observed only in the contact type ore, occurring as inclusions in gersdorffite or embedded in large skutterudite crystals.

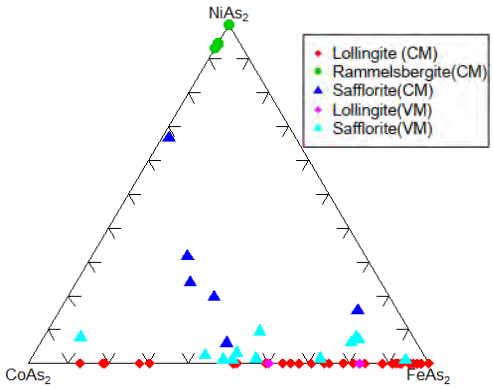

Fig. 3. $CoAs_2$-$FeAs_2$-$NiAs_2$ triangular plot (apfu) showing the variation of the chemical and mineralogical composition of diarsenides between the contact mineralization (CM) and vein mineralization (VM) of the F53 deposit.

- Triarsenides: EPMA analysis of triarsenides shows the presence of three skutterudite generation in F53 deposit from Aït Ahmane area. The first generation is the Ni-skutterudite (Skutterudite I) identified in the contact ore type; occurring as zoned crystals and in contact with gersdorffite. The second generation is Co-skutterudite (Skutterudite II), observed as a massive beach and more often as isolated cubic crystals in the quartz-carbonate gangue. The third generation is the relatively Fe-skutterudite (Skutterudite III) contains gold inclusions.
- Sulfoarsenide minerals (Fig. 4) are represented by gersdorffite identified only in the contact type ore. cobaltite is more abundant in the mineralized veins. the arsenopyrite occurs frequently at the edges of löllingite concretions and sometimes as prismatic crystals isolated in the gangue. the alloclasite was observed just in the contact mineralization adjacent to the edges of the nickeline and gersdorffite. the glaucodot isolated automorphic crystals in the quartz-carbonate gangue and westerveldite are observed as isolated automorphic crystals in the gangue and in association with skutterudite and sometimes as inclusions in cobaltite.

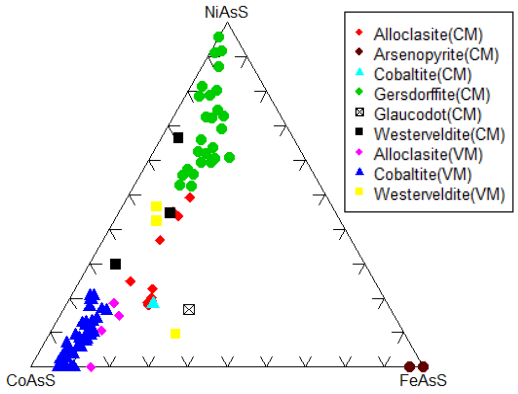

Fig. 4. CoAsS-FeAsS-NiAsS triangular plot (apfu) showing the variation of the chemical and mineralogical composition of sulfoarsenides between the contact mineralization (CM) and vein mineralization (VM) of the F53 deposit.

- Sulphides containing chalcopyrite fill the fractures in the arsenide ore and cavities in the quartz-carbonate gangue. Bornite was observed as filling of fractures through the arsenides. The covellite is included in chalcopyrite. Djurleite occurs as a microcrack filler in Co arsenide minerals. Roxbyite filling microcracks in Co arsenide minerals. Sphalerite constitutes the filling of the voids of the interstices and the microcracks in the skutterudite. Wurtzite occurs as a cavity and fissure filler in Co-Ni-Fe arsenide minerals. Molybdenite [MoS2], occurs in disseminated form in the gangue.
- Native bismuth [Bi] corresponds to the native element identified in the contact mineralization, it is observed either in inclusion in the löllingite or in association with nickeline, embedded in patches of the bornite.

4 Conclusion

The F53 deposit presents two morphological types of mineralization formed in different tectonic regimes and shows variable chemical and mineralogical compositions. The first is the

contact mineralization hosted in the N120° tectonic contact between the serpentinized peridotites and the quartz diorite. The analysis by EMPA show that this type is characterized by the presence of Ni-rich monoarsenide (Nickeline and langisite), diarsenides (Ni-safflorite, Co-löllingite, Fe-löllingite and rammelsbergite), the abundance of triarsenides rich in Ni, Co and Fe (Skutterudite I, skutterudite II and skutterudite III) and sulfoarsenide with Ni, Co and Fe (Gersdorffite, arsenopyrite, cobaltite, alloclasite, westerveldite and glaucodot), it is noted that cobaltite is very rare in this case, the presence of native elements (Bismuth) and sulfides of Cu, Zn, Pb and Mo filling voids and microcracks affecting Co-Ni-Fe arsenides and quartz-carbonate gangue. The second type is vein mineralization in the form of mineralized quartz-carbonate veins oriented N00° to N40° intersecting quartz diorite. The analysis by EMPA on the samples taken from the vein mineralization showed the absence of Ni-rich arsenides (Nickeline, langisite, rammelsbergite and gersdorffite) and also Fe sulfoarsenides (Arsenopyrite) and the presence of diarsenides poor in Ni and rich in Co and Fe (Co-safflorite, Fe-safflorite and Fe-löllingite), triarsenides low in Ni (Skutterudite II and Skutterudite III) and sulfoarsenides rich in Co and poor in Ni and Fe (Cobaltite, alloclasite, westerveldite) with the abundance of cobaltite, The sulfides of Cu, Zn, Pb are less abundant with the absence of molybdenite and native elements (Bismuth).

Acknowledgments

This study is part of Ph.D thesis of the first author (ME). Managem group is very thankful for their support and logistics during field work. The team of laboratory of the Siberian Branch of the Russian Academy of Sciences (Novosibirsk, Russia) for EMPA analysis.

References

Admou, H., Razin, P., Egal, E., Youbi, N., Soulaimani, A., Blein, O., Chèvremont, P., Gasquet, D., Barbanson, L., Bouabdelli, M., Anzar, C., 2013. Notice explicative de la Carte géologiques du Maroc (1/50 000), feuille Aït Ahmane. Notes Mém. Serv. Géol. Maroc.

Ez-Zghoudy, M., Ikenne, M., Souhassou, M., Alaeddine Belfoul, M., Gouiza, M., Ilmen, S., Ousbih, M., Karfal, A., Maacha, L., Zouhair, M., 2023. Structural controls on the Co and Ni-bearing arsenides from the Bou Azzer mine (Case of Aït Ahmane F53 vein deposit): Implications for mineral exploration. Journal of African Earth Sciences.

Leblanc, M., 1981. Ophiolites précambriennes et gîtes arséniés de cobalt (Bou Azzer, Maroc). Notes et mém. Serv. Géol. Maroc. 280, 311p. Leblanc, M., Billaud, P., 1982. Cobalt arsenide orebodies related to an upper Proterozoic ophiolite: Bou Azzer (Morocco). Econ. Geol. 77, 162–175. https://doi.org/10.2113/gsecongeo.77.1.162.

Maacha, L., 2013. Etudes Métallogéniques Et Géophysiques des Minéralisations Cobaltifères et Cuprifères de Bou-Azzer El Graara Anti-Atlas Maroc : Les Minéralisations de Cuivre de la Plateforme de Bleida. UNIVERSITE CADDI AYYAD FACULTE DES SCIENCES SEMLALIA- MARRAKECH, Maroc.

Mineralogical distribution of platinum-group elements (PGE) in the UG2 and Merensky Reefs at the Kalkfontein farm, Bushveld Igneous Complex

Anastasia M Nailana[1], Napoleon Q Hammond[1]
[1]University of Limpopo, Department of Geology and Mining, South Africa

Abstract. A study on the UG2 and Merensky Reefs at Kalkfontein farm located in the southern sector of the Eastern Limb of the Bushveld Igneous Complex, was undertaken to investigate the platinum-group elements (PGE) mineralogical characteristics, variation and distribution in these reefs. The distribution of the total platinum group minerals (PGM) in the UG2 show the following modal proportions, PGE sulphides (60%), PGE arsenides (13%), PGE alloys (10%), PGE sulphoarsenides (9%) and PGE bismuthotellurides (8%), while in the Merensky, PGE sulphides account for about 33% of the total PGM, PGE bismuthotellurides forms about 30%, PGE arsenides form 18%, PGE sulphoarsenides 10%, and PGE alloys, 6%. The PGM show close association with various mineral phases in both the UG2 and the Merensky. The base metal sulphides, which are dominated by pentlandite and chalcopyrite, show much closer association with the PGM in the UG2 than in the Merensky. The grain size of the PGM measured as equivalent circle diameter (ECD) vary from 0.73 to 32 µm and 0.87 µm to 27 µm in diameter in the UG2 and Merensky Reefs, respectively. Generally, more than 80% of the PGM are less than 10 µm in both the UG2 and Merensky.

1 Introduction

The platinum group minerals (PGM) are a diverse group of minerals that concentrate the platinum-group elements (PGE; Os, Ir, Ru, Rh, Pt, and Pd), and the mineralization is associated with mafic-ultramafic intrusions. The Bushveld Igneous Complex in South Africa hosts the world's largest resources of PGE. They are mostly mined from the Merensky Reef, UG2 Reef and Platreef ore deposits. They are situated in the complex's Rustenburg Layered Suite (RLS). The mineralogical and related metallurgical processing characteristics of Bushveld ores in the UG2 and Merensky Reefs has attracted many studies for some time now (e.g., Penberthy et al. 2000; Chetty et al. 2009) with an ultimate goal to provide vital information that can be used to improve the recovery of the PGE from the ore during beneficiation. This study investigated the PGE mineralogical variation and distribution in the Upper Group 2 (UG2) and the Merensky Reefs at the Kalkfontein farm, at the Two Rivers Platinum (TRP) Mine in the southern sector of Eastern Limb of the Bushveld Igneous Complex (Fig. 1), by determining the modal distribution of the PGM phases, their mineral association and their grain size distribution.

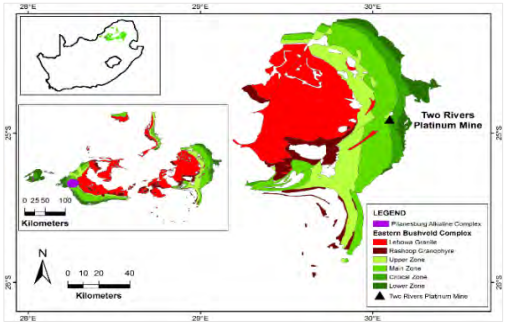

Figure 1. Simplified geological map of the Bushveld Igneous Complex with location of Two Rivers Platinum Mine indicated with a black triangle on the map.

1.2 Geology of the study area

Both the UG2 and Merensky Reefs are present in Kalkfontein farm. Three UG2 Reef facies are defined at the farm at the mine, namely, the UG2 Normal Reef, UG2 Split Reef and the UG2 Multiple Split Reef. The UG2 Normal Reef is approximately 1.5 m to 2 m thick and is characterized by a thick main chromitite layer (approximately 1.2 m thick). The UG2 Split Reef is approximately 2 m to 2.5 m thick, comprising of up to 2 m thick of main chromitite layer but separated into two by an internal pyroxenite/norite. The UG2 Multiple Split Reef is approximately 4.5 to 5 m thick and is characterized by main chromitite layer (2.5 m thick) and separated into three or more by internal pyroxenite/norite (McLaren and De Villiers 1982). In all the facies types, the main chromitite layers are underlain by pegmatoidal feldspathic pyroxenite and overlain by feldspathic pyroxenite.

2 Methodology

Six boreholes from in the Kalkfontein farm were logged and sampled for the study, samples were taken from two UG2 Normal Reef (BH 8206 and KFN 008), one UG2 Split Reef (KFN 014), one UG2 Multiple Split Reef (BH 8026) and two Merensky Reef (KFN 043 and BH 8026). Fifty-four polished blocks prepared from selected samples were analysed using A FEI600F field emission Mineral Liberation Analyser PGM characterization. Sixteen polished blocks selected from high PGE grade areas correlated with the assay data were analyzed for the PGM chemical composition using electron probe micro-analyses.

3 Results and discussion

3.1 Petrography and PGM characterization

Base metal sulphides (BMS) are uncommon in the UG2 samples, however when present, they occur as inclusions in silicates and chromite, or interstitial to the chromite grains and between chromite and silicates grain boundaries (Fig. 2a and b). In general, the BMS in the UG2 Reef are fine to medium grained with subhedral to anhedral morphology. The BMS in the UG2 and Merensky Reefs includes pentlandite, chalcopyrite, pyrrhotite, pyrite, millerite and galena. However, pentlandite and chalcopyrite are the most dominant in the UG2 Reef, while chalcopyrite, pentlandite and pyrrhotite dominate in the Merensky Reef. Cumulus chromite grains makes up about 60% of the total volume in the UG2 Reef, with silicates and BMS accounting for the balance. In the Merensky Reef, silicate minerals comprise 80% by volume with the remainder being BMS. Chromite grains occur in lesser extent in the reef and exhibit anhedral to subhedral morphology. The chromite grains are irregularly fractured with PGM filled within the fractures in some cases (Fig. 2a).

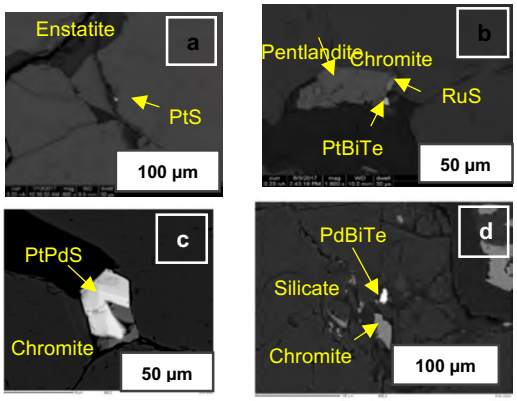

Figure 2. Backscattered electron images of PGM textural association in UG2 and Merensky Reefs. **a.** PtS within chromite fracture (from UG2 Reef). **b.** RuS_2 and PtBiTe associated with pentlandite (from UG2 Reef). **c.** Subhedral PtPdS interstitial to chromite (from the UG2 Reef). **d.** PdBiTe inclusion in silicate (from the Merensky Reef).

The PGM identified in the UG2 share grain boundaries with silicates, chromite and BMS (Fig. 2a, b and c) and in the Merensky PGM occur as silicates inclusions (Fig. 2d). The PGM occur in euhedral to anhedral shape and rounded to sub rounded shapes. Following Bachmann et al. (2018), the PGM in the UG2 and Merensky Reefs were grouped into PGE sulphides, PGE arsenides, PGE sulphoarsenides, PGE bismuthotellurides and PGE alloys. In the UG2, PGE sulphides accounted for nearly 60% of the total PGM grains (2480) counted, followed by PGE sulphoarsenides 13%, PGE alloys 10%, PGE arsenides 9%, and PGE bismuthotellurides 8% (Fig. 3a). In the Merensky Reef, PGE sulphides constitute about 34% of the total PGM grains (692) counted, followed by PGE bismuthotellurides at 31%, PGE arsenides 22%, PGE sulphoarsenides 7% and PGE alloys forming 6% (Fig. 3b). VIn the UG2, the PGE sulphides is dominated by cooperite (PtS, PtPdS), ranging from 50 to 75 % of the total PGE-sulphides, followed by laurite (RuS_2), forming about 16 to 40% of the total PGE sulphides. The PGE sulphoarsenides show a range between the hollingworthite (RhAsS)-irarsite (IrAsS)-platarite (PtAsS) solid-solutions, and sperrylite ($PtAs_2$), dominating the PGE arsenides. The PGE bismuthotellurides is dominated by michenerite (PdBiTe), ranging from 57 to 80% of the total grains followed by maslovite (PtBiTe). The PGE alloys is highly variable in composition. Like in the UG2, PGE sulphides in the Merensky Reef is dominated by cooperite (PtS) and braggite PtPdS), which together constitute between 71 to 80% of the total PGE sulphides. The PGE arsenide occur mostly as sperrylite, while the PGE sulphoarsenides form a PtAsS-PtRhAsS-PtPdAsS solid-solution series. The PGE bismuthotellurides occur as maslovite (PtBiTe) and michenerite (PdBiTe), and an intermediary PtPdBiTe, in almost equal proportions.

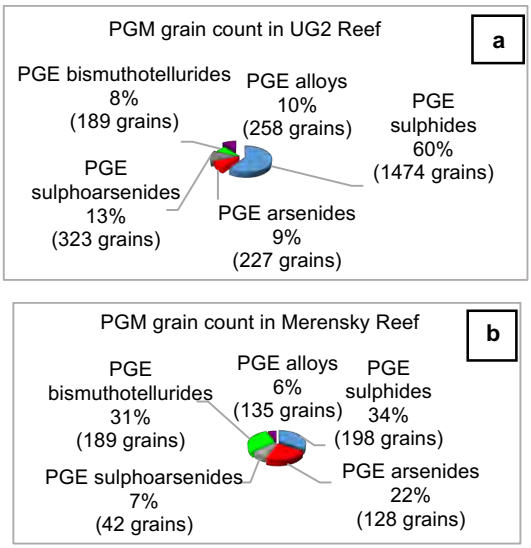

Figure 3. a. PGM grain count distribution in the UG2 Reef. **b.** PGM grain count distribution in the Merensky Reef.

3.2 PGM grain size distribution

The grain size of the PGM range from 0.73 to 32 µm and 0.87 µm to 27 µm in diameter in the UG2, Reef and Merensky Reef (equivalent circle diameter), respectively. The grain size distributions of the PGM in KFN 008 and KFN 014 are similar, where approximately, 97 wt. % of the grains passing through 19 µm, and approximately 70 wt. % passing 15 µm. Similarly, the cumulative grain size distribution in BH 8206 and BH 8026 also exhibit similar trend, with approximately 97 wt. % passing 19 µm, while approximately 50 wt. % 16 µm and 15 µm in BH 8206 and BH 8026, respectively (Fig. 4a). The cumulative grain size

distribution of the PGM in the Merensky Reef are slightly heterogeneous. Particularly, in the sieve size between 10 µm and 18 µm. The PGM in KFN 043 are much finner than the PGM in BH 8026. In KFN 043 the grain size of 30 wt. % passed 10 µm, while in BH 8026, less than 10 wt. % of PGM grain size passed 10 µm (Fig. 4b).

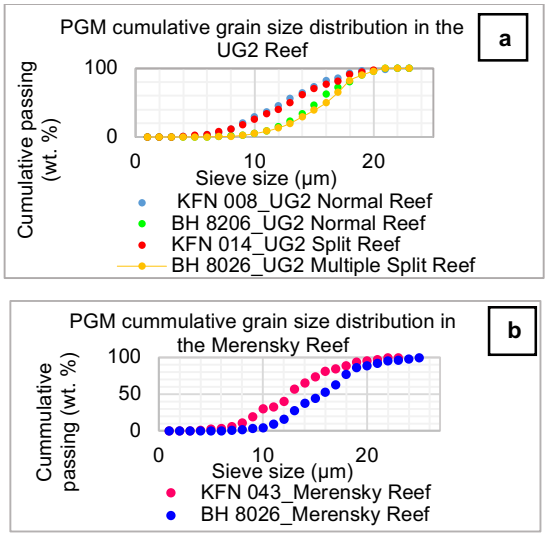

Figure 4. a. PGM cummulative grain size distribution in the UG2 Reef. **b.** PGM cumulative grain size distribution in the Merensky Reef.

3.3 PGM mineral association

The PGM mineral association is illustrated in Fig. 5 and shows mineral association with base metal sulphides, primary silicates, secondary silicates and oxides. Common minerals associated with the PGM in the UG2 are BMS, which are dominated by chalcopyrite, pentlandite and pyrrhotite, constitute a range between 35 to 65 area % of the total minerals associated with the PGM. However, chalcopyrite and pentlandite constitute over 80 area % of the base metal sulphides. Primary silicates indicate a range between 10 and 30 area % of the total mineral associated with the PGM, while secondary silicates constituting about 8 % of the total mineral association. In the Merensky Reef, primary silicates accounted for most of the minerals associated with the PGM. This is followed by base metal sulphides in a range from 20 to 32 area %, secondary silicates (14%) oxides (3%) which includes chromite.

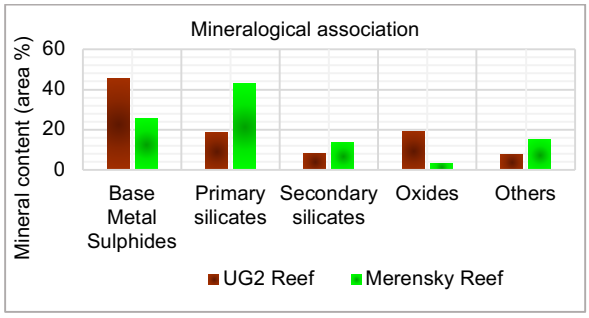

Figure 5. The minerals associated with the PGM in the UG2 Reef and in the Merensky Reef.

4 Conclusion

Magmatic Ni–Cu–PGE sulphide deposits form by segregation of immiscible droplets of dense sulphide melt from mafic to ultramafic magmas, where the PGE partition strongly into the sulphide melt S-saturation of the basaltic melts when emplaced in the crust, with the PGE having experimentally determined partition coefficients estimated between 1400–36000 (Barnes and Lightfoot 2005). Several theories have been proposed for the PGE mineralization in the UG2 and Merensky Reefs in the Bushveld Igneous Complex to explain their origin. For example, supersaturation of sulphides in the UG2 Reef may have been due to contamination or chromite precipitation (Naldrett and von Gruenewaldt 1989). Barnes and Maier (1999) proposed that the PGE supersaturation in the reef might have formed by sulphides solubility and ultimately sulphides immiscibility, which can be obtained by fractional crystallization of the magma as the temperature decreases, a reduction in the quantity of ferrous iron, or by mixing two compositionally distinct magmas. The Merensky Reef is thought to have formed from a magma pulse that contained entrained sulphides (Lee and Butcher 1990), hence the elevated sulphides content. Seabrooke et al. (2006) proposed that the Merensky Reef overall PGE concentration was the result of two independent mineralizing episodes, one linked to the creation of the chromitite layer and the other to sulphide mineralization. Other theories have documented that PGE enrichment is attributed to post-magmatic fluids (Ballhaus and Stumpfl 1986).

Although there are local variations in lithologies and mineralogy in the PGE-bearing reefs in the Bushveld Igneous Complex, the results from the study are consistent with general observation by several workers (e.g., Penberthy et al. 2000; Rose 2016) in the Eastern Bushveld Igneous Complex. The PGM show marked association with base metal sulfides (BMS). Approximately, 60% of the PGM in the UG2 Reef will be recovered considering that they occur as PGE sulphides, which have the fastest floating rates, while about 34% of the PGM will be recovered in the Merensky Reef under similar conditions. The PGM have significantly smaller average grain sizes of 7 and 10 µm for the UG2 and Merensky Reefs, respectively, and for optimum PGM recovery the ore needs to be milled to grain sizes of up to less than 3 µm. The PGM in UG2 Reef are mostly associated with base metal sulphides, and about 46% of PGM in the UG2 Reef are most likely to be recovered due to their association with the BMS which are naturally floatable. The secondary silicates minerals are more abundant in the Merensky Reef, and this may lead to poor recoveries. Therefore, longer flotation times would be required to increase

the flotation effectiveness. The marked association of PGE tellurides, arsenides and PGE alloys and secondary silicates, is consistent with the remobilisation and recrystallisation of some of the PGM during hydrothermal alteration subsequent to their initial primary crystallization.

Acknowledgements

National Research Foundation are thanked for funding the project from 2021 to 2022.

References

Bachmann K, Osbahr I, Tolosana-Delgado R, Chetty D, Gutzmer J (2018) Variation in platinum group mineral and base metal sulfide assemblages in the Lower Group chromitites of the western Bushveld Complex, South Africa. The Canadian Mineralogist 56(5):723-743

Ballhaus CG, Stumpfl EF (1986) Sulfide and platinum mineralization in the Merensky Reef: evidence from hydrous silicates and fluid inclusions. Contributions to Mineralogy and Petrology 94(2):193-204

Barnes SJ, Maier WD (1999) The fractionation of Ni, Cu and the noble metals in silicate and sulphide liquids. Short Course Notes-Geological Association of Canada 13:69-106

Barnes SJ, Lightfoot PC (2005) Formation of magmatic nickel sulfide deposits and processes affecting their copper and platinum group element contents. Int J Miner Process Int J Miner Process 93:246–255

Chetty D, Gryffenberg L, Lekgetho TB, Molebale IJ (2009) Automated SEM study of PGM distribution across a UG2 flotation concentrate bank: implications for understanding PGM floatability. J S Afr I Min Metall 109:587–593

Lee CA, Butcher AR (1990) Cyclicity in the Sr isotope stratigraphy through the Merensky and Bastard Reef units, Atok section, eastern Bushveld Complex. Economic Geology 85(4):877-883

Maier WD (2005) Platinum-group element (PGE) deposits and occurrences: Mineralization styles, genetic concepts, and exploration criteria. Journal of African Earth Sciences 41(3):165-191

McLaren CH, De Villiers JPR (1982) The platinum-group chemistry and mineralogy of the UG-2 chromitite layer of the Bushveld complex. Economic Geology 77(6):1348-1366

Penberthy CJ, Oosthuyzen EJ, Merkle RKW (2000) The recovery of platinum-group elements from the UG-2 chromitite, Bushveld Complex – a mineralogical perspective. Miner Petrol 68:213-222

Rose DH (2016) A process mineralogical investigation of the Merensky Reef and UG-2 at the Two Rivers Platinum mine with emphasis on ore characterization. University of Johannesburg (South Africa)

Seabrook CL, Cawthorn RG, Kruger FJ (2006) The Merensky Reef, Bushveld Complex: Mixing of Minerals Not Mixing of Magma. Economic Geology 100:1191-1206

Mineralogical constraints and evidence for crustal interaction in the Ni-rich systems of the Curaçá Valley mineral district, Bahia, Brazil.

Tercio Nunes[1], Gema Olivo[1], John Thompson[2], Filipe Porto[2]; Anderson Lima[2]; Pablo Graia[2] *[1]Department of Geological Science and Geological Engineering, Queen's University, Kingston, ON, Canada[2]Ero Copper corp., Vancouver, BC, Canada*

Abstract. The Curaçá Valley district is well-known for Cu sulfide mineralization in Proterozoic mafic-ultramafic intrusions with unusually high Cu:Ni ratios. Despite the overall predominance of chalcopyrite-bornite-rich mineralization in mafic-ultramafic intrusions, Ni-rich mineralized zones have been identified within the Vermelhos and Umburana sulfide systems. The Vermelhos system is associated to chalcopyrite-pyrrhotite-pentlandite mineralization predominantly hosted in orthopyroxenite, norite and gabbro-norite, with abundant phlogopite-spinel (+/- apatite-monazite and tellurides). The Umburana system is characterized by pyrrhotite- pentlandite-pyrite mainly hosted in hornblende-websteriteunits, which are overlain by orthopyroxenite with low-grademineralization. Both systems exhibit evidence of complex interactions with wall-rocks, including abundant country- rock xenoliths surrounded by reaction margins (e.g., phlogopite-rich rims). "Pegmatoidal" bodies are common at the contacts between the mafic-ultramafic intrusions and gneisses, and are interpreted as partial melts of country rocks during intrusion emplacement. The interaction of the mafic-ultramafic magmas with country rocks, including S-bearing gneisses, could have played an important role in forming the Ni-Cu sulfide mineralization associated with phlogopite-spinel-telluride-apatite-monazite. The mineralization in the Umburana system may represent crystallization from monosulfide solid solution (MSS), whereas Vermelhos was dominated by fractionated intermediate solid solution (ISS), overprinted by hydrothermal alteration.

1 Introduction

The mafic-ultramafic intrusions in the Curaçá Valley mineral district were emplaced in the highly metamorphosed terrains of the Paleoproterozoic Itabuna-Salvador-Curaçá belt, within the northern part of the São Francisco craton, Brazil (Oliveira et al 2004). These mafic-ultramafic intrusions host abundant Cu-mineralization (Figure 1), making the district the second largest Cu-producer in Brazil (Ero-Copper 2022a).

The mineralized zones are mainly characterized by chalcopyrite-bornite rich breccias hosted in orthopyroxenite and norite, containing abundant phlogopite-spinel, with local apatite-monazite and zircon (Maier and Barnes 1999; Teixeira et al. 2010). Within the Curaçá Valley's deposits, the Vermelhos and Umburana's systems host the highest Ni contents but display different Cu:Ni ratios and distinct host rock characteristics (Ero-Copper 2019, 2022b). The processes by which these systems were formed are still controversial, and little is known about the relationship between the Cu-rich and Ni-rich mineralization.

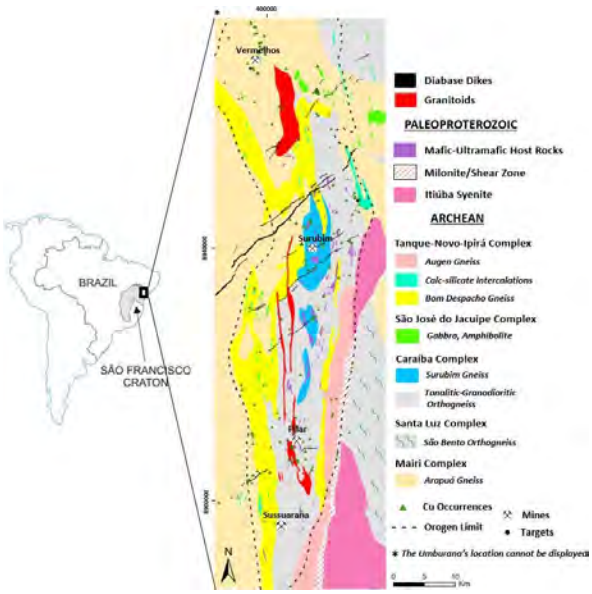

Figure 1. Geological map of the Curaçá Valley district, exhibiting the main Cu mines, occurrences, and mafic-ultramafic hosting intrusions.

2 Ni-rich mineralized systems

2.1 The Vermelhos system

Vermelhos has Cu:Ni values ranging from 6 to 40 in mineralized mafic-ultramafic rocks (Ero-Copper 2019). The Ni-rich zones are characterized by chalcopyrite(+/-bornite)-pyrrhotite-pentlandite in breccias with high content of phlogopite, various spinels and minor apatite (+/-monazite). PGE- bearing tellurides and electrum occur locally in the mineralized zones. The host rocks includeorthopyroxenite, norite, gabbro-norite with minor clinopyroxenite and websterite units.

The magmatic phases associated to the host rocks include (in different proportions) orthopyroxene, clinopyroxene, plagioclase, phlogopite, apatite, monazite and various types of spinels (some enriched in Al and Zn; Nunes et al. 2022). The earlymagmatic sulfides include pyrrhotite, pentlandite and minor Ni-tellurides. Chalcopyrite, several precious metals tellurides (including PGMs) and electrum, mostly occur filling corroded zones and fractures in the magmatic silicates, some Cr-spinels and pyrrhotite-pentlandite (Figure 2). Chalcopyrite is rarely seen in sharp contact with pyrrhotite- pentlandite. Chlorite, K-mica, epidote, carbonate,

serpentine, talc, and violarite replaced the early phases, which were also cut by late magnetite veins. Age-dating based on microprobe data (Suzuki and Adachi 1994) of monazite in the Ni-rich zones, confirmed late-overprinting of the mineralized system.

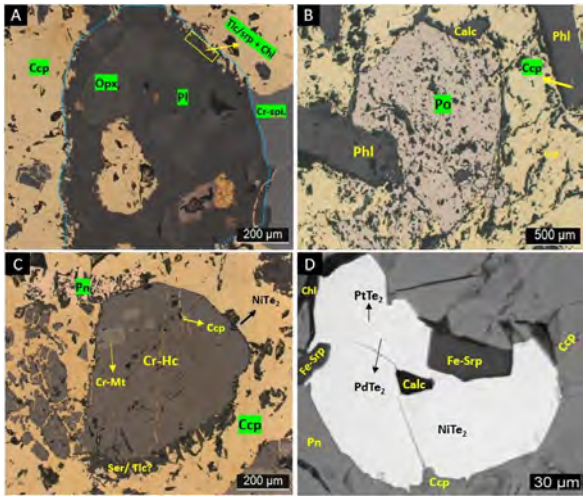

Figure 2. Optical (A-C) and backscattered-electron (BSE) images (D): **A)** Chalcopyrite (Ccp) filling corroded zones in orthopyroxene (Opx) and plagioclase (Pl), which are replaced by talc(Tlc)/serpentine (Srp) + chlorite (Chl) in the contact margins; **B)** Pyrrhotite (Po) and phlogopite (Phl) inclusions in Ccp, which fills cleavage plans in Phl and partially corroded zones in Po; **C)** Ccp filling fractures in the Cr-rich hercynite (Cr-Hc) which exhibit exsolutions of Cr-rich magnetite (Cr-Mt); **D)** Pd-Pt tellurides and Ccp filling fractures in Ni-telluride and spatially related to pentlandite (Pn), Fe-serpentine (Fe-Srp) and chlorite (Chl).

2.2 The Umburana system

Umburana contains mineralization with the lowest Cu:Ni ratios discovered to date hosted within mafic-ultramafic rocks in the district, ranging from 0.1 to 8 (Ero-Copper 2022b). The mineralization is composed of pyrrhotite-pentlandite-pyrite occurring as disseminated/blebs, net-textured, veins and massive/breccia, with only minor chalcopyrite, phlogopite and apatite (+/-monazite). The intrusion consists of an upper orthopyroxenite with minor mineralization overlying a hornblende-websterite with significant mineralization (Figure 3).

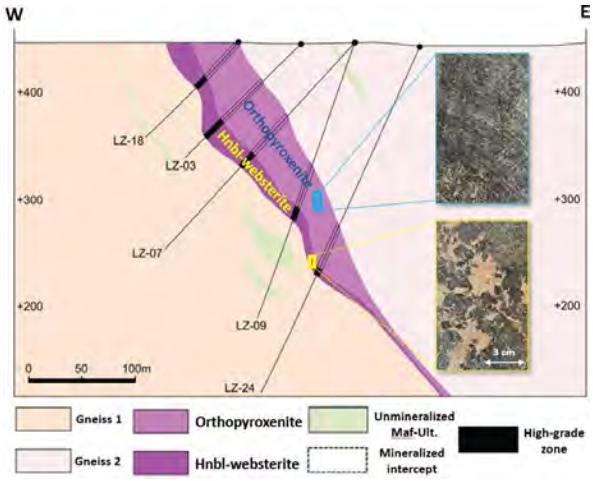

Figure 3. Geological section of the Umburana's LZ target, exhibiting the two main host rocks.

The orthopyroxenite unit (11-17.3% Mg; 0.09-0.16% Cr) contains orthopyroxene and minor clinopyroxene as cumulate phases with intercumulus plagioclase, hornblende and minor phlogopite (+/- apatite-monazite). Pyrrhotite and pentlandite occur as interstitial among the silicates (Figure 4).

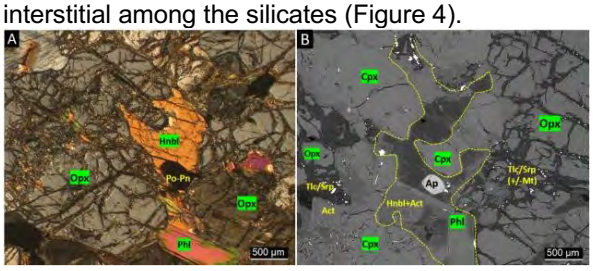

Figure 4. Optical (A) and BSE (B) images: **A)** Orthopyroxene (Opx) cumulates, and hornblende (Hnbl) and phlogopite (Phl) as intercumulus phases with interstitial pyrrhotite (Po) and pentlandite (Pn); **B)** Opx and clinopyroxene (Cpx) cumulates with Hnbl-plagioclase(Pl)-apatite(Ap)-Phl as intercumulus phases. Talc(Tlc)/serpentinte(Srp)-magnetite(Mt) occur filling corroded zones mostly in Opx, and actinolite (Act) in Hnbl and Cpx.

The hornblende-websterite (8.5-11% Mg; ~0.08% Cr) is the main mineralized unit, sitting stratigraphically below the orthopyroxenite. In this unit the orthopyroxene is highly altered by talc/serpentine and minor calcite, with remnants of intercumulus clinopyroxene, hornblende, plagioclase and minor apatite (+/- monazite). Pentlandite occurs in rims around pyrrhotite (forming loop textures in the high-grade zones) and both occur in sharp contact with chalcopyrite. Pyrite is mainly found as large inclusions in the pyrrhotite- pentlandite rich zones, with the latter two filling in corroded and fractured zones in the former (Figure 5).

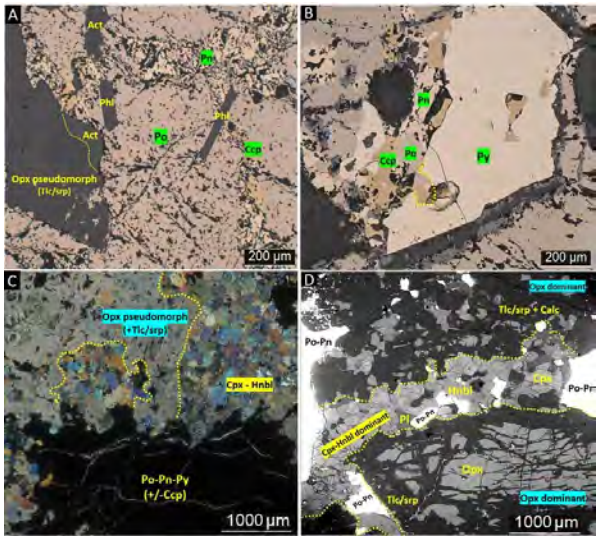

Figure 5. Optical (A-C) and BSE (D) images: **A)** Po with Pn rims and in sharp contact with Phl and Act inclusions; **B)** Po-Pn-Ccp and Tlc/Srp-Mt filling corroded zones in Py; **C)** Po-Pn-pyrite (Py) in contact with Cpx-Hnbl and highly altered Opx; **D)** Po-Pn as droplets/blebs in Cpx-Hnbl and filling corroded zones in altered Opx.

3 Evidence of crustal interaction

Complex interactions with wall-rocks are observed within the mineralized zones in the Umburana and Vermelhos systems. Wall-rock xenoliths have marginal reaction zones enriched in phlogopite and garnet. “Pegmatoidal” bodies are commonly presentin the contact zones of the mafic-ultramafic intrusions with the country rocks and surrounding some xenoliths in the mineralized zones. Some of the intercumulus phases of the Umburana host rocks exhibit similar mineralogy as the xenoliths, including plagioclase and apatite (+/- monazite; Figure 6). S-bearing paragneisses occur near the mineralized intrusions of both systems and might have introduced some S to the mafic-ultramafic magmas.

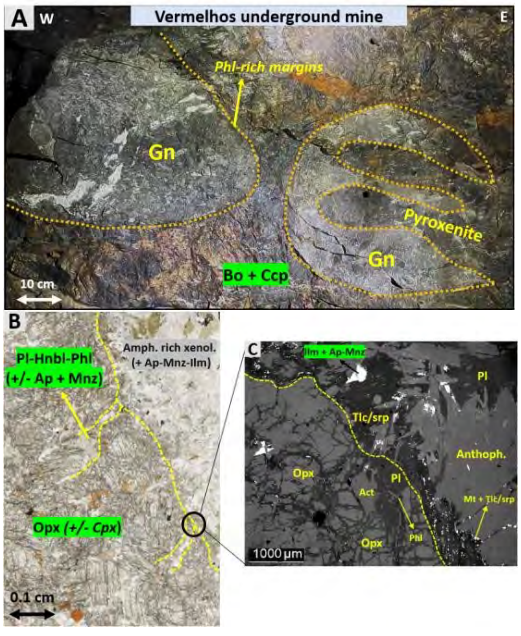

Figure 6. A) Country rock gneiss (Gn) xenoliths in highly mineralized zones of the Vermelhos underground mine; **B)**Pl-Hnbl-Phl-Ap-monazite (Mnz) as intercumulus phases inthe orthopyroxenite unit of Umburana, in contact withamphibole rich xenolith containing Ap-Mnz-ilmenite(Ilm); **C)** BSE image showing in detail the contact of the xenolith with cumulate Opx and intercumulus Pl-Act-Phl.

4 Preliminary interpretations

4.1 Parageneses

Based on the mineralogical and textural associations of this work, we propose the following paragenetic sequences (Figure 7) for the Umburana and Vermelhos systems:

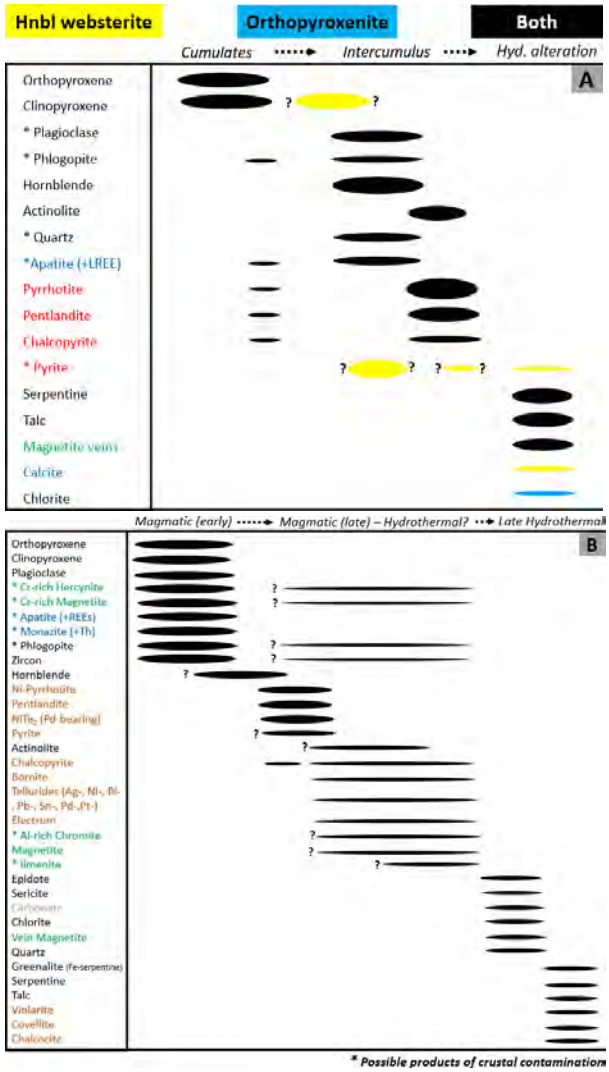

Figure 7. Paragenetic sequences of **A.** Umburana and **B.** Vermelhos.

4.2 Metallogenic model

Field and textural evidence suggest extensive interaction between wall-rocks and mafic-ultramafic magmas at the time of emplacement and crystallization. It is likely that contamination with crustal rocks influenced the igneous mineral assemblage with crystallization of orthopyroxene,

clinopyroxene, hornblende, phlogopite, various spinels (Al-Zn rich), apatite (+/- monazite) and sulfides.

The Umburana system is related to magmas that crystallized cumulus orthopyroxene, clinopyroxene +/- phlogopite) and intercumulus clinopyroxene-hornblende (+/- plagioclase-phlogopite-apatite-monazite). Based on the textural association seen in the hornblende-websterite unit where remnant clinopyroxene-hornblende-pyrrhotite-pentlandite occur between highly altered cumulus orthopyroxene, we interpret that the magma that formed the hornblende-websterite was emplacedinto the orthopyroxenite, and is the main host of thesulfide mineralization (Figure 8). The sulfide assemblage including pyrrhotite-pentlandite (+/- chalcopyrite) probably represents crystallizationfrom mono-sulfide solid solution (MSS).

The Vermelhos' host rocks were derived from mafic-ultramafic magmas that crystallized orthopyroxene, clinopyroxene and a greater amount of spinel (up to 50%), phlogopite (up to 60%) and plagioclase (up to 20%) in comparison to Umburana. Given the higher abundance of chalcopyrite and thus lower Cu:Ni values, mineralization may have crystallized largely from intermediate solid solution (ISS) to form chalcopyrite (+/- bornite) after early MSS (pyrrhotite-pentlandite).

Late hydrothermal alteration including chlorite, K-mica, epidote, carbonate, serpentine, talc, violarite and magnetite veins overprinted the system and locally remobilized the sulfides.

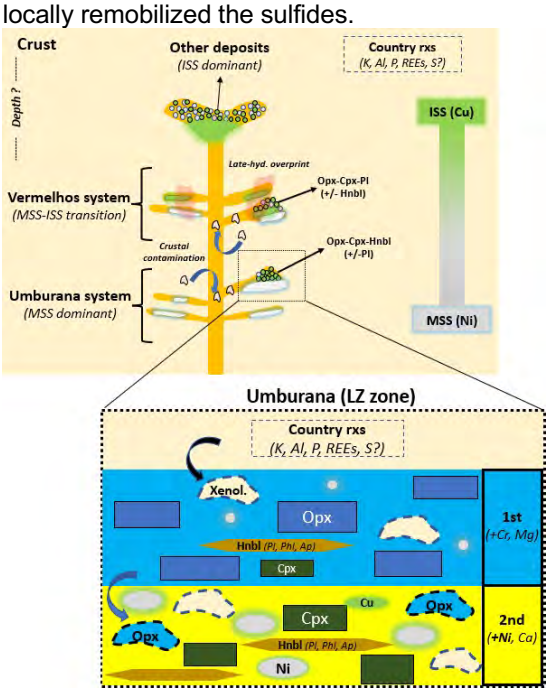

Figure 8. Metallogenic model of the Umburana and Vermelhos systems in the Curaçá Valley district.

5 Final remarks

- The host rocks in the Ni-rich Umburana and Vermelhos systems are pyroxene dominant, with the major differences related to the higher amount of clinopyroxene-hornblende in the highly mineralized zones of Umburana and more cumulate plagioclase and phlogopite-spinels- tellurides in Vermelhos.
- Chalcopyrite occurs as a minor phase and is coeval with pyrrhotite-pentlandite in the Umburana system, whereas in Vermelhos it is abundant and most of it postdates thosesulfides.
- Complex wall-rock interaction with mafic-ultramafic magmas likely led to crustal contamination within the mineralized zones of both systems, with possible addition of sulphur. This might explain the abundance of phlogopite, spinels (+Al-Zn) and minor apatite (+/-monazite), especially seen in Vermelhos. However, the exact timing and extent of the country rocks assimilation remains to be quantified.
- The different Cu:Ni ratios observed in both systems could be explained by extreme sulfide fractionation processes, in which Umburana would represent crystallization from MSS and Vermelhos predominantly ISS.

Acknowledgements

We thank Ero Copper Corp. for sponsoring this research, as well as Queen's University, Brian Joy and Agatha Dobosz for the analytical support.

References

Ero-Copper (2019): Ero-Copper news release, December 3, 2019. https://erocopper.com/news/ero-copper-intersects-51.8-meters-grading-3.49-copper-including-33.4-meters-grading-4.96-copper-in-pilar-mine-deepening/

Ero-Copper (2022a): Ero-Copper news release, January 6, 2022. https://erocopper.com/news/ero-copper-announces-updated-mineral-reserves-and-resources-for-the-mcsa-mining-complex-and-the-nx-gold-mine/

Ero-Copper (2022b): Ero-Copper news release, September 29, 2022. https://erocopper.com/news/ero-copper-announces-discovery-of-nickel-sulphide-system-in-the-curaca-valley-intercepts-16.5-meters-grading-1.22-nickel/

Maier W.D., and Barnes S.J. (1999): The origin of Cu sulfide deposits in the Curaca Valley, Bahia, Brazil; evidence fromCu, Ni, Se, and platinum-group element concentrations.Economic Geology, 94(2), 165-183.

Nunes, T. A. (2022). PDAC 2022 poster: "The Ni-PGE rich zones of the Vermelhos Cu-Deposits, Curaçá Valley District, Brazil: Constrains on the Spinel Composition".

Oliveira E.P. et al (2004): Contrasting copper and chromium metallogenic evolution of terranes in the Palaeoproterozoic Itabuna–Salvador–Curaçá orogen, São Francisco craton,Brazil: new zircon (SHRIMP) and Sm–Nd (model) ages and their significance for orogen-parallel escape tectonics.Precambrian Research, 128(1-2), 143-165.

Suzuki K., and Adachi M. (1994). Middle Precambrian detrital monazite and zircon from the Hida gneiss on Oki-Dogo Island, Japan: their origin and implications for the correlation of basement gneiss of Southwest Japan and Korea. Tectonophysics, 235(3), 277-292.

Teixeira J. B. G., et al. (2010): IV-Depósitos de Cobre do Valedo Rio Curaçá, Bahia. Modelos de Depósitos de Cobre do Brasil e sua Resposta do Intemperismo, 73-95.

Chemistry of major sulfides from Ni-Cu (PGE) mineralization at the Ransko ore district (Bohemian Massif): A result from LA-ICPMS study

Jan Pašava[1], Irina Andronikova[1], Vojtěch Wertich[1,2], Lukáš Ackerman[3], Petr Rambousek[1], Ondřej Pour[1], Karel Malý[4]

[1]*Czech Geological Survey, Prague, Czech Republic*
[2]*Masaryk University, Brno, Czech Republic*
[3]*Institute of Geology, Czech Academy of Sciences, Prague, Czech Republic*
[4]*Aurum Discovery Ltd., Kells, Republic of Ireland*

Abstract. The concentrations of platinum-group (PGE) and chalcophile elements in base metal sulfides (BMS) represented by pyrrhotite (Po), pentlandite (Pn), chalcopyrite (Cp) and cubanite (Cub) from the Ransko Ni-Cu (Co-PGE) deposit (Bohemian Massif) were determined by laser ablation-inductively coupled plasma-mass spectrometry (LA-ICPMS). In high-grade ore, the pyrrhotite shows a strong enrichment in Ag, Ir and Rh whereas the pentlandite is enriched in Cu, Pd and Ir. Cubanite is compared to chalcopyrite significantly enriched in Ag, Sb, Re, Os and Au whereas chalcopyrite shows slightly higher median Pd and Cd values. Rhenium, Os, Ir, Ru, and Rh occur mostly in solid solution in pyrrhotite and pentlandite from high-grade ore, which has been interpreted to represent monosulfide solid solution (mss) cumulates. The distribution of TABS (Te + As + Bi + Sb + Sn) in BMS indicates crustal contamination.

1 Geology and Mineralization

The Ransko massif is the ultra(mafic) body located in a transition zone between the Moldanubian, the Kutná Hora crystalline unit and the Hlinsko Zone in the Bohemian Massif, Czech Republic (Figure 1).

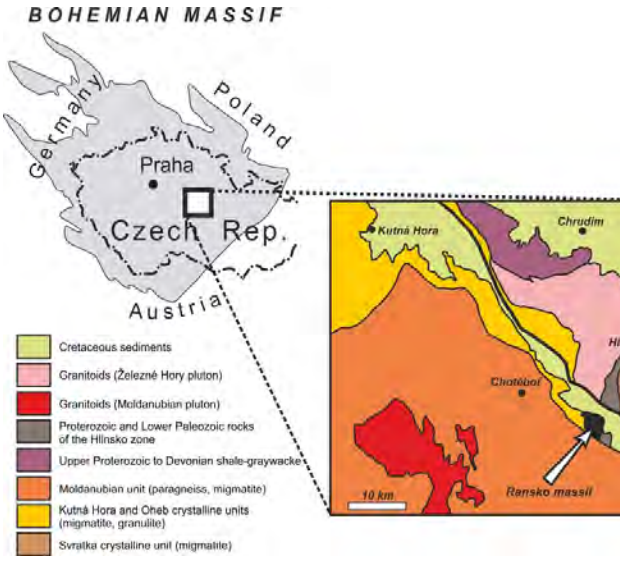

Figure 1. Geoloical position of the Ransko gabbro-peridotite massif (from Mísař 1974 modified by Ackerman et al. 2013).

It represents a strongly differentiated intrusive complex formed by peridotites and gabbroic rocks (gabbro, troctolite) with a magmatic segregation of low-grade Ni–Cu ores, a unique ore type in the Bohemian Massif. The exact geotectonic position of the Ransko massif and its relationship to adjacent units has been subject to several discussions (e.g. Synek and Oliveriová 1993, Štědrá and Nahodilová 2009, Pertoldová et al. 2010). While the Moldanubian and Kutná Hora units experienced polyphase Variscan high-grade metamorphism (~340 Ma), the adjacent part of the Hlinsko Zone was suggested to be Upper Proterozoic (Pitra and Guiraud 1994).

The Ransko massif has been subject of mining activity for a long time. For example, iron mining (oxidized, Fe-enriched caps) and smelting has been documented from the 14th until the end of the 19th century. Exploration for Ni-Cu-Co ores started in 1950s and resulted in finding of nine smaller ore bodies (e.g., Jezírka). Low grade Ni–Cu magmatic mineralization in troctolites is confined to a 3 km long and 1 km wide ore zone cutting the massif in a NE-SW direction (Mísař 1974). The ore zone is characterized by strong serpentinization and uralitization of the host rocks. Individual ore bodies are developed close to the contact of olivine-rich rocks (peridotite, troctolite) with gabbro, and particularly in the zones exhibiting varied alternation of troctolites with (olivine)gabbro. The Ni–Cu sulfide mineralization is not bound to a particular rock type but occur in various rock types as irregular lenses and horizons in a relatively strongly mineralized zone containing pyrrhotite and pyrite. Isolated and irregular occurrences of disseminated Cu-Ni ores were also discovered in troctolites and plagioclase-bearing peridotites. Within the Ni–Cu ores, Pašava et al. (2003) detected anomalous PGE concentrations with Pt+Pd contents up to ~0.7 ppm and revealed the presence of platinum-group minerals (PGM).

Based on paleomagnetic data, the Ransko massif was firstly assumed to be of Lower Cambrian age (Marek 1970). However, Re–Os data of barren and mineralized rocks from the Jezírka Ni–Cu body yield a regression of 341.5 ± 7.9 Ma assuming its Variscan age (Ackerman et al. 2013). This is exactly the same age of the mafic stock hosting Ni-Cu (PGE) mineralization at Aguablanca (Spain) (Romeo et al. 2006). Strongly mineralized Ransko peridotite with mantle like $^{187}Os/^{188}Os$ values suggest that PGE are predominantly of mantle origin. On the other hand, radiogenic $^{187}Os/^{188}Os$ values detected in barren and low mineralized samples indicate crustal

contamination of parental magmas during their emplacement.

2 Results and Discussion

2.1 Samples and Methods

The polished sections of low (RAN7- olivine gabbro with 0.11 wt% Cu and 0.09 wt% Ni and RAN17- troctolite with 0.46 wt.% Ni and 0.19 wt.% Cu) and high Cu-Ni (R1- troctolite with 2.3 wt% Cu and 1.6 wt% Ni) mineralization from the Jezírka deposit from Ransko were first studied using a reflected light microscopy and afterwards by a FE–SEM scanning microscopy using Tescan Mira3 GMU housed at the Czech Geological Survey (CGS).

Trace elements in sulfides were analyzed at the LA-ICPMS laboratory at the CGS using Agilent 7900 ICP-MS coupled with an Analyte Excite Excimer 193 nm LA system equipped with a two-volume HelEx ablation cell. Up to 30 isotopes were detected depending on the mineral (^{49}Ti, ^{51}V, ^{53}Cr, ^{55}Mn, ^{57}Fe, ^{59}Co, ^{60}Ni, ^{65}Cu, ^{66}Zn, ^{71}Ga, ^{74}Ge, ^{75}As, ^{77}Se, ^{101}Ru, ^{103}Rh, ^{107}Ag, ^{108}Pd, ^{111}Cd, ^{115}In, ^{118}Sn, ^{121}Sb, ^{125}Te, ^{185}Re, ^{188}Os, ^{193}Ir, ^{195}Pt, ^{197}Au, ^{201}Hg, ^{205}Tl, ^{208}Pb, and ^{209}Bi). We do not report Ru data for Pn and Rh data for Cp and Cub because of polyatomic interferences (Trubač et al. 2018).The laser was fired with spot size of 35-40 µm and fluence of 3.9-4.7 J/cm^2 with a laser pulse rate of 10 Hz. The GLITTER 3.0 software was used as a data reduction program. Internal standardization was based on Fe concentration determined by the SEM analysis and/or on the stoichiometric Fe values. Two reference materials were used for external calibration: the USGS MASS-1 (Wilson et al., 2002) and UQAC-FeS-1 (Savard et al. 2018, Duran et al. 2019) sulfide pellets. The UQAC-FeS-5 (Savard et al. 2018) and GSE-2g, a syntetic basalt material supplied by USGS (Mayers et al. 1976) were used for quality control.

2.2 Mineralogy

The ore minerals includes pyrrhotite, pentlandite, chalcopyrite and cubanite with minor pyrite, (Cr)magnetite, picotite, mackinawite, valleriite, ilmenite, galena, sphalerite, cobaltite–gersdorffite, native bismuth, gold, PGM represented by michenerite, froodite and sperrylite and tellurides represented by tsumoite, hessite and unnamed Bi-Ni telluride (Vavřín and Frýda 1998, Pašava et al. 2003 and references therein).

In this study, we newly identified an unnamed Pd-Bi-Sb phase in close association with michenerite and froodite, melonite (NiTe) in form of inclusions in pyrrhotite, and clausthalite (PbSe). Our high-grade ore sample (R1) is mainly composed of pyrrhotite, pentlandite and cubanite (Figure 2A) whereas low-grade ore (samples RAN-07 and RAN-17) is characterized by dominating pyrrhotite, pentlandite and chalcopyrite (Figure 2B).

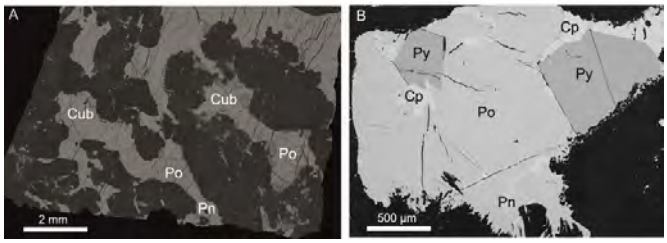

Figure 2. Photomicrographs of typical ore from Ransko. **A** – high-grade ore with pyrrhotite (Po), pentlandite (Pn) and cubanite (Cub). **B** – low-grade ore with pyrrhotite, pentlandite and chalcopyrite. Abbreviations: Cub – cubanite, Cp – chalcopyrite, Pn – pentlandite, Po – pyrrhotite and Py – pyrite.

2.3 Trace element concentrations in Base Metal Sulfides (BMS)

The ranges of concentrations of PGE in major base metal sulfides are shown on Figure 3.

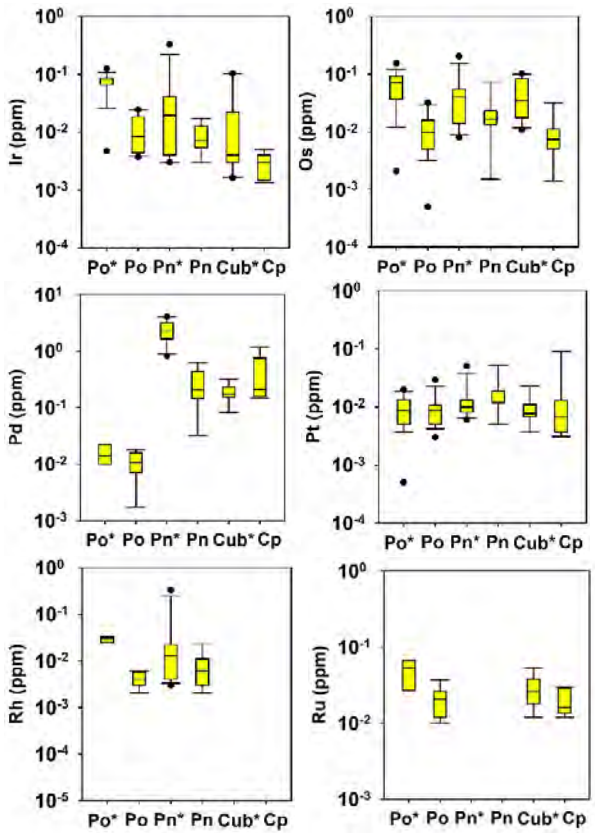

Figure 3. Box and whiskers plots for PGE in sulfides from Ransko. Po – pyrrhotite, Pn – pentlandite, Cub – cubanite, Cp – chalcopyrite, * sulfide from high-grade ore. The boxes are framed by 25th and 75th percentile, line within the box indicates median value. Whiskers displays 10th and 90th percentile and outliers are shown as one symbol representing 5th and 95th percentile.

The median concentrations of other selected trace elements (including TABS) in major BMS are shown in Table 1.

Iridium and Rh show the highest median values in Po from high-grade ore while Pt and Pd are dominating in high-grade ore Pn. Both the sulfides

have the highest median Os values. Such distribution reflects very likely concentration of these metals in monosulfide solid solution similarly as reported from other Ni-Cu deposits (e.g. Aguablanca, NW Spain - Piña et al. 2012). Chalcopyrite is characteristic of the highest median values of Te, Cd, In and Zn while Cub bear peak median values of Ag, Re, Bi and Sb.

To investigate the role of crustal assimilation on the metal contents, we used As and Sb concentrations (Samalens et al. 2017; Mansur et al. 2021) in Pn (Figure 4). Both elements are incompatible with MSS and ISS and therefore, their concentrations in the sulfide liquid tend to increase with progressive fractionation.

Table 1. The median concentrations of selected trace elements in major BMS from Ransko (values in ppm).

	Po	Pn	Cub	Po	Pn	Cp
	high-grade ore			***low-grade ore***		
Co	13	15883	0.28	62.11	33543	0.34
Cu	0.84	482.2	235770	1.025	28.92	329996
Zn	0.55	1.01	205.7	0.58	1.03	474.31
As	0.43	0.89	0.39	0.40	0.89	0.30
Se	84	72.4	73.9	55.9	62.0	47.5
Ag	1.2	6.2	14.6	0.13	2.5	1.32
Cd	0.08	0.18	11.0	0.05	0.18	19.30
In	0.003	0.006	0.10	0.005	0.004	0.15
Sn	0.14	0.15	0.19	0.15	0.17	0.12
Sb	0.19	0.15	12.87	0.17	0.21	0.16
Re	0.056	0.086	0.161	0.085	0.021	0.003
Au	0.005	0.016	0.017	0.005	0.022	0.005
Tl	0.01	0.05		0.003	0.03	
Pb	1.23	2.58	5.62	0.87	4.73	4.16
Bi	0.75	0.51	0.90	0.28	0.89	0.45
Te	0.22	0.28	2.22	0.52	0.6	2.54

The values of Sb/Se and As/Se ratios in Pn from both types of ore at Ransko are well comparable with other magmatic Ni-Cu deposits which show external input of As and Sb in the sulfide liquid through crustal assimilation (see Mansur et al. 2021). High Sb values and a negative correlation between Sb/Se and As/Se in low grade ore likely reflect different crustal sources (lithologies).

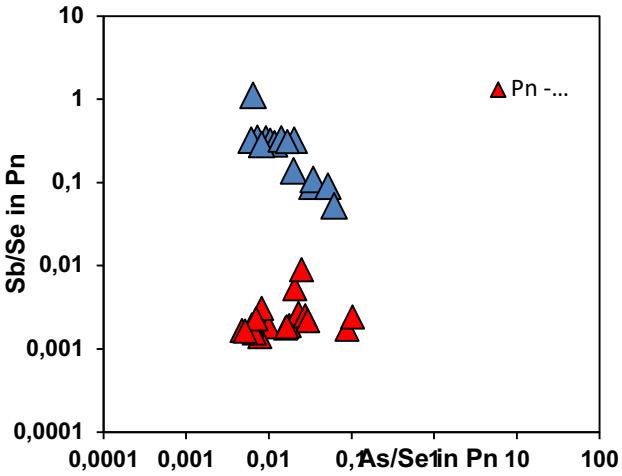

Figure 4. Binary plot of Sb/Se and As/Se in pentlandite (Pn) from the Staré Ransko Ni-Cu deposit.

In magmatic sulfide deposits, a fraction of the PGE is hosted by BMS, whereas the remaining PGE with TABS form PGM (e.g., Junge et al. 2015). Within Ni-Cu deposits, the effect of fractional crystallization on the composition of BMS is dominantly relative to the effect of PGM exsolution. Mansur et al. (2021) concluded that although there is no clear negative correlation between PGE and TABS concentrations in Pn, there is an increase in concentrations of both PGE and TABS from Cu-poor to Cu-rich ores (e.g., Pn from Noril'sk-Talnakh) which is consistent with the situation at Ransko (Figure 5).

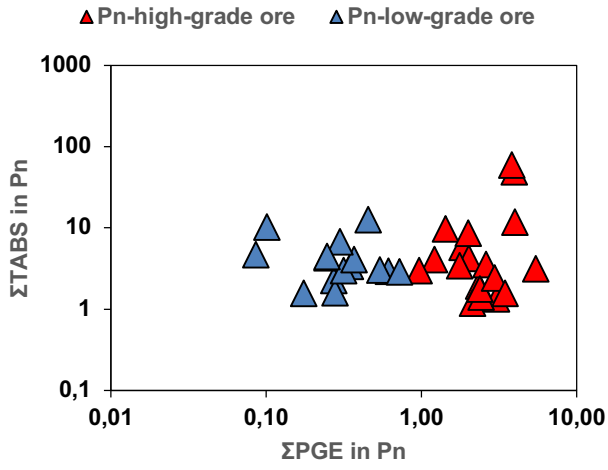

Figure 5. Binary plot of ΣTABS versus ΣPGE in Pn from Ransko Ni-Cu deposit. ΣTABS: Te + As + Bi + Sb + Sn. ΣPGE: Pt + Pd + Rh + Ir + Os.

To evaluate the influence of the R-factor on the BMS composition we used mantle normalized plots for strongly to highly (Figure 6 a,b), and slightly to moderately chalcophile elements (Figure 7 a,b). The elements are disposed from left to right in order of increasing partition coefficient into a sulfide liquid relative to silicate liquid ($D^{sulf/sil}$). The Po and Pn show similar shapes (Figure 6 a,b) suggesting similar R-factors during their formation.

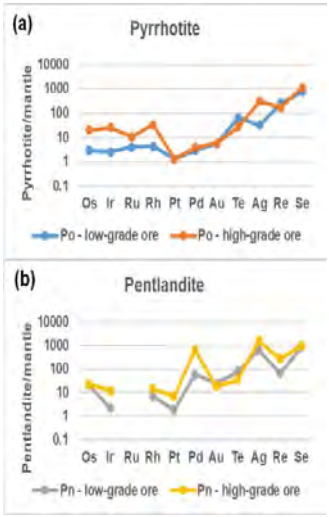

Figure 6. Strongly and highly chalcophile element primitive mantle normalized diagrams for median compositions of **(a)** Po and **(b)** Pn from Ransko. Primitive mantle values from Lyubetskaya and Korenaga (2007).

The median values of IPGE (Ir, Os, Ru) are higher in Po from high-grade ore in relation to Po from low-grade ore. The Pn from high-grade ore is typical of a strongly positive Pd and Ag anomalies while the Pn from low-grade ore shows more negative Ir, Pt and Re anomalies.

The mantle-normalized patterns for median Po composition are relatively flat and have slightly negative Cd, Co and In anomallies, a strong negative Zn anomaly and a strong positive Sb anomaly (Figure 7a). The patterns for median Pn compositions are similar to those for Po, but in contrast, Pn shows strongly positive Co anomaly not observed in Po patterns (Figure 7b).

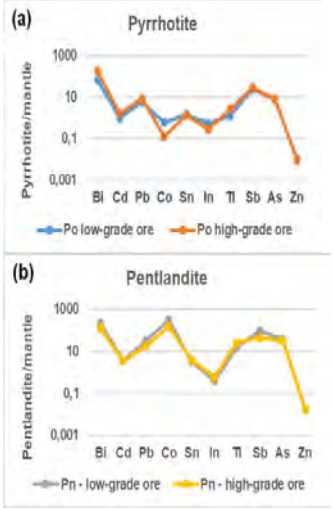

Figure 7. Slightly and moderately chalcophile element primitive mantle normalized TABS diagrams for median compositions of **(a)** Po and **(b)** Pn from Ransko.

Conclusions

The results of LA-ICPMS study of BMS at Ransko can be summarized as follows:

(1) In high-grade ore, the pyrrhotite shows a strong enrichment in Ag, Ir and Rh whereas the pentlandite is enriched in Cu, Pd and Ir. Cubanite is highly enriched in Ag, Sb, Re, Os and Au whereas chalcopyrite shows slightly higher median Pd and Cd values.

(2) Rhenium, Os, Ir, Ru, and Rh occur mostly in solid solution in pyrrhotite and pentlandite from high-grade ore representing monosulfide solid solution cumulates.

(3) The values of Sb/Se and As/Se ratios in pentlandite from both types of ore at Ransko most likely reflect external input of As and Sb in the sulfide liquid by crustal assimilation. This is also supported by the distribution of slightly to moderately chalcophile elements.

(4) There is an increase in concentrations of both PGE and TABS from Cu-poor to Cu-rich ores.

Acknowledgements

This study has been co-funded by the European Union (SEMACRET, Grant Agreement no. 101057741) and UKRI. It is also a contribution to the Strategic Research Plan of the Czech Geological Survey (DKRVO 2023-2027). We thank an anonymous reviewer for useful comments.

References

Ackerman L, Pašava J, Erban V (2013) Re–Os geochemistry and geochronology of the Ransko gabbro–peridotite massif, Bohemian Massif. Mineral Deposita 48:799-804

Duran CJ, Dube-Loubert H, Page P, Barnes SJ, Roy M, Savard D, Cave BJ, Arguin JP, Mansur ET (2019) Applications of trace element chemistry of pyrite and chalcopyrite in glacial sediments to mineral exploration targeting: Example from the Churchill Province, northern Quebec, Canada. J Geochem Explor 196:105-130

Faryad SW (2009) The Kutná Hora Complex (Moldanubian zone, Bohemian Massif): A composite of crustal and mantle rocks subducted to HP/UHP conditions. Lithos 109:193-208

Holub M, Jelínek E, Komínek E, Pluskal jr. O (1992) Genetic model of sulfide mineralization of the Ransko gabbro peridotite massif (Bohemia, Czechoslovakia). Sborník geologických věd, ložisková geologie, 30:7-42

Junge M, Wirth R, Oberthür T, Melcher F, Schreiber A (2015) Mineralogical siting of platinum-group elements in pentlandite from the Bushveld Complex, South Africa. Mineral Deposita 50:41–54

Lyubetskaya T, Korenaga J (2007) Chemical composition of earth's primitive mantle and its variance: 1. method and results. J Geophys Res 112:B03211

Mansur ET, Barnes SJ, Duran CJ (2021) An overview of chalcophile element contents of pyrrhotite, pentlandite, chalcopyrite, and pyrite from magmatic Ni-Cu-PGE sulfide deposits Mineral Deposita 56:179-204

Marek F (1970) Odhad stáří ranského bazického masívu podle paleomagnetických dat. Bulletin of the Czech Geological Survey 45:99-102 (in Czech with English abstract)

Mísař Z (1974) The Ransko gabbro - peridotite massif and its mineralization (Czechoslovakia). Prague, Charles University, 215 p.

Mísař Z (1979) Sulfide mineralization in the Ransko gabbro-peridotite massif, Czechoslovakia. Can Mineral 17:299-307

Myers AN, Havens RG, Connor JJ, Conklin NM, Rose HJ JR (1976) Glass Reference Standards for the Trace-Element Analysis of Geological Materials-Compilation of Interlaboratory Data. Geological Survey Professional Paper 1013 UNITED STATES Government printing Office, Washington

Pašava J, Vavřín I, Frýda J, Janoušek V, Jelínek E (2003) Geochemistry and mineralogy of Platinum-group elements in the Ransko gabbro-peridotite massif, Bohemian Massif, Czech Republic. Mineral Deposita 38:298-311

Pertoldová J, Verner K, Vrána S, Buriánek D, Štědrá V, Vondrovic L (2010) Comparison of lithology and tectonometamorphic evolutionof units at the northern margin of the Moldanubian Zone: implications for geodynamic evolution in the northeastern part of the Bohemian Massif. J Geosci 55:299-319

Piña R, Gervilla F, Barnes SJ, Ortega L, Lunar R (2012) Distribution of platinum-group and chalcophile elements in the Aguablanca Ni-Cu sulfide deposit (SW Spain): evidence from a LA-ICP-MS study. Chem Geol 302:61-75

Pitra P, Guiraud M (1996) Probable anticlockwise P-T evolution in extending crust: Hlinsko region, Bohemian Massif. J Metamorph Geol 14:49-60

Romeo I, Lunar R, Capote R, Quesada C, Dunning GR, Piña R, Ortega L (2006) U/Pb age constraints on Variscan Magmatism and Ni–Cu–PGE metallogeny in the Ossa-Morena zone (SW Iberia). J. Geol. Soc. London 163:837-846

Samalens N, Barnes SJ, Sawyer EW (2017) The role of black shales as a source of sulfur and semimetals in magmatic nickel-copper deposits: example from the Partridge River Intrusion, Duluth Complex, Minnesota, USA. Ore Geol Rev 81:173-187

Savard D, Bouchard-Boivin B, Barnes SJ, Garbe-Schönberg D (2018) UQAC-FeS: A new series of base metal sulfide quality control reference material for LA-ICP-MS analysis. In Proceedings of the 10th International Conference on the Analysis of Geological and Environmental Materials, Sydney, Australia, 8-13 July 2018

Synek J, Oliverová D (1993) Terrane character of the north-eastmargin of the Moldanubian Zone: the Kutná Hora Crystalline Complex, Bohemian Massif. Geol Rund 82:566-582

Štědrá V, Nahodilová R (2009) High-pressure metabasic rocks from the Kutna Hora Complex: geological position and petrology of exotic lithologies along the segmented Moldanubian margin, Bohemian Massif. J Geosci 54:135-157

Vavřín I, Frýda J (1998) Michenerite PdBiTe and froodite $PdBi_2$ from the Cu-Ni mineralization in the Ransko Massif, Czech Republic. Mineral. Petrol. 63:141-146

Wilson SA, Koenig AE, Ridley WI (2002) Development of sulfide calibration standards for the laser ablation inductively-coupled plasma mass spectrometry: J. Anal. At. Spectrom. 17: 406-409

Trubač J, Ackerman L, Gauert Ch, Ďurišová J, Hrstka T (2018) Platinum-Group Elements and Gold in Base Metal Sulfides, Platinum-Group Minerals, and Re-Os Isotope Compositions of the Uitkomst Complex, South Africa. *Econ Geol* 113: 439–461

Ilmenite-hosted fluid inclusions: Snapshot of magmatic fluid chemistry in mafic rocks

Anthony Pochon[1, 2], Daniel J. Kontak[3], Eric Gloaguen[1, 2], Johann Tuduri[1, 2], Giada Iacono-Marziano[1], Héctor R. Campos Rodríguez[1], Val Mollé[1], Tom Chatelin[1],
[1]ISTO, UMR 7327, Université d'Orléans, CNRS, BRGM, Orléans, France
[2]BRGM, Orléans, France
[3]Harquail School of Earth Sciences, Sudbury, Canada

Abstract. As volatiles play a major role in the igneous ore systems, this study aims to characterize the magmatic fluid chemistry of two early Carboniferous mafic magmatic systems related to Variscan Sb deposits, the Saint-Jean-du-Doigt intrusion in the French Armorican Massif and the San Antonio sill swarm in the Central Iberian zone. As unusual proxy, magmatic ilmenite from these two settings hosting abundant primary fluid inclusions were fully characterized texturally and chemically in order to assess their origin and determine their compositions. Results show that similar ilmenite textures and nature of fluid inclusions characterize the two mafic bodies. Qualitative studies, using SEM-EDS and LA-ICP-MS analyses of evaporate mound and LA-ICP-MS analyses of fluid inclusion rich areas, reveal the trapped fluids are multi-component and are dominated by Na-Ca-S-Sr in Saint-Jean-du-Doigt and San Antonio areas, but in different proportions. In addition, variable amounts of Sb, As, Zn, Mo, W, Pb, Cu, Zr and Hf are present. The data clearly demonstrate that mafic magmatic fluids may contain a non-negligible content of metals and metalloids. Although incomplete, the results reveal that magmatic fluids from the early Carboniferous mafic magmatism contain Sb and thus might constitute a source of Sb in the Variscan belt.

1 Introduction

Volatiles play a major role in the evolution of magmas from their generation in the mantle to eruption at the surface. In particular, water exerts a key control for ore forming processes (e.g., Hedenquist and Lowenstern 1994) and can be used as a vector for metals. Indeed, the abundance of H_2O leads to specific late-magmatic mineral assemblages and strongly controls replacement processes (Putnis and Austrheim 2010). The role and the importance of magmatic aqueous fluids in ore-forming processes is well established in classical felsic systems (e.g. porphyry deposits), but is markedly less constrained in upper crustal mafic magmas. Consequently, the magmatic-hydrothermal transition is not commonly investigated in mafic rocks.

Nevertheless, in the past few years the role of volatiles in mafic igneous ore systems has been revaluated, as well evidenced for conventional magmatic Ni-Cu sulfide deposits (Iacono-Marziano et al. 2022). In the European Variscan belt, spatial links have been demonstrated between mafic intrusions and "*unconventional*" Sb deposits (Pochon et al. 2016, 2018). Indeed, early Carboniferous mafic magmatism is spatially related with some Sb deposits in the external unthickened domains of the belt, *i.e.* the Central Iberian-Armorican zone (Figure 1, Pochon et al. 2016). Here the Sb is not directly associated with dolerite dikes and sills at surface, but instead with mafic bodies present at depth. This raises the question of whether magmatic fluids may supply Sb and related metal and metalloids to the hydrothermal system. In one of these early Carboniferous mafic intrusions ilmenite has been shown to be an excellent proxy of the magmatic-hydrothermal transition, as it has been shown to host fluid inclusions (FIs) enriched in metals and metalloids (Pochon et al. 2023).

In order to assess the role of mafic magmatic fluid as a metal carrier and potential source, we focussed on two mafic magmatic systems, the Saint-Jean-du-Doigt (SJDD) intrusion in the French Armorican Massif (Pochon et al. 2023) and the San Antonio sill swarm (SA) in the Central Iberian zone (Extremadura, Spain). These two intrusive complexes: (i) have similar emplacement ages (i.e. 347 ± 4 Ma for SJDD, Barboni et al. 2013 and 354 ± 5.4 Ma for SA, Campos et al. 2022); (ii) are located in the same geodynamical domain (Figure 1); and (iii) are likely to be the counterpart of early Carboniferous mafic bodies located below the Sb occurrences at depth.

To address the above, we have texturally and chemically characterized ilmenite-hosted FIs from the mafic rocks of these two magmatic systems. These data, when combined with detailed information about alteration history of the rocks, allow the tracking of the magmatic-hydrothermal transition of the intrusions and the composition of the fluids produced by magma degassing.

2 Methodology

Reflected light microscopy and SEM were used to characterize textures of ilmenites and their areas hosting FIs in samples from the SJDD gabbro (Armorican Massif) and the SA gabbroic sills (Central Iberian zone). As ilmenite absorbs infrared light, micro-thermometric studies could not be performed. However, as the ilmenites contain high abundances of FIs, qualitative information about their chemistry was obtained by comparing trace element compositions of FI-free and FI-bearing ilmenites obtained via LA ICP-MS.

In addition, qualitative measurements of key elements and complexing agents present in the trapped fluid were obtained in SJDD ilmenite with a procedure modified after Kontak (2004). Samples were rapidly heated around 500-600°C to induce FI decrepitation and subsequently quenched by

immediately switching off the heating source. The resulting evaporate mounds that formed on the sample surfaces were characterized for their major and trace element composition using a SEM-EDS technique, EPMA maps and LA ICP-MS traverses.

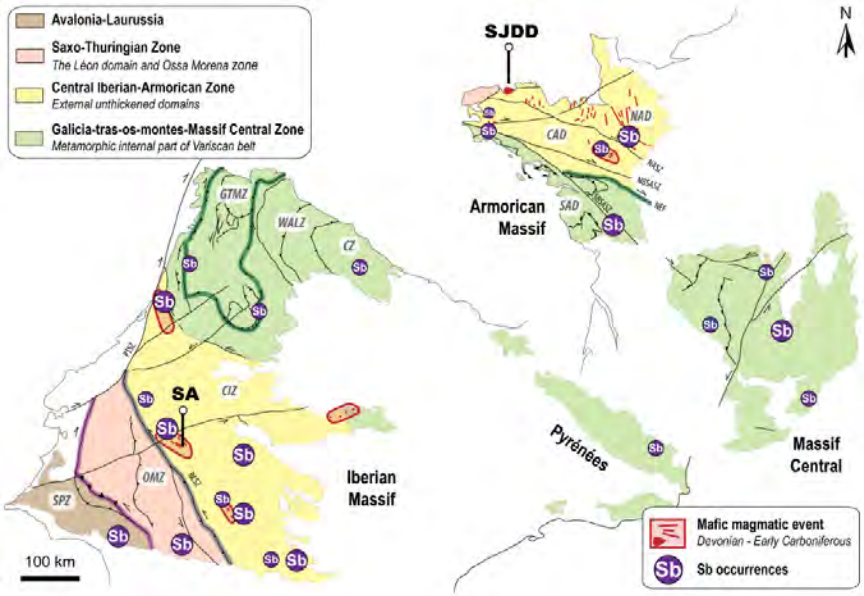

Figure 7. Schematic representation of the west European Variscan belt representing the main terranes and showing the relationship between early Carboniferous mafic magmatism and hydrothermal Sb deposits (modified from Ballouard et al. 2018). NAD: North Armorican domain, CAD: Central Armorican domain, SAD: South Armorican domain, GTMZ: Galicia-Trás-os-Montes zone, WALZ: West Asturian-Leonese zone, CZ: Cantrabrian zone, CIZ: Central Iberian zone, OMZ: Ossa Morena zone, SPZ: South Portuguese zone, NASZ: north Armorican shear zone, NBSASZ: northern branch of the south Armorican shear zone, SBSASZ: southern branch of the south Armorican shear zone, NEF: Nort-sur-Erdre fault.

3 Results

3.1 Textural relation and ilmenite composition

Both the SJDD gabbro and the SA dolerite host similar textured ilmenite with high abundances of FIs equally distributed in the host phase (Figure 2a).

Ilmenite crystals are subhedral to anhedral and occur in direct contact with almost all major minerals, i.e. along grain boundaries between plagioclase, clinopyroxene and amphibole. Ilmenite hosts a high density of crystal defects, which consist of vacancy aggregates, i.e. voids that likely formed during crystal growth and consist of trapped FIs (Pochon et al. 2023).

Most ilmenite crystals show both FI-free and FI-bearing areas, with FI-rich zones in the core areas (up to 15 % of the total crystal surface), whereas FI-free zones typically mantle the latter and also occur more rarely within the crystal (Figure 2a, b). Ilmenite is often rimmed by titanite (i.e. ~10 µm-thick zone around ilmenite) with the contact between the two phases being irregular (i.e. corroded), and some blocky rutile crystals are sometimes present in the rims. The FIs show either negative crystal or irregular shapes with sizes ranging between 0.5 and 5 µm and are either organized in sub-parallel trails, which occur parallel to the elongation (i.e. the c-axis) of the ilmenite, or are randomly distributed.

The contents of two relevant trace elements (Ni and Sb) in ilmenite are plotted in a univariate boxplot (Figure 2c) which distinguishes between FI-free and FI-rich zones. The Sb content shows a net enrichment from FI-free to FI-rich areas. For SJDD, FI-free ilmenite has a mean Sb value of 0.51 ppm, whereas FI-rich ilmenite has mean Sb value of 3.02 ppm. A similar enrichment is observed for SA where FI-free ilmenite has a mean Sb value of 3.22 ppm, whereas FI-rich ilmenite has a mean Sb value of 16.32 ppm. As Sb is strongly incompatible in ilmenite (Klemme et al. 2006), the Sb enrichment in the ilmenite clearly suggests it is carried by FIs. In contrast, Ni, a compatible element in ilmenite (Shepherd et al. 2022), does not seem to be affected by the presence of FIs with similar mean values for FI-free and FI-rich areas (Figure 2c).

Other trace elements (not shown) that are clearly enriched in FI-rich areas of SJDD ilmenite are Sr (FI-free: 0.17 ppm, FI-rich: 0.56 ppm), Mo (FI-free: 1.13 ppm, FI-rich: 11.1 ppm), Pb (FI-free: 0.14 ppm, FI-rich: 1.44 ppm), and W (FI-free: 0.32 ppm, FI-rich: 4.97 ppm).

3.2 Compositions of evaporate mounds

After heating, the presence of evaporate mounds is easily observed, using reflected light, at the ilmenite surface in the form of circular mounds that are commonly surrounded by an aureole of smaller debris. However, mounds with irregular or linear shape are also observed.

Chemically, the evaporate mounds are invariably multi-component and dominated by Na-Ca (∑ ≈ 70 wt. %) in variable proportions and by S (≈ 30 wt. %). These three elements are present in all mounds, whereas K, Ba and Cl are much less present (i.e. only to 36%, 6%, and 6% of analysed mounds, respectively). The K/Ca and K/Na ratios are relatively low, with a mean value of 0.06 and 0.03, respectively. An EPMA map of an evaporate mound is displayed in Figure 3 to illustrate its typical circular texture and the major element distribution.

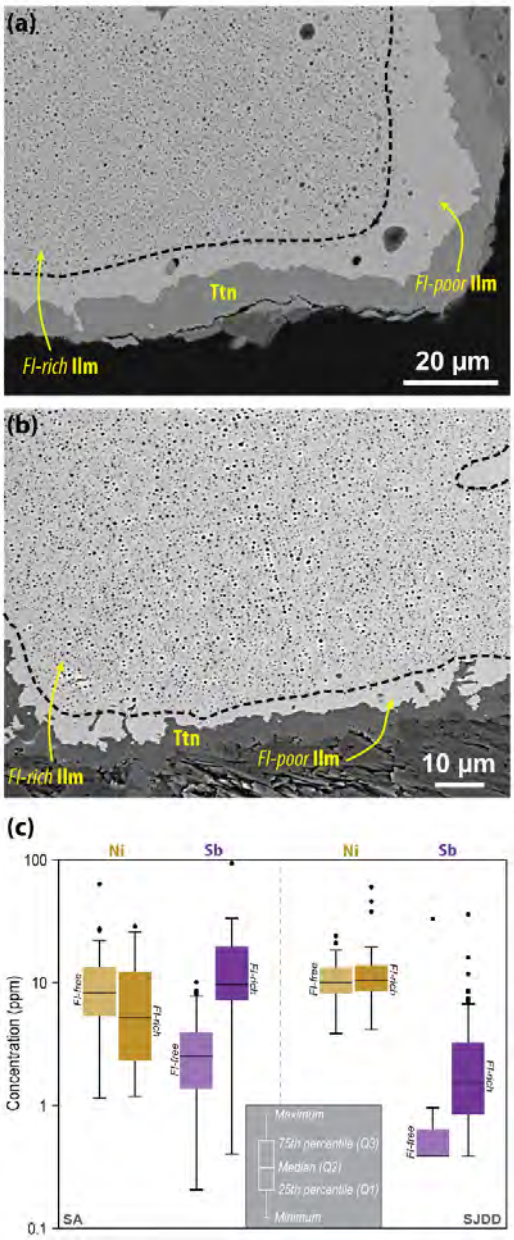

Figure 8. Selected BSE images illustrating the typical texture of ilmenite-hosted FIs from (a) SJDD and (b) SA mafic bodies. (c) Boxplot of the Ni and Sb contents obtained by LA ICP-MS for FI-rich and FI-poor ilmenites from the two study areas.

The LA ICP-MS traverses on the evaporate mounds give interesting information about the metal composition of the fluids. These traverses confirm that all the mounds are invariably dominated by Na-Ca-S, and always accompanied by Sr (Figure 4). In addition, variable amounts of Sb, As, Zn, Mo, Pb, and Cu, and more rarely Zr and Hf, are observed. Additionally, in the same ilmenite grain evaporate mounds may have different composition, that is either Na- or Ca-dominant, but the ∑(Na+Ca)/Ca (in wt. %) remains similar at 2-3:1.

The LA ICP-MS analyses indicate that As and Sb contents increase by 600-650% (i.e. a factor of 7-7.5, respectively) from ilmenite to the evaporate mound, whereas the Cu content increases by 300%. In contrast, the V and Ni contents are not affected by the presence of the mound.

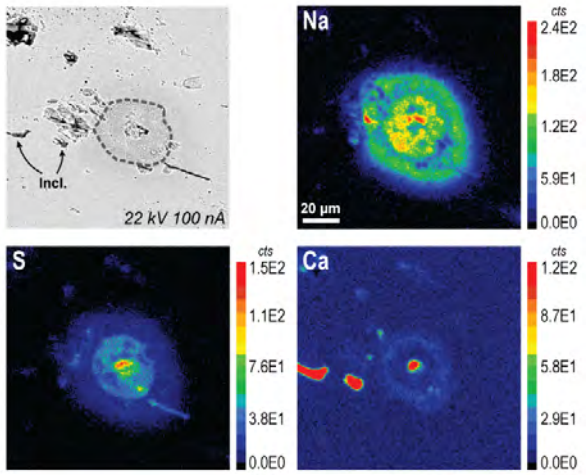

Figure 9. Selected BSE image of decrepitate mound on ilmenite, highlighted by dashed grey line, with X-ray elemental maps of Na, S, and Ca. Incl. = mineral inclusions.

4 Discussion and conclusions

Similar unusual textures suggesting FIs in magmatic ilmenite are observed in the SJDD gabbro (France) and the SA gabbroic sills (Spain), two mafic bodies belonging to the early Carboniferous mafic magmatic event in the Variscan belt. This raises the question of whether this type of texture is restricted to this particular magmatism or can be found in other mafic rocks. The peculiarity of SJDD and SA magmatic rocks is that they seem to crystallize from magmas with reduced redox conditions, as suggested by the occurrence of ilmenite in the absence of titano-magnetite. In the case of SJDD, a detailed study of mineral alteration suggests autometasomatism of the pluton via orthomagmatic fluids which induced plagioclase saussuritization, amphibole crystallization and clinopyroxene replacement, and ilmenite transformation into titanite and rutile (Pochon et al. 2023). This indicates a relatively high volatile content for the mafic magma and accounts for the occurrence of a fluid phase during the late magmatic and the high-temperature hydrothermal stages.

The presence of evaporate mounds clearly confirms that the voids decorating ilmenite surfaces represent evacuated FIs. The composition of the latter fluid is invariably dominated by Na-Ca-S; these

three elements are symptomatic of the presence of FIs (Kontak et al. 2004). In addition, it is important to note that: (i) whenever present, the K content is low; and (ii) Cl is rarely present, meaning S is the major solute anion in exsolved fluids.

Although they are both qualitative methods, “indirect” analyses (i.e. comparison of LA ICP-MS analyses of FI-free and FI-rich area) and the “direct” analysis (i.e. LA ICP-MS traverses) show similar information, namely a non-negligible content of metals and metalloids that are incompatible with ilmenite, firstly Sb, Mo and Pb.

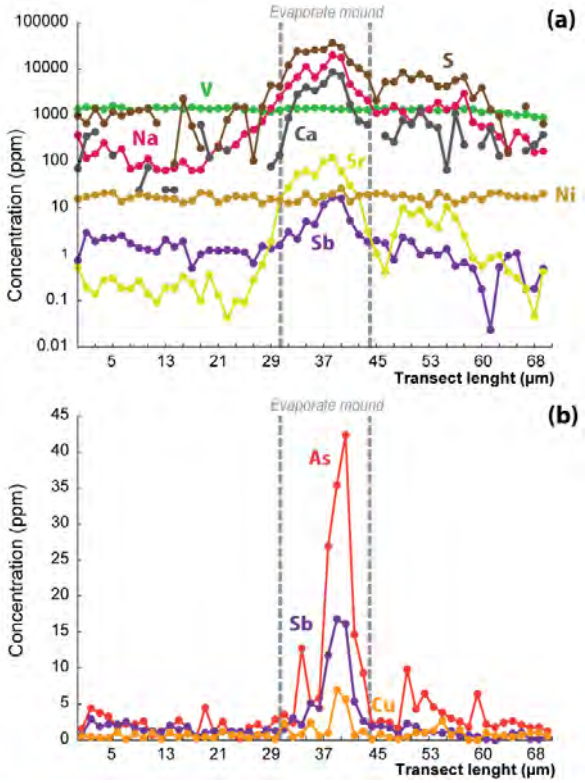

Figure 10. LA-ICP-MS traverse of decrepitate mound on ilmenite. All elements are in ppm except S, which is in count per second (CPS).

An additional important point to mention is the incompleteness of the information derived from the analyses of evaporate mounds. Indeed, the evaporate mounds only represent the tip of the iceberg, as an unknown amount of the decrepitated FI component is vaporized during it decrepitation. Thus, it is likely that some of the volatile component may have escaped, hence only a partial amount of the original metal budget was trapped in the newly crystallized evaporate mounds. Therefore, the next step should be the quantitative analyses of the trapped fluids and their metal and metalloid content, in order to estimate a possible contribution of magmatic fluids from the early Carboniferous mafic magmatism to Sb mineralization in the Variscan belt.

Acknowledgements

This work was achieved in the framework of the ERA-MIN2 Aureole project funded by the ANR (grant ANR-19-MIN2-0002) for the French partners. We also acknowledge the LabEx VOLTAIRE (ANR-10-LABX-100-01) and EquipEx PLANEX (ANR-11-EQPX-0036) for providing support to the EPMA and LA-ICP-MS laboratories.

References

Ballouard C, Poujol M, Mercadier J, Deloule E, Boulvais P, Baele JM, Cuney M, Cathelineau M (2018) Uranium metallogenesis of the peraluminous leucogranite from the Pontivy-Rostrenen magmatic complex (French Armorican Variscan belt): the result of long-term oxidized hydrothermal alteration during strike-slip deformation. Miner Deposita 53:601–628.

Barboni M, Schoene B, Ovtcharova M, Bussy F, Schaltegger U, Gerdes A (2013) Timing of incremental pluton construction and magmatic activity in a back-arc setting revealed by ID-TIMS U/Pb and Hf isotopes on complex zircon grains. Chem Geol 342:76–93.

Campos HR, Gloaguen E, Pochon A, Iacono-Marziano G, Mollé V, Higueras P, Lorenzo S, Maria Esbri J (2022) Mafic magmatism and Sb mineralization: geochemical insights from the Central Iberian Zone, Spain, SGA2022: 16th Biennial meeting, pp. 22.

Hedenquist JW, Lowenstern JB (1994) The role of magmas in the formation of hydrothermal ore deposits. Nature 370(6490):519–527.

Iacono-Marziano G, Le Vaillant M, Godel BM, Barnes SJ, Arbaret L (2022) The critical role of magma degassing in sulphide melt mobility and metal enrichment. Nat Commun 13:2359.

Klemme S, Günther D, Hametner K, Prowatke S, Zack T (2006) The partitioning of trace elements between ilmenite, ulvospinel, armalcolite and silicate melts with implications for the early differentiation of the moon. Chem Geol 234:251–263.

Kontak DJ (2004) Analysis of evaporate mounds as a complement to fluid-inclusion thermometric data: case studies from granitic environments in Nova Scotia and Peru. Canad Mineral 42:1315–1329.

Pochon A, Gapais D, Gloaguen E, Gumiaux C, Branquet Y, Cagnard F, Martelet G (2016a) Antimony deposits in the Variscan Armorican belt, a link with mafic intrusives? Terra Nova 28:138–145.

Pochon A, Gloaguen E, Branquet Y, Poujol M, Ruffet G, Boiron MC, Boulvais P, Gumiaux C, Cagnard F, Gouazou F, Gapais D (2018) Variscan Sb-Au mineralization in Central Brittany (France): A new metallogenic model derived from the Le Semnon district. Ore Geol Rev 97:109–142.

Pochon A, Iacono-Marziano G, Gloaguen E, Tuduri J, Erdmann S (2023) High-temperature alteration during cooling of mafic intrusions: Insights from the Saint-Jean-du-Doigt intrusive complex (Armorican Massif, France). Lithos 436–437:106977.

Putnis A, Austrheim H (2010) Fluid-induced processes: Metasomatism and metamorphism. Geofluids 10:254–269.

Shepherd K, Namur O, Toplis MJ, Devidal JL, Charlier B (2022) Trace element partitioning between clinopyroxene, magnetite, ilmenite and ferrobasaltic to dacitic magmas: an experimental study on the role of oxygen fugacity and melt composition. Contrib Mineral Petrol 177:90.

Magnetite composition as petrogenetic and fertility indicator for Fe-Ti-V-(P) mineralization in Archean mafic-ultramafic intrusions within the Superior Province, Canada

Anne-Aurélie Sappin[1], Michel G. Houlé[1]
[1] Geological Survey of Canada, Lands and Mineral Sector, Natural Resources Canada, Québec City

Abstract. Magnetite composition from several Archean mafic to ultramafic intrusions within the Superior Province was characterized to be used as petrogenetic and fertility indicator for Fe-Ti-V-(P) mineralization. The composition of magnetite could be partially influenced by a number of factors, including the presence of exsolutions and inclusions and the element partitioning with co-crystallized minerals. Nevertheless, the global composition of magnetite in compatible (e.g., Mg, V, Cr) and incompatible (e.g., Al, Mn, Ti) elements provides helpful information regarding the degree of differentiation of each host intrusion but also among themselves. In magnetite discrimination diagrams (e.g., Ca+Al+Mn versus Ti+V, Ni+Cr versus Ti+V), magnetite from these Archean intrusions is characterized by lower Ti+V values than expected, with magnetite composition mostly plotting within fields for hydrothermal deposits rather than within fields for Fe-Ti-V-(P) deposits. Considering that the Fe-Ti-V-(P) deposit fields in these diagrams were mainly defined based on Fe-oxides hosted within Proterozoic and Phanerozoic Fe-Ti deposits, the preliminary results suggest that magnetite from Archean Fe-Ti deposits has lower Ti and/or V contents than magnetite from younger deposits.

1 Introduction

It is now well established that magnetite is a useful petrogenetic tracer and suitable indicator mineral for mineral exploration (e.g., Dare et al. 2012, 2014; Duran et al. 2020 and references therein). However, despite the numerous studies published in recent years, only a few of them focussed on magnetite associated with Fe-Ti-V-(P) deposits hosted by Archean mafic and ultramafic intrusions (e.g., Polivchuk 2017; Arguin et al. 2018; Mathieu 2019). The Superior Province with its numerous prospective units for this type of mineralization appears as an ideal area to study the compositional variations of magnetite in Archean mafic-ultramafic intrusions hosting Fe-Ti-V-(P) mineralization. As part of this study, eight Meso- to Neoarchean mafic and ultramafic intrusions distributed throughout the province were selected to characterize their magnetite composition (Fig. 1). These intrusions include the Croal Lake (i.e., Kasabonika), Big Mac, and Butler (East and West) intrusions from the Ring of Fire intrusive suite and the Highbank-Fishtrap intrusive complex within the Oxford-Stull domain, the Oxtoby Lake and Wabassi Main intrusions within the Uchi domain, the Baie Chapus Pyroxenite within the La Grande Rivière domain, and the Rivière Bell and Lac Doré complexes within the Abitibi greenstone belt in the Wawa-Abitibi terrane. The determination of the chemical composition of their magnetite will help to understand which factors influence their composition, how magnetite can be used as petrogenetic and fertility indicator for Fe-Ti-V-(P) mineralization in Archean mafic to ultramafic intrusions, and the efficiency of discrimination diagrams to determine the mineral deposit setting in which magnetite formed.

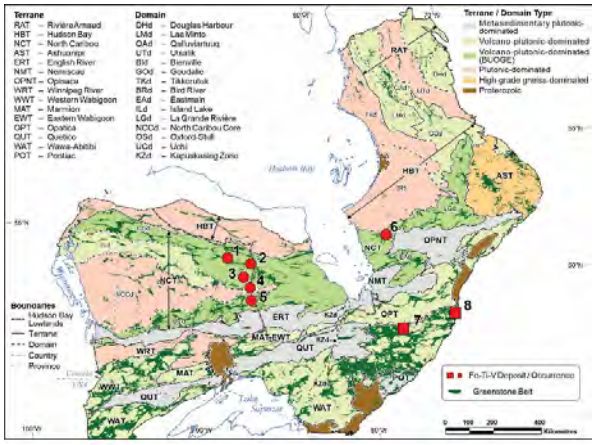

Figure 1. Geological map showing the location of the studied mafic to ultramafic intrusions across the Superior Province (after Houlé et al. 2020). Terrane and domain boundaries are modified from Stott et al. (2010), Percival et al. (2012), and SIGÉOM (2020). Intrusion names: 1 – Croal Lake; 2 – Big Mac; 3 – Butler West and East; 4 – Highbank-Fishtrap; 5 – Oxtoby Lake and Wabassi Main; 6 – Baie Chapus Pyroxenite; 7 – Rivière Bell; 8 – Lac Doré.

2 Sampling and methodology

Magnetite of the studied intrusions is hosted by either oxide-bearing mafic to ultramafic rocks (<40% Fe-Ti oxides) or by semi-massive to massive Fe-Ti oxides (40–80% and >80% Fe-Ti oxides, respectively). The oxide-bearing samples are from the mafic-dominated Croal Lake, Big Mac, Butler, Highbank-Fishtrap, Oxtoby Lake, Wabassi Main, and Lac Doré intrusions and the ultramafic-dominated Baie Chapus Pyroxenite. The semi-massive and massive Fe-Ti oxide samples are from the Croal Lake, Big Mac, Highbank-Fishtrap, and Baie Chapus intrusions and the mafic-dominated Rivière Bell intrusion.

Magnetite grains were analyzed by EPMA at the Université Laval (Québec, Canada) and by LA-ICP-MS at the Geological Survey of Canada (Ottawa, Canada) to determine their trace element contents.

The spot analyses by EPMA mostly exclude the ilmenite exsolutions/inclusions, whereas those by LA-ICP-MS include the ilmenite exsolutions formed during subsolidus exsolution-oxidation processes.

3 Magnetite composition from mafic to ultramafic intrusion

In the oxide-bearing mafic and ultramafic rocks, magnetite composition in compatible elements (e.g., Mg, V, Ni, and Cr) and incompatible elements (e.g., Al, Mn, and Ti) during fractionation processes varies from intrusion to intrusion (Figs. 2A, 2B). Magnetite from the Croal Lake, Big Mac, Butler, and Highbank-Fishtrap intrusions has high Cr and locally V contents. Magnetite from the Oxtoby Lake intrusion has low Mg contents, relatively low Cr, Al, and Mn contents, and the lowest Ti contents. Magnetite from the Wabassi Main intrusion has the highest Mg and Co contents and high V, Ni, Cr, Al, Mn, and Ti contents. Magnetite from the Lac Doré complex has low V contents, relatively low Mg and Cr contents, and the lowest Ni contents, but high Mn, Ti, and Zn contents. In addition, magnetite from the Baie Chapus Pyroxenite has the highest Ni contents, relatively high Mg contents, and low V, Cr, and Al contents.

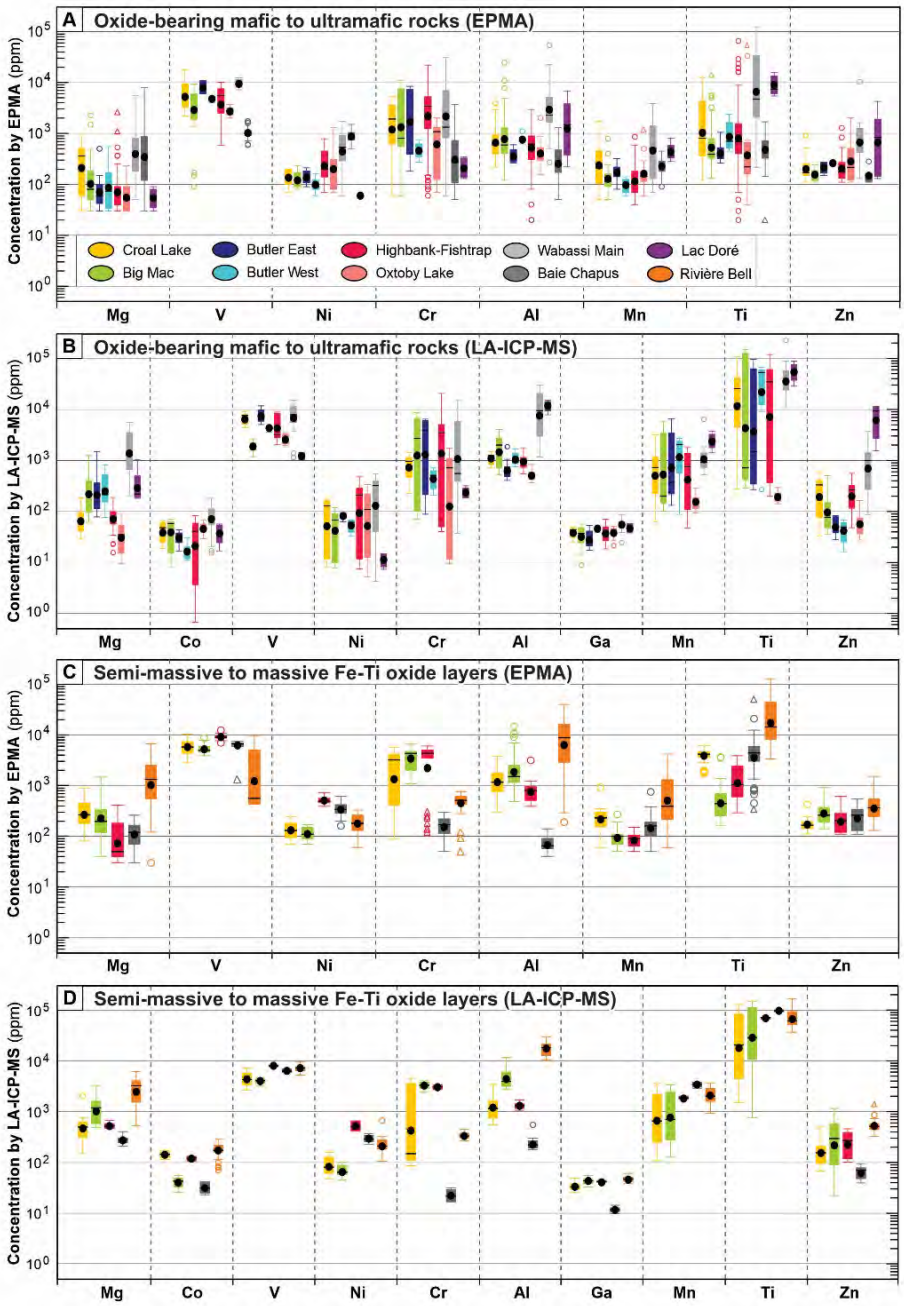

Figure 2. Box and whisker plots of selected trace elements in magnetite analyzed by (A) EPMA and (B) LA-ICP-MS in the oxide-bearing samples and (C) EPMA and (D) LA-ICP-MS in the semi-massive to massive Fe-Ti oxide layers. The upper and lower margins of the box represent the upper 75% and lower 25% of the data. The whiskers represent the upper and lower threshold values (95% of the data). Median values are shown as solid black lines and mean values as solid black circles. Outliers are shown as open circles and far outlier as open triangles along the whisker.

Similarly, the chemical signature of the magnetite from the semi-massive and massive Fe-Ti oxides differs from one intrusion to another (Figs. 2C, 2D). Magnetite from the Croal Lake and Big Mac intrusions has relatively high Mg and Cr contents. In contrast, magnetite from the Highbank-Fishtrap complex has relatively low Mg contents but high Cr contents. In the Rivière Bell complex, the Fe-oxides have been affected by regional/local metamorphism and most of their primary composition, except for V and Cr, has been modified (Polivchuk 2017); these Fe-oxides show relatively low V and Cr contents. Finally, magnetite from the Baie Chapus Pyroxenite has intermediate Ni contents, relatively high Mn contents, locally low Mg and Zn contents, and the lowest Co, Cr, Al, and Ga contents.

4 Discrimination diagram

In all the discrimination diagrams used to distinguish magnetite from hydrothermal or Fe-Ti-V-(P) deposits and defined based on Fe-oxide compositions determined by EPMA (e.g., Dupuis and Beaudoin 2011; Méric 2011; Fig. 3), magnetite from the studied Archean intrusions shows significantly lower Ti+V contents than expected and plots predominantly within the field for hydrothermal deposits rather than within the field for Fe-Ti-V-(P) deposits for our EPMA results. An exception is the Rivière Bell magnetite, which plots predominantly within the Fe-Ti-V deposit field. In contrast, the LA-ICP-MS data for the magnetite grains generally plot within the Fe-Ti-V-(P) deposit fields in these discrimination diagrams.

5 Discussion and conclusions

Trace element contents of magnetite obtained by EPMA are generally in good agreement with those obtained by LA-ICP-MS (Fig. 2). However, some of these data show small discrepancies, like for Al, Mn, Ti, and Zn (Fig. 2). These differences are related to the presence of exsolutions, in particular ilmenite exsolutions that are incorporated during the LA-ICP-MS analyses and not in the EPMA analyses and commonly explain the variations in Al, Mn, and Ti. But some of these variations (e.g., for Si, Ca, and Zn) are better explained by the presence of mineral inclusions (e.g., silicates, sulfides). The composition of magnetite is also influenced by the co-crystallizing minerals. In the Baie Chapus Pyroxenite, for example, magnetite grains in the pyroxenite have a relatively primitive composition with high Mg and Ni contents and low Al contents (Figs. 2A, 2B). However, they show lower Cr and V contents than expected (Figs. 2A, 2B). These low Cr contents could result from the fractional crystallization of chromite at depth, whereas the depletion in V of magnetite from the pyroxenite could be explained by the high proportion of clinopyroxene in this rock type, in which V also partitions ($D_V^{Cpx/Basaltic\ melt}$ = 3.1: Hart and Dunn 1993).

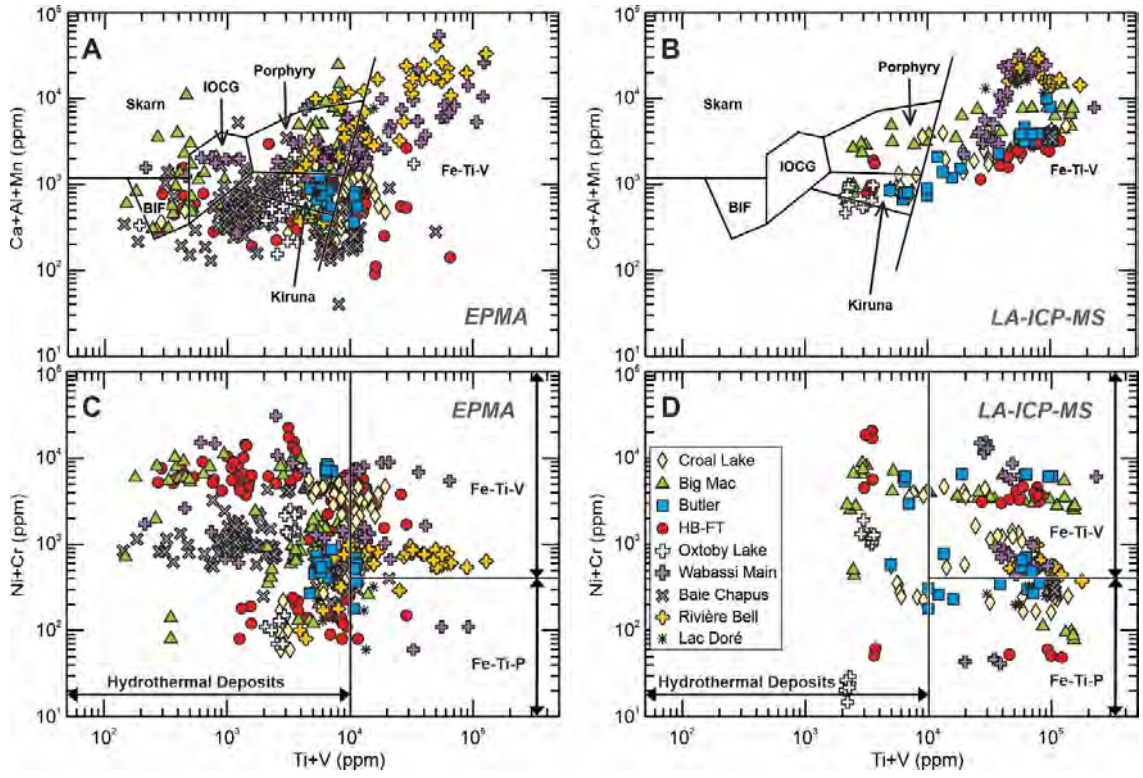

Figure 3. Discrimination diagrams of magnetite composition from hydrothermal and Fe-Ti-V-(P) deposits. Ca+Al+Mn versus Ti+V diagram for results determined by (A) EPMA and (B) LA-ICP-MS. Ni+Cr versus Ti+V diagram for results determined by (C) EPMA and (D) LA-ICP-MS. Each data point represents an individual magnetite grain. Abbreviations: BIF = banded iron formation, IOCG = iron oxide copper-gold. The fields in discrimination diagrams (A) and (B) are from Dupuis and Beaudoin (2011), and those in (C) and (D) are from Méric (2011).

The overall composition of magnetite, however, appears to be mainly independent of the host-rock type and gives us clues regarding the degree of fractionation of the host intrusion. Based on the chemical signature of magnetite from the studied mafic-dominated intrusions (Fig. 2), it appears that the Rivière Bell and Lac Doré complexes have the most evolved composition, whereas the Croal Lake, Big Mac, Butler, Highbank-Fishtrap and Wabassi Main intrusions are the most primitive. Identifying the most primitive and evolved intrusions will help detecting which intrusions in the Superior are most likely to host Fe-Ti-V-P mineralization.

In the discrimination diagrams, it appears that for results determined by EPMA (Figs. 3A, 3C), magnetite from the studied Archean intrusions has lower Ti+V contents than magnetite from the Proterozoic and Phanerozoic Fe-Ti deposits used to construct the diagrams. The distinct chemical signature of the Rivière Bell magnetite (higher Ti+V contents; Figs. 3A, 3C) could be due to omnipresent fine ilmenite exsolutions in the Fe-oxide grains and/or late Ti remobilization during metamorphism (Polivchuk 2017). Preliminary results suggest that the contradiction between the Archean and Proterozoic/Phanerozoic magnetite composition could be explained by lower Ti and/or V contents in magnetite from Archean Fe-Ti deposits than from younger deposits. Further investigations are necessary to explain this difference but factors such as the change in the fugacity of oxygen or a variation in the quantity of ilmenite exsolutions can be considered. Interestingly, the LA-ICP-MS data appear better at correctly predicting the deposit type in these diagrams (Figs. 3B, 3D) as the Ti contents determined by LA-ICP-MS are often higher than those determined by EPMA. However, a fair amount of the LA-ICP-MS data points still fall into other hydrothermal deposit types (Figs. 3B, 3D).

Acknowledgements

Support for this study was provided through the Ni-Cr-PGE Systems Project's "Activity NC-2.2: Ni-Cr metallotect: Synthesis, updates, and revised models for the Superior Province" of the NRCan's Targeted Geoscience Initiative Program. We thank Northern Shield Resources Inc. (C. Vaillancourt, I. Bliss, R.-L. Simard, and G. Budulan) and R. Metsaranta from the Ontario Geological Survey for supplying representative samples; M. Choquette (Université Laval) for its technical support during EPMA analysis; and Z. Yang, D. Petts, and S.E. Jackson (Geological Survey of Canada) for their assistance with LA-ICP-MS analyses.

References

Arguin J-P, Page P, Barnes S-J, Girard R, Duran C (2018) An integrated model for ilmenite, Al-spinel, and corundum exsolutions in titanomagnetite from oxide-rich layers of the Lac Dore Complex (Quebec, Canada). Minerals 8: 1-39.

Dare SAS, Barnes S-J, Beaudoin G (2012) Variation in trace element content of magnetite crystallized from a fractionating sulphide liquid, Sudbury, Canada: implications for provenance discrimination. Geochimica et Cosmochimica Acta 88: 27-50.

Dare SAS, Barnes S-J, Beaudoin G, Meric J, Boutroy E, Potvin-Doucet C (2014) Trace elements in magnetite as petrogenetic indicators. Mineralium Deposita 49: 785-796.

Dupuis C, Beaudoin G (2011) Discriminant diagrams for iron oxide trace element fingerprinting of mineral deposit types. Mineralium Deposita 46: 319-335.

Duran CJ, Barnes S-J, Mansur ET, Dare SAS, Bedard LP, Sluzhenikin SF (2020) Magnetite chemistry by laser ablation-inductively coupled plasma-mass spectrometry records sulphide fractional crystallization in massive nickel-copper-platinum group element ores from the Norilsk-Talnakh mining district (Siberia, Russia): implications for trace element partitioning into magnetite. Economic Geology 115: 1245-1266.

Hart SR, Dunn T (1993) Experimental cpx/melt partitioning of 24 trace elements. Contributions to Mineralogy and Petrology 113: 1-8.

Houlé MG, Lesher CM, Sappin A-A, Bédard M-P, Goutier J, Yang XM (2020) Overview of Ni-Cu-(PGE), Cr-(PGE), and Fe-Ti-V magmatic mineralization in the Superior Province: Insights on metallotects and metal endowment. In: Bleeker W, Houlé MG (eds) Targeted Geoscience Initiative 5: Advances in the understanding of Canadian Ni-Cu-PGE and Cr ore systems – Examples from the Midcontinent Rift, the Circum-Superior Belt, the Archean Superior Province, and Cordilleran Alaskan-type intrusions. Geological Survey of Canada, Open File 8722, pp. 117-139.

Mathieu L (2019) Origin of the vanadiferous serpentine–magnetite rocks of the Mt. Sorcerer area, Lac Doré layered intrusion, Chibougamau, Québec. Geosciences 9: 110.

Méric J (2011) Caractérisation géochimique des magnétites de la zone critique de l'intrusion magmatique de Sept-Îles (Québec, Canada) et intégration à une base de données utilisant la signature géochimique des oxydes de fer comme outil d'exploration. Internship report, Université du Québec à Chicoutimi.

Percival JA, Skulski T, Sanborn-Barrie M, Stott GM, Leclair AD, Corkery MT, Boily M (2012) Geology and tectonic evolution of the Superior Province, Canada. In: Percival JA, Cook FA, Clowes RM (eds) Tectonic Styles in Canada: The LITHOPROBE Perspective. Geological Association of Canada, Special Paper 49, pp. 321-378.

Polivchuk M (2017) The formation of vanadium deposits in the Archean Riviere Bell Complex, Quebec: insights from Fe-Ti oxide chemistry. MSc thesis, University of Ottawa.

SIGEOM (2020) Système d'information geominière du Québec. Ministère de l'Énergie et des Ressources naturelles du Québec. http://sigeom.mines.gouv.qc.ca. Accessed 9 February 2020.

Stott GM, Corkery MT, Percival JA, Simard M, Goutier J (2010) A revised terrane subdivision of the Superior Province. In: Summary of Field Work and Other Activities 2010. Ontario Geological Survey, Open File Report 6260, pp. 20-1–20-10.

Crustal S sources for komatiite hosted Ni deposits and implications for sulfide transport and deposition

Anne Brandt Virnes[1], Marco L. Fiorentini[1], Stefano Caruso[1,2], Kim Baublys[3], Quentin Masurel[1], Nicolas Thebaud[1]
[1]Centre for Exploration Targeting, School of Earth Sciences, The University of Western Australia, Perth, WA
[2]Commonwealth Scientific and Industrial Research Organization, Mineral Resources, Kensington, WA
[3]School of Earth and Environmental Sciences, The University of Queensland, Brisbane, Qld

Abstract. Previous S isotope works suggested that the Mount Keith and Cliffs komatiite hosted Ni deposits in the Yilgarn Craton of Western Australia formed in different volcanic environments. The Mount Keith deposit was interpreted to have formed near the komatiite vent and a VMS style S source in the felsic volcanic substrate, whereas the Cliffs deposit formed at a distal position on a basaltic substrate. It was inferred that the felsic stratigraphic substrate at Mount Keith was more prospective than the mafic substrate at Cliffs. However, recent modelling of metal upgrading during transport of assimilated crustal sulfides in komatiites indicates a positive relationship between the travel distance and the resulting metal tenors of the deposited sulfides. This relationship has not been observed between the Mount Keith and Cliffs deposits. New S isotope data from the Cliffs Ni deposit confirm the presence of a VMS style source in the immediate footwall to the deposit. We suggest that the Cliffs Ni deposit also formed in a rift environment, proximal to its crustal S source. This implies that rift environments where bimodal magmatism occurs, mafic-hosted systems may be as prospective as felsic-hosted ones, significantly increasing the search space for high-tenor mineralisation associated with komatiites.

1 Introduction

Komatiites require assimilation of crustal sulfur to form Ni deposits (e.g., Lesher and Burnham 2001; Ripley and Li 2013; Barnes et al. 2016). Sulfur isotopes applied to the Type I Cliffs and Type II Mount Keith komatiite hosted Ni deposits, Agnew-Wiluna Greenstone Belt (AWB), Western Australia, showed that both deposits likely assimilated Archaean seawater derived, volcanogenic massive sulfides (VMS; Bekker et al. 2009). Our previous work confirmed a VMS style sulfide source for the Mount Keith Ni deposit and showed that komatiite hosted Ni sulfides largely preserve their crustal mass-independent S isotopic signatures (MIF-S, denoted $\Delta^{33}S$; Virnes et al., 2023).

VMS style sulfides in the AWB were mainly identified in felsic volcanic rocks underlying the Mount Keith Ultramafic Unit (MKU), whereas basalt underlying the Cliffs Ultramafic Unit (CLU) was thought to only contain sedimentary sulfides (Bekker et al. 2009; Fiorentini et al. 2012; Perring 2015). The felsic volcanic rocks were interpreted to mark the central part of a palaeo-rift, with the basalt dominating in rift-distal environments (Fiorentini et al. 2012). As the Cliffs and Mount Keith Ni deposits both sourced VMS style sulfides, it was inferred that the deposits formed proximal and distal to the palaeo-rift and the VMS style S source, respectively. Most komatiite hosted Ni deposits in the AWB are associated with felsic volcanic substrates, with few exceptions such as Cliffs. Felsic hosted komatiites were thus deemed more prospective for Ni deposits than mafic hosted bodies in bimodal systems (Fiorentini et al. 2012).

Recent work by Yao and Mungall (2021) showed that metal tenors of magmatic sulfides are positively correlated with distance from their crustal S source. However, the metal tenors of the Cliffs Ni deposit are not markedly higher than those from the Mount Keith Ni deposit (Perring 2015). This questions whether Cliffs really formed distal to the rift axis and from its crustal S source as previously proposed. Perring (2015) reported potential VMS style sulfides from the basal footwall to CLU, which until now had not been analysed for S isotopes. Their presence, however, suggests that the Cliffs Ni deposit, and basaltic hosted komatiite ores in general, may also have formed close to the rift and crustal S source.

To test this hypothesis, we characterised the S isotopic composition of sedimentary and VMS style sulfide horizons in the predominantly basaltic footwall to the CLU and compared them to that of the magmatic sulfides from the Cliffs Ni deposit. This dataset is used to evaluate if even basaltic hosted systems in the AWB formed proximal to a rift environment and thus can be considered as prospective for Ni mineralisation. These results are also used to discuss the transport and depositional mechanisms for komatiite hosted ore systems.

2 Regional geology

The AWB is located in the central northern part of the Archaean Yilgarn Craton, Western Australia (Fig. 1; Cassidy et al. 2006) and consists of a ca. 2825-2655 Ma greenstone succession comprising basalt, komatiite, felsic volcanic and volcaniclastic rocks, conglomerate and minor shale and chert (Hayman et al. 2015; Gole et al. 2019; Masurel et al. 2022). The greenstone succession has been divided into 5 cycles comprising 1) early mafic-ultramafic volcanism related to crustal thinning of proto-Yilgarn; 2) craton-wide felsic and mafic volcanism likely related to uplift from plume impingement; 3) early rift related bimodal volcanism followed by a main ultramafic-mafic plume related LIP event, which formed the CLU; 4) felsic volcanism and granitic doming during late stage plume event; 5) basin inversion and formation of molasse style conglomerates (Masurel et al. 2022).

The Cliffs Ni deposit in located in the Mount Keith region in the northern part of the AWB (Fig. 1). The stratigraphic substate to the CLU hosting the Cliffs Ni deposit consists mainly of the massive to pillowed Never Can Tell Basalt (NCBT; Hayman et al. 2015), and minor Mount Keith Dacite (MKD; Rosengren et al. 2008), which are both part of the cycle 3 incipient rift related bimodal volcanism (Masurel et al. 2022).

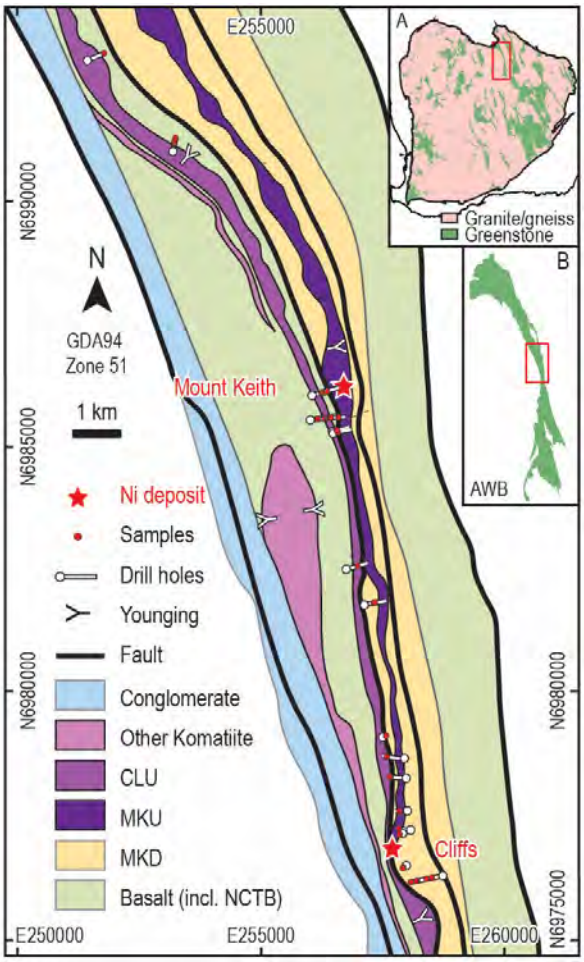

Figure 11. Geology of the Mount Keith region, Agnew-Wiluna Greenstone Belt (AWB; inset B), Yilgarn Craton (inset A), with drill hole traces and sample locations. CLU: Cliffs Ultramafic Unit, MKU: Mount Keith ultramafic Unit, MKD; Mount Keith Dacite, NCTB: Never Can Tell Basalt. Modified from Perring (2015).

3 Materials and methods

Fifty-one samples were collected from 18 drill cores from the Mount Keith region (Fig. 1). All samples were classified based on their sulfide parageneses, which was corroborated via petrographic analysis using optical microscopy. Eleven samples were magmatic Ni sulfides from the CLU at the Cliffs Ni deposit, 25 and 3 samples were of VMS style sulfides from NCTB and MKD, respectively, and 12 samples were interflow sediments from NCTB. All samples were analysed for multiple S isotopes by EA-IRMS at the Stable Isotope Geochemistry Laboratory, University of Queensland, following a modified procedure described in Baublys et al. (2004). Historical S isotope data from the CLU (Bekker et al. 2009) are presented with the results.

4 Results

Magmatic Ni sulfides from the CLU consist mainly of pyrrhotite, pentlandite and minor chalcopyrite. They vary from disseminated blebby and cloudy droplets in serpentinised olivine cumulate (Fig. 2A) to massive sulfide lenses at the base of the CLU unit (Fig 2B). Values of $\delta^{34}S$ range from ca. -5.8‰ to -0.3‰ with a median of ca. -3.1‰ (Fig. 3A). The $\Delta^{33}S$ values range from and ca. -1.3‰ to +0.1‰ with a median of ca. -0.51‰ (Fig. 3A).

Sedimentary sulfides occur as nodules or finely disseminated to bedding-parallel stringers in shales and mudstones (Fig 2C). Sulfide phases are mostly pyrrhotite and lesser chalcopyrite, partially replaced by metamorphic pyrite. Values of $\delta^{34}S$ range from ca. -5.7‰ to +4.8‰ with a median of ca. +2.0‰. The $\Delta^{33}S$ values range from ca. -0.3‰ to +3.9‰ with a median of ca. +1.2‰ (Fig. 3A). Sedimentary sulfides were observed in the central and northern part of the region, with the most positive $\Delta^{33}S$ values found mainly in the Mount Keith mine area (Fig. 3B).

The VMS style sulfides are pyrrhotite and lesser chalcopyrite, often replaced by metamorphic pyrite. Sulfides occur as disseminations, amygdule fillings, interpillow- and fragment vein fill (Fig. 2D and E) and semi-massive lenses in their host rocks. Values of $\delta^{34}S$ range from ca. -6.4‰ to +10.9‰ with a median of ca. +2.3‰. The $\Delta^{33}S$ values range from ca. -1.5‰ to +3.6‰ with a median of ca. -0.3‰ (Fig. 3A). The most negative $\Delta^{33}S$ values occur in the north and south of the region, while the least negative values coincide with the presence of sedimentary sulfides in the central part of the region (Fig. 3B).

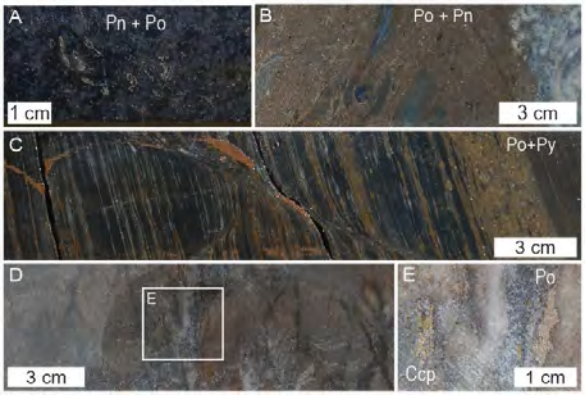

Figure 12. Examples of sulfide styles. A) Cloudy disseminations in CLU. B) Massive sulfide in CLU. C) Nodular and bedding-parallel stringer sulfides in shale. D) Vein sulfides in hydrothermally altered, bleached fragmental basalt. E) Close up on vein sulfides in D.

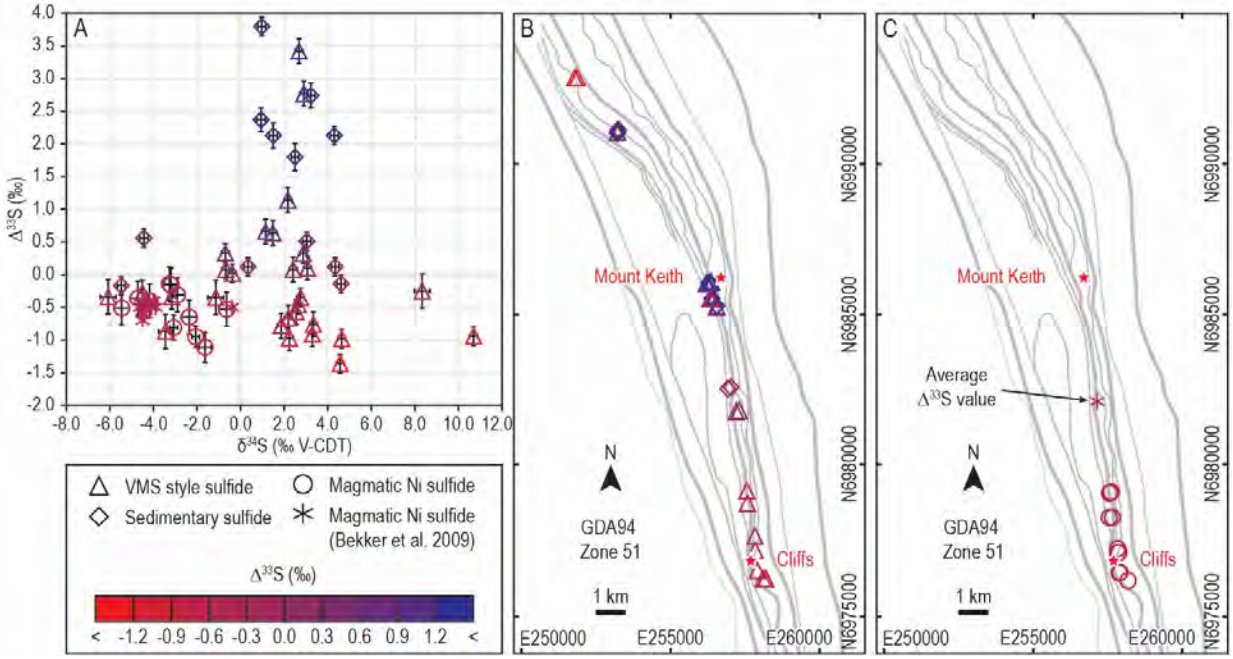

Figure 13. A) Plot of $\delta^{34}S$-$\Delta^{33}S$ coloured by $\Delta^{33}S$ variation. Error bars are 2σ absolute uncertainties. B) Spatial distribution and $\Delta^{33}S$ variability of sulfides in the stratigraphic footwall to the CLU. C) Spatial distribution and $\Delta^{33}S$ variability of magmatic Ni sulfides from the CLU.

5 Discussion

5.1 Sulfur source reservoirs in the Mount Keith region

The sedimentary sulfides in the Mount Keith region generally have positive $\delta^{34}S$ and $\Delta^{33}S$ values (Fig. 3A), consistent with a MIF-S reduced species transformed into sulfide without significant mass-dependent fractionation (Johnston 2011). The hydrothermal sulfides show a wider range in $\delta^{34}S$ values and are generally $\Delta^{33}S$ negative or plot around ~0‰ (Fig. 3A), indicative of being derived from both seawater and magmatic reservoirs (Johnston 2011). The wide range of $\delta^{34}S$ values suggests a predominantly closed system with respect to the sea water sulfate reservoir during the time of sulfide precipitation (Seal 2006), consistent with the AWB forming as a failed continental rift closed off from the wider ocean (Masurel et al. 2022). A minor set of hydrothermal sulfides have positive $\Delta^{33}S$ values (Fig. 3A) and coincide spatially with $\Delta^{33}S$ positive sedimentary sulfides (Fig. 3B), suggesting that the former may have reworked pre-existing sedimentary sulfides.

5.2 Mafic-hosted komatiite systems may form proximal to their crustal S source

Based on the dataset of by Bekker et al. (2009) the mafic hosted CLU and related Ni mineralisation was proposed to have formed at a distal position to the rift axis and its crustal S source (Fiorentini et al. 2012). Our new dataset has identified sulfides related to VMS style hydrothermal alteration in the NCTB immediately beneath the CLU-NCTB contact. The S-isotopic signatures of these hydrothermal sulfides (Fig. 3B) are similar to those in the overlying Cliffs Ni deposit (Fig. 3C), and generally provide a better fit compared to the other occurrences in the region. The correlation between the magmatic and hydrothermal $\Delta^{33}S$ values highlights the increased possibility that the Cliffs Ni deposit formed proximal to its S source. The Cliffs Ni deposit thus need not be a distal version of the komatiite system that formed the Mount Keith Ni deposit. This is consistent with the lack of significantly different metal tenors between the two deposits (Perring 2015) as otherwise predicted by the models of Yao and Mungall (2021).

5.3 Implications for the dynamics of sulfide metal enrichment during transport

Yao and Mungall (2021) showed that significant lateral travel distance of assimilated crustal sulfide droplets was needed for them to equilibrate with enough silicate melt to concentrate economic levels of metals. However, the fact that Cliffs Ni deposit formed proximal to its crustal S source precludes extensive lateral movement of the sulfide liquid. Consequently, this indicates that pre-enrichment of metals in the sulfide liquid must happen close to the S source, prior to deposition as a typical Type I basal massive sulfide mineralisation.

A possible mechanism for such proximal metal enrichment involves the komatiite lava flowing over topographical steps (such as faults) in the substrate (Yao and Mungall 2022). Complex flow patterns, vortices and eddies are created in the wake of these steps, significantly increasing the potential for entrapment and re-entrainment of transported sulfide droplets. This effectively increases the amount of silicate melt that the sulfide can interact

with during very limited lateral transport (Yao and Mungall 2022). The multitude of faults, high topographical variation, and increased likelihood of VMS style sulfide occurrences make proximal parts of rift settings ideal locations for the enhancement of this process (e.g., Corti et al. 2018). The magmatic $\Delta^{33}S$ signatures and the proximity to the potential crustal VMS style S source indicates that, similar to the Mount Keith deposit, the Cliffs Ni deposit also formed in such a rift proximal environment. This supports that mafic parts of bimodally hosted komatiite systems should be considered as prospective as the felsic counterparts.

6 Conclusions

Contrary to previous models, the mafic hosted Cliffs Komatiite Ni deposit likely formed proximal to a palaeo-rift axis and a VMS style crustal S source, suggesting that mafic hosted komatiite ore systems are equally prospective as felsic hosted systems in bimodal volcanic regions.

The proximity of the Ni deposit to its crustal S source emphasises the importance of complex flow dynamics and multistage entrapment and re-entrainment of assimilated and transported sulfide droplets rather than extensive lateral flow and distal deposition of sulfide mineralisation.

Acknowledgements

ABV is supported by the UWA Postgraduate Award for International Students and the UWA International Fee Scholarship. This project was funded by the Minerals Research Institute of Western Australia (MRIWA) M530 Yilgarn 2020 collaborative research project. BHP NickelWest is thanked for facilitating fieldwork, access to drill cores, sampling, and technical support.

References

Barnes SJ, Cruden AR, Arndt N, Saumur BM (2016) The mineral system approach applied to magmatic Ni–Cu–PGE sulphide deposits. Ore Geology Reviews 76:296-316. doi: https://doi.org/10.1016/j.oregeorev.2015.06.012.

Baublys KA, Golding SD, Young E, Kamber BS (2004) Simultaneous determination of δ33SV-CDT and δ34SV-CDT using masses 48, 49 and 50 on a continuous flow isotope ratio mass spectrometer. Rapid Communications in Mass Spectrometry 18:2765-2769. doi: https://doi.org/10.1002/rcm.1681.

Bekker A, Barley ME, Fiorentini ML, Rouxel OJ, Rumble D, Beresford SW (2009) Atmospheric Sulfur in Archean Komatiite-Hosted Nickel Deposits. Science 326:1086-1089. doi: https://doi.org/10.1126/science.1177742.

Cassidy KF, Champion DC, Krapez B, Barley ME, Brown SJA, Blewett RS, Groenewald P, Tyler IM (2006) A revised geological framework for the Yilgarn Craton, Western Australia. Geological Survey of Western Australia, Record 2006/8.

Corti G, Molin P, Sembroni A, Bastow ID, Keir D (2018) Control of Pre-rift Lithospheric Structure on the Architecture and Evolution of Continental Rifts: Insights From the Main Ethiopian Rift, East Africa. Tectonics 37:477-496. doi: https://doi.org/10.1002/2017TC004799.

Fiorentini ML, Beresford SW, Barley ME, Duuring P, Bekker A, Rosengren N, Cas R, Hronsky J (2012) District to Camp Controls on the Genesis of Komatiite-Hosted Nickel Sulfide Deposits, Agnew-Wiluna Greenstone Belt, Western Australia: Insights from the Multiple Sulfur Isotopes. Economic Geology 107:781-796. doi: https://doi.org/10.2113/econgeo.107.5.781.

Gole MJ, Western E, Diragitch A (2019) A revised stratigraphic model for the 2.7 Ga Agnew-Wiluna greenstone belt, Yilgarn Craton, Western Australia. Ore and Energy Resource Geology 1:100001. doi: https://doi.org/10.1016/j.oreoa.2019.100001.

Hayman PC, Thébaud N, Pawley MJ, Barnes SJ, Cas RAF, Amelin Y, Sapkota J, Squire RJ, Campbell IH, Pegg I (2015) Evolution of a ~2.7Ga large igneous province: A volcanological, geochemical and geochronological study of the Agnew Greenstone Belt, and new regional correlations for the Kalgoorlie Terrane (Yilgarn Craton, Western Australia). Precambrian Research 270:334-368. doi: https://doi.org/10.1016/j.precamres.2015.09.016.

Johnston DT (2011) Multiple sulfur isotopes and the evolution of Earth's surface sulfur cycle. Earth-Science Reviews 106:161-183. doi: https://doi.org/10.1016/j.earscirev.2011.02.003.

Lesher CM, Burnham OM (2001) Multicomponent elemental and isotopic mixing in Ni-Cu-(PGE) ores at Kambalda, Western Australia. The Canadian Mineralogist 39:421-446. doi: https://doi.org/10.2113/gscanmin.39.2.421.

Masurel Q, Thébaud N, Sapkota J, De Paoli MC, Drummond M, Smithies RH (2022) Stratigraphy of the Agnew-Wiluna Greenstone Belt: review, synopsis and implications for the late Mesoarchean to Neoarchean geological evolution of the Yilgarn Craton. Australian Journal of Earth Sciences 69:1149-1176. doi: https://doi.org/10.1080/08120099.2022.2102076.

Perring CS (2015) Volcanological and Structural Controls on Mineralization at the Mount Keith and Cliffs Komatiite-Associated Nickel Sulfide Deposits, Agnew-Wiluna Belt, Western Australia—Implications for Ore Genesis and Targeting. Economic Geology 110:1669-1695. doi: https://doi.org/10.2113/econgeo.110.7.1669.

Ripley EM, Li C (2013) Sulfide Saturation in Mafic Magmas: Is External Sulfur Required for Magmatic Ni-Cu-(PGE) Ore Genesis? Economic Geology 108:45-58. doi: https://doi.org/10.2113/econgeo.108.1.45.

Rosengren NM, Cas RAF, Beresford SW, Palich BM (2008) Reconstruction of an extensive Archaean dacitic submarine volcanic complex associated with the komatiite-hosted Mt Keith nickel deposit, Agnew-Wiluna Greenstone Belt, Yilgarn Craton, Western Australia. Precambrian Research 161:34-52. doi: https://doi.org/10.1016/j.precamres.2007.06.012.

Seal RR, II (2006) Sulfur Isotope Geochemistry of Sulfide Minerals. Reviews in Mineralogy and Geochemistry 61:633-677. doi: https://doi.org/10.2138/rmg.2006.61.12.

Virnes AB, Fiorentini ML, Barnes SJ, Caruso S, Martin LAJ, Aleshin ME, Schoneveld LE, Roberts MP, Masurel Q, Thebaud, N (2023) Decoupling of sulfur isotope signatures from platinum group elements in komatiite-hosted ore systems: evidence from the Mount Keith MKD5 Ni Deposit, Western Australia. Manuscript submitted for publication.

Yao Z-s, Mungall JE (2021) Kinetic controls on the sulfide mineralization of komatiite-associated Ni-Cu-(PGE) deposits. Geochimica et Cosmochimica Acta 305:185-211. doi: https://doi.org/10.1016/j.gca.2021.05.009.

Yao Z-s, Mungall JE (2022) Transport and deposition of immiscible sulfide liquid during lateral magma flow. Earth-Science Reviews 227:103964. doi: https://doi.org/10.1016/j.earscirev.2022.103964.

Magmatic Black Shale Assimilation and the Formation of Sulphide Deposits – Perspectives from Experiments and Thermodynamic Simulations

Ville J. Virtanen[1]
[1]*Institute des Sciences de la Terre d'Orléans (ISTO), CNRS-Université d'Orléans-BRGM, France*

Abstract. Magmatic assimilation of sulphur (S)-bearing black shales can lead to the formation of economically significant Cu-Ni(-PGE) sulphide deposits. Liberation of S from black shales as well as the chemical interaction between the black shale and magma are complex non-linear processes that are intricately linked to the deposition of sulphide, yet these remain poorly understood. Experimental work and computational thermodynamic simulations can shed light on the details of these processes and help in identifying key parameters for exploration purposes. Here, I review recent experiments and thermodynamic simulations of magmatic black shale assimilation related to the mineralized intrusions of the Duluth Complex. The experiments show what reactions contribute to progressive S liberation during black shale devolatilization and partial melting. The thermodynamic simulations demonstrate the effects of black shale assimilation on magmatic sulphide precipitation. Collectively, the results provide new details to many of the processes suggested previously on the basis of field observations and geochemical data, the two main pillars of any experimental or computational work.

1 Introduction

Assimilation of sedimentary sulphur (S) by high-temperature komatiitic and basaltic magmas greatly improves the probability for the formation of economically important Cu-Ni(-PGE) sulphide deposits (e.g., Ripley and Li 2013; Barnes et al. 2016). However, it has been established that a close spatial association between S-rich sedimentary rocks and magmas with high assimilation potential is not an unambiguous indicator for sulphide deposits (Barnes et al. 2016). Clearly, all S-rich sedimentary rocks are not equally suitable sources for S and our understanding of the processes controlling S liberation during assimilation is still inadequate to explain the reasons why.

The predominant mode of S assimilation depends on the type of sedimentary rock and can vary as a function of temperature. Magmatic assimilation of oxidized S from anhydrite evaporites is driven by dissolution and limited by sulphate-saturation of the magma (e.g., Iacono-Marziano et al. 2017). In the case of sulphide-bearing black shales, S can be mobilized by devolatilization fluids (e.g., Ripley 1981; Thériault and Barnes 1998; Virtanen et al. 2021) or it can be transported to the magma in the form of sulphide xenocrysts or xenomelts when the host silicate material melts (e.g., Thériault and Barnes 1998; Queffurus and Barnes 2014; Samalens et al. 2017; Virtanen et al. 2021). The S liberating processes in the black shales are controlled by the main silicate and sulphide phases as well as the carbonaceous materials. Characterizing the S liberating reactions from the natural rocks can be difficult as the reaction products may be overprinted upon cooling or alteration. Laboratory experiments enable constraining the up-temperature reactions in strictly controlled conditions and without the effects of overprinting processes.

For sulphide deposits to form by assimilation, the magma must react with the S-bearing material liberated from the host sedimentary rock, which changes the magma chemistry. Again, constraining the important chemical changes affecting the sulphide saturation based on the natural rock record can be difficult due to several possible overprinting processes during cooling, magmatic recharge, or alteration. Thermodynamic simulations have shown that addition of siliciclastic sedimentary material tends to lower the sulphur content at sulphide saturation (SCSS) of magmas, hence enhancing sulphide precipitation (e.g., Ripley and Li 2013). However, the most important assimilation-induced chemical factors that control sulphide precipitation remain elusive. Modern thermodynamic modelling software, such as the Magma Chamber Simulator, enable simulating phase equilibria in continuously assimilating magmas with strict constraints on mass and heat balance (Bohrson et al. 2014). These computational simulations can help us to characterize how assimilation changes the chemical composition and phase equilibrium in the magma and contribute to sulphide precipitation.

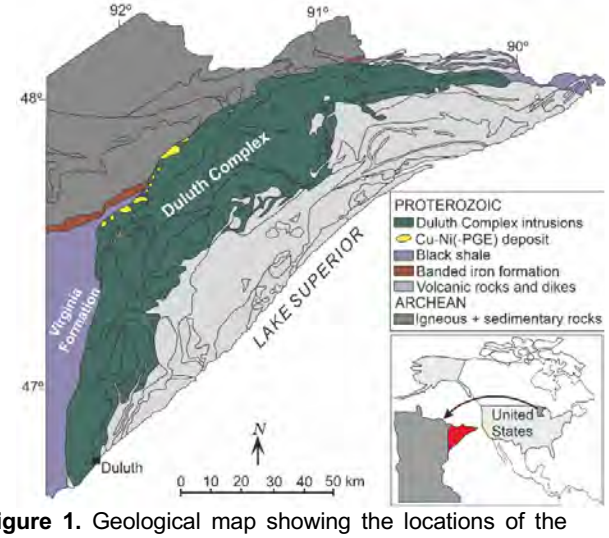

Figure 1. Geological map showing the locations of the Duluth Complex and the Virginia Formation.

The purpose of this abstract is to review the experimental work and thermodynamic simulations conducted by the author to study how black shale assimilation caused the formation of the Cu-Ni(-PGE) sulphide deposits (currently subeconomic) of the Duluth Complex, Minnesota (Fig. 1). The experiments highlight how S can be liberated from black shales, while the thermodynamic simulations focus on the sulphide precipitation in continuously assimilating magmas. A more comprehensive synthesis of the methodology and results is presented in Virtanen (2022).

2 Sulphur assimilation and magmatic sulphide saturation

2.1 Black shale devolatilization and partial melting

Virtanen et al. (2021) conducted heating experiments using a natural black shale from the Virginia Formation (Fig. 1) as the starting material. Several authors have proposed these black shales as the source of S in the Duluth Complex deposits (e.g., Ripley 1981; Thériault and Barnes 1998; Queffurus and Barnes 2014; Samalens et al. 2017). The experiments were done with externally heated pressure vessels at 200 MPa and the temperature range was 700–1000 °C. The experiments were rapidly quenched and the solid run products characterized using scanning electron microscopy. Speciation of the non-quenchable fluid phase was estimated based on mass balance calculations and thermodynamic simulations of the COHS (carbon, oxygen, hydrogen, sulphur) system.

The run products of the 700 °C experiment contain remnants of metastable muscovite and chlorite indicating incomplete devolatilization. The devolatilization fluid, however, is in equilibrium with homogeneous Cu-bearing pyrrhotite, which completely replaces the original sedimentary pyrite and chalcopyrite (Fig. 2a-b). This implies a faster equilibration rate for the sulfide-fluid system compared to that of the silicate devolatilization reactions. Mass balance calculation shows that 45 wt.% of the total S (as H_2S) and 60 wt.% of the total Cu are hosted in the fluid phase. Extrapolating these results to the devolatilized volume of the Virginia Formation, shows that the amount of liberated S is large enough to supply all of the inferred sedimentary S (ca. 75 wt.%; Ripley 1981) in the Cu-Ni(-PGE) deposits of the Duluth Complex. The same amount of fluid contains 4 Mt of Cu, which corresponds to the equivalent of roughly 15 wt.% of Cu in the Duluth Complex deposits (Listerud and Meineke 1977).

Progressing partial melting of the black shale is observed in the experiments conducted at 800–900 °C. The continuous silicate melt network hinders pervasive fluid percolation, as observed by isolated fluid bubbles and variable Cu contents in pyrrhotite. Compared to the experiment at 700 °C, pyrrhotite at 800–900 °C accommodates higher concentration of Cu at constant S/metal, which in a closed experimental system means that Cu and S partition back to the pyrrhotite from the fluid at increasing temperature. These observations imply impeded S and Cu liberation at low degrees of black shale partial melting.

At 1000 °C, silicate melt is the volumetrically dominant phase. Rounded Cu-(Ni-)bearing pyrrhotite is accompanied with Cu-rich sulphide melt and both are generally attached to fluid bubbles (Fig. 2c). The net density of the sulphide-fluid composite droplets is considerably lower than that of pure sulphide, which promotes sulphide transport between the extensively molten black shale and magma. Furthermore, if the magma is, or becomes, fluid-saturated, the sulphide-fluid pairing can aid transport of the suspended sulphides from the feeder system to the emplacement level.

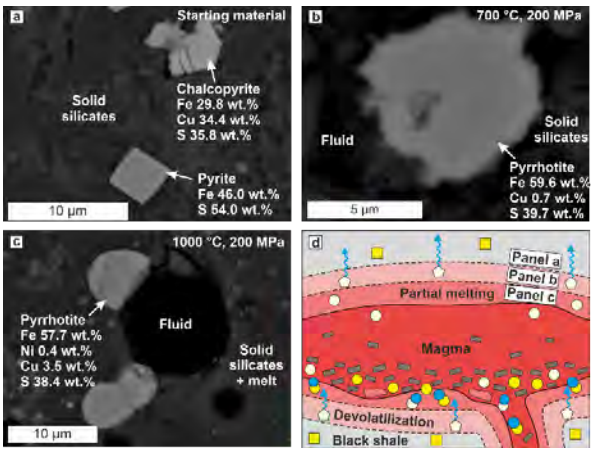

Figure 2. Back-scattered electron images of sulphides and associated phases in **a** the natural black shale starting material and the quenched experiment run product at **b** 700 °C, 200 MPa and **c** 1000 °C, 200 MPa. **d** a schematic assimilation model based on the experiment results. Yellow squares represent pyrite and chalcopyrite in the black shale host rock. White pentagons represent pyrrhotite and blue arrows fluid in devolatilization zone. White, yellow, and blue circles represent pyrrhotite and Cu-rich sulphide melt, and fluid bubbles, respectively, in partial melting zone. Silicate crystallization in the magma is indicated with brown rectangles.

Collectively, the experimental results support a view of two main stages for selective S liberation from black shales. First, devolatilization fluids can mobilize significant amounts of S and Cu, which can potentially be transported to the magma or become concentrated to suitable domains in the host rock (Fig. 2d). It should be noted that the formation of this S-bearing fluid requires the presence of pyrite and carbonaceous material in the sedimentary rock. In regionally metamorphosed black shales, pyrite may already be replaced by pyrrhotite, which is thermodynamically stable with the devolatilization fluid and hence S liberation is not expected. Subsequently, as the black shale becomes extensively partially molten, sulphide-fluid composite droplets tend to form (Fig. 2c-d). The composite droplets suspended in the partial melt are

more likely to be transported to the magma from the footwall and feeder conduit walls compared to denser unattached sulphides (Fig. 2d). This process requires extensive partial melting and is most likely to occur in xenoliths or in settings where heating is enhanced by flowing magma.

2.2 Magmatic black shale assimilation and sulphide saturation

Using the Magma Chamber Simulator, Virtanen et al. (2022) conducted thermodynamic simulations to study how black shale assimilation affects the SCSS in magma. For the simulations, we selected a basaltic parental magma composition relevant to the mineralized Duluth Complex intrusions and a black shale composition identical to the one used in the abovementioned experiments. The effects of selective assimilation of black shale partial melt and bulk assimilation on the SCSS were compared with closed-system fractional crystallization of the same magma. Mass balance of S in the magma was calculated by treating S as a trace element, because thermodynamic simulation of sulphide phase equilibrium is not currently possible with the Magma Chamber Simulator. As shown in the experiments, up-temperature S mobilization in a black shale is a complex non-linear process and cannot be precisely modelled with a constant partition coefficient. For that reason, three different coefficients were tested for S partitioning between the black shale residual and partial melt in the selective assimilation simulations: 1) completely compatible (Kd = 100), 2) equally compatible (Kd = 1), and 3) completely incompatible (Kd = 0.001). The simulation results were compared to the natural sulphide deposits to determine how effective S liberation from the black shale is required, which in turn was tentatively related to the S liberation processes identified in the experiments.

The simulations showed that the basaltic parental melt had thermodynamic potential to assimilate at least 40 wt.% of pre-heated black shale relative to the original mass of the magma regardless of the mode of assimilation (selective or bulk). Assimilation of >20 wt.% is required to replace the olivine-plagioclase dominant cumulates with orthopyroxene-plagioclase assemblages as observed in some of the natural Duluth Complex intrusions. All of the major element oxide contents, including H_2O, in the magma respond to the assimilation in such way that the SCSS diminishes. The change in magma chemistry is not only a result of the chemically mixed black shale material but is further enhanced by the changes in crystallizing phase assemblage. The formation of orthopyroxene-plagioclase cumulates as well as the first-order chemical changes affecting the SCSS are more pronounced with selective assimilation of partial melt than bulk assimilation.

One important observation is that although assimilation of S-poor black shale partial melt lowers the SCSS in the magma, the early sulphide precipitation is only slightly enhanced compared to closed-system fractional crystallization due to the diluting effect of the assimilated melt. In fact, this scenario leads to an overall sulphide grade of 0.3 wt.%, which is lower than 0.4 wt.% produced by fractional crystallization alone (Fig. 3). It is hence considered unlikely that assimilation of crustal rocks that are S-poor relative to the magma, could lead to formation of high-grade sulphide deposits.

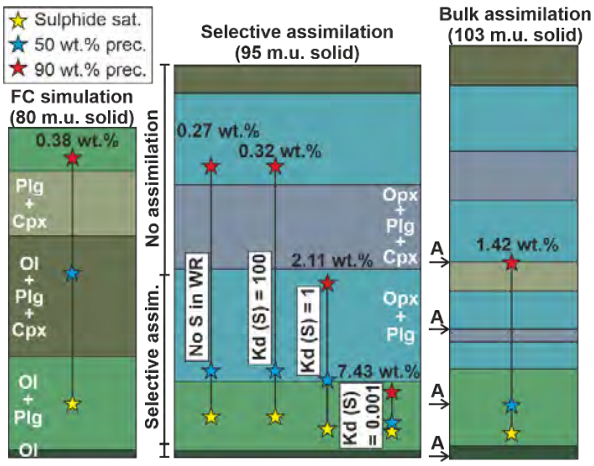

Figure 3. Thermodynamic simulation results showing cumulate stratigraphies with fractional crystallization (FC), FC + selective assimilation, and FC + bulk assimilation. Main minerals for each colour are indicated within the first two columns (Ol = olivine, Plg = plagioclase, Cpx = clinopyroxene, Opx + orthopyroxene). The column heights are scaled to the cumulates masses (mass units = m.u.). The stages of continuous selective assimilation and 10 wt.% bulk assimilation steps (A) are indicated left side of the relevant columns. The stars indicate the timing of sulphide saturation (yellow) as well as 50 (blue) and 90 wt.% (red) sulphides precipitated. The wt.% numbers indicate the average sulphide grade between the yellow and red stars without dynamic accumulation. The Kd values indicate bulk partition coefficients for sulphur (S) in the selectively assimilated black shale. See text for details about the simulations.

Based on the simulations, both selective and bulk assimilation can supply the magma with ca. 75 wt.% black shale-derived S as previously suggested for the Duluth Complex deposits (Ripley 1981). With bulk assimilation, this limit is reached when the amount of assimilated black shale is 40 wt.% relative to the original mass of the magma. Without dynamic accumulation, most of the sulphides will be scattered within the early olivine-plagioclase and the subsequent orthopyroxene-plagioclase cumulates with an average sulphide abundance of ca. 1.4 wt.% (Fig. 3). In the case of selective assimilation, S must be at least equally concentrated between the assimilated partial melt and residue (i.e., Kd ≤ 1) to fulfill the imposed natural constraint for the S mass balance. When S is equally compatible to the black shale residual and assimilated partial melt, the magmatic sulphides are distributed between the early olivine-plagioclase and orthopyroxene-plagioclase cumulates with an average grade of 2.1

wt.% (Fig. 3). Comparable S fluxes could arguably be generated either by S liberation via fluids or by sulphide transport via black shale partial melt. In the simulation where S is considered highly incompatible to the black shale residual (Kd = 0.001), the sulphides mostly reside within the olivine-plagioclase cumulates with an average grade of 7.4 wt.% (Fig. 3). It is clear that only fluid-mediated S assimilation could lead to comparably effective extraction of S from the residual black shale.

Roughly 70% of the Duluth Complex deposits are hosted in olivine-plagioclase cumulates, whereas the rest are within the orthopyroxene-plagioclase cumulates. Based on the data provided by Listerud and Meineke (1977), the average sulphide grade was tentatively estimated to be 7.3 wt.%. Comparing these natural data with the simulations, it seems that the olivine-plagioclase hosted sulphide deposits can readily form without significant dynamic accumulation if S extraction from the black shale is highly selective. With less effective S extraction from the black shale, more silicate melt is assimilated and the sulphides occur increasingly within the orthopyroxene-plagioclase cumulates. The grade of the simulated deposits is, however, low compared to the natural deposits, which means that subsequent dynamic sulphide accumulation is necessary.

3 Concluding remarks

The results from the experiments and thermodynamic simulations increase our understanding of the complexity behind the magmatic assimilation of S from black shales. As a black shale is heated by magma, it is first subjected to devolatilization and subsequently partial melting, which can both contribute to selective S and metal liberation from the solid residue. These processes are controlled by the mineralogy and carbonaceous materials in the black shale as well as by the heat flow from the magma, hence their relative importance has to be evaluated case specifically. The assimilated black shale material changes the chemistry and consequently phase equilibrium in the magma. These assimilation-induced changes tend to enhance sulphide precipitation from the magma but assimilation of external S seems to be required for economically important deposits to form.

Acknowledgements

Jussi S. Heinonen, Ferenc Molnár, Max Schmidt, Felix Marxer, Nicholas Barber, Nico Kueter, and Fabio Cafagna are thanked for their contributions to the conduction and interpretation of the experiments and numerical simulations.

References

Barnes SJ, Cruden AR, Arndt N, Saumur BM (2016) The mineral system approach applied to magmatic Ni-Cu-PGE sulphide deposits. Ore Geol. Rev. 76: 296–316. http://dx.doi.org/10.1016/j.oregeorev.2015.06.012

Bohrson WA, Spera FJ, Ghiorso MS, Brown GA, Creamer JB, Mayfield A (2014) Thermodynamic model for energy-constrained open-system evolution of crustal magma bodies undergoing simultaneous recharge, assimilation and crystallization: the Magma Chamber Simulator. J. Petrol. 55:1685–1717. https://doi.org/10.1093/petrology/egu036

Iacono-Marziano G. Ferrana C, Gaillard F, Di Carlo I, Arndt NT (2017) Assimilation of sulfate and carbonaceous rocks: Experimental study, thermodynamic modeling and application to the Noril'sk-Talnakh region (Russia). Ore Geol. Rev. 90:399–413. http://dx.doi.org/10.1016/j.oregeorev.2017.04.027

Listerud WH, Meineke DG (1977) Mineral resources of a portion of the Duluth Complex and adjacent rocks in St. Louis and Lake Counties, Northeastern Minnesota. Minnesota Department of Natural Resources Division of Minerals 93:1–84.

Queffurus M, Barnes S-J (2014) Selenium and sulphur concentrations in country rocks from the Duluth Complex, Minnesota, USA: Implications for formation of the Cu-Ni-PGE sulphides. Econ. Geol. 109:785–794. https://doi.org/10.2113/econgeo.109.3.785

Ripley EM (1981) Sulphur Isotopic Studies of the Dunka Road Cu-Ni Deposit, Duluth Complex, Minnesota. Econ. Geol. 76:610–620. https://doi.org/10.2113/gsecongeo.76.3.610

Ripley EM, Li C (2013) Sulfide saturation in mafic magmas: Is external sulfur required for magmatic Ni-Cu(-PGE) ore genesis? Econ. Geol. 108: 45–58. https://doi.org/10.2113/econgeo.108.1.45

Samalens N, Barnes S-J, Sawyer EW (2017) The role of black shales as a source of sulphur and semimetals in magmatic nickel-copper deposits: Example from the Partridge River Intrusion, Duluth Complex, Minnesota, USA. Ore Geol. Rev. 81:173–187. https://doi.org/10.1016/j.oregeorev.2016.09.030

Thériault RD, Barnes S-J (1998) Compositional variations in Cu-Ni-PGE sulphides of the Dunka Road Deposit, Duluth Complex, Minnesota; the importance of combined assimilation and magmatic processes. Canad. Mineral. 36:869–886.

Virtanen VJ (2022) Thermally induced processes in black shales and the formation of Cu-Ni(-PGE) deposits in and around mafic intrusions – an example from the Duluth Complex, Minnesota, United States. Dissertation, University of Helsinki.

Virtanen VJ, Heinonen JS, Barber ND, Molnar F (2022) Complex Effects of Assimilation on Sulfide Saturation Revealed by Modeling with the Magma Chamber Simulator: A Case Study on the Duluth Complex, Minnesota, USA. Econ. Geol. https://doi.org/10.5382/econgeo.4917

Virtanen VJ, Heinonen JS, Molnar F, Schmidt MW, Marxer F, Skyttä P, Kueter N, Moslova K (2021) Fluids as primary carriers of sulphur and copper in magmatic assimilation. Nat. Commun. 12:1–12. https://doi.org/10.1038/s41467-021-26969-3

Solubility of selected elements in the synthetic analogue of kotulskite (PdTe)

Anna Vymazalová[1], František Laufek[1], Marek Tuhý[1,2], Jan Kamenský[1,2],
[1]Czech Geological Survey, Prague, Czech Republic
[2]Institute of Geochemistry, Mineralogy and Mineral Resources, Faculty of Science, Charles University, Prague, Czech Republic

Abstract. The solubility of selected elements in the synthetic analogue of palladium telluride kotulskite (PdTe) was studied experimentally at 400 °C. We have investigated the solubility of ternary elements in kotulskite in the range 0 to 30 at. %, on the tie-line Pd-Te-X, with Pd = 50 at.%, with X = Ag, As, Bi, Cu, Sb, Sn, Se. For the purpose of this study silica-glass tube method was used, the experimental products were evaluated by means of X-ray powder-diffraction analysis, reflected light and electron microscopy. Assessed solid solution series and stable associations should be sought in assemblages with other PGM and known Pd tellurides, likely in magmatic Cu-Ni-PGE mineral deposits, associated with mafic and ultramafic igneous rocks.

1 Introduction

There are four known minerals among palladium tellurides: kotulskite (PdTe), merenskyite ($PdTe_2$), telluropalladinite (Pd_9Te_4), keithconnite ($Pd_{3-x}Te$). Further, there are known occurrences at natural conditions of phases $Pd_{13}Te_3$ and Pd_3Te_2 (e.g. Arnason et al., 1997). However, these occurrences have not yet been described as minerals. Among palladium tellurides, kotulskite (Genkin et al. 1963) and merenskyite (Kingston 1966) belong to the most abundant minerals, commonly found together among other platinum-group minerals and Cu-Ni-Fe sulphides. Palladium tellurides are generally found in Cu-Ni-PGE mineral deposits, associated with mafic and ultramafic igneous rocks. They also occur in other types of deposits, enriched in PGE, like porphyry copper/gold systems, sedimentary-hosted massive sulphides or metalliferous black shales.

We have experimentally investigated the solubility of selected elements (Ag, As, Bi, Cu, Sb, Sn, Se and Pb) in the synthetic analogue of kotulskite at 400 °C. Furthermore, we have studied the ternary Pd-X-tellurides in order to asses stable assemblages in the corresponding ternary systems. The evacuated silica tube method was applied for the purpose of this study. The experimental products were examined primarily with X-ray powder diffraction, and in polished sections by means of reflected light and electron microscopy.

2 Techniques and methods

2.1 Experimental

Experiments were performed in evacuated and sealed silica glass tubes in horizontal tube furnaces. Charges of about 300 mg were carefully weighed out from the native elements (palladium powder, 99.95% purity; tellurium ingot, 99.999% purity; and selected elements Ag, As, Bi, Cu, Sb, Sb, Se, Pb of 99.999% purity). The starting mixtures were first melted at 1000 °C for several hours. Then, the run products were ground in an agate mortar under acetone and reheated to 400 °C (for 3 to 4 months). After heating, quenching occurred by dropping the capsules in cold water. Phases in the run products were characterized by X-ray powder diffraction and, in polished sections examined under reflected light and with electron-microprobe techniques (EPMA).

2.2 Electron probe microanalyses

The EPMA analyses were performed with a JEOL JXA 8230 electron probe microanalyser in a wavelength-dispersion mode using an electron beam focussed to 1-2 μm. Pure elements were used as standards. Concentrations were quantified on the L_α lines for Pd, Te, As, Sb, Sn, Se, Pb; the L_β for Ag; the K_α for Cu and M_α for Bi; with an accelerating voltage of 15 keV, and a beam current of 10 nA. In a sample, compositional data were collected from several grains within a polished section.

2.3 X-ray diffraction analyses

The X-ray diffraction patterns (XRD) were collected in Bragg-Brentano geometry on Bruker D8 Advance diffractometer equipped with the Lynx Eye XE detector and Cu*K*α radiation source. The data were collected in the angular range from 10 to 140° 2Θ°.

3 Results and Discussion

We performed the experimental runs in a series Pd – X–Te, with X = Ag, As, Bi, Cu, Sb, Sn, Se and Pb, with compositional step from 5 to 10 at.%. In detail, the following experimental runs were studied Pd50(Te50-X) with X = 0.5, 10, 20, 30, some additional runs were also performed within Pd50-XTe50, with X= 10,20. Kotulskite dissolves up to 1 at.% Cu. Our investigations in the Pd-Sb-Te system, in the range up to $Pd_{50}(Te_{20}Sb_{30})$, confirmed the continuous solid solution (ss) between sudburyite and kotulskite (Figs 1-3). This is in agreement with the study of El-Boragy and Schubert (1971) at 400 °C, and also at 600 °C by Kim and Chao (1991). Furthermore, natural occurrences forming the

kotulskite – sudburyite (ss-PdTe – ss-PdSb) series are well established from various Cu-Ni-PGE deposits.

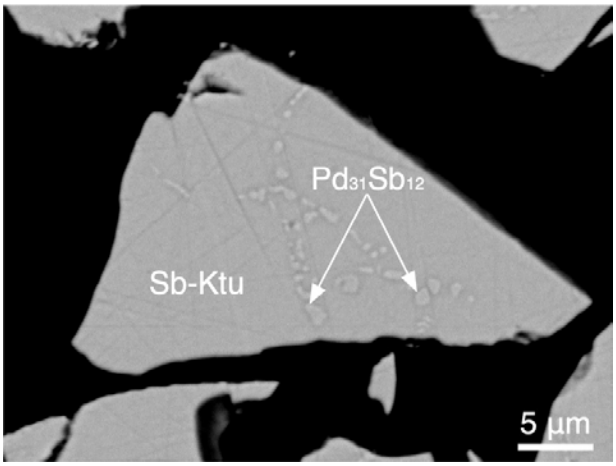

Figure 1. BSE image of kotulskite (dissolving 4.5 at. % Sb) forming a stable association with phase $Pd_{31}Sb_{12}$ (light). Run No KtSb 0.5, heated four months, T = 400 °C.

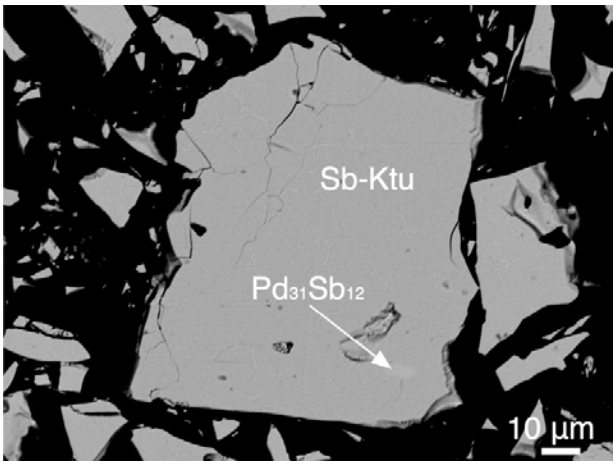

Figure 2. BSE image of kotulskite (dissolving 20 at. % Sb) Run No KtSb 20, heated four months, T = 400 °C.

Our experimental study has shown the maximum solubility of As in kotulskite up to 4 at.%. Kotulskite ss forms a stable association with palladoasrsenide and phase $PdAs_2$ at 400 °C(Fig.4). Kotulskite dissolves up to 19 at.% Sn as suggested by Vymazalová and Drábek (2010) and up to 10 at. % Se (Vymazalová et al. 2019).

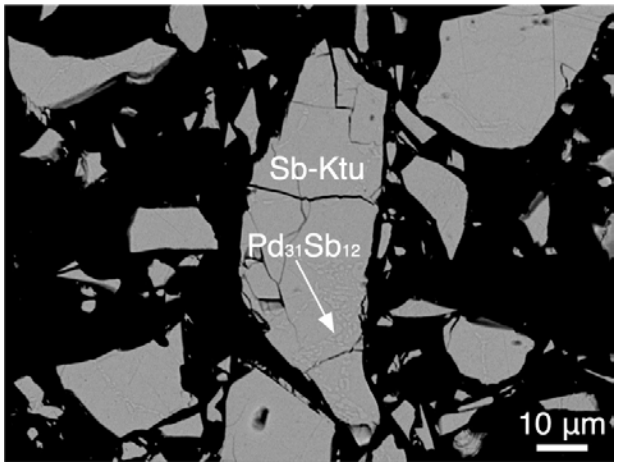

Figure 3. BSE image of kotulskite (dissolving 30 at. % Sb) in association with phase $Pd_{31}Sb_{12}$ (light inclusions). Run No KtSb 30, heated four months, T = 400 °C.

Kotulskite forms an extensive solid solution with Pb, dissolving up 30 at.% Pb (Vymazalová and Drábek 2011). It dissolves up to 10 at. % Se (Vymazalová et al. 2019). Kotulskite does not dissolve Ag at 400 °C which is in agreement with the experimental study of the system at 350 and 450 °C (Vymazalová et al. 2015). The system Pd-Bi-Te has been preliminarily experimentally studied by Evstigneeva et al. (2019) in the temperature range 350-550 °C. They detected the ss-PdTe – ss-PdBi association. The kotulskite – sobolevskite series were widely reported from a number of Cu-Ni-PGE mineral deposits associated with mafic and ultramafic igneous rocks (e.g. Evstigneeva et al. 1975, Sluzhenikin 2011, Cook et al. 2002, Barkov et al. 2002, among others).

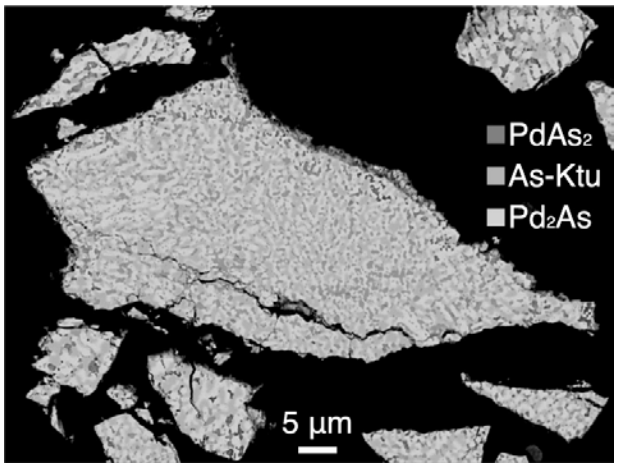

Figure 4. BSE image of stable association of kotulskite (dissolving 3 at. % As) in association with $PdAs_2$ and palladoarsenide Pd_2As. Run No KtAs30, heated four months, T = 400 °C.

The unit-cell parameters of selected kotulskite solid solutions are summarized in Table 1. Fig. 5 shows the evolution of unit-cell volume. The incorporation of Bi into the kotulskite structure results in a significant increase of the unit-cell

volume. Contrary to that, incorporation of Sb leads to a decrease up to 0.39 apfu of Sb, followed by a slight increase of the unit-cell volume. Minute incorporation of As (up to 0.05 apfu) results in a decrease of the unit-cell volume.

Table 1. The unit-cell parameters of selected kotulskite solid solutions

	Unit cell			Apfu 2		
	c (Å)	*c*(Å)	*V*(Å^3)	Te	X	Pd
PdTe	4.1523	5.6719	84.694	1	0	1
KtBi05	4.1602	5.669	84.971	0.87	0.13	0.99
KtBi10	4.1676	5.6676	85.252	0.80	0.20	0.99
KtBi20	4.1839	5.6744	86.024	0.60	0.40	1.00
KtBi30	4.1952	5.6824	86.609	0.40	0.60	1.01
KtSb05	4.1405	5.6544	83.951	0.93	0.09	0.98
KtSb10	4.1336	5.643	83.505	0.84	0.19	0.97
KtSb20	4.1098	5.6139	82.117	0.63	0.39	0.98
KtSb30	4.121	5.6252	82.735	0.39	0.61	1.00
KtAs05	4.1215	5.6474	83.082	1.01	0.03	0.96
KtAs10	4.1147	5.643	82.743	1.00	0.05	0.95

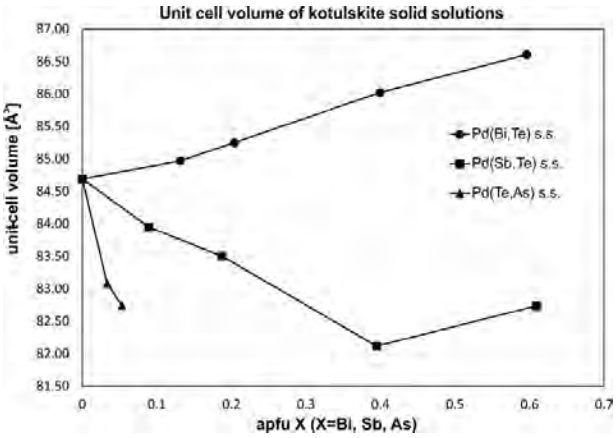

Fig. 5 The changes of unit-cell volume in kotulskite involving Bi, Sb and As.

3 Conclusions

We have proved a range of solid solutions in the systems Pd-X-Te, with X = Ag, As, Bi, Cu, Sb, Sn, Se and Pb at 400 ºC. We have assessed the maximum solubility of selected elements in kotulskite. In some cases, the solid solution series are misinterpreted as potential new minerals occurring in nature. We have further proved the stable association of kotulskite ss with palladoasrsenide and phase $PdAs_2$.The solid solution series established, and stable associations proved, can be found in Cu-Ni-PGE mineral deposits associated with mafic and ultramafic igneous rocks.

Acknowledgements

Financial support through the Project No 22-26485S from the Grant Agency of the Czech Republic (GACR) is gratefully acknowledged.

References

Arnason JG, Bird DK, Bernstein S, Kelemen PB (1997) Gold and platinum-group element mineralization in the Kruuse Fjord gabbro complex, east Greenland. Econ Geol 92: 490-501.

Barkov AY, Laflamme JHG, Cabri LJ, Martin RF (2002) Platinum-group minerals from the Wellgreen Ni-Cu-PGE deposit, Yukon, Canada. Can Min 40: 651-669.

Cook NJ, Ciobanu CL, Merkle RKW, Bernhardt H-J (2002) Sobolevskite, taimyrite, and Pt_2CuFe (tulameenite?) in complex massive talnakhite ore, Talnakh Orefield, Russia. Can Min 40: 329-340.

El-Boragy M, Schunert K (1971) Uber einige Varianten der NiAs-Familie in Mischungen des Palladiums mit B-Elementen. Z. Metallkunde 62: 314-323.

Evstigneeva PV, Nickolsky MS, Geringer NV, Vymazalová A, Nekrasov AN, Chareev DA (2019) Pt- and Pd-bismuthotellurides: phase relations in the Pt-Bi-Te and Pd-Bi-Te systems. Proceedings of the 15th Biennial SGA Meeting, 27-30 August 2019, Glasgow, UK.

Evstigneeva TL, Kovalenker VA (1975) Sobolevskite, a new bismuthide of palladium, and the nomenclature of minerals of the system PdBi-PdTe-PdSb. Int Geol Rev 18:856-866.

Genkin AD, Zhuravlev NN, Smirnova EM (1963) Moncheite and kotulskite - new minerals - and the composition of michenerite. Zapiski Vsesoyuznogo Mineralogicheskogo Obshchestva 92: 33-50.

Kim W-S, Chao GY (1991) Phase relations in the system Pd-Sb-Te. Can Min 29: 401-409.

Kingston GA (1966) The occurrence of platinoid bismuthotellurides in the Merensky Reef at Rustenburg platinum mine in the western Bushveld. Min Mag 35: 815-835.

Sluzhenikin SF (2011) Platinum-copper-nickel and platinum ores of Noril'sk region and their ore mineralization. Rus J Gen Chem 81: 1288–1301.

Vymazalová A, Chareev DA, Kristavchuk A, Laufek F Drábek M (2014) The system Ag-Pd-Se: Phase relations involving minerals and potential new minerals. Can Min 52: 77-89.

Vymazalová A, Drábek M (2010) The system Pd-Sn-Te at 400°C and mineralogical implications. II. The ternary phases. Canadian Mineralogist 48: 1051-1058.

Vymazalová A, Drábek M (2011) The Pd–Pb–Te system: phase relations involving pašavaite and potencial minerals. Can Min 49: 1679-1686.

Vymazalová A, Laufek F, Kristavchuk AV, Chareev DA, Drábek M (2015) The system Ag-Pd-Te: phase relations and mineral assemblages. Min Mag 79: 1813-1832.

Vymazalová A, Tuhý M, Laufek F (2019) Palladium and platinum seleno-tellurides and their associations. Proceedings of the 15th Biennial SGA Meeting, 27-30 August 2019, Glasgow, UK.

Mineralogical and geochemical insights of Fe-Ti-P-REE mineralization in alkaline igneous complexes: example from the Kodal deposit, Oslo Rift, Norway

Pierre Buelens[1], Vinciane Debaille[1], Sophie Decrée[2], Nolwenn Coint[3]
[1]Laboratoire G-Time, Université Libre de Bruxelles, Brussels, Belgium
[2]Royal Belgian Institute of Natural Sciences, Geological Survey of Belgium, Brussels, Belgium
[3]Geological Survey of Norway, Trondheim, Norway

Abstract. Phosphates are essential in our society to guarantee the global food production chain. They have been recognized as critical raw materials (CRM) by the EU. It is mostly extracted from apatite $[Ca_5(PO_4)_3(F, OH, Cl)]$, a mineral common to sedimentary, igneous and metamorphic rocks. Alkaline igneous deposits have so far received limited interest by comparison with other igneous or sedimentary-related type deposits. However, some of them show notable enrichments in P_2O_5 and could become exploitable, especially in Europe. In these systems, apatite is enriched in Rare Earth Elements (REE), which constitutes a potential byproduct, in addition to phosphorus. Here, we focus on the Early Permian Larvik Monzonitic Plutonic Complex (LPC; Oslo Rift, Norway), which displays Fe-Ti-P-REE mineralization whose formation remains unclear. We first described the mineralogical assemblages constituting the mineralization, the surrounding larvikites as well as the contacts between the two facies. Further geochemical investigations were performed on in-situ apatite from Kodal in order to establish its trace elements composition.

1 Introduction

The Fennoscandian Shield possesses a significant amount of igneous phosphorus mineralization in carbonatite, anorthosite and alkaline-related environments (e.g. the Fen, Sokli, Siilinjarvi carbonatitic complexes, the Bjerkreim-Sokndal layered intrusion, the alkalic Raftsund intrusion and Misvaerdalen Complex; Vartiainen & Woolley 1974; Vartiainen & Vuotovesi 1980; Gautneb et al 2013; Ihlen et al 2014; Coint et al 2020; Decrée et al 2022). Some occurrences have received much interest in recent decades, such as the Bjerkreim-Sokndal layered intrusion belonging to the Rogaland Anorthositic Province, southwestern Norway. By contrast, few deposits of alkaline affinity have been studied as possible target for apatite exploitation. The 297-256 Ma Oslo Rift (southeastern Norway) hosts the youngest magmatic rocks of the Fennoscandian Shield (e.g. Sundvoll et al 1990; Neumann et al 2004; Ziegler et al 2006; Larsen et al 2008; Decrée et al 2022), including the Larvik Plutonic Complex (LPC), which contains several Fe-Ti-P mineralizations. The LPC is organized into ten successive nested monzonitic intrusive units (numbered from I to X) with decreasing saturation in silica towards the west (Figure 1; Petersen, 1978). These intrusive units crystallized early in the formation of the Oslo Rift: U-Pb ages on zircons range from 302 Ma for the oldest (I) to 288 Ma for the youngest (X) (Dahlgren et al 1998; Rämö et al 2022).

The LPC contains several occurrences of Fe-Ti-P-rich rocks, particularly in the vicinity of the younger, silica-undersaturated plutons. The most

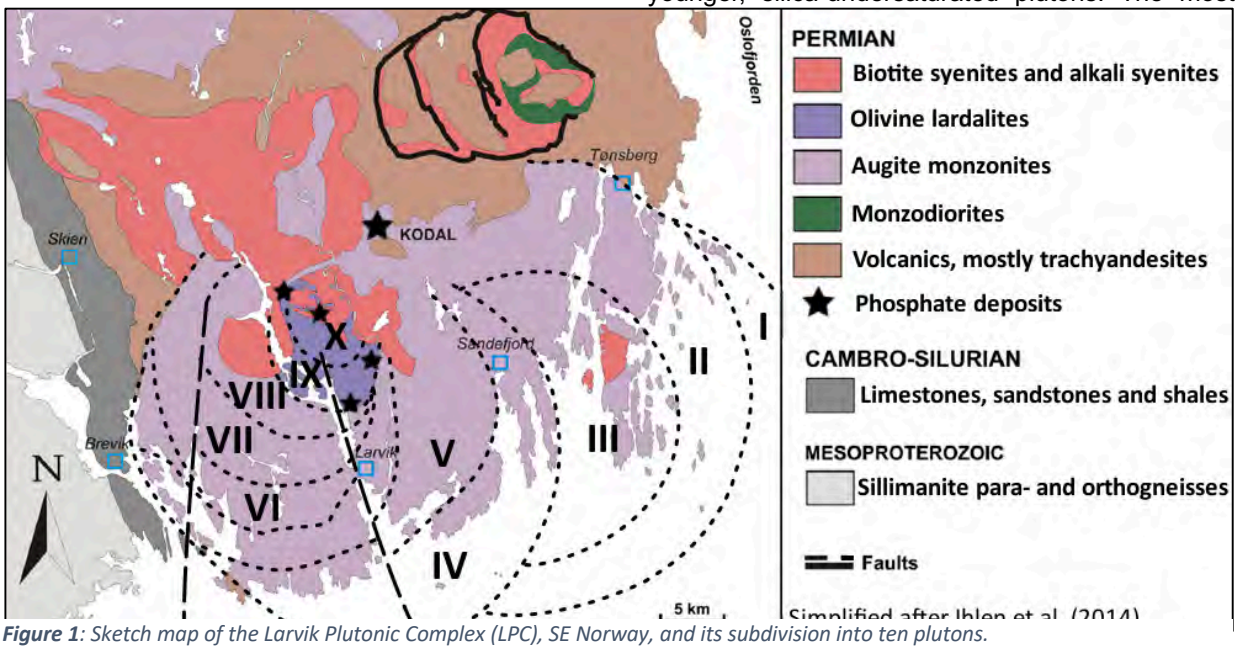

***Figure 1**: Sketch map of the Larvik Plutonic Complex (LPC), SE Norway, and its subdivision into ten plutons.*

notable deposit, Kodal, occurs in an area close to the plutons V and X (Figure 1). The mineralization occurs as dyke-like lenses within the monzonite, which are ~1900 m long, a few tens of meters wide, and at least several hundred meters deep, based on previous drill cores (Ihlen et al 2014). JORC compliant resources were recently estimated at 48.9 Mt (massive and disseminated mineralization), with 4.77% P_2O_5 and 21.5% Fe (Decrée et al 2022). In addition, the Kodal mineralization also concentrates rare earth elements and yttrium (TREEY) to high levels, with mean values of ~11000 ppm TREE (Ihlen et al 2014; Decrée et al 2022). Hypotheses for the formation of the Kodal deposit include silicate-liquid immiscibility (Bergstøl 1972; Kragh & Jensen 1991), in-situ accumulation (Lindberg 1985), and accumulation in the magma chamber prior to ascent (Andersen & Seiersten 1994), but have not reached consensus.

2 Petrology and mineralogy

2.1 Fe-Ti-P-REE mineralization

The mineralization mainly consists of titanomagnetite, ilmenite and apatite, with a predominance of titanomagnetite. Other common species include silicates in various proportions, such as titaniferous augite (with Ca>Mg>>Fe>Ti) and phlogopite. Massive ore often displays plurimillimetric to centimetric Fe-Ti-P rich clusters, dominated by automorphic magnetite along the {111} or {110} crystallographic planes, with ilmenite being exsolved as lamellae in its cleavages (Figure 2A). Apatite crystallized as circular, ovoid xenomorphic crystals or as elongated prisms, with rare signs of zonation. The most massive Fe-Ti-P-REE mineralization is limited to these three mineralogical phases, but the oxides and apatite can also be intercalated between variable amounts of fractured and subhedral titanaugite (Figure 2A). Phlogopite is a common mineral, usually separating the oxides from the plagioclases in the monzonitic facies.

2.2 Monzonitic rocks of the LPC

The most common rock-type in the LPC is coarse-grained larvikites (monzonites), whose main features are rhomb-shaped feldspar phenocrysts with Schiller effect (Le Maitre 2002). Plagioclase grains are predominantly sodic ($An_{<40}$) and show a frequent antiperthitic texture. In addition to the plagioclase and alkali feldspar phenocrysts, which make up most of the volume of the larvikites, the intergranular space comprises mafic clusters similar to the mineralization (Figure 2B). Magnetite is associated with ilmenite and apatite, displaying the same textures as in the mineralization but with a greater proportion augite, hornblende and phlogopite, all bearing titanium. Pegmatitic pockets also occur, containing frequent alkaline accessory minerals: Na-bearing pyroxenes and amphiboles, zircon, baddeleyite and zirconolite-3O $[(Ca,Y,REE)_2Zr_2(Ti,Nb)_3FeO_{14}]$.

Plutons IX and X of the LPC show a higher degree of silica undersaturation, expressing as lardalites (massive nepheline syenite, with rhomb-shaped feldspars and massive, squarish nepheline crystals; Neumann 1980; Le Maitre 2002). The higher (Na+K)/Si ratio of these rocks implies a higher proportion of mafic minerals such as phlogopite, aegirine, or various Na-amphiboles.

Larvikites do not show much chemical variation throughout the successive plutons, apart from the decreasing silica-saturation, which is the main evolutionary marker: plutons I and II are oversaturated and contain quartz, whereas plutons III-VIII oscillate between quartz saturation and moderate undersaturation that shows accessory nepheline (Petersen 1978; Neumann 1980).

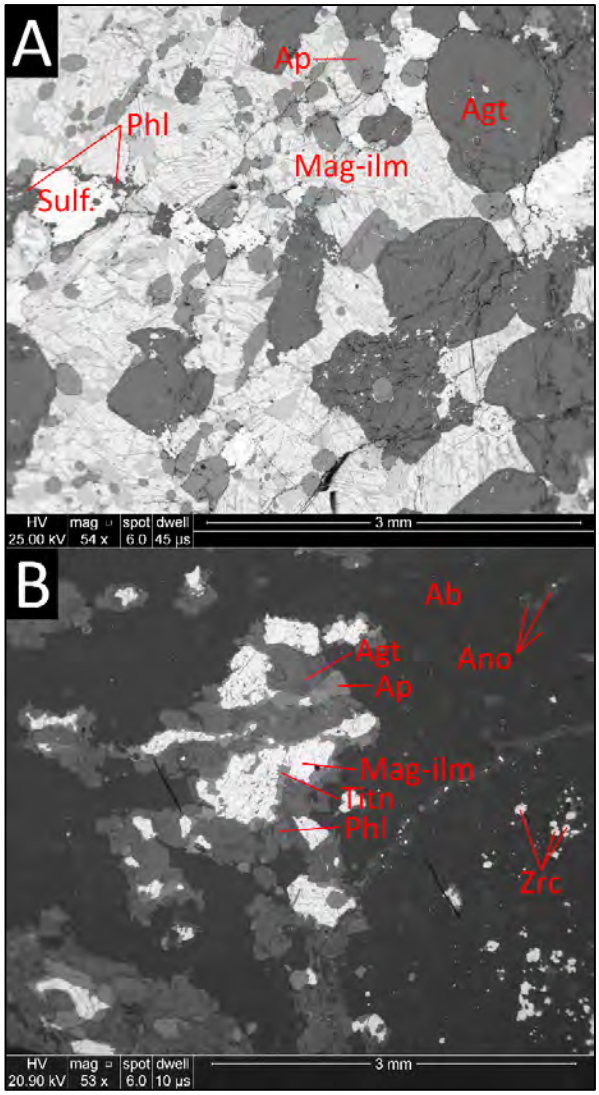

Figure 2. SEM backscatter electron pictures. A: massive mineralization of Kodal, with recurrent exsolutions of ilmenite lamellae in magnetite cleavages, and large roundish clinopyroxene grains. B: coarse-grained larvikite, very close to the disseminated ore of Kodal. Large phenocrysts of albite (top left, top right, bottom right) host minor phases and the same mineral assemblages in the intergranular space as in the mineralization. Mineral abbreviations: Ab: albite; Agt: Ti-augite; Ano: anorthoclase;

Ap: fluorapatite; Mag-ilm: magnetite and ilmenite; Phl: Ti-phlogopite; Sulf.: minor Fe-Cu sulfides; Titn: titanite; Zrc: zircon.

3 Material and methods

Priority was given to the sampling of the Fe-Ti-P-REE mineralization, especially from the Kodal deposit, which represents the most promising P_2O_5 and REE occurrences. Other lithologies sampled include nearby larvikites, larvikites from pluton V, lardalites from plutons IX and X, as well as a few other minor lithologies found in contact with the Kodal mineralization. Both mineralogical assemblages and petrographic textures were investigated in polished sections for 141 samples, using a SEM (Royal Belgian Institute of Natural Sciences).

In addition, whole-rock major and trace elements of 134 samples were analyzed at both the Laboratoire G-Time (ULB) and the Geological Survey of Norway (NGU). Major element measurements were performed using a ThermoScientific iCAP 7000 series ICP-OES (ULB) and a XRF PANalytical Axios 4kW (NGU), whereas trace elements were measured by an Agilent technologies 7700 series ICP-MS (ULB), a XRF PANalytical Axios 4kW (NGU) and a LA-ICP-MS (NGU), the latter consisting in a New Wave 193nm laser connected to a Thermo Fischer Scientific "Element XR" ICP-MS.

Trace elements composition on in-situ apatite were performed in the division of Geology, KULeuven (Belgium), as well as in NGU, in each case using a Teledyne-Cetac Analyte Excite 193 nm excimer laser coupled with an Agilent Technologies 8900 series Triple Quadrupole ICP-MS.

4 Geochemistry

4.1 Potential regarding the P mineralization

The Fe-Ti-P-REE massive mineralization of the LPC displays a very restricted mineralogy, particularly at Kodal. It includes three types of minerals: oxides (magnetite-ilmenite), silicates (titanaugite, phlogopite) and phosphates, mostly apatite. Each of these three groups preferentially concentrates distinct elements: apatite incorporates most of trace elements such as Sr and REE, due to the high difference between partition coefficients of these elements for apatite and other minerals of the mineralization (Li et al 2023). SEM investigations, combined with whole-rock elemental analyses show that apatite enrichment in the mineralization is quite variable (with whole-rock P_2O_5 content between 1.5% and 11.5%), with an average of about 6.5% P_2O_5 and about 3000 ppm TREEY. These observations suggest that the Kodal apatite contains REE in substitution on the order of 1%, in agreement with Ihlen et al (2014).

In-situ trace elements compositions from the Kodal deposit display strong enrichments in REE, particularly in LREE (Figure 3), with mean values of 11500 ppm TREEY, with an upper limit of 14700 ppm TREEY for unaltered massive mineralization. The actinide contents in apatite remain low, with typical values around 50 ppm Th and 12 ppm U. The apatite compositions obtained give the Kodal mineralization the status of potential P, REE, and F reserves (Andersen & Seiersten 1994), in a time where Europe seeks to assess its critical raw material resources.

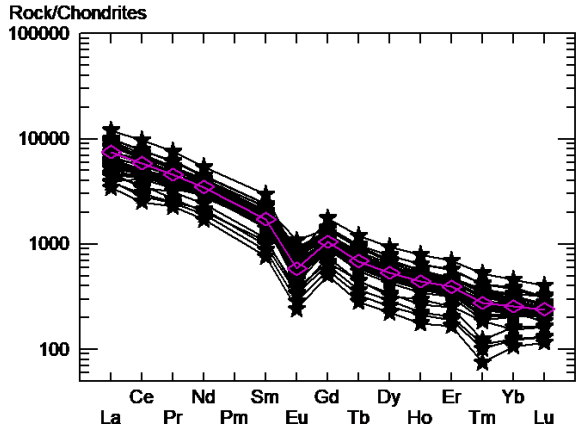

Figure 3. REE spider diagram of the apatite from the Kodal Fe-Ti-P-REE deposit (black stars), with the mean as the purple diamonds pattern. Normalized to C1 chondrites (Sun & McDonough 1989).

4.2 An onset closely related to the LPC

Whole-rock data, namely Nb/Ta and REE patterns and ratios, shows that the monzonitic rocks of the LPC share the same source as the Fe-Ti-P-REE mineralization. Moreover, the LPC plutons crystallized by successive emplacement of very similar plagioclase-rich mushes with a high Sr/Nd ratio and a positive Eu anomaly (Figure 4, A). In contrast, the mineralizations show a negative anomaly in Eu, coupled with ratios in La/Gd and Gd/Lu that differ from the range of monzonitic rocks (Figure 4, A,B). Regarding these first observations, we propose that the mineralized rocks could be a magmatic residue common to all the monzonitic plutons, dissociated in the magmatic chamber by either liquid-liquid immiscibility or fractional crystallization. Similarly to the model proposed by Andersen & Seiersten (1994), the residual P-rich magma would have ascended later, in an already emplaced and cooling larvikite.

5 Perspectives

Many questions remain, notably about the source of these mineralizations and their petrogenetic links with the LPC monzonitic rocks. Further elemental and isotopic analyses are therefore planned to bring further insights.

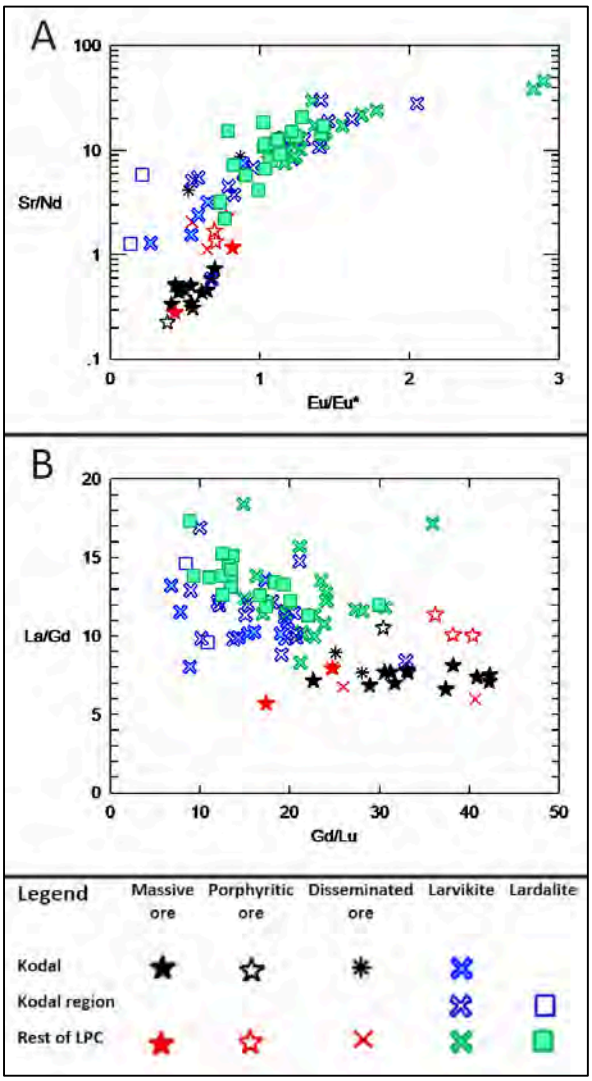

Figure 4. A : Trace element ratios underlying the enrichment of plagioclase (high Sr/Nd value, Eu/Eu*>1) for all monzonitic rocks, except for a few larvikites in and close to Kodal. B: (La/Gd) vs (Gd/Lu). Mineralizations constantly show a ratio in La/Gd distinctly lower than the range of monzonitic rock, hinting for a global segregation of the ore in the LPC. Low Gd/Lu values are believed to trace the enrichment in zircons.

Acknowledgements

We would like to thank the Geological Survey of Norway for granting access and allowing sampling of drill cores of the Kodal mineralization. We also acknowledge the Research Council of Norway for the support to the Norwegian Laboratory for the Mineral and Materials Characterization, MiMaC, project number 269842/F50. Many thanks to the Division of Geology from KULeuven (Belgium) for access and support to their geochemical facilities.

References

Andersen T and Seiersten M (1994): Deep cumulates in a shallow intrusion: Origin and crystallization history of a pyroxenite (jacupirangite s.l.) body in the Larvik Pluton, Oslo Region, South Norway; in Neues Jahrbuch fur Mineralogie Monatshefte 1994-6, p. 255-274

Bergstøl S (1972): The Jacupirangite at Kodal, Vestfold, Norway: in Mineralium Deposita 1972-7, p. 233-246

Coint N, Keiding JK and Ihlen PM (2020): Evidence for Silicate-Liquid Immiscibility in Monzonites and Petrogenesis of Associated Fe-Ti-P-rich rocks: Example from the Raftsund Intrusion, Lofoten, Northern Norway; in Journal of Petrology 2020-00(0), p.1-39

Dahlgren S, Corfu F and Heaman L (1998): Datering av plutoner og pegmatitter i Larvik pluton-kompleks, sydlige Oslo Graben, ved hjelp av U-Pb isotope i zircon og baddeleyitt; in Kongsberg Mineralsymposium 1998, Norsk Bergverksmuseum Skrift, 1998-14, p. 32-39

Decrée S, Coint N, Debaille V, Hagen-Peter G, Leduc T and Schiellerup H (2022): The Potential for REEs in Igneous-related Apatite Deposits in Europe; in Geological Society, London, Special Publications 2022-526(1)

Gautneb H, Ahtola T, Lintinen P, Bergman T, Gonzalez J, Hallberg A, Litvinenko V, Shchiptsov V and Voytekhovsky YL (2013): Industrial Mineral Deposit Map of the Fennoscandian Shield 1:2.000.000; in Geological Survey of Norway; Geological Survey of Finland; Geological Survey of Sweden; SC Mineral; Institute of Geology, Karelian Research Centre, RAS; Geological Institute of the Kola Science Centre, RAS

Ihlen PM, Schiellerup H, Gautneb H and Skår Ø (2014): Characterization of apatite resources in Norway and their REE potential – A review; in Ore Geology Reviews 2014-58, p. 126-147

Kragh K and Jensen OA (1991): An immiscible iron-rich liquid in a larvikite magma?; GeoSkrifter 1991-38, p. 32-34

Larsen BT, Olaussen S, Sundvoll B and Heeremans M (2008): The Permo-Carboniferous Oslo Rift through six stages and 65 million years; in Episodes 2008-31(1), p. 52-58

Le Maitre RW (Editor), Streckeisen A, Zanettin B, Le Bas MJ, Bonin B, Bateman P, Bellieni G, Dudek A, Efremova S, Keller J, Lameyre J, Sabine PA, Schmid R, Sørensen H and Woolley AR (2002): Igneous Rocks, A Classification and Glossary of Terms; Cambridge University Press

Lindberg A (1985): Fe-Ti-P Mineralizations in the Larvikite-Lardalite Complex, Oslo Rift; in Norges Geologiske Undersøkelse Bulletins 402, p. 93-98

Li W, Costa F, Oppenheimer C and Nagashima K (2023): Volatile and trace element partitioning between apatite and alkaline melts; in Contribution to Mineralogy and Petrology 2023-178(9), 24 p

Neumann E-R (1980): Petrogenesis of the Oslo Region Larvikites and Associated Rocks; in Journal of Petrology 1980-21(3), p. 499-531

Neumann E-R, Wilson M, Heeremans M, Ann Spencer E, Obst K, Timmerman MJ and Kirstein L (2004): Carboniferous-Permian rifting and magmatism in southern Scandinavia, the North Sea and northern Germany: a review; in Geological Society, London, Special Publications 223, p. 11-40

Petersen JS (1978): Structure of the Larvikite-Lardalite Complex, Oslo-Region, Norway, and it Evolution; in Geologische Rundschau 1978-67(1), p. 330-342

Sun S-s and McDonough WF (1989): Chemical and isotopic systematics of oceanic basalts: implications for mantle composition and processes; in Geological Society, London, Special Publications 1989-42, p. 313-345

Sundvoll B, Neumann E-R, Larsen BT and Tuen E (1990): Age relations among Oslo Rift magmatic rocks: implications for tectonic and magmatic modelling; in Tectonophysics 1990-178, p. 67-87

Rämö TO, Andersen T, and Whitehouse MJ (2022): Timing and Petrogenesis of the Permo-Carboniferous Larvik Plutonic Complex, Oslo Rift, Norway: New Insights from U-Pb, Lu-Hf, and O Isotopes in Zircon; in Journal of Petrology 2022-63, p. 1-29

Vartiainen H and Woolley AR (1974): The age of the Sokli carbonatite, Finland, and some relatioships of the North Atlantic alkaline igneous province; in Bulletins of the Geological Society of Finland 1974-46, p. 81-91

Vartiainen H, and Vuotovesi T (1980): The Sokli carbonatite complex; in Lithos 1980-13, p. 224-225

Ziegler PA, Schumacher ME, Dèzes P, Van Wees J-D and Cloetingh S (2006): Post-Variscan evolution of the lithosphere in the area of the European Cenozoic Rift System; in Geological Society, London, Memoirs 32, p. 97-112

Magmatic and hydrothermal processes in a carbonatite-related REE mineralization system: insights from the Maoniuping deposit, southwestern China

Zhe Chi[1,2], Pei Ni[1], Junyi Pan[1], Zengqian Hou[3], Dawid Szymanowski[2], Cyril Chelle-Michou[2]
1State Key Laboratory for Mineral Deposits Research, Institute of Geo-Fluids, School of Earth Sciences and Engineering, Nanjing University, Nanjing, China
2 Department of Earth Sciences, ETH Zürich, Zürich, Switzerland
3 Institute of Geology, Chinese Academy of Geological Sciences, Beijing, China

Abstract. In carbonatite-related REE systems, the relative importance of magmatic and hydrothermal processes is debated. Based on our new data on high-precision zircon geochronology and in situ geochemistry from the Maoniuping REE deposit, we suggest that the giant REE mineralization may be generated from a super-enriched fluid within a short period of time. Rejuvenation of the system upon magma recharge may play an important role in REE enrichment in alkaline complexes.

1 Introduction

Carbonatites are associated with most of the REE resources in the world. However, the magmatic and hydrothermal processes in carbonatitic systems that concentrate REE elements to economic levels (wt.%) are still poorly constrained. The Cenozoic Maoniuping deposit, China, displays a clear mineralization zonation, a well-established intrusion sequence, and limited supergene alteration, providing an outstanding case study to decipher the magmatic and hydrothermal processes for REE mineralization.

In this study, we obtained high-precision U-Pb zircon ages from pre- and post-ore intrusions, with the aim of constraining the duration of magmatic-hydrothermal ore formation. Spatially resolved geochemical information from zircon core and rim was collected to track the magmatic processes involved in the formation of REE mineralization. Additionally, REE concentration of fluids was obtained by LA-ICP-MS analysis of fluid inclusions in fluorite and quartz, which are closely associated with the ore mineral (bastnaesite). These data were included in a mass balance calculation to examine the REE mineralization lifespan determined by geochronology.

2 Geology of the Maoniuping deposit

The Maoniuping deposit, located in the western Yangtze craton, is the fifth largest REE mineralization in the world. It contains resources of 3.17 Mt REO with an average grade of 2.95 wt.%. It is hosted in an Oligocene syenite-carbonatite complex formed in a post-collisional environment.

The REE mineralization is centred around a composite alkaline intrusion made of lamprophyre dykes, quartz syenite pluton, carbonatite dykes, and alkaline granite porphyry (Fig. 1A). Syenitic plutonic rocks were emplaced first, followed by the intrusion of lamprophyre dykes. Ore-related carbonatite intruded into syenite and lamprophyre dykes, resulting in extensive fenitization superimposed on the earlier-formed magmatic rocks (Fig. 2A-E). Granite porphyry crosscuts all early intrusions and ore veins (Fig. 2F-G), representing the latest magmatic pulse.

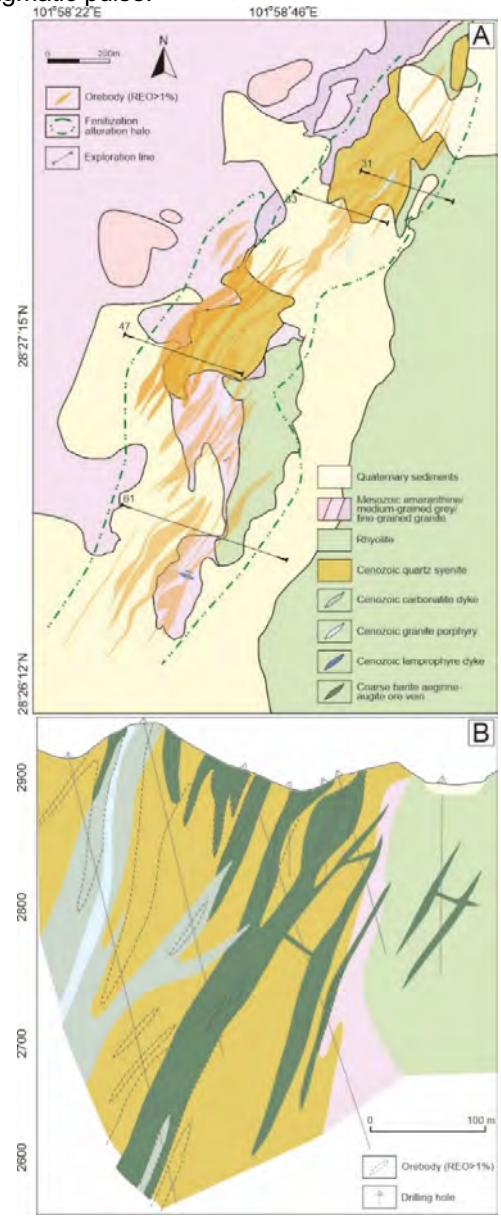

Figure 1. (A) Simplified geologic map showing the distribution of carbonatite-alkaline complexes and REE orebodies in the Maoniuping deposit (modified after Yuan et al. 1995); (B) Cross-section along exploration line 31 (modified after Yuan et al. 1995).

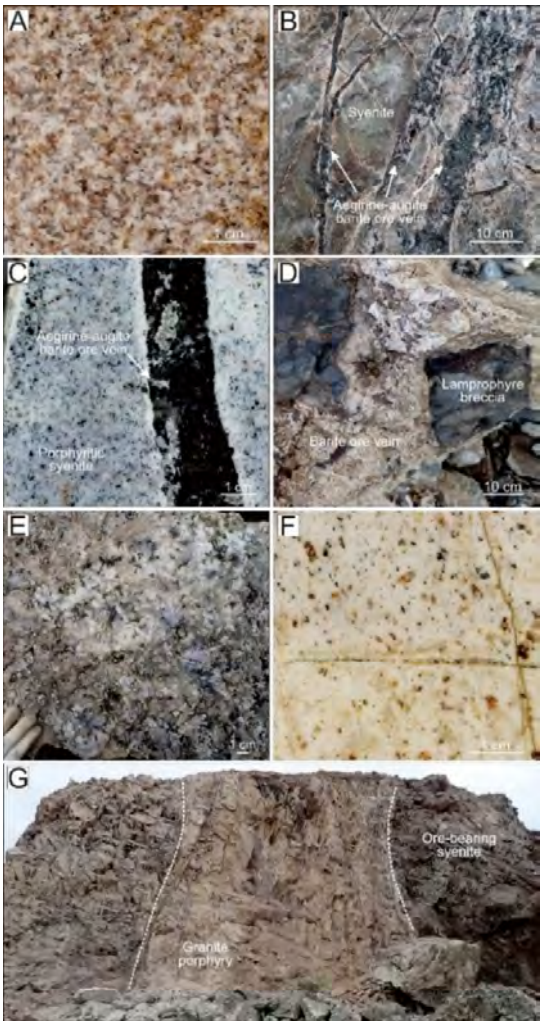

Figure 2. (A) Quartz syenite; (B) Aegrine-augite barite REE ore stockwork veins hosted in the syenite; (C) Aegrine-augite barite ore veins cutting porphyritic syenite; (D) Lamprophyre breccia in barite REE ore veins; (E) Pink calcite carbonatite with fluorite and barite; (F) Barren granite porphyry; (G) Barren granite porphyry intruding quartz syenite and cutting ore stockwork veins

The majority of the REE mineralization is hosted in two types of ore veins: aegirine-augite-barite stockwork veins (Fig. 1 B and C) and carbonatitic veins and dykes (Fig. 1E). These two types of veins are composed of broadly similar mineral assemblages but different mineral ratios, including aegirine-augite, feldspar, arfvedsonite, calcite, bastnaesite, quartz, fluorite, barite, and exhibit similar trending orientations at the deposit scale. At the location where carbonatite dyke is exposed, there is a transition from carbonatite veins to aegirine-augite-barite veins, indicating that both mineralization styles are generated by a single fluid pulse.

3 Samples and Methodology

One sample of pre-ore syenite (MNP018) and two samples of post-ore granite porphyry (MNP017 and MNP049) were collected. In situ LA-ICP-MS measurements and chemical abrasion-isotope dilution-thermal ionization mass spectrometry (CA-ID-TIMS) analysis were performed at ETH Zurich. The separated zircons were annealed for 48 h at 900 ℃, and then were mounted in epoxy. Polished zircons were imaged using SEM-CL, followed by in situ LA-ICP-MS analysis for trace elements and U-Pb isotopes. Based on the in-situ zircon compositions and the CL texture, some grains were plucked out of the mounts and processed for high-precision U-Pb analyses by CA-ID-TIMS.

Fluid inclusions in quartz and fluorite were analyzed by LA-ICP-MS at the fluid inclusion lab at Nanjing University to obtain their major and trace elemental compositions. The detailed procedure refers to the description by Pan et al. (2019). The sulfate concentrations of fluid inclusions were used as internal standards, which are obtained by combining microthermometric data with a calibrated sulfate solubility curve (Chen et al. 2020).

4 Timescales of ore formation: bracketed by the dates of pre-ore and post-ore intrusions

Previous in situ geochronology indicated that the magma evolution and REE mineralization of the Maoniuping syenite-carbonatite complex occurred over 2.5 Myr (Weng et al. 2020). Our new high-precision U-Pb dates of individual zircon crystals do not reveal a prolonged magmatic history but suggest a highly constrained magmatism and mineralization timescale (Fig. 3). The youngest zircons from each sample are interpreted as the closest approximation of the emplacement age of each intrusion. These youngest zircons in pre- and post-ore intrusions bracket the maximum duration of ore formation to a time interval of ca. 0.15 Myr.

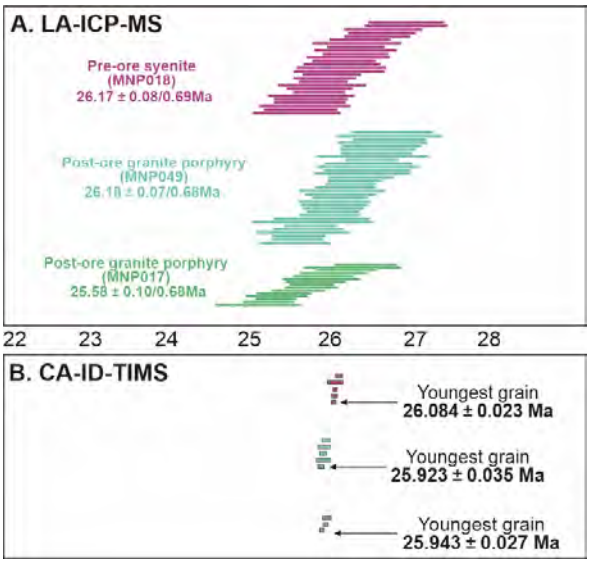

Figure 3. Geochronology of the Maoniuping magmatic system. (A) Ranked LA-ICP-MS $^{206}Pb/^{238}U$ dates. Weighted mean ages are given with two uncertainties: (1) 2σ internal uncertainty and (2) with propagated external uncertainty; (B) Ranked CA-ID-TIMS $^{206}Pb/^{238}U$ dates with date and uncertainty of the youngest zircons.

The fluid inclusions hosted in bastnaesite and associated minerals (quartz and fluorite) are polycrystalline inclusions, with sulfate and a small amount of carbonate as daughter minerals. REE concentrations of fluid inclusions in quartz and fluorite associated with bastnaesite ranged from 1070 to 17200 ppm, with an average of 4000 ppm. Mass balance calculation shows that assuming a maximum mineralization duration of 0.15 Ma, the fluid flow rate will be 0.15 kg/s. While it is on the low end of what has been reported in geothermal systems and hot springs (0.1 to 1000 kg/s, Moncada et al. 2019), the mineralizing pulse may have been much shorter than the bracketed interval duration, thereby allowing for higher fluid flow rates.

5 Magmatic processes: insights from zircon chemistry in pre-ore syenite

Four zircon CL textural categories were devised to classify the grains observed (Fig. 4). A-type zircon displays grey continuous oscillatory zoning. B-type zircon is characterized by a bright CL texture. C type has a core-rim texture with resorption textures on the core. D-type zircons contain rims with dark luminescence.

The LA-ICP-MS dates of the four types of zircon are overlapping. From core to rim, A-type zircon grains usually display a trend of declining Th/U ratio (Fig. 4A and B), indicating a fractionating trend jn the presence of co-crystallizing titanite and apatite (both abundant minerals in the magmatic rocks of Maoniuping). The REE content in A-type zircons usually decreases from core to rim (Fig. 4A). B-type zircon grains have the highest Th/U ratio and Ti content, and lowest Yb/Gd_N ratio (Fig. 4C and D). Most C-type zircon grains show a rejuvenation trend, manifested by decreased Th/U ratios and increased Yb/Gd_N ratios (Fig. 4E and F). In C-type zircons, the REE contents are generally higher at the rim (Fig. 4E). The dark rims of D-type zircons are characterized by elevated Hf concentrations and often display more evolved Yb/GdN and Th/U ratios (Fig. 4G and H).

The appearance of high-temperature and low-evolution B-type zircons and the tendency of C-type zircons to become less evolved from core to rim pinpoints toward magma recharges into the syenitic magma reservoir. As recorded in A-type zircons, magmas are progressively depleted in REE content as apatite and titanite crystallize. The less-evolved rims of C-type zircons usually have enriched REE contents compared to the core suggesting that the rejuvenation the magmatic system may contribute to the REE enrichment in alkaline complexes.

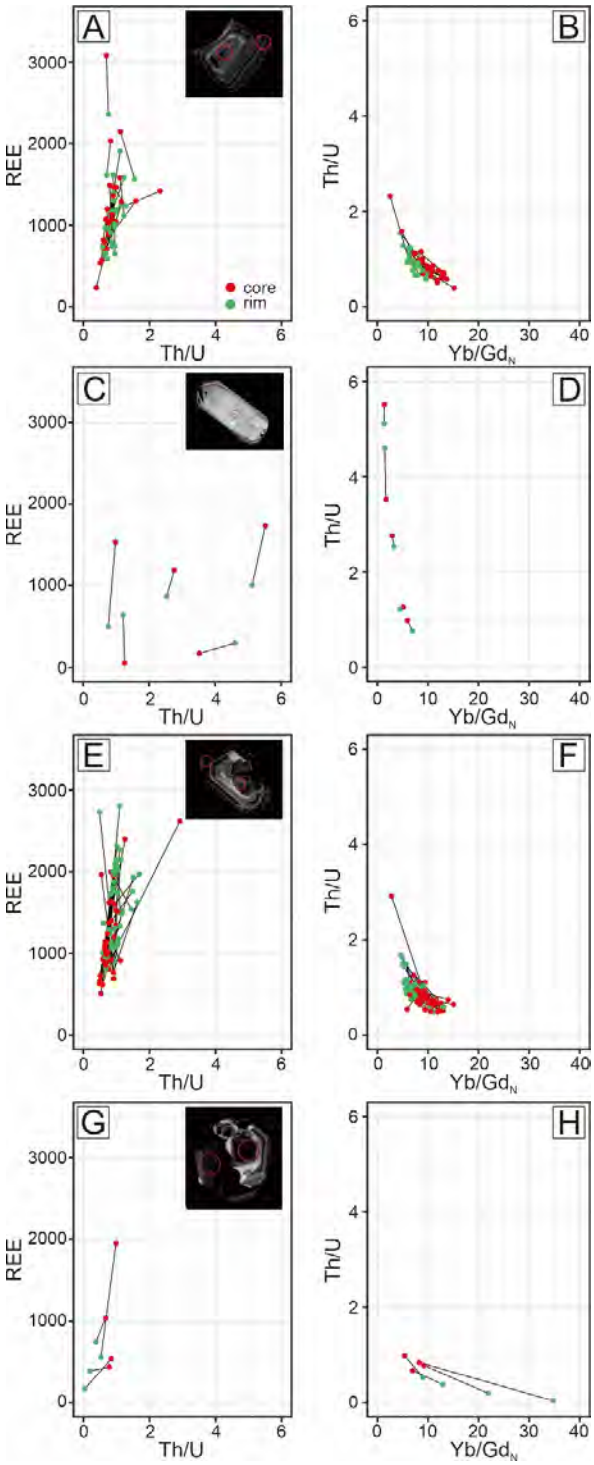

Figure 4. REE vs Th/U and Th/U vs Yb/Gd$_N$ trends from core to rim for each type zircons. (A-B) A-type; (C-D) B-type; (E-F) C-type; (G-H) D-type.

References

Chen H, Cui H, Zhong R, Xie Y, Yu C, Li Z, Ling Y (2020) Solubility of Na_2SO_4 in silica-saturated solutions: Implications for REE mineralization. AM MINERAL 105(11):1686-1694.

Moncada D, Rimstidt JD, Bodnar RJ (2019) How to form a giant epithermal precious metal deposit: Relationships between fluid flow rate, metal concentration of ore-forming fluids, duration of the ore-forming process, and ore grade and tonnage. ORE GEOL REV 113:103066.

Pan JY, Ni P, Wang RC (2019) Comparison of fluid processes in coexisting wolframite and quartz from a giant vein-type tungsten deposit, South China: Insights from detailed petrography and LA-ICP-MS analysis of fluid inclusions. AM MINERAL 104(8):1092-1116.

Weng Q, Yang WB, Niu HC, Li NB, Mitchell RH, Zurevinski S, Wu D (2022) Formation of the Maoniuping giant REE deposit: Constraints from mineralogy and in situ bastnäsite U-Pb geochronology. AM MINERAL 107(2): 282-293.

Yuan ZX, Shi ZM, Bai G, Wu CY, Chi RA, Li XY (1995) The Maoniuping rare earth ore deposit, Mianning County, Sichuan Province. Seismological Publishing House: Beijing 150 (in Chinese).

Dating multi-stage REE mineralization in Canada: the example of Thor Lake and Saint Honoré deposits

Hélène Legros[1,2,3], D. Graham Pearson[3], Sarah Dare[2], L. Paul Bédard[2]
[1]*Ministère des Ressources Naturelles et des Forêts, Gouvernement du Québec, Canada*
[2]*Department of applied sciences, CERM, Université du Québec à Chicoutimi, Chicoutimi, Canada*
[3]*Department of Earth and Atmospheric Sciences, University of Alberta, Edmonton, Canada*

Abstract. Geochronology applied to ore deposit geology is in constant development and aims to better define the timing of deposition of potential targets, and help to constrain petrogenetic models available for exploration. In the case of REE deposits, alkaline and carbonatite plutonic suites are generally targeted. However, many magmatic REE deposits are remobilized by late hydrothermal processes that could affect endowment. Therefore, it is crucial to constrain the timing of both magmatic and regional hydrothermal ore events. Here, we show results for the Thor Lake bastnaesite mineralization (Slave craton) and the apatite grains of Saint Honoré (Saguenay-Lac-Saint-Jean, Québec).

1 Introduction

REE resources are critical in most areas of the world due to the increasing demand for the development of new technologies (Dushyantha et al. 2020). Our understanding of ore deposition is linked to our understanding of the timing of formation.

Direct dating of ore minerals is not always possible due to the lack of proper matrix-match reference material. However, in the past decades, there has been an increasing interest in developing ore mineral reference materials for geochronology purposes and specifically, U-Pb dating.

Here, we focus on two REE-bearing minerals: one with major REE concentrations, bastnaesite ($(La,Ce,Y)CO_3F$), and one with trace or minor amount of REE, apatite ($Ca_5(PO_4)_3(F,Cl,OH)$).

Both minerals currently have at least one reference material available in the literature. However, both minerals show very low U concentrations and variable common Pb concentrations, which make acquisition as well as data processing challenging (Chew et al. 2014; Roberts et al. 2020).

Precise dating of these minerals is crucial to investigate mineralizing processes, also to define what the lifetime of these processes is. Most REE deposits are emplaced in association with a major magmatic event but exhibit replacement textures indicative of late hydrothermal remobilization of the minerals. Direct dating could highlight the eventual time gap between these two endowment events.

2 Preliminary results

2.1 Bastnaesite dating

Bastnaesite grains were selected from the world-class Thor Lake deposit, located in the Slave Craton in Canada. The analyses were done at the University of Alberta using an iCAP. No matrix-match reference material was available in the Archean age range; therefore, the analyses were run with two reference materials: the K9 bastnaesite and the WC-1 marine calcite. The K9 Bastnaesite is dated at ca. 116 Ma while WC-1 is dated at ca. 254 Ma. The alkaline plutonic suite associated with the Thor Lake mineralization is Mesoarchean (ca. 2.2 Ga).

The Thor Lake bastnaesite has concentrations of U from 0 to 10 ppm, Pb from 40 to 140 ppm and Th from 200 to 800 ppm. The low U concentration is a common feature of carbonate minerals (Roberts et al. 2020). The variation in U-Pb-Th in the bastnaesite grains is controlled by the zoning and the alteration of the grains into parasite, which is easily trackable with the elevation of the Ca concentration.

The first results show a spectrum of ages ranging from sub-concordant 2.0 Ga ages, close to the magmatic event, to ca. 1.77 Ga for the unaltered bastnaesite. However, altered grains give ages as young as 865 Ma. The meaning of such a large age gap and correspondence to regional events is currently being discussed.

2.2 Apatite dating

Apatite is a ubiquitous mineral in ore deposits (Webster and Piccoli 2015). We selected grains from various alkaline and carbonatite REE-Nb mineralization targets located in the Québec province in Canada (such as Saint- Honoré). Apatite has been the subject of U-Pb geochronology development, which is still being developed thanks to analytical advancements of ICP-MS, notably the LA-ICP-MS/MS mode. One of the main limitations of apatite U-Pb dating is the substantial amounts of initial (non-radiogenic, or common) Pb compared to U when it crystallizes (Chew and Spikings 2015), which leads to substantial Pb correction (Chew et al. 2014). LA-ICP-MS/MS mode allows to precisely correct common lead by removing the interference with Hg.

The apatite grains from the carbonatite of Saint-Honoré were analysed along with MAD and Durango reference material on an ICP-QQQ-MS at the Université du Québec à Chicoutimi. The large grain size and abundance of the samples allows us to acquire a substantial dataset that will document the timing of ore deposition for the first time. Several apatite textures are observed: disseminated, disseminated oriented, radial aggregated and in veins. These textures hint at distinct magmatic-

hydrothermal events consistently with observations made by previous studies (Néron et al. 2018). This study aims to date these events but also to document the potential reopening of the U-Pb system in apatite in different magmatic-hydrothermal conditions.

Acknowledgements

The bastnaesite work was supported by Metal Earth while the apatite work is supported by an MRNF postdoctoral grant. We thank Yan Luo, Andy DuFrane and Dany Savard for their help acquiring the data and for the discussions that lead to these preliminary results.

References

Chew DM, Petrus JA, Kamber BS (2014) U–Pb LA–ICPMS dating using accessory mineral standards with variable common Pb. Chemical Geology 363:185–199. https://doi.org/10.1016/j.chemgeo.2013.11.006

Chew DM, Spikings RA (2015) Geochronology and thermochronology using apatite: time and temperature, lower crust to surface. Elements 11:189–194

Dushyantha N, Batapola N, Ilankoon I, et al (2020) The story of rare earth elements (REEs): Occurrences, global distribution, genesis, geology, mineralogy and global production. Ore Geology Reviews 122:103521

Néron A, Bédard LP, Gaboury D (2018) The Saint-Honoré carbonatite REE zone, Québec, Canada: Combined magmatic and hydrothermal processes. Minerals 8:397–397

Roberts NMW, Drost K, Horstwood MSA, et al (2020) Laser ablation inductively coupled plasma mass spectrometry (LA-ICP-MS) U–Pb carbonate geochronology: strategies, progress, and limitations. Geochronology 2:33–61. https://doi.org/10.5194/gchron-2-33-2020

Webster JD, Piccoli PM (2015) Magmatic apatite: A powerful, yet deceptive, mineral. Elements 11:177–182

Stable isotope constraints on the source of ore fluids for the Hicks Dome REE+Y-HFSE-fluorspar deposit

Julia A. McIntosh[1], Craig A. Johnson[1], Allen K. Andersen[2], Albert H. Hofstra[1]
[1] U.S. Geological Survey, Denver CO, USA
[2] U.S. Geological Survey, Spokane WA, USA

Abstract. Hicks Dome is comprised of coarse crystalline Mississippi Valley Type deposits at shallow levels and an enigmatic, fine-grained fluorite, rare earth elements, Y, high field strength elements, Be, and Ba rich deposit at deeper levels. Phyllosilicates from a lamprophyre dike and a breccia from two Hicks Dome drill cores were sampled to resolve the fluid history of the entire deposit using light stable isotopes. Silicate fluorination coupled with isotope ratio mass spectrometry give $\delta^{18}O$ values from +6.9 to +16.0 ‰ (Vienna Standard Mean Ocean Water). Temperature conversion elemental analyzer and gas chromatography-isotope ratio mass spectrometry give $\delta^{2}H$ values from -54 to -33 ‰ (Vienna Standard Mean Ocean Water). Muscovite from metasomatized dikes and breccias are relatively enriched in ^{18}O compared to phlogopite from lamprophyre. Calculated isotopic compositions of the fluids from which the phyllosilicates precipitated indicate that phlogopite retained a magmatic composition while muscovite likely formed from magmatic fluids that exchanged with carbonate host rocks or from magmatic fluids that mixed with basinal brines. Enrichment of deuterium in fluids calculated from muscovite suggest that fluids were derived from hypothesized carbonatites or were acidic. These data demonstrate that the Hicks Dome critical mineral resource is magmatic hydrothermal in origin.

1 Introduction

The Illinois-Kentucky Fluorspar District (IKFD) in the midcontinent region of the USA (Figure 1) is comprised of fluoritic Mississippi Valley-Type (MVT) Pb-Zn deposits. Previous studies of coarsely crystalline fluorite, barite, and Pb-Zn deposits have suggested that the ores formed from basinal brines that migrated northward from the Arkoma Basin in response to uplift of the Alleghanian-Ouachita orogenic belt during the late Paleozoic (Figure 1; Plumlee et al. 1995; Denny et al 2008). The abundant fluorine is hypothesized to be magmatic, derived either from melts related to locally abundant lamprophyre dikes that were emplaced during the Permian (Denny et al. 2008), or from a carbonatite intrusion that is thought to underlie Hicks Dome in the southern IKFD (Figure 1; Andersen et al. 2021).

The deposit at Hicks Dome differs from other fluorspar Pb-Zn deposits in the IKFD in that it is 600 m lower in the stratigraphic section and has high concentrations of numerous elements and minerals on the current U.S. Geological Survey (USGS) list of critical mineral commodities (U.S. Geological Survey 2022). The estimated resource is 65.8 million tons containing critical 15.8% fluorspar, 4.8% barite, 0.16% Be, 1.3% TiO_2, 0.2% Nb_2O_5, and 0.3% rare earth elements plus Y (REEs+Y; Andersen et al. 2021). It has been hypothesized that the Hicks Dome deposit formed from a combination of magmatic and basinal brines following a cryptoexplosive event (e.g., Denny et al. 2008). However, incomplete understanding of the deposit paragenesis and geochemistry renders this hypothesis difficult to test (Andersen et al. 2021).

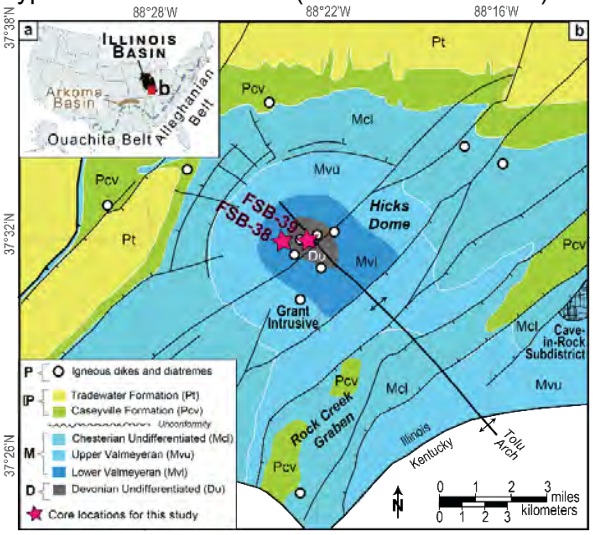

Figure 1. a. Geographic location of the Illinois basin, Alleghanian-Ouachita orogenic belt, and Arkoma basin; b. Geologic map of the Hicks Dome study area. Modified from Denny et al. (2008).

Here we present a new dataset of the oxygen and hydrogen isotopic composition of phyllosilicates in lamprophyre dikes and breccias from Hicks Dome. $\delta^{18}O$ and $\delta^{2}H$ values of phyllosilicate minerals precipitated from a fluid will vary systematically depending on physiochemical conditions and the $\delta^{18}O$ and $\delta^{2}H$ values of the associated fluid. By measuring the $\delta^{18}O$ and $\delta^{2}H$ values of phyllosilicates in the igneous and hydrothermally altered rocks, we can reconstruct the isotopic compositions of fluids involved in the formation of the critical mineral resource at Hicks Dome and test the hypotheses that have been raised regarding fluid sources.

2 Materials and methods

2.1 Core samples

The two drill cores examined in this study (Figure 1b) contain a lamprophyre dike (core FSB-38; Figure 2a–d) and a calcite cemented breccia (core FSB-39; Figure 2e,f). Dike and breccia samples were obtained from depths between 967–982 m, and 404–408 m below the surface, respectively. Samples were disaggregated using a mortar and pestle or

Selective Fragmentation (SelFrag), and then sieving. Phyllosilicates were separated from Ti oxides, sulfates, sulfides, and bertrandite by density separation and from quartz by hand picking.

Figure 2. Photographs of drill core sampled for this study. A. Lamprophyre dike from core FSB-38, 982 m depth; b. Example of a phlogopite; c. Altered lamprophyre dike from core FSB-38, 970 m depth; d. Example of a muscovite; e. Calcite cemented breccia from core FSB-39; f. Example of muscovite. Arrows point to phyllosilicates.

Phlogopite occurs in unaltered portions of the lamprophyre dike (Figure 2b) whereas muscovite is present in metasomatized portions (Figure 2d). Phyllosilicates separated from the calcite cemented breccia were also muscovite (Figure 2f).

2.2 Stable isotopic methods

A portion of the mineral separates were reacted with BrF_5, and the resulting oxygen converted to CO_2 gas using a silicate fluorination extraction line (method of Clayton and Mayeda 1963). Oxygen isotopic analyses were completed using a Micromass Optima isotope ratio mass spectrometer (IRMS) at the USGS in Denver.

The second portion of each separate was loaded into Ag capsules and decomposed in a Thermo Temperature Conversion Elemental Analyzer (TC/EA). Evolved H_2 gas was purified by gas chromatography and analyzed for hydrogen isotopes using a Thermo Delta V IRMS at the USGS in Denver (method of Sharp et al. 2001).

Oxygen and hydrogen isotope ratios are reported in conventional delta notation in units of per mil (‰), as follows: $\delta R = ((R_{sample}/R_{standard}) - 1) \times 1000$, where R is the isotopic ratio of $^{18}O/^{16}O$ or $^{2}H/^{1}H$. The reference standard used herein is Vienna Standard Mean Ocean Water (V-SMOW). Data were normalized so that analyses of reference materials NBS 28 silica gave a $\delta^{18}O$ value of 9.58 ‰ and analyses of USGS 57 and USGS 58 gave $\delta^{2}H$ values of -91.5 and -28.4 ‰, respectively. Analytical error was ±0.2‰ for oxygen and ±1 ‰ for hydrogen.

Isotopic compositions of fluids were calculated from the measured phyllosilicate compositions and the empirically or experimentally derived mineral-H_2O fractionation factors of O'Neil and Taylor (1969), Suzuoki and Epstein (1976), Bowers and Taylor (1985), and Zheng (1993).

3 Results

3.1 Measured phyllosilicates

Phlogopite from the unaltered lamprophyre dike give $\delta^{18}O$ values of 6.9 to 8.6 ‰ (V-SMOW; Figure 3). Muscovite from the altered dike give $\delta^{18}O$ values of 14.9 and 16.0 ‰ whereas those from the breccia give $\delta^{18}O$ values of 13.3 and 14.1 ‰.

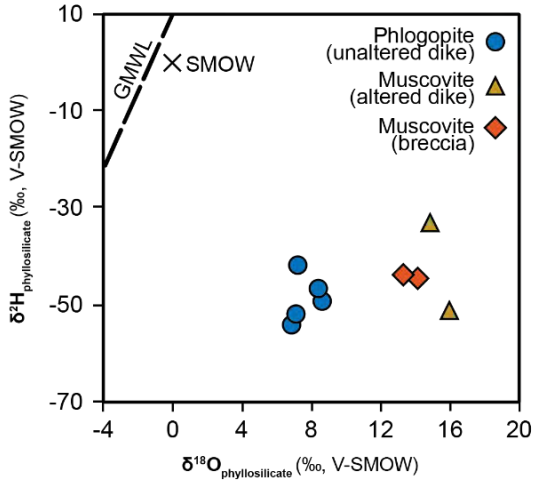

Figure 3. $\delta^{18}O$ and $\delta^{2}H$ (‰, relative to V-SMOW) of Hicks Dome phyllosilicates. GMWL= Global meteoric water line (Craig 1961).

Phlogopite from the unaltered lamprophyre dike give $\delta^{2}H$ values of -54 to -42 ‰ (V-SMOW; Figure 3). Muscovite from the altered dike give $\delta^{2}H$ values of -51 and -33 ‰, whereas those from the breccia give $\delta^{2}H$ values of -45 and -44 ‰.

3.2 Calculated fluid compositions

Phlogopite compositions measured herein are normal for ultramafic igneous rocks (e.g., Taylor and Sheppard 1986). If lamprophyre melts exsolved an aqueous fluid phase, the composition of that fluid phase would have reflected isotopic equilibrium exchange with melt and crystals near liquidus temperatures, which were probably around 1000°C. Assuming an equilibration temperature of 1000°C, calculated $\delta^{18}O_{H2O}$ values from phlogopite in the unaltered lamprophyre dike are 9.2 to 10.7 ‰, with an average of 9.9 ‰ (Figure 4). $\delta^{2}H_{H2O}$ values calculated from phlogopite in the unaltered lamprophyre dike are -66 to -54 ‰, with an average of -61 ‰ (Figure 4).

The relatively coarse (0.25–5 mm) crystalline muscovite in the metasomatized dike and calcite cemented breccia are likely precipitated from a hydrothermal fluid at temperatures between 200 to 600°C. The $\delta^{18}O_{H2O}$ values calculated from muscovite are 5.4 to 14.6 ‰ and 3.8 to 12.8 ‰ for the altered dike and breccia, respectively (Figure 4). $\delta^{2}H_{H2O}$ values calculated from muscovite are -60 to -10 ‰ and -53 to -21 ‰ for the altered dike and breccia, respectively (Figure 4).

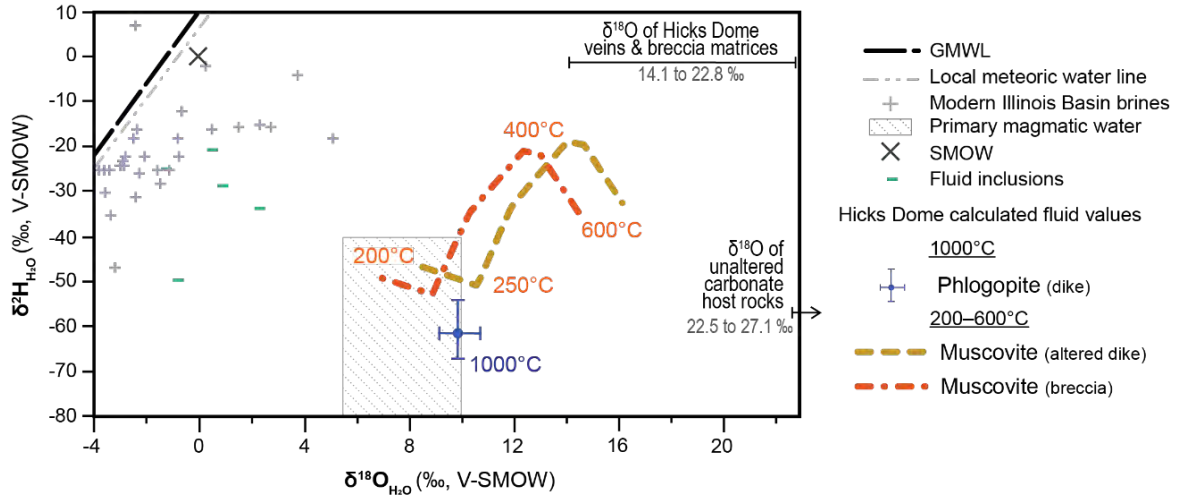

Figure 4. *Average $\delta^{18}O$ and $\delta^{2}H$ of calculated fluids over a range of temperatures relative to other fluid and rock compositions. Illinois Local meteoric water line from Kendall and Coplen (2001). Illinois Basin brine data from Clayton et al. (1966) and Labotka et al. (2015). Fluid inclusion data from Richardson et al. (1988). Illinois basin unaltered carbonate data from Pinckney and Rye (1972) and Moorehead (2013). Hicks Dome data from Moorehead (2013).*

4 Discussion

The $\delta^{18}O$ and $\delta^{2}H$ values of phlogopite from the lamprophyre dike measured herein preserve their primary magmatic compositions. This is demonstrated by the fact that their calculated fluid compositions are consistent with primary magmatic water at 1000°C (Figure 4). However, the two phlogopite samples with the most positive $\delta^{18}O$ values lie slightly outside the primary magmatic water box, which may implicate a more ^{18}O rich fluid component (Figures 3,4).

The measured $\delta^{18}O$ values of muscovite from the altered lamprophyre dike and calcite cemented breccia are more enriched in ^{18}O, which is typical of minerals that precipitate from fluids that are enriched in ^{18}O relative to meteoric water (Figure 4). If muscovite equilibrated isotopically at temperatures below 250°C, the calculated fluid compositions are consistent with mixing of a magmatic fluid related to lamprophyre emplacement, represented by the composition of $\delta^{18}O_{H2O}$ and $\delta^{2}H_{H2O}$ derived from phlogopite at 1000°C, and a basinal brine. This fluid composition supports the magmatic fluid-brine mixing model suggested by Plumlee et al. (1995). Modern brines in strata of the Illinois basin are a combination of connate water, residual brine produced by evaporation of seawater, halite dissolution brine, and meteoric water (Figure 4; Clayton et al. 1966; Labotka et al. 2015). Permian residual brines extracted from fluid inclusions in MVT fluorite and sphalerite in the Cave-in-Rock subdistrict of the IKFD (Figure 1b) are thought to represent main stage saline fluids (Figure 4; Richardson et al. 1988).

On the other hand, if muscovite equilibrated isotopically at temperatures above 250°C, the calculated fluid compositions are consistent with isotopic exchange with a magmatic fluid and Illinois basin carbonate rocks which have $\delta^{18}O$ values between +22.5 to +27.1 ‰ (Pinckney and Rye 1972; Moorehead 2013).

Although the isotopic equilibration temperature for hydrothermal muscovite is not precisely known, the calculated $\delta^{2}H_{H2O}$ value is higher than the corresponding value for the lamprophyre fluid no matter what temperature is assumed for equilibration (Figure 4). Thus, the muscovite did not form from pristine lamprophyre fluid. However, a magmatic origin for the muscovite fluid is not ruled out because a carbonatite melt could have evolved a more ^{2}H-enriched fluid than the lamprophyre melt.

A carbonatite source for hydrothermal fluids at Hicks Dome has been suggested due to its enrichment in REE+Y, Th, Ti, Nb, and F, which parallels that of sediment host mineralization on the periphery of the Bear Lodge carbonatite (Wyoming, USA; Andersen et al. 2021). Moreover, Moorehead (2013) measured the $\delta^{13}C$ and $\delta^{18}O$ values of calcite in veins and breccia matrices at Hicks Dome and determined that these values reflect magmatic-hydrothermal fluids that isotopically exchanged with carbonatite and Illinois basin host carbonate rocks. Lastly, Bradbury and Baxter (1992) characterized the nearby Grant Intrusive (Figure 1b) as a carbonatitic breccia, whose carbon and oxygen isotope compositions may indicate exchange between magmatic fluid and carbonate rock (Moorehead 2013).

$\delta^{2}H_{H2O}$ values ≥-40‰ are not uncommon for fluids condensed from magmatic vapors. Studies have found that aqueous fluids exsolved from melts are enriched in deuterium relative to the water dissolved in the melt. Separated vapor is further enriched in deuterium relative to conjugate hypersaline brine (Giggenbach 1992). The large volume of solution collapse breccias at Hicks Dome is consistent with a magmatic fluid origin because magmatic vapors are often acidic and therefore

corrosive to carbonate rock due to high concentrations of H_2CO_3, H_2SO_4, and HCl.

It is also possible that the high δ^2H_{H2O} values are secondary, as hydrogen isotopes values are more easily modified than oxygen isotope values in phyllosilicates without phase changes and at low temperature (≤350°C; O'Neil and Kharaka 1976). This may be why the oxygen isotope values of the muscovite are similar, whereas the hydrogen isotopes show one value that is ~20 ‰ heavier than the other values (Figure 3). Deuterium rich meteoric water or Illinois basin formation water may have migrated into basement rocks under low water/rock conditions, or shale membrane filtration.

The data and calculated fluid compositions presented here suggest that there were at least two episodes of phyllosilicate formation or alteration associated with, first, intrusion of lamprophyre melts (magmatic), and second, metasomatism of the lamprophyre dikes plus breccia formation associated with the inferred intrusion of carbonatite melts (orthomagmatic and metasomatic).

5 Summary

Stable isotope data on phlogopite from a lamprophyre dike and muscovite from a metasomatized dike and calcite cemented breccia have distinct compositions. At magmatic temperatures, phlogopite from an unaltered lamprophyre dike likely formed from primary magmatic water. Enrichment in ^{18}O for calculated $\delta^{18}O_{H2O}$ values from muscovite suggests that at these minerals formed from magmatic fluids that exchanged with the carbonate host rocks or from mixing between magmatic fluids and basinal brines. High δ^2H_{H2O} values calculated from muscovite indicate they did not form from a lamprophyre fluid but may be from a carbonatite or acidic fluid with condensed magmatic vapors.

Future work will entail analyzing more phyllosilicate separates from dikes and breccias for their oxygen and hydrogen isotope ratios, and further evaluate the magmatic hydrothermal system at Hicks Dome.

Acknowledgements

Support for sample preparation and mineral separation provided by William Benzel, Kristian Price, Christopher Holm-Denoma, and Derek Ensign. TC/EA analyses completed by Craig Stricker. This work benefitted from discussions with Mitchell Bennett. This work is funded by the U.S. Geological Survey's Earth Mapping Resources Initiative (Earth MRI) and the Mendenhall Postdoctoral Research Fellowship program to JAM. Any use of trade, firm, or product names is for descriptive purposes only and does not imply endorsement by the U.S. Government.

References

Andersen AK, Hofstra AH, Nuelle LM (2021) Hydrothermal HFSE(+HREE) mineralization in the Bear Lodge Alkaline Complex—a key to understanding the larger Hicks Dome critical mineral resource? Goldschmidt2021 Virtual Conference

Bowers TS, Taylor Jr. HP (1985) An integrated chemical and stable-isotope model of the origin of Midocean Ridge Hot Spring Systems. Journal of Geophysical Research: Solid Earth 90:12583–12606

Bradbury JC, Baxter JW (1992) Intrusive breccias at Hicks Dome Hardin County, Illinois. Illinois State Geological Survey, Champaign, IL

Clayton RN, Mayeda TK (1963) The use of bromine pentafluoride in the extraction of oxygen from oxides and silicates for isotopic analysis. Geochimica et Cosmochimica Acta 27:43–52

Clayton RN, et al (1966) The origin of saline formation waters: 1. Isotopic composition. Journal of Geophysical Research 71:3869–3882

Craig H (1961) Isotopic Variations in Meteoric Waters. Science 133:1702–1703

Denny FB, et al (2008) The Illinois-Kentucky Fluorite District, Hicks Dome, and Garden of the Gods in southeastern Illinois and northwestern Kentucky. In: Maria AH, Counts RC (eds) From the Cincinnati Arch to the Illinois Basin: Geological Field Excursions along the Ohio River Valley. Geological Society of America, pp 11–24

Giggenbach WF (1992) Isotopic shifts in waters from geothermal and volcanic systems along convergent plate boundaries and their origin. Earth and Planetary Science Letters 113:495–510

Kendall C, Coplen TB (2001) Distribution of oxygen-18 and deuterium in river waters across the United States. Hydrological Processes 15:1363–1393

Labotka DM, et al (2015) Isotopic and geochemical characterization of fossil brines of the Cambrian Mt. Simon Sandstone and Ironton–Galesville Formation from the Illinois Basin, USA. Geochimica et Cosmochimica Acta 165:342–360

Moorehead A (2013) Igneous intrusions at Hicks Dome, southern Illinois, and their relationship to fluorine-base metal-rare earth element mineralization. M.Sc. Thesis, Southern Illinois University

O'Neil JR, Taylor Jr. HP (1969) Oxygen isotope equilibrium between muscovite and water. Journal of Geophysical Research (1896-1977) 74:6012–6022

O'Neil JR, Kharaka YK (1976) Hydrogen and oxygen isotope exchange reactions between clay minerals and water. Geochimica et Cosmochimica Acta 40:241–246

Pinckney DM, Rye RO (1972) Variation of O^{18}/O^{16}, C^{13}/C^{12}, texture, and mineralogy in altered limestone in the Hill Mine, Cave-in-District, Illinois. Economic Geology 67:1–18

Plumlee GS, Goldhaber MB, Rowan EL (1995) The potential role of magmatic gases in the genesis of Illinois-Kentucky fluorspar deposits; implications from chemical reaction path modeling. Economic Geology 90:999–1011

Richardson CK, Rye RO, Wasserman MD (1988) The chemical and thermal evolution of the fluids in the Cave-in-Rock fluorspar district, Illinois; stable isotope systematics at the Deardorff Mine. Economic Geology 83:765–783

Sharp ZD, Atudorei V, Durakiewicz T (2001) A rapid method for determination of hydrogen and oxygen isotope ratios from water and hydrous minerals. Chemical Geology 178:197–210

Suzuoki T, Epstein S (1976) Hydrogen isotope fractionation between OH-bearing minerals and water. Geochimica et Cosmochimica Acta 40:1229–1240

Taylor Jr. HP, Sheppard SMF (1986) Igneous rocks: I. Processes of isotopic fractionation ad isotope systematics. In: Valley JW, Taylor Jr. HP, O'Neil JR (eds) Stable Isotopes in High Temperature Geological Processes. Mineralogical Society of America, pp 227–271

U.S. Geological Survey (2022) 2022 Final List of Critical Minerals [notice], Federal Register 87:10381–10382

Zheng Y-F (1993) Calculation of oxygen isotope fractionation in hydroxyl-bearing silicates. Earth and Planetary Science Letters 120:247–263

Iron-Ti oxide and apatite mineralisation associated with alkaline monzonitic rocks: An example from the Kodal deposit, Permian Oslo Rift, Norway

Ana Carolina R. Miranda[1], Nolwenn Coint[1], Sarah Dare[2] and Eduardo T. Mansur[1]
[1]*Geological Survey of Norway, Trondheim, Norway*
[2]*Department of Applied Sciences, Université du Québec à Chicoutimi, Chicoutimi, Canada*

Abstract. Iron-Ti oxide and apatite enriched rocks are typically associated with anorthosite–mangerite–charnockite–granite (AMCG) and layered intrusions in magmatic systems or related to iron oxide apatite (IOA) deposits, in hydrothermal systems. The origin of these non-cotectic rocks in magmatic systems has been widely debated and several petrogenetic models have been proposed. The Kodal deposit, located in the Permian Oslo rift, South Norway, is the largest occurrence of Fe-Ti oxide and apatite mineralisation hosted within alkaline monzonitic rock, differing from known occurrences hosted within AMCG suites and mafic layered intrusions. The Fe-Ti oxide and apatite mineralisation consists of disseminated and massive ore, which are mainly composed of variable amounts of titanomagnetite, apatite and augite and minor amphibole and biotite. We have systematically sampled four representative drill cores across the Kodal deposit. Further investigation of the concentration of the trace elements in titanomagnetite and apatite in the host rock, disseminated and massive ores will be performed by LA-ICP-MS. This will allow us to assess which petrogenetic processes, such as liquid-liquid immiscibility, fractional crystallization or mineral accumulation, contributed to the formation of Fe-Ti oxide and apatite mineralisation at Kodal.

1 Introduction

The Fe-Ti oxide and apatite-rich rocks (i.e. nelsonites) of magmatic origin are commonly associated with mafic and intermediate intrusive complexes related to anorthosite–mangerite–charnockite–granite (AMCG) and layered intrusions (Dymek and Owens 2001; Charlier et al. 2008; Coint et al. 2020). In hydrothermal systems, these are commonly related to iron oxide apatite deposits (IOA). Nevertheless, the origin of these non-cotectic rocks has been widely debated and petrogenetic models evoking fractional crystallization, liquid-liquid immiscibility, mineral accumulation and residual melts concentrated by filter pressing have been proposed as alternatives to explain their origin (Philpotts 1967; Emslie 1975).

Discovered in the late eighteen hundreds, the Kodal deposit is one of the largest Fe-Ti oxide and apatite deposits in Norway (Figure 1). Different from known occurrences hosted within AMCG suites and mafic layered intrusions, the Fe-Ti oxide and apatite mineralisation at Kodal is hosted within alkaline monzonite. Three distinct models have been proposed to explain the genesis of the Kodal deposit: (i) silicate-liquid immiscibility leading to the separation of an Fe-rich melt (Bergstøl 1972; Kragh and Jensen 1991); (ii) fractional crystallization and physical accumulation of apatite and Fe-Ti-oxides from a monzonitic magma (Peterson 1978); and (iii) apatite and Fe-Ti oxide crystallization at depth followed by upward transport, accompanied by mineral sorting, to shallow crustal levels (Andersen and Seiersten 1994).

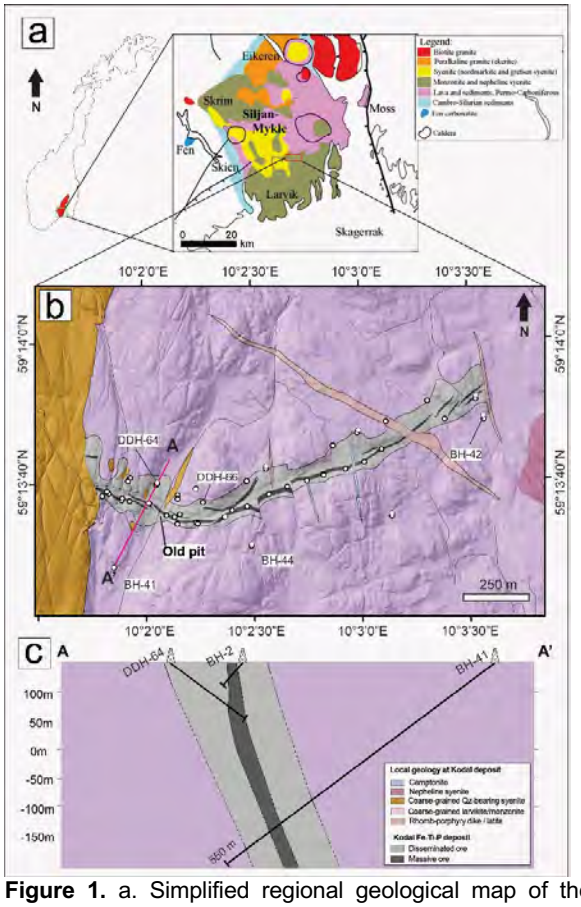

Figure 1. a. Simplified regional geological map of the southern part of Oslo rift showing the location of Kodal Fe-Ti-P deposit; b. Geological map showing the Kodal deposit. The white dots represent the location of drill cores; c. Profile containing three drillcores showing the shape and orientation of the ore body.

Considering that the genesis of Kodal deposit is poorly understood and that the Fe-Ti-P mineralisation is hosted in monzonitic rocks, the Kodal deposit offers the opportunity to understand a so far unique Fe-Ti-P mineralisation hosted in evolved, alkaline magmatic rocks.

In this work, we report preliminary results of fieldwork, and petrographic description of the host rock and Fe-Ti-P ores of the Kodal deposit. Further investigation of trace elements in titanomagnetite and apatite will be performed to test the different hypotheses for the formation of the Kodal deposit.

2 Geological setting of the Kodal Fe-Ti-P deposit

The Kodal deposit is located in the Permian Oslo Rift at the southern part of Norway (Figure 1). It represents the largest occurrence of Fe-Ti-P mineralisation in the Larvik Plutonic Complex (LPC), with a total indicated resource of 14.6 Mt at 5.18% P_2O_5 and 24.12% Fe (Kodal Minerals PLC 2014). The LPC comprises a slightly- to under-saturated, alkaline monzonite (regionally referred to as larvikite), syenite and nepheline-syenite (regionally referred to as lardalite), formed during the Permian rifting (Petersen 1978). These intrusions form several rings, which suggests sequential shifting of centres of magmatic activity towards the west, with the nepheline-syenite being the youngest phase (Petersen 1978; Rämö et al., 2022). The positioning of the Kodal deposit within the LPC is not well constrained, but it is possible that the deposit is associated with the latest magmatic pulses in the region.

The Kodal deposit is poorly exposed, except for an old mining pit area, where massive nelsonites can be observed (Figures 1 and 2a). The Fe-Ti-P orebody consists of an approximately 2 km long, and 100 meters thick, tabular, E-W trending orebody, steeply dipping (70-80 degrees) towards the south (Figure 1). The ore consists of variable amounts of titanomagnetite, apatite and augite, with minor amphibole and biotite. It can be massive or disseminated where it constitutes up to 40% of the total volume of the rock (Figure 2). The massive ore varies from a few centimetre intervals that occur as pockets within the monzonite, displaying sharp contacts, to zones with approximately 2 metres of thickness, normally surrounded by disseminated intervals (Figures 1 and 2).

Around 40 cores were drilled in the Kodal deposit in the early 1980's, which allows us to precisely constrain the geometry of the ore body and detailed sampling of different portions of the mineralisation. Whole-rock geochemical analyses for the cores yield in average 1.33 wt.% P_2O_5, 12.3 wt.% Fe_2O_3(T) and 2.4 wt.% TiO_2 for the host monzonite, 2.7 wt.% P, 19.1 wt.% Fe_2O_3(T) and 4.18 wt.% TiO_2 for the disseminated ore, and 7.3 wt.% P_2O_5, 44.7 wt.% Fe_2O_3(T) and 8.63 wt.% TiO_2 for the massive ore. Thus, the limit between the monzonite and the disseminated ore (Figure 1) is mostly based on Fe_2O_3(T), TiO_2 and P_2O_5 concentrations, but local variations are common and the profile showed in the Figure 1c is just a schematic simplification of the ore types.

The relationship between the host rocks and the different ore types is variable, but magmatic flow textures are commonly observed (Figure 2). In these cases, coarse-grained feldspar crystals from the host monzonite display a parallel alignment and accompany domains with massive Fe-Ti-P ore (Figure 2b). Moreover, although a gradual transition from host rock to disseminated and to massive ore has been observed, a sharp contact between massive ore and the host rock is also common (Figure 2c). Overall, the textures suggest that the host monzonite and the Fe-Ti-P-rich domains co-existed, and were eventually mobilized together, prior to complete crystallization.

3 Methods

We have systematically described and sampled four representative drill cores across the deposit (Figure 1). Over 100 samples have been collected, and 44 thin sections were prepared and characterized under reflected and transmitted light.

The concentration of trace element in Fe-oxides (Ti-magnetite and ilmenite) and apatite in the host rock, disseminated and massive ores will be obtained by LA-ICP-MS, at the Geological Survey of Norway.

4 Preliminary results

The host monzonite is predominantly composed of dark grey coarse-grained feldspar crystals (ternary feldspar), associated with accumulations of interstitial domains of fine-grained mafic minerals (Figure 3a). These interstitial domains (approximately <10% of the rock) comprise titanomagnetite, with ilmenite lamellae exsolutions, apatite and augite (Figures 3a and 4a). Apatite crystals occur as inclusions in magnetite and augite crystals, but also as euhedral crystals with well-defined contacts with other phases. Amphibole and biotite are observed as a product of augite alteration, normally concentrated in fractures and along augite rims (Figure 4a). Commonly, centimetre-scale agglomerates of titanomagnetite are surrounded by a thin rim of titanite crystals at the contact with surrounding silicates (Figure 4a). In weathered examples, the monzonite displays a pale/whitish colour as a result of the alteration of large feldspar crystals (Figure 2a). The degree of such alteration is variable, but can be pervasive, characterizing a complete change of feldspar colour, or partial, where only the rims of feldspar crystals are transformed to a very-fine grained aggregate of sericite. In cases where pervasive alteration is observed, the magmatic texture of the rock is still preserved, and the only remarkable feature is the change in the rock colour (Figure 2b).

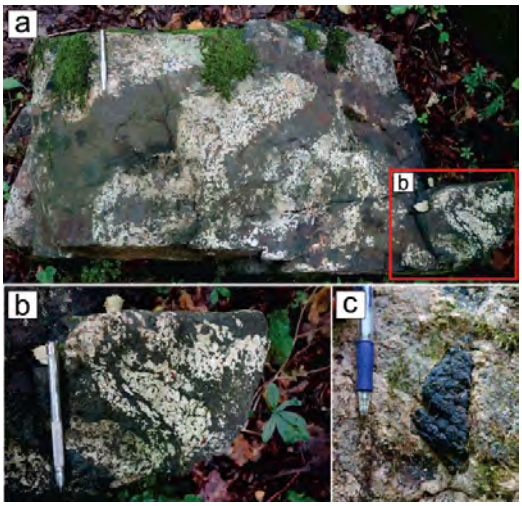

Figure 2. a. Sample close to the old excavation pit at Kodal deposit. The host monzonite displays a magmatic flow texture defined by the alignment of rhomb-shaped feldspar phenocrysts and centimetric domains of massive Fe-Ti-P ore; b. Monzonite with massive Fe-Ti-P ore displaying folded magmatic foliation. The white colour of coarse-grained euhedral feldspar crystals is a result of surface weathering; c. Outcrop near the old excavation pit displaying a centimetric massive oxide-apatite bleb within the host monzonite. Note the sharp contact between the massive ore and the host rock.

Disseminated ore is more abundant relative to massive ore within the Kodal deposit (Figure 1). Iron-Ti oxide (most commonly titanomagnetite and minor ilmenite), apatite and augite accumulations form a more or less connected interstitial network around alkali feldspar phenocrysts. Locally, a greater proportion of the interstitial mafic minerals relative to feldspar led to the development of a net-textured ore (Figures 3b-c). In these cases, the mafic minerals define an interstitial continuum within large feldspar crystals and their volume can reach up to 40%.

The massive ore is composed mainly of apatite and titanomagnetite with variable amounts of augite. It can be divided into augite-poor and augite-rich massive ore (Figure 3d). In the augite-rich domains, the augite crystals are medium- to fine-grained and commonly display amphibole and biotite alteration along the edges (Figures 4a and 4b). Augite-poor domains comprise predominantly titanomagnetite and apatite, with minor titanite. Apatite occurs included within larger magnetite crystals or displaying sharp contact with smaller crystals. The proportion of apatite varies, but is commonly greater than 30% of the rock volume.

The transition between disseminated and massive ore domains is variable and can be given by a progressive increase of apatite and magnetite, but most frequently is marked by a sharp contact. Round-shaped pockets of massive ore of few tens of centimetres are also commonly found embedded within the disseminated ore, but less frequently in direct contact with the host monzonite (Figure 2c).

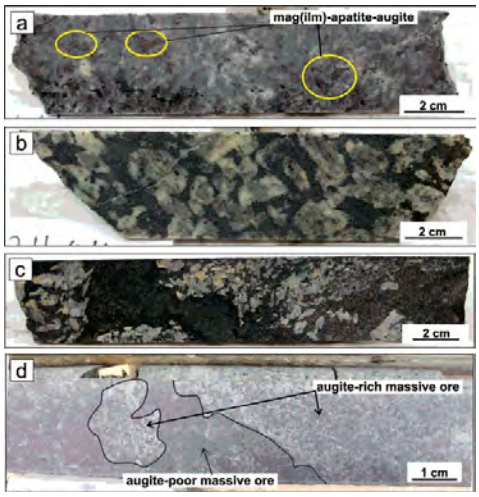

Figure 3. Representative facies of the Kodal Fe-Ti-P deposit. a. Monzonite hosting euhedral feldspar crystals surrounded by interstitial domains of mafic minerals (i.e., augite, titanomagnetite, apatite and minor ilmenite); b. Net-textured Fe-Ti-P ore (dark) surrounding grey-coloured, partially altered, feldspar crystals; c. Contact between the net-textured and massive Fe-Ti-P ores. Note the sharp contact between the two; d. Massive Fe-Ti-P ore with augite-rich and augite-poor domains. Note the sharp contact between both facies, and the occurrence of irregular blebs of the augite-rich ore within augite-poor domains.

5 Concluding remarks and next steps

A remarkable feature of the Kodal deposit is the presence of magmatic flow textures in the ore (Figure 2c), defined by the alignment of alkali feldspar. Although our preliminary results do not allow us yet to constrain the ore forming processes that led to the formation of the deposit, the textures are indicative that magmatic flow played a role in the segregation of the Fe-Ti-P ore minerals. This is important as a process leading to the non-cotectic accumulation of augite, apatite and magnetite is required in order to explain the origin of the Kodal deposit.

To improve our understanding of the formation of the Kodal deposit, we will systematically investigate the trace-element composition of magnetite and apatite in different portions and facies of the deposit. Recent contributions have shown that these results can be used to unveil processes, such as accumulation during fractional crystallization or silicate-liquid immiscibility (Dare et al. 2014; Arguin et al. 2018; Coint et al. 2020; Kieffer et al., 2023). Moreover, although studies assessing the composition of apatite and Fe-oxides in Fe-Ti-P-rich rocks formed at different geological settings has gained more attention in recent years, this is not yet the case for alkaline systems. As such, the Kodal deposit offers the opportunity to unveil the chemistry of these minerals in an Fe-Ti-P deposits formed at as part of alkaline system, which, to the best of our knowledge has not yet been assessed elsewhere.

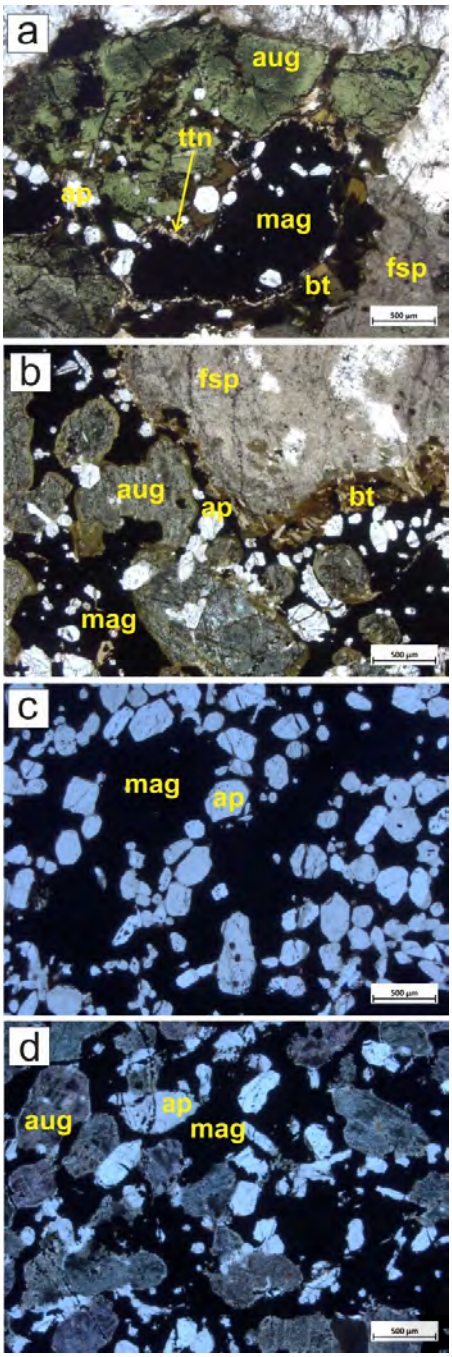

Figure 4. Transmitted light photomicrographs of the monzonitic host-rock of the Kodal deposit and different Fe-Ti-P ore types. a. Local accumulation of titanomagnetite and apatite within augite crystals in the monzonite. Note the occurrence of a thin rim of titanite at the contact between magnetite and surrounding silicates; b. Net-textured ore with titanomagnetite and apatite domains surrounding a coarse-grained. Note the partial alteration of the feldspar crystal and the biotite-rich contact between the feldspar and magnetite; c. Augite-poor massive ore comprising abundant euhedral apatite crystals both included within and at contact with magnetite; d. Augite-rich massive ore with partial alteration of the augite crystals along fractures and rims. Abbreviations: aug: augite; ap: apatite; bt: biotite; fsp: feldspar. ttn: titanite; mag: magnetite.

Acknowledgements

Part of the analyses for this study were performed in the Norwegian Laboratory for Mineral and Materials Characterisation (MiMaC) NGU node, supported by the Research Council of Norway project number 269842/F50. This work was also partly supported by a Canada Research Chair program grant (#950-231976) to Prof. Dr. Sarah Dare (UQAC) in Geochemistry Applied to Ore Deposits.

References

Andersen T and Seiersten M (1994) Deep cumulates in a shallow intrusion: Origin and crystallization history of a pyroxenite (jacupirangite s.l.) body in the Larvik Pluton, Oslo Region, South Norway. N. Jb. Miner. Mh., H. 6,255 - 274

Arguin J-P, Pagé P, Barnes S-J, Girard R, Duran C (2018) An Integrated Model for Ilmenite, Al-Spinel, and Corundum Exsolutions in Titanomagnetite from Oxide-Rich Layers of the Lac Doré Complex (Québec, Canada). *Minerals* 8(11):476. https://doi.org/10.3390/min8110476

Bergstøl S (1972) The Jacupirangite at Kodal, Vesffold, Norway. (A potential Magnetite, ilmenite and apatite ore). Mineral. Deposita 7:283-246

Charlier B, Sakoma E, Sauvé M, Stanaway K, Auwera JV, Duchesne JC (2008) The Grader layered intrusion (Havre-Saint-Pierre Anorthosite, Quebec) and genesis of nelsonite and other Fe–Ti–P ores. Lithos 101:359-378, https://doi.org/10.1016/j.lithos.2007.08.004.

Coint N, Keiding JK, Ihlen PM (2020) Evidence for Silicate–Liquid Immiscibility in Monzonites and Petrogenesis of Associated Fe–Ti–P-rich rocks: Example from the Raftsund Intrusion, Lofoten, Northern Norway, *Journal of Petrology* 61 (4) egaa045 https://doi.org/10.1093/petrology/egaa045

Dare SAS, Barnes SJ, Beaudoin G, *et al.* (2014) Trace elements in magnetite as petrogenetic indicators. *Miner Deposita* **49**, 785–796 https://doi.org/10.1007/s00126-014-0529-0

Dymek RF, and Owens BE (2001) Petrogenesis of Apatite-Rich Rocks (Nelsonites and Oxide-Apatite Gabbronorites) Associated with Massif Anorthosites. *Economic Geology* 96(4):797–815. doi: https://doi.org/10.2113/gsecongeo.96.4.797

Emslie RF (1975) Major rock units of the Morin Complex, southwestern Quebec: Geological Survey of Canada Paper 74-48, 37p.

Kieffer MA, Dare SA, and Namur O (2023) The use of trace elements in apatite to trace differentiation of a ferrobasaltic melt in the Sept-Iles Intrusive Suite, Quebec, Canada: Implications for provenance discrimination. *Geochimica et Cosmochimica Acta* 342:169-197

Kodal Minerals plc. (2014) *Group Annual Report and Financial Statements for the year ended 31 March 2014.* Kodal Minerals plc, London.

Kragh K and Jensen OA (1991) An immiscible iron-rich liquid in a larvikite magma? GeoSkrifter 38: 32-34

Petersen JS (1978) Structure of the larvikite-lardalite complex, Oslo Region, Norway, and its evolution. Geol. Rundschau 67,330-342.

Philpotts AR (1967) Origin of certain iron-titanium oxide and apatite rocks: Economic Geology, 62:303–315

Rämö OT, Andersen T, and Whitehouse MJ (2022) Timing and Petrogenesis of the Permo-Carboniferous Larvik Plutonic Complex, Oslo Rift, Norway: New Insights from U–Pb, Lu-Hf, and O Isotopes in Zircon. Journal of Petrology, 63(12), egac116

Fengchengite from Sierra La Vasca Complex, Mexico

Maria Grazia Perna[1], Antonio Rodriguez Vega[2], Emma Humpreys-Williams[3], Fabrizio Nestola[4], Biagioni Cristian[5], Gianluigi Rosatelli[1], Francesco Stoppa[1]

[1] Department of Psychological, Health and Territory Sciences, University "Gabriele d'Annunzio" Chieti-Pescara, 66100, Chieti, Italy

[2] Escuela Superior de Ingeniería (ESI) Universidad Autónoma de Coahuila. Boulevard Adolfo López Mateos s/n, Nueva Rosita, San Juan de Sabinas, Coahuila.

[3] The Natural History Museum, London SW7 5BD, UK

[4] Department of Geosciences, Padua University, 35121 Padova, Italy

[5] Department of Earth Sciences, Pisa University, 56126 Pisa, Italy

Abstract. Fengchengite is a member of eudialyte group-minerals, with a general formula $Na_{12}\square_3Ca_6(Fe^{3+},\square)_3Zr_3Si(Si_{25}O_{73})(H_2O)_3(OH)_2$. The cell parameters are *a*=14.2426 Å, *c*=30.1889 Å, *V*=5303.32 Å^3 and the space group is $R\bar{3}m$. The genetic environment is associated with highly evolved peralkaline igneous products. The associated paragenesis consists of alkali feldspars, aegirine, arfvedsonite, apophyllite, calcite and other mineral phases at REE, corresponding to the typical mineralogy of a kakortokite, a variety of agpaitic nepheline syenite displaying cumulate textures and igneous layering. Kakortokite is associated with wollastonite, containing goetzenite, brytholite and pyrite. Fengchengite is a rare mineral with a puzzling structure that is difficult to reconstruct.

1 Introduction

The economic importance and demand for high field strength elements (HFSE) and rare earth elements (REEs) have increased significantly in recent years (e.g. Weng et al. 2015; Goodenough et al. 2017), especially in the last period due to the political crisis. They form the basis for transitioning to a high-tech, green-tech and sustainable industry. This has led to the development and search for new deposits and sources that can lead to the extraction of such products. Alkaline complexes are placed in this perspective, where the close association between carbonatitic and alkaline rocks represents one of the largest reservoirs of REE and HFSE (e.g. Dostal 2017). Rocks from these complexes show an unusual enrichment in these elements and a typical mineralogy composed of REE-bearing rare and complex minerals.

Peralkaline igneous rocks are characterised by a molar ratio (Na+K)/Al >1. Depending on the HFSE-bearing minerals, a distinction is made between miaskitic rocks, in which HFSE are mainly hosted by zircon/baddeleyite and titanite/perovskite, and agpaitic rocks, in which HFSE are hosted by Na-Ca-HFSE complex minerals, in particular eudialyte group minerals (EGMs, hereafter), rinkite group minerals and wöhlerite group minerals (e.g. Marks and Markl 2017).

The EGMs are represented by HFSE-REE-rich Na-Ca-zirconosilicates and represent the index mineral for agpaitic peralkaline systems. The first occurrences were reported from Kangerdluarssuk, Ilìmaussaq, South Greenland (Stromeyer 1819).

The accepted IMA formula (Johnsen et al. 2003a) is as follows:
$\{N(1)_3N(2)_3N(3)_3N(4)_3N(5)_3\}\{[M(1a)_3M(1b)_3]_3M(2)_3M(3)M(4)Z_3[Si_{24}O_{72}]Ø_{0\text{-}6}\}X(1)X(2)$

EGMs are currently composed of 30 chemical species (for the empirical and corresponding CNMNC formulae of the IMA-approved members of the eudialyte group, see Mikhailova et al. 2022 and references therein).

This mineral group is known from various occurrences, including the Lovozero alkaline massif, Russia (e.g. Mikhailova et al. 2020), the Ilìmaussaq complex, South Greenland (e.g. Marks et al. 2020), Mont Saint Hilaire, Quebec, Canada (e.g. Johnsen et al. 2003b), Tamazeght, Morocco (e.g. Schilling et al. 2009), Norra Kärr alkaline complex, Southern Sweden (e.g. Sjoqvist et al. 2013) and many others. The minerals typically associated with EGMs in these occurrences are aegirine and arfvedsonite, various Na-Al silicates such as alkali feldspars, nepheline, sodalite, zeolites and various HFSE and LILE-rich minerals such as astrophyllite, lamprophyllite, tugtupite, wohlerite, rosenbuschite and rinkite) (Schilling et al. 2011).

2 Geological Setting

Sierra La Vasca represents a Tertiary magmatic complex with an extension of approximately 100 km^2 and. It consists of two main intrusive bodies of granitic and monzonitic composition, associated with numerous minor intrusive bodies, including dykes and sills, of compositions varying between diorite, andesite, dacite and rhyolite. The area also presents a series of satellite minor complexes characterised by mainly alkaline and carbonatitic magmatism. Generally, the contact between carbonatitic and syenitic bodies is characterised by centimetric bars of wollastonite rocks. The Cretaceous carbonate sequence represents the basement.

3 Methods

Minerals analysis and BSE images were obtained using a Phenom XL SEM hosted at the DATA Laboratory at "G. d'Annunzio" University of Chieti-Pescara.

Eudialyte-group minerals were analysed by a JEOL 8200 Super-probe at Natural History Museum,

London. The accuracy of these analyses in analysing REE is ~1.3%, based on the detection limit. The detection limit is two magnitude orders lower than the hellandite group members' REE concentration.

Trace element concentrations were acquired using an ESI 213 nm Laser Ablation system and Agilent 7700 ICP-MS system at the Natural History Museum, London.

Spectra data reduction was performed using the Thermo Scientific™ OMNIC™ 9.2.0 Spectral Software at Padua University, Padua, Italy. Single-crystal XRD data were collected using a Supernova Rigaku Oxford Diffraction four-circle diffractometer (Rigaku) equipped with a 200K Pilatus Dectris detector (Dectris). The diffractometer was operated with Mo Kα radiation at 50 kV and 0.12 mA X-ray tube conditions.

Powder XRD was carried out using the X-ray diffractometer Bruker D2 Phaser, located at DATA (Chieti, Italy). The acquisition parameters are Cu-Kα (1.540598 Å) radiation generated at 30 kV and 15 mA in an exploratory interval between 3 and 70° 2θ, 0.1 steps, and a scan rate of 0.15°/s. Once the diffractogram was obtained, background subtraction and indexing of peaks with semi-quantitative analysis were performed. Finally, the mineral identification was performed using the software EVA.

3 Petrographic context

EGMs samples comes from a kakortokite, an agpaitic nepheline syenite. Kakortokite has alkali feldspars, aegirine, arfvedsonite and apophyllite as its main minerals (Figure 1). Accessory minerals are represented by other phases of REE minerals, including F-britholite, stillwellite-(Ce), kainosite-(Y) and gittinsite, a typical alteration mineral of the eudialyte group.

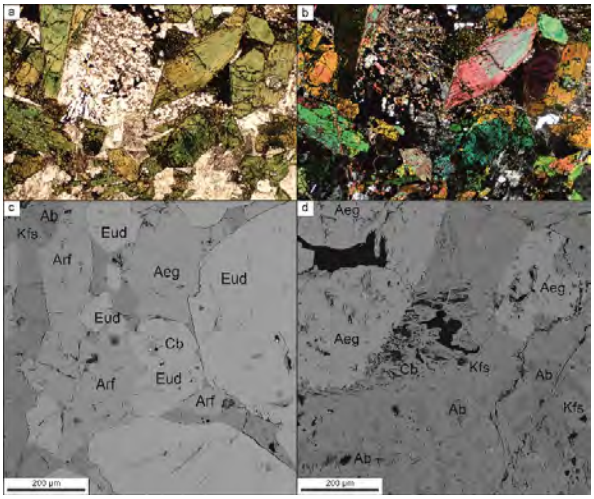

Figure 1. a-b. Plane-polarised (left) and cross-polarised (right) transmitted light images for kakortokite sample; c-d. BSE images of kakortokite sample. Abbreviation: Ab- albite; Kfs- k-feldspar; Eud- eudialyte group minerals; Aeg – aegirine; Arf – arfvedsonite; Cb – carbonate.

4 Crystal structure

The structure of the eudialyte group of minerals is hetero-polyhedral, with three layers alternating along the c-axis. The T-layer is characterised by three- or nine-membered SiO_4 tetrahedra, $[Si_3O_9]^{6-}$ or $[Si_9O_{27}]^{18-}$, respectively; the M-layer is formed by 6-membered rings of $[M(1)_6O_{24}]$ built by shared $M(1)O_6$ octahedra along one edge; and isolated octahedra of ZO6 form the Z-layer. They alternate in *TMTZ* mode (Rastsvetaeva 2007).

In the complex structure, the SiO_4 rings combined in $[Si_3O_9]^{6-}$ and $[Si_9O_{27}]^{18-}$ form layers perpendicular to [001]. Between two of these, rings of $[M(1)O_6]$ octahedra are connected by polyhedra of $[M(2)O_n]$, forming 2:1 layers. Zr cross-links these layers in octahedral coordination. The final presence of $[NaO_n]$ polyhedra, where Na can have different coordination, implies the filling of the structure. These structures form a trigonal system with space group *R3m*, $R\bar{3}m$ or *R3*. In the case of $R\bar{3}m$, the presence of the centre of symmetry between Si(1) and Si(2) reduces the number of different sites (Johnsen and Grice 1999). Furthermore, the N sites, which are 5 in the case of *R3m* and *R3*, are reduced to 3, with Na(1) equal to Na(2) and Na(3) equals Na(4). In this case, these N sites are entirely occupied by Na, except in the case of fengchengite, which is characterised by vacancies on the N(3) site (see Mikhailova et al. 2022).

The crystal structure of our eudialyte sample is solved on MoKα radiation and refined for 1929 unique reflections. The space group is trigonal, $R\bar{3}m$ with *a*=14.2426 Å and *c*=30.1889 Å, *V*=5303.32 Å^3.

5 Crystal chemistry

The chemical composition of eudialyte group minerals (in average and in wt.%) is SiO_2 51.2, ZrO_2 11.7, Nb_2O_5 0.3, TiO_2 0.8, Ta_2O_5 0.1, FeO 5.4, MnO 1.0, CaO 11.1, Na_2O 12.9, K_2O 0.2, La_2O_3 0.3, Ce_2O_3 0.9, Pr_2O_3 0.1, Nd_2O_3 0.4, Sm_2O_3 0.1, Gd_2O_3 0.1, Y_2O_3 0.4, HfO_2 0.2, Cl 2.2.

The formula recalculated based on Si+Zr+Ti+Hf+Nb= 29 (following Johnsen and Grice 1999) (in average and in a.p.f.u.) is Si 25.7, Zr 2.9, Nb 0.1, Ti 0.3, Fe 2.3, Mn 0.4, Ca 6.0, Na 12.5, K 0.1, La 0.1, Ce 0.2, Nd 0.1, Y 0.1, Cl 1.9.

6 Conclusion

Classifying minerals of the eudialyte group is a complex process which requires a thorough overview of the crystal structure and chemical composition.

Regarding the crystal structure, following Rastsvetaeva and Chukanov (2012), our sample turns out to be "12-layer eudialyte" being *a*=14.2426 Å and *c*=30.1889 Å, M(1)-disordered with spatial group $R\bar{3}m$ and, based on centring nine-membered Si, O rings by the additional Si-tetrahedra (T), M-octahedra (M) or vacancies (□) or combination of these, our sample falls into the T+T variant.

In terms of chemical composition, the classification was performed following Mikhailova et al. (2022). Our sample shows Zr> 2.25 belonging to the Zirconium eudialytes. The content of Ca is > 4.5 belonging to the subgroup of the Ca-rich Zirconium eudialytes. From the structural analysis, it belongs to the T+T variant with Si> 25.5, Nb < 0.5 and W < 0.5. Based on the content of Mn and Fe and their occupancy in the M(2) site, with $4.5 \geq {}^{M(2)}Mn + {}^{M(2)}Fe > 1.5$; ${}^{M(2)}Fe > {}^{M(2)}Mn$; $Fe^{3+} > Fe^{2+}$ our sample falls into the fengchengite group. This is in agreement with the structure as fengchengite is the only 12-layer end-member with space group $R\bar{3}m$.

The final formula is ${}^{N}\{[Na_{3.00}Na_{3.00}]_{\Sigma 6.00}(Na_{5.55}K_{0.13}Sr_{0.01}Ca_{0.31})_{\Sigma 6.00}(\square_{2.70}Ca_{0.08}Mn^{2+}_{0.22})_{\Sigma 3.00}\}_{\Sigma 15.00}$ ${}^{M(1)}(Ca_{5.61}La_{0.05}Ce_{0.13}Pr_{0.01}Nd_{0.06}Sm_{0.01}Gd_{0.01}Dy_{0.01}Er_{0.01}Yb_{0.01}Y_{0.10})_{\Sigma 6.00}{}^{M(2)}(Fe^{3+}_{2.52}Mn^{2+}_{0.21}Ti_{0.26}Ta_{0.01})_{\Sigma 3.00}$ ${}^{Z}(Zr_{2.87}Nb_{0.08}Ti_{0.03}Hf_{0.03})_{\Sigma 3.00}$ ${}^{M(3)}Si_{0.73}$ ${}^{M(4)}Si_{25}$ O_{73} ${}^{X(1)}(H_2O)_3$ ${}^{X(2)}(Cl_{1.89}OH_{0.11})_{\Sigma 2.00}$.

Acknowledgements

The authors sincerely thank Julia A. Mikhailova for valuable advice on crystallochemistry.

References

Dostal J (2017) Rare Earth Element deposits of alkaline igneous rocks. Resources 6(3):34. https://doi.org/10.3390/resources6030034

Goodenough KM, Wall F, Merriman D (2017) The Rare Earth Elements: demand, global resources, and challenges for resourcing future generations. Nat Resour Res 27:201-216. https://doi.org/10.1007/s11053-017-9336-5 https://doi.org/10.1134/S1075701512070069

Johnsen O, Grice JD (1999) The crystal chemistry of the eudialyte group. Canad Miner 37: 865–891.

Johnsen O, Ferraris G, Gault RA, Grice JD, Kampf AR, Pekov, IV (2003a) The nomenclature of eudialyte-group minerals. Canad Mineral 41(3):785-794. https://doi.org/10.2113/gscanmin.41.3.785

Johnsen O, Grice JD, Gault RA (2003b) Ferrokentbrooksite, a new member of the eudialyte group from Mont Saint-Hilaire, Quebec, Canada. Canad Mineral 41(1):55-60. https://doi.org/10.2113/gscanmin.41.1.55

Marks MAW, Eggenkamp HGM, Atanasova P, Mundel F, Kümmel S, Hagen M, Wenzel T, Markl G (2020) Review on the compositional variation of Eudialyte-group minerals in the Ilímaussaq Complex (South Greenland). Minerals 10(11):1011. https://doi.org/10.3390/min10111011

Marks MAW, Markl G (2017) A global review on agpaitic rocks. Earth Sci Rev 173:229-258. https://doi.org/10.1016/j.earscirev.2017.06.002

Mikhailova JA, Pakhomovsky YA, Panikorovskii TL, Bazai AV, Yakovenchuk VN (2020) Eudialyte group minerals from the Lovozero Alkaline Massif, Russia: occurrence, chemical composition, and petrogenetic significance. Minerals 10(12):1070. https://doi.org/10.3390/min10121070

Mikhailova JA, Stepenshchikov DG, Kalashnikov AO, Aksenov SM (2022) Who is who in the eudialyte group: a new algorithm for the express allocation of a mineral name based on the chemical composition. Minerals 12(2):224. https://doi.org/10.3390/min12020224

Rastsvetaeva RK (2007) Structural mineralogy of the eudialyte group: a review. Crystallogr Rep 52: 47-64.

Rastsvetaeva RK, Chukanov NV (2012) Classification of eudialyte-group minerals. Geol Ore Depos 54:487-497.

Schilling J, Marks MAW, Wenzel T, Markl G (2009) Reconstruction of magmatic to subsolidus processes in agpaitic system using eudialyte textures and composition: a case study form Tamazeght, Morocco. Canad Mineral 47(2):351-365. https://doi.org/10.3749/canmin.47.2.351

Schilling J, Wu F-Y, McCammon C, Wenzel T, Marks MAW, Pfaff K, Jacob DE, Markl G (2011) The compositional variability of eudialyte-group minerals. Mineral Mag 75(1):87-115. https://doi.org/10.1180/minmag.2011.075.1.87

Sjöqvist ASL, Cornell DH, Andersen T, Erambert M, Ek M, Leijd M (2013) Three Compositional Varieties of Rare-Earth Element Ore: Eudialyte-Group Minerals from the Norra Kärr Alkaline Complex, Southern Sweden. Minerals 3(1):94-120. https://doi.org/10.3390/min3010094

Stromeyer F (1819) Analyse einiger von dem Prof. von Giesecke in Grönland entdeckten Fossilien: Gieseckit, Saphirin, Apophyllit, Dichroit, Arragonit und Eudialit. Ann Phys 63:372–381 (in German).

Weng Z, Jowitt SM, Mudd GM, Haque N (2015) A detailed assessment of global Rare Earth Element Resources: opportunities and challenges. Econ Geol 110(8):1925-1952. https://doi.org/10.2113/econgeo.110.8.1925

The Mount Weld rare earth element deposit, Western Australia: a carbonatite-derived laterite

Philip L. Verplanck[1], Heather A. Lowers[1], Adam R. Boehlke[1], Jay M. Thompson[1], Ganesh Bhat[2], Cameron Mercer[1]
[1]US Geological Survey, Denver, Colorado, USA
[2]Lynas Rare Earths Ltd., Laverton, Australia

Abstract. Carbonatite-hosted rare earth element (REE) deposits are the primary source of the world's light REEs and have the potential to be a source of heavy REEs. The Mount Weld REE deposit in Western Australia is hosted in a lateritic sequence that reflects supergene enrichment of the underlying carbonatite complex. Similar to other carbonatite-related ore deposits, ore from Mount Weld displays extreme light REE (LREE) enrichment (La up to 4 wt. %), but in contrast also contains substantially higher concentrations of heavy REEs (HREEs). REE enrichment in the laterite is controlled by the breakdown of primary minerals, the release and transport of REEs, and the formation of secondary minerals. Secondary REE-bearing phosphate minerals are the primary REE-host phases in the laterite ore with monazite as the dominant phase; other REE-bearing phases include rhabdophane, cerianite, churchite, florencite, and crandallite subgroup minerals. Profiles through the laterite show that in the REE-rich zone, apatite and primary calcite have broken down, and dolomite decreases by approximately 60-100%, such that the loss of Ca and Mg, as well as Si and K, leads to a relative increase in the REEs. Sequestering of REEs in secondary mineral phases formed by groundwater further enhances the REE concentration.

1 Introduction

With the increasing reliance on high technology and green energy products, demand for critical metals has become an important driver in economic geology. The REEs are family of elements that have been defined as critical on most lists because of their unique magnetic and optical properties and their geographical-limited supply locations. Carbonatite-hosted REE deposits are the primary source of the world's LREEs and have the potential to be a source of HREEs. Carbonatites are defined by the International Union of Geological Sciences (IUGS) as igneous rocks composed of greater than 50 volume percent primary carbonate minerals, primarily calcite and/or dolomite, and containing less than 20 wt.% SiO_2 (Le Maître 2002). The Mount Weld REE deposit (Figure 1) in Western Australia is hosted in a lateritic sequence above an underlying carbonatite. It is one of four giant, active REE mines associated with carbonatites, the largest REE producer outside of China, and the only one of the four that is laterite hosted. Lynas Rare Earths Ltd. (2022) reported a total mineral resource (measured, indicated, and inferred) of 54.7 million tonnes with 5.3 percent TREO (total rare earth oxide).

The Mount Weld carbonatite occurs within Eastern Goldfields province of the Yilgarn craton, near Laverton, Western Australia. The laterite is covered by 20 to 40 m of lacustrine and alluvial sedimentary rocks, so there is no surface expression of the mineralization. The deposit was discovered by drilling a large, circular magnetic anomaly identified in a 1966 regional airborne geophysical survey undertaken by the Australian Bureau of Mineral Resources. Magnetite from the carbonatite was dated at 2025 ± 10 Ma by the Re-Os method (Graham et al. 2004), but the age of laterization is poorly constrained. Because of active mining and extensive exploration drilling, this is an ideal setting to evaluate REE enrichment associated with lateritically-weathered carbonatites.

Figure 1. Photograph of the Mount Weld mine with the active pit in the foreground, October 2018.

2 Methodology

This study is based on samples from drill cores and from the active pit. Mineralogical characteristics were determined through petrographic studies, scanning electron microscopy (SEM), and X-ray diffraction (XRD). Mineral chemistry on selected samples was determined by Laser Ablation-Inductively Coupled Plasma-Mass Spectrometry (LA-ICP-MS). Major and trace element whole-rock chemistry was determined by wavelength dispersive X-ray fluorescence spectrometry (WDXRF), inductively coupled plasma-optical emission spectroscopy (ICP-OES), and inductively coupled plasma mass spectroscopy (ICP-MS).

3 Results

3.1 The Carbonatite

The Mount Weld carbonatite is approximately 4 kilometers in diameter and is buried under approximately 20-40 meters of surficial sediment and up to 120 meters of weathered material.

Carbonatite samples from older drill core are either calcite- or dolomite-rich, with minor minerals including apatite, magnetite, olivine, biotite, pyrite, monazite, and pyrochlore (Figure 2). Carbonatite samples from core from recent drilling at the base of the active pit are primarily ankerite carbonatite and contain REE fluorcarbonate minerals, bastnäsite and parasite, as well as apatite and monazite. Chondrite-normalized REE diagrams of the Mount Weld carbonatite are LREE enriched, and samples with REE fluorcarbonate minerals are more LREE enriched and have a steeper negative slope (Figure 3). The neodymium isotopic composition (epsilon neodymium calculated at 2025 Ma of 0.7) and strontium isotopic composition ($^{87}Sr/^{86}Sr$ calculated at 2025 Ma of 0.70197) are consistent with the carbonatite being derived from a mantle source (Verplanck et al. 2016).

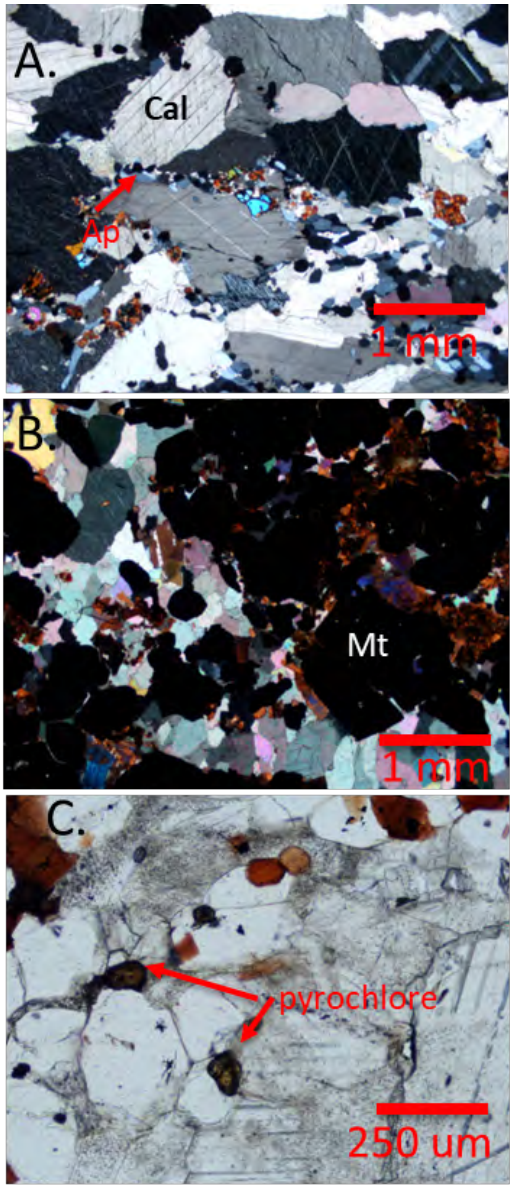

Figure 2. Plane- and cross-polarized light photomicrographs of the Mount Weld carbonatite. a. Calcite (Cal) carbonatite with apatite (Ap); b. Calcite carbonatite with magnetite (Mt); c. Calcite carbonatite with pyrochlore.

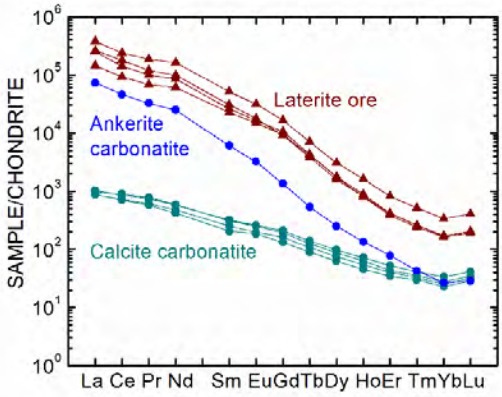

Figure 3. Chondrite-normalized rare earth element diagram displaying the Mount Weld calcite carbonatite, mineralized ankerite carbonatite, and laterite ore. Ankerite carbonatite data from Zhukova et al. 2021. Chondrite values from Anders and Ebihara (1982).

3.1 The Laterite

The laterite sequence, up to approximately 90 m thick, lies above a residual zone that overlays the carbonatite (Figure 4). Overall, the composition of the laterite samples is variable, most samples are iron rich with goethite, the dominant mineral phase. Other minerals include hematite, calcite, dolomite, apatite, hollandite, kaolinite, nacrite, illite, maghemite, montmorillonite, magnetite, pyrochlore, ilmenite, and rutile, and traces of quartz, barite, anatase, cryptomelane, and vermiculite. Calcite and barite appear to be secondary phases while dolomite, magnetite, and pyrochlore are residual phases from the carbonatite. The transition to the underlying carbonatite is termed the “residual zone” and is composed of apatite, magnetite, pyrochlore, and dolomite with secondary goethite, kaolinite, and hematite.

Figure 4. Photograph of an active face near the base of pit at the Mount Weld mine.

The REE mineralogy in the laterite is variable and complex (Figure 5). Within the active pit, medium-grained primary monazite is observed.

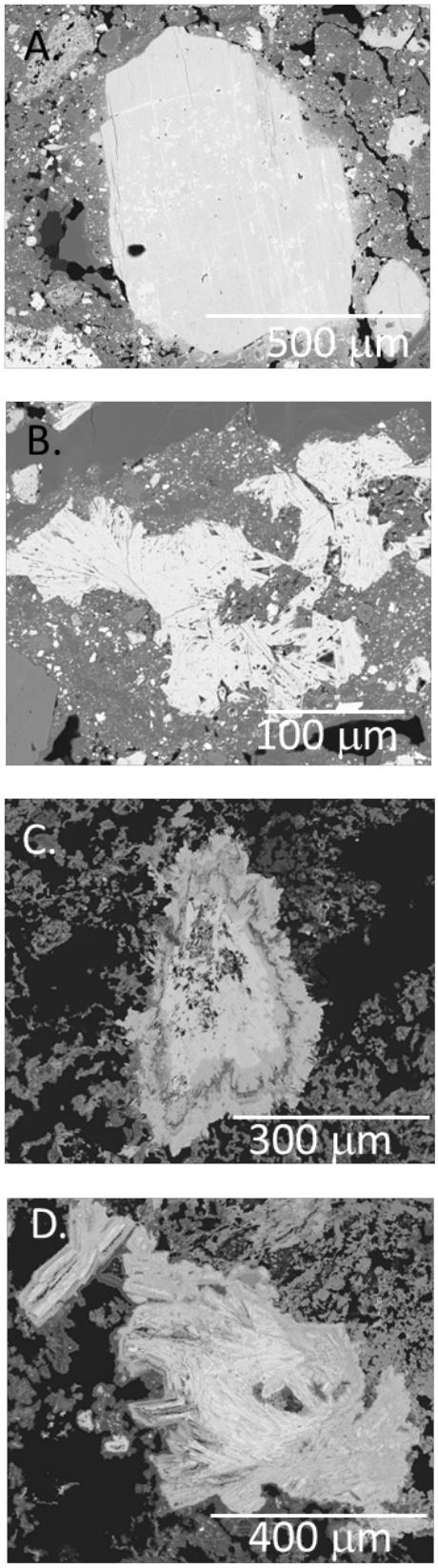

Figure 5. Backscatter electron images of REE phases in the laterite. a. Residual grain of primary monazite; b. LREE phase (rhabdophane); c. Zoned churchite; d. Complex phase relationships with intergrown LREE phases.

Secondary phosphate minerals include monazite, rhabdophane [$Ce(PO_4)\cdot 0.6H_2O$], crandallite subgroup minerals (goyazite [$(Sr,REE)Al_3(PO_4)(PO_3OH)(OH)_6$] and gorceixite [$(Ba,REE)Al_3(PO_4)(PO_3OH)(OH)_6$], florencite [$REEAl_3(PO_4)_2(OH)_6$], and churchite [$Y(PO_4)\cdot 2H_2O$]. Cerianite [$CeO_2$] are also observed. Mineral textures are complex displaying variable zoning and overprinting (Figure 5).

The chondrite-normalized REE patterns of samples from the laterite display LREE enrichment but have a range in HREE concentrations (Figure 3 and 6). Compared to the REE patterns of the underlying carbonatite, the ore laterite displays LREE enrichment and substantial HREE enrichment. The LREEs are moderately enriched compared to the ankerite carbonatite, and more substantially enriched compared to the calcite carbonatite (Figure 3). The chondrite-normalized REE patterns for laterite samples from drill core display a range in concentrations, range in slope, and variable sizes of cerium anomalies (Figure 6). These patterns reflect the variability in laterite mineralogy. Samples with more HREEs tend to contain greater proportions of churchite. Relative cerium enrichment or depletion is controlled by redox conditions, thus variations in the nature of the Ce anomalies reflect changing redox conditions during laterite evolution.

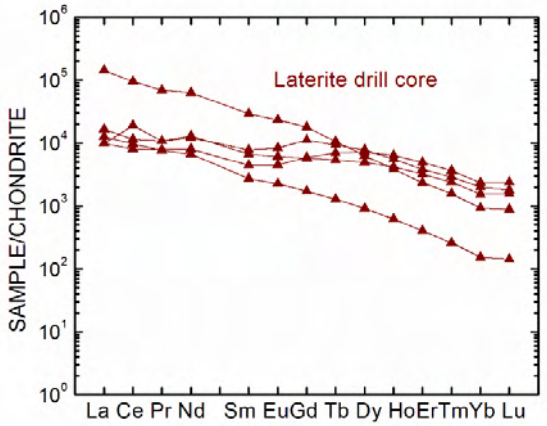

Figure 6. Chondrite-normalized rare earth element diagram displaying laterite samples collected from drill core. Chondrite values from Anders and Ebihara (1982).

4 Discussion

Lateritic weathering is an important process in ore deposit formation. The breakdown of primary minerals and the sequestration of elements in secondary phases may lead to economic enrichments. Carbonatites are characterized by minerals which are susceptible to chemical weathering and by REE concentrations that are enriched compared to most igneous rocks. Chemical weathering of the Mount Weld carbonatite caused the breakdown of minerals including calcite, dolomite, olivine, biotite, magnetite, pyrite, apatite, and monazite. Mass loss by mineral breakdown and elements mobilized in groundwater enhanced the

relative concentration of less mobile elements. Additionally, some elements are sequestered in secondary phases, further enriching the laterite.

In the Mount Weld laterite, primary calcite, olivine, biotite, magnetite, and pyrite are absent. Breakdown of these phases released Ca, Fe, Mg, Si, Al, K, and S. Compared to the carbonatite, dolomite in the laterite decreased by approximately 60-100%, leading to additional release of Ca and Mg. The breakdown of pyrite may have led to isolated zones of acidic conditions which further enhanced chemical weathering. In the carbonatite, the REEs were likely hosted by apatite, monazite, calcite, and dolomite. Weathering of apatite released phosphate as well as REEs. Although calcite and dolomite generally contain substantially lower REE concentrations than apatite, their higher modal abundance may make them a substantial REE host phase (Chebotarev et al. 2022; Verplanck et al. 2022).

The formation of secondary REE phosphate minerals is a major control on REE enrichment in the laterite, and these phases are the focus of REE processing at the deposit. Investigation of other REE sequestration processes, including adsorption by other secondary phases, will help identify if other processes play important roles in REE enrichment.

5 Conclusions

The Mount Weld deposit is an example of economically viable REE deposit formed by lateritic weathering of a carbonatite. For an economically viable deposit, there must be sufficient in grade and tonnage as well have a mineralogy that enables economic mining and processing. The REE concentrations and size of the underlying carbonatite provided an adequate endowment of REEs for the laterite. Apatite in the carbonatite provided sufficient phosphate during weathering to facilitate the formation of secondary REE minerals in the laterite. The successful mining of the Mount Weld deposit offers a framework for evaluation of other carbonatite-derived laterites as viable REE deposits.

Acknowledgements

This work was supported by the U.S. Geological Survey Mineral Resources Program. Any use of trade, firm, or product names is for descriptive purposes only and does not imply endorsement by the U.S. Government.

References

Anders E, Ebihara M (1982) Solar-system abundances of the elements. Geochimica et Cosmochimica Acta 46:2363-2280

Chebotarev DA, Wohlgemuth-Ueberwasser C, Hou T (2022) Partitioning of REE between calcite and carbonatitic melt containing P, S, Si at 650–900 °C and 100 MPa. Scientific Reports 12

Graham S, Lambert D, Shee S (2004) The petrogenesis of carbonatite, melnoite and kimberlite from the Eastern Goldfields Province, Yilgarn Craton. Lithos 76:519–533

Le Maître RW, ed. (2002) Igneous Rocks: a Classification and Glossary of Terms. Cambridge University Press, Cambridge, U.K. 193 p

Lynas Rare Earths LTD, 2022, Annual Report. 116 p

Verplanck PL, Farmer GL, Kettler RM, Lowers HA, Johnson CA, Koenig AE, Blessington MJ (2022) Petrogenesis and Rare Earth Element Mineralization of the Elk Creek Carbonatite, Nebraska, USA. Ore Geology Reviews 146

Verplanck PL, Mariano AN, Mariano AN Jr (2016) Rare earth element ore geology of carbonatites. In: Verplanck PL, d Hitzman MW (eds) Society of Economic Geologists Reviews in Economic Geology, v. 18, pp 5–32

Zhukova IA, Stepanov AS, Jiang S-Y, Murphy D, Mavrogenes JA, Allen C, Chen W, Bottrill R (2021) Complex REE systematics of carbonatites and weathering products from uniquely rich Mount Weld REE deposit, Western Australia. Ore Geology Reviews 39

Delineating the sulfur isotope signature of a VMS district by LA-ICP-QQQ-MS

Guillaume Barré[1], Crystal LaFlamme[1]
[1]Département de géologie et de génie géologique, Université Laval, Québec, Canada

Abstract. The demands for in situ sulfur isotopes analysis has increased in recent years. Yet, no rapid method for collecting high-resolution data with little sample preparation time is available. In this study, we developed a new analytical technique using LA-ICP-QQQ-MS, to rapidly acquire in situ $\delta^{34}S$ measurements on thin sections. This new method was tested on VMS samples from which the isotope signatures were previously characterized by bulk analyses. In situ lines of $\delta^{34}S$ analysis were performed on both pyrite and pyrrhotite from different types of VMS deposits (sub-seafloor replacement VMS, seafloor VMS and exhalites) with different bulk isotopic signatures. Overall, the in-situ measurements for each sample are consistent with the bulk signature. At the thin section scale, different analyses on the same grain return similar values that are individually slightly different from the bulk signature. However, the average signature from the different grains on a single sample is consistent with the bulk signature. It highlights the benefits of in situ analysis and validates the accuracy of this new in situ technique. This study opens new analytical opportunities for rapid in situ sulfur isotopes analysis in petrographically-characterized thin sections on different geological settings.

1 Introduction

Many metals are chalcophile and are often complexed with sulfur in the Earth's crust. Therefore, the understanding of sulfur reservoirs and the pathways of sulfur through the hydrosphere-geosphere, remain critical in ore deposit research. As sulfur can form many species and across a number of oxidation states, its pathways at the Earth's surface have been studied using its stable isotope signature $\delta^{34}S$ (e.g., Kump, 2012). Recently, the isotopic fractionation of sulfur has lent insight into its source reservoirs for a number of magmatic and/or hydrothermal deposit types, elucidating critical components for deposit formation (e.g., Seal, 2006; Hutchinson et al., 2020). For instance, in volcanogenic massive sulfide (VMS) systems, which form at, or near, the Earth's surface through the interaction of hydrothermal fluids with ocean water in often microbial-rich host rocks, sulfur isotopes have elucidated that thermochemically reduced seawater sulfate represents a significant sulfur reservoir (e.g., LaFlamme et al. 2021).

These deposit-scale sulfur isotope variations can be harnessed for an improved understanding of the spatial and temporal controls on sulfide precipitation and source reservoirs of sulfur and even metal endowment (see LaFlamme et al. 2018). However, interpreting growing $\delta^{34}S$ datasets necessitates in situ measurements, in order to analyse distinct micro-textures. Until presently, in situ $\delta^{34}S$ measurements have been commonly completed in 1-inch epoxy mounts using a secondary ion mass spectrometer (e.g., Caruso et al. 2018). However, the demand for in situ sulfur isotope analyses is growing and, therefore, rapid methods of high-resolution data collection with little sample preparation time must be developed.

Whereas other isotopic techniques requiring large, rapidly acquired datasets have moved to LA-ICPMS (e.g., U-Pb geochronology), sulfur isotope measurements have been hindered by poor ^{32}S and ^{34}S mass resolution on interfering oxides, hydroxides and argon of the plasma. New analytical developments, the LA-triple quadrupole (QQQ)-ICPMS, show promise in being able to precisely measure $\delta^{34}S$. Whereas the SIMS and LA-MC-ICP-MS instruments utilise a multi-collector to narrow the window of measurement to the very specific selected mass, the triple quadrupole places two quadrupoles (Q1 and Q3) in tandem, between which the ions of interest are reacted with a gas to change their masses and thus remove potential isobaric overlaps (known as MS/MS mode).

To demonstrate the benefit of rapidly collected $\delta^{34}S$ measurements completed in situ in petrographically-characterized thin sections by LA-QQQ-ICPMS, we present a case study in which we discriminate the sulfur isotope signature of massive sulfide lenses and exhalites in the Noranda and Matagami VMS districts of the Abitibi subprovince, Québec. Massive Cu-, Zn- and Fe-sulfides precipitated in seafloor hydrothermal systems are a result of complex water-rock interactions between magmas, hydrothermal fluids and circulating seawater as these processes influence heat and chemical fluxes and ultimately the precipitation of sulfides. When preserved in the ancient rock record these systems form VMS districts composed of three types of mineralized rock: stockwork, massive sulfide and exhalite (Huston et al. 2010). We monitor these processes by using the sulfur isotope signature and test the potential to deliver new vectoring methods that track the optimal conditions for the precipitation of massive sulfides in order to guide exploration in VMS districts.

2 Geology

The Abitibi Greenstone Belt is known to host one of the greatest Archean VMS endowments (e.g., Mercier-Langevin et al., 2011). The belt was formed between ca. 2790 to 2640 Ma and consists of a succession of volcanic and sedimentary rocks intruded by plutonic suites. All units were affected by low- to moderate-grade metamorphic overprint (Monecke et al., 2017 and references therein). Two VMS districts of the belt were sampled: the Noranda

and the Matagami districts. Three different types of deposits were sampled with different proportions of seawater sulfate incorporation and therefore different isotopic signatures are expected (Figure 1). These include: 1) The McLeod Deep mine (Matagami district) corresponds to a sub-seafloor replacement VMS where mostly magmatic isotopic signature is expected. Three different levels of the deposits were sampled: the semi massive sulfides zone, the massive sulfides lens and the stringer zone. The latter is mainly composed of large pyrite crystals with inclusions of sphalerite and chalcopyrite. The two other zones present similar sulfides assemblages of pyrite, sphalerite, chalcopyrite and pyrrhotite. Only the proportion of the different sulfides varied between the two zones. 2) Two seafloor VMS occurences in the Noranda district: Amulet and Moosehead. They are composed of pyrite, sphalerite and chalcopyrite with rare galena. Moosehead presents more sphalerite than Amulet and is associated with exhalite levels. Amulet shows alternating sphalerite-rich and chalcopyrite-rich layers always mixed with pyrite. 3) Noranda district exhalites include the 9191, 1244, 9187 and 9126. They mainly consist of laminated chert horizons with layers of pyrite ± chalcopyrite, sphalerite, pyrrhotite. They are often associated with VMS lenses and are formed from hydrothermal vents at or below the seafloor, with possible sedimentary influence (e.g., Huston et al., 2010).

3 Methodology

Analyses of pyrite and pyrrhotite were completed on 3 thin sections from the McLeod Deep VMS, 4 from the Noranda district exhalites and 1 from the Moosehead showing. They were first characterized petrographically by reflected light microscopy. In situ sulfur isotope measurements were completed on an Applied Spectra RESOlution-SE 193 nm ArF excimer laser ablation system with a large volume S155 sample cell coupled to an Agilent 8900 ICP-QQQ-MS. Four thin sections per analytical session were loaded into the cell together with reference materials in epoxy mounts. Straight or curved lines of a minimum length of 100 µm were acquired on single grains of pyrite and pyrrhotite, with a beam diameter of 38 µm. Mix of He ± Ar is used as carrier gas. In order to remove mass interferences that may be present during the analysis, oxygen was used in the reaction cell to react with isotopes S^{32} and S^{34} and increase their masses to 48 and 50, respectively. Thus, the interfering masses, which do not react with the oxygen, will be removed on the second quadrupole.

Primary matrix matched reference materials were used to calibrate instrumental mass fractionation and monitor drift throughout the session. Reference materials include Sierra pyrite ($\delta^{34}S$ = 2.17‰ ± 0.18; LaFlamme et al. 2016), and Pierre pyrrhotite ($\delta^{34}S$ = 4.73‰ ± 0.19; in-house). Secondary reference materials are used for quality control and include Iberia pyrite ($\delta^{34}S$ = 8.92‰ ± 1.11; in-house) and Montpelier pyrrhotite ($\delta^{34}S$ = 3.30‰ ± 0.19; in-house). All in-house reference materials have undergone a protocol for characterizing their chemical composition by CAMECA SX-100 electron probe micro-analyzer and isotopic signature by three sulfur extractions (by chromium-reduced sulfides solution; Canfield et al., 1986) measured by SF_6-fluorination-isotope ratio mass spectrometry at the Institut de Physique du Globe de Paris. Isotopic homogeneity was also verified by in situ measurements across multiple grains using the SIMS-1280 at University of Western Australia.

Data reduction was performed in Iolite v.4 (Paton et al., 2011) to select integration times and to identify, subtract the background and generate the $^{34}S/^{32}S$ ratios. Reference material normalization was completed by sample-standard bracketing by using the average of 2 standards before and after a series of 3 to 4 samples. Note that, standard values that differ by more than one standard deviation from the actual value are discarded and not used in data reduction processes. For unknown samples, outliers values are rejected when chemical equilibrium is assumed and their isotopic signatures differ by more than two standard deviations from the average of all similar analyses on the same sample. Uncertainty on each analysis varied from ± 1.22‰ to ± 2.17‰ and is calculated as the propagated error on the signature of the unknown determined from all the standards (primary and secondary).

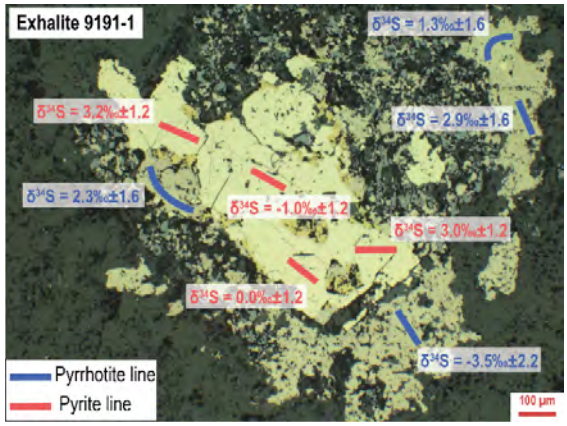

Figure 1. Reflected light microphotograph and location of analytical lines of pyrite and pyrrhotite and their respective $\delta^{34}S$ signature.

4 Results

A minimum of 4 lines of analyses were acquired on different grains of pyrite and pyrrhotite (when present) from each thin section (Figure 1). Note that uncertainties given in this section corresponds to the range of variation of the absolute values for a single sample and not the measurement error of an individual analysis. Pyrite and pyrrhotite from three samples (McLeod Deep 1, 2 and 3 on Figure 2) from the sub-seafloor replacement VMS (McLeod Deep mine, Matagami district) were analysed. All pyrite grains show similar $\delta^{34}S$ = -2.0‰ ± 1.2, when

pyrrhotite presents more variability with $\delta^{34}S$ = -0.3‰ ± 2.3. Only one exhalite from the Noranda district exhibited both pyrite and pyrrhotite (exhalite 9191), with isotopic signatures at $\delta^{34}S$ = 1.3‰ ± 2.1 and $\delta^{34}S$ = 2.6‰ ± 1.2, respectively. Pyrites from exhalites 9126 and 9187 show similar isotopic signatures at $\delta^{34}S$ = 3.3‰ ± 2.1 and $\delta^{34}S$ = 3.2‰ ± 1.4, respectively. Pyrites from exhalite 1244 and Moosehead showing (MO), also show similar values at $\delta^{34}S$ = 2.0‰ ± 1.0 and $\delta^{34}S$ = 1.7‰ ± 1.2, respectively (Figure 2). Overall, the obtained isotopic signatures are consistent within a single grain with high reproducibility between ± 0.1‰ and ± 2.2‰ (median at ± 0.7‰). The difference between two grains can be up to ± 5.1‰ in a single thin section (Figure 3).

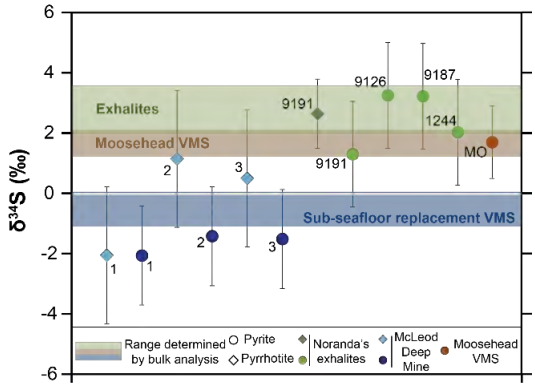

Figure 2. $\delta^{34}S$ values determined on pyrite and pyrrhotite from 8 thin sections from VMS and exhalite. Shaded areas show the range of $\delta^{34}S$ values obtained by bulk on the three different types of VMS. MO = Moosehead showing.

5 Discussion and conclusions

5.1 Suitable application of S isotopes by LA-ICPMS

The results obtained by LA-ICP-QQQ-MS were compared to the bulk isotopic signatures performed on the same samples (Barré et al., 2022). The pooling of all the pyrite and pyrrhotite data from a single thin section allows to better constrain the isotopic signature of the whole grain and to reduce the uncertainty of the values. The average of all lines of each thin section shows isotopic signatures broadly similar to bulk values. The maximum difference between the average of a single thin section and its associated bulk value is ± 1.1‰ (median at ± 0.3‰; Figure 2).

Exhalites 9126 and 1244 and the Moosehead showing have very similar isotopic signatures within a single grain with a maximum difference of ±0.7‰, while the difference between two grains of the same thin section can go up to 3.7‰. Nevertheless, for each sample the average of the two grains gives an isotopic signature similar to that of the bulk analysis (Figure 3).

Although different isotopic signatures between two pyrites can be observed in the same sample, the high reproducibility of the values within a single grain and the fact that the average of all the samples is consistent with the bulk signature, leads us to interpret isotopic variations as natural variation between grains, rather than associated to analytical error. Variations within larger grains can therefore likely be attributed to heterogeneous isotopic signatures within the same grain. Such variations cannot be observed with bulk techniques, so the reproducibility between bulk signatures and in situ averages value indicates high accuracy of the in-situ technique. The concordance between in situ and bulk isotopic signatures on a single sample show that LA-ICP-QQQ-MS is a suitable technique to determine sulfur isotopes at the thin section scale.

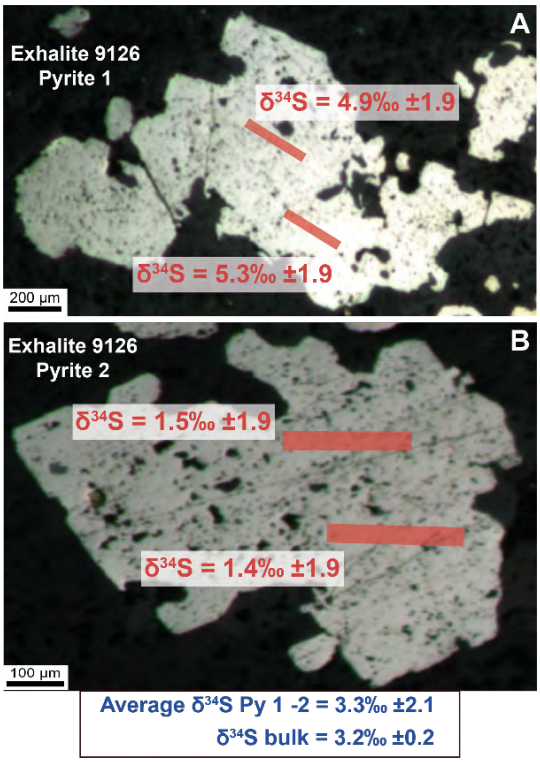

Figure 3. Reflected light microphotograph of two different pyrite grains from the same exhalite sample with the location of the lines of analysis carried out with their respective $\delta^{34}S$ signature. Note that the average of the $\delta^{34}S$ signatures of the two grains gives a value similar to the bulk value.

5.2 Delineating VMS district mineralisation using $\delta^{34}S$

Seawater sulfate influence changes depending on the type of VMS occurrences. Sub-seafloor replacement VMS will not record this influence, as sulfates precipitate before reaching the ore deposit area. Seafloor VMS will record a significant influence of seawater sulfate through the process of thermochemical sulfate reduction of seawater sulfate. In exhalite, the seawater influence can be important when it is close to a VMS deposit (Barré et al., 2022). Sulfur isotopes can be used as a vectoring tool to track this influence, discriminate

between these different VMS occurrences and determine the distance to a VMS deposit.

In this study, the analysis resolution of LA-ICP-QQQ-MS makes it possible to differentiate the isotopic signature of a sub-seafloor VMS deposit (McLeod Deep with $\delta^{34}S$ = -0.9‰ ± 2.1), from a seafloor VMS showing (Moosehead with $\delta^{34}S$ = 1.7‰ ± 1.2), and exhalite occurrences (9191, 9126, 9187 and 1244 with an average of $\delta^{34}S$ = 2.5‰ ± 1.6; Figure 4). Even though, so far, the error on a single measurement is relatively large (up to 2‰), when the data are pooled, the uncertainty decreases and leads to similar accuracy between bulk and LA-ICP-QQQ-MS. The resolution of this new technique is therefore sufficient to differentiate the types of VMS and exhalites within the same district.

Furthermore, we demonstrate here that this new technique can also differentiate between different generations of sulfides within a single thin section, which cannot be done with bulk techniques. The observation of such variations in situ is essential to better understand the variations within the deposit and thus better understand its formation. To date, only SIMS can perform such high-resolution sulfur isotope analysis. But sample preparation is time consuming, and it cannot be done on thin section. Sulfur isotopes analysis by LA-ICP-QQQ-MS in thin section is an important achievement that opens a new simple, rapid and high-resolution in situ sulfur isotopes technique. It will make it possible to increase the number of analyses that can be carried out on a single deposit and makes it possible to observe heterogeneity at the scale of the thin section or even at the grain scale.

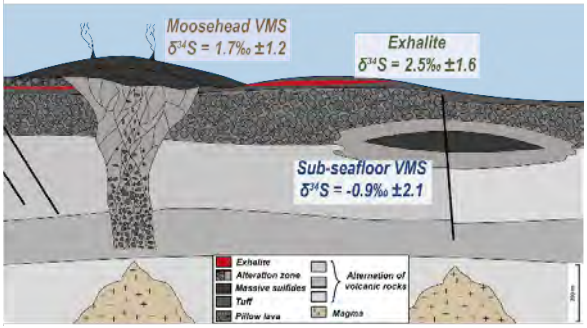

Figure 4. Sketch representing seafloor and replacement sub-seafloor VMS and exhalites with their respective $\delta^{34}S$ signature determined in bulk by SF_6 fluorination technique.

Acknowledgements

C.L. acknowledges support from the Canada Research Chair and John Evans Leaders Fund from the Canada Foundation for Innovation. The authors want to thank Pierre Cartigny from the Institut de Physique du Globe de Paris and Laure Martin from the University of Western Australia for their help on the isotopic characterization of the new sulfide reference materials by SF_6 fluorination and SIMS techniques, respectively. Marc Choquette from the Laboratoire de Microanalyses of Université Laval is also warmly thanked for the chemical characterization of these reference materials.

References

Barré, G, LaFlamme, C, Beaudoin, G, Goutier, J, Cartigny, P (2022) The application of multiple sulfur isotopes to determine the architecture of Archean VMS deposits. GAC-MAC, Abstract volume, v. 45.

Canfield, D.E, Raiswell, R, Westrich, JT, Reaves, CM, Berner, RA (1986) The use of chromium reduction in the analysis of reduced inorganic sulfur in sediments and shales. Chem Geol 54(1-2): 149-155.

Caruso S, Fiorentini ML, Hollis SP, LaFlamme C, Baugartner RJ, et al. (2018) The fluid evolution of the Nimbus Ag-Zn-(Au) deposit: an interplay between mantle plume and microbial activity. Precamb Res 317: 211-229. https://doi.org/10.1016/j.precamres.2018.08.012

Farquhar, J, Kim, ST, Masterson, A (2007) Implications from sulfur isotopes of the Nakhla meteorite for the origin of sulfate on Mars. EPSL 264(1-2): 1-8.

Huston DL, Pehrsson S, Eglington BM, Zaw K (2010) The Geology and Metallogeny of Volcanic-Hosted Massive Sulfide Deposits: Variations through Geologic Time and with Tectonic Setting. Econ Geol 105:571–591

Hutchison, W, Finch, AA, Boyce, AJ (2020) The sulfur isotope evolution of magmatic-hydrothermal fluids: Insights into ore-forming processes. Geochim Cosmo Acta 288: 176-198. https://doi.org/10.1016/j.gca.2020.07.042

Kump LR (2012) Sulfur isotopes and the stepwise oxygenation of the biosphere. Elements. DOI 10.2113/gselements.8.6.410

LaFlamme C, Barré G, Fiorentini ML, Beaudoin G, Occhipinti S, Bell J (2021) A significant seawater sulfate reservoir at 2.0 Ga determined from multiple sulfur isotope analyses of the Paleoproterozoic Degrussa Cu-Au volcanogenic massive sulfide deposit. Geochim Cosmochim Acta 295:178-193. https://doi.org/10.1016/j.gca.2020.12.018

LaFlamme C, Hollis SP, Jamieson JW, Fiorentini ML (2018) Three-dimensional spatially constrained sulfur isotopes highlight processes controlling sulfur cycling in the near surface of the Iheya North hydrothermal system, Okinawa Trough. Geochem Geophys Geosystems 19:2798-2812. https://doi.org/10.1029/2018GC007499

LaFlamme C, Martin L, Jeon H, et al. (2016) In situ multiple sulfur isotope analysis by SIMS of pyrite, chalcopyrite, pyrrhotite, and pentlandite to refine magmatic ore genetic models. Chem Geol 444.9:1-15. https://doi.org/10.1016/j.chemgeo.2016.09.032

Monecke, T, Mercier-Langevin, P, Dubé, B, Frieman, BM (2017) Geology of the Abitibi greenstone belt.

Mercier-Langevin, P, Goutier, J, Ross, PS, McNicoll, V, Monecke, T, Dion, C, Dubé, B, Thurston, P, Bécu, V, Gibson, H, Hannington, M, Galley, A (2011) The Blake River Group of the Abitibi greenstone belt and its unique VMS and gold-rich VMS endowment. Geol Surv Can 6869: 1-61.

Paton, C, Hellstrom, J, Paul, B, Woodhead, J, Hergt, J (2011) Iolite: Freeware for the visualisation and processing of mass spectrometric data. JAAS 26(12): 2508-2518.

Seal, RR (2006) Sulfur isotope geochemistry of sulfide minerals. Rev Mineral Geochem 61(1): 633-677.

Application of Next Generation Technology in Undercover Exploration

Nigel W. Brand [1,2], David J. Crook [3]
[1] *Portable Spectral Services, West Perth, Australia*
[2] *Centre for Exploration and Targeting, University of Western Australia*
[3] *Mount Ridley Mines Limited, West Perth, Australia*

Abstract. As mineral exploration increasingly pushes into concealed (covered) terrains, explorers must maximise the geochemical and mineralogical information gained to understand the geological setting, terrain prospectively and mineral potential at various scales. Routine, low-cost geochemical techniques enable explorers to look for anomalies within the cloud of data however mineralogical techniques that, at best provide data on the dominant mineral phases (e.g. x-ray diffraction, "XRD"), are expensive, low volume (e.g. scanning electron microscope "SEM") or qualitative (e.g. short-wave infrared "SWIR"). We present the findings of an ongoing regional evaluation study over concealed Proterozoic lithologies known to host magmatic nickel sulphides with potential to host other base-metal, gold and rare earth elements ("REE") systems within the Fraser Range, Western Australia. The data has been acquired by Micro-XRF mapping technology which can accurately quantify the chemical compositions, and through post-processing, identify and quantify mineralogy of the same geological sample. High-quality, quantitative analyses were undertaken of "end of hole" air core drill samples representing the freshest nature of the rock being drilled. The resulting datasets have identified new mineralogical features and detected chemical differences at a microscale. The Bruker M4^{PLUS} Tornado "Micro-XRF" was utilised in this study, providing rapid and non-destructive acquisition of data.

1. Introduction

Yet to be discovered mineral deposits are becoming more likely to occur in concealed terrains and the ability to see through cover to detect and understand the nature of the underlying bedrock ore environment has become a fundamental aspect of modern mineral exploration and ore deposit science (Winterburn et al 2020), with an increasing appetite for collecting and integration of mineralogical and chemical data.

Over the past two decades commercial laboratories have offered high volume, low-cost, routine, quantified multi-element geochemical analyses that are accurate and precise over ten (10) orders of magnitude, from 100 percent to parts per billion. This has given rise to an increasing demand for mineralogical information, however, a commercial high volume, low-cost, routine mineralogical identification technique does not currently exist. SEM techniques provide mineralogical data at the sub-percent range yet do not provide a routine solution due to high cost and very low production volumes; XRD at best covers analyses within three (3) orders of concentration magnitude (100% to ~1%); whilst techniques such as SWIR are high volume and low cost, however, are qualitative at best.

Advances in Micro-XRF technology, such as capillary optics, has enabled mapping at high spatial resolution, down to 20um, without sacrificing intensity or sensitivity, providing a non-destructive, quantitative method for geochemical analysis and mineralogy of samples whilst providing the spatial distribution of major, minor and abundant trace components at the mapped resolution (Fritz et al 2016; Hoehnel 2018). During mapping the entire X-ray spectrum for each pixel in the grid is collected. Geochemically, elements ranging from carbon (C) to uranium (U) are simultaneously measured with quantification limits ranging from percentages to parts per million.

Automated mineralogy is undertaken using BRUKER's Advanced Mineral Identification and Characterisation Software (AMICS) through spectral matching of an extensive real-world and synthetic mineral library. Through automation, high volume throughput can be achieved which enables the routine commercial application of this technology.

The applicability of this technology for a practical solution when exploring a concealed geological terrain is being tested under a research project sponsored by Mount Ridley Mines Limited. To date, the project has analysed over 600 drill samples collected within an area of 1,200km^2 concealed Proterozoic terrain. This forms an exploration workflow that identifies rock types to produce a geological map with overlays of potential ore-environment minerals utilising both mineralogical and chemical vectors.

The project area lies within the Biranup and Nornalup geological provinces of the Albany–Fraser Orogen which forms part of the West Australian Craton and is located along the south-eastern margin of the Archean Yilgarn Craton (Spaggiari et al 2011). The Albany–Fraser Orogen is hosted by predominantly Paleoproterozoic to Mesoproterozoic granites formed through a complex series of events.

2. Methodology

Over 600 end-of-hole drill samples have been scanned during this study. Initially, selected samples were scanned "as received" at a high resolution (25-30µm) to develop a working mineral reference library using the AMICS software. With the mineral reference library established, samples are rerun in a validation process at a lower resolution

(100-200µm) to test accuracy and precision for high volume throughput.

Once validation is completed, routine samples are cleaned and mounted "as received" in batches of ~ 24 samples with no additional preparation (Figure 1). These mounts are loaded and scanned using a BRUKER M4^{PLUS} TORNADO. Quantified geochemical analysis is undertaken using the M4 software and quantified mineralogical analysis is undertaken using AMICS. Any "unknown" minerals encountered at this stage are further assessed and when identification is verified, these will be added into the mineral reference library.

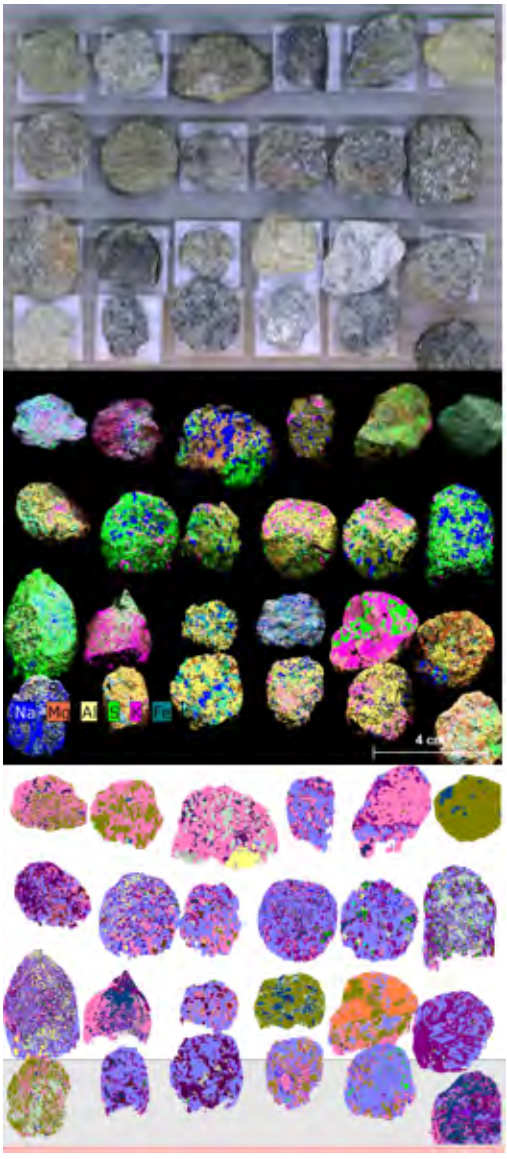

Figure 1: End of hole samples (top), chemistry (centre), mineralogy (bottom).

3. Results

Results from the study to date has identified thirty-one (31) minerals. Common rock forming minerals and minerals associated with regional metamorphism are abundant. Primary economic minerals as well as alteration minerals associated with ore environments are present in lower concentrations, typically less than 0.5% of the rock volume. Identification of ore environment minerals however is crucial when vectoring towards concealed ore deposits (Figure 2).

Given the nature of the cover sequence and weathering effects in the study area, the potential to generate false anomalies is recognised when interpreting geochemical data only. Identification of secondary mineral phases associated with a geochemical anomaly and then correlation of these minerals with the underlying basement or potential ore environment is a means of validating or discounting geochemical anomalies.

For each sample, mineralogical maps are generated showing the spatial distribution of the mineralogy, sample texture, mineral grain size, mineral associated etc (Figure 3).

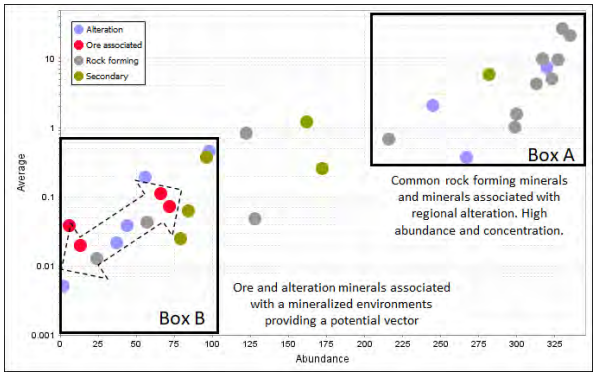

Figure 2: Abundance (number of times a mineral is identified in the data set) vs Average (average concentration of a mineral phase in the data set). "Box A" represents common rock forming minerals and minerals associated with regional alteration. "Box B" represents ore and alteration minerals associated with a mineralized environments providing potential vectors.

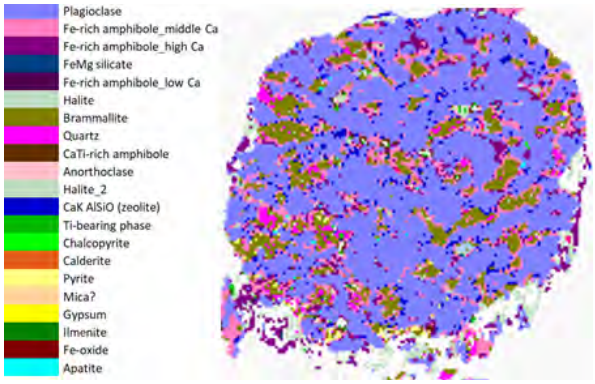

Figure 3: Mineralogical map of an "end of hole" sample, MRAC0112.

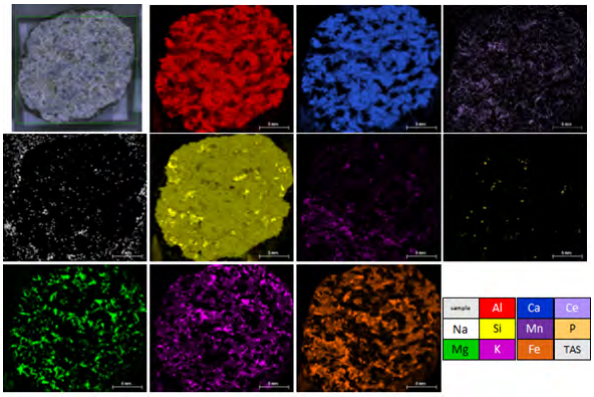

Figure 4: Individual element distribution maps show the relative element concentration within the sample MRAC0112.

Individual element distribution maps visually show the relative element concentration within the sample (Figure 4). Numerical data is used by the AMICS to ascertain the sample's constituent minerals. Common rock-forming minerals can be placed into standard IUGC petrographic diagrams to identify the underlying bedrock, which is then verified with standard geochemical plots using micro-XRF whole-of-sample geochemistry data (Figure 5).

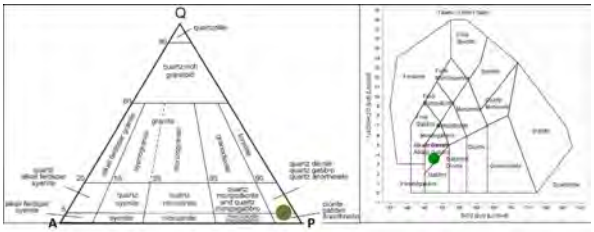

Figure 5: MRAC0112 mineral data *plotted in IUGC diagram (left) and chemical data plotted in Middlemost' 1994 TAS diagram (right).

From the end-of-hole drill sample data, the spatial distribution of individual mineral abundances can be shown (Figure 6). Common rock-forming and metamorphic minerals are used to map the underlying geology. Primary ore minerals and mineral alteration patterns associated with ore systems provide information on the terrain prospectivity, mineral potential and may act as a vector towards an ore deposit.

4. Conclusions

This paper demonstrates the application of next generation technology in undercover exploration and highlights the importance of detecting routine, high-volume low-cost quality "trace" mineralogy to identify a suite of "indicator" minerals with the potential to vector towards and detect economic mineral systems.

This pilot study forms part of a much larger regional program undertaken by Mount Ridley Mines Limited to understanding the basement geology, and mineral prospectively using a non-destructive micro-XRF technique to quantify mineralogy and chemistry and provide textural and petrography information that is "fit for purpose" for mineral exploration.

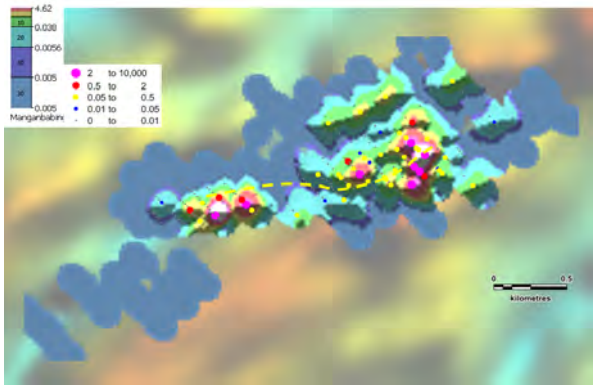

Figure 6: The spatial distribution of manganbabingtonite [$Ca_2(Mn,Fe)FeSi_5O_{14}(OH)$] a mineral associated with garnet-pyroxene-magnetite skarn.

Acknowledgments

Mt Ridley Mines Limited are thanked for their continuing support in method development and application of non-destructive technology in the mineral exploration.

References

Fritz, J., Tagle, T., Ashworth, L., Schmitt, R.-T., Hofmann, A., Luais, B., Harris, P.D.,Hoehnel, D., Ozdemir, S., Mohr-Westheide, T., Koeberl, C. (2016): Nondestructive spectroscopic and petrochemical investigations of paleoarchean SLs from the ICDP drill core BARB5, Barberton Mountain Land, South Africa. Meteorit. Planet. Sci. 51, 2441e2458.

Hoehnel, D., Reimold, W. U., Altenberger, U., Hofmann, A., Mohr-Westheide, T., Özdemir, S., & Koeberl, C. (2018): Petrographic and Micro-XRF analysis of multiple archean impact-derived spherule layers in drill core CT3 from the northern Barberton Greenstone Belt (South Africa). Journal of African Earth Sciences, 138, 264-288.

Middlemost, E.A.K. (1994): Naming materials in the magma/igneous rock system; Earth-Science Reviews, v. 37, pp. 215-224.

Spaggiari, CV, Kirkland, CL, Pawley, MJ, Smithies, RH, Wingate, MTD, Doyle, MG, Blenkinsop, TG, Clark, C, Oorschot, CW, Fox, LJ and Savage, J. (2011): The geology of the east Albany–Fraser Orogen — a field guide: Geological Survey of Western Australia, Record 2011/23, 97p.

Winterburn, P.A.; Noble, R.R. and Lawie, D. (2020): Advances in exploration geochemistry, 2007 to 2017 and beyond. Geochemistry: Exploration, Environment, Analysis, 20, 157-166.

Cassiterite: the zircon of mineral systems

Patrick A. Carr[1], Dawid Szymanowski[2], Lorenzo Tavazzani[2], Benita Pulitz[3], Torsten Vennemann[3], Cyril Chelle-Michou[2], Quentin Charbonnier[2], Zbigniew Galazka[4], Julien Mercadier[1]

[1]GeoRessources, Université de Lorraine, CNRS
[2]Institute of Geochemistry and Petrology, ETH Zürich, Switzerland
[3] Institute of Earth Sciences, University of Lausanne, Switzerland
[4]Leibniz-Institut für Kristallzüchtung, Germany

Abstract. New analytical developments and workflows are presented to determine the U–Pb age and εHf_i and $\delta^{18}O$ isotopic compositions of cassiterite (SnO_2), an ubiquitous mineral in magmatic-hydrothermal deposits. We present a multi-stage column chromatography scheme for the separation and purification of U, Pb and Hf for the determination of the U–Pb age and εHf_i from the same cassiterite solution by ID-TIMS and MC-ICP-MS, respectively. Additionally, new natural and synthetic cassiterite reference materials are presented for normalisation and validation of $\delta^{18}O$ data by ion microprobe analysis. The objective is to propose combined bulk and in-situ U–Pb age, εHf_i and $\delta^{18}O$ characterization of cassiterite in magmatic-hydrothermal mineralisation systems to constrain the temporal and genetic conditions leading to the formation of economic mineral deposits containing this mineral.

1 Introduction

Zircon ($ZrSiO_4$) is used widely by the geoscience community to determine the age (using the U–Pb decay systems) and provenance (with εHf_i and $\delta^{18}O$ isotopic compositions, for example) of the melt or fluid from which it precipitates. However, the use of zircon geochemistry for constraining these parameters in metal rich magmatic-hydrothermal systems is severely hampered by its notable absence in many mineralised environments (e.g., hydrothermal veins, greisen, breccias, skarns, pegmatites, and rare metal granites), and when present by its poor preservation due to metamictisation or secondary alteration (Figure 1). In contrast, cassiterite (SnO_2) is known to precipitate in both magmatic and hydrothermal environments associated with numerous economically important elements (Sn, W, Li, Nb, Ta, F, U, Cu, and Au) and can resist the subsequent hydrothermal alteration synonymous with these complex geological environments. Cassiterite has similar geochemical characteristics as zircon such that the age of crystallisation and the provenance of the forming melts and fluids can also potentially be determined by U-Pb geochronology, and εHf_i and $\delta^{18}O$ compositions, respectively.

To date, however, analytical protocols for the determination of U–Pb, Lu–Hf and oxygen isotopic composition of cassiterite are less advanced to that of zircon. We present new analytical developments and propose a logical workflow to determine U–Pb, Lu–Hf and oxygen isotopic composition by bulk and in-situ methods in cassiterite. The widespread availability of these techniques, and their application to mineral deposits worldwide can install cassiterite as 'the zircon of mineral systems' as initially proposed by Blevin and Norman in 2010.

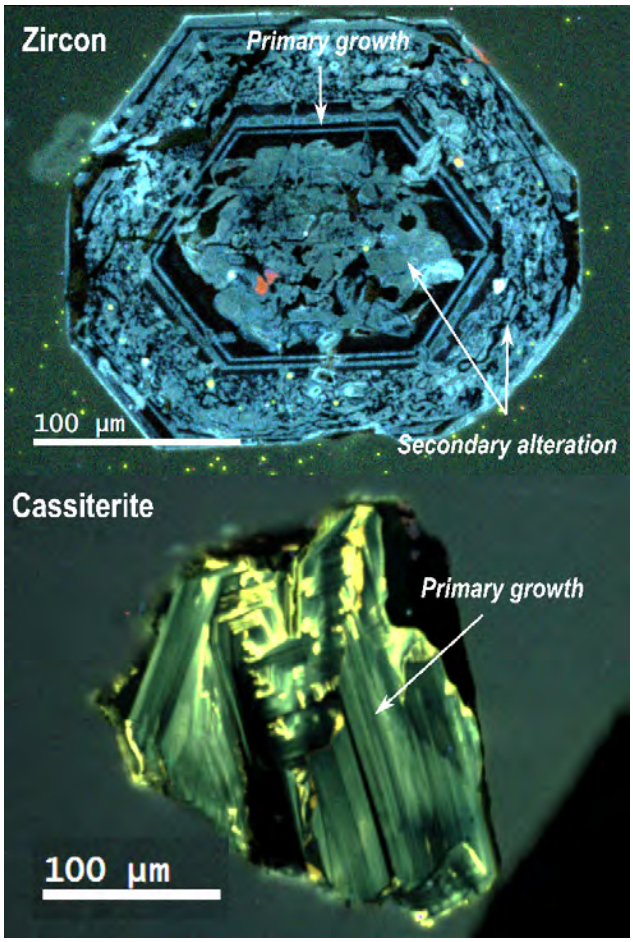

Figure 1. Cathodoluminescence images of a highly altered zircon (top) and primary cassiterite (bottom) from the magmatic-hydrothermal rare-metal prospect of St Mélany, Massif Central, France. In this context, zircon is often absent, or metamict and/or highly altered, such as its isotopic composition cannot be used to determine the age or provenance of mineralising melts and fluids. Cassiterite is commonly pristine and can be used in place of zircon for age and compositional information.

2 Analytical developments

Cassiterite can exhibit large variations in chemistry within a deposit, and within grains at the micron-scale, that highlights the need for geochemical imaging prior to isotopic analyses. The chemical heterogeneity within cassiterite also lends itself to in-

situ techniques (such as LA-[MC]-ICP-MS for U–Pb and εHf_i or SIMS for $\delta^{18}O$) to observe the range in compositions that can be found within a single crystal or an entire deposit. However, these in-situ techniques are less precise compared to bulk methods (such as ID-TIMS for U–Pb, MC-ICP-MS for εHf_i, and fluorination for $\delta^{18}O$) and require matrix-matched reference materials to correct for the artificial isotopic fractionation created during analysis. Preferably, both in-situ and bulk methods can be employed depending on the studies requirements (i.e., high analytical precision vs. high spatial precision), the degree of heterogeneity of the cassiterite to analyse or analytical tools available to researchers.

2.1 Combined U–Pb ages and εHf_i compositions

Cassiterite can contain several hundred ppm of both U and Hf such that it is suitable for isotopic analysis of these elements by both in-situ and bulk techniques. However, cassiterite often contains common Pb, such that U–Pb ages are typically determined from Discordia relationships from multiple analyses (n>20). U–Pb geochronology of cassiterite by ID-TIMS and LA-ICP-MS has been reported elsewhere (e.g., Carr et al. 2020, 2022, Tapster and Bright 2020). Current age uncertainty for U–Pb cassiterite ages is >0.1% for ID-TIMS data (Tapster and Bright 2020) and 1.9% for LA-ICP-MS (Carr et al. 2022).

A single study has presented εHf_i compositions of cassiterite by LA-MC-ICP-MS and MC-ICP-MS (Yang et al. 2023). Lu/Hf within cassiterite are generally low (<0.001) and calculation of εHf_i involves very minor corrections for in-situ decay of Lu. Solution based MC-ICP-MS can produce Hf isotopic measurement uncertainties of ± 0.2 ε, whilst LA-MC-ICP-MS is ± 2 ε (Yang et al. 2023).

Here we used a scheme based on 3-column separation and purification of U, Pb and Hf from a Sn-rich matrix and analysis at the ETH facilities, Zürich. Cassiterite dissolution is achieved with HBr decomposition in Teflon microcapsules assembled inside a Parr pressure vessel at 210°C for at least 5 days. Separation and purification of U, Pb and Hf aliquots from initial cassiterite solutions involved passes through TRU-Spec, AG1X-8 resins and TODGA resins. This method yields low Pb blanks that are insignificant relative to the Pb derived from the sample. For most cassiterite samples, between 200 and 1000 µg of concentrate is sufficient for a high precision U–Pb and εHf_i analysis by ID-TIMS and MC-ICP-MS, respectively.

2.2 $\delta^{18}O$ compositions

Previous studies have identified large variations in $\delta^{18}O$ within cassiterite (e.g., up to 10‰ variation; Sun and Eadington 1987) indicating large changes in fluid composition and/or variable degrees of fluid mixing and/or changes in the precipitation temperature of cassiterite. More recent *in-situ* SIMS studies have identified intra-grain variations up to 2‰ at the micron scale (Carr et al. 2017). When combined with $\delta^{18}O$ in co-precipitation quartz, temperature estimates can be made assuming isotopic fractionation factors determined independently by other methods (e.g., Li et al. 2021).

These factors indicate that $\delta^{18}O$ of cassiterite is generally more appropriately determined by in-situ methods, such as SIMS. Although SIMS do not compromise precision in oxygen-rich minerals such as cassiterite, it does require matrix-matched reference materials to account for matrix-effects causing the fractionation of oxygen isotopes (Carr et al. 2017). Currently only one reference cassiterite is available to the community (Li et al. 2021). Here we present two new reference materials that can be used for normalisation and validation of $\delta^{18}O$, and quantification of laboratory and inter-laboratory reproducibility.

Refence $\delta^{18}O$ values for cassiterite were determined by CO2-laser fluorination line connected to a Finnigan MAT 253 at the Université de Lausanne, Switzerland. Approximately 2 mg of cassiterite concentrate was required for each analysis. In-situ $\delta^{18}O$ compositions were determined on a CAMECA 1280 ion microprobe at the CRPG, Nancy, France (Bouden et al. 2021).

Natural cassiterite from the eastern Kareila, Russia (sample SPG) yields preliminary $\delta^{18}O$ reference values of 2.51 ± 0.02 (SD; n=2). In-situ analyses (n=20) of multiple grains of SPG yields a session reproducibility (2SD) of 0.58‰.

Synthetic cassiterite formed through physical vapour transport and subsequently annealed at 1400°C (sample IKZ-a; Galazka et al. 2013) yield preliminary laser fluorination $\delta^{18}O$ of 4.63 ± 0.05 (SD; n=3). Multiple analyses (n= 70) from traverses of multiple fragments of this cassiterite yields a session reproducibility of 0.47‰.

3 Analytical workflows for cassiterite isotope geochemistry

The proposed analytical workflow is shown in Figure 2. The heterogeneous composition common in cassiterite requires chemical imaging (SEM, cathodoluminescence and trace element mapping by LA-ICP-MS) prior to any quantification or isotope ratio analyses. These images can guide placement of $\delta^{18}O$ analyses and select zones rich in U and Hf that are favourable for *in-situ* analyses by SIMS and LA-(MC)-ICP-MS, respectively. Grains identified to have high U and Hf, and low common Pb and Lu/Hf by LA-ICP-MS can be plucked from epoxy mounts and selected for solution analyses involving sample dissolution, separation, and purification of U, Pb and Hf and analysis by ID-TIMS (U and Pb) and MC-ICP-MS (Hf) as in customary for zircon (e.g., Herriott et al. 2019).

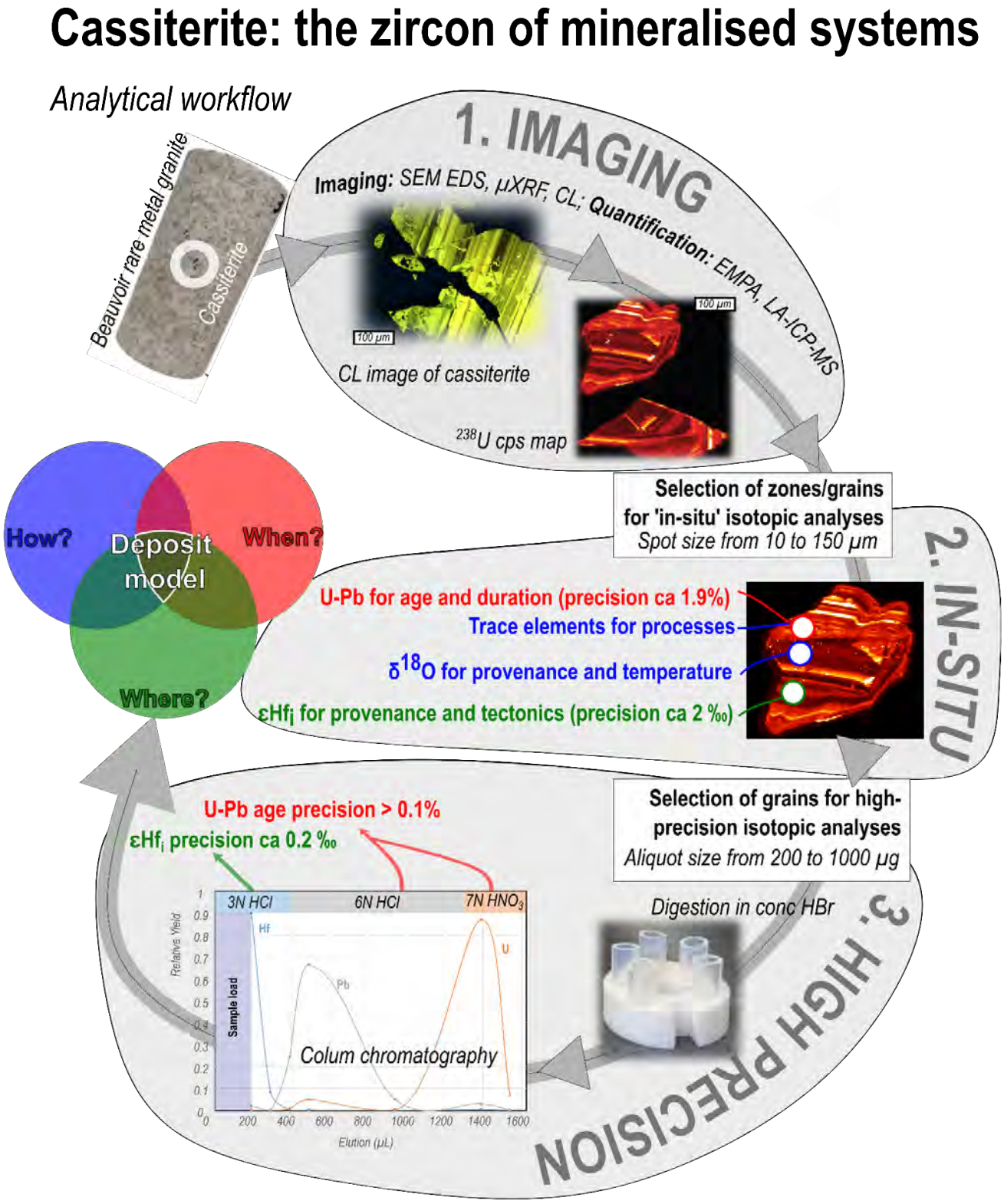

Figure 2. Analytical workflow for U–Pb, εHf_i and $\delta^{18}O$ isotopic analysis of cassiterite in three sequential steps including (1) chemical imaging, (2) *in-situ* isotopic ratio and trace element quantification and (3) high precision (bulk) isotopic ratio ID-TIMS. The combination of these data can provide unique temporal and genetic constraints on the formation of magmatic-hydrothermal deposits containing cassiterite.

4 Conclusions

The U–Pb age, εHf_i and $\delta^{18}O$ composition of cassiterite can provide direct constraints on the timing and source of fluids and melts responsible for its formation. We present a summary of recent analytical developments in high spatial resolution (i.e., LA-MC-ICP-MS and SIMS), and high measurement precision (i.e., ID-TIMS and MC-ICP-MS) analyses of cassiterite. The most appropriate methodology can be chosen based on the scientific problem to be defined and the characteristics of cassiterite (if alteration or primary zoning present). Isotopic compositions from cassiterite can be crucial in mineralised systems where zircon is absent and determining the age and source of mineralising melts and fluids is difficult. When zircon is present, this cassiterite geochemistry can also provide complementary interpretations such as cooling rates of magmatic-hydrothermal systems and fluid-rock or fluid-fluid mixing processes.

Acknowledgements

P.C. was funded by Institut Carnot ICEEL and the French National Agency through the national programme “Investissements d’avenir” of the Labex Ressources 21 (Reference ANR-10-LABX-21-RESSOURCES21). J. Cauzid and A. Lecomte are thanked for assistance with imaging techniques. L. Neymark provided the SPG cassiterite for oxygen isotope analysis. N. Bouden helped with $\delta^{18}O$ compositions by SIMS. Trace element images in Figure 2 were performed at Trinity College, Dublin with the help of D. Chew.

References

Blevin PL, Norman MD (2010) "Cassiterite: The zircon of mineral systems—A scoping study." Australian Earth Science Convention 2010, AESC2010. Poster GS2010/0483. 2010.

Bouden N, Villeneuve J, Marrocchi Y, Deloule E, Füri E, Gurenko A, Piani L, Thomassot E, Peres P, Fernandes F (2021) Triple oxygen isotope measurements by multi-collector secondary ion mass spectrometry. Frontiers in Earth Science, 8, 601169.

Carr PA, Norman MD, Bennett VC (2017) Assessment of crystallographic orientation effects on secondary ion mass spectrometry (SIMS) analysis of cassiterite. Chemical Geology, 467, 122-133.

Carr, PA, Zink S, Bennett VC, Norman MD, Amelin Y, Blevin PL (2020) A new method for U-Pb geochronology of cassiterite by ID-TIMS applied to the Mole Granite polymetallic system, eastern Australia. Chemical Geology, 539, 119539.

Carr PA, Moreira E, Neymark L, Norman MD, Mercadier J (2022) A LA-ICP-MS Comparison of Reference Materials Used in Cassiterite U-Pb Geochronology. Geostandards and Geoanalytical Research.

Galazka Z, Uecker R, Klimm D, Irmscher K, Pietsch M, Schewski R, Albrecht M, Kwasniewski A, Ganschow S, Schulz D, Guguschev C, Bertram R, Bickermann M, Fornari R (2014) Growth, characterization, and properties of bulk SnO2 single crystals. physica status solidi (a), 211(1), 66-73.

Li Y, He S, Zhang RQ, Bi XW, Feng, LJ, Tang GQ, Wang WZ, Huang F, Li XH (2021) Cassiterite oxygen isotopes in magmatic-hydrothermal systems: in situ microanalysis, fractionation factor, and applications. Mineralium Deposita, 1-19.

Sun SS, Eadington PJ (1987) Oxygen isotope evidence for the mixing of magmatic and meteoric waters during tin mineralization in the Mole Granite, New South Wales, Australia. Economic Geology, 82(1), 43-52.

Tapster S, Bright JW (2020) High-precision ID-TIMS cassiterite U–Pb systematics using a low-contamination hydrothermal decomposition: implications for LA-ICP-MS and ore deposit geochronology. Geochronology, 2(2), 425-441.

Herriott, TM, Crowley JL, Schmitz MD, Wartes MA, Gillis RJ - 2019) Exploring the law of detrital zircon: LA-ICP-MS and CA-TIMS geochronology of Jurassic forearc strata, Cook Inlet, Alaska, USA. Geology, 47 (11): 1044–1048.

Yang M, Yang YH, Romer RL, Wu ST, Wu T, Wang H (2023) In situ Hf isotope analysis of cassiterite by LA-MC-ICP-MS: Protocol and applications. Journal of Analytical Atomic Spectrometry.

Zircon and whole-rock geochemical fertility tools applied to porphyry copper deposits: case studies of Chachimbiro Volcanic Complex and Cerro Tolondro prospect, Ecuador.

Francesca Del Río[1], Massimo Chiaradia[1], Hugo Carrasco[1], Alexey Ulyanov[2], Angelo Aguilar[3], Sergio Cubelli[3], Carolina Rodríguez[3], and Carlos Urrutia[3].
[1]Section of Earth Sciences, University of Geneva, Rue des Maraîchers 13, 1205-Geneva, Switzerland.
[2]Institute of Mineralogy and Geochemistry, University of Lausanne, 1022 Chavannes-prés-Renens, 1015 Lausanne, Switzerland.
[3] CODELCO, Casa Matriz, Huérfanos 1270, Santiago, Chile.

Abstract. Bulk rock and mineral geochemical signatures commonly used in the exploration for porphyry copper deposits (PCDs) have been applied to the apparently barren Chachimbiro Volcanic Complex (CVC), and to the potentially mineralized Cerro Tolondro (CT) prospect, northern Ecuador, to understand the relationship between volcanic eruptions and the formation of PCDs.
Whole-rock geochemistry of both CVC and CT shows depleted LREE, and MREE differentiation trend, and lack an Eu negative anomaly with differentiation. CVC also portrays a MREE and HREE depletion, and an increase of Sr/Y values through time and chemical evolution.
Based on geochemical fertility indicators (e.g., Eu/Eu* versus (Ce/Nd)/Y and Dy/Yb) from trace elements measured in zircons, CVC and CT fall in the same field as mineralized PDCs, furthermore Cerro Tolondro might show a more complex magmatic evolution than Chachimbiro Volcanic Complex.

1 Introduction

The use of geochemistry for the exploration of porphyry copper deposits (PCDs) has migrated to more innovative techniques during the past decades. These techniques are designed to use bulk rock, mineral (e.g., zircon and apatite) geochemistry, and isotopic composition to quantify parameters that are considered crucial in the formation of PCDs, such as oxidation state, water content, and degree of fractionation of magmas associated with PCDs (Richards, 2015).

However, recent work by Chiaradia and Caricchi (2022) has shown that the use of geochemical tracers applied to zircon geochemistry is more complex, and that also barren volcanic centers that are associated with large eruptions (e.g., Fish Canyon Tuff, and Kneeling Nun Tuff) may present a comparable geochemical trend, as those from mineralized porphyry rocks.

For a better understanding of the meaning of zircon and apatites geochemistry in mineralized and non-mineralized volcanic systems, we are studying two nearby volcanic centers in northern Ecuador, one corresponding to the presumably barren CVC, and a target area for the potential occurrence of mineralized porphyry copper deposits, CT (Figure 1).

The Chachimbiro Volcanic Complex (CVC) is a compound volcano located in the Western Cordillera of northern Ecuador, with three Pleistocene eruptive events (405.7 ± 2.0 ka to 22'730 ± 120 ybp), and a fourth Holocene (5'760 ± 30 ybp) lateral blast explosion (Bellver Baca et al., 2020).

Cerro Tolondro (CT) corresponds to a prospect localized also in the Western Cordillera of Ecuador, few km to the north of CVC (Fig. 1). A preliminary study of geological features of the area of CT was carried out by "Exploraciones Mineras Andinas Ecuador S.A." which delineated a basement consisting of andesites and volcanoclastic sequence varying form tuff to volcanic breccias, intruded by dacitic porphyries and hydrothermal breccias (EM, 2021).

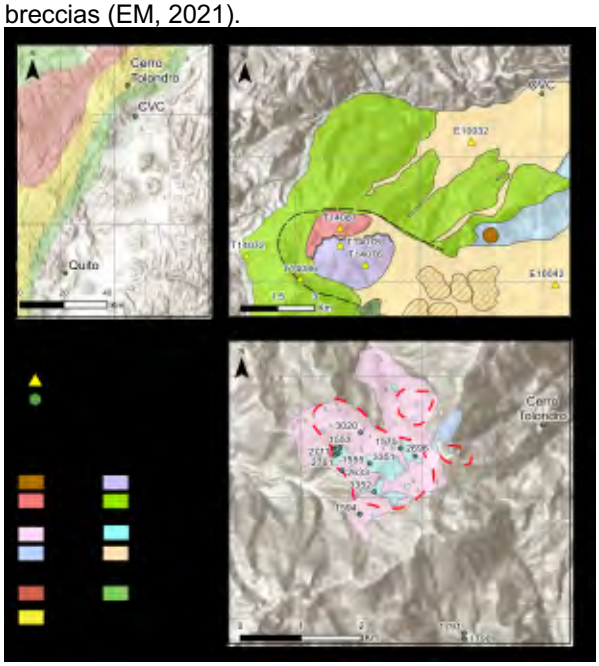

Figure 1. Location of Chachimbiro volcanic complex, and Cerro Tolondro, in northern Ecuador. Geology adapted from Bellver Baca et al. (2020), and EM (2021).

2 Methodology

Bulk rock analyses of representative Cerro Tolondro rocks were carried out at ALS Minerals Spain, whereas geochemical compositions of an extensive dataset of rocks from the Chachimbiro

Volcanic Complex are available from Bellver Baca et al. (2020).

We extracted zircon grains from samples of both volcanic centers, using conventional mineral separation techniques.

Representative zircon grains were handpicked under a binocular microscope, mounted in epoxy discs, and then polished to approximately half grain thickness. Cathodoluminescence (CL) images of both mineral phases were taken using the CamScan MV2300 instrument at Institute of Earth Sciences of the University of Lausanne, and the JEOL JSM7001F at the Faculty of Earth Sciences of the University of Geneva.

LA-ICP-MS analyses of zircons were conducted using a sector-field spectrometer Element XR in interfaced to an ASI (Australian Scientific Instruments) RESOlution 193 ArF excimer ablation system at the University of Lausanne, Switzerland, for U–Pb dating, REE and trace elements measurements.

3 Whole-rock geochemistry

Bulk rock analyses from the rock samples from the CVC have SiO_2 values between 59 – 69 wt. %, and vary from andesite to rhyodacites from the first eruptive episode (CH1) to the last one (CH4). Cerro Tolondro display a wider SiO_2 content range (52-70 wt.%), due to the hydrothermal alteration that is affecting the prospective area, Winchester and Floyd (1997) classification rock chart was used in order to examine immobile elements such as Zr/Ti_2O (Figure 2. A), the samples can be classified as andesites and dacites.

Chondrite-normalized REE patterns of CVC rocks display decreasing LREE and MREE values from the first eruptive episode to the last one, a drastic depletion of the HREE, and lack a negative Eu anomaly. Cerro Tolondro shows also a spoon-shaped pattern of the REE, but lacks the strong HREE depletion typical of the last CVC stage (CH4) and displays a small Eu negative anomaly (Figure 2. B and C).

Sr/Y values of CVC increase from CH1 to CH4, to values >50. Cerro Tolondro Sr/Y values remain mostly below 50. These low values of Sr/Y at CT are probably the result of the pervasive alteration affecting the rocks of this prospect; in fact, when plotted against the alteration index (A.I.), the lowest Sr/Y values coincide with the most altered samples (Figure 2. D).

4 U–Pb dating of zircons from Cerro Tolondro

$^{238}U/^{206}Pb$ ages of zircon spots from 4 samples of the Cerro Tolondro area are shown in Figure 3 and the mean ages of the zircon populations of each sample are reported. The fine-grained dacitic porphyry (FDP) unit yields an age of 11.48 ± 0.13 Ma (MSWD = 1.8), and the Andesite unit, 11.40 ± 0.32 Ma (MSWD = 0.84). The medium dacitic porphyry (MDP) corresponds to the youngest unit, with an age of 7.11 ± 0.14 Ma (MSWD = 1.1).

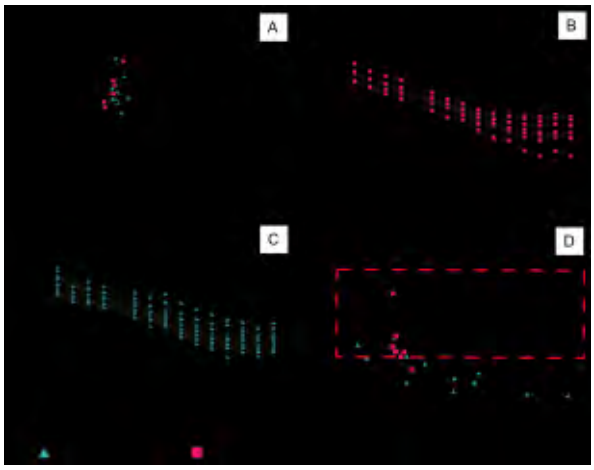

Figure 2. Whole rock chemistry. A. Winchester and Floyd (1997) classification rock chart, B. REE pattern for CVC, C. REE pattern for CT, and D. Sr/Y ratio vs Alteration Index (A.I.), where red field represents fertile signature, varying in between 50 < Sr/Y < 150.

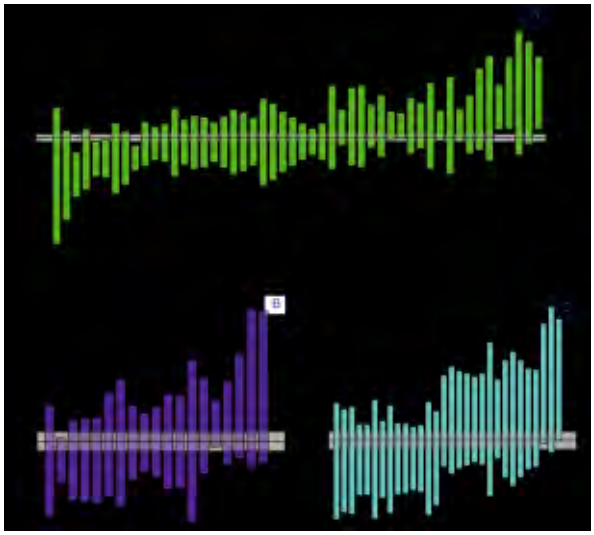

Figure 3. Weighted mean $^{238}U/^{206}Pb$ ages for Cerro Tolondro's units. A. Fine dacitic porphyry (FDP). B. Andesite. C. Intrusive porphyry. D. Medium dacitic porphyry (MDP).

5 Zircon geochemistry

The studied zircon grains present a prismatic morphology, varying from euhedral to sub-euhedral. Internal texture in most zircons exhibits oscillatory and sector zoning.

Chondrite-normalized REE patterns of zircons from CVC and Cerro Tolondro display a classic crustal zircons trend, with a depletion of LREE, a strong positive Ce anomaly, and enrichment of HREE (Figure 4. A and B).

Th/U can be used a fractionation index of the magma from which zircons have crystallized, with

zircons having higher Th/U values being those that have crystallized from less differentiated magma. Figure 4. C shows that CVC zircons are characterized by an increase of Yb/Dy with differentiation (increasing Th/U) passing from the oldest CH1 to the youngest CH4 unit (green arrow). This can be interpreted as the result of co-crystallization of zircons with amphibole and titanite, which are both minerals incorporating preferentially MREE (Dy) over HREE (Yb). For Cerro Tolondro, zircons display a similar fractionation trend, portraying an overall amphibole ± titanite fractionation, but have overall higher Th/U values. Additionally, Yb/Dy in CT extends to higher values with respect to CVC, possibly due to more extensive titanite fractionation.

We have used the classification diagrams of Lu et al. (2016) to discriminate between zircons from fertile and infertile magmatic rocks. In all these plots both CVC and CT fall in the fertile zircon fields associated with mineralized PCDs (e.g., Figure 4. D and E). The geochemical features of zircons plotting in the fertile fields in these plots are considered to indicate zircon crystallization from oxidized and hydrous magmas fractionating abundant amphibole (Lu et al., 2016).

To better understand the role that the oxidation state plays on the fertility of magmas, we applied the zircon oxybarometer proposed by Loucks et al. 2020). Figure 4 reports the range of the oxidation states of zircons from CVC and CT expressed as ΔFMQ values. The figure shows that all CVC stages and the older (ca 11-11-5 Myr old) rocks of CT have consistent ΔFMQ values around 0 or slightly above. Only the youngest (~7 Myr old) medium-grained dacitic porphyry has ΔFMQ slightly higher (~+0.5). All zircons from CVC and CT units have significantly lower ΔFMQ values than those of world-class PCDs (e.g., Chuquicamata, and El Salvador).

These comparisons highlight that whereas discrimination plots based on trace elements suggest that Cerro Tolondro and Chachimbiro volcanic complex plot in the fertile PCD field, the ΔFMQ values based on the oxybarometer of Loucks et al. (2020) display a significant difference between CVC and CT on one hand and world-class PCDs on the other.

6 Conclusion

Whole-rock geochemistry from CVC shows increasing Sr/Y values and decreasing HREE through time and with magmatic differentiation from CH1 to CH4, displaying Sr/Y values typical of fertile magmas. Cerro Tolondro lacks the heavy HREE depletion of CVC, and its Sr/Y values cannot be reliably used due to the pervasive alteration affecting the district.

Zircon mineral chemistry suggests that zircons of CVC crystallized from a magma that increasingly fractionated abundant amphibole ± titanite through time. Cerro Tolondro zircons also appear to follow an amphibole ± titanite fractionation trend although they have overall higher Th/U values and the trend is much less defined. This might suggest a more complex magmatic evolution at CT than at CVC.

Zircon trace elements of both volcanic complexes fall in the fertile fields of PCDs in various commonly used trace element plots, suggesting that the magmatic evolution of the two systems could be consistent with that of mineralized PCDs. However, the ΔFMQ values of CVC and CT are significantly lower than those of world-class deposits, suggesting that the oxidation state of magmas (expressed in the form of the equation of Loucks et al., 2020) should be assessed as an additional proxy for magma fertility in porphyry copper deposits.

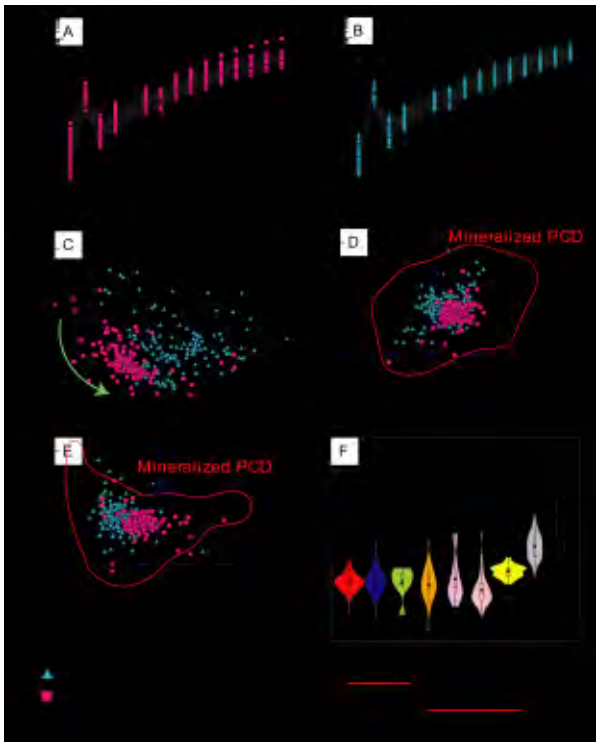

Figure 4. Zircon chemistry for CVC and CT. A. REE pattern for CVC, B. REE pattern for CT, C. Th/U vs Yb/Dy. D. Eu/Eu* compared with (Ce/Nd)/Y, E. Eu/Eu* anomaly values compared to Dy/Yb, and F. Δ FMQ variation regarding CVC and CT units, related to mineralized PCD.

Acknowledgements

We acknowledge Codelco S.A. for funding this research, carried out in the laboratories at the University of Geneva, and at the University of Lausanne. We are also grateful to Alexey Ulyanov, Agathe Martignier, Florence Begue, and Alexandra Demers-Roberge, for there help during the lab sessions.

References

Bellver-Baca M.T., Chiaradia, M., Beate, B., Beguelin, P., Deriaz, B., Mendez-Chazarra, N. & Villagómez, D. (2020). Geochemical evolution of the Quaternary Chachimbiro Volcanic Complex (frontal volcanic arc of Ecuador), Lithos, v. 356–357, 21 p.

Chiaradia, M. & Caricchi, L. (2022). Supergiant porphyry copper deposits are failed large eruptions. Communications earth & environment, v. 3, 107 p.

Exploraciones Mineras Andinas Ecuador S.A. (EM), (2021). Resultados del programa de levantamiento geoquímico y reconocimiento geológico, Proyecto Cerro Tolondro II.

Louck, R., Fiorentini, M., Henríquez, G. (2020). New magmatic oxybarometer using trace elements in zircon. Journal of Petrology, 1-30 p.

Lu, Y-J., Loucks, R., Fiorentni, M., McCuaig, C., Evans, N., Yang, Z-M, Hou, Z-Q., Kirkland, C., Parravilla, L., Kobussen, A. (2016). Zircon compositions as a pathfinder for porphyry Cu ± Mo ± Au mineral deposits. Society of Economic Geologists Special Publication, No. 19, chapter 13, 329-347 p.

Richards, J. (2015). The oxidation state, and sulfur and Cu contents of arc magmas: implications for metallogeny. Lithos, v. 233, 27-45 p.

Winchester JA, Floyd PA (1977) Geochemical discrimination of different magma series and their differentiation products using immobile elements. Chemical geology, 20, 325-343 p.

Identification and characterization of indicator minerals using µ-XRF

Léa Géring[1,2], Antoine Nadeau[1], Georges Beaudoin[1,2], Carl Guilmette[1]
[1] Département de géologie et de génie géologique, Faculté des sciences et de génie, Université Laval
[2] Centre de recherche sur la géologie et l'ingénierie des ressources minérales (E4m)

Abstract. This project aims at developing an automated method for identifying, counting, and characterizing indicator minerals (IM) of heavy mineral concentrates (HMC) based on µ-XRF data. Polycaprolactone grain mount provides homogeneous composition of non-detectable elements, and it allows grain top leveling. We develop a data processing workflow using µ-XRF raw counts maps as input. A binary image (grain/mount) is obtained using the sum of element counts and the counts in the spectral range that yield bremsstrahlung tube radiations. The next processing step use PyImageJ to recognize grain border and determine a region of interest (ROIs) at each grain centre. ROIs data is used in a decision tree that aims at identifying the mineralogy. The first layer of the decision tree classifies into a mineral group such as silicates, sulfides, phosphates, or oxides, based on count thresholds for Si, S, P. The following layers use thresholds for other element counts or count ratios. Once the mineralogy of each grain is determined, composition measurement can be performed using the appropriate calibrated method. Since µ-XRF is semi-quantitative, calibration curves need to be created to adjust the chemical method for each mineral. Calibration is achieved using Electron Probe Micro-Analyzer (EPMA) measurements on standard grains.

1 Introduction

Indicator minerals are an exploration method that enables targeting eroded deposits by sampling and analysing overburden sediments to find minerals derived from the mineralisation, its associated alteration or host rocks. This method led, for instance, to the discovery of the diamantiferous kimberlite of Lac de Gras (Canada), by Cr-pyrope counting in HMC of tills (Fipke et al 1995), and to the discovery of the Casa-Berardi gold deposit (Canada), by counting till gold grains and analysing their shape (Sauerbrei et al 1987).

IMs from the HMC are typically selected manually and analysed by a mineralogist with a binocular lense. This step is commonly called "picking". Since picking relies on visual interpretation, precision and reproducibility are highly dependent on the mineralogist expertise. The use of an automated method using µ-XRF would not only increase reproducibility for grains mineralogy identification and counting, but could also provide chemical compositions as well as grain shape information. Grain mineralogy that can be quickly derived from uXRF data, using intensity maps (counts/pixel), by implementing count thresholds or count ratios in a decision tree. This mineralogical analysis is part of a workflow (Figure 1). The objective of the automated method is to provide rapid HMC analysis as well as to improve QA/QC by making analysis reproductible.

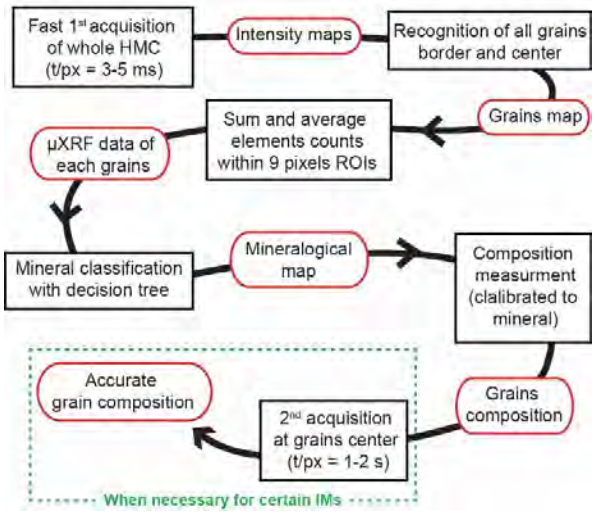

Figure 1. Proposed workflow for indicator minerals identification and composition measurement.

2 Method

2.1 Grain mount

The grain mounting method should enable optimization of data quality and to yield a low background signal. Carbon tape and polycaprolactone are suitable since they contain C, H and O, too light to be measured with x-ray fluorescence techniques.

Carbon tape is the simplest mount, allowing to directly deposit the grains on the adhesive surface. However, polycaprolactone resin enables grains top leveling, that prevents smaller grains to be hidden by bigger grains, a problem that is accentuated by the fact the source of X-ray is not orthogonal to the stage. Levelling is important because of the narrow focal depth of the beam. Intensity maps are more reliable and show less grain deformation if the z-focal plane encompasses all grain vertices. A polycaprolactone mount is thus preferred to carbon tape.

Polycaprolactone has a low temperature melting point (60°C), making it easy to manipulate. Polycaprolactone balls were placed in petri boxes and in an oven at 100°C for an hour. The top surface is levelled before it cools and solidify. After reheating the surface, it becomes ductile for about 15 minutes.

The selected grains are deposited on the surface and levelled with a press orthogonal to the surface.

2.2 Data acquisition

Micro-X-Ray Fluorescence (μ-XRF) is a spatially resolved, non-destructive technique that provides elemental analysis based on XRF spectra. Measurements were performed using a TORNADO M4 (Bruker Nano GmbH, Germany). The primary radiation is generated by applying a high voltage of 50 kV within a tube to a Rhodium anode. The Rh characteristic X-rays are focussed to a spot of 20 μm in diameter, at the chosen focal depth, by polycapillary lenses. The XRF signal emitted by the sample is collected by two detectors with a maximum rate of 130 x 10^3 counts per second (130 kcps) each. Acquisition is performed in lines, with the stage moving under the fixed primary beam. Data is acquired continuously, at a step size of 20 μm. The data for a single pixel is defined by averaging (or integrating) the signal over the time (measuring time) for the beam to cross the width of one pixel, (i.e., step width). Measuring time (t/px) must be optimized to allow the detection of light elements such as Mg, Al and Si while still offering a fast analysis. For example, 5 ms pixel time gives a fast result, but Al and Mg are not always detected over the background signal. A 30 ms pixel time gives accurate detection of lighter elements, but the complete analysis for a 1 cm^2 surface takes up to 6 hours. Different acquisition times are tested in this range to find the best compromise between timesaving and data quality. Counts are given in the number of counts per second per eV (cps/eV) to normalise counts to the energy resolution of the detector. This automated correction allows comparison of data acquired with different step widths.

2.3 Data processing

Each element intensity map can be exported from the Bruker Composite file (.bcf), as text files. These contain, for each pixel, the sum of counts in narrow energy ranges of the spectra that exhibit the characteristic peak for the element.

The software also gives the possibility to export total counts in a selected energy range. Counts within the energy range between 8.5 keV and 11.5 keV were exported. This energy range corresponds to a spectral range that exhibit bremsstrahlung radiation diffusion, referred to as the "brem. region" in the text and figures. This corresponds to primary x-ray, produced in the tube, not by Rh fluorescence, but by breaking and changing the trajectory of the electron under the effect of positive charge of Rh protons. Loss of energy of the braked electrons is converted into an x-ray. As observed for polycaprolactone (Figure 2), matter composed of light chemical elements shows generally high tube radiation diffusion because the latter are not absorbed. Total of counts in the brem. region is thus used to dissociate grains from the polycaprolactone resin.

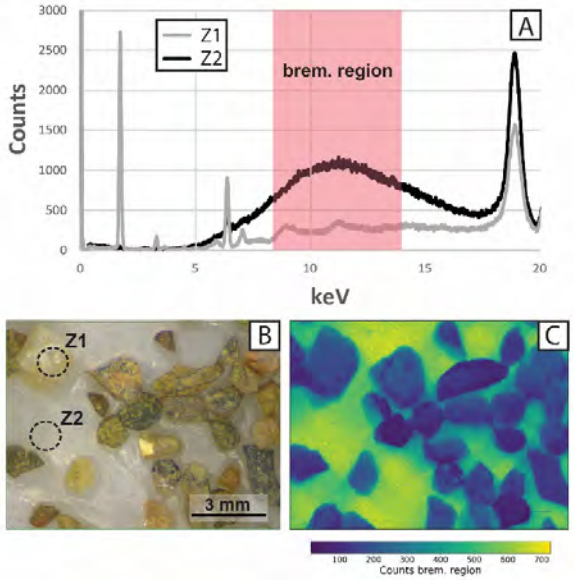

Figure 2. (A) Plot of total counts spectrum of two zones of 900 pixels, Zone 1 and 2, as referred on the optical image (B), taken by the TORNADO M4 camera. (C) Intensity map based on total counts within the brem. region, also shown in the diagram.

The primary dataset consists of intensity maps, stacked together to make a multilayered image. Each layer contains raw counts for an element, and an additional layer contains brem. region total counts. Processing of such a dataset instead of the whole spectra significantly decreases the processing time.

First, the multilayered image is converted into a *HyImage* to be treated with *hylite* (Thiele et al., 2021) an open-source python package. This package was designed to process hyperspectral data, but it works with any multi-channel image. *Hylite's* decision tree function is employed twice in the present workflow (Figure 1), (1) for the first step, to create a grain vs. mount binary image and, (2) for the mineralogical classification.

The grain/mount binary image is produced using a decision tree based on thresholds on the sum of element counts and on total counts in the brem. region. The decision tree output is further processed to define grain contours, count grains, and define a ROI at each grain centre. This step is performed with PyImageJ (Rueden et al 2022). PyImageJ implements a smoothing technique, median filtering to smooth noise while preserving sharpe edges. Next, a filter to remove holes, and, finally, the watershed function slices grains that are touching. PyImageJ also returns the coordinates of each grain 'centre from which are derived ROIs of 9 pixels. Centre coordinates are rounded to get a single pixel coordinate and derive the coordinates of the 8 other pixels in the square centred on the first pixel. The sum or the average of the element counts within the 9 pixels ROIs are the data input for the mineralogical

and compositional analysis. The mineralogical classification is realized using a second decision tree performed with *hylte*. Element counts used in the decision tree are in Figure 3.

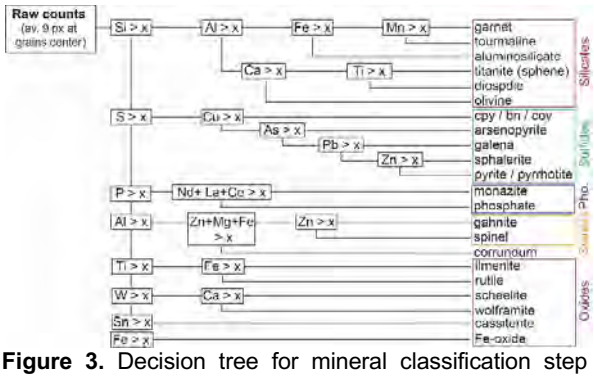

Figure 3. Decision tree for mineral classification step based on µ-XRF raw counts. Layers consist of thresholds.

The decision tree attributes, at first, a mineral group between silicates, sulfides, and phosphates by implementing thresholds for Si, S and P. If none of the thresholds are crossed, the decision tree attributes the pixel to the oxide group. Subsequent thresholds (and eventually counts rartios) are implemented to further classify within each mineral group.

2.4 Composition measurement calibration

Bruker M4 software allows the creation of composition measurement methods. Even if the absolute peak intensity for a given element is theoretically proportional to its concentration in the sample (Beckhoff et al 2006), the matrix effect of the sample is of great importance. Mineral lattice thus greatly influences the absolute peak intensity; however, this matrix effect is expected to be constant for a given mineral. To increase the precision of the µ-XRF's quantification, the software allows to input calibration parameters to correct this matrix effect. EPMA coupled with Wavelength-Dispersive X-Ray Spectroscopy (WDS) quantification is used as a reference for composition. Analysis of multiple grains with EPMA followed by µ-XRF of the same samples allows to create calibration line. Slope and offset of these linear trendlines are registered in Bruker M4 software as calibration parameters of a quantification method for the corresponding mineral group (e.g., garnet, spinel etc.).

3 Preliminary results

3.1 Grain count

Polycaprolactone mounts were tested with coarse and angular silicate grains of about 1 mm (Figure 4). Grain identification could not be done using the grayscale optical image (Figure 4A) because some grains are lighter than the polycaprolactone resin. However, in the case of HMC, grayscale image usefulness for grain identification is going to be tested. Pixels were classified as grain with the decision tree function if they fill two conditions: (1) the elements' sum is superior to 1.5% of the difference between the minimum and the maximum of the elements' sum of the dataset and (2) the brem. region counts are inferior to 35% of the difference between the maximum and the minimum brem. region counts in the dataset. Shape of grains of the produced binary image show some difference if compared to the optical image due to the fact the beam is not orthogonal to the stage, in contrast to the optical camera. Nevertheless, a good match is obtained.

The output of the decision tree is converted in a binary image (Figure 4B) that is then treated with PyImageJ functions as shown in Figure 4. The "watershed" filter did not work perfectly, for instance a grain in the middle was sliced in two particles (Figure 4D). The computed grain number is 33, whereas, the number of grains in the dataset Figure 4 is 32. Two grains were not detected and three were over-detected, i.e., two grains are detected when only one is present. The error percentage of under- and over- estimation is 6.25% and 9.37% respectively.

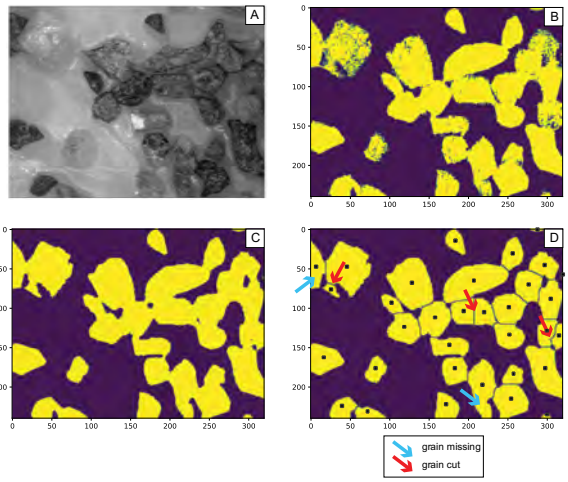

Figure 4. (A) Optical image in shades of gray. Different steps outputs after image processing: (B) binary image from first decision tree for grain and mount dissociation, (C) smoothed image of (B), (D) image with 'Fill Holes and 'Watershed' correction, black squares are nine pixels ROIs centred on grains centers.

Nine-pixel ROIs were defined based on the particle center output from PyImagej (Figure 4C). The average count for each element was calculated within each ROIs. These averages constitute the input in the mineral classification decision tree.

3.2 Mineralogy

The mineralogy decision tree was tested on multilayered images of µ-XRF data of common indicator minerals mounted on carbon tape. Tested thresholds were fixed numbers, chosen depending on counts variability of a given dataset. For

instance, the threshold for the silicate group for data acquired with measuring time of 30 ms per pixel is “Si > 5 cps”.

Figure 5 shows that minerals with simple stoichiometry such as ilmenite are easily classified, whereas for 4 olivine and 6 garnet grains are more challenging to classify. Border pixels were classified as grain based on the all elements count sum, but not as silicate, because the count for Si was too low because of “dilution” of the Si signal by matrix. Some pixels (red) are silicate because the count for Si was sufficient, but not for Al, so that the pixels were not classified into the garnet family. As a result, some pixels that belong to garnets grains were misclassified as diopside (Figure 5).

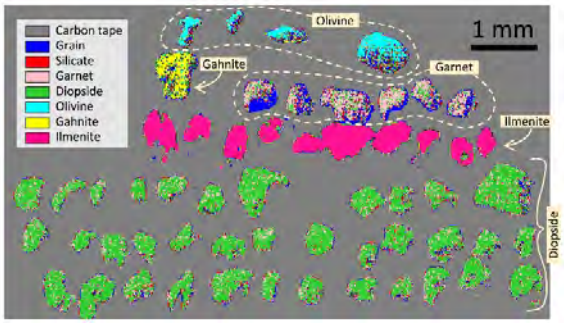

Figure 5. Decision tree output for mineral classification. Data are µ-XRF element intensity maps acquired at 50 keV, a measuring time of 30ms and a step size of 20 µm.

4. Conclusion

Grains identification based on grayscale image was not efficient in the example dataset because it contains grains that were too close in grayscale to the mount. Mineralogical and compositional analysis are based on ROI that must be at grain centre with respect to µ-XRF data, so if the ROI is based on optical image, it might be shifted and take grain border's XRF data. Grayscale optical image is however more loyal to real grain shape compared to XRF maps; thus, it is probably the most relevant dataset when it comes to automated grain shape measurements.

Classification pixel per pixel is not effective because some light elements are sometimes not detected and pixels at grain borders are not representative of grain composition. ROIs based mineral classification would have a better reliability since the classification would be based on counts integrated from several pixels. For example, 9-pixel ROIs integrate counts from the 9 spectrums that can be either summed (for thresholds) or averaged (for count ratios). The size of the ROIs can be modified according to the grain size of the analysed HMC.

Mineral classification with a simple decision tree can be considered on HMC samples because it contains minerals with a density over 3.0-3.2, which highly decrease mineralogy variability. Nevertheless, grain variety can still be extensive, and the mineralogy algorithm needs to be tested on HMC-type samples, doped with a known number of indicator minerals.

Grains topography and various grain sizes influence the absolute intensity of the characteristic peaks of the X-ray spectra. However, the relative intensity of characteristic peaks remains unchanged for a given measuring time. New branches with count ratios could be implemented in the mineral classification algorithm. Count ratios method could be efficient to classify solid solution minerals and minerals with similar compositions or stoichiometry. Grains from the garnet group, that typically have highly variable compositions, could be identified based on their Al/Si ratio since those elements are the most stable in the garnet lattice.

Crystal orientation may also influence peak intensity because of Bragg diffraction; however, it is expected to be negligible in our application.

Acknowledgements

Authors would like to thank the FRQNT, MERN, Agnico Eagle Mines, and Bruker for their financial and technical support.

References

Beckhoff, B., Kanngießer Habil, B., Langhoff, N., Wedell, R., Wolff, H. (Eds.) (2006) Handbook of practical x-ray fluorescence analysis. In: Springer Science & Business Media (ed) Springer Berlin, Heidelberg, pp 309-410. https://doi.org/10.1007/978-3-540-36722-2

Fipke, C.E., Gurney, J.J. and Moore, R.O. (1995) Diamond exploration techniques emphasising indicator mineral geochemistry and Canadian examples. Geological Survey of Canada, Canada, Bulletin 423.

Rueden, C. T., Hiner, M. C., Evans, E. L., Pinkert, M. A., Lucas, A. M., Carpenter, A. E., Cimini, B. A., Eliceiri, K. W. (2022) PyImageJ: A library for integrating ImageJ and Python, Nat Methods, 19:1326–1327, https://doi.org/10.1038/s41592-022-01655-4

Sauerbrei, J.A., Pattison, E.F., Averill, S.A. (1987) Till sampling in the Casa-Berardi gold area, Quebec: A case history in orientation and discovery. Journal of Geochemical Exploration 28:297–314. https://doi.org/10.1016/0375-6742(87)90054-9

Thiele S., Lorenz S., Kirsch M., Gloaguen R. (2020): *Hylite : A hyperspectral toolbox for open pit mapping* https://doi.org/10.5194/egusphere-egu2020-13563

Compositional variations of olivine in kimberlites: A new tool for diamond exploration

Andrea Giuliani[1], David Phillips[2], D. Graham Pearson[3], Soumendu Sarkar[2], Yaakov Weiss[4], Robin Preston[5], Michael Seller[6], Zdislav Spetius[7]
[1]ETH Zurich, Switzerland (andrea.giuliani@erdw.ethz.ch)
[2]The University of Melbourne, Australia
[3]University of Alberta, Canada
[4]The Hebrew University of Jerusalem, Israel
[5]De Beers Group, South Africa
[6]De Beers Group, Canada
[7]Novosibirsk State University, Russia

Abstract. Understanding the diamond potential of lithospheric roots traversed by kimberlites is a complex art that largely relies on geochemical and thermobarometric constraints provided by mantle-derived garnet, clinopyroxene and chromite (diamond indicator minerals). Although it is widely acknowledged that strongly melt-metasomatised lithospheric mantle keels are associated with poor diamond preservation, the mechanisms underpinning this relationship are far from clear. Here we show that the diamond grade of kimberlites worldwide is reflected by the composition of magmatic olivine. Kimberlites with low diamond grades contain iron-rich olivine, which is typical of kimberlites that entrain and assimilate substantial amounts of lithospheric mantle material metasomatised by earlier failed pulses of kimberlite (or similar) melt. Conversely, high diamond grades are exclusively associated with kimberlites featuring Mg-rich olivine composition which sampled lithospheric mantle keels only marginally modified by interaction with precursor kimberlite or related melts. This work provides a causal link between infiltration of the deep lithosphere by carbonate-rich kimberlite melts and diamond destruction, and shows that olivine chemistry is a new and inexpensive tool for diamond exploration.

1 Introduction

Diamond exploration is a multifaceted operation that relies on combinations of multiple geophysical and geochemical methods (Kjarsgaard et al., 2019). The composition of diamond indicator minerals (DIMs) in kimberlites, including mantle-derived garnet, clinopyroxene and chromite, provides important constraints on the diamond potential of the lithospheric mantle traversed and entrained by kimberlites (Gurney et al., 1993; Nowicki et al., 2007), including the thickness of the lithospheric roots (Grutter, 2009) and, therefore, of the diamond window (that is the lithospheric layer sandwiched between the graphite-diamond stability curve and the lithosphere-asthenosphere boundary). DIMs also provide indications of the extent of depletion vs metasomatic enrichment of the lithospheric mantle, as it is well established that diamonds brought to surface by kimberlites preferentially reside in compositionally depleted lithospheric mantle roots (Gurney et al., 1993; Nowicki et al., 2007). The connection between melt-metasomatism of the deep lithosphere and diamond potential of kimberlites is well-established empirically (Griffin and Ryan, 1995; Malkovets et al., 2007), but its geological context is not well understood, e.g., What is the origin and composition of these metasomatic melts? When did this metasomatic affect the lithospheric mantle? This work targets this knowledge gap and explores a new method to enhance the diamond exploration toolbox.

2 Background: olivine in kimberlites

Kimberlites are complex hybrid rocks that contain components of magmatic, hydrothermal and xenocrystic origin (Giuliani and Pearson, 2019). Olivine is the main constituent of fresh kimberlite rocks (Mitchell, 1973, 1986) and is generally zoned between xenocrystic cores derived from disaggregation of lithospheric mantle wall rocks, and magmatic rims (Giuliani, 2018). The olivine cores do not simply represent typical mantle peridotites, but may also be sourced locally from other lithologies (e.g., megacrysts; sheared peridotites) that have experienced metasomatism by precursor kimberlite melts. In fact, it is well established that the eruption of kimberlite magmas is preceded by 'priming' of lithospheric mantle conduits by earlier failed pulses of kimberlite melt (Giuliani et al., 2014, 2016).

Recent work has shown that the average Mg# [atomic proportions of Mg/(Mg+Fe)] of xenocrystic olivine cores is directly correlated to the average Mg# of olivine rims in kimberlites on a global (Giuliani et al., 2020) and regional scale (Dalton et al., 2020; Sarkar et al., 2021; Tovey et al., 2021). This correlation, combined with extensive petrographic and experimental evidence of assimilation of entrained lithospheric mantle material by kimberlites (Mitchell, 2008; Kamenetsky et al., 2009; Russell et al., 2012; Soltys et al., 2016), suggests that the composition of kimberlite melts at surface is directly related to the composition of lithospheric mantle wall rocks which interacts with kimberlite melts *en route* to surface (Giuliani et al., 2020). It further establishes that the more intensive the metasomatism, the more Fe-rich is the composition of magmatic olivine. Therefore, olivine chemistry provides a direct link between kimberlite melt composition and lithospheric mantle wall rocks, including the extent of

kimberlite-related metasomatism of the lithospheric mantle traversed by pulses of kimberlite magma that reach the surface.

3 Working hypothesis: A connection between kimberlite composition and diamond grade

Recent experimental work by Fedortchouk et al. (2022) has confirmed existing evidence (e.g., Robinson et al., 1989) that interaction of diamonds with carbonate-rich melts akin to kimberlites at lithospheric mantle depths leads to diamond resorption. Here, we test whether a correlation exists between olivine compositions and diamond grades in kimberlites worldwide, with the poviso that the composition of olivine in kimberlites constrains the extent of kimberlite-related metasomatism of the (diamond-bearing) lithospheric mantle roots. If this hypothesis is correct, we expect to observe lower diamond grades in kimberlites that sample lithospheric mantle wall rocks that have been extensively metasomatised by precursor kimberlite melts and, therefore, contain olivine with low (average) Mg# values.

4 Results

Building up on the compilation of Giuliani et al. (2020), we have assembled a revised database that includes new electron microprobe analyses of olivine in 12 kimberlites from Russia, Canada, Brazil and South Africa, and additional results from other localities published since the previous compilation. This new dataset confirms that the average Mg# of olivine cores in kimberlites (and also diamondiferous cratonic lamproites; see Sarkar et al., 2022) is directly correlated with the average Mg# of olivine rims. Of the 100 localities for which olivine data are now available, 74 have associated diamond grades (e.g., run of mines; exploration data). Comparison of average Mg# of either olivine cores or rims (which are linearly correlated) with diamond grades indicates that high diamond grades (>50-100 cpht or carats per hundred tonne) are exclusively. associated with high-Mg# olivine, i.e. >90 for olivine cores, ≥89 for olivine rims. Conversely, the diamond grades of kimberlites featuring low-Mg# olivine are always low (<20 cpht). It should be noted that low diamond grade can also occur in kimberlites with high-Mg# olivine.

5 Implications

The correlation between average olivine Mg# (cores or rims) and diamond grades confirms our working hypothesis that kimberlite-related metasomatism is detrimental to diamond preservation. This finding provides a sound explanation for the empirical observation, based largely on garnet xenocryst compositions (Gurney et al., 1993; Griffin and Ryan, 1995; Malkovets et al., 2007; Agashev et al., 2018), that melt-metasomatism of the lithospheric mantle leads to diamond destruction.

This study highlights that the major element composition of olivine in kimberlites represents a new inexpensive tool for diamond exploration. This tool does not replace other geochemical approaches such as analyses of garnet, but can be used to rapidly assess the likelihood of high diamond grades in a kimberlite based on the extent of kimberlite metasomatism of the lithospheric mantle roots. An important caveat is that olivine compositions are relatively invariant in kimberlite pipes and clusters of kimberlites, whereas diamond grades vary on every scale. Hence, olivine compositions provide constraints on the likelihood of diamond preservation in the lithospheric mantle, but do not allow prediction of the influence of other local-scale processes which impact diamond grade such as pre-existing diamond contents in the wall rocks, sampling efficiency by kimberlite melts, sorting of entrained mantle cargo during kimberlite ascent and emplacement, dilution by country rocks, etc. Nonetheless, used in combination with other geological constraints such as the depth of the lithosphere retrieved from mantle xenolith and xenocryst studies, the composition of olivine can provide an important tool for assessing the diamond potential of a kimberlite pipe or cluster before undertaking more detailed investigations.

References

Agashev AM, Nakai Si, Serov IV, Tolstov AV, Garanin KV, Kovalchuk OE (2018) Geochemistry and origin of the Mirny field kimberlites, Siberia. Mineralogy and Petrology 112(2):597-608 doi:10.1007/s00710-018-0617-4

Dalton H, Giuliani A, O'Brien H, Phillips D, Hergt J (2020) The role of lithospheric heterogeneity on the composition of kimberlite magmas from a single field: The case of Kaavi-Kuopio, Finland. Lithos 354-355:105333 doi:https://doi.org/10.1016/j.lithos.2019.105333

Fedortchouk Y, Chinn IL, Perritt SH, Zhang Z, Stern RA, Li Z (2022) Diamond-destructive mantle metasomatism: Evidence from the internal and external textures of diamonds and their nitrogen defects. Lithos 414-415:106616 doi:https://doi.org/10.1016/j.lithos.2022.106616

Giuliani A (2018) Insights into kimberlite petrogenesis and mantle metasomatism from a review of the compositional zoning of olivine in kimberlites worldwide. Lithos 312-313:322-342 doi:https://doi.org/10.1016/j.lithos.2018.04.029

Giuliani A, Pearson DG (2019) Kimberlites: From Deep Earth to Diamond Mines. Elements 15(6):377-380 doi:10.2138/gselements.15.6.377

Giuliani A, Pearson DG, Soltys A, Dalton H, Phillips D, Foley SF, Lim E, Goemann K, Griffin WL, Mitchell RH (2020) Kimberlite genesis from a common carbonate-rich primary melt modified by lithospheric mantle assimilation. Science Advances 6(17):eaaz0424 doi:10.1126/sciadv.aaz0424

Giuliani A, Phillips D, Kamenetsky VS, Goemann K (2016) Constraints on kimberlite ascent mechanisms revealed by phlogopite compositions in kimberlites and mantle xenoliths. Lithos 240–243:189-201 doi:http://dx.doi.org/10.1016/j.lithos.2015.11.013

Giuliani A, Phillips D, Kamenetsky VS, Kendrick MA, Wyatt BA, Goemann K, Hutchinson G (2014) Petrogenesis of Mantle Polymict Breccias: Insights into Mantle Processes

Coeval with Kimberlite Magmatism. Journal of Petrology 55(4):831-858
Griffin WL, Ryan CG (1995) Trace elements in indicator minerals: area selection and target evaluation in diamond exploration. Journal of Geochemical Exploration 53(1–3):311-337 doi:http://dx.doi.org/10.1016/0375-6742(94)00015-4
Grütter HS (2009) Pyroxene xenocryst geotherms: Techniques and application. Lithos 112, Supplement 2:1167-1178 doi:http://dx.doi.org/10.1016/j.lithos.2009.03.023
Gurney JJ, Helmstaedt H, Moore RO (1993) A review of the use and application of mantle mineral geochemistry in diamond exploration. Pure and Applied Chemistry 65(12):2423-2442 doi:doi:10.1351/pac199365122423
Kamenetsky VS, Kamenetsky MB, Sobolev AV, Golovin AV, Sharygin VV, Pokhilenko NP, Sobolev NV (2009) Can pyroxenes be liquidus minerals in the kimberlite magma? Lithos 112S:213-222
Kjarsgaard BA, Januszczak N, Stiefenhofer J (2019) Diamond Exploration and Resource Evaluation of Kimberlites. Elements 15(6):411-416 doi: 10.2138/gselements.15.6.411
Malkovets VG, Griffin WL, O'Reilly SY, Wood BJ (2007) Diamond, subcalcic garnet, and mantle metasomatism: Kimberlite sampling patterns define the link. Geology 35(4):339-342 doi:10.1130/g23092a.1
Mitchell RH (1973) Composition of olivine, silica activity and oxygen fugacity in kimberlite. Lithos 6(1):65-81 doi:http://dx.doi.org/10.1016/0024-4937(73)90080-7
Mitchell RH (1986) Kimberlites: Mineralogy, Geochemistry and Petrology. Plenum Publishing Company, New York
Mitchell RH (2008) Petrology of hypabyssal kimberlites: Relevance to primary magma compositions. Journal of Volcanology and Geothermal Research 174(1-3):1-8
Nowicki TE, Moore RO, Gurney JJ, Baumgartner MC (2007) Diamonds and Associated Heavy Minerals in Kimberlite: A Review of Key Concepts and Applications. In: Maria AM, David TW (eds) Developments in Sedimentology, vol Volume 58. Elsevier, pp 1235-1267
Robinson DN, Scott JA, Van Niekerk A, Anderson VG (1989) The sequence of event reflected in the diamonds of some southern African kimberlites. In: Ross J, Jaques AL, Ferguson J, Green DH, O'Reilly SY, Danchin RV, Janse AJA (eds) Kimberlites and Related Rocks 4th International Kimberlite Conference, vol 2. Geological Society of Australia, Perth, pp 990-1000
Russell JK, Porritt LA, Lavallee Y, Dingwell DB (2012) Kimberlite ascent by assimilation-fuelled buoyancy. Nature 481(7381):352-356
Sarkar S, Giuliani A, Ghosh S, Phillips D (2021) Petrogenesis of coeval lamproites and kimberlites from the Wajrakarur field, Southern India: New insights from olivine compositions. Lithos 406-407:106524 doi:https://doi.org/10.1016/j.lithos.2021.106524
Sarkar S, Giuliani A, Phillips D, Howarth GH, Ghosh S, Dalton H (2022) Sublithospheric melt input in cratonic lamproites. Geology 50(11):1296-1300 doi:10.1130/G50384.1
Soltys A, Giuliani A, Phillips D, Kamenetsky VS, Maas R, Woodhead J, Rodemann T (2016) In-situ assimilation of mantle minerals by kimberlitic magmas — Direct evidence from a garnet wehrlite xenolith entrained in the Bultfontein kimberlite (Kimberley, South Africa). Lithos 256–257:182-196 doi:http://dx.doi.org/10.1016/j.lithos.2016.04.011
Tovey M, Giuliani A, Phillips D, Pearson DG, Sarkar C, Nowicki T, Carlson J (2021) The spatial and temporal evolution of primitive melt compositions within the Lac de Gras kimberlite field, Canada: Source evolution vs lithospheric mantle assimilation. Lithos 392-393:106142 doi:https://doi.org/10.1016/j.lithos.2021.106142

In-situ Rb-Sr dating of mica: method refinement and application to mineral resources

Andrea Giuliani[1], Marcel Guillong[1], Senan Oesch[1], Roland Mass[2], Geoff H. Howarth[3], Marco L. Fiorentini[4]
[1]ETH Zürich, Switzerland (andrea.giuliani@erdw.ehtz.ch)
[2]The University of Melbourne, Australia
[3]University of Cape Town, South Africa
[4]University of Western Australia

Abstract. In-situ Rb-Sr dating of mica by laser ablation ICP-MS/MS has recently emerged as a new tool to date a range of geological processes including mineralisation events. The majority of age results presented to date are based on Rb/Sr calibration using the widely available MicaMG pressed-powder pellet. However, several studies have reported low accuracy associated with mica Rb-Sr ages using this method or large variations in calculated Rb/Sr for the same mica attributed to the different ablation properties of MicaMG and natural mica. In this work, we first report the results of a systematic comparison between isotope-dilution and in-situ Rb/Sr ages of micas in diamondiferous kimberlites from South Africa and Sierra Leone. We confirm that employment of MicaMG as calibration material may provide inaccurate results and present a new approach to obtain accurate ages, which relies on Rb/Sr calibration using the synthetic glass NIST610 SRM and an in-house mica standard. This updated procedure is then employed to constrain the ages of other diamond deposits and address the formation of Au mineralisation in the Eastern Goldfields (Australia).

1 Introduction

In-situ Rb-Sr dating of mica by laser ablation ICP-MS/MS (or QQQ) is increasingly employed to date a range of geological processes including magmatic intrusions, metamorphic and thermal events, crustal deformation and hydrothermal mineralisation. This analytical method overcomes the isobaric interference of ^{87}Rb on ^{87}Sr, which previously hampered analysis of Sr isotopes in Rb-rich phases such as mica, by reaction of Sr^+ ions with a gas reagent (SF_6 or N_2O) in a collision cell. Rb^+ ions are not affected by this reaction and, while the isotopes of Sr are quantified as reacted species (e.g., SrO^+), ^{87}Rb is determined by measuring the abundance of unreacted and interference-free ^{85}Rb.

The majority of age results presented to date are based on Rb/Sr calibration using the widely available MicaMG pressed-powder pellet (Hogmalm et al., 2017; Gorojovsky and Alard, 2020; Olierook et al., 2020; Zametzer et al., 2022; Kirkland et al., 2023). Strontium isotope ratios are routinely calibrated using the synthetic glass NIST610 SRM. However, various studies have reported low accuracy associated with mica Rb-Sr ages using this method (e.g., Li et al., 2020; Redaa et al., 2021, 2023; Subarkah et al., 2022) or large variations in calculated Rb/Sr for the same mica attributed to the different ablation properties of MicaMG and natural mica (Redaa et al., 2021). In this work we reassess the validity of this analytical approach by comparison of age data obtained for the same materials by in-situ and isotope-dilution methods. We then develop a new robust strategy to obtain accurate in-situ mica Rb/Sr ages and show its application to the formation of ore deposits.

2 Samples and methods

Micas tested in this study are predominantly sourced from kimberlites, including Bultfontein (South Africa; 88.3 ± 0.2 Ma; 2se; Fitzpayne et al., 2020), Wimbledon (South Africa; 114.4 ± 0.8 Ma; Sarkar et al., 2023), Koidu (Sierra Leone; ~145 Ma; De Beers unpublished data) and Tonguma (Sierra Leone; no previous age constraints available but assumed to be similar to Koidu) (**Figure 1**). The Bultfontein and Wimbledon localities have been selected to test the accuracy and reproducibility of in-situ mica Rb-Sr analyses, whereas obtaining new age data for multiple samples from Koidu and Tonguma represents the main target of this study. Additional samples from Au-mineralised carbonate-rich veins in the Smokebush dolerite (Eastern Goldfields, Western Australia) are also included to test the application of this method to the formation of Archean hydrothermal ore deposits.

Independent age constraints based on mica Rb-Sr dating by isotope dilution are available for Bultfontein (Fitzpayne et al., 2020) and Wimbledon (Sarkar et al., 2023). For Koidu and Tonguma, three samples were selected for isotope dilution analysis by multi-collector (MC) ICP-MS at the University of Melbourne. We also independently tested the Rb-Sr isotope composition of MicaMG by measuring an aliquot of the same powder used to manufacture the pellets we employ for calibration of mica Rb/Sr in situ analysis by isotope dilution (results reported in Redaa et al., 2023). In-situ Rb-Sr dating of mica in grain mounts and thin sections was undertaken by laser ablation ICP MS/MS using an Agilent 8800 housed at ETH Zurich.

3 Results and discussion

The Rb-Sr isotope compositions of mica fractions (bulk, leachate, residue) were used to construct Rb-Sr isochrons using IsoplotR. The only analysed sample from Tonguma yielded a 4-point isochron corresponding to an age of 138.2 ± 0.5 Ma (2se) (Fitzpayne et al., 2023). The two Koidu samples that

were analysed yielded 3-point isochron ages within uncertainties overlapping one another (145.7 ± 0.5 Ma, and 144.9 ± 0.5 Ma) (Fitzpayne et al., 2023). These ages are indistinguishable from previous age determinations for Koidu (145 Ma; De Beers unpublished).

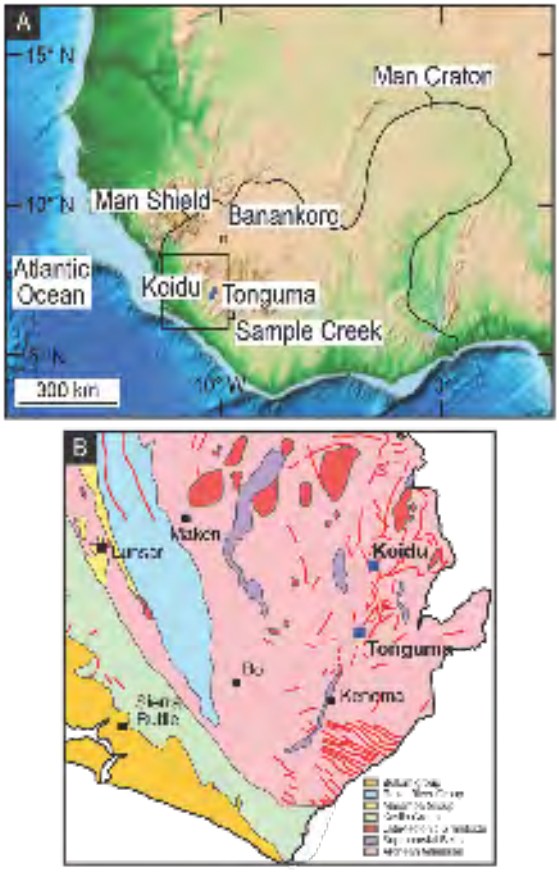

Figure 1. A) Tomographic map of West Africa showing the areal extent of the Man Craton and the positions of main kimberlite clusters; and B) inset showing a simplified map of south-eastern Sierra Leone including the positions of Tonguma and Koidu.

These ages and those previously obtained by isotope dilution for micas in South-African Cretaceous kimberlites were then compared with those obtained by laser ablation ICP-MS/MS using two different procedures. The first one is identical to the widely applied strategy of calibrating $^{87}Sr/^{86}Sr$ using the synthetic glass NIST610 SRM and $^{87}Rb/^{86}Sr$ using MicaMG. This procedure generates age results which generally do not overlap those obtained by isotope dilution with relative differences as high as 10% (**Figure 2**). We concur with Redaa et al. (2021) that this difference between solution-based and in-situ mica Rb-Sr ages probably stems from the different ablation properties of the pressed nano-powder pellet MicaMG. Poor reproducibility of Rb/Sr in MicaMG compared to NIST610 also confirms the heterogeneous behaviour of MicaMG during laser ablation.

We have therefore devised a new procedure where NIST610 is initially employed to estimate both $^{87}Sr/^{86}Sr$ and $^{87}Rb/^{86}Sr$, thus producing very stable splines for drift correction and initial calibration of Rb-Sr isotopes in mica. An in-house mica standard (from Wimbledon) is then utilised to re-calibrate $^{87}Rb/^{86}Sr$ in the mica unknowns. This procedure generates age data which match 'isotope-dilution' ages for the same micas (**Figure 1**).

For Tonguma and Koidu, pooling of laser ablation analyses of micas in multiple samples returns ages of 137.1 ± 2.0 Ma (n = 133; 5 samples) and 145.1 ± 2.4 Ma (n = 92; 4 samples), which are also indistinguishable from the solution-based age data. These data and a similarly narrow spread in mica Rb-Sr age data by individual samples for different units of each locality suggest that different intrusive units at Koidu and Tonguma were emplaced over a short time interval, which currently cannot be resolved.

Analyses of mica in carbonate-rich veins from Smokebush are currently underway and the results will be presented at the meeting.

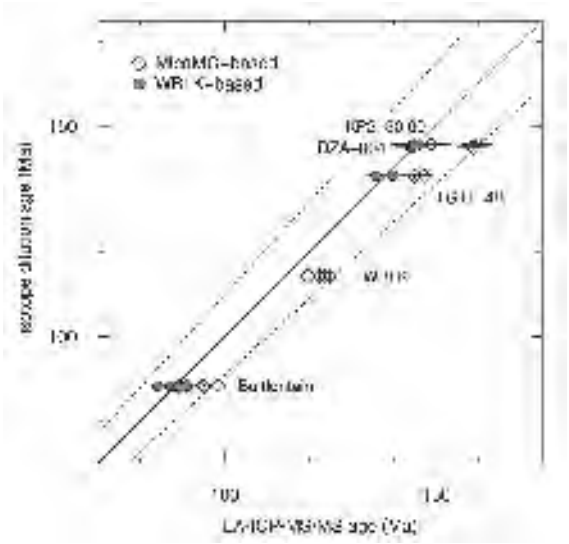

Figure 2. Comparison of mica Rb-Sr ages from LA-ICP-MS/MS vs isotope dilution. Note the difference between LA-ICP-MS/MS ages calculated using MicaMG or Wimbledon (WBLK) to calibrate Rb/Sr in the mica unknowns, where only the latter approach provides accurate results.

4 Conclusions

In-situ Rb-Sr dating of mica by LA-ICP-MS/MS can provide excellent age constraints and is much quicker and less expensive compared to conventional isotope-dilution methods. Although this method does not achieve the same level of precision of isotope dilution analyses, it allows to preserve textural context and can be combined with analysis of trace element concentrations thus enabling combination of petrological, geochemical and isotopic information. However, additional effort is required to improve the current limitations of in-situ mica Rb-Sr dating. This work shows that

employment of MicaMG as primary calibration standard is not recommended and developments of suitable mica reference materials showing large spread in Rb/Sr such as our Wimbledon mica is required.

References

Fitzpayne A, Giuliani A, Hergt J, Woodhead JD, Maas R (2020) Isotopic analyses of clinopyroxenes demonstrate the effects of kimberlite melt metasomatism upon the lithospheric mantle. Lithos 370-371:105595 doi:https://doi.org/10.1016/j.lithos.2020.105595

Fitzpayne A, Giuliani A, Howarth GH, Peters BJ, Fehr MA, Maas R (2023) Major-, trace-element and Sr-Nd-Hf isotope geochemistry of diamondiferous dykes from Tonguma and Koidu, Sierra Leone: Highly micaceous kimberlites formed by assimilation of metasomatised lithospheric mantle rocks. Chemical Geology 630:121475 doi:https://doi.org/10.1016/j.chemgeo.2023.121475

Gorojovsky L, Alard O (2020) Optimisation of laser and mass spectrometer parameters for the in situ analysis of Rb/Sr ratios by LA-ICP-MS/MS. Journal of Analytical Atomic Spectrometry doi:10.1039/D0JA00308E

Hogmalm KJ, Zack T, Karlsson AKO, Sjöqvist ASL, Garbe-Schönberg D (2017) In situ Rb–Sr and K–Ca dating by LA-ICP-MS/MS: an evaluation of N2O and SF6 as reaction gases. Journal of Analytical Atomic Spectrometry 32(2):305-313 doi:10.1039/C6JA00362A

Kirkland CL, Olierook HKH, Danišík M, Liebmann J, Hollis J, Ribeiro BV, Rankenburg K (2023) Dating mylonitic overprinting of ancient rocks. Communications Earth & Environment 4(1):47 doi:10.1038/s43247-023-00709-5

Li S-S, Santosh M, Farkaš J, Redaa A, Ganguly S, Kim SW, Zhang C, Gilbert S, Zack T (2020) Coupled U-Pb and Rb-Sr laser ablation geochronology trace Archean to Proterozoic crustal evolution in the Dharwar Craton, India. Precambrian Research 343:105709 doi:https://doi.org/10.1016/j.precamres.2020.105709

Olierook HKH, Rankenburg K, Ulrich S, Kirkland CL, Evans NJ, Brown S, McInnes BIA, Prent A, Gillespie J, McDonald B, Darragh M (2020) Resolving multiple geological events using in situ Rb–Sr geochronology: implications for metallogenesis at Tropicana, Western Australia. Geochronology 2(2):283-303 doi:10.5194/gchron-2-283-2020

Redaa A, Farkaš J, Gilbert S, Collins AS, Löhr S, Vasegh D, Forster M, Blades M, Zack T, Giuliani A, Maas R, Baldermann A, Dietzel M, Garbe-Schönberg D (2023) Testing Nano-Powder and Fused-Glass Mineral Reference Materials for In Situ Rb-Sr Dating of Glauconite, Phlogopite, Biotite and Feldspar via LA-ICP-MS/MS. Geostandards and Geoanalytical Research 47(1):23-48 doi:https://doi.org/10.1111/ggr.12467

Redaa A, Farkaš J, Gilbert S, Collins AS, Wade B, Löhr S, Zack T, Garbe-Schönberg D (2021) Assessment of elemental fractionation and matrix effects during in situ Rb–Sr dating of phlogopite by LA-ICP-MS/MS: implications for the accuracy and precision of mineral ages. Journal of Analytical Atomic Spectrometry 36(2):322-344 doi:10.1039/D0JA00299B

Sarkar S, Giuliani A, Dalton H, Phillips D, Ghosh S, Misev S, Maas R (2023) Derivation of lamproites and kimberlites from a common evolving source in the convective mantle: The case for southern African “transitional kimberlites”. Journal of Petrology:accepted pending minor revisions

Subarkah D, Nixon AL, Jimenez M, Collins AS, Blades ML, Farkaš J, Gilbert SE, Holford S, Jarrett A (2022) Constraining the geothermal parameters of in situ Rb–Sr dating on Proterozoic shales and their subsequent applications. Geochronology 4(2):577-600 doi:10.5194/gchron-4-577-2022

Zametzer A, Kirkland CL, Barham M, Hartnady MIH, Bath AB, Rankenburg K (2022) Episodic alteration within a gold-bearing Archean shear zone revealed by in situ biotite Rb–Sr dating. Precambrian Research 382:106872 doi:https://doi.org/10.1016/j.precamres.2022.106872

Standardized and Automated 3D Mineralogy of Ores

Jose R. A. Godinho[1]
[1] *Helmholtz-Zentrum Dresden-Rossendorf, Helmholtz Institute Freiberg for Resource Technology. j.godinho@hzdr.de*

Abstract. Quantitative mineralogy of geological materials has been limited to 2D imaging methods that use chemical information from cross-sections of a material to automatically classify it's mineral phases. A more comprehensive mineralogical analysis of the real microstructures inside a material can be done in 3D using X-ray Computed Tomography (CT). Nevertheless, a widespread use of the technique has been limited by the lack of standardized methods to classify and to quantify minerals from 3D images that do not contain chemical information. This is mostly due to 3D image artefacts that hinder the ability to process the data in a standardized way, which is hindered further by the variety of scanners and software available at different laboratories. Here, results from the first standardized workflow for automated 3D mineralogy using CT are presented. The results from different types of ores (Au, Cu, Fe, Cr and REE) are compared with other standard methods 2D-based automated mineralogy and XRD. The advantages and disadvantages of using 3D characterization are discussed as well as the advantages of using the proposed workflow relative to traditional 3D image analysis.

1 Introduction

Image artefacts and partial volume in voxels at interphases are inevitable in 3D images resulting from CT. This makes image processing based on the grey-scale of the whole 3D image time consuming and the results can be strongly influenced user input bias due to the lack of automation and standardization of the different image processing steps. These are strong reasons to prevent the adoption of CT and 3D imaging for routine ore characterization. For this to become a reality, two steps are required, 1) to reduce and account for the imaging artefacts with minimum subjective image processing, and 2) to standardize and automate the quantification workflow, similar to available 2D automated mineralogy methods.

The first standardized workflow, **M**ounted **S**ingle **Pa**rticle **C**haracterization for **M**ineralogical **An**alysis (MSPaCMAn) to implement these steps was recently proposed (Godinho et al. 2021; Godinho et al. 2023). Here, the workflow is applied to reference samples and different ore types, to quantify their mineralogical composition in a semi-automated way.

2 Methods

The MSPaCMAn workflow consists of the following sequence of steps (Fig.1): 1) sample preparation as a particle dispersion where a spacer is used to minimize the particles to touch. This step simplifies the image processing, which enables automation. 2) Particle segmentation is done using deep learning model that has been pre-trained in dozens of samples and can distinguish the particles from the background without user input (Gotkowski et al. 2023). 3) Phase classification is done using a decision tree with criteria based on the grey-scale and geometrical properties of each particle. This allows to reduce the complexity of the microstructures in the whole image into less complex subvolumes that are sample specific. 4) Phase quantification is calculated at the particle-level using the grey-values of all voxels in the particle, which allows taking in consideration the partial volume at interphases. This improves the detection limit of grains, improves accuracy and decreases user input bias.

3 Results

The MSPaCMAn workflow has been validated in several reference samples containing particles of known composition. For example, in Figure 2 several minerals typically present in sulphide concentrates are analysed in the same sample. With the exception of the denser arsenopyrite, the other phases have similar x-ray attenuation coefficients. Consequently, it would be difficult to distinguish those phases, especially if they appear associated as it is often the case in ores. Nevertheless using single particle histograms it is possible to distinguish the phase based on the distinctive grey-values at the maximum of the peaks. As shown in figure 1 magnetite and pyrite can be classified correctly even if they are associated in complex microstructures.

Figure 3 shows a sample containing quartz and biotite. Biotite has a characteristic thin shape, thus its characteristic grey-scale is shifted towards lower values that those expected based solely on the attenuation coefficient. Consequently, the two phases cannot be distinguished base only on the grey-scale. Nevertheless, the since the grey-values of the peaks from the single particle histograms are a function of the geometrical properties of the biotite particles, this function can be used as a classification criteria.

The method is currently being test in real ore with different degrees of complexity, e.g., chromite ore, sulphide-cupper ores, REE rich carbonates, iron ores, and gold-rich quartz-pyrite. Quantitative validation of the results is done using XRD, 2D-based automated mineralogy and chemical essays.

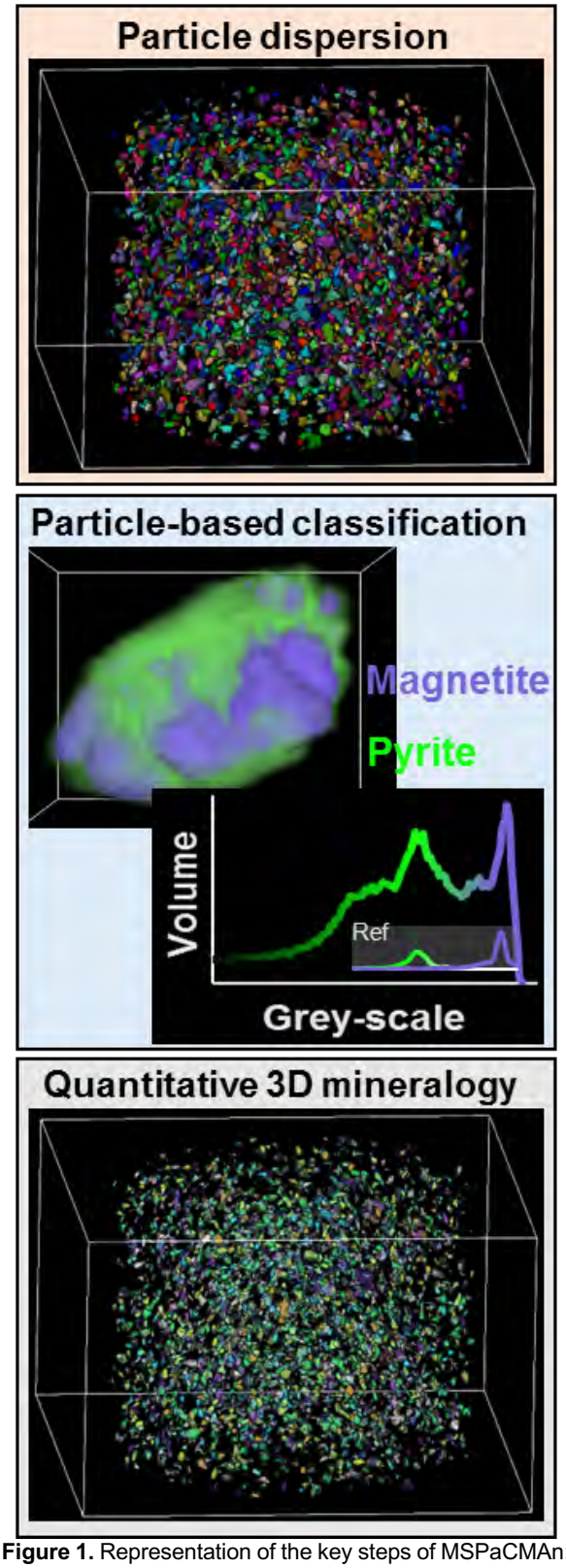

Figure 1. Representation of the key steps of MSPaCMAn: Sample preparation, particle-based histogram analysis, automatic classification and quantification of all particles.

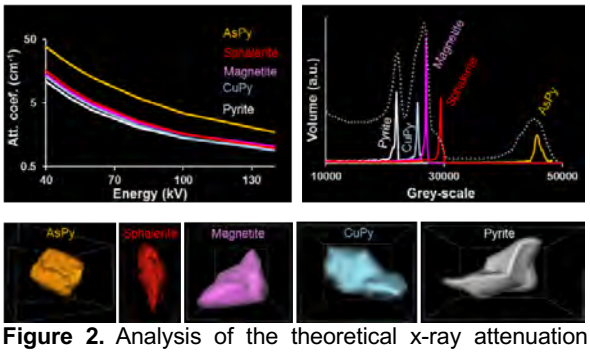

Figure 2. Analysis of the theoretical x-ray attenuation coefficient and particle histograms from a reference sample containing arsenopyrite (AsPy, orange), sphalerite (red), magnetite (pink), chalcopyrite (CuPy, blue) and pyrite (white). The histogram of the entire 3D image (dashed line) is compared with the histogram of individual particles, one per phase.

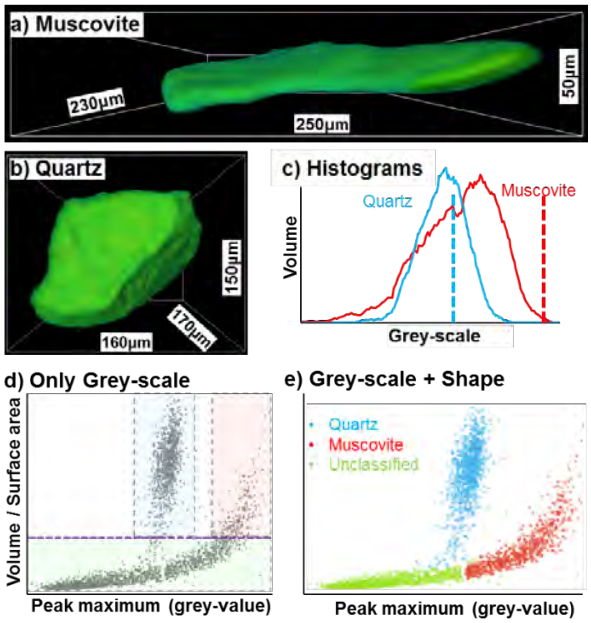

Figure 3. Comparison between particles with different composition and shape. **a)** muscovite particle, and **b)** quartz particle. **c)** histograms of the particles (a) and (b). The dashed lines correspond to the theoretical peak position of the pure phases. **d)** Representation of the variation of the volume to surface area ratio as a function of the maximum peak grey-value for a mixture of particles containing muscovite and quartz, similar to (a) and (b). Blue and red boxes identify the areas within which the particles could be identified as quartz or muscovite based only on the grey-scale; and the purple line marks the expected detection limit. **e)** Same data as (d) but the particles are individually analysed and the classification uses both the peak grey-value and the V/SA of each individual particle.

4 Conclusion

Similar to 2D-based automated quantitative mineralogy methods, the presented workflow includes sample preparation and criteria-based classification. Although in 3D these criteria are based on particle histograms instead of chemical spectra. This poses some limitations to distinguish

mineral phases especially for complex microstructures. Nevertheless, for large grains and for sparsely distributed phases (cases subject to 2D stereological bias), the method shows advantages relative to 2D methods. Additionally, when compared to traditional 3D image processing, the method lowers the size detection limit of grains and increases the contrast resolution.

Altogether, the MSPaCMAn workflow opens the door for standardized 3D characterization with particle-level resolution. The possibility to automate the workflow gives hope to reducing the costs and time for 3D characterization, thus making it more desirable to the raw materials industry. The third dimension can unleash new possibilities in minerals processing and particle technology.

References

Godinho, J.R.A.; Grilo, B.L.D.; Hellmuth, F.; Siddique, A. *Minerals* **2021**, *11*, 947. https://doi.org/10.3390/min11090947

Godinho, J.R.A.; Hassanzadeh, A.; Heinig, T. *Nat Resour Res* **2023,** *32*, 479–499. https://doi.org/10.1007/s11053-023-10169-5

Gotkowski, K.; Gupta, S.; Godinho, J.R.A.; Tochtrop, C.G.S.; Maier-Hein, K.H.; Isensee, F. *arXiv preprint* **2023**. arXiv:2301.13319

How trace elements are incorporated into pyrite, a view from mm- to nano-scale

Daniel D. Gregory[1], Anthony Chappaz[2], Sandra D. Taylor[3], Daniel E. Perea[4], Libor Kovarik[3], and John B. Cliff[4]
[1]Department of Earth Sciences, University of Toronto, Toronto, ON, M5S3B1, Canada
[2]STARLAB, Earth and Atmospheric Sciences, Central Michigan University, MI 48858 USA
[3]Physical and Computational Sciences Directorate, Pacific Northwest National Laboratory, Richland, WA 99354, USA
[4]Earth and Biological Sciences Directorate, Pacific Northwest National Laboratory, Richland, WA 99354, USA

Abstract. Pyrite trace element chemistry is important for understanding evolution of ore fluids in mineralizing systems. Much of the understanding of how metals are held in pyrite is based on micro-scale techniques such as LA-ICPMS and electron microprobe. This requires assumptions to be made when interpreting the results regarding whether elements are held as micro-inclusions versus as substitutions into the pyrite lattice. In this contribution, we use micro- to nano-scale analyses including LA-ICPMS, NanoSIMS, and atom probe tomography (APT) to investigate trace element deportment in pyrite from sites characterized by high trace element concentrations (Black Butte SEDEX deposit) and one characterized by medium to low trace element concentrations (Leicester pyrite member, New York). We further use synchrotron based XANES to investigate the redox state of As and how that relates to trace element enrichment. We find that trace elements are highly heterogeneous at all scales investigated and that interpretation of how trace elements are incorporated into pyrite using even micro-scale techniques must be pursued with caution.

1 Introduction

Pyrite is a common mineral in many different ore deposits and can incorporate several different elements into its structure. As such, pyrite trace element chemistry has received significant interest as a potential vector to mineralization as fluid composition is likely a significant factor in the end trace element chemistry of the pyrite (Belousov et al., 2016). However, several other factors may affect the trace element content of the pyrite including other mineral phases precipitating at the same time as the pyrite, fluid temperature, boiling, wall rock interactions and presence of other elements in the pyrite that may influence incorporation of other trace elements. This latter factor is the subject of this study, specifically the effect that As, and As redox state, has on trace element incorporation into pyrite.

It has been known for some time that As may affect the incorporation of some trace elements into the pyrite lattice and that its redox state can affect which elements are preferentially incorporated. When As^- substitutes for S it has been shown that elements similar to Fe are preferentially incorporated (e.g. Ni and Co) (Reich and Becker, 2006). Alternatively, from a charge balance perspective, if As(+III) substitutes for Fe(+II), then, for every 2 As atoms, there needs to be one cation gap in the pyrite structure to accommodate more large cations like Au(+I) or Pb(+II), leading to their relatively high concentration in the pyrite (Deditius et al., 2008). As can also be incorporated as amorphous Fe-S-As nano-inclusions (Deditius et al., 2009) which would not necessarily increase the incorporation of other elements. However, while it has been shown that these processes may increase the incorporation of various trace elements, and thus affect the partition coefficient of the trace elements into pyrite, it has not been shown that this is the dominant control of pyrite trace element incorporation. In this contribution we use a variety of different techniques applied to samples from two sites (high and medium trace element concentration) to determine the spatial variability of trace elements in pyrite, from the micrometer to nanometer scale, while considering the variation in redox state, to determine whether As content and/or redox state are the dominant controls on trace element concentration in pyrite.

2 Methods

We used a combination of in situ techniques to identify associations of different trace elements with As. These started in larger scale to guide higher chemical sensitivity and spatial resolution composition mapping techniques from identified textures to gain data at progressively finer scales. The first step involved using LA-ICPMS conducted at the University of Tasmania. This utilized a 193 nm ArF excimer ATL Atlex ILR laser coupled to an Agilent 7700 ICP-MS. 35 µm spot sizes were used and point spots were ablated in a pure He atmosphere at 5 Hz. The ablated material was then mixed with Ar to improve efficiency of the aerosol transport. LA-ICPMS maps were also constructed. These analyses utilizing a similar methodology with the spot analyses with the exception that line scans were employed and smaller spot size were used (13 µm); see Gregory et al., (2016) for more details.

Next, representative textures were analyzed with nanoscale secondary ion mass spectrometry (NanoSIMS) composition mapping using a Cameca NanoSIMS 50L housed at the Environmental Molecular Sciences Laboratory (EMSL) at the Pacific Northwest National Laboratory (PNNL) This provided 50 µm x 50 µm maps of the trace and major element abundances of selected textures of the pyrite. Two steps were used to produce the maps. The first maps were produced for negative ions ($^{12}C_2^-$, $^{12}C^{14}N^-$, $^{28}Si^-$, $^{34}S^-$, $^{75}As^-$, $^{78}Se^-$, and $^{80}Se^-$), then the

same area was mapped for positive ions ($^{58}Ni^+$, $^{63}Cu^+$, $^{66}Zn^+$, $^{68}Zn^+$, and $^{133}Cs^+$). A 2 pA primary beam with a probe diameter of 120-400 nm was used. This provided microscale spatial correlations of different elements with As.

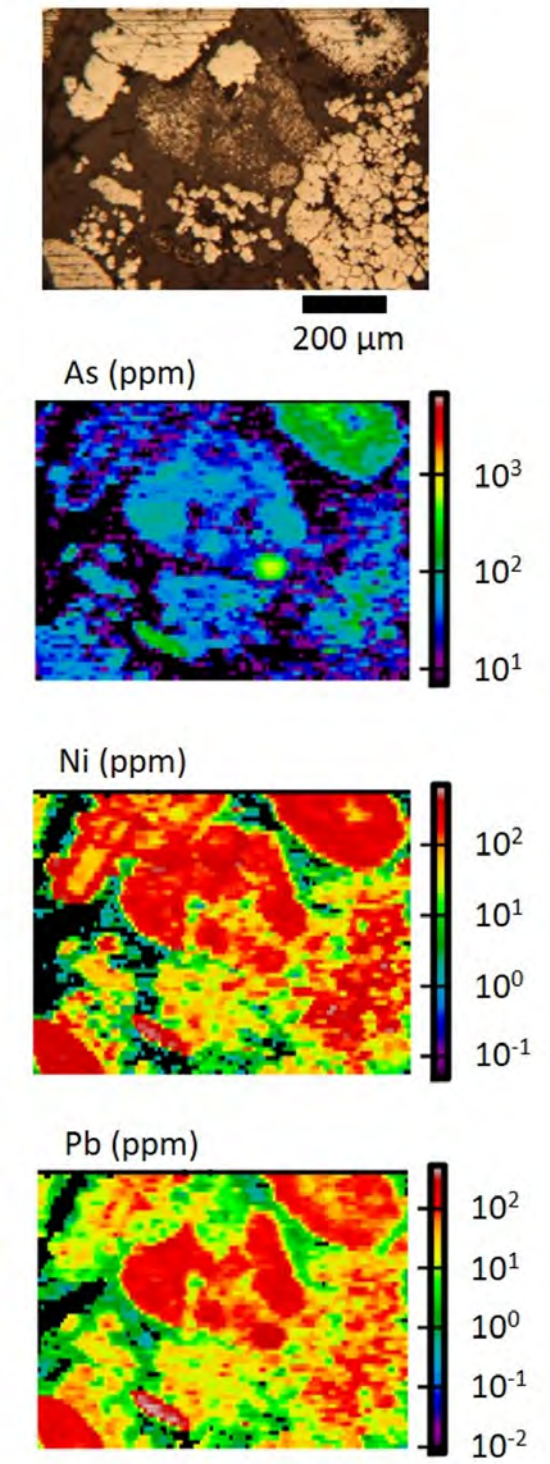

Figure 1. LA-ICPMS trace element maps of one sample from the Leicester pyrite member (low to medium trace element content. Note the variable correlation of the enrichment of the As, Ni, and Pb.

Regions of interest for Atom probe tomography (APT) analysis, were identified using the NanoSIMS data. Micro-sized regions of interest were prepared for APT analyses using a Thermo Fischer Scientific Helios Nanolab 600i focused ion beam (FIB) scanning electron microscope (SEM) which physically lifted it out and shaped the regions of interest into specimens needles. APT analysis was conducted on a CAMECA Local Electrode Atom Probe (LEAP) 4000X-HR in laser-assisted mode utilizing a 355 nm UV laser with an energy per pulse range between 35 and 65 pJ. A laser pulse repetition range of 100-250 kHz was used. A detection rate of 0.002 ions per pulse was maintained by varying the voltage applied to the specimen.

Synchrotron based spectroscopic techniques were applied to determine As speciation for a selection of four samples at the Advanced Photon Source (Argonne National Laboratory). Micro-focused XANES spectra were collected at sector 20. For each sample, 2-3 ROIs were targeted with a beam size of 50 μm^2. As a first step, we produced As elemental maps of 500 μm^2 for each ROIs using µ-XRF. Subsequently, we collected µ-XANES spectra for As at the following K-edge energy: 11,867 eV. At least three spectra per spot were be merged to improve signal to-noise ratio. Spectra were interpreted using four As standards. We processed and analyzed all the data using the Demeter software package.

3 Samples

A high trace element pyrite sample from the Black Butte SEDEX deposit, Montana and a medium to low trace element content pyrite sample from the Leicester Pyrite Member, New York state were chosen to investigate the effects of both the trace element content of the fluids from which the pyrite formed on its end trace element content and how the metals are held within it. The Leicester Pyrite Member is thought to have formed in Devonian-aged sedimentary rocks and later concentrated through re-sedimentation. It provides an example of a low temperature, relatively low trace element formation environment. The sample from the Black Butte SEDEX deposit formed at elevated temperatures (~200-350 °C) and in a relatively high trace element environment.

4 Results

In the laser ablation maps there was clear variation in trace element content in the different textures and parts of the pyrite within the samples (Figure 1). Of particular interest is the variable correlation between the As and other elements. In some regions, there is clear correlation between areas of As and areas of enrichment of Ni and Pb, as well as other trace elements. This is further supported in the NanoSIMS maps that, at a finer scale, show a similar variable enrichment of Se and Ni with no obvious visual

correlation with As (Figure 2). However, other samples show distinct correlation between As and other trace elements. The same observations are made at the nano-scale using atom probe tomography where there is a general association between trace metal enrichments and the presence of As in regions of the pyrite samples. However, this is not always the case as there are also regions where there are element enrichments independent of As.

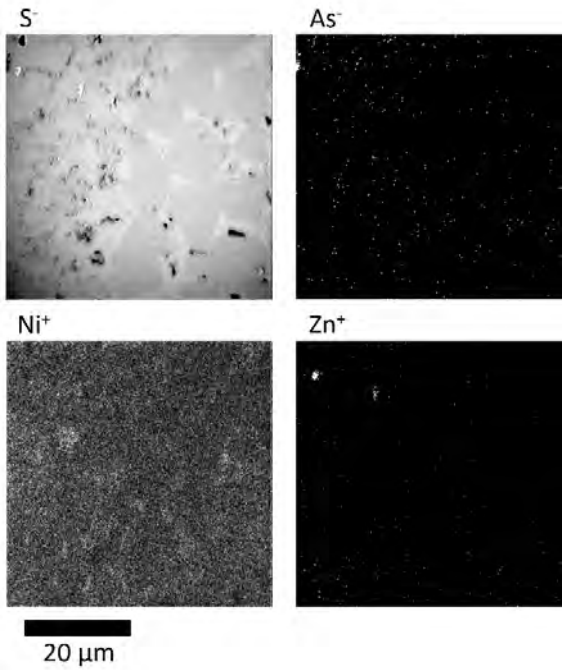

Figure 2. NanoSIMS trace element maps from the Leicester Pyrite Member, note the Zn and Ni enrichments that do not correlate with As enrichments. Modified after Gregory et al., (2019).

The speciation of As is highly variable intra and inter samples. The average As oxidation state ranges from 0.8 to 2.6 for 10 ROIs across four samples (Figure 3).

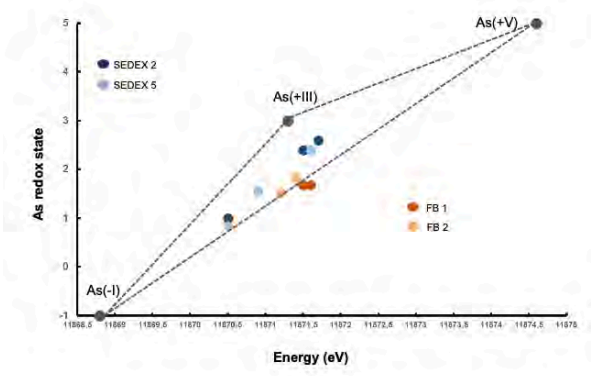

Figure 3. As average oxidation state for 10 ROIs

5 Discussion and Conclusions

The analyses conducted in this study show high variability in pyrite trace element content and As concentration. This suggests that in some cases As may facilitate the enrichment of trace elements in pyrite, such as Cu and Ni, as has been hypothesized. However, at the micro- to nano-scale, this is frequently not the case. Thus, interpretations of the manner and causes for enrichment of trace elements in pyrite must be done with caution as these enrichments can vary significantly across very small distances.

We argue that, general inferences of composition of the formative fluids can sometimes be made by investigating the concentrations of trace elements in pyrite. However, due to the high levels of heterogeneity observed at all scales investigated, attempts to tie specific elements with the uptake of other elements should be done with caution and that a direct calculation of fluid concentration from pyrite concentration is likely to be unachievable.

Acknowledgements

NanoSIMS and APT analyses were performed under a project award (#49860) from the Environmental Molecular Sciences Laboratory, a DOE Office of Science User Facility sponsored by the Biological and Environmental Research program under Contract No. DE-AC05-76RL01830. We also acknowledge the NSERC Discovery Grant to Daniel Gregory.

References

Belousov, I., Large, R., Meffre, S., Danyushevsky, L., Steadman, J., and Beardsmore, T. (2016) Pyrite compositions from VHMS and orogenic Au deposits in the Yilgarn Craton, Western Australia: Implications for gold and copper exploration. Ore Geology Reviews.

Deditius, A. P., Utsunomiya, S., Ewing, R. C., and Kesler, S. E. (2009) Nanoscale "liquid" inclusions of As-Fe-S in arsenian pyrite. American Mineralogist 94: 391-394.

Deditius, A. P., Utsunomiya, S., Renock, D., Ewing, R. C., Ramana, C. V., Becker, U., and Kesler, S. E. (2008) A proposed new type of arsenian pyrite: Composition, nanostructure and geological significance. Geochimica et Cosmochimica Acta 72: 2919-2933.

Gregory, D. D., Large, R. R., Bath, A. B., Steadman, J. A., Wu, S., Danyushevsky, L., Bull, S. W., Holden, P., and Ireland, T. R. (2016) Trace Element Content of Pyrite from the Kapai Slate, St. Ives Gold District, Western Australia. Economic Geology 111: 1297-1320.

Gregory, D., Mukherjee, I., Olson, S. L., Large, R. R., Danyushevsky, L. V., Stepanov, A. S., Avila, J. N., Cliff, J., Ireland, T. R., and Raiswell, R. (2019) The formation mechanisms of sedimentary pyrite nodules determined by trace element and sulfur isotope microanalysis. Geochimica et Cosmochimica Acta 259: 53-68.

Reich, M., and Becker, U. (2006) First-principles calculations of the thermodynamic mixing properties of arsenic incorporation into pyrite and marcasite. Chemical Geology 225: 278-290

Mineralization age of the Kar'ernoe ore occurrence, Polar Urals revealed by the U-Th/He dating of pyrite

Ekaterina Ivanova[1,2], Olga Yakubovich[1,2], Maria Anosova[3], Eugeniya Tuykova[4,5] and Ivan Sobolev[4]
[1]Institute of Earth Sciences, Saint-Petersburg University, Saint-Petersburg, Russia
[2]Institute of Precambrian Geology and Geochronology (IPGG), Russian Academy of Sciences (RAS), Saint-Petersburg, Russia
[3]Vernadsky Institute of Geochemistry and Analytical chemistry (GEOKHI), Russian Academy of Sciences, Moscow, Russia
[4]Institute of Geology of Ore Deposits, Petrography, Mineralogy and Geochemistry (IGEM), Russian Academy of Sciences, Moscow, Russia
[5]Geoinformation Research Centre (NGIC) Russian Academy of Sciences, Moscow, Russia

Abstract. The Kar'ernoe gold ore occurrence is located within the volcanogenic rocks of the Toupugol-Khanmeishor district on the eastern slope of the Polar Urals. The age of mineralization of the volcanogenic rocks was determined by the U-Th/He dating of pyrite. Two events of ore formation are established. The first stage (424±6 Ma (2σ); n=4) is coeval with sedimentation of the volcanogenic rocks. The later stage (400±6 Ma (2σ); n=3) reflects the newly formation/recrystallization of pyrite due to the emplacement of the diorites of the Sob complex. Thus, the Kar'ernoe gold ore occurrence might represent the initial sulfide stages of ore formation in the Toupugol-Khanmeishor ore district.

Introduction

The Toupugol-Khanmeishor ore district is a relatively understudied region in the Polar Urals, which is believed to have a potential for discovering gold deposits (Vikentyev et al. 2017). Regional provenance studies require reconstruction of the ore-magmatic systems of the Paleozoic island-arc system of the Polar Urals. Accurate geochronological data is essential to the developing of such models. Herein we applied a novel approach of U-Th/He dating of pyrite in order to estimate the age of mineralization of the Upper Silurian-Lower Devonian island-arc volcanogenic rocks of the Kar'ernoe ore occurrence and to establish its relation to the known magmatic and tectonic activity in the area.

1 Fundamentals of the U-Th/He dating of pyrite

The U-Th/He system is known to be widely used in the field of low temperature thermochronology (Farley et al. 2002; Flowers et al. 2022). Recent advances in understanding of the He behavior in native metals, pyrite and Fe oxyhydroxide phases made He dating technique suitable for geochronological studies (Shukolyukov et al. 2012; Farley et al. 2018; Yakubovich et al. 2019).

Radiogenic ^{4}He is produced by the alpha-decay of ^{235}U, ^{238}U, ^{232}Th isotopes. Uranium can be present in pyrite in the form of micron-size mineral inclusions (uraninite, apatite, monazite, rutile) and/or as a relatively homogeneous impurity (Baranov 1966). Concentration of U in pyrite in average varies from 0.2 to 11 μg/g (Melekestseva et al. 2014; Yakubovich et al. 2020). Long alpha-stopping distances (11–34 μm) prevent He accumulation within micron-size inclusions of U- and Th-bearing phases, which implies that U-Th/He age corresponds to the age of pyrite formation. High thermal retentivity of radiogenic He in pyrite is confirmed by step-heating experiments (Yakubovich et al. 2019) and by the results of pyrite dating from the slightly metamorphized VMS type Uzelga deposit, South Urals (Yakubovich et al. 2020).

2 Object of study

2.1 Geological setting

The Toupugol-Khanmeishor gold ore region is located in the northern part of the Voikar zone, which belong to the Polar-Ural island-arc system (Fig.1). The northwestern part of the Voikar zone is mainly composed of Late Ordovician oceanic formations of the ophiolite association and borders along the Main Ural Fault with the Paleozoic-Late Proterozoic formations of the West Ural megazone. The southeastern part of the zone is dominated by Late Ordovician-Middle Devonian island-arc rocks of the Malouralsk volcanoplutonic belt, overlain by a thick Mesozoic-Cenozoic sedimentary cover of the West Siberian Plate (Volchkov et al. 2008).

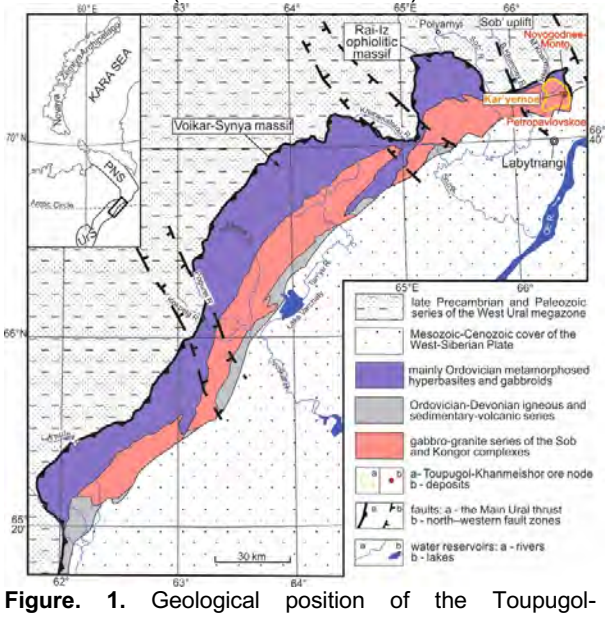

Figure. 1. Geological position of the Toupugol-Khanmeishor ore district in the structures of the Polar Urals using data from (Yazeva et al. 1984; Sobolev et al. 2017)

Two gold ore deposits are known in that area: gold-iron-skarn Novogodnee-Monto (7 t Au), and gold-porphyry Petropavlovskoe (26 t Au) deposits (Vikentyev et al. 2017).

The Kar'ernoe ore occurrence is located in a flank of the Novogodnensky ore field in 2 km southwest of the Novogodnee-Monto gold deposit. Estimated resources of the Kar'ernoe ore occurrence is 5 tons of Au (P_2 category; Volchkov et al. 2008). Mineralization is host by Upper Silurian-Lower Devonian volcanic-sedimentary (flyschoids, polymictic breccias with fragments of volcanic, intrusive and carbonate rocks) and volcanic rocks of the Tupugolskaya formation. Early-Middle Devonian diorite porphyrites and quartz diorites of the Sob complex, as well as Early Carboniferous dykes of dolerites, lamprophyres, and monzodiorite-porphyries of the Musyur complex cut these volcanic-sedimentary rocks (Volchkov et al. 2008). Intense shearing, cataclasis, brecciation, limited by the Tupugolsky and Eviegansky faults, are developed within the deposit. Interlayers of fine clastic carbonate rocks host layered sulfide and pyrite mineralization.

2.2 Sample description

A sample 14/32 of medium-fine clastic crystal-clastic ore, with abundant dissemination and layered dissemination of pyrite, was collected from the Kar'ernoe ore district (Fig. 2,3; 66°48'12"N, 66°26'05"E). The wavy-layered texture forms a successive alternation of tuffs and tuffites. The tuffaceous layers are grouped into gradation series with a gradual decrease in the dimension of the pyroclastic material up the section. The ore mineral is mainly distributed in the form of scattered small cubic sections (0.005×0.005 mm) and their intergrowths; larger crystals (up to 0.4×0.4 mm) are less common. Pyrite forms lenticular segregations, reaching a size of 0.04×0.4 mm, and clusters of 0.12×0.2 mm. Veinlets of quartz-carbonate (up to 1.8 mm) and carbonate compositions (up to 0.08 mm) cut the rocks.

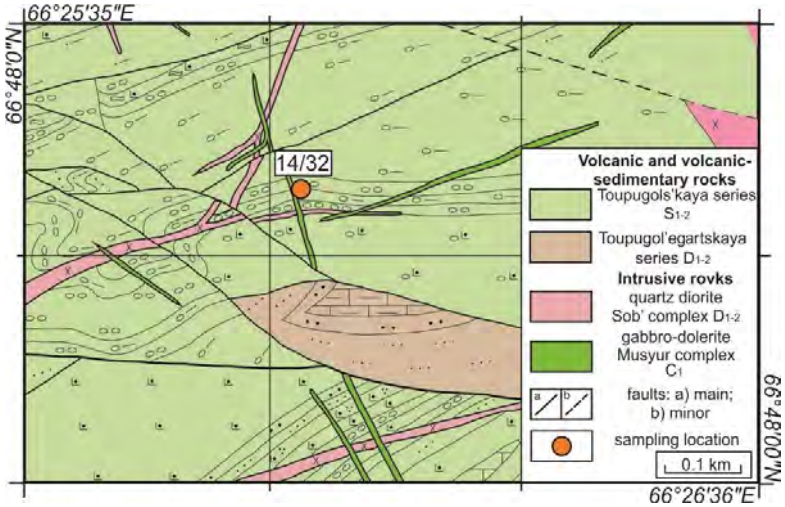

Figure 2. Geological scheme of the Kar'ernoe ore occurrence and sampling location, using data of Pryamonosov (2004).

3 Methodology

Pyrite grains were isolated from the rock sample 14/32 (Fig.2) by the separation in heavy liquids technique at the IGEM RAS (Moscow). Individual grains with sizes > 200 μm without visible inclusions (stereo microscope with an × 5 magnification) were selected for U-Th/He dating and electron microscopy study. Microanalyses of pyrite was done from the polished sections using a Hitachi S-3400N scanning electron microscope equipped with an AzTec Energy 350 X-ray spectral analysis detector at the Geomodel Resource Center of St. Petersburg State University (St. Petersburg).

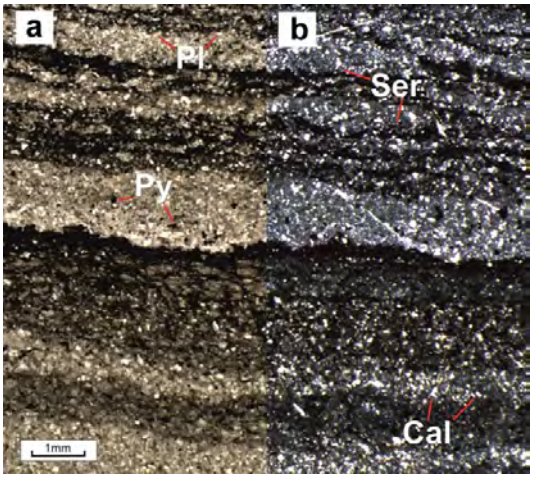

Figure. 3. Petrographic features of tuffites of the Kar'ernoe ore occurrence in thin section of sample 14/32: a) under plane polarized light; b) under crossed nicol. Cal-calcite; Pl-plagioclase; Py-pyrite; Ser-sericite.

3.1 Helium measurements

For each measurement 4–5 pyrite grains were combined in a joint sample with mass of 1.5–2.5 mg and placed in a quartz ampoule. Prior the He measurement the ampoule was sealed under forevacuum conditions (10^{-3} Torr). The gas content of radiogenic He was measured on a highly sensitive mass spectrometer MSU-G-01-M at the IPPG RAS (St. Petersburg) following the procedure described in Yakubovich et al., 2021.

3.2 Uranium and Th measurements

Mass fractions of U and Th were obtained by the isotopic dilution method. Degassed quartz ampoule was spiked with ^{230}Th-^{235}U tracer and dissolved in a mixture of acids (aqua regia (0.4 ml), HF conc (0.5 ml) and $HClO_4$ (0.05 ml)) in closed teflon vials at a temperature of 180°C within 24 hours. The $^{235}U/^{238}U$ and $^{230}Th/^{232}Th$ isotopic ratios were measured using the ELEMENT XR ICP MS at the GEOKHI RAS (Moscow). The accuracy of the analytical procedure was monitored by the parallel measurements of the Durango apatite, which is an international U-Th/He standard. Empty quartz ampoules were used in order to determine the He, U and Th blank of the measurements.

3.3 U-Th/He age calculation

U-Th/He ages were calculated using the IsoplotR software (Vermeesch 2018). Given the relatively large size of the analyzed grains alpha-recoil corrections were not applied.

4. Results

4.1 Electron microscopy

Pyrite grains from the sample 14/32 has a zonal distribution of arsenic impurities, which can reach mass fraction of up to 3 wt. % (Fig. 5). Most common mineral inclusion are galena and chalcopyrite. Less often pyrrhotite, sphalerite, and arsenopyrite were observed. Among U- and Th- bearing phases small (less than 10 μm) precipitates of titanite, rutile, rarely apatite, were established.

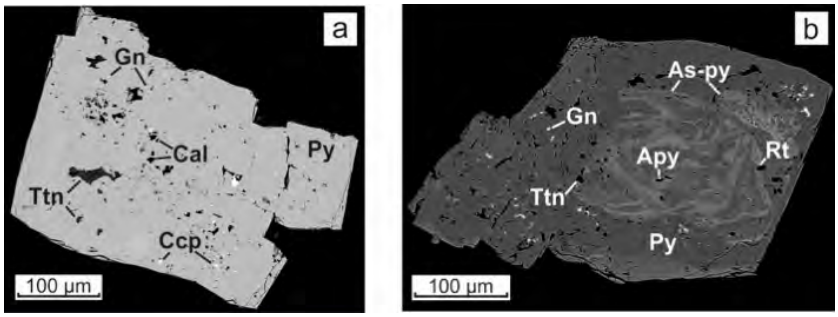

Figure 5. BSE images of pyrite from the Kar'ernoe ore occurrence: a) mineral inclusions in a pyrite crystal; b) zonal distribution of arsenic in pyrite. Apy – arsenopyrite; As-Py – arsenic pyrite; Cal – calcite; Ccp – chalcopyrite; Gn – galena; Py – pyrite; Rt – rutile; Ttn – titanite.

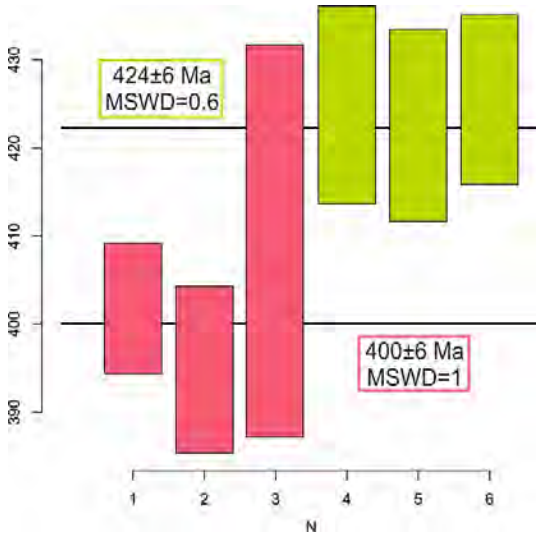

Figure 6. Weighted mean plot for pyrite from the Kar'ernoe ore occurrence, constructed in the IsoplotR software ver 5.2.

4.2 Dating results

In total six subsamples of pyrite from the sample 14/32 were dated. The He concentration is in a range of 9.40–3.27 10^{-8} cm^3/g, which is significantly higher than the concentration of trapped He (Yakubovich et al. 2019). The U mass fraction varies from 0.54 to 1.68 μg/g (Th/U ratio = 0.45-0.48). Four pyrite subsamples have shown age values that overlap within 95% level of confidence (Fig. 6) with weighted mean age of 424±6 Ma (2σ). Three subsamples overlap within 95% level of confidence and have weighted mean age of 400±6 Ma (2σ).

5. Discussion

The U-Th/He age of pyrite from the volcanogenic rocks of the Kar'ernoe ore occurrence, calculated for six subsamples, corresponds to the Late Silurian. U-Th/He ages show relatively large dispersion which might reflect several mineralization events. The age of 424±6 Ma (2σ) is coeval with the sedimentation age of the Toupugolskaya formation which is established as late wenlock – ludlow (biostratigraphy; Zyleva et al. 2014). Younger age of

400±6 Ma (2σ) might reflect pyrite formation/recrystallization due to the emplacement of plagiogranites of the late phase of the Sob complex (403±4 Ma; zircon U-Pb; Sobolev et al. 2018). Rocks of the Sob complex are developed within first tens of meters from the sampling location (Fig. 2). The interpretation of data is complicated by the fact that several grains were used to determine the age of subsample. The clusterisation of the U-Th/He ages requires us to propose higher U content in the one of the generations which allows to hide U-Th/He signal of the another one. Additional measurements of the single grains of pyrite are required in order to confirm that suggestion.

U-Th/He age of the pyrite from the Kar'ernoe ore occurrence (400–424 Ma) is remarkable older than U-Th/He age of pyrite from the Novogodnee Monto deposit (382±8 Ma; Yakubovich et al., 2021). Thus, despite its belonging to the the Novogodnensky ore field, Kar'ernoe ore occurrence represents initial stages of sulfide mineralization within the Toupugol-Khanmeishor gold ore region.

6. Conclusion

U-Th/He dating results of six subsamples of pyrite from the Kar'ernoe ore occurrence (400–424 Ma) indicates mineralization were formed at the initial stages of ore formation in the Toupugol-Khanmeishor ore cluster.

Funding

This research was supported by the RSF (project 22-77-10088).

References

Baranov, E.N. and Vertepov, G.I. (1966) Concentration of Uranium in Sulphides as an Indicator of Possible Uranium Deposit; At. Energy, v. 20, p. 170–171.

Farley, K.A. (2002) (U-Th)/He Dating: Techniques, Calibrations and Applications. Rev. Mineral. Geochem, v. 47, p. 819–843.

Farley, K.A. (2018) Helium diffusion parameters of hematite from a single-diffusion-domain crystal; Geochimica at Cosmochimica Acta, v. 231, p. 117–129.

Flowers, R.M.; Zeitler, P.K.; Danišík, M.; Reiners, P.W.; Gautheron, C.; Ketcham, R.A.; Metcalf J.R.; Stockli D.F.; Enkelmann E.; Brown R.W. (2022) (U-Th)/He Chronology: Part 1. Data, Uncertainty, and Reporting; GSA Bulletin, p. 1–33.

Volchkov, A.; Girfanov, M.; Kryazhev, S.; Andreev, A.; Cheremsin, A.; Mansurov, R. (2008) The Position of Gold Mineralization of the Toupugol-Khanmeyshor Ore Area in Ore-Containing Complexes, Their Mineral and Geochemical Characteristics and Comparison with the Reference Objects of the Novogodnee-Monto Mineralized Area; unpublished report, Moscow, Russia.

Zyleva L.I., Konovalov, A.L, Kazak, A.P., et al. (2014) Gosudarstvennaya geologicheskaya karta Rossiiskoi Federatsii. Masshtab 1:1000000 (3-e pokol.). Ser. Zap.-Sibirskaya. List Q-42, Salekhard; Ob. Zap. (State Geologica Map of the Russian Federation on a Scale 1 : 1000000 (3rd Generation). West Siberian Series. Sheet Q-42, Salekhard, Explanatory Note), SPb.: Kart. fabr. VSEGEI.

Melekestseva, I.Y.; Tret'yakov, G.A.; Nimis, P. et al. (2014) Barite-rich massive sulfides from the Semenov-1 hydrothermal field (Mid-Atlantic Ridge, 13°30.87′ N): evidence for phase separation and magmatic input; Marine Geology, v. 349, p. 37–54.

Shukolyukov, Y.A.; Yakubovich, O.V.; Mochalov, A.G.; Kotov, A.B.; Sal'nikova, E.B.; Yakovleva, S.Z.; Korneev, S.I.; Gorokhovskii, B.M. (2012) New Geochronometer for the Direct Isotopic Dating of Native Platinum Minerals (^{190}Pt-^{4}He Method); Petrology, v. 20, p. 491–505.

Sobolev, I.D.; Soboleva, A.A.; Udoratina, O.V.; Kaneva T.A.; Kulikova K.V.; Vikentiev I.V.; Khubanov V.B.; Buyantuev M.D.; Hourigan J.K. (2017) First Results of U-Pb (LA-ICP-MS) Dating of Detrital Zircons from Paleozoic Island Arc Clastic Rocks of Polar Urals; Bull. Moscow Soc. Nat. Geol. Ser., v. 92, p. 3–26.

Sobolev, I.D.; Vikentyev, I.V.; Soboleva, A.; Travin, A.V. (2018) Results of U/Pb SIMS Dating of Zircons and 39Ar/40Ar Age of Plagioclase from Rocks of the Sob Complex (Petropavlovsk Gold Deposit, Polar Urals); in Proc. Conf. Methods and Geological Results of Studying Isotopic Geochronometric Systems of Minerals and Rocks, IGEM RAS: Moscow, Russia, p. 398–401.

Yakubovich, O.V., Vikentyev, I.V., Bryanskiy, N.V., Zarubina, O.V., Gorokhovskii, B.M. (2019) Dating pyrite by radiogenic helium: new approach to determine the age of hydrothermal processes; Life with Ore Deposits on Earth – 15th SGA Biennial Meeting 2019 Proceedings, Glasgow, v. 1, p. 194–197.

Yakubovich, O.V.; Vikentyev, I.V.; Zarubina, O.V.; Bryanskiy, N.V.; Gorokhovskii, B.M. (2019) U–Th–He Dating of Pyrite from the Uzelga Copper-Zinc Massive Sulfide Deposit (South Urals, Russia): First Application of a New Geochronometer; Dokl. Earth Sci, v. 485, p. 368–371.

Yakubovich, O.; Podolskaya, M.; Vikentyev, I.; Fokina, E.; Kotov, A. (2020) U-Th-He Geochronology of Pyrite from the Uzelga VMS Deposit (South Urals) – New Perspectives for Direct Dating of the Ore-Forming Processes; Minerals, v. 10, 629.

Yakubovich O., Vikentyev I., Ivanova E., Podolskaya M., Sobolev I., Tyukova E., Kotov A. (2021) U-Th-He Geochronology of Pyrite from Alteration of the Au-Fe-Skarn Novogodnee-Monto Deposit (Polar Urals, Russia) — The Next Step in the Development of a New Approach for Direct Dating of Ore-Forming Processes. Geosciences, v. 11, 408.

Yazeva, R.G. and Bochkarev, V.V. (1984) Voikar Volcanoplutonic Belt, Polar Urals; Uralian Sci. Center, USSR Acad. Sci., Sverdlovsk, Ukraine.

Vermeesch P. (2018) Isoplot R: A free and open toolbox for geochronology; Geoscience Frontiers, v. 9 (5), p. 1479–1493.

Vikentyev, I.V.; Mansurov, R.K.; Ivanova, Y.N.; Tyukova, E.E.; Sobolev, I.D.; Abramova, V.D.; Vykhristenko, R.I.; Trofimov, A.P.; Khubanov, V.B.; Groznova, E.O.; et al. (2017) Porphyry-Style Petropavlovskoe Gold Deposit, the Polar Urals: Geological Position, Mineralogy, and Formation Conditions; Geol. Ore Depos, v. 59, p. 482–520.

Hyperspectral mineral mapping on exploration core from the Au-rich from LaRonde Penna VMS deposit, Quebec, Canada in the shortwave infrared

Friederike Körting [1], Julio Hernandez [1], Pesal Koirala [1], Miranda Lehman [2], Thomas Monecke [2], David Lindblom [3], Oskar Jonsson [3], Constantin Hildebrand [1]
[1]Norsk Elektro Optikk AS, Hyspex, www.hyspex.com
[2]Center to Advance the Science of Exploration to Reclamation in Mining, Department of Geology and Geological Engineering, Colorado School of Mines, https://caserm.mines.edu/
[3]Prediktera AB, www.prediktera.com

Abstract. Utilizing HySpex cameras covering the spectral range between 930 and 2500 nm, full core boxes from the LaRonde Penna deposit can be scanned within seconds. Using the newly developed Prediktera's Breeze GEO software, real-time mineral mapping is achieved. This includes an expert-system-based analysis using the publicly available USGS Material Identification and Classification Algorithm for mineral identification, a feature modelling via minimum wavelength mapping , and a comparison-based approach via the spectral angle mapper. Drill cores from the LaRonde Penna deposit are being scanned and interpreted. The deposit is located within the Archean Abitibi greenstone belt of Ontario and Quebec, Canada, which is home to numerous volcanogenic massive sulphide (VMS) deposits. LaRonde Penna contains an endowment of 71 Mt of ore grading on average 3.9 g/t Au and economic grades of Zn, Cu and Pd. Scanning cores hyperspectrally for this well-studied deposit opens up a unique opportunity for research and development. The HySpex system's mineral mapping capabilities are presented in close cooperation with renowned academic and industrial partners through the Center to Advance the Science of Exploration to Reclamation in Mining led by the Colorado School of Mines and Virginia Tech.

1 Introduction

Society's mineral demand is driven by the ongoing green energy transition and is expected to increase substantially in the next decades. This requires the identification of new mineral resources, which typically involves drilling of the subsurface. The amount of drilling performed per project depends on geological characteristics of the deposit under investigation such as the shape and sizes of the mineralized zones and associated alteration halos. Drill core is typically logged visually, which involves documentation of key parameters such as lithology, mineral assemblages, and the location and orientation of structures. The visual logging is often supplemented by sub-sampling for geochemical or mineralogical analysis. Sample analysis is destructive, expensive and time-consuming. Hyperspectral imagery (HSI) offers a fast, replicable, non-destructive method for logging drill core mineralogically(Bedini 2017; Krupnik and Khan 2019; Rajan Girija and Mayappan 2019).

2 The developed hardware and software solution

HSI imagery is used to identify areas of significance and visualize mineral-spectral changes downhole. To the best of our knowledge, all commercial solutions operate as offline, post-acquisition data analysis services using data processing and modelling algorithms customized for a specific exploration site. This limits the usability and access to the data beyond the initial requirements of the end user. An upgrade of the models or reprocessing of the data is often only possible at an additional cost. For research activities, this presents a limit as samples from a variety of sites or different campaigns are often necessary and need to be analysed flexibly. Identifying this need, the hyperspectral hardware developer HySpex and the software provider Prediktera developed a high-resolution, hyperspectral core imager to allow self-determination of data analysis for research projects. The system incorporates Prediktera's Breeze GEO software to offer seamless data acquisition, flexible modelling capabilities, user adjustment and real-time mineral analysis capabilities. The main aim of this development is to make the user fully independent to carry out their own data analysis.

The integrated solution for hyperspectral drill core imaging is being developed in close cooperation with academic and industrial partners through the Center to Advance the Science of Exploration to Reclamation in Mining (CASERM). CASERM is a collaborative research centre for geoscience data use in the mining industry lead by Colorado School of Mines and Virginia Tech. CASERM members actively research approaches to bridge the different scales in geoscientific research and aim to provide tangible research answers for the industry to provide "Mineralogy Across Scales".

As an example of the capabilities of the instrumentation, methods and analysis tools, an exploration drill hole from the LaRonde Penna volcanogenic massive sulphide (VMS) deposit was scanned and analysed. This drill hole displays the important alteration mineral assemblages surrounding the ore zone. LaRonde Penna is the largest gold-rich VMS deposits in the world and is

located within the southern portion of the Archean Abitibi greenstone belt of Ontario and Quebec, Canada.

3 Datasets

Endmember minerals of interest for this deposit were defined by a SEM-based thin section analysis at the Colorado School of Mines via the TESCAN Integrated Mineral Analyzer (TIMA) software. The core contains significant portions of plagioclase, amphibole, andalusite/kyanite, biotite, calcite, chlorite, clinozoisite, epidote, garnet, margarite, muscovite, quartz, staurolite, tourmaline as well as different sulphide mineralss (pyrite, sphalerite and chalcopyrite). Not the entirety of these minerals can be mapped in the SWIR spectral range. Figure 1 shows the plot of the spectrally active minerals for this study, the VNIR-SWIR reference spectra were obtained from the USGS spectral library version 7 (Kokaly et al. 2017).

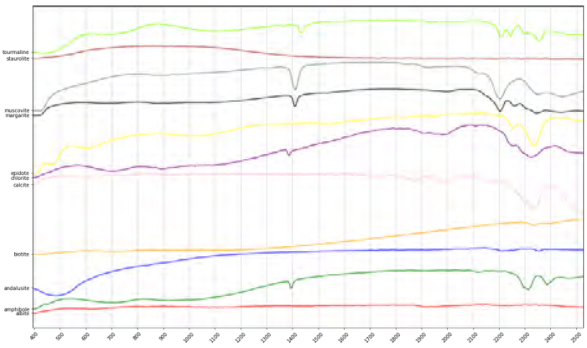

Figure 1. VNIR and SWIR spectra relevant to the LaRonde-Penna deposit from USGS spectral library version 7. X-axis shows the wavelength range from 400 – 2500 nm. The minerals plotted from top to bottom are tourmaline (light green), staurolite (maroon), muscovite (grey), margarite (black), epidote (yellow), chlorite (purple), calcite (pink), biotite (orange), andalusite (blue), amphibole (dark green) and albite (red).

Forty-nine core boxes from the LaRonde Penna deposits were scanned hyperspectrally, using the HySpex SWIR384 camera (specification see table 1) from diamond drill hole 3125-162A at a depth of 1135.6 to 1265.0 meters. Core depth logging was achieved within breeze GEO by manually logging the start and end depth of each box and adjusting the depth for eventual core loss. An example of the false-colour SWIR-RGB of core box #28 is given in Figure 2.

Table 1. HySpex SWIR384 main specifications.

SWIR 384	
Spectral range	930-2500 nm
Spatial pixels	384
Spectral channels	288
Spectral sampling	5.45 nm
FOV	16°
Linear field of view (FOV) for 1 m lens	294 mm
Pixel size on scene across/along	0.77/ 0.77 mm
Bit resolution	16 bit
Noise floor	150 e-
Dynamic range	7500
Peak SNR (at full resolution)	> 1100
Max speed (at full resolution)	400 fps
Camera interface	CameraLink

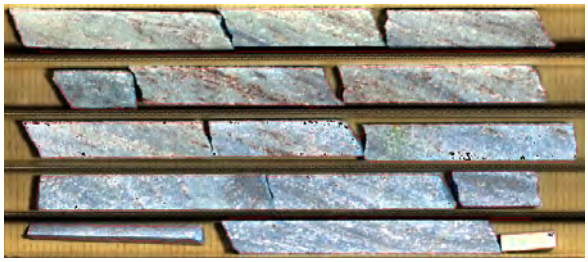

Figure 2. False-colour RGB image of a representative core box (R: 1225 nm, G: 1660 nm, B: 2150 nm).

4 Mineral and spectral anomaly classification in the SWIR

Near-real time classification of the core is achieved using the USGS Material Identification and Classification Algorithm (MICA; Kokaly 2011) and a feature modelling approach referred to as minimum wavelength modelling (MWL; van Ruitenbeek and van der Meer 2014; van der Meer et al. 2018; Hecker et al. 2019).

The prediction of USGS MICA and MWL takes about 6 min in Breeze GEO for the 49 core boxes measured (130 m of core). The SWIR file size for each core box is ~300 MB, with a total file size of ca. 13.5 GB. USGS MICA mapping is carried out via a publicly available MICA Command File (mcf) named “mica_cmds_2micron_usgshyspex_vswir3177_v4a_mtnpass” containing 91 materials described in the expert system. The pixel count is carried out for different, user-defined mapped minerals. MWL was performed between 2100 and 2450 nm. Different mineral feature products are explored that are commonly used and found in commercial HSI analyses tool and a staple for HSI mineral exploration (e.g., white mica chemistry, MgOH, Al/clay, $Fe^{2+}OH$). Simple spectral indices are explored on this dataset as well. The USGS MICA classification is shown in Figure 3.

The MWL modelling of the deepest feature in the chosen wavelength range (2100-2450 nm) highlights spectral changes in the core but is less straightforward to interpret than per-pixel mineral

maps. Figure 4 shows a representative core box in which a change from blue colours (2205 nm) to yellow (2330 nm) to green (2248 nm) occurs from top to bottom.

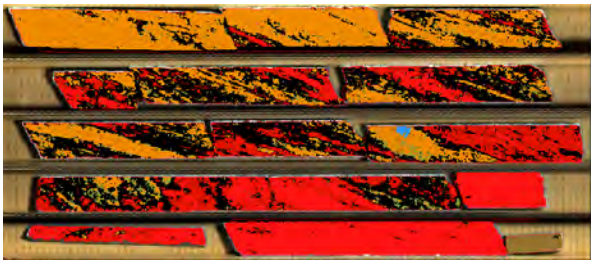

Figure 3. USGS MICA classification of a representative core box. Red colours indicate presence of epidote/chlorite, orange colours indicate presence of white micas. Green colours indicate serpentine mineral mixtures and blue colours indicate kaolinite-clay mixtures.

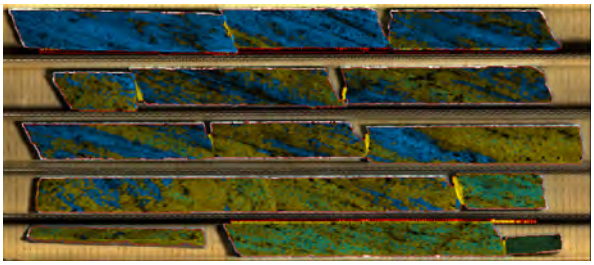

Figure 4. MWL mapping of a representative core box. Colour coding shows the wavelength position of the deepest mapped feature. Blue colours (2205 nm) to yellow (2330 nm) to green (2248 nm) is visible throughout the box indicating a gradual change with depth. Colour brightness indicates the depth of the feature, where brighter colours show deeper features.

5 Results

General trends in the white mica occurrence plot are visible in the USGS MICA analysis. The average white mica pixel counts were plotted for all 49 core boxes in Table 2. This average represents the pixel area classified as white mica in each box rather than the absolute percentages. It highlights the changes in white mica occurrence depth and shows changes that can be investigated further. Main rock-forming minerals cannot be classified (e.g., feldspars and quartz) in the SWIR. Bulk geochemistry or mineralogical analyses of the core via validation measurements have not been available for the example core but XRF-based geochemistry can be imported into breeze GEO to support the HSI-based mineralogy in user-defined segments. Mineral abundance determined in Breeze GEO will be further validated for the LaRonde Penna drill core in cooperation with CASERM.

Table 2. White mica pixel count [%] for a total of 49 core boxes from LaRonde-Penna. The USGS MICA analysis was used.

Box	Depth [m]	USGS all white mica [%]	USGS all white mica
1	1135.6	22.78	
2	1137.8	8.46	
3	1140.4	13.64	
4	1142.9	1.93	
5	1145.2	0.91	
6	1147.5	11.17	
7	1154.3	58.10	
8	1157.3	49.70	
9	1159.4	19.00	
10	1161.8	1.74	
11	1164.5	3.63	
12	1167.1	0.10	
13	1169.5	1.40	
14	1172.0	10.80	
15	1174.4	1.10	
16	1177.1	2.21	
17	1179.5	3.19	
18	1182.2	0.01	
19	1184.4	0.01	
20	1187.8	15.54	
21	1190.8	49.59	
22	1193.8	89.95	
23	1196.4	90.33	
24	1199.2	92.76	
25	1201.8	90.36	
26	1204.2	90.30	
27	1207.6	69.58	
28	1209.5	23.75	
29	1212.0	0.68	
30	1214.6	14.26	
31	1217.0	44.70	
32	1219.7	71.46	
33	1222.5	79.22	
34	1226.0	87.70	
35	1229.1	89.30	
36	1231.9	92.28	
37	1234.6	90.27	
38	1237.0	89.39	
39	1239.8	83.88	
40	1242.3	70.90	
41	1245.0	69.38	
42	1247.8	44.29	
43	1250.6	13.52	
44	1253.2	4.63	
45	1256.0	45.15	
46	1258.7	44.78	
47	1260.7	46.99	
48	1262.6	33.60	
49	1265.0	18.79	

In the USGS MICA analysis, epidote and chlorite are mapped frequently along the core, color-coded as red (Figure 5). The distinct absorption features for these minerals are as follows (the deepest features are marked with an asterisk): Epidote has distinct absorptions at 2255 nm and 2335* nm, chlorite has absorption features around 2245 nm, 2328* nm and 2386 nm. Muscovite exhibits

absorption features around 2205* nm and 2345 nm (Krupnik and Khan 2019).

The plot of chlorite (clinochlore and thuringite) against epidote shows the similarity of both spectra in the SWIR wavelength range (2100 nm and onwards; Figure 5). This complicates a clear distinction between these phases. The classification of chlorite in areas also indicate the potential presence of epidote and vice-versa and the two mineral groups cannot be distinguished well from each other.

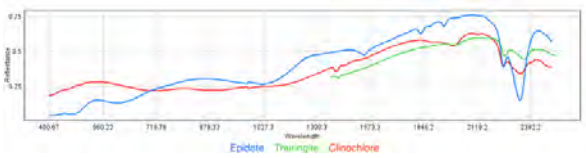

Figure 5. Spectral plot of chlorite vs. epidote. Spectra plotted within Breeze GEO. The color-coding of the spectra is different to the colours used in the USGS MICA classification. Minerals include epidote (blue), thuringite (green) and clinochlore (red).

6 Conclusions

The results presented in this paper show promising advancements in the development of both hardware and software for core scanning that enables the user to take matters into their own hands with minimum time spent on setting up hyperspectral imaging data acquisition and analysis routines. The visualization of the workflow with a plug-and-play approach allows for an automated approach to core segmentation, analysis and adjustments in each. The HySpex laboratory acquisition setup provided sufficiently high turnover rates of 300 meters a day in the controlled environment of the Core Scanning Lab facility at Colorado School of Mines but future hardware developments will focus on a more modular design, wider belt enabling to scan two boxes simultaneously and a wider field of view of the VNIR-SWIR cameras. A casing will protect the cameras from stray light, dust and other influencing factors and allow a more versatile hardware setup adaptable to different types of facilities and environments. The Breeze GEO software allows for a new level of interactivity with the data and enables a user-led setup of workflows including standard and expert-based classification routines. Near-real-time correction and classification and the possibility of adjustment of workflows following on-site interpretation of the data enable the user to adjust data analysis and interpretation based on new information from research.

Acknowledgements

This study was achieved in close collaboration with the Center to Advance the Science of Exploration to Reclamation in Mining, which is an industry-university collaborative research centre between Colorado School of Mines and Virginia Tech under NSF award numbers 1822108 and 1822146. Drill core from the LaRonde Penna deposit was made available by Agnico Eagle. We thank Patrick Mercier-Langevin from the Geological Survey of Canada for in-depth discussions on the geology of the LaRonde Penna deposit and the implications of this study. Raymond Kokaly and Todd Hoefen from the USGS as well as Katharina Pfaff from Colorado School of Mines are acknowledged for providing insights into hyperspectral data interpretation. The USGS PRISM MICA algorithms were implemented into Breeze GEO. This would not have been possible without obtaining the code and detailed documentation.

References

Bedini E (2017) The use of hyperspectral remote sensing for mineral exploration: A review, JHRS 7:189–211

Hecker C, van Ruitenbeek FJA, van der Werff HMA, Bakker WH, Hewson RD, van der Meer FD., (2019) Spectral absorption feature analysis for finding ore: A Tutorial on using the method in geological remote sensing, IEEE Geosci Remote Sens Mag 7:51–71

Kokaly R F (2011), PRISM: Processing Routines in IDL for Spectroscopic Measurements (Installation Manual and User's Guide, Version 1.0)

Kokaly RF, Clark RN, Swayze GA, Livo KE, Hoefen TM, Pearson NC., Wise RA, Benzel WM, Lowers HA, Driscoll RL, Klein AJ (2017) USGS Spectral Library Version 7"

Krupnik, D, and Khan, S, (2019) Close-range, ground-based hyperspectral imaging for mining applications at various scales: Review and case studies. Earth Science Review 198: 102952

Rajan Girija R, Mayappan S (2019) Mapping of mineral resources and lithological units: a review of remote sensing techniques. Int J Image Data Fusion **10:**79–106

Van der Meer F, Kopačková V, Koucká L, van der Werff HMA, van Ruitenbeek FJA, Bakker WH (2018) Wavelength feature mapping as a proxy to mineral chemistry for investigating geologic systems: An example from the Rodalquilar epithermal system. Int J Appl Earth Obs Geoinf 64:237–248

van Ruitenbeek FJA, Bakker WH, van der Werff HMA, Zegers TE, Oosthoek JHP, Omer ZA, Marsh SH, van der Meer FD (2014) Mapping the wavelength position of deepest absorption features to explore mineral diversity in hyperspectral images. Planet Space Sci 101**:**108–117

Characterisation of apatite-bearing magnetite ore in drillcores using µ-XRF

Carolina Månbro[1], Joanna Kolodziejczyk[2], Patrick Krolop[2], Eva Öberg[2], Mehdi Parian[1],
[1]Mineral and Metallurgical Engineering, Luleå University of Technology, Luleå, Sweden
[2]Process and Product Development, LKAB, Malmberget and Kiruna, Sweden

Abstract. The convention of using bulk chemical assays by XRF in determination of the grade of a deposit provides a somewhat erratic result since the element/s of interest often occur in more than just the target mineral/s. By analysing the chemical composition of individual mineral crystals in exploration drillcores a clearer picture of the deposit can be attained since it visualizes the distribution of elements in minerals. Furthermore, by investigating individual minerals the possibility of finding additional mineral/s of interest increases and the extraction process can be adapted to process all minerals of interest to get the best possible recovery.

1 Introduction

Northern Sweden is the type locality for iron oxide-apatite (IOA) deposits, commonly referred to as "Kiruna type" based on the special character of the ores (Geijer 1931, Martinsson et al. 2016).

To date, the apatite from these ores have been regarded waste since the demand for apatite/ phosphor has been too low for an economically viable extraction. However, the increased demand for mineral fertilisers in combination with the low cadmium content of the apatite in Swedish IOA (Håkansson et al. 2023) have caused extraction of phosphor from apatite to be more eligible. Furthermore, the apatite in Swedish iron oxide deposits hosts rare earth elements (REE) classified as critical raw materials (CRM) needed for the green transition (Blengini et al. 2020). Thus, apatite concentrate from Swedish iron oxide deposits can offer an intra-European production of materials that are now mainly imported from outside of the EU, making the supply chain less vulnerable to global events and politics.

Analysing samples using traditional X-ray fluorescence (XRF) for chemical assays is a good method if a bulk composition is sought. However, the recent decades have seen a rapid development of laboratory scale micro-X-ray fluorescence (µ-XRF). Thus, analyses that were previously only possible in synchrotron facilities are now possible to perform in benchtop µ-XRF instruments, making the technology more accessible (Flude et al. 2017). Elemental and mineralogical analysis by µ-XRF is a more detailed analytical method compared to XRF and provides spatial distribution of elements in the sample. The elemental information can further be converted to mineral maps using an automated mineralogy software. Also, the µ-XRF is capable of analysing powders as well as surface of whole rock samples, and so, these analyses can be performed in a non-destructive manner. Consequently, a modern µ-XRF can combine detailed analyses with good accessibility thus establishing an alternative workflow capable of reporting chemical assays as well as element – mineral affiliation/s and textural information.

Another feature in the µ-XRF is the large range of resolution in which the analyses can be performed. On the larger scale, resolutions on 100's of µm can be used, whereas on a smaller scale a resolution down to 10 µm is possible. Thus, in opting for a coarser resolution the analytical time can be very quick (minutes for dm-scale samples), whereas a fine resolution analysis is as time consuming as a scanning electron microscopy (SEM)-based analysis.

2 Methods

Drill core fragments representing various mineral associations from IOA occurrences in Northern Sweden were examined. The drillcores were cut and one half powdered for XRF analysis at LKAB chemical laboratory Malmberget. The remaining powdered samples and the other half of the drill-cores were sent to Luleå University of Technology (LTU) for further analyses.

The drillcore samples were analysed by a Bruker M4 Tornado µ-XRF instrument under medium vacuum (2 mbar), using a Rh-tube, 50 kV voltage, and 600 µA current. Samples with Fe content of 30 % or more were analysed at 300 µA current to avoid flooding the detectors. Analytical time per pixel was 10 ms, and the size of the area scanned 160x30 mm. Three different resolutions were applied, 500 µm, 200 µm, and 50 µm, in order to evaluate the impact of resolution on precision.

The powdered samples were ground to <10 µm using an X-ray diffraction (XRD) McCrone mill and fitted in Ø 26 mm XRD sample holders. These samples were analysed in the µ-XRF following the same procedure as for the drillcores but with an analysed area of 16x10 mm. The powdered samples were additionally analysed using a Malvern Panalytical Empyrean for X-ray diffraction analysis.

The data collected from the µ-XRF scans were analysed in both the M4 software for elemental distribution and association, and in Bruker's advanced mineral analysis and characterisation software (AMICS) for mineralogy, mineral distribution, and mineral association. Quantitative XRD analyses (Rietveld refinement) were

performed in the HighScore Plus software using the PDF-4 mineral database.

3 Results

The data collected from µ-XRF analysis of drillcores, and powdered samples were used for comparison with the results from XRF chemical assays. The µ-XRF drillcore analyses were also used to generate elemental maps and to produce mineral maps in AMICS.

3.1 Chemical composition

Data from the XRF chemical assays were compared to powder and drillcore samples analysed in µ-XRF.

Comparing the results from the chemical assays by XRF to that of the µ-XRF scanned powdered samples shows a good correlation with high R^2-values (Figure 1).

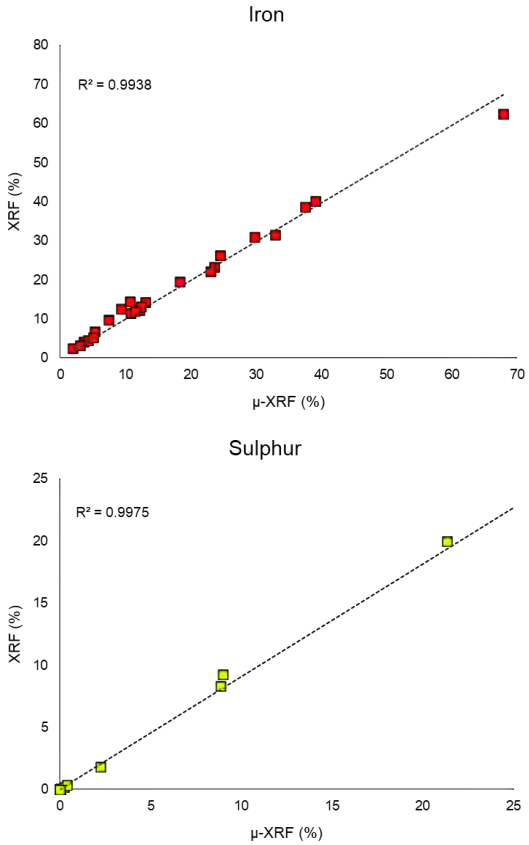

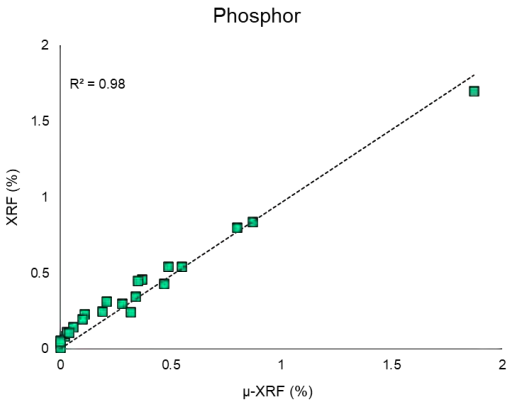

Figure 1. Comparison of XRF assays and µ-XRF data for Fe, S, and P in powdered samples.

However, when the assays are plotted against the results from drillcore analysis a correlation is still present, although it is lower than for the powdered samples based on sample inhomogeneity across different scales (Figure 2). The correlation between the beforementioned was not resolution dependent and chemical variation in the results from the three different resolutions used was negligible.

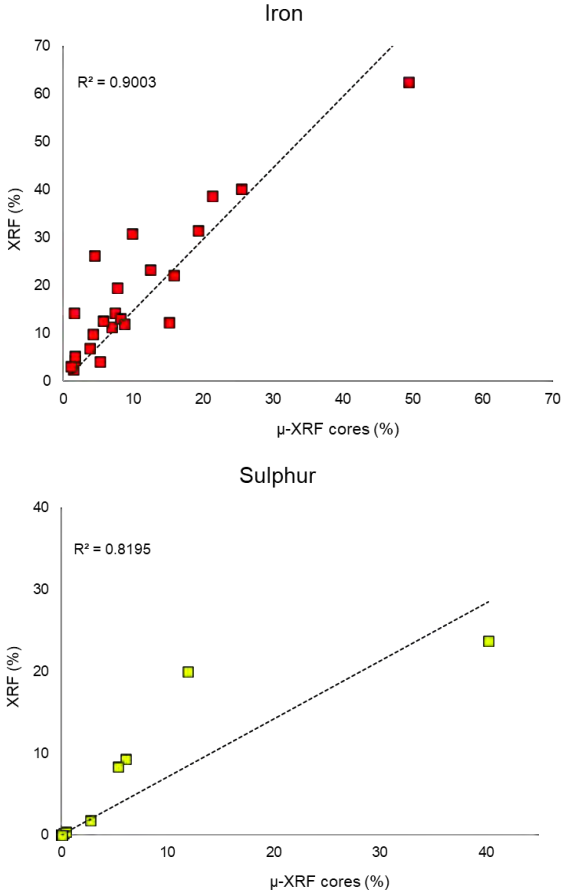

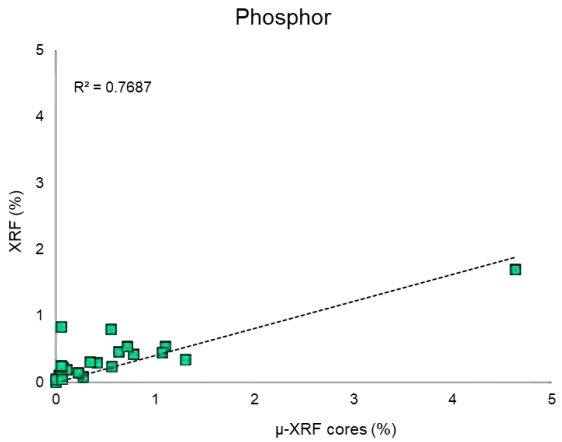

Figure 2. Comparison of XRF assays and µ-XRF data for Fe, S, and P in drillcore samples.

3.2 Elemental distribution

Elemental maps were produced for all drillcores. From these, two representable samples were selected for this work.

Figures 3 and 4 show the element distribution of Fe, P, and S in sample M19 and M09, respectively. From these it is clear that both samples contain minerals with a high Fe-content, mainly Fe-oxide/s, and that P occurs in discrete crystals. Sulphur, however, shows different distribution patterns in the two samples with S in sample M19 mainly occurring in discrete areas, e.g., the cross-cutting vein, whereas S in sample M09 is disseminated throughout the sample but also show a higher concentration in association with P. Thus, the S-bearing minerals differ between areas within the same deposit.

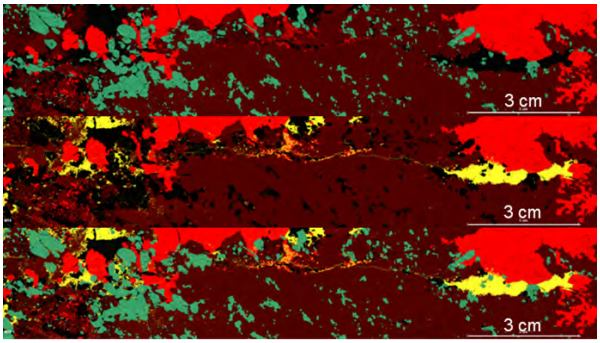

Figure 3. Elemental maps from drillcore sample M19 with Fe in red, P in green, and S in yellow. Top show Fe and P, middle Fe and S, and bottom Fe, P, and S.

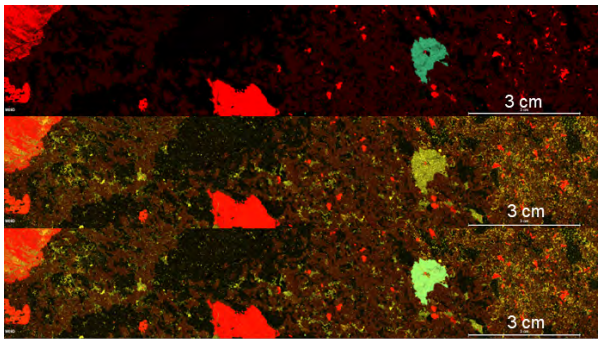

Figure 4. Elemental maps from drillcore sample M09 with Fe in red, P in green, and S in yellow. Top show Fe and P, middle Fe and S, and bottom Fe, P, and S.

3.3 Modal mineralogy

Mineral maps and modal abundance were acquired using AMICS. This is a Bruker specific software with a built-in mineralogical database.

X-ray images and mineral maps from AMICS as well as mosaic images acquired from the M4 software are shown in Figure 5 and 6. The minerals in the false colour mineral maps have been grouped to yield a more distinct transition between minerals and to enhance visibility of the modal distribution.

4 Discussion

Recent work has demonstrated the application of µ-XRF analysis on geological samples to be an efficient approach (e.g., Flude et al., 2017; Menzies et al., 2022; Parian et al. 2022; Månbro and Parian 2023).

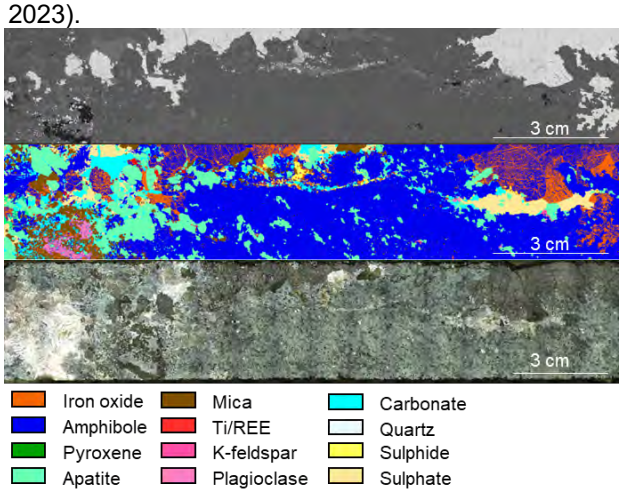

Figure 5. X-ray intensity image (top), mineral map (middle), and mosaic scan from µ-XRF (bottom) of sample M19.

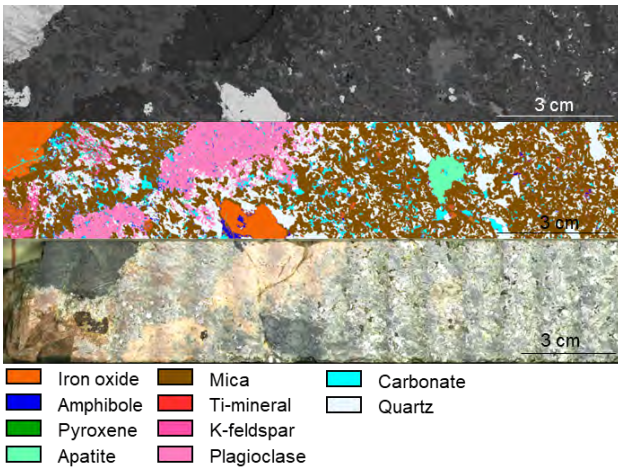

Figure 6. X-ray intensity image (top), mineral map (middle), and mosaic scan from µ-XRF (bottom) of sample M09.

Chemical assays normally require samples to be ground to a fine fraction on which XRF is performed. This approach gives a bulk rock composition and is destructive by nature. Chemical assay acquired by µ-XRF is here shown to perform as well on powdered samples as traditional XRF. The chemical information from scanning of the rock surface is dependent on a few additional parameters, e.g., texture and mineral distribution in the sample. However, the results from drillcore scanning show that even highly variable, textured samples like the ones used in this work provide good correlation with the XRF data, and therefore a representative chemical composition of the bulk rock composition.

Mineral identification and quantification are typically done on epoxy samples with fractions < 1 mm using SEM and an automated mineralogy software, e.g., QEMSCAN, although mineral identification by SEM is also possible on cm-scale, non-powdered samples. From the powdered sample analysis, liberation can also be determined.

When utilising a µ-XRF characterisation software like AMICS, dm-scale, whole rock samples can be analysed, and crushing is not needed. However, it is also possible to analyse the mineralogy of coarse powders. Thus, µ-XRF analyses can be performed in a non-destructive way. Since the sample size that can be analysed in the µ-XRF is larger than for the SEM, it could potentially provide more representative data, i.e., the µ-XRF can produce high quality data from larger, whole rock samples. Quantification of the mineralogy in a sample can also be extracted from the AMICS software, as can the degree of liberation.

However, the X-ray beam in the µ-XRF is of higher intensity than an electron beam in a SEM. This means that beam penetration in a sample is deeper in µ-XRF compared to SEM analyses. This penetration depth leads to signals from below the surface of the sample to be detected and might therefore cause a contamination of the signal from the underlying minerals. This impedes converting elemental spectra to mineralogy since the generated spectra may not match or mismatch existing known mineral standard spectra. This is especially common in samples where the ore includes elements with high atomic numbers, e.g., iron oxides, and the gangue mineralogy is lighter, e.g., feldspars. Furthermore, distinguishing iron oxide minerals, e.g., magnetite and hematite are not tangible by µ-XRF but has also been shown difficult with SEM-based software (Krolop et al. 2019).

One way to work around this is to cross-reference Fe oxides and the gangue mineralogy with an additional mineralogical analytical method, e.g., XRD, optical microscopy, or core logging, from which the parameters in AMICS can be changed to better suit the individual sample or deposit.

However, in some circumstances the beam penetration has proven beneficial when analysing for bulk chemistry since the area scan obtains a slight depth (Månbro and Parian 2023). The identification of heavy elements at depth in the sample can be valuable in REE and precious/heavy metal exploration. These elements are often present at low values in the rock (ppm to ppb), and therefore detection of signals from below the sample surface can provide information that otherwise could have been overlooked.

5 Conclusions

Characterisation of geological samples is an important part of several disciplines, but perhaps most so for the mining industry. At present, the typical workflow in analysing samples includes routine chemical analysis of exploration and mining drillcores, core logging, and selected XRD and SEM analyses as well additional optical microscopy. In processing plant, complementary information about mineral liberation after the comminution and separation stages are collected.

The work presented here shows that utilising the µ-XRF for characterisation of samples ranging from whole rock to fine powders is comparable to traditional methods that typically uses smaller sample sizes, are more time consuming, and that are destructive. When analysing high-grade samples however, some challenges are presented in correctly classifying the minerals at the sample surface due to the beam penetration. This however can be averted if the characterisation workflow includes an additional mineral identification method, e.g., XRD or core logging, from which a baseline mineralogy can be determined and the identification in the characterisation software improved to get a better fit data set.

An important factor in achieving a good recovery is to know which minerals are carrying the element/s of interest. In this aspect the µ-XRF analysis has some advantages compared to the traditional methods e.g., being able to analyse larger sample sizes compared to SEM analysis. Therefore, a workflow including µ-XRF analysis already in the

exploration stage could increase the sample throughput, provide a more holistic view of the deposit and consequently more correct predictions of processing quality and performance since identification of the minerals carrying the element/s of interest can be determined and these therefore possibly targeted more efficiently.

Acknowledgements

The authors would like to thank Dr. Andrew Menzies for his support during analytical work.

References

Blengini G A, Latunussa C EL, Eynard U, Matos CT de, Wittmer D, Georgitzikis K, Pavel C, Carrara S, Mancini L, Unguru M, Blagoeva D, Mathieux F, Pennington D (2020). European Commission, Study on the review of the list of Critical Raw Materials - Final Report, Critical Raw Materials Factsheets. https://doi.org/10.2873/11619

Geijer (1931) The iron ores of the Kiruna type. Sverige Geologiska Undersökning, C624, pp. 1-32

Flude S, Haschke M, Storey M (2017). Application of benchtop micro-XRF to geological materials. Mineral. Mag. 81, 923–948. https://doi.org/10.1180/minmag.2016.080.150

Håkansson U, Jonsén P, Jonsén R, Holmström Å, Larsson K, Jolsterå R, Vikström L (2023) Circular Production of Phosphorous and Rare Earth Elements. Conference in Minerals Engineering, Luleå, Sweden 7-8 Feb 2023, 111-116.

Krolop P, Jantschke A, Gilbricht S, Niiranen K, Seifert T (2019) Mineralogical imaging for characterization of the Per Geijer Apatite iron ores in the Kiruna District, Northern Sweden: A comparative study of mineral liberation analysis and raman imaging. Minerals, 9(9), 544.

Menzies A H, Tagle R, Reinhardt F, Hirschle C, Schellkopf L J, Kelly N, (2022). High-speed Micro-XRF Analysis of Rock Samples and Drill Cores. Microsc. Microanal. 28, 650–651. https://doi.org/10.1017/s1431927622003117

Martinsson O, Billström K, Broman C, Weihed P and Wanhainen C (2016) Metallogeny of the northern Norrbotten ore province, northern Fennoscandian Shield with emphasis on IOCG and apatite-iron ore deposits. Ore Geology Reviews, 78, 447-492.

Månbro C, Parian M (2023) Chemical and Mineralogical Characterisation of Iron Ore Drillcore Using µ-XRF. Conference in Minerals Engineering, Luleå, Sweden 7-8 Feb 2023, 157-171.

Continuous X-Ray Fluorescence Core Scanning: Application Examples and Methodology Developments

Miranda Lehman [1], Thomas Monecke [1], Erik Tharalson [1], Angus Tod [2], Annelie Lundström [3], Alexander Seyfarth [4], Susann Stolze [1], Katharina Pfaff [1]
[1]*Department of Geology and Geological Engineering, Colorado School of Mines, 1516 Illinois St. Golden, Colorado, USA*
[2]*Minalyze Australia, U6 175 Campbell Street, 9104 Belmont, Western Australia*
[3]*Minalyze Sweden, Industrivägen 4, 433 61 Sävedalen, Sweden*
[4]*SGS North America, 5576 West River Oaks Rd Janesville, Wisconsin, USA*

Abstract. Exploration drilling forms an integral part of mineral exploration programs. A great deal of time and money is spent on the logging of the drill core, the collection of data, and the preparation of samples for laboratory-based analysis. Workflows generally involve a high amount of human intervention. The Minalyzer continuous X-ray fluorescence core scanner can produce high-resolution photographs, 3D LiDAR point clouds, and depth associated major and minor element geochemical results of drill core in a non-destructive, timely manner. In addition to geochemical results, these outputs are used to accurately depth register drill core, perform RQD analysis, and calculate bulk densities. By implementing the core scanner into mineral exploration workflows, the processing and understanding of drill core can be sped up, and performed in a non-destructive manner with high accuracy and precision.

1 Introduction

The criticality of mineral and material resources is one of the greatest challenges for modern society and a major bottleneck as the world works toward the green energy transition. Ambitious net-zero carbon emission targets can only be achieved through a substantial increase in mineral resource discovery, development, and production. These factors will result in increased exploration drilling as drill core represents the only direct source of information constraining the subsurface geology.

Large exploration programs commonly face a range of workflow issues when working with drill core. This includes problems arising from the fact that core logging is subjective and inconsistencies between different core logging geologists complicate 3D modelling of the subsurface. In addition, laboratory-based geochemical analyses of core samples are slow and assay data are often obtained weeks to months following sample submission, preventing their use in decision making during ongoing drilling campaigns.

Many current workflow challenges can be overcome using modern core scanning technology such as the Minalyzer continuous X-ray fluorescence (XRF) core scanner (Fig. 1). This instrument, described in detail by Sjöqvist et al. (2015), is a patented, non-destructive analytical tool that offers a unique reorganization of drilling and logging program workflow. The continuous XRF core scanner is equipped with a high-resolution line scan camera for RGB photography, a 3D LiDAR scanner to create 3D point clouds, and a silicon drift detector (SDD) to produce quality geochemical results within an elemental range of Na to U. Analytical turn-around times are short when post-processing strategies are optimized.

The images, point clouds, and geochemical data that the Minalyzer continuous XRF core scanner produces can be used for a variety of calculations within the proprietary Minalogger software (ML2). These include rock quality designation (RQD) analysis, X-ray specific gravity, volume bulk density calculations, and down hole geochemical trends. All of these are accurately depth registered and calculated at a user defined interval (10 cm, 1 m, etc.). Scanning drill core using this instrument as the first step of a core logging workflow has the potential to replace the need for the initial time-consuming steps such as photography and RQD analysis. Continuous downhole geochemical results can be used to guide ongoing drilling programs and to create strategic assay sampling methods that cut down the number of samples that need to be sent out for laboratory-based analysis reducing cost.

The Minalyzer continuous XRF core scanner is currently being used in a variety of industrial settings as a reliable exploration tool and in academic settings, such as Colorado School of Mines to conduct research on drill core. Core scan data are uploaded to a cloud-based viewing and interpretation platform, minalogger.com, that allows permanent archiving and can be used to export data into industry-standard software packages such as Leapfrog Geo or ioGAS™.

2 Methodology

2.1 Sample preparation and core scanning

Preparing core to be scanned in the Minalyzer continuous XRF core scanner requires minimal effort. Full, uncut core is ideal for scanning with this instrument, but cut core can also be easily scanned. Core pieces should be arranged to be as level and flat as possible. Core must be cleaned if visually dirty. Each core box is loaded and placed into the same position on the instrument stage. Once a core box is loaded and correctly positioned, the instrument begins its pre-scan phase during which photographs, and a LiDAR scan are taken. The instrument uses the 3D point cloud to create the

scan path the X-ray detector can take along the core while also maintaining a

Figure 1. The Minalyzer continuous X-ray fluorescence (XRF) core scanner at Colorado School of Mines.

consistent distance from the core surface. The user has the ability to edit the scan paths if needed.

At the beginning and end of each day OREAS Certified Reference Materials (CRM) are scanned using the same scan settings used for the project. These CRMs are used day to day to check for detector drift and play an important role in post-processing as described below.

2.2 Scan settings

The Minalyzer continuous XRF core scanner can capture an elemental range of Na to U depending on the scanning settings (voltage, current, and scanning speed), the environment, and the X-ray tube anode. Typically, to capture all light and heavy elements of interest, two scans are performed on each core box. This includes one run at settings optimized for heavy elements and a second scan setting with a He purge optimal to capture light elements. If two or more scan settings are desired, the Minalyzer CS will conduct these scans using the same scan path created during the pre-scan phase.

The user also defines the scanning speed at which the detector nominally moves along the surface of the core. This speed ranges between 0.1 mm/sec up to 40 mm/sec, with 10 mm/sec offering the best trade off of detection limits and speed. During scanning, the detector maintains a consistent distance from the surface of the core, which is based on the 3D model. The collected X-ray spectra are binned and saved every 10 mm into a single multi-multi channel analyser (MMCA) file for each core box at each scan setting.

2.3 Depth registration

After scanning, the core must be depth registered in the Minalogger software (ML2). This is an important step of the post-processing routine that must be executed with consistency and accuracy. ML2 uses the 3D point cloud to display an image and height map for each core box while it is being depth registered. Depth logging can be done in feet or meters and the material in each box can be logged as competent core, weathered core, or rubble. When depth registering using the “core” function it is important to mark all the fractures along the core for later RQD calculations. A core loss function can be used to define areas of missing core. Depth blocks or true depth markers can also be added to mark the locations and corresponding depths of known depth measurements down hole. These functions all have an accuracy of several millimetres. Depth registration creates an accurate depth log outlining material type, fracture locations, and core recovery.

2.4 Rock quality designation

After the core is logged, the RQD function in Minalogger.com allows the user to define each fracture logged in the core during depth registration as a true break or a manmade break. Any core logged as rubble receives a 0% designation. These designations can be analysed at any interval defined by the user. Results are binned into the defined intervals corresponding to depth and output in a summary file.

2.5 Image stitching

RGB images are collected in four overlapping strips during the pre-scan phase and brought into the ML2 software to create a stitching and cropping template.

This template can be applied to all boxes in a given drill hole. Additional templates can be produced and applied to individually selected boxes as needed.

2.6 Multi-channel analyser (MCA) file generation

After depth registration is finalized, each 10 mm bin of collected spectral data in the MMCA file is assigned a depth based on its location on the drill core. After an interval is defined, such as 10 cm or 1 meter, spectra within the interval are collated to create an MCA file for each interval for the entire length of the drill hole. A summary_MCA file is generated during this step that contains the from and to depths of each interval along with other important metadata.

2.7 Spectral analysis

Collected spectra are de-convoluted and quantified based off of fundamental parameters. For each drill hole and scan setting a Multiple Least Squared (MLSQ) calibration file is produced from the CRM scanned during the project. The generated interval MCA files for an entire drill hole are then batch quantified against the corresponding MLSQ file. This initial step creates data that is calibrated using CRM, but it is not matrix matched which can cause deviations in the average accuracy of the data. The de-convolution software outputs a summary_XRF file for each drill hole that contains the processed elemental geochemistry.

Finally, the batched data is combined with depth data to create a preliminary depth-registered geochemistry data set. During post-processing, calibration factors derived from lab assay comparisons can be applied to the preliminary data to produce a matrix-matched calibrated dataset.

2.8 X-ray specific gravity

To calculate the X-ray specific gravity (X-SG™) a subset of varying samples is chosen from the scanned drill hole. Submerged specific gravity is calculated for each chosen sample in the set and then used as a calibration set.

By comparing the quantified Compton values and submerged specific gravity calculation values, a calibration factor is created for the sample set. The resulting calibration factor is applied to the entire drill hole to obtain accurate X-SG™.

2.9 Volume bulk density

The volume bulk density of drill core is calculated using the standard density formula. The volume for this calculation is derived from the point cloud produced for each core tray during the pre-scan phase and each box is weighed to determine the mass. The complete description of these calculations is outlined in Arthursson et al. (2021).

3 Methodology developments

Ongoing methodology improvements focus on the implementation of a digital pulse processor that will allow the count rate of the detector to be significantly increased. Implementation of the digital pulse processor will allow for lower detection limits while still maintaining a typical scan speed such as 10 mm/s. Alternatively, the scan speed could be increased to enhance the throughput of the core.

A long-wave ultra-violet (UV) light source is also being added as an additional imaging option during the pre-scanning phase. A long-wave UV light source can illuminate certain minerals of interest such as carbonate phases and is most widely used to identify oil bearing core during oil and natural gas exploration.

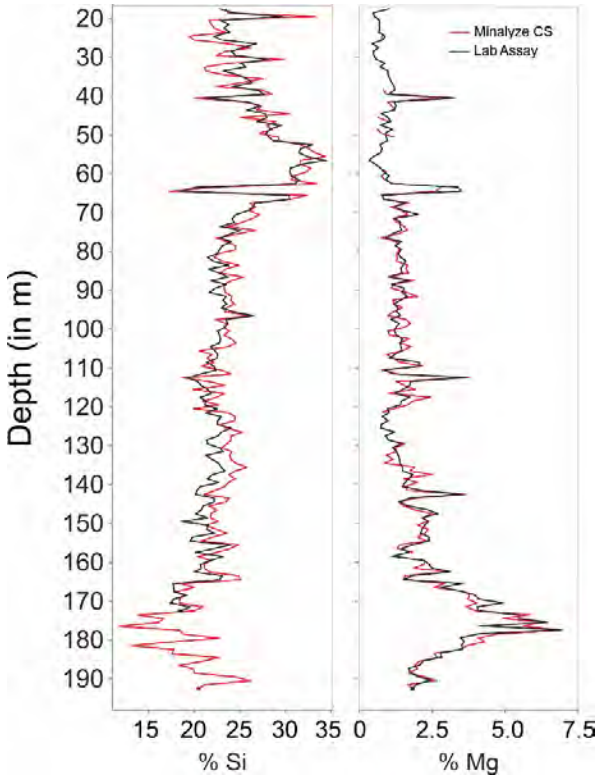

Figure 2. Comparison of XRF results for Si and Mg values collected using the Minalyzer CS (red) and lab assay results (black).

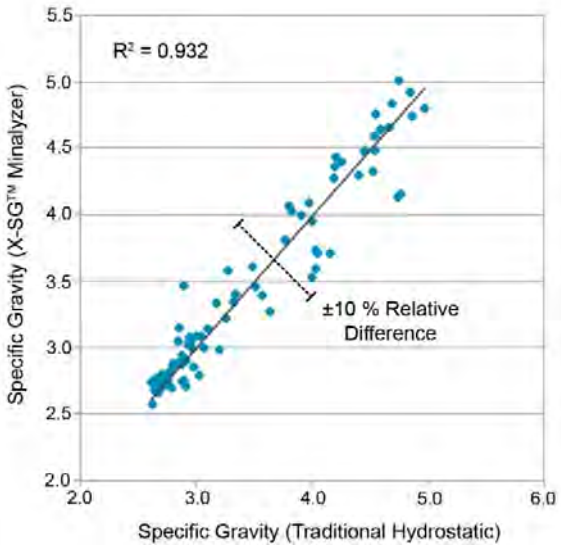

Figure 3. X-SG™ values versus traditional calculated hydrostatic values for the same drill hole showing a linear 1:1 ratio and the ±10 % relative difference.

4 Discussion and conclusions

The Minalyzer continuous XRF core scanner offers a variety of solutions for academic and industrial analysis. To test the accuracy of continuous XRF results, the core scanner data can be compared to laboratory-based assays obtained from the same core. Although it is not expected for these datasets to match perfectly due to differences in the instrumental methods used, sample volume analysed, and possible sample heterogeneities, it is expected that they correlate to one another. Figure 2 displays Minalyzer and laboratory-based assay datasets for Si and Mg values plotted down hole from a project in Mount Isa Inlier, Australia. A visual correlation can be seen in Figure 2, with associated R^2 values of 0.9819 for Si and 0.9785 for Mg.

RQD and fracture frequency calculated in Minalogger.com based on depth registration from an epithermal deposit in the western United States was compared to the RQD performed by a geologist at the mine site. The Minalogger analysis was performed using the same parameters used at the mine site. As expected, the results were very similar, and upon further inspection the Minalogger.com results were more accurate. Results from Minalogger.com had a higher accuracy because the calculations are based off the depth registration allowing measurements and fracture counts to be exact compared to using the traditional method of employing a tape measure.

Previous work has established that the volume bulk density calculation method using the 3D point clouds produced by the Minalyzer yields highly reliable data (Arthursson et al. 2021).

In general, calculating the specific gravity of drill core is important for resource estimation, but is a labour-intensive process that involves hydrostatic weight measurements for a large number of samples. A drill hole was scanned using the Minalyzer continuous XRF core scanner that already had an associated specific gravity dataset to compare results from each method. From the Minalyzer dataset, a variety of core segments were chosen to represent visually different rock types within the drill hole, and the hydrostatic weight was calculated. These values were used to create a calibration factor. The resulting calibrated X-SG™ values were plotted against the values calculated using the traditional method. Figure 3 shows that R^2 = 0.93 with relative difference between the datasets of ± 10 %.

The Minalyzer continuous XRF core scanner is a proven analytical tool that was introduced to the market in 2014 and is currently being implemented at multiple active mine sites. Though this is a robust system, method and hardware developments such as adding a UV light source for UV imaging and a digital pulse processor to increase detection limits are only going to increase the relevance and usefulness of this core scanner and cast a wider net of applications. The presented methods and calculations have a large upside because the values needed for the calculations are almost all collected during scanning or can be easily implemented into the workflow. Being able to digitise depth registered drill core with all of the associated datasets within days of drilling creates usable and accurate databases that can be accessed anywhere in the world.

Acknowledgements

This work was supported, in part, by the National Science Foundation and conducted within the Center to Advance the Science of Exploration to Reclamation in Mining (CASERM) which is a joint industry-university collaborative research centre between the Colorado School of Mines and the Virginia Tech under award numbers 1822146 and 1822108.

References

Arthursson M, Tod A, Dellar E, Lundström A (2021) Digitalizing the mining industry – 3D scanning of core trays to produce volumetric bulk densities. Third Australasian Exploration Geoscience Conference, Brisbane, 2021, Extended Abstracts, 5 p.

Sjöqvist ASL, Arthursson M, Lundström A, Calderón Estrada E, Inerfeldt A, Lorenz H (2015) An innovative optical and chemical drill core scanner. Sci Drill 19:13–16

XRD clustering and quantitative analysis as a fingerprinting technique to study ore deposits

Sheida Makvandi[1], Jean Cauzid[2], Alexandre Tarantola[2], Vasilios Melfos[3], Panagiotis Voudouris[4]
[1]*Application Competence Centre, Malvern Panalytical, Almelo, the Netherlands*
[2]*GeoRessources - Université de Lorraine-CNRS, Vandoeuvre-lès-Nancy CEDEX – France*
[3]*School of Geology, Aristotle University, Thessaloniki, Greece*
[4]*Faculty of Geology and Geoenvironment, National and Kapodistrian University of Athens, Athens, Greece*

Abstract. This study highlights the importance and efficiency of XRD clustering and quantitative analysis (using the Rietveld method) in metallogenic studies as a principal mineralogical assessment tool for the optimization of both field sampling and sample selection for further geochemical investigations. In this regard, 24 samples representative of various Oligocene epithermal and telescoped porphyry-epithermal deposits from Greece, their associated alteration zones and igneous host rocks were measured by XRD. The XRD scans were also investigated by PCA and cluster analysis in HighScore Plus software to distinguish their mineralogical similarity and differences; identify the representative scans of each cluster for phase identification and quantification. As a result, samples with mineral assemblages typical of epithermal and/or porphyry deposits cluster together or plot each other's vicinity, whilst those typical of advanced alteration zones also form (a) separate cluster(s). However, some felsic and mafic igneous host-rock samples are classified in the same clusters, which indicates the alteration of their original mineralogy over multiple phases of alteration and mineralization in their respective geological settings. The abundance of alteration minerals in these rocks reported in the XRD results supports this hypothesis. The XRD results were compared and showed very good agreement with trace element and bulk chemical data and VNIR-SWIR results.

1 Introduction

Identification and quantification of mineral assemblages in geological samples are primary steps after field sampling, which can serve two purposes: providing guidance for the optimization of the sampling strategy, and reducing the number of samples for further investigations using other mineralogical and geochemical techniques such as laser ablation inductively coupled plasma mass spectrometry (LA-ICP-MS), Laser Induced Breakdown Spectroscopy (LIBS) and/or scanning electron microscopy-energy dispersive X-ray spectroscopy (SEM-EDS). These methods despite their precision and efficiency are expensive and relatively slow, and the interpretation of the results requires petrographic data.

Whilst optical microscopy is conventionally accepted as a principal tool for mineralogical assessments, the precision of petrographic studies largely relies on the operator's knowledge and expertise. This is where hiring a complementary but more sophisticated technique, such as X-Ray Diffraction (XRD), seems essential. Over a million crystal structures are available in references libraries for mineral identification in XRD patterns. These structure data can also be used to create a calculated profile that through the Rietveld method (Rietveld 1969) can quantify the abundance of all minerals present in a sample. A distinct benefit of quantitative XRD (QXRD) is that the data can be further analyzed separately or in combination with data from other techniques with multivariate statistical methods to reveal hidden information in the dataset and provides insights for ore deposits or provenance discrimination studies. Thus, this study aims to highlight the value of XRD clustering and quantitative analysis as a rapid and cost-effective method in the study of porphyry and epithermal deposits.

2 Geological contexts

The Hellenides are part of the Alpine chain, resulting from the collision between the African and the Eurasian continents, which spread from the Alps to SE Asia. In Greece, the orogen consists of three continental blocks (Adria, Pelagonia and Rhodopia) accreted during the Hellenic subduction (Dewey et al. 1973, Ring et al. 2010), which evolved in two stages: a compressional event starting Late Jurassic and culminating Mid-Cretaceous, followed by an ongoing extension resulting from the slab rollback (Jolivet and Brun 2010, Jolivet et al. 2013). Therefore, large volumes of arc and post-collisional magmas intruded the thinned crust from Rhodope (Oligocene to Early Miocene) to the Cyclades (Middle Miocene to Pliocene). Many of these magmatic systems host porphyry-epithermal systems (Voudouris et al. 2019). This study focuses on the Rhodope province, which consists of four metamorphic core complexes -the Rhodope Massif -surrounded by a belt of slightly metamorphosed sedimentary and volcano-sedimentary rocks -the Circum-Rhodope belt.

Magmatism in the Rhodope Massif and the Circum-Rhodope belt ranges from calc-alkaline through high-K calc-alkaline to shoshonitic, and it is characterized by voluminous lavas and pyroclastics of andesitic to rhyolitic composition and their subvolcanic/plutonic equivalents. Outcropping alteration zones around porphyry bodies cover the entire series: potassic, sodic-calcic, propylitic, sericitic, argillic, advanced argillic, K-feldspar (adularia) and silicic.

3 Sampling and analytical methods

Sampling focused on building an exhaustive collection of the host rocks, intrusive bodies, alteration types, including overprinted ones, and mineralized veins of the district. A total of 40 samples were collected, from which, the samples without mineralized veins were cut in two pieces, and one piece was pulverized and sent for whole rock analysis at the SARM-CRPG facility (Service d'Analyse des Roches et Minéraux). The second piece was analyzed using a portable Spectral Evolution SR6500 VNIR-SWIR spectrometer at the GeoRessources laboratory.

A subset of 24 samples that were representative of all host igneous rocks, mineralization and associated alteration zones were analyzed by XRD at the Application Competence Centre, Malvern Panalytical, in the Netherlands. These samples originate from the Santa Barbara-Sykorachi (StB; 4 samples), Konos Hill (KH; 5 samples), Kassiteres (Ka; 3 samples), St Philippos (StP; 5 samples), Maronia (Ma; 4 samples), Pefka-Loutros (Pe; 1 sample) and Myli-Aisymi (My; 2 samples) prospects. All of them are Oligocene deposits either epithermal (StB, StP, Pe) or telescoped porphyry-epithermal (KH, Ma, My) systems (Voudouris et al. 2019). Table 1 summarizes the sample description, and cluster analysis results.

3.1 XRD measurements and Rietveld analysis

The XRD scans were collected using the Minerals Edition of Aeris compact X-Ray diffractometer from Malvern Panalytical with power settings of 40 kV–15 mA, equipped with a cobalt-anode X-ray tube, a goniometer radius of 145 mm, 0.04 rad. soller slits, 1/4° divergence slit, a 23 mm mask, low beam-knife position, step size 0.02° and acquisition time of 29 s/step. The Bragg-Brentano measurement covered a range of 5-75° 2θ allowing the detection of clay minerals and heavy minerals such as Fe oxides/hydroxides and sulfides. The use of cobalt radiation was applied to prevent the emission of Fe fluorescence. Fluorescence comes when using Cu radiation in analyzing Fe, Cu, and/or Mn-containing materials. This, therefore, improves the penetration depth of X-rays in the sample and improves counting statistics. The use of a linear PIXcel1D Medipix3 detector with an active length of 5.54° 2θ allows a scan acquisition time of a few minutes. The phase identification was done in the Malvern Panalytical's HighScore Plus software version 5.1 (Degen et al. 2014) using the ICDD PDF-4 database (Gates-Rector & Blanton 2019).

Table 1. Samples description and cluster analysis results. Number 0 indicates the samples that could not cluster with others because their district mineralogy (acting as outliers in the analysis).

Sample ID	Deposit	Lithology and alteration	Cluster number & colour
116-01	StB	Quartz vein	0 (black)
116-02		Andesite_Sericitic	0 (black)
116-03		Andesite_Chloritic-sericitic	1 (blue)
116-04		Andesite_Propylitic	2 (green)
118-05	KH	Granodiorite_Sodic-calcic	2 (green)
119-01		Clays_Serisitic	4 (brown)
119-02		Clays_Propylitic	4 (brown)
119-03		Monzodiorite_Serisitic	1 (blue)
119-04		Monzodiorite_Sotassic	5 (electric blue)
119-05	Ka	Diorite_Potassic	2 (green)
120-01		Monzodiorite_Chloritic-sericitic	4 (brown)
121-01		Rhyolite_Sericitic	4 (brown)
121-02	StP	Advanced clay alteration	0 (black)
121-04		Advanced clay alteration	3 (grey)
121-05		Advanced clay alteration	0 (black)
121-06		Advanced clay alteration	3 (grey)
121-07		Granodiorite_Propylitic	1 (blue)
122-01	Ma	Monzogabbro_Potassic	5 (electric blue)
122-02		Granite_Potassic	2 (green)
122-03		Monzogabbro_Propylitic	5 (electric blue)
123-02		Rhyolite_Sericitic	4 (brown)
123-03	Pe	Rhyolite_Chloritic-sericitic	0 (black)
124-03	My	Rhyolite_Sericitic	2 (green)
124-04		Rhyolite_Propylitic	4 (brown)

The peak position overlapping of critical minerals such as sphalerite with pyrite supports the use of Rietveld refinement as a full pattern fitting approach, in contrary to classical straight-line calibration methods that can cause a bias in the results. The Rietveld refinement requires XRD scans of a certain quality that includes a low and flat background and high diffraction intensities (most intense peak with >10,000 counts). In this study, every quality scan was collected within 7 minutes of measurement. A signal 3 times above the noise level is detectable, whilst a signal 10 times above the noise level is required for accurate phase quantification. The average signal-to-noise ratio in the collected XRD scans is 125. This means all minor and trace phases in the studied samples were detectable and quantifiable. The accuracy of XRD results was validated by comparison with the bulk chemistry, X-Ray fluorescence and VNIR-SWIR data published in previous studies (e.g., Jeong et al. 2016).

3.2 Extended cluster analysis

The phase identification was performed on specific XRD scans selected by extended cluster analysis (creation of correlation matrix, agglomerative hierarchical cluster analysis, grouping, and visualization) and Principal Component Analysis (PCA) and marked as a representative or outlier scan. Figure 2 shows a compare-view of 10 representative and outlier scans. Both PCA and cluster analysis of XRD scans were done in HighScore Plus software.

Cluster analysis aims to simplify the analysis of a large amount of data. It automatically sorts all (closely related) scans of an experiment into separate groups and marks the most representative scan of each group as well as the most outlying scans within each group (Degen et al. 2014). Samples that are clustered together show similar mineralogy. Therefore, it is only necessary to identify and quantify phases in the most representative scan of each cluster to create an

analytical routine (Degen et al 2014; Pernechele et al 2021). The other scans in the group can be inserted and automatically analysed in their corresponding routine. This is more efficient when analysing multiple samples originating from the same type of rocks/lithology or in quality control environments.

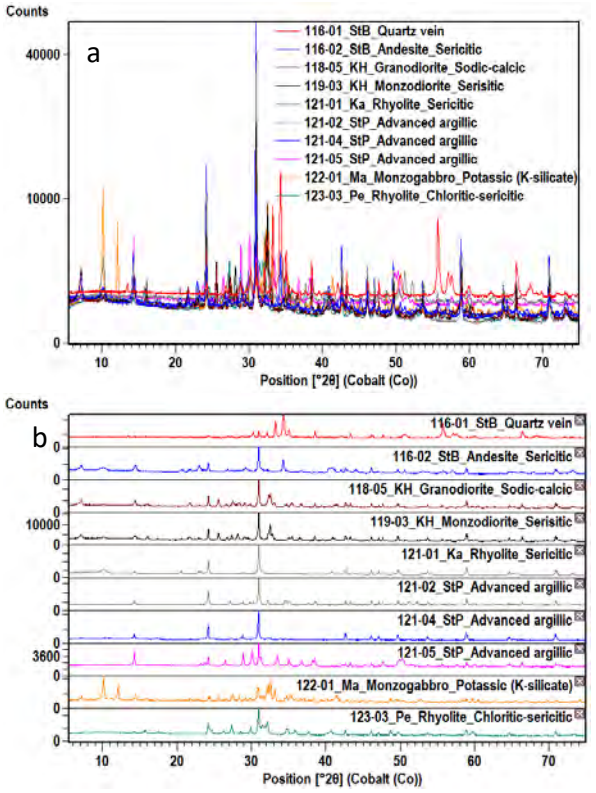

Figure 1. a) An overlay-view and **b)** a 2D-view of 10 XRD scans: 5 scans representative of 5 clusters and 5 so-called outliers (samples 116-01, 116-02, 121-02, 121-05, 123-03) that could not cluster with others because of their distinct mineralogy. A different XRD pattern simply corresponds to a different mineralogy.

4 Results and discussion

The dendrogram after cluster analysis (Figure 2) shows that 15 out of the 24 studied samples can be grouped into five clusters, whereas five samples do not belong to any of these groups given their distinct mineralogy. One of these so-called outliers is Sample 116-01 (Figure 3), which was collected from a quartz/sulfide vein at Santa Barbara-Sykorachi. The XRD analysis differentiates this sample as it consists of about 42.7 wt% calcite, 13.2 wt% chalcopyrite, 10.4 wt% sphalerite, and 2.9 wt% galena (a typical assemblage of epithermal mineralization; Voudouris et al 2019).

In addition, the XRD analysis discriminates this sample due to the occurrence of 9.0 wt% rudashevskyite (Fe-dominant member of sphalerite group) and 0.8 wt% cerussite ($PbCO_3$). In contrary, the other 3 samples from this area are from variably altered andesites (sericitic, chloritic-sericitic, and propylitic) and are mainly composed of feldspars (calcic and/or potassic) ± calcite ± clinochlore ± muscovite and quartz. Between 11.0 to 21.0 wt% illite was measured in sericitic and chloritic-sericitic andesites samples (116-02 and 116-03).

As depicted by the dendrogram in Figure 2, sample 116-01 despite its distinct mineralogical characteristics, shows some similarity to advanced argillic samples (samples 121-02 to 121-06) from St Philippos. This is consistent with their epithermal origin/association (Voudouris et al. 2019). According to the QXRD results, the advanced argillic samples are mainly composed of quartz (36.3 to 85.6 wt%), dickite (5.2 to 21.0 wt%), also variably contain pyrite (0.9 to 12.5 wt%) and a minor amount of galena (0.2 to 2.1 wt%). In contrast, the presence of 11.9 wt% anglesite ($PbSO_4$) and 2.4 wt% tennantite ($Cu_{12}As_4S_{12}$) in sample 121-02, and 42.6 wt% baryte and 1.3 wt% anglesite in sample 121-05 can also explain their dissimilarity to samples 121-04 and 121-06 (Figure 2).

In addition to samples 121-02 to 121-06, the presence of pyrite in association with clay minerals has been confirmed by the XRD-Rietveld analysis in other samples such as samples 118-05 and 119-01 to 119-04 from Konos Hill, sample119-05 from Kassiteres, and sample 123-02 from Maronia. This mineralogical association is characteristic of polymetallic epithermal deposits overprinting and/or occurring laterally from porphyry-style mineralization (Voudouris et al 2019).

Trace and major element composition of the 24 samples measured by ICP-MS and LIBS indicate that these samples averagely contain 18.4 ppm lithium. The XRD-Rietveld analysis identifies lepidolite, fluorannite, petalite, and griceite as the Li-containing minerals. The highest abundance of lepidolite is detected in rhyolite samples with sericitic alteration from Kassiteres and Myli-Aisymi (5.2 wt% in sample 121-1 and 2.7 wt% in sample 124-03) followed by monzogabbro with potassic (K-silicate) alteration from Maronia (sample 122-01) that contains 2.3 wt% lepidolite. The VNIR-SWIR results also confirmed the presence of lepidolite in samples 119-05-Ka, 122-01-Ma, 122-03-MA, 124-03-My and 124-04-My. They were tested using portable LIBS, which revealed the presence of Li.

In certain samples such as monzongabbro with potassic alteration from Maronia, fluoroannite is Li-bearing (5.3 wt% in sample 122-01, and 3.5 wt% in sample 122-03). This result emphasizes on one of the advantages of mineralogical analysis by XRD, which is indirect chemical fingerprinting (based on a stoichiometric formula of identified phases). The XRD reference databases commonly include multiple candidates for every mineral that may differ in their minor elements chemistry (e.g., Ni- or As-containing pyrite; Ni-, Cu-, Zn- or Ti-bearing magnetite). Elemental substitution or impurities can slightly affect the mineral's diffraction pattern. For instance, in the spinel structure of magnetite, the presence and increase in the Ti content results in an

increase in unit-cell parameter, oxygen fractional coordinate, and tetrahedral bond length, and a marginal decrease in the octahedral bond length (Bosi et al. 2009).

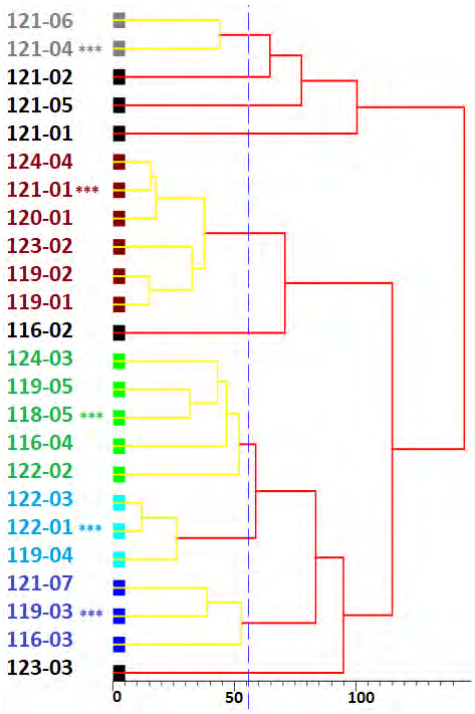

Figure 2. Dendrogram after cluster analysis based on the correlation matrix from 24 studied samples. X-axis shows the dissimilarity of the tie bars. Every colour represents a distinct cluster, except for black that specifies the outliers. The most representative scan of each cluster is indicated by ***.

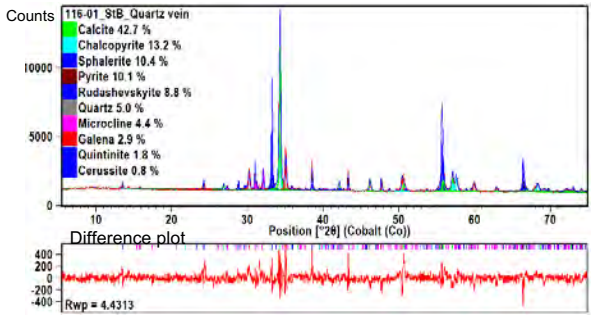

Figure 3. Rietveld analysis of XRD data of sample 116-01 in HighScore Plus. Distinct mineralogy that differentiates epithermal mineralization from alteration zones and host rocks. The difference plot shows the difference between the measured and calculated intensities/profiles. An Rwp = 4.4 indicates the reliability of the Rietveld refinement and accuracy of the phase quantification.

5 Conclusions

Quality scans collected in 7 minutes in Aeris compact XRD system show the potential of XRD as a time- and cost-effective technique for ore deposit mineralogical studies, and sample selection for further investigations with other techniques. PCA and cluster analysis of XRD patterns in HighScore Plus is an efficient approach to analyze many data as they simplify the complexity of such a dataset and reveal the hidden correlation between different observations. As a result, the XRD scans of 24 studied samples were grouped in 5 clusters and 5 outliers showing the diverse mineralogy of these samples. The Rietveld analysis of XRD patterns also indicates a different abundance of minerals in each sample. This study showed the presence of lepidolite, fluorannite, petalite, and griceite as Li-containing minerals in some of studied the lithologies (particularly in rhyolite samples with sericitic alteration). Pyrite occurrence in clay-rich assemblages was also detected as a signature of epithermal mineralization.

Acknowledgments

T. Degen, M. Sommariva, and M. Pernechele (Malvern Panalytical, the Netherlands) are thanked for their technical support on XRD measurements and data analysis. M. Fisher (GeoRessources, Université de Lorraine) is thanked for the VNIR-SWIR and geochemical data acquisition and interpretation as part of her master's degree thesis.

References

Bosi F, Hålenius U, Skogby H (2009) Crystal chemistry of the magnetite-ulvöspinel series. American Mineralogist 94, 181-189.

Degen T, Sadki M, Bron E, König U, Nénert G (2014) The High Score Suite. Powder Diffraction 29, S13–S18.

Dewey JE, Pittman WC III, Ryan WBF, Bonnin J (1973) Plate tectonics and the evolution of the Alpine system. Geol. Soc. Am. Bull., 84 (10) 3137-3180.

Gates-Rector S, Blanton T (2019) The Powder Diffraction File: A Quality Materials Characterization Database. Powder Diffraction 34, 352-360.

Jeong Y, Yu J, Koh SM, Heo CH, Lee J (2016) Spectral characteristics of minerals associated with skarn deposits: a case study of Weondong skarn deposit, South Korea. Geosciences Journal 20, 167-182.

Jolivet L, Brun J-P, (2010) Cenozoic geodynamic evolution of the Aegean region. Int. J. Earth Sci. 99, 109–138.

Jolivet L, Faccenna C, Huet B, Labrousse L, Le Pourhiet L, et al (2013) Aegean tectonics: strain localization, slab tearing and trench retreat. Tectonophysics 597, 1–33.

Pernechele M, López Á, Davoise D, Maestre M, König U, Norberg N (2021) Value of Rapid Mineralogical Monitoring of Copper Ores. Minerals 11, 1142.

Rietveld HM (1969) A profile refinement method for nuclear and magnetic structures. Journal of Applied Crystallography 2 (2), 65-71.

Ring U, Glodny J, Will T, Thomson S (2010) The Hellenic subduction system: high pressure metamorphism, exhumation, normal faulting, and large-scale extension. Ann. Rev. Earth Plan. Sci. 38, 45–76.

Voudouris P, Repstock A, Spry PG, Frenzel M, Mavrogonatos C, et al (2022) Physicochemical constraints on indium-, tin-, germanium-, gallium-, gold-, and tellurium-bearing mineralizations in the Pefka and St Philippos polymetallic vein- and breccia-type deposits, Greece. Ore Geol. Rev., 140, 104348.

Voudouris P, Mavrogonatos C, Spry PG, Baker T, Melfos V, et al (2019) Porphyry and epithermal deposits in Greece: An overview, new discoveries, and mineralogical constraints on their genesis. Ore Geol. Rev., 107, 654-691.

Integrated analysis of the Consorcio prospect in Cunas emerald mine (Colombia), tool to determine mineralization stages and related by-products

Andrés S. Martín-Ravelo[123]
[1]*Departamento de Geociencias, Universidad Nacional de Colombia, Bogotá, Colombia*
[2]*Society of Geology Applied to Mineral Deposits – Student Chapter UNAL, Bogotá, Colombia*
[3]*Caracterización Tecnológica de Minerales research group, Bogotá, Colombia*

Abstract. This work includes the main results and research proposal under development by students and researchers from the Universidad Nacional de Colombia (SGA Student Chapter and Caracterización Tecnológica de Minerales research group) linked to the "LitoCo" project, focused on determining the conditions of the mineralization stages that originated the emerald deposits located in Cunas emerald mine and the closes "Consorcio" prospect (Maripi-Boyacá, Colombia). This study is based on stratigraphy, petrography, geochemistry (XRD and XRF) and gamma-ray spectral geology, joining efforts to delimit new productive zones of emeralds through local-regional correlations, while the extraction potential of critical minerals present as stored by-products (REE elements, stone aggregates and clay minerals; for construction and industrial use) is evaluated.

1 Introduction

Colombia has been the largest emerald producer since ancient history. Nowadays, its role has passed to a second place due to arise of large producers in other parts of the world, occupying the third place in terms of emerald production, after Zambia and Brazil. Emeralds in the world are typically found in metamorphic aureoles or pegmatitic veins in countries like Zambia, Brazil, Pakistan, or Ethiopia (González-Durán et al. 2021). Colombian deposits are unique, due to mineralization occurs in sedimentary rocks by hydrothermal processes related to high diagenesis and low grade metamorphism (equal to found in sediment-hosted Pb-Zn or Mississippi Valley Type deposits) without magmatism or high-grade regional metamorphism (Giuliani et al. 2019), inside organic-rich black shales, calcareous mudstones, limestones and evaporitic siltstones of early-Cretaceous age (Valanginian to Hauterivian-Barremian), belonging to Rosablanca, Furatena and Muzo formations (González-Durán et al. 2021).

This work covers the lithostratigraphy and petrography of a deposit corresponding to Cunas emerald mine, within the Maripí District (MD), one of the Colombian emerald mining districts, all of them distributed N-NE along both flanks of the Andes eastern cordillera, between the provinces of Cundinamarca and Boyacá: Western Emerald Belt (WEB, including the municipalities-districts of Muzo-Quipama, Peñas Blancas, Coscuez and Maripí), and Eastern Emerald Belt (EEB, including the municipalities-districts Chivor, Macanal and Gachalá).

The Cunas mine has been exploited for at least 30 years since its discovery in the 1990's. Between Cunas and La Pita mine (Figure 1) there is a coarse-vein of high-quality emeralds, within the Consorcio prospect (consortium in Spanish, named for the joint exploitation of both companies). Since then, multiple studies have been conducting to determine the mineralization conditions that occurred to form these emeralds and how they vary with respect to other mines. Several additional proposals to better understand the genesis and potential of emerald deposits for not only gems but also by-products (REE's elements, stone aggregates and clay minerals) are X-ray diffraction, X-ray fluorescence and gamma spectrometry, that we are going to mention next.

The main structures in WEB are tight syncline-anticline folds oriented N30°E, parallel to SE-verging thrust faults, such as Coscuez, Peñas Blancas and Rio Minero (leader thrust fault), cut by the Rio Itoco strike fault, oriented 50°SE separating numerous mines. These are interpretated as fault propagation folds in a compressive and transpressive regime, where the detachment levels correspond to ductile beds of albitites and other evaporitic rocks of Cretaceous formations, juxtaposing these rocks and moving overpressured connate fluids (brines) between faults, escaping and triggering intense hydraulic fracturing. In each WEB deposit, there is evidence of complex deformation resulting in polyphasic duplex structure, as well as growth of chloritoid porphyroblasts and therefore a low-grade metamorphism process (Branquet et al. 1999).

According to Giuliani et al. (2019) in the hinges of the folds develops tectonic and hydrothermal breccias when fluids percolate and leach rocks during successive pulses of fault fluid flow and dilatant sites resulting from shear fracturing synchronous to thrust fault propagation, crystallizing emeralds after albitization, early sulphates reduction and carbonization. Thus, the large mines are developed recognize these structures (e.g. Peñas Blancas, Coscuez, La Pava and Puerto Arturo mines are following the Alto de la Chapa and Coscuez anticlines). At the Cunas mine and Consorcio prospect (Figure 1), mineralization occurs in WNW flank of Muzo syncline, along decimetres-thick carbonate veins and hydrothermal breccias cut bedding (Romero et al. 2021; Martín-Ravelo and Romero-Ordóñez 2022).

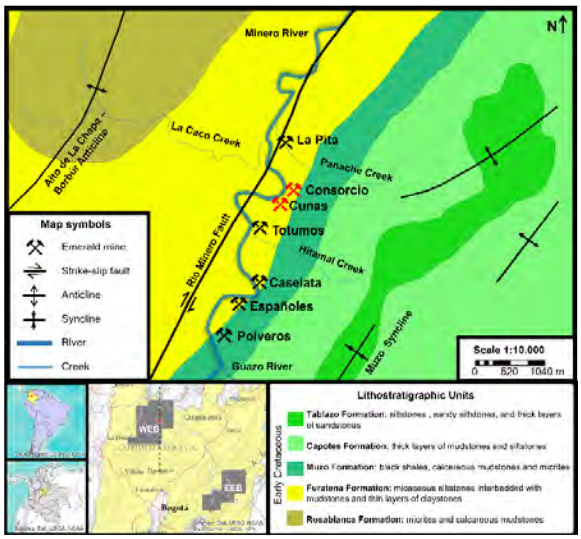

Figure 1. Maripí District (MD) geological map, showing Cunas mine and Consorcio prospect. Modified of Martín-Ravelo and Romero-Ordóñez (2022)

Mineralization stages occur simultaneously to develop the tectonic structures (González-Durán et al. 2021). Albitization occurs when brines leach the rocks and crystallizes metasomatic albite due to mobilization of solution of alkaline composition (Na^+, Ca^+, Fe^+, Mg^+) forming thrust-breccias parallel to the lamination called “cenicero” by the miners (Giuliani et al. 2019). Alkalinity then stimulates sulphate reduction in the presence of black shales organic matter, releases HCO_3^- and H_2S to form pyrite and carbonates as the solution acidifies. Carbonization receives its name due to crystallization of calcite and dolomite in veins in paragenesis with quartz + fluorite + parisite + emerald, resulting in an enrichment in light REEs and high Cr-V ratios and poor iron content as a chemical fingerprint of emerald gems. Finally, supergenic stage and compressional deformation occur, forming red tectonic breccias cemented by pyrite and ankerite. Mineralization conditions of emeralds are known at the Cunas mine (Romero-Ordóñez et al 2021) formed at low temperature ~260-340°C, pressure ~850-2400 bar, high density 1,03 g/cm^3 and elevated salinity ~39% wt., as result of the mixture of two hydrothermal fluids.

The mineralizations have been dated at different ages, both in EEB and WEB. Most accepted age for the WEB deposits corresponds to the Eocene-Oligocene (Giuliani et al. 2019) during a pulse of tectonic uplift of Andes eastern cordillera (38-32 Ma, using ^{40}Ar-^{39}Ar in muscovite) and are younger than EEB (65 Ma, using Ar method too), framing this latest age in extensive deformation during Cretaceous-Paleogene margin. However, other authors propose similar ages for EEB and WEB, with important tectonic implications. Romero-Ordóñez (1999) gives an age of 67 Ma (using Rb-Sr in cogenetic carbonates) and Altenberger et al. (2022) gives ~47 to 51 Ma (using U-Pb-Th in parisite), so the discussion remains open to define the time and processes that formed the Colombian emeralds.

3 Methods

Petrography and stratigraphy studies were conducted in field and Universidad Nacional de Colombia, which are the baseline for the analyses developed within the "LitoCo" project fully financed by the same university.

A 1:1000 scale stratigraphic section was built along the Consorcio prospect, consisting of an ascending stratigraphic tunnel in an E direction and parallel to dip of W flank of the Muzo syncline (Figure 1). It consists of 444 m of non-poorly altered siliciclastic and mixed rocks, composed of mudstones, siltstones and grey blackish claystones interbedded with beds of decimetres and meters of fine-medium grained sandstones. Some beds are calcareous, locally fossiliferous and correspond to mudstone-wackestone rocks.

120 hand samples from the Consorcio prospect and Cunas mine were collected and classified to elaborate eleven polished thin sections (PTS). Together 3 PTS from CDTEC Gemlab (Bogotá, Colombia) underwent petrography and complementary micro-Raman spectroscopy. Were used Zeiss Axio Scope-A1 microscope and Horiba Scientific LabRAM Evolution Raman spectrometer coupled Olympus BX41 microscope. Nineteen rock samples from the Consorcio stratigraphic section (Figure 2) were ground and sieved with 60 mesh, separating 100 µm fraction to perform x-ray diffraction and x-ray fluorescence (thin fraction), as well as characterization of organic matter macerals (coarse fraction) with reflected light petrography. The Briquettes were prepared based on the ASTM D 2797 standard in ore and coal petrography 223-220 lab of Universidad Nacional de Colombia.

4 Results

4.1 Stratigraphy

Eight segments were recognized along the Consorcio section (Figure 2), grouping into two formations described from base to top, and defined in WEB and other mines (Terraza 2019).

Furatena formation covers the first 7 segments, consisting in ~133 m of black siltstones and mudstones with plane-parallel lamination of quartz, mica and organic matter interbedded with dm-thick sheet of very fine to medium grained sandstones, with more or less pyrite (associated with black levels rich in organic matter), either as massive microcrystalline crystals and red-orange ferruginous patinas, or as mm-thick concordant veins (especially in segment 4). Concordant veins of calcite+pyrite appear in segments 5 and 6, being more fissile due to grow of muscovite interbedded with black claystones and orange patinas. All formation has calcite patinas, except for a sporadic layer of mudstone-wackestone present in segment 7.

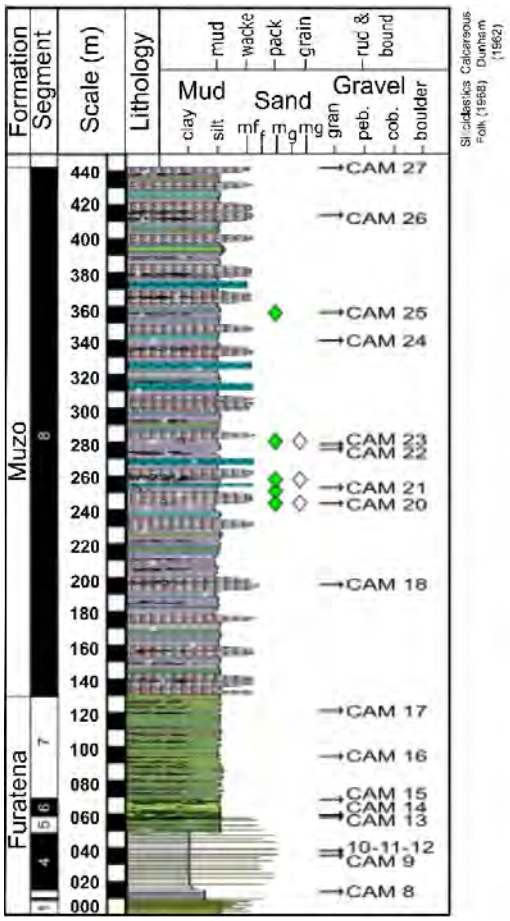

Figure 2. Stratigraphic column of Consorcio prospect, showing each of nineteen samples collected. Modified of Martín-Ravelo and Romero-Ordóñez (2022)

Muzo formation covers the upper part of segment 7 and segment 8, above to Furatena formation in net contact, marked by change from siliciclastics to more calcareous rocks without leaving the mixed character. They consist in ~311 m of organic-rich black siltstones and mudstones with plane-parallel lamination (organic levels up to 50 cm thick); interbedded with beds of very fine-fine sandstone meters thick (up to 5 m), with wavy plane-parallel surfaces cemented by carbonates and foraminifera fossils levels, which can be classified as mudstone-wackestone. Siltstones and mudstones have more fissility surfaces than lithologies of the Furatena formation, due to micas decrease. Muzo formation have millimetric veins of pyrite with ferruginous patinas concordant, also tangential- almost orthogonal (to stratification) fibrous calcite veins dm thick, in paragenesis with Cr-muscovite or fuchsite. These veins are cut by rhombohedral calcite and dolomite concordant veins, forming hydrothermal breccias with quartz, fluorite, parisite and emeralds.

Thickness of Muzo formation is greater than the reported in type section (~180 m) and the same as other mines (Jiménez 2017). All these observations (reported jointly by Martín-Ravelo and Romero-Ordóñez (2022)) for rocks from Furatena and Muzo formations allowed to interpret them as transgressive onlap deposits over inner ramp, as storm-influence lagoon, due to sedimentation regime change from siliciclastics to calcareous deposition. Contrast in thickness between the Consorcio section and type section may be due to half-graben basin geometry to explain the high angle thrust system and folds developed in WEB (Terraza 2019).

4.2 Petrography

Five stages of mineralization were recognized based on textures and cross-cut relations. From older to younger: premineral, albitization, carbonization (I), carbonization (II) and supergene.

Premineral is represented by low or unaltered rocks that show relictic textures and partial replacements, such as organic matter with clastic texture (lamination), recrystallization of foraminifera, and diagenetic cement (Figure 3a). Albitization occurs when albite replaces pre-existing minerals and introduce euhedral pyrite and muscovite. Carbonization (I) and (II) receive their names due to the development of fibrous calcite veins cut by rhombohedral carbonates veins (calcite+dolomite) (Figure 3b) in paragenesis with quarz, fluorite, parisite and emerald (Figure 3c, 3d).

Similarly, LitoCo project contemplates the evaluation of macerals combining micro-Raman spectrometry to evaluate the reflectance and thermal maturity reached by rocks during emerald mineralization and diagenesis.

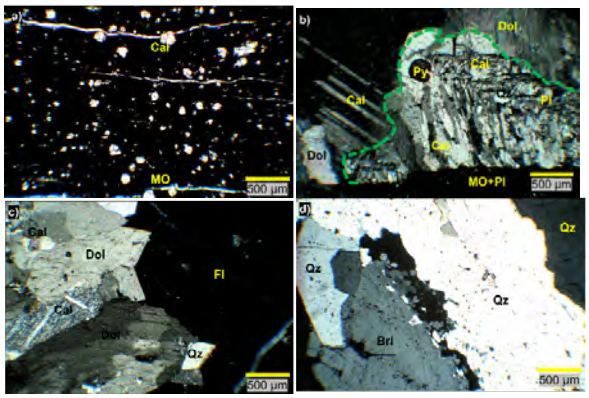

Figure 3. a Premineral stage (with foraminifera). **b** Rhombohedral carbonate veins (calcite and dolomite) cut fibrous calcite+pyrite veins. **c** Calcite + dolomite + quarz + fluorite ± parisite paragenesis in emerald veins. **d** Emerald (beryl) in paragenesis with quartz forming lamellae texture.

5 Research proposal (in development)

5.1 X-ray diffraction (XRD) and x-ray fluorescence (XRF)

Based on previous studies (González-Durán et al. 2021), we as research team of LitoCo project propose new methodologies to contribute to the exploration of emeralds and by-products, considering the proximity to other mines and taking advantage of the work near two important emerald

mines. XRD and XRF provide information of spatial variations in metasomatism because of evolution of main trapping emerald structures, even complementing diagenesis observation considering analysis as differential thermal curves (Araujo et al. 2004) and determining the paleo-conditions of host rock deposit (Mantilla et al. 2004). In addition, XRD-XRF analysis (low-cost geochemistry) provides information on the crystalline structure and composition of phosphates (monazite, xenotime, apatite), clay minerals, carbonates and feldspars present in emerald host rocks, so it can be evaluated the potential to produce fertilizers, pottery, and construction materials.

5.2 Gamma-ray spectrometry

Gamma-ray spectrometry allows the measure the radiation emitted by radioactive isotopes in host rock, seeking to quantify and allowing to determine the natural content of light REEs (e.g. Y, Sc, La, Ce, Nd, Sm, Eu, Tb) and other associated elements (V, Co, Cs and U), due to basin reduction conditions and presence of high phyllosilicates content (Condie 1991; Jiménez 2017), with a greater exploitation potential than conventional sources such as zircon, complementing the unassessed amounts of (Ce,La)-Parisite, Monazite and Ce-Bastnaesite in Colombian emerald deposits (Giuliani et al. 2019). As in the oil and gas industry, gamma ray spectrometry can be used to build logs like open hole logs, and therefore for use in regional exploration if combined with lithological logging (e.g., extant stratigraphic section) (Serra 1984).

6 Conclusions

Five mineralization stages were recognized in Cunas mine and Consorcio prospect, equally to other emerald mines (Puerto Arturo, Tequendama, La Pava, Coscuez). Therefore, there are great possibilities of developing this deposit and discover new opportunities in coming years. With a growing demand of REEs and raw materials, mining must be rethought to extract the maximum amount of materials that the mine produces and that are currently wasted, using relative new technologies.

Acknowledgements

To Universidad Nacional de Colombia, especially to PGP program with LitoCo project for support. To "Caracterización Tecnológica de Minerales" research group for gamma-spectrometry analysis and lattice lab (224-106A, Ciudad Blanca, Bogotá) for XRD-XRF analysis. Likewise, to professors Ariel Cadena, Gustavo Sarmiento, Juan Carlos Molano, Jimmy Fernández, Thomas Cramer and Fernando Romero. To the Rotlewicz brothers (Jimmy and Paul), the Rodríguez brothers (Orlando and Hugo), Carlos Rodríguez, and the countless emerald lovers (miners, businesspeople, researchers) who allowed samples, financial support and fieldtrip, laboratories, and experience.

References

Altenberger U, Rojas-Agramonte Y, Yang Y, Fernández-Lamus J, Häger T, Guenter C, Gonzalez-Pinzón A, Cahrris-Leal F, Artel J (2022) In Situ U–Th–Pb dating of parisite: Implication for the age of mineralization of Colombian emeralds. Minerals 12(10), 1232: 1-16. https://doi.org/10.3390/min12101232

Araujo JH, Francisco SN, Acchar W, Gomez UU (2004) Thermal Decomposition of Illite. Materials Research 7(2) http://doi.org/10.1590/S1516-14392004000200024

Branquet Y, Laumonier B, Cheilletz A, Giuliani G (1999) Emeralds in the eastern cordillera of Colombia: Two tectonic settings for one mineralization. Geology 27: 597-600. https://doi.org/10.1130/0091-7613(1999)027%3C0597:EITECO%3E2.3.CO;2

Condie KC (1991) Another look at rare earth elements in shales. Geochimica et Cosmochimca Acta 55(9): 2527-2531. https://doi.org/10.1016/0016-7037(91)90370-K

Giuliani G, Groat LA, Marshall D, Fallick AE, Branquet Y (2019) Emerald deposits: A review and enhanced classification. Minerals 9(2), 105: 1-63. https://doi.org/10.3390/min9020105

González-Durán AF, García-Toloza J, Bonilla GE, Cedeño-Ochoa CJ, Angarita-Sarmiento LG, Castañeda-Gómez AJ, Parra-Bastidas SD, Bocanegra-Rodríguez LC, Montaña-Cárdenas J, López-Castillo CL (2021) Geoquímica y mineralogía de la mina La Pava, Muzo-Quípama: Implicaciones en la exploración de esmeraldas en Colombia. Boletín de Geología, 43(2): 117-142. https://doi.org/10.18273/revbol.v43n2-2021007

Jiménez J (2017) Estudio químico, mineralógico y espectroscópico de las esmeraldas colombianas en los distritos mineros de Chivor, Muzo y Coscuez y su aplicación en la determinación de origen geográfico. MSc Thesis, Universidad Nacional de Colombia. Recovered from https://repositorio.unal.edu.co/handle/unal/63927

Mantilla FL, García RC, Uribe PE (2004) Caracterización y significado de la alofana y la haloysita en rocas de la formación Paja (Cretácico inferior). Borde occidental de la cordillera oriental, Colombia. Boletín de Geología, 26(43): 11-22. Recovered from https://revistas.uis.edu.co/index.php/revistaboletindegeologia/article/view/914

Martín-Ravelo AS, Romero-Ordóñez FE (2022) Petrografía de las rocas de Consorcio en la mina de esmeraldas de Cunas (Maripí, Boyacá). Relación estratigráfica con rocas del Valle Medio del Magdalena (Colombia). Boletín de Geología 44(2): 125-143. https://doi.org/10.18273/revbol.v44n2-2022006

Romero-Ordóñez FH, González-Durán AF, García-Toloza J, Rotlewicz-Cohen J, Cedeño-Ochoa CJ, Alvarado-González HR, Angarita-Sarmiento LG (2021) Mineralogy and fluid inclusions of the Cunas emerald mine, Maripí – Boyacá, Colombia. Earth Sciences Research Journal 25(2): 139-156. https://doi.org/10.15446/esrj.v25n2.90210

Romero-Ordóñez FH, Schultz-Güttler RA, Kogi K (1999) Geoquímica del Rubidio-Estroncio y edad de las esmeraldas colombianas. Geología Colombiana 25: 221-239. Recovered from https://repositorio.unal.edu.co/handle/unal/42082

Serra O (1984) 7. Natural gamma-ray spectrometry. In: Serra O (ed) Fundamentals of Well-Log Interpretation,15 vol. Amsterdam – Oxford – New York – Tokyo, pp 113-134. https://doi.org/10.1016/S0376-7361(08)70421-7

Terraza R (2019) Notas sobre el context tectonoestratigráfico de formación de las esmeraldas colombianas. Boletín Geológico 45: 37-48. https://doi.org/10.32685/0120-1425/boletingeo.45.2019.486

LA-ICP-MS trace element composition of stibnite from the Kizhnica-Hajvalia-Badovc ore field, Kosovo

Sławomir Mederski[1], Jaroslav Pršek[1], Konrad Kluza[1], Dimitrina Dimitrova[2]
[1]AGH University of Science and Technology, Kraków, Poland
[2]Geological Institute, Bulgarian Academy of Sciences, Sofia, Bulgaria

Abstract. The chemical composition and trace element concentration in stibnite from the Kizhnica-Hajvalia-Badovc (KHB) ore field (Kosovo) was studied. Trace element measurements in stibnite from 2 localities (Janjevo stibnite-quartz vein and Badovc stibnite-rhodochrosite breccia) were conducted using LA-ICP-MS technique. In addition to the typical enrichments in As, Pb, Hg, or Cu known from the literature, stibnite from the KHB ore field shows the highest known concentrations of Tl (up to 213 ppm) and Ag (up to 146 ppm). In addition, elevated concentrations of As (up to 4,100 ppm), Pb (up to 2,000 ppm), Hg (up to 316 ppm), and Cu (up to 46.9 ppm) are observed. The following three independent mechanisms of incorporation of the above-mentioned trace elements into the stibnite structure are presented: (1) $As^{3+} \leftrightarrow Sb^{3+}$; (2) $(Cu^{+} + Ag^{+}) + Pb^{2+} \leftrightarrow Sb^{3+} + \square$; and (3) $Tl^{+} + Hg^{2+} \leftrightarrow Sb^{3+} + \square$.

1 Introduction

Stibnite is the most common ore mineral of antimony and is present in a variety of deposit genetic types. Most of them are associated with hydrothermal systems - epithermal and mesothermal veins, sediment-hosted and Carlin-type Au deposits, but also hot-spring deposits (Seal et al. 2017). These deposits are often located on the periphery of orogenic Au deposits, intrusion-related Au deposits, and porphyry Cu-Mo deposits. The main production of antimony ores comes from quartz-stibnite veins and replacement Sb deposits (Fu et al. 2020; 2022).

Antimony deposits are usually mineralogically monotonous with the only economic mineral - stibnite. However, stibnite can occur in either Sb-Au, Sb-W, or Sb-As±Tl association, and thus can be characterized by various trace elements (Fu et al. 2020). Stibnite can incorporate into its structure both trivalent As^{3+}, but also, through heterovalent substitutions, divalent elements such as Pb^{2+}, or Hg^{2+}, and monovalent elements such as Cu^{+}, Ag^{+}, and Tl^{+}. The trace element data in stibnite measured by the LA-ICP-MS technique began to be published relatively recently (only after 2020), mainly from the world's largest Sb deposits located in China such as Xikuangshan, Daocaowan, Woxi, and Banxi (Fu et al. 2020; 2022; Song et al. 2022). However, some genetic types, particularly Carlin-type and sediment-hosted gold deposits (SHGD), have no data. And consequently, the nature of the behavior of the diagnostic pathfinder elements known for these environments (such as thallium, mercury, or arsenic) in the context of substitution mechanisms in stibnite, is not known.

In addition, data from numerous European deposits are lacking, with the only data coming from the Gerakario deposit in Greece (Stergiou et al. 2022). In Europe, there are several Sb-As±Tl deposits and mineral occurrences within the Mediterranean Region (Janković 1989). These can be divided into two groups - the Triassic and the Neogene. The first are associated with the intercontinental rift and volcanogenic-sedimentary sequences and are hosted mainly by carbonate rocks. On the other hand, Neogene deposits are associated with calc-alkaline volcanism along the closure zone of the ocean (Janković 1989). One of the regions of Neogene Sb mineralization is the Kizhnica-Hajvalia-Badovc (KHB) ore field in the Kosovo in Vardar Zone (Fig. 1). Hydrothermal mineralization that is responsible for the formation of stibnite-rich veins and breccias in the KHB ore field is associated with a concealed porphyry system (Mederski et al. 2022b). In this paper, we present data on trace elements in stibnite obtained by LA-ICP-MS technique and demonstrate possible substitution mechanisms in stibnite.

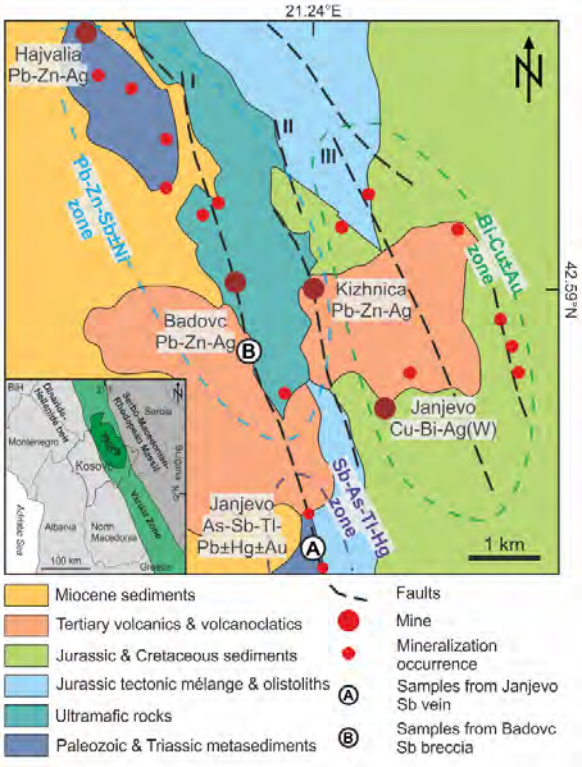

Figure 1. Simplified geological map of Kizhnica- Hajvalia-Badovc ore field with the sampling locations. Abbreviations: I = Hajvalia- Badovc Zone; II = Kizhnica Zone; III = Okosnica Zone.

2 Geology

The Kizhnica-Hajvalia-Badovc ore field is situated in the southern part of the Trepça Mineral Belt (TMB). In the KHB ore field area are present Paleozoic-Triassic metasedimentary complex (schists and marbles), Triassic-Jurassic ultramafic complex, Jurassic tectonic mélange with olistoliths, Jurassic-Cretaceous flysch series, Neogene volcanic and volcanoclastic rocks (mainly andesites), and Miocene sediments (Fig. 1). Moreover, the area is intersected by 3 major tectonic zones that controlled hydrothermal mineralization (Fig. 1).

The study area shows the presence of many styles of polymetallic hydrothermal mineralization: veins, stockwork-impregnation, carbonate-replacement, listvenite-hosted, and skarn/hornfels. Three documented Pb-Zn-Ag deposits occur within the KHB ore field (Kizhnica, Hajvalia, and Badovc) and they are associated with the Pb-Zn-Sb±Ni zone described by Mederski et al. (2021; 2022a) (Fig. 1). In addition, mineral occurrences associated with the Bi-Cu±Au system are described in the eastern part of the KHB ore field (Mederski et al. 2021), while a distal Sb-As-Tl-Hg mineralization is observed in its southern part (Mederski et al. 2022b) (Fig. 1).

3 Samples and methods

3.1 Investigated material

The studied samples containing stibnite were collected from 2 localities in the KHB ore field: Janjevo stibnite-quartz vein and Badovc stibnite-rhodochrosite breccia (Fig. 1).

Janjevo is a recently discovered location with As-Sb-Tl-Pb±Hg±Au mineralization hosted by Upper Triassic marbles (Mederski et al. 2022b). Two generations of stibnite have been distinguished here. The first generation occurs in the quartz-stibnite vein that intersects marbles. Stibnite forms prismatic needles up to about 5 cm (Fig. 2a) and occurs in association with quartz, minor dolomite, pyrite, As-Tl-Sb-Hg pyrite, sphalerite, and secondary minerals: gypsum, valentinite, and native sulfur. The second generation forms small, disseminated aggregates inside the dolomitized lenses in the As-Sb-Tl-Pb profile in the marbles. First-generation stibnite was used for the study using the LA-ICP-MS technique.

Stibnite samples from the second locality were collected from alteration zones and andesite-listvenite contacts of the Pb-Zn-Ag Badovc deposit on the hills north of Shashkofc. The dominant here are massive-banded Pb-Zn-Sb ores, as well as Pb-Zn-Sb±Ni listvenite hosted ores (Mederski et al. 2022a). The rhodochrosite-stibnite breccia ores that are the subject of this research, with stibnite crystals up to 2 cm in size (Fig. 2b-c), have also been discovered here. Stibnite occurs in simple paragenesis with rhodochrosite, sphalerite, and pyrite. In addition, some ore fragments show strong brecciation, while stibnite was found in breccias cutting across the previously mentioned massive-banded Pb-Zn-Sb ores. In addition, one sample with massive stibnite was found in association with quartz, pyrite, sphalerite and berthierite.

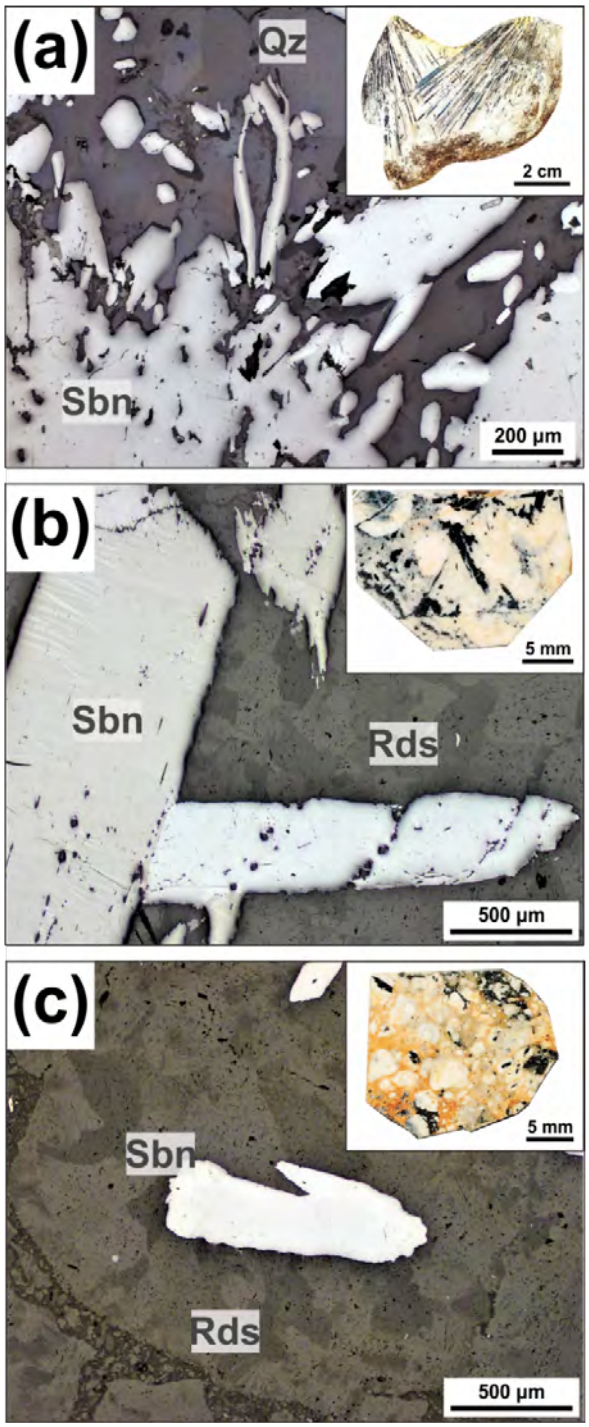

Figure 2. Hand specimen and reflected light microphotographs of selected stibnite from the KHB ore field. **(a)** Typical stibnite needles from quartz vein - Janjevo. **(b)** Idiomorphic stibnite crystal with visible polysynthetic twinning from rhodochrosite ore, Badovc. **(c)** Euhedral stibnite crystal in rhodochrosite breccia, Badovc. Qz = Quartz; Rds = Rhodochrosite; Sbn = Stibnite.

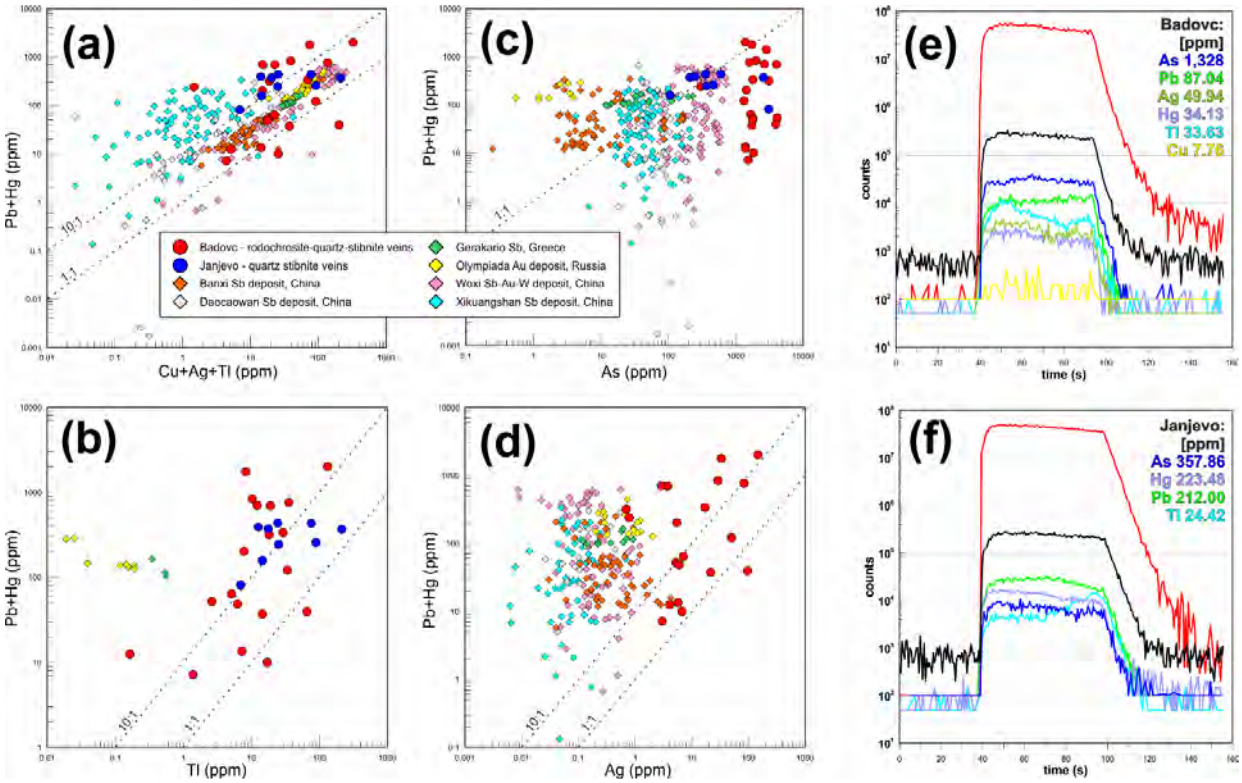

Figure 3. Compositional relationships in stibnite from the KHB ore field compared with available literature data (Fu et al. 2020; 2022; Silyanov et al. 2022; Song et al. 2022; Stergiou et al. 2022) **(a-d)**. Selected time-resolved laser ablation ICP-MS depth profiles of stibnite from Badovc **(e)** and Janjevo **(f)**.

3.2 Analytical techniques

Preliminary chemical analyses of stibnite were carried out by electron microprobe (EPMA) - JEOL Super Probe 8230 in the Laboratory of Critical Elements at Faculty of Geology, Geophysics, and Environmental Protection, AGH-UST, Kraków Poland.

Trace element concentrations in stibnite were measured by laser ablation inductively coupled plasma mass spectrometry (LA-ICP-MS) using a PerkinElmer ELAN DRC-e ICP mass spectrometer combined with a New Wave UP193-FX excimer laser ablation system at the Geological Institute, Bulgarian Academy of Sciences, Sofia, Bulgaria. The ablation was conducted in He medium. To maximize sensitivity, the ICP-MS was optimized daily concerning the oxide production rate of ThO/Th (0.5%). Operating conditions of the laser system include 6 Hz repetition rate; 20 to 35 µm spot size; and energy density on analyzed minerals and standards of 3.3-3.4 J/cm^2 (at 35 µm spot) and 2.9-3.1 J/cm^2 (at 20 and 25 µm spot). The nebulizer gas flow rate was 0.8 L/min, while auxiliary and make-up gas flows rates were 0.92 L/min. The analysis time was 100 s (background: 40 s, laser-on the sample: 60 s). The acquisition dwells time was set to 0.02 s for ^{71}Ga, ^{74}Ge, ^{107}Ag, ^{125}Te, ^{202}Hg, ^{205}Tl; to 0.03 s for ^{115}In, ^{118}Sn; to 0.04 s for ^{197}Au, and 0.01 s for all other monitored isotope masses - ^{34}S, ^{49}Ti, ^{51}V, ^{53}Cr, ^{55}Mn, ^{57}Fe, ^{59}Co, ^{60}Ni, ^{65}Cu, ^{66}Zn, ^{75}As, ^{77}Se, ^{82}Se, ^{95}Mo, ^{111}Cd, ^{121}Sb, ^{181}Ta, ^{182}W, ^{208}Pb, and ^{209}Bi. Targeted spots in the polished sections were predefined to avoid obvious mineral inclusions. Repeated external standardization was conducted by analyzing NIST SRM 610 glass standard and the USGS Mass 1 sulfide standard. Data reduction was undertaken using antimony (determined by EPMA) as an internal standard and by SILLS software (Guillong et al. 2008).

4 Stibnite geochemistry

The main trace elements found in stibnite from the KHB ore field are As, Pb, Hg, Tl, Cu and Ag. Stibnite from both localities shows a similar geochemical signature, although they differ mainly in Cu and Ag content.

Arsenic is the major substituting element in the studied stibnite (Fig. 3c). Higher contents of As are observed in stibnite from Badovc (302–4,100 ppm) - the median is 1,760 ppm, while in Janjevo it is 206–3,080 ppm (median: 368 ppm).

The main divalent elements are **lead** and **mercury**. The medians for lead content are, respectively: 120 ppm for Janjevo and 144 ppm for Badovc. However, individual analyses reach up to 2,000 ppm of Pb with evident homogeneous spectra (Fig. 3e-f). On the other hand, stibnite from Janjevo shows significantly higher Hg contents (45.40–316 ppm; median 102 ppm) than in Badovc (0.53–34.13 ppm; median 6.09 ppm).

Both localities show the presence of **thallium**: in Janjevo the concentrations range 6.94–213 ppm (median 24.42 ppm), and in Badovc 0.16–132 ppm

(median 12.18 ppm) (Fig. 3b). In addition, lower **copper** concentrations are observed, with ranges of 1.08–2.79 ppm (median 1.89 ppm) in Janjevo and 0.69–46.9 ppm (median 7.76 ppm) in Badovc. In addition, stibnite from Badovc exhibits a **silver** concentration between 0.69 and 146 ppm (median 6.30 ppm) (Fig. 3d).

5 Discussion

The mechanisms of trace elements incorporation in stibnite have previously been described by Fu et al. (2020) - $2Sb^{3+} \leftrightarrow Cu^{+} + Pb^{2+} + As^{3+}$, and Song et al. (2022) - $3Sb^{3+} \leftrightarrow As^{3+} + 2Cu^{+} + Hg^{2+} + Pb^{2+}$. Analysis of trace elements in stibnite from the KHB ore field, as well as higher concentrations of some elements such as Ag and Tl, suggests the presence of several independent substitutions in stibnite. In addition, LA-ICP-MS spectra show a homogeneous distribution that suggests the presence of these metals in the stibnite structure rather than inclusions (Fig. 2e-f).

First, the arsenic in the KHB ore field does not correlate significantly with any other trace element, suggesting the presence of a simple $As^{3+} \leftrightarrow Sb^{3+}$ substitution.

Secondly, stibnite from the KHB ore field shows the highest concentrations of other monovalent cations, such as Cu^{+} reported so far, including Tl^{+} (Fig. 3b) and Ag^{+} (Fig. 3d). In addition to the character of the fluids, this is because the rhodochrosite breccia from Badovc and the quartz vein from Janjevo lack typical base-metal sulfides like galena or chalcopyrite, which could preferentially incorporate these elements (Pb, Cu, Ag, Tl).

Copper as in other localities correlates well with Pb (0.82) (Fu et al. 2020; 2022), but is also well correlated with Ag (0.82), while Ag also correlates with Pb (0.57), and no relationship is seen between Ag and Hg (-0.01). These results suggest the presence of heterovalent $(Cu^{+} + Ag^{+}) + Pb^{2+} \leftrightarrow Sb^{3+} + \square$ substitution in stibnite from Badovc. In contrast to other known localities, silver, rather than copper, is more important in this substitution in Badovc.

In addition, stibnite from the KHB ore field shows the highest enrichment in thallium reported in the literature so far (Fig. 3b). The mechanism of thallium incorporation is related to mercury, both metals can be named diagnostic pathfinder elements for Carlin-type gold deposits and are found in numerous hydrothermal sediment-hosted systems. The suggested mechanism for incorporation of Tl and Hg is $Tl^{+} + Hg^{2+} \leftrightarrow Sb^{3+} + \square$. Furthermore, observing the complex graph of Pb+Hg *vs.* Cu+Ag+Tl (Fig. 3a), it is visible that the stibnite from China's sediment-hosted Sb deposits Xikuangshan and Daocaowan does not follow the trend observed in other known deposits caused by $Cu^{+} + Pb^{2+} \leftrightarrow Sb^{3+}$ substitution. Stibnite from these locations has the highest Hg content, even above 100 ppm (Fu et al. 2020; Song et al. 2022), and clearly some not-measured monovalent element is missing - probably thallium, which is very common in such systems.

Investigations on stibnite from the KHB ore field show that at low hydrothermal temperatures stibnite (Badovc: 180-240°C, Janjevo: 230-260°C; Mederski et al. 2022a) can incorporate a wide range of trace elements such as As, Pb, Hg, Tl, Ag, and Cu.

Acknowledgements

The research was funded by the Society of Economic Geologists Canada Foundation (SEGCF) Student Research Grant 2019 and the Society of Economic Geologists Foundation (SEGF) Newmont Mining Corporation Student Grant 2020.

References

Fu S, Hu R, Bi X, Sullivan NA, Yan J (2020) Trace element composition of stibnite: Substitution mechanism and implications for the genesis of Sb deposits in southern China. Appl Geochem 118:104637

Fu S, Wang T, Yan J, Pan L, Wei L, Lan Q, Fu S (2022) Formation of the Banxi Sb deposit in Eastern Yangtze Block: Evidence from individual fluid inclusion analyses, trace element chemistry, and He-Ar-S isotopes. Ore Geol Rev 146:104949

Guillong M, Meier DL, Allan MM, Heinrich CA, Yardley BWD (2008) Appendix A6: SILLS: A MATLAB based program for the reduction of laser ablation ICPMS data of homogeneous materials and inclusions. In: Sylvester P (ed). Laser Ablation ICP–MS in the Earth Sciences: Current Practices and Outstanding Issues. Vancouver, Mineral Assoc Canada, Short Course 40:328–333

Janković S (1989) Sb-As-Tl Mineral Associations in the Mediterranean Region. Int Geol Rev 31:262–273

Mederski S, Pršek J, Dimitrova D, Hyseni B (2021). A Combined EPMA and LA-ICP-MS Investigation on Bi-Cu-Au Mineralization from the Kizhnica Ore Field (Vardar Zone, Kosovo). Minerals 11:1223

Mederski S, Pršek J, Dimitrova D (2022a) Trace elements in sphalerite from the Kizhnica-Hajvalia-Badovc ore field, Kosovo: an example of In-bearing sphalerite. In: The Critical Role of Minerals in the Carbon-Neutral Future 16th Biennial SGA Meeting: Rotorua, New Zealand, 2022. Proceedings Volume 1:239–242

Mederski S, Pršek J, Majzlan J, Kiefer S, Dimitrova D, Milovský R, Bender Koch C, Kozień D (2022b) Geochemistry and textural evolution of As-Tl-Sb-Hg-rich pyrite from a sediment-hosted As-Sb-Tl-Pb±Hg±Au mineralization in Janjevo, Kosovo. Ore Geol Rev 151:105221

Seal RR, Schulz KJ, De Young JH, Sutphin DM, Drew LJ, Carlin JF, Berger BR (2017) Antimony. In: Critical mineral resources of the United States–Economic and environmental geology and prospects for future supply. U.S. Geological Survey, pp. 1–30

Silyanov SA, Sazonov AM, Naumov EA, Lobastov BM, Zvyagina YA, Artemyev DA, Nekrasova NA, Pirajno F (2022) Mineral Paragenesis, formation stages and trace elements in sulfides of the Olympiada gold deposit (Yenisei Ridge, Russia). Ore Geol Rev 143:104750

Song X, Lai J, Xu J, Liu X, Li B, He H, Wang Y, Shi J, Wang C, Wen C (2022) Material Source and Genesis of the Daocaowan Sb Deposit in the Xikuangshan Ore Field: LA-ICP-MS Trace Elements and Sulfur Isotope Evidence from Stibnite. Minerals 12:1407

Stergiou CL, Melfos V, Voudouris P, Papadopoulou L, Spry PG, Peytcheva I, Dimitrova D, Stefanova E (2022) A Fluid Inclusion and Critical/Rare Metal Study of Epithermal Quartz-Stibnite Veins Associated with the Gerakario Porphyry Deposit, Northern Greece. Appl Sci 12:909

Rapid and on-site elemental quantitative analyses using handheld LIBS : the Beauvoir granite case study

Naila Mezoued[1], Cécile Fabre[1], Jean Cauzid[1], Michel cathelineau[1], Christophe Ballouard[1]
[1]GeoRessources CNRS-Université de Lorraine, BP 70239, 54506 Vandoeuvre-les-Nancy, France

Abstract. Acquiring geochemical data during mineral exploration is long and costly. Thus, using portable spectroscopic tools such as a handheld LIBS device to obtain qualitative and quantitative data on-site within seconds represents a breakthrough for the mining industry. In this context, light elements Li and Be as well as trace elements Rb and Cs were targeted to develop quantitative models using a handheld LIBS device. Hole core portions from the Beauvoir granite deposit were analyzed with limited sample preparation to reproduce field conditions. Different normalization methods (SNV, total spectrum area, and internal standard) were assessed to enhance model performances. Both univariate and multivariate approaches were evaluated. The final calibration curve for each element was chosen based on the lowest RMSE obtained. Furthermore, considering the heterogeneous character of rock samples and potential signal fluctuation due to laser or/and plasma fluctuation, the repeatability of the technique was tested using successive LIBS measurements on the same sample.

1. Introduction

One of the key steps to locate potential ore deposits is acquiring reliable geochemical data representative enough to highlight the prevalence of targeted elements across a study area. To do so, samples from outcrops or drilled cores, are prepared and analyzed to determine the whole rock elemental composition. It can take several weeks to months before results are available, which delays considerably effective decision-making and strategy optimization during prospecting.

In this framework, the use of portable spectroscopic devices such pLIBS to develop innovative geochemical methods seems more promising than ever(Senesi and al 2021). The spectral signal obtained provides qualitative both quantitative data in near real-time with minimal sample preparation(Fabre and al 2021; Wise and al 2022). Therefore, beyond field observations, geologists have now the ability to generate valuable geochemical information on the field to optimize rocks sampling, identify geochemical pathfinders, and improve decision-making during field exploration or drilling campaigns. This extended abstract focuses on how to estimate the elemental composition of unprepared core samples, in particular, lithium content using a handheld LIBS device.

2. Methodology

2.1 laser-induced breakdown spectroscopy (LIBS) technique

Similar to a laboratory setup(Miziolek 2006), a handheld LIBS device uses a high-energy laser to vaporize a fraction of the material at the surface of a sample initiating a micro-plasma plume. As the excited atoms, ions, and molecules forming the plasma return to low energy levels, photons are expelled. The emitted light is then collected and processed through detectors and broadband spectrometers. The atomic spectrum obtained records the signal intensity at specific wavelengths. The distinct position of emission lines reveals the elemental composition of a sample while measuring the concentration of these elements requires individual calibration curves.

The specific model used is the Z300 portable LIBS (SciAps) which is characterized by a 1064 nm pulsed Nd-YAG laser that delivers 5-6 mJ per pulse at a repetition rate set at 10 Hz. its spectrometers cover a large spectral band from 190 to 950 nm allowing elements detection from H to U. The analyses are performed at atmospheric pressure and ambient temperature but under constant argon flush to enhance signal intensity. No sample preparation is required except for a relatively flat surface to guarantee signal quality.

2.2 The Beauvoir granite Although the superficial part of the Beauvoir granite was exploited since the 19th for kaolin, it was only in 1985 during the first Geologie profonde de la France (GPF) drilling project that the lithium potential of the unaltered granite was discovered(Cuney and al 1992). This rare metals leucogranite characterized by high Li, Rb, Cs, Nb, Ta, P, and F content is composed mainly of quartz, albite, and Li-rich micas (lepidolite and zinnwaldite) while phosphate minerals, fluorite, topaz, and orthoclase can be found in varied proportions through the magmatic body(Rossi and al 1987). Since GPF, two drilling campaigns were conducted by Imerys. The first one explores the northern, central, and southern parts of the granite. While, the second, more extensive, started in 2021, and will continue till 2023 as part of the EMILI project. The project intend to confirm the economic potential of the deposit for lithium extraction and refine the Beauvoir granite geological model to achieve Imerys provisional plan to start production by 2028.

2.2 Samples

LIBS technique is sensitive to chemical matrix effects (El Haddad and al 2014). thus, to quantify effectively an element, it is recommended to use reference samples of the same matrice composition to calibrate the spectral signal. Hence, to represent best the homogeneous composition of the Beauvoir granite and determine lithium content in hole core portions (Figure 1), 15 granite samples from the 2018 and 2021 drilling campaigns were analyzed as references. The samples selected cover the broad range of lithium concentrations observed in the beauvoir granite, ranging from low (Li < 1000 ppm) to high (Li > 6000 ppm) values. Only unaltered or very low alteration percentage rock samples were considered. The greisen and kaolinized facies, not targeted for lithium extraction, were excluded. To extend the calibration curve to lithium-depleted samples, three more granite samples from massif central containing low grades (70-334ppm) were also included.

2.3 Data acquisition and processing The LIBS analyses were acquired according to a

Figure 1. Major Li emission lines from handheld LIBS spectrum.

vertical profile covering the total length of the core portions, with 1 point placed every

Figure 1. Major Lithium emission lines from the NIST LIBS database.

centimeter. Each point is in fact 36 zones analyzed arranged in a rectangular shape grid (2.7x2.5 mm). The signal obtained for a point corresponds to the average signal of 4 laser shots for each zone. The mean size of a LIBS micro-plasma crater is around 300 um. Thus, Acquiring a significant number of shots per sample allows us to i) reduce any shot-to-shot variability caused by the plasma fluctuation and ii) obtain representative LIBS spectra of the entire sample, especially in heterogenous compositions such as rocks.

The emission lines of the targeted elements were identified using the handheld LIBS spectral database and NIST database. Then, a processing sequence was implemented using Spectragryph 1.3 software to perform individual spectrum baseline correction and extract the peak area at specific spectral intervals. The handheld LIBS software (ProfileBuilder) can be used to generate internal calibration curves accessible on the tool(Fabre 2022). However, due to the large number of data acquired on whole core portions (> 300 points per sample), external regression models were built using statistical computing software. The R-squared (R^2) and root mean squared error (RMSE) were used to evaluate statistically each model.

3. Results and discussion

3.1 LIBS elements detection Using handheld LIBS allows us to detect both major elements (Si, Al, Na, K, and Li) forming most of the Beauvoir granite minerals as well as elements such as Rb, Cs, and Be occuring in smaller amounts. The lithium signal is mostly observed in 4 intervals at 460, 610, 670, and 812 nm (Figure 1). The triple peak at 460 nm appears to be correlated with the highest lithium concentrations.

Rb and Cs, were also investigated, considering their potential to be co-extracted from lepidolite(Zhang 2022), the main Li-bearing mineral in the Beauvoir granite. The atomic emission lines of these elements are mostly visible in the near-infrared region at 779-794 nm for Rb and 852-894 nm for Cs. Since, the average content of Be in the Beauvoir granite is above the detection limit of the LIBS tool, the Be signal could be identified at 225, 569, and 555 nm.

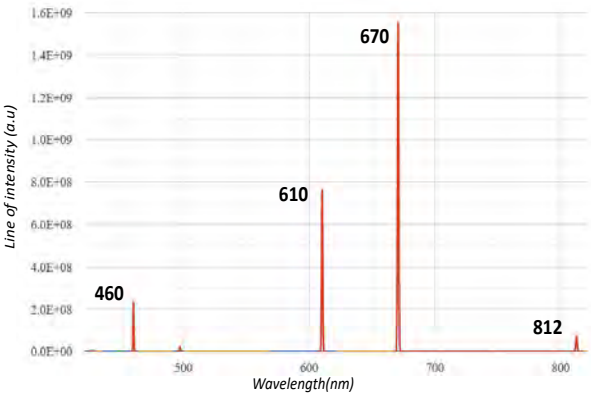

3.2 Quantitative analysis

Figure 2 displays the quantitative models for lithium developed on the Beauvoir granite samples. Multiple approaches were tested (unshown data) either using the sum of lithium signal over the selected emission lines or calculating the ratio of the total lithium signal to the signal of chosen elements on normalized and raw LIBS spectra. Overall, the lithium signal acquired by the LIBS tool correlates linearly with the geochemical data (70 to 7950 ppm) of the reference samples. The results obtained show that the statistical performances of the Li calibration curve (R2=0.95, RMSE=608 ppm) were improved by using Si, Al, Rb, and Mn as internal standards and normalizing the LIBS

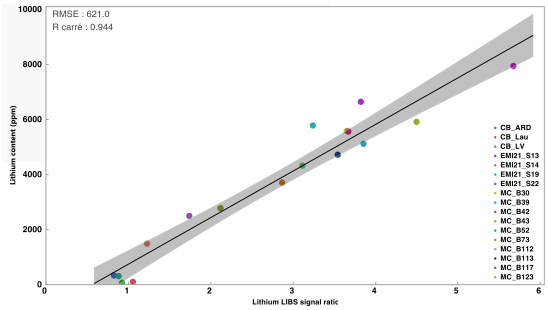

Figure 2. Lithium and Rubidium quantitative models developped using Handheld LIBS analyses.

spectra acquired by the total area of each individual spectrum. Although tested, no distinct improvement was made using multivariate models for lithium quantification.

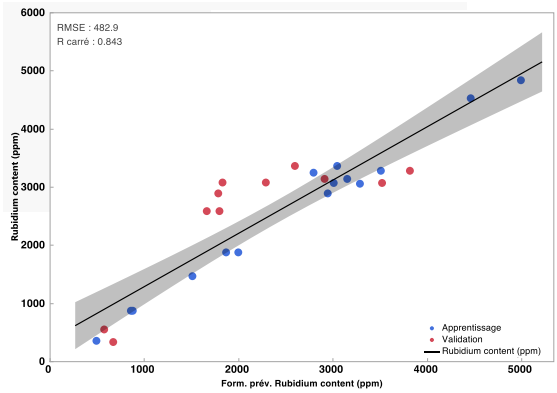

Considering the inhomogeneous character of rock samples, the shift observed on some samples could reflect physical matrix effects such as texture, hardness, or alteration proportion on the ablation process. In fact, work is still going on to determine how specific facies and grain size as well as veins occurrence can impact models prediction.

While the trace elements Rb, Cs, and Be were well detected by the LIBS device, none of the univariate models tested produced robust results, hence multivariate models were implemented to improve the overall quantification performance for these elements. The particular method used is interval PLS regression which allows building models to include multiple explanatory variables by selecting specific spectral intervals. The results illustrate the relation between the actual values of these elements in the reference samples and the predicted values of the multivariate models developed. The best model calculated for Rb includes five components and shows R^2=0.84 and RMSE=482 ppm (Figure 2). For Cs, 6 components were used to obtain R^2=0.89 and RMSE=131 ppm. Beryllium model shows a performance of R^2 =0.99 and RMSE of 4 ppm. Although, Be and Cs models should be completed by further analyses since only a limited number of the overall granite samples were included due to the lack of geochemical data.

3.3 Measures repeatability

One of the challenges of quantitative LIBS analyses is to guarantee a similar signal during separate measurements on the same sample due

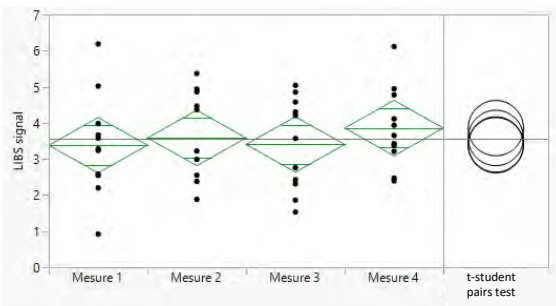

to potential fluctuation of laser or plasma parameters, especially in heterogeneous samples such as rocks. In order to compare the LIBS signal obtained on the same sample, during successive measurements with same portable tool and identical acquisition settings, 4 separate measurements performed at 2 different locations on the granite sample were acquired (Figure 3).

Next, an one way ANOVA test was computed to assess the variation of the LIBS ratio signal normalized at the total area between different measurements.The results obtained for all groups (F-value = 0.33/ p-value = 0.80) and between pairs groups revealed no statistically significant difference in the LIBS signal ratio obtained between the 4 measures on the same sample. This implies that the sampling strategy used which consists of analyzing a consequent number of points organized according to a vertical profile, helps to ensure a reliable LIBS signal during separate measurements of the same sample.

Figure 3. Analysis of variance performed on whole rock signals obtained from 4 separate LIBS measurements acquired on the same granite sample

Conclusion

This work aims to develop analytical methodologies to generate rapid quantitative geochemical data on unprepared core samples during mineral prospection. For this purpose, the handheld LIBS, which can detect both light and heavy elements, was used to build quantitative models to predict the concentration of light elements Li and Be as well as trace elements Rb and Cs. Reference samples were selected from the targeted deposit, the Beauvoir granite, in order to limit chemical matrix effects. Depleted granite samples from massif central were also analyzed to cover low-concentration values. Considering the heterogeneous character of granite samples, multiple analysis points were acquired then averaged to obtain a representative LIBS signal over 4m core portions. Both, Univariate and multivariate analyses were applied on normalized (total area spectrum, SNV, internal standard) and raw LIBS spectra to assess the most statistically robust model for each element. Finally, the evaluation of separate measurements of the same sample reveals no statistically significant difference between the mean LIBS signal ratio obtained on the same sample. Overall, LIBS demonstrate great potential to generate rapid and reliable geochemical data on unprepared granite sample to support-effective decision-making during exploration campaigns on potential ore deposits.

Acknowledgments

We would like to acknowledge Imerys and LabEx RESSOURCES 21 [ANR-10-LABX-21-01] for providing financial support to this study. M.Cathelineau and C.Ballouard for providing a number of the granite samples analyzed and the related geochemical data.

References

Cuney, M., Marignac, C., Weisbrod, A., 1992. The Beauvoir topaz-lepidolite albite granite (Massif Central, France); the disseminated magmatic Sn-Li-Ta-Nb-Be mineralization. Economic Geology 87, 1766–1794. https://doi.org/10.2113/gsecongeo.87.7.1766

El Haddad, J., Canioni, L., Bousquet, B., 2014. Good practices in LIBS analysis: Review and advices. Spectrochimica Acta Part B: Atomic Spectroscopy 101, 171–182. https://doi.org/10.1016/j.sab.2014.08.039

Fabre, C., Ourti, N.E., Ballouard, C., Mercadier, J., Cauzid, J., 2022. Handheld LIBS analysis for in situ quantification of Li and detection of the trace elements (Be, Rb and Cs). Journal of Geochemical Exploration 236, 106979. https://doi.org/10.1016/j.gexplo.2022.106979

Fabre, C., Ourti, N.E., Mercadier, J., Cardoso-Fernandes, J., Dias, F., Perrotta, M., Koerting, F., Lima, A., Kaestner, F., Koellner, N., Linnen, R., Benn, D., Martins, T., Cauzid, J., 2021. Analyses of Li-Rich Minerals Using Handheld LIBS Tool. Data 6, 68. https://doi.org/10.3390/data6060068

Miziolek, A.W., Palleschi, V., Schechter, I., 2006. Laser Induced Breakdown Spectroscopy. Cambridge University Press.

ROSSI, P., AUTRAN, A., BURNOL, L., CUNEY, M., OHNENSTETTER, D., MONIER, C., PIANTONE, P., RAIMBAULT, L., VIALLEFOND, L., 1987. Logs pétrographiques et géochimiques du granite de Beauvoir dans le sondage Echassières I. Minéralogie et géochimie comparées. Géol. Fr 111–135.

Senesi, G.S., Harmon, R.S., Hark, R.R., 2021. Field-portable and handheld laser-induced breakdown spectroscopy: Historical review, current status and future prospects. Spectrochimica Acta Part B: Atomic Spectroscopy 175, 106013. https://doi.org/10.1016/j.sab.2020.106013

Wise, M.A., Harmon, R.S., Curry, A., Jennings, M., Grimac, Z., Khashchevskaya, D., 2022. Handheld LIBS for Li Exploration: An Example from the Carolina Tin-Spodumene Belt, USA. Minerals 12, 77. https://doi.org/10.3390/min12010077

Zhang, X., Chen, Z., Rohani, S., He, M., Tan, X., Liu, W., 2022. Simultaneous extraction of lithium, rubidium, cesium and potassium from lepidolite via roasting with iron(II) sulfate followed by water leaching. Hydrometallurgy 208, 105820. https://doi.org/10.1016/j.hydromet.2022.105820

Pyrite analysis enhanced by dimensionality reduction: investigating texture, trace elements, and sulphur isotope signatures in the Kibali gold district, DRC.

Yann Mpaka Waku[1, 2, 3], Bjorn P. von der Heyden[1], Gary Hurst[2], David Lawrence[2], Etienne Mwandale[2], Sarah Glynn[4, 5]

[1] Department of Earth Sciences, Stellenbosch University, South Africa
[2] Barrick Gold Corporation, Toronto, ON, Canada
[3] Department of Geosciences, University of Kinshasa, DR Congo
[4] School of Geosciences, University of the Witwatersrand, Johannesburg, South Africa
[5] GFZ German Research Centre for Geosciences, Potsdam, Germany

Abstract. Pyrite is the most abundant sulphide mineral in the various ore zones hosted within the world-class Kibali gold district. Because of its affinity for trace elements and gold incorporation, pyrite mineral chemistry is increasingly being used as a powerful tool to assess the characteristics of ore formation. This study presents a novel dimensionality reduction-based approach for pyrite classification. This approach incorporates the strengths of both Uniform Manifold Approximation and Projection (UMAP) and Principal Component Analysis (PCA) with k-Means clustering to analyse the large trace element datasets derived from in-situ laser ablation inductively coupled plasma mass spectrometry (LA-ICP-MS) including sulphur isotope from Secondary Ion Mass Spectrometry (SIMS). The results suggest that 8 clusters may be defined from the pyrite mineral chemistry signatures. This clustering served to direct a refined classification relative to the initial textural analysis. We anticipate that our approach may be adopted by other workers who wish to disentangle complex pyrite growth and gold mineralisation histories in a variety of geological contexts.

1. Introduction

Archean greenstone belts are well-known metallogenic settings known for hosting a significant number of orogenic gold deposits (e.g. Kalgoorlie, Kurnalpi, Pilbara, Abitibi, Barberton, Kibalian, and others). Deciphering the timing and mechanisms of gold mineralisation within these belts is a non-trivial task, given that they have commonly experienced protracted and complex geological histories. Increasingly, studies are utilising pyrite trace element signatures as one of the suites of tools to better understand the conditions giving rise to ore formation. The utility of pyrite mineral chemistry is ensured by its ubiquity within orogenic gold deposits (where auriferous pyrites commonly represent a significant ore mineral), and by its propensity to incorporate a range of trace elements into its mineral structure. Laser-Ablation Inductively Coupled Plasma Mass Spectroscopy (LA-ICP-MS) is increasingly applied as the analytical tool of choice, especially when coupled to traditional microscopy investigations that detail the pyrite mineral textures. The power of LA-ICP-MS approaches is that they can quantify the concentration of multiple elements simultaneously at a spatial resolution as small as 15 µm and in either spot or mapping mode. The large and rich datasets that emanate from LA-ICP-MS studies are highly amenable to further detailed investigation using dimensionality reduction and 'big data' techniques.

The Kibali gold district, located in the Congo Craton, comprises a number of deposits with a total Au endowment of greater than 23 Moz (Allibone et al. 2020). Within these deposits, Au is hosted primarily (~90%) in auriferous pyrite (Lawrence 2011; Bird 2016; Allibone et al. 2020). Therefore, a careful investigation of pyrite would provide a significant opportunity to investigate the genesis of gold mineralisation in this district. This study aims to provide further insight into the textures, trace elements, and sulphur isotope characteristics of pyrite in the Kibali gold district using LA-ICP-MS and Secondary Ion Mass Spectrometry (SIMS) analyses. We developed a new combination of dimensionality reduction methods, comprising Uniform Manifold Approximation and Projection (UMAP) and Principal Component Analysis (PCA) with k-Means clustering to classify and analyse trace elements in pyrites. Our work thus highlights the benefits of dimensionality reduction in mineral chemistry analyses and highlights its utility towards improving pyrite trace element classification and interpretation.

2. Regional and local geology

The Kibalian Moto greenstone belt is located in the Neoarchean northeastern Congolese Congo Craton (Fig. 1a). The belt comprises volcanosedimentary rocks deposited from before 2640 Ma until ~2625 Ma (Allibone et al. 2020). The central part of the Moto greenstone belt is the most gold endowment zone, where several deposits and prospects are aligned within the ca. 60 km boundary belt structure known as the "KZ trend".

The Karagba-Chauffeur-Durba (KCD) deposit contains 85 to 90% of the current gold resources in the Kibali Gold Mine permit. The deposit (Fig. 1b) is hosted by metamorphosed volcanosedimentary rocks and is characterised by large hydrothermal alteration. The pre-ore stage ACSA-a alteration —

an acronym for "Albite, Carbonate, Silica, Alteration" with -a indicating less destructive alteration and -b denoting total destruction of the original rock texture—occurred during the tight to the isoclinal folding event, while the ore-stage exhibits a quartz-carbonate-sulphides-gold paragenesis associated with the more texturally damaging ACSA-b alteration (Lawrence 2011; Bird, 2016; Allibone et al., 2020). The mineralisation penetrates and replaces the siliclastic rocks, BIF, and chert host rocks lithologies, typically manifesting as fine disseminations or cm to mm-sized sulphide veins. Recent studies suggest the possibility of pre-metamorphic gold mineralisation in the KCD area, as gold grains in conglomerate units were found to be larger in size and to occur mainly within the gangue mineral assemblage as free gold, distal to sulphide minerals (Mpaka et al. submitted).

Apart from the KCD deposit and its peripheral deposits (Gorumbwa, Kombokolo, Rhino and Agbarabo), the Pakaka-Tete Bakangwe and Kalimva deposits were also considered in this study. The latter deposits are located respectively towards the northeast and northwest of the KCD deposit along the regional KZ trend (Fig. 1b). The geology is divided into two sequences: the hanging wall consisting of metamorphosed and altered basalt and volcaniclastic and the footwall comprising immature gritstone, sandstone, minor pebbly conglomerate, and BIF (Allibone et al. 2020). Gold mineralisation at Pakaka and Kalimva is found within a km-scale shear zone, while at Tete Bakangwe and KCD, folded footwall rocks are the main host for mineralisation (Allibone et al. 2020).

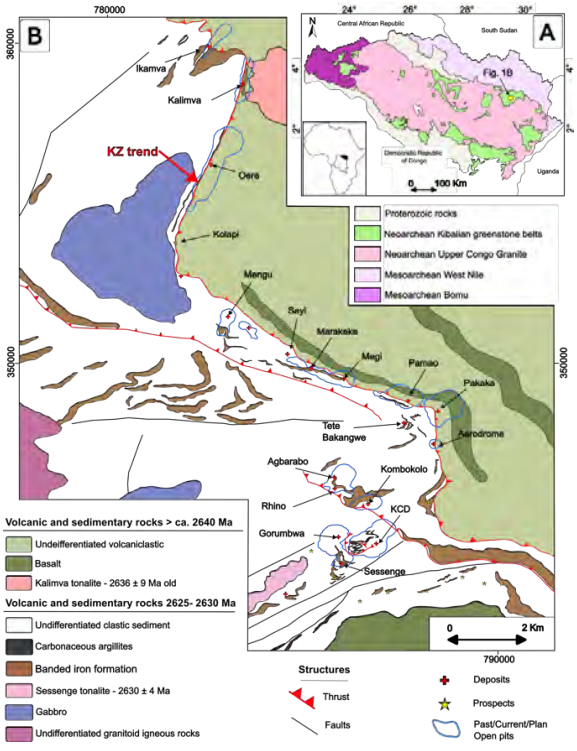

Figure 1. Summary geologic map of: (A) northeastern Congolese Congo Craton and (B) Kibali gold district. Modified after Bird (2016) and Allibone et al. (2020).

3. Methods

A total of 91 samples were collected from 26 diamond drill holes at eight deposits. 101 Polished sections were prepared, and 12 samples were selected for trace element analyses. Scanning Electron Microscopy (SEM) analyses at the Central Analytical Facility in Stellenbosch University were conducted on carbon-coated mounts using Zeiss EVO MA15VP with an OXFORD INCA Electron Dispersive Spectrometer (SEM-EDS) and Wavelength Dispersive Spectrometer (WDS). LA-ICP-MS at the Central Analytical Facility in Stellenbosch University was used for trace element analyses of pyrite, with monitored isotopes including ^{34}S, ^{47}Ti, ^{51}V, ^{52}Cr, ^{55}Mn, ^{57}Fe, ^{59}Co, ^{60}Ni, ^{63}Cu, ^{66}Zn, ^{69}Ga, ^{71}Ga, ^{72}Ge, ^{75}As, ^{77}Se, ^{95}Mo, ^{107}Ag, ^{111}Cd, ^{115}In, ^{118}Sn, ^{121}Sb, ^{128}Te, ^{133}Cs, ^{139}La, ^{157}Gd, ^{182}W, ^{197}Au, ^{202}Hg, ^{205}Tl, ^{208}Pb, and ^{209}Bi. The study also used SIMS to measure the $\delta^{34}S$ sulphur isotope composition in a different pyrite generation within six samples. The SIMS analyses were conducted using the virtual SIMS facility at the University of the Witwatersrand, which is connected via an internet-based link to the Cameca 1280-HR instrument located at the Helmholtz Zentrum Potsdam in Germany.

4. Results

4.1. Pyrite textures

Five main types of pyrite have been identified in samples from the Kibali Gold District based on occurrence, grain size, morphology, and detailed textural analysis (Fig. 2). Pyrite-0 (Fig. 2a) is microcrystalline and occurs in the Kalimva deposit. Pyrite-1 (Fig. 2b) is small and commonly found along phyllosilicate mineral foliation. Pyrite-2 (Fig. 2c) appears as euhedral to subhedral grains with a core-rim texture (core = py-2a, core with inclusions = py-2b, homogeneous rims = py-2c, and zoned rims with arsenic-rich bands = py-2cz, Fig. 2d). Pyrite-3 (Fig. 2e) occurs as massive pyrite-veinlets and often replaces pyrrhotite. Pyrite-4 (Fig. 2f) is characterised by large pyrite grains and often occurs as isolated grains in the matrix or within quartz veins.

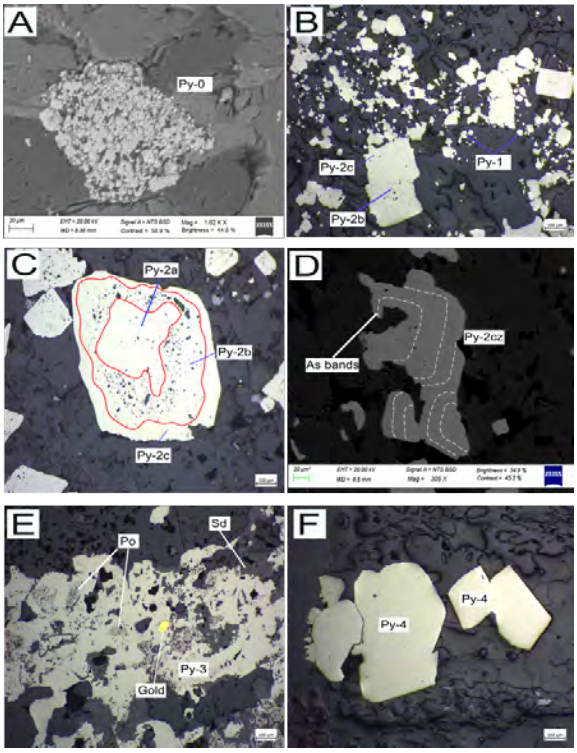

Figure 2. BSE and reflected light photomicrographs from the Kibali Gold district show different pyrite types' textural characteristics. A. Fine microcrystalline grains of pyrite (py-0). B. Disseminated fine-grained py-1 and coarse-grained py-2. C. Subhedral pyrite grain showing core-rim texture with core free-inclusion (py-2a) rimmed by rich-inclusion pyrite (py-2b) and surrounded by free-inclusion pyrite (py-2c). D. Subhedral core-rim pyrite with As-rich bands zonation (py-2cz). E. Irregular pyrite veinlet (py-3) replacing pyrrhotite and replaced by siderite. F. Coarse euhedral to subhedral poor-inclusion pyrite (py-4) grains. Abbreviations: Py: pyrite; Po: pyrrhotite; Au: gold; Sd: Siderite

4.2. Multivariate statistical analyses of trace elements

Using a dataset of 310 individual chemical measurements, distinct clusters were determined using the UMAP algorithm (Fig. 3). The data reduction process was performed using ioGAS software. The k-Means algorithm yielded 8 clusters, which is 68% different from the classification obtained visually (Fig. 3a, b). Furthermore, PCA analysis supports different groups with specific trace element vectors. The findings indicate a negative correlation between PC1 and Se, Ni, Co ± Ge, which are typically found in conjunction with py-4b and py-2c. Conversely, Pb and Sb exhibit a positive correlation with PC1. The dominant positive contributors to PC2 are W, Cr, and V, which are spatially linked with py-0, py-1, py-2a, and py-2b. On the other hand, Bi, Ag, Au, and Cu are part of a negative vector group associated with PC2, which is spatially linked with py-2cz (Fig. 3c, d).

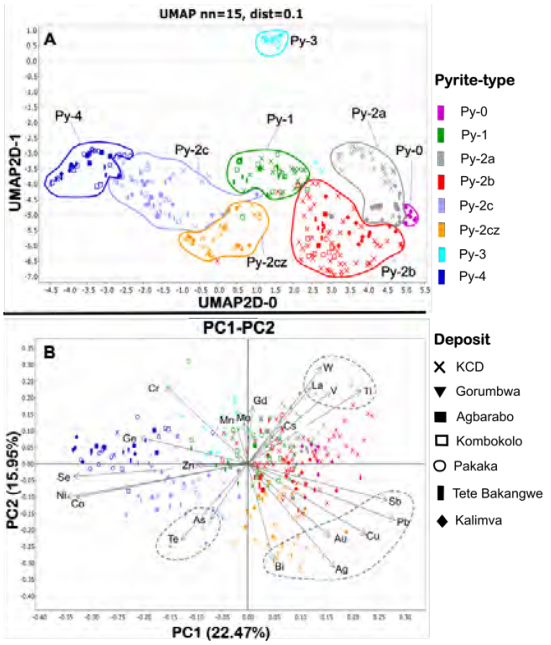

Figure 3. Selected bivariate plots of UMAP and PCA. A. 2D UMAP projection plot with sample grouping using K-means clustering (K = 8). B. PCA plot with trace elements against pyrite types.

4.3. Trace element patterns and maps

The trace element analyses indicate significant differences among the pyrite types. Py-4, py-2c, and py-3 show depleted gold content, while py-0, py-1, py-2b, and py-2cz exhibit a higher concentration of gold. Arsenic displays low concentrations in py-3 and high values in other types, with py-0 having the highest median value. Py-4 and py-2c contain significant amounts of Co and Ni, respectively, with varying distributions across the Kibali district.

LA-ICP-MS elemental mapping was performed on seven pyrite grains from various deposits in the Kibali gold district. The spatial distribution pattern of trace elements in pyrite-2 grains from KCD and Tete Bakangwe are similar. Py-2a (cores) hosted in barren quartz-carbonate altered BIF protolith have low concentrations of most elements, except for Co, Ni, Mn, Cu, Cr, Zn, and As, which are concentrated in the outer zone. Py-2b (cores with inclusions) have elevated levels of Au, As, Bi, Cr, Cu, Gd, La, Mn, Pb, Sb, Ti, V, W, and Zn, while py-2c (homogenous rims) is relatively enriched in Co, Ni, Se, and Te in the outer zone.

4.4. Sulphur isotopes of pyrite

The $\delta^{34}S$ values of pyrite were analysed at 60 spots, ranging from -0.05 to 7.65‰ with a mean of 3.34‰ (stdv=1.89). The py-0 (n=6) ranged from 0.56 to 1.85‰, while py-1 (n=3) yielded values between 2.27 and 2.61‰. Py-2 exhibited a wide range, with py-2a ranging from 2.21 to 2.75‰, py-2b (n=20) ranging from -0.05 to 5.41‰, py-2c (n=14) ranging from 1.65 to 5.78‰, and py-2cz

(n=6) ranging from 5.36 to 7.65‰. Py-3 (n=7) ranged between 3.15 and 4.64‰.

5. Preliminary discussion and conclusions

Orogenic gold deposits formed during the Precambrian era exhibit a complex evolution that involves multiple stages of metamorphism, ductile to brittle deformation, and cycling of ore fluids (Pitcairn and Goldfarb, 2022). Determining the timing of gold incorporation in sulphides can be challenging in these deposits due to the overlapping later stages of deformation. This phenomenon was observed in the Kibali gold district, where pyrite displayed a wide degree of grain size and morphology variation.

The discrimination of the different pyrite generations by applying new dimensionality reduction methods to the trace element data combined with sulphur isotope analyses has allowed us better to constrain the evolution of mineralisation in the Kibali district. Importantly, consideration of the pyrite trace element signatures in multi-parameter space has assisted in refining the pyrite classification relative to the initial textural classification. Thus, the PC graphs help show the spot analyses' multivariate nature. This allows for a data description and straightforward interpretation that is not possible using the basic statistics.

These mineral chemistry, sulphur isotope and textural insights help to develop and constrain the genetic model for the various pyrite generations in the Kibali gold district. The fine-grained and nodular texture and the elevated trace element content of the py-0 generation suggest an early sedimentary origin with S isotope composition averaging 1.39‰ (e.g., Large et al. 2009), likely by rapid formation within the pore waters in a basaltic-volcaniclastic basin. The py-1, py-2a and py-2b generations show distinctive similarities in their trace element behaviour, notably showing correlation with the elements V, La, Ti and Cr. These signatures may be related to micro to nanoscale inclusions, an insight which is supported by SEM analyses. These siderophile elements suggest that the pyrite may have formed by the interaction between a fluid and oxide minerals such as magnetite. Sulphidation reactions such as these are commonly observed in the banded iron formation units of the Kibali district. The py-3 generation has chemical signatures most strongly correlating with Mn, Zn and Mo and particularly the Mn content may suggest that this generation forms by carbonate replacement, again a phenomenon that is common in the alteration haloes of orogenic gold deposits. The most auriferous pyrites are py-2cz which show high Ag, Ag, As, Bi, Cu, Pb, Sb and Te, and which also have the highest sulphur isotope signature. This is likely to represent the ore fluid. Py-4 has high Co, Ni and Se content which may derive from interaction between fluid and more mafic lithologies. This generation is paragenetically late and postdates the mineralisation event.

To summarise, the application of dimensionality reduction methods not only facilitates improved pyrite classification based on their chemistry but also aids in interpreting their genesis. This research outcome can substantially enhance the accuracy of differentiating between pyrite types in diverse geological settings. Our investigation establishes a groundwork for potential dimensionality reduction-based research on trace element incorporation in minerals, extending beyond pyrite. This technique may advance our comprehension of mineral formation mechanisms, which is pivotal in succeeding in mineral exploration.

1 Acknowledgements

The authors would like to thank Barrick Gold Corporation for their financial support and for granting access to data. The valuable contribution of Frédéric Couffignal in assisting with the SIMS analyses is much appreciated. Mrs. Madelaine Frazenburg, Dr. Alicia Botes and Mrs. Riana Rossouw are acknowledged for their assistance during the SEM and LA-ICP-MS analyses. Furthermore, the authors express their gratitude to the Kibali geologists for their helpful assistance and constructive discussions.

2 References

Allibone, A., Vargas C., Mwandale E., Kwibisa J., Jongens R., Quick S., Komarnisky N., Fanning M., Bird P., MacKenzie D., Turnbull R., Holliday J. (2020): Orogenic Gold Deposits of the Kibali District, Neoarchean Moto Belt, Northeastern Democratic Republic of Congo, Society of Economic Geologists, SEG Special Publications, no. 23, pp. 185–201.

Bird, P.J., (2016): Evolution of the Kibali Granite-Greenstone Belt, North East Democratic Republic of the Congo, and Controls on Gold Mineralisation at the Kibali Gold Deposit. PhD, Kingston University London. 325p.

Groves, D.I., Goldfarb R.J., Robert F., Hart C.J. R. (2003): Gold Deposits in Metamorphic Belts: Overview of Current Understanding, Outstanding Problems, Future Research, and Exploration Significance Economic Geology. Vol. 98, pp. 1–29.

Large, R.R., Maslennikov, V., Robert, F., Danyushevsky, L.V., and Chang, Z., (2007): Multistage sedimentary and metamorphic origin of pyrite and gold in the giant Sukhoi Log deposit, Lena gold province, Russia: Economic Geology, v. 102, p. 1232–1267.

Lawrence, D.M. (2011): Petrographic Studies on the Kibali Gold Deposit, NE Democratic Republic of Congo: D. Lawrence 2011 Sample Suite. Unpublished Kibali internal report, Kingston University London, 21 p.

Mpaka Y.W, von der Heyden B.P, Bampata T., Luzolo F.N, Mwandale E. (submitted): Gold characteristics in the conglomeratic units of the mineralised Archean Moto Greenstone Belt, DRC.

Pitcairn I. and Goldfarb R.J. (2022): Orogenic gold: is a genetic association with magmatism realistic? Mineralium Deposita 58, 5–35.

Phytoremediation, a less costly prospect for tailings rehabilitation

Phumudzo G. Munyai[1], Humbulani R. Mundalamo[1], Jason S. Ogola[1], Luke Chimuka[2]
[1]Department of Earth Sciences, University of Venda, Private Bag X5050, Thohoyandou, 0950, South Africa
[2]Department of Environmental Analytical Chemistry, Wits University, Private Bag 3, Johannesburg, 2050, South Africa

Abstract. Gold mine waste is considered as the major source of toxic metals in the environment however these toxic metals can be removed from the mine waste, soil and water by a process called phytoremediation which involves the use of plants to remove and immobilize toxic metals. A mineralogical characterization was conducted at Klein Letaba tailings storage facility (TSF) to quantify the presence of metals. Previous studies revealed an abundance of metals such as Pb, Cr, Ni and As. However, the extent of remediating metals from the TFS has not been adequately investigated in the Giyani Greenstone Belt (GGB). The TSF mainly comprises high metal concentrations of Pb, Ni, As and Cr. Plants and tailings were seasonally collected on the TFS for chemical and mineralogical characterization. XRF and ICP-OES analysis revealed the metal concentrations and distribution. The focus of the study was to investigate the potential of metal extraction from native plant species growing on the mine TSF which could not be extracted by the mine using physical-chemical techniques.

1 Introduction

The Giyani Greenstone Belt is known for its gold mineralisation, and it has been exploited at Klein Letaba, Louis Moore, Birthday, Golden Osprey and Fumani mines (Weilers 1956). All these mines are closed but the metals within their respective TSF can cause environmental and health problems.

Mining operations produce different sorts of wastes, frequently in huge amounts. The vast majority of these wastes are discarded into surface facilities, making extensive structures that require exploration and support to guarantee their long load solidness (Karlsson et al. 2014). Metals are essential in living organisms at lower concentrations and as such when they are absent living organisms suffer from deficiency, alternatively when these metals are available in excess concentrations, they result in being toxic to both human health and the surrounding environment (Sabine 2009). Large amounts of waste have been generated and mobilized due to mining, agricultural and industrial activities.

Tailings are a by-product of the gold mining industry, and the discharge of this waste material can have a significant environmental impact. To reduce this impact, phytoremediation has been proposed as an effective and economically viable method for removing metals from gold mine tailings (Peer et al. 2005). Both metal and non-metal mining activities generate huge quantity of waste rocks, which damages the aesthetics of the area. Particularly, in case of metal mining, activities such as crushing, grinding, washing, smelting and all the other process used to extract, concentrate metals, generate a large amount of waste rocks and tailings which scars the landscape, disrupts the ecosystems, and destroys microbial communities. Waste materials that remain after the extraction of usable ores are dumped on the surrounding land, which is the sources of toxic metals, leave the land devoid of topsoil, nutrients and supportive microflora and vegetation, thus remains barren (Mukhopadhyay and Maiti 2010).

Phytoremediation efforts have largely focused on the use of plants to accelerate the degradation of organic contaminants, usually in concert with root rhizosphere microorganisms, or remove hazardous metals from the soil and water (Peer et al. 2005). Phytoremediation of contaminated sites is a relatively inexpensive and aesthetically pleasing to the public compared to alternate remediation strategies which involve excavation or chemical in-situ stabilization. This is one of the best remediation strategies for metal extraction and stabilisation of the mine tailings using native plant species (Peer et al. 2005).

The Giyani Greenstone Belt (GGB) situated in the north-eastern part of the Limpopo Province in South Africa is home to abandoned mine sites. These mine sites are a constant danger to nearby communities due to the risks associated with tailings dam, disused mine shafts, pit lakes and dilapidated mine buildings (Mhlongo et al. 2020).

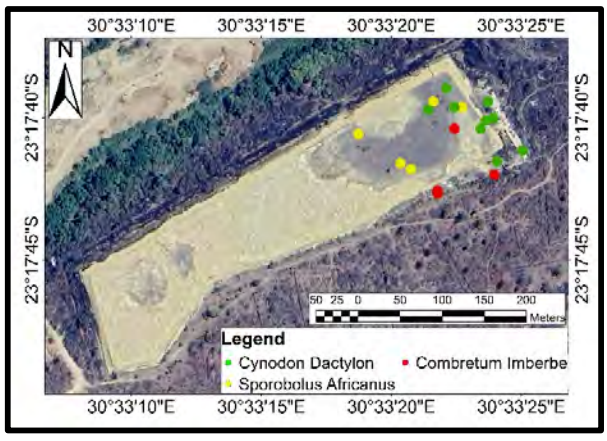

Figure 1. Sample locations of native plant species growing on the TSF for summer 2020.

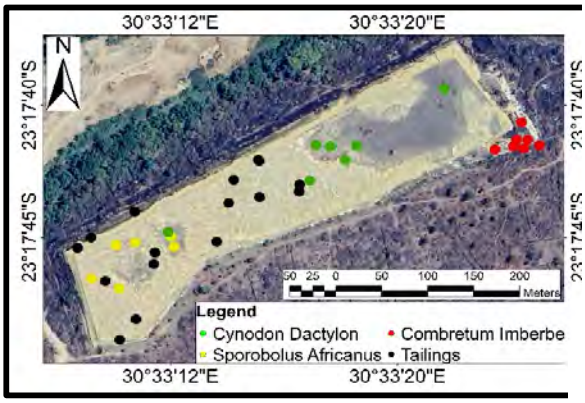

Figure 2. Sample locations of native plant species growing on the TSF for winter 2021.

A. Combretum imberbe *B. Cynodon dactylon* *C. Sporobolus africanus*

Figure 3. Dominant plant species growing on the TSF.

2 Methodology

A total of 80 plants and tailings samples were randomly and seasonally collected at Klein Letaba TFS for metals concentration analysis as part of the feasibility study. 5 ccontrol samples were collected away from the mine site but within similar geological setting. This helped during comparative study to ascertain that these metals are indeed extracted from the mine due to anthropogenic activities. The metal concentration results from the reconnaissance study were used to develop evidential uptake of the dominant plants in the study area.

Each composite sample was split into two representative aliquots for chemical and mineralogical analysis. The first aliquot was analysed using X-ray fluorescence spectrometry (XRF) at University of Venda Mining and Environmental Geology laboratory and the second aliquot was digested using microwave digestion technique at University of Venda Hydrology and Water Resources laboratory then sent out to Madzivhandila Agricultural Centre for Inductively coupled plasma optical emissions spectrometry (ICP-OES) analysis.

3 Results

3.1 Identification of native plant species

Three dominant plant species growing and thriving well were identified growing on the TSF: *Combretum imberbe, Cynodon dactylon and Sporobolus africanus*. These plant species were found to be hyperaccumulators of Pb and Ni (> 1000 mg kg^{-1}) because they were able to uptake and translocate metals from the roots to the shoot then leaves.

3.2 Geochemistry of Klein Letaba TSF

Major trace elements were identified namely, Pb, Cr, As, Ni, Cu and Co in their order of abundance indicates the distribution and dispersion of metals across the study area. A high geochemical signature across the entire area was revealed high to moderate concentrations.

3.3 Metal concentrations of plants: summer season

Pb (KLT1S14) recorded 1700 mg kg^{-1} on the and Ni (KLT1S14) recorded metal concertation of 1101.03 mg kg^{-1} on the roots for the Combretum imberbe plant, whereas Pb (KLT1S1) had concentration of 1525.8 mg kg^{-1} on the roots and 1204.3 mg kg^{-1} on the stem. These values exceed the ground tissues in concentration which are present in the soil (Baker and Brooks 1989).

Table 1. Metal concentrations of plants on different parts during summer (wet) season where red denotes high concentrations and yellow indicates intermediate concentrations.

SAMPLE ID	Pb (mg/kg)	Ni (mg/kg)	As (mg/kg)	Zn (mg/kg)	Cu (mg/kg)	Co (mg/kg)	Cr (mg/kg)	Cd (mg/kg)
KLT1S14 ROOT	1700,71	1101,03	511,25	80,41	25,12	16,12	510,1	0,01
KLT1S14 STEM	980,33	507,14	90,87	23,04	15,85	9,4	358,23	0
KLT1S14 LEAF	750	810,23	305,25	62,35	18,32	13,3	200,61	0
KLT1S22 ROOT	2307,25	1407	984,04	62,7	20,04	10,01	609,32	0,01
KLT1S22 STEM	1150	670,02	270,02	15,32	12,01	5,23	460,1	0
KLT1S22 LEAF	810	890,36	547,01	54,1	17,24	8,11	216,45	0
KLT1C1 ROOT	11,1	58	1,5	15,5	2,1	1,1	48,3	0,01
KLT1C1 STEM	9,2	23,1	0,5	8,4	0,8	0,2	35,8	0
KLT1C1 LEAF	2,9	37,1	1,1	10,2	1,6	0,9	22,5	0
KLT1C2 ROOT	12,3	52,2	2,1	23,4	16,7	2,2	36,5	0,01
KLT1C2 STEM	8,2	15,3	1,3	115	10,4	1,1	29,4	0
KLT1C2 LEAF	6,4	25,4	1,6	15,4	12,2	2,1	21,6	0,01
KLT1S1 ROOT	1525,8	754,6	741,2	95,1	25,2	13,7	740,5	0,1
KLT1S1 STEM AND LEAF	1204,3	521,4	245,6	114,23	14,03	4,65	314,8	0,01
KLT1S5 ROOT	513,2	60,1	56,7	52,2	16,1	25,6	241,8	0,1
KLT1S5 STEM AND LEAF	250,1	24,5	32,4	58,1	9,4	15,9	65,7	0,01
KLT1S15 ROOT	1370,9	1230,7	580,8	123,5	78,5	12,4	873,96	0,01
KLT1S15 STEM AND ROOT	750,4	780,6	350,7	260,9	50,6	3,5	563,58	0

Table 1 shows that uptake of metals by *Combretum imberbe, Cynodon dactylon* and *Sporobolus africanus* was following the order roots>stem>leaves. The uptake was high on the *Combretum imberbe* plant as compared to the grass species (*Cynodon dactylon* and *Sporobolus africanus*).

3.4 Metal concentrations of plants: winter season

During winter season, the order of abundance of uptake shows that the leaves have high metal concentration followed by the stem then the roots (Table 2) whereas the grass species (*Cynodon dactylon*) the concentration is high in roots followed by the shoot.

Table 2. Metal concentrations of plants on different parts during winter (dry) season

Sample ID	Name	Cr (ppm)	Cu (ppm)	Co (ppm)	Ni (ppm)	Pb (ppm)	Zn (ppm)	Mn (ppm)	Fe (ppm)
KLP1S1S	Shoot	3.878	2.175	1.337	0.425	3.502	1.327	315.9	172.2
	Root	3.589	2.180	1.262	0.040	3.573	0.370	200.50	31.99
KLP1S4S	Shoot	3.522	2.250	1.212	0	3.458	0.996	128.9	59.57
	Root	3.309	2.339	1.155	0	3.476	0.274	78.10	103.8
KLP2S1S	Shoot	3.571	2.172	1.158	0.621	3.437	1.915	333.9	185.2
	Root	3.781	2.461	1.960	1.990	3.525	2.589	259.4	209.9
KLP3S2C	Shoot	3.552	2.345	1.722	0.183	3.299	1.049	99.55	166.2
	Root	4.006	3.252	1.994	5.989	3.335	7.381	255.1	200.1
KLP3S4C	Shoot	3.505	2.338	1.628	0	3.488	1.424	112.8	72.48
	Root	2.690	2.207	1.598	0	3.702	1.242	93.84	53.24
KLP3S7C	Shoot	1.965	2.250	1.683	0	3.733	1.261	153.2	149.5
	Root	2.318	2.173	1.726	2.854	3.778	7.270	208.1	210.2
KLP4S1Cl	Leaves	2.261	2.114	1.567	0	3.00	0	55.3	26.88
	Stem	2.384	2.373	1.810	1.479	3.167	1.733	65.59	45.87
	Root	2.481	2.487	2.013	4.053	3.743	18.09	50.43	136.2
KLP4S3Cl	Leaves	2.110	2.063	2.533	0.524	3.071	7.167	55.3	156.3
	Stem	2.206	2.055	2.375	3.089	3.639	7.140	57.96	106.7
	Root	1.990	2.899	2.134	3.120	3.572	10.75	69.86	125.6
KLP4S5Cl	Leaves	1.775	1.886	2.464	0.909	3.021	6.402	292.5	195.2
	Stem	1.223	1.817	2.309	8.523	3.067	2.384	0	14.24
	Root	1.409	1.862	2.294	0	2.864	0.244	0	13.92
KLP4S7	Leaves	1.429	1.891	2.418	0.842	3.394	3.193	104.9	125.5

Table 2 shows very little up to no concentrations at all due to the fact that the plants are dormant during winter season. The leaves accumulate more concentration, bind and die then re-circulate the metals in leaves and metals in soil in the same location. Rate of metal uptake during winter season is very little and previous studies revealed that the plants tend to uptake more nutrients in wet seasons as compared to dry season. This will help to determine the best time to harvest the plants.

4 Conclusions

This study revealed that the native plant species growing and thriving well on the TSF are hyperaccumulators of Pb and Nickel during summer (wet) season, whereas during winter (dry) season the plant species are dormant and tend to take up very minimal up to no concentration of metals because they bind and die resulting in withering of the leaves on the TSF. This phenomenon is known as the re-circulation of metals in leaves and metals in soil in the same location. These hyperaccumulator plant species can accumulate metals in their above ground tissues in concentrations far exceeding those present in the soil.

3 Acknowledgements

Special thanks to DSI-NRF-CIMERA for funding this project. Prof. J.S. Ogola, Prof. L. Chimuka, Dr. H.R. Mundalamo, University of Venda, Wits University and SANBI are thanked for supervision, guidance, analysis and pot culture experiments and Klein Letaba mine tailings owners for granting permission to access the mine tailings and acquiring samples.

4 References

Baker AJM, Brooks RR (1989) Terrestrial higher plants which hyperaccumulate metallic elements - A review of their distribution, Ecology and Phytochemistry. Journal of Biorecovery 1: 81-126.

Karlsson S, Sjöberg V, Ogar A, Bäckström M et al (2014) Leachability of Cu, Zn, As, Ba, and Pb from refuse in the Zelany most tailings dam. An Interdisplinary response to mine water challenges. In: Sun and Wang (eds), pp. 121-125.

Mhlongo S E, Amponsah-Dacosta F, Kadyamatimba A et al (2020) Appraisal of strategies for dealing with the physical hazards of abandoned surface mine excavations: A case study of frankie and nyala mines in South Africa, J Minerals. https://doi.10.3390/min10020145

Mukhopadhyay S, Maiti, SK (2010) Phytoremediation of metal mine waste. Journal of Applied Ecology and Environmental Research 8(3): 207-222.

Peer WA, Freeman JL, Baxter IR, Richards EL, Murphy AS et al (2014). Phytoremediation and hyperaccumulator plants. Dissertation. University of Maryland, College Park.

Sabine M and Wendy G (2009). Human health effects of metals. Dissertation. Kansas State University.

Weilers WF, (1956) The geology of Klein Letaba gold mine in the Sutherland Range, North-Eastern Transvaal. Dissertation. Stellenbosch University 33: 445-479.

Continuous element mapping of drill cores from the Bushveld Complex, SA using LIBS and µEDXRF

Wilhelm Nikonow[1], Dieter Rammlmair[2], Jeannet A. Meima[1]
[1]Federal Institute for Geosciences and Natural Resources (BGR), Stilleweg 2, 30655 Hannover, Germany
[2]Institute of Mineralogy, Leibniz University Hannover, 30167 Hannover, Germany

Abstract. This paper discusses the complexity of mechanisms responsible for the variation in element composition in magnetitite layers within the Upper Zone of the Bushveld Complex in South Africa. It presents a methodological approach to obtain continuous data on element distributions along several drill core metres using micro energy dispersive X-ray fluorescence microscopy (µEDXRF) and laser-induced breakdown spectroscopy (LIBS). The focus is on magnetitite layer 21 at about 223 m depth of the drill core BH7772 from the Eastern Limb.
The data shows that the method of using µEDXRF and LIBS for element mapping at the micrometre scale is promising for providing continuous data on element distributions along several drill core metres. The results indicate that the variability in the composition of the magnetitite layers is even more complex than the large scale data known from the literature describe. This underlines the problem of obtaining a sufficient number of samples for representative data, while considering practical limitations of sampling and analysis in regards to time and effort. The combination of LIBS and µEDXRF can help to understand the complex processes responsible for the variation in element composition within the magnetitite layers.

1 Introduction

The Bushveld Complex in South Africa hosts the largest ultramafic-mafic intrusion in the world. Its Upper Zone contains a series of magnetitite layers, which hold vast resources of vanadium and chromium. These layers display certain trends in element composition along their occurrence within the Upper Zone. While titanium and chromium generally decrease with depth, vanadium increases with concentrations of two wt.-% V_2O_5 in the lowest layers (Scoon and Mitchell 2012; Molyneux 1974; Klemm et al. 1985). Chromium is also known to show rapid upwards depletion within magnetite layers (Cawthorn and McCarthy 1980).

Several processes have been discussed in the literature to be responsible for the variation: fractional crystallisation, magma mixing and compositional convection, partial recrystallization and assimilation as well as reactive melt infiltration (e.g. Kruger and Latypov 2020a; Veksler and Charlier 2015; Yao and Mungall 2022).

The forming processes are still in discussion. This demonstrates the complexity of the mechanisms taking place at different scales. While the general trends are known, they can change and even be inverted on a smaller scale. Considering the large variation over the drill core depth, results will differ depending on the sampling distance of each data point. The variability raises the question of what sampling distance is necessary to have representative data of the magnetitite layers. While it is practically impossible to sample at micrometre resolution over the full Upper Zone, the complexity requires high data density.

The methodological progress in the areas of element mapping using micro energy dispersive X-ray fluorescence microscopy (µEDXRF) and laser induced breakdown spectroscopy (LIBS) seems promising to provide a solution to the aforementioned problem. Scanning drill core halves in 2D over several metres on a micrometre scale can provide the information needed. This work provides a method to obtain continuous data on element distributions along several drill core metres.

2 Materials and methods

The samples for this work were donated for academic research by Impala Platinum Ltd. The core BH7772 was drilled in the Eastern Limb of the Bushveld Complex at N -24.5092° E 29.8945°, about 20 km east of the Marula Mine and 50 km northwest of Burgersfort. It covers about 1337 m of the Upper Zone with some of the underlying Main Zone. The geology is dominated mostly by gabbro-norites, norites and mottled anorthosites with some granites and ultramafic pegmatites. The Upper Zone contains more than 20 layers or seams of magnetitite. This work deals with the layer 21 at about 223 m depth; the main magnetite layer is located at 1068 m. The numbering of these layers varies in the literature, but layer 21 is easily identifiable due to its thickness of more than 10 m containing mostly magnetite, with some ilmenite, plagioclase, clino- and orthopyroxene, olivine and sulphides (Molyneux 1974; Von Gruenewaldt 1973).

About 10 m of core from layer 21 were analysed using µEDXRF, LIBS, electron microprobe analysis (EMPA) and thin section microscopy. For the LIBS analysis the GeoLIBScanner from Laser Technik Berlin (LTB) was used with a Nd:YAG laser operating at 1064 nm with a mapping step size of 75 µm. The system has a wide-band spectrograph and CCD (210 – 1000 nm) with a spectral resolution of 0.047 – 0.222 nm. A stripe of about 1 cm was measured along the core providing spectra that can be used for element distribution maps of almost all elements (Meima et al. 2022b; Meima et al. 2022a; Kuhn et al. 2016).

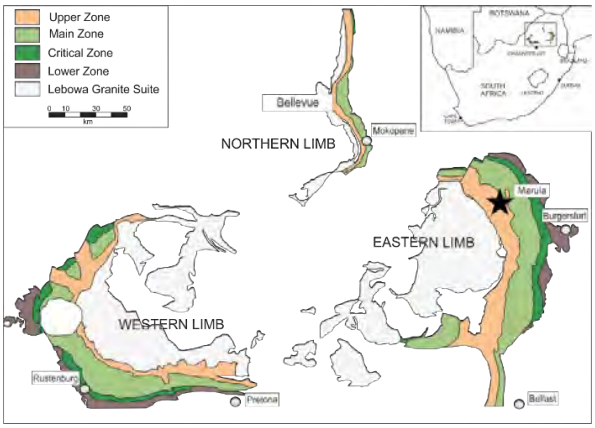

Figure 1. Overview of the Bushveld Complex adapted after Junge et al. (2015). Samples of this work are from the Eastern Limb; a star marks the drill core location, which is about 20 km east of the Marula Mine and 50 km northwest of Burgersfort.

In order to display the chemical variability within the magnetite, the procedure from Meima et al. (2022b) was adapted, where spectra are assigned a mineral name using the supervised classification algorithm spectral angle mapper (SAM) and a mineral database. The area of magnetite was cleaned off mixed pixels using unsupervised classification and thresholds for intensities of Si, Ti, S and Li. The resulting areas display the mostly pure magnetite. Within this area, median values of Cr intensities per pixel row are calculated and plotted along the drill core. Meima et al. (2022b) showed that intensity ratios with narrow spectral ranges from LIBS within one mineral matrix can be considered proportional to element concentrations measured with EMPA. Single spot EMPA data will be used to calibrate the element intensities from LIBS.

For µEDXRF analysis, the M4 Tornado Plus from Bruker was used (Nikonow et al. 2019; Kaskes et al. 2021; Barnes et al. 2016). It operates with a Rh tube at 50 kV and 600 µA providing energy dispersive spectra for areas of up to 15 x 20 cm. The samples were measured with a spatial resolution of 40 µm and a dwell time of 5 ms per spot. The X-ray spot size is focussed by a poly-capillary to about 20 µm (Nikonow and Rammlmair 2016).

The spectra are classified using SAM and a mineral database that has been created over time at BGR, based mostly on EMPA data and containing more than 8000 mineral spectra including solid solution minerals (Nikonow and Rammlmair 2017).

3 Results and discussion

The results from the LIBS and EDXRF analysis are displayed in figure 2. The LIBS data provides a contiguous overview of the Cr variation along the drill core at a spatial resolution of 75 µm (figure 2a). It shows a great variation on the 10 m scale. According to EMPA data from about 130 analyses on magnetite of this core section, the Cr_2O_3 content varies between below detection limit and 1.5 wt.-% with a median of 0.2 wt.-% Cr_2O_3 (median values per four thin section in figure 2a). There is no general trend along the profile, but rather a wave-like behaviour reaching lows at about 218 m and 213.5 m and a high at about 216.5 m with several distinct excursions in both directions. Several authors have described apparent cyclic variations within the monomineralic layers of the Bushveld Complex on a macro scale, proposing ideas on the formation of these layers (Tegner et al. 2006; Junge et al. 2014; Scoon and Mitchell 2012). However, on a micro scale, the general trends can differ or even be inverted (Yao and Mungall 2022; Kruger and Latypov 2020b) and, therefore, contradicting a model of fractional crystallisation. Consequently, the scale has to be considered in order to study and explain rhythmic cycles or reversals of general trends.

Figure 2b shows a zoom-in from 215 to 216 m, with the corresponding mineral distribution map from µEDXRF in figure 2c. The continuous spatial resolution of 75 µm from LIBS provides detailed information on the Cr distribution showing that in the upper 30 cm with mostly massive magnetite there is a small but steady trend towards higher Cr intensities. At about 215.3 m depth, the proportions of plagioclase, pyroxene and biotite increase resulting in a greater variation of Cr intensity with many smaller increases and decreases within the magnetite layers. The peak at 215.55 m can be attributed to the occurrence of small-grained clinopyroxene, plagioclase, amphibole, apatite and ilmenite within a groundmass of magnetite. There are several other steep increases of Cr intensities at 215.3 m, 215.45 m and 215.75 m, all of them seem connected to the presence of pyroxenes. However, the Cr_2O_3 concentration in clinopyroxene does not exceed 0.05 wt.-% with a median below the detection limit, according to EMPA. Other authors observed a relation of higher Cr content with the presence of plagioclase, interpreted as magma replenishment or reactive melt infiltration (Yao and Mungall 2022; Scoon and Mitchell 2012). The plagioclase in the upper part of figure 2b) has mostly no effect on the Cr intensity. Only where plagioclase occurs in combination with reaction rims of clinopyroxene, olivine, amphiboles and biotite Cr shows higher variability. Thus, the mechanisms resulting in the variability of Cr in magnetitite are not yet fully understood. However, continuous element mapping of several drill core metres at micrometre resolution in combination with mineral information from µEDXRF including neighbouring minerals can contribute to the understanding of these processes.

4 Conclusions

A drill core section of about 10 m length from the Bushveld Complex was analysed by LIBS and µEDXRF. LIBS data provide element distributions along the drill core at high spatial resolution in the micrometre range, while being able to analyse full core boxes. The combination of metre and micrometre scale with chemical and mineralogical

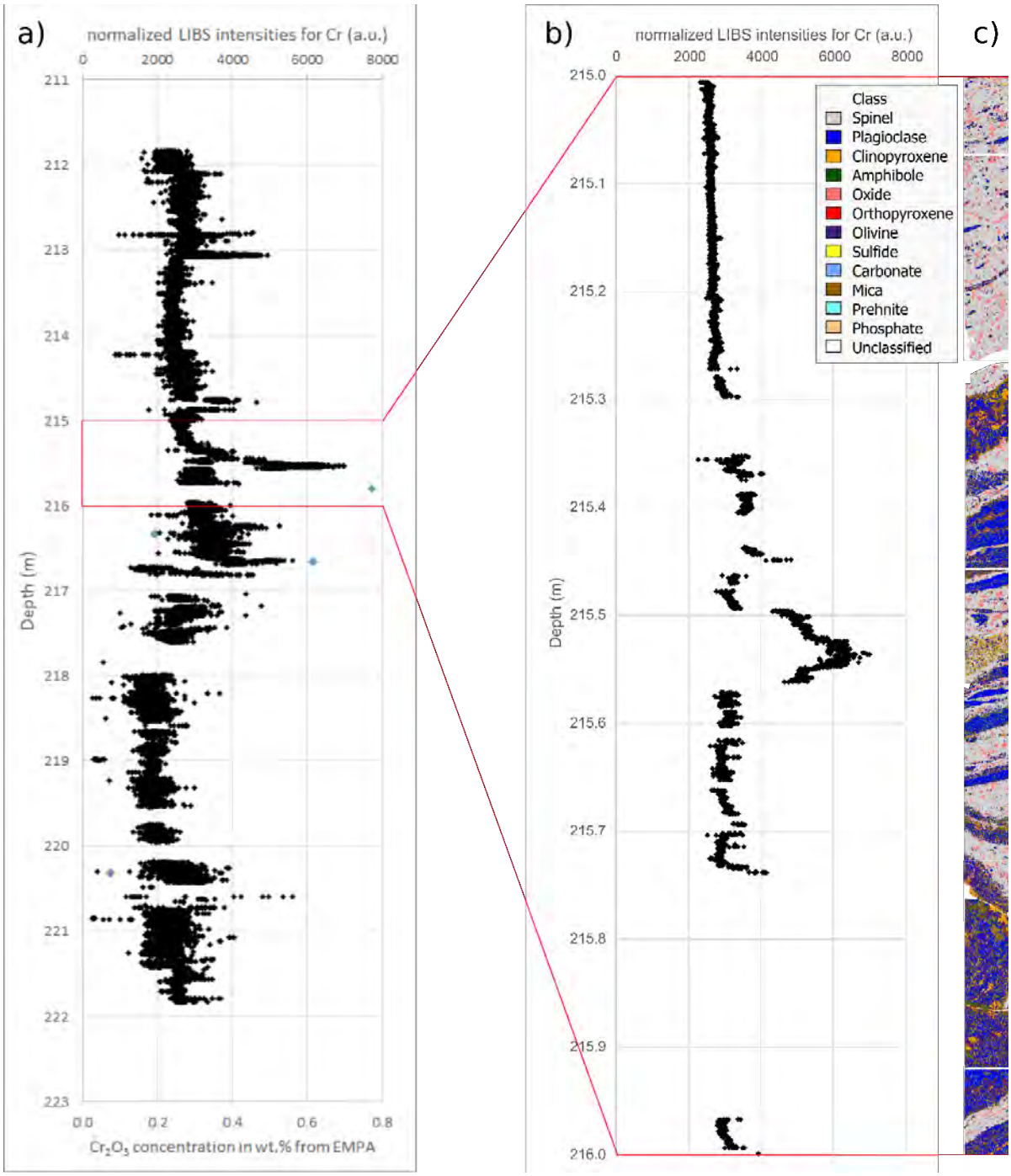

Figure 2. Cr intensities normalized to sum intensities from LIBS (a,b) along the drill core. Each point reflects the median of a 75 µm row. The median Cr_2O_3 concentrations (blue) per thin section from EMPA are plotted on the lower axis. EMPA data at 215.8 m has no corresponding LIBS data, since the grains were too small to receive a pure LIBS pixel. A one meter zoom-in is displayed in the middle (b). The mineral distribution from µEDXRF for sub-section b) is shown in c).

information in 2D opens new possibilities to analyse and understand the mechanisms of magnetitite layer formation and the metasomatic influence triggered by late magma emplacement.

Acknowledgements

The results of this work are part of research that is funded by the German Research Foundation (DFG) within the Project Spectroscopic mineral - chemical analysis of drill cores: Development of fast 2D LIBS, EDXRF and hyperspectral scanning with application to outstanding problems of the Bushveld Complex layered intrusion (457479532). We would like to express our gratitude to Impala Platinum Ltd. for donating the core, Prof. Roelofse from the University of the Free State, Bloemfontein for logging the core and Dr. Veksler from GFZ Potsdam for logistics. We thank Dr. Simon Goldmann, Christian Wöhrl and

Dominic Göricke for assistance with EMPA and M4 Tornado Plus measurements.

References

Barnes SJ, Mole DR, Le Vaillant M, Campbell MJ, Verrall MR, Roberts MP, Evans NJ (2016) Poikilitic textures, heteradcumulates and zoned orthopyroxenes in the Ntaka Ultramafic Complex, Tanzania: implications for crystallization mechanisms of oikocrysts. J Pet 57:1171-1198.

Cawthorn RG, McCarthy TS (1980) Variations in Cr content of magnetite from the upper zone of the Bushveld Complex — evidence for heterogeneity and convection currents in magma chambers. Earth Planet Sci Lett 46:335-343. doi: https://doi.org/10.1016/0012-821X(80)90049-7.

Junge M, Oberthür T, Melcher F (2014) Cryptic variation of chromite chemistry, platinum group element and platinum group mineral distribution in the UG-2 chromitite: an example from the Karee Mine, western Bushveld Complex, South Africa. Econ Geol 109:795-810.

Junge M, Wirth R, Oberthür T, Melcher F, Schreiber A (2015) Mineralogical siting of platinum-group elements in pentlandite from the Bushveld Complex, South Africa. Miner Depos 50:41-54. doi: 10.1007/s00126-014-0561-0.

Kaskes P, Déhais T, de Graaff SJ, Goderis S, Claeys P (2021) Micro–X-ray fluorescence (μXRF) analysis of proximal impactites: High-resolution element mapping, digital image analysis, and quantifications In: Reimold WU, Koeberl C (eds) Large Meteorite Impacts and Planetary Evolution VI. Geological Society of America, pp 0.

Klemm D, Henckel J, Dehm R, Von Gruenewaldt G (1985) The geochemistry of titanomagnetite in magnetite layers and their host rocks of the eastern Bushveld Complex. Econ Geol 80:1075-1088.

Kruger W, Latypov R (2020a) Fossilized solidifications fronts in the Bushveld Complex argues for liquid-dominated magmatic systems. Nat Commun 11:2909. doi: 10.1038/s41467-020-16723-6.

Kruger W, Latypov R (2020b) Fossilized solidification fronts in the Bushveld Complex argue for liquid-dominated magmatic systems. Nat Commun 11:2909. doi: 10.1038/s41467-020-16723-6.

Kuhn K, Meima JA, Rammlmair D, Ohlendorf C (2016) Chemical mapping of mine waste drill cores with laser-induced breakdown spectroscopy (LIBS) and energy dispersive X-ray fluorescence (EDXRF) for mineral resource exploration. J Geochem Explor 161:72-84.

Meima J, Rammlmair D, Junge M, Nikonow W (2022a) Continuous measurement of Mg/Fe and Ca/Na ratios with scanning Laser Induced Breakdown Spectroscopy in 6 meter of drill core through Merensky Reef, Bushveld Complex, South Africa EGU General Assembly 2022. Copernicus Meetings, Vienna, Austria.

Meima JA, Rammlmair D, Junge M (2022b) The use of Laser Induced Breakdown Spectroscopy for the mineral chemistry of chromite, orthopyroxene and plagioclase from Merensky Reef and UG-2 chromitite, Bushveld Complex, South Africa. Chem Geol 589:120686. doi: 10.1016/j.chemgeo.2021.120686.

Molyneux T (1974) A geological investigation of the Bushveld Complex in Sekhukhuneland and part of the Steelpoort valley. South Afr J Geol 77:329-338.

Nikonow W, Rammlmair D (2016) Risk and benefit of diffraction in Energy Dispersive X-ray fluorescence mapping. Spectrochim Acta B: At Spectrosc 125:120-126.

Nikonow W, Rammlmair D (2017) Automated mineralogy based on micro-energy-dispersive X-ray fluorescence microscopy (μ-EDXRF) applied to plutonic rock thin sections in comparison to a mineral liberation analyzer. Geosci Instrum Method Data Syst 6:429-437. doi: 10.5194/gi-6-429-2017.

Nikonow W, Rammlmair D, Meima JA, Schodlok MC (2019) Advanced mineral characterization and petrographic analysis by μ-EDXRF, LIBS, HSI and hyperspectral data merging. Mineral Petrol 113:417-431. doi: 10.1007/s00710-019-00657-z.

Scoon R, Mitchell A (2012) The Upper Zone of the Bushveld Complex at Roossenekal, South Africa: geochemical stratigraphy and evidence of multiple episodes of magma replenishment. South Afr J Geol 115:515-534.

Tegner C, Cawthorn RG, Kruger FJ (2006) Cyclicity in the Main and Upper Zones of the Bushveld Complex, South Africa: crystallization from a zoned magma sheet. J Pet 47:2257-2279.

Veksler IV, Charlier B (2015) Silicate liquid immiscibility in layered intrusions Layered intrusions. Springer, pp 229-258.

Von Gruenewaldt G (1973) The main and upper zones of the Bushveld Complex in the Roossenekal area, eastern Transvaal. Trans Geol Soc SA 76:207-227.

Yao Z, Mungall JE (2022) Magnetite layer formation in the Bushveld complex of South Africa. Nat Commun 13:1-11.

Exploring mineral chemistry variations in tourmaline and chlorite at the Triangle orogenic gold deposit (Val-d'Or, Québec): Implications for mineralisation vectors

Giovanni Pedemonte[1,2], Bertrand Rottier[1,2], Georges Beaudoin[1,2], Jacques Simoneau[3], Pape Mactar-Dieng[3]

[1]*Département de géologie et de génie géologique, Université Laval, Québec, Canada*
[2]*Centre de Recherche sur la Géologie et L'ingénierie de Ressources Minérales (E4m), Université Laval, Québec, Canada*
[3]*Eldorado Gold Corporation, Québec, Canada*

Abstract: Recent efforts in the research of ore deposits focus on the chemical characterisation of key minerals in mineralised systems to define vectors and indicator minerals constituting new and powerful exploration tools. The present study reports systematic tourmaline and chlorite chemical variability from the Triangle orogenic gold deposit (Val-d'Or, Québec). A detailed study of the paragenetic sequence allows defining at least three main mineralisation events. This study focuses on the characterisation of tourmaline and chlorite chemistries contained in the Au-bearing quartz-tourmaline- ankerite-chlorite veins of the second and main mineralising event, in the two main shear zones of the deposit, named C2 and C4. Chemical variability of chlorite and tourmaline have been explored using Principal Component Analysis, which allows to find some elemental ratios that strongly correlate with the elevation and Au grade of the samples along both shears. Further investigation on the physicochemical factors, including the effect of host rocks, controlling tourmaline and chlorite chemistries is in progress to define potential tracers that will allow vectorisation towards the high-grade ore shoots in the Triangle deposit and other shear-hosted orogenic gold deposits.

1 Introduction

1.1 Geology of the Sigma-Lamaque-Triangle district

Triangle is an orogenic gold deposit located in the Val-d'Or mining district. The main rock types of the district are the Val-d'Or Formation, a sequence of andesitic to rhyolitic lavas (Pilote 2000; Scott et al. 2002) and of mafic to intermediate pyroclastic rocks (Robert and Brown 1986a, b; Robert and Kelly 1987). This formation is strongly deformed, and show an E-W trending, sub-vertical schistosity (Latulippe 1976; Pilote et al. 1998; Pilote 2000; Scott et al. 2002) and are crosscut by different intrusive units mainly gabbroic and dioritic in composition (Pilote 2000; Neumayr et al. 2000; Scott et al. 2002). The Triangle deposit is structurally controlled and developed along third-order shears associated to the Larder Lake-Cadillac Break, crosscutting mafic tuffs belonging to the Val-d'Or Formation and dioritic intrusions such as the *Triangle Plug* and the *Dyke North* (Figures. 1 and 2). Gold mineralisation is hosted in several parallel shear zones trending approximately NW-SE, in veins composed of quartz, tourmaline, ankerite and chlorite associated with a strong quartz-sericite-feldspar alteration. The present study focuses on the characterisation of the geochemical variability of tourmaline and chlorite present in the orogenic veins from the two main shear zones of the deposit, named C2 and C4.

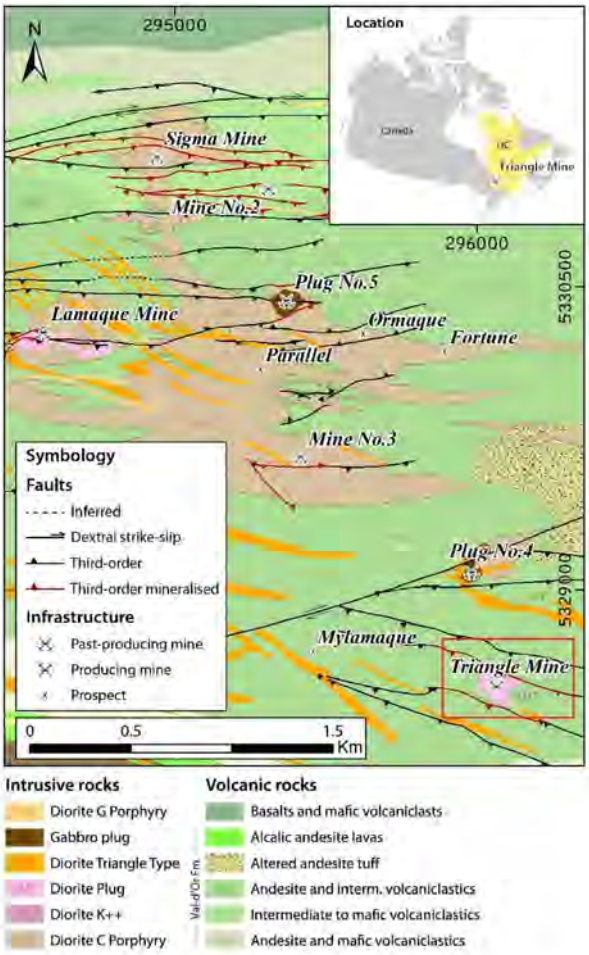

Figure 1. Geological map of the Triangle deposit (prepared with data from Eldorado Gold Corporation).

1.2 Mineralising events and paragenesis

Three main mineralisation events have been recognised at the Triangle deposit. The first event is characterised by early, deformed quartz-chlorite-sericite-carbonate veins with disseminated pyrite and minor gold mostly as inclusions in quartz. This event is accompanied by an intense deformation of the host rock and by an epidote, chlorite, and carbonate alteration associated with deformed pyrite. The second event consists of a proximal alteration zone at the contact of the shear,

characterised by widespread quartz-sericite-feldspar with traces of chlorite and undeformed pyrite. This event includes the main vein-filling stage, formed by massive quartz-tourmaline-ankerite-pyrite-chlorite veins emplaced along the shears. This second event is the most important for Au mineralisation, where Au occurs as inclusions associated with Au-Ag tellurides (krennerite and petzite) in pyrite. Finally, the third event consists of small pyrite-tourmaline-quartz veinlets crosscutting the veins of the second event. Those veinlets are associated to a third generation of gold commonly occurring as fracture filling inclusions (mainly in pyrite) associated with chalcopyrite and Pb-Bi tellurides (altaite and tellurobismuthite).

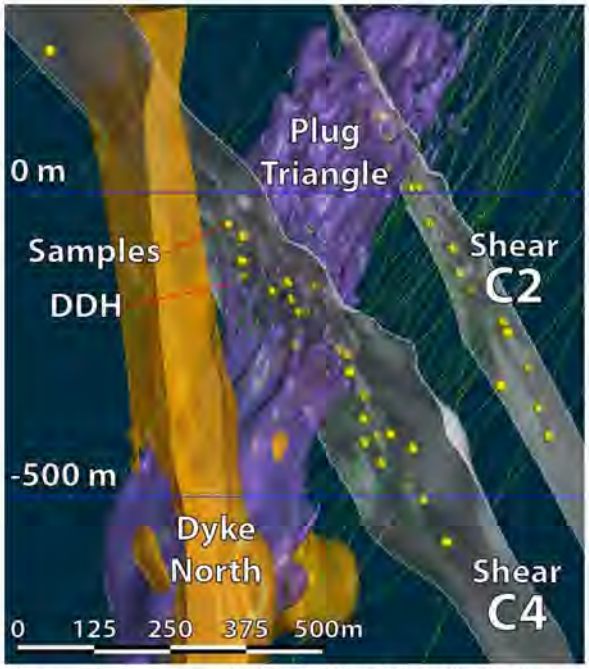

Figure 2. 3D view (facing NW) of the distribution of samples used for the present study (yellow spheres), along the two main shear zones (C2 and C4) in the Triangle deposit, and the influence of the intrusive rocks in the area. Empty areas in the 3D render correspond to the mafic tuffs of the Val-d'Or formation (Leapfrog Geo® model from Eldorado Gold Corporation).

2 Analytical methods and mineral chemistry

Tourmaline and chlorite from the quartz-tourmaline-ankerite-pyrite-chlorite veins of the second event have been analysed for major elements by EPMA and for minor and trace elements by LA-ICP-MS. Selected samples are from the shears C2 and C4, between -355.2 to +130.6m, and between -445.6 to 231.7 m, respectively (Figure 2). The Au grade of the samples varies between <0.01 (under detection limit, <d.l.) to 197.66 ppm and <0.01 to 151.93 ppm for shears C2 and C4 respectively. Grades has been classified in four intervals: barren (<0.01 – 0.5 ppm), low to cut-off grade (0.5 – 3 ppm), high grade (3 – 10 ppm) and above 10 ppm. For shear C2 most of the analysed vein samples crosscut the mafic tuffs whereas for C4 some veins also crosscut the Triangle plug (Figure 2). Tourmaline from shears C2 and C4 show contrasting mean composition of the following elements (Δ is the percentage of variation): Cr (144 vs 266 ppm, Δ=84%), K (1813 vs 3824 ppm, Δ=111%), Ti (1758 vs 2884 ppm, Δ=64%), Cu (3.94 vs 0.96 ppm, Δ=-76%), Ba (37.2 vs 88.6 ppm, Δ=138%), W (3.78 vs 16.5 ppm, Δ=336%), Pb (10.3 vs 155 ppm, Δ=1414%). Some elements remain almost constant between the two shears (Δ<5%), like Fe (4.4 vs 4.5 wt%), and Al (15.5 vs 15.2 wt%).

Conversely, the chlorite from shears C2 and C4 shows contrasting mean composition of B (11.3 vs 57.9 ppm, Δ=412%), Ca (2952 vs 6660 ppm, Δ=126%), Cr (85 vs 43.5 ppm, Δ=-49%), Cu (0.46 vs 1.12 ppm, Δ=144%), Sr (19.4 vs 9.1 ppm, Δ=-53%), La (2.54 vs 0.51 ppm, Δ=-80%) and Pb (1.49 vs 5.39 ppm, Δ=263%). Some elements remain relatively constant between the two shears (Δ<5%), such as Mg (7.9 vs 8.2 wt%), V (227 vs 230 ppm) or Fe (15.7 vs 15.8 wt%).

In shear C4, samples hosted in the dioritic Triangle Plug have been analysed. The preliminary results seem to indicate that tourmaline and chlorite chemistry varies as function of the host rock. In this sense, tourmaline from the veins that crosscuts the intrusive rocks compared to those crosscutting the mafic tuffs shows contrasting content of Sc (28 vs 50.1 ppm, Δ=79%), Cr (276 vs 191 ppm, Δ=-31%), Mn (109 vs 188 ppm, Δ=72%), Fe (3.86 vs 5.1 wt%, Δ=32%), Co (3.45 vs 13.2 ppm, Δ=283%), Cu (1.09 vs 2.75 ppm, Δ=153%) and Zn (499 vs 370 ppm, Δ=-26%). Similarly, chlorite shows contrasting content of Ca (1.6 vs 0.4 wt%, Δ=-73%), Sc (12.9 vs 32.9 ppm, Δ=155%), V (150 vs 241 ppm, Δ=60%), Cr (133 vs 52.9 ppm, Δ=-60%), Co (9.4 vs 16.1 ppm, Δ=71%), Sr (40.7 vs 9.5 ppm, Δ=-77%) and La (3.7 vs 0.5 ppm, Δ=-87%).

2.1 Tourmaline and chlorite geochemistry as a function of Au grade and elevation

Both tourmaline and chlorite show systematic change of composition as function of the Au grade of the samples and of their position along the shear. However different trends are observed for samples from shears C2 and C4. For samples from shear C2, there is a correlation between the Au grades and the sample elevation, where higher grades are recorded in shallower samples. Therefore, as Au grade increases (from <0.01 to >10 ppm) and as elevation increases (from -288.1 to 217.6 m), tourmaline shows a systematic decrease in V (574 to 440 ppm), Fe (5.16 to 3.77 wt%) and an increase in Ni (10.3 to 33.5 ppm), Zn (309 to 378 ppm) and Sr (233 to 475 ppm). Chlorite shows a systematic increase of Li (86.8 to 140 ppm), Sc (8.6 to 39.8 ppm) and Zn (408 to 637 ppm), and a decrease in Mn (1204 to 405 ppm) and Co (25.9 to 3.8 ppm).

In the case of shear C4, following an increase in the Au grade (from <0.01 to >10 ppm), tourmaline shows a systematic increase in Zn (228 to 407 ppm)

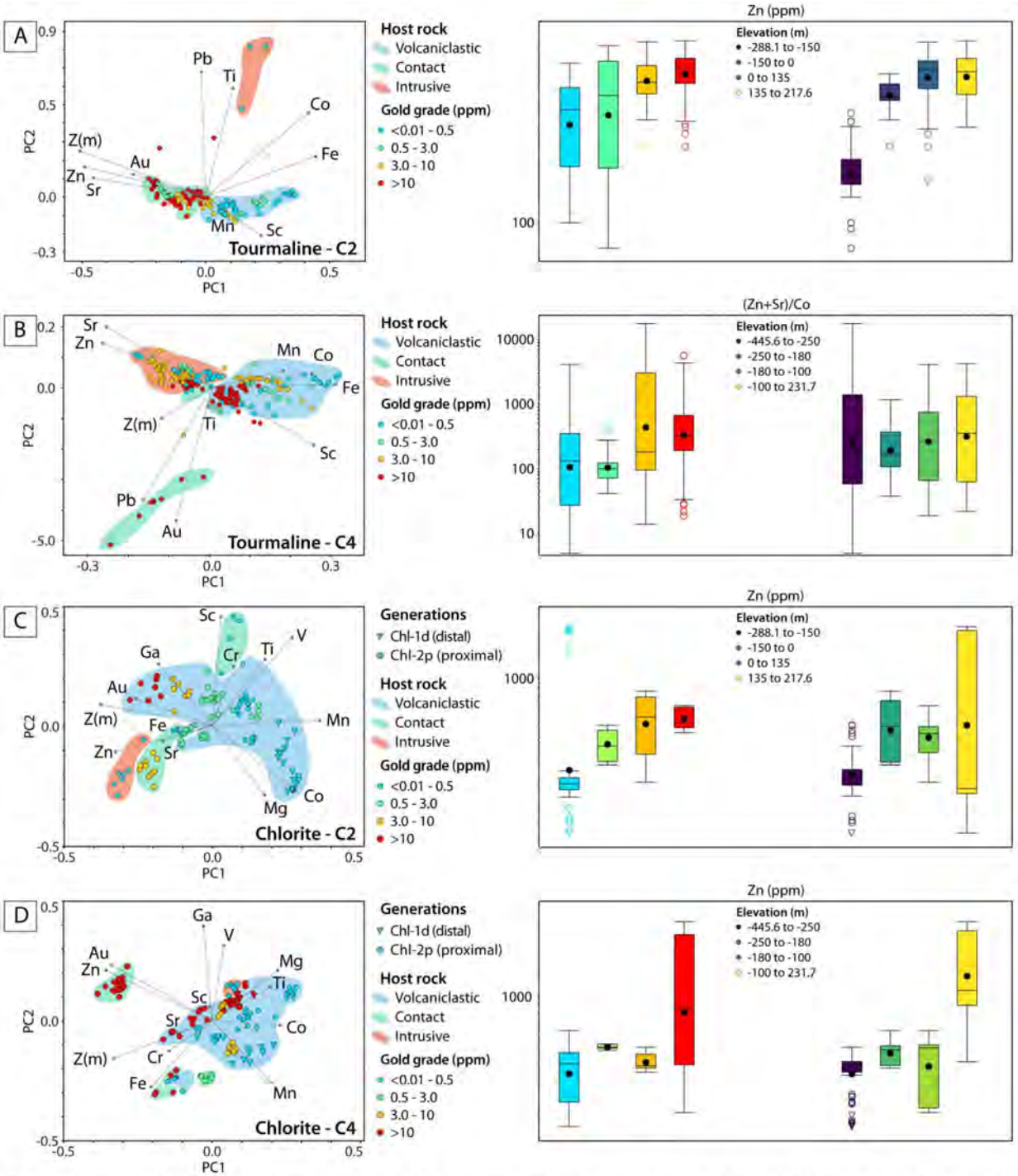

Figure 3. Principal Component Analysis of selected elements in tourmaline and chlorite from the shears C4 and C2, and the elements selected that better control the distribution of Au grades (ppm) and elevation (m) of the samples.

and Cr (34.8 to 216 ppm), and a decrease in Ca (3248 to 2872 ppm). Chlorite shows a systematic increase in Li (78.8 to 148 ppm) and Zn (413 to 2199 ppm) contents. With variations in elevation for C4 (from -445.6 to 231.7 m), tourmaline shows a systematic decrease in Sc (42 to 32 ppm), V (506 to 212 ppm) and an increase in Ni (35 to 70 ppm); chlorite shows a systematic increase in Zn (357 to 498 ppm) and Li (65 to 101 ppm). Therefore, Zn contents in chlorite seems to be sensitive to variations in Au grade and elevation in both shear C2 and C4.

2.2. Principal Component Analysis (PCA) and elemental ratios

Principal Component Analysis (PCA) allows to define the main elements controlling the chemical variabilities and correlating with either the elevation or the Au grade of the samples. Each PC explains

part of the variance of the data, with the first (PC1) capturing the greatest variance, followed by the second (PC2), and so forth. For tourmaline from shear C2, PC1 is mainly controlled by Au grade, elevation, Zn Sr, Co and Fe; and PC2 by Ti, Pb, Mn and Sc (Figure 3A). For tourmaline from shear C4, PC1 is mainly controlled by Zn, Mn and Fe, PC2 is controlled by Au grade, Pb and Ti, and both PC1 and PC2 are controlled by elevation, Sr, Co and Sc (Figure 3B). For shear C2, the PCA confirm the strong correlation between samples elevation, Au grades, and the Zn content (Figure 3A). For shear C4, the (Zn+Sr)/Co ratio increases with the Au grade of the samples and it is also controlled by the elevation (Figure 3B). For chlorite from shear C2, PC1 is controlled by Mn, Zn, Fe, Sr, elevation and Au grades. PC2 is controlled by Sc and Cr. Both PC1 and PC2 are controlled by Mg, Co, V, Ti and Ga. In the case of shear C4, both PC1 and PC2 are controlled by Mn, Zn, Au grades, elevation, Mg and Ti. PC1 is controlled by Co and Sr, and PC2 is controlled by Sc, Ga and V. The Zn content increases with Au grades and elevation for both shear C2 and C4 (Figure 3C and 3D).

3 Discussion

As show by the PCA, the chemical variation of chlorite and tourmaline as a function of sample elevation and Au grade are different between shears C2 and C4, for both chlorite and tourmaline, with the only exception of Zn. The reason of the discrepancy still needs to be evaluated. It can also be noted in the PCA that the vein host rock can have a strong effect on the chemistry of both minerals, which requires further investigation (Figure 3).

Most of the chemical variation of tourmaline and chlorite along both shears C2 and C4 are associated with variation of the Au grade and elevation of the samples. This correlation complicates the interpretation of the observed chemical variation as they can be either due to changes of the physicochemical conditions of the mineralising fluid associated with Au precipitation, or it can reflect the progressive evolution of the ascending mineralising fluid along the shears.

In shear C2, where most of the samples come from the shear that crosscut the mafic tuffs, both tourmaline and chlorite display an enrichment of Zn and Sr with an increase of the sample elevation, along with a depletion of Co. This variation may be linked to an increase content of those elements in the fluid, in response of the alteration of the mafic tuffs along the pathway of the ascending mineralising fluids, as suggested by Sciuba et al. (2021). However, further analyses need to be performed to clearly identify the different factors controlling the chemical variability of tourmaline and chlorite along the two shear zones.

4 Conclusions

Preliminary mineral chemistry results for tourmaline and chlorite in the Triangle deposit show that the chemistry of both minerals vary as a function of the Au grade and/or the elevation of the samples. These results also demonstrate that both minerals have the potential to be used as vector to target high grade zones in orogenic Au mineralised shear zones. However, some discrepancies between the chemical variation of both tourmaline and chlorite along the two investigated shear zones need to be explained before the development of such exploration tools. Further analysis will be performed to investigate the effects of host rock composition on chlorite and tourmaline trace element content along the two shears, and to identify the different factors controlling the chemical variability observed in both minerals.

Acknowledgements

This research is supported by the *Fonds de Recherche du Québec Nature et Technologies* (FRQNT), grant #FT130375. The authors would like to thank Eldorado Gold Corporation for allowing access to the property and for all the support during logging and sampling.

References

Latulippe M (1976) Excursion géologique: la région de Val-d'Or-Malartic.(Ed.) Ministère des richesses naturelles du Québec: Institut canadien des mines et de la métallurgie.

Neumayr P, Hagemann SG, Couture J-F (2000) Structural setting, textures, and timing of hydrothermal vein systems in the Val d'Or camp, Abitibi, Canada: implications for the evolution of transcrustal, second- and third-order fault zones and gold mineralization. Can J Earth Sci 37:95–114. https://doi.org/10.1139/e99-105

Pilote P (2000) Géologie de la région de Val d'Or, Sous-province de l'Abitibi-Volcanologie physique et évolution métallogénique

Pilote P, Moorhead J, Mueller W (1998) Développement d'un arc volcanique, le région de Val d'Or, ceinture de l'Abitibi - volcanologie physique et évolution métallogénique : guide d'excursion A2, 14-17 mai 1998

Robert F, Brown AC (1986a) Archean gold-bearing quartz veins at the Sigma Mine, Abitibi greenstone belt, Quebec; Part II, Vein paragenesis and hydrothermal alteration. Economic Geology 81:593–616. https://doi.org/10.2113/gsecongeo.81.3.593

Robert F, Brown AC (1986b) Archean gold-bearing quartz veins at the Sigma Mine, Abitibi greenstone belt, Quebec; Part I, Geologic relations and formation of the vein system. Economic Geology 81:578–592. https://doi.org/10.2113/gsecongeo.81.3.578

Robert F, Kelly WC (1987) Ore-forming fluids in Archean gold-bearing quartz veins at the Sigma Mine, Abitibi greenstone belt, Quebec, Canada. Economic Geology 82:1464–1482. https://doi.org/10.2113/gsecongeo.82.6.1464

Sciuba M, Beaudoin G, Makvandi S (2021) Chemical composition of tourmaline in orogenic gold deposits. Minerallium Deposita 56:537–560. https://doi.org/10.1007/s00126-020-00981-x

Scott CR, Mueller WU, Pilote P (2002) Physical volcanology, stratigraphy, and lithogeochemistry of an Archean volcanic arc: evolution from plume-related volcanism to arc rifting of SE Abitibi Greenstone Belt, Val d'Or, Canada. Precambrian Research 115:223–260. https://doi.org/10.1016/S0301-9268(02)00011

Exploring semi-supervised generation of mineral list for automated mineralogy systems

L. Pereira[1], R. Tolosana-Delgado[1], S. Thiele [1], R. Japarov[1], M. Frenzel[1], K. Bachmann[1], K.G. van den Boogaart[1], J. Gutzmer[1]

[1] Helmholtz-Zentrum Dresden-Rossendorf, Helmholtz Institute Freiberg for Resource Technology, Germany

Abstract. The quality of results obtained by a scanning electron microscope-based automated mineralogy system strongly depend on the project-specific list of spectra of the minerals being mapped [1]. Mineral lists can be selected manually from existing universal lists that construct theoretical spectra from typical mineral composition, and/or can be constructed based on spectra measured in the samples of a specific project. Regardless of the source, the choice of mineral list is subjective: One can prefer extensive mineral lists to enhance the chances of capturing variations in chemical composition of specific minerals (e.g., splitting chlorite compositions); or else smaller, compact (lumped) mineral lists to reduce misclassification [2]. No general, perfect balance within generality-specificity or extension-compaction exists, so that users end up interactively and iteratively building the spectral library for each project in tedious steps of adding and removing mineral spectral candidates. This process is also project-, ore-and operator-specific. While some automated mineralogy devices provide operating modes for automatically constructing mineral lists throughout a measurement, these commonly offer only limited settings and are not clear about the data processing steps. Additionally, these established strategies do not provide the user with any measure of uncertainty, essential for geometallurgy [3].

The goal of this contribution is to compare the performance of several components of a strategy to automatically and objectively construct automated mineralogy mineral lists, making use of several machine learning algorithms, for the specific case of dataset collected with the Mineral Liberation Analyser (MLA). The strategy, which is illustrated in Figure1, has five steps: (1) preliminary data transformation, (2) dimension reduction, (3) endmember detection, (4) phase detection, and (5) spectral unmixing.

For each of these steps, several options were tested. These included for data transformation peak extraction and Box-Cox transformations [4], which at the same time embraces logarithm/log-ratio transformations, square root transformations and the identity transformation. Regarding dimension reduction, principal component analysis [5]. In step three, we considered QHull convex hull detection, and N-FINDER [6], a conventional linear endmember detection method. In step four, the goal is to find the groups of spectra that can be identified with the members of the mineral list, not all of them being necessarily endmembers. Algorithms tested here correspond to model-free unsupervised classification algorithms, such as k-means [7]. Finally, in step five we tried several sparse and non-negative-constrained linear unmixing algorithms. This unmixing was done within the sample of spectra forming the training data only in order to determine the number of necessary groups (or clusters) to extract from step four, as the actual final phase attribution will be done by the MLA software for the whole project after delivering the mineral list. Some of the results obtained in a Chromite deposit from the Bushveld complex are presented in Fig. 2. The strategy presented here offers not only improvements to the workflow of scanning electron microscope-based automated mineralogy systems but also is a step stone for compiling mineral lists in analytical devices such as µX-Ray Fluorescence automated mineralogy, where spectra mixing is a bigger issue.

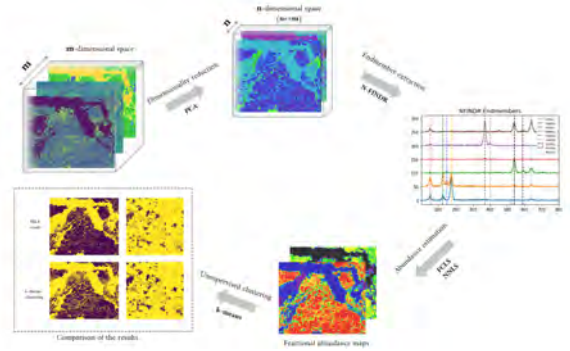

Figure 1. Schematic representation of the methodology applied in here.

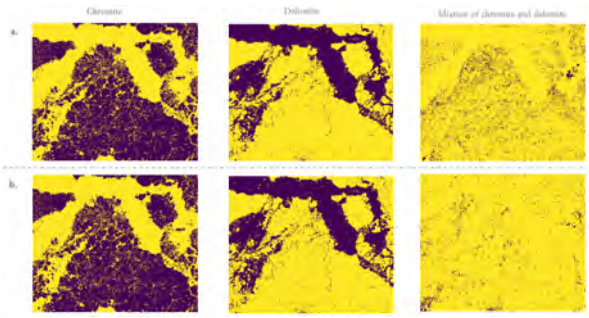

Figure 2. Summary of classification results obtained with the MLA (a) and the proposed method (b), illustrating the issue of mixed spectra.

References

Y. Gu, R. P. Schouwstra, and C. Rule, “The value of automated mineralogy,” *Miner. Eng.*, vol. 58, pp. 100–103, Apr. 2014, doi: 10.1016/j.mineng.2014.01.020.

M. Kern, R. Möckel, J. Krause, J. Teichmann, and J. Gutzmer, “Calculating the deportment of a fine-grained and compositionally complex Sn skarn with a modified approach for automated mineralogy,” *Miner. Eng.*, vol.

116, pp. 213–225, Jan. 2018, doi: 10.1016/j.mineng.2017.06.006.
K. G. van den Boogaart and R. Tolosana-Delgado, “Predictive Geometallurgy: An Interdisciplinary Key Challenge for Mathematical Geosciences,” in *Handbook of Mathematical Geosciences: Fifty Years of IAMG*, B. S. Daya Sagar, Q. Cheng, and F. Agterberg, Eds., Cham: Springer International Publishing, 2018, pp. 673–686. doi: 10.1007/978-3-319-78999-6_33.
“The Box-Cox Transformation Technique: A Review - Sakia - 1992 - Journal of the Royal Statistical Society: Series D (The Statistician) - Wiley Online Library.” https://rss.onlinelibrary.wiley.com/doi/abs/10.2307/2348250 (accessed May 15, 2023).
N. Kambhatla and T. K. Leen, “Dimension Reduction by Local Principal Component Analysis,” *Neural Comput.*, vol. 9, no. 7, pp. 1493–1516, Jul. 1997, doi: 10.1162/neco.1997.9.7.1493.
M. E. Winter, “N-FINDR: an algorithm for fast autonomous spectral end-member determination in hyperspectral data,” in *Imaging Spectrometry V*, M. R. Descour and S. S. Shen, Eds., SPIE, 1999, pp. 266–275. doi: 10.1117/12.366289.
A. Likas, N. Vlassis, and J. J. Verbeek, “The global k-means clustering algorithm,” *Pattern Recognit.*, vol. 36, no. 2, pp. 451–461, Feb. 2003, doi: 10.1016/S0031-3203(02)00060-2.

Critical Minerals: Germanium and Cobalt in the Bornite Deposit, Southwestern Brooks Range, Alaska

Katharina Pfaff[1] , Garth Graham[2] , Alexander Jones[1] , Karen Kelley[2]
[1]Center to Advance the Science of Exploration to Reclamation in Mining (CASERM), Department of Geology and Geological Engineering, Colorado School of Mines, USA
[2]U.S. Geological Survey, Geology, Geophysics, and Geochemistry Science Center, Denver, USA

Abstract. Increasing demand for Ge and Co has led to a renewed interest and focus on advancing our understanding of the occurrence, distribution, and sequestration of these critical elements in known ore deposits. A workflow using a variety of analytical techniques and co-registered datasets has been developed and was applied to the carbonate hosted Bornite Cu-Co (Zn,-Ge) deposit in Alaska, where a new orebody ("the South Reef") was discovered in 2011. The South Reef is host to substantial amounts of high-grade Cu, Co, and appreciable Zn, but also contains localised elevated concentrations of Ge. We describe the mineralogy and paragenesis of the South Reef based on detailed optical petrography, scanning electron microscopy, scanning electron microscopy-based automated mineralogy, and mapping µ-X-ray fluorescence analysis. Germanium was found to exist in renierite, white mica, illite, galena and feldspars within the South Reef. Cobalt was found to occur in cobaltiferous pyrite, carrollite, and cobaltite.

1 Introduction

Our society has become increasingly dependent on mineral commodities to facilitate our transition to green energy and ever advancing technologies. The United States government recently included Ge and Co as "critical minerals", which are necessary for the manufacture of a product, but where we currently have a dependency on foreign sources. The absence of these commodities can have significant consequences for the U.S. economy or national security (Executive Office of the President 2017, U.S. Geological Survey, 2022). Identification of domestic sources of critical mineral commodities is an important step toward independence from foreign sources which may be unreliable. However, little is known about the occurrence, distribution, and sequestration of many critical minerals in known ore deposits.

The aim of this study was to develop a workflow that efficiently and effectively characterises the ore, gangue, and alteration mineralogy to inform us about the occurrence, distribution, and sequestration of all critical minerals in the South Reef. Improved understanding of the nature of mineralised zones provides fundamental information for development of systems models that unravel ore forming processes that can guide critical mineral exploration and assessment.

The Bornite deposit is located in the Cosmos Hills, on the southern flank of the western Brooks Range, approximately 260 km east of Kotzebue and 460 km north of Fairbanks (Fig. 1).

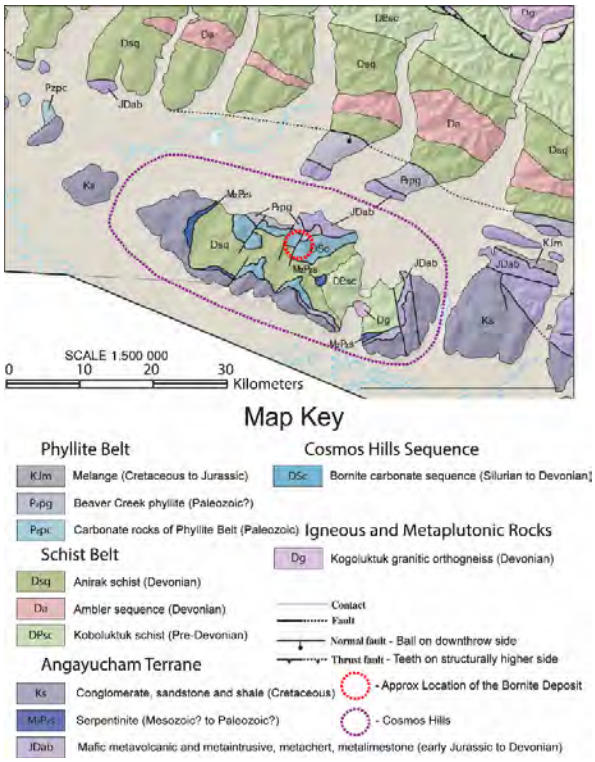

Figure 1. Regional geology and location of the Bornite deposit. Geology modified after Hitzman (1986) and Till et al. (2008).

Mostly Devonian schists and carbonates are exposed in a N-W trending, double plunging anticline (Hitzman 1986). The Bornite Cu-Co (Zn, Ge) deposits are hosted in the Devonian-Silurian Bornite carbonate sequence. Ore forming processes appear to have included brecciation and replacement of carbonates, and influx of copper-rich metalliferous fluids that led to a complex paragenesis, dominated by chalcopyrite (with high grade zones containing bornite, chalcocite and tennantite). The deposit has an indicated Cu resource of 40.5 Mt with an average grade of 1.02% and a total inferred 141.9 Mt at an average grade of 1.74%. The deposit is also host to a significant amount of Co with an inferred 182.4 Mt of Co at an average grade of 0.019% (Davis et al. 2008). Germanium resource values have not been published.

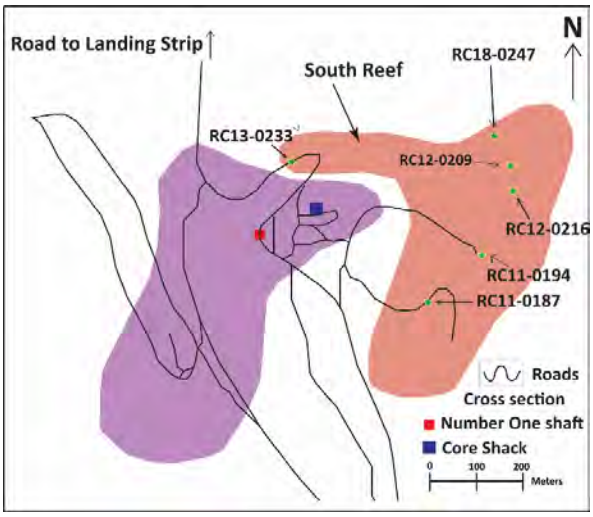

Figure 2. Plan view map of the location of the historical main Number One orebodies (purple) and the South Reef (orange), and drill hole collars from which samples were collected.

Although standard analytical methods are effective at accurately measuring the abundance of numerous elements including Cu, Co, and Zn, Ge concentrations are commonly under-represented because of volitisation during sample digestion. However, limited multi-element data (Grannito et al. 2019, Trilogy Metals, Written Communication, 2018) demonstrate that elevated Ge concentrations occur locally in the Bornite deposit.

Reconnaissance, high-quality data indicate that Ge-rich intervals correlate with bornite-rich copper zones. Cobalt mainly occurs as cobaltiferous pyrite within and around the copper mineralised zones and as carrollite and cobaltite directly associated with copper bearing minerals. Therefore, areas with visibly high chalcocite, bornite and chalcopyrite were chosen for sampling.

The aim of this study was to improve our understanding of the occurrence and sequestration of Ge in the South Reef of the Bornite deposit and to develop a workflow using co-registered datasets to better understand the critical mineral endowment. Optical microscopy, μ-X-ray fluorescence (μ-XRF) mapping, field emission scanning electron microscopy (FE-SEM) backscattered electron (BSE) imaging coupled with energy dispersive spectroscopy (EDS) for semi-quantitative chemical analysis, and SEM-based automated mineralogy were employed on samples taken from the South Reef orebody.

2 Samples and Methods

2.1 Samples

Quarter-core samples were collected from variably mineralised Cu intercepts from 6 drill holes in the South Reef (shown in Fig. 2). Drill hole RC11-0187 was the most extensively sampled (48 of the 98 total samples) because of its extremely thick Cu-mineralised intercept. Samples from the Number One ore body were provided by the U.S. Geological Survey (USGS) prior to sample collection for the purpose of initial reconnaissance. The South Reef samples were chosen based on the availability of modern drill core, modern reconnaissance Ge assay data, and the opportunity to sample different intensities of mineralisation.

2.2 Methods

Forty-one of the 98 drill core samples collected were selected for analysis in the Mineral and Materials Characterization Facility at the Colorado School of Mines because they reflect different intensities of mineralisation. Our workflow was multi-step. First, a mapping μ-XRF (M4 Tornado, Bruker) was used as a reconnaissance tool to determine elemental distributions in these 41 samples so that a sub-sampling strategy could be determined. Next, billets from selected areas on 25 samples were cut for thin section preparation for more detailed study. These billets were mapped using the μ-XRF at a higher resolution prior to thin section preparation. Third, the finished thin sections were inspected under transmitted and reflected light, FE-SEM BSE (MIRA, Tescan) and EDS (XFlash® 6/30 silicon drift detector, Bruker) and SEM-based automated mineralogy (TIMA, Tescan) to understand mineral paragenesis and related occurrence and distribution of cobalt and germanium in the South Reef.

3 Results and Discussion

Mineral paragenesis of the South Reef was determined based on a combination of petrography and co-registered micro-analytical methods such as mapping μ-XRF, SEM-based automated mineralogy, and traditional FE-SEM BSE and EDS analyses. The South Reef consists of localised high grade Cu intercepts, including massive bornite and chalcocite that extend laterally into more abundant chalcopyrite-rich zones.

Micro-XRF mapping (Fig. 3) showed that Co is hosted in cobaltiferous pyrite, carrollite, and cobaltite and revealed a strong correlation between Cu and Fe, and that high Co values almost always correspond to high Ni values. Barium and K as well as Ge and K show a significant spatial correlation. A notable correlation was seen between Co, Bi, As, and Pb in some samples. Within areas showing high Cu (Cu sulphides), bright areas of Ge could be found.

Five paragenetic stages were delineated: (I) dolomitisation, (II) ferroan alteration, (IIIa) veining, (IIIb) brecciation, (IV) main ore forming event (Fig. 4), and (V) a post ore forming event. Stage I predominantly consists of diagenetic low-temperature dolomite and pyrite, followed by ferroan stage II dolomite and pyrite as reported by Hitzman (1986). Stage III includes different carbonates, pyrite, cobaltiferous pyrite, and the Ba-minerals cymrite and alstonite. During the main ore forming

stage IV, cobaltiferous pyrite was replaced by mainly chalcocite and subordinately bornite. Trace elements in stage III cobaltiferous pyrite (Co, As, Pb) were liberated and precipitated as cobaltite, carrolite, galena, tennantite (Mahaffey 2021; this study). Petrographic observations reveal a distinct precipitation succession of the different Cu-sulphide minerals in stage IV. Chalcocite, bornite, and chalcopyrite did not precipitate in equilibrium but are staggered in space and time, with chalcocite precipitating first in the centre of the deposit,

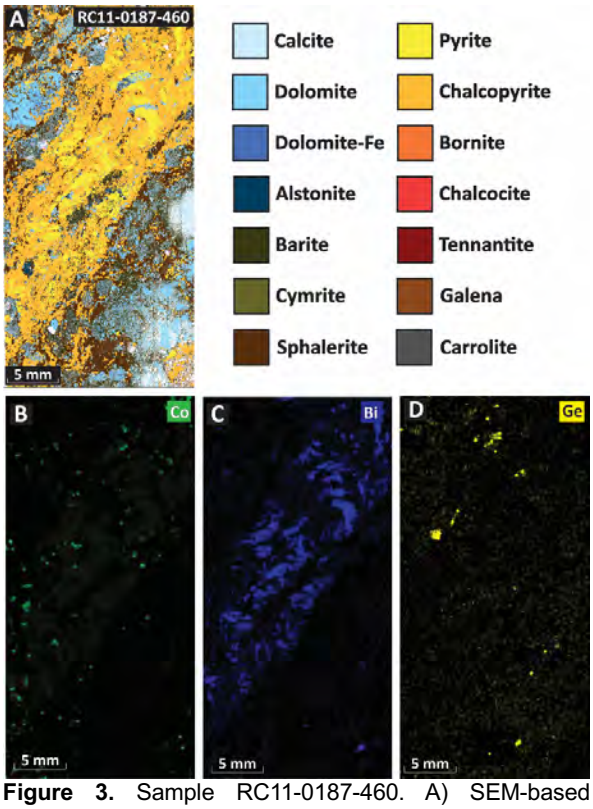

Figure 3. Sample RC11-0187-460. A) SEM-based automated mineralogy images, and µ-XRF element maps of B) Co, C) Bi, and D) Ge.

followed by bornite and then chalcopyrite (Hitzman 1986, Conner 2015, this study). The mineral renierite is the Ge bearing sulphide in the South Reef orebody. Renierite predominantly occurs as inclusions in chalcocite and bornite and is significantly less abundant in chalcopyrite. Renierite grains in chalcopyrite are commonly in contact with residual bornite and are always much smaller than renierite inclusions in chalcocite and bornite. These textures suggest that renierite, like bornite and chalcocite, is no longer in equilibrium in the presence of chalcopyrite. Discrete cobalt minerals occur in high-grade Cu zones and are represented by carrolite and cobaltite.

Hitzman (1986) suggested that the mineralizing fluid was a warm (100 to 215°C) basinal brine, rich in hydrocarbons, suggesting that the fluid responsible for ore formation was highly reduced. A reduced and acidic basinal brine at 200°C is able to transport significant amounts of Cu, Ba, and Zn (Cooke et al. 2000; Pfaff and Graham 2013).

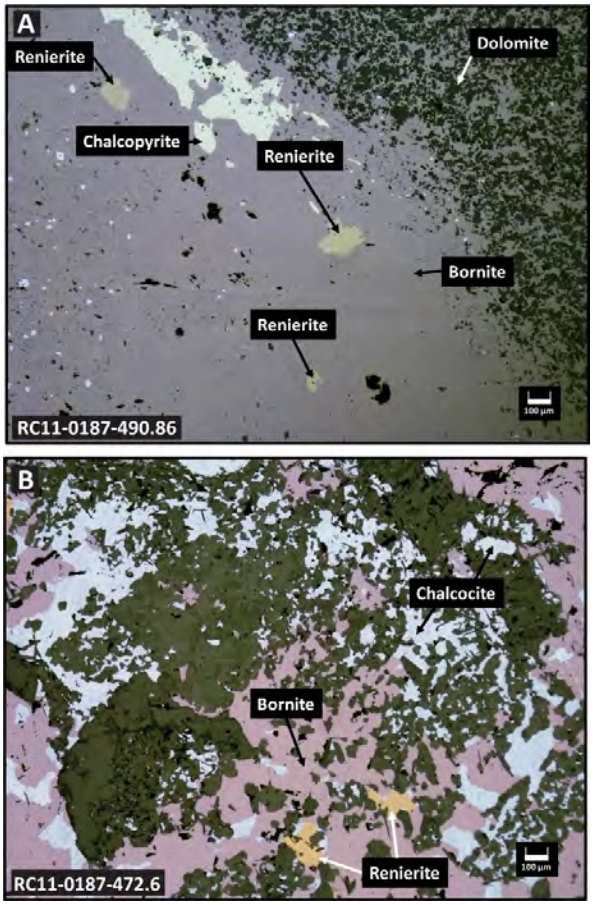

Figure 4. Stage IV ore mineralogy. Renierite hosted in bornite and in association with chalcocite and minor chalcopyrite.

This is consistent with observations from other carbonate hosted Cu-sulphide deposits such as the Black Butte deposit in Montana (Pfaff and Graham 2013) or the lead-zinc clastic sediment hosted Sullivan Deposit (Cooke et al. 2000). It is suggested here that reduced acidic basinal brines ascended along basin faults and interacted with carbonates at the site of ore deposition, causing the fluid to shift in pH towards more alkaline conditions, resulting in the precipitation of ore minerals. The succession of Cu-sulphide minerals is interpreted to reflect the evolving fluid during fluid-rock interaction leading to more alkaline conditions and to a concomitant decrease in sulphide activity in the mineralizing fluid over space and time. When the sulfur activity in the fluid decreases, chalcopyrite is formed at the expense of bornite and pyrite and renierite is destabilised (Einaudi et al. 2005). Similar textural evidence can also be observed at Kipushi where renierite preferentially occurs in chalcocite and bornite (De Vos et al. 1974, Schneider et al. 2007).

5 Conclusions

The South Reef of the Bornite Cu-Co-(Ge) deposit is host to substantial amounts of high-grade Cu, Co, and Zn, but also hosts elevated concentrations of

Ge. With an increasing demand for Co and Ge and the lack of literature on their occurrence and sequestration within primary ore deposits, understanding known Co- and Ge-bearing ore deposits is critical for future exploration efforts. Five paragenetic stages have been delineated at the South Reef of the Bornite Cu-Co-(Ge) deposit: (I) dolomitisation, (II) ferroan alteration, (IIIa) veining, (IIIb) brecciation, (IV) ore forming event, and (V) post ore forming event. Cobalt occurs in cobaltiferous pyrite, carrollite, and cobaltite. Germanium occurs in renierite as well as enrichments in white mica, illite, galena and feldspars within the South Reef. Highest Ge-mineral (renierite) as well as Co-minerals (carrolite and cobaltite) abundances appear to correlate with highest bornite and chalcocite concentrations.

We propose that reduced acidic basinal brines capable of transporting significant amounts of Cu entered the organic matter rich carbonates and phyllites, leading to fluid-rock interaction at the site of deposition. The ore-forming basinal brine was subsequently buffered to an intermediate oxidation state and a near-neutral pH. Petrographic observations and SEM-based automated mineralogy reveal a distinct spatial and temporal precipitation succession from chalcocite, bornite, followed by chalcopyrite. This succession in Cu-minerals is interpreted to reflect the evolving ore forming fluid at the site of deposition, characterised by a decrease in temperature and a concomitant decrease in sulphide activity of the mineralizing fluid. This shift in pH towards more alkaline conditions, and subordinately a decrease in temperature and concomitant decrease in sulphide activity, are thought to have been the predominant precipitation mechanism leading to the distinct mineral zonation in space and time. Cobalt, which predominantly occurs in pre-main ore stage cobaltiferous pyrite, was replaced and Co was liberated during the ore forming process, leading to the formation of discrete Co-minerals (carrolite and cobaltite). Germanium is interpreted to have precipitated contemporaneously with chalcocite and bornite when the sulphur activity in the fluid was still high, forming discrete renierite minerals.

The Bornite deposit shares many similarities with other Ge-bearing carbonate hosted base metal deposits in Africa such as the Tsumeb, Kipushi, Khusib Springs, Kombat, and Kabwe deposits, however it seems to be of lower germanium grade than these deposits.

Acknowledgements

We thank Trilogy Minerals, and specifically Andy West, Bonnie Broman, and Dave Szumigala for access to drill core. Thanks to Heather Lowers and Mitchel Bennett for thorough reviews, which improved this contribution significantly.

Disclaimer

Any use of trade, firm, or product names is for descriptive purposes only and does not imply endorsement by the U.S. Government

References

Cooke D, Bull S, Large R, McGoldrick P (2000) The importance of oxidized brines for the formation of Australian Proterozoic stratiform sediment-hosted Pb-Zn (sedex) deposits. Econ Geol 95: 1-18.

Conner DT (2015) Geology of the Bornite copper-zinc-cobalt carbonate-hosted deposit, southwestern Brooks Range, Alaska, Masters Thesis, Colorado School of Mines, 70p.

Davis B, Rim R, Austin J (2008) NI 43-101 Technical Report on the Bornite Project, Northwest Alaska, USA. Prepared for Trilogy Metals Inc.

De Vos W, Viaene W, Moreau J (1974) Minéralogy du gisement de Kipushi, Shaba, Zaïre. Cent de la Soc Géol 165-183.

Einaudi MT, Hedenquist JW, Esra Inan E (2005) Sulfidation state of fluids in active and extinct hydrothermal systems: Transitions from porphyry to epithermal environments. In: Volcanic, Geothermal, and Ore-Forming Fluids: Rulers and Witnesses of Processes with the Earth, Sturart F. Simmons, Ian Graham. https://doi.org/10.5382/SP.10.15

Granitto M, Wang B, Shew NB, Karl SM, Labay KA, Werdon MB, Seitz SS, Hoppe JE (2019) Alaska Geochemical Database Version 3.0 (AGDB3) including best value data compilations for rock, sediment, soil, mineral, and concentrate sample media: U.S. Geological Survey data release, https://doi.org/10.5066/P98NHRAD.

Hitzman M (1986) Geology of the Ruby Creek copper deposit, southwestern Brooks Range, Alaska, Economic Geology 81: 1644-1674 https://doi.org/10.2113/gsecongeo.81.7.1644

Jones A (2021) Germanium occurrence in the Bornite deposit, southwestern Brooks Range, Alaska, Masters Thesis, Colorado School of Mines, 103p. https://hdl.handle.net/11124/176411

Mahaffey ZB (2021) The mineralogical associations, distribution, and mineral zoning of cobalt in the Bornite deposit, southwest Brooks Range, Alaska, University of Alaska Fairbanks, Masters Thesis, 134 p. plus appendices., http://hdl.handle.net/11122/12625

Pfaff K, Graham GE (2013) The Black Butte Cu-(Co-Ag) deposit, Montana: A thermodynamic model. GSA Annual Meeting & Exposition, Denver, Colorado, USA. https://gsa.confex.com/gsa/2013AM/webprogram/Paper229705.html

Schneider J, Melcher F, Brauns M (2007) Concordant ages for the giant Kipushi base metal deposit (DR Congo) from direct Rb-Sr and Re-Os dating of sulfides. Miner Depos 42: 791-797.

Till AB, Dumoulin JA, Harris AG, Moore TE, Bleick H, Siwiec B (2008) Preliminary integrated geologic map databases for the United States: digital data for the geology of the southern Brooks Range, Alaska: U.S. Geological Survey Open-File Report 2008-1149.

U.S. Geological Survey, 2016, 2022 Final List of Critical Minerals: Federal Register/Vol. 87, No.37/Thursday, February 24, 2022/Notices: 10381-10382.

Exploring the preservation potential of mineral deposits in the northern Canadian Cordillera through low temperature thermochronology: preliminary insights

Nicolas Pinet[1], Dawn Kellett[2], Isabelle Coutand[3], Patrick Sack[4]
[1]Geological Survey of Canada, Québec, QC, Canada
[2]Geological Survey of Canada, Dartmouth, NS, Canada
[3]Department of Earth Sciences, Dalhousie University, Halifax, NS, Canada
[4]Yukon Geological Survey, Whitehorse, YK, Canada

Abstract. In northern Canada and eastern Alaska, Late Cretaceous to Eocene mineral deposits formed at upper crustal levels, after the accretion of allochthonous terranes against North America. To analyse their preservation potential, an orogen-scale study of multiple low temperature thermochronometers has been initiated. This study will enable a large-scale investigation into spatio-temporal variations in exhumation, and thus delineate areas favourable for preservation of mineral deposits formed at shallow depths.

1 Introduction

Reflecting its complex geological history, the northern Cordillera, which spans northern British Columbia, Yukon (Canada) and eastern Alaska (USA), is endowed with diverse mineral deposit types of various ages. Some deposits were formed before or during the primarily Jurassic accretion of allochthonous terranes against ancestral North America, whereas others are linked to post-accretionary tectonism and magmatism. Post Jurassic mineral deposits include (Fig. 1A; Allan et al., 2013; Nelson et al., 2013):

1) mid-Cretaceous gold mineralization occurring in an elongated belt extending from eastern Alaska to easternmost Yukon, associated with the emplacement of several mid-Cretaceous (115-98 Ma) intrusive suites. Mineralization includes intrusion breccia complexes, Au- and W-skarns, reduced intrusion-related deposits and epithermal mineralization, and polymetallic veins.
2) Late Cretaceous (79-72 Ma) Cu-Mo-Au porphyries, skarns and epithermal deposits that are significantly enriched in Au. In Alaska and west-central Yukon, some of the mineral deposits are associated with small volume, high-level intrusive bodies that have isotopic signatures and geochemical affinities to mantle-derived magmas with minor crustal inheritance. Carlin-type deposits located in east-central Yukon also formed during this metallogenic event.
3) Latest Cretaceous to Eocene (70-50 Ma) porphyry Cu, Mo systems and polymetallic veins, carbonate replacements, skarn bodies and epithermal systems. Some of the mineralized zones overlap in age with extensive regional emplacement of the volcanic rocks of the 71-68 Ma Carmacks Group that once covered much of central-southwest Yukon (Fig. 1)

Aside from exposed magmatic rocks, and the Tintina and Denali faults, parallel, major right-lateral strike-slip faults with ~ 370 and ~ 430 km of mainly Cenozoic displacement, respectively (Fig. 1A), there are few constraints on the mid-Cretaceous to Eocene geological history of the northern Cordillera. However, this time interval was marked by a change in plate-margin geometry, possible variations in lithospheric thickness and a subtropical climate, that collectively likely have had a profound impact on landscape evolution of the mountain belt. Late Cretaceous to Cenozoic geological history potentially resulted in variations in exhumation distribution and intensity across the orogen that may have impacted the preservation potential of shallow-crustal level hydrothermal deposits. We are undergoing a regional-scale multi-thermochronology study to quantify spatio-temporal variations in crustal exhumation and hereby introduce preliminary insights.

2 Geomorphological setting

Between the Denali and Tintina faults, the Yukon uplands represent a relatively low erosional surface that truncates metamorphic rocks and intrusions. The base of the shallowly dipping (generally < 10°) volcanic rocks of the Carmacks Group preserved in central Yukon represent the paleo-topography at 71-68 Ma. This suggests that the age of the planation of the Yukon uplands is at least Late Cretaceous. This led Ryan et al. (2017) to propose that there has been little net incision since the late Mesozoic. However, the amount of eroded, post 71 Ma rocks is poorly constrained (Dusel-Bacon et al., 2016).

3 Low-temperature thermochronology

Figure 1B shows available published and unpublished low-temperature thermochronology data including (U-Th)/He analyses on zircon (ZHe), apatite fission track analyses (AFT) and (U-Th)/He analyses on apatite (AHe) with closure temperature ranges of ~20–200°C, ~80–120°C and ~30–120°C, respectively (Ault et al., 2019).

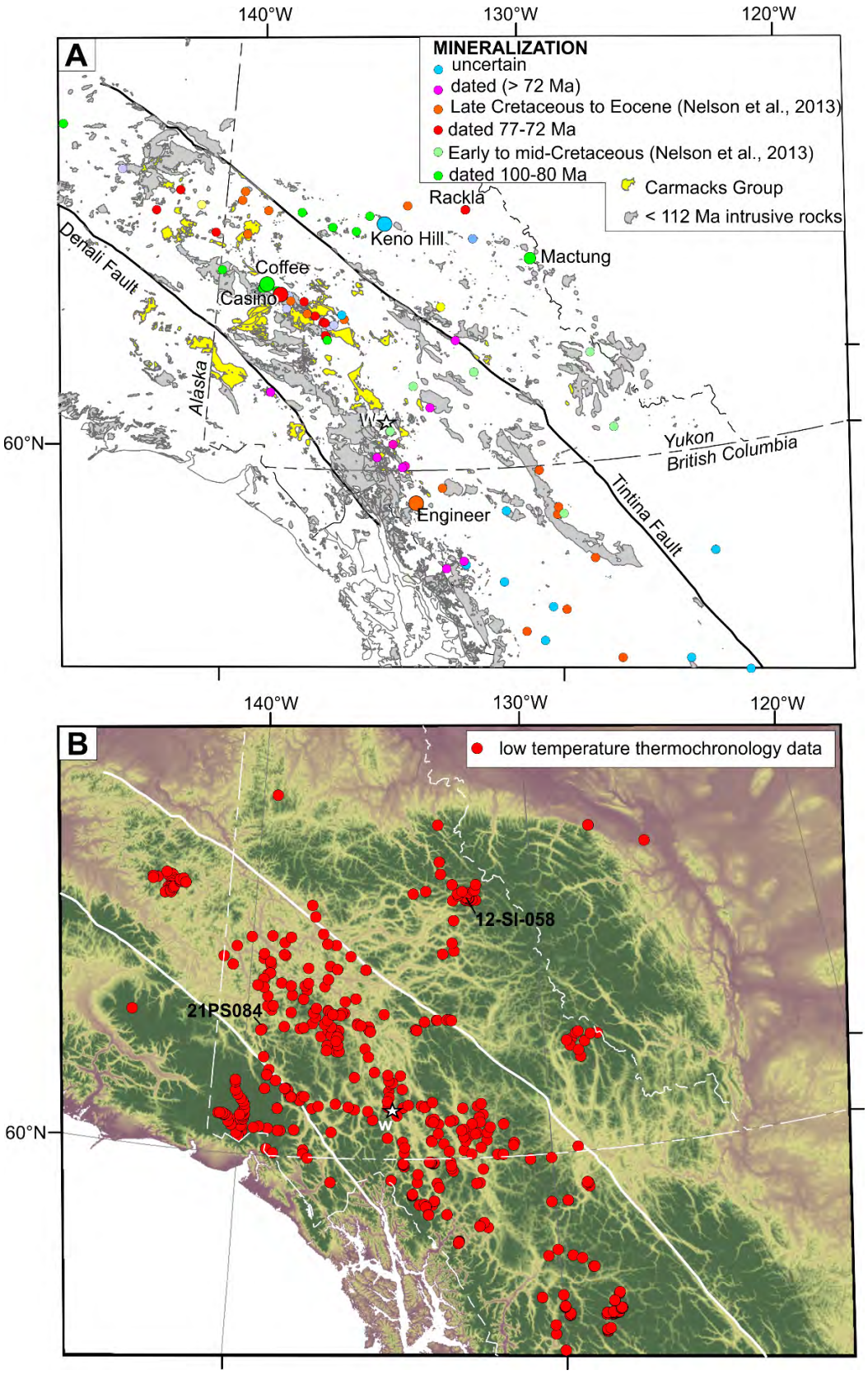

Figure 1. A- Geological setting of the northern Cordillera with location of the mid-Cretaceous to recent mineralized zones; Methods to constrain the age of dated mineralized zones include Re–Os, $^{40}Ar/^{39}Ar$ and U-Pb. Volcanic rocks of the Carmacks Group (71-68 Ma) and intrusive rocks younger than 112 Ma are located. B- Available low-temperature thermochronology data. W, Whitehorse.

Among the > 600 compiled samples, ca. 32% include several thermochronometers, providing independent information on the T-t path in the upper crust.

When several thermochronometers are used on the same sample, dates usually conform to the expected order, with ZHe > AFT > AHe, especially in young orogens (Whipp et al., 2022). The time difference between ZHe, AFT and/or AHe dates on a single sample varies significantly within the dataset, which indicates a difference in exhumation rates (i.e., rapid exhumation is expected to yield minimal difference between dates).

Dated samples represent a wide range of sedimentary, metamorphic and plutonic rocks of various ages, collected at various elevations which add complexity to the interpretation of regional exhumation patterns. However, for each sample, predictable ZHe, AFT and/or AHe dates are expected for various T-t scenarios (Fig. 2). To facilitate T-t modelling, recently collected data target Cretaceous magmatic rocks which record only thermal events postdating crystallization.

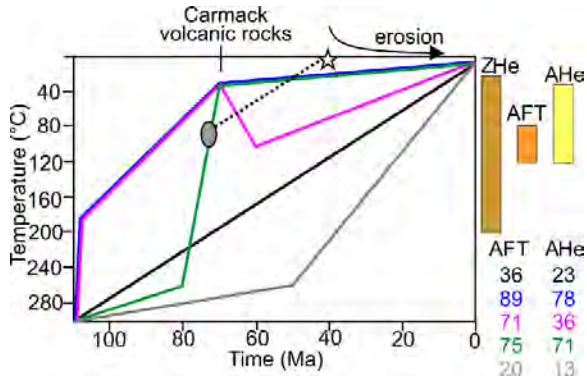

Figure 2. Time-temperature diagram for an intrusive rock emplaced at ca. 110 Ma and showing expected AFT and AHe dates (in Ma) for different potential T-t paths. The closure temperature windows of thermochronometers are indicated. The ellipse, dashed line and star illustrate the T-t path of a hypothetical mineral deposit formed at 2-3 km depth during the Late Cretaceous (ca. 74 Ma) in an area characterized by constant cooling (black T-t path). Such deposit would be eroded at ca. 40 Ma.

4 Preliminary results

Figure 3 shows two examples that illustrate how independent geological constraints may help to define Late Cretaceous to Cenozoic T-t paths.

Sample 12-SI-058 (location in Fig. 1B) yields an AFT age of 49.2 ± 5.3 Ma, with a mean track length of 13.6 µm. It was sampled from Neoproterozoic sedimentary rocks located 2 km from Carlin-type deposits in central Yukon (Pinet et al., 2023). Pyrobitumen reflectance and programed pyrolysis results constrain the maximum temperature during the Late Cretaceous to 230-150 °C (constraint 1, Fig. 3A). Maximum temperature during mineralization at ca. 74 Ma is 91 °C based on fluid inclusion and clumped isotope thermometry on late ore stage minerals (constraint 2, Fig. 3A). Inverse modeling suggests a period of rapid cooling at ca. 35 Ma.

Sample 21PS084 (location in Fig 1B) yields an AFT date of 34.8 Ma ± 2.6 Ma, with a mean track length of 14.5 ± 0.4 µm. It is an intrusive sample collected from the mid-Cretaceous Whitehorse magmatic suite (constraint 1: temperature > 300°C at 112-98 Ma, Fig. 3B). This sample is located 4.2 km from exposed Carmacks Group at an elevation only 125 m lower than the base of the group (constraint 2: temperature < 60 °C during volcanic rocks emplacement at ca. 70 Ma, Fig. 3B). Inverse modelling indicates that only scenarios with one or several heating episode(s) during the Cenozoic may account for the data if geological constraint 2 is considered, even if no rock younger than the Carmacks Group is known in the area.

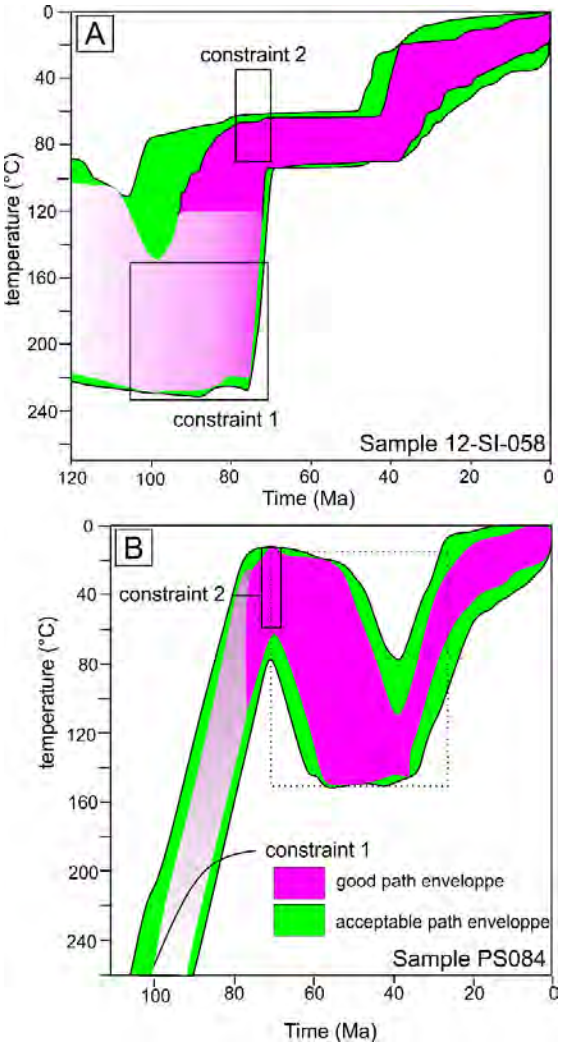

Figure 3. Inverse modelling results using *HeFTy* software (Ketcham, 2013). The black boxes are geological constraints used during modelling. The part of the magenta envelope with a colour gradient is almost unconstrained by modelling.

5 Future work

New low-temperature thermochronology analyses are in the process of being added to this compiled ZHe, AFT and AHe dataset with the aim to apply a large spatial- and temporal- coverage to investigate rates, patterns and drivers of orogen-wide exhumation, within a regionally consistent framework. This approach should help to depict spatial trends of exhumation, possibly linked to plate-boundary processes, tectonic activity, magmatism and post-orogenic surface processes and ultimately provide insight on the preservation of Late Mesozoic to Cenozoic mineral deposits.

Acknowledgements

All the participants of the GEM GeoNorth project 'Faults, fluids and landscape evolution: Cretaceous to Cenozoic in the Northern Cordillera' are warmly acknowledged.

References

Allan M.M., Mortensen J.K., Hart C.J.R., Bailey L.A., Sanchez M.G., Ciolkiewicz W., McKenzie G.G., Creaser R.A. (2013) Magmatic and metallogenic framework of west-central Yukon and eastern Alaska: Society of Economic Geologists, Special Publication 17, p. 111–168.

Ault A.K., Gautheron C, King G.E. (2019) Innovations in (U-Th)/He, fission track, and trapped charge thermochronometry with applications to earthquakes, weathering, surface-mantle connections, and the growth and decay of Mountains. Tectonics, 38:3705-3739.

Dusel-Bacon C., Bacon C., O'Sullivan P.B., Day W.C. (2016) Apatite fission-track evidence for regional exhumation in the subtropical Eocene, block faulting, and localizes fluid flow in east-central Alaska. Can. J. Earth Sci., 53:260-280.

Ketcham RA (2013) HeFTy, version 1.8.2. Manual user dated 2 october 2013.

Nelson J.L., Colpron M., Israel S., 2013. The Cordillera of British Columbia, Yukon and Alaska: tectonics and metallogeny. Soc. Econ. Geol., Special Publication 17, pp. 53-109.

Pinet, N., Haeri-Ardakani O., Jautzy J., Savard M.M., Sack P., Mercier-Langevin P., 2023. Thermal history of Carlin-type gold deposits in Yukon (Canada) as revealed by organic matter geothermometry, clumped isotope data, fluid inclusion microthermometry, and apatite fission-track analyses. Mineralium Deposita, https://doi.org/10.1007/s00126-023-01162-2

Ryan J.J., Hayward N., Jackson Jr., L.E. (2017). Landscape antiquity and Cenozoic drainage development of southern Yukon, through restoration modeling of the Tintina Fault. Can. J. Earth Sci., 54:1085-1100.

Whipp D.M., Kellett D.A., Coutand I. and Ketcham R.A. (2022) Modeling competing effects of cooling rate, grain size, and radiation damage in low-temperature thermochronometers. Geochronology, 4:143-152.

A hyperspectral detailed view on a magnetitite horizon in the Bushveld Complex, SA.

Dieter Rammlmair[1], Wilhelm Nikonow[2]
[1]Institute of Mineralogy, Leibniz University Hannover
[2]Federal Institute of Geosciences and Natural Resources

Abstract. More than 20 individual magnetitite layers occur within the Upper Zone of the layered Bushveld igneous complex, South Africa. Three individual layers from drill core BH7772, Marula Mine, Eastern Lobe were analyzed, offering a wide range of textural patterns. Investigations by LIBS, µEDXRF and HSI revealed mineralogical, mineral chemical, rock chemical and textural information in a continuous mode. Whilst mineralogical information can be quite easily derived by either method, the access to proper mineral grain information such as area grain size, grain shape and orientation, as well as deformation needs more effort. Both, µEDXRF and LWIR HSI are sensitive for individual grain orientation by changing the chemical signal due to diffraction, or the spectral reflectance or absorbance feature, respectively. By applying ENVI spectral angle mapper (SAM) an evaluation of either method can be performed given that a proper endmember collection is provided. Whilst spatial resolution of µEDXRF provide detailed information for selected parts, LWIR mapping with 400 µm step size can be acquired from large core intervals. The evaluation of signals controlled by orientation within an individual mineral mask allows the extraction of size, shape and orientation of individual grains within a continuous core section, providing a new insight into the genesis of magnetite layers.

1 Introduction

Drill cores provide continuous information of parts of the Bushveld igneous complex, the worldwide largest layered mafic to ultramafic intrusion hosting huge PGE, Cu/Ni sulphides, chromitite, and Ti and V in magnetitite deposits (Scoon and Mitchell 2012; Molyneux 1974). Optical, chemical and physical hyperspectral methods such as VNIR, SWIR, LWIR, LIBS, µEDXRF next to remanent magnetization, radiation, electric resisti-vity, heat capacity, x-ray absorption, CT, spectral CT provide among others information in 1D, 2D and even 3D. These methods provide the basis for detailed mineralogical, chemical and textural investigation (Nikonow et al., 2019) in a more objective way that logging geologists could perform for later interpretation and further sampling for more detailed investigation of exceptional samples by quantitative methods such as EPMA, LA-ICP-ToF-MS among others.

Sample handling and data acquisition and turnover time of results are crucial aspects for the mining industry. Therefore, the focus is based on easy-to-handle fast methods. Unfortunately, a single method will not cover all aspects of interest and combining methods is necessary.

LIBS, despite strong matrix effects, has become an outstanding tool to identify individual phases based on chemical patterns by ENVI spectral angle mapper (SAM) algorithm. It can further be used to monitor Mg# and An# of orthopyroxene, clinopyroxene, olivine, chromite, and plagioclase, respectively, in relation to the pixel neighbourhood, to highlight fractionation and reversal pattern comparable to EPMA derived pattern down to 50 µm spatial resolution (Meima et al. 2022a,b). It further provides detailed information on the changes of trace element chemistry of individual mineral phases in a continuous mode for several meters. With µEDXRF at 20 µm spatial resolution even more details can be extracted in an automated way providing SAM based phase modality, area grainsize distribution and phase orientation as far segmentation of grains works in an acceptable way. But, monomineralic aggregates are a challenge for a correct grainsize attribution on a chemical basis. µEDXRF on coarse materials is governed by diffraction signals based on the crystallographic orientation of individual mineral grains. This aspect can promote the extraction of individual grains within aggregates to obtain better area grainsize and grain shape and orientation (Nikonow and Rammlmair 2016). An additional aspect is, that by selection of areas of interest a direct 2D correlation of modality and chemistry can be achieved.

Hyperspectral imaging (HSI) of visible-near Infrared, short and long wave infrared, VNIR, SWIR and LWIR, respectively, can be used as an alternative method. It is the fastest screening method - despite the aspect of proper core surface cleaning - of full core prior to cutting applied by the mining industry to highlight mineral distribution and lithological changes in drill core boxes at spatial resolution of approx. 1.4 mm. Since most pixels will record mineral mixtures spectral unmixing has to be obtained to highlight the mineral fractions within individual pixels. By scanning a half core at higher resolution, a strong reduction of mixed pixels, always in relation to the grain size of the investigated phases, can be obtained down to 25 µm for VNIR and SWIR and 400 µm for LWIR thus monomineralic spectra are obtained. This brings in a new aspect for data interpretation. Since spectra of individual grains have to be interpreted the orientation of the mineral grain might change a signal pattern dramatically. This needs an enormous development of individual mineral endmembers referring to the changes in orientation, thus being able to identify a mineral distribution pattern with SAM. But as a positive side effect the grain orientation signals within a mineral mask can

be used to extract again individual grains for further textural analyses, namely optimization of area grainsize distribution, grain shape and grain orientation.

The fusion of data sets based on LIBS or µEDXRF derived phase maps used to mask phases of interest with HSI can promote the acquisition of textural details on larger scale at sub-mm level for identification of grain size changes.

2 Materials and methods

Core BH7772 from the Marula Mine was donated to the University of Bloemfontain for the ICDP by Impala Platinum Ltd.. Logging and logistics were done by Prof. Roelofse (Univ. Bloemfontain). Three magnetite layers from the lower central and upper portion were selected each with transitions to foot and hanging wall, anorthosites, lithologies and sampling of continuous slices through three magnetitites, in total 11.33 m was done by Dr. Veksler from GFZ, Potsdam.

Data acquisition by spectral methods followed a scheme of minimum disturbance of primary setting. Hyperspectral imaging was performed as the first step by SisuRock scanner from Specim. An approx. 15 cm field of view was used for long wave infrared, (LWIR) resulting in 400µm pixel resolution, whilst for short wave infrared (SWIR) and visible to near infrared (VNIR) a 5 cm FOV was applied generating 125 and 42 µm pixels, respectively. Measurement started with LWIR followed by SWIR and VNIR to reduce preheating artefacts. Row data were radiometrically and geometrically corrected to obtain reflectance. The noise was minimized by MNF transformation and spike removal was performed to obtain a calibrated and corrected reflectance data set. For individual minerals, the focus was on LWIR, a number of endmembers were extracted reflecting different grain orientation to be used for ENVI hyperspectral software based spectral angle mapper (SAM) classification.

Laser induced breakdown spectroscopy (LIBS) imaging was applied prior to cutting samples into subsample. The GeoLIBS Scanner from Laser Technik Berlin (LTB) with a 1064 nm Nd:YAG laser was applied to map a 1 cm stripe with 75 µm step size. For LIBS results refer to Nikonow et al. 2023 at SGA 2023.

Continuous element mapping of drill core sections was done by a Bruker M4-Tornado Plus micro energy dispersive x-ray fluorescence (µEDXRF) system, too. Samples were cut to a size of 20 cm length to feed the system. Analysis was performed under vacuum with a Rh tube at 50 kV, 30 µA, with a poly-capillary beam guide with 51° incidence angle, without filters, and two opposing detectors with 51° take off angle, 90 ° to the tube. Mapping was performed in 40 µm steps in x and y direction and at 5 msec acquisition time. Data from both detectors were extracted and the minimum per pixel per channel of both detectors was calculated to obtain a minimum dataset (*min) with reduced diffraction signal side effects for 165 region of K/L/M lines of elements of interest as an ENVI database. Additionally a dataset (*D1-D2) of the difference of both detectors was used reflecting the signal deviation for each of the detectors regarding the minimum per channel per pixel thus reflecting the diffraction signals of individual grains (Nikonow and Rammlmair, 2016).

3 Results and discussion

The results from the LIBS and EDXRF data evaluation are presented by Nikonow et al. at SGA 2023. LIBS profiles reflect the chemical changes within an individual mineral distribution. Meima et al. (2022a,b) showed in a section through 6 m Merensky Reef, and a section from UG2 chromitite from Karee Mine, Western Lobe of the Bushveld Complex how detailed and accurate - validated by EPMA analysis - Mg# of pyroxenes, olivine and chromite, as well as anorthite content of plagioclase reflects changes related to fractional crystallization and reversals due to new magma input. Similar effects can be observed in the upper zone magnetitite layers, too (Nikonow et al. at SGA2023). The µEDXRF data evaluation provide very detailed mineral distribution pattern based on supervised ENVI SAM classification using approx. 8000 mineral spectra as a data base, but elemental analysis of individual grains might be disturbed by prominent diffraction signals influencing the intensities of other elements, due to not complete pattern removal in some grains.

These disturbing diffraction signals can provide additional thus quite valuable information. By masking a classified individual phase distribution, all changes in signal within this frame would represent changes in crystal orientation, and therefore form a basis for further segmentation of individual grains in monomineralic compounds in a better way then watershed segmentation could do.

To achieve this, an elevated effort is needed to obtain a reliable grain orientation data base per mineral for millions of possibilities. Focusing on the most prominent signals of a selected mineral like magnetite the number of endmembers to be created could be reduced to a minimum by using a wider threshold. Since grains are often randomly orientated conflicts due to identical orientation are minimized. Figure 1 shows an example of some almost massive magnetite layers with ilmenite and a late clinopyroxene rich aggregate with fine interstitial magnetite. Wang 2023 assumes for Hongge layered Intrusion in China that fractional crystallization-based aggregation of magnetite will range around maximum 60%. He stated that hydrothermal input is needed to get higher magnetite concentrations in a layer. The hydrothermal input is supported by extremely light delta $\delta^{56}Fe$ in secondary magnetite compared to primary magnetite thus 20% to 30% could be hydrothermally mobilized from deeper units. The hydrothermal addition of Fe coinciding

with silicate resorption and therefore increasing compaction would generate a relative loss Cr, Ti, V, Mn etc..

This brings us back to the element variability in the Bushveld magnetitites, documented by both LIBS profiles and µEDXRF mapping (Figure 1a) and to the partial strong magnetite enrichment, where grains are compacted and only diffraction signals (Fig.1b) would record grain size changes within the system prior to applying other time-consuming methods.

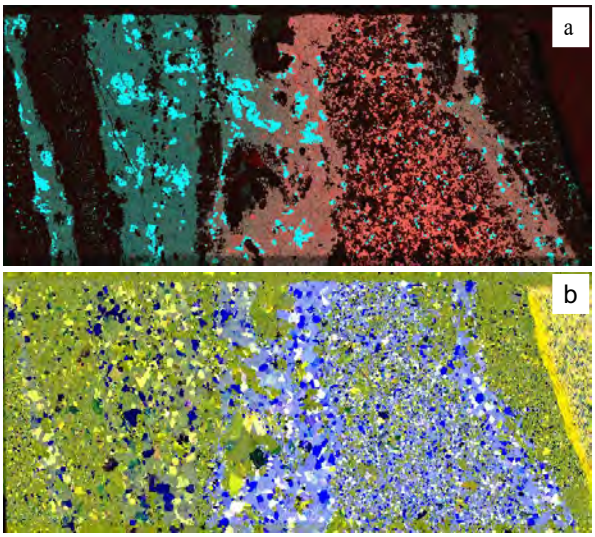

Figure 1. a) Distribution of Cr, V and Ti as RGB image showing strong gradient of Cr from interstitial fine-grained magnetite within a clinopyroxene, plagioclase, apatite aggregate via a massive proximal magnetite layer with coarse ilmenite at intermediate values into a distal massive magnetite with coarse ilmenite at low values.
b) shows the grain size pattern of two strongest lines at RhLa (D1-D2) and RhLb D1-D2) in RGB with D1 (red) and D2 (green) and superimposed Cr min (blue) for magnetite with bluish background and silicates and ilmenite in greenish. Note the rapid grain size changes displayed by diffraction pattern (Length 18cm)

The extremely elevated Cr content within fine grained magnetite in the clinopyroxene aggregate. A number of models exist discussing replenishment, reactive melt infiltration, fractional crystallisation, inversals etc. (Tegner et al. 2006; Junge et al. 2014; Scoon and Mitchell 2012, Yao and Mungall 2022; Kruger and Latypov 2020b). What definitely can be observed is an extreme complexity of textural features which all do influence the chemical pattern of magnetite, and in the case of figure 1 showing a prominent metasomatic Cr halo around a relatively thin clinopyroxene rich feature. Similar pattern occurs at some anorthosite layers, too.
Besides evaluation of EDXRF diffraction pattern, suitable for spinels, LWIR can be helpful to obtain a quick overview of misorientation of silicates. But data extraction on a grain size basis for LWIR is a huge challenge since signals related to remote sensing reflect homogeneous powder samples with sum signals that can easily be compared with available

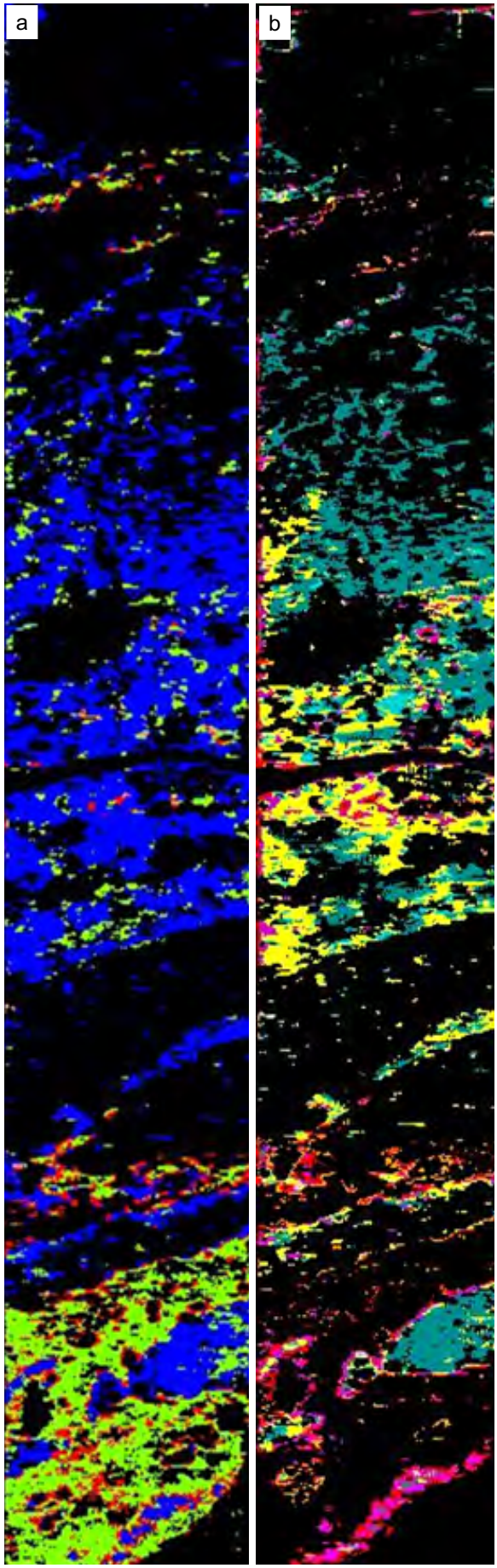

Figure 2. LWIR Endmember based classification showing silicate distribution in magnetite layer (Sample UZ223-15_24 from 217.86m to 218.15m) showing a) plagioclase in blue, clinopyroxene in green and biotite in red, Fayalite in purple and magnetite, ilmenite and sulfide in black, and b) different orientation of plagioclase grains in different color (Length 29 cm).

spectral data sets. At 400µm resolution where single grains at different 3D orientation are measured each signal appears to be individual showing changes in the number and ratio of spectral features. One way to solve this problem is to acquire hundreds of individual spectral patterns of each mineral, and adding spectra of not recognized grains to the database.

Spectral sets for individual minerals can be combined to obtain a mineral distribution (Fig. 2a), but even individual pattern can be used to outline similar orientation or even individual grains (Fig. 2b). By translation of the information into grains, evaluation can be performed for size, shape and orientation of single grains, for neighbourhoods providing additional information to modality, mineral and rock chemistry. If automatized this evaluation scheme will promote detailed view to a drill core to achieve a highly valuable pattern identification and comparison in a continuous mode.

4 Conclusions

The analyses of magnetitite core sections from the Bushveld Complex by HSI, LIBS, and µEDXRF provides huge chemical, mineralogical and textural data sets (Nikonow et al. 2019). Whilst chemical and mineralogical aspects are relatively easy to be achieved by hyperspectral evaluation methods, micro textural information such as proper area grain size characterization require new tools. For both µEDXRF and HIS, disturbing signals based on diffraction and mineral grain orientation dependent distortion of reflectance as well as absorption signals, respectively, can be used to identify individual grain boundaries in monomineralic aggregates. By obtaining a better grain area size, grain shape and grain orientation of individual minerals without elevated analytical effort in a continuous mode detail such as hidden grading, recrystallized shear zones etc. can be extracted which could be used for better interpretation of chemical anomalies in a magnetitite core section.

Acknowledgements

This project is funded in the frame of ICDP by the German Research Foundation (DFG). Project 457479532 “Spectroscopic mineral - chemical analysis of drill cores: Development of fast 2D LIBS, EDXRF and hyperspectral scanning with application to outstanding problems of the Bushveld Complex layered intrusion”. We would like to thank Impala Platinum Ltd. for donating the core, Prof. Roelofse from the University of the Free State, Bloemfontein for logging the core and Dr. Veksler from GFZ Potsdam for logistics. Data acquisition was performed by Dr. Meima, Dr. Goldmann, Christian Woehrl, Dominic Goericke, Christopher Specht at BGR.

References

Junge M, Oberthür T, Melcher F (2014) Cryptic variation of chromite chemistry, platinum group element and platinum group mineral distribution in the UG-2 chromitite: an example from the Karee Mine, western Bushveld Complex, South Africa. Economic Geology 109:795-810.

Kruger W, Latypov R (2020a) Fossilized solidifications fronts in the Bushveld Complex argues for liquid-dominated magmatic systems. Nat Commun 11:2909. doi: 10.1038/s41467-020-16723-6.

Kruger W, Latypov R (2020b) Fossilized solidification fronts in the Bushveld Complex argue for liquid-dominated magmatic systems. Nature Communications 11:2909. doi: 10.1038/s41467-020-16723-6.

Meima J, Rammlmair D, Junge M, Nikonow W (2022a) Continuous measurement of Mg/Fe and Ca/Na ratios with scanning Laser Induced Breakdown Spectroscopy in 6 meter of drill core through Merensky Reef, Bushveld Complex, South Africa EGU General Assembly 2022. Copernicus Meetings, Vienna, Austria.

Meima JA, Rammlmair D, Junge M (2022b) The use of Laser Induced Breakdown Spectroscopy for the mineral chemistry of chromite, orthopyroxene and plagioclase from Merensky Reef and UG-2 chromitite, Bushveld Complex, South Africa. Chem Geol 589:120686. doi: 10.1016/j.chemgeo.2021.120686.

Nikonow W, Rammlmair D (2016) Risk and benefit of diffraction in Energy Dispersive X-ray fluorescence mapping. Spectrochimica Acta Part B: Atomic Spectroscopy 125:120-126.

Nikonow W, Rammlmair D, Meima JA, Schodlok MC (2019) Advanced mineral characterization and petrographic analysis by µ-EDXRF, LIBS, HSI and hyperspectral data merging. Mineralogy and Petrology 113:417-431. doi: 10.1007/s00710-019-00657-z.

Scoon R, Mitchell A (2012) The Upper Zone of the Bushveld Complex at Roossenekal, South Africa: geochemical stratigraphy and evidence of multiple episodes of magma replenishment. South African Journal of Geology 115:515-534.

Tegner C, Cawthorn RG, Kruger FJ (2006) Cyclicity in the Main and Upper Zones of the Bushveld Complex, South Africa: crystallization from a zoned magma sheet. Journal of Petrology 47:2257-2279.

Wang D (2023) The formation of Hongge Fe-Ti-V oxide deposit hosted in layered intrusion, Emeishan Large Igneous Province, Southwest China. PhD Thesis. 210.pp., LUH, Hanover, Germany

Yao Z, Mungall JE (2022) Magnetite layer formation in the Bushveld complex of South Africa. Nature communications 13:1-11.

Petrography and geochemistry of rare earth element occurrences in the Koumbizick Massive (South Region, Cameroon)

Benjamin Ndobe Tarkang[1], Wilson Tasing Ngirnyu[1]
[1]*University of Maroua Faculty of Earth Science, P.O. Box 16, maroua* Cameroon
[2]*National Advance School of Mines and Petroleum Industries* Kaele, P.O. Box 08, kaele Cameroon

Abstract. The Koumbizick Massive (South Region, Cameroon) occurs in the north-western part of the Congo Craton in the Nyong Complex, and is a target for rare earth element (REE) mineralization. The objective of this work is to evaluate the occurrence of rare earth elements of some geological formations such as Gneiss that crop out in the Koumbizick massive. The Nyong unit is characterised by metamorphic rock units of different grades associated with Magnetite-Bearing gneisses and magmatic intrusions that are generally oriented NE-SW. Six representative samples were collected during fieldwork. Geochemical and outlook evaluation approach methods were used to evaluate the REE potential of the samples. The results show that the samples are strongly enriched in REE, especially light REE (La, Ce, Nd, Sm). Petrographic analysis shows that the host rock has a porphyroblastic to granoblastic texture and mineral phases of quartz, plagioclase feldspar, biotite, pyroxenes, and amphibole. According to Pearson's correlation coefficient value, REE show good positive correlation among themselves and fair correlation with other elements such as Cr, Cu, V Zn. These data suggest that the REE concentration outcropping the Koumbizick massive are high.

1 Introduction

Koumbizick is a village located southeast of the Lolodorf subdivision in ocean division of the South Region of Cameroon (Figure 1). The village of Koumbizick has a surface area of 120 km^2 and is located about 30 km north from the town of Lolodorf. It is bound to the east by Abam and west by Mbango.

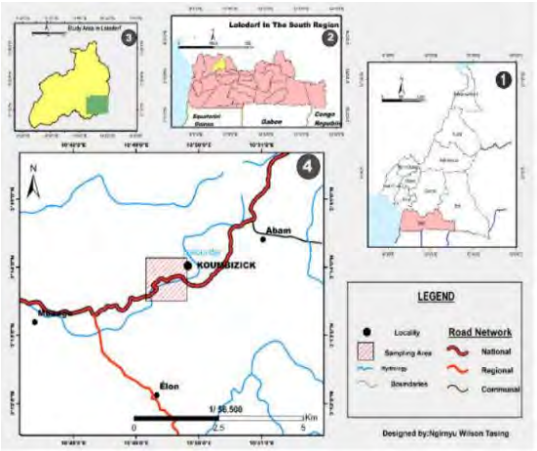

Figure 1. Sketch localization map (1) of Cameroon with South Region of Cameroon highlighted (2) Lolodorf in the South Region of Cameroon (3) position of Koumbizick and study area in the Lolodorf sub-division. (4) Localised map of Koumbizick within the study area.

The Koumbizick massive is located in the western part of the Congo craton. The Koumbizick massive covers a total area of 50km^2 Comprising Archean crust, early to mid- Proterozoic fold belt. This massive consist of Migmatite Gneiss, plutonic rocks of the charkokite suit, Granodiorite. The Koumbizick massive dates the same age as the Congo craton making it favourable for various mineralogical prospection.

2 Methodology

Fieldwork and sampling was conducted in conjunction with satellite imagery. The maps were made at the IRGM Spatial Imaging Research Center. Geological, topographical, hydrographic, location, relief, sampling map and the three-dimensional maps of the study area were also produced. The study of the geological map makes it possible to obtain information on the local geological context and the geological formations present. The topographic map shows the relief units bearing the work area. The mineral resource map shows the mineral indices in the work area and the geology to which these mineral resources are assigned. The sampling map represents the sampling points taken in the field. Petrographic analysis was carried out in order to analyze the occurrence of REE in the rock mass formation using the binocular microscope of the OPTIC IVYMEM SYSTEM brand

X-Ray diffraction (XRD) mineralogical analysis was conducted which uses X ray beams by accelerating the electron into a copper target and directed toward the sample, were the atoms deflect them. Angles of constructive interference will diffract X-rays into the detector which transduces the x-ray intensity and plots them in form of curves (diffractogram) which presents peaks at very specific diffraction angles. The position of these peaks is a true signature of the arrangement of atoms inside a crystal (distance between atoms, and between intracrystalline planes). The empirical relation that connects the angles at which the peaks are observed and the distances between atomic planes is the Bragg's Law. X-ray diffraction makes it possible to distinguish products having the same chemical composition but different atomic arrangements. X-ray fluorescence (XRF) was also use which is a method used to measuring the wavelength and intensity of "light" (X-rays in this case) emitted by energized atoms in the sample. In XRF, irradiation with a primary X-ray beam from an X-ray tube causes the emission of fluorescent X-rays

with discrete energies with characteristics of the elements present in the sample

Figure 2. Graphical illustration of major element variation

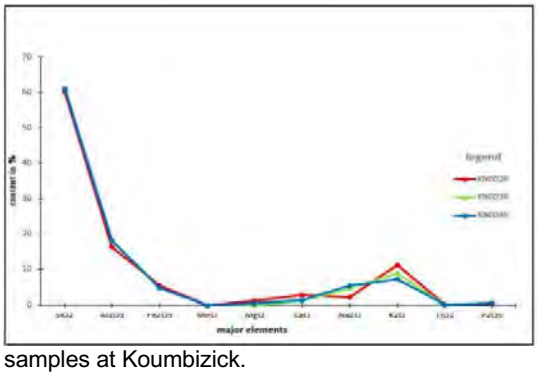

in samples at Koumbizick.

Table 1: Rare earth element concentration of samples from the Koumbizick massive.

Elements	KN001S	KNR005C	KNR006C
	%wt.	%wt.	%wt.
SiO2	60.37	59.12	61.28
Al2O3	16.57	19.03	17.8
Fe2O3	5.09	3.65	4.71
MnO	0.06	0.06	0.06
MgO	1.14	0.71	0.01
CaO	2.54	1.88	1.04
Na2O	3.47	4.65	3.73
K2O	9.19	7.18	9.27
TiO2	0.24	0.4	0.22
P2O5	0.4	0.91	0.5
L.O.I.	0.92	2.02	0.79
TOTAL	99.99	99.61	99.41
Elements	KN002R (ppm)	KN003R (ppm)	KN004R (ppm)
La	825	471	900
Ce	1604	600.5	1716.5
Pr	182.5	100	208.5
Nd	624	296.5	676.5
Sm	87	28	94
Eu	8.5	6.5	9
Gd	68.5	23.5	74
Tb	6.76	2.05	7.1
Dy	34.88	7.01	35.65
Ho	5.94	1.36	5.99
Er	15.21	3.96	15.25
Tm	1.88	0.67	1.83
Yb	9.5	2.71	9.78
Lu	1.45	0.67	1.45
Y	138	59.5	151.5

3 Results and Discussion

The study of rock samples under an optical microscope shows that they have a porphyroblastic to granoblastic texture. The mineral phases identified are quartz, plagioclase feldspar, biotite, pyroxenes, and amphibole. Quartz crystals occupy 50-55% of the rock and are sub-automorphic to xenomorphic. The sub automorphic crystals vary in size between 0.5 and 2 mm and are interstices of potassium feldspar and biotite lamellae or are included in amphibole and potassium feldspar. The xenomorphic crystals appear in the form of stretched bands with dimension up to 1 cm in the long axis and in some places, occurring as clusters of quartz with a triple junction. Rare earth minerals are disseminated in the various sampling profiles, but only a few occurrences have values high enough to be classified as “showings”. Microscope and electron microprobe work has shown that the minerals hosting REEs are allanite($A_2M_3Si_3O_{12}[OH]$), bastnasite($Ce(CO_3)F$), and monazite ($(Ce, La, Th) PO_4$).

Figure 3. (a) Fragmented blocks at site 2 (b) photo of sample KN004R from site 2

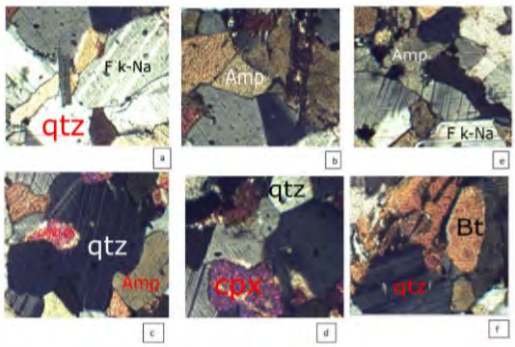

Figure 4. Thin section of gneiss sample showing the different mineral phases present in thin section. (define the minerals)

Cerium is the most enriched LREE in all the samples with a maximum concentration of 2715 ppm recorded in sample KNR006C, and minimum concentration of 1300 ppm in samples KNR001S. Europium has the lowest content for light REE in all samples with maximum concentration of 11.5 ppm in samples KNR005C and minimum concentration of 8.3 ppm in samples KNR001S. After cerium in concentration, Lanthanum, Neodymium, Praseodymium, Samarium, Gadolinium respectively follow in the order for light REE abundant in all the samples Generally, sample KNR006C records the highest concentration in light REE, ranging from 2715 ppm for Cerium to 11.3 ppm for Europium. Meanwhile, sample KNR001 records the lowest light REE concentrations (Fig5.).

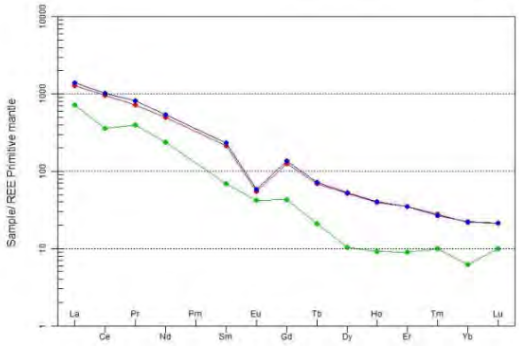

Figure 5. Primitive mantle-normalised (McDonough and Sun 1995) multi-element diagram of samples from the Koumbizick Massive.

4 Conclusions

After analyses, mineralogical result reveals the presents of REEs mineralogy of allanite's as the main mineral in samples which is made up of about 2.01% to 2.22%. Followed by monazite and bastnaesite. Light REEs are concentrated to a greater degree than other REEs (up to 2715 ppm). It appears that the rocks have a syenitic lithological nature rich in REEs, Making koumbizick massive highly favourable for REE prospection.

Acknowledgements

Thanks to the IRGM laboratory in Yaoundé were all the analysis were carried out.

References

Tchouankoue JP 1992. The Bangangte syenite: A Pan-African complex with intermediate characters: petrology and geochemistry. Doctorate of Third Cycle thesis. Cameroon: University of Yaoundé; p.160.

Peng Guo, Dmitri A. Ionov., Mantle and Recycle Oceanic crustal components in mantle Xenolith from north-eastern china and their mantle sources p. 7.

U-Pb dating and trace-element characterisation of potential cassiterite reference materials applicable to Sn-W mineralisation systems

Tonny B. Thomsen*,[1], Benjamin Heredia[1], Jakub Ryznar[2], Wladyslaw Zygo[3], Hugh O'Brien[4], Matthew Goodey[5], Simon Tapster[5], Anouk M. Borst[6], Nynke Keulen[1], Sebastian Malkki[1], Diogo Rosa[1]
[1] Geological Survey of Denmark and Greenland (GEUS), Øster Voldgade 10, 1350 Copenhagen, Denmark, tbt@geus.dk
[2] PROXIS Sp. z o.o. ul. Cieszyńska 23G, 43-170 Łaziska Górne, Poland
[3] AGH University of Science and Technology, Kraków, Poland
[4] Geological Survey of Finland (GTK)
[5] Geochronology and Tracers Facility, British Geological Survey (BGS), UK
[6] KU Leuven & Royal Museum for Central Africa, Belgium

Abstract. To support the traceability of Sn and W minerals to their deposit type (i.e., skarn, greisen or vein), various cassiterite and scheelite materials were investigated for their potential as quality standard reference materials. One cassiterite material in particular, the Kivu-2, revealed encouraging results when measured by laser-ablation inductively coupled plasma mass spectrometry (LA-ICPMS) at GEUS and GTK, which showed that e.g., this cassiterite contains virtually no common-Pb. ID-TIMS analyses of the Kivu-2 cassiterite material are being obtained at the BGS to further constrain the isotopic composition. It is anticipated that the ID-TIMS results will support this cassiterite's potential to be an international standard reference material for matrix matched U-Pb dating. In contrast, the internal variations in trace elements abundance as measured by LA-ICPMS most probably are too large to constitute a robust element quantification standard material. The complete data set of this study will be presented at the meeting together with an assessment of the potential applicability of the studied cassiterite materials to Sn-W ore systems.

1 Introduction

Sn and W occurrences in East Greenland were extensively studied by the Nordmine exploration company during the late 1960s to early 1980s. Their survey was succeeded by 40 years of investigations by GEUS and the Greenlandic Ministry of Mineral Resources (MMR), of which the latest work was during the Summer of 2022. As described in the abstract by Keulen et al. (this conference), Sn and W occur in the minerals cassiterite and scheelite, respectively, and most of the Sn and W occurrences are associated with the East Greenland Caledonian orogeny. These minerals occur in skarn, greisen, and hydrothermal veins, depending on their host rock and the proximity of adjacent granites (Hallenstein & Pedersen, 1982). Literature data shows that skarn, greisen, and vein-type deposits show distinct mineral trace element compositions (e.g., Wang et al. 2022, Sciuba et al. 2020 and many others). Thus, a good understanding of the mineral trace element content and associated element patterns together with the age of the mineralisation would help characterise the deposit type(s) in which cassiterite and/or scheelite occur. However, well characterized standard reference materials for microanalysis of this kind of minerals are required, in particular for U-Pb mineral dating. Unfortunately, for cassiterite and scheelite these are rare to non-existent. The aim of this study is therefore to analyse different cassiterites and scheelites to evaluate their potential as robust standard reference materials.

2 Cassiterite materials studied

Several cassiterite and scheelite mineral samples were investigated, however, focus of this study was put on cassiterite, because none of the scheelite materials studied proved to hold potential as robust standard reference material. The investigated cassiterites included two samples from the western province of the Rubavu District in Rwanda, three samples from the Musha-Ntunga pegmatite quartz veins in Eastern Rwanda (Kivu rift), two from the Manono-Kitotolo pegmatites in DR Congo, two samples from East Greenland, and samples from three different locations in Portugal (Montesinho, Panasqueira, Vale das Gatas). Separated mineral grains or small chunks of rock with a high proportion of cassiterite were encapsulated in epoxy pucks and polished prior to analysis. In addition, 5 samples of standard or potential standard cassiterite material (Jian-1, CH1, SPG4, ELS, and RZMEGA) provided by the BGS along with the Yankee cassiterite standard provided by courtesy of Patrick Carr from Université de Lorraine, CNRS, CREGU, France, were included in the study for testing the reproducibility and repeatability of the LA-ICPMS measurements.

3 Laboratory investigations

3.1 SEM

The epoxy mounts with cassiterite were studied by Scanning Electron Microscopy (SEM) to identify textural and compositional variations. Cathodo-luminescence (CL) and back-scattered electron (BSE) images were obtained to identify features such as internal zoning and inclusions in the cassiterite mineral grains. Automated quantitative mineralogy (AQM) software on the SEM was used for some samples to locate smaller cassiterite mineral grains and to establish compositional and spatial homogeneity within individual grains. AQM is a scanning electron microscope technique that combines BSE imaging with chemical analyses by energy dispersive spectroscopy in a mosaic with a small step-size (Keulen et al. 2020).

3.2 LA-ICPMS and ID-TIMS

Laser-ablation inductively coupled plasma mass spectrometry (LA-ICPMS) was performed at GEUS and GTK using both non-matrix matched and matrix matched analysis protocols. Analyses at GEUS were performed using a NWR213 solid state Ng:YAG laser ablation system from ESL coupled to a Thermo Scientific Element2 SF-ICPMS. At GTK a Teledyne ArF excimer 193 nm laser system coupled to a Nu Instruments TM AttoM high resolution ICP-MS was used. The U-Pb Geochronology and Trace Element data reduction schemes of iolite 4 were used to obtain U-Pb dates and trace elements abundances of the cassiterite grains analysed.

It is well-known that cassiterite is challenging to decompose by regular acid dissolutions protocols. For ID-TIMS analyses, protocols were implemented and performed at BGS following Tapster and Bright (2020), this to assess the potential of the non-matrix matched results obtained by LA-ICPMS analyses, and the evaluation of a correction factor. It is anticipated that the ID-TIMS measurements confirm the LA-ICPMS data, and further improve the accuracy and precision of the U-Pb dating for the Kivu-2 cassiterite sample material.

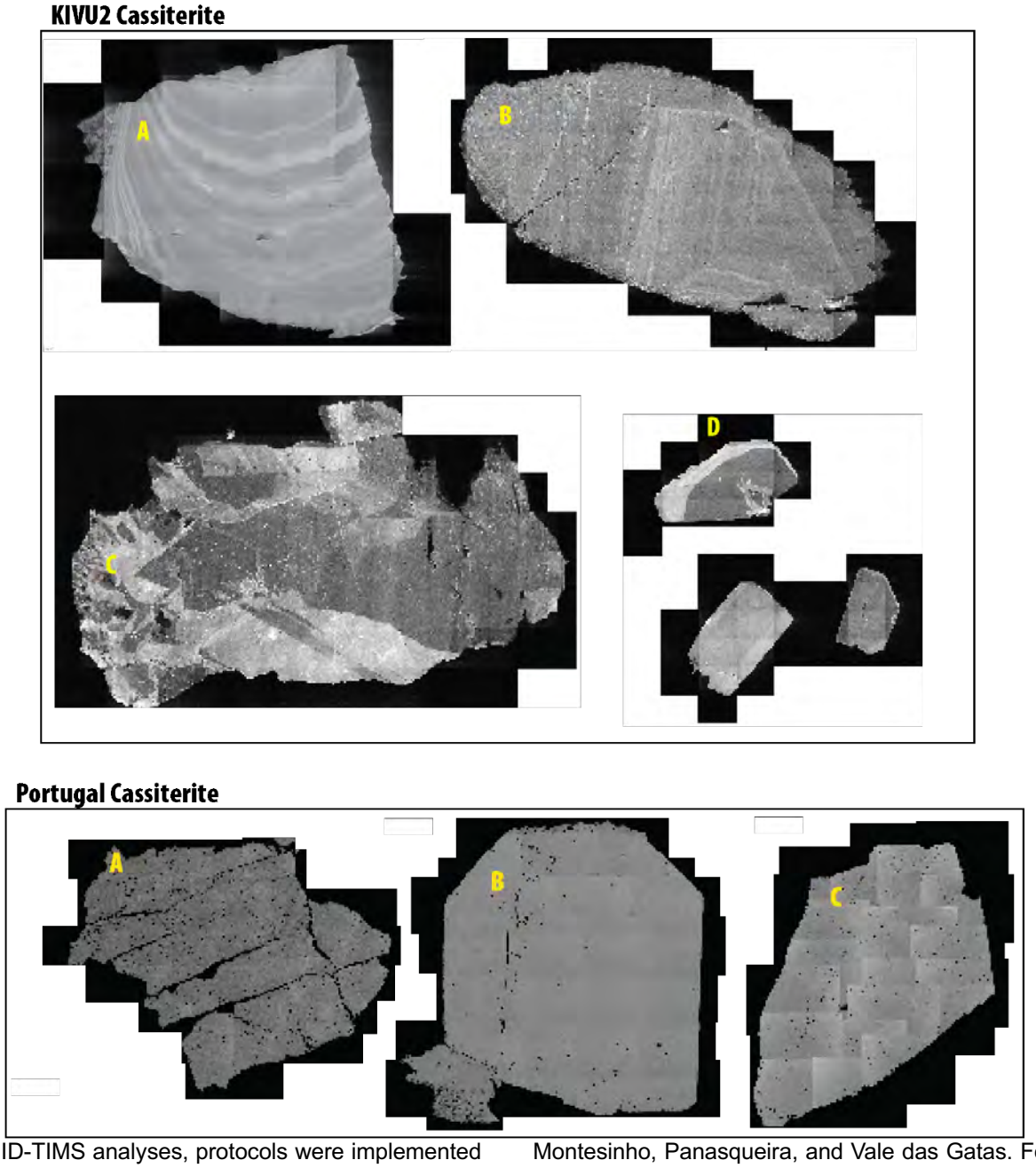

Figure 1. SEM CL images showing distinct section zoning in Kivu-2 (A to D mineral grains in top image), and cassiterites from Portugal (lower image; A: Montesinho; B: Panasqueira; C: Vale das Gatas.

4 Textural and compositional variations

CL images are presented in figure 1 to show the typical appearance of the cassiterites Kivu-2, Montesinho, Panasqueira, and Vale das Gatas. For Kivu-2 in particular, four different samples were collected from the same rock at the very same sample site (A to D), of which three samples (B, C and D) showed a low U content at around 1 ppm on

average, whereas the sample A contains much more U (~several hundred ppm U on average). Despite this large difference in the U and Pb abundances and clear zoning of the grains, all Kivu-2 samples yield comparable dates within error or each other. The clear zonation that can be observed in these grains does not seem to significantly influence the U/Pb dates. The trace element abundances, however, show significant variations that, based on the current analyses, do not appear to constitute a robust reference for determination of elemental contents. Comparable variations are observed in the analysed cassiterite grains from Portugal that show a less pronounced zoning and have low common-Pb content. The cassiterites from Greenland contain a high proportion of common-Pb and are less suitable as reference material for both dating and trace element determination, but nevertheless show reasonably comparable dates within single occurrences.

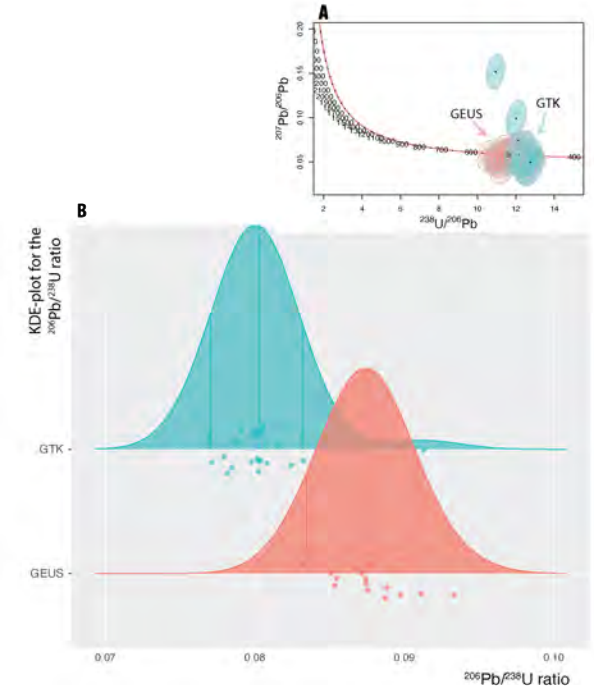

Figure 2. LA-ICPMS analyses of the Kivu-2 cassiterite obtained at GEUS (red) and GTK (blue), respectively, shown in $^{206}Pb/^{238}U$ ratio plot and Tera-Wasserburg diagram (A). The smaller discrepancy observed in the raw 206Pb/238U ratios (B) most probably result from the different analytical setup and the non-matrix matched analysis approach employed in the two laboratories. A more complete data set and data also from other cassiterite materials will be presented at the meeting.

5 Kivu-2 – a new cassiterite standard?

The results of two independent laser ablation sessions from the two laboratories show that the non-matrix matched U/Pb dating analyses plot near concordia (Fig. 2A) indicative of a very low initial-Pb contribution. The apparent variation can thus be represented by the $^{206}Pb/^{238}U$ ratios on a KDE graph as in Figure 2B. The mean dates of 516±11 Ma (GEUS) and 509±9 Ma (GTK) correspond to a <2-5 % difference. This deviation is most probably related mainly to the differences between the analytical protocol and to different matrix-related elemental fractionation instrumental setup rather than representing true variations in the isotope systematics of both U and Pb. The ID-TIMS U-Pb analyses will constrain the isotopic ratios and assess the LA-ICPMS results. Further absolute LA-ICPMS geochronometry and trace elements measurements will constrain the data towards a very robust data set for U/Pb dating with minimal requirements for common Pb correction, and a constrained trace elemental characterisation of the Kivu-2 material. The dating of cassiterite offers a potential platform for linking time relations between magmatism and hydrothermal processes, and our contribution is thus beneficial for the development of well characterised materials to use for calibration and verification of U/Pb dates and elemental databases generated by microbeam analysis methods.

6 Acknowledgements

The study is financed by GEUS and EIT-RM project MinExTarget #109674 and the Greenlandic Ministry of Mineral Resources, Government of Greenland. M. Alaei and H. Vesturklett are thanked for laboratory assistance.

7 References

Hallenstein, C. & Pedersen, J. 1982: Study of Scheelite Mineralization in Central East Greenland. Nordisk Mineselskab A/S, 152 pp. GEUS Dodex file report 20688.

Keulen N, Malkki SN, Graham S (2020) Automated Quantitative Mineralogy Applied to Meta-morphic Rocks. Minerals 10, 47, 29pp. DOI: 10.3390/min10010047.

Sciuba, M., Beaudoin, G., Grzela, D. & Makvandi, S. (2020) Trace element composition of scheelite in orogenic gold deposits. Mineral Dep 55:1149-1172.

Tapster, S., Bright, JWG. 2020: High-precision ID-TIMS cassiterite U–Pb systematics using a low-contamination hydrothermal decomposition: implications for LA-ICP-MS and ore deposit geochronology. GChron 2, 425-441. doi: 10.5194/gchron-2-425-2020.

Wang, C, Zhao, K, Chen, J & Ma, X (2022) Examing fingerprint trace elements in cassiterite: Implications for primary tin deposit exploration. Ore Geol Rev 149:105082, 13 pp.

Nation-wide low-density geochemical mapping using composite sample, Korea

Seung-Jun Youm [1], Joo Sung Ahn [2], Yong-Chan Cho[2], Gil-Jae Yim [2], Sang-Woo Ji [2], Jung-Hwa Lee[2], Jung-Ho Lee[1]
[1]Critical Minerals Research Centre, Korea Institute of Geoscience and Mineral Resources, Korea
[2]Geo-Environment Research Centre, Korea Institute of Geoscience and Mineral Resources, Korea

Abstract. Nation-wide low-density geochemical maps are being constructed using composite samples of stream sediments for 10 elements (As, Be, Bi, Cd, Mo, Sb, Sn, Tl, U, W) that have not been previously mapped at the national level. To obtain high-quality geochemical data, rigorous quality control (QC) procedures were implemented, which included (1) the randomization of project samples, (2) the introduction of project standards, and (3) the insertion and analysis of analytical replicates. Threshold values were calculated and geochemical maps were created for five elements (Be, Bi, Sn, Tl, U). The remaining five elements that did not pass the QC are currently undergoing re-analysis. Low-density geochemical mapping can result in a loss of detailed geochemical information, but it is useful for identifying regional geochemical patterns and establishing threshold values.

1 Introduction

An efficient way to obatin the geochemical information of crustal constituents is to create a geochemical map that shows the spatial distribution of element concentration within terrestrial materials (Zhizhong et al. 2014). The geochemical map is useful not only for mineral resource exploration but also for various fields, such as agricultural and livestock productivity, forest management, human health, environmental standard setting, water quality, and land use planning. Therefore, many countries have created multi-element and multi-media geochemical maps at different scales to better understand the geochemical distribution in various environment. In the fast-changing global metal market, the demand for metal minerals continues to rise due to the development of high-tech industries. Meanwhile, industrial development and urbanization have led to artificial pollution in the surface environment. Recently, the natural concentration of harmful elements of geological origin has been reported across the country, possibly due to the effects of rapid climate change. Therefore, preparing a national-scale geochemical map is essential for effectively addressing these issues. However, in Korea, the number of elements covered in national-scale geochemical maps is currently limited to only 18 elements (Ba, CaO, Co, Cr, Cu, Fe_2O_3, K_2O, Li, MgO, MnO, Ni, Pb, Rb, Sr, TiO_2, V, Zn, Zr) (KIGAM 2007).

The number of samples collected in geochemical exploration is determined by the purpose and area of the survey. The more the number of samples (i.e., the higher the sample density), the more detailed geochemical information can be obtained. However, if the investigation area is large, sampling and chemical analysis can become costly and time-consuming. Therefore, conducting geochemical mapping over a national-scale or larger area may not even be feasible. To address this, it is necessary to create a low-density geochemical map that can reduce the number of required samples, thereby reducing the cost and time required for sample collection and analysis (Negrel et al. 2019). Composite sampling is a technique for mixing and homogenizing several spatially spaced samples and treating them as one individual. Lately, low-density geochemical maps have been prepared in this way (Birke et al. 2015).

The purpose of this study is to create nation-wide low-density geochemical maps using composite sample of stream sediments for 10 elements (As, Be, Bi, Cd, Mo, Sb, Sn, Tl, U, W) that have not been previously mapped on a national-scale.

2 Geology

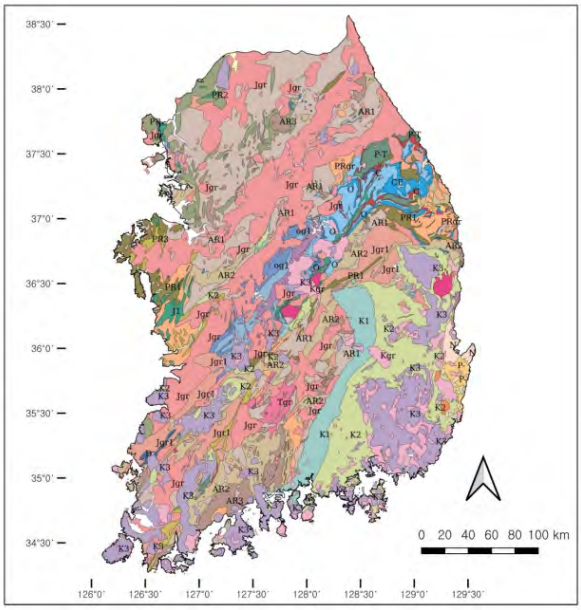

Figure 1. Geological map of Korea (1:1,000,000 scale; KIGAM 1995)

The geology of Korea is composed of complex rocks that have been formed over a long geological period, from the Precambrian to the Cenozoic era (Figure 1).

The late Archean-late Proterozoic gneisses and schists (AR, PR) form the base of geologic setting in Korea and are widely exposed on the surface due to uplift and erosion. The Ogcheon group (Og), which is distributed in the NE-SW direction from central region, is composed of metasedimentary rocks from the Cambrian-Ordovician period. The Chosun Supergroup (O) is composed mainly of carbonate rocks from the early Paleozoic era, while the

Pyongan Group (C, P, T) is composed of various sedimentary rocks from the late Paleozoic era. Both groups are distributed in the NE region. During the Jurassic period, igneous activity occurred extensively throughout the country, and granitic rocks (Jgr) were distributed widely in a NE-SW direction. In the SE region, the Gyeongsang Supergroup (K), composed of Cretaceous sedimentary rocks and volcanic-clastic rocks, was intruded by late Cretaceous granitic rocks (Kgr) and early Tertiary acidic rocks (P). In the Quaternary period, small-scale basic volcanic rocks were formed.

3 Methodology

It is both time consuming and costly to collect geochemical samples. Therefore, we decided to utilize about 23,500 stream sediments (particle size <0.015 mm; sampling density, 1 sample per 3.6 km^2), that had been collected and stored in the previous project (KIGAM 2007). To prepare the composite sample, we divided a 1:50,000 scale topographical map (approximately 600 km^2) into six cells by splitting it into three horizontally and two vertically. All of stream sediment samples (2 gr. each) within each cell were combined into a single composite sample (Figure 2). To maintain sampling consistency, the entire procedure was performed by the same person.

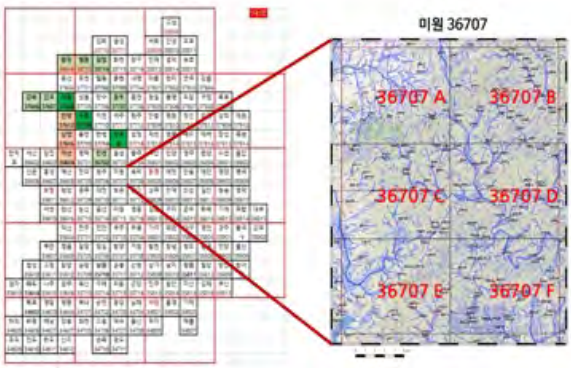

Figure 2. Cells for preparation of composite sample

Overall, 953 project samples were prepared across the country covering an area of ca. 100,000 km2 (sample density, 1 sample per 100 km2). Prior to analysis, all samples underwent a 4-acid decomposition (hydrofluoric acid, nitric acid, perchloric acid, hydrochloric acid) and were analysed using HR-ICP-MS (High Resolution Inductively Coupled Plasma Mass Spectrometer) in KIGAM laboratory. Rigorous quality control measures were carried out, including the randomization of project samples, the insertion and analysis of project standard, which was prepared from standards the project samples, and the insertion and analysis of analytical replicate (Eggen et al. 2019). All project samples were divided into 25 batches, and each batch contained two project and two analytical replicates. Certified reference standards (NCSDC73308 and NCSDC73301) were also inserted and analysed three times for each batch by the lab.

The colour surface maps were produced by IDW method with a circular window of radius of 30 km in QGIS. The locations of the composite samples were determined as the centre point of the cell, and if the centre point was located in the sea, it was moved to the centre point of the inland (Figure 3). Class boundaries for the maps were based on percentiles (5, 10, 15, 25, 50, 75, 90, 95, 99%).

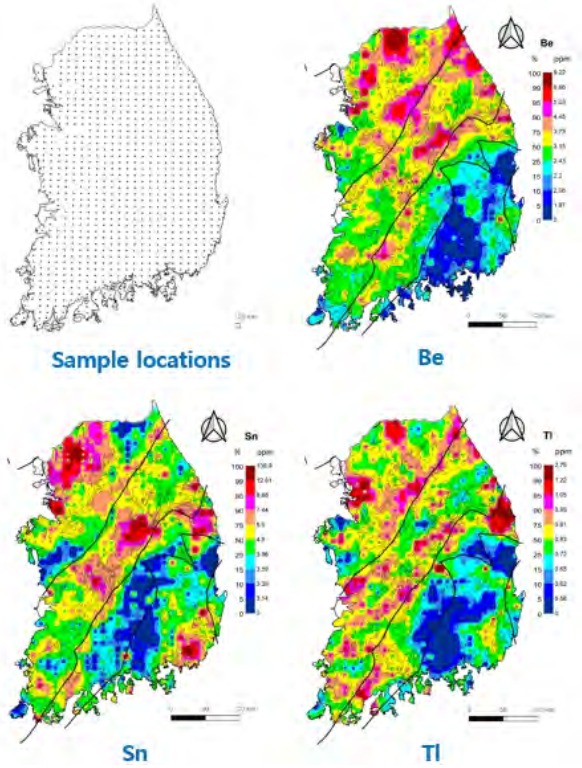

Figure 3. Composite sample locations and geochemical maps for Be, Sn and Tl. Bold line indicates geotectonic boundaries

4 Results and Discussion

After all data were received from the laboratory, simple graphics for the quality control data were drawn. In the random plots for the project samples, most elements (Be, Bi, Cd, Sb, Sn, Tl, U, W) displayed random variation over all samples. However, in the case of As, the weakly increasing trend in observed variation was found, and Mo showed breaks in concentration range during late-stage.

To determine repeatability, X-Charts for the project standard was drawn. Black line was plotted for the median and then stippled line either for 20% (green) and 30% (red) precision around the median. In the X-Chart, five elements (Be, Bi, Sn, Tl, U) did not deviate from the agreed precision (20%), but rest of the elements, especially As, showed deviations in lots of batches. In some last batch, Mo represented

poor precision, which is consistent with the result of the random plot (Figure 4).

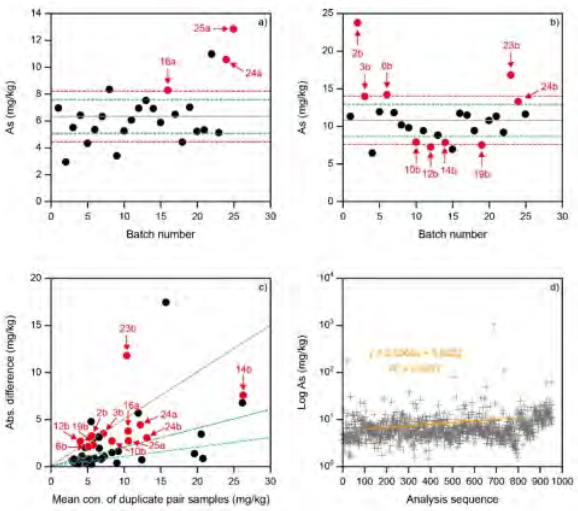

Figure 4. Quality control results for As (a & b, X-Chart; c, Thompson and Howarth plot; d, random plot). Red circle indicates re-analyses batch

To assess the overall analytical precision, the mean of each replicate pair was plotted against the absolute difference between the two analyses. On these plots, stippled lines were drawn for predefined precision level (10%, blue; 20%, green; 50% brown). Similar to QC result for the project samples, many replicate pairs deviated from the predefined level (20%) for As and less for Mo, Cd, Sb, Sn and W. All samples in the batches that deviated from the predefined precision (20%) of project standards, and at the same time, from the predefined level (20%) of analytical replicates, were selected and currently, 339 project samples are being reanalysed (Figure 4).

Table 1. Statistics for Be, Bi, Sn, Tl, U (ppm)

	Be	Bi	Sn	Tl	U
Minimum	1.3	0.1	1.4	0.3	1.7
25%	2.3	0.3	3.6	0.7	3.3
Median	2.9	0.4	4.4	0.8	4.6
90%	4.6	0.8	7.5	1.1	9.7
95%	5.6	1.2	9.0	1.2	11.5
98%	7.1	1.9	12.7	1.3	14.4
Maximum	9.2	9.5	137.1	2.8	38.3
Mean	3.2	0.5	5.2	0.8	6.0
Stdev.	1.3	0.6	5.1	0.2	3.4

Statistics was calculated for the 5 elements (Be, Bi, Sn, Tl, U) that passed the quality control test (Table 1). Threshold value was calculated using two robust methods, which are not significantly affected by statistical assumptions: (1) Tukey Inner Fence (TIF) = Q75 (75 percentile) + 1.5 x IQR (interquartile range), and (2) MAD = Median + 2 x median absolute deviation (Table 2).

Low-density geochemistry can lead to loss of detailed geochemical information compared to high density. Therefore, in order to confirm whether the low-density geochemical mapping method applied in this project was valid, the concentration of main elements (e.g. CaO) was analysed in the same way as the target elements, and compared with the result of high-density geochemical data in the previous project (KIGAM 2007).

Table 2. Threshold values for Be, Bi, Sn, Tl, U (ppm)

	Be	Bi	Sn	Tl	U
Threshold values					
MAD	4.8	0.7	7.1	1.1	9.1
TIF	7.7	1.5	12.3	1.5	20.9
Number of samples above threshold					
MAD	90	117	121	76	122
TIF	11	28	24	6	6

When comparing the distributions of CaO content between the high-density and the low-density geochemical maps, it becomes apparent that the detailed geochemical information in the latter was lost, specifically, the decreasing of highest value and the increasing of lowest value. However, the mean/median values and content ranges of 10-90% were similar, and the regional distribution pattern of the two geochemical maps was also similar, which confirm that low-density geochemical mapping can be used to identify regional distribution pattern and establish threshold value (Figure 5).

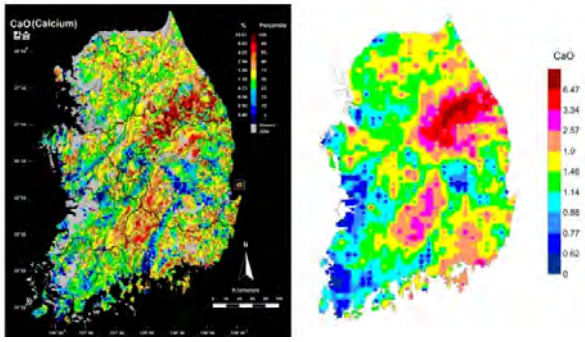

Figure 5. Comparison of high-density (KIGAM 2007) and low-density (in this study) geochemical maps for CaO

Regional geochemical distribution patterns of the geochemical maps generally reflects the underlying geology, but the effects of mineralization related to metal deposits have also been identified. For example, the regional distribution pattern of uranium is consistent with the geological distribution (Figure 6). Areas with high U concentration are associated with gneiss and granite, and low content is found in sedimentary rock.

In the case of bismuth, high concentrations are found in the gneiss and limestone, whereas low concentrations are found in Jurassic granite. Limestone is generally known to have a low Bi content, but it is thought to have a high content due to the formation of the Skarn deposits such as W, Mo, Pb, and Zn in this type of rock (Figure 7).

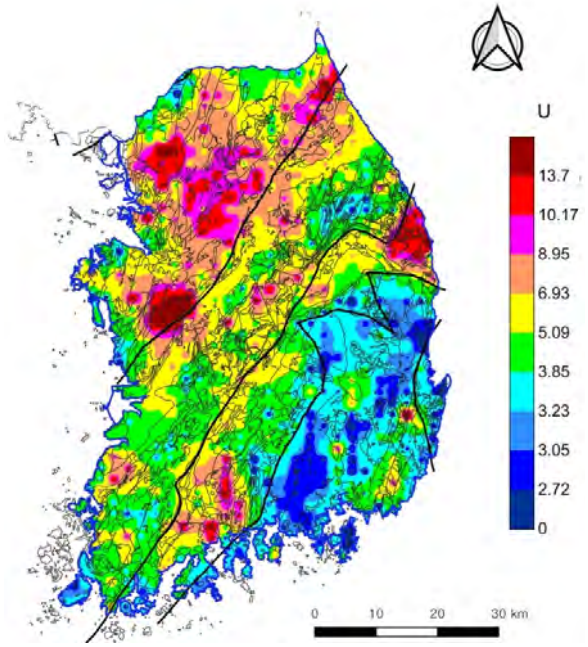

Figure 6. Low-density geochemical map for U. Bold line indicates geotectonic boundaries

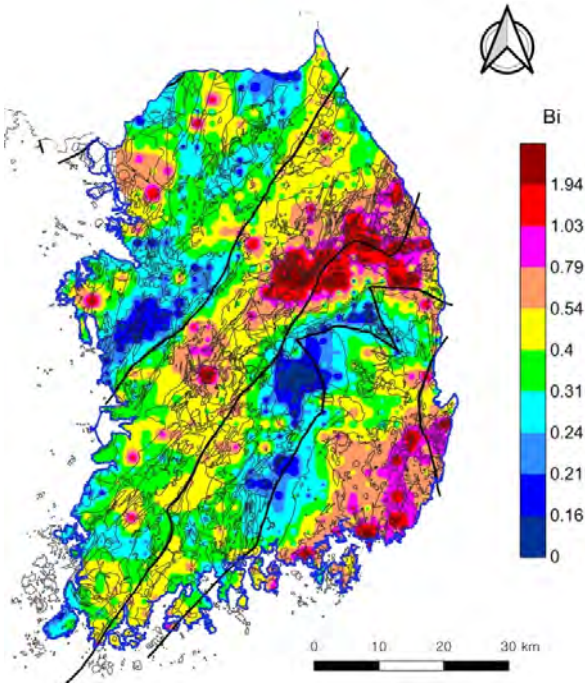

Figure 7. Low density geochemical map for Bi. Bold line indicates geotectonic boundaries

5 Conclusions

To create regional geochemical maps efficiently, we have chosen the composite sampling method that can save costs and time in sampling and analysis. A total of 953 composite samples were divided into 25 batches and analyzed for 10 elements (As, Be, Bi, C d, Mo, Sb, Sn, Tl, U, W) using ICP-MS. To obtain accurate analytical results, we conducted rigorous quality control. All project samples in batches that did not pass the QC procedure are currently undergoing re-analysis. Meanwhile, for the five elements that passed the QC, we calculated statistics and threshold values, and created national-scale geochemical maps. The regional distribution patterns of the elements largely reflect the underlying geology, but some can also show the influence of mineralization. Compared to the high-density geochemical map, it has been confirmed that low-density geochemical mapping using composite samples can be applied to identify regional geochemical distribution patterns and establish threshold values. However, low-density geochemical mapping can result in the loss of detailed geochemical information. To address this drawback, it would be necessary to carry out high-density geochemical surveys for anomalous areas.

8 Acknowledgements

This research was supported by the Basic Research Project of the Korea Institute of Geoscience and Mineral Resources (KIGAM) funded by the Ministry of Science and ICT of Korea (Code: 22-3412-2).

9 References

Birke, M., Rauch, U. and Stummeyer, J. (2015) How robust are geochemical patterns? A comparison of low and high sample density geochemical mapping in Germany, Journal of Geochemical Exploration, 154, p. 105-128

Eggen, O.A., Reimann, C. and Flem, B. (2019) Reliability of geochemical analyses: Déjà vu all over again, Science of the Total Environment, 670, p. 138-1148

KIGAM (1995) Geological Map of Korea 1:1,000,000. Korea Institute of Geoscience $ Mineral Resources.

KIGAM (2007) Geochemical Atlas of Korea (1:1,800,000), Series 9. Korea Institute of Geoscience & Mineral Resources, 68p [in Korean]

Negrel, P. Ladenberger, A., Reimann, C., Birke, M., Demetriades, A., Sadeghi, M., and The GEMAS Project Team (2019) Geochemical background and mineral potential of emerging tech-critical elements in Europe revealsed from low-sampling density geochemical mapping, Applied Geochemistry, 111, p. 104424

Zhizhong, C., Xuejing, X., Wensheng, Y., Jizhou, F., Qin, Z. and Jindong, F. (2014) Multi-element geochemical mapping in Southern China, Journal of Geochemical Exploration, 139, p. 183-192

Resistivity imaging over porphyry copper systems in the Red Mountain district, southwest Colorado, USA

Eric Anderson[1], Maryla Desczc-Pan[1], Doug Yager[1], Kyle Eastman[2], Bennett Hoogenboom[1]
[1]U.S. Geological Survey, Denver, Colorado, USA
[2]Montana Bureau of Mines and Geology, Butte, Montana, USA

Abstract. The Red Mountain district in southwestern Colorado produced base and precious metals hosted in breccia pipes and vein structures related to an extensive lithocap that overlies pervasive quartz-sericite-pyrite alteration. A helicopter-borne time-domain electromagnetic survey flown over the district yielded resistivity values that range from tens to thousand or more ohm-m, with lesser resistivity values in the lithocap and greater resistivity values in the rocks with propylitic alteration. A 60 m-thick, low resistivity zone subparallel to topography characterizes the magmatic-hydrothermal breccia pipes. A broad zone of low resistivity that may envelope epithermal deposits spans multiple flight lines and occurs beneath rocks with argillic alteration. A 50 m-thick low resistivity zone occurs beneath quartz-sericite-pyrite alteration and may indicate porphyry deposit at depth.

1 Introduction

The Red Mountain district is located along the structural margin of the Silverton caldera in southwest Colorado (Figure 1). Past production includes precious (Au, Ag) and base metals (Pb, Zn, Cu) hosted in breccia pipes and vein structures (Gonzales and Larson 2017). The district provides a unique opportunity to image the subsurface of porphyry copper systems because extensive erosion in rugged topography has exposed nearly a kilometer of crust from the mountain peaks to the valley floors. Surface alteration assemblages have been mapped using a combination of field mapping with X-ray diffraction analysis and imaging spectroscopy (Bove et al. 2007; Dalton et al. 2007), which provide a detailed understanding of surface mineralogy.

In this contribution, we build upon previous geophysical investigations of the Silverton caldera (Anderson et al. 2023) and focus on the lithocap in the Red Mountain district that is underlain by pervasive quartz-sericite-pyrite alteration. Airborne time-domain electromagnetic data are used to show the distribution of conductive material from the surface to depths around 300 m. We present resistivity inversion results along select flight lines that traverse outcropping components of the lithocap and underlying quartz-sericite-pyrite alteration and integrate these results into a three-dimensional modelling environment to discuss the implications for exploration.

2 Geologic setting

The Red Mountain district along the Silverton caldera margin is composed predominantly of Paleogene volcano-plutonic rocks that intrude and overlie variably metamorphosed sedimentary, volcanic, and intrusive rocks of Precambrian age and relatively undeformed sedimentary rocks of Paleozoic and Mesozoic age (Figure 1: Burbank and Luedke 1964; Yager and Bove 2007). The caldera margin consists of zones of concentric and radial faults and fractures. The flat-lying volcanic rocks include lava flows and related volcaniclastic rocks ranging in composition from andesite to rhyolite (Yager and Bove 2007) and have thickness around 850 m inside the caldera (Luedke and Burbank 2000).

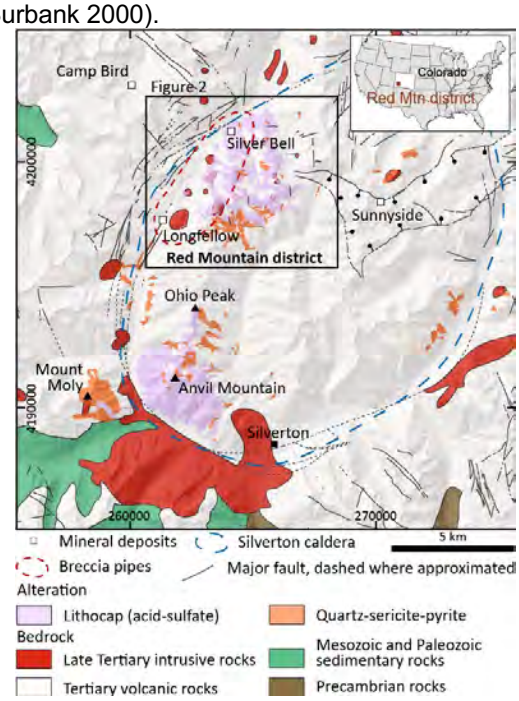

Figure 1. Generalized geologic map of the Silverton caldera in southwest Colorado. The Red Mountain district is along the caldera margin and consists of pervasively altered Tertiary volcanic and lesser intrusive rocks. Modified from Casadevall and Ohmoto (1977).

In the Red Mountains, an extensive lithocap formed around 23 Ma (Figure 2: Bove et al. 2001). The lithocap includes silicified rock surrounded by argillic alteration, and additional areas mapped as variations of quartz-alunite-pyrophyllite (Bove et al. 2007). Rocks having pervasive quartz-sericite-pyrite alteration crop out in the valleys below. Propylitic alteration assemblages and local areas of vein-related quartz-sericite-pyrite occur outward of the lithocap. Drill hole observations show that with increasing depth the alteration changes from advanced argillic to argillic to phyllic to weakly propylitic to strongly potassic at depths around 800 to 1200 m (Gilzean 1984). Magmatic-hydrothermal

breccia pipes formed along a north-northeast trending zone that is 2 km-wide extending from the Longfellow to Silver Bell mines (Gonzales and Larson 2017). The pipes have diameter around 150 m and are known to extend to depths of 300 m. The deposits have a high-sulfidation mineral assemblage that includes dickite, alunite, and pyrophyllite with enargite and pyrite. In addition, polymetallic veins occur in caldera-related structures. Ferricrete deposits that mark the emergence of paleowater tables are common east of the Red Mountains in the valley floors.

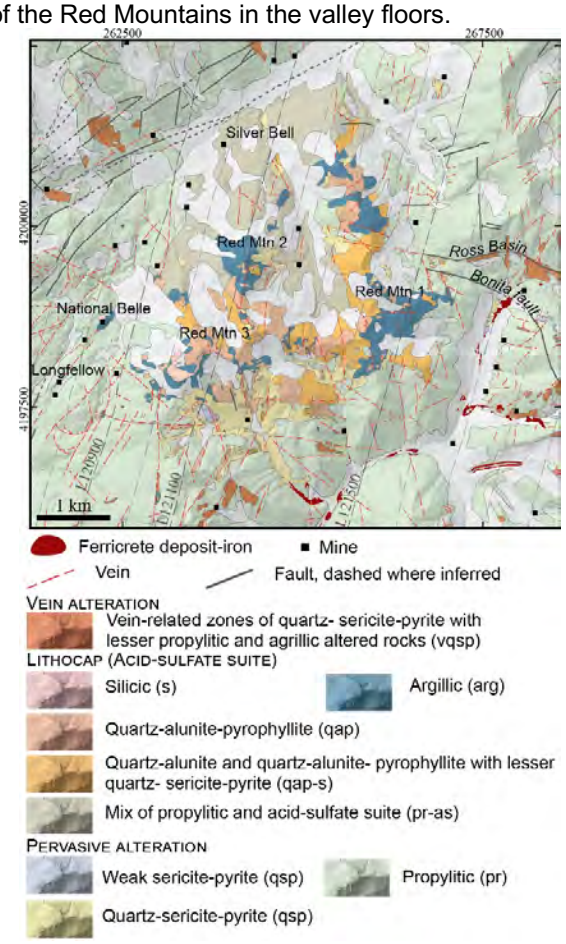

Figure 2. Alteration map of the Red Mountain district (modified from Bove et al. 2007). Dashed grey lines are flight lines with labelled lines shown in Figure 4.

3 Methodology

A helicopter-borne time-domain electromagnetic survey was flown by Geotech Ltd. over the Silverton caldera in 2019 (Hoogenboom et al., 2022). These data were subset to the Red Mountains district and had parallel flight lines oriented north-northeast with 600 m spacing and nominal terrane clearance for the transmitter-receiver loop of 110 m. Data were collected in 54-time channels ranging from 4.63 to 8254 µsec. A tau map, which measures the inductive response of a conductive target, was used for qualitative interpretation. Tau spans the measured time range and is dependent on conductance, not response magnitude, and, therefore, the presence of a good conductor is amplified and emphasized independently of its depth.

The time-domain electromagnetic data were inverted (Hoogenboom et al. 2022) along survey profile lines using the method described by Auken et al (2015). The 1D inversions used a 30-layer model with a 500 m maximum depth allowing for significant variations in depth of investigation beneath resistive and conductive areas. The inversion result is sensitive to sensor-to-source distance and may therefore be less resolved when sensor height is too large. The results were gridded with cell size of 5 m and provide a 2D quantitative estimate of the resistivity changes from the surface to around 300 m depth.

4 Results

The Tau map shows lateral changes in areas that exhibit good conductance, or low resistivity (Figure 3). The zone of magmatic-hydrothermal breccia deposits shows low resistivity along the entire length from Longfellow to Silver Bell mine where the bedrock is altered to propylitic and a mix of acid-sulfate assemblages. Low resistivity is also mapped on Red Mountain 1 and westward to Red Mountain 3 where the bedrock is variably altered to silicic, quartz-alunite-pyrophyllite, and lesser quartz-sericite-pyrite assemblages. North and south of Red Mountain 1 are rocks with propylitic assemblages that exhibit relatively high resistivity.

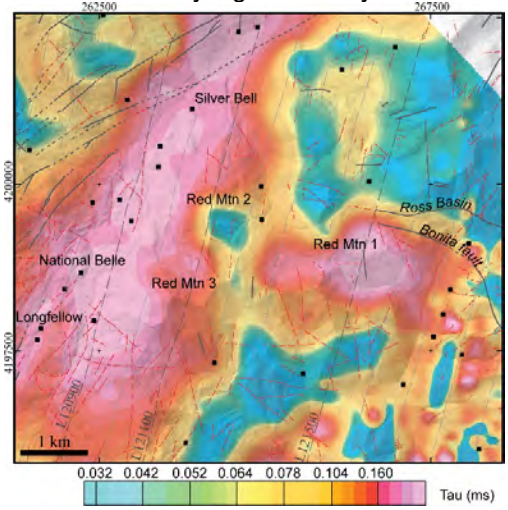

Figure 3. Contour map of Tau showing a qualitative distribution of resistivity changes with warm and cool colours indicating low and high resistivity, respectively.

The inverted resistivity sections provide estimates of how resistivity varies with depth beneath the flight lines (Figure 4). The sections extend approximately 7 km over pervasively altered rock. Line L120900 over the breccia deposits and rocks with propylitic alteration exhibits a prominent zone of low resistivity at 50 m depth with thickness around 60 m and is subparallel to topography (Figure 4a). The zone deepens and thickens to the north near the structural margin of the caldera. Line L121100 traverses the lithocap over Red Mountains

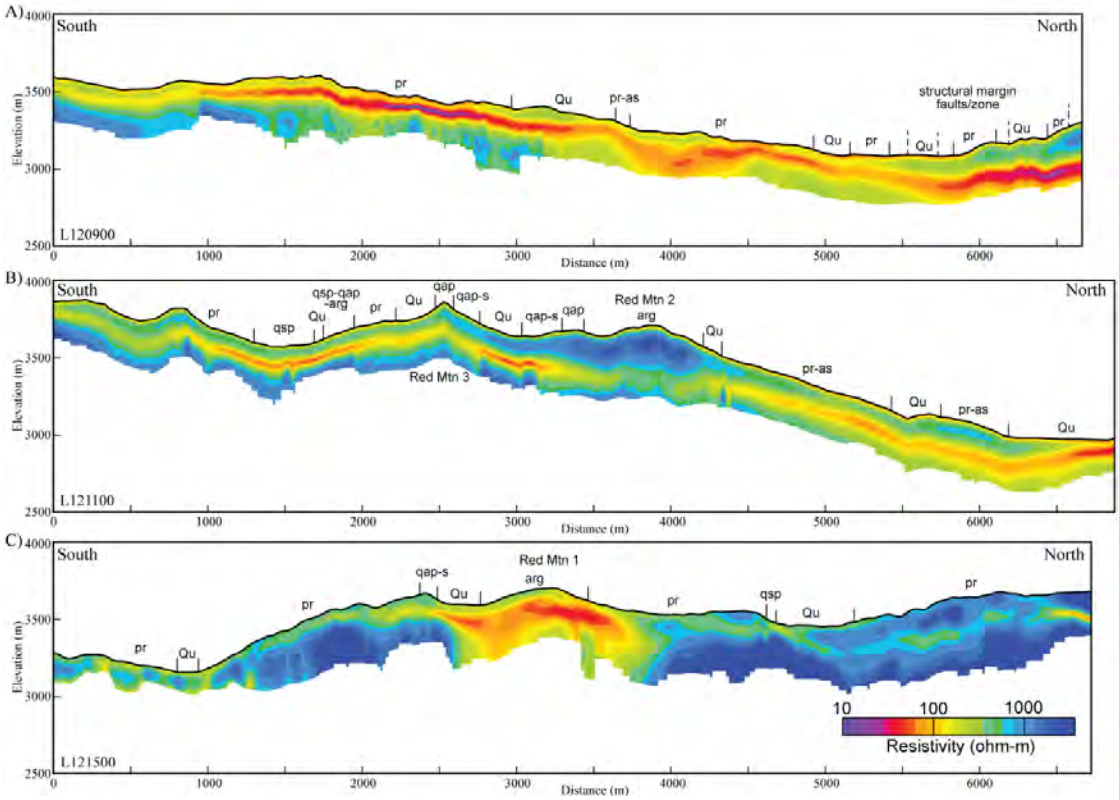

Figure 4. *Resistivity sections for flight lines A) L120900, B) L121100, and C) L121500. Mapped surface alteration extent indicated with abbreviations and vertical lines. Abbreviations: arg=argillic, pr=propylitic, pr-as=mix of propylitic and acid-sulfate suite, qap=mix of quartz-alunite and quartz-alunite-pyrophyllite, qap-s=quartz-alunite and quartz-alunite-pyrophyllite with lesser quartz-sericite-pyrite, qsp=quartz-sericite-pyrite stockwork veins, Qu=Quaternary deposit. See Figure 2 for flight line location.*

2 and 3 (Figure 4b). A zone of low resistivity subparallel to topography occurs on the south and north flanks of Red Mountain 3. The argillic alteration mapped on Red Mountain 2 has high resistivity and a zone of low resistivity parallels topography along the northern flank where the surface alteration consists of mixed propylitic and acid-sulfate assemblages. Line L121500 shows a zone of low resistivity on Red Mountain 1 where the rocks have argillic alteration assemblages, and high resistivity to the north and south (Figure 4c).

5 Discussion and implications

The Red Mountain district exhibits outcropping alteration patterns that show silicified ridges underlain by argillic and quartz-alunite-pyrophyllite alteration with quartz-sericite-pyrite assemblages at lower elevations. The lithocap formed at 23 Ma and has variable resistivity (Figure 5). Supergene processes commonly occur in the weathering environment of porphyry copper systems (Sillitoe 2005) and the formation of clay minerals and groundwaters with high dissolved solids can reduce subsurface resistivity (Dentith and Mudge 2014). Anderson et al. (2023) used reported drill hole observations of oxidized minerals to attribute low resistivity zones subparallel to topography in areas of pervasively altered rocks on Mount Moly, Anvil Mountain, and Ohio Peak (Figure 1) to supergene processes. In addition, ferricrete deposits are spatially distributed downslope from areas of intense alteration (Verplank et al. 2007; Yager and Bove 2007) and an indication that such processes have occurred.

The north-northeast-trending zone of breccia deposits from Longfellow to Silver Bell exhibits a prominent low resistivity response in the Tau map (Figure 3). In this area, the inverted resistivity sections show a blanket-like low resistivity zone (Figures 4,5). The highly fractured rocks in the pipes and along the structural margin of the caldera are permeable areas for paleo- and present-day groundwater to oxidize sulfides to depths near the top of the low resistivity zone. The flight line spacing (600 m) is likely too wide to image individual pipes that have diameters around 150 m. Thus, the Tau map provides a reconnaissance tool when exploring for breccia pipes and the inversions provide estimate to the depth at which enrichment may be expected.

At higher elevations in the Red Mountains, a broad area of low resistivity is imaged from the surface to depths around 300 m in adjacent flight lines (Figure 5). The Tau map indicates low resistivity on Red Mountain 1 that continues eastward to Red Mountain 3, and high resistivity on Red Mountain 2 (Figure 3). Argillic alteration assemblages are mapped on Red Mountains 2 and 3, yet the inverted resistivity sections show that these areas are underlain by high and low resistivity, respectively. Argillic alteration is clay rich and

characterized by the presence of dickite and trace to 40% fine-grained quartz, along with varying amounts of pyrite (Bove et al. 2007). The discrepancy in subsurface resistivity may be due to quartz content where an increase in quartz would increase resistivity. The low resistivity zone on Red Mountain 1, is therefore, likely due to the presence of clay, and the weathering of pyrite may have produced acidic conditions favorable for supergene processes. The area is surrounded by rocks having propylitic alteration and high resistivity. Thus, the low resistivity zone may contain epithermal deposits.

On the north and south flanks of Red Mountain 3, a thin low resistivity zone parallels the topography (Figures 4,5). This area is underlain by quartz-sericite-pyrite assemblages, most notably to the south (Figure 2). The veinlets associated with such alteration may have provided the necessary permeability and source metals for supergene processes. The geometry of the lithocap overlying rocks having quartz-sericite-pyrite assemblage is suggestive of porphyry deposit at depth. Thus, a thin low resistivity zone beneath mapped quartz-sericite-pyrite assemblages may be a good indicator of underlying porphyry-style mineralization.

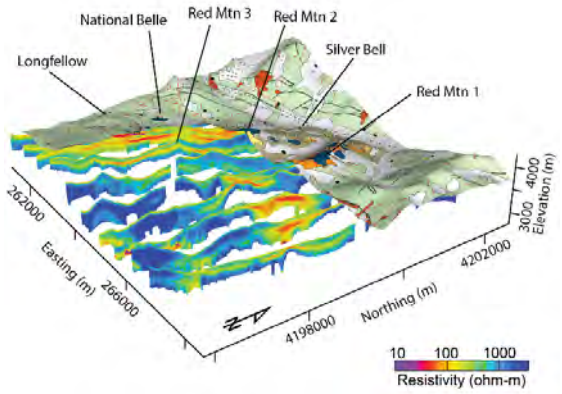

Figure 5. Three-dimensional perspective view of the Red Mountain district showing alteration patterns mapped at the surface and resistivity sections at depth.

Acknowledgements

We thank the U.S. Forest Service (USFS) and the Mineral Resources Program of the U.S. Geological Survey (USGS) for funding the airborne time-domain survey. Jean Legault and the Geotech team are thanked for data acquisition and thoughtful discussions. Any use of trade, firm, or product names is for descriptive purposes only and does not imply endorsement by the U.S. government.

References

Anderson ED, Yager DB, Deszcz-Pan M, Hoogenboom BE, Rodriguez BD, Smith BD (2023) Geophysical data provide three dimensional insights into porphyry copper systems in the Silverton caldera, Colorado, USA. Ore Geology Reviews 152:105223. https://doi.org/10.1016/j.oregeorev.2022.105223

Auken E, Christiansen AV, Kirkegaard C, Fiandaca G, Schamper C, Behroozmand AA, Binley A, Nielsen E, Effersø F, Christensen NB, Sørensen K, Foged N, Vignoli G (2015) An overview of a highly versatile forward and stable inverse algorithm for airborne, ground-based and borehole electromagnetic and electric data. Exploration Geophysics 46:223-235

Bove DJ, Hon K, Budding KE, Slack JF, Snee LW, Yeoman RA (2001) Geochronology and geology of late Oligocene through Miocene volcanism and mineralization in the western San Juan Mountains, Colorado. US Geological Survey Professional Paper 1642, 30 p. http://doi.org/10.3133/pp1642

Bove DJ, Yager DB, Mast MA, Dalton JB (2007) Alteration map showing major faults and veins and associated water-quality signatures of the Animas River watershed headwaters near Silverton, southwest Colorado. US Geological Survey Scientific Investigations Map 2976, 18-p. pamphlet, 1 plate, scale 1:24,000

Burbank WS, Luedke RG (1964) Geology of the Ironton quadrangle, Colorado, Geologic Quadrangle: US Geological Survey Geologic Quadrangle Map GQ-291, scale 1:24,000. http://doi.org/10.3133/gq291

Casadevall T, Ohmoto H (1977) Sunnyside Mine, Eureka mining district, San Juan County, Colorado; geochemistry of gold and base metal ore deposition in a volcanic environment. Econ. Geol. 72:1285-1320

Dalton JB, Bove DJ, Mladinich CS, Rockwell BW (2007) Imaging spectroscopy applied to the Animas River watershed and Silverton caldera. US Geological Survey Professional Paper 1651, Ch. E2, 141-159

Dentith M, Mudge ST (2014) Geophysics for the mineral exploration geoscientist. Cambridge University Press, Cambridge, United Kingdom

Gilzean MN (1984) The Nature of the Deep Hydrothermal System, Red Mountain District, Silverton, Colorado. Dissertation, University of California

Gonzales DA, Larson RA (2017) An overview of the mineral deposits of the Red Mountain mining district, San Juan Mountains, Colorado. In Karlstrom KE, Gonzales DA, Zimmerer MJ, Heizler M, Ulmer-Scholle DS (eds) The Geology of the Ouray-Silverton Area, New Mexico Geological Society 68th Annual Fall Field Conference Guidebook 133-140.

Hoogenboom BE, Deszcz-Pan M, Anderson ED, Rodriguez BD, Smith BD, Yager DB (2022) Airborne electromagnetic and magnetic survey data, Silverton, Colorado, 2019. US Geological Survey data release, https://doi.org/10.5066/P92IADBP

Luedke RG, Burbank WS (2000) Geologic map of the Silverton and Howardsville quadrangles, southwestern Colorado. US Geological Survey Geologic Investigation Series Map I–2681, scale 1:24,000. http://doi.org/10.3133/i2681

Sillitoe RH (2005) Supergene oxidized and enriched porphyry copper and related deposits. Economic Geology 100th Anniversary Volume 29:723-768

Verplank PL, Yager DB, Church SE, Stanton MR (2007) Ferricrete classification, morphology, distribution, and carbon-14 age constraints. In Church SE, von Guerard P, Finger SE (eds) Integrated investigations of environmental effects of historical mining in the Animas River watershed, San Juan County, Colorado, US Geological Survey Professional Paper 1651, 723–744

Yager DB, Bove DJ (2007) Geologic framework. In Church SE, von Guerard P, Finger SE (eds) Integrated investigations of environmental effects of historical mining in the Animas River watershed, San Juan County, Colorado, US Geological Survey Professional Paper 1651, 107–140

Multi-scale and multi-source hyperspectral imaging for mapping lithium-bearing minerals

René Booysen[1,2], Moritz Kirsch[1], Samuel T. Thiele[1], Sandra Lorenz[1], Yuleika Madriz[1], Paul A. M. Nex[2], Judith Kinnaird[2], Richard Gloaguen[1]
[1]*Helmholtz Institute Freiberg for Resource Technology, Helmholtz-Zentrum Dresden-Rossendorf, Germany*
[2]*School of Geosciences, University of the Witwatersrand, South Africa*

Abstract. The transition towards a net-zero economy has led to an increased need for several critical raw materials required for green technologies. Lithium (Li) is one of these materials. Significant mineral exploration using sustainable, efficient and innovative methods is required to not only improve mineral detection and mapping, but also to foster social acceptability for the mining and exploration industry. Hyperspectral imaging (HSI) allows for fast and systematic identification of key minerals. In this contribution, we propose an innovative approach for exploration by using hyperspectral data from multiple sensors at various scales to non-invasively map ore and pathfinder minerals. We showcase this approach in an open-pit and under-ground sites in South Africa, Namibia and Germany by acquiring data in the short-wave infrared (SWIR) with both a tripod and a drone. Hand-samples and drill-cores were used to identify the relevant minerals as well as for training/validation purposes. Using computer vision techniques, we were able to create a three-dimensional (3D) point cloud of the sites with HSI attributes to allow for the subsequent spectral mapping of relevant Li-bearing minerals. Results were validated using drill-core data, LIBS measurements and geochemical analyses of hand samples.

1 Introduction

The transition towards a green economy has led to a rise in demand for certain raw materials. Among these materials, Lithium (Li) stands out, as it is increasingly used in green technologies such as in rechargeable batteries for electric vehicles (Herrington 2021). Recycling alone cannot sustain this increased demand, which has reignited the focus on primary raw materials. Conventional exploration methods are typically involve laborious fieldwork, supported by geophysical surveying, which can prove to be costly, time-consuming, and often encounter low social acceptance of mining and exploration activities. Thus, a renewed approach to mineral identification and exploration is required.

We propose to use hyperspectral imaging (HSI) as a non-invasive method for the sustainable exploration and mapping of Li-bearing minerals. HSI is a method whereby a single image is acquired at hundreds of different wavelengths of the electromagnetic spectrum. Each pixel of the resulting data cube contains spectral information that can ultimately be used to identify mineral types (Shippert 2003). HSI allows us to acquire data safely from a distance as some targets might not be easily accessible. Furthermore, it allows for fast and systematic identification of key minerals and can provide information about mineral abundances and associations.

In recent years, the use of HSI for identifying and mapping minerals directly in the field has set particular emphasis on satellite and plane-based platforms (Van der Meer et al. 2012). We suggest using an innovative approach where hyperspectral data is acquired from both drone-borne and ground-based platforms at various scales (from open-pit and underground outcrops to drill-cores) to map ore pathfinder minerals for the targeting of Li.

To demonstrate our approach, we acquired data in the visible and near-infrared (VNIR) as well as short-wave infrared (SWIR) range of the electromagnetic spectrum at various Li-bearing deposits in South Africa, Namibia and Germany. In South Africa we acquired data from various pegmatite outcrops containing Li. One such example is from the Noumas 1 pegmatite body that contains spodumene and lepidolite (Figure 1). In Namibia, we acquired data from the main open-pit at the Uis tin mine. The LCT pegmatite hosts Li-bearing minerals such as cookeite and petalite amongst others (Booysen et al. 2022). In Germany, we acquired data from the historic underground Zinnwald mine, which is a Sn-W-Li greisen-type deposit and contains the Li-bearing mineral zinnwaldite (Kirsch et al. 2023, *in review*).

By using computer vision techniques, we created hyperclouds of the targeted outcrops, i.e., three-dimensional (3D) point cloud that are attributed with the full hyperspectral information (Thiele et al. 2021). This allowed us to map the relevant mineralization directly on the within the context of the outcrop geometry and easily integrate information from hand-samples and drill-cores (where possible) to identify relevant minerals as well as for training and validation purposes. This approach enables rapid and efficient mapping of complex terrains in a sustainable exploration scheme, and can be used for monitoring and optimisation of ore extraction.

Figure 1. Large green spodumene crystals found at the Noumas 1 pegmatite body in South Africa. The spodumene is surrounded by large white feldspar crystals.

2 Methodology and results

Due to emerging development of sensor technology towards small and robust solutions, hyperspectral sensors have become available for geological fieldwork. Not only can hyperspectral SWIR sensors be used on tripods in the field, but can now be deployed on civilian unmanned aerial vehicles (UAVs; also known as drones). This has allowed more flexible data acquisitions of targets at a relatively high spectral and spatial resolution.

For ground-based hyperspectral data acquisition, we used a tripod mounted Specim AisaFENIX that acquires data in the VNIR and SWIR range of the electromagnetic spectrum (400 nm – 2500 nm). A generator and a work-station are required in order to capture data in the field (Figure 2. a). For underground acquisition, adequate artificial lighting was required in addition. For UAV-based data acquisition we used a HySpex Mjolnir VS-620. The Mjolnir also acquires data in the VNIR and SWIR range (400 nm – 2500 nm). The UAV that we used is a custom-built octocopter, with the entire system, including the sensor and gimbal, weighing below 20 kg (Figure 2. b).

3D models of the various outcrops were produced through Structure-from-Motion, Multi-View-Stereo (SfM-MVS) photogrammetry. The RGB photos were captured in the field with a Sony camera, and were used for the SFM-MVS workflow in Agisoft Metashape. The 3D models were used to properly correct the hyperspectral data in the python-based toolbox *Hylite* (Thiele et al. 2021). The hyperspectral data is back-projected on the 3D model and transformed to a so-called hypercloud. The attributes of the 3D model allow us to correct for varying illumination conditions. Ultimately, by transforming the hyperspectral image into a hypercloud, we create a 3D pointcloud containing x, y and z coordinates as well as hyperspectral reflectance attributes.

Figure 2. a The tripod mounted AisaFENIX sensor in the field with a workstation consisting of a computer and generator. **b** The HySpex Mjolnir attached to the gimbal and mounted to a custom-built octocopter.

Hand samples and drill-cores were used to identify the minerals present at each outcrop. The samples were analysed in the laboratory with LWIR (long-wave infrared) and SWIR sensors. Spectra extracted from the data were compared to spectral libraries (the USGS and CSIRO spectral libraries) to identify the minerals in the samples. This allowed us to identify Li-bearing minerals such as lepidolite found at Noumas 1 (Figure 3), and other path finder minerals. We used these extracted spectra to create spectral libraries specific to each outcrop. With this information, we used machine learning algorithms (such as supervised classifications), minimum wavelength mapping and band ratios to map the relevant minerals directly on the hypercloud. In Figure 4 we show one such example where Li-bearing minerals were mapped in 3D at the main open-pit at the Uis mine. The results were validated using spectral point measurements, in-situ LIBS measurements and geochemical analyses such as XRF and XRD.

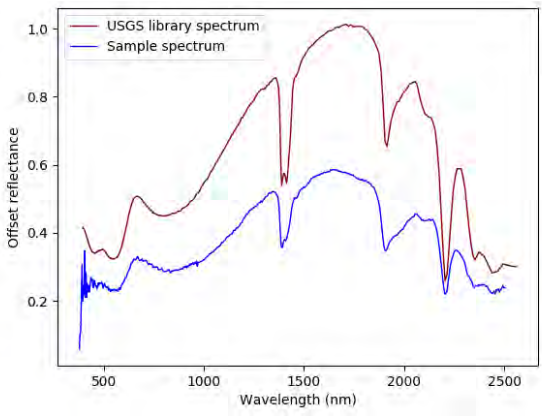

Figure 3. Spectrum of lepidolite taken from hyperspectral SWIR data of a hand sample (in blue) compared with a lepidolite spectrum taken from the USGS spectral library (in red).

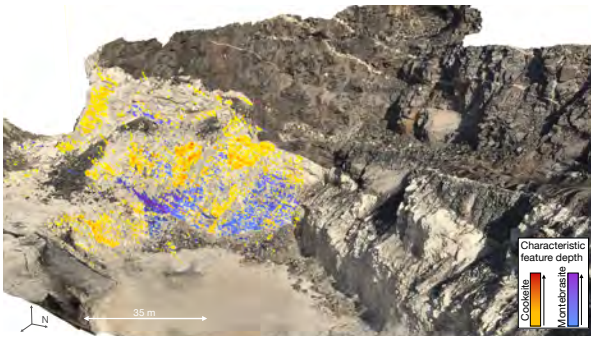

Figure 4. 3D model of the main open-pit at the Uis tin mine. Mapped Li-bearing minerals are shown in yellow and blue. Cookeite is shown in yellow and red, with red indicating a higher abundance of cookeite. Montebrasite is shown in blue and purple, with purple indicating a higher abundance (Booysen et al. 2022).

3 Discussion

In this contribution, we demonstrate the use of hyperspectral data from both UAV and tripod platforms for the exploration of open-pit and underground Li-hosting deposits. There are many unique challenges that accompany the acquisition of hyperspectral data on both tripod and drone platforms. For tripod data acquisition, a stable and good vantage point is required to capture optimal data of the targeted body, however, finding such a vantage point is not always possible. This is where UAV-based platforms can be useful. On the other hand, data acquired from a drone requires more complex corrections due to the platform's continuous movement during acquisition. Although the usage of both platforms has their own challenges to overcome, the fact that we have both options available allow us to use the most appropriate platform for each situation.

Proper data corrections are imperative for the successful use of the data. More conventional remote sensing methods such as satellite- and plane-based HSI have widely accepted and standardized correction steps. However, the correction procedure of data acquired with ground-based and drone-borne platforms are still considered novel. With this demonstration, we show a robust workflow with our advanced python-based toolbox, Hylite. Hylite corrects for various effects such as different incident angles and ambient light. Thiele et al. 2021).

By acquiring hyperspectral data of the hand samples and drill-cores first, we can not only identify and map the Li-bearing minerals directly, but also identify mineral associations. This aids us in directing focus to certain alterations that may be associated with mineralization. Furthermore, by creating a hypercloud we transform a normal hyperspectral image into a 3D data set with each point containing its own spectrum, latitude, longitude and elevation. This allows us to produce a geometrically correct and spatially continuous mineral map. By producing a 3D mineral map, geologists can improve their sampling strategy for further investigations. This approach is also meant to supplement geological fieldwork by providing a qualitative discrimination of geological domains in order to rapidly direct mining or exploration activities. It may be possible to selectively mine specific areas within the deposit based on this kind of data. The same approach can be used to map key mineralization in underground mines with the addition of artificial lighting (Kirsch et al. 2023, *in review)*.

Taking a hyperspectral multi-source approach has allowed us to acquire geological information rapidly and efficiently, allowing us to save time and keep costs down compared to conventional methods. Additionally, by using innovative and non-invasive methods during mining and exploration activities we can foster a higher degree of social acceptance in the mining and exploration industry.

4 Conclusion and outlook

Our study demonstrates the potential of a multi-source hyperspectral approach in generating mineral maps that are both geometrically accurate and spatially continuous. This approach has proven to be a valuable asset for the exploration and optimised extraction of critical raw materials such as Li, despite certain limitations. Notably, HSI promotes more socially acceptable methods for mining and exploration by using innovative and non-destructive methods. The next step would be to incorporate the time component, and with repeated acquisitions and real-time processing, we can provide 4D models that allow the monitor of the evolution of a geological target.

Acknowledgements

We would like to acknowledge Andrada Mining for their valuable support during the field campaign and data acquisition at the Uis tin mine. Additionally,

we would like to thank the South African Council of Geosciences for their assistance and support during fieldwork in South Africa. We would also like to acknowledge the Zinnwald visitors mine in Germany for their support during our hyperspectral campaign at the mine. This work received funding from HIF, the DSI-NRF Centre of Excellence; CIMERA as well as the European Regional Development Fund and the Land of Saxony.

References

Herrington, R., (2021) Mining our green future. *Nature Reviews Materials*, 6(6), 456-458. https://doi.org/10.1038/s41578-021-00325-9

Shippert, P., (2003). Introduction to hyperspectral image analysis. *Online Journal of Space Communication*, 2(3), 8.https://ohioopen.library.ohio.edu/spacejournal/vol2/iss3/8

Van der Meer, F. D., Van der Werff, H. M., Van Ruitenbeek, F. J., et al., (2012) Multi-and hyperspectral geologic remote sensing: A review. *International Journal of Applied Earth Observation and Geoinformation*, 14(1), 112-128. https://doi.org/10.1016/j.jag.2011.08.002

Booysen, R., Lorenz, S., Thiele, S. T., et al., (2022) Accurate hyperspectral imaging of mineralised outcrops: An example from lithium-bearing pegmatites at Uis, Namibia. *Remote Sensing of Environment*, 269, 112790. https://doi.org/10.1016/j.rse.2021.112790

Kirsch, M., Mavroudi, M., Thiele, S. T., et al., (2023) Underground hyperspectral outcrop scanning for automated mine-face mapping — the Lithium deposit of Zinnwald/Cínovec. *Photogrametric Record.* Under review

Thiele, S. T., Lorenz, S., Kirsch, M., et al. (2021) Multi-scale, multi-sensor data integration for automated 3-D geological mapping. *Ore Geology Reviews*, 136, 104252. https://doi.org/10.1016/j.oregeorev.2021.104252

Remote sensing and radiometric data for the detection of hydrothermal alteration zones with mineral potential at Yarra Wurta cliff, Australia

Juan E. Mosquera R.[1]
[1]*Geology department, National University of Colombia, Bogotá, Colombia*

Abstract. This study aimed to investigate the mineralization potential of the Yarra Wurta Cliff area, located approximately 45 km northeast of the Olympic Dam deposit in Australia, using spectral analysis and interpretation of geophysical data. This research used an integrated approach combining Landsat and ASTER satellite imagery, along with radiometry data provided by the Australian government, to detect and map hydrothermal disturbance in a study area in Australia. The results showed a good correlation between the radiometry data and the distribution of hydrothermal alteration, especially iron, copper and gold alteration. Although certain rocks showed clear signs of hydrothermal alteration, it is unclear whether they are more susceptible to alteration or whether other factors, such as their proximity to the source of the hydrothermal fluids, play a more important role. Overall, these findings
findings suggest that hydrothermal alteration in the Yarra Wurta Cliff area may be of interest for prospecting for minerals of economic interest.

1 Introduction

In mineral resource exploration, the detection of hydrothermal alterations is a key tool for identifying potential mineral deposits. Remote sensing is an important tool for the detection of these alterations over large areas, as it provides an aerial perspective and wide coverage. In this work, information from two remote sensors, Landsat and ASTER, was used to detect and characterize hydrothermal alterations in the Yarra Wurta cliff area in South Australia (Figure 1-2).

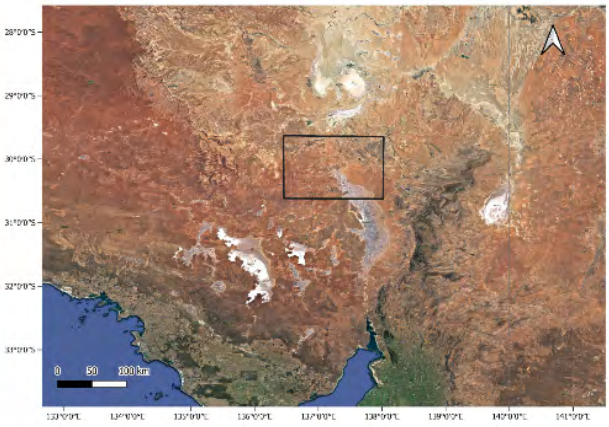

Figure 1. Location of the study zone, located in South Australia. Basemap: Google Hybrid, Map data ©2023 Google.

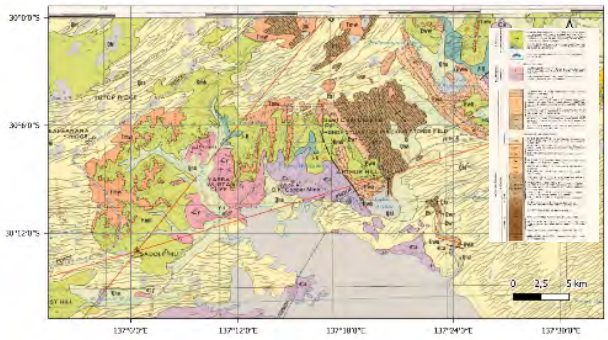

Figure 2. Geological map 1:250000 of Andamooka, the area is smaller than figure 1. Adapted from Raymond, O.L. (2002)

In addition to the remote sensing information, radiometric data were also used to corroborate the information and determine if the alterations were related to areas with anomalies in radioactive elements.

The methodology used to detect and characterize the hydrothermal alterations in the Yarra Wurta cliff area is presented and the results obtained are discussed.

2 Materials and methods

2.1 multi-sensor data

For this study, Was used Landsat-8/OLI data scenes LC09_L2SP_099081_20230217_20230220_02_T1 .The processing level corresponds to collection 2, level 2.

In addition, ASTER L1T satellite scenes, (AST_L1T_00303242001011242_20150415081131_13760),(AST_L1T_00303242001011250_20150415081132_61472) were used.

Landsat 9-OLI and ASTER data used in this study were acquired from the USGS Earth Explorer program.

No geometric, atmospheric, or radiometric corrections were applied to the Landsat 9-OLI and ASTER images, as both images were already rectified.

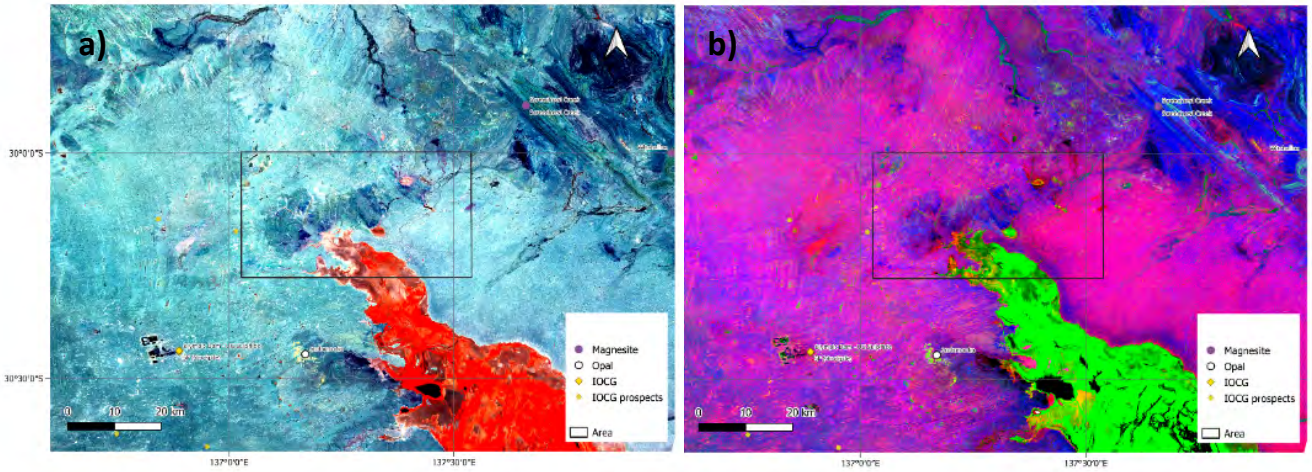

Figure 3. Landsat colour composites and band ratios: (a) RGB bands (5,6,7) dark blue represents hydrothermally altered rocks, (b) RGB bands (4/2,6/7,6/5) Blue represents altered rocks.

2.2 Colour composite

Colour composite is a technique used in remote sensing and image processing to combine three or more separate monochrome images into a single image.

Each monochrome image is typically derived from a different spectral band, with each band capturing different characteristics of the scene or object being imaged. By combining these bands into a single colour image, the resulting image provides more information and can be easier to interpret.

Colour composites are often used to highlight specific mineralogy and lithology in rocks, allowing geologists to more easily identify and characterize geological features. Githenya, L.et al. (2019)

2.3 Band ratio

Band ratios are a technique used to enhance specific features in satellite imagery by combining two or more spectral bands. In remote sensing, certain combinations of spectral bands can provide unique information about the earth's surface.

Band ratios are calculated by dividing the digital number (DN) values of one spectral band by the DN values of another spectral band. The resulting ratio values can then be displayed as a new image, with areas of interest highlighted based on the chosen spectral bands. The choice of spectral bands for band ratios depends on the application and the specific features of interest. The resulting images can be further processed using techniques such as false colour composites or image classification to extract information about the earth's surface.

2.4 Supervised classification

Supervised classification is a widely used technique in remote sensing for land cover mapping. In this study, we used supervised classification to identify different land cover classes in the study area.

The plugin SCP in Qgis was used to perform the classification, a set of training samples was selected for each land cover class based on visual interpretation of high-resolution satellite imagery and ground truth data.

2.5 Radiometric Data

Gamma-ray spectrometry-geophysics is a method used to determine the levels of potassium (K), uranium (eU), and thorium (eTh) on the surface of the Earth.

Radiometry data were obtained from the Geoscience Australia portal, identified as GSSA Andamooka percent Potassium grid geodetic, GSSA Andamooka ppm Thorium grid geodetic and GSSA Andamooka pmm Uranium grid geodetic. These data were used to provide information on the geology, including the identification of hydrothermal altered zones.

3 Results

3.1 Colour Composite

A colour compositing technique was used to generate a composite RGB (red, green, blue) image to highlight areas of hydrothermal disturbance. The combination of bands used was 5 (near infrared), 6 (shortwave infrared) and 7 (mid-infrared) .(Figure 3a).

This combination of bands allows obtaining a composite image in which hydrothermal alterations are highlighted (Figure 3a). According to Githenya, L.et al. (2019), this technique is widely used for the detection of hydrothermal alterations in mining areas and has proven to be effective in the identification of alteration minerals and the characterization of rocks at surface.

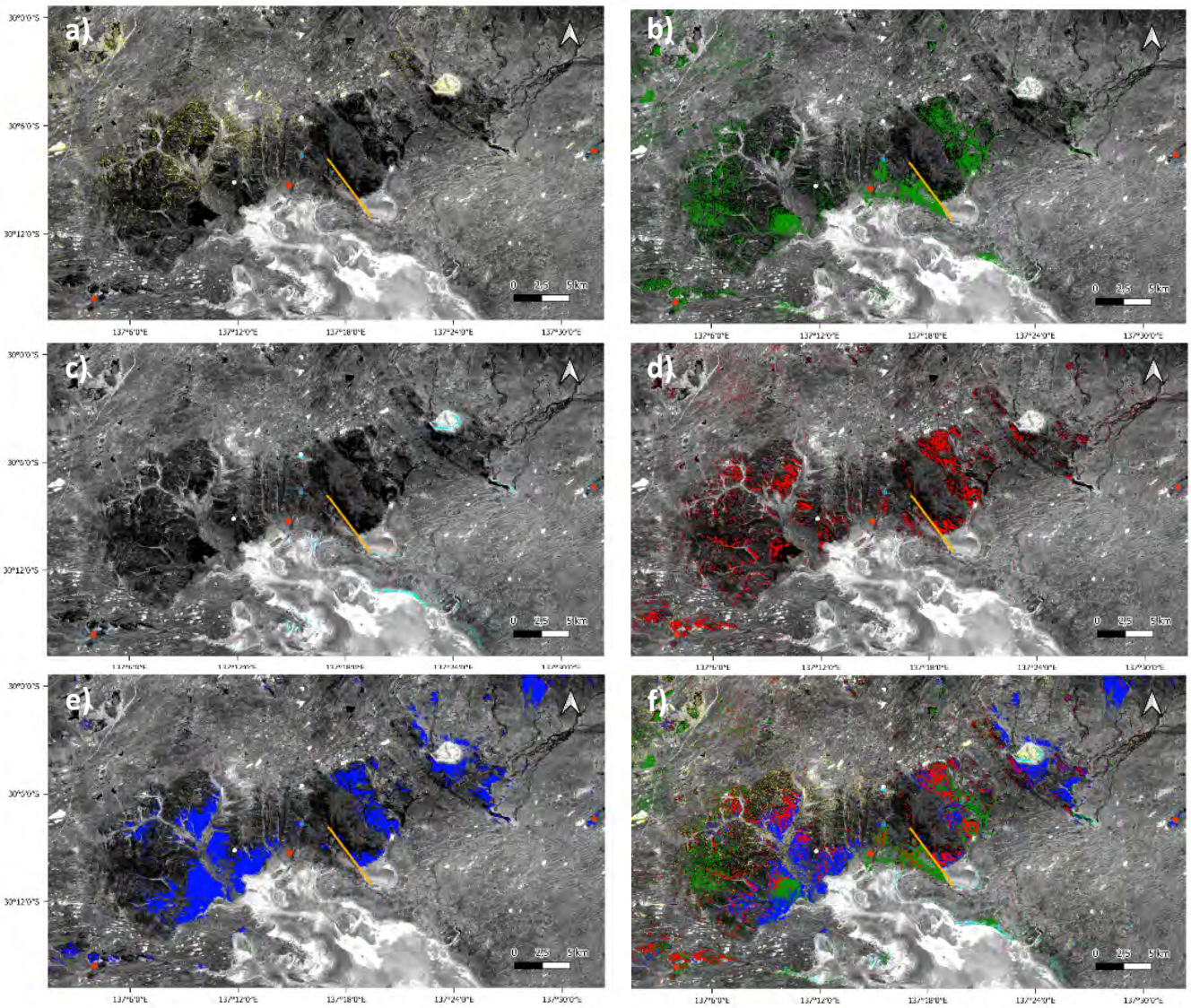

Figure 4. ASTER band ratio results in colour overlaid on Landsat B4: (a) Phyllic alteration (B5+B7)/B6, (b) Propylitic alteration (B6+B9)/(B7+B8), (c) Argillic alteration (B4+B6)/B5, (d) Fe oxide Cu-Au alteration (B5/B4), (e) Fe oxide Cu-Au alteration (B5/B4), (f) alterations exposed in the same scene. Orange dots (copper), White dots (Opal), Blue dot (Agate), gray dot (Clay) , orange line (fault). Mineral occurrences from Department for Energy and Mining(n.d)

3.1 Band ratio

Landsat image processing using band ratios also revealed valuable information about mineralization in the study area. According to Githenya, L. et al. (2019), the combination of the RGB band ratios(4/2,6/7,6/5) (Figure 3b). allowed the identification of areas with hydrothermal alteration that are identified in dark blue (Figure 3b).

The results of Aster image processing using the ratios of phyllic, argillic, propylitic, ferrous iron and iron oxide Cu and Au alteration (Figure 4). revealed a spatial distribution of these types of alteration in the study area.

Propylitic alteration is associated with alteration of feldspars, micas and amphibole, suggesting copper mineralization.

The presence of ferrous iron is due to the presence of minerals such as hematite and goethite.

Argillic alteration is characterized by the presence of clay minerals such as kaolinite, illite and montmorillonite, as well as the presence of quartz, potassium feldspars and plagioclase.

The phyllic alteration is recognized by the presence of sericite, muscovite, illite and smectite.

The Fe oxide, Cu-Au alterations is highly related to ferrous silicates.

The Aster band ratios were taken from Younes et al. (2022) and Oliver, S,et al. (2004).

3.2 Radiometric data

The results obtained (Figure 5) indicate a good correlation between the radiometry data of potassium, thorium and uranium The highest concentrations of radioactive elements (up to 4.50% K, 22 ppm eTh and more than 8 ppm eU), and the distribution of hydrothermal alteration in the study

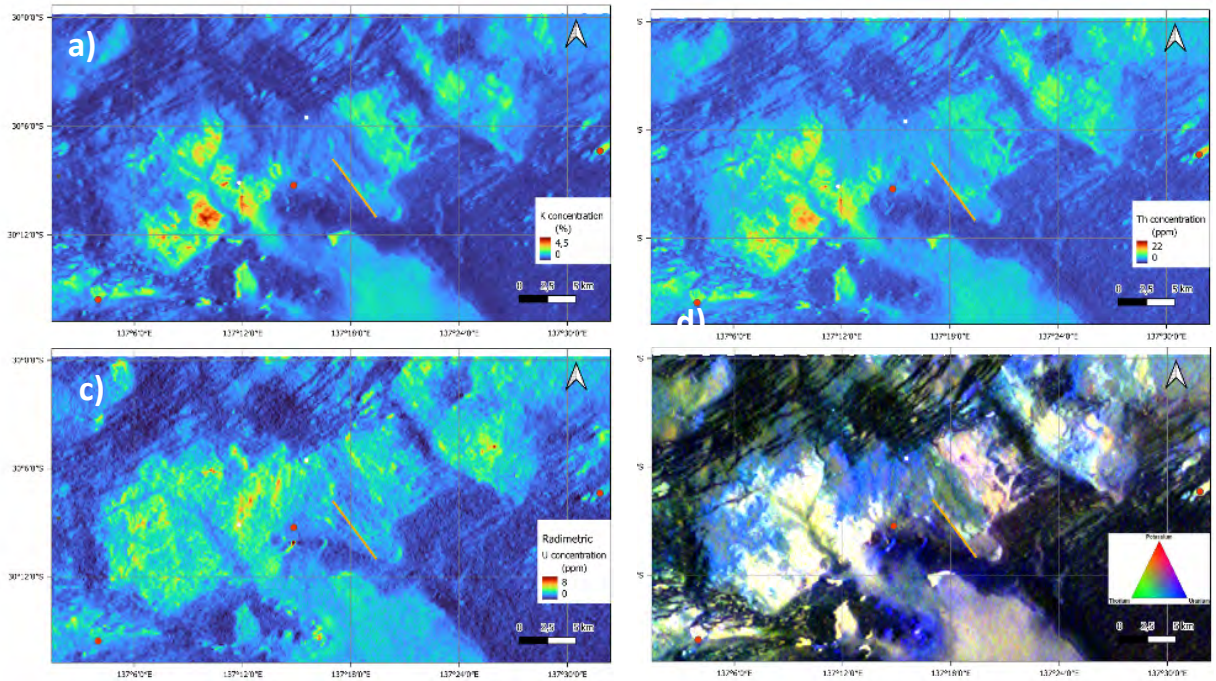

Figure 5. Maps of natural gamma-ray spectrometry : (a) Potassium (b) Thorium , (c) Uranium, (d) RGB bands (U,Th,U) Orange dots (copper), White dots (Opal), Blue dot (Agate), Gray dot (Clay) , orange line (fault). Mineral occurrences from Department for Energy and Mining(n.d)

area. Specifically, iron, copper and gold alteration was found to correlate strongly with thorium and potassium radiometry data. This suggests that these elements may be useful for the detection and exploration of mineral deposits in the area. It also reinforces the usefulness of radiometry as an important tool in mineral exploration. Uranium anomalies appear not to be associated with hydrothermal alteration zones.

4 Conclusion

hydrothermal alterations seem to be more concentrated in certain types of rocks, especially calcareous rocks. This is also because there may be more than one alteration event since some alterations are found exclusively in certain rocks.
Reported copper occurrences are mostly associated with iron, copper and gold oxide alteration, and propylitic alteration, opal is related to argillic alteration. The hydrothermal alterations are consistent with high values of thorium and potassium and can be of great help in determining alterations in other zones.

Further investigations are needed to determine more properties by means of other geophysical methods such as gravimetry and magnetometry, as well as field visits to verify the concordance of hydrothermal alterations, and to gather information associated with the IOCG type deposits in the area and the possible relationship between these and the study area.

Department for Energy and Mining, the Government of South Australia, mineral ocurrences (new versión), https://portal.geoscience.gov.au/.Accessed 2 March 2023

Geophysical Acquisition & Processing Section (2020): GSSA Andamooka percent Potassium grid geodetic. .dataset. Geoscience Australia, Canberra. http://pid.geoscience.gov.au/dataset/ga/67973

Geophysical Acquisition & Processing Section (2020): GSSA Andamooka pmm Uranium grid geodetic. .dataset. Geoscience Australia, Canberra. http://pid.geoscience.gov.au/dataset/ga/143519

Geophysical Acquisition & Processing Section (2020). GSSA Andamooka ppm Thorium grid geodetic.dataset. Geoscience Australia, Canberra. http://pid.geoscience.gov.au/dataset/ga/143523

Githenya, Lincoln & Kariuki, P. & Waswa, Aaron K.. (2019). Application of Remote Sensing in Mapping Hydrothermal Alteration Zones and Geological Structures as Areas of Economic Mineralization in Mwitika-Makongo Area, SE Kenya.

Google Maps (2023). *South Australia*, Google Maps [QGIS].https://mt1.google.com/vt/lyrs=y&x={x}&y={y}&z={z}.Accessed 07 March 2023

Oliver, S., Kalinowski, A (2004). ASTER Mineral Index Processing Manual. Geoscience Australia, Canberra.

Raymond, O.L. 2002. Scanned 250K Geological Maps. Geoscience Australia, Canberra. http://pid.geoscience.gov.au/dataset/ga/71367

Younes, Mamouch & Attou, Ahmed & Abdelhalim, Miftah & Ouchchen, Mohammed & Dadi, Bouchra & Achkouch, Lahsen & Et-Tayea, Yassine & Allaoui, Abdelhamid & Boualoul, Mustapha & Randazzo, Giovanni & Lanza, Stefania & Muzirafuti, Anselme. (2022). Mapping of Hydrothermal Alteration Zones in the Kelâat M'Gouna Region Using Airborne Gamma-Ray Spectrometry and Remote Sensing Data: Mining Implications (Eastern Anti-Atlas, Morocco). Applied Sciences. 12. 957. 10.3390/app12030957.

The use of total-field data for mineral exploration

Christopher Parker[1]
[1]*Gap Geophysics Australia Pty Ltd*

Abstract. Fast sampling magnetometers make it possible to collect total b-field data for use in mineral exploration. Total-field data is collected in Sub-Audio Magnetics (SAM) and SAMSON surveys.
The surveys can be deployed as a galvanic source to measure magnetometric conductivity (MMC) or through inductive source to measure the secondary eddy currents from conductors.
Total-field surveys are customisable and scalable depending on the requirements.
SAM surveys can be deployed on foot or in the air with a UAV or helicopter (HeliSAM). The SAM technique in galvanic mode excels at mapping electrical pathways of faults, shears, conductors.
Inductive surveys are comparable to standard electromagnetic surveys. The surveys can be undertaken as stationary measurements (SAMSON mode), walking or by air. SAMSON is the most sensitive technique and can detect large conductors that are greater than 1 km from surface. Walking or aerial surveys are known to have detected conductors in excess of 600 m below the surface.
Total-field surveys are cost effective as they allow for measurements to be taken continuously. The sensor does not suffer from rotational or vibration noise. Surveys can cover large survey areas rapidly for cost effective deep exploration.

1 Introduction

Gap Geophysics Australia Pty Ltd (GAP) developed a fast-sampling receiver that is capable of recording magnetic fields up to 9600 Hz when coupled with a Cs vapor magnetometer. The receiver samples the Larmor frequency from a compatible Cs magnetometer, such as a Geometrics G822A, very accurately. The Larmor frequency is directly proportional to the ambient magnetic field where the frequency is converted by using the gyromagnetic constant for Cs 133 which is 3.498572 Hertz per nT. Prior to this system being available, there were few other systems available that were fast enough sampling with low noise and high sensitivity. Noise levels of this system are lower than systems utilising the MFAM sensor developed by Geometrics in 2015.

2 Sub-Audio Magnetics

Sub-Audio Magnetics (SAM) (Boggs et al. 1998), was developed by Dr Malcolm Cattach as part of his PhD project in 1996. The SAM method requires a time-varying electric current to be artificially applied to the ground.

For SAM magnetometric (MMC) surveys, this is achieved with a geophysical transmitter producing a low frequency square wave (Figure 1) that is introduced into the ground through distant electrodes as for conventional gradient array electrical resistivity (ER) or induced polarisation (IP) surveys (Figure 2). SAM fixed loop electromagnetic (FLEM) surveys use a geophysical transmitter to transmit electrical current through a loop as for conventional FLEM surveys (Figure 3).

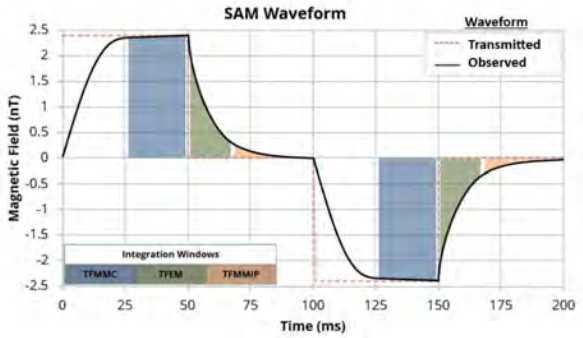

Figure 1. SAM transmitted waveform and integration windows.

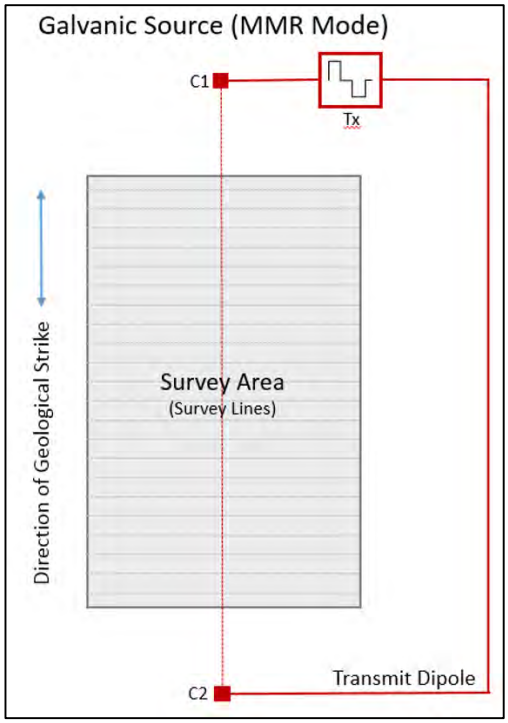

Figure 2. SAM - Galvanic mode.

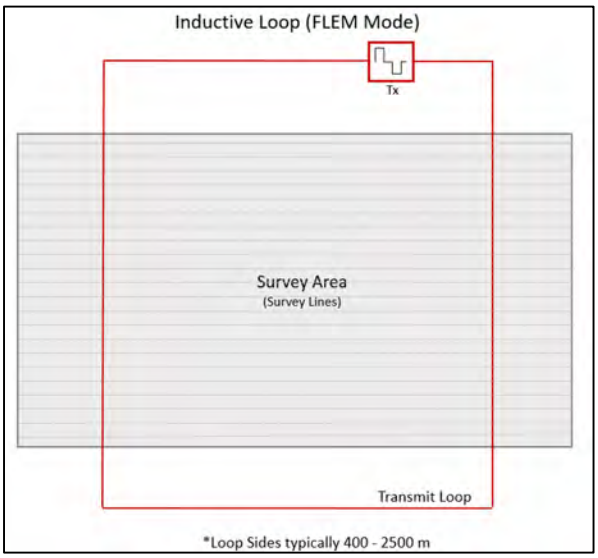

Figure 3. SAM - Inductive mode.

2.1 Galvanic mode

Galvanic mode SAM surveys are suitable for structural mapping trends, faults, shear zones and dislocations. Multiple survey orientations can be surveyed for maximum insight. Electrical pathways of least resistance or flows around resistive features are highlighted. The technique does not require highly conductive targets but rather a conductivity contrast between target geologies or structures.

2.2 Inductive mode

Fixed loop electromagnetic surveys are conducted to conducted to identify ore-bearing strata and ore-controlling structures in the mining area's periphery (Wu et al. 2022). Fixed loop surveys allow for a large magnetic moment which allows for excitation of deep targets.

3 Magnetometric Conductivity Data Recovery

SAM waveforms are separated from the spatial magnetic field and stacked to enhance the signal to-noise ratio. Raw TFMMC values are then computed by integrating beneath the waveform during the transmitter on-time. Normalisation of TFMMC values is performed by dividing by the transmitter current used. The uncorrected TFMMC values thus determined have units of picoteslas per amp (pT/A).

3.1 Primary and Normal Corrections

The theoretical electromagnetic fields produced by the wire feeding the electrodes (primary field) and current flowing through a homogenous half-space (normal field) are computed and subtracted from the raw TFMMC data. The resulting corrected TFMMC data then represent the anomalous part of the signal and the consequence of perturbations in current flow caused by lateral conductivity variations.

3.2 Magnetometric Conductivity Transformation

The TFMMC parameter is a total-field measurement that is made in the presence of the large background magnetic field of the Earth. This results in the TFMMC field being a pseudo-component measurement made in the direction of the Earth's magnetic field. As this component direction is variable from site to site and grid to grid, TFMMC data are generally non-standard and not intuitively interpreted.

The MMC transform was developed by David Boggs (Boggs et al. 1999) to provide a standard, intuitive presentation format for TFMMC data. This can be done via a 2D fast Fourier transform resulting in a horizontal component grid file. This transform is routinely applied to the gridded TFMMC data along the traverse line direction and magnetometric conductivity (MMC) images generated from these grid files.

MMC data are more readily related to underlying conductivity structure than TFMMC data. In general terms, MMC highs may be associated with underlying features that are relatively conductive and lows with resistive features.

4 Off-time Data Recovery

Total-field electromagnetic (TFEM) data are measured in the transmitter off-time. In the off-time both electromagnetic (EM) and induced polarisation (IP) responses can manifest, though the latter normally requires transmit frequencies as low as 0.125 Hz to be visible above the EM response. Due to the requirement that dynamic mode SAM uses higher frequencies, the successful extraction of IP parameters is generally restricted to resistive ground or stationary mode (SAMSON). However, EM responses can usually be detected in Total-field data and may be of significant exploration benefit. Total-field off-time data are extracted by integrating under the decay curve and involves summing the off-time data under the decay curve for each time gate and stacking readings in a moving window.

5 Platforms

Data can be collected by stationary measurements, whilst walking or flying the system with a UAV or helicopter. Highest resolution data is achieved with ground-based surveys whereas UAV and helicopter systems can be deployed in more challenging terrain or where rapid data acquisition is required.

6 Fixed loop case study – Lalor

6.1 The Lalor deposit

The Lalor deposit is a volcanogenic massive sulphide (VMS) deposit located in Manitoba, Canada. The Lalor deposit was discovered by

Hudbay Minerals using down-hole electromagnetics. The bore hole for the survey was a target from a Crone fixed-loop electromagnetics survey.
The Lalor Lake VMS deposit is flat lying, with mineralisation beginning at approximately 570 m from surface and extending to a depth of approximately 1,170 m (Blakley 2008).
Lalor deposit is geophysically characterised as a deeply buried good conductor that exhibits electrical responses that are distinct from the relatively resistive background (Yang et al. 2017).

6.2 Survey configuration

A fixed-loop electromagnetics survey was conducted over the deposit in 2014 by GAP. A total of 93 line-kilometres were acquired at 100 m line spacing in 4 hours with a towed bird receiver. The transmit loop was energised at 7.5 Hz by a Phoenix TXU-30 transmitter producing a magnetic moment of 57 MA m^2. Using this configuration, total-field was the first technique to detect the Lalor deposit with an airborne sensor.

6.3 Test lines

A test line was flown at three different transmit frequencies. The peak responses at 23 ms after the transmitter shutoff are detailed in Figure 4 with the response ranging from 3.6 pT/A at 7.5 Hz to 5.15 pT/A at 3.75 Hz.

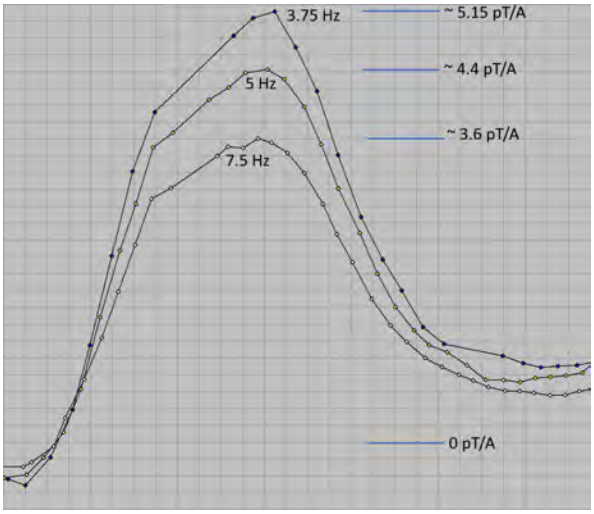

Figure 4: Peak response from the Lalor deposit.

6.4 EM response

The gridded results from channel 1, channel 9 and channel 13 are shown in Figures 5-7. The transmit loop is shown as a black outline on top of the EM response. North is up in these figures. Early time data (channel 1) is contaminated by cultural infrastructure. The response from the ore body is clear in channel 9 and channel 13.

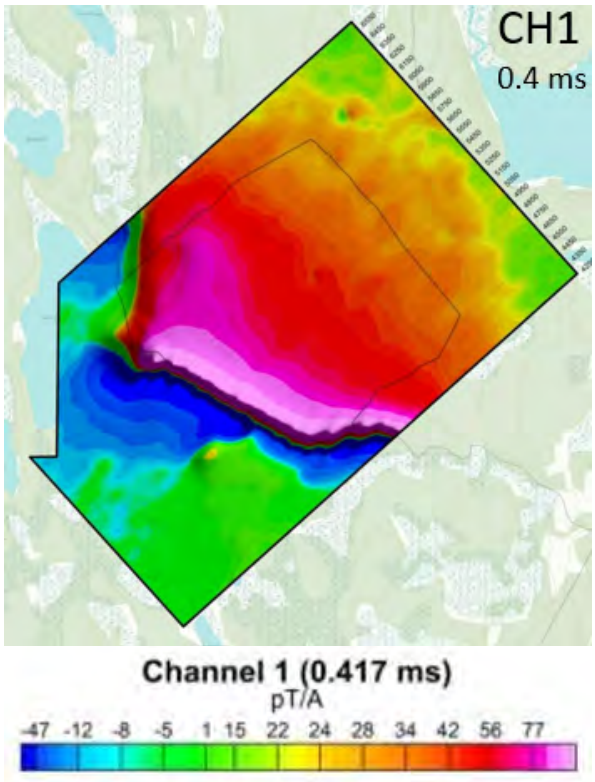

Figure 5. Lalor EM response - Channel 1.

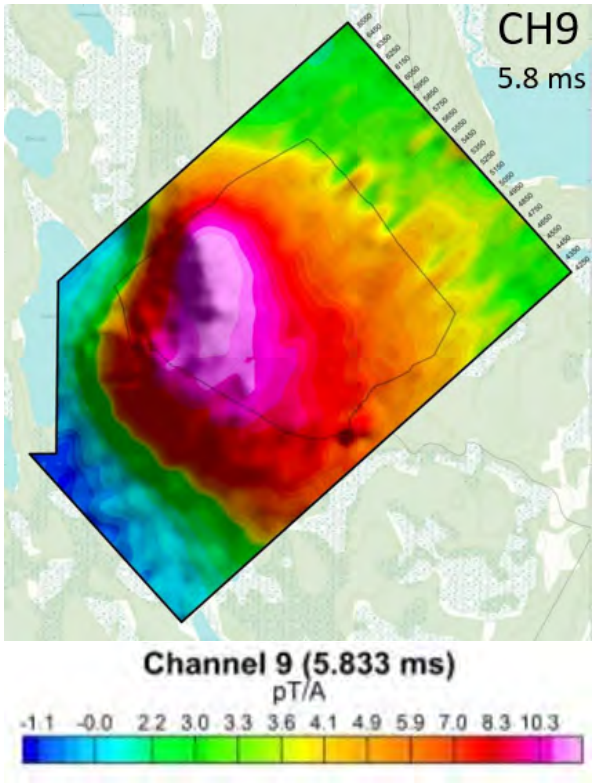

Figure 6. Lalor EM response - Channel 9.

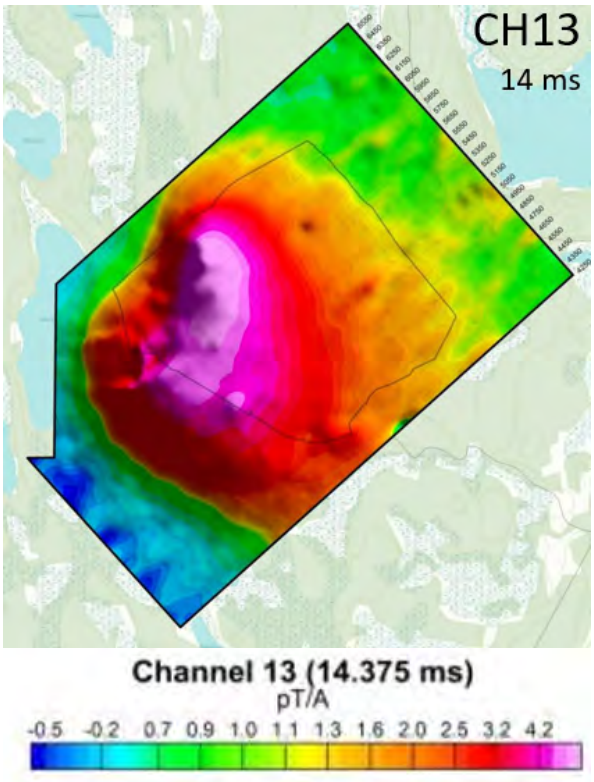

Figure 7. Lalor EM response - Channel 13.

6.5 Inversion

Inversion of the dataset was performed by Dikun Yang and Douglas W. Oldenburg. Both blind and warm-start inversions were performed. A good fit was achieved in the late time channels after the response from infrastructure was minimal.

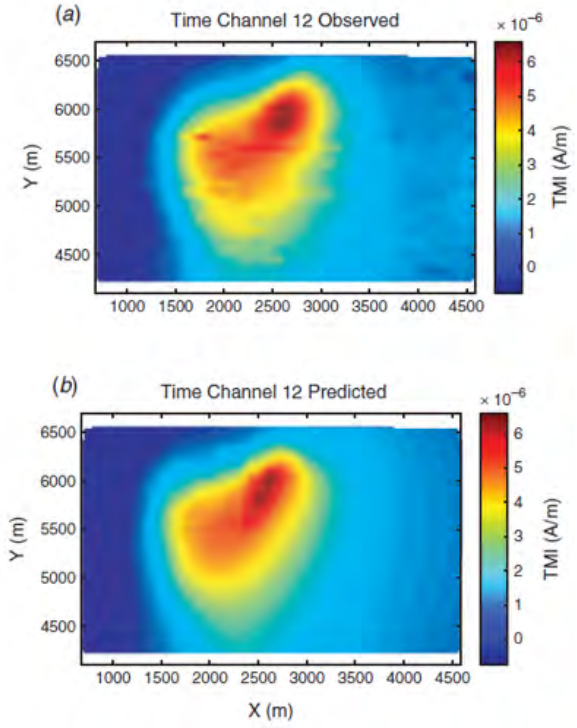

Figure 8. Lalor model Channel 12 (Yang et al. 2017)

7 Conclusion

Total-field is capable of rapid and cost-effective data collection. As the magnetometer does not require leveling or orientation, data is able to be collected from a variety of platforms resulting in an adaptable and scalable system. The Lalor deposit detection shows that the system is capable of detecting conductors at depth.

Acknowledgements

Dr Malcolm Cattach for sharing your knowledge and wisdom and for driving the development of total-field magnetometers for mineral exploration in Australia.

Dikun Yang and Douglas W. Oldenburg for inverting the HeliSAM data for the Lalor deposit.

Hudbay Minerals for allowing the HeliSAM survey to take place.

References

Blakley, I. T., 2008, Report on the Lalor Lake Deposit,SnowLake: NI 43–101 Report, Scott Wilson Roscoe Postle Associates.

D.B. Boggs, M.K. Cattach & J.M. Stanley (1998) Feasibility studies of TFMMIP and TFEM surveying with Sub-Audio Magnetics, Exploration Geophysics, 29:3-4, 290-295, https://doi.org/10.1071/EG998290

D.B. Boggs, J.M. Stanley & M.K. Cattach (1999) Three-dimensional numerical modelling of Sub-Audio Magnetic data, Exploration Geophysics, 30:3-4, 147-156, https://doi.org/10.1071/EG999147

Dikun Yang & Douglas W. Oldenburg (2017) 3D inversion of total magnetic intensity data for time-domain EM at the Lalor massive sulphide deposit, Exploration Geophysics, 48:2, 110-123, https://doi.org/10.1071/EG15070

Junjie Wu, Qingquan Zhi, Xingchun Wang, Xiaohong Deng, Yuge Liu, Xiaodong Chen, Fixed-loop TEM surveying using the SQUID magnetometer for deep mineral exploration in a conductive area, Journal of Geophysics and Engineering, Volume 19, Issue 6, December 2022, Pages 1300–1307, https://doi.org/10.1093/jge/gxac084

Smit, J.P., Stettler, E.H., Price, A.B.W. et al. Use of drones in acquiring B-field total-field electromagnetic data for mineral exploration. Miner Econ 35, 455–465 (2022). https://doi.org/10.1007/s13563-021-00292-1

New lithostructural map of the Doropo region, northeast Côte d'Ivoire: insight from structural and aeromagnetic data

Zaindjêdé H. Siagné[1,2], Tahar Aïfa[2], Alain Nicaise Kouamelan[1], N'guessan Nestor Houssou[1], Wilfried Digbeu[1], Bi Koffi Fidèle Kakou[3], Pierrick Couderc[3]

[1]*Université Félix Houphouët-Boigny, Abidjan-Cocody, 22 BP 582 Abidjan 22, Côte d'Ivoire*

[2]*Univ Rennes, Géosciences Rennes – CNRS UMR6118, Bat.15, Campus de Beaulieu, 35042, Rennes cedex, France*

[3]*Ampella-Centamin, 20 BP 945 Abidjan 20, Côte d'Ivoire*

Abstract. This study, performed in the Doropo region (northeastern Côte d'Ivoire) in the Paleoproterozoic domain (southern part of the West African Craton), aims to produce a detailed lithostructural map of this area. The geology of this region is less known due to the thick lateritic overburden and the scarcity of outcrops. Recent airborne geophysical data integrated with field structural and lithological observations allowed to distinguish several lithologies. Filtering techniques (derivatives, upward continuation, etc.) showed the presence of faults, shear zones and intrusions. The structural analysis revealed four deformation events : D1 is a N-S compression marked by E-W foliation, conjugate NE-SW and NW-SE sinistral and dextral shears, respectively, as well as folds with E-W axial planes; D2 is a major transpressive phase characterized by an intense NE-SW foliation, E-W dextral shear zones, a weakly dipping stretching lineation plunging N-E, and NE-SW faults; D3 is a NE-SW compressional phase generated NW-SE foliation with ~E-W shears, and NW-SE axial plane folds; D4 is a late, rather brittle phase characterized by brittle structures (faults, fractures, etc.) and the emplacement of NE-SW and NW-SE dolerite dykes. This tectonic evolution demonstrates that the Doropo region was subject to ductile and then brittle deformations.

1 Introduction

The Paleoproterozoic terrains of the West African Craton (WAC), particularly those of the Man-Leo Shield (Figure 1), are composed of granitoid and greenstone belts. They represent an interesting target for mineral exploration because they contain numerous mineral deposits (Goldfarb et al. 2017). Unfortunately, these regions are very often characterized by surface weathering (lateritization) and limited outcrops that can hinder cartographic surveying, mineral exploration and structural studies. The recourse to use high resolution aeromagnetic data processing appears then as an essential tool to study these terrains. Magnetism has shown its effectiveness in the study of similar terrains, especially within the WAC by producing new geological data .

Thus, the recently acquired (2015) aeromagnetic data in the Doropo region (northeast Côte d'Ivoire) present an opportunity to investigate this region where no significant geological studies have been done. This region appears promising for mineral prospects, with the current presence of several exploration companies (e.g., Ampella-Centamin Co). Based on this mining interest, detailed geological studies have become a necessity, as most mineral deposits (e.g., gold) are structurally controlled (Mériaud et al. 2019; Murray et al. 2019; Tourigny et al. 2019).

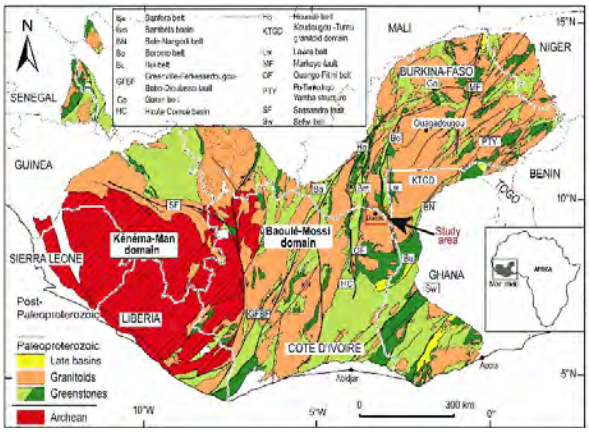

Figure 1. Simplified geological map of the Man-Leo Shield with the location of study area (modified from BRGM SIGAfrique map, Milési et al. 2004)

2 Methodology

Two major approaches (field and geophysical data analysis) were necessary to produce a detailed map of the region. A field phase was used to collect lithological, structural and magnetic susceptibility data followed by the processing of aeromagnetic data. All data acquired (geophysical, lithological and structural) were integrated within a GIS software for interpretation.

Field work resulted in: - Identifying the different lithologies encountered, describing them macroscopically. The macroscopic description focused on textural and mineralogical features. The structural framework was described by highlighting the structures that are manifestation of deformations that have affected these different lithologies while specifying their direction and dip if possible.

Above all, by establishing their spatial, crosscutting relationships and relative chronology between different deformation events. The aeromagnetic data were acquired within the framework of the Doropo Project in northeast Côte d'Ivoire. A total of 21,589 km of lines were flown. The flight lines were spaced at intervals of 200 m and 100 m (filling) in the direction N160–N340 while the control lines were spaced 2000 m and 1000 m (filling) in the direction N070–N250 at an average flight altitude of 100 m. The aeromagnetic data obtained underwent a first processing by making

specific corrections to be used and reliable for the further processing (Allard and Bois 1999).

Diurnal, altitude, topography and latitude corrections were applied. After that, the data from these corrections were gridded on a 25 m × 25 m cell size using Geosoft Oasis Montaj software. This allowed to obtain the total magnetic intensity map on which several filters were applied in order to highlight the geological properties.

3 Results

3.1 Petrography

Field observations complemented by drill core samples allowed to distinguish several lithologies in the Doropo region. The main lithologies in order of abundance are: (i) ***Biotite granite*** is the dominant lithology in the region and it is encountered all across the study area. It may occur in massive or circular or dome or slab of extremely variable size (meter to kilometer). It can also be observed as a cluster of large blocks exposed by erosion.

The rock is leucocratic to mesocratic and ranging from fine-to coarse-grained (Figure 2a). Based on visual estimation, the rock is mainly composed of quartz (~60%), feldspar (~30%), biotite (~10%) and sometimes small euhedral crystal of sulphides (ii) ***Gneissic and migmatitic granites*** are found in the south, east and north of the study area. They appear as circular or large slabs and are cross-cut by several quartzo-feldspathic veins (Figure 2b) and contain mafic enclaves (Figure 2c). They are light-to grey coloured, medium-to coarse-grained, and show a gneissic texture defined by alternating light colour (quartz, feldspar) and dark colour mineral (mica, amphibole) rich beds, which sometimes are migmatitic. Furthermore, the rocks contain quartz (~55%), feldspar (~35%), biotite (~5%), and some rare amphibole (~3%) and magnetite. (iii) ***Granodiorite*** are most often found in contact with or as enclaves within the biotite granite. They occur as circular or slab or meter-size block, and are mesocratic, medium-to coarse-grained (Figure 2d).

The rocks also show a granitic texture and contain feldspar (~60%), quartz (~25%), amphibole (~10%), biotite (~5%) and accessory sulphide minerals. These rocks sometimes show a weak foliation defined by aligned amphibole and biotite grains. (iv) ***Gabbro*** occurs in the shape of small decimeter-size nodules or as enclaves within the biotite granite and is found in the northern part of the study area. The rock is melanocratic, medium-to coarse-grained, and consists of feldspar (~70%), pyroxene (~25%), and rare amphibole (<5%) (Figure 2e). (v) ***Amphibolite*** generally occurs as enclaves within the biotite granite, gneissic and migmatitic granites, granodiorite and tonalite. The rock is dark green, fine-to medium-grained, and is crossed by numerous deformed thin quartz and feldspar veins (Figure 2f). It is mainly composed of amphibole (~80-70%) and feldspar (~30%). (vi) ***Rhyolite*** is less represented in the study area and appears as small meter-size boulders or dome-like outcrops in its central part. To the naked eye, the rock is light in colour, glassy, and composed of quartz and feldspar phenocrysts and some disseminated pyrite crystals (Figure 2g). It is the only felsic volcanic unit encountered in the Doropo region and show no apparent metamorphic alteration.

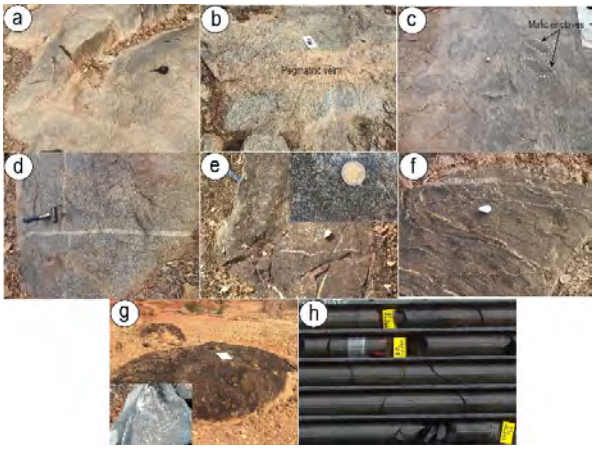

Figure 2. Field photographs of the main lithologies from the Doropo region. (**a**) Biotite granite, (**b**) Gneissic granite crossed by pegmatitic vein, (**c**) Migmatitic granite with mafic enclaves, (**d**) Outcrop of granodiorite, (**e**) Gabbro crossed by quartzofeldspathic vein, (**f**) Amphibolite with numerous thin quartz and feldspar veins, (**g**) Rhyolite boulders, and (**h**) Dolerite dyke in drill core.

3.2 Structural analysis Arial Bold 10pt

The Doropo region owes its structure to four deformation phases (D1, D2, D3 and D4) among which D1 to D3 played a major role. All of these deformation events have affected the granitoid terrains. The first deformation phase is characterized by a tectonic fabric obtained during recrystallization and migmatization (Figure 3).

This D1 deformation phase having generated: (i) a E-W S1 foliation, (ii) conjugate sinistral and dextral shear zones oriented NE-SW and NW-SE, respectively and (iii) F1 folds with plunging axis 45◦ towards the southwest. It is the result of a N–S compression which is less expressed in the region. This deformation phase has been reported in other areas of the Man-Leo Shield.

This first deformation phase (D1) is followed by a NW-SE transpressive phase (D2) which is the most important in the Doropo region (Figure 4). It is also recognized as one of the major phases at the WAC scale: (i) Northwestern and Southwestern Ghana, (ii) Northeastern Côte d'Ivoire (iii) in Burkina-Faso and (iv) in the Kédougou-Kéniéba Inlier (KKI) in Sénégal. It is distinguished by intense NE-SW oriented S2 foliations, intrafolial F2 folds, mineral stretching L2 lineations slightly sloping towards the northeast, NE-SW oriented faults (highlighted on the aeromagnetic maps) plunging, and E-W shear zone. These large-scale NE-SW oriented faults are affected by a later NNW-SSE faults. Furthermore, folding observed within granitoids could be explained by the

deformation intensity which prevailed in the Doropo region.

The D2 deformation phase is followed by two late phases: D3 and D4. D3 seems to be responsible for the shear bands, micro-folds as well as the S3 foliation present in the granitoids (Figure 5). It is related to NE-SW compression, described as late by Vidal et al. (1996) and Block et al. (2016).

The D4 deformation phase is characterized by a set of brittle structures and also the emplacement of the NE-SW and NW-SE dolerite dykes (Figure 6). These dykes may have been emplaced along the large NE-SW and NW-SE oriented faults which were reactivated during this deformation event.

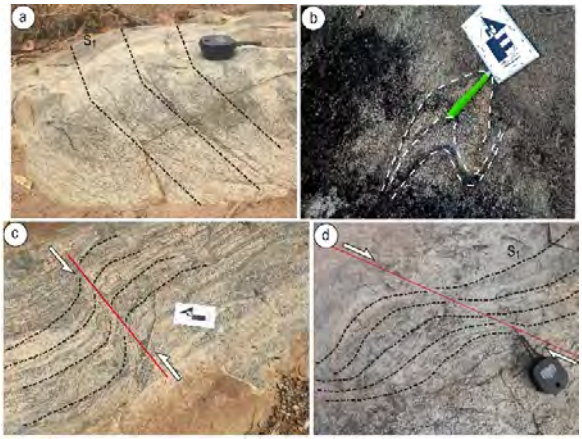

Figure 3. Structures of the D1 deformation observed in the field. **(a)** E-W Foliation (S1) in the gneissic granite of Doropo; **(b)** F1 Fold in the gneissic granite of Bouko; **(c)** NE-SW sinistral shear in the migmatitic granite of Lagbo; **(d)** NW-SE dextral shear in the gneissic granite of Doropo.

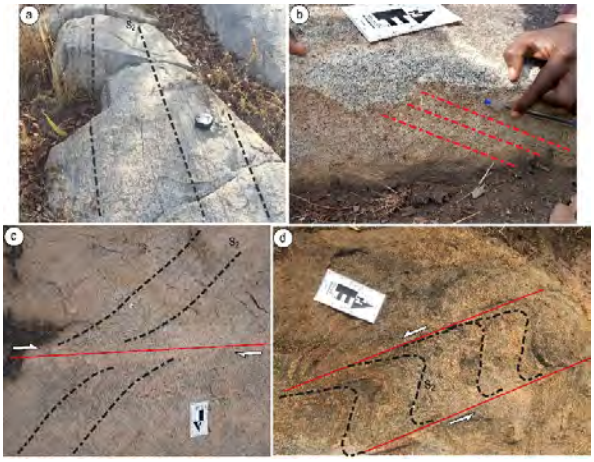

Figure 4. Representative structures of the D2 deformation. **(a)** NE-SW Foliation (S2) within the gneissic granite of Bouko; **(b)** Stretching L2 lineation within Bouko's gneissic granite; **(c)** E-W dextral shear observed at Bouko and **(d)** S-C fabrics in the Lagbo's migmatitic granite.

3.3 Aeromagnetic data and field observations integration

The particularity of these filters is to increase the contrasts between positive and negative anomalies. This allows to obtain three directional derivative maps according to X, Y and Z (Figure 7a-c). Figure 7a-c all show numerous linear and curvilinear structures strongly to weakly magnetic oriented in several directions. These different structures show NE-SW and NW-SE but also ENE-WSW to E-W preferential orientations.

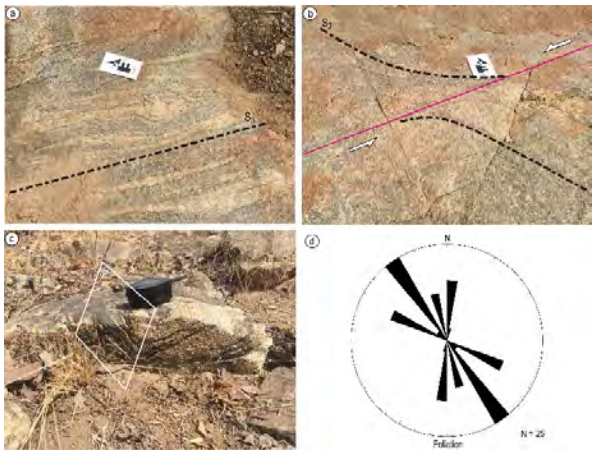

Figure 5. Structures of the D3 deformation. **(a)** NW-SE Foliation (S3) in the migmatitic granite of Lagbo; **(b)** WNW-ESE sinistral shear in Lagbo migmatitic granite; **(c)** F3 Fold with an NW-SE axial plane observed at Gbabedjou and **(d)** directional rose diagram of the S3 foliation. P denotes the axial plane of the fold.

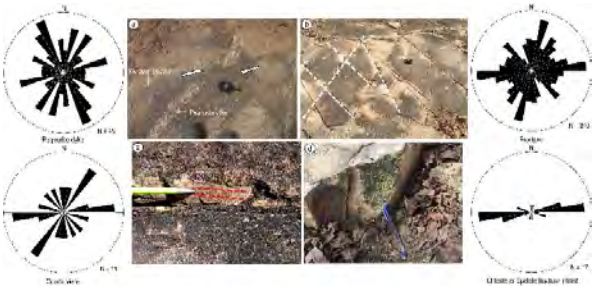

Figure 6. Structures of the D4 deformation. **(a)** Microgranite dyke dextrally shearing a pegmatite dyke; **(b)** Conjugated fractures within the Gbabedjou microgranite; **(c)** Fault mirror with subhorizontal slickenslide lineations reflecting a sinistral shear; **(d)** Fracture plan showing an infill with epidote or chlorite.

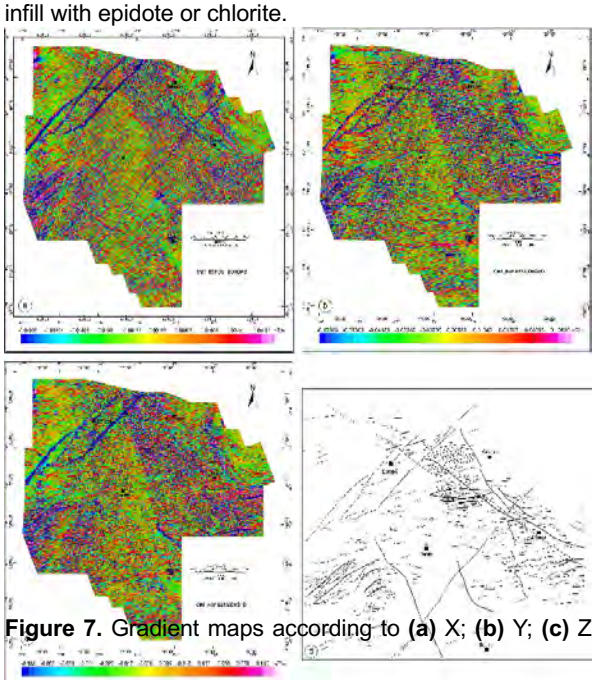

Figure 7. Gradient maps according to **(a)** X; **(b)** Y; **(c)** Z

and **(d)** Structural sketch related to faults, shears, dykes and magnetic lineaments.

The combination of geophysical data and field observations made it possible to establish the first lithostructural map of the Doropo region (Figure 8).

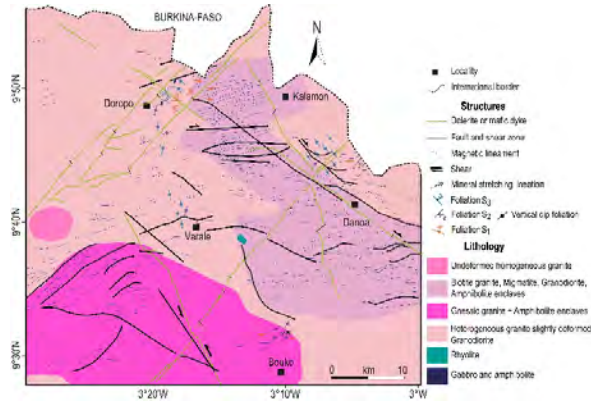

Figure 8. Lithostructural map of the Doropo region (reduction of the 1:50,000 scale map).

4 Conclusion

The geological investigations in the Doropo area have generated new lithological and structural data for the northeastern part of Côte d'Ivoire. A new interpretative lithostructural map of the region at 1:50,000 has been produced by coupling the aeromagnetic data to the field observations.

The Doropo region was deformed by four tectonic phases: (i) N-S compressional phase (D1) characterized by an E-W foliation (S1), conjugate dextral (NW-SE) and sinistral (NE-SW) shear zones, and as well as F1 folds with an E-W axial plane; (ii) most prominent NW-SE transpressional phase (D2) responsible for the regional NE-SW foliation (S2), slightly steep stretching L2 lineation plunging towards the northeast, NE-SW faults, and E-W dextral shear zones; (iii) NE-SW compressional phase (D3) marked by NW-SE foliation (S3), NW-SE axial plane F3 folds, and E-W sinistral shears, and finally (iv) late phase (D4), responsible for brittle structures (faults, fractures, etc.) and also the emplacement of NE-SW and NW-SE dolerite dykes that intersecting all the lithologies of the region.

These different deformation events suggest that the geodynamic model that has prevailed in the Doropo region was due to collisional tectonics. These new geological data are a contribution to previous studies in northeastern Côte d'Ivoire where no detailed geological study has been carried out for several decades. With the previous studies carried out in the neighboring regions of Ghana and Burkina Faso, they contribute to a better understanding of the WAC geodynamics.

Acknowledgements

We would like to thank the Managing Director of Ampella-Centamin Co. (Côte d'Ivoire) for providing us with the airborne data. This project, funded by Ampella-Centamin Co., also received funding from the West African Economic and Monetary Union (UEMOA) through its "Support Program for Training and the Research for Excellence 2019–2020 Edition".

References

Allard, M. and Bois, D. (1999): La géophysique appliquée à l'exploration minérale. Dans la magnétométrie et la radiométrie. *Centre collégial de développement de matériel didactique* (CCDM), Montréal (Québec), pp. 161–311.

Block, S., Jessell, M., Ailleres, L., Baratoux, L., Bruguier, O., Zeh, A., Bosch, D., Caby, R., Mensah, E. (2016): Lower crust exhumation during Paleoproterozoic (Eburnean) orogeny, NW Ghana, West African Craton: interplay of coeval contractional deformation and extensional gravitational collapse. Precambrian Res. 274, 82–109.

Goldfarb, R.J., André-Mayer, A.-S., Jowitt, S.M., Mudd, G.M. (2017): West Africa: the world's premier paleoproterozoic gold province. Econ. Geol. 112 (1), 123–143.

Mériaud, N., Masurel, Q., Thébaud, N., Tourigny, G. (2019): Fluid Pressure Dominated Orogenic Gold Mineralization under Low Differential Stress: Case of the Yaouré Gold Camp, Côte d'Ivoire, West Africa. Mineralium Deposita, pp. 1-18.

Milési, J.P., Feybesse, J.L., Pinna, P., Deschamps, Y., Kampunzu, H., Muhongo, S., Lescuyer, J.L., Le Goff, E., Delor, C., Billa, M., Ralay, F., Heinry, C. (2004): Geological map of Africa 1: 10,000,000, SIGAfrique project. In *20th conference of African geology, BRGM, Orléans,* France.

Murray, S., Torvela, T., Bills, H. (2019): A geostatistical approach to analyzing gold distribution controlled by large-scale fault systems-an example from Côte d'Ivoire. J. Afr. Earth Sci. 151, 351-370.

Tourigny, G., Tranos, M.D., Masurel, Q., Kreuzer, O., Brammer, S., Owusu-Ansah, K., Yao, D., Hayford, T. (2019): Structural controls on granitoid-hosted gold mineralization and paleostress history of the Edikan gold deposits, Kumasi Basin, southwestern Ghana. Miner. Deposita 54, 1033-1052.

Vidal, M., Delor, C., Pouclet, A., Simeon, Y., Alric, G. (1996): Evolution geodynamique de l'Afrique de l'Ouest entre 2.2 Ga et 2 Ga: Le style archéen des ceintures vertes et des ensembles s´edimentaires birimiens du nord-est de la Côte d'Ivoire. Bull. Soc. Geol. Fr. 167, 307-319.

National- to continental-scale governmental geophysical efforts for critical mineral mapping, USA

Anne E. McCafferty[1], Chelsea M. Amaral[1], and Garth Graham[1]
[1]U.S. Geological Survey, Geology, Geochemistry and Geophysics Science Center, Box 25046, Mail Stop 964, Denver Federal Center, Denver, Colorado 80225 USA

Abstract. The U.S. Geological Survey (USGS) has established robust collaborations with domestic state and international geological surveys to provide geophysical and other types of earth science data that act to underpin critical mineral research efforts across the United States, Canada, and Australia. The Earth Mapping Resource Initiative (EMRI) is a national-scale collaborative effort with state geological surveys to improve geophysical and geological data to advance our understanding of the United States' critical mineral endowment. The Critical Mineral Mapping Initiative (CMMI) is a tri-national collaboration with the federal geological surveys of Canada and Australia to conduct research that will aid in identifying new areas with potential for critical mineral deposits across all three countries. This study describes the important interplay between the EMRI and CMMI and how each act in a complementary fashion to advance critical mineral research. We present examples that illustrate how magnetic anomaly data are used to define critical mineral prospectivity for Mississippi Valley-type (MVT) Zn-Pb mineral systems and illustrate how CMMI magnetic derivative maps were considered into USGS' EMRI efforts to acquire modern high-resolution airborne geophysical data over a large area within the US Midcontinent.

1 Introduction

Within the last four years, the USGS has established two significant research collaborations with US State Geological Surveys and with federal government surveys of Canada (Geological Survey of Canada) and Australia (Geoscience Australia). In 2019, the USGS launched the Earth Mapping Resource Initiative (EMRI) in collaboration with the Association of American State Geologists (AASG). EMRI's goals are to improve our understanding of the geologic framework of the country by mapping aspects of the surface and subsurface. Interpretations of subsurface geology and architecture are being greatly improved with the acquisition of new high-resolution geophysical surveys (Day 2019). EMRI activities were accelerated in 2021 with the passage of the Bipartisan Infrastructure Law, which provides a significant increase in funding for geologic mapping and geophysical surveys to better understand the United States' critical mineral endowment. The tri-national Critical Mineral Mapping Initiative, a collaboration among the federal geological surveys of the United States (U.S. Geological Survey), Canada (Geological Survey of Canada) and Australia (Geoscience Australia) was formed in 2019. The mission of the CMMI is to conduct research to better understand critical mineral resources in known deposits, determine the geological controls on known critical mineral deposits, and identify new sources of supply through mineral prospectivity mapping and resource assessment (Kelley 2020).

Both the EMRI and CMMI are multi-faceted in their research approaches to mapping critical mineral geology and prospectivity. The CMMI is concentrating one aspect of its research on mapping mineral prospectivity for basin-hosted Zn-Pb deposits, including Mississippi Valley-type (MVT) deposits, using machine learning techniques (Lawley et al. 2022). In parallel, EMRI has identified 'focus' areas across the United States with potential for critical minerals (Dicken et al. 2022). Focus areas are defined collaboratively with the state geological surveys and are selected based on criteria such as areas undergoing active mining, areas currently or previously having been mined with by-product critical mineral production, or areas identified as prospective via exploration and research. The EMRI focus areas incorporate a wide range of system and deposit types (Hofstra and Kreiner 2020) and include known world class MVT districts. Collaborative discussions with state geological surveys define planning and collection of new data including high-resolution airborne magnetic and radiometric surveys.

Mississippi Valley-type deposits, including those in the United States, account for a significant proportion of the world's base metal production and resources. These enormous hydrothermal systems, formed from evaporative brines and hosted in sedimentary basins are also a high-potential target for a long list of critical minerals including Ba, Be, Co, F, Ga, Ge, In, Nb, Ni, Sn, Ti, and Zn as well as principal commodities such as Ag, Cu, Pb, Th, and Y (Hofstra and Kreiner 2020; Dicken et al. 2022).

This paper highlights geophysical efforts that support the goals of both projects by providing examples of how the CMMI and EMRI have worked in a complementary way to leverage legacy and modern magnetic data to identify MVT deposit potential in the southern Midcontinent of the United States.

2 Methods

Mineral prospectivity modelling requires ingestion of numerous earth science-related datasets, including surface geology, structure, and deposit location data, as well as geophysical data that can image rock properties in the subsurface to depths that can reach tens to hundreds of kilometres. These latter

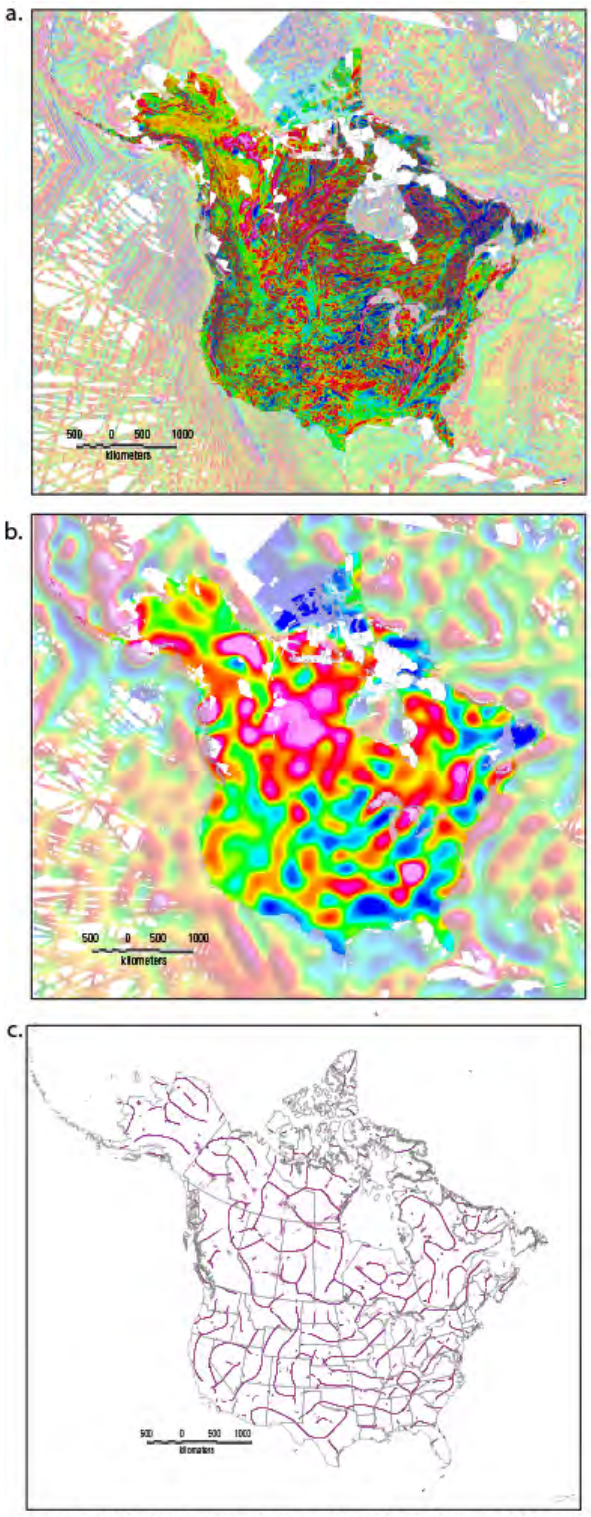

Figure 1. (a) Magnetic anomaly map of the US and Canada; (b) Long-wavelength magnetic anomaly; (c) Deep crust magnetic boundaries (McCafferty et al., 2023).

data can inform researchers on deeper crustal frameworks and former geologic processes that could have focused ore deposit formation. The significance of individual data types (e.g., magnetics) to geology and known deposits can be investigated on a layer-by-layer basis to investigate empirical relationships. The data can be then feature engineered to further enhance the empirical relationships prior to incorporating individual layers into the modelling process.

Efforts to create CMMI mineral prospectivity models (Lawley et al. 2020) involved processing of geologic deposit location, geologic, and geophysical data to evidential layers for input into a machine learning environment. National-scale magnetic anomaly data for the US, Canada, and Australia were filtered to enhance long-wavelength magnetic anomalies (McCafferty et al. 2023) for this purpose.

The rationale for emphasizing the long wavelengths in the magnetic anomaly field arose from recent studies that show geophysical data related to physical property changes within the deep lithosphere are instrumental in mapping locations of major tectonic features and craton boundaries that are spatially associated with the distribution of sedimentary hosted deposits including MVT deposits (Hoggard et al. 2020; Huston et al. 2022).

In general, deep-seated geologic sources give rise to long- wavelength anomalies. To enhance the footprint of the deep-crustal magnetic sources, the horizontal gradient magnitude (HGM) of the long-wavelength magnetic field (reduced-to-pole then transformed to pseudo gravity) was calculated. The edges outlining the magnetic source, often referred to as 'worms', track the maxima of the HGM and are interpreted to map the outer extent of the deep crustal magnetic sources (Fig. 1c).

3 Results

Processing of total magnetic field data to emphasize only long-wavelength (deep) magnetic features, as used in CMMI prospectivity modelling, permits simplification of a complex total magnetic anomaly map at the continental scale (e.g., Fig 1a) to more digestible broad scale trends (Fig.1b and 1c).

The Midcontinent of the US is host to the largest MVT Zn-Pb province in world and includes the world-class districts of the Old Lead Belt, Viburnum Trend, and Tri-State districts among others. Eighteen MVT EMRI focus areas present (Fig. 2b). Of the 18 focus areas, 12 (67%) have overlap with one of four deep magnetic boundaries. Seventeen of the 18 focus areas (94%) occur within a 40 km distance of a deep boundary.

Analyses of other non-MVT EMRI focus areas (Dicken et al. 2022) show a similar spatial relationship with the locations of the deep boundaries. This region of world class MVT deposits also hosts several other igneous mineral systems including the southeast Missouri IOA/IOCG province (i.e., Pea Ridge, MO IOA, Boss, MO IOCG), mafic magmatic systems (i.e., Glen Mountain PGE complex), and magmatic REE systems (i.e., Hicks Dome, IL and Magnet Cove, AR carbonatites). A total of 21 EMRI focus areas are mapped related to these 3 mineral systems, with 16 or 76% of the focus areas either overlapping or falling within 40 km of a magnetic boundary.

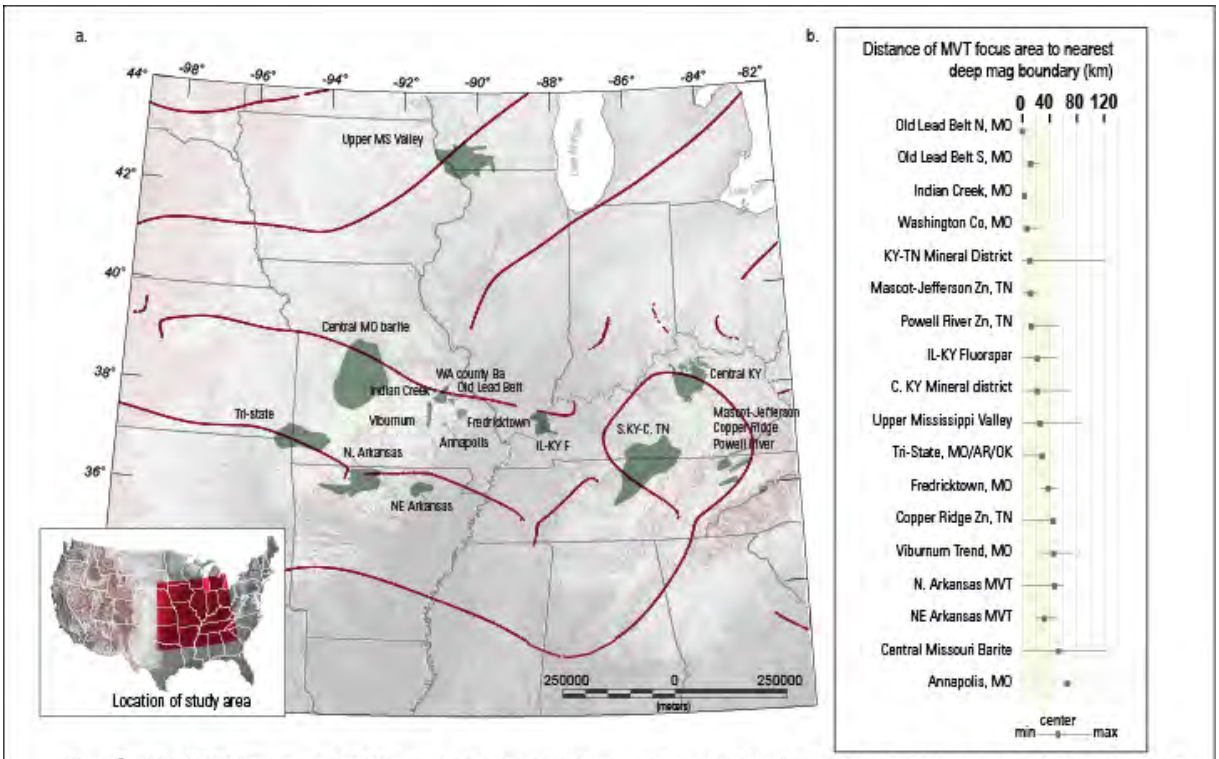

Figure 2. (a) Earth MRI focus areas for MVT mineralization (green) and deep crust magnetic boundaries (dark red); (b) chart showing distance of an Earth MRI MVT focus area to the nearest deep magnetic boundary..

4 Discussion

The deep crust magnetic boundaries are interpreted to map the edges of ancient geologic terranes that acted to preferentially control overlying sedimentary geometries and subsequent younger mineralizing events. Comparison of paleo-reconstruction models from a global terrane database of Eglington et al. (2013) show many of the magnetic boundaries parallel and lie close to the edges of ancient basement terranes.

Depth to the deep magnetic boundaries is estimated to be approximately equivalent to the depth to the Moho from studies done on Curie depth across this region. The Moho ranges in depth from 32 to 44 km in this area. We assume these depths approximate the lower boundary on magnetic susceptibility related to changes in mineralogy across the crust/mantle boundary. This assumption is supported by a study using the North America magnetic compilation (Ravat 2007) that determined the cold Archean and Proterozoic provinces within the Midcontinent of the U.S. were generally characterized by a non-magnetic mantle (Ravat and Purucker 2012).

The close coincidence of the deep crust magmatic boundaries to the locations of known MVT districts hints at a fundamental control by deep crustal boundaries on the siting of these mineralized districts within an old, broadly stable craton. We hypothesize that these deep-–seated structures influenced the sedimentary facies patterns in the overlying sedimentary basins, which may have influenced the flow paths of the brines responsible for MVT mineralization at least in the US Midcontinent. Preliminary examination of focus areas for some other deposit types (not shown) suggest that deep crustal boundaries may also control the siting of other deposit types. Further research is required to affirm causation. Nonetheless, these results suggest that, in some geological environments, deep geophysics may help to concentrate the prospective search area for ore deposits. Identifying ore-deposit locations through EMRI studies is thus consequential in advancing our understanding of our earth and improving responsible management of its resources.

5 Conclusion

National-scale magnetic anomaly data generated as part of the CMMI project, show spatial association with MVT mineral systems across the US Midcontinent. The vast majority (94%) of EMRI MVT focus areas occur within 40 kilometres of a deep magnetic boundary. The boundaries are estimated to represent geologic sources near the Moho and map the edges of ancient geologic terranes. Acquisition of modern high-resolution magnetic and radiometric surveys are being designed and flown for the EMRI program over this area of the Midcontinent. The new data will shed light on the shallow expression of magnetic anomalies that allow for refinement of the first-order

controls on mineralization provided by the deep magnetic boundary analyses.

Acknowledgements

The authors wish to thank Ani Tikku (USGS reviewer) and an SGA reviewer for constructive comments.

Disclaimer

Any use of trade, firm, or product names is for descriptive purposes only and does not imply endorsement by the U.S. Government

References

Day WC (2019) The Earth Mapping Resources Initiative (Earth MRI)—Mapping the Nation's critical mineral resources (ver. 1.2, September 2019). U.S. Geological Survey Fact Sheet 2019–2007. https://doi.org/10.3133/fs20193007

Dicken CL, Woodruff LG, Hammarstrom JM, Crocker KE (2022) GIS, supplemental data table, and references for focus areas of potential domestic resources of critical minerals and related commodities in the United States and Puerto Rico. US Geological Survey data release. https://doi.org/10.5066/P9DIZ9N8. Accessed 6 March 2023

Eglington B, Pehrsson S, Ansdell K, Lescuyer J, Quirt D, Milesi J, Brown P (2013) A domain-based digital summary of the evolution of the Palaeoproterozoic of North America and Greenland and associated unconformity-related uranium mineralization. Precambrian Research. https://doi.org/10.1016/j.precamres.2013.01.021

Hofstra AH, Kreiner DC (2020) Systems-Deposits-Commodities-Critical Minerals Table for the Earth Mapping Resources Initiative (ver. 1.1, May 2021). US Geological Survey Open-File Report 2020–1042. https://doi.org/10.3133/ofr20201042.

Hoggard MJ, Czarnota K, Richards FD, Huston DL, Jaques AL, Ghelichkhan S (2020) Global distribution of sediment–hosted metals controlled by craton edge stability. Nature Geoscience 13:504–510. https://doi.org/10.1038/s41561-020-0593-2.

Huston DL, Champion DC, Czarnota K, Duan J, Hutchens M, Paradis S, Hoggard M, Ware B, Gibson GM, Doublier M, Kelley K, McCafferty A, Hayward N, Richards F, Tessalina S, Carr G (2022) Zinc on the edge—isotopic and geophysical evidence that cratonic edges control world-class shale-hosted zinc-lead deposits. Mineralium Deposita. http://dx.doi.org/10.1007/s00126-022-01153-9.

Kelley KD (2020) International geoscience collaboration to support critical mineral discovery. US Geological Survey Fact Sheet 2020– 3035. https://doi.org/10.3133/fs20203035.

Lawley CJM, McCafferty AE, Graham GE, Huston DL, Kelley KD, Czarnota K, Paradis S, Peter JM, Haward N, Barlow M, Emsbo P, Coyan J, San Juan CA, Gadd MG (2022) Data-driven prospectivity modelling of sediment-hosted Zn-Pb mineral systems and their critical raw material. Ore Geology Reviews 141:104635. https://doi.org/10.1016/j.oregeorev.2021.104635.

McCafferty AE, San Juan CA, Lawley CJ, Graham GE, Gadd MG, Huston DL, Kelley KD, Paradis S, Peter JM, Czarnota K (2023) National-Scale Geophysical, Geologic, and Mineral Resource Data and Grids for the United States, Canada, and Australia- Data in Support of the Critical Minerals Mapping Initiative. US Geological Survey data release. https://doi.org/10.5066/P970GDD5

Ravat D (2007) Crustal magnetic fields. In: Gubbins D, Herrero-Severa E (eds) Encyclopedia of Geomagnetism and Paleomagnetism. Springer, New York, pp 140-144

Ravat D, Purucker M (2012) Unraveling the magnetic mystery of the Earth's lithosphere: The background and the role of the CHAMP Mission. In: Reigber C, Lühr H, Schwintzer P (eds) First CHAMP Mission Results for Gravity, Magnetic and Atmospheric Studies. Springer, New York, pp 251-260

A GIS-based mineral prospectivity analysis of the Neoproterozoic Arabian Shield

Christophe Bonnetti[1], Arnaud Fontaine[1], Célestine Berthier[1,3], Julien Feneyrol[1], Joffrey Corbet[1], Virginie Masson[1], Rémi Bosc[1,2], Adil M. Hashim[2]
[1]Arethuse Geology EURL, 29 Allée de Saint Jean, 13710 Fuveau, France
[2]Arethuse Arabia Mining, King Abdul Aziz Street, 13315 Riyadh, Kingdom of Saudi Arabia
[3]GeoRessources, Université de Lorraine, CNRS, 54000 Nancy, France

Abstract. The Neoproterozoic Arabian Shield formed following three major tectono-magmatic events during the Cryogenian–Ediacaran Nabitah orogenic cycle, including the pre-accretion, syn-orogenic and late- to post-orogenic stages, representing fertile environment for various mineral systems related to precious, base and rare metals. At the shield scale, the mineral prospectivity analysis that was performed, based on the selective review and reclassification of multiple geological and geophysical datasets, identified a series of mineral belts correlated with suture and shear zones concentrating the majority of mineral deposits and occurrences. (i) Pre-accretion arc-related porphyry, epithermal, VMS mineral systems and magmatic deposits related to ultramafic rocks are predominantly distributed along the Nabitah, Al Amar, Bi'r Umq and Yanbu suture zones. (ii) Orogenic gold veins mainly developed in the N-trending Nabitah shear zone that is coaxial with the Nabitah and Al Amar sutures. Gold was remobilised from source rocks during this syn-collisional tectonic event associated with a peak M1 of low-grade metamorphism. Orogenic gold mineralisation also occurred sporadically along the NW-trending Najd strike-slip fault system developed during late orogenic extension and associated with a peak M2 of high-grade metamorphism, locally. (iii) Finally, magmatic-hydrothermal rare metal deposits formed in association with late- to post-orogenic alkaline, peralkaline and peraluminous granites.

1 Introduction and geological setting

The Arabian Shield (AS) is part of a larger geological Neoproterozoic assemblage, the Arabian-Nubian Shield (ANS) spreading over parts of Egypt, Eritrea, Ethiopia, Saudi Arabia, Somalia, Sudan and Yemen (Nehlig et al. 1999), which represents an area > 1,100,000 km^2 of fertile environment for various mineral systems related to precious, base and rare metals (Technip Group et al. 2015). However, the availability of geological and geophysical data is highly variable depending on the country, and historical surveys as well as exploration works are heterogeneously distributed and do not always cover areas of interest from a mineral prospectivity point of view. Although many of the geological data collected over the past decades in the AS have been digitalised into a Geographical Information System (GIS), an overall review of the major geological events that occurred through the geodynamic evolution of the shield, and their roles in providing the favourable conditions for ore genesis is currently lacking. Therefore, we reviewed and combined a broad variety of datasets collected over the past ten years into an in-house GIS database to assess the prospectivity potential of certain areas at the shield scale based on modern tectonic concepts (e.g. suture-structural-mineral belts) and the mineral systems approach, which can then be applied as exploration targeting criteria for different mineralisation styles at the belt or district scale (e.g. McCuaig et al. 2010).

The ANS evolved between ~870 and 550 Ma as one of the largest tracts of juvenile Neoproterozoic crust in the world (Johnson 2014; Figure 1). Within this domain, the AS is differentiated by a series of variably oriented sutures punctuated by ophiolite complexes (Stern et al. 2004), shear zones and fold belts (Meyer et al. 2014; Elisha et al. 2017; Figure 2). Suture zones and coaxially developed shear belts highlight the boundaries of magmatic arc remnants and micro-continental blocks (Stern and Johnson 2010; Johnson 2014) that were accreted during the Cryogenian-Ediacaran Nabitah orogeny (Nehlig et al. 2002) as a result of the Greater Gondwana assembly at 544 Ma (Stern and Johnson 2010).

The geodynamic evolution of the AS can be summarized by three main tectono-magmatic phases reflecting a 300-million-year process of continental crustal growth represented by amalgamated juvenile magmatic arcs and associated volcano-sedimentary basins, syn-orogenic intrusive bodies and molassic basins, and late to post-orogenic granitoid intrusions (Stern and Johnson 2010; Figures 1 and 2):

(i) a Late Tonian–Early Cryogenian (~880–660 Ma) pre-orogenic rifting episode that triggered Rodinia break-up, which was followed by the formation of multiple magmatic island arcs together with fore- and back-arc volcano-sedimentary basins within an intra-oceanic subduction setting (Johnson et al. 2011; Johnson 2014). This episode corresponds with a major stage of juvenile crust formation in the northern East African Orogen, between West and East Gondwana (Stern and Johnson 2010). As the convergence progressed, these arcs were progressively amalgamated to form the AS, with a peak accretion age at ca. 780 Ma (Stern et al. 2004);

(ii) a Late Cryogenian–Early Ediacaran (~690–590 Ma) syn-orogenic stage marked by the onset of the Nabitah collision or orogeny (Nehlig et al. 2002; Johnson et al. 2011, 2013), which is dominantly characterised by an early peak M1 of low grade (greenschist) metamorphism at ca. 710 Ma (Elisha et al. 2017), the development of the N-trending, dextral transpressional Nabitah shear and fold belt

(~680–640 Ma; Johnson et al. 2011), deformed syn-orogenic granitoids and post-accretion molassic basins (e.g. Murdama Group sediments; ~670–570 Ma; Johnson et al. 2013);

(iii) a Late Cryogenian–Ediacaran (~650–530 Ma) late to post-orogenic phase of extensional collapse (Blasband et al. 2000) marked by the offset of the Nabitah structures by the NW-trending, sinistral Najd strike-slip fault system (Stern and Johnson 2010; Meyer et al. 2014), with local development of a late peak M2 of high grade (> amphibolite) metamorphism at ca. 620 Ma associated with a series of gneissic domes (Johnson et al. 2013; Elisha et al. 2017), late sediments infill in molassic basins (e.g. Jibalah Group > 640 Ma; Johnson et al. 2013) and numerous intrusions of late- to post-orogenic granitoids and dykes (~650–530 Ma) with post-collisional anorogenic signatures (Eyal and Eyal 1987; Lehmann et al. 2020).

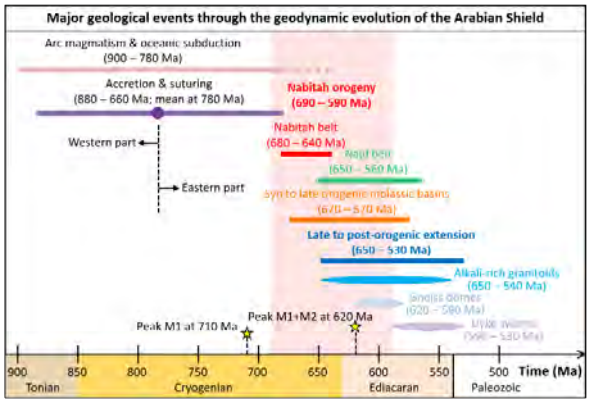

Figure 1. Chronology of major geological events through the geodynamic evolution of the Arabian Shield (modified after Eyal and Eyal 1987; Blasband et al. 2000; Nehlig et al. 2002; Stern et al. 2004; Stern and Johnson 2010; Johnson et al. 2011, 2013; Johnson 2014; Meyer et al. 2014; Elisha et al. 2017; Lehmann et al. 2020).

2 Methodology

The mineral prospectivity analysis (i.e. Carranza 2021) was performed on QGIS software by reviewing multiple datasets of geological and geophysical information including airborne magnetic and satellite imagery data, stratigraphic units, lithologies, structures, ore deposits and mineral occurrences inventory compiled from the literature and publicly available data provided by the Saudi Geological Survey. Lithologies were then classified based on their petrologic features, stratigraphic ages and related tectono-magmatic event through the Nabitah orogenic cycle. Similarly, structures were reclassified based on their nature, distribution and kinematic indicators with a particular attention in locating terrane boundaries and suture zones along which major structural belts developed. Finally, a selective review of the mineral occurrence database (Nehlig et al. 1999; Technip Group et al. 2015) was conducted to determine key criteria and favourable contexts for ore genesis to assess the prospectivity potential of the main mineral systems developed in major structural belts of the AS that are presented in the litho-tectonic and metallogenic map of Figure 2.

Mineral occurrences previously classified by commodities were reclassified according to their mineralisation styles and deposit types following the mineral system approach (McCuaig et al. 2010) and using criteria such as metal association, morphology, host rock, structural control, alteration pattern, and the local geological context. This mineral system approach was integrated into the geodynamic context as a precursor to statistical and spatial analyses that will be performed in the future.

3 Mineral prospectivity analysis

3.1 Pre-accretion, magmatic arc-related mineral systems

The pre-accretion stage of the AS was dominated by arc magmatism within an oceanic subduction domain and provided favourable geological setting for the formation of VMS, epithermal and porphyry mineral systems, as well as magmatic mineralisation related to ultramafic igneous rocks. To date, no porphyry Cu-Mo deposit has been discovered and only few occurrences hosted in granodiorite mainly located at the edge of the Ad Dawadimi terrane in eastern AS were reported. Orthomagmatic Cr-Ni-Cu deposits and occurrences are predominantly hosted in mantle-derived or oceanic crust remnants ultramafic rocks (e.g. serpentinite, gabbro, peridotite) and distributed along the Yanbu, Nabitah and Al Amar suture zones. Syngenetic VMS Cu-Zn-(±Au) deposits and occurrences are mainly hosted in arc-related volcano-sedimentary basins showing bimodal volcanic records. Hence, their spatial distribution follows the orientation trend of their host lithologies, which are highlighted by the suture zones (Nabitah, Bi'r Umq, Al Amar, Yanbu) as a result of magmatic arcs collage during the accretion phase. For instance, the giant Jabal Sayid deposit (estimated resources of 56.4 Mt at 2.2% Cu, 0.1% Zn, 0.2 g/t Au, 5.0 g/t Ag; Technip Group et al. 2015) is hosted in bimodal volcanic rocks within the accretionary complex of a forearc volcano-sedimentary basin, south of the contact with the Bi'r Umq suture zone. Finally, prominent epithermal deposits and associated occurrences are mainly hosted in the contact zone between arc-related plutonic and volcanic rocks along the Al Amar (e.g. Al Amar deposit with estimated resources of 6.8 Mt at 14.0 g/t Ag, 5.2 g/t Au, 4.5% Zn; Technip Group et al. 2015) and Bi'r Umq (e.g. Mhad Ahd Dhahab deposit with estimated resources of 3.4 Mt at 44.2 g/t Ag and 9.2 g/t Au; Technip Group et al. 2015) suture zones.

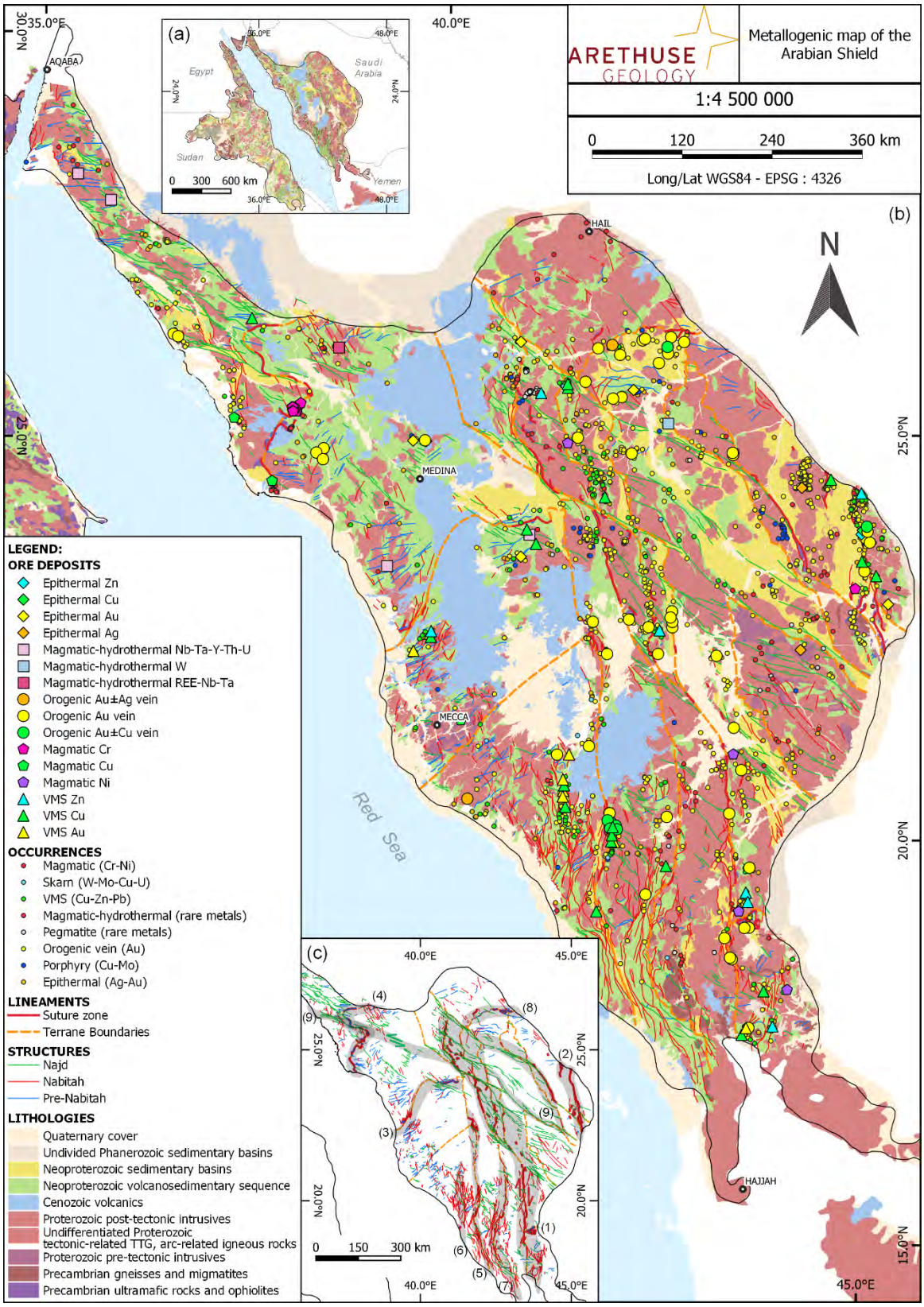

Figure 2. a Litho-tectonic map of the Arabian-Nubian Shield. **b** Litho-tectonic and metallogenic map of the Arabian Shield. **c** Structural map of the Arabian Shield showing the distribution of the main mineral belts. The grey zones correspond with the mineral belts as follow: (1) the Nabitah suture/shear zone, (2) the Al Amar suture zone, (3) The Bi'r Umq suture zone, (4) the Yanbu suture zone, (5) The Umm Farwah shear zone, (6) the Baydah shear zone, (7) the Tadj/Ibran shear zone, (8) the Hibashi suture/fault zone, (9) the Najd shear zone (modified after Nehlig et al. 1999, 2002; Blasband et al. 2000; Stern et al. 2004; Stern and Johnson 2010; Johnson et al. 2011, 2013; Johnson 2014; Meyer et al. 2014; Technip Group et al. 2015; Lehmann et al. 2020).

3.2 Syn- to late orogenic gold systems

Orogenic gold system is widespread throughout the AS and was related to two major tectono-metamorphic events: (i) the syn-collisional development of the N-trending Nabitah shear and fold belt that is coaxial with the Nabitah and Al Amar sutures across the shield and associated with parallel shear zones in its southern part. Gold deposits and occurrences (e.g. Ar Rjum deposit with estimated resources of 84.0 Mt at 1.3 g/t Au in the Zalim district; Technip Group et al. 2015) are structurally-controlled by shear zones, often overprinting pre-accretion mineral systems, and occur as auriferous quartz-carbonate-(±sulfide) veins, which are hosted in various lithologies that experienced the peak M1 of metamorphism at the origin of fluid-mediated gold remobilization from source rocks; and (ii) the development of the NW-trending Najd strike-slip fault system during the late orogenic extension associated with the peak M2 of metamorphism,. In this context, gold mineralisation is hosted in Nabitah/Nadj related shears within the contact zone of late orogenic intrusions (e.g. Ad Duwayhi deposit with estimated resources of 31.0 Mt at 2.4 g/t Au; Technip Group et al. 2015).

3.3 Late to post-orogenic magmatic-hydrothermal rare metal systems

The AS also experienced a relatively intense episode of magmatism during the late- to post-orogenic stage of the Nabitah orogenic cycle, with emplacement favoured along major crustal discontinuities represented by the Nabitah and Najd structural belts. The distribution and typology of associated rare metal magmatic-hydrothermal deposits and occurrences were mainly controlled by the chemical affinities of magma sources with Nb-Ta-REE-Th-U-Sn mineralisation related to alkaline and peralkaline granites and W-Sn-Nb-Ta-Li-Be associated with peraluminous granite and pegmatite.

4 Conclusions and perspectives

The synthesis of the main geological and metallogenic events through the geodynamic evolution of the Arabian Shield allowed the characterisation of various mineral systems that formed during the pre-accretion, syn-orogenic and late- to post-orogenic phases of the Nabitah orogenic cycle. The mineral prospectivity analysis identified a series of mineral belts that concentrate the large majority of ore deposits and occurrences with suture zones (Nabitah, Al Amar, Bi'r Umq and Yanbu) and structural belts (Nabitah and Najd shear zones) as a major pathfinder at the shield scale. This study was therefore a necessary step to define prospective areas and narrow down the prospect generation for spatial and statistical analyses at the belt or district scale to provide guidance for exploration and generate future metallogenic research studies in the AS.

Acknowledgements

The authors thank Arethuse Geology for funding this study and providing its in-house GIS database.

References

Blasband B, White S, Brooijmans P, De Boorder H, Visser W (2000) Late Proterozoic extensional collapse in the Arabian-Nubian Shield. J Geol Soc London 157:615-628

Carranza EJM (2021) Mineral Prospectivity Analysis. In: Daya Sagar B, Cheng Q, McKinley J, Agterberg F (eds) Encyclopedia of Mathematical Geosciences. Encyclopedia of Earth Sciences Series. Springer, Cham

Elisha B, Katzir Y, Kylander-Clark A (2017) Ediacaran (~620 Ma) high-grade regional metamorphism in the northern Arabian Nubian Shield: U-Th-Pb monazite ages of the Elat schist. Precambrian Res 295:172-186

Eyal Y and Eyal M (1987) Mafic Dykes in the Arabian-Nubian Shield. J Earth Sci 36:195-211

Johnson PR (2014) An Expanding Arabian-Nubian Shield geochronologic and isotopic dataset: Defining limits and confirming the tectonic setting of a Neoproterozoic accretionary orogen. Open Geol J 8:3-33

Johnson PR, Anderson A, Collins AS, Fowler AR, Fritz H, Ghebreab W, Kusky T, Stern RJ (2011) Late Cryogenian-Ediacaran history of the Arabian-Nubian Shield: A review of depositional, plutonic, structural, and tectonic events in the closing stages of the northern East African Orogen. J African Earth Sci 61:167-232

Johnson PR, Halverson GP, Kusky TM, Stern RJ, Pease V (2013) Volcanosedimentary basins in the Arabian-Nubian Shield: Markers of repeated exhumation and denudation in the Neoproterozoic accretionary orogen. Geosciences 3:389-445

Lehmann B, Zoheir B, Neymark L, Zeh A, Emam A, Radwan A, Zhang R, Moscani R (2020) Monazite and cassiterite U-Pb dating of the Abu Dabbab rare-metal granite, Egypt: Late Cryogenian metalliferous granite magmatism in the Arabian-Nubian Shield. Gondwana Res 84:71-80

McCuaig TC, Beresford S, Hronsky J (2010) Translating the mineral systems approach into an effective exploration targeting system. Ore Geol Rev 38:128-138

Meyer SE, Passchier C, Abu-Alam T, Stuwe K (2014) A strike-slip core complex from the Najd fault system, Arabian Shield. Terra Nova 26:387-394

Nehlig P, Salpeteur I, Asfirane F, Bouchot V, Eberlé JM, Genna A, Kluyver HM, Lasserre JL, Leister JM, Nicol N, Récoché G, Shanti M, Thiéblemont D (1999) The mineral potential of the Arabian Shield: A reassessment. In proceedings of the IUGS/UNESCO Meeting on the "Base and Precious Metal Deposits in the Arabian Shield", Jeddah

Nehlig P, Genna A, Asfirane F (2002) A review of the Pan-African evolution of the Arabian Shield. GeoArabia 7:103-124

Stern RJ and Johnson P (2010) Continental lithosphere of the Arabian Plate: A geologic, petrologic, and geophysical synthesis. Earth Sci Rev 101:29-67

Stern RJ, Johnson PR, Kröner A, Yibas B (2004) Neoproterozoic ophiolites of the Arabian-Nubian Shield. Develop Precambrian Geol 13:95-128

Technip Group, Arethuse Geology, brgm (2015) Comprehensive mining strategy study project – Metals inventory for the kingdom of Saudi Arabia. Technical Report 064856C001-430, unpublished

Large-scale structural controls on hot spring mineral deposits of geothermal systems (Mt. Amiata, Italy) highlighted by machine learning algorithms?

Paolo S. Garofalo[1], Lara Capitanio[1], Elisa Mariarosaria Farella[2], Simone Rigon[2], Fabio Remondino[2], Ivan Callegari[3], Daniele Rappuoli[4]

[1] Dept. of Biological, Geological and Environ. Sciences, University of Bologna, I
[2] 3D Optical Metrology Unit, Fondazione Bruno Kessler – Trento, I
[3] German University of Technology – Sultanate of Oman
[4] Parco Nazionale Museo delle Miniere del Monte Amiata, Piancastagnaio, I

Abstract. The cinnabar (±stibnite) deposits of the Mt. Amiata geothermal system and the associated hot springs and gas vents, occur along a N-S directed, narrow longitude region.

In this study, we combine a geological and geophysical dataset gathered from the early stages of geothermal exploration of the district with a multivariate statistical analysis carried out by Machine Learning (ML) algorithms to highlight possible correlations between the distribution of the geothermal expressions of Mt. Amiata and its geological/structural features. We used 5 distinct ML supervised models (Ordinary Least Squares Linear Regressor, Multilayer Perceptron Regressor, Support Vector Regressor, CatBoost, and Random Forest) to determine which set of geological or geochemical features of the dataset reproduces the distribution of the geothermal expressions of the area with sufficient accuracy.

The regressors CatBoost and Random Forest, which use decision trees for probability calculations, are the most efficient in predicting the narrow-longitude distribution of the geothermal expressions of Mt. Amiata. Also, the only combination of predictors generating probability maps that accurately reproduce the distribution of the geothermal expressions is the one considering permeability, Hg solubility, T, and distances from faults and folds. This shows that only a combination of geological/geochemical factors can explain the peculiar regional distribution.

1 Introduction

With an historical production of c. 117 kt of Hg at a grade of 0.2-8 wt% (Segreto, 1991), the cinnabar(±stibnite) deposits of Mt. Amiata (south Tuscany, Italy) form one of the largest mercury districts ever documented. Here, 14 deposits of distinct sizes and economic importance were exploited between the years 1846 and 1982. Most of these deposits occurred along with uneconomic prospects within an area that is >30 km long in the N-S direction – from the Pietrineri deposit to the N to the Catabbio deposit to the S – and c. 15 km wide in the E-W direction (Fig. 1).

The district is located within a geothermal system that was explored with a set of geophysical methods since 1953 (Cataldi, 1967). Presently, close to the cities of Piancastagnaio and Bagnore (Fig. 1) this system hosts 5 power plants having 88 MW installed capacity, which exploit two distinct wet-steam reservoirs (Barelli et al., 2010). The first is 2500-4000 m deep at c. 300-350 °C, and the second is 500-1000 m deep at 150-230 °C. In the district, CO_2-rich gas vents and hot springs were documented in detail (e.g., Frondini et al., 2009; Magi et al., 2019).

The area belongs to the Apennine thrust-and-fold belt, which consists of a stack of tectonic units detached from the Adria plate that migrated progressively eastwards from the Late Oligocene to the Early Miocene (Marroni et al., 2015). Since the Late Miocene, the migration of this deformation front was followed by a stage of extensional tectonics and post collisional magmatism.

A young volcano-plutonic system controls the geothermal system of Mt. Amiata, although only indirect evidence exists on the nature, shape, and depth of emplacement of the pluton (Gianelli et al., 1988). Several data suggest the presence of this pluton at 4-7 km depth, with an apophysis located below Monte Labbro (Fig. 1).

The Mt. Amiata volcano is a 305-231 ka old, small size volcano fed by a SSW-NNE eruptive fissure. From base to top, it is made of trachydacitic flows, olivine latitic to trachydacitic domes and flows, and olivine latites (Conticelli et al., 2015). Geochemical and isotopic compositions indicate a genesis from mixing between a high silica, high-K calc-alkaline magma and a mafic ultrapotassic magma.

The volcano-plutonic system intruded the folded and faulted stratigraphic sequence made of allochthonous flysch units deposited onto oceanic crust (Ligurian Domain), Mesozoic carbonatitic and Cenozoic terrigenous formations (Tuscan Domain), and a poorly outcropping Carboniferous sequence made of graphitic quartz-phyllites, metagreywackes, and carbonate-bearing quartz-phyllites (Gianelli et al., 1988).

The Mt. Amiata deposits consisted mostly of disseminations, massive stratabound, stockworks, and breccias cemented by cinnabar, metacinnabar, and marcasite (Arisi Rota et al., 1971). Stibnite, native Hg, pyrite, chalcopyrite, realgar, and orpiment were reported as minor phases. The most common gangue was calcite with minor celestite, fluorite, gypsum, zeolites, dawsonite, and amorphous silica (opal, chalcedony).

The deposits share many similarities with those of the near-surface hot spring deposits formed close to volcanic centers (Pirajno, 2020).

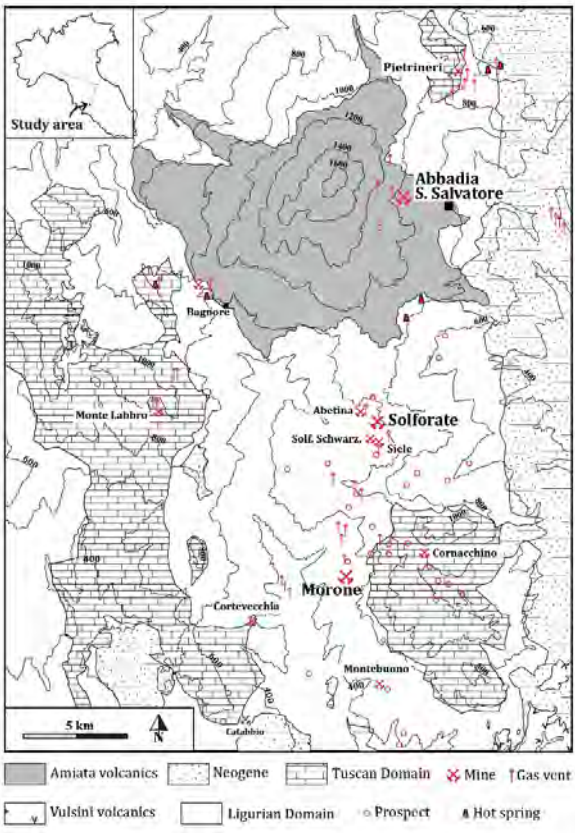

Figure 1. Geological map of the Mt. Amiata ore district and location of cinnabar(±stibnite) deposits, prospects, gas vents, and hot springs (modified from: Calamai et al., 1970). The three largest deposits are shown with larger symbols, and one of the 14 deposits of the district (Cerreto Piano) is located outside this map. Notice that all occurrences formed within a narrow longitude region.

A distinct characteristic of these deposits is their location within a wide latitude but narrow longitude region (Fig. 1). Such distribution was known since early geological documentation of the area (e.g., De Castro, 1914); however, the controlling factors of such peculiar regional distribution were never explored to a sufficient extent. For instance, recent work (Brogi et al., 2011) showed that the location of the Morone deposit (Fig. 1) was controlled by the formation of sinistral shear zones during the Pleistocene, in particular by focussing of the ore fluid within extensional jogs and pull apart structures. While very important at the deposit scale, these structures alone do not explain why the deposits formed within a narrow longitude region at the district scale, leaving unanswered a fundamental question on the genesis of these deposits.

The aim of our work is to apply Machine Learning (ML) algorithms to couple geological and geophysical data in order to explore possible correlations between the peculiar narrow-longitude distribution of the geothermal expressions of the area and its geological/structural features. Moreover, we apply a multivariate statistical analysis to predict the distribution of geothermal expressions in areas without surveys. We deliberately choose a limited dataset of surveys collected during the early stages of geothermal exploration because we want to simulate as much as possible a reconnaissance stage of mineral exploration, i.e., one in which a typical multidisciplinary mineral exploration dataset (from remote sensing, field mapping, geophysical and geochemical surveys, limited drilling) would be coupled with the statistical tools provided by ML algorithms.

2 Methodology

2.1 The dataset

The geological data used for our predictions consists of the documented lithologies of the study area (Fig. 1) and of its relevant structural data. In detail, we considered all antiforms, synforms, and faults (inverse, normal) mapped in the geothermal database (Cataldi, 1967) and in recent studies (Bonciani et al., 2005). The lithologies were grouped into 4 complexes according to their established permeability, and care was taken to determine the positions of the top of the shallow reservoir (500-1000 m deep) within the study area. These data were used to construct 2D and 3D geological models of the area.

The ore deposit data consists of the locations of all the geothermal expressions of the area, which include cinnabar (±stibnite) ore deposits, (uneconomic) prospects, gas vents, springs (cold, hot), geothermal wells, and power plants.

The physical-chemical dataset consists in the temperature (T) gradient, heat flow data, Bouguer anomaly data, and Hg solubility in the geothermal fluid, which was considered equal to the experimentally determined solubility of $Hg°_{aq}$ in water in the 0-350 °C interval (Clever et al., 1985).

This information was used to prepare a set of 24,398 points that mark the entire study area. Each point was univocally identified (via longitude, latitude, and depth) and characterized by unique predictor values of permeability, T, T gradient, Hg solubility, heat flow, Bouguer anomaly, distance from the nearest fold, distance from the nearest fault, and vertical distance from the top of the reservoir.

2.2 Machine Learning models

We calculated probability maps of the study area using five distinct ML supervised models (i.e., regressors). They are (1) Ordinary Least Squares Linear Regressor, (2) Multilayer Perceptron Regressor, (3) Support Vector Regressor, (4) CatBoost, and (5) Random Forest. These regressors differ from each other in that (1)-(2)-(3) calculate probability values by linear regression while (4)-(5) calculate probabilities by decision trees (Sun et al., 2019). Each regressor calculated the probability that a specific combination of geological or geochemical features of the dataset can reproduce the distribution of the geothermal expressions of the area. We

divided these features into two categories, namely geometric and ore predictors (Table 1), which distinguish features that identify potential structural or lithological controls (distance from folds, faults, and reservoir) from physical-chemical controls (permeability, T, Hg solubility, etc.). Kriging-based spatial interpolation was used later to calculate 2-D probability maps, which were generated at distinct depths up to 1 km.

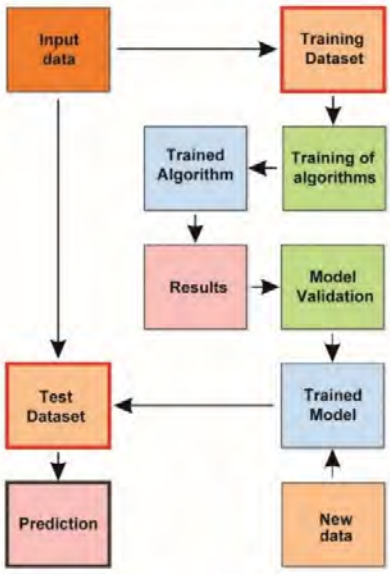

Figure 2. Block diagram showing the typical workflow of a ML algorithm.

Following typical ML methodologies, the available data were split into two subsets, namely the Training dataset and the Test dataset (Fig. 2). The first one was used to train the regressors, generate the ML model, and validate it. The Test dataset was used to carry out the predictions (Pedregosa et al., 2011). The Training dataset consisted of points where the occurrence of cinnabar deposits and/or prospects are historically known. This dataset was augmented following three established techniques (Farella et al., 2021) to improve the training of the distinct regressors when dealing with unbalanced classes of data. This generated three distinct datasets with which algorithms were trained and probability predictions were subsequently carried out.

Correlations and predictions were calculated for eight combinations of predictors (Table 1) using the Scikit-learn Python libraries (Pedregosa et al., 2011), which integrate the five regressors listed above and other state-of-the-art ML algorithms. Our combinations do not consider all possible permutations of ore and geometric predictors, but rather favor the role of permeability, Hg solubility, and faults in the formation of the geothermal expressions. Each combination of predictors was analyzed with the 5 regressors, but out of the 24 combinations of augmented datasets and regressors only seventeen provided results whose statistical significance was evaluated. We evaluated the accuracy of our prediction through three parameters: RMSE, MAE and R^2. Below, we present and discuss two representative results of this work.

3 Results

The Ordinary Least Squares Linear Regressor, the Multilayer Perceptron Regressor, and the Support Vector Regressor generate probability maps that do not reproduce the spatial distribution of the geothermal expressions of Mt. Amiata with any of the considered combination of predictors. In contrast, CatBoost and Random Forest generate maps that reproduce with good accuracy the distribution using the augmented Training dataset and a specific combination of predictors (Test 8).

Figure 3 shows two examples of interpolated probability maps generated with the described method using Random Forest. These maps highlight the different correlations that a given set of predictors generate with a given ML algorithm. Thus, the exclusive use of ore predictors (Test 1) by the Random Forest regressor generates high probability areas (Fig. 3a) that do not fit the established distribution of the geothermal expressions of Mt. Amiata (e.g., black triangles denoting deposits/prospects). Similar results are obtained by almost all other regressors using the combination of predictors presented in Table 1.

Table 1. Combination of predictors used in this study.

	Ore Predictors						Geometric Predictors		
Test no.	Permeability	Hg Solubility	Heat flux	T	T gradient	Bouguer Anomaly	Distance from fold	Distance from fault	Distance from top of C4
1	X	X	X	X	X	X			
2							X	X	X
3	X	X	X	X	X	X	X	X	X
4	X	X					X	X	X
5	X	X						X	
6	X	X	X					X	
7	X	X		X				X	
8	X	X		X			X	X	

Note: C4 denotes “Complex 4”, i.e., the permeable reservoir

The only combination of predictors that allowed CatBoost and Random Forest to generate probability maps that approximate accurately the distribution of the geothermal expressions is the one that considers permeability, Hg solubility, T, and distances from faults and folds (Fig. 3b, Test 8).

4 Interpretation

ML algorithms based on decision trees for probability calculations (i.e., CatBoost, Random Forest) prove to be the most efficient in predicting the true distribution of geothermal expressions of Mt. Amiata for this dataset. The evidence that only a combination of physical-chemical and geological

predictors (Test 8) is able to reproduce the narrow-longitude distribution of all geothermal expressions suggests that not all geological/structural factors play the same role in controlling ore precipitation, gas venting, and hot spring discharge in a geothermal field.

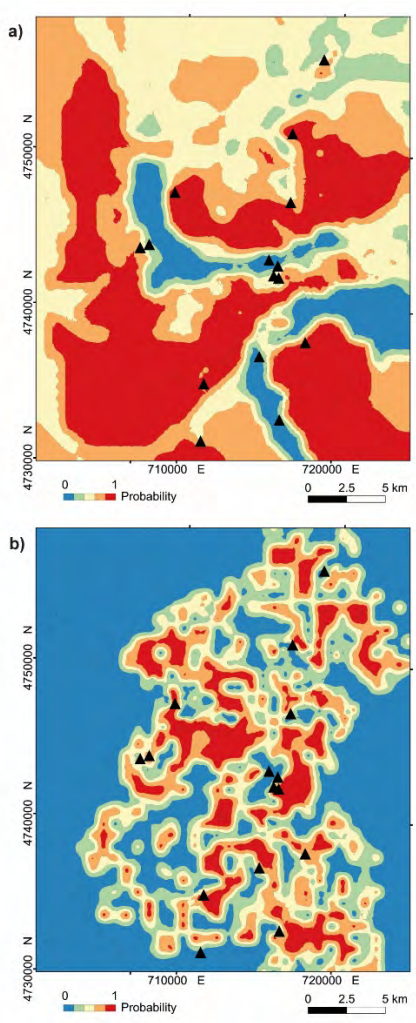

Figure 3. Correlation maps based on the Random Forest regressor and calculated for the entire study area. The black triangles are the known cinnabar (±stibnite) deposits/prospects (Fig. 1). (a) Map calculated considering only the ore predictors (Test 1, Table 1). (b) Map calculated considering a selection of ore and geometric predictors (Test 8).

Also, fault density alone is probably unable to control the regional distribution of all expressions of a geothermal system, but must combine with other factors that favor underground transport and precipitation, i.e. presence of folds, fluid T, and solubility. This is true also for the distribution at depth of geothermal expressions. Distributions of ore features similar to those reported here were documented in the Goldstrike Gold System, North Carlin Trend (Dobak et al., 2020).

References

Arisi Rota, F., Brondi, A., Dessau, G., Franzini, M., Monte Amiata SpA, Stabilimento Minerario del Siele SpA, Stea, B. and Vighi, L., 1971. I Giacimenti Minerari. In: SIMP (Editor), La Toscana Meridionale, Società Italiana di Mineralogia e Petrologia, pp. 357-571.

Barelli, A., Ceccarelli, A., Dini, I., Fiordelisi, A., Giorgi, N., Lovari, F. and Romagnoli, P., 2010. A Review of the Mt. Amiata Geothermal System (Italy), World Geothermal Congress 2010, Bali, Indonesia, pp. 1-6.

Bonciani, F., Callegari, I., Conti, P., Cornamusini, G. and Carmignani, L., 2005. Neogene post-collisional evolution of the internal Northern Apennines: insights from the upper Fiora and Albegna valleys, (Mt. Amiata geothermal area, southern Tuscany). Bollettino della Societa Geologica Italiana, Vol Spec 3: 103-118.

Brogi, A., Fabbrini, L. and Liotta, D., 2011. Sb–Hg ore deposit distribution controlled by brittle structures: The case of the Selvena mining district (Monte Amiata, Tuscany, Italy). Ore Geology Reviews, 41(1): 35-48.

Calamai, A., Cataldi, R., Squarci, P. and Taffi, L., 1970. Geology, Geophysics and Hydrogeology of the Monte Amiata Geothermal Field. Geothermics, 1(Special Issue 1): 1-9.

Cataldi, R., 1967. Remarks on the geothermal research in the region of Monte Amiata (Tuscany - Italy). Bulletin Volcanologique, 30(1): 243-269.

Clever, H.L., Johnson, S.A. and Derrick, M.E., 1985. The Solubility of Mercury and Some Sparingly Soluble Mercury Salts in Water and Aqueous Electrolyte Solutions. Journal of Physical and Chemical Reference Data, 14(3): 631-680.

Conticelli, S., Boari, E.L., Burlamacchi, L., Cifelli, F., Moscardi, F., Laurenzi, M.A., Ferrari Pedraglio, L., Francalanci, L., Benvenuti, M.G., Braschi, E. and Manetti, P., 2015. Geochemistry and Sr-Nd-Pb isotopes of Monte Amiata Volcano, Central Italy: evidence for magma mixing between high-K calc-alkaline and leucititic mantle-derived magmas. Italian Journal of Geosciences, 134(2): 266-290.

De Castro, C., 1914. Genesi dei giacimenti cinabriferi del Monte Amiata, Memorie Descrittive Carta Geologica d'Italia, pp. 1-77.

Dobak, P.J., Robert, F., Barker, S.L.L., Vaughan, J.R., Eck, D., 2020. Chapter 15: Goldstrike Gold System, North Carlin Trend, Nevada, USA, Geology of the World's Major Gold Deposits and Provinces. Society of Economic Geologists, 23: 313-334.

Farella, E.M., Özdemir, E. and Remondino, F., 2021. 4D Building Reconstruction with Machine Learning and Historical Maps. Applied Sciences, 11(4): 1445.

Frondini, F., Caliro, S., Cardellini, C., Chiodini, G. and Morgantini, N., 2009. Carbon dioxide degassing and thermal energy release in the Monte Amiata volcanic-geothermal area (Italy). Applied Geochemistry, 24(5): 860-875.

Gianelli, G., Puxeddu, M., Batini, F., Bertini, G., Dini, I., Pandeli, E. and Nicolich, R., 1988. Geological model of a young volcano-plutonic system: the geothermal region of Monte Amiata (Tuscany, Italy). Geothermics, 17(5/6): 719-734.

Magi, F., Doveri, M., Menichini, M., Minissale, A. and Vaselli, O., 2019. Groundwater response to local climate variability: hydrogeological and isotopic evidences from the Mt. Amiata volcanic aquifer (Tuscany, central Italy). Rendiconti Lincei. Scienze Fisiche e Naturali, 30(1): 125-136.

Marroni, M., Moratti, G., Costantini, A., Conticelli, S., Benvenuti, M.G., Pandolfi, L., Bonini, M., Cornamusini, G. and Laurenzi, M.A., 2015. Geology of the Monte Amiata region, Southern Tuscany, Central Italy. Italian Journal of Geosciences, 134(2): 171-199.

Pedregosa, F., Varoquaux, G., Gramfort, A., Michel, V., Thirion, B., Grisel, O., Blondel, M., Prettenhofer, P., Weiss, R. and Dubourg, V., 2011. Scikit-learn: Machine learning in Python. The Journal of Machine Learning Research, 12: 2825-2830.

Pirajno, F., 2020. Subaerial hot springs and near-surface hydrothermal mineral systems past and present, and possible extraterrestrial analogues. Geoscience Frontiers, 11(5): 1549-1569.

Segreto, L., 1991. Monte Amiata. Il mercurio italiano. Strategie internazionali e vincoli extraeconomici. Ciriec. Storie d'impresa pubblica e di pubblico interesse. Franco Angeli (Ed.), 1-355 pp.

Sun, T., Chen, F., Zhong, L., Liu, W. and Wang, Y., 2019. GIS-based mineral prospectivity mapping using machine learning methods: A case study from Tongling ore district, eastern China. Ore Geology Reviews, 109: 26-49.

Imputation methods for REE and Y in zircon

Carlos Carrasco-Godoy[1], Ian H. Campbell[1]
[1]Research School of Earth Sciences, Australian National University, Australia

Abstract. The shape of chondrite normalized zircon rare earth element (REE) patterns and Cerium (Ce) and Europium (Eu) anomalies provide insights into the conditions under which a zircon was crystallized. Therefore, using these elements as variables is common during machine learning algorithms training. However, several predictive models do not tolerate missing observations. Here, we propose two new methods, based on the lattice strain theory (Chondrite-Lattice) and Onuma diagrams (Chondrite-Onuma), using chondrite normalized values instead of partition coefficient. We compiled a dataset of ~1500 zircons, with known REE + Y concentrations, and used it to test and calibrate these methods. They require analyses of as few as five REEs to impute the missing REE in incomplete or legacy datasets and to estimate La, Pr, or Ce* in magmatic zircons. This allows for magma fertility models to have more variables available for model training and testing, in addition to providing a standardized method to calculate Ce*, La and Pr in zircon.

1 Introduction

Zircon is one of the most resilient accessory minerals in nature and is present in a wide range of geological environments. The geochemical and isotopic information it contains provides insights to understand fundamental earth processes (Finch and Hanchar 2003).

The rare earth elements (REE) and Y have been widely studied in zircon. Their concentration and shape of their chondrite normalized pattern give information about their source rock (e.g. Rubatto 2002; Zhu et al. 2022), and insights into the conditions under which the zircon crystallized (e.g. redox state, Loucks et al. 2020), among others.

Several studies have attempted to establish geochemical discriminants that identify zircons that were crystallized from “fertile” magma. Here we refer to fertility as the capacity of a magma to form a porphyry copper deposit. Pizarro et al. (2020), based on traditional statistical analysis, suggested the term porphyry indicator zircon (PIZ) for a zircon with characteristics that are considered indicators of fertility (for instance, Eu/Eu* > 0.4 or Ce/Nd > 1, among others).

Recent studies have applied machine learning algorithms to discriminate fertility among zircons, giving better predictions than traditional methods (e.g., Zou et al. 2022; Zhou et al. 2022). However, a drawback of several machine learning models is that they are unable to deal with missing data (Kuhn 2020). If the amount of missing information is small, imputation techniques can be used during model training and cross-validation. Some of the common methods for imputation include the replacement of missing values for the mean or median of the variable or more complex methods that use predictive models based on the non-missing variables (Kuhn 2020). Particularly, in the case of REE, it is possible to impute using the geometric mean of adjacent chondrite-normalized REE of the element to replace. However, this method does not consider the curvature of the zircon pattern and it cannot be applied if two or more consecutive REE are missing or next to Ce and Eu.

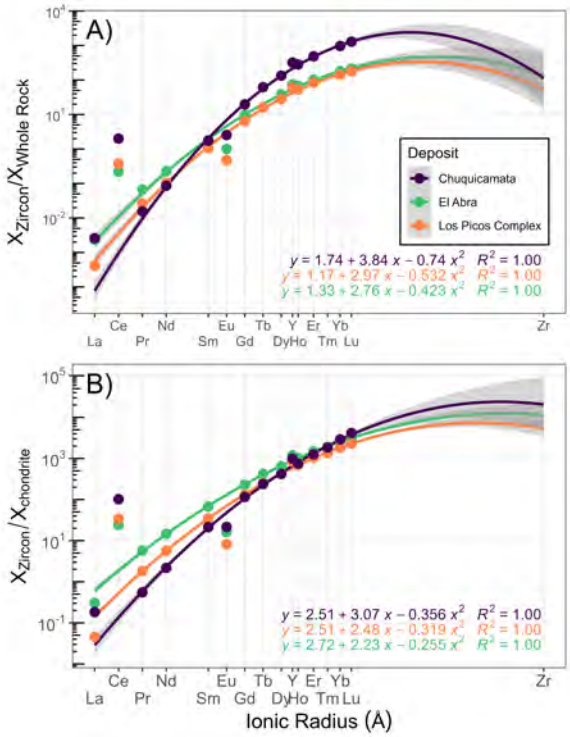

Figure 1. Onuma diagrams for three zircons from Ballard et al. (2002). Equations for each parabola are colour-coded, where y = $\log_{10}$(x). The X-axis is reversed. The shading indicates a 95% confidence interval for the quadratic fit. **A** Partition coefficient estimates vs Ionic radii. **B** Chondrite normalised values vs ionic radii. Chondrite values were taken from Palme and O’Neill (2014)

We demonstrate two methods that derive from Onuma diagrams (Chondrite-Onuma) and the lattice strain theory (Chondrite-Lattice), but using chondrite normalized values instead of partition coefficients, to impute missing REE and to calculate La and Pr where their concentrations are low; together with Ce* and Eu* anomalies in magmatic zircons.

2 Onuma diagrams and the lattice strain theory

Onuma et al. (1968) showed a relationship between an element's ionic radius and its partition coefficient

for a given mineral. All the elements of the same charge (e.g., +3 for most REE), describe a quadratic function with decreasing partition coefficient as the ionic radii are further displaced from the ionic radii of the lattice site where the substitution occurs (Figure 1A).

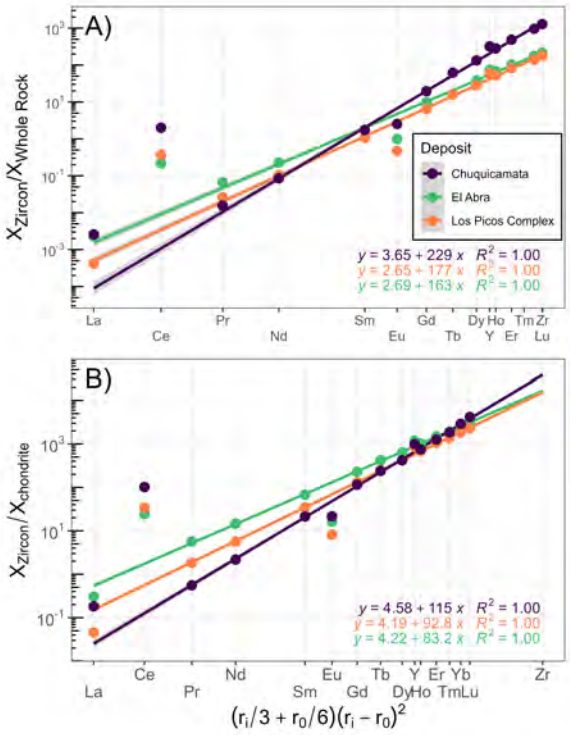

Figure 2. Lattice strain regression for the same zircons as Figure 1. Equations for each parabola are colour-coded, where y = $\log_{10}$(x). The X-axis is reversed and represents the misfit parameter from the lattice strain equation. The shading indicates a 95% confidence interval for the quadratic fit. **A** Partition coefficient estimates vs Ionic radii. **B** Chondrite normalised values vs ionic radii. Chondrite values from Palme and O'Neill (2014)

The lattice strain theory (Blundy and Wood 1994) explains the relationship between the partition coefficients and the misfit between the lattice site in the crystal and the actual ionic radius of an element occupying that space. The elements with the same charge describe a linear relationship (Figure 2A) where the partition coefficient decreases as the difference between the effective lattice site (r_0) and the cation radius increases (r_i).

These methods can be used to impute missing REE, or to calculate La or Ce* in zircons (e.g., Burnham 2020; Loader et al. 2022). However, they require precise knowledge of the melt composition, which is often unavailable or cannot be analysed (e.g., detrital zircons). However, if chondrite-normalized values are used instead of partition coefficients, they have the same quadratic and linear relationship for the Onuma diagrams and the lattice strain theory, respectively. Therefore, we have used this empirical observation to overcome the limitations of using partition coefficients.

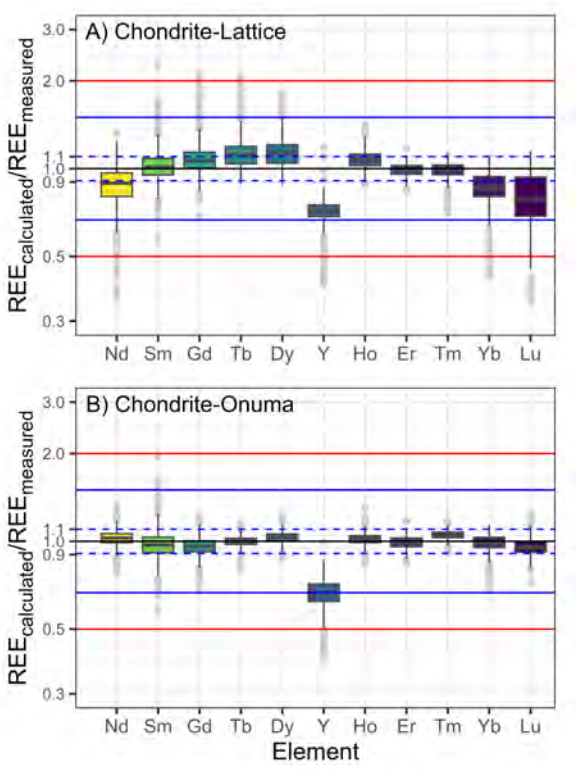

Figure 3. Boxplots for the ratio between calculated and measured concentrations for each REE, excluding La, Pr, Ce and Eu. Calculated values will plot along the y = 1 line if they are equal to the measured values. The blue segmented lines, blue continuous lines and red lines are reference lines for a discrepancy between measured and calculated values of 10%, 50% and 100%, respectively. Each box contains 50% of the data. Each box and whiskers represent 99.3% of the data. The grey dots are outliers and represent 0.7% of the data. **A** Chondrite-Lattice. **B** Chondrite-Onuma methods.

Figures 1 and 2 show the comparison of Onuma diagrams and lattice strain regressions for three zircons from Ballard et al. (2002) using partition coefficients and chondrite normalized values. We have used whole rock compositions as a proxy for melt composition and excluded Ce and Eu because can be present in more than one oxidation state. We have also excluded La and Pr due to their susceptibility to LREE contamination (Claiborne et al. 2018; Zou et al. 2019; Zhong et al. 2019; Burnham 2020). Both cases have an R^2 higher than 0.99.

3 Data Compilation

We have compiled nearly 1500 zircons from the literature that have the whole range of REE + Y analysed with no missing values (Ballard et al. 2002; Buret et al. 2016, 2017; Burnham and Berry 2017; Loader et al. 2017; Large et al. 2018, 2020, 2021; Lu et al. 2019; Zhu et al. 2020; Pizarro et al. 2020). Most of this data has been filtered for LREE-rich or titanite inclusions in their original publications. This dataset was used to evaluate the performance of the Chondrite-Onuma and Chondrite-Lattice

methods for different scenarios of missing REE. We have used a separate small dataset (Colombini et al. 2011; Taylor et al. 2015; Claiborne et al. 2018) of melt-zircon pairs to calculate La, Ce* and Pr using the lattice strain theory. The calculated values were used to compare the methods proposed in this study with those of Zhong et al. (2019). We have tested almost exclusively magmatic zircons.

4 Imputation of REE + Y

Figures 3A and 3B show the ratio between predicted and measured concentrations for the complete dataset for each REE and Y for the Chondrite-Lattice and Chondrite-Onuma methods, respectively.

Overall, the Chondrite-Lattice method (Figure 3A) gives predictions that disagree, in median, up to ~30% (Figure 3A), which is higher for the HREE section of the REE pattern. In contrast, the Chondrite-Onuma method (Figure 3B) gives predicted values that disagree by <5% with respect to the measured concentrations. Yttrium is underestimated by both methods, which is also observed in Figures 1 and 2 where the measured values fall above the regression line. In both cases, if the disagreement is systematic, the predictions can be calibrated by projecting them to the ratio = 1 line.

The cases in Figure 3 are overfitted models because all the REEs are used for prediction. We have reproduced 6 different scenarios where a different number of REEs are missing or censored (e.g., where not analysed or below detection limits). Both methods give good results if only three evenly distributed REEs, and identical results to those in Figure 3 if 4 or more REEs are used, excluding La, Pr, Ce, Eu and Y during modelling.

5 Calculated La, Ce* and Pr

Measured La and Pr concentrations in zircon are often considered unreliable (Claiborne et al. 2018; Zou et al. 2019; Zhong et al. 2019; Burnham 2020) and Ce anomalies are traditionally calculated using the geometric mean of these elements to obtain Ce*. Thus, their concentrations cannot be used as reference values. Therefore, we have used the best estimates for La and Pr, which are those derived from the lattice strain theory (using partition coefficients).

Figure 4 shows the calculated values for different methods vs the lattice strain estimates for La and Ce. The calculated Ce is equal to Ce*. Both cases tend to slightly overestimate La and Ce* when compared to the lattice strain theory.

Zhong et al. (2019) proposed a method to calculate Ce anomalies based on a logarithmic regression between the REE atomic number and their chondrite normalized concentrations. However, their method gives values that underestimate La and Ce* up to 2 and 1 orders of magnitude, respectively, compared to the lattice strain estimates. There is no difference between the methods for estimating Pr.

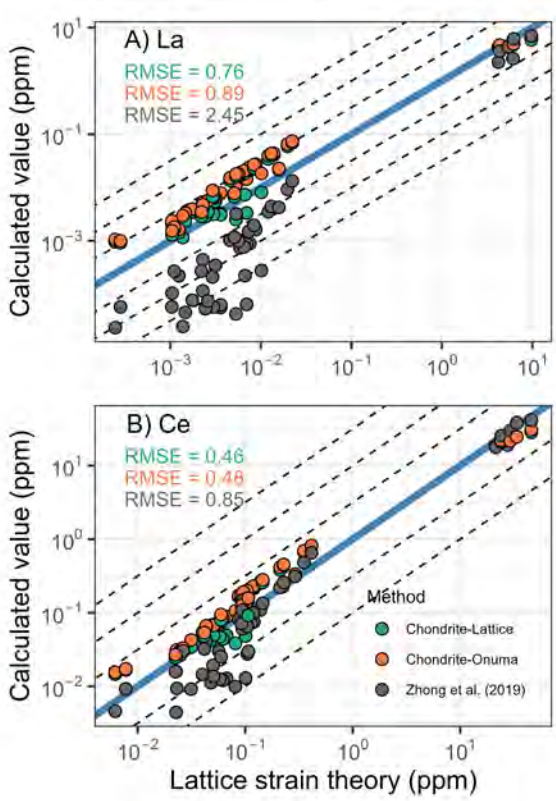

Figure 4. A La and **B** Ce concentrations obtained by the lattice strain theory vs the calculated values using the chondrite-lattice strain, chondrite-Onuma and the Zhong et al. (2019) methods. Calculated Ce is equal to Ce* in this case. The blue line is the identity line. The segmented lines are 0.5 orders of magnitude apart. Root mean square errors (RMSE) are colour coded according to the method, lower values are better. Zircon-glass pairs are from Colombini et al. (2011), Taylor et al. (2015) and Claiborne et al. (2018)

6 Implications and conclusions

The Chondrite-Lattice and Chondrite-Onuma can be used to impute missing REE in zircon, which gives complete datasets for training and testing of machine learning models. This is especially useful in the case of legacy data. Furthermore, the methods provide a standardized procedure for calculating La, Ce* and Pr so they can be used as input variables for new fertility models based on zircon geochemistry. We recommend the Chondrite-Onuma method for imputation and the Chondrite-Lattice to calculate La, Ce* and Pr.

7 Code availability

The methods used in the work have been compiled in the ImputeREE package for the R programming language. The package is accessible in the CRAN network and on the development site at https://github.com/cicarrascog/imputeREE. A

companion app is accessible from the development website.

Acknowledgements

This work was funded by the National Agency for Research and Development (ANID) / Scholarship Program / DOCTORADO BECAS CHILE/2019 - 72200364.

References

Ballard JR, Palin MJ, Campbell IH (2002) Relative oxidation states of magmas inferred from Ce(IV)/Ce(III) in zircon: application to porphyry copper deposits of northern Chile. Contributions to Mineralogy and Petrology 144:347–364. https://doi.org/10.1007/s00410-002-0402-5

Blundy J, Wood B (1994) Prediction of crystal–melt partition coefficients from elastic moduli. Nature 372:452–454. https://doi.org/10.1038/372452a0

Buret Y, von Quadt A, Heinrich C, et al (2016) From a long-lived upper-crustal magma chamber to rapid porphyry copper emplacement: Reading the geochemistry of zircon crystals at Bajo de la Alumbrera (NW Argentina). Earth and Planetary Science Letters 450:120–131. https://doi.org/10/f8242b

Buret Y, Wotzlaw J-F, Roozen S, et al (2017) Zircon petrochronological evidence for a plutonic-volcanic connection in porphyry copper deposits. Geology 45:623–626. https://doi.org/10.1130/G38994.1

Burnham AD (2020) Key concepts in interpreting the concentrations of the rare earth elements in zircon. Chemical Geology 551:119765. https://doi.org/10.1016/j.chemgeo.2020.119765

Burnham AD, Berry AJ (2017) Formation of Hadean granites by melting of igneous crust. Nature Geoscience 10:457–461. https://doi.org/10.1038/ngeo2942

Claiborne LL, Miller CF, Gualda GAR, et al (2018) Zircon as Magma Monitor: Robust, Temperature-Dependent Partition Coefficients from Glass and Zircon Surface and Rim Measurements from Natural Systems. In: Moser DE, Corfu F, Darling JR, et al. (eds) Geophysical Monograph Series. John Wiley & Sons, Inc., Hoboken, NJ, USA, pp 1–33

Colombini LL, Miller CF, Gualda GAR, et al (2011) Sphene and zircon in the Highland Range volcanic sequence (Miocene, southern Nevada, USA): elemental partitioning, phase relations, and influence on evolution of silicic magma. Miner Petrol 102:29. https://doi.org/10.1007/s00710-011-0177-3

Finch RJ, Hanchar JM (2003) Structure and Chemistry of Zircon and Zircon-Group Minerals. Reviews in Mineralogy and Geochemistry 53:1–25. https://doi.org/10.2113/0530001

Kuhn M (2020) Feature engineering and selection: a practical approach for predictive models. CRC Press, Taylor & Francis Group, Boca Raton London New York

Large SJE, Buret Y, Wotzlaw JF, et al (2021) Copper-mineralised porphyries sample the evolution of a large-volume silicic magma reservoir from rapid assembly to solidification. Earth and Planetary Science Letters 563:116877. https://doi.org/10.1016/j.epsl.2021.116877

Large SJE, Quadt A von, Wotzlaw J-F, et al (2018) Magma Evolution Leading to Porphyry Au-Cu Mineralization at the Ok Tedi Deposit, Papua New Guinea: Trace Element Geochemistry and High-Precision Geochronology of Igneous Zircon. Economic Geology 113:39–61. https://doi.org/10.5382/econgeo.2018.4543

Large SJE, Wotzlaw J-F, Guillong M, et al (2020) Resolving the timescales of magmatic and hydrothermal processes associated with porphyry deposit formation using zircon U–Pb petrochronology. Geochronology 2:209–230. https://doi.org/10.5194/gchron-2-209-2020

Loader MA, Nathwani CL, Wilkinson JJ, Armstrong RN (2022) Controls on the magnitude of Ce anomalies in zircon. Geochimica et Cosmochimica Acta. https://doi.org/10.1016/j.gca.2022.03.024

Loader MA, Wilkinson JJ, Armstrong RN (2017) The effect of titanite crystallisation on Eu and Ce anomalies in zircon and its implications for the assessment of porphyry Cu deposit fertility. Earth and Planetary Science Letters 472:107–119. https://doi.org/10.1016/j.epsl.2017.05.010

Loucks RR, Fiorentini ML, Henríquez GJ (2020) New magmatic oxybarometer using trace elements in zircon. J Petrology. https://doi.org/10.1093/petrology/egaa034

Lu Y, Smithies R, Wingate M, et al (2019) Zircon fingerprinting of magmatic-hydrothermal systems in the Archean Yilgarn Craton

Onuma N, Higuchi H, Wakita H, Nagasawa H (1968) Trace element partition between two pyroxenes and the host lava. Earth and Planetary Science Letters 5:47–51. https://doi.org/10.1016/S0012-821X(68)80010-X

Pack A, Russell SS, Shelley JMG, van Zuilen M (2007) Geo- and cosmochemistry of the twin elements yttrium and holmium. Geochimica et Cosmochimica Acta 71:4592–4608. https://doi.org/10.1016/j.gca.2007.07.010

Pizarro H, Campos E, Bouzari F, et al (2020) Porphyry indicator zircons (PIZs): Application to exploration of porphyry copper deposits. Ore Geology Reviews 126:103771. https://doi.org/10.1016/j.oregeorev.2020.103771

Rubatto D (2002) Zircon trace element geochemistry: partitioning with garnet and the link between U–Pb ages and metamorphism. Chemical Geology 184:123–138. https://doi.org/10.1016/S0009-2541(01)00355-2

Taylor RJM, Harley SL, Hinton RW, et al (2015) Experimental determination of REE partition coefficients between zircon, garnet and melt: a key to understanding high-T crustal processes. Journal of Metamorphic Geology 33:231–248. https://doi.org/10.1111/jmg.12118

Zhong S, Seltmann R, Qu H, Song Y (2019) Characterization of the zircon Ce anomaly for estimation of oxidation state of magmas: a revised Ce/Ce* method. Miner Petrol 113:755–763. https://doi.org/10.1007/s00710-019-00682-y

Zhou Y, Zhang Z, Yang J, et al (2022) Machine Learning and Singularity Analysis Reveal Zircon Fertility and Magmatic Intensity: Implications for Porphyry Copper Potential. Nat Resour Res. https://doi.org/10.1007/s11053-022-10122-y

Zhu Z, Campbell IH, Allen CM, et al (2022) The temporal distribution of Earth's supermountains and their potential link to the rise of atmospheric oxygen and biological evolution. Earth and Planetary Science Letters 580:117391. https://doi.org/10.1016/j.epsl.2022.117391

Zhu Z, Campbell IH, Allen CM, Burnham AD (2020) S-type granites: Their origin and distribution through time as determined from detrital zircons. Earth and Planetary Science Letters 536:116140. https://doi.org/10.1016/j.epsl.2020.116140

Zou S, Chen X, Brzozowski MJ, et al (2022) Application of Machine Learning to Characterizing Magma Fertility in Porphyry Cu Deposits. Journal of Geophysical Research: Solid Earth 127:e2022JB024584. https://doi.org/10.1029/2022JB024584

Zou X, Qin K, Han X, et al (2019) Insight into zircon REE oxybarometers: A lattice strain model perspective. Earth and Planetary Science Letters 506:87–96. https://doi.org/10.1016/j.epsl.2018.10.031

Zircon geochemistry: insights into porphyry copper deposits fertility from machine learning applications

Carlos Carrasco-Godoy[1], Ian H. Campbell[1], Yamila Cajal[1,2]
[1]Research School of Earth Sciences, The Australian National University
[2]Centre for Ore Deposit and Earth Sciences, University of Tasmania

Abstract. Zircon is a widespread mineral in igneous rocks and its geochemistry allows the reconstruction of the age and conditions of magma formation. This makes it possible to assess how a zircon that grew from a magma that formed a porphyry deposit differs from one that did not. Several studies have proposed geochemical signatures of zircon that can be used to distinguish between ore-bearing and barren magmas, such as Eu and Ce anomalies. For this study, ca. 18,000 zircons were compiled, including zircons from more than thirty deposits, which are compared with zircons from barren intrusions and rivers. We have trained different models for predicting fertility, focusing on the insights that can be obtained from these models. An oversampled random forest gave the best results with a ROC AUC of 0.977. The results suggest that the fertility signal in zircons becomes stronger as the porphyry systems evolve. The model reveals that there are differences in the LREE content of fertile and barren zircons but not in the HREE. The results show that the changes in the Ce anomaly in zircon are controlled by changes in Pr and La rather than changes in Ce.

1 Introduction

Porphyry copper deposits are the source of ~75% of the world's copper and ~20% of its gold (Sillitoe 2010). Although global consumption of copper is expected to increase in the next 50 years, the discovery of new deposits has decreased over the last decades (Elshkaki et al. 2016; Schodde 2019). Furthermore, the use of copper has become fundamental in the transition from fossil fuels to renewable energies (Månberger and Stenqvist 2018). Therefore, it is critical to improve our current exploration methods to assure copper's future demand.

Zircon is a widespread accessory mineral present in a range of geological environments. It contains diagnostic elements and isotopes in its crystal structure, which in addition to its resistance to chemical and physical weathering (Finch and Hanchar 2003), make it suitable for a wide range of applications from geochronology (e.g., Compston and Pidgeon 1986) to identifying Earth's major periods of mountain building (Zhu et al. 2022).

Zircon can be found in igneous rocks that range in composition from intermediate to felsic and are important reservoirs for incompatible elements (e.g., U, Hf, REE, among others) in their host rock (Finch and Hanchar 2003). The content of several of these elements in the zircon lattice varies as physicochemical properties of the magma change, such as temperature (e.g. Ti, Ferry and Watson 2007), oxygen fugacity (Ce and U, Loucks et al. 2020), the magma composition or co-crystallizing minerals (Loader et al. 2017, 2022; Zhong et al. 2018)

Therefore, we consider the hypothesis that the conditions required for the formation of an economic porphyry copper deposit led to zircons with a unique trace elements geochemistry that can be used to predict fertility. Several studies have used traditional methods (e.g., univariate statistics) to define geochemical characteristics to classify fertile zircons (Dilles et al. 2015; Lu et al. 2016; Pizarro et al. 2020; Leslie et al. 2021). Pizarro et al., (2020) summarized these characteristics and suggest the term porphyry indicator zircon (PIZ) to be used for zircons with high Hf concentrations (> 8,750 ppm), high Ce/Nd (> 1), Eu/Eu* (> 0.4), (10,000xEu/Eu*)/Y (> 1), (Ce/Nd)/Y (> 0.01) ratios, intermediate Th/U ratios and low Dy/Yb (< 0.3).

Recent studies (Zou et al. 2022; Zhou et al. 2022) have used machine learning algorithms to distinguish fertility in zircon crystals. They show that univariate criteria (e.g., Pizarro et al. 2020) have accuracies, depending on the dataset, of between 80 to 90% whereas machine learning algorithms can reach up to 94% accuracy depending on the model used.

2 Data and Methods

For this study, ca. 18,000 zircons from ore-bearing and barren igneous rocks, and detrital grains from rivers, have been carefully compiled from the literature. The global dataset includes zircons from more than thirty porphyry copper deposits. The porphyry dataset contains nearly 5,000 zircons. The geological information of each grain (e.g., age, host rock composition, etc.) was carefully compiled where available. Furthermore, each zircon was labelled according to the deposit as Cu, Cu±Au, Cu±Mo or Cu±Au±Mo porphyry deposits, as well as according to their temporal distribution within the deposit as precursor or pre-, syn- or post-mineralization if indicated in the literature. The barren dataset considers 13,000 zircons from barren sources divided into three subsets: the river (n ~7,000, Zhu et al. 2020), GEOROC (n ~5,000, excluding porphyry-associated publications, Lehnert et al. 2000) and the barren subsets (n ~ 800). Considering that economic porphyry copper deposits are rare (Richards 2022) it is a reasonable assumption to consider that the detrital zircons, from Earth's major rivers, are barren. The GEOROC subset considers zircon from the GEOROC database. The barren subset considers zircon grains spatially or

temporally associated with porphyry copper deposits but that are considered barren within the district.

Cerium anomalies have been associated with an increase in the oxygen fugacity of the magma, but its calculation is difficult due to the low La and Pr content of zircon (Ballard et al. 2002; Zou et al. 2019; Zhong et al. 2019). Here, we have used a new empirical method to calculate Ce (Carrasco-Godoy and Campbell, in review), based on the lattice strain theory, to impute any missing REE and to calculate standardized La, Pr concentrations and Ce anomalies.

We have trained a random forest (Breiman 2001), decision tree and logistic regression. Each model was trained using five times repeated 10-fold cross-validation, considering raw and oversampled datasets to account for class unbalance. Each model was trained with and without centred log-ratio (CLR) transformation of the data (Aitchison 1984). The models were ranked according to their performance metrics: the area under the receiver operating characteristic curve (ROC-AUC) which indicates the possibility of a random fertile zircon ranked higher than a randomly selected barren zircon; sensitivity which is the proportion of fertile zircons correctly identified among the fertile zircons; and specificity which is the proportion of barren zircons correctly identified among the total of barren zircons. The three best models had their hyperparameters tuned using a mix of grid search and simulated annealing (Kuhn and Silge 2022).

Here, we present the results of the best model with a detailed analysis of the model predictions on individual probabilities in addition to the outcome prediction. Then, we link the results of the models to geological processes than can lead to the formation of fertile zircons.

Data processing, feature selection and model training and testing were performed in R programming language using the base (R Core Team 2022), tidyverse (Wickham et al. 2019) and tidymodels (Kuhn and Wickham 2020) metapackages. Random forest and decision trees were fitted with the Rpart and ranger packages (Wright et al. 2021; Therneau and Atkinson 2022).

3 Results and discussions

The best model was an oversampled random forest without CLR transformation. Centred log-ratio transformation has been widely applied to remove the effects of the constant sum in closed data (e.g., major elements that sum 100%, Aitchison 1984). However, we did not observe any improvement between CLR and the raw data. We attribute this to the closed nature of the zircon crystal lattice which would not allow more elements than their formula unit can hold or the non-parametric nature of Random Forest models (Nathwani et al. 2022).

The metrics during model training were the area under the receiving operating characteristic (ROC AUC) of 0.977 ± 0.05%, sensitivity of 0.87 ± 0.28% and specificity of 0.95 ± 0.11%, whereas in the testing set where a ROC AUC of 0.978, sensitivity of 0.89 and specificity of 0.94.

An additional set with zircons neither in the testing nor training set was used for external validation. Most of the data are from deposits, rivers or barren intrusions that were not present in the training or testing sets. The results are ROC AUC of 0.978, but with a lower sensitivity (0.707) and a higher specificity (0.98).

Most binary classification algorithms estimate membership probabilities and use 0.5 as a boundary. Figure 1 shows a normalized histogram of the fertile zircon membership probability according to each subset for the predictions in the testing set. Only the deposit dataset contains zircons labelled as fertile. In this histogram, each bin represents the relative proportions of each class rather than the total counts. The individual probabilities in the testing set show that most of the zircons, with more than 50% probability of being fertile, belong to the testing set and misclassified zircons fall to a minimum after the probability is higher than 90%. Therefore, depending on the degree of confidence the boundary to define fertile zircons can be adjusted. A shift of the classification boundary (red line in Figure 1) to the right would increase the confidence of a zircon being fertile at the cost of discarding more fertile zircons as barren (an increase in the specificity and a decrease in the sensitivity).

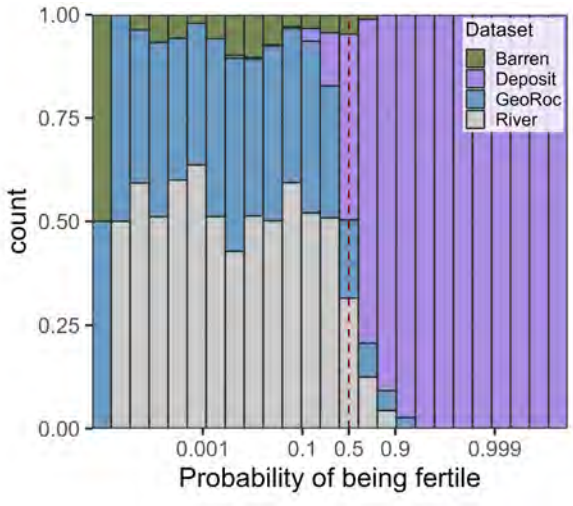

Figure 1. Normalized histogram of the predicted probabilities from oversampled random forest in the testing set. The colours indicate the different subsets from the main dataset. X-axis is logit-transformed. The red dashed line indicates a probability of 0.5. Each bin shows the proportion of zircons from each dataset that falls within that probability.

The analysis of the misclassified grains for each class membership, considering a probability boundary of 0.5, decreases from precursor (34%) to post-mineral (1.6%) which suggests an increase in the fertile signature as the porphyritic systems evolve. In contrast, barren zircons mislabelled as fertile reach 18% for the barren subset, 14% for I-type granites, 5% for detrital zircons from rivers and

1.9% for S-type granites. The misclassification percentage can be used as a benchmark of how many mislabelled zircons can be expected when applying a predictive model to unknown data.

The random forest corrected Gini impurity importance ranking (Nembrini et al. 2018) for the features included in the model training indicates that Eu anomaly and Ce anomalies are the most important variables, which is consistent with observations by other authors (Loader et al. 2017; Zou et al. 2022; Zhou et al. 2022). There is a decrease in the importance from LREE to HREE. The study of the median between ore-associated and barren zircon shows little to no difference for the HREE. In contrast, there is an increase in the median difference from pre-mineral to post-mineralization zircons as the ionic radius of the REE increases. Lanthanum and Pr have the highest variation, a factor of 6 and 4, respectively. However, these variations should be taken as indicative only, due to the difficulty of measuring LREE in zircon makes it difficult to gauge the real magnitude of these changes. In contrast, Ce concentrations are relatively constant with a maximum median variation of less than 1.6. This is consistent with the observations of Loader et al. 2022. We suggest that the variation in Ce anomaly in zircon is mainly controlled by the depletion of La and Pr, rather than the variation of Ce.

3 Conclusions and future work

We have shown that random forest models provide an improvement in predictions of zircon fertility when applied to porphyry copper deposits over traditional methods based on univariate statistics. We have compiled the largest and most complete dataset to date for training fertility models using zircon geochemistry.

Insights obtained from the model suggest that there is an increase in the fertility signal in zircons as porphyry systems evolve. Ce and Eu anomalies are the best predictors of fertility and the LREE have more weight in the prediction of fertility than HREE. Changes in Ce anomaly are likely controlled by variations in La and Pr rather than Ce concentrations.

Future work considers a model pipeline to classify detrital zircons according to the deposit type they are associated with, Cu, Cu-Au or Cu-Mo, and their temporality (pre- to post-mineralization).

Finally, each model can be tailored to increase the probability of correct classification by taking into account their geological and geographic context.

Acknowledgements

This work was funded by the National Agency for Research and Development (ANID) / Scholarship Program / DOCTORADO BECAS CHILE/2019 - 72200364.

References

Aitchison J (1984) The statistical analysis of geochemical compositions. Mathematical Geology 16:531–564. https://doi.org/10.1007/BF01029316

Ballard JR, Palin MJ, Campbell IH (2002) Relative oxidation states of magmas inferred from Ce(IV)/Ce(III) in zircon: application to porphyry copper deposits of northern Chile. Contributions to Mineralogy and Petrology 144:347–364. https://doi.org/10.1007/s00410-002-0402-5

Breiman L (2001) Random Forests. Machine Learning 45:5–32. https://doi.org/10.1023/A:1010933404324

Compston W, Pidgeon RT (1986) Jack Hills, evidence of more very old detrital zircons in Western Australia. Nature 321:766–769. https://doi.org/10.1038/321766a0

Dilles JH, Kent AJR, Wooden JL, et al (2015) Zircon Compositional Evidence For Sulfur-Degassing From Ore-Forming Arc Magmas. Economic Geology 110:241–251. https://doi.org/10.2113/econgeo.110.1.241

Elshkaki A, Graedel TE, Ciacci L, Reck BK (2016) Copper demand, supply, and associated energy use to 2050. Global Environmental Change 39:305–315. https://doi.org/10.1016/j.gloenvcha.2016.06.006

Ferry JM, Watson EB (2007) New thermodynamic models and revised calibrations for the Ti-in-zircon and Zr-in-rutile thermometers. Contrib Mineral Petrol 154:429–437. https://doi.org/10/bzbzdw

Finch RJ, Hanchar JM (2003) Structure and Chemistry of Zircon and Zircon-Group Minerals. Reviews in Mineralogy and Geochemistry 53:1–25. https://doi.org/10.2113/0530001

Kuhn M, Silge J (2022) Tidy Modeling with R: A Framework for Modeling in the Tidyverse. O'REILLY MEDIA, INC, USA, S.l.

Kuhn M, Wickham H (2020) Tidymodels: a collection of packages for modeling and machine learning using tidyverse principles.

Lehnert K, Su Y, Langmuir CH, et al (2000) A global geochemical database structure for rocks. Geochemistry, Geophysics, Geosystems 1:. https://doi.org/10.1029/1999GC000026

Leslie C, Meffre S, Cooke DR, et al (2021) Complex Petrogenesis of Porphyry-Related Magmas in the Cowal District, Australia: Insights from LA ICP-MS Zircon Imaging. 24:22

Loader MA, Nathwani CL, Wilkinson JJ, Armstrong RN (2022) Controls on the magnitude of Ce anomalies in zircon. Geochimica et Cosmochimica Acta. https://doi.org/10.1016/j.gca.2022.03.024

Loader MA, Wilkinson JJ, Armstrong RN (2017) The effect of titanite crystallisation on Eu and Ce anomalies in zircon and its implications for the assessment of porphyry Cu deposit fertility. Earth and Planetary Science Letters 472:107–119. https://doi.org/10.1016/j.epsl.2017.05.010

Loucks RR, Fiorentini ML, Henríquez GJ (2020) New magmatic oxybarometer using trace elements in zircon. J Petrology. https://doi.org/10.1093/petrology/egaa034

Lu Y-J, Loucks RR, Fiorentini M, et al (2016) Zircon Compositions as a Pathfinder for Porphyry Cu ± Mo ± Au Deposits. In: Richards JP (ed) Tectonics and Metallogeny of the Tethyan Orogenic Belt. Society of Economic Geologists, p 0

Månberger A, Stenqvist B (2018) Global metal flows in the renewable energy transition: Exploring the effects of substitutes, technological mix and development. Energy Policy 119:226–241. https://doi.org/10.1016/j.enpol.2018.04.056

Nathwani CL, Wilkinson JJ, Fry G, et al (2022) Machine learning for geochemical exploration: classifying metallogenic fertility in arc magmas and insights into porphyry copper deposit formation. Miner Deposita. https://doi.org/10.1007/s00126-021-01086-9

Nembrini S, König IR, Wright MN (2018) The revival of the Gini importance? Bioinformatics 34:3711–3718. https://doi.org/10.1093/bioinformatics/bty373
Pizarro H, Campos E, Bouzari F, et al (2020) Porphyry indicator zircons (PIZs): Application to exploration of porphyry copper deposits. Ore Geology Reviews 126:103771. https://doi.org/10.1016/j.oregeorev.2020.103771
R Core Team (2022) R: A Language and Environment for Statistical Computing. R Foundation for Statistical Computing, Vienna, Austria
Richards JP (2022) Porphyry copper deposit formation in arcs: What are the odds? Geosphere 18:130–155. https://doi.org/10.1130/GES02086.1
Schodde R (2019) Trends in exploration
Sillitoe RH (2010) Porphyry Copper Systems. Economic Geology 105:3–41. https://doi.org/10.2113/gsecongeo.105.1.3
Therneau T, Atkinson B (2022) rpart: Recursive Partitioning and Regression Trees
Wickham H, Averick M, Bryan J, et al (2019) Welcome to the Tidyverse. Journal of Open Source Software 4:1686. https://doi.org/10.21105/joss.01686
Wright MN, Wager S, Probst P (2021) ranger: A Fast Implementation of Random Forests
Zhong S, Feng C, Seltmann R, et al (2018) Can magmatic zircon be distinguished from hydrothermal zircon by trace element composition? The effect of mineral inclusions on zircon trace element composition. Lithos 314–315:646–657. https://doi.org/10.1016/j.lithos.2018.06.029
Zhong S, Seltmann R, Qu H, Song Y (2019) Characterization of the zircon Ce anomaly for estimation of oxidation state of magmas: a revised Ce/Ce* method. Miner Petrol 113:755–763. https://doi.org/10.1007/s00710-019-00682-y
Zhou Y, Zhang Z, Yang J, et al (2022) Machine Learning and Singularity Analysis Reveal Zircon Fertility and Magmatic Intensity: Implications for Porphyry Copper Potential. Nat Resour Res. https://doi.org/10.1007/s11053-022-10122-y
Zhu Z, Campbell IH, Allen CM, et al (2022) The temporal distribution of Earth's supermountains and their potential link to the rise of atmospheric oxygen and biological evolution. Earth and Planetary Science Letters 580:117391. https://doi.org/10.1016/j.epsl.2022.117391
Zhu Z, Campbell IH, Allen CM, Burnham AD (2020) S-type granites: Their origin and distribution through time as determined from detrital zircons. Earth and Planetary Science Letters 536:116140. https://doi.org/10.1016/j.epsl.2020.116140
Zou S, Chen X, Brzozowski MJ, et al (2022) Application of Machine Learning to Characterizing Magma Fertility in Porphyry Cu Deposits. Journal of Geophysical Research: Solid Earth 127:e2022JB024584. https://doi.org/10.1029/2022JB024584
Zou X, Qin K, Han X, et al (2019) Insight into zircon REE oxybarometers: A lattice strain model perspective. Earth and Planetary Science Letters 506:87–96. https://doi.org/10.1016/j.epsl.2018.10.031

Building up a new mineral exploration indicator (MEI) system based on big data and AI technology

Junling Zhang[1], Huayong Chen[1*]
[1]Key Laboratory of Mineralogy and Metallogeny, Guangzhou Institute of Geochemistry, Chinese Academy of Sciences, Guangzhou 510640, China

Abstract: In this paper we present a new mineral exploration indicator system based on big data. It focusses on specific types of mineral deposits and is guided by ore-forming models, driven by AI, statistical analysis, and other algorithm libraries. It intelligently extracts and integrates multi-scale and multi-type exploration indicators to form a system that can automatically evolve with exploration activities. The new system is a bridge that connects big data for mineral exploration and accurate prospect prediction, and may be an effective tool for guiding exploration.

1 Introduction of MEI

The concept of a "mineral exploration indicator" (MEI) in this paper refers to the characteristic of exploration results obtained through variable mineral exploration methods that have a mineralization-indicating effect. It is the integration of prospecting signs and exploration methods, which can fully reflect the relationship between prospecting signs, exploration activities, and exploration methods.

MEI has three key features: (1) spatial features, i.e., all exploration indicators are associated with specific spatial locations; (2) exploration method, i.e., all exploration indicators are obtained through specific exploration activities, within a certain range of exploration scales, and through the use of certain exploration methods; and (3) mineralization-indicating effect, i.e., the essential features of all MEI is that they have direct or indirect mineralization-indicating effects.

2 Classification of MEI

MEI can be subdivided in detail according to different classification criteria such as exploration methods, mineralization-indicating effect, spatial dimensions, data types, exploration scales, and types of mineral deposits.

(1) According to the exploration methods, they can be divided into geological indicators, mineral indicators, geophysical indicators, geochemical indicators, remote sensing indicators. (2) According to the mineralization-indicating types, they can be classified into abundance indicators, proximity indicators, and anomaly indicators (Yousefi et al., 2019). (3) According to the spatial dimensions, they can be classified into one-dimensional indicators, two-dimensional indicators, three-dimensional indicators, and four-dimensional spatiotemporal indicators. (4) According to the information expression types, they can be divided into qualitative indicators, morphological indicators, and quantitative indicators. (5) According to different exploration scales, they can be classified into global indicators, mineralization domain indicators, metallogenic province indicators, metallogenic belt indicators, ore field indicators, and deposit indicators. (6) According to the types of mineral deposit, they can be classified into MEI for porphyry copper deposits, skarn-type deposits, ion-adsorption type rare earth deposit, orogenic gold deposit.

3 Extraction of MEI

The key point of the method for extracting MEI is to analyse and judge whether the exploration data has a mineralization-indicating effect. The extraction methods for different types of MEI have similarities but also significant differences.

The extraction method for abundance indicators mainly includes statistical analysis methods such as ore grade calculating and information quantity method. The extraction method for proximity indicators mainly includes adjacency analysis methods such as buffer zone analysis and nearest neighbour analysis, as well as distance field analysis method. The extraction method for anomaly indicators mainly includes traditional statistical methods, probability plot method, multivariate statistical methods, geological morphology analysis method, multifractal method, wavelet analysis method, machine learning method (Mokhtari and Sadeghi, 2021; Cracknell and Reading, 2014; Chen *et al.*, 2023). However, the extraction methods for anomaly indicators vary for different exploration methods, such as probability density distribution method and two-dimensional empirical mode method for extracting geophysical anomaly indicators, interference removal and principal component thresholding method for extracting remote sensing anomaly indicators.

4 Construction of MEI system

The mineralization-indicating effect of a single MEI is limited, and prospect prediction is a complicated process that requires the integration of multiple exploration indicators to form a system that can jointly improve the accuracy and precision of ore prediction. The MEI system proposed in this paper is a combination of multi-scale exploration indicators according to the type of ore deposit (Fig. 1).

Therefore, the MEI system consists of two major elements: (1) a set of multi-scale exploration indicators with different exploration scales, exploration methods, and deposit types; (2) integration methods for combining the exploration indicators in the system, which can be divided into knowledge-driven methods, data-driven methods (Yousefi et al., 2021), and AI-driven methods.

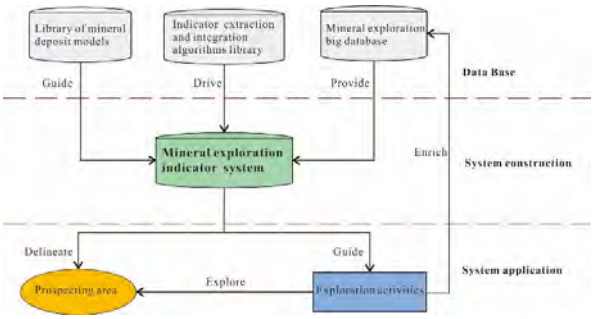

Fig. 1 The construction and application process of mineral exploration indicator system

The knowledge-driven method mainly relies on expert experience to drive the integration of indicators and is suitable for blind ore prediction in areas with low levels of mineral exploration and limited exploration data. It includes methods such as Boolean logic model, index overlay method, fuzzy logic model, and evidence belief method. The data-driven method mainly uses traditional data statistics algorithms to drive indicator integration. It is suitable for prediction in regions with high levels of exploration and rich exploration data. It includes methods such as statistical analysis, comprehensive information value method, evidence weight method, and Bayesian network classifier.

The AI-driven method mainly uses big data and artificial intelligence methods to drive indicator integration and is currently a hot and cutting-edge research topic, including methods such as logistic regression analysis, random forest method, support vector machine method, neural network method, and deep learning method (Barak et al., Wang et al., 2020; Chen et al., 2022; Roshanravan et al., 2023).

5 Future of MEI system

With the continuous development of the theoretical disciplines of ore deposits, mineral exploration, computer science, information science, and the continuous improvement of technologies such as big data, artificial intelligence, and exploration methods, the development of the MEI system research will also enter a new stage. The future research trend of the MEI system will generally develop from "simple dispersion" to "intelligent integration", which will be specifically manifested as: (1) the development of simple indicator towards complex indicator; (2) the development of two-dimensional indicator towards three/four-dimensional indicator; (3) the development of single-element indicator towards multi-element indicator; (4) the development of fuzzy indicator towards precise indicator; (5) the development of manual extraction indicator towards intelligent extraction indicator; and (6) the development of data-driven indicator integration towards intelligent-driven indicator integration.

Acknowledgements

This study was funded by the National Natural Science Foundation of China (42230810).

References

Barak, S., Imamalipour, A., Abedi, M., Bahroudi, A. and Khalifani, F.M. (2021): Comprehensive modeling of mineral potential mapping by integration of multiset geosciences data; Geochemistry, Mineral exploration: a journey from fieldwork, to laboratory work, computational modelling and mineral processing, V.81, P.125824.

Chen, G.X., Huang, N., Wu, G.P., Luo, L., Wang, D.T. and Cheng, Q.M. (2022): Mineral prospectivity mapping based on wavelet neural network and Monte Carlo simulations in the Nanling W-Sn metallogenic province; Ore Geology Reviews, V143, P.104765.

Chen, Z.Y., Xiong Y.H., Yin .BJ., Sun B.J. and Zuo R.G. (2023): Recognizing geochemical patterns related to mineralization using a self-organizing map; applied geochemistry, p.105621.

Cracknell, M.J. and Reading, A.M.(2014): Geological mapping using remote sensing data: A comparison of five machine learning algorithms, their response to variations in the spatial distribution of training data and the use of explicit spatial information; Computers & Geosciences, V.63,P. 22–33.

Mokhtari, Z. and Sadeghi, B. (2021): Geochemical anomaly definition using multifractal modeling, validated by geological field observations: Siah Jangal area, SE Iran; Geochemistry, Mineral exploration: a journey from fieldwork, to laboratory work, computational modelling and mineral processing, V.81, P.125774.

Yousefi, M., Kreuzer, O.P., Nykänen, V., Hronsky, J.M.A., (2019): Exploration information systems – A proposal for the future use of GIS in mineral exploration targeting; Ore Geology Reviews 111, 103005.

Roshanravan, B., Kreuzer, O. P., Buckingham, A., Keykhay-Hosseinpoor, M. & Keys, E. (2023): Mineral potential modelling of orogenic gold systems in the granites-tanami Orogen, Northern Territory, Australia: A multi-technique approach; Ore Geology Reviews, V.152, P.105224.

Xiong, Y.H. and Zuo, R.G. (2020): Recognizing multivariate geochemical anomalies for mineral exploration by combining deep learning and one-class support vector machine; Computers & Geosciences, V.140, P.104484.

Wang, J., Zuo, R.G. and Xiong, Y.H. (2020): Mapping Mineral Prospectivity via Semi-supervised Random Forest.; Natural Resources Research, V.29(1), P.189–202.

Yousefi, M., Carranza, E.J.M., Kreuzer, O.P., Nykänen, V., Hronsky, J.M.A. and Mihalasky, M.J. (2021): Data analysis methods for prospectivity modelling as applied to mineral exploration targeting: State-of-the-art and outlook.; Journal of Geochemical Exploration, V.229, P.106839.

Plate convergence, orogenic uplift, and tectonic preconditioning for giant porphyry copper formation in the central Andes

Alexander D. Farrar[1], Matthew J. Cracknell[1], David R Cooke[1], Thomas Schaap[1]
[1] Centre for Ore Deposit and Earth Sciences (CODES), University of Tasmania

Abstract. The central Andes is the world's highest altitude cordilleran mountain belt and contains nearly half the world's reserves of copper – a critical mineral for global clean energy technologies. While previous studies have debated the relative importance of deep-seated structural corridors, plate motion, and cordilleran development in the formation of porphyry copper deposits and the Andes, a formal, data-driven approach that assesses these relationships has not been undertaken. To address this gap, we conduct time-series and statistical analysis of published orogenic proxies in the central Andes and compare them to different plate convergence models. We identify both linear and causal tectonic processes that are occur prior to and simultaneously with the formation of these deposits. By identifying the most suitable plate motion models, we provide a novel perspective into the complex interplay between plate motion, orogenic uplift, and porphyry Cu mineralisation in the central Andes. Our data-driven results advance our understanding of how plate convergence and orogenic processes in the central Andes interact and provide insight into tectonic preconditioning processes that are required for the formation of giant porphyry copper ore deposits.

1 Introduction

The central Andes represents the type example of a cordilleran orogenic system. Because of this, there are a plethora of studies that have investigated the orogenic evolution of the central Andes, based on structural geology and basin evolution, petrology, geochronology, thermochronology, paleoelevation, seismology, and geodynamic modelling, and there have been many models produced for the plate tectonic motions of the Farallon-Nazca plate (NAZ) and South American plate (SAM). Given the myriad different models that exist for the tectonic evolution of the central Andes, how does one decide which model(s) are most the useful for further tectonic analysis related to porphyry mineralisation processes in the central Andes?

In this study, we employ data-driven analysis to compare competing plate motion models to orogenic processes in the central Andes since the late Cretaceous using the Pearson correlation coefficient (r), and we apply Granger causality, a robust method for identifying causal linkages between time-series variables that exhibit temporal lag. Granger causality has been widely employed in economic, medical, and climatic studies, however, its application in geology has remained largely unexplored. Using Granger causality, we investigate temporal linkages between plate convergence parameters and orogenic variables, and we assess their statistical correspondence.

Our data-driven method yields critical insight into the relationships between plate tectonic and cordilleran orogenic processes, including the necessary tectonic conditions for metallogenic episodes, which form giant porphyry copper deposits (PCDs; >3 Mt contained Cu) at the intersections of continental-scale structural corridors during high strain episodes (Farrar et al. In Press).

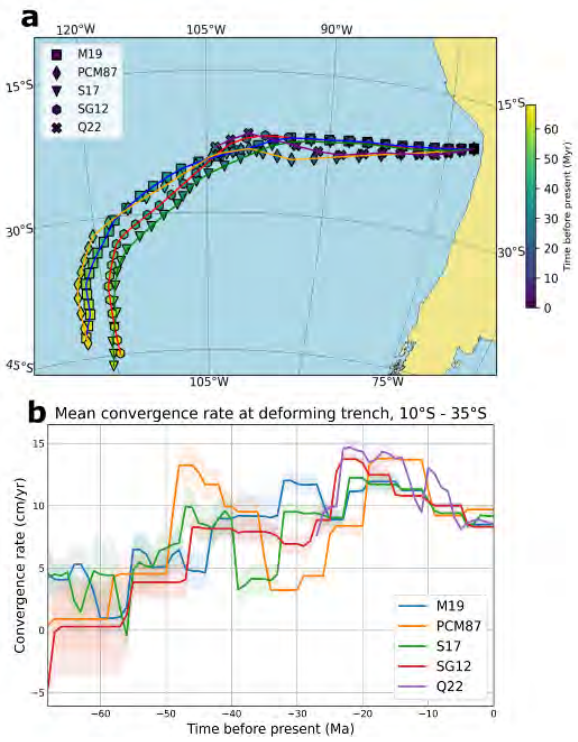

Figure 1. a) Retro-projected trajectory for a point on the Nazca plate relative to South America. We selected a seed point that is currently entering the trench at 20°S and retro-projected it to 68 Ma, using the five plate models analysed in this study (see Methodology). b) Mean convergence rate per Myr along the trench for each plate motion model, shading represents one standard deviation of the mean.

2 Methodology

Five plate tectonic motion models representing a diversity of available models for SAM-NAZ convergence (Pardo-Casas and Molnar 1987; Somoza and Ghidella 2012; Schepers et al. 2017; Müller et al. 2019; Quiero et al. 2022; hereafter referred to as PCM87; SG12; S17; M19; Q22; Figure 1) were output from pyGPlates in 1 Myr age bins. Linear correlation analysis of these models

was conducted at 1 Myr temporal intervals. The mean and standard deviation of convergence obliquity and convergence rate for each plate tectonic motion model, every 1 Myr was calculated for each trench sample point.

Time-series data representing orogenic proxies for the central Andes since the Late Cretaceous were compiled (Figure 2). These consist of paleoelevation of geomorphological domains (Boschman 2021) tectonic stress (Sr/Y) and crustal thickening (La/Yb) proxies from unaltered volcanic rocks (Loucks 2021), flat slab subduction events (Ramos and Folguera 2009) and exhumation rate history (Stalder et al. 2020) and the cumulative contained Cu associated with giant porphyry copper deposits (this study) per metallogenic epoch (Sillitoe and Perello 2005), Figure 3).

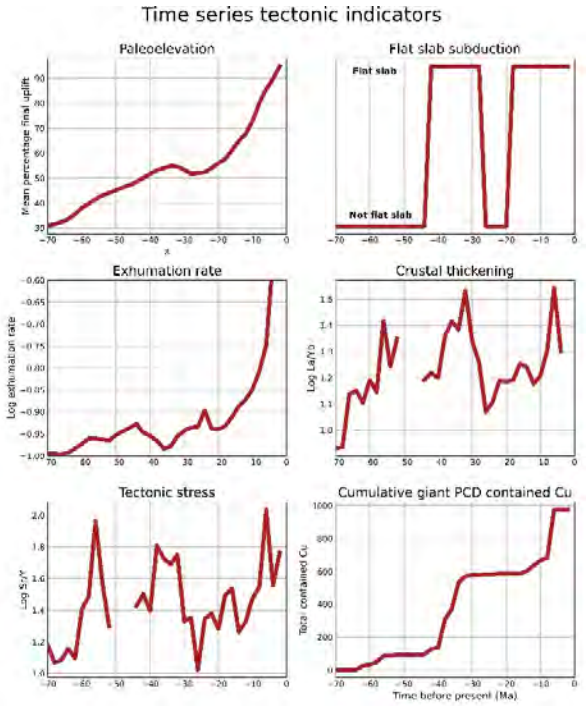

Figure 2. Time series tectonic indicators

To enable a direct temporal comparison of orogenic and plate tectonic datasets, we binned model proxies into two-million-year time intervals for linear correlation analysis (Figure 4) and G-causality analysis (Figure 5). Due to positive skewness in Sr/Y, La/Yb, and exhumation data, we log10 transformed these variables, resulting in approximately Gaussian distributions. We conducted autocorrelation and Augmented Dickey Fuller (ADF) tests on the time series datasets using the python statsmodels ADF package and we performed the G-causality tests using the statsmodels grangercausalitytests package in Python (Seabold and Perktold 2010).

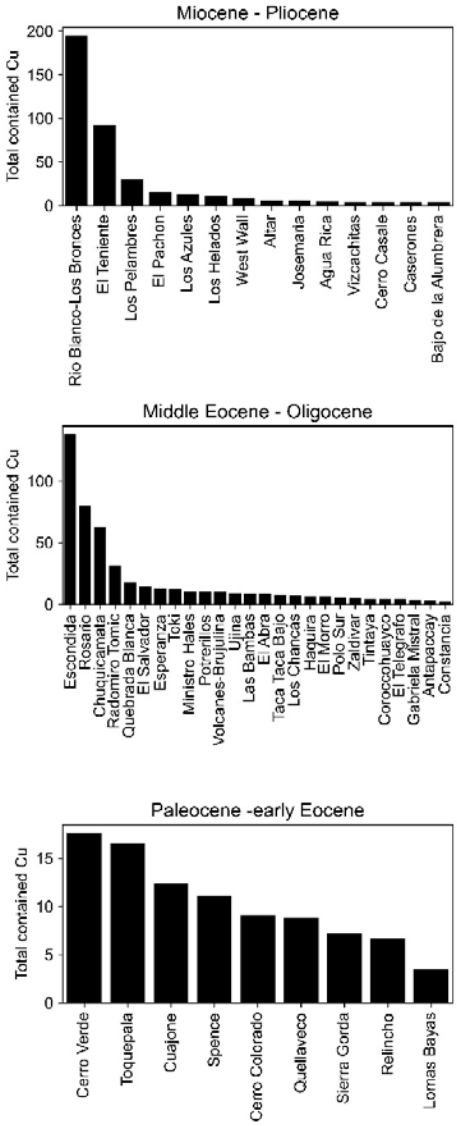

Figure 3. Pareto charts of the total contained Cu of giant porphyry copper deposits, per Cenozoic metallogenic epoch (Sillitoe and Perello 2005) in the central Andes.

3 Results

3.1 Linear correlation analysis

Our investigation of orogenic proxy pairs demonstrates significant positive correlation (r > 0.7) between tectonic stress and crustal thickening as well as between exhumation rate and paleoelevation (Figure 4). These results indicate that as tectonic stress increases, so does crustal thickening, and changes in paleoelevation are broadly synchronous with changes in exhumation rate. These results are consistent with visual analysis of Figure 3, which illustrates the cyclic nature of crustal thickening processes over the temporal range.

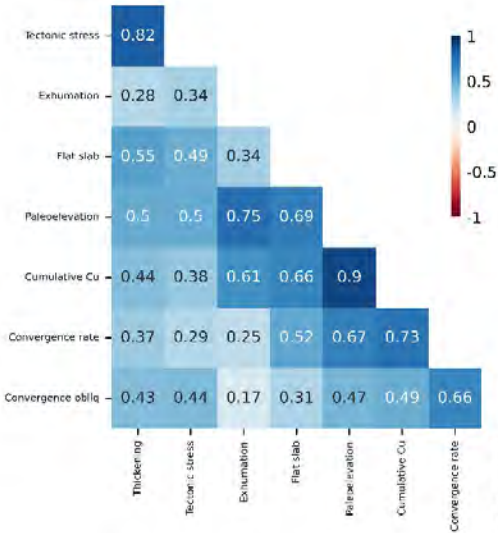

Figure 4. Pearson correlation of the means of orogenic proxies, SG12 convergence rate, PCM87 convergence obliquity, cumulative giant PCD tonnage, since 70 Ma.

Incorporating plate convergence parameters and cumulative Cu tonnage allows for the simultaneous assessment of non-orogenic proxies. Figure 4 shows that paleoelevation and cumulative Cu tonnage exhibit a significant linear relationship (r = 0.9) and convergence rate and cumulative Cu tonnage are also significantly linearly correlated (r = 0.73; Figure 5).

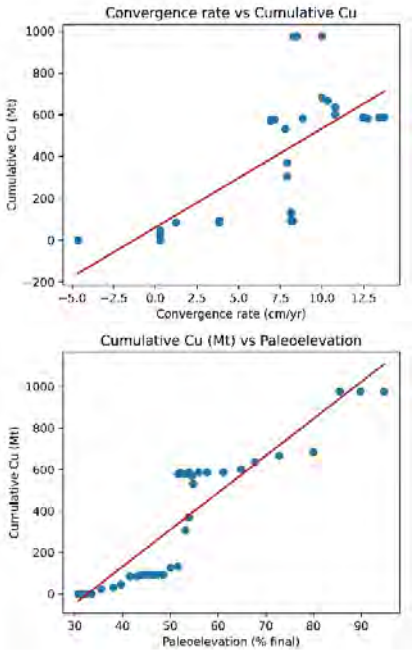

Figure 5. Scatter plots of cumulative Cu tonnage and Paleoelevation against SG12 convergence rate. Red line is the linear correlation coefficient for each pair.

3.2 Granger causality

Our investigation using Granger causality analysis (Figure 6) revealed several significant lagged causal relationships that were not detected in the linear correlation analysis for the orogenic proxies (Figure 4). These relationships include a causal effect of crustal thickening on paleoelevation, exhumation rate, and flat slab state, as well as a feedback loop where paleoelevation and exhumation rate both affect crustal thickening. Our results also indicate that changes in tectonic stress drive variations in paleoelevation, exhumation rate, and crustal thickening, while flat slab subduction leads to increased paleoelevation and exhumation rate.

Incorporating the five plate motion models to the G-causality analysis with the orogenic uplift proxies enables us to investigate causal relationships between plate motion and orogenesis. The results showed whilst many models exhibit causal linkages with orogenic proxies, the SG12 convergence rate model exhibits 7 causal linkages with orogenic proxies, indicating its suitability for further metallogenic analysis.

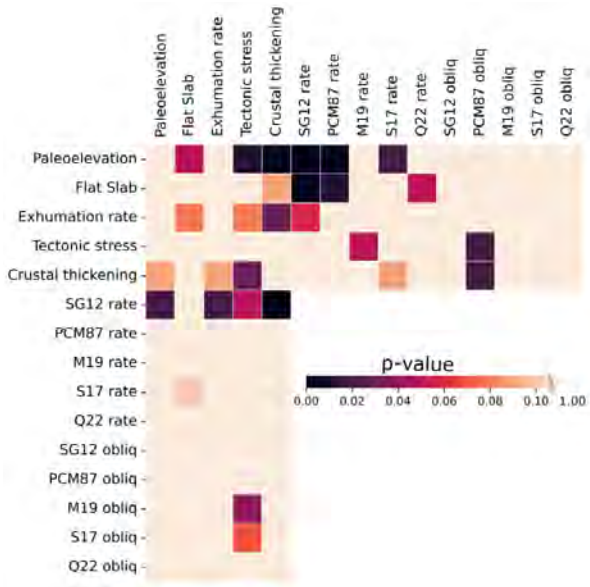

Figure 6. G-causality matrix of plate motion and orogenic proxy pairs. H_0 = x-axis variable does not G-cause the y-axis variable, H_0 is rejected if p-value of the F-test <0.10. p-values of variable pairs, non-background-colored intersections represent variable pairs that exhibit statistically significant G-causality (p-value < 0.10).

The SG12, PCM87, and S17 convergence rate models were found to strongly G-cause paleoelevation responses, while the SG12, PCM87, and Q22 models G-caused flat slab events. Additionally, the SG12 model was found to G-cause exhumation, while the M19 model was found to G-cause tectonic stress. Interestingly, the orogenic proxies themselves were found to exhibit strong causality on SG12 convergence rate, with paleoelevation, exhumation rate, crustal thickening and tectonic stress proxies all exhibiting feedback

with SG12 (Figure 6). The PCM87 convergence obliquity was found to strongly G-cause changes in crustal thickening and tectonic stress proxies and was thus defined as the most useful convergence obliquity model (Figure 6).

4 Conclusions

Our study provides a novel approach for the evaluation of plate motion models based on their relationship with convergent margin tectonics. Our data driven analysis shows that there is a significant linear relationship between increasing Cu tonnage in metallogenic epochs and increasing rate of convergence and increasing Andean elevation. There are also lagged correlations that are not able to be determined by linear analysis alone. By determining the direction of temporally lagged variables using Granger causality analysis, causal relationships between plate motion and orogenic processes can be detected that are not identified using linear correlation techniques.

Future research will build on this tectonic process model, as well as incorporating the best correlated plate motion models with orogenic proxies, to examine the causal spatial and temporal relationships between giant PCDs and plate tectonic processes in the central Andes.

Acknowledgements

This research forms part of a PhD by AF at the University of Tasmania (CODES). AF acknowledges the financial support provided by First Quantum Minerals to carry out this research. We thank G. Begg and J. Hronsky for discussions that improved this study.

References

Balázs, A., Faccenna, C., Ueda, K., Funiciello, F., Boutoux, A., Blanc, E. J. P., and Gerya, T., 2021, Oblique subduction and mantle flow control on upper plate deformation: 3D geodynamic modeling: Earth and Planetary Science Letters, v. 569.

Boschman, L. M., 2021, Andean mountain building since the Late Cretaceous: A paleoelevation reconstruction: Earth-Science Reviews, v. 220.

DeCelles, P. G., Ducea, M. N., Kapp, P., and Zandt, G., 2009, Cyclicity in Cordilleran orogenic systems: Nature Geoscience, v. 2, p. 251-257.

Farrar, A. D, Cooke, D. R., Hronsky, J. M. A., Wood, D. G., Benavides, S. B., Cracknell, M. J., Banyard, J. F., Gigola, S., Ireland, T., Jones, S. M., Piquer, J., (In Press) A model for the lithospheric architecture of the central Andes and the localization of giant porphyry copper deposit clusters. Economic Geology.

Iaffaldano, G., Bunge, H.-P., and Dixon, T. H., 2006, Feedback between mountain belt growth and plate convergence: Geology, v. 34.

Loucks, R. R., 2021, Deep entrapment of buoyant magmas by orogenic tectonic stress: Its role in producing continental crust, adakites, and porphyry copper deposits: Earth-Science Reviews, v. 220.

Meade, B. J., and Conrad, C. P., 2008, Andean growth and the deceleration of South American subduction: Time evolution of a coupled orogen-subduction system: Earth and Planetary Science Letters, v. 275, p. 93-101.

Müller, R. D., Zahirovic, S., Williams, S. E., Cannon, J., Seton, M., Bower, D. J., Tetley, M. G., Heine, C., Le Breton, E., Liu, S., Russell, S. H. J., Yang, T., Leonard, J., and Gurnis, M., 2019, A global plate model including lithospheric deformation along major rifts and orogens since the Triassic: Tectonics, v. 38, p. 1884-1907.

Pardo-Casas, F., and Molnar, P., 1987, Relative motion of the Nazca (Farallon) and South American plates since Late Cretaceous time: Tectonics, v. 6, p. 233-248.

Quiero, F., Tassara, A., Iaffaldano, G., and Rabbia, O., 2022, Growth of Neogene Andes linked to changes in plate convergence using high-resolution kinematic models: Nat Commun, v. 13, p. 1339.

Ramos, V. A., and Folguera, A., 2009, Andean flat-slab subduction through time: Geological Society, London, Special Publications, v. 327, p. 31-54.

Schepers, G., van Hinsbergen, D. J. J., Spakman, W., Kosters, M. E., Boschman, L. M., and McQuarrie, N., 2017, South-American plate advance and forced Andean trench retreat as drivers for transient flat subduction episodes: Nat Commun, v. 8, p. 15249.

Seabold, S., and Perktold, J., 2010, Statsmodels: Econometric and statistical modeling with python: Proceedings of the 9th Python in Science Conference, 2010, p. 10.25080.

Sillitoe R, Perello J (2005) Andean copper province: Tectonomagmatic settings, deposit types, metallogeny, exploration, and discovery. Economic Geology 100th Anniversary Volume 100:845-890.

Somoza, R., and Ghidella, M. E., 2012, Late Cretaceous to recent plate motions in western South America revisited: Earth and Planetary Science Letters, v. 331, p. 152-163.

Stalder, N. F., Herman, F., Fellin, M. G., Coutand, I., Aguilar, G., Reiners, P. W., and Fox, M., 2020, The relationships between tectonics, climate and exhumation in the Central Andes (18–36°S): Evidence from low-temperature thermochronology: Earth-Science Reviews, v. 210.

Suárez, R. J., Guillaume, B., Martinod, J., Ghiglione, M. C., Sue, C., and Kermarrec, J.-J., 2022, Role of convergence obliquity and inheritance on sliver tectonics: Insights from 3-D subduction experiments: Tectonophysics, v. 842.

The importance of hierarchical data structures for the interpretation of mineral trace-element data

Max Frenzel[1]
[1]*Helmholtz-Zentrum Dresden-Rossendorf, Institute Freiberg for Resource Technology, Germany*

Abstract. Recent years have seen a sharp increase in the generation and use of mineral trace-element data in geological research. However, while much new data is being generated and published, relatively little work has been done to develop appropriate methods for statistical analysis and interpretation. Several characteristic features of mineral trace-element data require careful consideration during evaluation and interpretation to avoid biased results. In particular, the generally hierarchical structure of the data must be considered. Unfortunately, this is not done in most current studies. This contribution provides a brief overview of what hierarchical data structures are, and what consequences they have for statistical analysis and data interpretation.

1 Introduction

Modern laser ablation inductively coupled plasma mass spectrometry (LA-ICP-MS) systems enable the rapid, spatially resolved collection of mineral trace-element data at relatively high sensitivity and low cost. This has led to their widespread use in geological research (Sylvester and Jackson 2016).

Unfortunately, the accompanying increase in the generation and use of mineral trace-element data has not been accompanied by a commensurate increase in understanding of how best to use and interpret it. Specifically, the time lag between the capabilities for data generation and interpretation seems to be chiefly due to a lack of appreciation by many workers for the key mathematical features of the data and their consequences for statistical analysis.

While the requirements arising from the compositional nature of trace-element have already been discussed in detail elsewhere (van den Boogaart and Tolosana-Delgado 2013, Frenzel et al. 2016), this contribution focusses on hierarchical data structures. After a short description of what is meant by this term, different approaches for dealing with these data structures are described. An example is then given to illustrate the biases that may be introduced into the analysis of a dataset by ignoring them. Finally, recommendations are made for future work.

2 What are hierarchical data structures?

In hierarchical data structures, each datapoint is characterized by multiple attributes, each referring to a different level of organization. In mineral trace-element datasets, such data structures typically arise from both the nature of the data as well as the sampling and analysis processes (Dimitrijeva et al. 2018, Godefroy-Rodriguez et al. 2020).

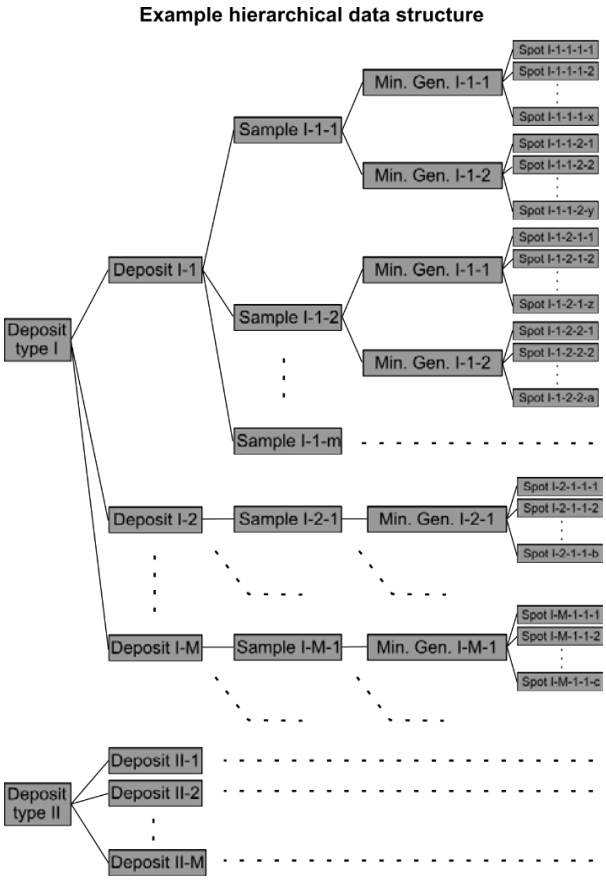

Figure 1. Example hierarchical data structure for mineral trace-element data collected on different deposit types. A more detailed description is provided in the main text.

For example, in a high-level LA-ICP-MS study each data point may be described by the following attributes, in order of increasing level of organization: “analysis spot” < “mineral generation” (if several are present) < “sample” < “deposit” < “deposit type”. This is also illustrated in Fig. 1 and has several consequences for the expected mathematical properties of the data.

Most importantly, one would expect two datapoints from such a dataset to be more similar, the more attributes they have in common. That is, two datapoints from the same sample and same mineral generation would be expected to be more similar than two points from different samples but from within the same deposit, which would in turn be expected to be more similar than datapoints collected on samples from different deposits, and so on. The chief reason for this is that the further two datapoints are separated in the data hierarchy, the further they are also separated in space and time,

and the greater should be the differences in the geological conditions they reflect.

One can mathematically express these ideas by a formula describing the observed variability in trace-element concentrations in terms of the different effects caused by differences at each of the hierarchical levels. For the data structure described above and shown in Fig. 1, one may write:

$$\log\left(c^A_{ijklmn}\right) = Ref^A + Type^A_i + Deposit^A_{ij} + Sample^A_{ijk} + Generation^A_{ijl} + \varepsilon^A_{ijklm} \quad (1)$$

Where c^A_{ijklmn} is the concentration of trace-element A measured in analysis spot m, in mineral generation l on sample k, from deposit j, belonging to deposit type i; Ref^A is a reference value for the concentration of A, e.g., a global mean; $Generation^A_{ijl}$ is the mean effect of mineral generation l in deposit j in district i on $log(c^A)$, expressed as an additive value, and corrected for variations between samples, deposits, and deposit types; $Sample^A_{ijk}$ is the mean effect of sample k in deposit j of type i, and so on. Finally, ε^A_{ijklm} is the residual value of the specific analysis spot. Note that this description assumes that the identified mineral generations are only consistently identifiable within the same deposit ij, and that the effects of the different factors, or hierarchical levels are statistically independent. Alternative models are possible, where consistent identification of mineral generations is feasible over smaller or larger scales, and where interactions between the different factors occur (cf. Winter 2013, Dmitrijeva et al. 2018).

If one assumes that the dataset is balanced, i.e., the same number of observations are available for each unique combination of the different attributes, then the total variance of the observed data following model (1) would be:

$$var\left[\log\left(c^A_{ijklmn}\right)\right] = var\left(Type^A_i\right) + var\left(Deposit^A_{ij}\right) + var\left(Sample^A_{ijk}\right) + var\left(Generation^A_{ijl}\right) + var\left(\varepsilon^A_{ijklm}\right) \quad (2)$$

This is just another way of expressing the ideas described above, namely, that knowing the value of one measurement with a set of attributes $ijklm$ already narrows the expected range of values for the next measurement with the same, or some of the same attributes. This may seem obvious to most geologists. However, it has dramatic consequences for the statistical analysis of the data. Namely, it means that individual datapoints are not expected to be statistically independent (cf. Dmitrijeva et al., 2018). Nor is it obvious that individual sets of observations $ijklmn$ can be assumed to be identically distributed, i.e., to follow the same probability distribution. For instance, the mean effects of the samples, $Sample^A_{ijk}$, within one deposit should have different mean and variance than those from the next deposit, resulting in a different distribution of the corresponding $log(c^A)$.

However, both statistical independence and identical distribution (iid) are key assumptions in virtually all statistical methods. To further complicate matters, mineral trace-element data is often unbalanced, i.e., different numbers of observations are available for each specific combination of attributes. The combination of these features means that standard statistical methods cannot be sensibly applied to the raw spot data. Biases are introduced into data analysis if this is done, as illustrated below.

Finally, we note that hierarchical data structures and unbalanced datasets also occur frequently in other areas of geochemistry. Some attention had been paid to this in the past, e.g., in the hierarchical estimation of Clarke values describing crustal abundances (Ketris and Yudovich, 2009). However, this has unfortunately not entered universal practice.

3 Dealing with hierarchical data

To sensibly apply standard statistical methods to hierarchically structured data, one must find a way to modify this data such that the iid assumption generally required for data analysis is satisfied. This can be achieved by aggregation of the data to the hierarchical level relevant for the analysis.

Consider the case where one is interested in the differences in trace-element signatures between deposit types for a dataset with the same structure as our example in Fig. 1. The relevant hierarchical level for analysis would be that of individual deposits. The mean trace-element concentrations for the deposits can relatively safely be assumed to be independent from each other and follow a simple probability distribution, i.e., to be iid. The main task then is to infer the probability distribution of deposit means for each deposit type from the available data and use this to answer any question(s).

Different methods exist to achieve the necessary aggregation of the data to the desired hierarchical level. In the present example, the simplest way of doing so would be to compute hierarchical means for the individual deposits and use these means for further analysis (cf. Ketris and Yudovich, 2009). Hierarchical computation in this case would mean, that the mean for each mineral generation on each sample is first calculated from individual analysis spots, then the mean for each sample is estimated from the means per mineral generation, and finally the deposit mean is calculated from the sample means (cf. Fig. 1). This removes the biases due to the different numbers of observations available from each sample, deposit, generation etc.

However, this approach is cumbersome. The unbalanced nature of the data also means that some hierarchical means are more uncertain than others, i.e., means will generally be more certain for deposits where more samples were taken. This can be dealt with in the further statistical analysis by giving weights to each of the means to reflect its uncertainty. However, the relevant uncertainties themselves are not always easy to quantify, particularly where only single observations are

available, e.g., where only one sample has been taken for a given deposit. Such cases are in fact relatively common (cf. Frenzel et al. 2016).

A more sophisticated way of performing the hierarchical estimation of mean values and the corresponding uncertainties is to fit a model of the form of eq. (1) to the data. The relevant class of models for this purpose are linear mixed effects (LME) models (Winter, 2013; Dmitrijeva et al., 2018). These models can be used to simultaneously make unbiased estimates of the mean effects (including uncertainties) of the different attributes at each hierarchical level. Such estimates can then be used in further data analysis.

In fact, LME models are much more versatile than this, and can be used to analyse many different problems. Where the capabilities of LME models are suitable to address a specific question, it is therefore best to apply them directly to a given dataset. This may remove the need for cumbersome hierarchical aggregation of the data prior to analysis.

4 Effects of ignoring hierarchical data structures

Disregard for hierarchical data structures is typically expressed in mineral trace-element studies by the treatment of individual datapoints from the lowest hierarchical level of a dataset as iid observations. Thus, in an LA-ICP-MS dataset all individual spot measurements belonging to one deposit type may be taken to represent this type, regardless of how many deposits the data covers, or how many samples were analysed per deposit.

What does this do to the analysis and interpretation of the data? It will have two major effects. First, it will suggest that there are far greater numbers of independent observations, and thus greater statistical power, than are actually present in the dataset. Second, it will introduce bias into the analysis whenever the data is unbalanced, i.e., nearly always. Finally, it will introduce artefacts to the shapes of the observed data distributions. These effects are illustrated graphically in Figure 2 using an example from the literature.

Figure 2a shows a PCA biplot from Bélissont et al. (2014) indicating different “fields” of sphalerite composition for different types of Pb-Zn deposits, based on a “large” set of LA-ICP-MS point analyses. On the other hand, Fig. 2b shows the same data reduced to its relevant hierarchical level, i.e., the hierarchical means for individual deposits, including their associated uncertainties. Several features are apparent from this comparison.

First, the data distribution in Fig. 2a shows many blob-like features, or clusters. Second, each of these clusters appears to be defined by many datapoints. Since the statistical power of a dataset increases with $1/\sqrt{n}$ (think of the standard error of the mean), where n is the number of available iid observations, Fig. 2a would suggest that such complex distributional shapes reflect the real distribution of the data for the different deposit types. For instance, if one was to analyse a new sample from another MVT deposit not represented in the original dataset, surely it would plot inside one of the MVT fields delineated in Fig.2a.

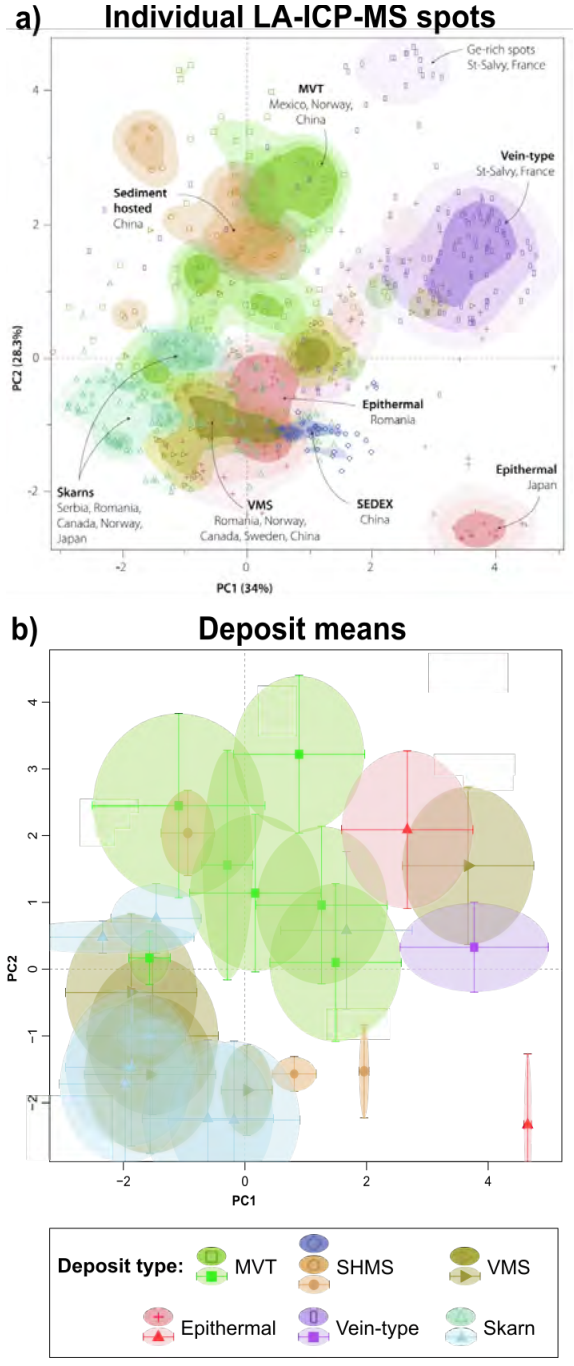

Figure 2. Graphical illustration of the typical effects of treating individual LA-ICP-MS analysis spots as independent observations: a) reproduction of Fig. 13c of Bélissont et al. (2014), a PCA-biplot of several hundred individual analysis spots of sphalerite from different types of Pb-Zn deposits; b) reconstruction of a) showing deposit means and associated 95% confidence intervals. Note that the somewhat imperfect reconstruction in panel b) is chiefly due insufficient documentation in Bélissont et al. (2014) regarding the assumptions made to run PCA. They do not describe whether they used scaled or unscaled input variables, nor how they treated missing values (i.e., below detection limit or missing at random).

In fact, nothing could be further from the truth. As Fig. 2b shows, most of the clusters observed in Fig. 2a in fact appear to reflect individual deposits, although the reconstruction is not perfect (cf. explanation in figure legend). This reduction also highlights how very few iid observations are really available. The total number of deposits in the dataset is only 26. That is, the statistical power of the dataset is in fact so low, that no reliable distinction between deposit types is possible. This clearly illustrates the major effect of ignoring hierarchical data structures: it creates overconfidence in potentially biased results.

4.1 Overfitting of data by ML methods

A specific type of overconfidence in erroneous results occurs when disregard for hierarchical data structures (and sometimes other features) is coupled to the use of machine learning (ML) methods, e.g., for classification problems. As illustrated in Fig. 2a, disregard for hierarchical data structures will generally create datasets with apparently complex, clustered data distributions. ML methods are excellent at picking out the irregular, high-dimensional boundaries between such clusters for classification or regression purposes (Bishop 2006). Thus, any ML models fitted to such data will generally have a much greater degree of complexity than is justified by the true nature of the data.

To make matters worse, the false assumption that individual observations are iid also short-circuits the key quality-control measure typically used to assure the reliability of the ML results: application of the fitted model to a test dataset randomly subsampled from the original data, and therefore assumed to be independent of it. However, because the test data will again contain only individual spot analyses, which must necessarily come from the same clusters already included in the training data (samples/deposits), the assumption of independence will be violated. Thus, the apparent classification accuracy is usually greatly overestimated, providing exaggerated confidence in the potentially flawed results.

While this may seem like a rather specialized issue, the recent surge in the popularity of both ML methods and mineral trace-element data has led to the publication of many articles suffering from this problem (e.g., Sun and Zhou 2022, Li et al. 2023). Given the potentially complex interactions between high-dimensional data structures and the classification algorithms typically used (random forests, neural nets etc.), it is difficult to say which of the results reported in such studies are reliable.

5 Conclusions and future work

Hierarchical data structures are currently ignored by most workers using mineral trace-element data. This introduces biases into data analysis and may result in conclusions that are not justifiable given the data. To avoid such issues in the future, appropriate methods must be used for data analysis. Hierarchical aggregation and the use of LME models for data analysis both provide adequate approaches. In fact, the use of these methods offers significant potential for interesting discoveries regarding the nature and causes of the often-substantial variance observed in the trace-element signatures of many of the common and less-common minerals occurring in mineral deposits. Specifically, the quantitative understanding of the variance structure of the data via LME models may be useful in this regard (e.g., Dmitrijeva et al. 2018, Frenzel et al. 2022).

Acknowledgements

I would like to thank all those colleagues, particularly Raimon Tolosana-Delgado, Marija Dmitrijeva, Nigel Cook, and others from Freiberg, Adelaide, and elsewhere, who have over the past 10 years made significant contributions to my understanding of this research area by many fruitful, though sometimes heated, discussions. Without their intellectual input, I would not have been able to write this contribution.

References

Belissont R, Boiron M-C, Luais B, Cathelineau M (2014) LA-ICP-MS analyses of minor and trace elements and bulk Ge isotopes in zoned Ge-rich sphalerites from the Noailhac – Saint-Salvy deposit (France): Insights into the incorporation mechanisms and ore deposition processes. Geochim Cosmochim Acta 126:518-540.

Bishop CM (2006) Pattern recognition and machine learning. Springer, New York, 738 p.

Dmitrijeva M, Metcalfe AV, Ciobanu CL, Cook NJ, Frenzel M et al. (2018) Discrimination and variance structure of trace element signatures in Fe-oxides: a case study of BIF-mineralisation from the Middleback Ranges, South Australia. Math Geosci 50:381-415.

Frenzel M, Hirsch T, Gutzmer J (2016) Gallium, germanium, indium, and other minor and trace elements in sphalerite – A meta-analysis. Ore Geol Rev 76:52-78.

Frenzel M, Voudouris P, Cook NJ, Ciobanu CL, Gilbert S, Wade BP (2022) Evolution of a hydrothermal ore-forming system recorded by sulfide mineral chemistry: A case study from the Plaka Pb-Zn-Ag deposit, Lavrion, Greece. Miner Depos 57:417-438

Godefroy-Rodriguez M, Hagemann S, Frenzel M, Evans NJ (2020) Laser ablation ICP-MS trace element systematics of hydrothermal pyrite in gold deposits of the Kalgoorlie district, Western Australia. Miner Depos 55:823-844

Ketris MP, Yudovich YaE (2009) Estimations of Clarkes for carbonaceous biolithes: World averages for trace element contents in shales and coals. Int J Coal Geol 78:135-148.

Li X-M, Zhang Y-X, Li Z-K, Zhao X-F, Zuo R-G et al. (2023) Discrimination of Pb-Zn deposit types using sphalerite geochemistry: New insights from machine learning algorithm. Geosci Front 14:101580.

Sun G-T, Zhou J-X (2022) Application of machine learning algorithms to classification of Pb-Zn deposit types using LA-ICP-MS data for sphalerite. Minerals 12:1293.

Sylvester PJ, Jackson SE (2016) A brief history of laser ablation inductively coupled plasma mass spectrometry (LA-ICP-MS). Elements 12:307-310.

Van den Boogaart KG, Tolosana-Delgado R (2013) Analyzing compositional data with R. Springer, Berlin, 258 p.

Winter B (2013) Linear models and linear mixed effects models in R with linguistic applications. arXiv preprint https://arxiv.org/abs/1308.5499.

The role of data science in modern mineral exploration and mining: adding machine learning tools to the geoscientist's toolbox

Dina Klimentyeva[1], Britt Bluemel[1], McLean Trott[1]
[1] ALS GoldSpot Discoveries Ltd., Vancouver, Canada

Abstract. Geodatascience is an emerging field that combines traditional geoscience expertise with the (data) science of artificial intelligence and machine learning. The pace and volume of data acquisition is rapidly increasing in mineral exploration campaigns, at mining operations, and in near-mine environments, leading to the accumulation of large datasets that can be challenging to process and interpret using conventional methods. Machine learning and data science techniques add speed and consistency to interpretation of large datasets, aid in the amalgamation of new and historic datasets, and facilitate the integration of disparate data types with varying resolutions. All these factors help shorten the gap between discovery and development, and companies across the entire mining value chain, in a variety of commodities, are realizing the value of incorporating machine learning workflows and machine-assisted modelling to assist in the discovery and development of ore bodies.

1 Machine learning in mineral exploration and mining

1.1 Significance of ML tools for exploration

Machine learning (ML) and data science are increasingly gaining acceptance as exploration tools, with applications ranging from core image analysis (Acosta et al. 2019), prospectivity mapping (Carranza 2010, Sun et al. 2019) to chemostratigraphy (Bluemel 2021), and large language models helping to query the corpus of geoscientific literature (Deng et al. 2023).

1.2 Practical applications of machine learning for exploration

The most important components of any successful mineral exploration campaign are a robust geological map and a realistic geological model that represent the synthesis of field observations with interpretations from fundamental datasets such as geochemistry, mineralogy, and geophysics.

1.3 Interpretability of ML results

To integrate traditional geological interpretations with results obtained from ML models, it is necessary to understand the entire ML process from start to finish. This includes selecting fit-for-purpose data types, choosing appropriate transformations and data pre-processing, and utilizing appropriate algorithms. The results must then be critically evaluated and integrated with geological insights and field observations, to ensure the final result most closely resembles geological reality.

1.4 Linking ML results with geological reality

We can pinpoint several examples where machine learning algorithms can be easily interpreted and linked to geological insights, thereby providing a good starting point for increased acceptance and adoption of machine learning processes in exploration, for example:

- Dimensionality reduction applied to geochemical data extracts insights about different styles of mineralization. For instance, principal component analysis (PCA), which is a dimensionality reduction technique, allows the integration of statistics with geology by illustrating which geochemical elements exhibit similar behaviour, thereby adding clarity to the interpretation of datasets from new jurisdictions.

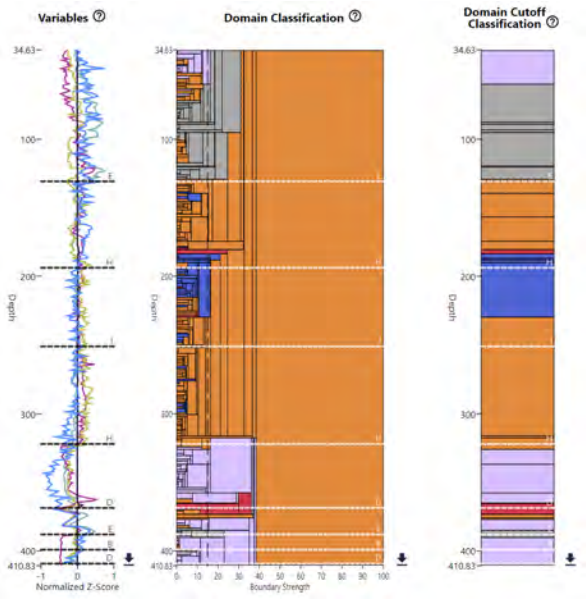

Figure 1. Drillhole domaining based on geochemistry, using Al (blue), Hf (dark blue), Ti (navy blue), Y (violet), Zr (dark red) and Nb (light green) as input signals. Zr and Hf curves are overlapping. Colours of the domains refer to inferred geological units. The dataset is processed by the ALS Goldspot Tessellation app (https://tessellation.app.goldspot.ca/), with dataset of Halley (2020) as an example

- Drillhole domaining based on geochemical information (Fig. 1). By selecting relevant

input signals, it is possible to routinely classify drillhole samples for the purpose of defining lithology, alteration, or mineralization styles.

- Reconciliation of clustering results and logged lithology or alteration labels (Fig. 2) helps derive objective criteria which can be utilized by logging geologists to differentiate and classify rock types and alteration assemblages,
- Assessment of relative importance of geochemical signal for the prediction of stratigraphy (Fig. 3) by calculating and plotting the SHapley Additive exPlanations (SHAP) values. The SHAP values represent the importance of each feature and are calculated by comparing the model's predictions with and without the involvement of each input variable (Lundberg et al. 2020). The comparison of SHAP values for different input variables can assist in selecting the most fit-for-purpose assay techniques

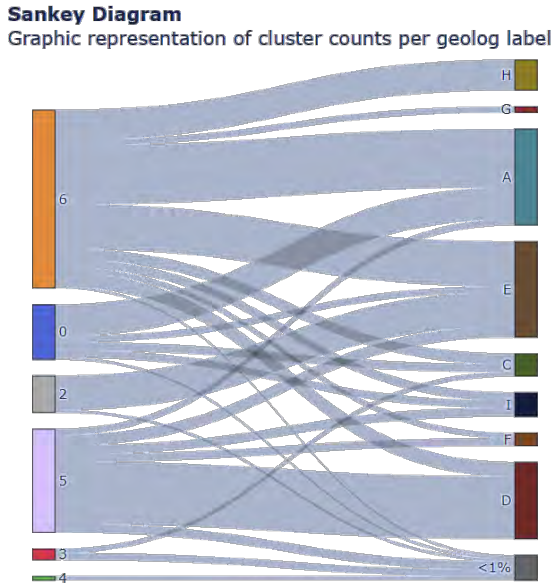

Figure 2. Relating geochemical information (left, also illustrated in the downhole plot of Figure 1) to logged alteration labels (right), using Al, Hf, Ti, Y, Zr and Nb as input signals. The dataset is processed by the ALS Goldspot Tessellation app (https://tessellation.app.goldspot.ca/), with dataset of Halley (2020) as an example

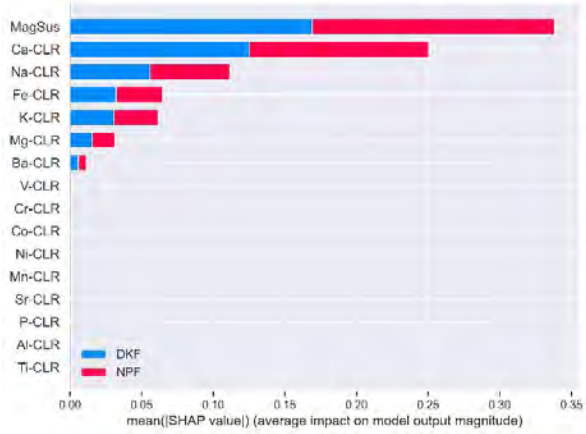

Figure 3. Defining a quantitative metric for the importance of geochemistry for predicting the stratigraphy (SHAP curve). Centred log-ratio transformed geochemical data and magnetic susceptibility (MagSus) were used as the model's inputs

1.5 Data limitations and considerations

Machine learning techniques are becoming more prevalent as computational costs continue to lower, and traditional barriers to entry like the necessity of in-depth knowledge of an object-oriented programming language (such as Fortran, C++, or Python) are overtaken by the rapid increase of the availability of GUI-based applications, such as Orange Data Mining. It is now possible to create robust ML models that can produce accurate results by memorizing the input data, and this creates the illusion of a good fit to the test dataset, but lacks the capacity to be successfully deployed and generalize to the new data! However, the diligent data scientist can recognize that these high accuracies are the result of data leakage and model overfitting.

By understanding the limitations of machine learning algorithms, and combining robust exploratory data analysis, transparent scaling and transformation procedures, we can ensure the successful deployment of many state-of-the-art ML techniques. Meticulous attention to cataloguing of metadata, consistent logging of categorical variables, and robust treatment of missing data can ensure that the data is fit-for-purpose, and properly cleaned and homogenized before use in the machine learning model. The resulting model is robust and flexible, and produces realistic results that are more easily interpretated.

2 Case study

This presentation will showcase various tools, techniques, and case studies where Artificial Intelligence, Data Science, and expert geoscientific approaches are combined to add understanding to the geological system with the goal of discovery. By enhancing the ability of an exploration team to interpret rock textures based on core photos, as well as integrating geochemistry, textural information,

and geophysics to improve understanding of already known orebodies, we can leverage our knowledge from well-defined systems to increase our understanding as we interpret data from new mineral systems. This case study combines structured data (extracted from drillcore photography) with geochemical and petrophysical data to create ML predictions of the presence of mineralization, which can be modelled in 3D. This case study provides a workflow for exploration targeting when dealing with challenges like complex deposit models, and subtle differences in geochemical or textural signal. This case study will also highlight the importance of a strong geological framework to underpin the successful deployment of machine learning algorithms.

Acknowledgements

We gratefully acknowledge the client company for permission to share the results of the project.

References

Acosta ICC, Khodadadzadeh M, Tusa L, Ghamisi P (2019) A Machine Learning Framework for Drill-Core Mineral Mapping Using Hyperspectral and High-Resolution Mineralogical Data Fusion. IEEE Journal of Selected Topics in Applied Earth Observations and Remote Sensing 12:4829–4842. https://doi.org/10.1109/JSTARS.2019.2924292

Bluemel B (2021) Chemostratigraphic discrimination assisted by machine learning to enhance 3d modelling. In: Goldschmidt2021 abstracts. European Association of Geochemistry, Virtual

Carranza EJM (2011) From Predictive Mapping of Mineral Prospectivity to Quantitative Estimation of Number of Undiscovered Prospects. Resource Geology 61:30–51. https://doi.org/10.1111/j.1751-3928.2010.00146.x

Deng C, Zhang T, He Z, et al (2023) Learning A Foundation Language Model for Geoscience Knowledge Understanding and Utilization. arXiv preprint arXiv:2306.05064.

Halley S (2020) Mapping Magmatic and Hydrothermal Processes from Routine Exploration Geochemical Analyses. Economic Geology 115:489–503. https://doi.org/10.5382/econgeo.4722

Lundberg SM, Erion G, Chen H, et al (2020) From local explanations to global understanding with explainable AI for trees. Nat Mach Intell 2:56–67. https://doi.org/10.1038/s42256-019-0138-9

Sun T, Chen F, Zhong L, et al (2019) GIS-based mineral prospectivity mapping using machine learning methods: A case study from Tongling ore district, eastern China. Ore Geology Reviews 109:26–49. https://doi.org/10.1016/j.oregeorev.2019.04.003

ALS Goldspot Tessellation app (2022) https://tessellation.app.goldspot.ca/. Accessed 10 August 2023

Predicting mineral abundances from geochemistry in a heavy mineral sand deposit

Kat Lilly[1], Michael Gazley[2,3], Muhammet Kartal[4], Tom Ritchie[5]
[1]RSC, 245 Stuart St, Dunedin, New Zealand
[2]RSC, 225 Thorndon Quay, Wellington, New Zealand
[3]School of Geography, Environment and Earth Science, Victoria University of Wellington, New Zealand
[4]RSC, 13 Rheola St, West Perth, Australia
[5]Hardie Pacific, 57 Leith St, Dunedin, New Zealand

Abstract. Scanning electron microscopy (SEM)-based automated mineralogical studies were undertaken on samples from a heavy mineral sands project on West Coast, South Island, New Zealand, to characterise the mineral assemblage and to quantify the abundance of garnet and ilmenite. These data were used as a training dataset to build linear regression models that predict garnet and ilmenite abundances from major element geochemistry from X-ray fluorescence spectroscopy (XRF) data. The model-performance metrics indicate that the models robustly predict the abundances of these minerals, which allows us to rapidly and inexpensively derive garnet and ilmenite abundances which can be used as an input for subsequent mineral resource estimates (MREs).

1 Introduction

Automated, quantitative analysis of a mineral assemblage in an SEM with energy-dispersive X-ray spectroscopy (EDS) can provide a precise and accurate measurement of the abundance of mineral phases within a sample. However, it is also time-consuming, relatively expensive, and requires very careful sample preparation to ensure that the sample presented to the SEM is representative. XRF analysis is relatively cheap, rapid, and requires less complicated and time-consuming sample preparation.

A statistical model can be built to accurately predict the mineral abundances from the XRF geochemistry. This makes sense theoretically – the geochemistry is directly related to the mineralogy – and does indeed work well in practice; furthermore, for mineral deposits with simple mineralogy (Ritchie et al., 2019, Tay et al., 2021), this can be effective with a limited number of training data.

2 Methodology

2.1 Sample collection and preparation

A set of 30 samples that were representative (based on geochemistry) of the heavy mineral sand deposit were chosen for automated mineralogy, 28 of which were selected from hand auger samples to cover the full variability in garnet and ilmenite abundance across the deposit, and two of which were processing-plant concentrate to provide high-abundance samples. Samples were sieved to be between 53 µm and 2 mm; and a split was taken for automated mineralogy and another taken for pulverisation and XRF analysis.

Care was taken to ensure that the ~10 g of sample taken for each SEM analysis was representative of the original sample. Samples were mounted in 25 mm epoxy rounds, and then cut in half and remounted to present the cut faces in 30 mm epoxy rounds so as to minimise bias in the sample caused by differential settling by grain size and density.

2.2 XRF analysis

The pulverised portion of the sample was analysed by SGS Westport, New Zealand, by flux fusion XRF on a Bruker S8 TIGER instrument resulting in a dataset of 11 major elements reported in wt.% oxide.

2.3 Automated Mineralogy

The 30-mm epoxy rounds were analysed in a Hitachi 3900SU SEM using 2 Bruker EDS detectors and Bruker's Advanced Mineral Analysis and Characterization System (AMICS) software.

More than 99% (by cross-sectional area) of mineral grains were successfully classified. As a test on the quality of the AMICS results, a comparison was made between the major element chemistry as measured by XRF, and the inferred chemistry calculated from the measured abundances of the AMICS-classified minerals. This test work showed a high level of agreement between the two methods, verifying that the SEM sample preparation and analysis methods are robust.

3 Linear Regression Modelling

A multiple linear regression model was built in Python to predict both garnet and ilmenite concentrations from the XRF chemistry, using the SEM-derived mineral abundances as training data. The following elements were used as model inputs: Si, Al, Fe, Ca, Mn and Ti.

The performance of the models were evaluated by holding out a random 30% of the samples, and using bootstrap resampling on the remaining training data. The performance of the models on this unseen test data is presented in Figures 1 and 2.

The garnet model reports a root mean square error (RMSE) of 1.9 wt.%, and the ilmenite model a

RMSE of 2.7 wt.%. We consider this model performance to be fit for purpose to provide inputs for mineral resource estimates (MREs), and it is consistent with the performance of similar models that we have built for similar heavy mineral sand projects on West Coast.

An initial model such as that presented here, coupled with an examination of the geochemistry of the entire dataset, provides an approach to optimise sampling. That is to say that additional samples can be located to summarise both the geochemical variability of the dataset, and to in-fill any gaps in the mineral abundances. For example, in the dataset presented here, particular attention should be given to samples that have a predicted garnet abundance of 12–20 wt.% and a predicted ilmenite abundance of 8–20 wt.% as these samples are missing in the dataset. Care should also be taken to ensure that there is adequate sample support around the cut-off grade of any subsequent MRE; this is likely in the 1–3 wt.% garnet and ilmenite range which are not adequately sampled here.

4 Summary

In a heavy mineral sand project, where the mineralogy is quite simple, it is possible to build statistically robust models to predict garnet and ilmenite abundance with limited training data. These models can be validated by selection of additional samples to analyse by automated mineralogy based on an initial model – such as that presented here. Additional sampling and analysis is currently underway, based on the strategy we have used at other West Coast heavy mineral sand projects.

Planned future work involves building models to predict the output of the processing plant directly from the whole-sample major element geochemistry of the raw starting material. The relationship between geochemistry of the raw material and the mineral abundances in the concentrate is less direct, but it is still possible to model the latter from the former.

We also plan to do this with portable XRF results that can be acquired on site and within a matter of hours, without the need to send batches of samples away for laboratory XRF analysis.

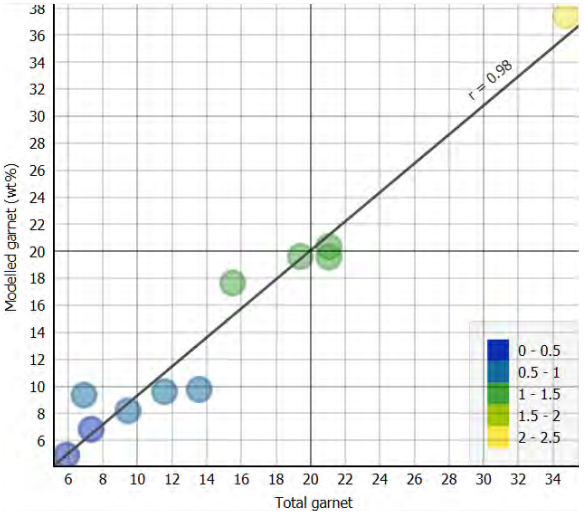

Figure 1. Modelled garnet vs measured garnet for a 30% holdout test dataset. These samples were excluded from the training dataset for the purposes of evaluating model performance, and the model trained on the remaining dataset using bootstrap resampling. Colour scale shows MnO wt.%.

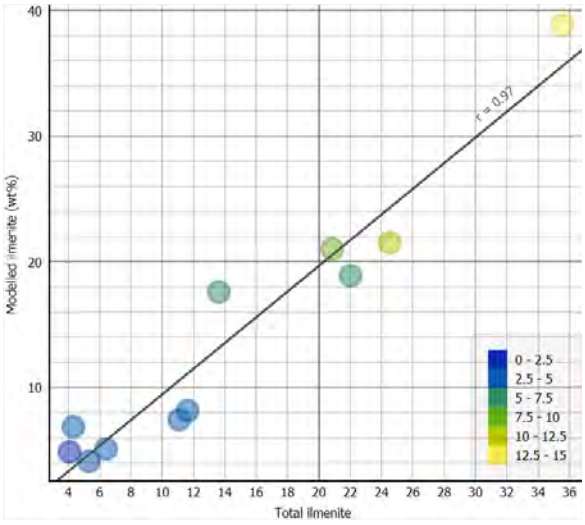

Figure 2. Modelled ilmenite vs measured ilmenite for a 30% holdout test dataset. These samples were excluded from the training dataset for the purposes of evaluating model performance, and the model trained on the remaining dataset using bootstrap resampling. Colour scale shows TiO_2 wt.%.

References

Ritchie, T. W., Scott, J. M., & Craw, D. (2019). Garnet compositions track longshore migration of beach placers in western New Zealand. Economic Geology, 114:513-540.

Tay, S. L., Scott, J. M., Palmer, M. C., Reid, M. R., & Stirling, C. H. (2021). Occurrence, geochemistry and provenance of REE-bearing minerals in marine placers on the West Coast of the South Island, New Zealand. New Zealand Journal of Geology and Geophysics, 64: 89-106.

Machine learning in mineral prospectivity mapping and target generation for critical raw materials

Vesa Nykänen
Information Solutions, Geological Survey of Finland, P.O. Box 77, FI-96101 Rovaniemi, Finland

Abstract The aim of mineral prospectivity mapping (MPM) is to delineate areas that are favourable for certain mineral deposit types. This can be based on prior knowledge using a so-called empirical or data-driven approach or by translating expert knowledge into a mathematical formula by using a conceptual or knowledge-driven approach. Both approaches can benefit from machine learning methods using advanced computer algorithms that can learn from data. This learning can either be supervised or unsupervised. Geographical information systems (GIS) provide a perfect platform for conducting MPM, as in these systems, we can automate and build complex systems to construct models that can be used to predict where the best exploration terrains are hidden. This paper aims to describe how machine learning methods can be utilized in MPM in various steps. This is demonstrated via examples of several past and ongoing research and innovation projects.

1 Mineral prospectivity mapping

A mineral prospectivity mapping (MPM) process may be split into several steps (Fig. 1) (Nykänen et al. 2023). It starts from mineral systems modelling (Step 1), in which the important ingredients of a mineral system that formed the ore body are defined. These critical factors are then translated into mappable parameters that can later be used in GIS for MPM. Then, based on the characterization of the mineral system model, the data are either acquired from existing databases or from the field (Step 2). In the data pre-processing step (Step 3), data are transformed to represent proxies for critical parameters of the mineral systems. This is quite often the most time-consuming part of an MPM-related project if the data acquisition part is not considered. Then follows the actual mineral prospectivity analysis (Step 4), in which two main approaches (or a combination of them) can be used. The final phase in MPM is model validation (Step 5), when statistical methods are applied to test how well the model has performed.

1.1 Data-driven (empirical) approach

The first approach in MPM is data driven (empirical), where prior knowledge of mineral deposits or occurrences is used to train the models. These techniques include many traditional MPM methods, as well as advanced machine learning and deep learning techniques requiring large amounts of training data to be successful. Weights of evidence (WoE) is a traditional statistical technique that is often used in data analysis and modelling for MPM (Bonham-Carter 1994). It is not considered as a form of machine learning, however, as it does not involve the use of algorithms that can learn patterns from data. Logistic regression, another popular classical data-driven MPM method, belongs to the machine learning category, and can be used for classification tasks. It is a statistical method that applies a logistic function to model the likelihood of a binary or categorical result based on one or more input features. Logistic regression is a supervised learning procedure, which means that this method requires labelled, i.e., previously known training data to learn the relationships connecting the input features and the outcome. It is a linear model, which means that it assumes a linear relationship between the input features and the log-odds of the outcome. An artificial neural network (ANN) can be seen as a form of machine learning that is constructed based on the structure and function of the human brain (Tsoukalas and Uhrig 1997; Looney 1997; Nykänen 2008; Cracknell and Reading 2014). ANNs are designed to recognize patterns in multidimensional data, learn from these patterns, and make estimates or conclusions that are derived from this learning. ANNs are comprised of joined nodes, or neurons, processing and transmitting data through a series of layers. The input layer receives the data, which is then passed through one or more hidden layers before reaching the output layer, where the final prediction or decision is made. ANNs can be used for both supervised and unsupervised learning tasks, and they can handle complex non-linear relations between the variables. Artificial neural networks are a form of machine learning, specifically deep learning algorithms, that are used to identify arrays in data and make predictions or decisions based on this learning.

Deep learning is a subfield of machine learning involving the use of ANNs with multiple layers to model and analyse complex relationships in data (LeCun et al. 2015). Deep learning algorithms are constructed to learn from large and complex datasets by automatically extracting features and patterns from the input data. Convolutional neural networks (CNNs) are common examples of deep learning model architectures. The advantage of using deep learning is its ability to learn hierarchical descriptions of the data so that each successive layer within the network learns increasingly from the features. This may be computationally intensive and may also require large amounts of training data, which can limit the applicability of CNNs in data-poor areas. Furthermore, as with all ANNs, deep learning methods also tend to be “black box” in nature, so it can be difficult to interpret their decisions and to understand the reasoning behind their predictions.

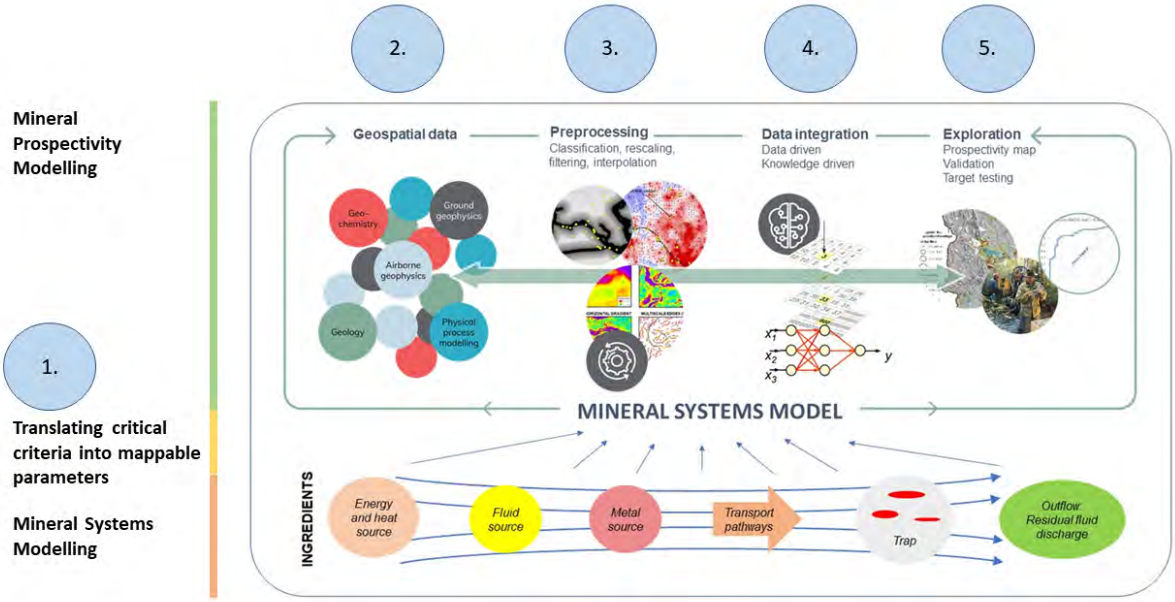

Figure 1. The mineral prospectivity mapping workflow (modified from Nykänen et al. 2023).

Applicable fields of use of ANNs include those where there is a need to analyse complex relationships in data and apply the technique to tasks, e.g., pattern recognition in images for structural geology.

Self-organizing map (SOM) is a machine learning method that uses unsupervised learning to create a low-dimensional representation of high-dimensional data (Kohonen 1990). It can be used for data visualization and exploration, feature extraction, clustering, and pattern recognition assignments. SOM is a powerful and widely used machine learning method that can be applied to different data analysis purposes, and it has also recently been applied to mineral prospectivity mapping (Chudasama et al. 2022b). In MPM, SOMs can be used to identify spatial relationships and patterns in geological, geochemical, and geophysical data that may be indicative of mineralization. The SOM technique can use as input a large exploration dataset, including geological, geochemical, and geophysical data, and find clusters of similar data within the multidimensional feature space. When these datapoints also have spatial information (i.e., coordinates), the resulting map can then be used to identify areas that are most likely to contain mineral deposits based on the patterns and relationships within the data.

1.2 Knowledge-driven (conceptual) approach

The second approach in MPM is knowledge driven (conceptual), where expert knowledge is translated into a mathematical formula or model, and it does not require any known deposit within the study area to be used as training sites (McKay and Harris 2016). Conceptual or knowledge-driven mineral prospectivity methods rely on understanding of geological processes and mineral deposit models to identify areas that are most likely to contain mineral occurrences or deposits. These methods assume that certain geological, geochemical, and geophysical features, and especially an explicit combination of them, are commonly associated with specific types of mineral deposits, and that by mapping these features from various exploration datasets, areas of high mineral potential can be identified.

Fuzzy logic is one example of a conceptual or knowledge-driven approach. It is a method that deals with problem solving and decision making under uncertainty, having no crisp boundaries between sets (true and false). It is based on fuzzy set theory (Zadeh 1965). It is not a subset of machine learning, but it can be used in machine learning as a form of reasoning, allowing a computer code to make decisions based on data. Fuzzy logic overlay is used in geospatial analysis and decision making. It involves the integration of multiple layers of data, each of which represents a different variable or factor that is relevant to a specific decision or analysis. In MPM, these factors are related to the critical mineral systems parameters.

The Boolean logic method or index overlay method uses a set of geological rules or constraints to create a model of the geological environment that is favourable for mineralization. The rules are based on expert knowledge and geological concepts, and the model is then used to identify areas of high mineral potential.

The expert system method uses a set of rules and decision trees based on expert knowledge to identify areas of high mineral potential. The rules are based on geological concepts and the decision trees are used to guide the user through the prospectivity mapping process.

2 Tools developed for public use

The Geological Survey of Finland (GTK) has been maintaining and updating a toolbox called ArcSDM, which was originally established by the U.S. Geological Survey and the Geological Survey of Canada (Sawatzky et al. 2009) and includes some of the key methodologies described by Bonham-Carter (1994). This toolbox can be freely downloaded from GitHub (Geological Survey of Finland 2023a). The tools were updated in the project Mineral Prospectivity Modeller (MPM), funded by the Finnish Funding Agency for Technology (Tekes) (Geological Survey of Finland 2023b). The same project also developed an online web service called MPM Online Tool (Fig. 2) (Geological Survey of Finland 2023c), which can be used to build simple Fuzzy logic overlay models using public geodata from Northern Finland on a web browser-based platform.

Later, in 2018–2021, GTK developed a SOM toolbox, GisSOM (Geological Survey of Finland 2023d), in an EU-funded project entitled NEXT. This toolbox can be used to cluster and visualize data, as described earlier. These SOM tools are currently being further developed in an on-going EIT RawMaterials-funded project entitled DroneSOM (DroneSOM 2023).

The most recent development concerning MPM tools at GTK is the EU-funded project Exploration Information System (EIS), in which the project team is developing new geomodels of selected mineral systems and novel, fast, and cost-efficient spatial data analysis tools for mineral exploration on top of an open GIS platform (EIS 2023). This work is being conducted together with 17 partners from leading research institutes, academia, service providers, and the mining industry. The tools created will also eventually be freely downloadable from GitHub. The project duration is from May 2022 to April 2025.

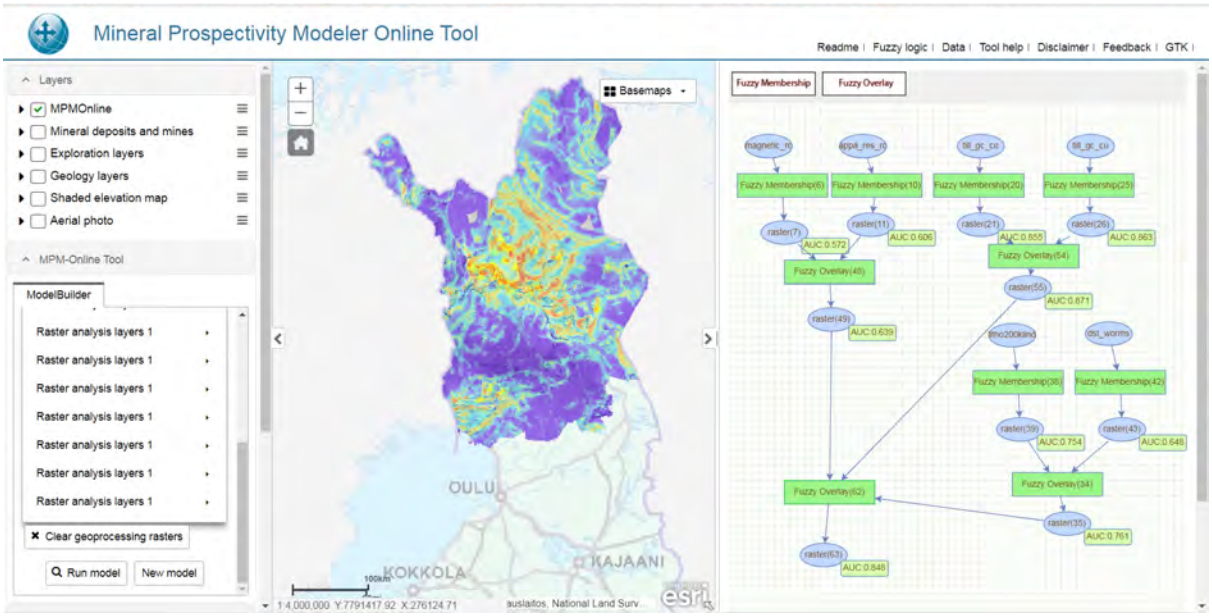

Figure 2. The MPM online tool (Geological Survey of Finland 2023c).

3 Case studies

While developing tools for MPM, the team at GTK has also tested the tools on numerous mineral deposit types using real exploration data from GTK's public databases (Geological Survey of Finland 2023e). The main target test area has been Northern Finland, which is potential for many deposit types, including orogenic gold (Nykänen 2008, Nykänen et al 2008a, Niiranen et al. 2015; Niiranen et al. 2019), orogenic gold with an atypical metal association (Chudasama et al. 2022a, 2022b), IOCG (Nykänen et al. 2008b), magmatic Ni–Cu (Nykänen et al. 2015), and various cobalt-bearing deposit types (Nykänen et al. 2023). In addition to peer-reviewed scientific papers and conference papers, some of these published models are available from the Mineral Deposits and Exploration web map service MDaE of GTK (Geological Survey of Finland 2023f).

Acknowledgements

The MPM project was funded by the Finnish Funding Agency for Technology (Tekes). The NEXT project was funded by the European Union's Horizon 2020 research and innovation program under grant agreement no. 776804–H2020-SC5-2017. The EIS project is funded by the European Union's Horizon Europe research and innovation program under grant agreement no. 1010557357, and DroneSOM is funded by EIT RawMaterials.

References

Bonham-Carter GF (1994) Geographic information systems for geoscientists–modelling with GISComputer Methods in the Geosciences 13. Pergamon, Oxford, 398 p

Chudasama B, Torppa J, Nykänen V, Kinnunen J, Lerssi J, Salmirinne H (2022a) Target-scale prospectivity modeling for gold mineralization within the Rajapalot Au-Co project area in northern Fennoscandian Shield, Finland. Part 1: Application of knowledge-driven- and machine learning-based-hybrid- expert systems for exploration targeting and addressing model-based uncertainties. Ore Geology Reviews, 147, https://doi.org/10.1016/j.oregeorev.2022.104937.

Chudasama B, Torppa J, Nykänen V, Kinnunen J (2022b) Target-scale prospectivity modeling for gold mineralization within the Rajapalot Au-Co project area in northern Fennoscandian Shield, Finland. Part 2: Application of self-organizing maps and artificial neural networks for exploration targeting, Ore Geology Reviews, 147, https://doi.org/10.1016/j.oregeorev.2022.104936.

Cracknell MJ, Reading AM (2014) Geological mapping using remote sensing data: A comparison of five machine learning algorithms, their response to variations in the spatial distribution of training data and the use of explicit spatial information. Computers & Geosciences 63, 22-33.

DroneSOM (2023) DroneSOM accessed April 3rd, 2023, from https://dronesom.com/

EIS 2023 Exploration Information System. Accessed April 3rd, 2023, from https://eis-he.eu/

Geological Survey of Finland (2023a) ArcSDM. Spatial Data Modeler for ArcGIS. Accessed March 29th, 2023, from https://github.com/gtkfi/ArcSDM

Geological Survey of Finland (2023b) Mineral Prospectivity Modeller, MPM project. http://projects.gtk.fi/mpm/index.html

Geological Survey of Finland (2023c) MPM Online Tool http://projects.gtk.fi/mpm/online_tool/

Geological Survey of Finland (2023d) GisSOM. Accessed April 3rd, 2023, from https://github.com/gtkfi/GisSOM.

Geological Survey of Finland (2023e) Hakku. Spatial Data Products. Accessed April 4th, 2023, from https://hakku.gtk.fi/en

Geological Survey of Finland (2023f) Mineral Deposits and Exploration – MdaE. Accessed April 3rd, 2023, from https://gtkdata.gtk.fi/mdae/index.html

Kohonen T (1990) The Self-Organizing Map. Proceedings of the IEEE, 78 (9), pp. 1464-1480. doi: 10.1109/5.58325

LeCun Y, Bengio Y, Hinton, G (2015) Deep learning. Nature 521, 4326-444.

Looney CG (1997) Pattern recognition using neural networks: theory and algorithms for engineers and scientists: Oxford University Press, New York, 458 p

McKay G, Harris JR (2016) Comparison of the Data-Driven Random Forests Model and a Knowledge-Driven Method for Mineral Prospectivity Mapping: A Case Study for Gold Deposits Around the Huritz Group and Nueltin Suite, Nunavut, Canada. Natural Resources Research, 25, DOI: 10.1007/s11053-015-9274-z

Niiranen T, Lahti I, Nykänen V (2015) The orogenic gold potential of the Central Lapland greenstone belt, northern Fennoscandian shield. In Maier, W.; Lahtinen, R. and O'Brien (eds). Mineral Deposits of Finland. Elsevier. pp. 733-752.

Niiranen T, Nykänen V, Lahti I (2019) Scalability of the mineral prospectivity modelling – An orogenic gold case study from northern Finland. Ore Geology Reviews, Volume 109, 2019, Pages 11-25, ISSN 0169-1368, https://doi.org/10.1016/j.oregeorev.2019.04.002.

Nykänen V (2008) Radial Basis Functional Link Nets Used as a Prospectivity Mapping Tool for Orogenic Gold Deposits Within the Central Lapland Greenstone Belt, Northern Fennoscandian Shield. Natural Resources Research, 17, DOI: 10.1007/s11053-008-9062-0

Nykänen V, Groves DI, Ojala VJ, Gardoll SJ (2008a) Combined conceptual/empirical prospectivity mapping for orogenic gold in the northern Fennoscandian Shield, Finland. Australian Journal of Earth Sciences 55 (1), 39-59.

Nykänen V, Groves DI, Ojala VJ, Eilu P, Gardoll SJ (2008b) Reconnaissance-scale conceptual fuzzy-logic prospectivity modelling for iron oxide copper-gold deposits in the northern Fennoscandian Shield, Finland. Australian Journal of Earth Sciences 55 (1), 25-38.

Nykänen V, Törmänen T, Niiranen T (2023) Cobalt prospectivity using a conceptual fuzzy logic overlay method enhanced with the mineral systems approach. Natural Resources Research (Manuscript submitted for publication).

Sawatzky DL, Raines GL, Bonham-Carter GF, Looney CG (2009) Spatial DataModeller (SDM): ArcMAP 9.3 geoprocessing tools for spatial data modelling using weights of evidence, logistic regression, fuzzy logic and neural networks http://arcscripts.esri.com/details.asp?dbid=15341.

Tsoukalas LH, Uhrig RE (Eds.) (1997) Fuzzy and neural approaches in engineering: John Wiley & Sons, Inc., New York, 587 p

Zadeh LA (1965) Fuzzy sets 8. Institute of Electric and Electronic Engineering, Information and Control, pp. 338–353.

Navigating the complexities of decision-making for Critical Mineral Exploration Campaigns: Insights form AI-based Geological Prospectivity and Risk Models

Mohammad Parsa
[1]*Geological Survey of Canada, Ottawa, Ontario, K1A 0E8, Canada*

Abstract. This study presents an integrated framework for interpreting geological prospectivity models, which are central to decision-making and land-use planning for critical mineral exploration campaigns. Besides geological prospectivity, there are other factors that are essential to policymaking. Different uncertainties linked to prospectivity models are of factors affecting geological prospectivity and, therefore, their interpretation. In addition, mineral deposits usually form in clusters and follow certain spatial patterns, making spatial distribution another important factor for the interpretation of geological prospectivity models. Herein, an integrated approach to interpreting geological prospectivity models is presented. This approach combines geological prospectivity, uncertainty, and spatial distribution to help make informed decisions while narrowing down the search space for mineral exploration. An example of using this approach is further demonstrated for national-scale delineation of exploration targets for REEs in Canada.

1 Introduction

Critical minerals are essential for renewable energy technologies and play an inevitable role in transitioning to a carbon-free economy. The demand for renewable energy sources continues to surge, leading to an ever-increasing demand for critical minerals. Ensuring a secure and sustainable supply of critical minerals is, thus, crucial for the transition to a carbon-free economy.

Geological prospectivity models can help policymakers make informed decisions about critical mineral exploration campaigns. These models can help identify areas where critical minerals are likely to be discovered, thereby helping understand the potential supply of critical minerals and make decisions about where to invest in exploration and mining activities.

Geological prospectivity models are mostly derived by the application of various supervised regression techniques. These are probability models in which high probability values pertain to favourable zones for discovering a given type of mineral deposits. These models, therefore, are continuous models that are devoid of interpretation. One must, thus, assign a threshold value to these models for demarcating exploration targets.

Methods used for interpreting geological prospectivity models range from subjective assigning of a threshold value to objective interpretation of these models. The former method entails intrinsic problems. There is a chance of overestimating or underestimating exploration targets while setting a subjective value for interpreting geological prospectivity models. Turning to the latter methods, abrupt changes in the probability values (Porwal et al. 2003), spatial distribution of probability values (Parsa et al. 2017), and risk-return analysis (Parsa and Pour 2021) have been applied to objective interpretation of geological prospectivity models. Although these objective solutions address the problem of subjective bias, there is a need for a holistic approach to interpreting geological prospectivity models that considers spatial and statistical distribution of prospectivity values together with uncertainties linked to prospectivity models.

Herein, an integrated methodology is proposed that considers the above aspects while interpreting geological prospectivity models. This methodology has been applied to national-scale geological prospectivity models of a suite of critical minerals, helping select high priority exploration targets.

2 Methodology

There are data- and model-related uncertainties that affect the results of geological prospectivity models. An open-source framework for measuring different uncertainty types for geological prospectivity mapping is presented in this study.

This framework starts with selecting random sub-samples from the labelled samples. Each set of random sub-samples is fed into different machine and deep learning algorithm, leading to a set of geological prospectivity models. These models are derived with different labelled samples and different regression models, helping measure the data- and model-related uncertainties. This is followed by the application of risk-return analysis and spatial measurements for objectively interpret the geological prospectivity models. This framework was exploited for generating exploration targets of several critical minerals, including REEs.

The proposed framework is an open-source, versatile approach allowing for addition of algorithms or datasets.

Acknowledgements

I am grateful for the invitation of the organizers of the machine learning session, Chetan Nathwani, Francisca M. Maepa, and Daniel Gregory.

References

Parsa M, Maghsoudi A, Yousefi M (2017) An improved data-driven fuzzy mineral prospectivity mapping procedure; cosine amplitude-based similarity approach to delineate exploration targets. International journal of applied earth observation and geoinformation. 1;58:157-67.

Parsa M, Pour AB. A (2021) simulation-based framework for modulating the effects of subjectivity in greenfield mineral prospectivity mapping with geochemical and geological data. Journal of Geochemical Exploration. 1;229:106838.

Porwal A, Carranza EJ, Hale M (2003) Knowledge-driven and data-driven fuzzy models for predictive mineral potential mapping. Nat Resour RES. 12:1-25.

Assessing tourmaline as an indicator mineral using multivariate statistics

Eduardo Valentin dos Santos[1], Georges Beaudoin[1], Bertrand Rottier[1]
[1]Département de géologie et génie géologique, Université Laval, Quebec, Canada

Abstract. Tourmaline chemistry from different geological environments, including granite, Li-rich and -poor pegmatite, porphyry Cu-Mo, granite-related Sn, volcanogenic massive sulphide (VMS), unconformity U, orogenic gold, epithermal Au-Ag, and metapelite, were analysed by electron probe micro-analyser (EPMA) and laser ablation inductively coupled plasma mass spectrometry (LA-ICP-MS). The data was processed and analysed using principal component analysis (PCA) and partial least squares discriminant analysis (PLS-DA). Most tourmaline from the majority of the investigated geological environments straddle along dravite-schorl, with the exception of unconformity U (Mg-foitite), Li-bearing pegmatite, and some granite-related Sn (elbaite-liddicoatite). LA-ICP-MS trace element PCA analysis results in good separation of Li-rich pegmatite, and unconformity U deposits. Granite-related Sn deposits tend to plot between Li-pegmatite and other magmatic rocks and magmatic-hydrothermal deposits on the first, second, and third components. Both Li-pegmatite and granite-related Sn are inversely correlated to orogenic gold deposits. PLS-DA analysis results in good separation of Li-rich and Li-poor pegmatite, and unconformity U. There is considerable overlap between other classes using PCA and PLS-DA. Further data collection and classification using machine learning (Random Forest) methods are the next steps of this project, as they will likely allow better discrimination of tourmaline from the investigated geological environments.

1 Introduction

Tourmaline is a common mineral in several geological environments and mineral deposits (Slack 1996, Trumbull et al. 2020). It has one of the largest stability ranges of crustal minerals and is characterized by low volume diffusion rates, so it usually preserves its original chemical composition and zonings reflecting the physicochemical conditions of its crystallization environments (van Hinsberg et al. 2011, Slack and Trumbull 2011).

Tourmaline compositional data can be utilized as a pathfinder for different types of deposits. Sciuba et al. (2021) demonstrated that the tourmaline composition from orogenic gold deposits is controlled by the fluid composition, metamorphic facies, and composition of the country rocks, and is overall rich in Sr, V, and Ni and poor in Li, Be, Ga, Sn, Nb, Ta, U, and Th compared to tourmaline from other deposit types and geological environments.

Nonetheless, the published tourmaline trace element datasets are often inconsistent and incomplete in the number of analyzed elements, making it difficult to compare different deposit types using statistical and machine learning methods. In this context, this project aims to build a homogeneous database and develop criteria for

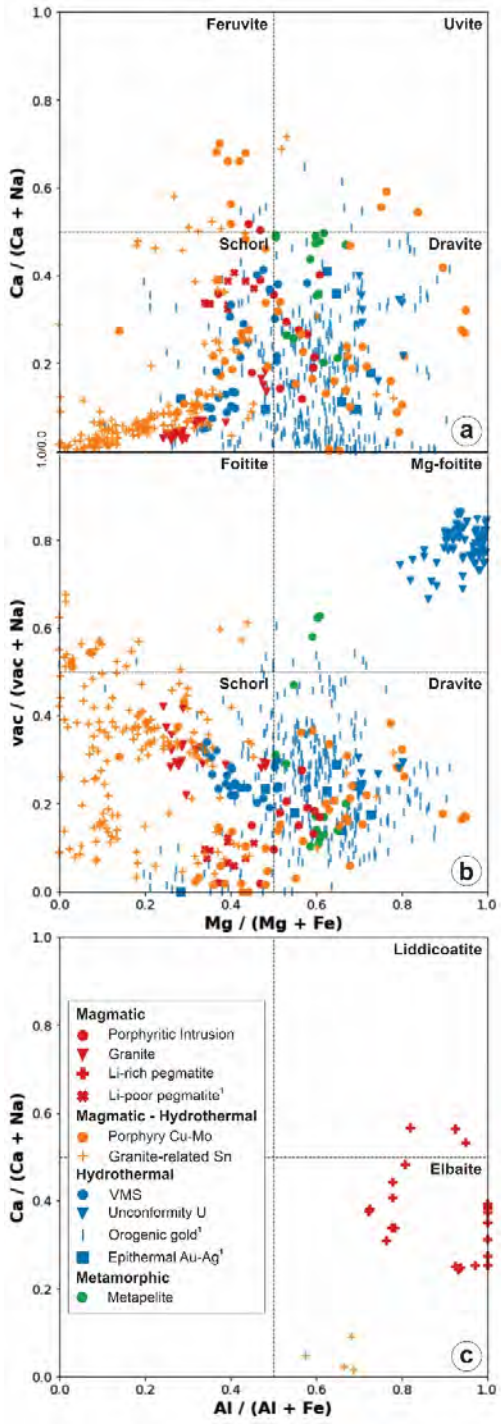

Figure 1. *Composition of tourmaline from different geological environments. Tourmaline classification diagrams from Henry et al. (2011).* ***a.*** *Mg/(Mg+Fe) vs. Ca/(Ca+Na),* ***b.*** *Mg/(Mg+Fe) vs. X-vac/(X-vac+Na), and* ***c.*** *Ca/(Ca+Na) vs. Al/(Al+Fe). 1 – Sciuba et al. (2021).*

using tourmaline chemistry as a geochemical prospecting tool.

2 Methods

2.1 Electron probe micro-analysis (EPMA)

Major and minor elements were measured with a CAMECA SX-100 electron probe micro-analyzer equipped with five WDS spectrometers at Université Laval. Silicon, Ti, Al, V, Sc, Fe, Mg, Mn, Zn, Cu, Ni, Co, Ca, Sr, Na, K, F, and Cl were analysed using a 5 µm beam, 15 kV acceleration voltage, and 20 nA current, counting 10s on background and 20s on peak.

Tourmaline structural formula were calculated according to Henry et al. (2011), on the basis of 31 anions, 29 oxygen atoms, and 3 apfu B.

2.2 Laser ablation-inductively coupled plasma-mass spectrometry (LA-ICP-MS)

Major, minor, and trace elements were measured using an Agilent 8900 ICP-QQQ-MS coupled with a RESOlution-SE 193nm excimer at Université Laval. Acquisition parameters were 38 µm lines, at a 5 µm/s line speed, 10 Hz laser frequency, and fluence of 4.67~8.25 J.cm^{-2}.

The Si concentration measured by EPMA was used as internal standard. The reference materials NIST-610 (^{7}Li, ^{9}Be, ^{23}Na, ^{27}Al, ^{44}Ca, ^{47}Ti, ^{53}Cr), NIST-612 (^{39}K, ^{45}Sc, ^{59}Co, ^{60}Ni, ^{71}Ga, ^{85}Rb, ^{86}Sr, ^{89}Y, ^{107}Ag, ^{111}Cd, ^{115}In, ^{118}Sn, ^{133}Cs, ^{137}Ba, ^{139}La, ^{140}Ce, ^{141}Pr, ^{146}Nd, ^{152}Sm, ^{153}Eu, ^{155}Gd, ^{159}Tb, ^{163}Dy, ^{165}Ho, ^{166}Er, ^{169}Tm, ^{172}Yb, ^{175}Lu, ^{178}Hf, ^{181}Ta, ^{182}W, ^{197}Au, ^{232}Th, ^{238}U), and GSE-1g (^{11}B, ^{24}Mg, ^{51}V, ^{55}Mn, ^{56}Fe, ^{57}Fe, ^{65}Cu, ^{66}Zn, ^{92}Zr, ^{93}Nb, ^{95}Mo, ^{207}Pb) were used as primary standards depending on the element. When not used for quantification, NIST-610, NIST-612, GSE-1g, KL2-G, and ML3B-G were used as secondary standards to control data quality.

Data reduction was carried out using the Iolite package for Igor Pro software (Paton et al. 2011).

2.3 Multivariate statistical analysis

Prior to PCA and PLS-DA, the dataset was processed for variables (elements) with values below the detection limit (censored values). Elements with more than 40% censored values were excluded. For the remaining, censored values were imputed using the log-ratio Expectation-Maximization (lrEM) algorithm (R package zCompositions; Palarea-Albaladejo and Martín-Fernández 2015). This algorithm ensures that censored values are replaced by imputed values between zero and the detection limit. After imputation the dataset was transformed using centered log-ratios to overcome the closure effect in compositional data (Aitchison 1986).

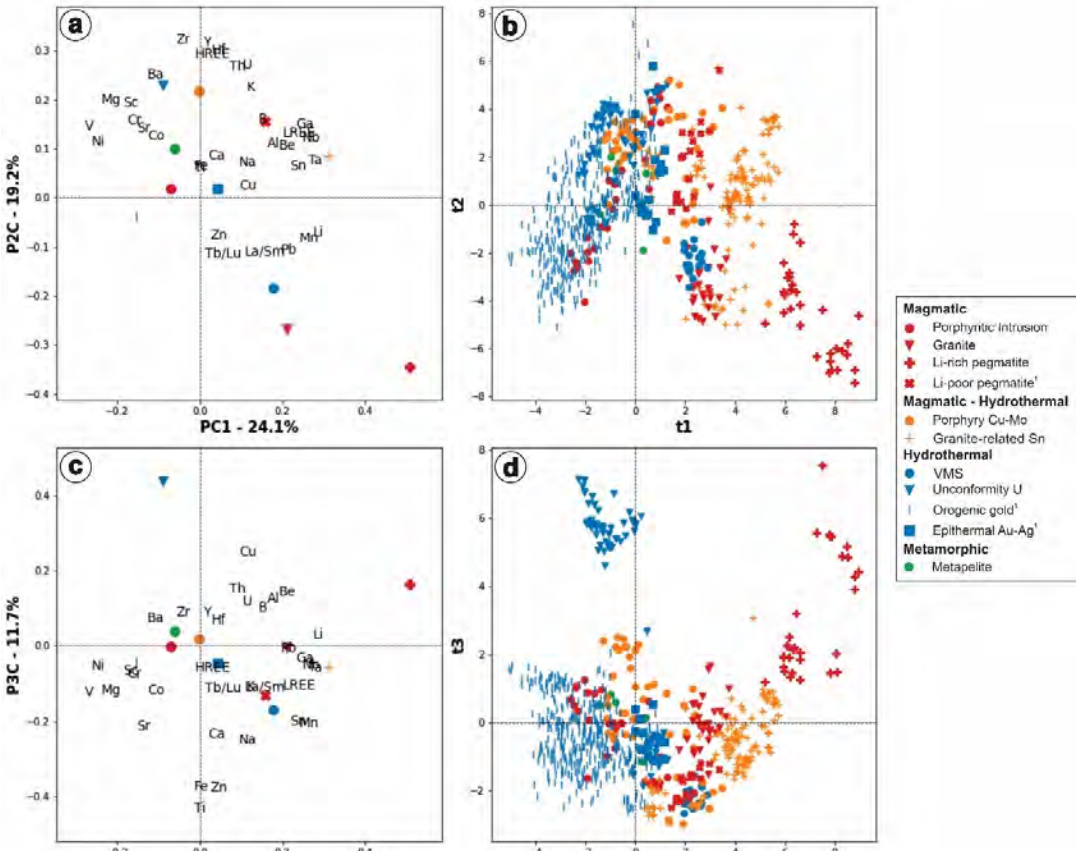

Figure 2. *PCA diagrams of tourmaline trace elements measured by LA-ICP-MS. Loadings (PC1-PC2) and scores (t1-t2) on the first and second components are shown on* ***a*** *and* ***b****. Loadings (PC1-PC3) and scores (t1-t3) on the first and third components are shown on* ***c*** *and* ***d****. 1 – Sciuba et al. (2021).*

The PCA is an unsupervised method used to reduce a larger set of variables to a smaller number of uncorrelated variables called principal components (PC). Each PC explains part of the variance of the data, with the first (PC1) capturing the greatest variance, followed by the second (PC2), and so forth. The PCA loadings are the correlation coefficients between original variables and PCs, and provide information on the impact of a variable on a given PC. The PCA Scores are composite values for each sample on each PC, calculated using the original variable values and factor weights (Makvandi et al. 2019 and references therein).

The PLS-DA, on the other hand, is a supervised classification method that combines partial least squares regression using a continuous data matrix X (elements), and discriminant analysis, using a categorical outcome matrix Y (different classes). The PLS components (scores; t1, t2, etc.) and loadings (wq*1, wq*2, etc.) are among the main PLS-DA outcomes. Another significant output is the variable importance on the projection (VIP) plot (Fig. 3e), where elements with VIP values larger than 1.0 are the most influential variables in the model, variables between 0.8 and 1.0 are moderately influential, and values smaller than 0.8 do not contribute significantly in the sample classification (Makvandi et al. 2021 and references therein).

For both PCA and PLS-DA plots, positively correlated variables are shown grouped, whereas negatively correlated variables plot diametrically opposed. The location of variables is dependent on their contribution to discrimination. Variables near the origin contribute weakly to classification, whereas the outer variables are highly variable between classes (Caraballo et al. 2022).

3 Results and discussion

Thirty tourmaline-bearing samples from granite, porphyritic intrusion, Li-rich pegmatite, porphyry Cu-Mo, granite-related Sn, VMS, unconformity U, and metapelite were investigated by EPMA and LA-ICP-MS. The Sciuba et al. (2021) dataset was added to this study, because the same set of elements were analysed.

Tourmaline major element composition shows large compositional ranges, reflected in different tourmaline species (Fig. 1). Most of the investigated geological environments present tourmaline that ranges from schorl (Fe-rich, sodic) to dravite (Mg-rich, sodic). Porphyritic intrusion, granite-related Sn, porphyry Cu-Mo, and orogenic gold have foitite (Fe-rich, X-site vacant), feruvite (Fe-rich, calcic), and uvite (Mg-rich, calcic), but these represent minor members of a dominantly schorl-dravite population of the same deposit types. Unconformity U deposits and Li-rich pegmatite are Mg-foitite (Fe-rich, X-site vacant) and elbaite (Li-rich, sodic) or liddicoatite (Li-rich, calcic), respectively.

The trace element compositions, variance, and correlations along different classes were analyzed by PCA and PLS-DA. From the PCA score and

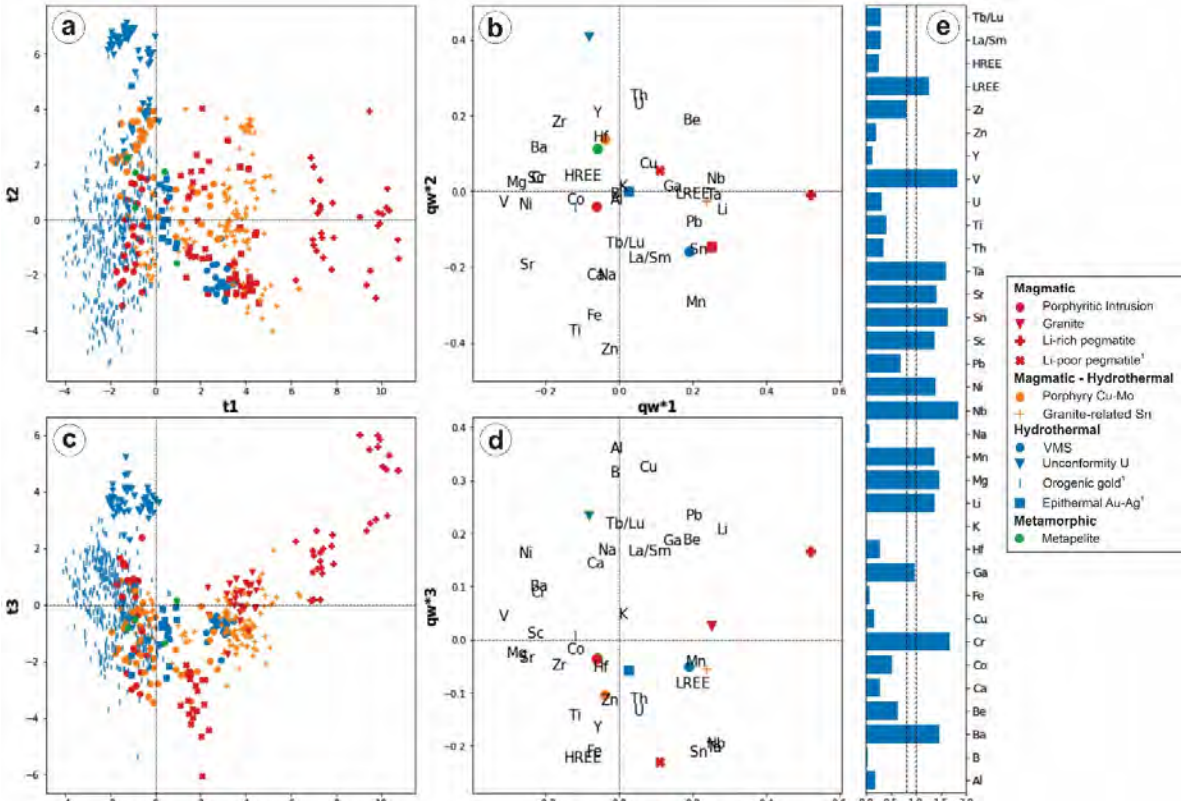

Figure 3. *PLS-DA diagrams of tourmaline trace elements measured by LA-ICP-MS. Loadings (qw*1-qw*2) and scores (t1-t2) on the first and second components are shown on* ***a*** *and* ***b****. Loadings (qw*1-qw*3) and scores (t1-t3) on the first and third components are shown on* ***c*** *and* ***d****. The VIP plot is shown on* ***e****. 1 – Sciuba et al. (2021).*

loadings plots (Fig. 2), unconformity U and Li-rich pegmatite are well separated from the other classes on the t1 vs. t3 (Fig. 2b) and t1 vs. t2 and t3 (Fig. 2b and 2d) score plots.

On the loadings plot of the first two principal components (Fig. 2a), Li-rich pegmatite is influenced by high contents of the elements on the lower right quadrant (i.e., Li, Mn, Pb, La/Sm, Tb/Lu, Zn), and by extremely low contents of the elements on the opposed quadrant (i.e., Ni, V, Cr, Co, Sc, Sr, Mg, Ba, Zr). On the first and third loadings plot (Fig. 2c), Li-rich pegmatite is influenced by a similar set of elements, with the addition of Be, Al, B, U, Th, Cu, Y, and Hf. Nonetheless, unconformity U deposits are characterized by a low concentration of most elements, especially Fe, Zn, and Ti.

All other groups are largely overlapping, but granite-related Sn tends to plot between Li-rich pegmatite and granite, Li-poor pegmatite, and VMS on both diagrams. Granite-related Sn deposits are positively correlated with LREE, Na, Al, Ga, Sn, Nb, and Ta.

Epithermal Au-Ag, metapelite, porphyritic intrusion, and porphyry Cu-Mo tend to plot near the origin. The first slightly tends toward elements enriched in felsic rocks, whereas the rest tends to the elements enriched in mafic rocks. Orogenic gold deposits are inversely correlated to Li-rich pegmatite and characterized by high Sr, V, Ni, Co, Cr, Mg, and Sc concentrations.

The PLS-DA score and loading plots (Fig. 3a, 3b, 3c, and 3d) highlight the separation of Li-rich pegmatite and unconformity U on the first, second, and third components. Lithium-poor pegmatite is well-defined on the first and third components. The Li-rich pegmatite class is evidenced by high concentrations of Be, Li, Mn, Nb, Pb, Sn, Ta, and LREE, and low concentrations of Ba, Cr, Mg, Ni, Sc, Sr, and V. Unconformity U is characterized by high Th, U, Y, and Zr and low Ca, Fe, Mn, Na, Sn, Sr, Ti, and Zn. Li-poor pegmatite (Fig. 3f) is well separated by the third component and is evidenced by high Fe, Nb, Sn, Ta, and U and low Al, B, Cu, Ni, and V.

The VIP plot (Fig. 3e) highlights the importance of Ba, Cr, Li, Mg, Mn, Nb, Ni, Sc, Sn, Sr, Ta, V, and LREE for the PLS-DA model.

4 Conclusions

Both PCA and PLS-DA are good at classifying Li-rich pegmatite and unconformity U. However, these classes are different from the other geological environments by their major element composition since they are elbaite-liddicoatite and Mg-foitite.

Both models suggest that tourmaline from orogenic gold deposits has a high concentration of elements enriched in mafic rocks. In contrast, Li-rich pegmatite and granite-related Sn deposits tourmaline have a high concentration of elements enriched in evolved felsic rocks. This suggests that tourmaline chemistry can record the nature of the magmatic source of hydrothermal fluids for magmatic-hydrothermal deposits, or the composition of buffering rocks for metamorphic fluids, as shown by Sciuba et al. (2021).

Further data collection, PLS-DA algorithm tuning with the best-performing elements, and classification using machine learning (Random Forest) methods are the next steps of this project, as they will likely allow better discrimination of tourmaline from the investigated geological environments.

Acknowledgements

This research project was funded by the Natural Sciences and Engineering Research Council of Canada (NSERC), Agnico Eagle Mines Ltd. (AEM), and the Ministère des Ressources Naturelles et des Forêts du Québec (MRNF).

References

Aitchison J (1986) The statistical analysis of compositional data. Chapman and Hall, London

Caraballo E, Dare S, Beaudoin G (2022) Variation of trace elements in chalcopyrite from worldwide Ni-Cu sulfide and Reef-type PGE deposits: implications for mineral exploration. Mineral Deposita 57:1293-1321

Henry DJ, Novak M, Hawthorne FC, Ertl A, Dutrow BL, Uher P, Pezzotta F (2011) Nomenclature of the tourmaline-supergroup minerals. Am Mineral 96:895-913

Makvandi S, Beaudoin G, McClenaghan MB, Quirt D, Ledru P (2019) PCA of Fe-oxides MLA data as an advanced tool in provenance discrimination and indicator mineral exploration: case study from bedrock and till from the Kiggavik U deposits area (Nunavut, Canada). J Geochem Explor 197:199-211

Makvandi S, Huang X, Beaudoin G, Quirt D, Ledru P, Fayek M (2021) Trace element signatures in hematite and goethite associated with the Kiggavik-Andrew Lake structural trend U deposits (Nunavut, Canada). Mineral Deposita 56:509-535

Palarea-Albaladejo J, Martín-Fernández JA (2015) zCompositions – R package for multivariate imputation of left-censored data under a compositional approach. Chemometr Intell Lab Syst 143:85-96

Paton C, Hellstrom J, Paul B, Woodhead J, Hergt J (2011) Iolite: Freeware for the visualisation and processing of mass spectrometric data. J Anal At Spectrom 26:2508-2518

Sciuba M, Beaudoin G, Makvandi S (2021) Chemical composition of tourmaline in orogenic gold deposits. Mineral Deposita 56:537-560

Slack JF (1996) Tourmaline associations with hydrothermal ore deposits. In: Grew ES, Anovitz LM (eds) Boron: mineralogy, petrology and geochemistry. Rev mineral, vol 33, pp 559-643

Slack JF, Trumbull RB (2011) Tourmaline as a recorder of ore-forming processes. Elements 7 321-326

Trumbull RB, Codeço MS, Jiang S-Y, Palmer MR, Slack JF (2020) Boron isotope variations in tourmaline from hydrothermal ore deposits: a review of controlling factors and insights for mineralizing systems. Ore Geol Rev 125:103682

van Hinsberg VJ, Henry DJ, Dutrow BL (2011) Tourmaline as a petrologic forensic mineral: a unique recorder of its geologic past. Elements 7: 327-332

17th Biennial SGA Meeting

ETH Zurich, Switzerland

August 28 – September 1